

Advanced biomaterials and 3D printing technologies in bone repair

Edited by

Yanjin Lu, Chunguang Yang, Yujing Liu, Guogang Ren
and Changhui Song

Published in

Frontiers in Bioengineering and Biotechnology
Frontiers in Materials



FRONTIERS EBOOK COPYRIGHT STATEMENT

The copyright in the text of individual articles in this ebook is the property of their respective authors or their respective institutions or funders. The copyright in graphics and images within each article may be subject to copyright of other parties. In both cases this is subject to a license granted to Frontiers.

The compilation of articles constituting this ebook is the property of Frontiers.

Each article within this ebook, and the ebook itself, are published under the most recent version of the Creative Commons CC-BY licence. The version current at the date of publication of this ebook is CC-BY 4.0. If the CC-BY licence is updated, the licence granted by Frontiers is automatically updated to the new version.

When exercising any right under the CC-BY licence, Frontiers must be attributed as the original publisher of the article or ebook, as applicable.

Authors have the responsibility of ensuring that any graphics or other materials which are the property of others may be included in the CC-BY licence, but this should be checked before relying on the CC-BY licence to reproduce those materials. Any copyright notices relating to those materials must be complied with.

Copyright and source acknowledgement notices may not be removed and must be displayed in any copy, derivative work or partial copy which includes the elements in question.

All copyright, and all rights therein, are protected by national and international copyright laws. The above represents a summary only. For further information please read Frontiers' Conditions for Website Use and Copyright Statement, and the applicable CC-BY licence.

ISSN 1664-8714
ISBN 978-2-8325-4272-9
DOI 10.3389/978-2-8325-4272-9

About Frontiers

Frontiers is more than just an open access publisher of scholarly articles: it is a pioneering approach to the world of academia, radically improving the way scholarly research is managed. The grand vision of Frontiers is a world where all people have an equal opportunity to seek, share and generate knowledge. Frontiers provides immediate and permanent online open access to all its publications, but this alone is not enough to realize our grand goals.

Frontiers journal series

The Frontiers journal series is a multi-tier and interdisciplinary set of open-access, online journals, promising a paradigm shift from the current review, selection and dissemination processes in academic publishing. All Frontiers journals are driven by researchers for researchers; therefore, they constitute a service to the scholarly community. At the same time, the *Frontiers journal series* operates on a revolutionary invention, the tiered publishing system, initially addressing specific communities of scholars, and gradually climbing up to broader public understanding, thus serving the interests of the lay society, too.

Dedication to quality

Each Frontiers article is a landmark of the highest quality, thanks to genuinely collaborative interactions between authors and review editors, who include some of the world's best academicians. Research must be certified by peers before entering a stream of knowledge that may eventually reach the public - and shape society; therefore, Frontiers only applies the most rigorous and unbiased reviews. Frontiers revolutionizes research publishing by freely delivering the most outstanding research, evaluated with no bias from both the academic and social point of view. By applying the most advanced information technologies, Frontiers is catapulting scholarly publishing into a new generation.

What are Frontiers Research Topics?

Frontiers Research Topics are very popular trademarks of the *Frontiers journals series*: they are collections of at least ten articles, all centered on a particular subject. With their unique mix of varied contributions from Original Research to Review Articles, Frontiers Research Topics unify the most influential researchers, the latest key findings and historical advances in a hot research area.

Find out more on how to host your own Frontiers Research Topic or contribute to one as an author by contacting the Frontiers editorial office: frontiersin.org/about/contact

Advanced biomaterials and 3D printing technologies in bone repair

Topic editors

Yanjin Lu — Fujian Institute of Research on the Structure of Matter, Chinese Academy of Sciences (CAS), China

Chunguang Yang — Institute of Metal Research, Chinese Academy of Sciences (CAS), China

Yujing Liu — Changsha University of Science and Technology, China

Guogang Ren — University of Hertfordshire, United Kingdom

Changhui Song — South China University of Technology, China

Citation

Lu, Y., Yang, C., Liu, Y., Ren, G., Song, C., eds. (2024). *Advanced biomaterials and 3D printing technologies in bone repair*. Lausanne: Frontiers Media SA.
doi: 10.3389/978-2-8325-4272-9

Table of contents

- 06 **3D printing polylactic acid polymer-bioactive glass loaded with bone cement for bone defect in weight-bearing area**
Yurun Ding, Xiaolin Liu, Jue Zhang, Zhuocheng Lv, Xiangchao Meng, Zhiguo Yuan, Teng Long and You Wang
- 23 **Effect of laser scanning speed on microstructure and mechanical properties of SLM porous Ti-5Al-5V-5Mo-3Cr-1Fe alloy**
Wei Yuan, Xiaoli Zhao, Shujun Li and Yue Zhu
- 33 **A TMPS-designed personalized mandibular scaffolds with optimized SLA parameters and mechanical properties**
Xiaoxiao Zheng, Feng Duan, Zhenyu Song, Hongbing Mo, Zhehao Li, Yihan Song, Yucheng Su and Xinyu Wang
- 48 **Advances in the superhydrophilicity-modified titanium surfaces with antibacterial and pro-osteogenesis properties: A review**
Hanyu Shao, Mingchen Ma, Qiang Wang, Tingting Yan, Baohong Zhao, Shu Guo and Shuang Tong
- 64 **Progress in partially degradable titanium-magnesium composites used as biomedical implants**
Jianping Wang, Zhifan Bao, Chenliang Wu, Song Zhang, Ningwei Wang, Qiang Wang and Zhe Yi
- 79 **Digital chain for pelvic tumor resection with 3D-printed surgical cutting guides**
Vincent Biscaccianti, Henri Fragnaud, Jean-Yves Hascoët, Vincent Crenn and Luciano Vidal
- 92 **Case Report: Three-dimensional printed prosthesis reconstruction for patello-femoral large osteochondral defects in a patient with distal femoral giant cell tumour: A case report**
Dechao Yuan, Xiang Fang, Senlin Lei, Nishant Banskota, Fuguo Kuang, Yawei Gou, Wenli Zhang and Hong Duan
- 99 **Femtosecond laser treatment promotes the surface bioactivity and bone ingrowth of Ti₆Al₄V bone scaffolds**
Su Wang, Miao Zhang, Linlin Liu, Rongwei Xu, Zhili Huang, Zhang'ao Shi, Juncai Liu, Zhong Li, Xiaohong Li, Peng Hao and Yongqiang Hao
- 110 **Engineered electrospun poly(lactic-co-glycolic acid)/Si₃N₄ nanofiber scaffold promotes osteogenesis of mesenchymal stem cell**
Changsong Zhou, Shenghui Su, Jiwen Fan, Jiuzao Lin and Xiaoyong Wang
- 119 **Comparison of degradation behavior and osseointegration of 3D powder-printed calcium magnesium phosphate cement scaffolds with alkaline or acid post-treatment**
Katharina Kowalewicz, Anja-Christina Waselau, Franziska Feichtner, Anna-Maria Schmitt, Manuel Brückner, Elke Vorndran and Andrea Meyer-Lindenberg

- 144 **Biological properties of Cu-bearing and Ag-bearing titanium-based alloys and their surface modifications: A review of antibacterial aspect**
Yidan Ma, Jiao Yan, Tingting Yan, Qiang Wang, Zhifan Bao and Zhe Yi
- 164 **NiFe₂O₄/ZnO-coated Poly(L-Lactide) nanofibrous scaffold enhances osteogenic differentiation of human mesenchymal stem cells**
Shiva Shariati, Ehsan Seyedjafari, Fatemeh Sadat Mahdavi, Amirhosein Maali and Elaheh Ferdosi-Shahandashti
- 180 **Definition, measurement, and function of pore structure dimensions of bioengineered porous bone tissue materials based on additive manufacturing: A review**
Wen Peng, Yami Liu and Cheng Wang
- 196 **Three-dimensional-printed porous prosthesis for the joint-sparing reconstruction of the proximal humeral tumorous defect**
Yuqi Zhang, Minxun Lu, Xin Hu, Zhuangzhuang Li, Jie Wang, Taojun Gong, Yong Zhou, Li Luo, Li Min and Chongqi Tu
- 205 **Influence of porosity on osteogenesis, bone growth and osteointegration in trabecular tantalum scaffolds fabricated by additive manufacturing**
Juyang Jiao, Qimin Hong, Dachen Zhang, Mingqi Wang, Haozheng Tang, Jingzhou Yang, Xinhua Qu and Bing Yue
- 221 **Cu-loaded polyurethane to reduce ureteral stent microbes adherence and regulation of the inflammation response to RAW264.7**
Hongwei Li, Jing Zhao, Zhenyu Wang, Jiyuan Hu, Jinlong Zhao, Bukola O. Awonusi, Jianzhong Li and Lianhui Fan
- 233 **Biocompatibility and osseointegration properties of a novel high strength and low modulus β - Ti10Mo6Zr4Sn3Nb alloy**
Jiantao Liu, Kao Wang, Xingyuan Li, Xiwei Zhang, Xi Gong, Yihan Zhu, Zhiwei Ren, Bin Zhang and Jun Cheng
- 247 **Preparation of fish decalcified bone matrix and its bone repair effect in rats**
Zichao Liu, Xiaorui Jiang, Kai Wang, Yongshun Zhou, Tingting Li, Jianfeng Gao and Lei Wang
- 262 **Study on the influence of scaffold morphology and structure on osteogenic performance**
Jingyu Zhou, Shilang Xiong, Min Liu, Hao Yang, Peng Wei, Feng Yi, Min Ouyang, Hanrui Xi, Zhisheng Long, Yayun Liu, Jingtang Li, Linghua Ding and Long Xiong
- 276 **A novel three dimensional-printed biomechanically evaluated patient-specific sacral implant in spinopelvic reconstruction after total *en bloc* sacrectomy**
Zhaorui Lv, Jianmin Li, Zhiping Yang, Xin Li, Qiang Yang and Zhenfeng Li

- 285 **Mussel-inspired HA@TA-CS/SA biomimetic 3D printed scaffolds with antibacterial activity for bone repair**
Cheng Ji, Chengcheng Zhang, Zeya Xu, Yan Chen, Yanming Gan, Minghui Zhou, Lan Li, Qinying Duan, Tingting Huang and Jinxin Lin
- 302 **A comparative study of Sr-loaded nano-textured Ti and TiO₂ nanotube implants on osseointegration immediately after tooth extraction in Beagle dogs**
Yongfeng Li, Li Tang, Mingming Shen, Zhen Wang and Xiaofeng Huang
- 311 **3D printed hybrid scaffolds for bone regeneration using calcium methoxyethoxide as a calcium source**
Agathe Heyraud, Francesca Tallia, David Sory, Hung-Kai Ting, Anna Tchorzewska, Jingwen Liu, Hannah L. Pilsworth, Peter D. Lee, John V. Hanna, Sara M. Rankin and Julian R. Jones



OPEN ACCESS

EDITED BY
Chunguang Yang,
Institute of Metal Research, (CAS), China

REVIEWED BY
Liqun Yang,
China Medical University, China
Farnaz Ghorbani,
University of Erlangen Nuremberg,
Germany
Peng Wan,
Dongguan University of Technology,
China

*CORRESPONDENCE
You Wang,
drwangyou@163.com

[†]These authors have contributed equally
to this work and share first authorship

SPECIALTY SECTION
This article was submitted to
Biomaterials,
a section of the journal
Frontiers in Bioengineering and
Biotechnology

RECEIVED 18 May 2022
ACCEPTED 27 June 2022
PUBLISHED 25 July 2022

CITATION
Ding Y, Liu X, Zhang J, Lv Z, Meng X,
Yuan Z, Long T and Wang Y (2022), 3D
printing polylactic acid polymer-
bioactive glass loaded with bone
cement for bone defect in weight-
bearing area.
Front. Bioeng. Biotechnol. 10:947521.
doi: 10.3389/fbioe.2022.947521

COPYRIGHT
© 2022 Ding, Liu, Zhang, Lv, Meng,
Yuan, Long and Wang. This is an open-
access article distributed under the
terms of the [Creative Commons
Attribution License \(CC BY\)](#). The use,
distribution or reproduction in other
forums is permitted, provided the
original author(s) and the copyright
owner(s) are credited and that the
original publication in this journal is
cited, in accordance with accepted
academic practice. No use, distribution
or reproduction is permitted which does
not comply with these terms.

3D printing polylactic acid polymer-bioactive glass loaded with bone cement for bone defect in weight-bearing area

Yurun Ding^{*†}, Xiaolin Liu[†], Jue Zhang, Zhuocheng Lv,
Xiangchao Meng, Zhiguo Yuan, Teng Long and You Wang^{*}

Department of Bone and Joint Surgery, Renji Hospital, School of Medicine, Shanghai Jiaotong University, Shanghai, China

The treatment of bone defects in weight-bearing areas is mainly to transplant filling materials into the defect area, to provide immediate and strong support for weight-bearing. At present, the commonly used filling material is bone cement, which can only provide physical support without bone regeneration effect. The long-term stress at the interface may cause the loosening of bone cement. The ideal filling material should provide not only strong mechanical support but also promote bone regeneration. We introduce a 3D printing frame-filling structure in this study. The structure was printed with polylactic acid/bioactive glass as the frame, and bone cement as the filler. In this system, bone cement was used to provide immediate fixation, and the frame provided long-term fixation by promoting osteogenic induction and conduction between the interface. The results showed that the degradation of bioactive glass in the frame promoted osteogenic metabolism, induced M2 polarization of macrophages, and inhibited local inflammatory response. The *in vivo* study revealed that implantation of the frame-filling structure significantly promoted bone regeneration in the femoral bone defect area of New Zealand white rabbits. For a bone defect in a weight-bearing area, long-term stability could be obtained by bone integration through this frame-filling structure.

KEYWORDS

bone cement, bioactive glass, 3D printing, bone regeneration, polylactic acid

1 Introduction

Bone defect in the weight-bearing area is difficult to treat clinically. The treatment requires providing instant and stable support for the defect site, which can enable the affected limb to carry out the weight-bearing exercise as soon as possible. Currently, the main treatment is to place filling materials at the defect site to provide mechanical support for the weight-bearing area (Stahl and Yang, 2021). These materials include autologous bone, allogeneic bone, and bone cement. Polymethylmethacrylate (PMMA) is commonly applied to bone cement clinically, which is used to fill local bone defects such as joint replacement and percutaneous vertebroplasty (Laende et al., 2021; Prost et al., 2021).

PMMA has high mechanical strength after curing and can provide sufficient initial mechanical support. However, due to its inert characteristic, PMMA is not easy to degrade and does not have bone regeneration bioactivity. After filling the bone defect in the weight-bearing area with bone cement alone, long-term weight-bearing may produce fatigue damage to bone cement, resulting in the failure of fixation.

For a bone defect in the weight-bearing area, the ideal treatment needs to restore weight-bearing function immediately, and more importantly, to promote new bone formation effectively for long-term biological stability. The filling material needs to provide strong initial mechanical support and show degradability and bone regeneration ability. Moreover, the filling material should display plasticity to meet the morphological diversity of bone defects. Some studies modified bone cement by adding bioactive agents, such as calcium, phosphorus, or bone morphogenesis protein, in order to increase bone induction activity (Castro-Raucci et al., 2018; Ruskin et al., 2020). However, the mixture reduced the compressive strength of bone cement and could not meet the initial stable fixation of bone defects in the weight-bearing area. Moreover, the active components were wrapped in bone cement and could not effectively exert their bioactivity.

Poly(lactic acid) (PLA) is a polyester polymer material polymerized with lactic acid as the main raw material, which has good biocompatibility and degradability. PLA has been widely used in clinics, such as absorbable anchors for ligament or meniscus fixation, absorbable sutures, vascular stents, and other implant materials (Matsuki et al., 2018; Singhvi et al., 2019; Zhang et al., 2019). PLA has a low melting point and good plasticity. However, the disadvantage of PLA is its low biological activity, which needs to be modified to improve its performance. Bioactive glass (BG) is a silicate glass composed of SiO_2 , Na_2O , CaO , and P_2O_5 . It has good biocompatibility, bioactivity, and degradability. The trace elements released during the degradation, such as calcium, silicon, phosphorus, magnesium, and strontium, can exchange ions with body fluids, form a hydroxyapatite (HA) layer similar to the natural bone on the material surface, and then form a solid chemical bond with the adjacent bone surface, which can promote the formation of new bone. In addition, silicon and calcium released by BG can up-regulate osteoblast activity at the gene level to promote osteogenesis (El-Rashidy et al., 2017; Zheng et al., 2021). However, BG itself lacks reliable plasticity and low mechanical strength, which is difficult to meet the biomechanical requirements of bone defects in weight-bearing areas.

According to the requirements of mechanical support and bone induction for bone defects in weight-bearing areas, we designed a frame-filling structure with PLA, BG, and bone cement. We blended PLA with BG nanomicrospheres, and then constructed a PLA-BG framework structure by 3D printing additive manufacturing technology. 3D printing technology can prepare scaffolds

according to the shape of bone defects, and the preparation process does not change the physical and chemical properties of the raw materials. The frame structure not only has the plasticity of PLA but also has the bone-induced bioactivity of BG. The degradability of the frame structure provides space for bone growth. PMMA bone cement, as the filler of the frame-filling structure, ensures the initial mechanical requirements for the bone defect in the load-bearing area.

2 Materials and methods

2.1 Fabrication of 3D-printed scaffold using PLA-BG filaments

PLA-BG filaments (diameter: 400 μm) were prepared according to a previous study (Distler et al., 2020). Composite filaments were produced using PLA as the bulk matrix material and BG as a filler. 45S5 BG (composition: 45 wt% SiO_2 –24.5 wt% CaO –24.5 wt% Na_2O –6 wt% P_2O_5 , d50 (4.0 ± 1.0) μm , d95: $\leq 20\mu\text{m}$, Schott VitryxxR, Schott AG, Germany) was used. A PLA powder was selected (PLA RXP 7503, Resinex GmbH, Germany).

Cubical scaffolds (length: 10 mm, width: 10 mm, height: 1 mm) were designed with an interconnected porosity and pore diameter of 400 μm using computer-aided design software solid edge (Siemens AG, Germany) and the browser-based CAD tool, Tinkercad (Autodesk Inc., United States). PLA-BG filaments with 1 and 5% (wt) BG content were fed into a fused deposition modeling (FDM) 3D printer (Ultimaker S5 Premium, Ultimaker B.V., Netherlands), and scaffolds were produced.

2.2 Characterization of PLA-BG with different concentrations of BG

The composite scaffold PLA-BG containing 1% and 5% BG was prepared by the aforementioned method. The samples were divided into 3 groups: PLA group (PLA scaffold), 1% PBG group (PLA +1% BG composite scaffold), and 5% PBG group (PLA +5% BG composite scaffold).

2.2.1 Scanning electron microscopy

The scaffolds were frozen in liquid nitrogen and fractured with a scalpel to expose the interior. The scaffolds were examined from the top. Scaffolds were sputter-coated with gold for 40 s and imaged (SEM, 15 kV, Hitachi s-4800).

The formation of bone-like phosphorite on the surface was also observed by SEM. Briefly, the samples were immersed in SBF solution for 3 days, then frozen in liquid nitrogen and fractured with a scalpel to expose the interior. Scaffolds were sputter-coated with gold for the 40s and imaged (SEM, 15kV, Hitachi s-4800).

2.2.2 Fourier transform infrared spectrometer

The chemistry of the scaffolds was measured by FTIR (Nicolet Magna 550, Thermo-Nicolet, Madison, WI). Spectra were recorded in the ATR (attenuated total internal reflectance) mode using a Split Pea accessory (Harrick Scientific Corp., Ossining, NY) featuring a 200- μm Si internal reflection element. All the scans were recorded at a resolution of 4 cm^{-1} . OMNIC software (Nicolet) was used for data acquisition and spectrum processing.

2.2.3 X-ray photoelectron spectrometer

The surface elemental composition of the scaffolds was assessed using XPS (Eden Prairie, MN). The photoelectrons emitted from the surface of the samples under X-ray excitation were collected at a take-off angle of 45° and were analyzed with a hemispheric electron energy analyzer operating at a pass energy of 187.9 eV. During the analysis, the base chamber pressure was in the order of 1,010 Torr.

2.2.4 Inductively coupled plasma mass spectrometer

The samples were soaked in the buffer solution (PBS) at the ratio of 0.1 g/ml, and placed on the shaking table at 37 °C for 1, 3, and 7 days. 0.5 ml of solutions were collected after 1 day, 3 days, and 7 days, and kept in the refrigerator at 4°C. After dilution, the ion concentration of the extracted solution was tested by ICP-MS to obtain the ion concentration of the final leaching solution.

2.3 Biocompatibility of PLA-BG *in vitro*

2.3.1 Cell culture

SD rats from the laboratory animal research center of Renji Hospital Affiliated with Shanghai Jiaotong University School of Medicine were used in this study. The experimental protocol was approved by the Animal Ethical Committee of Renji Hospital Affiliated with Shanghai Jiaotong University School of Medicine. All surgical procedures were performed under general anesthesia with an intraperitoneal injection of 1% pentobarbital.

Bone marrow mesenchymal stem cells (BMSCs) from SD rats were obtained as previously described (Yu et al., 2021). SD rats (age: 2 weeks) were sacrificed by dislocating the cervical spine. Tibias and femurs were immediately dissected under aseptic circumstances. Osteoepiphysis were removed, then marrow tissues were dispersed through repeated flushing. The dispersed tissues were forcefully passed through a 19-gage needle to obtain a single-cell suspension. The cells were cultured in α -MEM (Invitrogen, Carlsbad, CA, United States) supplemented with 10% FBS, 1% penicillin, and streptomycin. The cell suspensions were seeded in 10-cm tissue culturing dishes in a humidified atmosphere containing 5% CO_2 at 37°C. The medium was changed every 2–3 days to remove nonadherent

cells, and adherent cells were passaged until they get confluent. BMSCs were passaged after digestion with 0.25% trypsin/1 mM EDTA. BMSCs at third passage were used for the experiments.

The scaffolds were placed in 48-well tissue-culture polystyrene plates for cell culture experiments. Wells without scaffolds were used as controls. The scaffolds were put into polystyrene 96-well plates (non-tissue culture treated) for cell culture experiments. Scaffolds were sterilized with ethylene oxide (Anderson Products) and degassed for 2 d under a house vacuum.

2.3.2 Immunofluorescence staining of cells

The polarization of macrophages was evaluated by immunofluorescence staining of RAW cells (RAW264.7). PLA, 1%, and 5% BG-PLA extracts were immersed within DMEM respectively for 1d, the leaching solutions were collected. RAW cells were co-cultured with leaching solutions from PLA, 1% and 5% BG-PLA extracts respectively, then fixed with 3.7% formaldehyde (mass/volume in PBS buffer) for 15 min, washed in PBS, and permeabilized with 0.2% by mass Triton X-100 for 5 min. The cells were labeled with iNOS rabbit polyclonal antibody (PA3-030A, ThermoFisher) at 1:250 dilution in 0.1% BSA and incubated for 3 h s at room temperature, and then labeled with goat anti-rabbit IgG secondary antibody, Alexa Fluor 488 conjugate (green, A27034, ThermoFisher) at a dilution of 1:2000 for 45 m at room temperature. The cells were labeled with CD206 polyclonal antibody (ThermoFisher) using a dilution of 1:200 (1 h, 37°C), followed by goat anti-rabbit IgG Alexa Fluor 594 (Red, ThermoFisher). Nuclei were stained with DAPI (Blue, S36938, ThermoFisher).

2.3.3 Confocal microscopy

Confocal microscopy (Nikon A1R) was used to measure cell morphology on PLA, 1% and 5% BG-PLA scaffolds. High-resolution images were captured for nuclei (Blue, DAPI, Beyotime) and actin (Red, 5 $\mu\text{g}/\text{ml}$, FITC-Phalloidin, Cytoskeleton). DAPI staining of nuclei was used to make sure that cell morphology was assessed for single cells. FITC-phalloidin stained actin images were used to assess cell morphology.

2.3.4 Osteogenic differentiation analysis

Osteogenic differentiation of BMSCs was measured by Alkaline Phosphatase (ALP) assay, alizarin red staining, and Sirius red staining.

For ALP assay, PLA, 1%, and 5% BG-PLA extracts were immersed within DMEM respectively for 7 days. Supernatants from each group ($n = 5$) were co-cultured with BMSCs for 7 and 14 days. Cells were extracted into an assay buffer containing 50 mM Tris-HCl, 0.1% Triton-X-100, and 0.9% NaCl (pH 7.6), and the lysate was frozen at -70°C . The lysate samples were thawed, and enzyme activity was analyzed using 0.1 mM

4-p-nitrophenylphosphate as a substrate in an assay buffer containing 0.1 M Tris and 1 mM $MgCl_2$ (pH 10.0, Sigma-Aldrich). After incubation at room temperature for 30 min, the reaction was stopped by the addition of 0.1 M NaOH, and the absorbance was measured at 405 nm with a plate reader (Spectramax plus384, United States). Five parallel samples were measured in triplicate. The protein content was determined by Bio-Rad Protein Assay (Bio-Rad Laboratories) with bovine serum albumin as standard. The specific ALP activity was calculated as absorbance at 405 nm/protein mg/ml. For ALP histochemical staining ($n = 4$), the cells were washed with PBS, fixed with citrate-acetone formaldehyde fixative, washed with deionized water, and stained for enzyme activity with the alkaline solution containing naphthol AS-BI phosphate and fast red violet LB base according to the manufacturer's instruction (alkaline phosphate kit, Sigma-Aldrich).

For alizarin red staining, BMSCs were washed two times with PBS followed by fixation in 96% ethanol for 15 min at room temperature. 1% of Alizarin red solution (Sigma-Aldrich) was added to the fixed cells and incubated for 60 min at room temperature with gentle rotation. Finally, cells were carefully washed three times with PBS and dried. Pictures were taken with an optical microscope (DFC295, Leica) at $\times 20$ magnification.

For Sirius red staining, cells were washed two times with PBS followed by fixation in 96% ethanol for 15 min at room temperature, then incubated in 0.1% Sirius Red solution (Sigma-Aldrich) for 60 min, washing twice in PBS, dehydrating in 100% ethanol, and then clearing in xylene. Pictures were taken with an optical microscope (DFC295, Leica) at $\times 20$ magnification.

2.3.5 Cell viability test

Cell viability was assessed by the CCK-8 test. BMSCs were plated at a density of 5×10^3 cells/well in a 96-well plate in a 0.1 ml culture medium. The cells were cultured for 24 h and then starved for 24 h in a serum-free DMEM medium. Then the cells were co-cultured with supernatants from each group ($n = 5$) for 1, 3, and 7 days at $37^\circ C$. On each day, the culture medium and supernatants were replaced and the cells were counted using CCK-8 (Dojindo, Kyushu Island, Japan). Briefly, 10 μL of the kit reagent was added to each well and the cells were incubated for 2 h. Cell viability was determined by measuring the absorbance at 450 and 655 nm with a microplate reader (Microplate Reader 680; Bio-Rad Laboratories, Hercules, CA, United States). Each experimental condition was analyzed in five wells.

2.3.6 RT-PCR

The difference in osteogenic differentiation ability in gene expression level was examined by quantitative RT-PCR. After BMSCs were co-cultured with leaching solutions from PLA, 1% and 5% BG-PLA extracts respectively, the mRNA expression of OPN, OCN, ALP, and RUNX2 were examined for 3, 7, and 14 days. Total RNA was isolated using TRIzol reagent

(Invitrogen), according to the manufacturer's standard instructions. For reverse transcription of mRNA, random-primed cDNA was synthesized from 2 mg of total RNA using a PrimeScript RT reagent kit (TaKaRa, Dalian, China). Real-time PCR was performed using 2 μL of cDNA product in a 25 μL reaction volume with a 7,500 Real-Time PCR System (Applied Biosystems, Singapore). SYBR Premix Ex Taq II (Takara Biotechnology), specific primers, and 2 μL of cDNA were used in each PCR reaction ($95^\circ C$ for 30 s, 40 cycles of denaturation at $94^\circ C$ for 5 s, annealing, and extension at $60^\circ C$ for 30 s). Sense and antisense primers were designed with Primer Express 5.0 based on published cDNA sequences. GAPDH was used as an internal control gene. All real-time PCR reactions were performed in triplicate, and results after calibration with GAPDH expression were calculated using the $\Delta\Delta CT$ method and are presented as fold increase, relative to non-stimulated control.

2.4 Characteristics and biocompatibility of PLA-BG/BC

2.4.1 Preparation of PLA-BG/BC

The silica gel mold was prepared through 3D printing mold pouring. The mold had a hole of 1 cm wide, 1 cm long, and 2 mm high, which was fit for the printing stent. The bone cement was prepared after the printing stent was placed. As soon as the viscosity of BC met the requirements, 100 mg of BC was added to each stent and extruded into the gap structure of the stent. The samples were obtained after drying.

The samples were divided into 4 groups: PLA group (PLA polylactic acid scaffold), PBG group (PLA +1% BG composite scaffold), PLA-BC group (PLA + PMMA bone cement composite scaffold), and PBG-BC group (PLA +1% BG + PMMA bone cement composite scaffold).

2.4.2 Scaffold characteristic test

The micromorphology of the scaffolds was detected by SEM. The chemistry of the scaffolds was measured by FTIR. The surface elemental composition of the scaffolds was assessed using XPS. The degradation of the complex was detected by ICP. The specific methods were mentioned earlier.

PLA, PBG, PLA/BC, and PBG/BC were respectively soaked in Tris HCl for 6 months. PH values and sample weight changes were detected for all the samples each week for 6 months.

2.4.3 Cell experiments of PLA-BG/BC

Cytotoxicity and Cell viability tests were conducted using CCK-8 and MTT assay. Cell morphology was measured by confocal microscopy. The polarization of macrophages was evaluated by immunofluorescence staining of RAW cells. Osteogenic differentiation of BMSCs was measured by ALP assay and RT-PCR. The specific methods were mentioned earlier.

2.5 In vivo experiment

3D printed composite scaffolds were implanted into the femoral tunnel of New Zealand rabbits to detect the short-term and long-term fixation effects of various implants (BC, PLA, PBG, PLA-BC, and PBG-BC). The operation process and animal feeding were carried out in Shanghai Jiagan Biotechnology Co., Ltd., with the approval of its ethics committee. The animal experiment was strictly in accordance with the relevant regulations and provisions on the protection of experimental animals formulated by it.

2.5.1 Surgical procedure and scaffold implantation

Thirty New Zealand white rabbits (aged 8–12 weeks and average weight of 3 kg) were randomly divided into 5 groups (BC group, PLA group, PBG group, PLA-BC group, and PBG-BC group), with 6 rabbits in each group. Each rabbit were implanted a sample scaffold in the femoral trochanter of the right hind limb, and the materials were randomly labeled.

Before surgery, samples (BC, PLA, PBG, PLA-BC, and PBG-BC, 5 mm × 5 mm × 1 mm) were sterilized by γ Radiation. The rabbits were injected with 1% Pentobarbital Sodium (pentobarbital, 80 mg/kg) intravenously. Local disinfection was carried out after skin preparation of the right hind limb. A 1–2 cm longitudinal incision was conducted at the trochanter, exposing the femoral trochanter, and peeling off the periosteum. Using a 1 mm wide bone chisel, a transverse slotting was made at the tuberosity, with a depth of 5–6 mm and the length of 5–6 mm. Then the sample was implanted into the slot so that the lateral edge of the sample was submerged into the femoral trochanter by about 0.5 mm. The wound was closed layer by layer. Penicillin (800000 units/day) was given intravenously 1–3 days after the operation to prevent infection. The rabbits were sacrificed at 4 and 12 weeks after the operation, and the femoral were removed for general observation, then the specimens were fixed with 10% formalin solution for the following analysis.

2.5.2 Micro-CT

The femur samples were photographed by X-ray and then scanned by micro-CT (sky scan 1,076, aartselaar, Belgium). The parameters were 100 kV and 80 μ A. The resolution is 18 μ m. The rotation angle of scanning was set to 360°. The sky scan TM CT analyzer software was used for three-dimensional reconstruction and quantitative analysis. The parameters included: bone volume fraction (BV/TV), bone area volume ratio (BS/BV), number of trabeculae (TB.N), and trabecular thickness (TB.Th).

2.6 Statistical analysis

Data were presented as mean \pm standard deviation (SD). Two-tailed analysis of variance (ANOVA) was used for statistical analysis. The differences were considered significant when $p < 0.05$.

3 Results

3.1 % PLA-BG had better properties and biocompatibility

The scaffolds were successfully prepared by the FDM method (Figure 1). The *in vitro* results showed that 1% BG-PLA had good biocompatibility, and could promote adhesion, proliferation, and differentiation of BMSCs. 1% BG-PLA showed no toxicity, and the degradation environment of which was neutral. Moreover, it could promote the polarization of macrophages toward M2, and inhibit its polarization towards M1, which is conducive to tissue repair. Therefore, 1% BG-PLA was chosen for the next experiments.

3.1.1 Both 1% and 5% PLA-BG had an amorphous structure

XPS and FTIR were performed to identify the characteristics of PLA, 1% and 5% BG-PLA (Figure 2). The results of XPS revealed that the 3 groups showed obvious steamed bread peaks, indicating the amorphous structure prepared by the 3D method. After adding BG, the waveform did not change significantly, because BG is also amorphous material. The results of FTIR showed peaks at 1,650, 1,250, and 1,130 cm^{-1} , which are the characteristic peaks of PLA. After adding BG, there were stretching vibration peaks of Si-O and Si-O-Si around 950 and 1,100 cm^{-1} . While no significant difference was observed between 1% and 5% BG-PLA, which might be due to the small content of BG that participated in the energy reaction of the infrared spectrum.

3.1.2 The surface of PLA-BG was rough and presented some micron granular substances. 5% PLA-BG showed more BG particles on the surface

The surfaces of three different 3D printing scaffolds were observed by SEM (Figure 3). The diameter of the scaffold fiber was 400 microns, and the gap was also 400 microns. Further amplification revealed that the surface of PLA was relatively smooth. After adding BG, the surfaces became rough and presented some micron granular substances, corresponding to the doped BG particles. The amount of BG particles on the scaffold surface with 5% content was significantly more than that with 1% BG content.

3.1.3 Bone-like phosphorite were formed on the surface of PLA-BG. Ion exchange was more intense on the surface of 5% PLA-BG

After the samples were immersed in SBF solution for 3 days, the formation of bone-like phosphorite on the surface was observed by SEM (Figure 4). Barely any changes were found on the surface of PLA, which was still relatively smooth. Mineralized sediments were found on the surface of 1% and

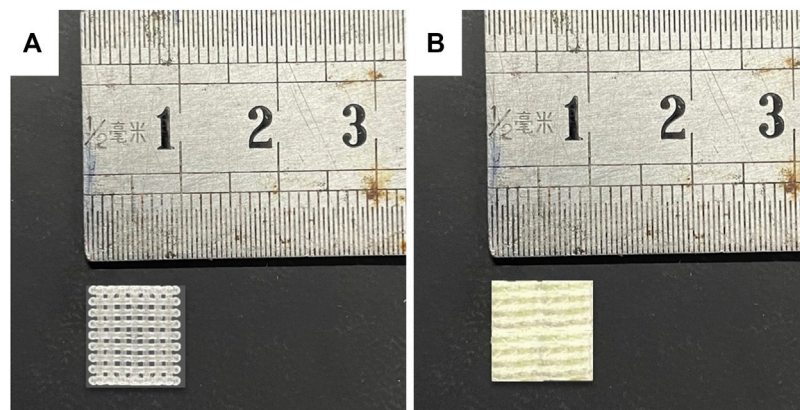


FIGURE 1
Photos of samples. (A) PBG; (B) PBG-BC.

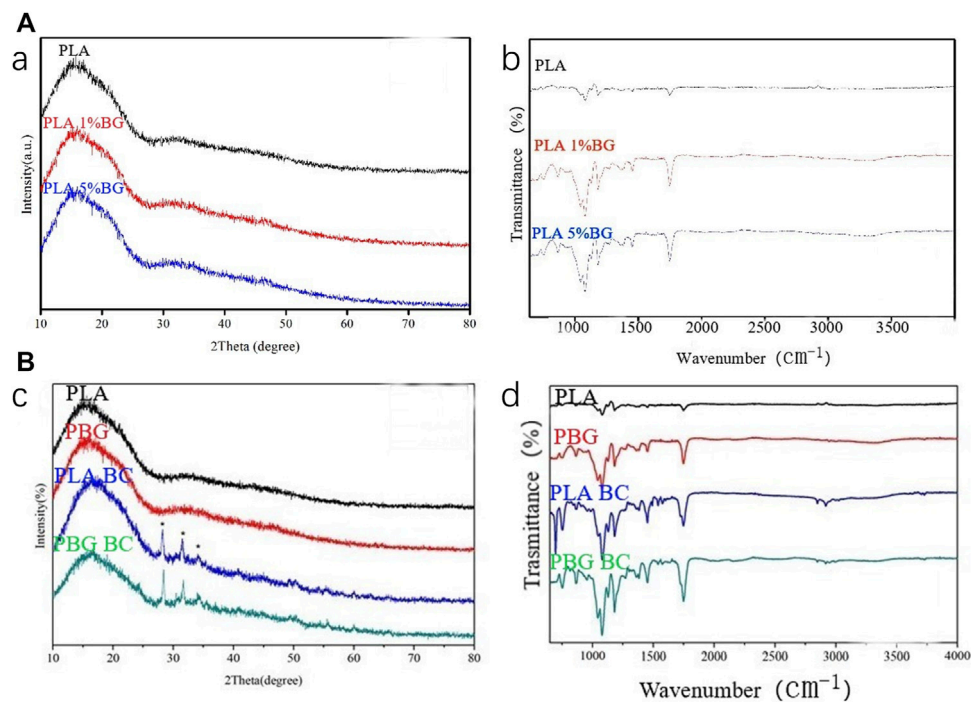
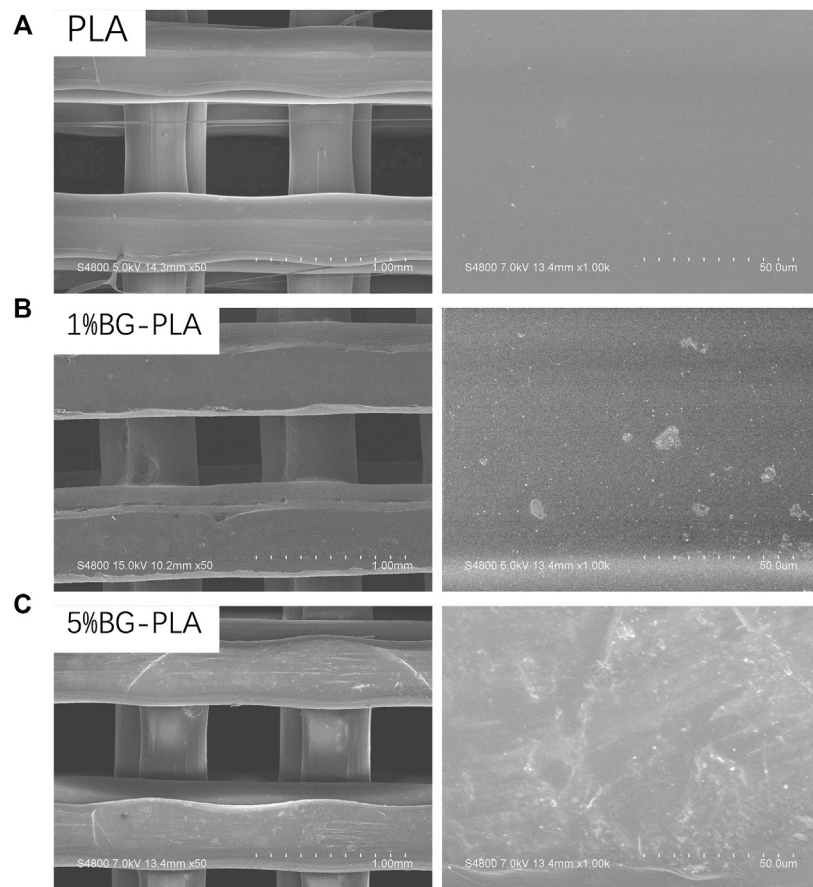


FIGURE 2
(A) XPS and IR spectra of PLA, 1% and 5% BG-PLA; (B) XPS and IR spectra of PLA, PBG, PLA-BC, and PBG-BC.

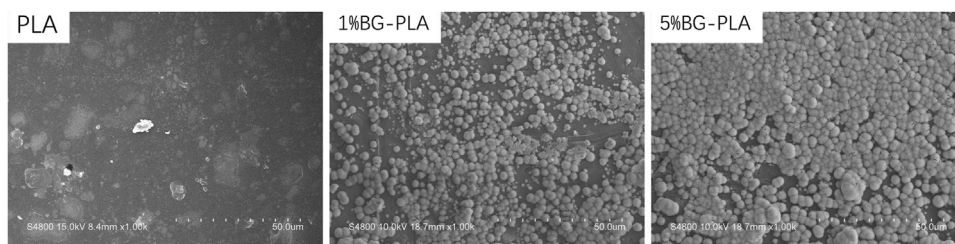
5% BG-PLA samples, which were typically bone-like phosphorite morphology. This might be due to the fact that BG can induce the formation of surface mineralization by ion exchange and silicon hydroxyl. The amount and distribution of bone-like phosphorite on the 1% surface were less than that on the 5% sample surface, indicating that the ion exchange on the 5% sample surface was more intense, and more mineralized deposits were formed.

3.1.4 PLA-BG could promote M2 polarization of macrophages

RT-PCR and immunofluorescence staining were used to evaluate the inducing effect on macrophage polarization of the scaffolds (Figure 5). The results of PCR showed that PLA-BG significantly inhibited the expression of IL-1 and iNOS, while promoting the expression of ARG1 and IL-10. It was

**FIGURE 3**

SEM of scaffolds. (A) PLA; (B) PLA with 1% BG (1%BG-PLA); (C) PLA with 5% BG (5% BG-PLA).

**FIGURE 4**

SEM of PLA, 1% and 5% BG-PLA after soaking in SBF solution for 3 days.

suggested that the addition of BG was conducive to the M2 polarization of macrophages. For immunofluorescence staining, green fluorescence represented iNOS and red fluorescence was CD206. The results showed that the degradation or dissolution products of PLA were conducive to the polarization of macrophages towards M1. While after BG was added, the dissolution or degradation

products were conducive to the polarization of macrophages in the M2 direction.

3.1.5 1% PLA-BG showed a better proliferation effect

Cell proliferation was evaluated by the CCK-8 experiment (Figure 6). The results revealed that 1% PLA-BG had a significant

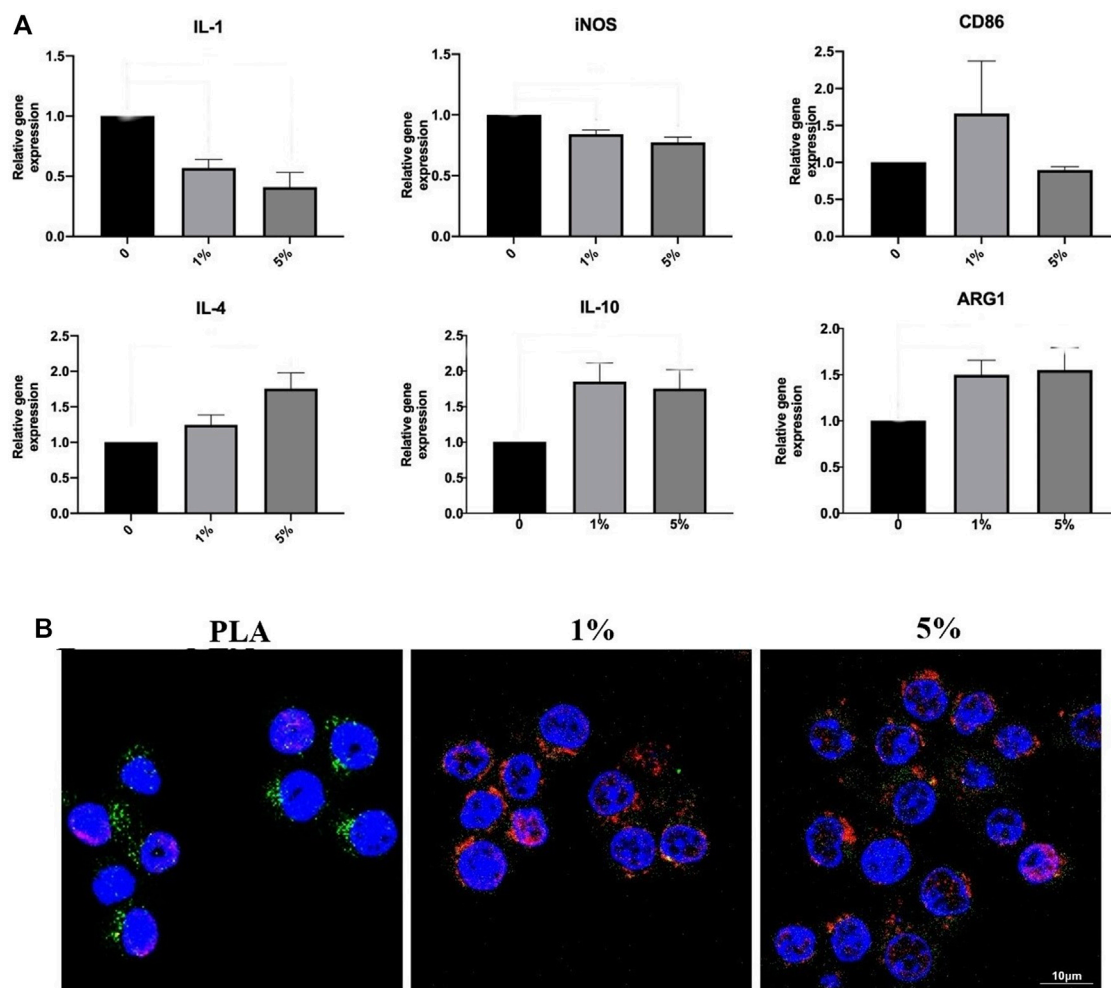


FIGURE 5

Inducing effect on macrophage polarization of cells RAW264 cultured with leaching solutions from PLA, 1% and 5% BG-PLA. (A). RT-PCR; (B) Immunofluorescence.

promoting effect on cell proliferation during full-time period. While 5% BG-PLA did not show a better promoting effect compared with 1% PLA-BG, even the inhibition of cell proliferation was detected relative to PLA at some time points such as 12 h.

3.1.6 1% and 5% PLA-BG both had better adhesion morphology with more pseudopodia

BMSCs were cultured on PLA scaffolds, 1% and 5% BG-PLA scaffolds for 12 or 24 h. Cell adhesion was observed using CLSM (24 h) and SEM (12 h), respectively (Figure 6). After a coculture of 12 h, the cells began to attach to the sample surface, cells on both 5% and 1% BG-PLA scaffolds had more pseudopodia extending out and attached more rapidly. After coculture of 24 h, the cells exhibited typical spindle morphology. Both 1% and 5% BG-PLA had better adhesion morphology with more pseudopodia.

3.1.7 BG-PLA showed osteogenic differentiation ability

The osteogenic activity was evaluated by ALP staining, Alizarin red staining, and Sirius red staining (Figure 7). In 1% and 5% PLA-BG groups, more ALP expression was found by ALP staining, more calcium nodule deposition was found *via* Alizarin red staining, and more collagen formation was found by Sirius red staining. Statistical analysis showed that the positive dyeing areas in 1% and 5% PLA-BG groups were significantly larger than that of the PLA group.

RT-PCR was performed to evaluate the relative expression of osteogenesis-related genes (Figure 7). In 1% and 5% BG-PLA groups, an increased expression of osteoblast markers was shown in comparison to that of the PLA group, indicating that BG induced osteogenic activity.

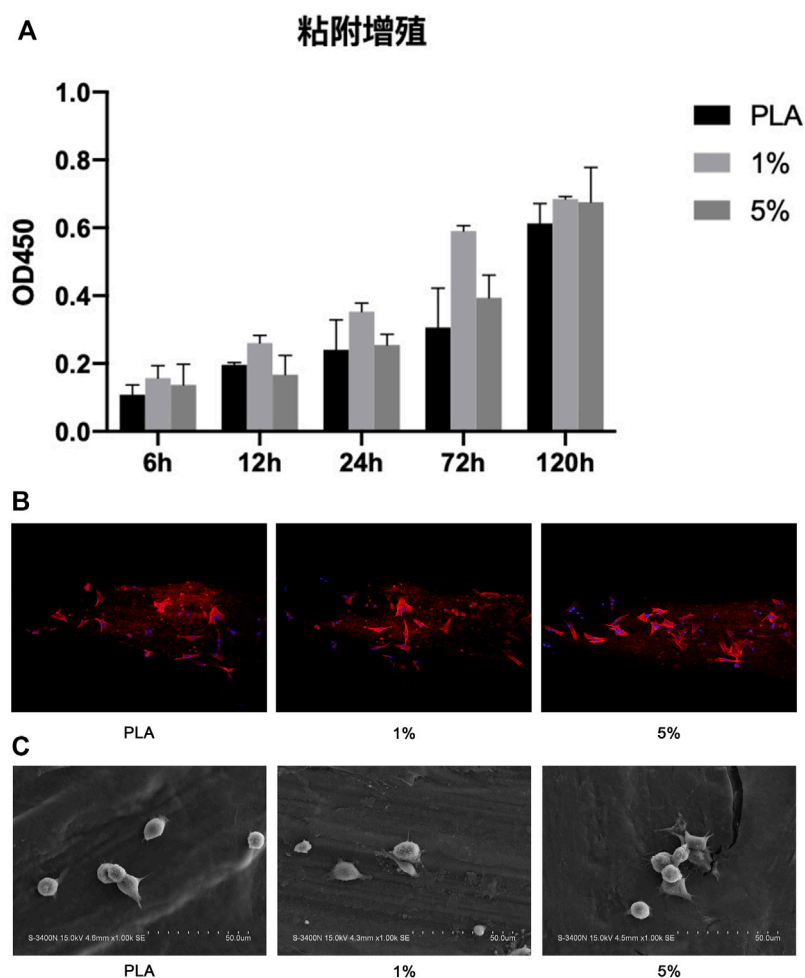


FIGURE 6

Coculture of BMSCs with scaffolds. (A) CCK-8 experiment; (B) 3D CLSM pictures of cells on scaffolds (24 h); (C) SEM images of cells adhered on scaffolds (12 h).

3.2 PBG-BC provided sufficient initial mechanical strength, good biocompatibility, and effective osteogenic induction

The addition of BC provided the initial mechanical strength, without affecting the biocompatibility and osteogenic induction of PBG.

3.2.1 Addition of BC maintained the amorphous structure of PBG

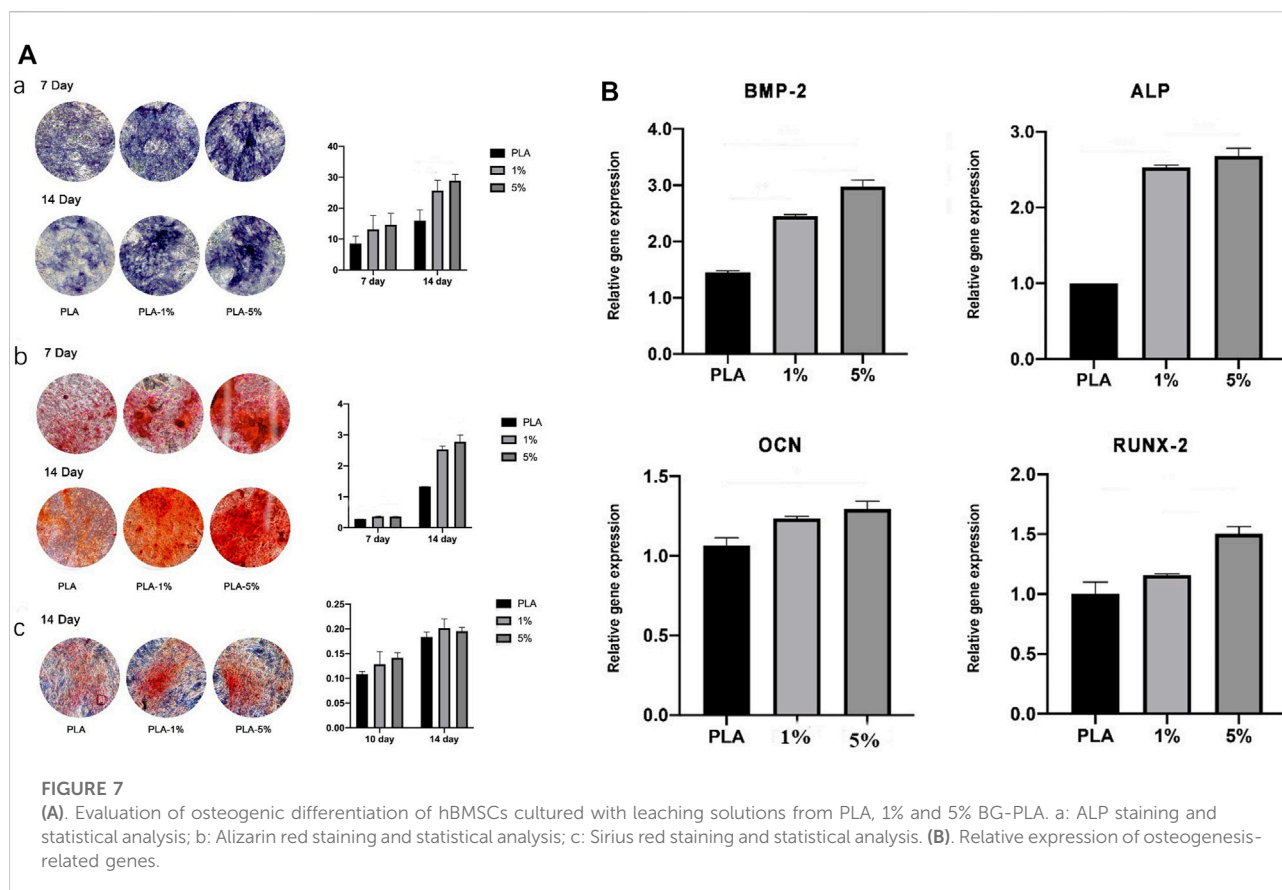
The composition of the PBG-BC surface was analyzed by XPS and FTIR (Figure 2). The characteristic peak of PBG and PMMA was found after BC was filled into PBG, indicating the completion of composite scaffolds containing PMMA and changes in the characteristics of the original PBG.

3.2.2 BC was completely filled into the gap of PBG

The surface was observed by SEM and EDS (Figures 8, 9). The surface of PLA was relatively smooth, while BG particles could be observed on the surface of PBG. The results of EDS confirmed the main elements of the skeleton structure of these scaffolds. BC was filled into the gaps of PLA-BC and PBG-BC, and the boundaries were obvious between BC and the composite scaffolds.

3.2.3 Addition of BC did not change the surface properties of PBG

The 3D confocal microscope revealed the surfaces of the scaffolds (Figure 9). The surface roughness was significantly improved after the addition of BC. There was an obvious boundary between the surface of PBG and BC, indicating that BC did not change the original properties of the scaffolds.



3.2.4 PBG-BC showed enough compressive strength

The results of the compressive strength test showed that the compressive strength of PLA and PBG was only about 20 MPa (Figure 10). The values of PLA-BC and PBG-BC reached about 80 MPa, which was similar to that of PBG, indicating that the addition of BC significantly improved the compressive strength of the scaffolds.

3.2.5 The weight and pH of PBG-BC changed slightly during degradation

Samples were soaked in Tris HCl for 24 weeks to analyze the degradation performance (Figure 10). After soaking for 4 and 12 weeks, SEM was performed to observe the surface of the samples. There was no obvious change on the surface of BC, while PLA and PBG were degraded to varying degrees. There were some defects on the surface of PLA, and small holes were observed on the surface of PBG. Similar degradation morphologies were found on the surfaces of PLA-BC and PBG-BC.

After soaking for 24 weeks, the sample weighing results showed that the weight gradually decreased in PLA and PBG groups, while the value changed slightly in PLA-BC and PBG-BC

groups, indicating that the addition of BC influenced the degradation rate of scaffolds. The pH test results showed that the pH values gradually decreased in PLA and PLA-BC groups, while the values were relatively stable in PBG and PBG-BC groups, indicating that the degradation of BG could regulate the pH of the local microenvironment.

3.2.6 BC had little influence on the cell adhesion of PBG-BC.

The morphology and adhesion of BMSCs were observed by SEM and laser confocal microscope (Figure 11). The results of SEM showed that the cells had well-formed pseudopodia on the surface of PLA-BC and PBG-BC similar to that of PLA and PBG. The results of laser confocal microscopy showed that large amounts of cells were attached on the surface of PLA and PBG, except that the cells did not attach on the surface of BC.

3.2.7 BC influenced little on the osteogenic induction ability of PBG

The osteogenic differentiation of BMSCs was evaluated by ALP staining, Alizarin red staining, and Sirius red staining (Figure 12). The results showed that PBG-BC could still induce osteogenic differentiation after adding BC. In the PBG-

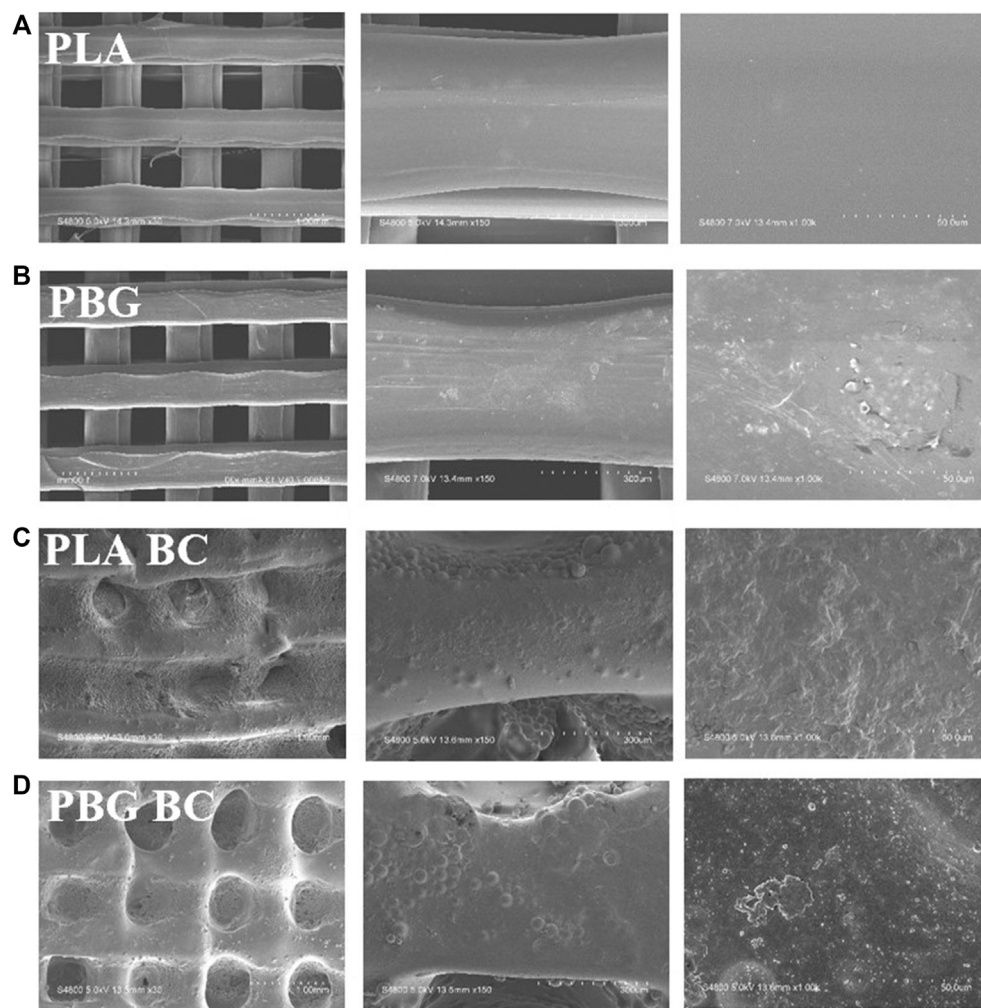


FIGURE 8
SEM of the scaffolds. (A): PLA; (B) PBG; (C) PLA-BC; (D) PBG-BC.

BC group, the staining area of calcium nodules was larger than that of PLA and PLA-BC, but smaller than PBG, indicating that BC affected the osteogenic ability of PBG.

RT-PCR was conducted to detect gene expressions of RUNX2, BMP-2, ALP, and OCN (Figure 12). The results showed that both PBG and PBG-BC significantly enhanced the relative expression of osteogenesis-related genes, and the addition of BC did not influence the promoting effect.

3.2.8 Ca, P, and Si were cumulatively released from both PLA-BG and PBG-BC.

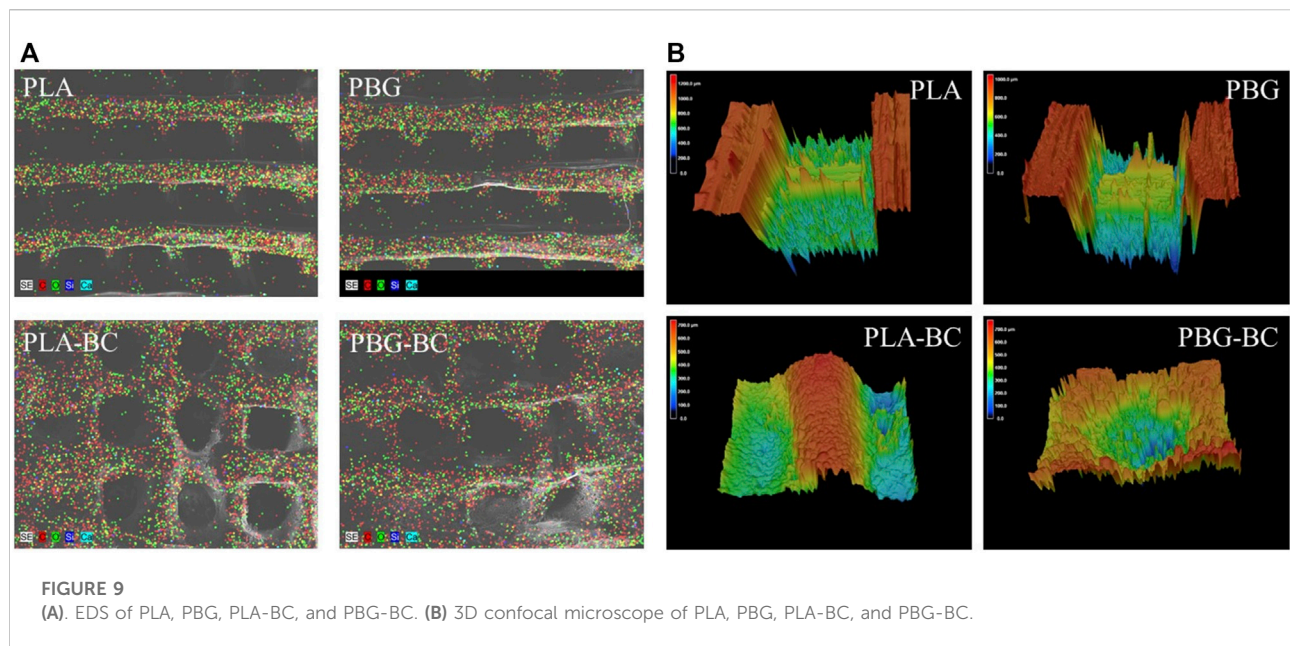
Elemental concentration analysis was conducted to detect releasing profiles of PBG and PBG-BC (Figure 10). Ca, P, and Si was cumulatively released in all the groups, and tended to plateau after 2 weeks. The releasing amounts of ions were higher in PLA-BG groups than that in PBG-BC groups, indicating that BC

influenced ion release. The results also suggested that the concentration of BG also affected the releasing amounts of ions. The higher the concentration of BG, the more ions were released.

3.3 PBG-BC were firmly fixed in the femoral tunnel of New Zealand rabbits and induced new bone formation at the interface

3.3.1 PBG-BC began to induce new bone formation after 4 weeks of implantation

4 weeks after implantation, Micro-CT showed that PLA and PBG were partially degraded and replaced by a small amount of new bone (Figure 13). In PLA-BC and PBG-BC groups, the



implants maintained a good cubic structure. A small amount of new bone was found in the gap, and new bone in the PBG-BC group was more dense. However, a clear boundary between bone and BC could still be seen in BC groups. The measurement of local areas showed that the groups containing BG (PBG and PBG-BC) were superior to pure PLA groups (PLA and PLA-BC) and BC group in terms of BV/TV, BS/TV, TB, Th, TB.N, and BMD (Figure 13). This result further proves that BG can induce osteogenesis and bone integration.

3.3.2 PBG-BC was firmly fixed in the femoral tunnel and induced new bone constantly at the interface 12 weeks after implantation

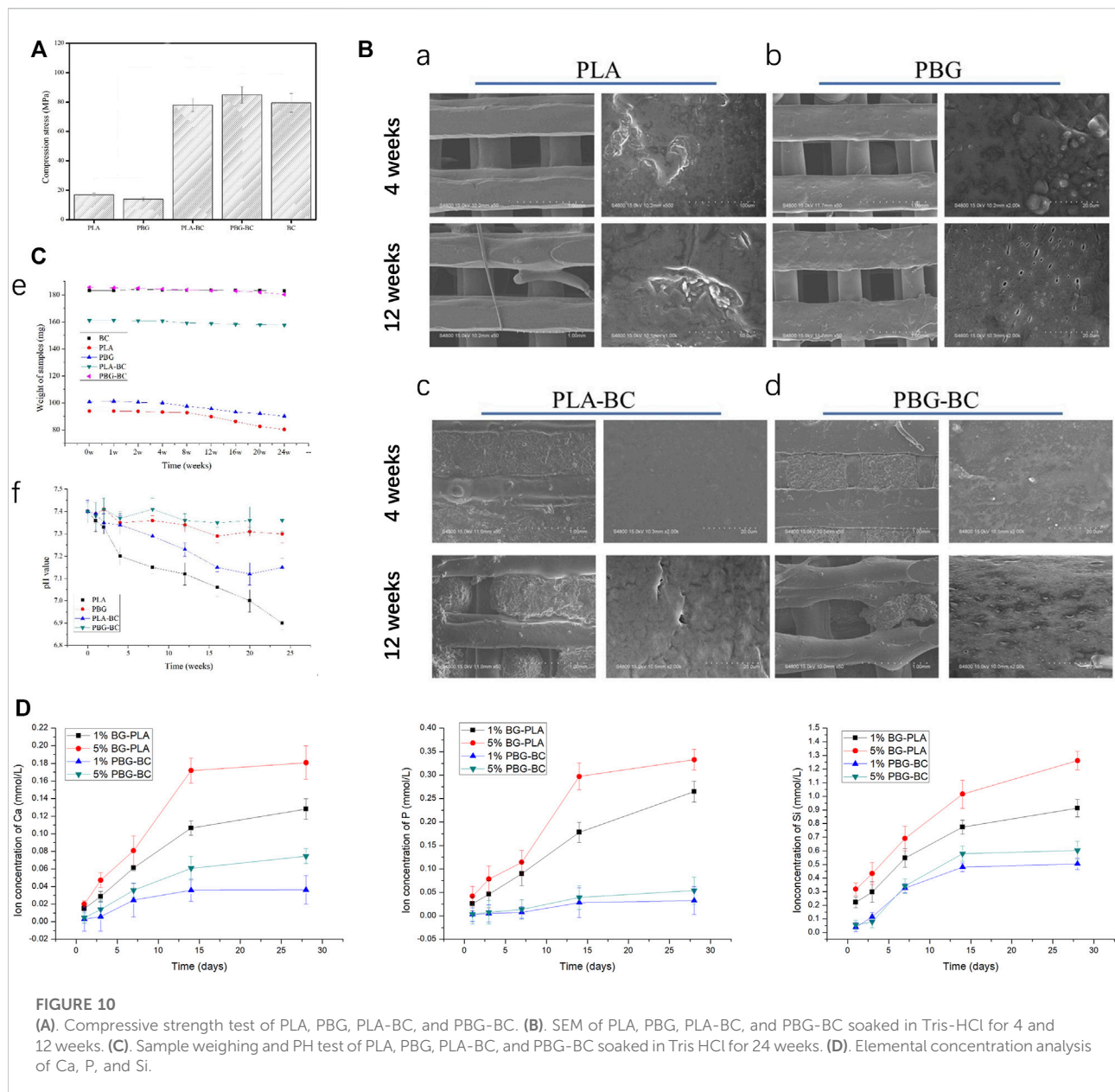
12 weeks after implantation, micro-CT showed that PLA and BG were further degraded, more bone tissues were found in the gap, new bone was more dense in PBG and PBG-BC groups, and PLA-BC and PBG-BC groups still maintained a good cube structure (Figure 14). A clear boundary was still found in the BC group. Local area measurement of BV/TV, BS/TV, TB, Th, TB.N, and BMD showed that PBG was better than PLA, and PBG-BC was better than PLA-BC, indicating that the addition of BG promoted new bone formation (Figure 14). The values also showed that PLA-BC was lower than that of PLA, and PBG-BC was lower than that of PBG, indicating that BC had some impact on new bone formation.

4 Discussion

An ideal filling system for bone defects in the weight-bearing area should provide strong initial mechanical support and bone

regeneration ability. In this study, PLA and BG were prepared as frame structures by 3D printing technology, with PMMA as the filling structure. The composite has sufficient initial mechanical stability. BG can induce ion exchange during degradation, forming a local microenvironment conducive to bone regeneration, which significantly improves the long-term stability of the interface.

The frame structure is composed of PLA and BG. BG is silicate glass with good biocompatibility, degradability, and bioactivity. It is a commonly used bone tissue repair material clinically (Bento et al., 2021; Zheng et al., 2021; Daskalakis et al., 2022). BG has bone inducing effect. When BG is implanted into the body, it can exchange ions with extracellular fluid, and form a HA layer on its surface, to build a solid chemical bond with the bone surface (Daskalakis et al., 2022). In addition, different ions released by BG, such as silicon and calcium, can regulate osteoblast activity, promote extracellular matrix mineralization and accelerate new bone formation (Daskalakis et al., 2022). C Wu found that silicon ions at a certain concentration could stimulate cell proliferation, differentiation, and enhance bone mineralization and metabolism (Wu et al., 2007). P Valerio found that silicon ions could increase the cell viability of osteoblasts (Valerio et al., 2004). However, the mechanical strength of BG is too weak to be used for bone tissue repair alone. To provide mechanical strength, PLA was selected as the loading scaffold for BG. PLA is known as a degradable polymer, the degradation product is nontoxic and has good mechanical properties (Kaseem et al., 2021). The results of the study showed that the composite of the two materials not only improved the mechanical properties and elastic modulus but also met the requirements of bone induction.



The results of the degradation performance test showed that the degradation rate of pure PLA was about 20%, while the degradation rate of PLA-BG rose to 25%, indicating that the addition of BG significantly improved the degradation rate. This phenomenon may result from the interaction of degradation products of PLA and BG. After the degradation of pure PLA, the local internal environment became acidic, which resulted in the decrease in the degradation rate (Vaid et al., 2021). The degradation products of BG are alkaline (Daskalakis et al., 2022), which has an acid-base neutralization effect on the local internal environment, maintains the steady-state of the internal environment, and is conducive to the continuous occurrence of degradation. After adding bone cement, the

degradation rate of PBG-BC decreased significantly to 10%, which may be due to the significant reduction of the direct contact area between the material and the surrounding tissue. The results of the ion releasing test showed that the ion concentration released by PBG-BC was significantly lower than that of PLA-BG. In addition, bone cement itself is of high quality and is barely degradable, which also may affect the degradation rate.

Cell adhesion rate and protein adsorption of the material have a significant impact on cell activity (Li et al., 2021). Pure PLA produced an acidic degradation environment, which was not conducive to cell adhesion and proliferation, so the cell adhesion and proliferation rate were low. It is reported that the

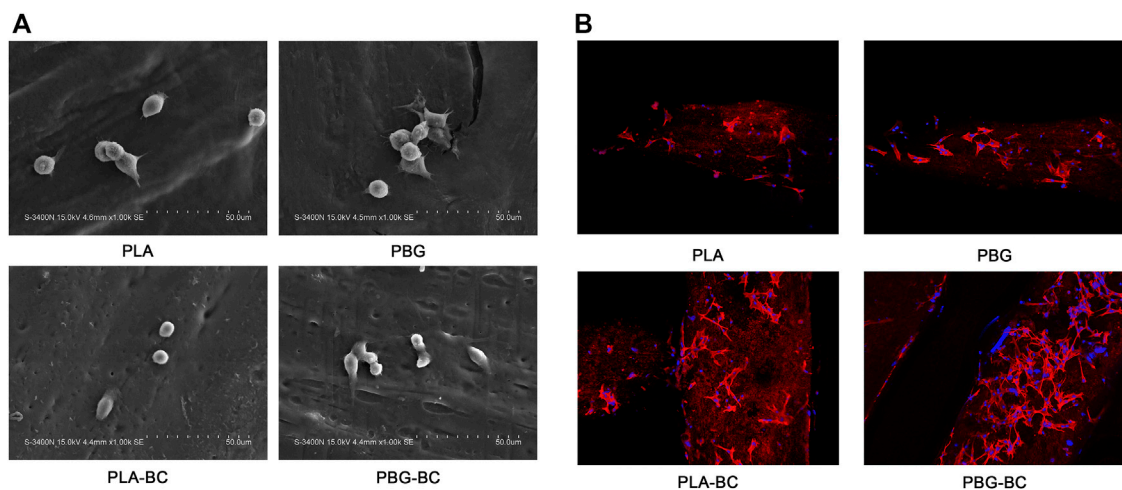


FIGURE 11

(A). SEM of BMSCs cultured on the surface of PLA, PBG, PLA-BC, and PBG-BC. (B). Laser confocal microscope of BMSCs cultured on the surface of PLA, PBG, PLA-BC, and PBG-BC.

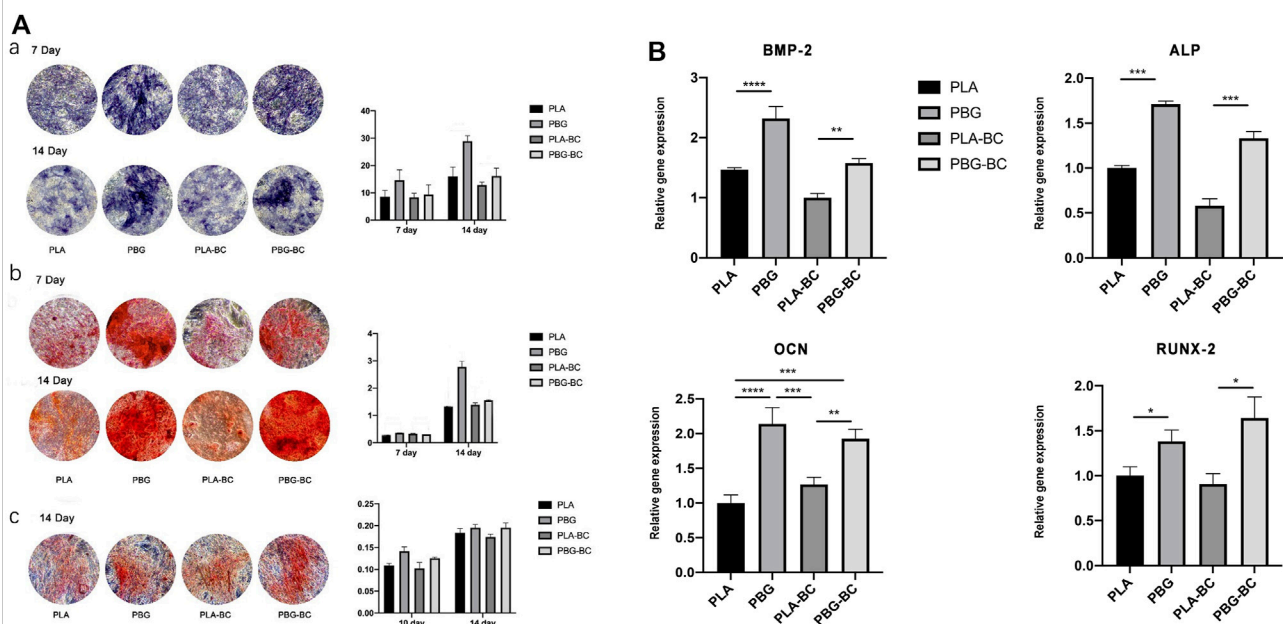
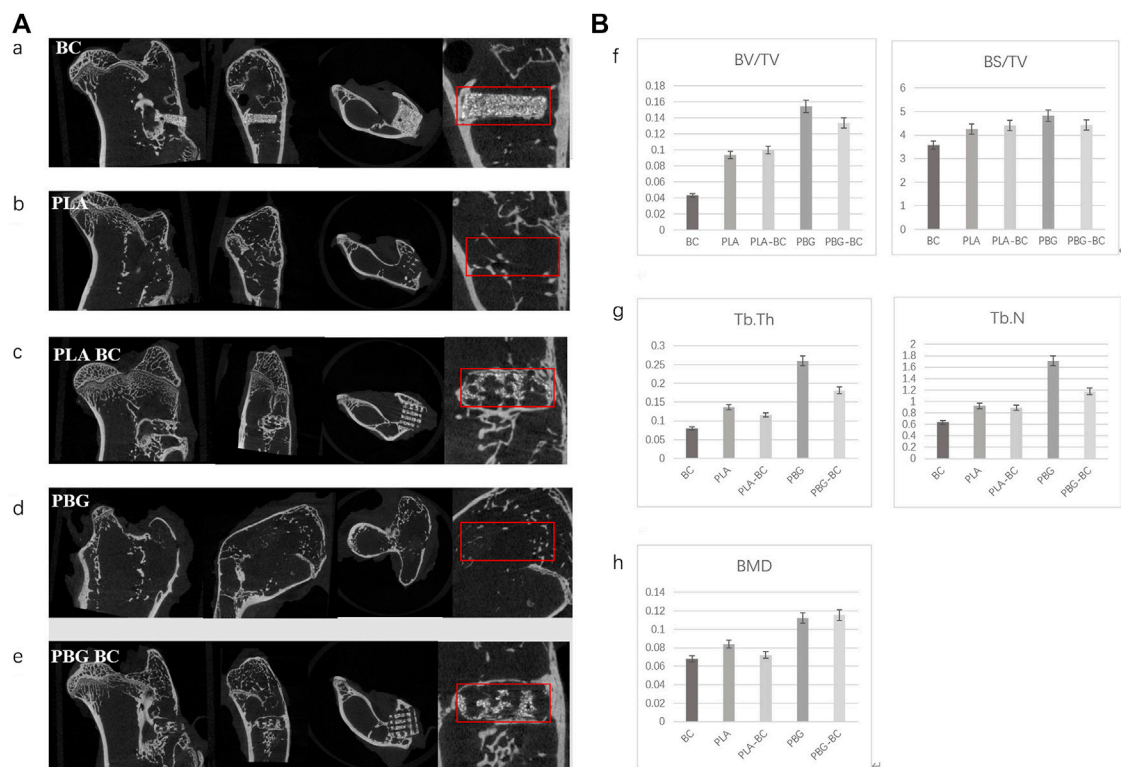


FIGURE 12

(A). Evaluation of osteogenic differentiation of hBMSCs cultured with leaching solutions from PLA, PBG, PLA-BC, and PBG-BC. a: ALP staining and statistical analysis; b: Alizarin red staining and statistical analysis; c: Sirius red staining and statistical analysis. (B). Relative expression of osteogenesis-related genes.

pure BG powders usually resulted in a high pH value in the implanted site (Zhu et al., 2020). In our study, the combination of BG and PLA made the pH value stable within the normal physiological range, and the cell adhesion and proliferation rate were significantly higher than that of pure PLA. BG

degradation products such as Ca, P, and Si are also conducive to cell proliferation and adhesion (Daskalakis et al., 2022). As for the filling structure in the system, bone cement is bioinert material, the addition of bone cement has little impact on the local environment and cell activity.

**FIGURE 13**

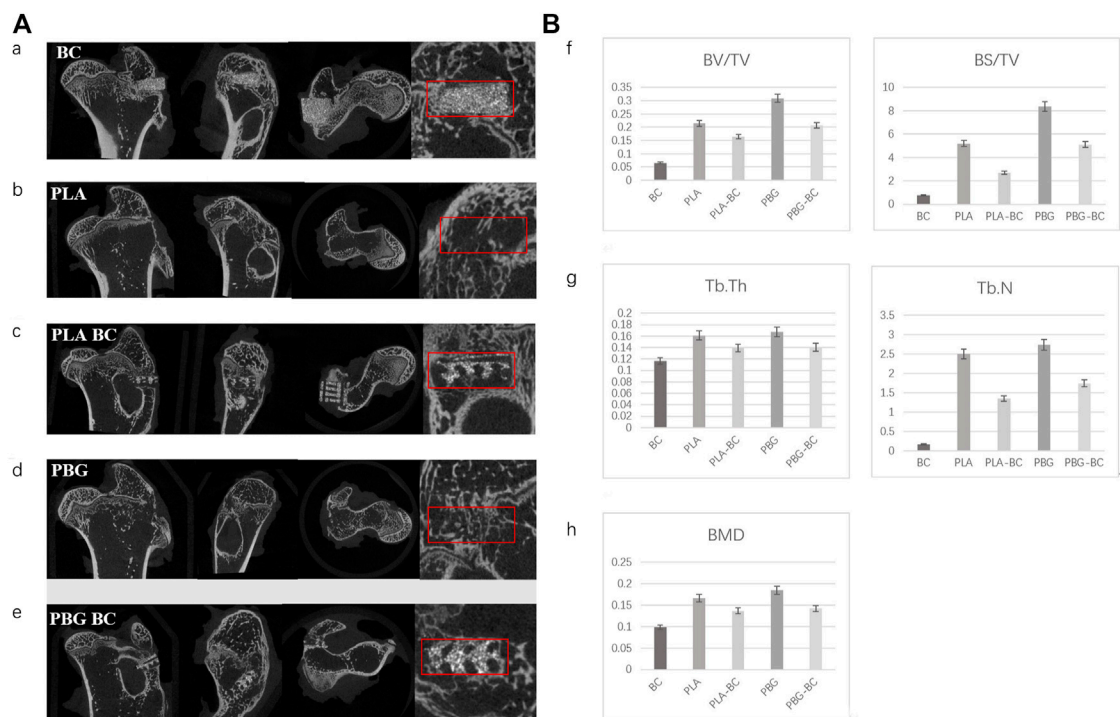
(A). Coronal, sagittal, cross-sectional, and local enlarged images of micro-CT 4 weeks after sample implantation. a: BC; b: PLA; c: PLA-BC; d: PBG; e: PBG-BC. (B). Statistical comparative analysis of local area (2 mm × 2 mm × 1 mm around the stent) of micro-CT 4 weeks after sample implantation. f bone volume/tissue volume (BV/TV), bone surface area/tissue volume (BS/TV); g: trabecular thickness (Tb. Th), trabecular number (Tb. N); h: bone mineral density (BMD). *: $p < 0.05$.

Once the scaffolds are implanted into the defect site, foreign body responses occur because of the inflammatory reactions of the host to the implants, which could delay the repairing process (Williams, 2008). An improved understanding suggested that the biomaterial-immune system interaction plays a far more important role in tissue regeneration (Loi et al., 2016; Vishwakarma et al., 2016). The interactions between implants and macrophages have an important impact on interface inflammatory response and tissue reconstruction (Liu et al., 2021). Studies have shown that macrophages can support bone formation by recruiting mesenchymal stem cells (MSC) to the defect site (Freytes et al., 2013; Wynn and Vannella, 2016). Macrophages can also enhance the angiogenesis of endothelial cells (Dong et al., 2017). It is known that the change in the microenvironment can polarize macrophages in either direction of M1 or M2 (Ma et al., 2021). M1 macrophages can secrete pro-inflammatory cytokines while M2 macrophages take part in tissue remodeling and resolution of inflammation (Loi et al., 2016). It was reported that macrophages of the M2 phenotype could enhance the expression of bone morphogenetic protein-2 (BMP-2) in macrophages, which regulated osteogenic

differentiation of BMSC (Chen et al., 2014). The results of this study showed that pure PLA promoted M1 polarization of macrophages, which may be due to the acidic environment produced by PLA, and some particles dissolved by PLA have a pro-inflammatory effect. PBG induced M2 polarization of macrophages, which may be due to the degradation microenvironment caused by BG. Studies have shown that ionic products of BG could activate macrophages toward the M2 phenotype and stimulate macrophages to secrete anti-inflammatory growth factors (Dong et al., 2017).

The composites were prepared by 3D-based FDM, which is a physical process without additives in the preparation process (Grivet-Brancot et al., 2022). The method can ensure the original characteristics of the material. The preparation time is short and can be customized according to different anatomical information. The high porosity of biomaterials is conducive to the growth of cells and blood vessels. PLA-BG prepared in this study has a completely interconnected channel network, which is conducive to bone growth.

The *in vivo* experiments revealed the structural relationship and bone integration between scaffolds and surrounding bone tissue.

**FIGURE 14**

(A). Coronal, sagittal, cross-sectional, and local enlarged images of micro-CT 12 weeks after sample implantation. a: BC, b: PLA, c: PLA-BC; d: PBG; and e: PBG-BC. (B). Statistical comparative analysis of local area (2 mm × 2 mm × 1 mm around the stent) of micro-CT 12 weeks after sample implantation. f: BV/TV, BS/TV; g: Tb. Th, Tb.N; h: BMD. *: $p < 0.05$.

4 weeks after implantation, the composite scaffold with BG, whether or not containing bone cement, had better bone integration, indicating that BG could promote new bone formation in the early stage. The composite scaffold containing bone cement maintained a good frame structure, but no obvious osteogenic reaction was found in the simple bone cement group, indicating that bone cement can only provide the initial stability of the scaffold. After 12 weeks of implantation, with the continuous degradation of PBG, a large number of new bones filled the space after degradation, while new bone formation in the simple bone cement group was still not obvious, indicating that PBG can continuously promote osteogenesis. PBG-BC maintained a good cubic structure, but the formation of new bone was worse than PBG, which may be due to the space occupied by bone cement could not form new bone. Although PBG had the best bone ingrowth performance, the scaffold may fail in the early stage without the support provided by bone cement.

5 Conclusion

PBG-BC could provide immediate and stable fixation for a bone defect in a load-bearing area. It also had the

characteristics of continuous osteogenic induction. The continuous degradation of PBG provided space for bone growth. During the degradation process, the release of various elements promoted osteogenic metabolism, regulated the local microenvironment, induced M2 polarization of macrophages, inhibited local inflammatory response, and provided long-term stability via bone integration.

Data availability statement

The original contributions presented in the study are included in the article/Supplementary Material, further inquiries can be directed to the corresponding author.

Ethics statement

The animal study was reviewed and approved by the Laboratory animal research center of Renji Hospital Affiliated with Shanghai Jiaotong University school of medicine.

Author contributions

YW and YD contributed to the conception and design of the study. YD, JZ, ZL, XM, and XL participated in the *in vitro* experiment. YD and YW participated in the *in vivo* experiment. YD and XL performed the statistical analysis. YD and XL wrote the first draft of the manuscript. ZY and TL wrote sections of the manuscript. All authors contributed to manuscript revision, read, and approved the submitted version.

Funding

This work was supported by the National Natural Science Foundation of China (Youth Program, 81802140).

References

- Bento, R., Gaddam, A., and Ferreira, J. M. F. (2021). Sol-gel synthesis and characterization of a quaternary bioglass for bone regeneration and tissue engineering. *Mater. (Basel)* 14 (16), 4515. doi:10.3390/ma14164515
- Castro-Raucci, L. M. S., Teixeira, L. N., Barbosa, A. F. S., Fernandes, R. R., Raucci-Neto, W., Jacobovitz, M., et al. (2018). Calcium chloride-enriched calcium aluminate cement promotes *in vitro* osteogenesis. *Int. Endod. J.* 51 (6), 674–683. doi:10.1111/iej.12883
- Chen, Z. T., Wu, C. T., Gu, W. Y., Klein, T., Crawford, R., Xiao, Y., et al. (2014). Osteogenic differentiation of bone marrow MSCs by beta-tricalcium phosphate stimulating macrophages via BMP2 signalling pathway. *Biomaterials* 35 (5), 1507–1518. doi:10.1016/j.biomaterials.2013.11.014
- Daskalakis, E., Huang, B., Vyas, C., Acar, A. A., Fallah, A., Cooper, G., et al. (2022). Novel 3D bioglass scaffolds for bone tissue regeneration. *Polym. (Basel)* 2214 (3), 445. doi:10.3390/polym14030445
- Distler, T., Fournier, N., Grünwald, A., Polley, C., Seitz, H., Detsch, R., et al. (2020). Polymer-bioactive glass composite filaments for 3D scaffold manufacturing by fused deposition modeling: Fabrication and characterization. *Front. Bioeng. Biotechnol.* 24 (8), 552. doi:10.3389/fbioe.2020.00552
- Dong, X., Chang, J., and Li, H. Y. (2017). Bioglass promotes wound healing through modulating the paracrine effects between macrophages and repairing cells. *J. Mat. Chem. B* 5 (26), 5240–5250. doi:10.1039/c7tb01211j
- El-Rashidy, A. A., Roether, J. A., Harhaus, L., Kneser, U., and Boccaccini, A. R. (2017). Regenerating bone with bioactive glass scaffolds: A review of *in vivo* studies in bone defect models. *Acta Biomater.* 62, 1–28. doi:10.1016/j.actbio.2017.08.030
- Freytes, D. O., Kang, J. W., Marcos-Campos, I., and Vunjak-Novakovic, G. (2013). Macrophages modulate the viability and growth of human mesenchymal stem cells. *J. Cell. Biochem.* 114 (1), 220–229. doi:10.1002/jcb.24357
- Grivet-Brancot, A., Boffito, M., and Ciardelli, G. (2022). Use of polyesters in fused deposition modeling for biomedical applications. *Macromol. Biosci.*, e2200039. doi:10.1002/mabi.202200039
- Kaseem, M., Ur Rehman, Z., Hossain, S., Singh, A. K., and Dikici, B. (2021). A review on synthesis, properties, and applications of polylactic acid/silica composites. *Polym. (Basel)* 813 (18), 3036. doi:10.3390/polym13183036
- Laende, K. E., Richardson, C. G., Meldrum, A. R., and Dunbar, M. J. (2021). Tibial component migration after total knee arthroplasty with high-viscosity bone cement. *J. Arthroplasty* 36 (6), 2000–2005. doi:10.1016/j.arth.2021.01.081
- Li, H., Zheng, L., and Wang, M. (2021). Biofunctionalized nanofibrous bilayer scaffolds for enhancing cell adhesion, proliferation and osteogenesis. *ACS Appl. Bio Mat.* 4 (6), 5276–5294. doi:10.1021/acsbm.1c00414
- Liu, X., Chen, M., Luo, J., Zhao, H., Zhou, X., Gu, Q., et al. (2021). Immunopolarization-regulated 3D printed-electrospun fibrous scaffolds for bone regeneration. *Biomaterials* 276, 121037. doi:10.1016/j.biomaterials.2021.121037
- Loi, F., Cordova, L. A., Pajarinen, J., Lin, T. H., Yao, Z. Y., Goodman, S. B., et al. (2016). Inflammation, fracture and bone repair. *Bone* 86, 119–130. doi:10.1016/j.bone.2016.02.020
- Ma, Y., Yang, H., Zong, X., Wu, J., Ji, X., Liu, W., et al. (2021). Artificial M2 macrophages for disease-modifying osteoarthritis therapeutics. *Biomaterials* 274, 120865. doi:10.1016/j.biomaterials.2021.120865
- Matsuki, K., Sugaya, H., Takahashi, N., Kawasaki, T., Yoshimura, H., Kenmoku, T., et al. (2018). Degradation of cylindrical poly-lactic Co-Glycolide/Beta-Tricalcium phosphate biocomposite anchors after arthroscopic bankart repair: A prospective study. *Orthopedics* 41 (3), e348–e353. doi:10.3928/01477447-20180226-08
- Prost, S., Pesenti, S., Fuentes, S., Tropiano, P., and Blondel, B. (2021). Treatment of osteoporotic vertebral fractures. *Orthop. Traumatology Surg. Res.* 107 (1S), 102779. doi:10.1016/j.otsr.2020.102779
- Ruskin, E. I., Coomars, P. P., Sikder, P., and Bhaduri, S. B. (2020). Magnetic calcium phosphate cement for hyperthermia treatment of bone tumors. *Mater. (Basel)* 13 (16), 3501. doi:10.3390/ma13163501
- Singhvi, M. S., Zinjarde, S. S., and Gokhale, D. V. (2019). Polylactic acid: Synthesis and biomedical applications. *J. Appl. Microbiol.* 127 (6), 1612–1626. doi:10.1111/jam.14290
- Stahl, A., and Yang, Y. P. (2021). Regenerative approaches for the treatment of large bone defects. *Tissue Eng. Part B Rev.* 27 (6), 539–547. doi:10.1089/ten.teb.2020.0281
- Vaid, R., Yildirim, E., Pasquinielli, M. A., and King, M. W. (2021). Hydrolytic degradation of polylactic acid fibers as a function of pH and exposure time. *Molecules* 26 (24), 7554. doi:10.3390/molecules26247554
- Valerio, P., Pereira, M. M., Goes, A. M., and Leite, M. F. (2004). The effect of ionic products from bioactive glass dissolution on osteoblast proliferation and collagen production. *Biomaterials* 25, 2941–2948. doi:10.1016/j.biomaterials.2003.09.086
- Vishwakarma, A., Bhise, N. S., Evangelista, M. B., Rouwkema, J., Dokmeci, M. R., Ghaemmaghami, A. M., et al. (2016). Engineering immunomodulatory biomaterials to tune the inflammatory response. *Trends Biotechnol.* 34 (6), 470–482. doi:10.1016/j.tibtech.2016.03.009
- Williams, D. F. (2008). On the mechanisms of biocompatibility. *Biomaterials* 29 (20), 2941–2953. doi:10.1016/j.biomaterials.2008.04.023
- Wu, C., Ramaswamy, Y., Kwik, D., and Zreikat, H. (2007). The effect of strontium incorporation into CaSiO₃ ceramics on their physical and biological properties. *Biomaterials* 28, 3171–3181. doi:10.1016/j.biomaterials.2007.04.002
- Wynn, T. A., and Vannella, K. M. (2016). Macrophages in tissue repair, regeneration, and fibrosis. *Immunity* 44 (3), 450–462. doi:10.1016/j.immuni.2016.02.015
- Yu, H., Liu, Y., Yang, X., He, J., Zhang, F., Zhong, Q., et al. (2021). Strontium ranelate promotes chondrogenesis through inhibition of the Wnt/ β -catenin pathway. *Stem Cell Res. Ther.* 2021 (1), 296. doi:10.1186/s13287-021-02372-z
- Zhang, J., He, L., Wei, G., Jiang, X., Fu, L., Zhao, Y., et al. (2019). Zwitterionic polymer-grafted polylactic acid vascular patches based on a decellularized scaffold for tissue engineering. *ACS Biomater. Sci. Eng.* 5 (9), 4366–4375. doi:10.1021/acsbomaterials.9b00684
- Zheng, X., Zhang, X., Wang, Y., Liu, Y., Pan, Y., Li, Y., et al. (2021). Hypoxia-mimicking 3D bioglass-nanoclay scaffolds promote endogenous bone regeneration. *Bioact. Mat.* 216 (10), 3485–3495. doi:10.1016/j.bioactmat.2021.03.011
- Zhu, Y., Ma, Z., Kong, L., He, Y., Chan, H. F., Li, H., et al. (2020). Modulation of macrophages by bioactive glass/sodium alginate hydrogel is crucial in skin regeneration enhancement. *Biomaterials* 256, 120216. doi:10.1016/j.biomaterials.2020.120216

Conflict of interest

The authors declare that the research was conducted in the absence of any commercial or financial relationships that could be construed as a potential conflict of interest.

Publisher's note

All claims expressed in this article are solely those of the authors and do not necessarily represent those of their affiliated organizations, or those of the publisher, the editors, and the reviewers. Any product that may be evaluated in this article, or claim that may be made by its manufacturer, is not guaranteed or endorsed by the publisher.



OPEN ACCESS

EDITED BY

Yanjin Lu,
Fujian Institute of Research on the
Structure of Matter (CAS), China

REVIEWED BY

Liang-Yu Chen,
Jiangsu University of Science and
Technology, China
Yi Yang,
University of Shanghai for Science and
Technology, China
Chao Chen,
Central South University, China

*CORRESPONDENCE

Shujun Li,
shjli@imr.ac.cn
Yue Zhu,
zhuyuedr@163.com

SPECIALTY SECTION

This article was submitted to
Biomaterials,
a section of the journal
Frontiers in Materials

RECEIVED 20 June 2022

ACCEPTED 08 July 2022

PUBLISHED 04 August 2022

CITATION

Yuan W, Zhao X, Li S and Zhu Y (2022),
Effect of laser scanning speed on
microstructure and mechanical
properties of SLM porous Ti-5Al-5V-
5Mo-3Cr-1Fe alloy.
Front. Mater. 9:973829.
doi: 10.3389/fmats.2022.973829

COPYRIGHT

© 2022 Yuan, Zhao, Li and Zhu. This is an
open-access article distributed under
the terms of the [Creative Commons
Attribution License \(CC BY\)](#). The use,
distribution or reproduction in other
forums is permitted, provided the
original author(s) and the copyright
owner(s) are credited and that the
original publication in this journal is
cited, in accordance with accepted
academic practice. No use, distribution
or reproduction is permitted which does
not comply with these terms.

Effect of laser scanning speed on microstructure and mechanical properties of SLM porous Ti-5Al-5V-5Mo-3Cr-1Fe alloy

Wei Yuan¹, Xiaoli Zhao², Shujun Li^{3*} and Yue Zhu^{1*}

¹Department of Orthopedics, The First Hospital of China Medical University, Shenyang, China,

²Institute of Materials Science, School of Materials Science and Engineering, Northeastern University, Shenyang, China, ³Shi-changxu Innovation Center for Advanced Materials, Institute of Metal Research, Chinese Academy of Sciences, Shenyang, China

In this study, porous Ti-55531(Fe) was fabricated by selective laser melting (SLM) with different laser scanning speeds. The microstructures, surface morphology, inner defects, porosity, microhardness, and compressive behaviors were studied. The variation of lattice constant and hardness were analyzed. The results show that all the specimens have a density of $\sim 1 \text{ g/cm}^3$, and a Vicker's hardness with a range of 280–320 Hv0.1. The porosity of the SLM-produced materials is greater than the designed value (77%) and increases from 77.33% to 82.33% with the increase of laser scanning speed from 500 mm/s to 1,500 mm/s. Continuous irregular columnar dendrites, a large number of gas-induced defects with small size between 20 and 60 μm and a deep molten pool form in the specimens fabricated with a laser scanning speed less than 1,000 mm/s. Some defects, elongated voids and interrupted columnar dendrites are identified in the specimens fabricated with the laser scanning speed more than 1,000 mm/s caused by the insufficient input energy. All specimens with different laser scanning speeds show the single β phase patterns. The compressive strength of the specimens with the laser scanning speed of 500 mm/s is maintained at 32 MPa and the compressive strength decreases with the increase of laser scanning speed. The specimens with a scanning speed of 500 mm/s present the best mechanical properties and surface quality.

KEYWORDS

metamaterial, beta-titanium, microstructure, mechanical behavior, selective laser melting

Introduction

Recently, 3D-architected metamaterials with micro-lattice structures have shown considerable weight reduction efficiency, flexible design capability and especially potential applications in battery electrodes, shock energy damping, acoustic, biological implants, and thermal sensors or stretchable electronics (Barba et al., 2020; Yu et al., 2020; Zhang et al., 2020; Kelly et al., 2021a; Kelly et al., 2021b; Salmi, 2021; Timercan et al., 2021; du Plessis et al., 2022). Meanwhile, additive manufacturing (AM) is widely accepted as a new

forming process for high performance components in aerospace, medical, energy and automotive applications due to its unique features of rapid prototyping, complex or customized processing and high efficiency (Chen et al., 2021). Various micro truss lattice structures can be achieved by AM method without limit of configuration of cell and the complexity of the structural surface. Selective laser melting (SLM) emerging as an advanced manufacturing technologies to fuse powders track-by-track and grow layer-by-layer under the control of a CAD model, is capable of fabricating porous 3D-architectures with optimal properties for various applications. Developing metallic lattice structures (e.g., aluminum alloys, titanium alloys, and superalloys) with high strength and good ductility has become the mainstream of additive manufacturing.

Based on the chemical compositions and relative amounts of the α phase with hexagonal close-packed (hcp) structure and β phase with body-centered cubic (bcc) structure at room temperature, titanium alloys are typically classified as α alloy, near- α alloy, $\alpha + \beta$ alloy, near- β alloy, and β alloy. Due to the superior strength, cold workability, corrosion resistance and biocompatibility, β alloys have attracted lots of attentions in aerospace, marine and biomedical industry (Chen et al., 2020; Zhang and Chen, 2020; Liu et al., 2021). Beta titanium alloy Ti-5553 (Ti-5Al-5V-5Mo-3Cr-0.5Fe) alloy is known as a heat treatable beta titanium alloy for its high strength and good ductility and has been widely applied as large aerospace components such as landing gears, arresting hooks and flap tracks (Huang et al., 2011; Ghosh et al., 2013; Cotton et al., 2015; Qin et al., 2016). The mechanical performance can be further improved by increasing the iron content from 0.5 wt% to 1 wt% (Guan et al., 2008). The strength and elongation of Ti-55531 (Fe) (Ti-5Al-5V-5Mo-3Cr-1Fe) alloy can be maintained at 1,350 MPa and 15.5%, respectively after STA heat treatment (Guan et al., 2008). To date, there have been some basic studies of dense SLM Ti-5553 components on the machinability (Grove et al., 2018) and the evolution of microstructure and tensile properties after isothermal heat treatments (Carton et al., 2019). The strength and the ductility of SLM dense Ti-5553 are approximately as 1,088 MPa and 14%, respectively after heat treatment (Carton et al., 2019), which is comparable to those of SLM Ti64 (Ti-6Al-4V) product (Simonelli et al., 2014). For Ti64, the mechanical properties are sensitive to the cooling rates. Further factors such as process parameters, build geometry, scanning strategy and surrounding conditions affecting the thermal history and cooling rates will determine the microstructure and resulted properties (Chen et al., 2021). Therefore, there could be similar changes in SLM porous Ti-55531(Fe), which may contribute to the high strength and ductility of porous metallic materials (Yuan et al., 2018; Ren et al., 2019; Liu et al., 2020; Chen et al., 2021). However, to the best of our knowledge, there are few reports on the fabrication and mechanical properties of SLM porous Ti55531(Fe) in the literature.

In this study, porous Ti-55531(Fe) specimens were fabricated by SLM process with different laser scanning speeds. The effects of scanning speed on the microstructure, surface morphology, porosity and compressive behaviors were investigated.

TABLE 1 Chemical composition of Ti-55531(Fe) powders used for SLM process (wt%).

	Al	V	Cr	Mo	Fe	Ti
Ti-55531(Fe)	5.11	5.53	2.87	3.56	1.13	Balanced

Materials and methods

The chemical compositions of the gas atomization (GA) Ti-55531(Fe) pre-alloyed powder are shown in Table 1. The Ti-55531 powders show a regular spherical morphology and a size distribution with a range of 20–70 μm and an average particle size (d_{50}) of 45 μm (Figure 1). The surface morphology and chemical compositions of the GA powders and the as-SLMed specimens were analyzed by SEM (JSM-6510A) assembled with an energy dispersive spectrometer (EDS). And a laser scattering particle size distribution analyzer (Horiba, LA-920) was used to determine the powder size distribution.

A 10 mm³ × 10 mm³ × 10 mm³ 3D scaffold architecture cube arrayed by rhombic dodecahedron unit cells was generated using Magic software (Materialise, Belgium) and built in an SLM system (Realizer SLM 100 machine with a 200 W Yb: YAG fiber laser). The schematic diagram for SLM process of rhombic dodecahedron designed 3D lattice structure is shown in Figure 2. The laser power was 190 W, the diameter of the focused spot was 20 μm , the thickness of the fixed powder layer and scanning interval was 30 and 60 μm , and the scanning rate were between 500 and 1,500 mm/s. The phase constitution of the lattice samples was determined by Rigaku Smartlab X-ray diffraction (XRD). Metallography was performed to determine microstructural changes of porous structures with different laser scanning speeds. These samples were prepared by grinding to 3,000 mesh, mirror polishing with SiO₂ suspension and followed by etching in acid mixture (HF: HNO₃: H₂O = 1:2:50). The shape of the molten pool is approximated by an arc in the building direction and the depth of the molten pool is reflected by the curvature radius of the approximate arc. The pool size could be changed along the building direction, so the average curvature radius of the fusion line was calculated by measuring more than fifteen fusion lines in the metallography figures.

The X-ray tomography (micro-CT) has been reported as computed tomography (CT) technology to check the surface roughness and of mesh struts and inner defects in the metallic cellular structures (Chan and Young, 2013; Wang et al., 2013). An XRT work was carried out using an Xradia Versa XRM-500 system (Carl Zeiss X-ray Microscopy Inc., Pleasanton, California, United States) with a spatial resolution of micron even dozens of nanometers to check the topological mesh and the size and count distribution of the defects inside the samples. Surface roughness

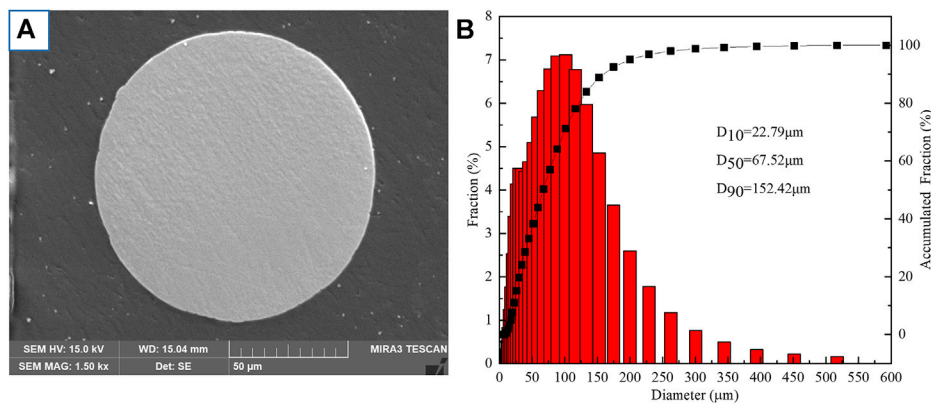


FIGURE 1
SEM micrographs of cross-section (A), particle size distribution (B) of Ti55531 powders.

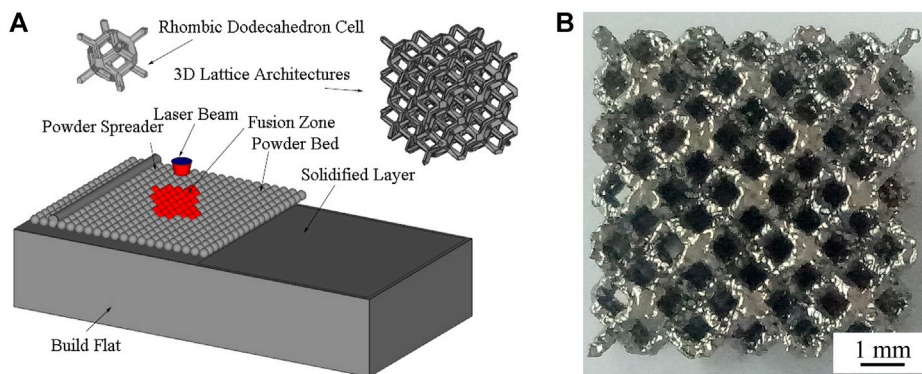


FIGURE 2
Schematic diagram of SLM process (A) and side view of mesh arrays part (B) for rhombic dodecahedron designed 3D lattice architecture.

is evaluated by analyzing the surface morphology based on the Micro-CT slicing data. The average roughness (R_a) is calculated as Eq. 1 (Chen et al., 2021)

$$R_a = \frac{1}{N} \sum_{i=1}^N |f_n| \quad (1)$$

where f_n is the length of the protruding at N locations on the surface of the struts based on the Micro-CT slicing data.

The porosity can be calculated by Eq. 2.

$$P = \frac{V_0 - V}{V_0} \times 100\% = 1 - \frac{D}{D_t} \quad (2)$$

where the V_0 is the total volume of the material, V is the volume of solid material, D is the measured density and the D_t is the theoretical density. The theoretical density (D_t) of Ti-55531(Fe) is presented as Eq. 3.

$$D_t = \sum_{i=1}^n d_i \cdot \eta_i \quad (3)$$

where D_t is the theoretical density, d_i is the atomic density of the i th atom and η_i is the atomic percentage of the i th atom in Ti-55531(Fe) alloys. The measured density of the SLM Ti-55531(Fe) was determined by the modified Archimedes method using a direct reading electronic hydrometer (ET-320), as is shown in Eq. 4 (Liu et al., 2016b)

$$D = \frac{W_1 \cdot D_0}{W_3 - W_2} \quad (4)$$

where D_0 is the density of the water, W_1 is the weight of porous specimens in air, W_2 is the weight of porous specimens in water after water osmosis stabilization and W_3 is the weight of porous specimens in air after water osmosis stabilization.

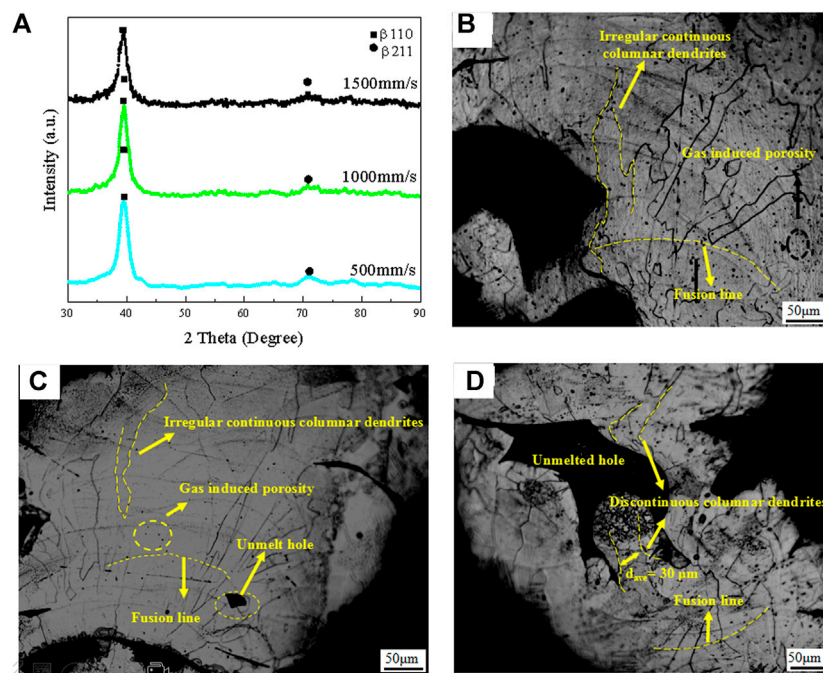


FIGURE 3
XRD profiles (A), optical micrographs of materials built at 500 mm/s (A), 1000 mm/s (B), 1500 mm/s (C).

Vicker's microhardness tests were conducted by 401 MVDTM with a 100 g load and a 10 s dwell time. The hardness was measured at the horizontal surface with the maximum number of the struts which is around 9 mm from the substrate depending on the different porous structure. Random measurement of five points was conducted on the surface of the cellular samples using a single point mode. The lattice constant was quantitatively calculated by Kohn least square method (Zhang et al., 2009) according to Eq. 4.

$$\sum_{j=1}^M \sum_{i=1}^N C_{ji} C_{li} X_j = \sum_{i=1}^N \frac{1}{d_i^{\text{exp}2}} C_{li} \quad (l = 1, \dots, M) \quad (5)$$

where N is the number of the crystal planes for calculation, and for b.c.c. structure $M = 1$, $X_1 = 1/a^2$, $C_1 = h^2 + k^2 + l^2$, d_i^{exp} is the experimental value of the crystal plane spacing. And the variance of X_1 can be calculated according Eq. 5.

$$\sigma^2(X_{ii}) = \frac{2\chi^2 A_{ii}^{-1}}{N - M} \quad (6)$$

A is a matrix with an element $a_{ij} = \sum_{l=1}^M C_{il} C_{jl}$, A_{ii}^{-1} is the i th diagonal element of the inverse matrix of matrix A , $\chi^2 = \frac{1}{2} \sum_{i=1}^N \left(\frac{1}{d_i^{\text{exp}2}} - \sum_{j=1}^M X_j C_{ji} \right)^2$

Uniaxial compression tests were carried out by a uniaxial testing machine (Shimadzu AG-X plus, 100 KN) with a speed of 0.5 mm/min at ambient temperature. The loading direction was parallel to

the building direction. The specimens were continually loaded and all the tests were stopped near 3 kN. Specific strength was calculated based on compressive strength and the measured density.

Results and discussion

Microstructure

As is shown in Figure 3A, the single β phase peaks are identified in as-built SLM Ti-55531 (Fe) alloy. This is different from the α (hcp) and β phases found in EBM Ti-24Sn-4Zr-8Sn component reported by Liu et al. (2016a) and the complicated structure in NiTiNb alloy prepared by eutectic reaction reported by Wang et al. (2018). As the cooling rate in SLM process is very high, the microstructure (β phase) at high temperature can be retained at ambient temperature. The laser scanning speed has limited effect on the phase type of the Ti55531 (Fe) alloys. When the laser scanning speed is less than 1,000 mm/s, the joints of the samples consist of irregular continuous columnar dendrites along the building direction, and fusion lines with small average radius of curvature (923–1,003 μ m) are obvious (Figures 3B,C). Discontinuous columnar dendrites can be identified in the sample fabricated with a laser scanning speed of 1,500 mm/s, and fusion line is hard to be found due to a larger

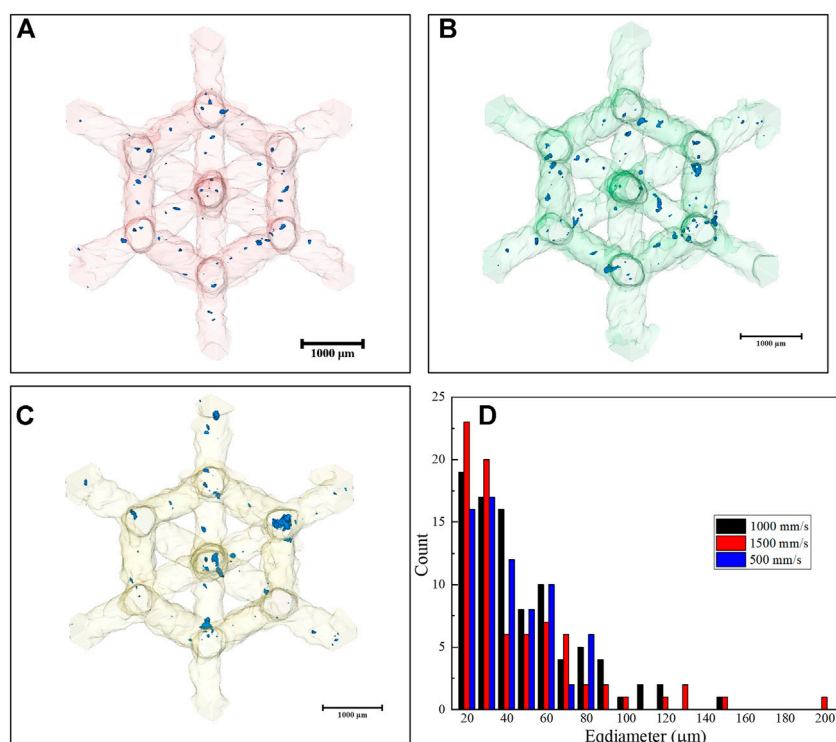


FIGURE 4

Morphology of the inner defects in the materials built at 500 mm/s (A), 1000 mm/s (B), 1500 mm/s (C), and size and distribution of the inner defects in the materials fabricated with different laser scanning speeds (D).

average radius of curvature ($\sim 1,095 \mu\text{m}$) (Figure 3D). The irregular columnar dendrites along the thermal flow direction can be ascribed to the cyclic heat treatment response during the layer-by-layer SLM process.

The porosity of porous materials is determined by the open holes (apparent porosity), surface morphology (surface roughness) and inner defects.

There is an energy volume density (E_v) to investigate the porosity, it is calculated as (Chen et al., 2021):

$$E_v = \frac{P}{v \cdot t_1 \cdot h_s} \quad (7)$$

where v is laser scanning speed, t_1 is layer thickness and h_s is hatch spacing. The laser scanning speed is inversely proportional to the input energy. Input energy density decrease with the increase of the laser scanning speed.

Inner defects

The morphologies of the inner defects in the samples built at 500 mm/s, 1000 mm/s, 1500 mm/s are shown in Figures 4A–C, respectively. The size and number of the defects inside the samples built at different laser scanning

speeds are shown in Figure 4D. Lower scanning speed (500 mm/s) leads to a large number of inner defects with a small size in the range of 20–80 μm (Figures 4A,D). Small size defects is still visible, but medium size defects (90–150 μm) appears when the scanning speed increases from 500 mm/s to 1,000 mm/s (Figures 4B,D). Inner defects with average size larger than 150 μm form and the number of small size inner defects decreases when the scanning speed increases from 1,000 mm/s to 1,500 mm/s (Figures 4C,D).

Homogenous porous structures always own advantages over both of the relative density of porous structure and the mechanical strength (Zhang and Wang, 2018). Besides the change of the microstructure and surface roughness on the mesh struts with different laser scanning speed, the size and count distribution of defects inside the basic cell may be responsible for the mechanical performance. The inner defects with small particle size distribution (20–60 μm) are mainly induced by the element volatilization in keyhole mode (Chen et al., 2021), are distributed in all samples built at different scanning speeds. But the number of the small size defects decreases slightly and the inner defects with large size increase by an increase of laser scanning speed. This phenomenon is because the input energy density at higher scanning speed is

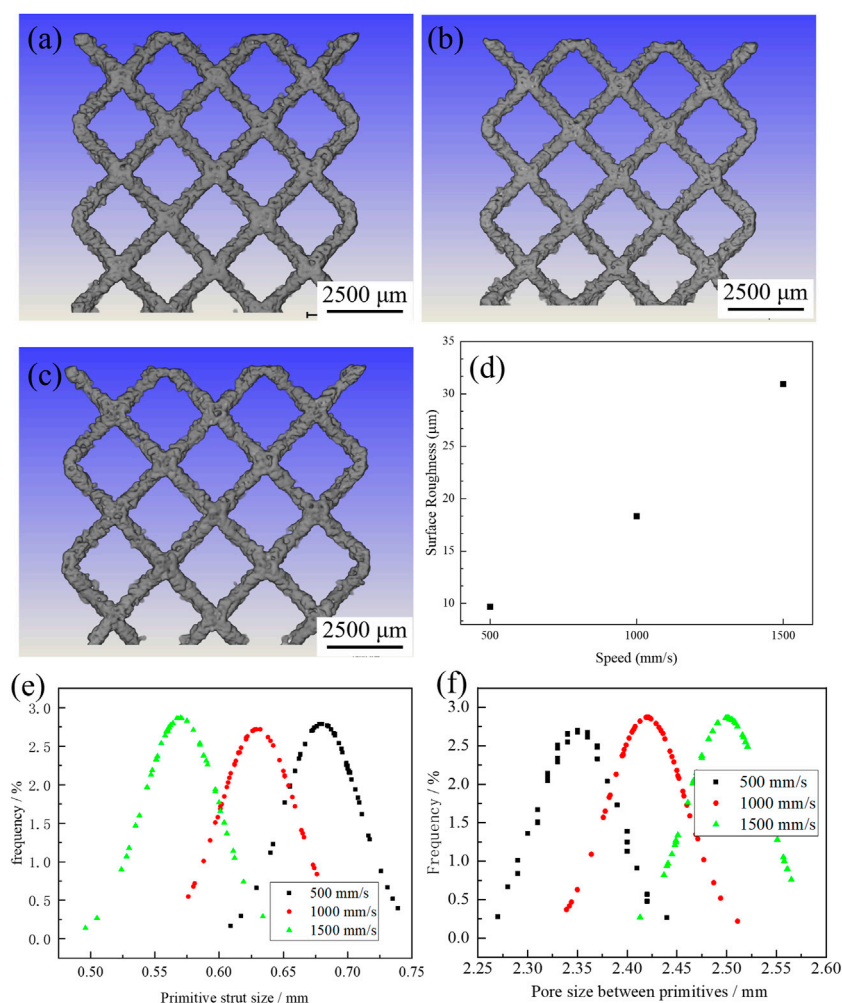


FIGURE 5

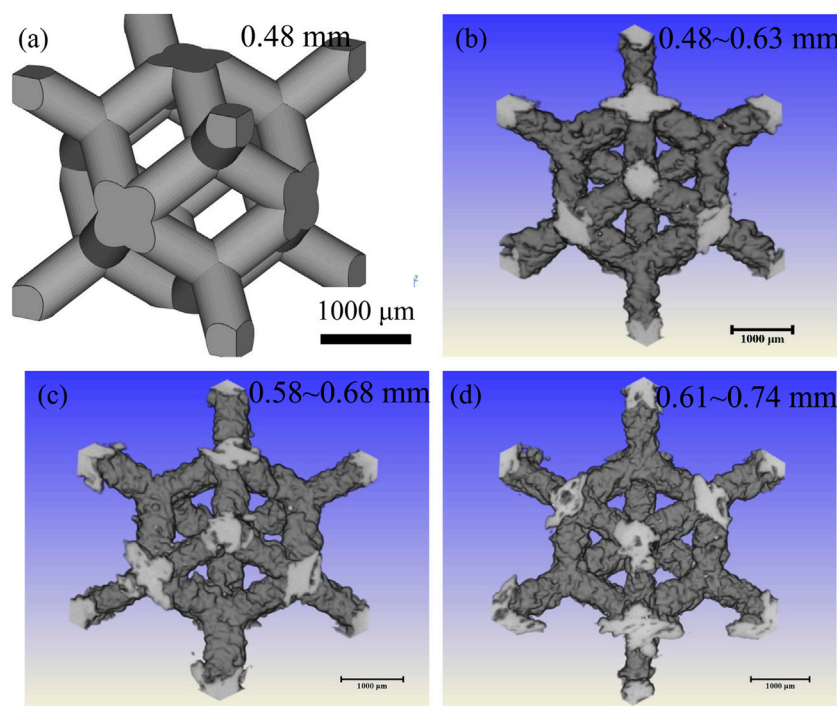
Micro-CT surface morphologies of the materials built at 500 mm/s (A), 1,000 mm/s (B), 1,500 mm/s (C). Surface roughness (D), strut size (E), and pore size (F) of porous structures built at different laser scanning speeds.

insufficient to maintain the keyhole mode, and insufficient depth of molten pool enhances the susceptibility of the lack of fusion zone.

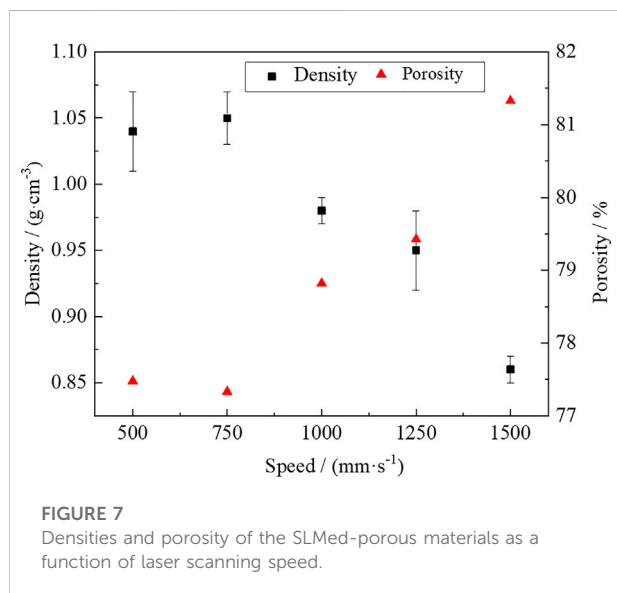
Surface morphology

The surface morphology of the materials built at different laser scanning speeds is shown in Figures 5A–C. The surface roughness, pore size, and the strut size of the mesh arrays are analyzed according to the Micro-CT surface morphology and shown in Figures 5D–F, respectively. The surface of the material built at 500 mm/s is the smoothest ($R_a = 10 \mu\text{m}$) (Figure 5A,D) with the largest strut of 0.62 mm and the smallest pore of 2.35 mm. The surface roughness increases from 10 to 31 μm with the laser scanning speed increased to 1,500 mm/s. And the

strut size decreases from 620 to 570 μm and hole size increases from 2.35 to 2.50 mm, accordingly. Sample fabricated with a scanning speed of 500 mm/s has a structure with an average hole size of 2.35 mm and an average strut size of 680 μm . The strut size decreases to 630 μm and hole size increase to 2.42 mm in the sample fabricated with a scanning speed of 1,000 mm/s. And the strut size continues to decrease to 570 μm and hole size continue to increase to 2.50 mm in the sample fabricated with a scanning speed of 1,500 mm/s. The porous material consists primarily of struts and holes. Larger holes and smaller struts mean more unfilled space in the porous sample and higher apparent porosity. As shown in Figure 6, the scanning speed also has effect on the actual strut size, with increasing the scanning speed from 500 mm/s to 1,500 mm/s, the strut size change from 0.48–0.63 mm to 0.61–0.74 mm, which is larger than the designed value of 0.48 mm.

**FIGURE 6**

The size of the designed rhombic dodecahedral scaffold (A), compare it with the actual size of the strut fabricated using different scanning speeds of 500 mm/s (B), 1,000 mm/s (C) and 1,500 mm/s (D).

**FIGURE 7**

Densities and porosity of the SLMed-porous materials as a function of laser scanning speed.

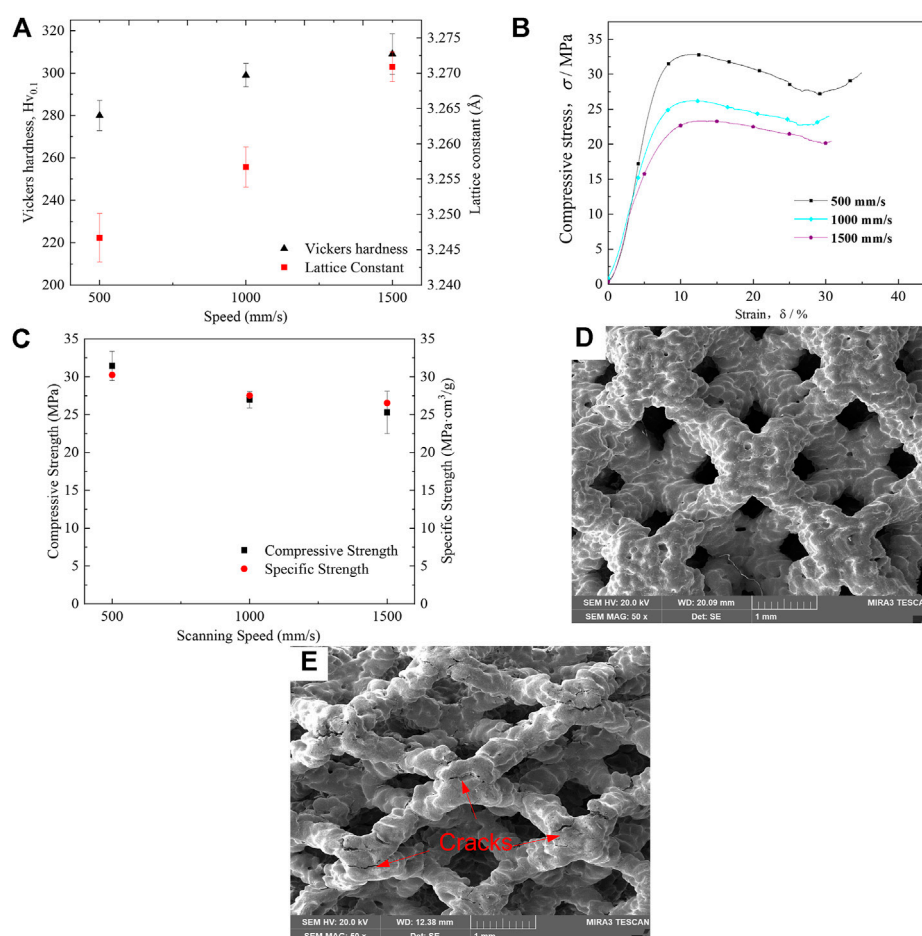
Surface roughness is one of the important indicators of both of the porous and dense components prepared in SLM process and can ultimately affect the part performance. When a high laser scanning speed is used, the energy

input is insufficient to fully melt the metallic powders (Chen et al., 2021). Some of the powders remain in the surface of the porous structure. Small balls form in the molten pool due to the plateau Raleigh capillary instability and move to the edge of the molten pool with the surface tension of molten pool. The surface roughness increases by an increase of the scanning speed because of an insufficient melting of metallic powders in total.

Porosity

The density and porosity of the SLM porous samples built at different scanning speed are shown in Figure 7. The densities of the samples decrease from 1.05 g/cm³ to 0.85 g/cm³ with the increase of laser scanning speed. The measured porosity is a little higher than the designed porosity (77%) and increase from 77.33% to 82.33% with the increase of laser scanning speed from 500 mm/s to 1,500 mm/s.

A high input energy density at a low scanning speed leads to a deep molten pool with a small average radius of curvature of 923 μm. Deep molten pool can promote the full melting of the metallic powders and reduce the defects of large size on the surface. The molten pool is elongated and can be broken into small islands at high scanning speed due

**FIGURE 8**

Lattice constant and microhardness (A), the compressive stress-strain curves of the materials with different scanning speeds (B), compressive strength and specific strength for SLM porous Ti-55531(Fe) alloys with different laser scanning speeds (C), SEM micrographs of materials with scanning speed of 1,000 mm/s in pre-compression (D) and post-compression state (E), respectively.

to the plateau Raleigh capillary instability (Chen et al., 2021). Inadequate penetration of molten pool will cause the lack of fusion defects. The shallower molten pool leads to unmelted holes and even discontinuous columnar dendrites.

In higher energy volume density, deep molten pool promotes element volatilization, and the volatilization gas can induce porosity. In this study, gas induced porosities with small size are dominated and both of the apparent porosity and the surface roughness are the lowest in the samples built at a scanning speed of 500 mm/s. Rapid scanning reduces the pool depth and enhances the stability of elongated lack of fusion defects and even interrupted the continuous growth of the columnar grains due to the plateau Raleigh capillary instability. Elongated voids with sharp edge form in the final parts and can be a resource of stress concentration under applied loads.

Microhardness and compressive behavior

The microhardness ($H_{V0.1}$) and the lattice constant increase with increasing scanning speed (Figure 8A). The factors affecting microhardness may include the phase constitution, the surface roughness and the surface residual thermal stress. All the samples show the same phase constitution as mentioned in Figure 3A. In this study, the residual thermal stress is evaluated by the lattice distortion based on the XRD data. The lattice distortion is mainly related to the vacancy concentration (Hu et al., 2010). The vacancies concentration can be lowered by decreasing the molten pool temperature. A higher scanning speed can lead to a shallower molten pool with a lower temperature because of a lower input energy density. The energy required to form Schottky vacancies is much less than that of Frenkel vacancies (Hu et al., 2010). Therefore, the atoms leaving the equilibrium position

mainly form Schottky defects, which results in the decrease of lattice constant. The lattice constant decreases with increasing vacancy concentration. Thus, the lattice distortion decreases by increasing the laser scanning speed. Larger Schottky-mode lattice distortion enhances the tensile residual thermal stress on the surface of the samples. Residual thermal tensile stress on the surface reduces the resistance of the indenter head of the hardness tester to enter the material surface, thus showing low hardness.

Figure 8B shows the compressive stress-strain curves of materials prepared with different scanning speed. It can be seen that they exhibit the similar curve shape but different strength. Figure 8C shows the compressive strength and specific strength of samples built at different laser scanning speed. The compressive strength can reach 31 MPa in the sample fabricated with a laser scanning speed of 500 mm/s and decreases with the increase of the laser scanning speed. The compressive strength decreases to 25 MPa in the samples built at 1,500 mm/s. The highest specific strength of as-built SLM porous Ti-55531 (Fe) specimens is 30.2 MPa cm³/g at the scanning speed of 500 mm/s and decreases with the increase of the laser scanning speed. The specific strength decrease to 26.5 MPa cm³/g when the scanning speed increase to 1,500 mm/s.

Porosity is the dominant factor on the compressive stress (Kadirgama et al., 2018). In this study, porosity increase with the increase of laser scanning speed, and high porosity can induce low compressive strength. High porosity is mainly related to large size unfused defects and small size of strut size. Firstly, rapid scanning speed reduced the size of the molten pool, and insufficient penetration of molten pool led to large size unfused defects. Large size unfused defects can be resources of the stress concentration under applied loads and reduce the compressive strength. Secondly, an increase of the scanning speed can decrease the size of the mesh strut which reducing the bearing capacity of the porous sample.

After compression, some structural units of the sample are deformed along the loading direction in two-dimensional: the hole spacing along the loading direction decreases, and the hole spacing perpendicular to the loading direction increases. All the samples fabricated with different laser scanning speeds show breakdown in cell nodes perpendicular to the direction of loading after the compression (Figures 8D,E), indicating that the strength of 3D rhombic dodecahedron cell designed porous structure is significantly depending on the design of the unit structure.

Conclusion

In this work, different laser scanning speed was used to fabricate a β type Ti-55531(Fe) meta-material with a 3D rhombic

dodecahedron cell designed porous structure. The effects of scanning speed on microstructural change, porosity, and compressive behaviors were systematically studied and discussed. The results are summarized as follows: 1) The columnar grains are continuous and deep molten pool forms with the laser scanning speed of 500 mm/s. The melt pool becomes shallower with increasing the scanning speed from 500 mm/s to 1,500 mm/s. The continuous growth of β columnar grains can be interrupted due to plateau Raleigh capillary instability or inadequate melting when the laser speed is 1,500 mm/s. 2) Experimental porosities (77.33–82.33%) are higher than expected (77%). The surface roughness (10–30 μ m) of porous SLMed Ti-55531(Fe) alloys is at the range level of particle size distribution. The inner defects with a size of 20–60 μ m are distributed all over the samples built at different scanning speed. And the number of tiny inner defects with a range of 20–80 μ m decreases and large inner defects with a range of 120–200 μ m form by an increase of scanning speed. 3) All the specimens show a range of 280–310 for Hv0.1 and 25–31 MPa for compressive strength. The specific strength of samples with scanning speed less than 1,000 mm/s is in a range of 27.5–30.2 MPa cm³/g and the roughness is less than 20 μ m. The specific strength is 26.5 MPa cm³/g and the surface roughness increase to near 30 μ m when the scanning speed increase to 1,500 mm/s. Scanning speed of 500 mm/s is good for both of the mechanical properties and surface quality.

Data availability statement

The original contributions presented in the study are included in the article/supplementary material, further inquiries can be directed to the corresponding authors.

Author contributions

WY and XZ: Concept, data curation, investigation, writing-original draft. SL and YZ: Conceptualization, writing-original draft, formal analysis, review and editing.

Funding

This work was supported partially by Chinese MoST (2017YFC1104903), Key Research Program of Frontier Sciences, CAS (QYZDJ-SSW-JSC031-02), National Natural Science Foundation of China (81902191, 51871220, 51922026), Scientific Research Foundation of Educational Department of Liaoning Province (QN2019001), China Postdoctoral Science Foundation (2021M693523), State Key Laboratory of Light Alloy Casting Technology for High-end Equipment (LACT-007), Shenyang Talents program

(RC200230) and CAS Interdisciplinary Innovation Team Project (JCTD-2020-10).

Conflict of interest

The authors declare that the research was conducted in the absence of any commercial or financial relationships that could be construed as a potential conflict of interest.

References

- Barba, D., Alabort, C., Tang, Y. T., Viscasillas, M. J., Reed, R. C., Alabort, E., et al. (2020). On the size and orientation effect in additive manufactured Ti-6Al-4V. *Mat. Des.* 186, 108235. doi:10.1016/j.matdes.2019.108235
- Carton, H. D., Klein, K. D., and Elmer, J. W. (2019). Evolution of microstructure and mechanical properties of selective laser melted Ti-5Al-5V-5Mo-3Cr after heat treatments. *Sci. Technol. Weld. Join.* 24, 465–473. doi:10.1080/13621718.2019.1594589
- Chan, Y. S., and Young, I. K. (2013). Void ratio and durability properties of porous polymer concrete using recycled aggregate with binder contents for permeability pavement. *J. Appl. Polym. Sci.* 126, E338–E348. doi:10.1002/app.36974
- Chen, L. Y., Cui, Y. W., and Zhang, L. C. (2020). Recent development in beta titanium alloys for biomedical applications. *Metals* 10 (9), 1139. doi:10.3390/met10091139
- Chen, L. Y., Liang, S. X., Liu, Y., and Zhang, L. C. (2021). Additive manufacturing of metallic lattice structures: Unconstrained design, accurate fabrication, fascinated performances and challenges. *Mater. Sci. Eng. R Rep.* 146, 100648. doi:10.1016/j.mser.2021.100648
- Cotton, J. D., Briggs, R. D., Boyer, R. R., Tamirisakandala, S., Russo, P., Shchetnikov, N., et al. (2015). State of the art in beta titanium alloys for airframe applications. *JOM* 67, 1281–1303. doi:10.1007/s11837-015-1442-4
- du Plessis, A., Razavi, S. M. J., Benedetti, M., Murchio, S., Leary, M., Watson, M., et al. (2022). Properties and applications of additively manufactured metallic cellular materials: A review. *Prog. Mat. Sci.* 125, 100918. doi:10.1016/j.pmatsci.2021.100918
- Ghosh, A., Sivaprasad, S., Bhattacharjee, A., and Kar, S. K. (2013). Microstructure-fracture toughness correlation in an aircraft structural component alloy Ti-5Al-5V-5Mo-3Cr. *Mater. Sci. Eng. A* 568, 61–67. doi:10.1016/j.msea.2013.01.017
- Grove, T., Denkena, B., Maiss, O., Krodol, A., Schwab, H., Kuhn, U., et al. (2018). Cutting mechanism and surface integrity in milling of Ti-5553 processed by selective laser melting. *J. Mech. Sci. Technol.* 32, 4883–4892. doi:10.1007/s12206-018-0936-8
- Guan, J., Liu, Y. Y., and Lei, J. F. (2008). *The influences of heat-treatment and alloying on the microstructures and mechanical properties of Ti-5Al-5Mo-5V based alloys*. Beijing: Master, Graduate School of the Chinese Academy of Science.
- Hu, G. X., Cai, X., and Rong, Y. H. (2010). *Fundamentals of materials science*. Shanghai: Shanghai Jiaotong University Press.
- Huang, J., Wang, Z. R., and Xue, K. M. (2011). Cyclic deformation response and micromechanisms of Ti alloy Ti-5Al-5V-5Mo-3Cr-0.5Fe. *Mater. Sci. Eng. A* 528, 8723–8732. doi:10.1016/j.msea.2011.08.045
- Kadrigama, K., Harun, W. S. W., Tarlochan, F., Samykano, M., Ramasamy, D., Azir, M. Z., et al. (2018). Statistical and optimize of lattice structures with selective laser melting (SLM) of Ti6Al4V material. *Int. J. Adv. Manuf. Technol.* 97 (1–4), 495–510. doi:10.1007/s00170-018-1913-1
- Kelly, C. N., Kahra, C., Maier, H. J., and Gall, K. (2021a). Processing, structure, and properties of additively manufactured titanium scaffolds with gyroid-sheet architecture. *Addit. Manuf.* 41, 101916. doi:10.1016/j.addma.2021.101916
- Kelly, C. N., Wang, T., Crowley, J., Wills, D., Pelletier, M. H., Westrick, E. R., et al. (2021b). High-strength, porous additively manufactured implants with optimized mechanical osseointegration. *Biomaterials* 279, 121206. doi:10.1016/j.biomaterials.2021.121206
- Liu, Y. J., Li, S. J., Hou, W. T., Wang, S. G., Hao, Y. L., Yang, R., et al. (2016a). Electron beam melted beta-type Ti-24Nb-4Zr-8Sn porous structures with high strength-to-modulus ratio. *J. Mat. Sci. Technol.* 32 (6), 505–508. doi:10.1016/j.jmst.2016.03.020
- Liu, Y. J., Li, S. J., Wang, H. L., Hou, W. T., Hao, Y. L., Yang, R., et al. (2016b). Microstructure, defects and mechanical behavior of beta-type titanium porous structures manufactured by electron beam melting and selective laser melting. *Acta Mat.* 113, 56–67. doi:10.1016/j.actamat.2016.04.029
- Liu, Y. J., Ren, D. C., Li, S. J., Wang, H., Zhang, L. C., Sercombe, T. B., et al. (2020). Enhanced fatigue characteristics of a topology-optimized porous titanium structure produced by selective laser melting. *Addit. Manuf.* 32, 101060. doi:10.1016/j.addma.2020.101060
- Liu, Z. Y., He, B., Lyu, T. Y., and Zou, Y. (2021). A review on additive manufacturing of titanium alloys for aerospace applications: Directed energy deposition and beyond Ti-6Al-4V. *JOM* 73 (6), 1804–1818. doi:10.1007/s11837-021-04670-6
- Qin, D. Y., Li, Y. L., Zhang, S. Y., and Zhou, L. (2016). On the tensile embrittlement of lamellar Ti-5Al-5V-5Mo-3Cr alloy. *J. Alloys Compd.* 663, 581–593. doi:10.1016/j.jallcom.2015.12.158
- Ren, D. C., Li, S. J., Wang, H., Hou, W. T., Hao, Y. L., Jin, W., et al. (2019). Fatigue behavior of Ti-6Al-4V cellular structures fabricated by additive manufacturing technique. *J. Mat. Sci. Technol.* 35, 285–294. doi:10.1016/j.jmst.2018.09.066
- Salmi, M. (2021). Additive manufacturing processes in medical applications. *Materials* 14 (1), 191. doi:10.3390/ma14010191
- Simonelli, M., Tse, Y. Y., and Tuck, C. (2014). Effect of the build orientation on the mechanical properties and fracture modes of SLM Ti-6Al-4V. *Mater. Sci. Eng. A* 616, 1–11. doi:10.1016/j.msea.2014.07.086
- Timercan, A., Sheremetyev, V., and Brailovski, V. (2021). Mechanical properties and fluid permeability of gyroid and diamond lattice structures for intervertebral devices: Functional requirements and comparative analysis. *Sci. Technol. Adv. Mat.* 22, 285–300. doi:10.1080/14686996.2021.1907222
- Wang, L. Q., Xie, L. C., Zhang, L. C., Chen, L. Y., Ding, Z. H., Lv, Y. T., et al. (2018). Microstructure evolution and superelasticity of layer-like NiTiNb porous metal prepared by eutectic reaction. *Acta Mat.* 143, 214–226. doi:10.1016/j.actamat.2017.10.021
- Wang, S. G., Wang, S. C., and Zhang, L. (2013). Application of high resolution transmission X-ray tomography in material science. *Acta Metall. Sin.* 49 (8), 897. doi:10.3724/sp.j.1037.2013.00107
- Yu, G. S., Li, Z. B., Li, S. J., Zhang, Q., Hua, Y., Liu, H., et al. (2020). The select of internal architecture for porous Ti alloy scaffold: A compromise between mechanical properties and permeability. *Mat. Des.* 192, 108754. doi:10.1016/j.matdes.2020.108754
- Yuan, W., Hou, W. T., Li, S. J., Hao, Y. L., Yang, R., Zhang, L. C., et al. (2018). Heat treatment enhancing the compressive fatigue properties of open-cellular Ti-6Al-4V alloy prototypes fabricated by electron beam melting. *J. Mat. Sci. Technol.* 34, 1127–1131. doi:10.1016/j.jmst.2017.12.003
- Zhang, L. C., and Chen, L. Y. (2020). A review on biomedical titanium alloys: recent progress and prospect. *Adv. Eng. Mat.* 21 (4), 1801215. doi:10.1002/adem.201801215
- Zhang, L., and Wang, S. G. (2018). Correlation of materials property and performance with internal structures evolution revealed by laboratory X-ray tomography. *Materials* 11 (10), 1795. doi:10.3390/ma11101795
- Zhang, M. K., Yang, Y. Q., Qin, W. T., Wu, S. B., Chen, J., Song, C. H., et al. (2020). Optimizing the pinch-off problem for gradient triply periodic minimal surface cellular structures manufactured by selective laser melting. *Rapid Prototyp. J.* 26, 1771–1781. doi:10.1108/rpj-11-2019-0298
- Zhang, Q. L., Wang, Y. S., Xiao, J., Li, D. Q., and Yin, S. T. (2009). Lattice distortion by the least square method. *Chin. J. Quantum. Elec.* 26, 177–186. doi:10.3969/j.issn.1007-5461.2009.02.010

Publisher's note

All claims expressed in this article are solely those of the authors and do not necessarily represent those of their affiliated organizations, or those of the publisher, the editors and the reviewers. Any product that may be evaluated in this article, or claim that may be made by its manufacturer, is not guaranteed or endorsed by the publisher.



OPEN ACCESS

EDITED BY

Chunguang Yang,
Chinese Academy of Sciences (CAS),
China

REVIEWED BY

Shujun Li,
Chinese Academy of Sciences (CAS),
China
Junlei Li,
Affiliated Zhongshan Hospital of Dalian
University, China
Rui Liu,
Shanghai Jiao Tong University, China

*CORRESPONDENCE

Xinyu Wang,
wangxinyu@jmsu.edu.cn

SPECIALTY SECTION

This article was submitted to
Biomaterials,
a section of the journal
Frontiers in Materials

RECEIVED 10 June 2022

ACCEPTED 01 July 2022

PUBLISHED 19 August 2022

CITATION

Zheng X, Duan F, Song Z, Mo H, Li Z,
Song Y, Su Y and Wang X (2022), A
TPMS-designed personalized
mandibular scaffolds with optimized
SLA parameters and
mechanical properties.
Front. Mater. 9:966031.
doi: 10.3389/fmats.2022.966031

COPYRIGHT

© 2022 Zheng, Duan, Song, Mo, Li,
Song, Su and Wang. This is an open-
access article distributed under the
terms of the [Creative Commons
Attribution License \(CC BY\)](https://creativecommons.org/licenses/by/4.0/). The use,
distribution or reproduction in other
forums is permitted, provided the
original author(s) and the copyright
owner(s) are credited and that the
original publication in this journal is
cited, in accordance with accepted
academic practice. No use, distribution
or reproduction is permitted which does
not comply with these terms.

A TPMS-designed personalized mandibular scaffolds with optimized SLA parameters and mechanical properties

Xiaoxiao Zheng^{1,2}, Feng Duan^{1,2}, Zhenyu Song², Hongbing Mo²,
Zhehao Li², Yihan Song^{1,2}, Yucheng Su^{3,4} and Xinyu Wang^{1,5*}

¹Key Laboratory of Oral Biomedical Materials and Clinical Application, Jiamusi University, Jiamusi, China, ²Experimental Center of Stomatology Engineering, Jiamusi University, Jiamusi, China, ³Beijing Implant Training College (BITC), Beijing, China, ⁴Dental Implant Center, Peking Union Medical College Hospital, China Academy of Medical Science, Beijing, China, ⁵Key Laboratory of Microecology-immune Regulatory Network and Related Diseases School of Basic Medicine, Jiamusi University, Jiamusi, China

With the rapid development of 3D printing technology, porous titanium scaffolds have provided a new restoration method to repair bone defects. Compared with the traditional body-centered cubic (bcc) dot matrix structure with a simple arrangement and repetitive structure, the topology-driven properties of triply periodic minimal surfaces (TPMS) can offer a continuous surface and smooth curvature, an excellent platform for cell proliferation. In this study, we used reverse engineering techniques to model the mandible. Sheet and solid networks of gyroid structure, the most common type of TPMS, were selected for porous design and then molded using metal 3D printing technology. At the same time, the surface treatment parameters of sandblasted, large-grit, and acid-etched (SLA) were optimized by orthogonal experimental design. Then, the optimized SLA parameter was used to treat the gyroid with 70% porosity. The result showed that reverse engineering reconstructed the TPMS-based mandibular model had good formability. Furthermore, the best surface morphology, wettability, and roughness were obtained for 3D printed Ti6Al4V under the treatment of 80 mesh Al₂O₃, blasting distances of 4 cm, and a 1:1:2 acid ratio. Moreover, the mechanical properties of Sheet-Gyroid and Solid-Gyroid were significantly different at 70% porosity. The porosity of the scaffolds was close to the design porosity after SLA treatment. However, no significant changes were found in its mechanical properties, all matching the mandible's mechanical properties to meet the implantation conditions.

KEYWORDS

triply periodic minimal surfaces, SLA, selective laser melting, orthogonal experimental design, mechanical behavior, bone defects, 3D printing, porous scaffolds

Highlights

- 1) Personalized porous design of bone defect sites was designed by using TPMS structures.
- 2) Optimal SLA surface treatment parameters were screened using an orthogonal experimental design for the pre-implantation treatment of 3D printed Ti6Al4V.
- 3) TPMS porous mechanical parts were processed with the screened SLA parameters to verify whether the mechanical properties match the bone defect site.
- 4) Our findings provided a new approach to bone defect regeneration.

Introduction

As people's aesthetic requirements increase, it is essential to restore the shape of the mandible, not only the original contour of the face but also the physiological function of the mandible. So, the repair and reconstruction of mandibular defects have been a hot topic of research in oral and maxillofacial surgery. Yet it still relies mainly on host autologous bone grafting to date, which is currently the best method for repairing minor segmental bone defects (Becker et al., 1996). Autologous non-vascularized free fibular grafts are also very common in the oral cavity (Dimitriou et al., 2011). Autologous bone grafting with vascularized is commonly used, but its surgical damage is more significant (Wei et al., 2016). Therefore, a bionic substitute of natural bone for bone grafting is now generally considered a more desirable treatment. Recent advances in tissue engineering techniques and personalized manufacturing (Zhu et al., 2016) hold promise in this setting.

Three main elements of tissue engineering are bone scaffolds, bone marrow mesenchymal stem cells (BMSCs) and induction factors (Zha et al., 2021). This study focuses on bone scaffolds, for which a variety of personalized scaffolds are available for the repair of mandibular defects (Milovanovic et al., 2020). However, none of the existing repair solutions achieves an ideal mandibular morphology, and mechanical properties are still to be improved. Ideal reconstruction of mandibular defects requires a complex curved restoration that conforms to the original form and restores function and good biomechanical compatibility with the remaining bone tissue. With the development of computer-aided design (CAD), computer-aided manufacturing (CAM) and 3D printing technology, it is possible to mimic the internal three-dimensional structure of the jaw anatomy and the external spatial shape, from microscopic to macroscopic structures, to meet the needs of individualized restorations (Tack et al., 2016; Memon et al., 2020).

The development of reverse-engineering techniques (Fucile et al., 2019) has made it possible to design scaffolds close to the shape of the original host bone defect. Therefore, the design of bone scaffolds focuses on mimicking the original morphology as closely as possible to reduce stress shielding and thus prolong

service life. The morphological design of scaffolds has moved from solids that would lead to stress shielding into the era of porosity. However, the restoration designs of the porous scaffolds are very complex. Structures based on simple cubic struts are among the most commonly used in 3D printed tissue engineering scaffolds, and this arrangement leads to severe anisotropy. Anisotropic structures are stiff in the axial direction and weak in the diagonal direction. They are considered detrimental in bone tissue engineering, especially when used as a load-bearing bone site (Pei et al., 2017; Zhang et al., 2018).

Recently, research interest has focused on triply periodic minimal surfaces (TPMS) designs due to their unique mechanical and biological characteristics (Yoo, 2011; Yoo, 2012; Walker et al., 2017). TPMS describes the scaffold's structure through mathematical functions. By adjusting its parameters, the pore parameters can be adjusted to achieve changes in the structural and mechanical properties of the scaffold. Compared to conventional dot-matrix structures, the TPMS method produces a continuous surface structure that is inherently topologically optimized and provides better self-support during selective laser melting (SLM) processing (Lu et al., 2020). TPMS scaffolds have a very high surface area to volume ratio, and this high specific feature of TPMS scaffolds helps to enhance cell adhesion, migration, and proliferation (Yoo, 2014). Many cellular and biological functions, such as ion exchange, oxygen diffusion and nutrient transport, occur on its surface (Pei et al., 2020). Therefore, TPMS scaffolds provide better biological signaling platforms for cells cultured on them. In addition, the infinitely continuous surface with smooth joints ensures fewer stress concentrations and higher mechanical properties than a regular lattice structure support. TPMS function enables a more straightforward implementation of structural parameter variations (Al-Ketan and Abu Al-Rub, 2021), overcomes the drawbacks of traditional truss cell structure design and allows automatic acquisition of digital models of porous bone support with complex microstructures and high-quality surfaces.

To enable good osseointegration of the metal scaffolds after implantation and facilitate osteoblasts' adhesion, proliferation, and differentiation, sandblasted, large-grit, and acid-etched (SLA) (Chambrone et al., 2015), anodizing (Ross and Webster, 2013), micro-arc oxidation (Zhang et al., 2021), and SLActive (Chambrone et al., 2015) surface treatment technologies for titanium alloys are proposed. The SLA forms a surface with a certain number of nested pores, which increases the microscopic surface area of the material and facilitates the mineralization of the extracellular matrix and the differentiation of osteoblasts in contact with the surface. At the same time, SLA as a treatment for cell growth scaffolds increases the adhesion between tissue and material. Further, the nanoscale morphology facilitates the synthesis and adsorption of specific proteins in the extracellular matrix, promoting cell adhesion (Kohal et al., 2013).

In biomedical applications, particularly in artificial implants, a combination of appropriate porous materials, porous structures, and

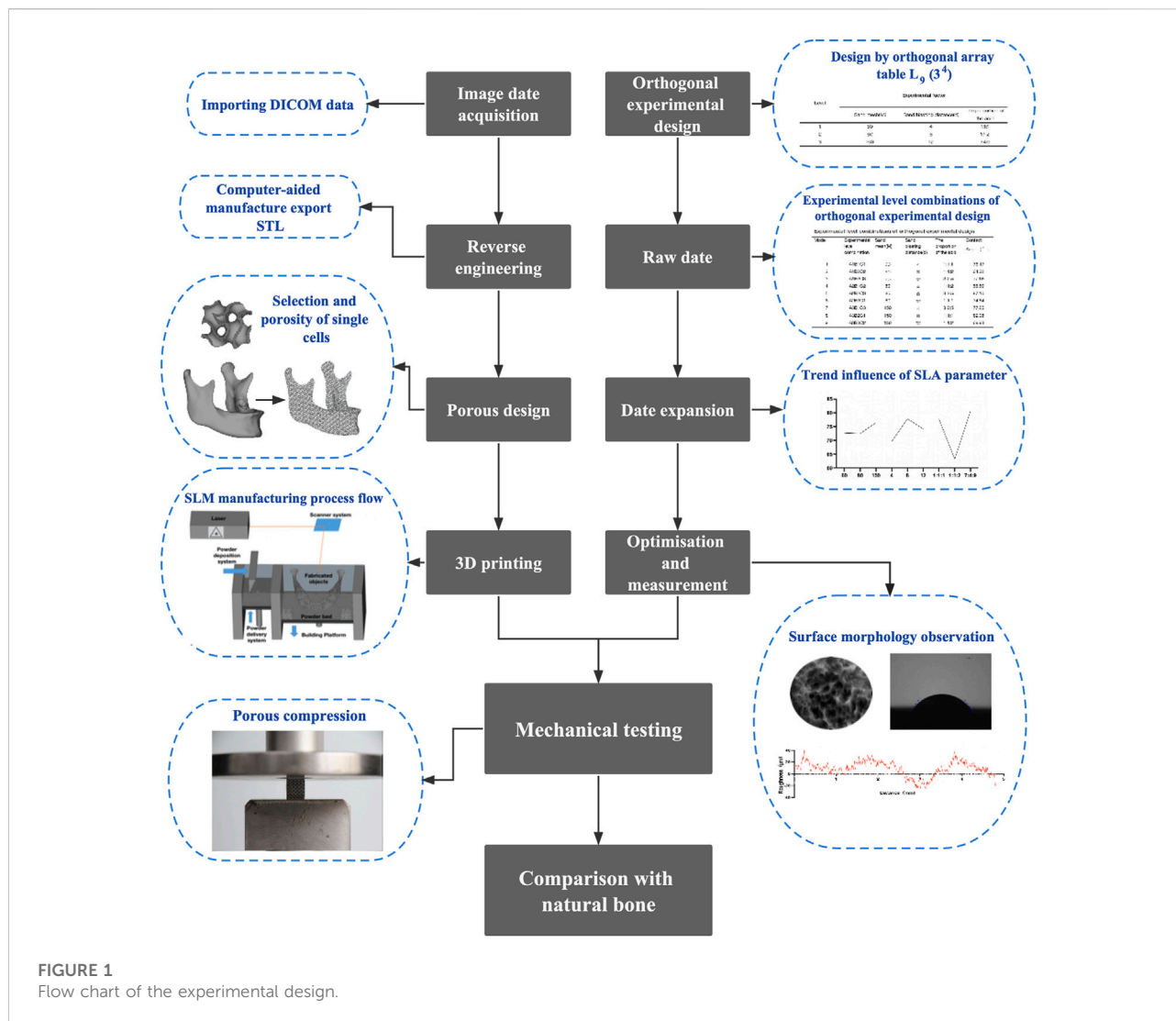


FIGURE 1
Flow chart of the experimental design.

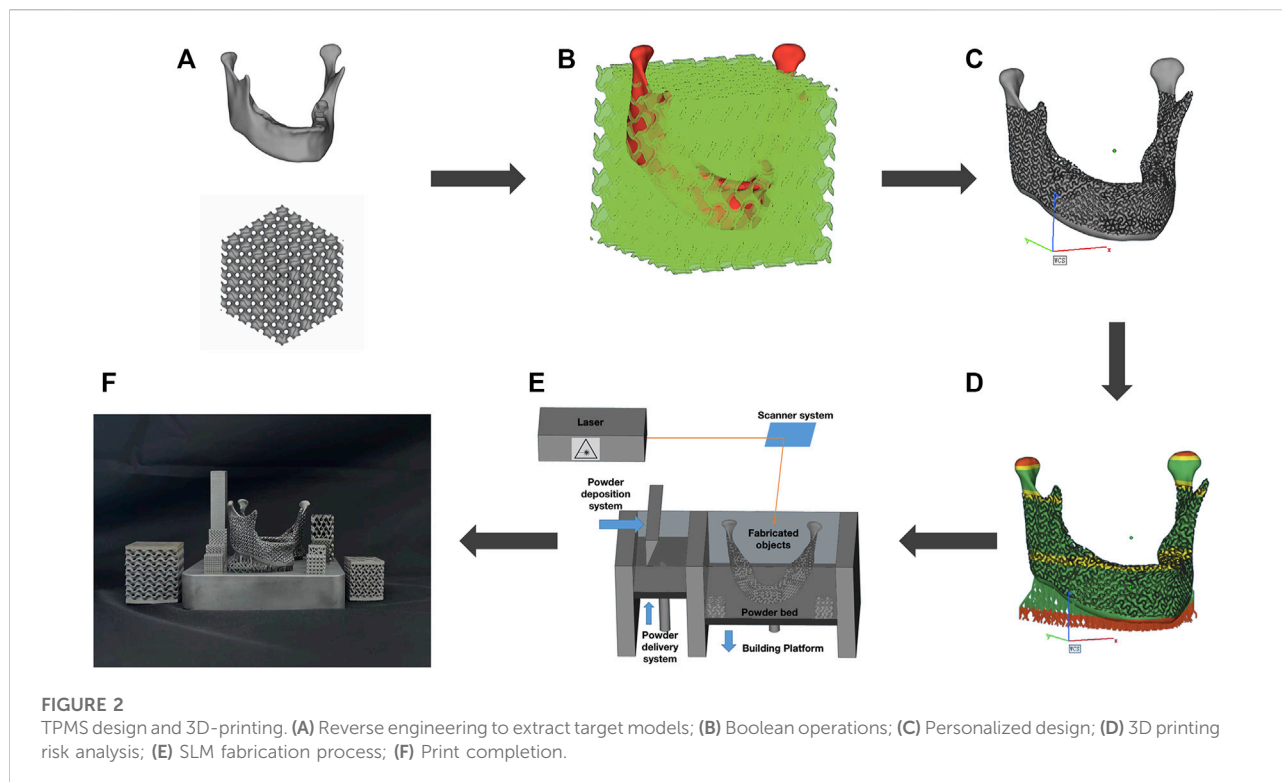
optimum parameters can reduce the elastic modulus of the implant, thus overcoming the stress shielding effect and preventing loosening of the implant (Arabnejad et al., 2016). Optimized morphological parameters, such as pore size and porosity, are also essential to ensure the success of bone implants. For ideal osseointegration, the optimum porosity should exceed 60%. Furthermore, the pore size should be between 600 and 900 μm (Zaharin et al., 2018; Pei et al., 2020). Yan et al. (2015) customized the TPMS scaffolds with SLM to match the elastic modulus of human bone, thus avoiding stress shielding of the implant and improving its durability. Melchels et al. (2010) designed TPMS scaffolds with gyroid on which BMSCs were grown. The results showed that the TPMS scaffolds had a greater cell density and cell distribution than scaffolds prepared by traditional salting. And its permeability was improved by a factor of 10. Lan Li et al. (2019) implanted the 3D printed P-structured TPMS metal scaffolds into the mini-pigs tibia and explored the osseointegration ability of TPMS-based bone substitutes for the first time in an *in vivo*

study, confirming the potential of TPMS-based bone substitutes in bone tissue repair.

In this research, 3D printed Ti6Al4V scaffolds with 70% porosity based on the gyroid structure design in TPMS were printed to investigate the relationship between the sheet and solid networks. The optimum parameters for SLA surface treatment were selected by orthogonal experiment design. After SLA treatment, the Sheet-Gyroid and Solid-Gyroid scaffolds were verified to be in good accordance with the requirements for human mandibular implantation through porous mechanical compression testing.

Materials and methods

Figure 1 shows the main flow of this experiment. First, reverse engineering techniques reconstruct the imaging data in



three dimensions. An orthogonal experimental design was performed to screen the optimal SLA approach. After that, mechanical tests were carried out on the SLA-treated TPMS. And the results were compared with that of the normal bone to determine if its mechanical properties were compatible with the normal mandible.

Personalized TPMS scaffolds design and 3D printing

Scaffolds design

The design is simplified, as shown in Figure 2, and the study is approved by Jiamusi University stomatological hospital ethics committee (NO.2022-KQYY-XS-06), and the volunteer and his family members signed informed consent. The image was scanned by the cone-beam computed tomography (CBCT; Dentsply Sirona, Germany) at 85 kV and 6 mA, 11×10 cm field of view (FOV), voxel size of 0.16 mm for 14.4 s, and the scans were saved in Digital Imaging and Communication in Medicine (DICOM) file format.

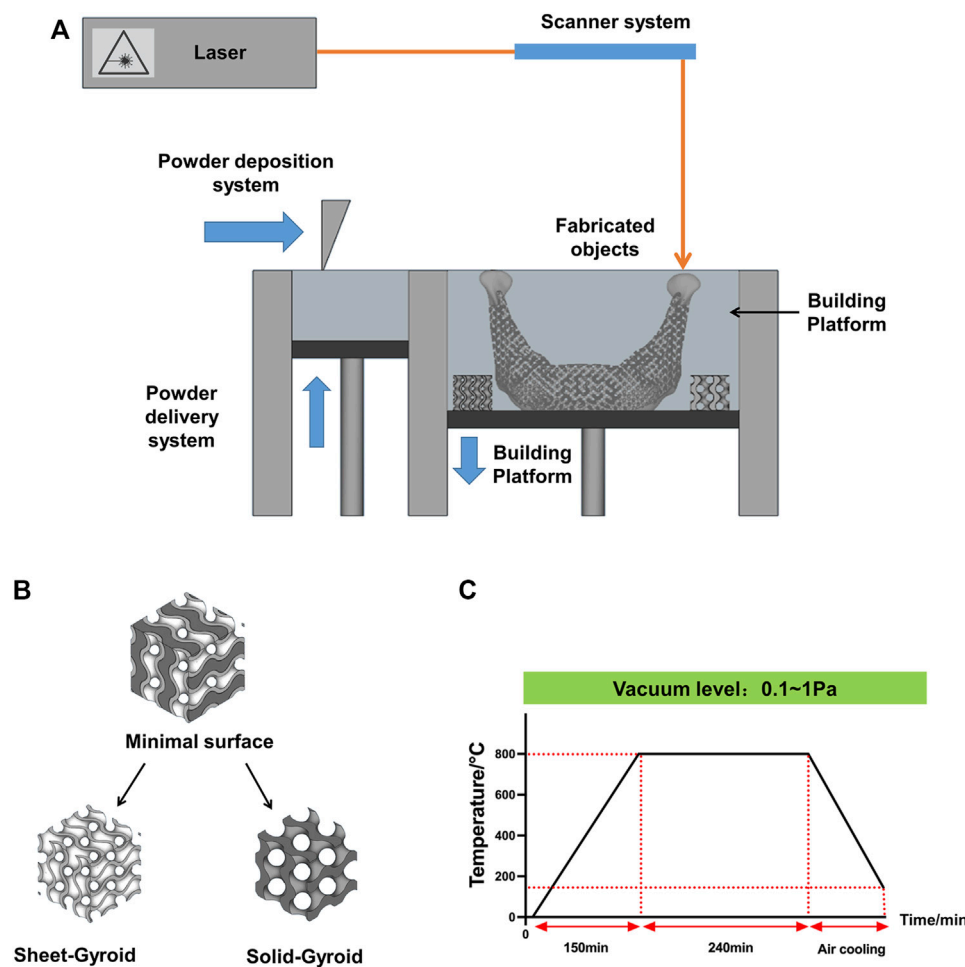
In reverse engineering, as shown in Figure 2A, the mandibular DICOM file was threshold segmented using Mimics 19.0 software (Materialise, Belgium), 3D-reconstructed, smoothed, and denoised to create customized models of bone defects such as whole mandible, half mandible, and partial mandible. Data was saved in the standard triangular language (STL) file format.

The STL data was then entered into MSLattice software (New York University Abu Dhabi, Abu Dhabi), based on the principle of Boolean operations shown in Figure 2B. The gyroid structure in TPMS with a unit cell size of 2 mm, a porosity of 70%, and a mesh density of 30 points was selected. It is important to note that during mandibular re-placement surgery or arthroplasty, the subarticular cavity was opened; the condyle should be solidified to avoid soft-tissue growth during the healing process. In this research, an interconnected biomimetic porous TPMS structure was designed, and their relationship was sheet networks and solid networks, as shown in Figure 3B.

2 mm supports were generated in Magics 26.0 software (Materialise, Belgium), as shown in Figure 2C, and fitted with superstructure adjustment coordinates. Then, the file was subjected to a print risk analysis, as shown in Figure 2D. Once the analysis was complete, slicing was carried out with a slice thickness of 0.025 mm, and a Concept Laser Slicer (CLS) format file was exported as a print prep file and then transferred to a 3D printer (Figure 2E).

3D printing and post-processing

The Mlab cusing 100R (Concept laser, Germany) was used to produce the personalized scaffolds and rectangular mechanical specimens, as shown in Figure 3A. Furthermore, the Ti6Al4V powder (Concept laser, Germany) of 10–53 μm was used as printing material. The



To remove stress, enhance the toughness of 3D printed Ti6Al4V specimens and improve their mechanical properties, they had to be heat-treated by a vacuum heat treatment furnace (Beijing Hangxin AM Technology Co. Ltd., China). Firstly, vacuum circumstance was achieved by vacuum pumping for 10 min (vacuum degree below 1 Pa). A temperature of 800 °C was achieved at 150 min under a vacuum state and preserved for 240 min. Then with the air cooling to 150 °C, open the chamber and remove the specimens. The heat treatment process is shown in [Figure 3C](#).

Orthogonal experimental design and optimization analysis

SLA's surface morphology and contact angle are affected by various factors, including the blasting distance, grit mesh, proportion of the acid, blasting angle, blasting time, acid etching time, and temperature (Rupp et al., 2004). Based on the results of previous exploratory experiments and the surface treatment methods used as previously described (Perrin et al., 2002), the controlled temperature of 75°C and reaction time of 30 min were selected for the surface treatment of the 3D printed porous Ti6Al4V scaffolds. Three surface treatment parameters, A (grit mesh), B (sandblasting distance), and C (the proportion of the acid), were chosen as orthogonal experimental factors, Where Al₂O₃ (Beijing Hangxin AM Technology Co. Ltd., China) is chosen as the grit for sandblasting, the ratio of an acid refers specifically to the ratio of sulfuric acid (Tianjin Kaitong Chemical Reagent Co. Ltd., China), hydrochloric acid (Tianjin Kaitong

TABLE 1 Orthogonal experimental design.

Level	Experimental factor		
	Grit mesh	Sandblasting distance	The proportion of the acid
1	60	4	1:1:1
2	80	8	1:1:2
3	150	12	7:4:9

Chemical Reagent Co. Ltd., China) and deionized water (Tianjin Kaitong Chemical Reagent Co. Ltd., China). Three levels were selected for each factor (Table 1), and an orthogonal table $L_9(3^4)$ was selected.

The sample surface morphology was characterized by field emission scanning electron microscopy (FE-SEM; FJEOL, Japan). The biocompatibility of 3D-printing Ti6Al4V scaffolds is directly related to their surface wettability (Yu et al., 2020). The contact angle is an important feature in determining materials' wettability. The smaller the intact angle is, the better the wettability is. Two microliters of deionized water were dropped onto the sample's surface after the spread was completed, and the contact angle was detected using a contact angle goniometer (Power each, China). The droplet image was captured and frozen for angle measurement. And we measured surface roughness with a compact roughness measuring instrument MarSurf PS10 (Mahr GmbH, Germany). Its maximum measuring range is 350 μm ($-200 \mu\text{m}$ to $+150 \mu\text{m}$).

According to the orthogonal experimental design, nine groups of experimental level combinations (the combinations of surface treatment parameters) were determined. The impact of different SLA parameters on the contact angle was determined and put in order through orthogonal experimental optimization analysis, and an optimal combination was then obtained.

Porosity measurement and mechanical properties of TPMS

Porosity

Porosity is measured by weight and drainage methods. In the weight method, M_a and M_{theory} is the weight of the specimens in air and the theoretical weight of Ti6Al4V, the porosity 'P' was calculated with the equation

$$P = 1 - \left(\frac{M_a}{M_{\text{theory}}} \right) \times 100\%$$

Another method is the drainage method, where the suspension derives the object's mass in water ' M_w '. The ρ_{water} and ρ_{theory} are the density of water, and Ti6Al4V is 1 g cm^{-3} and

4.41 g cm^{-3} , respectively. And the porosity is calculated according to the buoyancy of the specimens.

$$P = \frac{\frac{M_a \times \rho_{\text{water}}}{M_w}}{\rho_{\text{theory}}} \times 100\% = \frac{M_a}{4.41 \times M_w} \times 100\%$$

Design porosity can be derived directly from CAD software.

Mechanical properties

Porous rectangular specimens were subjected to a quasi-static compressive test using a Universal tester Machine (Jinan Heng Rui Jin Testing Machine Co., Ltd., China). According to ISO13314:2011 standard (Standard, 2011), porous rectangular specimens (Sheet-Gyroid or Solid-Gyroid structures; length: 12 mm, width: 10 mm, with one 0.5 mm rectangular sheet on both ends to avoid stress concentrations during the 3D printing process and the removal of supports after printing; five rectangular specimens for each type) before and after SLA were compressed at a head speed of 1.2 mm min^{-1} . The compression stop condition is compressed until the displacement is 8 mm or the force reaches 99 KN.

In this study, elastic modulus (E) was defined as the slope of the stress-strain curve within the elastic deformation region, offset yield strength (σ_s) was set at compressive 0.2% offset stress, and compressive strength (σ_{bc}) was determined as the first local maximum in the stress-strain curve.

Result

Orthogonal experimental design results

First, we measured the contact angle and observed the SEM. The contact angle of the 3D printed titanium samples is shown in Table 2. Among the nine groups, the highest contact angle was 82.24° (group $A_2B_2C_3$, Figure 4E), and the lowest value was 54.55° (group $A_2B_1C_2$, Figure 4D). According to these results, minor variations in surface treatment parameters of the SLA could lead to a significant change in contact angle (the maximum change value was 27.69°), indicating the significance of the surface treatment method.

TABLE 2 Experimental level combinations of orthogonal experimental design.

No.	Experimental level combination	Grit mesh	Sandblasting distance	The proportion of the acid	Contact angle (°)
1	A ₁ B ₁ C ₁	60	4	1:1:1	75.37
2	A ₁ B ₂ C ₂	60	8	1:1:2	64.03
3	A ₁ B ₃ C ₃	60	12	7:4:9	77.72
4	A ₂ B ₁ C ₂	80	4	1:1:2	54.55
5	A ₂ B ₂ C ₃	80	8	7:4:9	82.24
6	A ₂ B ₃ C ₁	80	12	1:1:1	73.74
7	A ₃ B ₁ C ₃	150	4	7:4:9	77.66
8	A ₃ B ₂ C ₁	150	8	1:1:1	81.66
9	A ₃ B ₃ C ₁	150	12	1:1:2	69.94

Analysis of the SEM of these nine groups of samples shows that as the concentration of hydrochloric acid decreases, grit residues from sandblasting begin to appear. In the third group, residual sandblasted particles can be observed in Figure 4C. Their grits are proven to affect osseointegration (Pei et al., 2020) and need to be removed prior to implantation. As shown in Table 2, the contact angle was also larger in these groups than in the remaining two groups.

The contact angle range of nine surface treatments was analyzed. Table 3 presents the results of the orthogonal experiment design, in which K represents the mean of the contact angle for the same experimental factor at the same level. The range was calculated by using the following formula:

$$R = \max_k - \min_k$$

where R represents the range of the same experimental factor. In other words, R is the extreme difference of the same factor.

According to the results of the range analysis of the orthogonal experimental design, the greater the R was, the more significant their influence was. The proportion of the acid had the most significant effect, followed by the sand mesh. In contrast, the sandblasting distance had the slightest effect. Through the range analysis (Figure 5), the optimal SLA parameters for the 3D printed Ti6Al4V were A₂B₁C₂. Specifically, the optimal SLA parameters were 80 mesh Al₂O₃, blasting distance of 4 cm, and the proportion of the acid of 1:1:2.

Verification of the optimized SLA parameters derived from the orthogonal experimental design

To verify the optimization results, we repeated the experiment. SEM results showed that the sandblasting process formed irregular pits and many sharp protrusions with several

tens of microns on the surface of the specimens. This caused partial exfoliation of the substrate (Figures 6B,E). Compared with Figures 6A,D, sandblasting removed the half-melted powder during the additive fabrication process and residual titanium alloy powder, which could not be removed by simple cleaning and is harmful to implantation (Wang et al., 2017; Song et al., 2019). So, the surface matrix exfoliation and grit residue due to sandblasting require further acid etching to remove.

Figure 6C showed that the simple sandblasting treatment creates an irregular surface roughness of several tens to hundreds of microns, and they were the first surface roughness level. Upon further magnification (Figure 6F), the treated sample's surface forms a pore-like roughness with a micro-nano composite. Further magnification can be observed that there are also many small pore structures of several microns in size within the large pores. There were some nano-convex structures within these tiny pores, which were the tertiary pores formed by the surface treatment.

Results also demonstrated that the surface contact angle of the SLA optimized specimens was 53.07° (Figure 6I). The surface contact angle of the sandblasted specimens was 49.98° (Figure 6H), both of which were statistically significant compared to the surface contact angle of the untreated specimens of 80.25° (Figure 6G), indicating that the SLA treatment can increase the surface hydrophilicity. Compared with the samples only treated by sandblasting, SLA treatment slightly increased the contact angle (Figure 6K).

The roughness of the surface is presented in Figures 6J,L, I. Both the SLA treatment and the sandblasting treatment reduced the surface roughness. The roughness was significantly lower in the sandblasted group ($R_a = 2.66 \mu\text{m}$, $R_q = 3.36 \mu\text{m}$) and SLA group ($R_a = 3.37 \mu\text{m}$, $R_q = 4.24 \mu\text{m}$) only compared to the untreated group ($R_a = 7.97 \mu\text{m}$, $R_q = 9.73 \mu\text{m}$). An ideal roughness should be between 1–10 μm (Yu et al., 2020), both treatments resulted in roughness within this range.

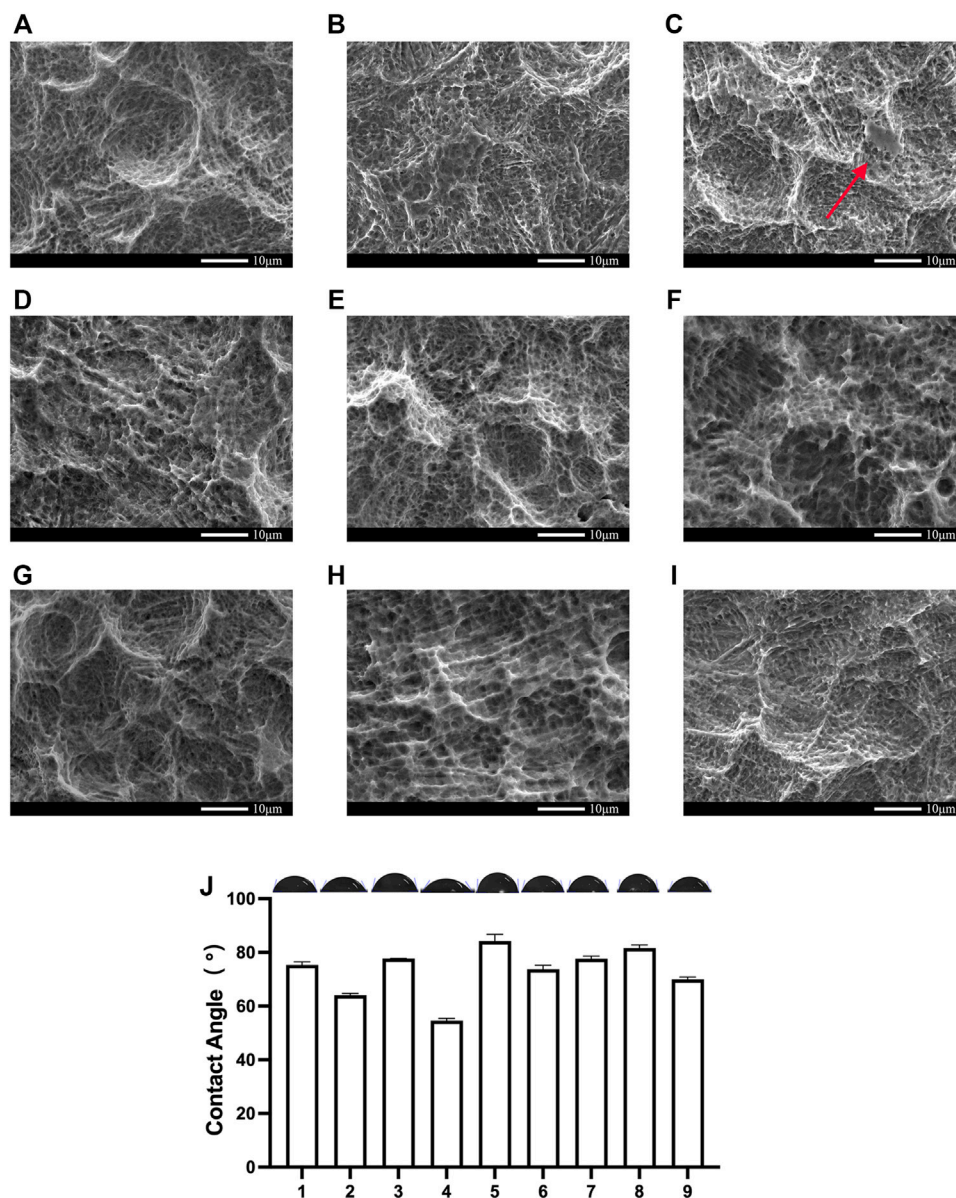


FIGURE 4

SEM and contact angle of the Orthogonal experimental design. (A) group; (B) group; (C) group; (D) The group; (E) The group; (F) The group; (G) The group; (H) The group; (I) The group; (J) The contact angle of the Orthogonal experimental design. Error bars represent means \pm SD and specimens number $n = 3$.

Porosity test results

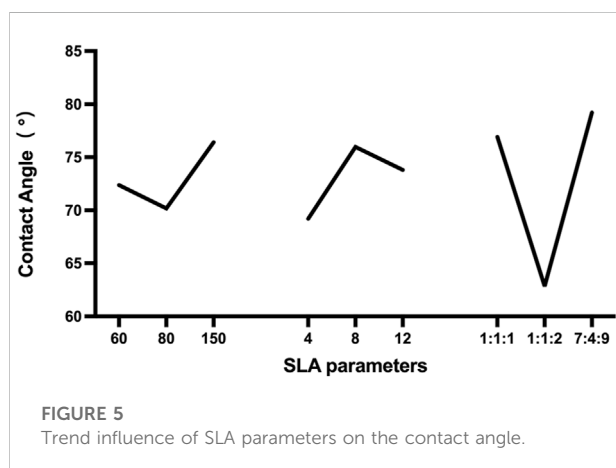
After 3D printing, the porosity was measured and presented in Table 4. Generally, as-built specimens' porosities were 15% lower than designed porosity. After surface treatment, porosity increased and approached the designed value. There was no statistical significance between porosity measurement by weight method and drainage method.

Mechanical properties results and comparison with bone defect sites

Sets of compressive stress-strain curves of Sheet-Gyroid and Solid-Gyroid structures before and after SLA treatment are depicted in Figure 7A, respectively, and their strain pictures under compression (Figure 7B). The specimens cracked along a 45-degree highly stressed band where the red color indicates, and

TABLE 3 Optimization of the results of the orthogonal experimental design.

No.	Experimental factor				Contact angle (°)
	A	B	C	D	
1	1	1	1	1	75.37
2	1	2	2	2	64.03
3	1	3	3	3	77.72
4	2	1	2	3	54.55
5	2	2	3	1	82.24
6	2	3	1	2	73.74
7	3	1	3	2	77.66
8	3	2	1	3	81.66
9	3	3	2	1	69.94
K1	72.373	69.193	76.923	—	—
K2	70.177	75.977	62.840	—	—
K3	76.420	73.800	79.207	—	—
Range R	6.243	6.784	16.367	—	—
Ranking	C > B > A	—	—	—	—
Optimal level	A2	B1	C2	—	—



all the structures tend to present a severe drop in strength associated with shear collapse.

SLA removed the remaining unmelted particles on the surface, weakening the specimen's strength, but not statistically significant, as shown in Figures 7C–E. From Table 5, the effect on mechanical properties before and after surface treatment was insignificant. The yield strength of the Sheet-Gyroid decreased only 15.37 MPa, and compressive strength decreased only 17.15 MPa. In contrast, the yield strength of Solid-Gyroid decreased only 10.36 MPa, and compressive strength decreased only 12.85 MPa. Both were not statistically significant, proving that SLA treatment could

increase the porosity without affecting the mechanical properties. This result was certainly good news for the subsequent clinical implantation of TPMS, as we hope to have the best mechanical properties while obtaining a higher specific surface area. We also found that the mechanical properties of the Sheet-Gyroid were better than those of the Solid-Gyroid in all cases. The elastic modulus of gyroid without SLA decreased from sheet to solid by 1.09 GPa, and the yield and compressive strength decreased by 79.81 and 96.22 MPa, respectively. After SLA, The Sheet-Gyroid and the Solid-Gyroid elastic module decreased by 1.36 GPa, and the yield and compressive strength decreased by 74.8 and 91.92 MPa, respectively.

To make metal scaffolds to be suitable for replacing natural bone, their mechanical properties must match that of the normal bones. The material's mechanical strength can be easily manipulated by changing equation. A comparison of the elastic modulus of all porous structures was performed with that of natural bone. The mechanical properties of the porous scaffold had to be within the range of that of the normal bone to avoid stress shielding. The modulus of elasticity of cortical bone and cancellous bone are 4–30 MPa and 0.2–2 GPa (Li et al., 2014), respectively, and the modulus of elasticity of the human mandible is 0.56–12.7 GPa (Novaes et al., 2010). All specimens in this experiment had a modulus of elasticity within the range. Another factor to be considered when selecting a suitable porous structure is the yield strength of the sample. The yield strength of natural bone is reported in the literature to be between 20–193 MPa (Li et al., 2014). All specimens were within the required yield strength range except for the untreated Sheet-Gyroid group in this experiment (Figure 7F). The individual values were slightly higher than the yield strength of natural bone, but the average values were still within the required range (Figure 7G).

Discussion

Porous structures have many application scenarios in the field of bone tissue regeneration (Guvendiren et al., 2016; Jammalamadaka and Tappa, 2018). Yet, the performance of porous structures designed by existing techniques in cell adhesion and proliferation is not ideal, mainly due to their unsmooth surfaces (Pei et al., 2020). Researchers have found that TPMS has the property of generating continuous surface and smooth curvature, hence, we adopted TPMS to design porous supports in this paper. In the fabrication of porous structures, 3D printing has its unique advantages because of its ability to precisely control cytoskeletal elements such as pore size, trabeculae, and wall thickness of porous structures. In addition, 3D printing can meet the needs of individual designs. In this study, we used reverse engineering techniques to extract the mandibular model, completed the porosity design based on the TPMS functions, and finally, the product molding

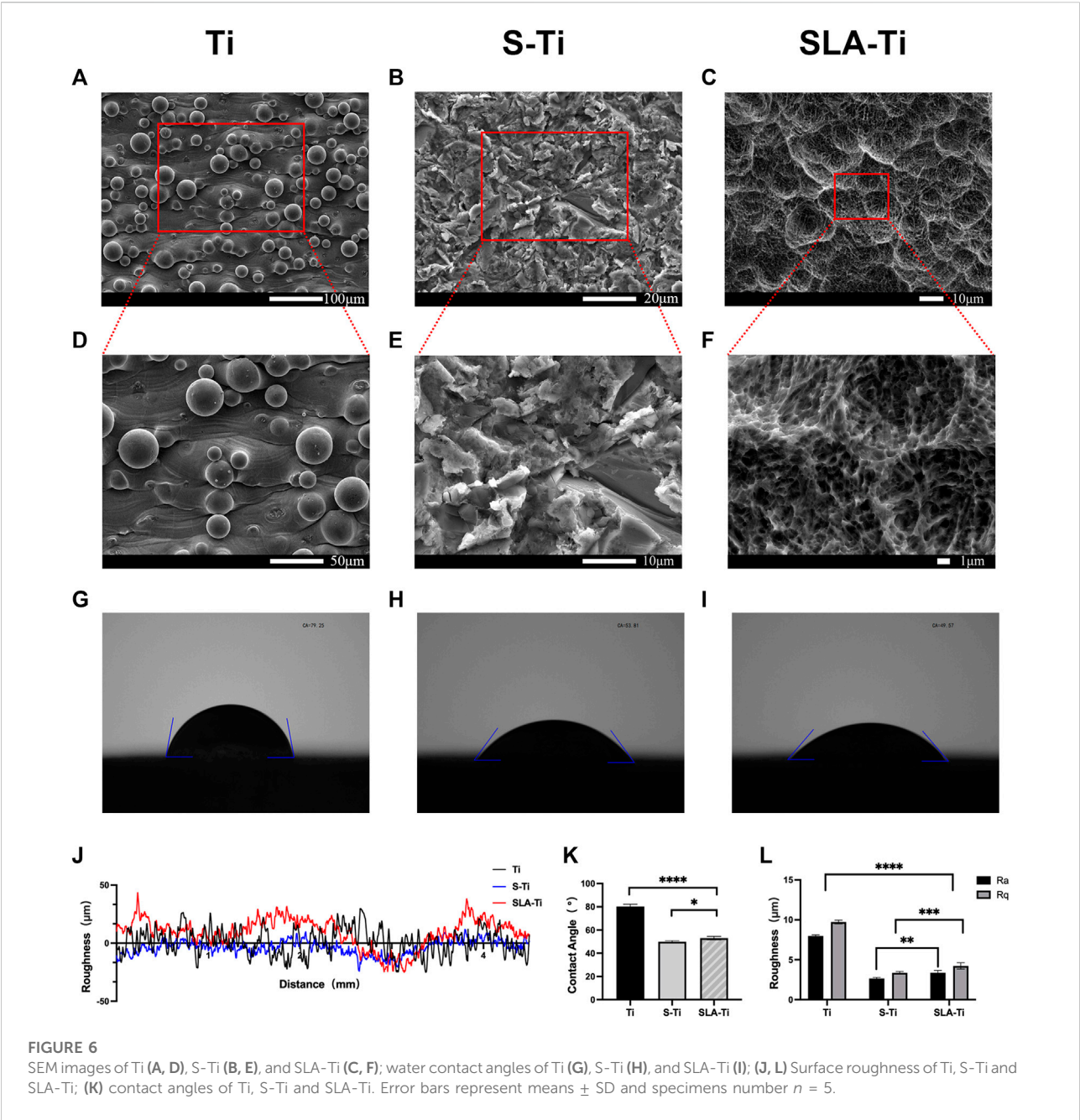


TABLE 4 Pore characterization of the porous structure.

Design porosity (%)		Weight method		Drainage method	
		As-built porosity (%)	Post-SLA porosity (%)	As-built porosity (%)	Post-SLA porosity (%)
Sheet-Gyroid	70	55.26	66.18	56.03	67.69
Solid-Gyroid	70	57.37	70.08	56.87	69.65

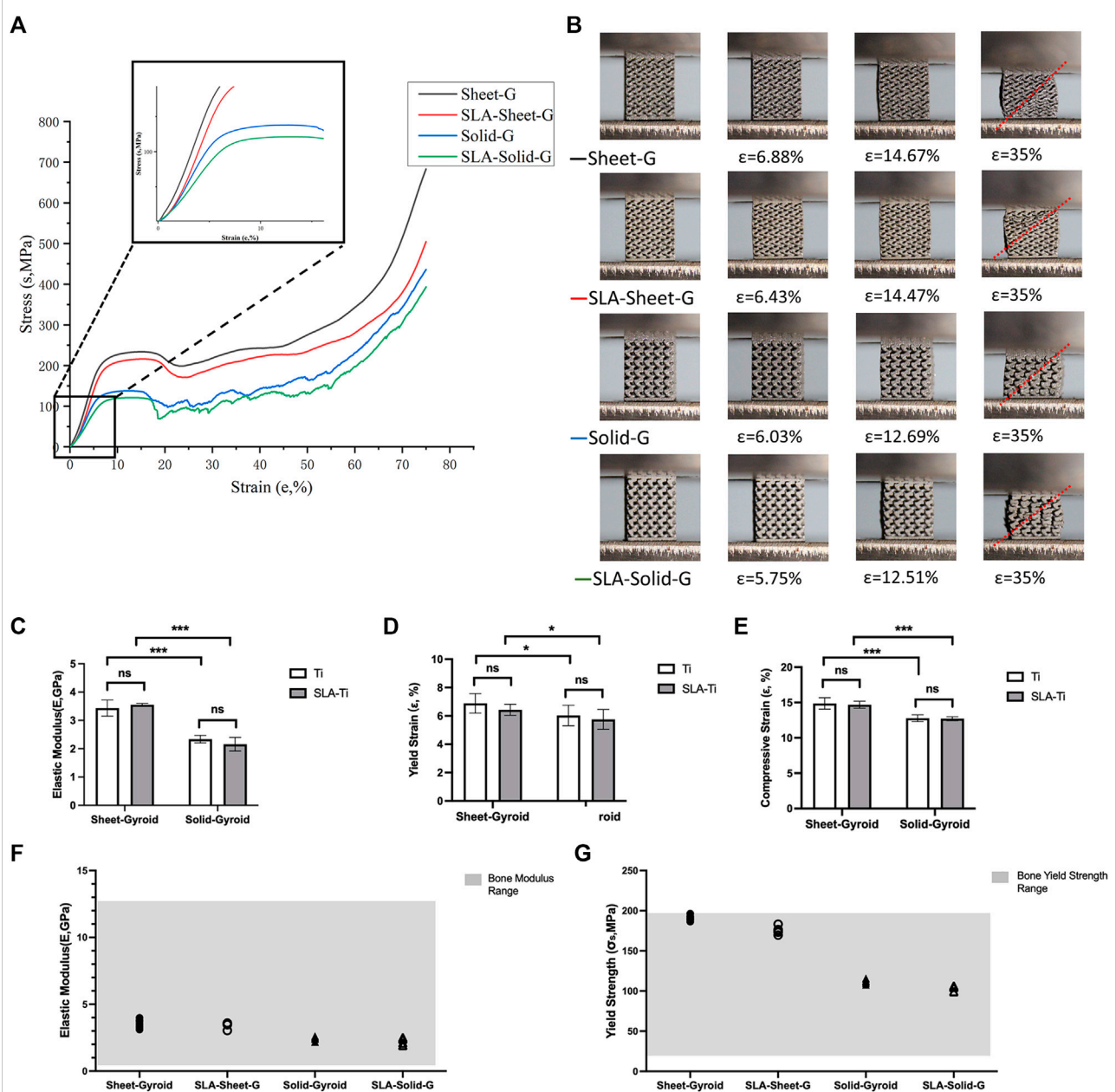


FIGURE 7

(A) Compressive stress-strain curves of Sheet-Gyroid and Solid-Gyroid structures before and after SLA; (B) Pictures of the corresponding strain from the compression; Elastic Modulus (C), corresponding yield strain (D) and corresponding compressive strain (E) of Sheet-Gyroid and Solid-Gyroid before and after SLA. Comparison between numerical and experimental elastic modulus (F) and yield strength (G) for Sheet-Gyroid and Solid-Gyroid samples before and after SLA in the range of bone modulus. Error bars represent means \pm SD and specimens number $n = 5$.

was carried out by 3D printing. Meanwhile, we performed an orthogonal experimental design to filter and optimize the SLA parameters. Surface treatment of 3D printed Ti6Al4V scaffolds was carried out, and porous compression experiments were conducted to evaluate its mechanical properties. The results demonstrated that the porous scaffold matched well with the

mechanical properties of the bone and met the implantation criteria.

In the metal additive manufacturing process, the TPMS-based printed product was slightly different from the designed one. We believed that the melt pool's temperature and geometry affected the products' density, ultimately leading to the difference

TABLE 5 Results of static compressive tests.

		Elastic modulus (E,GPa)	Yield strength (σ_s ,MPa)	Compressive strength (σ_{bc} ,MPa)
Sheet-Gyroid	Ti	3.43 \pm 0.28	192.17 \pm 2.84	233.44 \pm 2.37
	SLA-Ti	3.55 \pm 0.05	176.80 \pm 3.72	216.29 \pm 2.92
Solid-Gyroid	Ti	2.34 \pm 0.13	112.36 \pm 2.42	137.22 \pm 1.33
	SLA-Ti	2.16 \pm 0.24	102.00 \pm 3.06	124.37 \pm 2.44

between the as-built products and the design. The main parameters affecting the temperature and geometry of the melt pool are the layer thickness, scanning speed, laser power, hatch distance, and spot diameters (Casati et al., 2016). The Mlab series we chose in this paper was an SLM device with minor spot diameters on the market. Therefore, we should optimize the parameters other than the spot diameters, such as scanning speed, layer thickness and hatch distance, by controlling the energy density formula to improve the printing accuracy. In addition, by observing the gyroid structure, we found powder staining at the interface between its parallel and lower surfaces, which was due to the limited heat dissipation during the printing process (Vaithilingam et al., 2016). This reason caused the half-melted powder to remain on the porous support, which may also be one of the reasons for the difference between the product and the design.

To solve the limited heat dissipation during the 3D-printing process mentioned above, we usually need to add additional supports to enhance heat dissipation. Supports can be divided into solid and non-solid supports. Solid supports are responsible for anchoring the part, and non-solid supports safeguard the quality of the lower surface of the part. However, we found that the SLM-printed gyroid structure met the requirement of self-supporting. The tilt angle of each layer was less than 45°, which further validated that SLM technology was suitable for printing gyroid structures.

Reportedly, the TPMS surpasses conventional porous titanium scaffolds in several aspects. First, although the mechanical properties of the conventional cube structures are slightly better than those of the gyroid structures, only the cube porous structures with a pore size of 0.3–0.5 mm are suitable for implant application according to implantation young's modulus (Zaharin et al., 2018). In contrast, the gyroid structures for implant application have a more comprehensive range of pore sizes. Secondly, the mechanical properties of this paper's 70% gyroid structures were better than those of the Voronoi structures but worse than those of the gradient varying Voronoi structures (Wang et al., 2018). Finally, when compared with the diamond structure in TPMS, the gyroid exhibits better performances than the diamond in terms of the elastic modulus, ultimate strength and ductility (Liu et al., 2020).

As we all know, porous structures' mechanical properties have different applications in different fields (Wang et al., 2018). When the porous structure is used as a load-bearing structure, the porous

structure mainly works in the elastic phase and yield phase, and the focus is on the elastic modulus and yield stress of the porous material; when the porous structure is used as an impact-resistant material, the porous structure mainly works in the platform phase and densification phase. The maximum compressive strength of the porous material is crucial for its function. Relatively speaking, the performance in the elastic phase is of more interest for biological scaffolds. The elastic modulus needs to match the human bone to reduce the stress shielding of the implant, and the high yield stress has a positive effect on improving the fatigue resistance of the implant (Liu et al., 2016). According to the Gibson–Ashby model (Gibson, 2005), the porosity of the porous structure can be adjusted to match the actual requirements of elastic modulus and yield stress at the implant site. However, these studies were based on porous structures of the same unit cell size. They did not consider the effect of pore size variation on mechanical properties. In this paper, we confirmed whether there was no significant difference in mechanical properties between sheet networks and solid networks for TPMS, including elastic modulus and yield strength, which provides a new consideration for the design of scaffolds.

According to the above discussion of porous structure mechanical properties, we can reversely model the bone defect site preoperatively and match the mechanical properties with it during the porosity design of the porous scaffolds. For example, the mechanical properties of the defect site can be matched by changing the unit cell size and porosity and selecting different TPMS structures as well as sheet networks or solid networks in MSLattice software (Al-Ketan and Abu Al-Rub, 2021). Then, we consider using Finite Element Analysis (FEA) simulated the forces in the natural bone. The pre-process for the implant can be performed if the mechanical properties match the implantation criteria. If not, the mechanical properties can be fine-tuned by changing these four parameters for further optimization.

We also found that the SLA treatment formed a multi-level pore structure on the surface of the titanium alloy. Also, enhanced hydrophilicity and reduced roughness were observed. Among the pore structures, the formation of the first-class structure was caused by the local stress concentration phenomenon on the surface of the samples during the sandblasting process. These stress concentrations manifest as uneven corrosion during acid etching, where large

craters of several tens of microns formed during the blasting process with large grains of grit, while small pore structures of several microns and nanometers were formed during the acid etching process (Xing et al., 2014). To be specific, the acid etching process can not only form a multi-level hole structure on the highly irregular surface after sandblasting, release the local stress concentration caused by sandblasting, pin down the sharp peaks formed after sandblasting, but also remove the residual sandblasting grit on the surface of the substrate after sandblasting (Stepanovska et al., 2020). In addition, according to the results of orthogonal experiments, more sandblasted particles were left on the sample surface when the concentration of hydrochloric acid decreased. According to the literature (Yu et al., 2020), the attachment of more metal powder on the metal surface of 3D-printed titanium alloy may be the reason for the higher R_a and R_q value. Furthermore, the surface chemistry of 3D-printed titanium alloy was changed by acid etching to increase its hydrophilic properties.

The above discussion of this experiment was based on 3D printing, surface treatment and mechanical properties. Based on the present experiments, we will expand the selection of porosity and choose more minimal surface structures to explore the mechanics of TPMS and conduct further cellular and animal experiments to verify its effect on osseointegration. Moreover, we can follow the irregular variation of natural bone and design a porous gradient structure for further study.

Conclusion

The TPMS-based design of the mandible model reconstructed by reverse engineering has good formability. Under 80 mesh Al_2O_3 , sandblasting distance of 4 cm and 1:1:2 acid ratio, the 3D-printed Ti6Al4V resulted in the best surface finish morphology, wettability, and roughness. At 70% porosity, the mechanical properties of Sheet-Gyroid and Solid-Gyroid were significantly different. The SLA treatment resulted in a scaffold with porosity close to the design porosity and had no significant effect on its mechanical properties. The study can be applied not only to the mandible but also to any bone defect in any part of the body by adjusting the parameters. It also provides an idea for SLA surface treatment of metal implants.

Data availability statement

The raw data supporting the conclusion of this article will be made available by the authors, without undue reservation.

Ethics statement

The studies involving human participants were reviewed and approved by the Ethics Committee of Jiamusi University. The patients/participants provided their written informed consent to participate in this study.

Author contributions

Conceptualization: XZ and XW; methodology: XZ; software: XZ; validation: FD and ZS; data curation: HM; writing—original draft preparation: XZ; writing—review and editing: ZL and YS; supervision: YS; and funding acquisition: XW. All authors contributed to the article and approved the submitted version.

Funding

This work was funded by the “Touyan” Project of Heilongjiang Province of China and the National Key Research and Development Program of China (2016YFC1102603).

Acknowledgments

The first author would like to acknowledge the help of Professor Oraib Al-Ketan of New York University Abu Dhabi in certain aspects of the software.

Conflict of interest

The authors declare that the research was conducted in the absence of any commercial or financial relationships that could be construed as a potential conflict of interest.

Publisher's note

All claims expressed in this article are solely those of the authors and do not necessarily represent those of their affiliated organizations, or those of the publisher, the editors and the reviewers. Any product that may be evaluated in this article, or claim that may be made by its manufacturer, is not guaranteed or endorsed by the publisher.

References

- Al-Ketan, O., and Abu Al-Rub, R. K. (2021). MSLattice: A free software for generating uniform and graded lattices based on triply periodic minimal surfaces. *Mat. Des. Process. Comms.* 3 (6), e205. doi:10.1002/mdp2.205
- Arabnejad, S., Burnett Johnston, R. B., Pura, J. A., Singh, B., Tanzer, M., Pasini, D., et al. (2016). High-strength porous biomaterials for bone replacement: A strategy to assess the interplay between cell morphology, mechanical properties, bone ingrowth and manufacturing constraints. *Acta biomater.* 30, 345–356. doi:10.1016/j.actbio.2015.10.048
- Becker, W., Urist, M., Becker, B. E., Jackson, W., Party, D. A., Bartold, M., et al. (1996). Clinical and histologic observations of sites implanted with intraoral autologous bone grafts or allografts. 15 human case reports. *J. Periodontology* 67 (10), 1025–1033. doi:10.1902/jop.1996.67.10.1025
- Casati, R., Lemke, J. N., Tuissi, A., and Vedani, M. (2016). Aging behaviour and mechanical performance of 18-Ni 300 steel processed by selective laser melting. *Metals* 6 (9), 218. doi:10.3390/met6090218
- Chambrone, L., Shibli, J. A., Mercúrio, C. E., Cardoso, B., and Preshaw, P. M. (2015). Efficacy of standard (SLA) and modified sandblasted and acid-etched (SLActive) dental implants in promoting immediate and/or early occlusal loading protocols: A systematic review of prospective studies. *Clin. Oral Impl. Res.* 26 (4), 359–370. doi:10.1111/clr.12347
- Dimitriou, R., Jones, E., McGonagle, D., and Giannoudis, P. V. (2011). Bone regeneration: Current concepts and future directions. *BMC Med.* 9 (1), 66. doi:10.1186/1741-7015-9-66
- Fucile, P., Papallo, I., Improta, G., De Santis, R., Gloria, A., Onofrio, I., et al. (2019). “Reverse Engineering and Additive Manufacturing towards the design of 3D advanced scaffolds for hard tissue regeneration,” in *Proceeding of the 2019 II Workshop on Metrology for Industry 4.0 and IoT (MetroInd4.0&IoT)*, Naples, Italy, June 2019 (IEEE), 33–37. doi:10.1109/metro4.2019.8792891
- Gibson, L. J. (2005). Biomechanics of cellular solids. *J. biomechanics* 38 (3), 377–399. doi:10.1016/j.jbiomech.2004.09.027
- Guvendiren, M., Molde, J., Soares, R. M., and Kohn, J. (2016). Designing biomaterials for 3D printing. *ACS Biomater. Sci. Eng.* 2 (10), 1679–1693. doi:10.1021/acsbomaterials.6b00121
- Jammalamadaka, U., and Tappa, K. (2018). Recent advances in biomaterials for 3D printing and tissue engineering. *J. Funct. Biomater.* 9 (1), 22. doi:10.3390/jfb9010022
- Kohal, R. J., Bächle, M., Att, W., Chaar, S., Altmann, B., Renz, A., et al. (2013). Osteoblast and bone tissue response to surface modified zirconia and titanium implant materials. *Dent. Mater.* 29 (7), 763–776. doi:10.1016/j.dental.2013.04.003
- Li, Y., Yang, C., Zhao, H., Qu, S., Li, X., Li, Y., et al. (2014). New developments of Ti-based alloys for biomedical applications. *Materials* 7 (3), 1709–1800. doi:10.3390/ma7031709
- Li, L., Shi, J., Zhang, K., Yang, L., Yu, F., Zhu, L., et al. (2019). Early osteointegration evaluation of porous Ti6Al4V scaffolds designed based on triply periodic minimal surface models. *J. Orthop. Transl.* 19, 94–105. doi:10.1016/j.jot.2019.03.003
- Liu, Y., Li, S., Wang, H., Hou, W., Hao, Y., Yang, R., et al. (2016). Microstructure, defects and mechanical behavior of beta-type titanium porous structures manufactured by electron beam melting and selective laser melting. *Acta mater.* 113, 56–67. doi:10.1016/j.actamat.2016.04.029
- Liu, F., Ran, Q., Zhao, M., Zhang, T., Zhang, D. Z., Su, Z., et al. (2020). Additively manufactured continuous cell-size gradient porous scaffolds: Pore characteristics, mechanical properties and biological responses *in vitro*. *Materials* 13 (11), 2589. doi:10.3390/ma13112589
- Lu, Y., Cui, Z., Cheng, L., Li, J., Yang, Z., Zhu, H., et al. (2020). Quantifying the discrepancies in the geometric and mechanical properties of the theoretically designed and additively manufactured scaffolds. *J. Mech. Behav. Biomed. Mater.* 112, 104080. doi:10.1016/j.jmbbm.2020.104080
- Melchels, F. P., Barradas, A. M., van Blitterswijk, C. A., de Boer, J., Feijen, J., Grijpma, D. W., et al. (2010). Effects of the architecture of tissue engineering scaffolds on cell seeding and culturing. *Acta biomater.* 6 (11), 4208–4217. doi:10.1016/j.actbio.2010.06.012
- Memon, A. R., Wang, E., Hu, J., Egger, J., and Chen, X. (2020). A review on computer-aided design and manufacturing of patient-specific maxillofacial implants. *Expert Rev. Med. devices* 17 (4), 345–356. doi:10.1080/17434440.2020.1736040
- Milovanovic, J. R., Stojkovic, M. S., Husain, K. N., Korunovic, N. D., and Arandjelovic, J. (2020). Holistic approach in designing the personalized bone scaffold: The case of reconstruction of large missing piece of mandible caused by congenital anatomic anomaly. *J. Healthc. Eng.* 2020, 1–13. doi:10.1155/2020/6689961
- Novaes Jr, A. B., Jr, Souza, S. L. S. d., Barros, R. R. M. d., Pereira, K. K. Y., Iezzi, G., Piattelli, A., et al. (2010). Influence of implant surfaces on osseointegration. *Braz. Dent. J.* 21 (6), 471–481. doi:10.1590/s0103-64402010000600001
- Pei, X., Zhang, B., Fan, Y., Zhu, X., Sun, Y., Wang, Q., et al. (2017). Bionic mechanical design of titanium bone tissue implants and 3D printing manufacture. *Mater. Lett.* 208, 133–137. doi:10.1016/j.matlet.2017.04.128
- Pei, X., Wu, L., Zhou, C., Fan, H., Gou, M., Li, Z., et al. (2020). 3D printed titanium scaffolds with homogeneous diamond-like structures mimicking that of the osteocyte microenvironment and its bone regeneration study. *Biofabrication* 13 (1), 015008. doi:10.1088/1758-5090/abc060
- Perrin, D., Szmukler-Moncler, S., Echikou, C., Pointaire, P., and Bernard, J. P. (2002). Bone response to alteration of surface topography and surface composition of sandblasted and acid etched (SLA) implants. *Clin. Oral Implants Res.* 13 (5), 465–469. doi:10.1034/j.1600-0501.2002.130504.x
- Rupp, F., Scheidegger, L., Rehbein, D., Axmann, D., and Geis-Gerstorf, J. (2004). Roughness induced dynamic changes of wettability of acid etched titanium implant modifications. *Biomaterials* 25 (7–8), 1429–1438. doi:10.1016/j.biomaterials.2003.08.015
- Song, P., Hu, C., Pei, X., Sun, J., Sun, H., Wu, L., et al. (2019). Dual modulation of crystallinity and macro-/microstructures of 3D printed porous titanium implants to enhance stability and osseointegration. *J. Mat. Chem. B* 7 (17), 2865–2877. doi:10.1039/c9tb00093c
- Standard, I. (2011). ISO 13314: 2011 (E)(2011) mechanical testing of metals—ductility testing—compression test for porous and cellular metals. *Ref number ISO 13314(13314)*, 1–7.
- Stepanovska, J., Matejka, R., Rosina, J., Bacakova, L., and Kolarova, H. (2020). Treatments for enhancing the biocompatibility of titanium implants. *Biomed. Pap.* 164 (1), 23–33. doi:10.5507/bp.2019.062
- Tack, P., Victor, J., Gemmel, P., and Annemans, L. (2016). 3D-printing techniques in a medical setting: A systematic literature review. *Biomed. Eng. OnLine* 15 (1), 115. doi:10.1186/s12938-016-0236-4
- Vaithilingam, J., Goodridge, R. D., Hague, R. J., Christie, S. D., and Edmondson, S. (2016). The effect of laser remelting on the surface chemistry of Ti6Al4V components fabricated by selective laser melting. *J. Mater. Process. Technol.* 232, 1–8. doi:10.1016/j.jmatprotec.2016.01.022
- Walker, J. M., Bodamer, E., Kleinfehn, A., Luo, Y., Becker, M., Dean, D., et al. (2017). Design and mechanical characterization of solid and highly porous 3D printed poly(propylene fumarate) scaffolds. *Prog. Addit. Manuf.* 2 (1), 99–108. doi:10.1007/s40964-017-0021-3
- Wang, Z., Wang, C., Li, C., Qin, Y., Zhong, L., Chen, B., et al. (2017). Analysis of factors influencing bone ingrowth into three-dimensional printed porous scaffolds: A review. *J. Alloys Compd.* 717, 271–285. doi:10.1016/j.jallcom.2017.05.079
- Wang, G., Shen, L., Zhao, J., Liang, H., Xie, D., Tian, Z., et al. (2018). Design and compressive behavior of controllable irregular porous scaffolds: Based on voronoi-tessellation and for additive manufacturing. *ACS Biomater. Sci. Eng.* 4 (2), 719–727. doi:10.1021/acsbomaterials.7b00916
- Webster, A. P., and Ross, T. J. (2013). Anodizing color coded anodized Ti6Al4V medical devices for increasing bone cell functions. *Int. J. Nanomedicine* 8, 109–117. doi:10.2147/ijn.s36203
- Wei, J., Herrler, T., Dai, C., Liu, K., Han, D., Li, Q., et al. (2016). Guided self-generation of vascularized neo-bone for autologous reconstruction of large mandibular defects. *J. craniofacial Surg.* 27 (4), 958–962. doi:10.1097/scs.0000000000002680
- Xing, H., Komasa, S., Taguchi, Y., Sekino, T., and Okazaki, J. (2014). Osteogenic activity of titanium surfaces with nanonetwork structures. *Int. J. Nanomedicine* 9, 1741–1755. doi:10.2147/ijn.s58502
- Yan, C., Hao, L., Hussein, A., and Young, P. (2015). Ti-6Al-4V triply periodic minimal surface structures for bone implants fabricated *via* selective laser melting. *J. Mech. Behav. Biomed. Mater.* 51, 61–73. doi:10.1016/j.jmbbm.2015.06.024
- Yoo, D. J. (2011). Porous scaffold design using the distance field and triply periodic minimal surface models. *Biomaterials* 32 (31), 7741–7754. doi:10.1016/j.biomaterials.2011.07.019
- Yoo, D. (2012). New paradigms in internal architecture design and freeform fabrication of tissue engineering porous scaffolds. *Med. Eng. Phys.* 34 (6), 762–776. doi:10.1016/j.medengphys.2012.05.008

- Yoo, D.-J. (2014). Advanced porous scaffold design using multi-void triply periodic minimal surface models with high surface area to volume ratios. *Int. J. Precis. Eng. Manuf.* 15 (8), 1657–1666. doi:10.1007/s12541-014-0516-5
- Yu, M., Wan, Y., Ren, B., Wang, H., Zhang, X., Qiu, C., et al. (2020). 3D printed Ti-6Al-4V implant with a micro/nanostructured surface and its cellular responses. *ACS omega* 5 (49), 31738–31743. doi:10.1021/acsomega.0c04373
- Zaharin, H. A., Abdul Rani, A. M., Azam, F. I., Ginta, T. L., Sallih, N., Ahmad, A., et al. (2018). Effect of unit cell type and pore size on porosity and mechanical behavior of additively manufactured Ti6Al4V scaffolds. *Materials* 11 (12), 2402. doi:10.3390/ma11122402
- Zha, Y., Li, Y., Lin, T., Chen, J., Zhang, S., Wang, J., et al. (2021). Progenitor cell-derived exosomes endowed with VEGF plasmids enhance osteogenic induction and vascular remodeling in large segmental bone defects. *Theranostics* 11 (1), 397–409. doi:10.7150/thno.50741
- Zhang, B., Pei, X., Zhou, C., Fan, Y., Jiang, Q., Ronca, A., et al. (2018). The biomimetic design and 3D printing of customized mechanical properties porous Ti6Al4V scaffold for load-bearing bone reconstruction. *Mater. Des.* 152, 30–39. doi:10.1016/j.matdes.2018.04.065
- Zhang, R., Zhong, S., Zeng, L., Li, H., Zhao, R., Zhang, S., et al. (2021). Novel Mg-incorporated micro-arc oxidation coatings for orthopedic implants application. *Materials* 14 (19), 5710. doi:10.3390/ma14195710
- Zhu, W., Ma, X., Gou, M., Mei, D., Zhang, K., Chen, S., et al. (2016). 3D printing of functional biomaterials for tissue engineering. *Curr. Opin. Biotechnol.* 40, 103–112. doi:10.1016/j.copbio.2016.03.014



OPEN ACCESS

EDITED BY

Chunguang Yang,
Institute of Metal Research, (CAS), China

REVIEWED BY

Yanjin Lu,
Fujian Institute of Research on the
Structure of Matter, (CAS), China
Rui Liu,
Shanghai Jiao Tong University, China

*CORRESPONDENCE

Baohong Zhao,
bhzhao@cmu.edu.cn
Shu Guo,
sguo@cmu.edu.cn
Shuang Tong,
tongshuang@cmu.edu.cn

[†]These authors contributed equally to
this work and share first authorship

SPECIALTY SECTION

This article was submitted to
Biomaterials,
a section of the journal
Frontiers in Bioengineering and
Biotechnology

RECEIVED 22 July 2022

ACCEPTED 17 August 2022

PUBLISHED 06 September 2022

CITATION

Shao H, Ma M, Wang Q, Yan T, Zhao B,
Guo S and Tong S (2022), Advances in
the superhydrophilicity-modified
titanium surfaces with antibacterial and
pro-osteogenesis properties: A review.
Front. Bioeng. Biotechnol. 10:1000401.
doi: 10.3389/fbioe.2022.1000401

COPYRIGHT

© 2022 Shao, Ma, Wang, Yan, Zhao, Guo
and Tong. This is an open-access article
distributed under the terms of the
[Creative Commons Attribution License](#)
(CC BY). The use, distribution or
reproduction in other forums is
permitted, provided the original
author(s) and the copyright owner(s) are
credited and that the original
publication in this journal is cited, in
accordance with accepted academic
practice. No use, distribution or
reproduction is permitted which does
not comply with these terms.

Advances in the superhydrophilicity-modified titanium surfaces with antibacterial and pro-osteogenesis properties: A review

Hanyu Shao^{1†}, Mingchen Ma^{2†}, Qiang Wang², Tingting Yan³,
Baohong Zhao^{2*}, Shu Guo^{1*} and Shuang Tong^{1*}

¹Department of Plastic Surgery, First Hospital of China Medical University, Shenyang, China, ²School
and Hospital of Stomatology, China Medical University, Shenyang, China, ³Faculty of Materials Science
and Engineering, Kunming University of Science and Technology, Kunming, China

In recent years, the rate of implant failure has been increasing. Microbial infection was the primary cause, and the main stages included bacterial adhesion, biofilm formation, and severe inhibition of implant osseointegration. Various biomaterials and their preparation methods have emerged to produce specific implants with antimicrobial or bactericidal properties to reduce implant infection caused by bacterial adhesion and effectively promote bone and implant integration. In this study, we reviewed the research progress of bone integration promotion and antibacterial action of superhydrophilic surfaces based on titanium alloys. First, the adverse reactions caused by bacterial adhesion to the implant surface, including infection and bone integration deficiency, are briefly introduced. Several commonly used antibacterial methods of titanium alloys are introduced. Secondly, we discuss the antibacterial properties of superhydrophilic surfaces based on ultraviolet photo-functionalization and plasma treatment, in contrast to the antibacterial principle of superhydrophobic surface morphology. Thirdly, the osteogenic effects of superhydrophilic surfaces are described, according to the processes of osseointegration: osteogenic immunity, angiogenesis, and osteogenic related cells. Finally, we discuss the challenges and prospects for the development of this superhydrophilic surface in clinical applications, as well as the prominent strategies and directions for future research.

KEYWORDS

titanium, superhydrophilicity, UV photo-functionalization, plasma treatment, antibacterial, osseointegration, biocompatibility

1 Introduction

Implants are used in orthopedic, dental care, and cardiovascular devices. The most commonly used metallic materials for implants are stainless steel [Arciola et al. \(2018\)](#), titanium, and titanium alloys. Metal implants have been used in biomedicine since the 19th century. They are used as temporary and permanent implants in the body. Several properties of metals are suitable for bone repair. The tensile strength of metals is greater than that of polymers, their toughness is 20 times higher than that of ceramics, and their fatigue life is reasonable. Metals can be alloyed, thereby making them resistant to corrosion. In addition, using elements that do not adversely affect the body can improve biocompatibility. Thus, metals have been used for implantable device applications, and this trend is not expected to change soon. Titanium was developed for aerospace applications in the 1950's; however, after the 1960's, it was used in surgical implants. Titanium has gained popularity because of its excellent combination of strength, Young's modulus, and biocompatibility compared with other metal implant materials ([Kaur and Singh, 2019](#)). For all their advantages, metal implants pose potential risks to bacterial infection, either from the patient's body or the surgical instruments in the operating room ([Jaggessar et al., 2017](#)). Bacteria easily adheres to the implant materials, and microbial infection accelerates the corrosion and loosening of the implant as well as increases the probability of repeated surgery. For example, joint replacement prosthetic infections occur in approximately 1% of joint replacements, a proportion that increases significantly during revision surgery ([Campoccia et al., 2006](#); [Moran et al., 2010](#)). In dentistry, clinical studies at five years of follow-up have shown that up to 14.4% of implants are surrounded by implant infections, with the incidence increasing over time ([Norowski and Bumgardner, 2009](#)). Microbial infection implants can lead to prolonged hospitalization and increase bacterial drug resistance while contributing to the evolution of superbugs, which can lead to death or amputation in severe cases. It may also turn into a chronic infection ([Ferraris and Spriano, 2016](#)).

When bacteria adhere to the implant, periprosthetic biofilm layers predominantly consisting of proteins and polysaccharides that are highly resistant to antimicrobial therapy are formed, which can lead to local infections or even deeper and more serious systematic infections ([Jaggessar et al., 2017](#)). Timely bone integration plays a critical role in the occurrence of bacterial adhesion. If bacterial adhesion occurs before tissue repair, host defense cannot prevent surface colonization and biofilm formation ([Arciola et al., 2018](#)), and bacterial adhesion during the first few hours of cell contact with the biomaterial may impair the entire process of bone healing; that is, processes such as cell adhesion, cell differentiation, and subsequent nutrition are impaired by bacterial colony formation on the implant surface. In addition, local inflammatory processes may be

established, leading to changes in tissue pH and the migration of defense cells, such as macrophages, fibroblasts, and white blood cells, consequently affecting bone healing ([Kunrath et al., 2020](#)). Osseointegration results from inflammatory driving processes on and around the implant surface. A favorable immune response can promote osseointegration and wound repair, whereas an undesirable immune response can lead to excessive inflammation, pain, tissue destruction, fiber wrapping, and even implant failure ([Anderson et al., 2008](#)). To avoid the adverse effects of bacterial adhesion, scientists have also proposed several methods, and the main modes of action of commonly used antibacterial agents can be summarized as follows ([Zhan et al., 2021](#)): 1) Destroying or inhibiting the cell wall synthesis process; 2) Inhibiting the function of the cell membrane; 3) Inhibiting the protein synthesis process of bacterial cells; 4) Combining with components of DNA or RNA synthesis process to inhibit nucleic acid synthesis and affect the normal reproduction process of bacteria; 5) Inhibiting other metabolic processes, such as the destruction of folic acid, which is important for DNA synthesis.

The ideal implant material should have antibacterial properties as well as favorable biocompatibility. In recent years, studies have increasingly been conducted on superhydrophilic surfaces. Among numerous antibacterial methods, superhydrophilic surfaces exhibit antibacterial effects while achieving excellent biocompatibility. It was found that osteoblasts proliferated faster, and they were larger, longer, and more active on superhydrophilic Ti surfaces ([Henningsen et al., 2018](#)). More filamentous extension of macrophages was also observed on the surface of anodized and hydrogenated titanium (with superhydrophilic properties), and the stretched appearance of these macrophages was significantly less after 24 h ([Gao et al., 2020](#)). Compared with the micro-smoothness of nano-titanium, nano-rough particles, nanotubes, and nano-braided titanium can enhance the adhesion of osteoblasts and also provides other functionalities, such as alkaline phosphatase synthesis, calcium deposition, and collagen secretion ([Puckett et al., 2010](#); [Wennerberg et al., 2014](#)). As the superhydrophilic surfaces are rough, well-organized topography at nano/microscales could improve bio-compatibility and promote bone formation, which is crucial for successful osseointegration between the implant and bone. The cell filopodia can enter the pore of nanotubes to form a locked-in cell structure for bone ingrowth ([Zhao et al., 2020](#)). The hydrophilicity of implants has been identified as an important factor that may affect the early bone response, i.e., high hydrophilicity, faster healing, and therefore superior stability and the possibility of early loading, with favorable clinical predictability ([Rupp et al., 2004](#)). High hydrophilicity can improve the biological activity of biomaterials and promote cell adhesion ([Li et al., 2019](#)). [Table 1](#) summarizes several studies on superhydrophilicity surfaces that promote osseointegration and the cells they affect. The antibacterial

TABLE 1 Example of superhydrophilic surfaces promoting osseointegration.

Type of alloy	Preparation methods	CA	Cell culture	Mechanism of action	Reference
Tantalum	Electrochemical anodization	0°	MC3T3-E1	Triggering FAK and YAP/RUNX2 cell signaling pathways	Zhang Z. et al. (2021)
Si-TiO ₂	<i>In situ</i> anodization and Si plasma immersion ion implantation (PIII)	11.25 ± 0.88°	MC3T3-E1	The expression of Runx2 and ALP increased on Si-TiO ₂ -NTs	Zhao et al. (2020)
Ti	Acid etching Thermal alkali	<10°	RAW 264.7	Inhibition of osteoclast related markers, most osteoclasts growing on the surface of the material were mononuclear	Kartikasari et al. (2022)
Ti6Al4V	Electrochemical anodization	5°	Osteoblast MG63 cells	The MTT results exhibited high cell viabilities of 98.1%	Rahnamaee et al. (2020)
Hydrogenated titanium dioxide (H ₂ -TNT)	Electrochemical anodization Hydrogenation	3.65 ± 0.52°	Macrophages	H ₂ -TNT surface elicited up-regulated gene expression of M2 surface markers and down-regulation of M1 surface markers	Gao et al. (2020)

mechanisms and optimal biocompatibility of superhydrophilic surfaces were discussed, mainly with regard to anti-inflammatory properties and osteogenesis promotion.

2 Superhydrophilicity principle

Superhydrophilic structures are usually characterized by a contact angle (CA) less than 10°. CA is the reaction of surface wettability, and surface roughness and surface energy together determine wettability (Si et al., 2018). The surface energy calculated from the CA data shows that increasing the surface roughness increases the surface energy and at the same time increases the surface wettability, making the material superhydrophilicity (Puckett et al., 2010). More importantly, surface roughness and surface energy are key to favorable biocompatibility, and osteoblasts are more inclined to adhere to surfaces with high roughness and surface energy (Salido et al., 2007; Puckett et al., 2010).

Superhydrophilic materials were first inspired in 1970 *via* research on the human cornea, in which tears can completely diffuse across the cornea, forming a water membrane to eliminate the scattering of light (Si et al., 2018). In 2010, Zheng et al. (2010) reported that spider silk can efficiently collect water from the air, with the surface energy gradient and Laplacian pressure difference, generated by spider silk with a spindle structure, allowing continuous directional water condensation around the spider silk. The superhydrophilicity of the pitcher plant was discovered in 2016 (Chen et al., 2016), opening a new pathway for the study of superhydrophilicity structures. Currently, scientists have established a few relatively mature manufacturing methods for superhydrophilic materials, and they can be roughly divided into two categories: physical and chemical methods. Physical methods include laser treatment, physical vapor deposition, and spraying. Vorobyev and Guo created a novel method for achieving regular

superhydrophilicity of silicon using high-intensity femtosecond laser pulses (Vorobyev and Guo, 2010). Because of its superhydrophilicity, water resists gravity by spreading vertically upwards. The driving force of water motion is the surface energy generated by the surface structure and the Laplacian pressure (Vorobyev and Guo, 2010; Si et al., 2018). Zheng et al. (2016) reported spray-dried superhydrophilicity TiO₂/SiO₂ nanoparticle coatings. Numerous procedures can be used to form a superhydrophilicity surface, on which a drop of water or blood will immediately spread and wet the surface. To achieve superhydrophilic surfaces, plasma treatment and ultraviolet (UV) irradiation are commonly used (Albrektsson and Wennerberg, 2019). Li et al. (2008) prepared a long-term stable superhydrophilicity-layered TiO₂ via pulse laser deposition technology and annealing. The TiO₂-layered particle array exhibits superhydrophilicity, with the water CA approaching 0°, without requiring further UV exposure. Chemical methods, such as a novel underwater superhydrophilic polyacrylamide hydrogel coated mesh, are relatively complex, and can be used to achieve the selective separation of oil and water mixtures with high separation rates (Si et al., 2018).

3 Effect of superhydrophilicity surface on bacteria

3.1 Bacterial adhesion

As shown in Figure 1, when bacteria stick to the implant surface, the human body shows inflammation in response to foreign metals and pathogens. The inflammatory response of the host contributes to the formation of biofilms, because molecules produced as part of this response help the bacteria adhere to the surface of the medical device (Lin and Bumgardner, 2004). Therefore, inflammation can cause implant trauma and

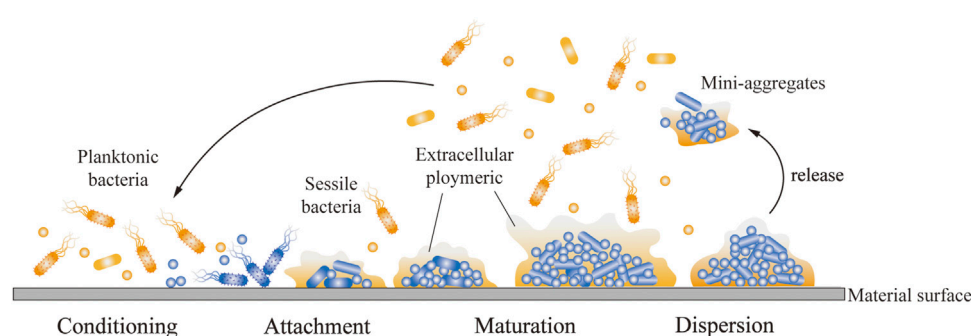


FIGURE 1

Process of bacterial adhesion on implant surface. The planktonic bacteria attach and adhere to the implant surface and bind to the sessile bacteria. The bacteria covered by EPS gradually mature and continue secreting EPS to attract more bacteria to adhere and form biofilms. An aggregate of bacteria began to break up into mini-aggregates, which were released.

damage to the underlying bone. The implantation of infected bacteria is generally not a sparse distribution of single adherent cells, but rather a biofilm in which bacterial aggregates adhere tightly to the surface of the biomaterial and are encased in a large matrix of extracellular polymers (EPSs) (Arciola et al., 2018). The growth of biofilms, harsh physical environment, and sublethal concentrations of antibiotics can serve as stress signals to stimulate persistent cell formation, which is responsible for the persistence of implant infections and the source of the spread of bacteria to other parts of the body. In addition, chronic inflammation occurs, because host immune defenses and traditional antimicrobial therapies are often ineffective against bacteria growth in biofilms. Different microbial species, including Gram-negative bacteria, Gram-positive bacteria, and fungi can form biofilm to against adverse factors. In addition, the high cell density in biofilms alters microbial gene expression, contributes to their increased virulence, and enhances inter-bacterial adhesion, consequently resulting in more frequent binding between biofilm community members than that between planktonic bacteria (Arciola et al., 2018).

3.2 Antibacterial mechanism of superhydrophilic surface

A thin oxide layer, TiO_2 , was formed on the titanium surface when titanium was exposed to air, and the oxide layer surface generally absorbed organic hydrocarbon contaminants from the atmosphere (Zhao et al., 2007; Att et al., 2009). Surface modification technologies can diminish hydrocarbon contamination, increase the content of functional OH groups on the material surface, and endow titanium with superhydrophilicity without altering the surface topography (Choi et al., 2016; Matsumoto et al., 2020). Furthermore,

treatments, such as UV irradiation and plasma treatment, can directly inactivate bacteria and biofilms on the titanium surface while obtaining superhydrophilicity (Koban et al., 2011; Guo et al., 2021), thereby creating a sterile environment for implantation. However, resistance to bacterial adhesion during or after implantation is also an aspect that cannot be ignored. Bacterial adhesion is a complex physical and chemical process that includes three stages: transport of bacteria towards a surface, reversible bacterial adhesion, and transition from reversible to irreversible adhesion (Yang et al., 2022). A 6 h post-implantation period has been identified as a “decisive period,” during which the inhibition of bacterial adhesion is critical to the long-term success of an implant (Zilberman and Elsner, 2008). Thus, the antibacterial effects on the first day are crucial to ensuring successful implantation.

The effect of surface wettability, that is, whether the material is hydrophilic or hydrophobic, on bacteria adhesion is currently inconclusive. Studies have indicated that hydrophobic surfaces could reduce the velocity of bacteria through collisions and slightly increase the collision duration when bacteria approach the surface, thereby promoting the landing and adhesion of bacteria (Qi et al., 2017), whereas hydrophilic surfaces could form more hydrogen bonds with bacteria, leading to increased adhesive forces, even exceeding the adhesion force on the hydrophobic surface (Boks et al., 2008).

The mechanisms of bacterial adhesion on the surface of materials are complex; they are related to the characteristics of the material itself, such as surface patterning, roughness, wettability, and surface charge as well as the characteristics of different bacteria (Pajerski et al., 2020; Yang et al., 2022). Without considering the addition of antibacterial ingredients or changing surface morphology, superhydrophilic surfaces can be obtained with certain bacteriostatic properties (Lan et al., 2015; Jeong et al., 2017). Bacteria were generally not completely eliminated on the titanium surface, so the reduction in the

TABLE 2 Examples of bacteriostasis on superhydrophilic surfaces.

Material	Processing mode		Bacterial	Experimental results	Reference
	Equipment	Processing time			
Ti	UV light	12 min	<i>S. aureus</i>	Higher antibacterial activity with increased culture time, and enhance the phagocytic ability of macrophages	Yang et al. (2021)
Ti	PECVD system (F and O dual plasma-base)	—	<i>S. aureus</i>	Antibacterial rates: fresh F-O-Ti 100%, after 1 day 96.6%, after 3 days 90.5%, after 7 days 89.8%	Chen et al. (2019)
Ti/Ti-Ag	Non-thermal atmospheric pressure plasma jet (NTAPPJ)	10 s	<i>S. sanguinis</i>	Bacterial adhesion was significantly reduced, the change of ions had no obvious effect on bacterial adhesion resistance	Lee et al. (2017)
Ti	NTAPPJ	10 min	<i>S. sanguinis</i>	The structure of aggregates changed from a long-chain shape to a short-chain form	Jeong et al. (2017)
Ti/Ti6Al4V	UV ($\lambda = 254$ nm, 8–10 mW/cm ²)	15 min	<i>S. aureus</i>	The antimicrobial activity was maintained for seven days after UV irradiation	Itabashi et al. (2017)
Ti	UV ($\lambda = 254$ nm, 100 mW/cm ²)	15 min	<i>Actinomyces oris</i>	During the initial attachment period, <i>Actinomyces oris</i> colonization is reduced and biofilm formation is inhibited for up to 6 h	Zhang et al. (2017)
Ti	NTAPPJ	2–10 min	<i>S. mutans</i> <i>S. aureus</i> <i>Klebsiella oxytoca</i> <i>K. pneumoniae</i>	Both adhesion and the biofilm formation rate were significantly lower for Gram-negative bacteria than Gram-positive bacteria on samples treated for longer durations with the NTAPPJ	Lee et al. (2019)
Ti	UV ($\lambda = 365$ nm, 10 mW/cm ²)	5 min	<i>P. aeruginosa</i> <i>S. aureus</i>	After 30 min, <i>P. aeruginosa</i> decreased by 90%, but by 240 min, <i>S. aureus</i> reduced by more than 99%	Pan et al. (2021)

number of bacteria was attributed to the anti-adhesion effect, and the bacterial viability was inhibited by the treatment on the superhydrophilic titanium surface. This type of superhydrophilic surface with short-term antibacterial effects can meet the requirements of clinical implantation without infection, and its antibacterial mechanisms are largely dependent on surface treatment methods. Therefore, we selected the typical surface modification methods, UV photo-functionalization and plasma treatment, and their several potential bacteriostatic mechanisms. Table 2 lists several examples of superhydrophilic surfaces with antibacterial properties.

3.2.1 Ultraviolet photo-functionalization

The naturally occurring oxide film on the titanium surface generally exists in an amorphous state and does not exhibit photocatalytic ability; however, the three crystal structures of TiO₂, anatase, rutile, and brookite, show photocatalytic activity and can be obtained via various oxidation methods, including sol-gel method, sputtering, chemical vapor deposition, atomic layer deposition, plasma immersion ion implantation, cathodic arc deposition, and anodization (Yeniyol et al., 2015; He et al., 2019). Under the excitation of UV light, the TiO₂ surface with semiconductor properties can generate electron-holes pairs, inducing a series of photocatalytic reactions, and facilitating the antibacterial effect (Chouirfa et al., 2019). UV treatment on titanium surfaces leads to the excitement of electrons from the valence band to the conduction band, followed by the abundant

production of electron-hole pairs. Gallardo-Moreno et al. (2010), reported that the irradiation of Ti6Al4V surfaces with UV-C light produced residual post-radiation effects that directly affected the viability of adhered bacteria, and the antibacterial effects are likely due to the return of the absorbed energy and the formation of little electrical currents caused by the surface charge during the relatively slow recombination process of electron-holes pairs of TiO₂ after irradiation. Hatoko et al. reported that UV-treated titanium surface inhibited the proliferation of *S. aureus* owing to the increased intracellular reactive oxygen species (ROS) (Hatoko et al., 2019). ROS can damage bacterial membranes and cell walls; thus, additional to destroying the bacterial defense system, they can also penetrate bacterial membranes, and destroy proteins and lipids, directly or indirectly disrupting cellular respiration and other physiological activities (Ren et al., 2020). UV treatment renders the titanium surface with a bacteria repellent; however, the effect is time-dependent (de Avila et al., 2015; Zhang et al., 2017). Electrochemical anodization, a surface modification method, is often used to obtain a functional TiO₂ film in the preparation of superhydrophilicity surfaces treated using UV. This anodized surface is inherently antibacterial. The surface of the titanium implant was placed in a sodium chloride solution and anodized by forming TiCl₃ surface layer (Han et al., 2016). Subsequently, the modified surface gradually hydrolyzes, resulting in the formation of

Ti-OH and bactericidal hypochlorous acid. Ti-OH endows the titanium surface with superhydrophilicity (Shibata et al., 2010), thereby facilitating favorable biocompatibility. Hypochlorous acid can be continuously released from titanium the surface for eight weeks (Shibata and Miyazaki, 2014), endowing the titanium surface with antibacterial properties (Shibata et al., 2010).

3.2.2 Cold plasma treatment

Cold plasma, a neutral-ionized gas regarded as the fourth fundamental state of matter (other than solid, liquid, and gas) (Burm, 2012), is currently applied in the surface modification of materials. Plasma is a mixture that contains UV and heavy (molecules, atoms, free radicals, ions) and light (electrons and photons) species generated by the excitation of gas via electric discharges (Moreau et al., 2008). The oxide layer on the titanium surface can be modified using ions, such as COOH^- , NO^- , OH^- , N^{3-} , and O^{2-} , after plasma treatment, and reactive oxygen and nitrogen species are the main effective components of cold plasma, enabling the titanium surface to perform reductive potential, which can oxidize the surrounding matter. Additionally, plasma-treated superhydrophilic titanium surfaces can exert bacteriostatic function through the ROS pathway (Yoo et al., 2015). Lee et al. (2019) reported that plasma-treated superhydrophilic titanium surfaces can inhibit the growth of Gram-negative bacteria; this inhibitory effect on Gram-negative bacteria is stronger than that on Gram-positive bacteria because of the thickness of the peptidoglycan layer in the bacterial cell wall (Lee et al., 2019). However, the contents of the reactive species in the materials were time-dependent, with the bacteriostatic effects decreasing over time (Park et al., 2018; Yang et al., 2021).

These two treatments show strong antimicrobial activity against Gram-negative bacteria, and the superhydrophilic surfaces also have a certain inhibitory effect on the formation of Gram-negative bacteria biofilm, such as the *P. aeruginosa* biofilm. After UV treatment of Ti plate, the growth of *P. aeruginosa* density and coverage decreased significantly, after 16 h of biofilm formation, UV treatment of titanium plate compared with untreated plate, the cumulative biomass significantly reduced and UV treatment on the surface of engraftment significantly sparser, cells less, smaller and more fragmented. The titanium discs were covered with larger, higher, and more extensive microcolonies (de Avila et al., 2015). Plasma nitriding Ti surface had excellent biofilm performance, and no large bacterial clusters of *P. aeruginosa* were observed after 3 or 6 h of culture, which may be related to the trivalent titanium ions produced by nitriding mechanism (Nunes Filho et al., 2018). Furthermore, the surface of Ti treated with non-thermal plasma (NTP) alone did not show the performance of effective inhibition of *P. aeruginosa* biofilm, but after the combination with gentamicin (GTM), the biofilm coverage area was significantly reduced. When treated with

0.25 h NTP and then 8.5 mg/L GTM, *P. aeruginosa* ATCC 15442 mature biofilm was completely eliminated from the surface. Therefore, NTP can be used as a suitable antibiofilm agent in combination with antibiotics for the treatment of biofilm-associated infections caused by this pathogen (Paldrychová et al., 2019; Paldrychova et al., 2020).

The chemical change, in which carbon content decreases and oxygen content increases on the surface of titanium after superhydrophilic modification (Hotchkiss et al., 2016; Jeong et al., 2017; Lee et al., 2017; Wang et al., 2020), can induce bacterial adhesion resistance. The effect of chemical composition on bacterial adhesion may be more important than surface energy, but further studies are needed to confirm this hypothesis (Lee et al., 2017). The bacteriostatic ability of the surface is optimal when the surface modification is completed, so in practical application, it is required to properly determine the ideal time point of surface treatment and implantation to better exert the bacteriostatic properties.

3.3 Comparison of antibacterial principle with superhydrophobic surface

Superhydrophobic surfaces have attracted extensive attention owing to their excellent self-cleaning and anti-fouling effects. If superhydrophobic surfaces are applied to implant surfaces, they can effectively reduce infection caused by microorganisms, reduce the rate of secondary surgery, as well as reduce thrombosis, thereby facilitating patient recovery (Kattula et al., 2017). Unlike superhydrophilicity surfaces, which are chemically antibacterial by changing some reactive oxygen groups or charges, superhydrophobic surfaces tend to directly kill bacteria that adhere to the surface. The antibacterial effect of superhydrophobic surfaces can be reflected in two aspects. On the one hand, superhydrophobic materials can prevent or reduce bone marrow-derived cells and bacterial adhesion (*S. aureus* and *verdigris*); this is owing to the reduction in the surface energy of the superhydrophobic surface and the amount of protein adsorption on the surface, thereby making the bacteria harder to adhere and more likely to be removed before the biofilm is generated, known as the self-cleaning effect of the superhydrophobic surface (Vanithakumari et al., 2013; Bartlet et al., 2018; Cao et al., 2018). On the other hand, the nanopillar structure on the superhydrophobic surface can kill the bacteria attached to the surface, but the mechanisms of microbial repulsion on superhydrophobic surfaces are complex and little understood currently. However, the characteristic of the hydrophobic surface repelling bacteria has certain limitations, most Gram-negative microorganisms exhibit repulsion, and Gram-positive microorganisms tend to adhere to these surfaces (Jaggessar et al., 2017). Table 3 lists a few examples of antibacterial superhydrophobic surfaces.

TABLE 3 Examples of bacteriostasis on superhydrophobic surfaces.

The name of the alloy	The preparation methods	Bacterial	The antibacterial effect	Reference
5,083 aluminum alloy	Ammonia etching and PFDTES modification	SRB	Greatly reduce the adhesion, growth, and proliferation of SRB.	Zhang et al. (2019)
Micro-nano structured titanium	Thermochemical treatment after silane modification	<i>S. aureus</i> <i>E. coli</i>	Decreased bacterial adhesion significantly (>90%) and prevented biofilm formation	Manivasagam et al. (2022)
Flower-like micro-nano titanium particles	Electrophoretic deposition	<i>E. coli</i>	Repel <i>E. coli</i> adhesion	Zeng et al. (2020)
Aluminum	Passivation with low surface energy OTES molecules after chemical etching	<i>S. aureus</i> <i>P. aeruginosa</i> <i>E. coli</i>	An antibiofouling property of 99.9% against <i>S. aureus</i> , 99% against <i>P. aeruginosa</i> and 99% against <i>E. coli</i> bacteria	Agbe et al. (2020)
Superhydrophobic basalt scales (SiO ₂)	Fluorinated with PFDTES after NaOH solution chemical etching	<i>P. aeruginosa</i>	Inhibited the adhesion of the <i>P. aeruginosa</i> cells	Zheng et al. (2021)

PFDTES: 1H, 1H, 2H, and 2H-Perfluorodecyltriethoxysilane. OTES, octyltriethoxysilane; SRB, Sulfate-reducing bacteria.

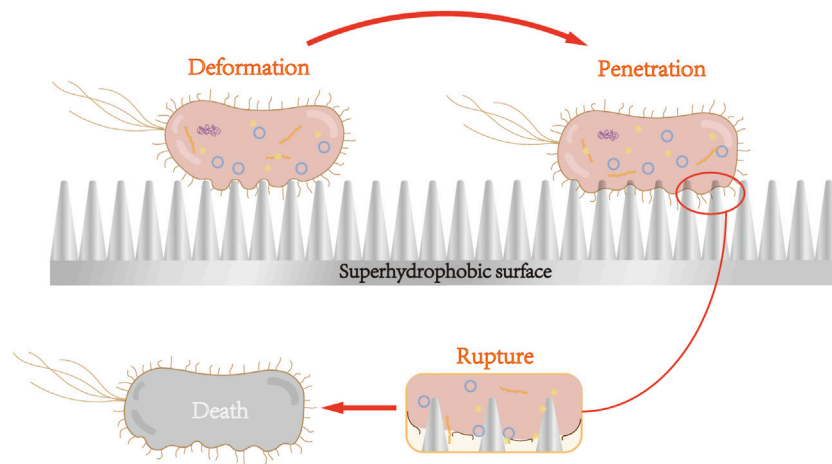


FIGURE 2

Nanoparticles of superhydrophobic surface cause bacterial cell membrane deformation, penetration, and rupture. After adhering to the surface of superhydrophobic nanoparticles, Gram-negative bacteria underwent cell membrane deformation, penetration, and rupture, and subsequent death.

The self-cleaning effect of superhydrophobic surfaces is attributable to their low surface energy, the structure of bacteria, and surface roughness. Suitable surface roughness reduces the contact area, and low surface energy coating limits adhesion (Kavitha Sri et al., 2020). *S. aureus* is more likely to adhere to titanium surfaces than *P. aeruginosa*, because spherical bacteria require lower surface energy to successfully adhere to titanium (Fadeeva et al., 2011). However, compared with that on smooth titanium surfaces, the adhesion of bacteria on the surface of superhydrophobic titanium nanoparticles after treatment is relatively reduced.

This resistance to bacterial colonization may be due to the greatly reduced surface area required for bacterial adhesion (Zhan et al., 2021).

Jenkins et al. (2020) reported that *Escherichia coli* adhering to the treated superhydrophobic nanoparticle titanium surface was first deformed under the action of nanoparticles, but the particles did not penetrate the cell membrane. Such deformation generally occurred in the area between the nanoparticles, namely air pockets, owing to the secretion of EPS layer. The bacterial cells then attached strongly to the nanostructure, and gradually, the nanoparticles penetrated the bacterial

membrane. When the adhesion is sufficiently strong, the bacterial membrane ruptures owing to the resistance that occurs. Figure 2 shows the process of the bacterial rupture. By contrast, *S. aureus*, which clung to the surface, is not penetrated, likely because the cell walls of Gram-positive bacteria have thicker peptidoglycan layers, hindering the penetration of the nanoparticles.

Superhydrophobic surfaces can cause the attached Gram-negative bacteria to rupture and die *via* the surface morphology. Superhydrophilic surface is formed with antibacterial groups on the titanium surface through special surface treatment, which produces ROS to destroy bacterial cell membranes and cell walls, consequently leading to the death of bacteria.

4 Effect of superhydrophilicity titanium surface on osseointegration

The direct integration of bone and metal leads to structural and functional integration between the living bone and the implant surface, known as osseointegration, which is the rapid activation of the immune response to tissue injury *via* endosteal injury (Overmann et al., 2020). The osteoblast lineage is required for rapid osseointegration, and endothelial cell (EC)-mediated angiogenesis is required for new bone formation (Noble and Noble, 2014). Osseointegration can be divided into three stages: inflammation, repair, and remodeling (Sakka and Coulthard, 2009).

According to the sequence of the occurrence of osseointegration, we classified it into three parts as follows: immune response, angiogenesis, and osteogenesis. The effects of superhydrophilic surfaces will be introduced respectively.

4.1 Effect of superhydrophilicity titanium surface on immune response during osseointegration

The immune system is the most effective weapon against foreign body invasion and tissue damage. Osseointegration is actually an immune-driven process that relies on favorable inflammatory pathways that promote new bone formation as part of the host response to bioactive implants and reduce negative tissue responses that can lead to rejection. The primary driving force of bone immunology is host innate immunity, particularly macrophage activation (Lee and Bance, 2019). The immune cells that interact with the implant surface can release a variety of cytokines for regulating the microenvironment of the surrounding tissue, affecting the initial host response to the implants, the process of osseointegration, and the long-term effects of the implants (Zhang et al., 2021).

4.1.1 Promotion of anti-inflammatory macrophage polarization through NETosis of neutrophils

After the degranulation of platelets (Terheyden et al., 2012), the neutrophils invade the blood clot via amoeboid migration, squeezing through little gaps in the walls of the blood vessels (Terheyden et al., 2012). Neutrophils can immediately dominate as the “first responders” after the tissue damage triggered by biomaterial implantation, and function in three primary abilities: the generation of oxidative bursts, release of granules, and formation of neutrophil extracellular traps (NETs), which enable neutrophil involvement in inflammation, recruitment of macrophages, M2 macrophage differentiation, resolution of inflammation, angiogenesis, and immune system activation (Selders et al., 2017).

Neutrophils dominate immediately after tissue injury (Wang, 2018). Although neutrophils exist for a considerably short time, they still play an indispensable role in promoting the polarization of macrophages. A role of neutrophils, NETosis, can be triggered in sterile inflammation (Thiam et al., 2020). It is a specific form of cell death caused by neutrophils, which is characterized by the release of cytokines, enzymes, immune cell recruitment chemokines, and DNA fibrils into the extracellular space referred to as NETs (Brinkmann et al., 2004; Yang et al., 2016). Abaricia et al. (2020) observed conditioned media from neutrophils grown on superhydrophilic titanium surfaces lead to anti-inflammatory macrophage polarization, and this anti-inflammatory effect was enhanced by the pre-treatment of neutrophils with a pharmacologic NETosis inhibitor. Therefore, a superhydrophilic titanium surface could reduce the neutrophil-induced pro-inflammatory transformation of macrophages regulated by NETosis.

4.1.2 Regulation of macrophage polarization

The early inflammatory response of macrophages to the material surface prior to osteogenesis and angiogenesis determines the fate of the implant *in vivo* through bone immunoregulation (Bai et al., 2018). The effect of superhydrophilic surfaces on the immune system is predominantly reflected in promoting the polarization of macrophages to the anti-inflammatory phenotype (Bai et al., 2018; Gao et al., 2020; Huang et al., 2021). The surfaces induced the immune response of macrophages, which secreted initial levels of proinflammatory cytokines and ultimately the highest concentrations of anti-inflammatory and immunomodulatory factors (Hotchkiss et al., 2016). Anti-inflammatory factors, IL-4, IL-10, IL-13, and TGF- β , were upregulated, whereas the pro-inflammatory factors, IL-1, IL-6, and TNF- α , were significantly down-regulated. The superhydrophilic surface effectively inhibited the inflammation of the implant-bone interface via down-

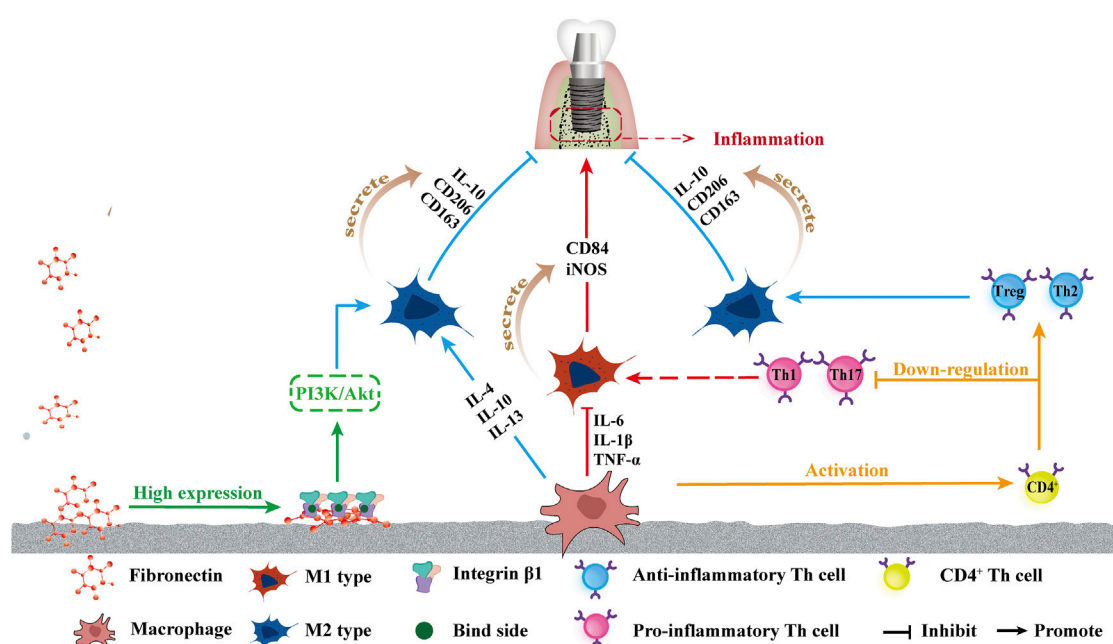


FIGURE 3
Schematic of influence of superhydrophilicity surface on osteogenic immune response. From left to right: the increased attachment of Fn provides more binding sites for integrin $\beta 1$, which in turn promotes the polarization of macrophages towards M2 by promoting the PI3K/Akt pathway. The superhydrophilic surface up-regulates IL-4, IL-10, and IL-13, promotes the polarization into M2, and promotes M2 phenotype secretion of IL-10, CD206, and CD136, promoting anti-inflammatory effects. The down-regulation of IL-6, TNF- α , and IL-1 β inhibited the polarization into M1 polarization, and inhibited the secretion of CD84 and iNOS of the M1 phenotype, inhibiting inflammation. Macrophages activated CD4⁺T cells, and the superhydrophilic surface promoted the differentiation of CD4⁺T cells into the anti-inflammatory phenotype Th2 and Treg and inhibited the differentiation into the pro-inflammatory phenotype Th1 and Th17.

regulating the expression of iNOS and CD86 in the M1 phenotype and up-regulating the expressions of IL-10, CD163, and CD206 in the M2 phenotype (Bai et al., 2018).

TNF- α , a key proinflammatory regulator that is predominantly released by stimulated macrophages, enhanced osteoclast differentiation and resorption activity, inhibited osteoblast activity and bone formation (Theiss et al., 2005), also combined with NF- κ B through NF- κ B-TNF- α pathway to attenuate the macrophage immune response (Robson et al., 2004). The activation of the NF- κ B pathway, a key intercellular regulator of inflammatory signaling, promotes the secretion of proinflammatory cytokines, including TNF- α and IL-1 β (Dai et al., 2015).

In addition to the TNF- α -NF- κ B pathway, integrin $\beta 1$ has also been observed to contribute to osteogenesis via superhydrophilic surfaces in a study by lv et al. (2018) and the high expression of integrin $\beta 1$ was detected on the UV-Ti surface, likely because fibronectin (Fn) maintains a more active conformation on the hydrophilic surface, leading to more cell binding sites (RGD) exposure, allowing integrin $\beta 1$ to better bind to the hydrophilic surface (Li et al., 2020). The highly expressed integrin $\beta 1$ is likely to drive macrophages to the M2 phenotype through the Phosphoinositol-3-kinase (PI3K)/

Serine/threonine kinase (Petzold et al., 2017) signaling pathway. PI3K also signals through Akt to inhibit NF- κ B activation, which induces a proinflammatory phenotype of macrophages, thereby inhibiting the polarization of macrophages toward the M1 phenotype (Lv et al., 2018). Hotchkiss et al. (2016) also reported that the combination of increased surface roughness and hydrophilicity may have a synergistic effect on increasing anti-inflammatory macrophage activation and yielding a suitable microenvironment, which may improve osseointegration and lead to a superior implant effect. Figure 3 shows the effects of a superhydrophilic surface on macrophage polarization.

4.1.3 Promotion of the macrophage-induced adaptive immune response towards Th2 pro-wound healing phenotype

Newly recruited adaptive immune cells known as T cells are activated via antigen presentation by macrophages or dendritic cells (Lazarevic et al., 2013). Activated T cells, particularly CD4⁺ helper T cells, are considered the most influential cells for generating long-term immune responses. Helper T cell subsets have several phenotypes: helper cell type 1 (Th1), helper cell type 2 (Th2), helper cell type 17 (Th17), and T

regulatory cells (Tregs). Th1 and Th17 are broadly considered proinflammatory (Lazarevic et al., 2013; Song et al., 2014), whereas Th2 and Treg helper cells are considered the most important for tissue regeneration (Lei et al., 2015; Schiaffino et al., 2017). In Hotchkiss' *in-vivo* research, rough superhydrophilicity surfaces produced the maximum up-regulation of Th2 and Treg genes and down-regulation of Th1 and Th17 genes three days after implantation, demonstrating that M ϕ could polarize the adaptive immune response toward Th2, pro-wound healing phenotype, promoting the resolution of inflammation and increasing stem cell recruitment around implants (Hotchkiss et al., 2018), as shown in Figure 3.

4.2 Effect of superhydrophilicity titanium surface on angiogenesis

Newly formed capillaries play a critical role in this process and provide a favorable biological basis for implant osseointegration. The capillary system is the most basic structure to maintain the normal metabolism of the body, providing nutrients required for metabolism, exchange of oxygen and carbon dioxide, and a huge network of official channels for the exchange of the body and metabolites (Zhao et al., 2018).

An et al (2009) reported that superhydrophilic surfaces promote vascular EC proliferation by up-regulating related markers and expression factors, such as endothelial markers and angiogenic factors, Von Willebrand factor, thrombomodulin, and endothelial protein C receptors.

In the inflammatory stage, macrophages are stimulated by an intracellular transcription factor known as hypoxia-inducible factor (HIF-1), which may interact with VEGF to increase angiogenesis during osseointegration on the surface of superhydrophilicity implants (Calciolari et al., 2018; Zhang et al., 2020). The binding of VEGF-A to its receptor (VEGFR2) can activate various signaling pathways (El Chaar et al., 2019), leading to promoted cell survival, proliferation, infiltration, and migration (Lu et al., 2018). After the homodimerization of VEGF and VEGFR2, NO is stimulated, contributing to vascular permeability and long-term response of EC survival, migration, and proliferation (Rabelink and Luscher, 2006). Osteoblast-derived VEGF acts on adjacent ECs and stimulates osteoclast formation and differentiation (Hoebe et al., 2004; Liu et al., 2012; Hu and Olsen, 2016). Raines et al. (2019). showed that superhydrophilicity titanium surfaces increased osteogenic VEGF-A expression. Upon binding of VEGF-A to VEGFR2, occurs homologous dimerization and undergoes intense autophosphorylation, inducing downstream phosphorylation of PI-3 kinase in ECs (Maes et al., 2010; Calciolari et al., 2018; Raines et al., 2019).

4.3 Effect of superhydrophilic titanium surface on osteogenesis

Bones are continually adapted and remodeled by the activity of two cell types: mesenchymal stem cells that differentiate into osteoblasts, the immature cell-rich braided bone that forms through ossification, and osteoclasts that act on the resorption of bone derived from macrophage/monocyte lines (Sartori et al., 2019). The phenotypic differentiation of MSCs into osteoblasts is an important step in bone formation and implant integration (Kunrath et al., 2020). This process is regulated by the TGF- β /BMP2 signal, and TGF- β , as well as BMP2 expressions, are significantly increased on the superhydrophilic surface (Ivanovski et al., 2011). The surface interaction between titanium implants and osteoblastic membranes consists of two stages: the nonspecific interactions of membranes using electrostatic forces and environmental binding involving the entire assembly in local contact (Rahnamaee et al., 2020). Calciolari reported that specific signaling pathways, such as Wnt, VEGF, and mitogen-activated protein kinases (MAPK) at the genomic and proteome levels have been identified as modulated by differences in titanium surface hydrophilicity; additionally, the enhanced osteogenic response on the hydrophilic surface may be caused by the up-regulation of the PI3K/Akt signaling pathway (Calciolari et al., 2018).

4.3.1 Superhydrophilicity surface with osteoblasts

Osteoblasts cultured on superhydrophilic surfaces showed a favorable diffusion performance, increased the contact area with materials, triggered osteogenic stimulation (da Silva et al., 2020), further promoted cell proliferation and differentiation (Li et al., 2019), and up-regulated related genes (Zhao et al., 2005). Studies have demonstrated that the osteoblasts cultured on the superhydrophilic titanium surface exhibited the enhancement of migration and proliferation ability (Henningesen et al., 2018; Smeets et al., 2019). Cold plasma treatment can promote the high expression of osteogenesis-related genes, such as alkaline phosphatase (ALP), Runt-related transcription factor 2 (Runx2), osteocalcin (OCN), and osteopontin (OPN) in precursor osteoblasts (Seo et al., 2014). An *in vivo* study by Tsujita et al, (2021) demonstrated that plasma-treated titanium could inhibit oxidative stress in cells and promote new bone formation around implants. In addition, Ann Wennerberg et al. (2014) compared the effects of the hydrophobic structure, hydrophobic structure of nano-structure, low-density nano-hydrophilic structure, and high-density nano-hydrophilic structure on the bone healing of adult rabbits via animal experiments *in vitro*, and concluded that the bone reaction was realized under the combination of wettability and the presence of nano-structure. The modified hydrophilic surface increased the absorption of plasma fibronectin (Rupp et al.,

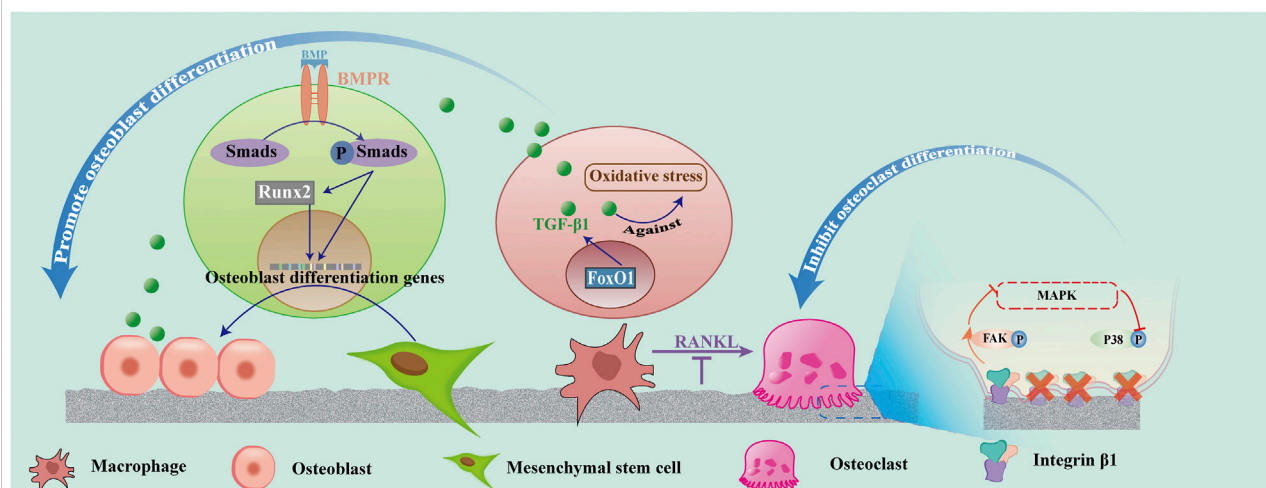


FIGURE 4

Effect of superhydrophilicity surface on osteogenic associated cells. Superhydrophilic surfaces promote osteogenic differentiation by promoting the activation of the BMP-Smad-Runx2 pathway in MSC, up-regulating FoxO1-TGF- β 1 expression in macrophages, and promoting osteogenic differentiation. Osteoclast differentiation was suppressed by inhibiting RANKL and integrin β 1/FAK/MAPK pathways.

2004), promoted the differentiation of osteoblast cells, and upregulated related genes (Zhao et al., 2005).

The BMP-Runx2 pathway is a potential pathway that promotes osteogenesis on superhydrophilicity surfaces. Bone morphogenetic protein (BMP) is a member of the multifunctional cytokine transforming growth factor- β (TGF- β) superfamily and is an important factor for osteogenesis. After BMP binds to its receptor (BMPR), BMPR is recruited to form an activated quaternary complex, which subsequently phosphorylates and activates the intracellular Smad protein. The receptor Smad binds to co-Smad and is transported to the nucleus as a transcription factor. Runx2 is a key transcriptional regulator of osteoblast differentiation, and one of the BMP-Smad target genes is Runx2. Runx2 binds to the OCN promoter and is involved in the early expression of osteochondral progenitor cells and osteoblast differentiation. Runx2 also induces the expression of osteogenic markers such as OCN and OPN (Lin and Hankenson, 2011). Both BMP and Runx2 are highly expressed on superhydrophilic surfaces, indicating that the superhydrophilicity promotion of bone integration may be closely related to the BMP-Runx2 pathway.

Additionally, the forkhead box transcription factor O1 (FoxO1) involves the interaction between the superhydrophilic surface and osteoblasts. Huang reported that the hydrophilic surface can reduce the level of ROS in macrophages under oxidative stress, and promote the inflammatory response to the anti-inflammatory type by upregulating FoxO1 (Huang et al., 2021). FoxO1 mediated the antioxidant and osteo-differentiation effects. Previous studies have also demonstrated that the appropriate upregulation of FoxO1 activates

transforming growth factor- β 1 (TGF- β 1), a key growth factor in wound repair, and protects the cells against oxidative stress (Ponugoti et al., 2013). Further molecular mechanism experiments showed that hydrophilic surfaces promoted FoxO1 expression under oxidative stress and also promoted osteogenic differentiation (Huang et al., 2021).

In conclusion, superhydrophilic surfaces might up-regulate the high expression of BMP and Runx2 and promote FoxO1 gene expression to up-regulate TGF- β 1, inhibit inflammation, as well as promote osteoblast proliferation and differentiation. Figure 4 shows the process of the BMP-Smad-Runx2 pathway and FoxO1-TGF- β 1 pathway. Thus, controlling the inflammation of the bone and surrounding tissues at an appropriate level is the key to promoting ideal osseointegration and reducing peri-implant bone resorption.

4.3.2 Superhydrophilicity surface with osteoclasts

Osteoclasts, a key cell in the remodeling stage, can be formed via macrophage differentiation stimulated by the receptor activator nuclear factor-Kappa B ligand (RANKL) in the presence of at least three nuclei (He et al., 2022). ECs support vascular-associated osteoclast differentiation through RANKL-RANK signaling (Zhang et al., 2020).

The inflammatory mediators, such as IL-1, IL-6, and TNF- α , secreted by the M1 macrophages, can increase the level of RANKL, an important cytokine that regulates the formation of osteoclasts, induce the death of osteoblasts (Sun et al., 2021), and promote the activation of macrophages into osteoclasts (Insua et al., 2017). Osteoclasts appeared in the

wound several days after surgery. They begin to create space for new bone formation and remove primary bone contact. The remodeling phase may continue for several years until most of the old bone in contact with the original bone is replaced by the newly formed, load-oriented bone (Terheyden et al., 2012). Studies have demonstrated that superhydrophilic surfaces increase macrophage recruitment and decrease osteoclast formation. However, the integrin $\beta 1$ expression was decreased in osteoclasts on the nanotube surface compared with the untreated titanium surface. The surfaces of superhydrophilicity titanium nanotubes inhibited the differentiation of osteoclasts and promoted osteogenesis by decreasing integrin $\beta 1$ -mediated FAK phosphorylation and its downstream MAPK pathway (P-P38). Moreover, the activity of osteoclasts on the nanotube surfaces was decreased (He et al., 2022).

5 Conclusion and perspectives

Owing to the unfavorable osseointegration and implant failure caused by microbial-related infections in clinical practice, implant materials that combine antibacterial properties and biocompatibility have always been an important goal for obtaining the perfect initial implantation effect and for maintaining the long-term survival of implants. Among the various surface modification methods, improving the wettability of the implant surfaces has been considered to regulate the host response to the implants, thereby accelerating the osseointegration speed; the superhydrophilic surfaces can possess the above functionality as well as show certain antibacterial effects. In this study, advances in superhydrophilicity titanium alloys, including antibacterial function and improved biocompatibility, are reviewed, and the related mechanisms in recent research are summarized. The post-treated titanium surfaces usually perform their antibacterial function by inhibiting bacteria adhesion and cell viability and even partially eliminating bacteria. Moreover, because of the favorable biocompatibility, a superhydrophilic titanium surface could effectively modulate the macrophages with an enhanced immune response against bacteria and influence the race between macrophages and bacteria to adhere to biomaterial surfaces (Yang et al., 2021). Thus, the superhydrophilic surface considerably reduces the likelihood of failure of the implant to bond to the bone surface owing to microbial infection. It promotes osteogenic immune responses as well as angiogenesis and osteogenic differentiation.

However, numerous challenges remain to be overcome. First, the mechanisms of the obtained antibacterial properties, based on the treatment methods, require further investigation. Current studies have observed that the superhydrophilicity of titanium treated with UV or cold plasma could inhibit bacterial adhesion and proliferation in a time-dependent manner which commonly

lasts for over 24 h, longer than the 6-h decisive period post-implantation. The different durations of the surface antibacterial properties are related to multiple factors, including the treatment methods, bacterial species, and inherent composition of the biomaterials. Furthermore, the duration of the superhydrophilic surface treatment could influence the antibacterial effect, but the effect has certain limitations compared with other antibacterial methods. Therefore, it is of significance to combine superhydrophilicity treatment with other surface modifications to exert better antibacterial properties while obtaining superior biocompatibility. Secondly, the specific effects of surface chemical composition changes on osteoblast-related cells need to be further studied. It has been found that the decrease of carbon content on the titanium surface is beneficial to improve the biological activity, and the increase of oxygen content is beneficial to increase the oxygenated fraction that can absorb fibronectin, and improve the protein adsorption rate to regulate the proteoglycan and cytoskeleton structure. Therefore, the effect of chemical composition changes on osteogenesis is worthy of further study. Thirdly, more *in vivo* studies are required, particularly to assess its effect on long-term implantation, which will be key to long-term clinical use. The biocompatibility and mechanical strength of the coating, such as the mechanical stability of the superhydrophilicity surface of titanium alloy, whether the propagation of the biological coating can withstand the biological environment of the human body, and whether the exposure to metal oxides will interfere with the function of cells and organs, have not been confirmed. Therefore, it is important to determine the stability and cytotoxic behavior of this material/implant. Fourthly, the durability of the structure has not been proven, and despite the significant efforts made to date, achieving superhydrophilic surfaces with high mechanical strength, favorable chemical stability, and durability to meet demanding applications remains a challenge, and further research is required. For numerous applications that do not require wear resistance, superhydrophilic surfaces can be used for a favorable performance. For example, superhydrophilic surfaces can be applied to permanent implants, reduce bacterial adhesion, and promote implant bone integration. Therefore, it is important to understand the durability requirements of the target application to adopt the appropriate treatment methods when preparing suitable superhydrophilic surfaces. Finally, the artificial structure is far from emulating the natural structure. The superhydrophilicity of natural structures and other properties conferred by them cannot be fully reflected in artificial surfaces.

In conclusion, while the superhydrophilicity obtained by treating titanium alloys alone holds considerable promise for the development of next-generation orthopedic and dental implants, more work and sustained effort are required to translate them into devices for clinical applications. In addition, determining methods to prove the sustainable superhydrophilicity of the material surface in the body

after implantation remains a challenge to be overcome at present.

Author contributions

BZ, SG, and ST conceived the concept of this review. HS and MM wrote the manuscript. QW and TY edited the manuscript. All authors contributed to manuscript revision, read, and approved the submitted version.

Funding

This work was supported by the Natural Science Foundation of Liaoning Province (2019-BS-281), National Natural Science Foundation of China (No. 82071151), Yanglei academician expert workstation of Yunnan Province (202205AF150025) and Guangxi Key Laboratory of the Rehabilitation and

Reconstruction for Oral and Maxillofacial Research Funded Project (No. Q13 GXKLRR02107).

Conflict of interest

The authors declare that the research was conducted in the absence of any commercial or financial relationships that could be construed as a potential conflict of interest.

Publisher's note

All claims expressed in this article are solely those of the authors and do not necessarily represent those of their affiliated organizations, or those of the publisher, the editors and the reviewers. Any product that may be evaluated in this article, or claim that may be made by its manufacturer, is not guaranteed or endorsed by the publisher.

References

- Abaricia, J. O., Shah, A. H., Musselman, R. M., and Olivares-Navarrete, R. (2020). Hydrophilic titanium surfaces reduce neutrophil inflammatory response and NETosis. *Biomater. Sci.* 8 (8), 2289–2299. doi:10.1039/c9bm01474h
- Agbe, H., Sarkar, D. K., and Chen, X. G. (2020). Tunable superhydrophobic aluminum surfaces with anti-biofouling and antibacterial properties. *Coatings* 10 (10), 982. doi:10.3390/coatings10100982
- Albrektsson, T., and Wennerberg, A. (2019). On osseointegration in relation to implant surfaces. *Clin. Implant Dent. Relat. Res.* 21, 4–7. doi:10.1111/cid.12742
- An, N., Schedle, A., Wieland, M., Andrukhov, O., Matejka, M., and Rausch-Fan, X. (2009). Proliferation, behavior, and cytokine gene expression of human umbilical vascular endothelial cells in response to different titanium surfaces. *J. Biomed. Mater. Res. A* 93 (1), 364–372. doi:10.1002/jbm.a.32539
- Anderson, J. M., Rodriguez, A., and Chang, D. T. (2008). Foreign body reaction to biomaterials. *Seminars Immunol.* 20 (2), 86–100. doi:10.1016/j.smim.2007.11.004
- Arciola, C. R., Campoccia, D., and Montanaro, L. (2018). Implant infections: adhesion, biofilm formation and immune evasion. *Nat. Rev. Microbiol.* 16 (7), 397–409. doi:10.1038/s41579-018-0019-y
- Att, W., Hori, N., Takeuchi, M., Ouyang, J., Yang, Y., Anpo, M., et al. (2009). Time-dependent degradation of titanium osteoconductivity: an implication of biological aging of implant materials. *Biomaterials* 30 (29), 5352–5363. doi:10.1016/j.biomaterials.2009.06.040
- Bai, L., Du, Z., Du, J., Yao, W., Zhang, J., Weng, Z., et al. (2018). A multifaceted coating on titanium dictates osteoimmunomodulation and osteo/angiogenesis towards ameliorative osseointegration. *Biomaterials* 162, 154–169. doi:10.1016/j.biomaterials.2018.02.010
- Bartlett, K., Movafaghi, S., Dasi, L. P., Kota, A. K., and Popat, K. C. (2018). Antibacterial activity on superhydrophobic titania nanotube arrays. *Colloids Surfaces B Biointerfaces* 166, 179–186. doi:10.1016/j.colsurfb.2018.03.019
- Boks, N. P., Busscher, H. J., van der Mei, H. C., and Norde, W. (2008). Bond-strengthening in staphylococcal adhesion to hydrophilic and hydrophobic surfaces using atomic force microscopy. *Langmuir* 24 (22), 12990–12994. doi:10.1021/la801824c
- Brinkmann, V., Reichard, U., Goosmann, C., Fauler, B., Uhlemann, Y., Weiss, D. S., et al. (2004). Neutrophil extracellular traps kill bacteria. *Science* 303 (5663), 1532–1535. doi:10.1126/science.1092385
- Burm, K. T. A. L. (2012). Plasma: The fourth state of matter. *Plasma Chem. Plasma process.* 32 (2), 401–407. doi:10.1007/s11090-012-9356-1
- Calciolari, E., Hamlet, S., Ivanovski, S., and Donos, N. (2018). Pro-osteogenic properties of hydrophilic and hydrophobic titanium surfaces: Crosstalk between signalling pathways in *in vivo* models. *J. Periodontol. Res.* 53 (4), 598–609. doi:10.1111/jre.12550
- Campoccia, D., Montanaro, L., and Arciola, C. R. (2006). The significance of infection related to orthopedic devices and issues of antibiotic resistance. *Biomaterials* 27 (11), 2331–2339. doi:10.1016/j.biomaterials.2005.11.044
- Cao, Y., Su, B., Chinnaraj, S., Jana, S., Bowen, L., Charlton, S., et al. (2018). Nanostructured titanium surfaces exhibit recalcitrance towards *Staphylococcus epidermidis* biofilm formation. *Sci. Rep.* 8 (1), 1071. doi:10.1038/s41598-018-19484-x
- Chen, H., Zhang, P., Zhang, L., Liu, H., Jiang, Y., Zhang, D., et al. (2016). Continuous directional water transport on the peristome surface of *Nepenthes alata*. *Nature* 532 (7597), 85–89. doi:10.1038/nature17189
- Chen, M., Li, H., Wang, X., Qin, G., and Zhang, E. (2019). Improvement in antibacterial properties and cytocompatibility of titanium by fluorine and oxygen dual plasma-based surface modification. *Appl. Surf. Sci.* 463, 261–274. doi:10.1016/j.apsusc.2018.08.194
- Choi, S. H., Jeong, W. S., Cha, J. Y., Lee, J. H., Yu, H. S., Choi, E. H., et al. (2016). Time-dependent effects of ultraviolet and nonthermal atmospheric pressure plasma on the biological activity of titanium. *Sci. Rep.* 6, 33421. doi:10.1038/srep33421
- Chouirfa, H., Bouloussa, H., Migonney, V., and Falentin-Daudre, C. (2019). Review of titanium surface modification techniques and coatings for antibacterial applications. *Acta Biomater.* 83, 37–54. doi:10.1016/j.actbio.2018.10.036
- Da Silva, R. A., da Silva Feltran, G., Ferreira, M. R., Wood, P. F., Bezerra, F., and Zambuzzi, W. F. (2020). The impact of bioactive surfaces in the early stages of osseointegration: An *in vitro* comparative study evaluating the HAnano[®] and SLActive[®] super hydrophilic surfaces. *BioMed Res. Int.* 2020, 1–11. doi:10.1155/2020/3026893
- Dai, X., Wei, Y., Zhang, X., Meng, S., Mo, X., Liu, X., et al. (2015). Attenuating immune response of macrophage by enhancing hydrophilicity of Ti surface. *J. Nanomater.* 2015, 1–8. doi:10.1155/2015/712810
- De Avila, E. D., Lima, B. P., Sekiya, T., Torii, Y., Ogawa, T., Shi, W., et al. (2015). Effect of UV-photofunctionalization on oral bacterial attachment and biofilm formation to titanium implant material. *Biomaterials* 67, 84–92. doi:10.1016/j.biomaterials.2015.07.030
- El Chaar, E., Zhang, L., Zhou, Y., Sandgren, R., Fricain, J.-C., Dard, M., et al. (2019). Osseointegration of superhydrophilic implants placed in defect grafted bones. *Int. J. Oral Maxillofac. Implants* 34 (2), 443–450. doi:10.11607/jomi.7172
- Fadeeva, E., Truong, V. K., Stiesch, M., Chichkov, B. N., Crawford, R. J., Wang, J., et al. (2011). Bacterial retention on superhydrophobic titanium surfaces fabricated by femtosecond laser ablation. *Langmuir* 27 (6), 3012–3019. doi:10.1021/la104607g

- Ferraris, S., and Spriano, S. (2016). Antibacterial titanium surfaces for medical implants. *Mater. Sci. Eng. C* 61, 965–978. doi:10.1016/j.msec.2015.12.062
- Gallardo-Moreno, A. M., Pacha-Olivenza, M. A., Fernandez-Calderon, M. C., Perez-Giraldo, C., Bruque, J. M., and Gonzalez-Martin, M. L. (2010). Bactericidal behaviour of Ti6Al4V surfaces after exposure to UV-C light. *Biomaterials* 31 (19), 5159–5168. doi:10.1016/j.biomaterials.2010.03.005
- Gao, S., Lu, R., Wang, X., Chou, J., Wang, N., Huai, X., et al. (2020). Immune response of macrophages on super-hydrophilic TiO₂ nanotube arrays. *J. Biomater. Appl.* 34 (9), 1239–1253. doi:10.1177/0885328220903249
- Guo, T., Oztug, N. A. K., Han, P., Ivanovski, S., and Gulati, K. (2021). Influence of sterilization on the performance of anodized nanoporous titanium implants. *Mater. Sci. Eng. C* 130, 112429. doi:10.1016/j.msec.2021.112429
- Han, A., Tsoi, J. K. H., Rodrigues, F. P., Leprince, J. G., and Palin, W. M. (2016). Bacterial adhesion mechanisms on dental implant surfaces and the influencing factors. *Int. J. Adhesion Adhesives* 69, 58–71. doi:10.1016/j.ijadhadh.2016.03.022
- Hatoko, M., Komasa, S., Zhang, H., Sekino, T., and Okazaki, J. (2019). UV treatment improves the biocompatibility and antibacterial properties of crystallized nanostructured titanium surface. *Int. J. Mol. Sci.* 20 (23), 5991. doi:10.3390/ijms20235991
- He, J., Du, Y. E., Bai, Y., An, J., Cai, X., Chen, Y., et al. (2019). Facile formation of anatase/rutile TiO₂ nanocomposites with enhanced photocatalytic activity. *Molecules* 24 (16), 2996. doi:10.3390/molecules24162996
- He, Y., Li, Z., Ding, X., Xu, B., Wang, J., Li, Y., et al. (2022). Nanoporous titanium implant surface promotes osteogenesis by suppressing osteoclastogenesis via integrin β 1/FAKpY397/MAPK pathway. *Bioact. Mater.* 8, 109–123. doi:10.1016/j.bioactmat.2021.06.033
- Henningsen, A., Smeets, R., Hartjen, P., Heinrich, O., Heuberger, R., Heiland, M., et al. (2018). Photofunctionalization and non-thermal plasma activation of titanium surfaces. *Clin. Oral Investig.* 22 (2), 1045–1054. doi:10.1007/s00784-017-2186-z
- Hoebe, A., Landuyt, B., Highley, M. S., Wildiers, H., Van Oosterom, A. T., and De Bruijn, E. A. (2004). Vascular endothelial growth factor and angiogenesis. *Pharmacol. Rev.* 56 (4), 549–580. doi:10.1124/pr.56.4.3
- Hotchkiss, K. M., Clark, N. M., and Olivares-Navarrete, R. (2018). Macrophage response to hydrophilic biomaterials regulates MSC recruitment and T-helper cell populations. *Biomaterials* 182, 202–215. doi:10.1016/j.biomaterials.2018.08.029
- Hotchkiss, K. M., Reddy, G. B., Hyzy, S. L., Schwartz, Z., Boyan, B. D., and Olivares-Navarrete, R. (2016). Titanium surface characteristics, including topography and wettability, alter macrophage activation. *Acta Biomater.* 31, 425–434. doi:10.1016/j.actbio.2015.12.003
- Hu, K., and Olsen, B. R. (2016). Osteoblast-derived VEGF regulates osteoblast differentiation and bone formation during bone repair. *J. Clin. Invest.* 126 (2), 509–526. doi:10.1172/jci82585
- Huang, J., Li, R., Yang, J., Cai, M., Lee, Y., Wang, A., et al. (2021). Bioadaptation of implants to *in vitro* and *in vivo* oxidative stress pathological conditions via nanotopography-induced FoxO1 signaling pathways to enhance Osteoimmunological regeneration. *Bioact. Mater.* 6 (10), 3164–3176. doi:10.1016/j.bioactmat.2021.02.023
- Insua, A., Monje, A., Wang, H. L., and Miron, R. J. (2017). Basis of bone metabolism around dental implants during osseointegration and peri-implant bone loss. *J. Biomed. Mater. Res. A* 105 (7), 2075–2089. doi:10.1002/jbma.36060
- Itabashi, T., Narita, K., Ono, A., Wada, K., Tanaka, T., Kumagai, G., et al. (2017). Bactericidal and antimicrobial effects of pure titanium and titanium alloy treated with short-term, low-energy UV irradiation. *Bone Jt. Res.* 6 (2), 108–112. doi:10.1302/2046-3758.6.2.2000619
- Ivanovski, S., Hamlet, S., Salvi, G. E., Huynh-Ba, G., Bosshardt, D. D., Lang, N. P., et al. (2011). Transcriptional profiling of osseointegration in humans. *Clin. Oral Implants Res.* 22 (4), 373–381. doi:10.1111/j.1600-0501.2010.02112.x
- Jaggessar, A., Shahali, H., Mathew, A., and Yarlaga, P. K. D. V. (2017). Biomimicking nano and micro-structured surface fabrication for antibacterial properties in medical implants. *J. Nanobiotechnol.* 15 (1), 64. doi:10.1186/s12951-017-0306-1
- Jenkins, J., Mantell, J., Neal, C., Gholinia, A., Verkade, P., Nobbs, A. H., et al. (2020). Antibacterial effects of nanopillar surfaces are mediated by cell impedance, penetration and induction of oxidative stress. *Nat. Commun.* 11 (1), 1626. doi:10.1038/s41467-020-15471-x
- Jeong, W. S., Kwon, J. S., Lee, J. H., Uhm, S. H., Ha Choi, E., and Kim, K. M. (2017). Bacterial attachment on titanium surfaces is dependent on topography and chemical changes induced by nonthermal atmospheric pressure plasma. *Biomed. Mater.* 12 (4), 045015. doi:10.1088/1748-605X/aa734e
- Kartikasari, N., Yamada, M., Watanabe, J., Tiskratok, W., He, X., Kamano, Y., et al. (2022). Titanium surface with nanospikes tunes macrophage polarization to produce inhibitory factors for osteoclastogenesis through nanotopographic cues. *Acta Biomater.* 137, 316–330. doi:10.1016/j.actbio.2021.10.019
- Kattula, S., Byrnes, J. R., and Wolberg, A. S. (2017). Fibrinogen and fibrin in hemostasis and thrombosis. *Arterioscler. Thromb. Vasc. Biol.* 37 (3), e13–e21. doi:10.1161/ATVBAHA.117.308564
- Kaur, M., and Singh, K. (2019). Review on titanium and titanium based alloys as biomaterials for orthopaedic applications. *Mater. Sci. Eng. C* 102, 844–862. doi:10.1016/j.msec.2019.04.064
- Kavitha Sri, A., Deeksha, P., Deepika, G., Nishanthini, J., Hikku, G. S., Antinate Shilpa, S., et al. (2020). Super-hydrophobicity: Mechanism, fabrication and its application in medical implants to prevent biomaterial associated infections. *J. Ind. Eng. Chem.* 92, 1–17. doi:10.1016/j.jiec.2020.08.008
- Koban, I., Holtfrete, B., Hubner, N. O., Matthes, R., Sietmann, R., Kindel, E., et al. (2011). Antimicrobial efficacy of non-thermal plasma in comparison to chlorhexidine against dental biofilms on titanium discs *in vitro* - proof of principle experiment. *J. Clin. Periodontol.* 38 (10), 956–965. doi:10.1111/j.1600-051X.2011.01740.x
- Kunrath, M. F., Dos Santos, R. P., de Oliveira, S. D., Hubler, R., Sesterheim, P., and Teixeira, E. R. (2020). Osteoblastic cell behavior and early bacterial adhesion on macro-micro- and nanostructured titanium surfaces for biomedical implant applications. *Int. J. Oral Maxillofac. Implants* 35 (4), 773–781. doi:10.11607/jomi.8069
- lan, G., Li, M., Tan, Y., Li, L., Yang, X., Ma, L., et al. (2015). Promoting bone mesenchymal stem cells and inhibiting bacterial adhesion of acid-etched nanostructured titanium by ultraviolet functionalization. *J. Mater. Sci. Technol.* 31 (2), 182–190. doi:10.1016/j.jmst.2014.08.007
- Lazarevic, V., Glimcher, L. H., and Lord, G. M. (2013). T-Bet: a bridge between innate and adaptive immunity. *Nat. Rev. Immunol.* 13 (11), 777–789. doi:10.1038/nri3536
- Lee, J. H., Jeong, W. S., Seo, S. J., Kim, H. W., Kim, K. N., Choi, E. H., et al. (2017). Non-thermal atmospheric pressure plasma functionalized dental implant for enhancement of bacterial resistance and osseointegration. *Dent. Mater.* 33 (3), 257–270. doi:10.1016/j.dental.2016.11.011
- Lee, J. W. Y., and Bance, M. L. (2019). Physiology of osseointegration. *Otolaryngol. Clin. North Am.* 52 (2), 231–242. doi:10.1016/j.otc.2018.11.004
- Lee, M. J., Kwon, J. S., Jiang, H. B., Choi, E. H., Park, G., and Kim, K. M. (2019). The antibacterial effect of non-thermal atmospheric pressure plasma treatment of titanium surfaces according to the bacterial wall structure. *Sci. Rep.* 9 (1), 1938. doi:10.1038/s41598-019-39414-9
- Lei, H., Schmidt-Bleek, K., Dienelt, A., Reinke, P., and Volk, H. D. (2015). Regulatory T cell-mediated anti-inflammatory effects promote successful tissue repair in both indirect and direct manners. *Front. Pharmacol.* 6, 184. doi:10.3389/fphar.2015.00184
- Li, Y., Sasaki, T., Shimizu, Y., and Koshizaki, N. (2008). A hierarchically ordered TiO₂ hemispherical particle array with hexagonal non-close-packed tops: Synthesis and stable superhydrophilicity without UV irradiation. *Small* 4 (12), 2286–2291. doi:10.1002/smll.200800428
- Li, Y., Li, B., Song, Y., Ma, A., Li, C., Zhang, X., et al. (2019). Improved osteoblast adhesion and osseointegration on TiO₂ nanotubes surface with hydroxyapatite coating. *Dent. Mater. J.* 38 (2), 278–286. doi:10.4012/dmj.2018-118
- Li, K., Liu, S., Hu, T., Razanau, I., Wu, X., Ao, H., et al. (2020). Optimized nanointerface engineering of micro/nanostructured titanium implants to enhance cell-nanotopography interactions and osseointegration. *ACS Biomater. Sci. Eng.* 6 (2), 969–983. doi:10.1021/acsbomaterials.9b01717
- Lin, H.-Y., and Bumgardner, J. D. (2004). *In vitro* biocorrosion of Co-Cr-Mo implant alloy by macrophage cells. *J. Orthop. Res.* 22 (6), 1231–1236. doi:10.1016/j.orthres.2004.04.005
- Lin, G. L., and Hankenson, K. D. (2011). Integration of BMP, Wnt, and notch signaling pathways in osteoblast differentiation. *J. Cell. Biochem.* 112 (12), 3491–3501. doi:10.1002/jcb.23287
- Liu, Y., Berendsen, A. D., Jia, S., Lotinun, S., Baron, R., Ferrara, N., et al. (2012). Intracellular VEGF regulates the balance between osteoblast and adipocyte differentiation. *J. Clin. Invest.* 122 (9), 3101–3113. doi:10.1172/jci61209
- Lu, L., Deegan, A., Musa, F., Xu, T., and Yang, Y. (2018). The effects of biomimetically conjugated VEGF on osteogenesis and angiogenesis of MSCs (human and rat) and HUVECs co-culture models. *Colloids Surfaces B Biointerfaces* 167, 550–559. doi:10.1016/j.colsurfb.2018.04.060
- Lv, L., Xie, Y., Li, K., Hu, T., Lu, X., Cao, Y., et al. (2018). Unveiling the mechanism of surface hydrophilicity-modulated macrophage polarization. *Adv. Healthc. Mater.* 7 (19), e1800675. doi:10.1002/adhm.201800675

- Maes, C., Goossens, S., Bartunkova, S., Drogat, B., Coenegrachts, L., Stockmans, I., et al. (2010). Increased skeletal VEGF enhances beta-catenin activity and results in excessively ossified bones. *EMBO J.* 29 (2), 424–441. doi:10.1038/emboj.2009.361
- Manivasagam, V. K., Perumal, G., Arora, H. S., and Popat, K. C. (2022). Enhanced antibacterial properties on superhydrophobic micro-nano structured titanium surface. *J. Biomed. Mater. Res. A* 110, 1314–1328. doi:10.1002/jbm.a.37375
- Matsumoto, T., Tashiro, Y., Komasa, S., Miyake, A., Komasa, Y., and Okazaki, J. (2020). Effects of surface modification on adsorption behavior of cell and protein on titanium surface by using quartz crystal microbalance system. *Mater. (Basel)* 14 (1), 97. doi:10.3390/ma14010097
- Moran, E., Byren, I., and Atkins, B. L. (2010). The diagnosis and management of prosthetic joint infections. *J. Antimicrob. Chemother.* 65, iii45–54. doi:10.1093/jac/dkq305
- Moreau, M., Orange, N., and Feuilloley, M. G. (2008). Non-thermal plasma technologies: new tools for bio-decontamination. *Biotechnol. Adv.* 26 (6), 610–617. doi:10.1016/j.biotechadv.2008.08.001
- Noble, F. I., and Noble, J. I. (2014). Bone biology: vessels of rejuvenation. *Nature* 507 (7492), 313–314. doi:10.1038/nature13210
- Norowski, P. A., Jr., and Bumgardner, J. D. (2009). Biomaterial and antibiotic strategies for peri-implantitis: a review. *J. Biomed. Mater. Res.* 88 (2), 530–543. doi:10.1002/jbm.b.31152
- Nunes Filho, A., Aires, M. M., Braz, D. C., Hinrichs, R., Macedo, A. J., and Alves, C., Jr. (2018). Titanium surface chemical composition interferes in the *Pseudomonas aeruginosa* biofilm formation. *Artif. Organs* 42 (2), 193–199. doi:10.1111/aor.12983
- Overmann, A. L., Aparicio, C., Richards, J. T., Mutreja, I., Fischer, N. G., Wade, S. M., et al. (2020). Orthopaedic osseointegration: Implantology and future directions. *J. Orthop. Res.* 38 (7), 1445–1454. doi:10.1002/jor.24576
- Pajerski, W., Duch, J., Ochonska, D., Golda-Cepa, M., Brzychczy-Wloch, M., and Kotarba, A. (2020). Bacterial attachment to oxygen-functionalized graphenic surfaces. *Mater. Sci. Eng. C* 113, 110972. doi:10.1016/j.msec.2020.110972
- Paldrychová, M., Vaňková, E., Scholtz, V., Julák, J., Sembolová, E., Matátková, O., et al. (2019). Effect of non-thermal plasma on AHL-dependent QS systems and biofilm formation in *Pseudomonas aeruginosa*: Difference between non-hospital and clinical isolates. *AIP Adv.* 9 (5), 055117. doi:10.1063/1.5090451
- Paldrychova, M., Vankova, E., Kasparova, P., Sembolova, E., Matatkova, O., Masak, J., et al. (2020). Use of non-thermal plasma pre-treatment to enhance antibiotic action against mature *Pseudomonas aeruginosa* biofilms. *World J. Microbiol. Biotechnol.* 36 (8), 108. doi:10.1007/s11274-020-02891-6
- Pan, F., Altenried, S., Zuber, F., Wagner, R. S., Su, Y. H., Rottmar, M., et al. (2021). Photo-activated titanium surface confers time dependent bactericidal activity towards Gram positive and negative bacteria. *Colloids Surfaces B Biointerfaces* 206, 111940. doi:10.1016/j.colsurfb.2021.111940
- Park, C., Park, S. W., Yun, K. D., Ji, M. K., Kim, S., Yang, Y. P., et al. (2018). Effect of plasma treatment and its post process duration on shear bonding strength and antibacterial effect of dental zirconia. *Mater. (Basel)* 11 (11), 2233. doi:10.3390/ma11112233
- Petzold, A., Balcer, L. J., Calabresi, P. A., Costello, F., Frohman, T. C., Frohman, E. M., et al. (2017). Retinal layer segmentation in multiple sclerosis: a systematic review and meta-analysis. *Lancet Neurol.* 16 (10), 797–812. doi:10.1016/s1474-4422(17)30278-8
- Ponugoti, B., Xu, F., Zhang, C., Tian, C., Pacios, S., and Graves, D. T. (2013). FOXO1 promotes wound healing through the up-regulation of TGF- β 1 and prevention of oxidative stress. *J. Cell Biol.* 203 (2), 327–343. doi:10.1083/jcb.201305074
- Puckett, S. D., Taylor, E., Raimondo, T., and Webster, T. J. (2010). The relationship between the nanostructure of titanium surfaces and bacterial attachment. *Biomaterials* 31 (4), 706–713. doi:10.1016/j.biomaterials.2009.09.081
- Qi, M., Gong, X., Wu, B., and Zhang, G. (2017). Landing dynamics of swimming bacteria on a polymeric surface: effect of surface properties. *Langmuir* 33 (14), 3525–3533. doi:10.1021/acs.langmuir.7b00439
- Rabelink, T. J., and Luscher, T. F. (2006). Endothelial nitric oxide synthase. *Arterioscler. Thromb. Vasc. Biol.* 26 (2), 267–271. doi:10.1161/01.Atrv.0000196554.85799.77
- Rahnamaee, S. Y., Bagheri, R., Vossoughi, M., Ahmadi Seyedkhani, S., and Samadikuchaksaraei, A. (2020). Bioinspired multifunctional TiO₂ hierarchical micro/nanostructures with tunable improved bone cell growth and inhibited bacteria adhesion. *Ceram. Int.* 46 (7), 9669–9679. doi:10.1016/j.ceramint.2019.12.234
- Raines, A. L., Berger, M. B., Patel, N., Hyzy, S. L., Boyan, B. D., and Schwartz, Z. (2019). VEGF-A regulates angiogenesis during osseointegration of Ti implants via paracrine/autocrine regulation of osteoblast response to hierarchical microstructure of the surface. *J. Biomed. Mater. Res. A* 107 (2), 423–433. doi:10.1002/jbm.a.36559
- Ren, Y., Liu, H., Liu, X., Zheng, Y., Li, Z., Li, C., et al. (2020). Photoresponsive materials for antibacterial applications. *Cell Rep. Phys. Sci.* 1 (11), 100245. doi:10.1016/j.xcrp.2020.100245
- Robson, M. C., Dubay, D. A., Wang, X., and Franz, M. G. (2004). Effect of cytokine growth factors on the prevention of acute wound failure. *Wound Repair Regen.* 12 (1), 38–43. doi:10.1111/j.1067-1927.2004.012109.x
- Rupp, F., Scheideler, L., Rehbein, D., Axmann, D., and Geis-Gerstorf, J. (2004). Roughness induced dynamic changes of wettability of acid etched titanium implant modifications. *Biomaterials* 25 (7–8), 1429–1438. doi:10.1016/j.biomaterials.2003.08.015
- Sakka, S., and Coulthard, P. (2009). Bone quality: a reality for the process of osseointegration. *Implant Dent.* 18 (6), 480–485. doi:10.1097/ID.0b013e3181bb840d
- Salido, M., Vilches, J. I., Gutierrez, J. L., and Vilches, J. (2007). Actin cytoskeletal organization in human osteoblasts grown on different dental titanium implant surfaces. *Histol. Histopathol.* 22 (12), 1355–1364. doi:10.14670/HH-22.1355
- Sartori, E. M., das Neves, A. M., Magro, O., Mendonca, D. B. S., Krebsbach, P. H., Cooper, L. F., et al. (2019). The role of MicroRNAs in the osseointegration process. *Int. J. Oral Maxillofac. Implants* 34 (2), 397–410. doi:10.11607/jomi.6581
- Schiaffino, S., Pereira, M. G., Ciciliot, S., and Rovere-Querini, P. (2017). Regulatory T cells and skeletal muscle regeneration. *FEBS J.* 284 (4), 517–524. doi:10.1111/febs.13827
- Selders, G. S., Fetz, A. E., Radic, M. Z., and Bowlin, G. L. (2017). An overview of the role of neutrophils in innate immunity, inflammation and host-biomaterial integration. *Regen. Biomater.* 4 (1), 55–68. doi:10.1093/rb/rbw041
- Seo, H. Y., Kwon, J. S., Choi, Y. R., Kim, K. M., Choi, E. H., and Kim, K. N. (2014). Cellular attachment and differentiation on titania nanotubes exposed to air- or nitrogen-based non-thermal atmospheric pressure plasma. *PLoS One* 9 (11), e113477. doi:10.1371/journal.pone.0113477
- Shibata, Y., and Miyazaki, T. (2014). “Biological activity of titanium,” in *Handbook of oral biomaterials Research*, 317–338. doi:10.1201/B15644-10
- Shibata, Y., Suzuki, D., Omori, S., Tanaka, R., Murakami, A., Kataoka, Y., et al. (2010). The characteristics of *in vitro* biological activity of titanium surfaces anodically oxidized in chloride solutions. *Biomaterials* 31 (33), 8546–8555. doi:10.1016/j.biomaterials.2010.07.098
- Si, Y., Dong, Z., and Jiang, L. (2018). Bioinspired designs of superhydrophobic and superhydrophilic materials. *ACS Cent. Sci.* 4 (9), 1102–1112. doi:10.1021/acscentsci.8b00504
- Smeets, R., Henningsen, A., Heuberger, R., Hanisch, O., Schwarz, F., and Precht, C. (2019). Influence of UV irradiation and cold atmospheric pressure plasma on zirconia surfaces: an *in vitro* study. *Int. J. Oral Maxillofac. Implants* 34 (2), 329–336. doi:10.11607/jomi.7017
- Song, X., Gao, H., and Qian, Y. (2014). Th17 differentiation and their pro-inflammation function. *Adv. Exp. Med. Biol.* 841, 99–151. doi:10.1007/978-94-017-9487-9_5
- Sun, Y., Li, J., Xie, X., Gu, F., Sui, Z., Zhang, K., et al. (2021). Macrophage-osteoclast associations: Origin, polarization, and subgroups. *Front. Immunol.* 12, 778078. doi:10.3389/fimmu.2021.778078
- Terheyden, H., Lang, N. P., Bierbaum, S., and Stadlinger, B. (2012). Osseointegration—communication of cells. *Clin. Oral Implants Res.* 23 (10), 1127–1135. doi:10.1111/j.1600-0501.2011.02327.x
- Theiss, A. L., Simmons, J. G., Jobin, C., and Lund, P. K. (2005). Tumor necrosis factor (TNF) α increases collagen accumulation and proliferation in intestinal myofibroblasts via TNF receptor 2. *J. Biol. Chem.* 280 (43), 36099–36109. doi:10.1074/jbc.M505291200
- Thiam, H. R., Wong, S. L., Wagner, D. D., and Waterman, C. M. (2020). Cellular mechanisms of NETosis. *Annu. Rev. Cell Dev. Biol.* 36, 191–218. doi:10.1146/annurev-cellbio-020520-111016
- Tsujita, H., Nishizaki, H., Miyake, A., Takao, S., and Komasa, S. (2021). Effect of plasma treatment on titanium surface on the tissue surrounding implant material. *Int. J. Mol. Sci.* 22 (13), 6931. doi:10.3390/ijms22136931
- Vanithakumari, S. C., George, R. P., and Mudali, U. K. (2013). Enhancement of corrosion performance of titanium by micro-nano texturing. *Corrosion* 69 (8), 804–812. doi:10.5006/0902
- Vorobyev, A. Y., and Guo, C. (2010). Laser turns silicon superwicking. *Opt. Express* 18 (7), 6455–6460. doi:10.1364/oe.18.006455
- Wang, J. (2018). Neutrophils in tissue injury and repair. *Cell Tissue Res.* 371 (3), 531–539. doi:10.1007/s00441-017-2785-7

- Wang, L., Wang, W., Zhao, H., Liu, Y., Liu, J., and Bai, N. (2020). Bioactive effects of low-temperature argon-oxygen plasma on a titanium implant surface. *ACS Omega* 5 (8), 3996–4003. doi:10.1021/acsomega.9b03504
- Wennerberg, A., Jimbo, R., Stübinger, S., Obrecht, M., Dard, M., and Berner, S. (2014). Nanostructures and hydrophilicity influence osseointegration: a biomechanical study in the rabbit tibia. *Clin. Oral Implants Res.* 25 (9), 1041–1050. doi:10.1111/clr.12213
- Yang, H., Biermann, M. H., Brauner, J. M., Liu, Y., Zhao, Y., and Herrmann, M. (2016). New insights into neutrophil extracellular traps: Mechanisms of formation and role in inflammation. *Front. Immunol.* 7, 302. doi:10.3389/fimmu.2016.00302
- Yang, Y., Zhang, H., Komasa, S., Morimoto, Y., Sekino, T., Kawazoe, T., et al. (2021). UV/ozone irradiation manipulates immune response for antibacterial activity and bone regeneration on titanium. *Mater. Sci. Eng. C* 129, 112377. doi:10.1016/j.msec.2021.112377
- Yang, K., Shi, J., Wang, L., Chen, Y., Liang, C., Yang, L., et al. (2022). Bacterial anti-adhesion surface design: Surface patterning, roughness and wettability: A review. *J. Mater. Sci. Technol.* 99, 82–100. doi:10.1016/j.jmst.2021.05.028
- Yeniyol, S., Mutlu, I., He, Z., Yuksel, B., Boylan, R. J., Urgen, M., et al. (2015). Photocatalytic antibacterial activity of mixed-phase TiO₂ nanocomposite thin films against aggregatibacter actinomycetemcomitans. *Biomed. Res. Int.* 2015, 705871–705910. doi:10.1155/2015/705871
- Yoo, E. M., Uhm, S. H., Kwon, J. S., Choi, H. S., Choi, E. H., Kim, K. M., et al. (2015). The study on inhibition of planktonic bacterial growth by non-thermal atmospheric pressure plasma jet treated surfaces for dental application. *J. Biomed. Nanotechnol.* 11 (2), 334–341. doi:10.1166/jbn.2015.2030
- Zeng, Q., Zheng, C., Han, K., Wu, W., Qi, H., Wang, K., et al. (2020). A biomimic superhydrophobic and anti-blood adhesion coating. *Prog. Org. Coatings* 140, 105498. doi:10.1016/j.porgcoat.2019.105498
- Zhan, Y., Yu, S., Amirfazli, A., Siddiqui, A. R., and Li, W. (2021). Recent advances in antibacterial superhydrophobic coatings. *Adv. Eng. Mater.* 24, 2101053. doi:10.1002/adem.202101053
- Zhang, B., Guan, F., Zhao, X., Zhang, Y., Li, Y., Duan, J., et al. (2019). Micro-nano textured superhydrophobic 5083 aluminum alloy as a barrier against marine corrosion and sulfate-reducing bacteria adhesion. *J. Taiwan Inst. Chem. Eng.* 97, 433–440. doi:10.1016/j.jtice.2019.01.031
- Zhang, B., Su, Y., Zhou, J., Zheng, Y., and Zhu, D. (2021a). Toward a better regeneration through implant-mediated immunomodulation: Harnessing the immune responses. *Adv. Sci. (Weinh.)* 8 (16), e2100446. doi:10.1002/advs.202100446
- Zhang, H., Komasa, S., Mashimo, C., Sekino, T., and Okazaki, J. (2017). Effect of ultraviolet treatment on bacterial attachment and osteogenic activity to alkali-treated titanium with nanonetwork structures. *Int. J. Nanomed.* 12, 4633–4646. doi:10.2147/IJN.S136273
- Zhang, J., Pan, J., and Jing, W. (2020). Motivating role of type H vessels in bone regeneration. *Cell Prolif.* 53 (9), e12874. doi:10.1111/cpr.12874
- Zhang, Z., Li, Y., He, P., Liu, F., Li, L., Zhang, H., et al. (2021b). Nanotube-decorated hierarchical tantalum scaffold promoted early osseointegration. *Nanomed. Nanotechnol. Biol. Med.* 35, 102390. doi:10.1016/j.nano.2021.102390
- Zhao, G., Schwartz, Z., Wieland, M., Rupp, F., Geis-Gerstorf, J., Cochran, D. L., et al. (2005). High surface energy enhances cell response to titanium substrate microstructure. *J. Biomed. Mater. Res. A* 74A (1), 49–58. doi:10.1002/jbm.a.30320
- Zhao, G., Raines, A. L., Wieland, M., Schwartz, Z., and Boyan, B. D. (2007). Requirement for both micron- and submicron scale structure for synergistic responses of osteoblasts to substrate surface energy and topography. *Biomaterials* 28 (18), 2821–2829. doi:10.1016/j.biomaterials.2007.02.024
- Zhao, D., Liu, M., Li, Q., Zhang, X., Xue, C., Lin, Y., et al. (2018). Tetrahedral DNA nanostructure promotes endothelial cell proliferation, migration, and angiogenesis via notch signaling pathway. *ACS Appl. Mater. Interfaces* 10 (44), 37911–37918. doi:10.1021/acsami.8b16518
- Zhao, X., You, L., Wang, T., Zhang, X., Li, Z., Ding, L., et al. (2020). Enhanced osseointegration of titanium implants by surface modification with silicon-doped titania nanotubes. *Int. J. Nanomed.* 15, 8583–8594. doi:10.2147/IJN.S270311
- Zheng, Y., Bai, H., Huang, Z., Tian, X., Nie, F.-Q., Zhao, Y., et al. (2010). Directional water collection on wetted spider silk. *Nature* 463 (7281), 640–643. doi:10.1038/nature08729
- Zheng, S., Wang, D., Tian, Y., and Jiang, L. (2016). Superhydrophilic coating induced temporary conductivity for low-cost coating and patterning of insulating surfaces. *Adv. Funct. Mater.* 26 (48), 9018–9025. doi:10.1002/adfm.201602843
- Zheng, H., Li, Z., Liu, L., Meng, F., Cui, Y., and Wang, F. (2021). Superhydrophobic composite coatings in bacterial culture media: Durable antibacterial activity and enhanced corrosion resistance. *Compos. Commun.* 27, 100857. doi:10.1016/j.coco.2021.100857
- Zilberman, M., and Elsner, J. J. (2008). Antibiotic-eluting medical devices for various applications. *J. Control. Release* 130 (3), 202–215. doi:10.1016/j.jconrel.2008.05.020



OPEN ACCESS

EDITED BY

Yanjin Lu,
Fujian Institute of Research on the
Structure of Matter (CAS), China

REVIEWED BY

Lenka Kuncicka,
Institute of Physics of Materials (ASCR),
Czechia
Cijun Shuai,
Jiangxi University of Science and
Technology, China

*CORRESPONDENCE

Song Zhang,
songzhang_sy@163.com
Zhe Yi,
zheyi@cmu.edu.cn

[†]These authors have contributed equally
to this work and share first authorship

SPECIALTY SECTION

This article was submitted to
Biomaterials,
a section of the journal
Frontiers in Bioengineering and
Biotechnology

RECEIVED 17 July 2022

ACCEPTED 15 August 2022

PUBLISHED 07 September 2022

CITATION

Wang J, Bao Z, Wu C, Zhang S, Wang N,
Wang Q and Yi Z (2022), Progress in
partially degradable titanium-
magnesium composites used as
biomedical implants.
Front. Bioeng. Biotechnol. 10:996195.
doi: 10.3389/fbioe.2022.996195

COPYRIGHT

© 2022 Wang, Bao, Wu, Zhang, Wang,
Wang and Yi. This is an open-access
article distributed under the terms of the
[Creative Commons Attribution License](https://creativecommons.org/licenses/by/4.0/)
(CC BY). The use, distribution or
reproduction in other forums is
permitted, provided the original
author(s) and the copyright owner(s) are
credited and that the original
publication in this journal is cited, in
accordance with accepted academic
practice. No use, distribution or
reproduction is permitted which does
not comply with these terms.

Progress in partially degradable titanium-magnesium composites used as biomedical implants

Jianping Wang^{1,2†}, Zhifan Bao^{2†}, Chenliang Wu¹, Song Zhang^{1*},
Ningwei Wang³, Qiang Wang² and Zhe Yi^{2*}

¹School of Materials Science and Engineering, Shenyang University of Technology, Shenyang, China, ²School and Hospital of Stomatology, China Medical University, Liaoning Provincial Key Laboratory of Oral Diseases, Shenyang, China, ³School of Materials Science and Engineering, Northeastern University, Shenyang, China

Titanium-magnesium composites have gained increasing attention as a partially degradable biomaterial recently. The titanium-magnesium composite combines the bioactivity of magnesium and the good mechanical properties of titanium. Here, we discuss the limitations of conventional mechanically alloyed titanium-magnesium alloys for bioimplants, in addition we summarize three suitable methods for the preparation of titanium-magnesium composites for bioimplants by melt: infiltration casting, powder metallurgy and hot rotary swaging, with a description of the advantages and disadvantages of all three methods. The titanium-magnesium composites were comprehensively evaluated in terms of mechanical properties and degradation behavior. The feasibility of titanium-magnesium composites as bio-implants was reviewed. In addition, the possible future development of titanium-magnesium composites was discussed. Thus, this review aims to build a conceptual and practical toolkit for the design of titanium-magnesium composites capable of local biodegradation.

KEYWORDS

titanium-magnesium composite, degradation, implant, mechanical property, galvanic corrosion

Introduction

Tissue injury is an unavoidable part of everyone's existence. In some circumstances, tissue injury cannot heal itself, which means hard tissue repair components must be implanted to help the injured tissue heal (Zhang L. et al., 2019). Autologous bone grafts are without a doubt the greatest material for restoration (Rodriguez-Merchan, 2022), with no rejection and a high graft success rate. Nonetheless, due to the limited availability of materials and the difficulty of adjusting shapes and properties, it is difficult to apply them on a large scale. In order to overcome the limitations of self-bone grafting, research into synthetic bone repair materials is gradually gaining attention. And with the help of computer aided design and numerical simulations, synthetic bone repair materials have been vigorously developed (Zach et al., 2014). Metals, ceramics and polymers are commonly used as hard tissue replacement materials. Metallic materials play a role in

most plastic surgery devices and dental implants, including temporary implants and permanent implants (Taddei et al., 2004; Chen and Liu, 2016). Nowadays many types of industrial metals are available, however, since bio-implants are implanted in the human body, only a few metals can meet the requirements for development as bio-implants. Conventional implants, which have been extensively used for orthopedic applications and are constructed of Ti-based alloys (Liu et al., 2019; Yan et al., 2019), stainless steel (Brooks et al., 2017; Teo et al., 2021), and cobalt-based alloys (Mas Ayu et al., 2019), will remain inside the body permanently after its implantation. Magnesium (Maier et al., 2020; Wu et al., 2021; Zeller-Plumhoff et al., 2021) are also classified as implants as biodegradable materials, in addition to the metals indicated above. In general, stainless steels and Co-based alloys suffer from a major biological drawback. For example, these two permanent alloys suffer from corrosion, which causes the liberation of allergenic/toxic Ni and Cr ions into bodily fluids. The release of these harmful ions will activate adverse inflammatory and immune responses *in vivo*, which becomes a primary shortcoming for long-term use in the biological surroundings (Wong and Man, 2018). Low density and high strength are advantages of titanium, and a dense oxide film will form on the surface of titanium and titanium alloys when titanium and titanium alloys come into contact with air or an oxygen-containing medium (Tang et al., 2018). Titanium alloys have been widely used in the field of biomedical applications due to their excellent biocompatibility and mechanical properties (Fan et al., 2021). Magnesium is a light metal with a density of 1.74 g/cm³, which is equal to the density of human bone (1.75 g/cm³) (Zhou H. et al., 2021). Due to their superior mechanical compatibility, biocompatibility, and degradability, magnesium and magnesium alloys have a wide range of biomedical uses. Magnesium is one of the body's macronutrients and is involved in a number of metabolic activities. The most important of these is that it promotes calcium deposition, which is good for bone formation (Makkar et al., 2018).

The respective shortcomings of titanium and magnesium materials limit their widespread use. The disadvantage of titanium is that its Young's modulus (E), although lower than that of other metals, is still somewhat different from that of human bone, which inevitably leads to "stress shielding" (Chen and Thouas, 2015). As a result, past studies have focused on reducing the E of biomedical titanium materials. β -phase titanium has been found to be a phase with a low E (Zhou L. et al., 2021), so increasing the content of β -phase in titanium alloys has become a significant focus of research (Koizumi et al., 2018; Aguilar et al., 2019; Pellizzari et al., 2020). Titanium alloys with E as low as 33 GPa have been developed (Hao et al., 2007). In addition to increasing the content of the β -phase to reduce the E, the introduction of a porous structure is also considered as an excellent way to reduce the E (Khodaei et al., 2018). Due to its unique pore design, porous titanium deforms more than bulk

materials when subjected to the same force. As β -phase titanium alloys require the addition of a number of β -phase stabilizing elements (Qazi et al., 2005), the addition of these heavy elements increases the risk of cytotoxicity caused by release of metal ions (Yu et al., 2015). Furthermore, titanium alloys enhance the likelihood of a patient's allergy after implantation (Fage et al., 2016). Weighing the pros and cons, porous titanium is considered to be an effective way to avoid the "stress shielding" phenomenon. By altering the porosity of porous titanium, the modulus of elasticity may be accurately regulated, allowing it to conform exactly to that of human bone tissue. The presence of a porous structure provides not only a channel for the movement of nutrients, but also space for tissue cell proliferation (Meenashisundaram et al., 2020). However, as titanium is a biologically inert material, certain surface modifications to the surface of the metal titanium are required to enable it to induce the formation of human bone tissue (Su et al., 2020). The surface modification treatment would make the preparation process more complicated and increase the production cost, which limits the wide application of porous titanium. The main problem faced by magnesium and magnesium alloys when implanted into the human body is their rapid degradation rate (Bütev Öcal et al., 2020), which can lead to an increase in pH in local areas of the tissue and a series of problems caused by rapid hydrogen precipitation. Rapid corrosion rates will eventually lead to premature loss of mechanical properties of magnesium and magnesium alloys. In this regard, reducing the degradation rate *in vivo* is a major problem for Mg based materials. High purity Mg alloy has a lower content of impurity elements, and although the degradation rate is lower than that of commercially pure Mg, the mechanical strength of high-purity magnesium is so low that it is not suitable for biological implants. For magnesium, alloying is an important step to improve its corrosion resistance. Magnesium alloys such as AZ91D, WE43 and ZK60 are considered to last longer than commercially pure magnesium in the human body (Witte et al., 2005; Asri et al., 2017).

In view of the inherent drawbacks of the Ti-based and Mg-based materials, titanium-magnesium composites for partially biodegradable implants have drawn the attention of researchers in recent years, which might circumvent the disadvantages of the permanent and non-permanent implants currently in use. Initially, scholars began to research the feasibility of titanium-magnesium composites as orthopedic load-bearing implants (Li et al., 2015). Subsequently, the mechanical and fatigue properties of titanium-magnesium composites have been shown to be comparable to Grade 4 Ti (Balog et al., 2017). Therefore, titanium-magnesium composites are also a viable option for dental implants. In addition, titanium-magnesium composites have also been developed for use in bioinspired fish scales (Liu X. et al., 2021). In summary, titanium-magnesium composites have a wide range of application prospects.

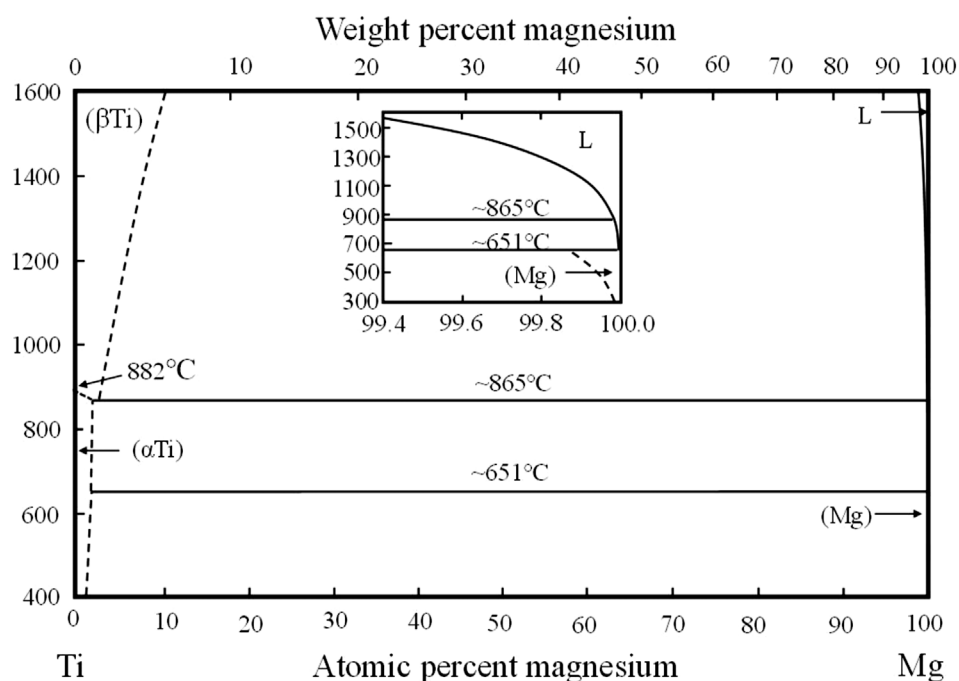


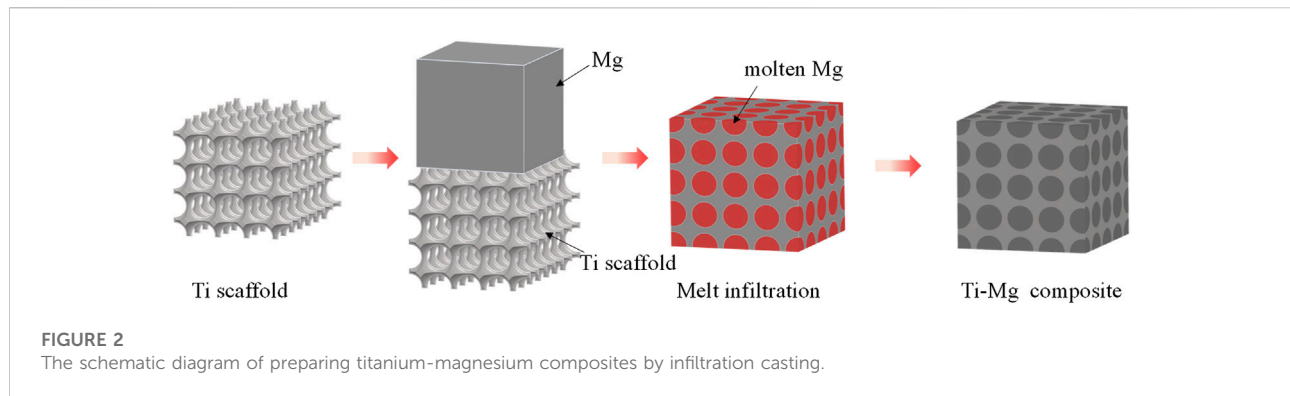
FIGURE 1
Titanium-magnesium binary phase diagram.

This paper presents an overview of recent research and developments of titanium-magnesium composites used as biomedical materials. It can be divided into three main sections, beginning with preparation of titanium-magnesium composites, outlining three suitable methods for the preparation of titanium-magnesium composites. This section is followed by summarizing mechanical properties of various titanium-magnesium composites and discussing the effects of all phases and alloying elements in titanium-magnesium composites on mechanical properties. The third section considers effect of material ingredient, volume ratio, and other factors on corrosive properties, describing the status of current titanium-magnesium composites used as biomaterials and their limitations. Overall, efforts have been made to reveal the latest scenario of biomedical titanium-magnesium composites. The goal of this review is to create a conceptual and practical toolset for the design of titanium-magnesium composites that can degrade locally.

Processing methods

Alloying Ti with Mg is a common strategy for preparing titanium-magnesium alloy. There are two inherent obstacles in the traditional method of preparing titanium-magnesium alloys. On the one hand, titanium is a high temperature resistant metal, with a melting point of 1668°C, which is much higher than the

boiling point of magnesium (1070°C). On the other hand, magnesium only acts as solute atoms in the titanium matrix. It was reported that the solid solubility of magnesium in titanium at room temperature is only 0.9 at. % and that of titanium in magnesium is 0.02 at. % (Yao et al., 2022). Figure 1 shows the phase diagram of titanium-magnesium binary alloy. As can be seen obviously, titanium and magnesium cannot be mutually soluble in the full composition range, and there are no eutectic phases or stable intermetallic compounds in the temperature of 600–1000°C. Owing to the significant difficulty of alloying between titanium and magnesium, producing titanium-magnesium alloys by traditional melting processes is nearly impossible. However mechanical alloying can extend the solid solubility of solid atoms and is considered as an effective method to increase the solid solubility of magnesium in titanium (Liang and Schulz, 2003). Cai et al. (2018) carried out ball-milling tests through titanium powder and magnesium powder for 50 h, and then compacted in a cubic-anvil press under a pressure of 4 GPa at RT. After annealed for 1 h, they prepared the Mg-1.5 at.% Ti alloy. In addition, Liang et al. (2021) have also prepared titanium-magnesium alloy with Mg content ranging from 0.312 wt.% to 2.5 wt.% by mechanical alloying method. According to their study, when the Mg content is low, Mg could improve the mechanical strength of Ti due to the co-strengthening effects of precipitation and solid solution. When the Mg content reaches 1.25 wt.%, it will be detrimental to the mechanical properties of



the material. As a consequence, mechanical alloying can effectively enhance the solid solubility of magnesium in titanium. Nevertheless, the magnesium content in titanium is still too low to exert obvious influence on the titanium-magnesium alloys. Due to the low solid solution of magnesium in titanium, titanium-magnesium composites prepared by infiltration casting, powder metallurgy and hot press forging have drawn scholars' attention.

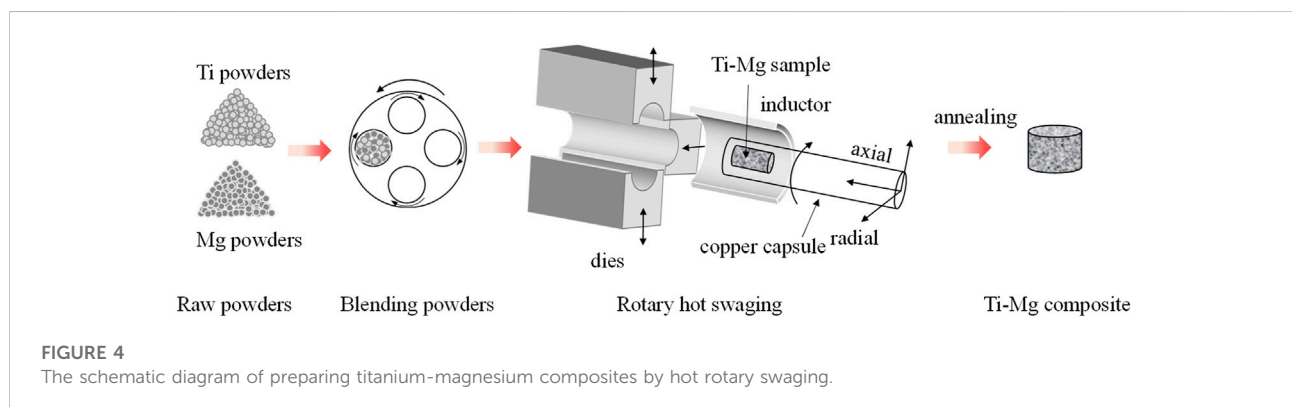
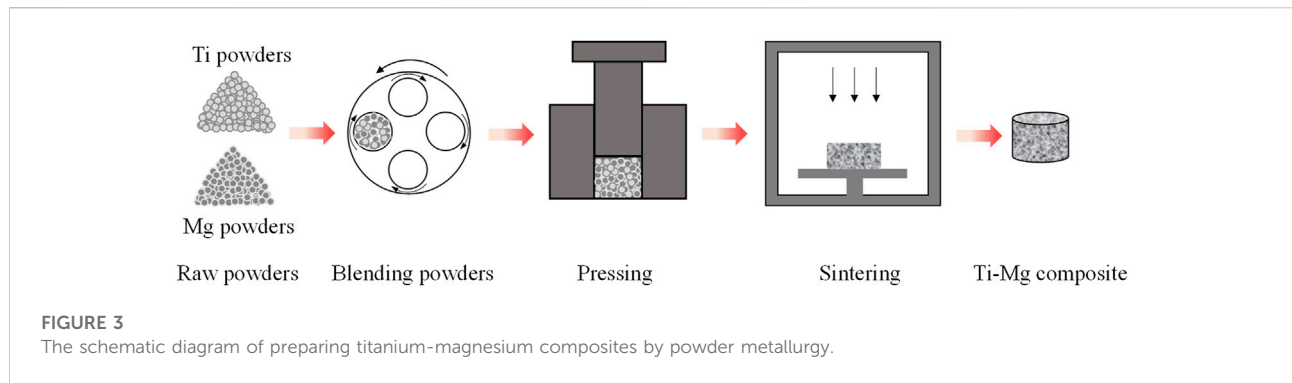
Infiltration casting

Infiltration is a liquid-state fabrication method, in which a porous preform is impregnated in a molten matrix metal to fill the pores. Mechanical winding, powder metallurgy, 3D printing and other techniques were used to prepare porous titanium, and then molten magnesium was used to fill the pores of the porous titanium, resulting in a titanium-magnesium composite (Li et al., 2015; Esen et al., 2016; Meenashisundaram et al., 2020). The schematic diagram of preparing titanium-magnesium composites by infiltration casting is shown in Figure 2. Li et al. (2015) twisted titanium wire into a spiral form, which was then stretched and woven into a 2D mesh. The mesh was formed into a 3D material and pressed in a mold to make the cylindrical porous titanium (p-Ti) preform. Subsequently, molten Mg was infused into the porous titanium, and the titanium-magnesium composite material was formed after cooling to room temperature. According to their research, the stiffness of p-Ti/Mg composites is greatly improved compared to entangled titanium, but only comparable to that of pure magnesium. The strength of p-Ti/Mg needs to be further improved as a biomedical implant. However, its residual strength after degradation is favorable for biomedical applications. Esen et al. (2016) obtained porous structures of Ti and Ti-6Al-4V skeletons by loose powder sintering and obtained titanium-magnesium composites with better mechanical properties by capillary penetration of molten magnesium. Meenashisundaram et al. (2020) 3D inkjet

printing technology to mix titanium powder and polyvinyl alcohol to prepare porous titanium parts, followed by pressureless infiltration of molten magnesium to obtain titanium-magnesium composites. 3D printing enables faster and more cost-effective manufacture of net shapes for biomedical implants that meet patient needs and improves precision, fit and load distribution, and is also considered an excellent technology for machining and preparing titanium alloys (Yi et al., 2021). In summary, the advantages of titanium-magnesium composites prepared by infiltration casting method are simple operation, low manufacturing cost, and large-scale industrial production. The disadvantage is that the bonding strength of the titanium-magnesium interface is low, and the wettability and fluidity of the metal solution need to be further improved.

Powder metallurgy

Powder metallurgy preparation of titanium-magnesium composite materials is a technology that uses titanium powder and magnesium powder as raw materials, which are mixed, pressed and sintered by ball milling. The schematic diagram of preparing titanium-magnesium composites by powder metallurgy is shown in Figure 3. With relatively low powder metallurgical sintering temperature, titanium-magnesium composites are easy to operate, with low energy consumption and high precision. Sintering is the most critical part of powder metallurgy and has a direct impact on the mechanical properties of the material. According to the different sintering processes, powder metallurgy can be divided into spark plasma sintering (SPS), microwave sintering, atmosphere sintering, etc. SPS is a fast, low-temperature, energy-saving and environmentally friendly new material preparation technology (Hu et al., 2020). Ouyang et al. (2020) prepared titanium-magnesium composites by SPS technique through irregularly shaped commercial titanium powders and x vol% (x = 10, 20 and



30) Mg-3Zn powders as raw materials, and the relative density values of titanium-magnesium composites are all higher than 98%. However, the content of Mg is low in the titanium-magnesium composites prepared by SPS. Therefore, the distribution of Ti phase in the prepared composites was continuous, while the distribution of Mg-3Zn phase was uniform rather than discontinuous, and these Mg-3Zn did not form continuous channels but independent pores after degradation. The MgO was also found according to XRD analysis, while the effect of MgO on the properties of the titanium-magnesium composites has not been investigated in depth. In order to avoid generation of oxides during the preparation process, Ibrahim et al. (2020) successfully prepared Ti-xMg ($x = 0, 12, 17$ and 24 vol.%) at a temperature below 450°C , and did not find the aggregation of oxygen elements at the titanium-magnesium interface. The powder metallurgy method can prepare titanium-magnesium composites quickly and efficiently. However, powder metallurgy also has many serious problems. For example, the oxidation of raw materials during the sintering process and the lack of metal compound phase formation at the interface between titanium and magnesium phases lead to poor interfacial bonding strength.

Hot rotary swaging

Hot rotary swaging is an incremental shaping process, which is commonly used to modify the cross-sections of rotationally symmetric metal objects such as rods, tubes, and wires, as well as to link various materials or components. The hot rotary swaging procedure reduces grain-size in metallic materials, and effectively improves the mechanical properties of the material, and hot rotary swaging has been used for various demanding materials and alloys (Chi et al., 2019; Kunčická et al., 2020; Strunz et al., 2020). The schematic diagram of preparing titanium-magnesium composites by hot rotary swaging is shown in Figure 4. Esen et al. (2013) used titanium and magnesium powder as raw materials, the titanium-magnesium composites with Mg volume fractions of 50, 60, 70 and 80% were prepared by hot rotary forging technology, followed by a 1-h annealing treatment at 600°C aiming at obtaining homogeneous microstructure of the material. The SEM micrographs of titanium-magnesium composites containing 80 vol% Mg are shown in Figure 5. Figure 5A illustrates the presence of oxygen enrichment between Mg-Mg, which indicated the presence of a very thin oxide layer between Mg-Mg. As shown in Figure 5B, the elemental oxygen content between titanium-magnesium was

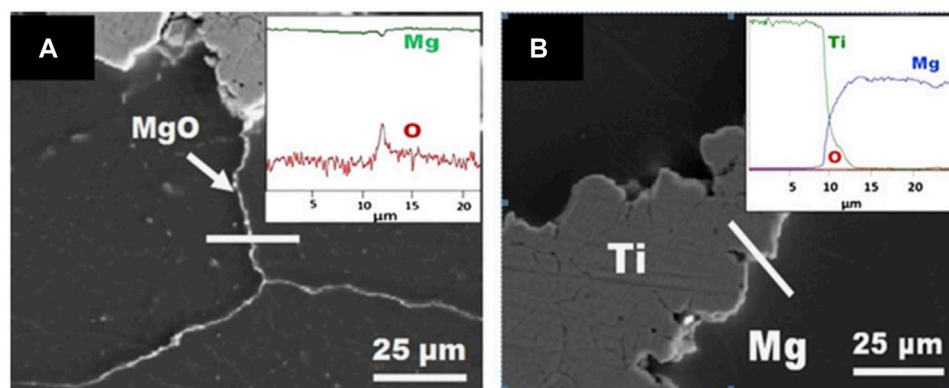


FIGURE 5
SEM micrograph of titanium-magnesium composites containing 80 vol% Mg (A) MgO layers and EDS line scan taken along white line and (B) titanium-magnesium interface and EDS line scan across titanium and magnesium (Esen et al., 2013).

only slightly increased because MgO was present only on the Mg powder of the original material. The titanium-magnesium composite prepared by hot press forging method has high density and good plasticity, but it should pay attention to the various reactions of magnesium powder with oxygen during the processing.

As a consequence, it is challenging to produce titanium-magnesium composite materials, and it is even harder to create them using conventional techniques. The three processes listed above had successfully prepared titanium-magnesium composites and each method has its own advantages. The titanium-magnesium composites prepared by powder metallurgy method will inevitably encounter magnesium volatilization during the preparation process, so the manufactured titanium-magnesium composites may differ from the initial design of the titanium-magnesium content. The titanium-magnesium composites prepared by powder metallurgy method often have low magnesium content, and the volatilization of magnesium will result in the presence of holes in the prepared composites. Hot rotary swaging technique can produce titanium-magnesium composites with a high magnesium content. However, its preparation process and subsequent heat treatment process inevitably react with oxygen to generate oxides such as MgO, which may adversely affect the properties of the composites. Therefore, it is not the best way to produce titanium-magnesium composites. The infiltration casting method meets the requirements of mass production, and can also control the total porosity, pore size and pore distribution of porous titanium scaffolds through 3D printing and other technologies to produce titanium-magnesium composites with specific structures to replace bone in different parts. In addition to the preparation techniques mentioned above, various cutting-edge technologies have been applied to the production of alloys with low miscibility. For instance, due to

the extremely quick cooling rate, laser rapid solidification is also known as a potential method for creating metastable structures and alloys with low miscibility.

Mechanical properties

Ti and Ti-6Al-4V are commonly used as support structures for the preparation of titanium-magnesium composites (Wang et al., 2011; Esen et al., 2020). Commercially-pure Ti (CP-Ti) as an α titanium alloy, only the CP-Ti with grade 4 is used for dental applications or for fabrication of porous coatings rather than joint implants due to its low mechanical strength at room temperature (Chen and Thouas, 2015). Ti-6Al-4V is the most widely used bio-applicable Ti-based $\alpha+\beta$ alloy. The properties of Ti-6Al-4V can be optimized by adjusting the volume fraction of the α and β phases through different heat treatments due to the presence of both, an α stabilizer (Al) and a β stabilizer (V) (Vrancken et al., 2012). Compared with CP-Ti, Ti-6Al-4V exhibits better mechanical properties. However, the V and Al elements added in Ti-6Al-4V are considered to be cytotoxic, especially that Al ions may depress bone growth and even exert a potential danger of Alzheimer's disease (Tamilselvi et al., 2006; Li et al., 2014). Currently, research and development in the field of Ti-based alloys is focused on two main objectives. The initial goal is to change the chemical compositions of the alloys in order to replace problematic components. The second goal is to create alloys with characteristics that are as near to bone as possible (Kunčická et al., 2017). The β -type titanium alloys containing more β -phase stabilizers (Mo, Zr and Ta) possess lower modulus of elasticity and higher toughness than Ti-6Al-4V bulk (Zhang Y. S. et al., 2019). The corrosion resistance of β -type titanium alloys in the human body is also higher than that of ($\alpha + \beta$) titanium alloys such as Ti-6Al-4V (Carman et al., 2011). The

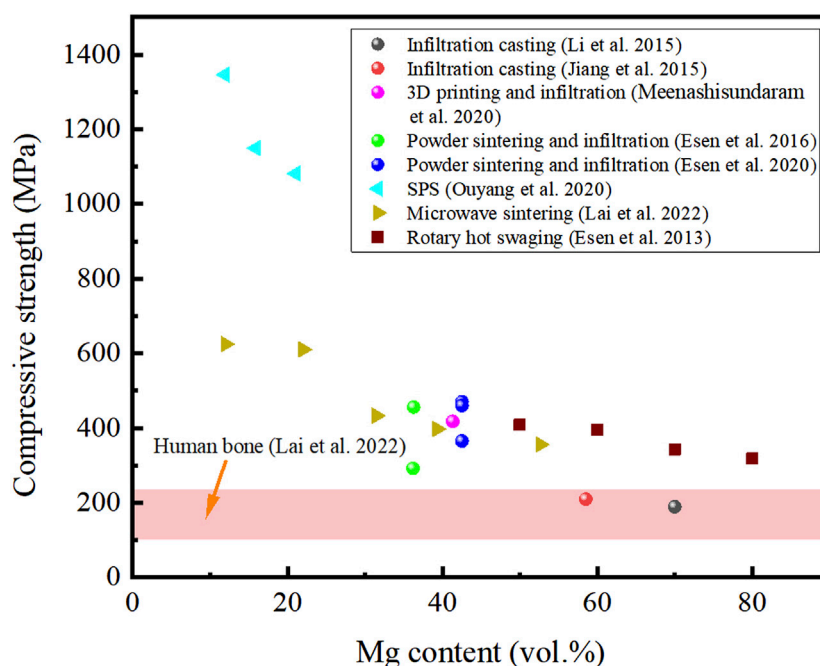


FIGURE 6

The UCS of human bone and titanium-magnesium composites as a function of Mg content prepared by different preparation processes.

incorporation of these rare metal elements makes the preparation of β -titanium alloys complex and increases the cost of raw materials (Narita et al., 2012). The design of low-cost β -titanium alloys has been in progress and will be used on a large scale for biomedical applications in the foreseeable future (Gepreel and Niinomi, 2013). Most titanium-magnesium composites currently use pure titanium as the raw material due to safety and cost-effectiveness considerations.

The mechanical properties of titanium and titanium alloys with porous structures are greatly reduced compared to the bulk titanium and titanium alloys. However, the mechanical properties of the composite can be correspondingly improved with magnesium completely filling the internal pores, while it is still far less than that of bulk titanium and titanium alloys. According to recent study, titanium-magnesium composites with specific spatially aligned structures can promote effective stress transfer, delocalize damage and arrest cracking, thereby bestowing improved strength and ductility (Zhang et al., 2022). In addition, extensive studies revealed that the mechanical properties of the titanium-magnesium composite are sufficient to meet the performance requirements of human implants. The human skeleton mainly plays a load-bearing role in the human body, so the study of ultimate compressive strength (UCS) is more relevant compared to the ultimate tensile strength. Figure 6 shows the UCS of human bone and titanium-magnesium composites as a function of Mg content prepared by different preparation processes. It is noticed that the UCS for all titanium-

magnesium composites in Figure 6 is higher than that of human bone. Since the mechanical properties of titanium are higher than those of magnesium and the interface between titanium and magnesium cannot be alloyed, the UCS of titanium-magnesium composites prepared by the same preparation process decreases with increasing Mg content. As the E of titanium is higher than that of magnesium, Ti will be subjected to a higher force when the titanium-magnesium composites withstand external forces. Therefore, cracks preferentially appear in the Ti phase or at the titanium-magnesium interface where the bond strength is not high. It can also be found that Ti tends to exhibit a ductile fracture mode, while magnesium exhibits a typical brittle fracture (Ouyang et al., 2020). Ibrahim et al. (2020) compared the mechanical properties of two composites prepared from the same magnesium powder and different titanium powders, and found that the titanium-magnesium composites prepared from hydrogenated-dehydrogenated titanium powder showed an improvement in yield strength and ultimate tensile strength compared to that prepared from plasma atomized titanium powder. This may be because the hydrogenated-dehydrogenated titanium powder surface has a larger concentration of TiO_2 , and the Ti-O solid solution may act as a strengthening agent, resulting in stronger mechanical characteristics. However, the load transfer from Ti to Mg during straining, may be hampered by the presence of TiO_2 dispersoids at the contact. Esen et al. (2016) prepared titanium-magnesium composites using Ti and Ti-6Al-4V powders with

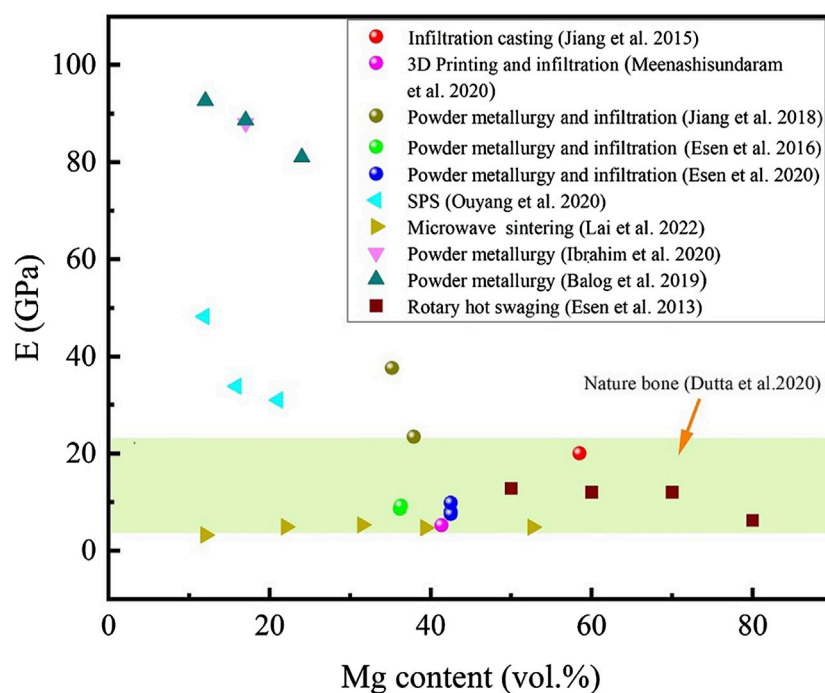


FIGURE 7

The E of nature bone and titanium-magnesium composites as a function of Mg content prepared by different preparation processes.

Mg, and the mechanical properties of the obtained Ti-6Al-4V/Mg were superior to those of Ti/Mg composites. In addition, according to the research of Jiang et al. (2018), the mechanical properties of titanium-magnesium composites prepared with an average diameter of 100 μm Ti powders are better than those prepared by 230 μm Ti powders. This is due to stress concentration in the sintered neck region of Ti particles, leading to pre-fracture. And smaller Ti particles means more sintering neck in the same volume. Although the contribution of magnesium to the composites is not very obvious, the mechanical properties of titanium-magnesium composites prepared with AZ91 and WE43 are higher than those prepared with pure Mg (Esen et al., 2020). In addition to the use of different raw materials to optimize the mechanical properties of the titanium-magnesium composites, a unique preparation process can also improve the mechanical properties of the composites. Lai et al. (2022) obtained titanium-magnesium composites by microwave sintering and found that the UCS of the titanium-magnesium composites were greatly improved compared with other preparation processes under the same Mg content. Ouyang et al. prepared titanium-magnesium composites by SPS, aiming at improving the mechanical properties. Due to the influence of the nanograin size microstructure produced by the SPS process, the UCS of the titanium-magnesium composites was as high as 1346.3 MPa (Ouyang et al., 2020).

Figure 7 shows the E of nature bone and titanium-magnesium composites as a function of Mg content prepared by different preparation processes. Overall, the E of the titanium-magnesium composites showed a decrease tendency with the increase of the volume fraction of Mg. According to the study reported by Balog et al. (2019), if the Mg component ($E = 45 \text{ GPa}$) is expected to contribute to elastic load transmission following a simple mixing rule, the E of the Titanium-magnesium composite should drop at a rate of 0.55 GPa per one vol% Mg. Another boundary condition is that if Mg does not contribute to elastic load transfer, the E of the titanium-magnesium composite should theoretically drop at a rate of 0.99 GPa per one vol% Mg. According to the results of their study show that the volume share of Mg share decreases by 0.78 GPa for every one vol% increase in the volume of Mg. This indicates that the interface between titanium and magnesium is often not an ideal metallurgical bonding and has a limited contribution to the load transfer in the elastic region. Theoretically, the E of titanium-magnesium composites should decrease with the increase of Mg content between the E of pure titanium and pure magnesium, but not lower than that of pure magnesium. The volume percentage of Mg in the microwave sintered titanium-magnesium composites is not very high, but its E is as low as below 10 GPa (Lai et al., 2022). This phenomenon can be attributed to the fact that the material prepared by microwave sintering will volatilize part of the Mg during processing because

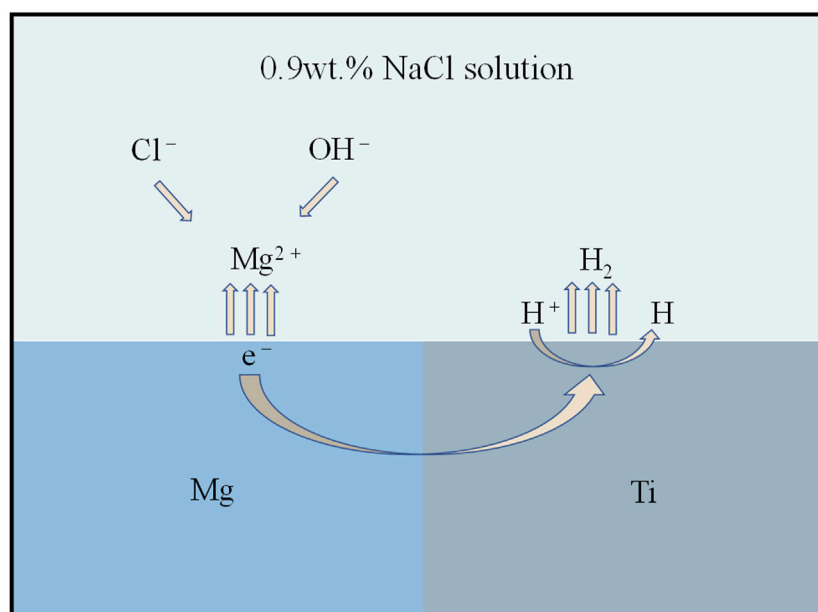


FIGURE 8
The schematic diagram of galvanic corrosion of titanium-magnesium composites.

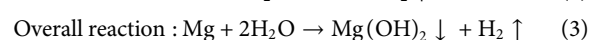
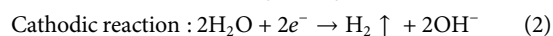
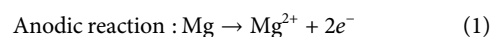
of the faster heating temperature, which leads to more pores in the composite. According to research of [Rivera-Salinas et al. \(2020\)](#), the holes in the composite materials significantly reduce the E of the overall material. The E of titanium-magnesium composites should theoretically be between Ti ($E = 110$ GPa) and Mg ($E = 45$ GPa), and decrease correspondingly with the increase of Mg content. If the dense density of the composite is 100%, the E of titanium-magnesium composites will not be lower than 45 GPa. However, the E of many titanium-magnesium composites were found to be lower than 45 GPa. These composites with low E may be due to the imperfect preparation process, which leads to the existence of pores in the composites and makes the material bonding not tight enough, thus the E of titanium-magnesium composites may be lower than that of pure magnesium. The composition of titanium-magnesium composites can be varied, and the strength and E can be adjusted in a wide range by selecting the appropriate titanium-magnesium composition ratio according to different parts of the skeleton.

Degradation performance

Degradation behavior

Since a dense oxide film forms on the surface of titanium and titanium alloys, it effectively prevents further corrosion of the material by the solution ([Zhou X. et al., 2021](#)). Mg is more active

and will degrade in human body. Therefore, the corrosion behavior of titanium and magnesium composites in these solutions, such as Hanks' solution, Ringer's solution and SBF solution, is mainly dominated by the degradation of Mg. The pH, electrolytes, amino acids and proteins of these solutions are as close as possible to the actual human environment ([Bahraminasab et al., 2019](#); [Heywood et al., 2019](#); [Tiyyagura et al., 2020](#)). Ti plays an important role in the degradation process of Mg. The electrochemical potential of the standard hydrogen electrode of Mg is -2.37 V, and that of the standard hydrogen electrode of Ti is -1.63 V. Because of the potential difference between Ti and Mg, galvanic corrosion occurs when Ti and Mg are in direct contact. Galvanic corrosion is an electrochemical process in which the reduction potential of an ion usually determines its ability to gain electrons and form a solid metal. The "active" metal with the lower reduction potential of the two metals will be corroded (anode). In comparison, the "noble" metal with the higher reduction potential will be deposited (cathode) ([Koh et al., 2015](#)). Thus, when metals with different reduction potentials pair, micro-movement and pitting will occur. The schematic diagram of the galvanic corrosion of the titanium-magnesium composite is shown in [Figure 8](#). The galvanic corrosion reaction of titanium-magnesium composites is as follows ([Wu et al., 2013](#)).



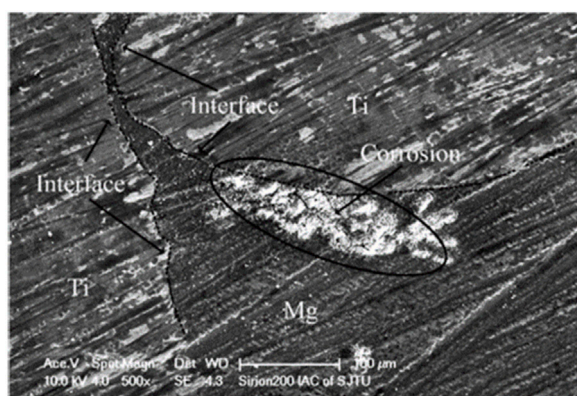


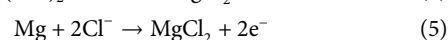
FIGURE 9

Surface morphology of the p-Ti/Mg composite after immersion in Hanks' solution for 10 min (Li et al., 2015).

Li et al. (2015) compared the corrosion rates of p-Ti/Mg and pure Mg in Hanks' solution through hydrogen precipitation experiments. It was found that the hydrogen evolution rates of p-Ti/Mg with a duplex microstructure were much higher than that of pure Mg. A maximum value of 1.49 ml/cm² h was reached at 52 h. Figure 9 shows the traces of galvanic corrosion observed for titanium-magnesium in Hanks' solution. It can be seen from Figure 9 that the Mg near the Ti phase is preferentially corroded, while the Mg farther away from the Ti corrodes to a lesser extent. Although the electrochemical differences between titanium and magnesium were minimal, the less electronegative magnesium was sacrificed as the anode, thus accelerating the corrosion of magnesium. The magnesium around the titanium wire was rapidly corroded away, causing the magnesium substrate further away from the wire to an "island structure", thus increasing the contact area between the magnesium and the solution and further accelerating the corrosion of magnesium. The electrocoupling corrosion will make the corrosion rate greatly accelerated, so how to reduce or avoid the electrocoupling corrosion in titanium-magnesium composites has become the focus of the research scholars. According to the study of Esen et al. (2013), it was found that the titanium-magnesium area ratio on the surface of titanium-magnesium composites will affect the degree of galvanic corrosion occurrence. When the surface area of Mg phase in the composite is smaller than that of Ti, a large cathode and small anode corrosion type will occur, and this corrosion mode will lead to the rapid transfer of electrons generated by the reaction of Mg with the solution through the Ti phase and generate hydrogen gas with the hydrogen ions in the reducing solution. When the area of Mg phase is much larger than that of Ti phase, a large anode and small cathode corrosion type will occur. And this corrosion mode is thought to slow down the rate of Mg corrosion rate, so the relatively small cathode area will lead

to saturation of electron transfer, electrons cannot pass through the limited Ti timely reduction of hydrogen ions, so that the anode magnesium corrosion is mitigated. In addition, Esen et al. (2016) also found that reducing the potential difference between the two metals by alloying can also significantly attenuate the galvanic corrosion in titanium-magnesium composites. They found that the corrosion rate of Ti-6Al-4V/Mg composites was lower than that of Ti/Mg composites because Ti, by alloying with Al and V, effectively changed the electrochemical potential of Ti, thus alleviating the galvanic corrosion between the two metals in the composites. Unlike Ti, the alloying of Mg should be kept cautiously, because the electrochemical potential between different phases and impurities of Mg alloy also produces potential difference, and unreasonable alloying may lead to the cathodic center of Mg alloy itself, which in turn will accelerate the corrosion rate of Mg phase (Song and Atrons, 2003). Truncating the electron transfer between metals is considered to be the most effective method to inhabit electrocoupling corrosion. During the preparation of titanium-magnesium composites, a layer of MgO film will be produced at the interface of titanium and magnesium, this may adversely affect the bond strength of the material, but the continuous MgO layer will make an insulating layer between Ti and Mg, thus blocking the electron transfer channel, avoiding the occurrence of galvanic coupling corrosion and changing the corrosion response of the material, which can effectively reduce the corrosion rate of composite materials (Esen et al., 2013; Ouyang et al., 2020).

Galvanic corrosion is the main form of corrosion in the first stage of titanium-magnesium composites, with the degradation of Mg, a layer of Mg (OH)₂ will be formed on the surface of the composite. Theoretically, this layer of Mg (OH)₂ can hinder the further reaction between the internal Mg and the solution (Lai et al., 2022), but it is found that Mg (OH)₂ only has a protective effect when the pH is higher than 11.5 (Tsakiris et al., 2021). And as a human implant, it tends to induce inflammation in the tissues around the implant at the early stage of implantation, thus creating an acidic environment (Liu Y. et al., 2021), which is unfavorable to magnesium hydroxide. In addition, it is found that when the chloride ion in the solution exceeds 30 mmol/L, magnesium hydroxide will be gradually eroded by chloride ion and further transformed into the more soluble MgCl₂ (Zhao et al., 2016), and there is still abundant chloride ion in human body fluid. It will gradually erode this protective film of magnesium hydroxide, so that it can expose the Mg inside the matrix and promote the further dissolution of Mg. The specific reaction is as follows.

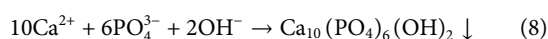
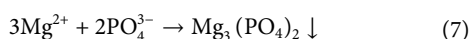
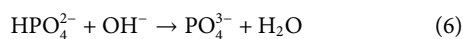


Soluble MgCl₂ is converted to magnesium phosphate by a series of reactions in a human environment rich in various ions

TABLE 1 Corrosion properties of titanium-magnesium composites in simulated body fluids.

Sample	Solution	Corrosion current density (mA/cm ²)	Corrosion potential (V)	References
Ti-10 Mg	SBF	0.00546 ± 0.00064	−0.499 ± 0.0232	Ouyang et al. (2020)
Ti-20 Mg	SBF	0.00349 ± 0.00052	−0.4289 ± 0.0148	Ouyang et al. (2020)
Ti-30 Mg	SBF	0.00359 ± 0.0036	−0.5046 ± 0.0126	Ouyang et al. (2020)
Ti-5Mg	SBF	0.0125	−0.970	Ouyang et al. (2020)
Ti-10 Mg	SBF	0.0258	−1.312	Lai et al. (2022)
Ti-20 Mg	SBF	0.0581	−1.427	Lai et al. (2022)
Ti-30 Mg	SBF	0.479	−1.469	Lai et al. (2022)
Ti6Al4V-Mg	Ringer's	0.429 ± 0.12	−1.47 ± 0.30	Esen et al. (2020)
Ti6Al4V-AZ91	Ringer's	0.367 ± 0.09	−1.44 ± 0.30	Esen et al. (2020)
Ti6Al4V-WE43	Ringer's	0.381 ± 0.08	−1.45 ± 0.36	Esen et al. (2020)
Ti-50 Mg	Ringer's	1.90	−1.472	Esen et al. (2013)
Ti-60 Mg	Ringer's	1.57	−1.493	Esen et al. (2013)
Ti-70 Mg	Ringer's	1.07	−1.490	Esen et al. (2013)
Ti-80 Mg	Ringer's	1.12	−1.512	Esen et al. (2013)

or in a solution that mimics the human environment. Magnesium phosphate is then further reacted to produce hydroxyapatite. These insoluble apatite components are predicted to act as nucleation sites for the inward growth of new bone after the implantation process, thereby improving biocompatibility and osseointegration standards (Heywood et al., 2019; Zhou H. et al., 2021). The reactions are follows.



Dynamic potential polarization testing is considered to be the most direct electrochemical method to evaluate *in vitro* corrosion processes. The corrosion potential and corrosion current of the material can be obtained by Tafer extrapolation. In Table 1, the corrosion potentials and corrosion currents of titanium-magnesium composites with different compositions are given. It can be seen that the corrosion potential of titanium-magnesium composites decreases with increasing Mg content, and the corrosion current increases rapidly with increasing Mg content. However, according to the research of Ouyang et al. (2020), the corrosion rate of Ti-30 Mg in SBF solution is higher than that of Ti-20 Mg. Since Mg agglomerates with increasing content during SPS preparation, the aggregation of Mg reduces the contact area between Mg and Ti phases, thus weakening the galvanic corrosion between Ti and Mg. Mg^{2+} concentrations of Ti-20 Mg grow quicker than those of Ti-10 Mg and Ti-30 Mg in the first 3 days, according to a follow-up study by Ouyang et al. (2020), Mg^{2+} concentrations are high in the cathode area,

TABLE 2 Conventional scale for assessing corrosion resistance (Tsakiris et al., 2021).

Resistance	i_{corr} (mA/cm ²)	Stability group
Completely stable	<0.001	4
Very stable	0.001–0.01	3
Stable	0.01–0.1	2
Low stable	0.1–1	1
Unstable	>1	0

generating an ion cloud that obstructs the electrode process. Traditionally, the corrosion resistance of the materials is evaluated according to the grades in Table 2. According to the classification in Table 2, the corrosion resistance of titanium-magnesium composites is within the class 0–3. For magnesium and magnesium alloys, the poor corrosion resistance means that the rate of degradation is too fast and may face rapid failure of the implant, but for titanium-magnesium composites, due to the stable presence of titanium, even if magnesium degrades rapidly after implantation, it will not cause the titanium-magnesium composite to lose its proper mechanical support. Therefore, it is not comprehensive to evaluate whether titanium-magnesium composites have the possibility of implantation into human body only by the rate of degradation. The bone repair process in human implants consists of three phases: the inflammatory phase, the repair phase and the remodeling phase (Chae et al., 2020). The ideal bone repair scaffold degradation and tissue repair curve is shown in Figure 10A. As time increases, the scaffold gradually degrades and the mechanical support curve

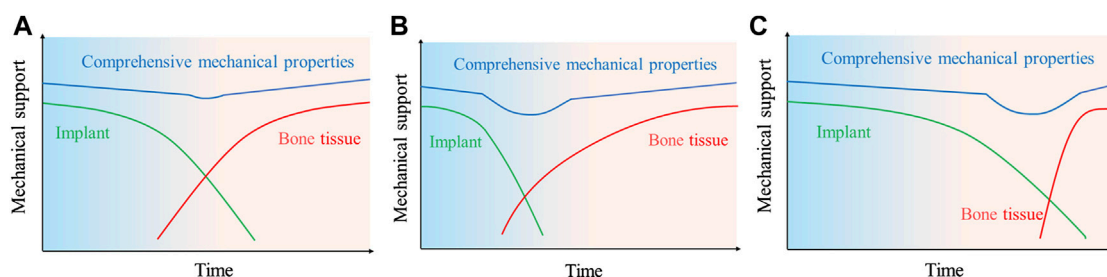


FIGURE 10

Schematic diagram of the mechanical support match between bone repair scaffold and tissue; green: red curves of scaffold implantation *in vivo* degradation, tissue repair at bone defect site; (A) ideal condition; (B) too rapid scaffold degradation; (C) too slow scaffold degradation.

decreases with time, while the curve of new tissue formation gradually increases with time, and the two complement each other, thus maintaining the mechanical support strength during the bone repair process. However, the majority of existing scaffolds have a changing mechanical support strength curve after implantation as shown in Figure 10B. On the one hand, the scaffold degrades quickly resulting in insufficient mechanical support for the healing tissue formed initially; on the other hand, the scaffold does not degrade or degrades too slowly, resulting in the growth of new bone tissue being impeded and a stress masking effect, leading to difficulties in providing sufficient mechanical support for the new bone once the mechanical properties of the scaffold are insufficient at a later stage, as shown in Figure 10C. As titanium-magnesium composites are partially degradable materials, only the surface Mg will be rapidly degraded after implantation into the body, the exposed porous structure of the titanium will provide mechanical support in the form of a skeleton. The degradation of Mg *in vivo* also serves to induce the formation of bone tissue, and the voids formed by the degraded Mg also provide space for bone tissue to grow. From this point of view, titanium-magnesium composites have an advantage over other human implants that cannot be matched.

Negative effects of corrosion and mitigation measures

The degradation of Mg and Mg alloys increases the OH^- concentration in the environment (Atrons et al., 2013), which can lead to an increase of pH around the local implant tissues and increase the risk of alkalosis in the human body. Esen et al. (2020) found that the pH of a variety of titanium-magnesium composites soaked in physiological solutions for up to 48 h increased dramatically to 10 or even higher. High pH can lead to severe internal injuries, but as mentioned earlier, the implant induces inflammation in the tissues surrounding the implant during the pre-implantation phase, creating an acidic environment where these acids may neutralize the OH^-

produced by the titanium-magnesium composite, which is helpful for the body and the implant. In addition to the high pH associated with the degradation of Mg, Ti at the cathode precipitates large amounts of hydrogen gas (Cao et al., 2013). The accumulation of large amounts of this hydrogen in the patient's body causes local discomfort rather than being harmful to the tissue. Over time, this hydrogen may be eliminated from the body or can be eliminated by a puncture procedure (Brooks et al., 2016). Although large amounts of hydrogen are not harmful to humans, they are extremely harmful to the properties and structure of the material. It has been found that excessive hydrogen pressure can exceed the self-strength of porous materials, causing the composite to lose its mechanical integrity and eventually face failure (Esen et al., 2013). The rapid corrosion rate of titanium-magnesium composites is a major factor limiting their use in human implants. Reducing the degradation of magnesium in composites is a pressing issue. Surface modification is considered to be the most widely used method to reduce the degradation rate of Mg-containing materials. Surface modification can be achieved by mechanical or chemical treatment. Chemical pre-washing can eliminate Mg from the composite surface in advance, thus exposing the porous structure, and this gradient composite has less effect on force properties (Jiang et al., 2015), but these surface pores can act as deep pockets for post-implantation bacterial infection (Weber and Cochran, 1998), and this method cannot be applied to mass production. Subsequently, Ibrahim et al. (2021) obtained flat, smooth and undamaged surfaces by mechanical treatment with grinding and polishing, and found that the degradation rate of mechanically treated titanium-magnesium composites was reduced by a factor of five compared to untreated ones. In addition, Xu et al. (2021) successfully generated a layer of oxide film on the surface of titanium-magnesium composites by micro-arc oxidation. Subsequently they found that the hydrogen precipitation rate of the micro-arc-oxidized titanium-magnesium composites was alleviated, and the degradation rate of the composites was significantly reduced. The microarc oxidation technique can not only reduce the

corrosion rate of Mg phase in composites, but also stimulate the adhesion, value addition and differentiation of cells on Ti phase (Chen et al., 2019). Taken together, micro-arc oxidation technology has a positive effect on both Ti and Mg phases in titanium-magnesium composites, and it is one of the technologies with more outstanding advantages in the surface modification scheme of titanium-magnesium composites. The human body is a complex chemical environment, and factors such as inorganic ions, amino acids and oxidative stress reactions in the human body may affect the degradation behavior of magnesium. The effect of this environmental factor on the corrosion rate of titanium-magnesium composites has not been studied in depth, and these studies are necessary before titanium-magnesium composites are implanted into the human body as bio-implants.

Conclusion and future perspectives

This work summarizes the recent progress of titanium-magnesium composites. Titanium-magnesium composites have shown significant promise for orthopedic applications. The titanium-magnesium composites have the following advantages:

- 1) The E of the composite may be modified across an extensive range by adjusting the titanium and magnesium composition ratios. In contrast, the inclusion of magnesium compensates for porous titanium's probable lack of strength.
- 2) The addition of magnesium to the composites also addresses titanium's lack of bioactivity.
- 3) Magnesium decomposition increases bone tissue formation and offers space for it to expand. The porous titanium in the composite can give long-term mechanical support for bone tissue growth.

The fabrication of partially degradable titanium-magnesium composites shows promise from a processing standpoint because all three preparation techniques successfully combined titanium and magnesium and displayed favorable properties that are either difficult to obtain or impractical through conventional melting or deformation processing. The mechanical properties of the currently prepared titanium-magnesium composites can meet the performance requirements of human implants, but researchers are still exploring the development of titanium-magnesium composites with lower E and higher UCS. Researchers are attempting to create titanium-magnesium composites with lower degradation rates from the perspective of composition selection, such as by lowering the surface volume share of magnesium in the composites and creating titanium-magnesium composites using either titanium alloys or magnesium alloys. Nevertheless, the partial

degradability and post-degradation strength of Ti-Mg composites are advantageous for biological applications. However, research on titanium-magnesium composites is still in its early stages compared to that of titanium alloys, stainless steel, and cobalt-based alloys. Before titanium-magnesium composites may be used in biomedical domains, much more work needs to be done. In order to consistently and easily produce high-quality samples, novel preparation techniques should be investigated and implemented. Second, the current studies on the mechanical characteristics of titanium-magnesium composites primarily focus on the E test and few works looking into the compressive and tensile properties performance, while studies on fatigue testing have been noted to be insufficient. In addition, corrosion fatigue, a complicated relationship between mechanical and corrosion features in a body fluid environment, is still absent. Finally, the relationship of mechanical behavior-corrosive properties-porosity is not to be established.

Author contributions

JW and ZB conceived and wrote the article; CW discussed and edited its contents; SZ: discussed and edited its contents and provided funding acquisition; NW: discussed and edited its contents; QW: discussed and edited its contents and provided funding acquisition. YZ: discussed and edited its contents and provided funding acquisition.

Funding

This work was supported by the Key Research Project from Shenyang Science and Technology Funded Project (Nos. 22-101-0-16, 19-109-1-03), Science and Technology Project of Liaoning Province (2018020205-101), the Key Research and Development Projects of Liaoning Province (2020020184-JH2/103).

Conflict of interest

The authors declare that the research was conducted in the absence of any commercial or financial relationships that could be construed as a potential conflict of interest.

Publisher's note

All claims expressed in this article are solely those of the authors and do not necessarily represent those of their affiliated organizations, or those of the publisher, the editors and the reviewers. Any product that may be evaluated in this article, or claim that may be made by its manufacturer, is not guaranteed or endorsed by the publisher.

References

- Aguilar, C., Arancibia, M., Alfonso, I., Sancy, M., Tello, K., Salinas, V., et al. (2019). Influence of porosity on the elastic modulus of Ti-Zr-Ta-Nb foams with a low Nb content. *Metals* 9, 176. doi:10.3390/met9020176
- Asri, R. I. M., Harun, W. S. W., Samykano, M., Lah, N. A. C., Ghani, S. A. C., Tarlochan, F., et al. (2017). Corrosion and surface modification on biocompatible metals: A review. *Mater. Sci. Eng. C* 77, 1261–1274. doi:10.1016/j.msec.2017.04.102
- Atrens, A., Song, G. L., Cao, F., Shi, Z., and Bowen, P. K. (2013). Advances in Mg corrosion and research suggestions. *J. Magnesium Alloys* 1, 177–200. doi:10.1016/j.jma.2013.09.003
- Bahraminasab, M., Bozorg, M., Ghaffari, S., and Kavakebian, F. (2019). Electrochemical corrosion of Ti-Al₂O₃ biocomposites in Ringer's solution. *J. Alloys Compd.* 777, 34–43. doi:10.1016/j.jallcom.2018.09.313
- Balog, M., Ibrahim, A. M. H., Krizik, P., Bajana, O., Klimova, A., Catic, A., et al. (2019). Bioactive Ti + Mg composites fabricated by powder metallurgy: The relation between the microstructure and mechanical properties. *J. Mech. Behav. Biomed. Mat.* 90, 45–53. doi:10.1016/j.jmbbm.2018.10.008
- Balog, M., Snajdar, M., Krizik, P., Schaperl, Z., Stanec, Z., and Catic, A. (2017). "Titanium-magnesium composite for dental implants (BIACOM)," in TMS 2017 146th Annual Meeting & Exhibition Supplemental Proceedings, San Diego, CA: Springer International Publishing, 271–284. doi:10.1007/978-3-319-51493-2_26
- Brooks, E. K., Brooks, R. P., and Ehrensberger, M. T. (2017). Effects of simulated inflammation on the corrosion of 316L stainless steel. *Mater. Sci. Eng. C* 71, 200–205. doi:10.1016/j.msec.2016.10.012
- Brooks, E. K., Der, S., and Ehrensberger, M. T. (2016). Corrosion and mechanical performance of AZ91 exposed to simulated inflammatory conditions. *Mater. Sci. Eng. C* 60, 427–436. doi:10.1016/j.msec.2015.11.059
- Bütev Öcal, E., Esen, Z., Aydinol, K., and Dericioğlu, A. F. (2020). Comparison of the short and long-term degradation behaviors of as-cast pure Mg, AZ91 and WE43 alloys. *Mat. Chem. Phys.* 241, 122350. doi:10.1016/j.matchemphys.2019.122350
- Cai, X. C., Song, J., Yang, T. T., Peng, Q. M., Huang, J. Y., and Shen, T. D. (2018). A bulk nanocrystalline Mg-Ti alloy with high thermal stability and strength. *Mat. Lett.* 210, 121–123. doi:10.1016/j.matlet.2017.09.021
- Cao, F., Shi, Z., Hofstetter, J., Uggowitzer, P. J., Song, G., Liu, M., et al. (2013). Corrosion of ultra-high-purity Mg in 3.5% NaCl solution saturated with Mg(OH)₂. *Corros. Sci.* 75, 78–99. doi:10.1016/j.corsci.2013.05.018
- Carman, A., Zhang, L. C., Ivasishin, O. M., Savvakini, D. G., Matviychuk, M. V., and Pereloma, E. V. (2011). Role of alloying elements in microstructure evolution and alloying elements behaviour during sintering of a near-β titanium alloy. *Mater. Sci. Eng. A* 528, 1686–1693. doi:10.1016/j.msea.2010.11.004
- Chae, K., Jiang, W. Y., Park, K., Lee, J., Kim, H., Lee, K., et al. (2020). Antibacterial infection and immune-evasive coating for orthopedic implants. *Sci. Adv.* 6, eabb0025. doi:10.1126/sciadv.abb0025
- Chen, F. M., and Liu, X. (2016). Advancing biomaterials of human origin for tissue engineering. *Prog. Polym. Sci.* 53, 86–168. doi:10.1016/j.progpolymsci.2015.02.004
- Chen, J., Li, J., Hu, F., Zou, Q., Mei, Q., Li, S., et al. (2019). Effect of microarc oxidation-treated Ti6Al4V scaffold following low-intensity pulsed ultrasound stimulation on osteogenic cells *in vitro*. *ACS Biomater. Sci. Eng.* 5, 572–581. doi:10.1021/acsbiomaterials.8b01000
- Chen, Q., and Thouas, G. A. (2015). Metallic implant biomaterials. *Mater. Sci. Eng. R Rep.* 87, 1–57. doi:10.1016/j.mser.2014.10.001
- Chi, F., Wießner, L., Gröb, T., Bruder, E., Sawatzki, S., Löwe, K., et al. (2019). Towards manufacturing of Nd-Fe-B magnets by continuous rotary swaging of cast alloy. *J. Magn. Magn. Mat.* 490, 165405. doi:10.1016/j.jmmm.2019.165405
- Dutta, S., Gupta, S., and Roy, M. (2020). Recent developments in magnesium metal-matrix composites for biomedical applications: A review. *ACS Biomater. Sci. Eng.* 6, 4748–4773. doi:10.1021/acsbiomaterials.0c00678
- Esen, Z., Butev, E., and Karakas, M. S. (2016). A comparative study on biodegradation and mechanical properties of pressureless infiltrated Ti/Ti6Al4V-Mg composites. *J. Mech. Behav. Biomed. Mat.* 63, 273–286. doi:10.1016/j.jmbbm.2016.06.026
- Esen, Z., Dikici, B., Duygulu, O., and Dericioğlu, A. F. (2013). Titanium-magnesium based composites: Mechanical properties and *in-vitro* corrosion response in Ringer's solution. *Mater. Sci. Eng. A* 573, 119–126. doi:10.1016/j.msea.2013.02.040
- Esen, Z., Öcal, E. B., Akkaya, A., Gürçay, B., Özcan, C., Özgümüş, B. A., et al. (2020). Corrosion behaviours of Ti6Al4V-Mg-Alloy composites. *Corros. Sci.* 166, 108470. doi:10.1016/j.corsci.2020.108470
- Fage, S. W., Muris, J., Jakobsen, S. S., and Thyssen, J. P. (2016). Titanium: A review on exposure, release, penetration, allergy, epidemiology, and clinical reactivity. *Contact Dermat.* 74, 323–345. doi:10.1111/cod.12565
- Fan, D. Y., Yi, Z., Feng, X., Tian, W. Z., Xu, D. K., Cristino Valentino, A. M., et al. (2021). Antibacterial property of a gradient Cu-bearing titanium alloy by laser additive manufacturing. *Rare Met.* 41, 580–593. doi:10.1007/s12598-021-01826-w
- Gepreel, M. A. H., and Niinomi, M. (2013). Biocompatibility of Ti-alloys for long-term implantation. *J. Mech. Behav. Biomed. Mat.* 20, 407–415. doi:10.1016/j.jmbbm.2012.11.014
- Hao, Y. L., Li, S. J., Sun, S. Y., Zheng, C. Y., and Yang, R. (2007). Elastic deformation behaviour of Ti-24Nb-4Zr-7.9Sn for biomedical applications. *Acta Biomater.* 3, 277–286. doi:10.1016/j.actbio.2006.11.002
- Heywood, M., Shi, Z., Li, Y., Wen, C., Kanwar, J., Xiao, Y., et al. (2019). Corrosion of porous Ti35Zr28Nb in Hanks' solution and 3.5 wt% NaCl. *Mater. Corros.* 70, 529–536. doi:10.1002/maco.201810423
- Hu, Z. Y., Zhang, Z. H., Cheng, X. W., Wang, F. C., Zhang, Y. F., and Li, S. L. (2020). A review of multi-physical fields induced phenomena and effects in spark plasma sintering: Fundamentals and applications. *Mat. Des.* 191, 108662. doi:10.1016/j.matdes.2020.108662
- Ibrahim, A. M. H., Balog, M., Krizik, P., Novy, F., Cetin, Y., Svec, P., et al. (2020). Partially biodegradable Ti-based composites for biomedical applications subjected to intense and cyclic loading. *J. Alloys Compd.* 839, 155663. doi:10.1016/j.jallcom.2020.155663
- Ibrahim, A. M. H., Takacova, M., Jelenska, L., Csaderova, L., Balog, M., Kopacek, J., et al. (2021). The effect of surface modification of TiMg composite on the *in-vitro* degradation response, cell survival, adhesion, and proliferation. *Mater. Sci. Eng. C* 127, 112259. doi:10.1016/j.msec.2021.112259
- Jiang, G., Li, Q., Wang, C., Dong, J., and He, G. (2015). Fabrication of graded porous titanium-magnesium composite for load-bearing biomedical applications. *Mat. Des.* 67, 354–359. doi:10.1016/j.matdes.2014.12.001
- Jiang, S., Huang, L. J., An, Q., Geng, L., Wang, X. J., and Wang, S. (2018). Study on titanium-magnesium composites with bicontinuous structure fabricated by powder metallurgy and ultrasonic infiltration. *J. Mech. Behav. Biomed. Mat.* 81, 10–15. doi:10.1016/j.jmbbm.2018.02.017
- Khodaei, M., Fathi, M., Meratian, M., and Savabi, O. (2018). The effect of porosity on the mechanical properties of porous titanium scaffolds: Comparative study on experimental and analytical values. *Mat. Res. Express* 5, 055401. doi:10.1088/2053-1591/aabfa2
- Koh, J., Berger, A., and Benhaim, P. (2015). An overview of internal fixation implant metallurgy and galvanic corrosion effects. *J. Hand Surg. Br.* 40, 1703–1710.e4. doi:10.1016/j.jhsa.2015.03.030
- Koizumi, H., Ishii, T., Okazaki, T., Kaketani, M., Matsumura, H., and Yoneyama, T. (2018). Castability and mechanical properties of Ti-15Mo-5Zr-3Al alloy in dental casting. *J. Oral Sci.* 60, 285–292. doi:10.2334/josnusd.17-0280
- Kunčická, L., Kocich, R., and Lowe, T. C. (2017). Advances in metals and alloys for joint replacement. *Prog. Mat. Sci.* 88, 232–280. doi:10.1016/j.pmatsci.2017.04.002
- Kunčická, L., Macháček, A., Lavery, N. P., Kocich, R., Cullen, J. C. T., and Hlaváč, L. M. (2020). Effect of thermomechanical processing via rotary swaging on properties and residual stress within tungsten heavy alloy. *Int. J. Refract. Met. Hard Mat.* 87, 105120. doi:10.1016/j.jrmhm.2019.105120
- Lai, T., Xu, J. L., Huang, J., Wang, Q., Zhang, J. P., and Luo, J. M. (2022). Partially biodegradable Ti Mg composites prepared by microwave sintering for biomedical application. *Mat. Charact.* 185, 111748. doi:10.1016/j.matchar.2022.111748
- Li, Q., Jiang, G., Wang, C., Dong, J., and He, G. (2015). Mechanical degradation of porous titanium with entangled structure filled with biodegradable magnesium in Hanks' solution. *Mater. Sci. Eng. C* 57, 349–354. doi:10.1016/j.msec.2015.08.008
- Li, Y., Yang, C., Zhao, H., Qu, S., Li, X., and Li, Y. (2014). New developments of Ti-based alloys for biomedical applications. *Materials* 7, 1709–1800. doi:10.3390/ma7031709
- Liang, G., and Schulz, R. (2003). Synthesis of Mg-Ti alloy by mechanical alloying. *J. Mat. Sci.* 38, 1179–1184. doi:10.1023/A:1022889100360
- Liang, L., Huang, Q., Wu, H., Ouyang, Z., Liu, T., He, H., et al. (2021). Stimulation of *in vitro* and *in vivo* osteogenesis by Ti-Mg alloys with the sustained-release function of magnesium ions. *Colloids Surfaces B Biointerfaces* 197, 111360. doi:10.1016/j.colsurfb.2020.111360
- Liu, W., Liu, S., and Wang, L. (2019). Surface modification of biomedical titanium alloy: Micromorphology, microstructure evolution and biomedical applications. *Coatings* 9, 249. doi:10.3390/coatings9040249

- Liu, X., Yuan, W., Shen, D., Cheng, Y., Chen, D., and Zheng, Y. (2021). Exploring the biodegradation of pure Zn under simulated inflammatory condition. *Corros. Sci.* 189, 109606. doi:10.1016/j.corsci.2021.109606
- Liu, Y., Yu, Q., Tan, G., Zhang, M., Tang, E., Wang, S., et al. (2021). Bioinspired fish-scale-like magnesium composites strengthened by textures of continuous titanium fibers: Lessons from nature. *J. Magnes. Alloy.* doi:10.1016/j.jma.2021.06.023
- Maier, H. J., Julmi, S., Behrens, S., Klose, C., Gartzke, A.-K., Wriggers, P., et al. (2020). Magnesium alloys for open-pored bioresorbable implants. *Jom* 72, 1859–1869. doi:10.1007/s11837-020-04078-8
- Makkar, P., Sarkar, S. K., Padalhin, A. R., Moon, B. G., Lee, Y. S., and Lee, B. T. (2018). *In vitro* and *in vivo* assessment of biomedical Mg-Ca alloys for bone implant applications. *J. Appl. Biomater. Funct. Mat.* 16, 126–136. doi:10.1177/228080017750359
- Mas Ayu, H., Daud, R., Kurniawan, T., Alias, J., Izman, S., Shah, A., et al. (2019). Improving biocompatibility of cobalt based alloy using chemical etching and mechanical treatment. *Materwiss. Werkstofftech.* 50, 254–259. doi:10.1002/mawe.201800210
- Meenashisundaram, G. K., Wang, N., Maskomani, S., Lu, S., Anantharajan, S. K., Dheen, S. T., et al. (2020). Fabrication of Ti + Mg composites by three-dimensional printing of porous Ti and subsequent pressureless infiltration of biodegradable Mg. *Mater. Sci. Eng. C* 108, 110478. doi:10.1016/j.msec.2019.110478
- Narita, K., Niinomi, M., Nakai, M., Hieda, J., and Oribe, K. (2012). Development of thermo-mechanical processing for fabricating highly durable β -type Ti-Nb-Ta-Zr rod for use in spinal fixation devices. *J. Mech. Behav. Biomed. Mat.* 9, 207–216. doi:10.1016/j.jmbbm.2012.01.011
- Ouyang, S., Liu, Y., Huang, Q., Gan, Z., and Tang, H. (2020). Effect of composition on *in vitro* degradability of Ti-Mg metal-metal composites. *Mater. Sci. Eng. C* 107, 110327. doi:10.1016/j.msec.2019.110327
- Pellizzari, M., Jam, A., Tschon, M., Fini, M., Lora, C., and Benedetti, M. (2020). A 3D-printed ultra-low young's modulus beta-Ti alloy for biomedical applications. *Materials* 13, 2792. doi:10.3390/ma13122792
- Qazi, J. I., Marquardt, B., Allard, L. F., and Rack, H. J. (2005). Phase transformations in Ti-35Nb-7Zr-5Ta-(0.06–0.68)O alloys. *Mater. Sci. Eng. C* 25, 389–397. doi:10.1016/j.msec.2005.01.022
- Rivera-Salinas, J. E., Gregorio-Jáuregui, K. M., Romero-Serrano, J. A., Cruz-Ramírez, A., Hernández-Hernández, E., Miranda-Pérez, A., et al. (2020). Simulation on the effect of porosity in the elastic modulus of SiC particle reinforced Al matrix composites. *Metals* 10, 391. doi:10.3390/met10030391
- Rodriguez-Merchan, E. C. (2022). Bone healing materials in the treatment of recalcitrant nonunions and bone defects. *Int. J. Mol. Sci.* 23, 3352. doi:10.3390/ijms23063352
- Song, G., and Atrons, A. (2003). Understanding magnesium corrosion—a framework for improved alloy performance. *Adv. Eng. Mat.* 5, 837–858. doi:10.1002/adem.200310405
- Strunz, P., Kocich, R., Canelo-Yubero, D., Machackova, A., Beran, P., and Kratka, L. (2020). Texture and differential stress development in W/Ni-Co composite after rotary swaging. *Materials* 13, 2869. doi:10.3390/ma13122869
- Su, J. L., Teng, J., Xu, Z. L., and Li, Y. (2020). Biodegradable magnesium-matrix composites: A review. *Int. J. Min. Metall. Mat.* 27, 724–744. doi:10.1007/s12613-020-1987-2
- Taddei, E. B., Henriques, V. A. R., Silva, C. R. M., and Cairo, C. A. A. (2004). Production of new titanium alloy for orthopedic implants. *Mater. Sci. Eng. C* 24, 683–687. doi:10.1016/j.msec.2004.08.011
- Tamilselvi, S., Raman, V., and Rajendran, N. (2006). Corrosion behaviour of Ti-6Al-7Nb and Ti-6Al-4V ELI alloys in the simulated body fluid solution by electrochemical impedance spectroscopy. *Electrochim. Acta* 52, 839–846. doi:10.1016/j.electacta.2006.06.018
- Tang, J., Luo, H., Qi, Y., Xu, P., Lv, J., Ma, Y., et al. (2018). Effect of nano-scale martensite and β phase on the passive film formation and electrochemical behaviour of Ti-10V-2Fe-3Al alloy in 3.5% NaCl solution. *Electrochim. Acta* 283, 1300–1312. doi:10.1016/j.electacta.2018.07.047
- Teo, A. Q. A., Yan, L., Chaudhari, A., and O'Neill, G. K. (2021). Post-processing and surface characterization of additively manufactured stainless steel 316L lattice: Implications for BioMedical use. *Materials* 14, 1376. doi:10.3390/ma14061376
- Tiyyagura, H. R., Puliyalil, H., Filipić, G., Kumar, K. C., Pottathara, Y. B., Rudolf, R., et al. (2020). Corrosion studies of plasma modified magnesium alloy in simulated body fluid (SBF) solutions. *Surf. Coat. Technol.* 385, 125434. doi:10.1016/j.surfcoat.2020.125434
- Tsakiris, V., Tardei, C., and Clicoschi, F. M. (2021). Biodegradable Mg alloys for orthopedic implants — a review. *J. Magnesium Alloys* 9, 1884–1905. doi:10.1016/j.jma.2021.06.024
- Vrancken, B., Thijs, L., Kruth, J. P., and Van Humbeeck, J. (2012). Heat treatment of Ti6Al4V produced by selective laser melting: Microstructure and mechanical properties. *J. Alloys Compd.* 541, 177–185. doi:10.1016/j.jallcom.2012.07.022
- Wang, Y. Q., Tao, J., Zhang, J. L., and Wang, T. (2011). Effects of addition of NH_4HCO_3 on pore characteristics and compressive properties of porous Ti-10% Mg composites. *Trans. Nonferrous Metals Soc. China* 21, 1074–1079. doi:10.1016/S1003-6326(11)60824-8
- Weber, H. P., and Cochran, D. L. (1998). The soft tissue response to osseointegrated dental implants. *J. Prosthet. Dent.* 79, 79–89. doi:10.1016/S0022-3913(98)70198-2
- Witte, F., Kaese, V., Haferkamp, H., Switzer, E., Meyer-Lindenberg, A., Wirth, C. J., et al. (2005). *In vivo* corrosion of four magnesium alloys and the associated bone response. *Biomaterials* 26, 3557–3563. doi:10.1016/j.biomaterials.2004.09.049
- Wong, M. H., and Man, H. C. (2018). Low-temperature fabrication of Ag-doped HA coating on NiTi. *Mat. Lett.* 229, 229–231. doi:10.1016/j.matlet.2018.07.003
- Wu, C. L., Zai, W., and Man, H. C. (2021). Additive manufacturing of ZK60 magnesium alloy by selective laser melting: Parameter optimization, microstructure and biodegradability. *Mat. Today Commun.* 26, 101922. doi:10.1016/j.mtcomm.2020.101922
- Wu, G., Ibrahim, J. M., and Chu, P. K. (2013). Surface design of biodegradable magnesium alloys A review. *Surf. Coat. Technol.* 233, 2–12. doi:10.1016/j.surfcoat.2012.10.009
- Xu, J. L., Tang, J., Hu, J., Zhang, J. L., Luo, J. M., Hao, G. D., et al. (2021). Microstructure, degradation properties and cytocompatibility of micro-arc oxidation coatings on the microwave sintered Ti-15Mg metal-metal composite. *J. Mat. Res. Technol.* 11, 1654–1664. doi:10.1016/j.jmrt.2021.02.004
- Yan, X., Li, Q., Yin, S., Chen, Z., Jenkins, R., Chen, C., et al. (2019). Mechanical and *in vitro* study of an isotropic Ti6Al4V lattice structure fabricated using selective laser melting. *J. Alloys Compd.* 782, 209–223. doi:10.1016/j.jallcom.2018.12.220
- Yao, F., You, G., Wang, L., Li, Q., Zeng, S., and Ming, Y. (2022). Design, fabrication, microstructure, and mechanical properties of interlayer-free vacuum diffusion bonding Mg/Ti composites. *Vacuum* 199, 110947. doi:10.1016/j.vacuum.2022.110947
- Yi, Z., Liu, Y., Ma, Y. D., Liu, Z. G., Sun, H., Zhou, X., et al. (2021). Surface treatment of 3D printed Cu-bearing Ti alloy scaffolds for application in tissue engineering. *Mat. Des.* 213, 110350. doi:10.1016/j.matdes.2021.110350
- Yu, F., Addison, O., and Davenport, A. J. (2015). A synergistic effect of albumin and H_2O_2 accelerates corrosion of Ti6Al4V. *Acta Biomater.* 26, 355–365. doi:10.1016/j.actbio.2015.07.046
- Zach, L., Kuncicka, L., Ruzicka, P., and Kocich, R. (2014). Design, analysis and verification of a knee joint oncological prosthesis finite element model. *Comput. Biol. Med.* 54, 53–60. doi:10.1016/j.compbio.2014.08.021
- Zeller-Plumhoff, B., Tolnai, D., Wolff, M., Greving, I., Hort, N., and Willumeit-Römer, R. (2021). Utilizing synchrotron radiation for the characterization of biodegradable magnesium alloys—from alloy development to the application as implant material. *Adv. Eng. Mat.* 23, 2100197. doi:10.1002/adem.202100197
- Zhang, L., Yang, G., Johnson, B. N., and Jia, X. (2019). Three-dimensional (3D) printed scaffold and material selection for bone repair. *Acta Biomater.* 84, 16–33. doi:10.1016/j.actbio.2018.11.039
- Zhang, M., Zhao, N., Yu, Q., Liu, Z., Qu, R., Zhang, J., et al. (2022). On the damage tolerance of 3-D printed Mg-Ti interpenetrating-phase composites with bioinspired architectures. *Nat. Commun.* 13, 3247. doi:10.1038/s41467-022-30873-9
- Zhang, Y. S., Hu, J. J., Zhang, W., Yu, S., Yu, Z. T., Zhao, Y. Q., et al. (2019). Discontinuous core-shell structured Ti-25Nb-3Mo-3Zr-2Sn alloy with high strength and good plasticity. *Mat. Charact.* 147, 127–130. doi:10.1016/j.matchar.2018.10.021
- Zhao, C., Wu, H., Hou, P., Ni, J., Han, P., and Zhang, X. (2016). Enhanced corrosion resistance and antibacterial property of Zn doped DCPD coating on biodegradable Mg. *Mat. Lett.* 180, 42–46. doi:10.1016/j.matlet.2016.04.035
- Zhou, H., Liang, B., Jiang, H., Deng, Z., and Yu, K. (2021). Magnesium-based biomaterials as emerging agents for bone repair and regeneration: From mechanism to application. *J. Magnesium Alloys* 9, 779–804. doi:10.1016/j.jma.2021.03.004
- Zhou, L., Chen, J., Huang, W., Ren, Y., Niu, Y., and Yuan, T. (2021). Effects of Ta content on phase transformation in selective laser melting processed Ti-13Nb-13Zr alloy and its correlation with elastic properties. *Vacuum* 183, 109798. doi:10.1016/j.vacuum.2020.109798
- Zhou, X., Xu, D., Geng, S., Fan, Y., Yang, C., Wang, Q., et al. (2021). Microstructural evolution and corrosion behavior of Ti-6Al-4V alloy fabricated by laser metal deposition for dental applications. *J. Mat. Res. Technol.* 14, 1459–1472. doi:10.1016/j.jmrt.2021.07.006



OPEN ACCESS

EDITED BY

Chunguang Yang,
Chinese Academy of Sciences (CAS),
China

REVIEWED BY

Hong Duan,
Sichuan University, China
Da Sun,
Wenzhou University, China
Liqun Yang,
China Medical University, China

*CORRESPONDENCE

Vincent Crenn,
vincent.crenn@chu-nantes.fr
Luciano Vidal,
luciano.vidal@ec-nantes.fr

[†]These authors have contributed equally
to this work

[‡]These authors have contributed equally
to this work

SPECIALTY SECTION

This article was submitted to
Biomaterials,
a section of the journal
Frontiers in Bioengineering and
Biotechnology

RECEIVED 11 July 2022

ACCEPTED 16 August 2022

PUBLISHED 08 September 2022

CITATION

Biscaccianti V, Fragnaud H, Hascoët J-Y,
Crenn V and Vidal L (2022), Digital chain
for pelvic tumor resection with 3D-
printed surgical cutting guides.
Front. Bioeng. Biotechnol. 10:991676.
doi: 10.3389/fbioe.2022.991676

COPYRIGHT

© 2022 Biscaccianti, Fragnaud, Hascoët,
Crenn and Vidal. This is an open-access
article distributed under the terms of the
[Creative Commons Attribution License](https://creativecommons.org/licenses/by/4.0/)
(CC BY). The use, distribution or
reproduction in other forums is
permitted, provided the original
author(s) and the copyright owner(s) are
credited and that the original
publication in this journal is cited, in
accordance with accepted academic
practice. No use, distribution or
reproduction is permitted which does
not comply with these terms.

Digital chain for pelvic tumor resection with 3D-printed surgical cutting guides

Vincent Biscaccianti^{1†}, Henri Fragnaud^{2†}, Jean-Yves Hascoët¹,
Vincent Crenn^{2,3*‡} and Luciano Vidal^{1*‡}

¹Research Institut in Civil Engineering and Mechanics (GeM), CNRS, UMR 6183, Centrale Nantes, Nantes Université, Nantes, France, ²Department of Orthopedic, Nantes Hospital, CHU Hotel-Dieu, Nantes, France, ³INSERM UMR 1307, CNRS UMR 6075-Team 9 CHILd (Chromatin and Transcriptional Deregulation in Pediatric Bone Sarcoma), Nantes Université, CRCI2NA (Centre de Recherche en Cancérologie et Immunologie Nantes-Angers), Nantes, France

Surgical cutting guides are 3D-printed customized tools that help surgeons during complex surgeries. However, there does not seem to be any set methodology for designing these patient-specific instruments. Recent publications using pelvic surgical guides showed various designs with no clearly classified or standardized features. We, thus, developed a systematic digital chain for processing multimodal medical images (CT and MRI), designing customized surgical cutting guides, and manufacturing them using additive manufacturing. The aim of this study is to describe the steps in the conception of surgical cutting guides used in complex oncological bone tumor pelvic resection. We also analyzed the duration of the surgical cutting guide process and tested its ergonomics and usability with orthopedic surgeons using Sawbones models on simulated tumors. The original digital chain made possible a repeatable design of customized tools in short times. Preliminary testing on synthetic bones showed satisfactory results in terms of design usability. The four artificial tumors (Enneking I, Enneking II, Enneking III, and Enneking I+IV) were successfully resected from the Sawbones model using this digital chain with satisfactory ergonomic outcomes. This work validates a new digital chain conception and production of surgical cutting guides. Further works with quantitative margin assessments on anatomical subjects are needed to better assess the design implications of patient-specific surgical cutting guide instruments in pelvic tumor resections.

KEYWORDS

surgical cutting guides, patient-specific instruments, pelvic bone tumor, reconstruction surgery, 3D printing, additive manufacturing, digital chain

Introduction

Surgical cutting guides (SCGs) are customized tools that help surgeons during complex surgeries (Scolozzi, 2015; Wong et al., 2016). They are patient specific, meaning they are designed and manufactured for a single specific case and tailored to the patient's anatomy (Vidal et al., 2020a). SCGs are increasingly studied and used in

orthopedic and maxillofacial surgeries (Abou-Elfetouh et al., 2011; Krishnan et al., 2012; Wong, 2016). The most common applications are currently for mandibular defect reconstruction and knee surgery. In addition, tumor resection surgeries, orthognathic surgery, or total knee arthroplasty (TKA) also often use this technology (Krishnan et al., 2012; Cartiaux et al., 2014; Gouin et al., 2014; Mazzoni et al., 2015; Greenberg et al., 2021).

There is abundant literature on this topic, and the efficiency of these guides seems to be established (Vidal et al., 2020b). However, there does not seem to be any set methodology for designing such guides (Numajiri et al., 2018). Recent publications, using pelvic surgical guides, showed a wide variety of designs with no clearly classified or standardized features (Wang et al., 2017; Evrard et al., 2019; Siegel et al., 2020; Gkagkalis et al., 2021). The only feature that is common to any surgical guide is the positioning, which uses the negative shape of the bone. García-Sevilla et al. (2021) mentioned that a common strategy was to design wide SCGs to ensure correct placement. The downsides of this strategy are also mentioned (larger SCGs, modification of the surgical procedure to fit the SCG). Another aspect of standardization is the ability to reduce delays (and costs) in the design process. Wong et al. (2015) mentioned a 2-month wait for design and manufacturing. Rustemeyer et al. (2014) mentioned a 2–4-week delay in computer-aided design/computer-aided manufacturing (CAD/CAM) assisted surgeries for maxillofacial applications. In a 2016 review, Martelli et al. (2016) reported that 19.6% of studies using 3D-printed devices found the production delays limiting. We believe that introducing a precise methodology for designing SCGs will improve production times. This methodology should still make extreme customization possible and precisely respond to each case of tumor resection. Pelvic tumor resection SCGs have been documented since 2014 (Cartiaux et al., 2014; Gouin et al., 2014).

The efficiency of SCGs is proven, and the solution they provide might even be preferred to surgical navigation (Wong et al., 2016). However, the descriptions of SCG design digital chains are insufficient, especially for pelvic tumor resections. Numajiri et al. (2018) published a detailed workflow they have developed for patient-specific cutting and reconstruction guides used in fibula free flap maxillary reconstruction. Popescu (2014) described an in-house online platform for the design of SCGs, covering various applications. They highlighted the crucial need for close collaboration and communication between surgeons and designers/engineers to obtain relevant SCGs. They also give a detailed analysis of the numerical workflow, with each step's input and output file format. Chen et al. (2016) developed a semi-automatic computer-aided method for surgical template design, covering various applications. The method presented focuses on making use of stereolithography (STL) to produce SCGs of various designs by thickening local surfaces directly on the 3D model's mesh. This then makes it possible to customize the

fixation features. However, in-house trials of this approach revealed that direct surface thickening of STL surfaces often failed. Additionally, SCG designs for maxillary resections, long bone resections, or pelvic resections are not similar and need specialized design strategies (Rauch et al., 2021; Vidal et al., 2022).

In this research work, we focused primarily on pelvic bone tumor resections. The aim of our study was to first propose a systematic methodology for designing the SCGs used in pelvic tumor resections. The semi-automatic method we described was assessed in terms of its capacity to produce 3D SCGs, as was the duration of the digital chain process. A complementary experimental approach with the use on a radiopaque synthetic pelvis (Sawbones, Vashon, WA, United States) was performed by trained surgeons.

Materials and methods

Study objectives

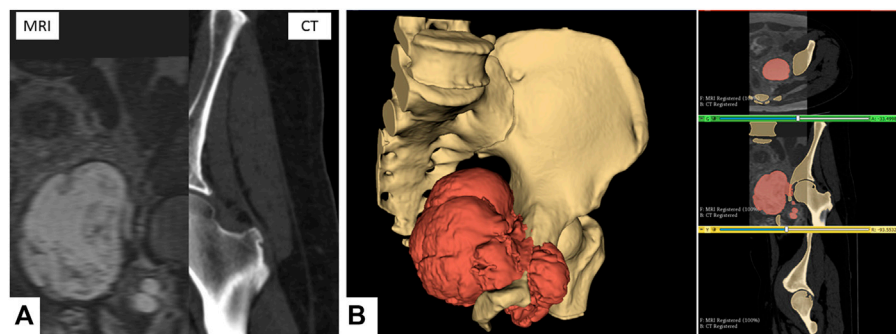
The aim of this study was to first describe and obtain functional 3D-printed SCGs using our original digital chain methodology, measuring the whole duration of the digital chain process, and evaluating its qualitative efficiency in the hands of specialized orthopedic tumor surgeons on a Sawbones model with regard to ergonomic aspects.

Systematic digital chain design on patient images

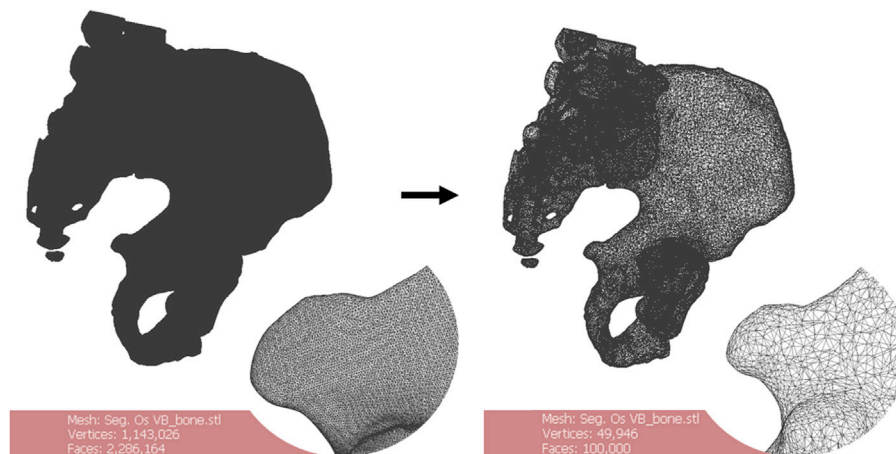
In this study, a systematic workflow (Supplementary Figure S1) was developed to process the DICOM (Digital Imaging and Communication in Medicine) files, design customized SCGs, and manufacture them using additive manufacturing (AM). To carry out the whole process, four types of software were used: 3D Slicer (Fedorov et al., 2012), MeshLab, Siemens NX (Siemens PLM, Plano, TX, United States), and Sinterit Studio. The Segment Editor Extra Effects and Elastix (Klein et al., 2010) of 3D Slicer were also used. The systematic digital chain was first tested on anonymized patients' images with magnetic resonance imaging (MRI) and computed tomography (CT) sequences.

DICOM file processing

To process DICOMs, the 3D Slicer was used. Anatomical 3D reconstruction was obtained by segmenting DICOM image stacks. The chosen approach was multimodal with the use of CT and MRI DICOMs together. To study and test the workflow, archive images of pelvic tumor cases available at the CHU Nantes were studied with full anonymization. The CT images used standard parameters, with a mean slice thickness of 1 mm. The presence of a contrasting agent was not mandatory for

**FIGURE 1**

Multimodal segmentation. (A) CT and MRI images, non-rigid B-Spline registration (3D Slicer's Elastix). (B) Multimodal segmentation using Watershed (right) and 3D reconstruction (left) of the bone tissues and tumor. Scale = 50 mm.

**FIGURE 2**

Remeshing of a 3D bone model. The starting number of faces of the mesh (left) is greater than 2,000,000. The oversampling is visible. Remeshing brings the number of faces to 100,000 (right). There is no noticeable quality downgrade for this application. Scale = 50 mm.

selection. MRI images were preferably T1 sequences, with gadolinium contrast agent and a slice thickness between 1 and 2 mm. Other sequences (T2 and STIR) were included if they met the thickness requirements and displayed enough contrast on the tumor. The images were obtained from different machines, such as the GE Medical Systems Optima CT660 (GE Healthcare, Chicago, IL, United States) for CT images, and the Siemens MAGNETOM Sola (Siemens PLM, Plano, TX, United States) for the MRI images.

The multimodal segmentation required prior registration of the DICOM images. CT and MRI were registered using the 3D Slicer's Elastix module's B-Spline registration with the "CT/MR-based pseudo-CT (pelvis prostate)" preset (Figure 1A).

One segmentation for each sequence was performed, focusing on the tissue of interest (bone on CT and tumor on MRI). The primary segmentation method used was the Watershed method implemented in the 3D Slicer module Segment Editor Extra Effects (Figure 1B). The reconstructed anatomical 3D models of the bone tissues and tumor were exported in the STL format.

STL file processing

The files were remeshed to reduce unnecessary computational load during the computer-aided design (CAD) phase. The quadratic edge collapse decimation function was used to reduce the mesh complexity (Figure 2). Topological differences between the original model and the remeshed

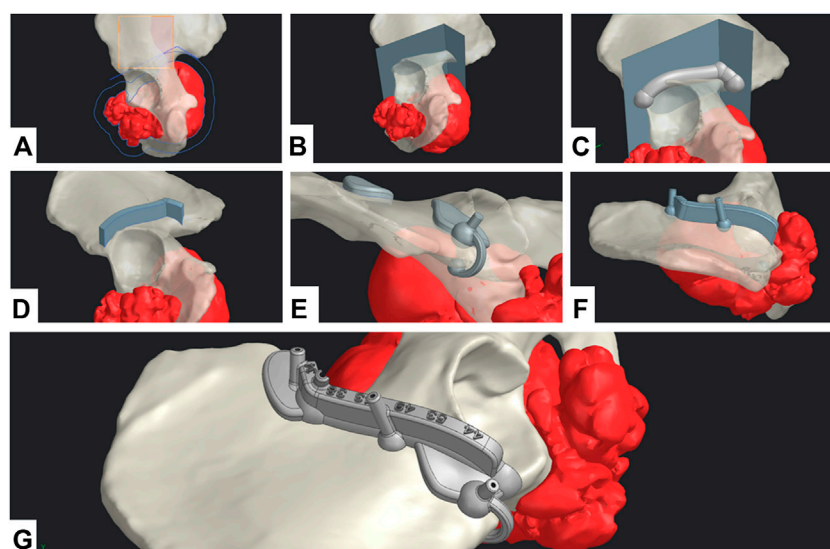


FIGURE 3
CAD design digital chain. (A) Geometrical definition. (B) Extrusion of the resection surface. (C) Main body generation. (D) Guiding feature generation. (E) Positioning feature generation. (F) Fixation feature generation. (G) Final SCG with united bodies and finishing features.

model in this case did not exceed 0.68 mm with an absolute mean of 0.01 mm difference (Hausdorff distance computation, sampling on all vertices). The quality downgrade was not noticeable.

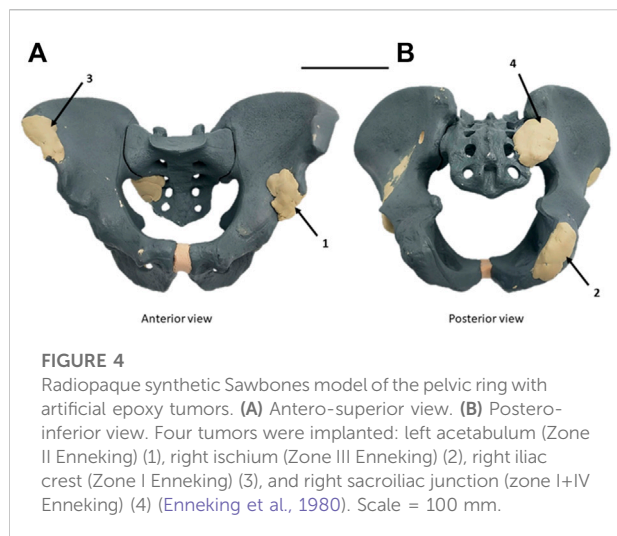
CAD process and surgical cutting guide design

For the CAD process, Siemens NX was used. The workflow was divided into two main phases: geometrical definition and SCG generation.

A straight collaboration between clinicians and engineers was established for the geometrical definition phase. A 3-point plane was defined, representing the main surgical direction of the approach. A polyline sketch on this plane defined the broad trajectory of resection (Figure 3A). The tumor's silhouette was projected on to the sketch and expanded by a 12 mm margin to conserve the oncological surgical margin of resection. The polyline was extruded as a surface body with a 5° draft angle (resection surface, Figure 3B). The SCG was generated in five steps: main body, guiding feature, positioning features, fixation features, and finishing. A 3D-trajectory was created along the resection surface for the main body: the intersection curve between the resection surface and bone model was displayed. Then, two extremities were defined for the cut. The intersection curve was simplified by approximating it to a 3D-spline between the nodes (nodes = extremity or intersection point between the bone model and resection plane junctions). The main body was generated as a solid circular sweep of diameter 16 mm along the 3D trajectory. The segments of the body were linked by spherical anchors (Ø20 mm) at each node (Figure 3C). The 3D trajectory

was offset from 15 mm upward along the resection surface. This defined the upper limit of the guiding feature. The surface was then cut using both 3D trajectories (initial and offset) to create the inner guiding surface. This surface was thickened by 7 mm to create the guiding feature's solid body (Figure 3D). The blade and pin axis were designed to avoid hurting any critical anatomical structures.

For the positioning features, two options were available: local contact surface widening (CSW) and deformable clip. A thin surface adherent to the bone in the area was thickened by 5 mm to create an additional contact surface. The width of the CSW could be limited to maximum defined by the surgeon. An offset copy of the cutting surface was used as a limiting element for the cutting guide's width. A Boolean subtraction was made to remove all parts of the SCGs outside the defined limits. These positioning features should not bring any risk or unnecessary exposure to noble anatomical structures. Finally, if the edge of the bone at the extremity was thin enough, a deformable clip was added. Two spheres were positioned on each side of the edge and linked with a thin bridge. Both local CSW and deformable clips could be used simultaneously (Figure 3E). The fixation features were designed as a drilled cylinder (Ø6 mm exterior, Ø2.1 mm interior) with a spherical anchor. Fixation feature axes were contained in the respective outer planes of the guiding feature. The axes were tilted from the direction of approach, so that none would be parallel with any other (Figure 3F). Finally, finishing was done by uniting all the solid bodies, and then creating corner gaps and cutting depth indications (Figure 3G).



Additive manufacturing

For the additive manufacturing process, the selective laser sintering (SLS) technology was chosen. The SCG prototypes were additively manufactured using a Sinterit Lisa SLS 3D (Sinterit, Krakow, Poland) printer with the affiliated software, Sinterit Studio. The material chosen was a nylon polyamide, Sinterit Polyamide 12 (PA12).

Evaluation method on a radiopaque synthetic pelvis

Experimental conditions

Bone tumor simulation

The experimental study was performed to validate our design digital chain. In a radiopaque synthetic pelvis (Sawbones, Vashon, WA, United States), four artificial epoxy tumors were

developed: right acetabulum (Enneking Zone II), left ischium (Enneking zone III), left iliac crest (Enneking zone I), and left sacroiliac junction (Enneking zone I+IV) as shown in Figure 4 (Enneking et al., 1980).

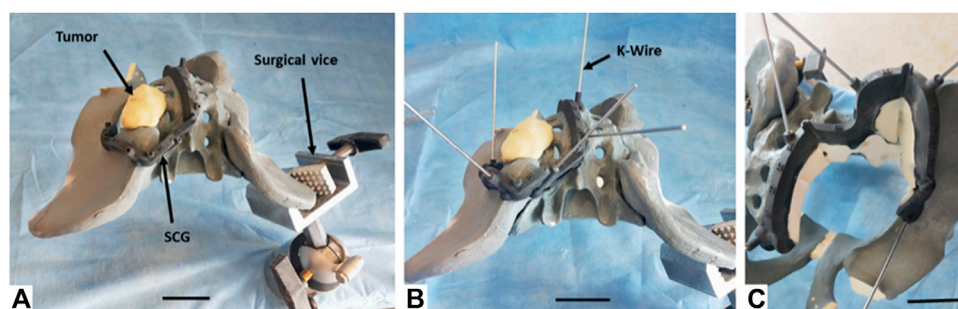
A CT image was then acquired on the modified synthetic pelvis, using the Philips Ingenuity Flex scanner (Philips International B.V., Amsterdam, Netherlands). Unlike the first method described previously for patient images, and given that no MRI sequence was acquired as dry synthetic bones are not MRI compatible, only a mono-modal (CT only) segmentation was thus performed in the 3D Slicer. Watershed segmentation was used as described. The contrast on artificial tumors was enough to clearly distinguish them from the synthetic cancellous bone. Some minor uncertainties remained on cortical bone (similar Hounsfield Units), requiring corrections in the first Watershed iteration. The 3D model was then exported in the STL format and remeshed. The STL was imported into Siemens NX for the CAD design of each SCG. The duration of the digital chain process was assessed for each simulated tumor.

Margins and cut planning

Surgical margins with a 10 mm margin baseline and local reductions to 5 mm for bone preservation considerations were defined by the surgeons. They helped establish baseline parameters for the CAD design (geometrical definition). On each case, a close clinician/engineer collaboration was needed to determine the correct surgical approach and the number of resection planes.

Resection protocol

Three surgeons (two senior specialized surgeons and one junior surgeon) participated in this study. Using our design digital chain, SCGs were produced for the four pelvic tumor resection cases. Iterations were made to test out different positioning features and different resection strategies. In total,



the digital chain was used 12 times on the synthetic pelvis. All resections were carried out on the same day by the same team of surgeons, using the same process. The SCGs were fixed to the synthetic bone with Ø2mm K-Wires.

The resections were carried out with a Stryker™ motor and a $90 \times 13 \times 1.27$ mm oscillating sawblade. A Sawbones model was fixed to a universal Sawbones clamp which can swivel 360° and rotate to any position, vertical or horizontal, aiming to reproduce patient positioning during the conventional surgery. During and after surgery simulation, the clinician was asked to evaluate the quality of the SCG's positioning, as well as its stability.

Qualitative assessment

The evaluation was made based on the subjective feelings of the surgeon: was the correct position of the SCG easy to find and maintain? (Primary positioning: Very easy/Easy/Medium/Hard/Very Hard/Impossible). Was the SCG stable prior to fixation? (Primary stability: Excellent/Good/Medium/Unstable). Was the SCG stable after fixation? (Secondary stability: Excellent/Good/Medium/Unstable). Was the SCG stable during resection? (Stability during the cut: Excellent/Good/Medium/Unstable). Was the resected piece easy to remove? (Extraction of resected piece: Easy/Medium/Complex/Impossible). The presence of bone fractures was also assessed (Yes/No). Finally, on a side note, the damage sustained by the SCG were also evaluated: did the guide sustain significant damage? (Overall integrity: No damage/Non-critical damage/Critical damage) Were there particle deposits due to the sawblade's friction with the SCG? (Particle deposits: No deposits/Small deposits/Significant deposits). The time taken by the surgeon to accomplish the various phases was also measured.

Results

Evaluating digital chain production and assessing duration

The digital chain could be used in every case and produced the expected results. No major glitch in the workflow was experienced, with the main difficulty being local holes in bone shape on the path of the SCG. This happened in two distinct anatomical areas: in the sacroiliac area (sacral foramen) and the ischiopubic ramus (obturator foramen).

The variety of cases made it possible to test SCGs with one–four resection planes. A first fit-test was a simple positioning of the guides on the dry bone around the simulated tumors. This made it possible to test the primary positioning for all 12 iterations. In total, two SCGs presented one resection plane, six SCGs presented two resection planes, two SCGs presented three resection planes, and two SCGs presented four resection planes. SCGs with three resection planes or more were easier to position and to maintain in place before K-Wire

fixation. SCGs with two resection planes were slightly less stable and thus needed good positioning features. SCGs with one resection plane were difficult to position, significantly less stable, and were thus not used for the cutting test. The most convincing version for each SCG was then selected to perform the resection.

Evaluation on a radiopaque synthetic pelvis

Using selected SCGs from the previous experimental step, the four artificial tumors implanted in the radiopaque Sawbones model (Sawbones, Vashon, WA, United States) were successfully resected using the digital chain (Figure 5). No traces of epoxy were found on the resection planes. During and after the simulated surgery, the clinician was asked to evaluate the quality of positioning the SCG, as well as its stability and ergonomics, with mostly very good and excellent results (Table 1).

Installing the SCG took between 60 and 92 s (primary positioning + fixation) (Table 2). The exact surgical margin achieved was not evaluated, but as there was no resin on the Sawbones cut, we can assume that it was at least a “macroscopically complete” resection.

The inclined resection planes proved to be efficient in easing the extraction of the resected piece (the resected piece either fell out directly or took a few seconds to extract (Table 2)). No fracture was observed with the Sawbones specimen piece removal. Finally, the SCGs sustained the cutting efforts with no critical damage. However, some particle deposits were observed, in variable amounts. These deposits were due to the oscillating blade, superficially damaging the cutting guide during the resection. Minor misalignments of the blade on the cutting plane by the operator and vibrations of the blade caused this damage. The damage translated into small particles of PA12 being ripped from the guide and deposited on the cutting site. The amount of PA12 deposited could not be accurately determined as the particles were mixed with Sawbones dust. However, most of the damaged parts remained attached to the guide because of PA12's ductility.

Discussion

The efficiency of 3D-printed surgical cutting guides seems proven in the recent literature (Sallent et al., 2017; Wang et al., 2017; Bosma et al., 2018). However, there is a lack of description of design digital chains for these guides. Maxillofacial reconstruction seems to be the most prominent field for developing SCG design workflows (Numajiri et al., 2018; Ostas et al., 2021), but it remains rare. To the best of our knowledge, such workflows do not exist for pelvic applications in the literature, especially for tumor resection surgeries.

TABLE 1 Evaluation of the four artificial tumor resections.

Criteria	Evaluation modality	Tumor 1 (acetabulum)	Tumor 2 (ischium)	Tumor 3 (iliac crest)	Tumor4 (sacroiliac junction)
Enneking zone	Enneking classification (Enneking et al., 1980)	II	III	I	I + IV
Number of cutting planes	—	3	2	2	4
Epoxy traces on cutting planes?	Yes/no	No	No	No	No
Number of positioning trials	—	1	1	1	2
Primary positioning (without fixation)	Very easy/easy/medium/hard/very hard/impossible	Very easy	Easy	Very easy	Medium
Primary stability (without fixation)	Excellent/good/medium/unstable	Good	Medium	Good	Excellent
Secondary stability (with fixation)	Excellent/good/medium/unstable	Excellent	Excellent	Excellent	Excellent
Stability during the cut	Excellent/good/medium/unstable	Excellent	Excellent	Excellent	Excellent
Extraction of resected piece	Easy/medium/complex/impossible	Easy	Easy	Easy	Medium
Fracture	Yes/no	No	No	No	No
Overall integrity of SCG	No damage/non-critical damage/critical damage	No damage	No damage	No damage	No damage
Particle deposits	No deposits/small deposits/significant deposits	Small deposits	Significant deposits	Small deposits	Significant deposits

The surgeon evaluated the SCG during the resections.

TABLE 2 Duration measurements (seconds) for each phase of use of the SCG.

Time (s)	Tumor 1 (acetabulum)	Tumor 2 (ischium)	Tumor 3 (iliac crest)	Tumor 4 (sacroiliac junction)
Primary positioning (without fixation)	7	6	10	21
Fixation (K-Wire installation)	85	54	60	59
Cut	157	41	68	240
Extraction of resected piece	0 (fall)	0 (fall)	0 (fall)	2
SCG dismounting	23	15	20	24
Total	272	116	158	346

The mention “fall” indicates that the resected piece fell on its own when the surgeon completed the resection.

Literature review concerning pelvic tumor resection SCGs

Different articles making use of pelvic SCGs (Table 3) were analyzed to build the digital chain described in our study in material and methods. The analyzed literature included articles about pelvic tumor resection (with reconstruction or not) that showed images of the SCG. Sawbones, cadaveric, and clinical studies were included. We also included two studies on the cut precision for pelvic osteotomy guides (Sallent et al., 2017; García-Sevilla et al., 2021). These articles did not display a tumor resection situation, with its complexity, but were still valuable for understanding SCG placement on pelvic bones. The examples of SCGs for all four zones of the pelvis (Enneking classification, F. Enneking et al., 1980) were found. A total of 13 publications were identified.

SCG workflow

The complexity of the resection also varied between one and four cutting planes. The analysis was based on workflow explanations in the articles (Wong et al., 2016; García-Sevilla et al., 2021) or visual assessments (Cernat et al., 2016; Jentzsch et al., 2016; Gkagkalis et al., 2021). It showed that the design workflow of SCGs for pelvic tumor resections has rarely been detailed, justifying our methodology-based original article.

SCG designs

Concerning the SCG design, we highlighted high heterogeneity in designs in the literature. Nonetheless, elevated open border guiding appeared to be the most common guiding feature in the batch (6 out of 13). It was not possible to precisely determine the height of the guiding surfaces due to the lack of information in the Materials and methods

TABLE 3 Literature analysis for pelvic tumor resection guide designs.

Author reference	Date	Enneking zone	Number of resection planes per SCG	Detailed design workflow	Design software	Types of blade guiding	General thickness	Positioning method	Fixation method	Additional features	Manufacturing process	Material
M. García-Sevilla et al. (García-Sevilla et al., 2021)	Mar-21	I, III	1	Yes	Meshmixer	Flat open border	1	Negative cortical bone shape + global contact surface widening	Screws		LFS	Dental SG resin
K.-C. Wong et al. (Wong et al., 2016)	Feb-16	I, II	3	Yes	Magics RP (Materialize)	Elevated closed slit	4	Negative cortical bone shape + global contact surface widening + stretched positioners	K-Wires		FDM	ABS
F. Gouin et al. (Gouin et al., 2014)	Jul-14	II, IV	1–4	No	Blender	Elevated open border	1 SCG = 2, 1 SCG = 3, 1 SCG = 5	Negative cortical bone shape + global contact surface widening	K-Wires	Metal sleeves for K-Wires	SLS	PA12
A. Sallent et al. (Sallent et al., 2017)	Oct-17	I, II, III, IV	1–2	No	3Matic (Materialise)	Elevated open border	2	Negative cortical bone shape + global contact surface widening	K-Wires		SLS	PA12
O. Cartiaux et al. (Cartiaux et al., 2014)	Jan-14	I, III	1–2	Yes (rough)	In-house software	Elevated open border	5	Negative cortical bone shape + global contact surface widening	K-Wires		SLS	PA12
K. C. Wong et al. (Wong et al., 2015)	Jan-15	II, III	1–3	Yes	3Matic (Materialise)	Elevated open slit	3	Negative cortical bone shape + global contact surface widening	K-Wires		SLS	PA12
T. Jentzsch et al. (Jentzsch et al., 2016)	Dec-16	I	2	No	CASPA	Elevated open border	5	Negative cortical bone shape + global contact surface widening	Not mentioned or visible		SLS	PA12
R. Evrard et al. (Evrard et al., 2019)	Jun-19	I, II, IV	1	Yes (rough)	Outsourced to 3D-Side, Leuven, Belgium	Elevated open border	2	Negative cortical bone shape + local contact surface widening + stretched positioners	K-Wires		SLS	PA12
G. Gkagkalis et al. (Gkagkalis et al., 2021)	Apr-21	II, III	1–2	No	Outsourced to Materialise	Elevated closed slit	3	Negative cortical bone shape + global contact surface widening	K-Wires		Unknown	Unknown
M. A. Siegel et al. (Siegel et al., 2020)	Nov-20	IV	3	No	Outsourced to BodyCad, Montreal, Canada	Elevated closed slit	3	Negative cortical bone shape + local contact surface widening	Unknown	Series of drill guides	SLS	PA12
E. Cernat et al. (Cernat et al., 2016)	Oct-16	I, IV	2–4	No	Unknown	Elevated open border	3	Negative cortical bone shape + local contact surface widening	K-Wires		SLS	PA12
		I	2	No	Unknown		1		K-Wires		Unknown	Unknown

(Continued on following page)

TABLE 3 (Continued) Literature analysis for pelvic tumor resection guide designs.

Author reference	Date	Enneking zone	Number of resection planes per SCG	Detailed design workflow	Design software	Types of blade guiding	General thickness	Positioning method	Fixation method	Additional features	Manufacturing process	Material
B. Wang et al. (Wang et al., 2017)	Mar-18					Flat open border		Negative cortical bone shape + global contact surface widening + stretched positioners				
X. Fang et al. (Fang et al., 2018)	Dec-18	I, II, III, IV	2	No	Creo 2.0 (PTC, Needham, MA, United States)	Elevated open border	3	Negative cortical bone shape	K-Wires		Unknown	Unknown
Z. Yu et al. (Yu et al., 2021)	Apr-21	I, IV	2	No	Creo 2.0 (PTC, Needham, MA, United States)	Elevated closed slit		Negative cortical bone shape + local contact surface widening	K-Wires	Fixation on both sides of cutting planes	Unknown	Unknown

The information is based on article contents. The general thickness was estimated visually (1 = very thin/2 = thin/3 = medium/4 = thick/5 = very thick). The main positioning features were also considered. The negative cortical bone shape feature was common to every guide. 10 guides used global contact surface widening (wide guides). Three guides used local widening (thin guides overall with wider local features). Three guides additionally used stretched positioners (features distant from the resection planes, supposedly to stabilize the guide and use specific bone landmarks). Most guides used K-Wire fixation and SLS additive manufacturing in PA12 material. FDM, Fused deposition modelling; SLS, selective laser sintering; and LFS, low-force stereolithography.

sections in these publications. The more recent studies display thinner cutting guides. The baseline feature for positioning was always that the SCG was designed as a negative shape of the cortical bone. However, the evaluation of the design of the contact surface was also made: in most cases (10 out of 13), the contact surface was globally wide, along the entire length of the guide. This observation was also made by García-Sevilla et al. (García-Sevilla et al., 2021). Two examples showed very thin guides with widening in local areas. Three cases showed SCGs with additional stretched positioners. These features provide an additional contact area far from the cutting planes. In 10 out of 13 cases, fixation was made with the Kirschner wires (K-Wires). Finally, eight out of 13 SCG examples used selective laser sintering (SLS) with nylon (PA12) for the manufacturing process.

Evaluating digital chain production

3D processing steps

DICOM processing phase

For the DICOM processing phase, the 3D Slicer (Fedorov et al., 2012) was selected. As it is open-source and customizable, an in-house Slicelet (3D Slicer module) that translated the DICOM processing part of the digital chain was built. To develop this part, we chose CT and MRI as the main image modalities. In the orthopedic field, CT is the gold standard for bone tissue segmentation. In the oncologic field, MRI is preferred for tumor segmentation. From these gold standards, our approach was to propose multimodal segmentation. 3D bone tissue models are reconstructed using CT images, and tumor models are reconstructed using MRI images. CT images are usually naturally suited for segmentation (high resolution, low slice thickness, and good bone contrast). The range for MRI settings is wider. T1 sequences using gadolinium as the contrast agent were the most efficient for highlighting the tumor well. The slice thickness should be between 1 and 2 mm for easier registration and semi-automatic segmentation. Using thicker MRI (4- or 5-mm slice thickness) is also possible, but less adapted to semi-automatic segmentation methods. The multimodal registration was performed using B-Spline registration. We found Elastix to be the best performing automatic registration module in 3D Slicer (Figure 1A) (Klein et al., 2010) for pelvic images and chose to use it in the study. We also found the Watershed method to be an excellent segmentation method for this digital chain: the manual part (initialization) was fast and simple and did not require high user accuracy. The calculation then expanded the initialized segments automatically, creating plain and smooth 3D models, natively suited to CAD processing (Figure 1B). The major downside of the Watershed model was the intensive calculation. We also noted that Watershed performed poorly on hollow structures, such as the skull or structures with numerous small details/ramifications, such as the brain's grey matter or small vascularization. It produced very good performances on blocky

or clearly defined features, such as pelvic bones on CT or tumors on MRI. It could also efficiently segment the main vascularization system (aorta, major arteries, and veins) if a contrast agent was used in the CT or MRI acquisition. The efficiency of Watershed segmentation has been shown in the literature for automatic and semi-automatic segmentation processes. It is said to perform adequate segmentation while saving time (Fan et al., 2019). The segmentation process could be improved by automating the initialization part. A hybrid thresholding approach is presented by Kim et al. (Kim et al., 2018) for an acetabulum automated segmentation process.

STL processing phase

For STL processing, MeshLab (Cignoni et al., 2008) was used for its easily accessible remeshing functions (Figure 2). STL files exported from 3D Slicer were in general very heavy. This was due to the extra fine default settings used by 3D Slicer on complex models. Such heavy meshes are translated into computational stress on the CAD software. The process is fully automatable, providing fixed size requirements for the STL (target number of faces or file weight for example) (Figure 2).

CAD processing phase

For the CAD phase, Siemens NX (Siemens PLM, Plano, TX, United States) was used. The lattice structure generation capabilities of the software were also considered very profitable, especially from the perspective of integrating a reconstruction phase into the digital chain. During this study, an engineer performed the geometrical definition with the information provided by surgeons. However, the goal in this digital chain would be to have the geometrical definition performed directly by clinicians to obtain optimal translation of surgical planning in the CAD 3D space. This phase aims at translating surgical constraints and objectives into geometrical objects. These objects are then used as references to generate solid bodies. The essential surgical parameters, such as the surgical margins, were defined with an orthopedic surgeon and included the blade thickness (10 mm margin + 2 mm thick blade). An interactive planning between the engineer and surgeon is mandatory not only for the surgical margins but also for cutting plane choices and K-Wire localization to avoid hurting noble anatomical structures with the saw or pins (vessels, nerves, bowels, and bladder).

SCG generation

The steps for generating SCG were performed manually by an engineer following a systematic method. However, provided there is development of an in-house platform, most of the steps could be automated.

SCG design choices

Most design choices were based on the analysis of the literature: the main body was made as a cylindrical 3D sweep to ensure continuous contact with the cortical bone in all

situations. An extrusion-based design (Wong et al., 2016) can be an efficient technique, but we found that high topological variations and resection complexity are detrimental to the repeatability of this method. We also acknowledged that most cutting guides are designed with a wide contact surface on the whole cutting length (Cartiaux et al., 2014; Gouin et al., 2014; Wong et al., 2015; Jentzsch et al., 2016; Sallent et al., 2017). However, to avoid additional trauma, we chose to design thin guides. For this reason, the main body of the SCG is only up to 8 mm wide (half of the cylindrical sweep diameter). Nevertheless, the main body alone was not enough to correctly position the SCG. Therefore, added positioning features were added that were similar to what Siegel et al. (2020), Evrard et al. (2019), and Cernat et al. (2016) recommended. These positioning features were added preferably in accessible areas of the bone to limit additional dissection, and their width can be limited to a maximum defined by the surgeon. The deformable clips are a test feature aimed at improving the first positioning of the guide and stabilizing it before K-Wire fixation. The 5 mm thick bridge is easily deformable to pinch the bone's edge and maintain the guide. It is unclear if this feature would be beneficial in actual surgery. The 15 mm guiding height was decided in collaboration with the experienced surgeons. We also confirmed it visually in the literature, as Sallent et al. used a height of 20 mm, although in other cases the guiding height is rarely specified. The 7 mm thickness was also a parameter defined by surgeons to avoid unnecessary dissection while withstanding the effort and oscillations of the blade. On this specific thickness point, the literature identifies two global conceptions: wide thickness SCGs and thinner ones.

We also added corner clearances that prevent the blade from damaging the guide at the intersections of resection planes, as described in the literature (Gouin et al., 2014). We found it impractical to implement a physical limitation on the depth of the blade. Displaying depth information to help the surgeon seemed a better option. Nonetheless, any extensive dissection toward noble structures (nerve roots and iliac vessels) was avoided. The blade and pin axes were also designed to avoid these critical anatomical areas if the tumor resection strategy did not plan for their resection.

SCG production

For additive manufacturing, SLS printing with PA12 is a certified process and material in the medical field. SLS is a powder-based additive manufacturing technology. It makes it possible to print complex objects in a powder volume. The powder is sintered layer by layer using a laser. This technology supports various materials from polymers (PA12 and TPE) to metals (steel and titanium). In this study, we chose polymer SLS printing for its ability to print complex free-form objects without using a support material (unlike fused deposition modeling (FDM)). It produced accurate printing of the SCGs. It is also the most popular choice in pelvic resection

guides in the literature (Cartiaux et al., 2014; Gouin et al., 2014; Wong et al., 2015; Jentzsch et al., 2016; Sallent et al., 2017; Evrard et al., 2019; Siegel et al., 2020). PA12 was the material selected for this study. It is a common material that is easy to work with in SLS printing, and its manufacturing parameters are perfectly well-known for the Sinterit Lisa machine. It is also biocompatible and suited to AutoClave sterilization. PA12 was thus indicated to produce the SCGs used in this study. SLA printing with Dental SG resin (or a similar material) could also be a viable option, as shown by García-Sevilla et al. (2021).

SCG and duration assessment

Using our semi-automated method, the digital chain succeeded in producing one SCG in less than 20 h, without taking into account the duration of the CT imaging procedure for the pelvic Sawbones. The longest step in the process was the printing of the SCG itself (11 h for one SCG), making printing batches for multiple SCGs might critically reduce the duration of this step (46 h for seven SCG). It should be noted that automating several CAD steps (which were designed to ultimately be automated) will reduce the duration of the SCG design in the near future.

The 20-h process, we report, to produce a single SCG does not take into account all the waiting time between each step, which may have biased our result. Moreover, discussion between the clinician and conception team might slow down the process. It is mandatory that feedback be obtained quickly from the surgeons and engineers to reduce the duration of the SCG process. This might be of major importance in an acute emergency oncological context and in trauma case situations, which might become an ongoing field for patient-specific tools in a reconstructive context.

Nonetheless, our results seem critical as most production times in the literature are of more than 2 weeks (Rustemeyer, 2014; Martelli et al., 2016). We believe that the semi-automated methodology we describe here could reduce production times for the patient-specific SCG instruments.

Evaluating a radiopaque synthetic pelvis

The surgically simulated evaluation with experienced bone tumor surgeons highlights good ergonomics and repeatability on Sawbones models. Interestingly, the easier-to-fit SCG were those with more than two planes in our experiment. The one-plane SCGs were rapidly left aside due to a lack of initial stability, meaning that this one-plane design might need complementary cross-sectional supports, if mandatory. An overall ergonomic assessment by surgeons was very good and excellent for most parameters. No resection piece fracture was identified, and nor was there any critical damage to the SCGs. These results transposed to human cases are nonetheless very debatable, due to the easy access of the

Sawbones on a clamp, and to the lack of any soft tissue that might complicate exposure and SCG placement. Nonetheless, the aim of this study with this Sawbones evaluation remains a qualitative assessment, and at this point, the results seem positive, with fast and easy use of the generated SCGs. The four artificial tumors were successfully resected from the Sawbones model using this digital chain. This provided the first confirmation of the usability of the SCGs generated, as they showed repeatable results both in terms of their designs and their performance.

Limits and strengths

In this preliminary methodological original publication, we do not assess margin quality with precise CT measurements. Nonetheless, no traces of epoxy were found on the cut evaluations, and we can consider this to be a “macroscopically complete” resection. This work mainly focused on the SCG design, a description of digital chain production, and quality assessment with qualitative and ergonomic data. The surgeon’s qualitative analysis of the SCG’s strength during its use seemed satisfying, but no quantitative force analysis has been performed. Such analysis would require the evaluation of the effort applied by the operator on the SCG with the oscillating saw, and specific methodology on this point might be developed for better assessing the SCG strength. Given that this is an experimental pilot study to validate our digital chain, no statistical analysis was performed.

Further study with greater sample size and quantitative assessment is needed to compare the design impact on scheduled margins and to validate this pilot study. This next step experiment will focus on Sawbones models and anatomical subjects, in order to take into account the importance of “real surgery” situations, such as patient soft tissue with surgical exposure difficulties and more constraints against the SCG. We may assume that with anatomical subjects, resection times might be much longer than the one we identified in our Sawbones qualitative assessment, with more pitfalls. Extending the images used in our digital chain to 3DMMI (3D multimodality image) that include CTA (CT angiography) and MRN (Magnetic Resonance Neurography) would be valuable to include the tumor adjacent noble vital structures in the surgical planning phase 3D models. (Fang et al., 2018; Yu et al., 2021).

Finally, our multimodal workflow brings new insight. If there are publications focusing on combined MRI and CT use for SCG design purposes (Table 3), to the best of our knowledge, documented and repeatable pipeline designs have not been fully documented, especially for pelvic resections.

Conclusion

In this study, we developed an original and fully detailed new design digital chain for pelvic tumor resection surgical guides.

The digital chain covers multimodal DICOM segmentation, STL processing, CAD design, and additive manufacturing. It was developed in an in-depth surgical collaboration context. This digital chain could be adapted to different clinical specialties and extended to additional applications outside the bone tumor field.

SCG production was considered successful on Sawbones experiments, and its surgical simulation was satisfactory in terms of ergonomics. Four artificial tumors were successfully resected from a Sawbones model using the digital chain. The design and production delays were also satisfying. The multimodal workflow could have been validated through this experimental study. Cadaveric and clinical case studies are scheduled to confirm these results with a quantitative assessment of various SCG designs.

Data availability statement

The raw data supporting the conclusions of this article will be made available by the authors, without undue reservation.

Author contributions

Conceptualization: VC and LV; methodology: LV; software: VB; validation: VC, LV, and J-YH; formal analysis: VB and HF; investigation: VB and HF; data curation: VB and HF;

References

- Abou-ElFetouh, A., Barakat, A., and Abdel-Ghany, K. (2011). Computer-guided rapid-prototyped templates for segmental mandibular osteotomies: A preliminary report: Computer-guided rapid-prototyped templates for segmental mandibular osteotomies. *Int. J. Med. Robot. Comput. Assist. Surg.* 7, 187–192. doi:10.1002/rcs.387
- Bosma, S. E., Wong, K. C., Paul, L., Gerbers, J. G., and Jutte, P. C. (2018). A cadaveric comparative study on the surgical accuracy of freehand, computer navigation, and patient-specific instruments in joint-preserving bone tumor resections. *Sarcoma* 2018, 1–9. doi:10.1155/2018/4065846
- Cartiaux, O., Paul, L., Francq, B. G., Banse, X., and Docquier, P.-L. (2014). Improved accuracy with 3D planning and patient-specific instruments during simulated pelvic bone tumor surgery. *Ann. Biomed. Eng.* 42, 205–213. doi:10.1007/s10439-013-0890-7
- Cernat, E., Docquier, P.-L., Paul, L., Banse, X., and Codorean, I.-B. (2016). Patient specific instruments for complex tumor resection-reconstruction surgery within the pelvis: A series of 4 cases. *Chir.* 111, 439. doi:10.21614/chirurgia.111.5.439
- Chen, X., Xu, L., Yang, Y., and Egger, J. (2016). A semi-automatic computer-aided method for surgical template design. *Sci. Rep.* 4 (6), 20280. doi:10.1038/srep20280
- Cignoni, P., Callieri, M., Corsini, M., Dellepiane, M., Ganovelli, F., and Ranzuglia, G. (2008). MeshLab: An open-source mesh processing tool. *Computing* 1, 129–136. doi:10.2312/LocalChapterEvents/ItalChap/ItalianChapConf2008/129-136
- Enneking, W. F., Spanier, S. S., and Goodman, M. A. (1980). A system for the surgical staging of musculoskeletal sarcoma. *Clin. Orthop. Relat. Res.* 153, 106–120. doi:10.1097/00003086-198011000-00013
- Evrard, R., Schubert, T., Paul, L., and Docquier, P.-L. (2019). Resection margins obtained with patient-specific instruments for resecting primary pelvic bone sarcomas: A case-control study. *Orthop. Traumatology Surg. Res.* 105, 781–787. doi:10.1016/j.otsr.2018.12.016
- Fan, Y., Beare, R., Matthews, H., Schneider, P., Kilpatrick, N., Clement, J., et al. (2019). Marker-based watershed transform method for fully automatic mandibular

writing—original draft preparation: VB and LV; writing—review and editing: VC and J-YH; and visualization and supervision: VC and LV.

Conflict of interest

The authors declare that the research was conducted in the absence of any commercial or financial relationships that could be construed as a potential conflict of interest.

Publisher's note

All claims expressed in this article are solely those of the authors and do not necessarily represent those of their affiliated organizations, or those of the publisher, the editors, and the reviewers. Any product that may be evaluated in this article, or claim that may be made by its manufacturer, is not guaranteed or endorsed by the publisher.

Supplementary material

The Supplementary Material for this article can be found online at: <https://www.frontiersin.org/articles/10.3389/fbioe.2022.991676/full#supplementary-material>

segmentation from CBCT images. *Dentomaxillofacial Radiol.* 48, 20180261. doi:10.1259/dmfr.20180261

Fang, X., Yu, Z., Xiong, Y., Yuan, F., Liu, H., Wu, F., et al. (2018). Improved virtual surgical planning with 3D- multimodality image for malignant giant pelvic tumors. *Cancer Manag. Res.* 7 (10), 6769–6777. doi:10.2147/CMAR.S185737

Fedorov, A., Beichel, R., Kalpathy-Cramer, J., Finet, J., Fillion-Robin, J.-C., Pujol, S., et al. (2012). 3D slicer as an image computing platform for the quantitative imaging network. *Magn. Reson. Imaging* 30, 1323–1341. doi:10.1016/j.mri.2012.05.001

García-Sevilla, M., Mediavilla-Santos, L., Ruiz-Alba, M. T., Pérez-Mañanes, R., Calvo-Haro, J. A., and Pascau, J. (2021). Patient-specific desktop 3D-printed guides for pelvic tumour resection surgery: A precision study on cadavers. *Int. J. Comput. Assist. Radiol. Surg.* 16, 397–406. doi:10.1007/s11548-021-02322-3

Gkagkalis, G., Moerenhout, K., Rüdiger, H. A., Müller, D. A., Letovanec, I., and Cherix, S. (2021). Pelvic chondrosarcoma treated by *en bloc* resection with patient-specific osteotomy guides and reimplantation of the extracorporeally irradiated bone as an osseocartilaginous structural orthotopic autograft: A report of two cases with description of the surgical technique. *Case Rep. Orthop.* 2021, 1–9. doi:10.1155/2021/5512143

Gouin, F., Paul, L., Odri, G. A., and Cartiaux, O. (2014). Computer-assisted planning and patient-specific instruments for bone tumor resection within the pelvis: A series of 11 patients. *Sarcoma* 2014, 1–9. doi:10.1155/2014/842709

Greenberg, S., Buchbinder, D., Turner, M. D., Dhillon, P., and Afshar, A. A. (2021). Three-Dimensional repositioning of the maxilla in orthognathic surgery using patient-specific titanium plates: A case series. *J. Oral Maxillofac. Surg.* 79, 902–913. doi:10.1016/j.joms.2020.11.031

Jentsch, T., Vlachopoulos, L., Fürnstahl, P., Müller, D. A., and Fuchs, B. (2016). Tumor resection at the pelvis using three-dimensional planning and patient-specific instruments: A case series. *World J. Surg. Oncol.* 14, 249. doi:10.1186/s12957-016-1006-2

- Kim, J. J., Nam, J., and Jang, I. G. (2018). Fully automated segmentation of a hip joint using the patient-specific optimal thresholding and watershed algorithm. *Comput. Methods Programs Biomed.* 154, 161–171. doi:10.1016/j.cmpb.2017.11.007
- Klein, S., Staring, M., Murphy, K., Viergever, M. A., and Pluim, J. P. W. (2010). Elastix: A toolbox for intensity-based medical image registration. *IEEE Trans. Med. Imaging* 29, 196–205. doi:10.1109/TMI.2009.2035616
- Krishnan, S. P., Dawood, A., Richards, R., Henckel, J., and Hart, A. J. (2012). A review of rapid prototyped surgical guides for patient-specific total knee replacement. *J. Bone Jt. Surg.* 94, 1457–1461. doi:10.1302/0301-620X.94B11.29350
- Martelli, N., Serrano, C., Pineau, J., Prognon, P., Borget, I., Batti, S. E., et al. (2016). Advantages and disadvantages of 3-dimensional printing in surgery: A systematic review. *Surgery* 159, 1485–1500. doi:10.1016/j.surg.2015.12.017
- Mazzoni, S., Bianchi, A., Schiariti, G., Badiali, G., and Marchetti, C. (2015). Computer-aided design and computer-aided manufacturing cutting guides and customized titanium plates are useful in upper maxilla waferless repositioning. *J. Oral Maxillofac. Surg.* 73, 701–707. doi:10.1016/j.joms.2014.10.028
- Numajiri, T., Morita, D., Nakamura, H., Yamochi, R., Tsujiko, S., and Sowa, Y. (2018). Designing CAD/CAM surgical guides for maxillary reconstruction using an in-house approach. *J. Vis. Exp.* 138, 58015. doi:10.3791/58015
- Ostas, D., Hedesiu, M., Roman, C. R., Cosma, C., Ciurea, M., and Rotaru, H. (2021). Design workflow for mandibular reconstruction. Opportunities and limitations of in-house virtual surgical planning. *J. Med. Biol. Eng.* 41, 482–493. doi:10.1007/s40846-021-00633-z
- Popescu, D. (2014). *Workflow for additive manufacturing of an individualized surgical template*. Bucharest, Romania: Proceedings in Manufacturing systems, 10–11. ISSN 2067-9238.
- Rauch, M., Hascoët, J. Y., and Vidal, L. (2021). *Additive manufacturing challenges and opportunities: From naval and aeronautics parts to biomufacturing applications*. Frankfurt, Germany: 3dPrintech Int Conf.
- Rustemeyer, J., Melenberg, A., and Sari-Rieger, A. (2014). Costs incurred by applying computer-aided design/computer-aided manufacturing techniques for the reconstruction of maxillofacial defects. *J. Cranio-Maxillofacial Surg.* 8, 2049–2055. doi:10.1016/j.jcms.2014.09.014
- Sallent, A., Vicente, M., Reverté, M. M., Lopez, A., Rodríguez-Baeza, A., Pérez-Domínguez, M., et al. (2017). How 3D patient-specific instruments improve accuracy of pelvic bone tumour resection in a cadaveric study. *Bone Jt. Res.* 6, 577–583. doi:10.1302/2046-3758.610.BJR-2017-0094.R1
- Scolozzi, P. (2015). Computer-aided design and computer-aided modeling (CAD/CAM) generated surgical splints, cutting guides and custom-made implants: Which indications in orthognathic surgery? *Revue de Stomatologie de Chir. Maxillo-faciale de Chir. Orale* 116, 343–349. doi:10.1016/j.revsto.2015.09.005
- Siegel, M. A., Balach, T., Sweeney, K. R., Nystrom, L. M., and Colman, M. W. (2020). Sacroiliac joint cut accuracy: Comparing new technologies in an idealized sawbones model. *J. Surg. Oncol.* 122, 1218–1225. doi:10.1002/jso.26124
- Vidal, L., Crenn, V., and Hascoët, J. Y. (2022). *The digital chain in orthopedic surgery: From CT and MRI data to 3D printing and digital twins*. Nantes, France: Journée Sante Du Futur Conf. Agence Régionale de Santé.
- Vidal, L., Kampleitner, C., Brennan, M. Á., Hoornaert, A., and Layrolle, P. (2020a). Reconstruction of large skeletal defects: Current clinical therapeutic strategies and future directions using 3D printing. *Front. Bioeng. Biotechnol.* 12 (8), 61. doi:10.3389/fbioe.2020.00061
- Vidal, L., Kampleitner, C., Krissian, S., Brennan, M. Á., Hoffmann, O., Raymond, Y., et al. (2020b). Regeneration of segmental defects in metatarsus of sheep with vascularized and customized 3D-printed calcium phosphate scaffolds. *Sci. Rep.* 10 (1), 7068. doi:10.1038/s41598-020-63742-w
- Wang, F., Zhu, J., Peng, X., and Su, J. (2017). The application of 3D printed surgical guides in resection and reconstruction of malignant bone tumor. *Oncol. Lett.* 14, 4581–4584. doi:10.3892/ol.2017.6749
- Wong, K.-C., Sze, K.-Y., Wong, I. O.-L., Wong, C.-M., and Kumta, S.-M. (2016). Patient-specific instrument can achieve same accuracy with less resection time than navigation assistance in periacetabular pelvic tumor surgery: A cadaveric study. *Int. J. Comput. Assist. Radiol. Surg.* 11, 307–316. doi:10.1007/s11548-015-1250-x
- Wong, K. C. (2016). 3D-printed patient-specific applications in orthopedics. *Orthop. Res. Rev.* 8, 57–66. doi:10.2147/ORR.S99614
- Wong, K. C., Kumta, S. M., Geel, N. V., and Demol, J. (2015). One-step reconstruction with a 3D-printed, biomechanically evaluated custom implant after complex pelvic tumor resection. *Comput. Aided Surg.* 20, 14–23. doi:10.3109/10929088.2015.1076039
- Yu, Z., Zhang, W., Fang, X., Tu, C., and Duan, H. (2021). Pelvic reconstruction with a novel three-dimensional-printed, multimodality imaging based endoprosthesis following enneking type I + IV resection. *Front. Oncol.* 11, 629582. doi:10.3389/fonc.2021.629582



OPEN ACCESS

EDITED BY

Changhui Song,
South China University of Technology,
China

REVIEWED BY

Feifei Pu,
Wuhan Hospital of Traditional Chinese
and Western Medicine, China
Yong Lu,
Ruijin Hospital, School of Medicine,
Shanghai Jiao Tong University, China

*CORRESPONDENCE

Hong Duan,
duanhong1970@126.com
Wenli Zhang,
zwlbox@163.com

[†]These authors contributed equally to
this work and share first authorship

SPECIALTY SECTION

This article was submitted to
Biomaterials,
a section of the journal
Frontiers in Bioengineering and
Biotechnology

RECEIVED 16 July 2022

ACCEPTED 07 September 2022

PUBLISHED 21 September 2022

CITATION

Yuan D, Fang X, Lei S, Banskota N,
Kuang F, Gou Y, Zhang W and Duan H
(2022), Case Report: Three-dimensional
printed prosthesis reconstruction for
patello-femoral large osteochondral
defects in a patient with distal femoral
giant cell tumour: A case report.
Front. Bioeng. Biotechnol. 10:995879.
doi: 10.3389/fbioe.2022.995879

COPYRIGHT

© 2022 Yuan, Fang, Lei, Banskota,
Kuang, Gou, Zhang and Duan. This is an
open-access article distributed under
the terms of the [Creative Commons
Attribution License \(CC BY\)](#). The use,
distribution or reproduction in other
forums is permitted, provided the
original author(s) and the copyright
owner(s) are credited and that the
original publication in this journal is
cited, in accordance with accepted
academic practice. No use, distribution
or reproduction is permitted which does
not comply with these terms.

Case Report: Three-dimensional printed prosthesis reconstruction for patello-femoral large osteochondral defects in a patient with distal femoral giant cell tumour: A case report

Dechao Yuan^{1†}, Xiang Fang^{1†}, Senlin Lei¹, Nishant Banskota¹,
Fuguo Kuang², Yawei Gou², Wenli Zhang^{1*} and Hong Duan^{1*}

¹Department of Orthopedics, West China School of Medicine/West China Hospital, Sichuan University, Chengdu, China, ²Department of Orthopedics, People's Fourth Hospital of Sichuan Province, Chengdu, China

Background: The restoration and reconstruction of patello-femoral large osteochondral defects caused by bone tumours are challenging because of the local recurrence rate and the joint's mechanical complexity. Although three-dimensional (3D)-printed prostheses are commonly adopted for tumour-induced bone defect reconstruction, patello-femoral osteochondral reconstruction with 3D-printed prostheses is rarely reported.

Case presentation: A 44-year-old female patient with progressive swelling and pain in the left knee for 6 months was diagnosed with Campanacci Grade II giant cell tumour (GCT). She underwent intralesional curettage combined with autografting and internal fixation, after which complications of deep infection arose. The patient then underwent internal fixation removal and cement packing. Afterwards, the pain of the affected knee persisted for 11 months, and bone cement removal plus 3D-printed modular prosthesis reconstruction was performed. At the last follow-up 27 months after surgery, she was pain free, the Musculoskeletal Tumour Society (MSTS) score improved from 15/30 to 29/30, the Visual Analogue Scale (VAS) score decreased from 7 to 0, and knee flexion increased from 50° to 130°. X-ray images 22 months after surgery showed that the prosthesis and screws were in a stable position, and callus formation was found at the prosthesis-bone interface.

Conclusions: A 3D-printed modular prosthesis may be a useful treatment option for the surgical reconstruction of GCT-induced patello-femoral large osteochondral defects. The firm fixation, osseointegration, and favourable

Abbreviations: GCT, Giant cell tumour; CT, Computed tomography; 3D, Three-dimensional; VAS, Visual Analogue Scale; ROM, Range of Motion; MSTS, Musculoskeletal Tumour Society.

congruency of the 3D-printed prosthesis with the adjacent articular surface can achieve long-term knee function and stability.

KEYWORDS

patello-femoral, three-dimensional printed prosthesis, osteochondral reconstruction, osteochondral defects, distal femoral, giant cell tumour

Background

Giant cell tumour (GCT) is an intermediate (locally aggressive), rarely metastasising bone tumour, accounting for 5% of all primary bone neoplasms (Palmerini et al., 2019). Surgery is the main treatment option for GCT, including intralesional curettage with various reconstruction methods and wide resection when the tumour destroys the bone structure extensively (Teng et al., 2019; Ippolito et al., 2020). It is challenging to restore and reconstruct patello-femoral large osteochondral defects caused by bone tumours because of the local recurrence rate and functional mechanical reconstruction (Wu et al., 2018; Andrade et al., 2019). Synthetic biphasic scaffold

plugs, fresh osteochondral allografts, and osteochondral autograft transfer are suited more for treating focal osteochondral defects than large osteochondral defects of the patello-femoral joint (Degen et al., 2017; Lattermann et al., 2018). Considering the large trauma, many complications, and difficult revision, patello-femoral arthroplasty or total knee arthroplasty should be used cautiously to reconstruct large osteochondral defects of the patello-femoral joint (Beard et al., 2020). Although three-dimensional (3D) printed prostheses with titanium alloy are commonly adopted for tumour-induced bone defect reconstruction (Fang et al., 2018; Yu et al., 2021), patello-femoral osteochondral reconstruction with 3D-printed prostheses is rarely reported. Our team recently encountered a

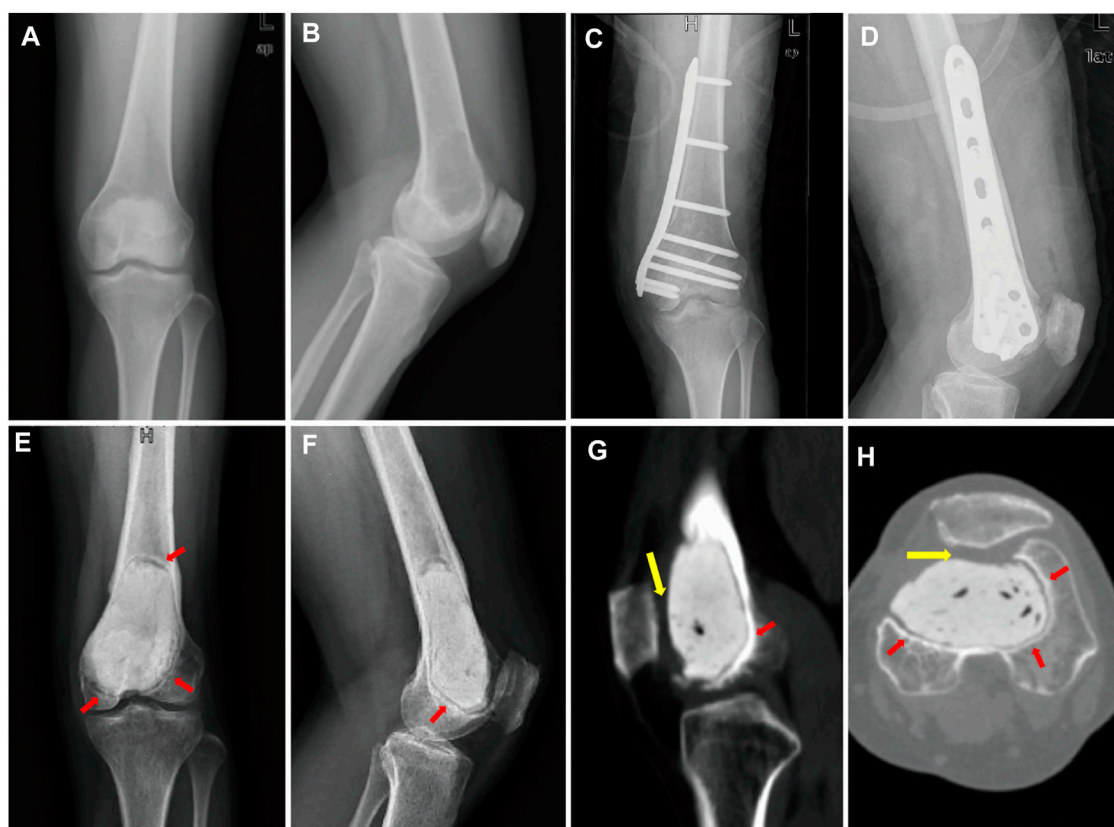


FIGURE 1

(A) Anterior–posterior and (B) lateral X-ray images show a large radiolucent area in the epiphyseal part of the left distal femur. (C) Anterior–posterior and (D) lateral X-ray images after intralesional curettage combined autografting and internal fixation. (E) Anterior–posterior and (F) lateral X-ray images. (G) sagittal and (H) transverse planes on CT images after cement packing at 11 months. Sclerotic rim occurs around cement (red arrow). (G,H) Distal femur articular cartilage defects mainly lie in the patello-femoral joint (yellow arrow).

case of a patient with a distal femoral GCT treated with intralesional curettage followed by a deep infection complication. Wound debridement was then performed, which resulted in patello-femoral large cartilage defects. The patient achieved a poor functional outcome with knee pain due to patello-femoral large cartilage defects, and we performed osteochondral reconstruction with a novel 3D-printed modular prosthesis that has never been reported.

Case presentation

History

A 44-year-old female patient with progressive swelling and pain in the left knee for 4 months was admitted to West China Hospital in July 2018. X-ray images showed a large radiolucent area of bone caused by osteolytic deconstruction in the epiphyseal part of the left distal femur (Figures 1A,B). Computed tomography (CT), magnetic resonance imaging, emission computed tomography, and pathological biopsy were performed, and the patient was diagnosed with Campanacci Grade II GCT. In August 2018, the patient underwent intralesional curettage combined with autografting and internal fixation (Figures 1C,D). There were complications of deep infection 7 days after surgery and wound dressing change, and intravenous antibiotics were ineffective. Then, wound debridement and removal of internal fixation were performed. After the infection was controlled, the patient underwent cement packing. Afterwards, the pain persisted in the affected knee for 11 months (Figures 1E–H), and bone cement removal plus 3D-printed modular prosthesis reconstruction for patello-femoral large osteochondral defects was performed at our hospital on 15 August 2019. Pain and knee joint function were evaluated according to the Visual Analogue Scale (VAS), Range of Motion (ROM), and Musculoskeletal Tumour Society (MSTS) scores. The VAS and MSTS scores were 7 and 15/30, respectively, before surgery. Knee flexion was 50°, and knee extension was normal before surgery.

Design and manufacture of the prosthesis

The 3D-printed modular prosthesis consisting of front and back modular components was designed according to the bone and patello-femoral cartilage defects. The front modular component of the prosthesis was made of titanium alloy for articulation with the patella. The back components, consisting of two parts for bone support, had four screw holes in three directions, including two horizontal screws for bicortical fixation and two bilateral screws for internal and lateral condylar cancellous bone fixation. The back components were designed to be porous with an average porosity of 50%–80% and

a pore diameter of 400–500 µm for bone ingrowth. The front and back components were combined using a press-fit structure (Figure 2). The prosthesis was made of Ti-6Al-4V with good biocompatibility and osseointegration (Wang et al., 2019; Yu et al., 2020). The prosthesis was designed using the Mimics software (version 20.0; Materialise Corp. Belgium) and manufactured by Chun Li Co., (Beijing, People's Republic of China) using a 3D printing technique. A model of the prosthesis was printed and tested before the final production to verify our plan (Figure 3). It took approximately 2 weeks from the time patient data were collected until the prosthesis was printed out.

Surgical procedure

Surgery was performed using an anteromedial approach under general anaesthesia. After bone cement removal, the bony cortex around the tumour 1–2 mm was excised using a circular 3D-printed guided plate (Figure 4A). The tumour cavity was then cauterised with an electric knife, expanded with a high-speed burr, and irrigated with anhydrous alcohol and distilled water. The back components were inserted into the cavity and fixed to the surrounding bone with four screws (Figure 4B). Autogenous iliac bone was inserted into the gap between the prosthesis and the adjacent bone to facilitate bone ingrowth. The front modular component was firmly fixed on the back components through a press-fit structure (Figure 4C). The surgery took 325 min, the intraoperative blood loss was 400 ml, and postoperative X-ray images showed that the implant was in a good position (Figures 5A,B).

Postoperative management

The patient started passive functional knee exercises on postoperative day 2, active exercise on postoperative day 7, partial weight-bearing exercises with crutches on postoperative day 30, and full weight-bearing exercises gradually. We followed up with the patient every month for the first 3 months, every 3 months for the first year, and every 6 months thereafter. Clinical outcomes and imaging findings were evaluated at each follow-up visit.

Follow-up

At the last follow-up visit 27 months after surgery, the patient was pain free with full weight-bearing (Video 1). The MSTS score was 29/30, and the VAS score was 0. Knee flexion was 130°, which was better than the initial 88° after surgery for 2 months (Figure 5), and knee extension was normal after surgery. There was no local rejection, indicating good biocompatibility and security of the prosthesis. The X-ray images showed that the

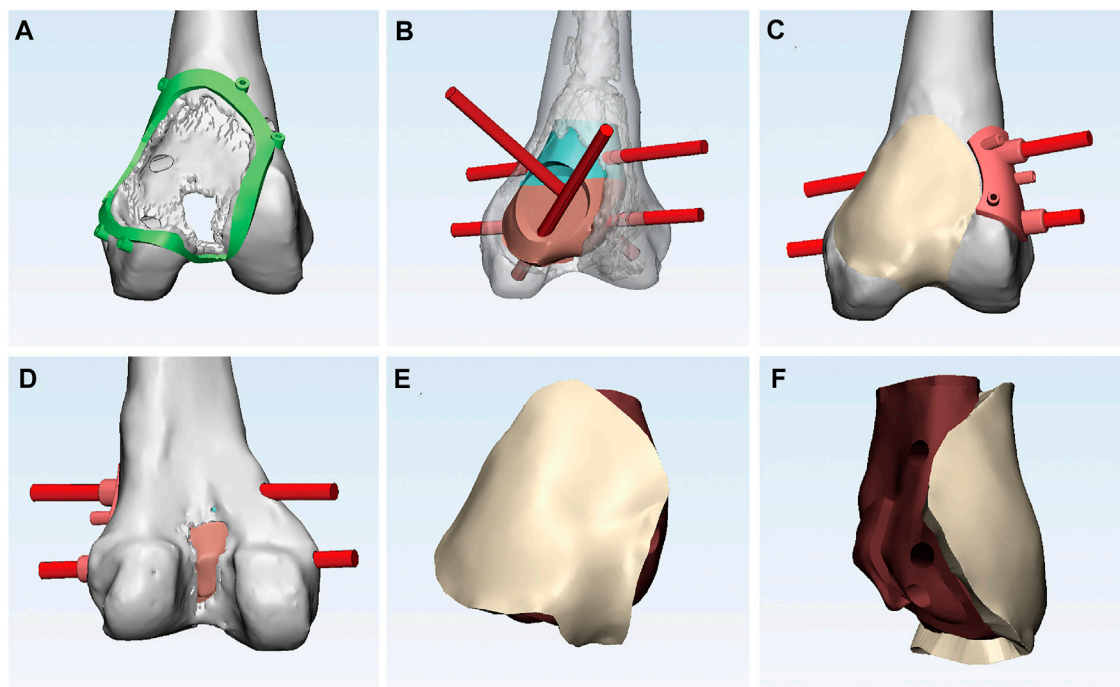


FIGURE 2

(A) Anterior view of the bone and articular cartilage defects and the circular 3D-printed guided plate. (B) Anterior view of the back components with four screw holes in three directions. (C) Anterior view of the front component connecting smoothly with the adjacent articular surface and two horizontal screws directed by guided plate. (D) Posterior view of bone defects. (E) Anterior and (F) lateral view of the 3D-printed modular prosthesis.

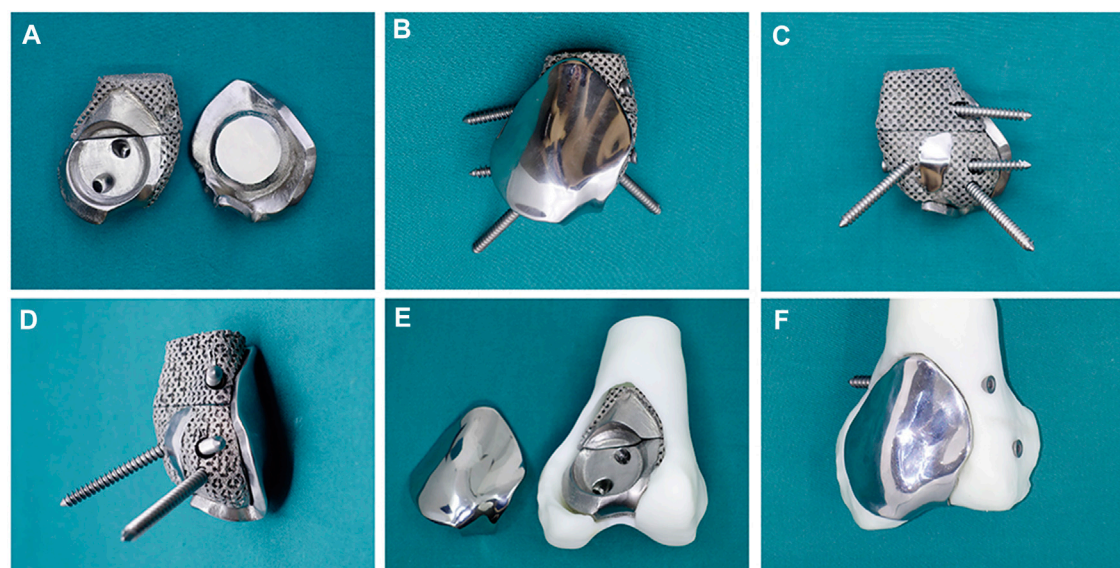


FIGURE 3

(A) The back components (left) combine with the front component (right) through a press-fit structure. (B) Anterior and (C) posterior and (D) lateral view of the assembled 3D-printed modular prosthesis with four screws. The prosthesis is tested on the femur model before surgery: (E) the back components fill in the bone cavity, and (F) the front component is fixed on the back components and connected to the adjacent articular surface.

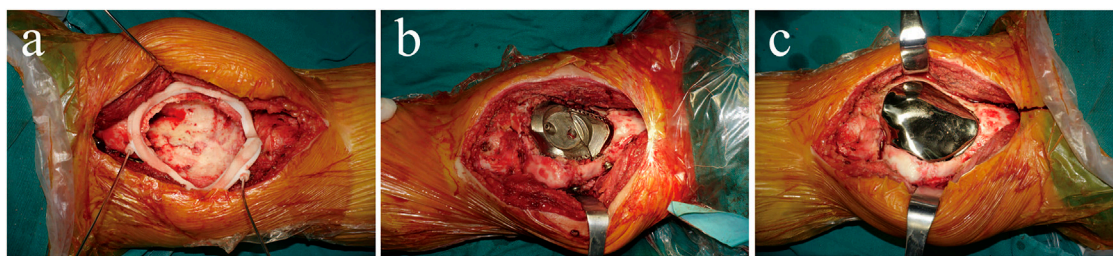


FIGURE 4

(A) The circular 3D-printed guided plate is fixed on the bone margin of the tumour. (B) The back components are inserted into the bone cavity and firmly fixed to the surrounding bone with four screws. (C) The front component is firmly fixed on the back components through a press-fit structure and conforms to the surrounding articular surface.

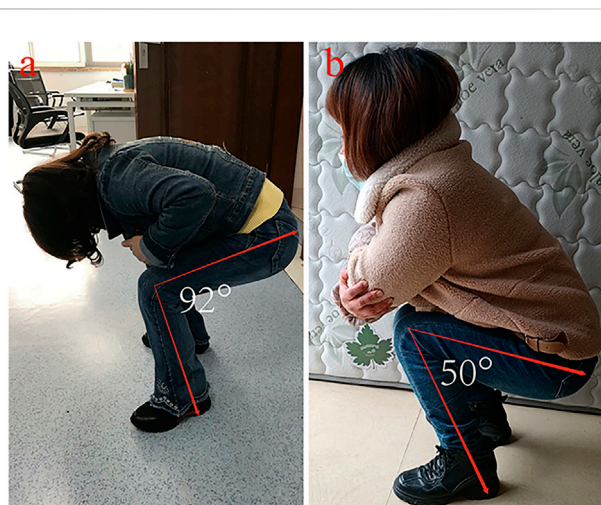


FIGURE 5

Knee flexion is (A) 88° and (B) 130° 2 months and 27 months after surgery, respectively.

prosthesis and screws were stable, and no recurrence was observed in the affected knee 22 months after surgery (Figure 6).

Discussion and conclusions

Intralesional curettage combining bone graft with internal fixation with or without local adjuvants is the most accepted surgical treatment for grade II GCT around the knee (Kamal et al., 2016), as encountered in our first surgery. Local recurrence, infection, and internal fixation failure are serious events that must be considered (Yu et al., 2010; Xu et al., 2013). Unfortunately, the patient experienced a deep infection after intralesional curettage. Although the deep infection was controlled, the patient suffered severe pain (VAS score of 7) and limited knee function (knee flexion was 50°) due to patello-femoral large cartilage defects. Fortunately, she eventually

achieved a satisfactory outcome with a 3D-printed prosthesis, a novel reconstruction method for patello-femoral large osteochondral defects. At the last follow-up, she was pain free with full weight-bearing, the MSTS score improved from 15/30 to 29/30, the VAS decreased from 7 to 0, and knee flexion recovered from 50° to 130°. These values were above the overall MSTS score and ROM after intralesional curettage and wide resection reported in the literature (Ayerza et al., 2009; Kundu et al., 2015), indicating that the 3D-printed prosthesis we used may be useful for patello-femoral osteochondral reconstruction.

Patello-femoral arthroplasty is commonly used for symptomatic patello-femoral osteoarthritis or isolated osteochondral lesions without ligament instability (Cotic et al., 2017; Jeong et al., 2020; Rezzadeh et al., 2020). The patient suffered from patello-femoral large osteochondral defects in our case, but patello-femoral arthroplasty could not achieve mechanical stability because of mass bone defects. Although the cement packing had adequate strength for the bone defects, we failed to reconstruct the patello-femoral cartilage, which led to knee pain; and the bone-cement interface is a non-biological integration, which can lead to secondary degenerative changes and fractures (Kundu et al., 2015; Teng et al., 2019). Consequently, a sclerotic rim was found around the bone-cement interface after 11 months of cement packing. Considering this, a porous endoprosthesis produced by a 3D technique that enables bone ingrowth may solve this problem. Lu et al. (2019) reported a patient treated with a 3D-printed porous implant combined with bone grafting for subchondral GCT of the proximal tibia and found excellent osseointegration between the graft and retained subchondral bone during a follow-up period of 29 months. In our case, we found that the prosthesis was fixed firmly, and that there was callus formation at the prosthesis-bone interface after surgery for 22 months, indicating the feasibility of a 3D-printed porous prosthesis to achieve osseointegration.

Total knee arthroplasty and unicompartmental knee hemiarthroplasty are also acceptable reconstruction

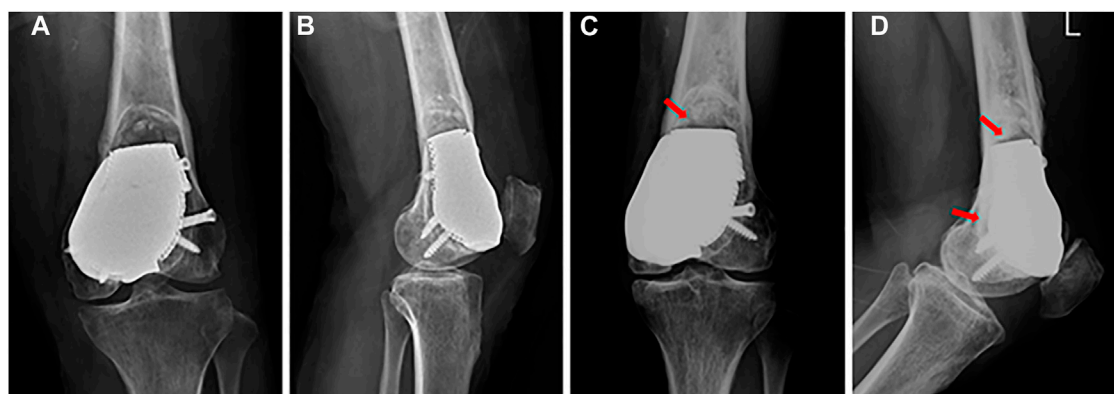


FIGURE 6

(A) Anterior–posterior and (B) lateral X-ray images after surgery. (C) Anterior–posterior and (D) lateral X-ray images 22 months after surgery: the prosthesis and screws are stable, and callus formation is found at the prosthesis–bone interface (red arrow).

procedures for osteochondral lesions around the knee (Garner et al., 2019; Beard et al., 2020). In our case, the large osteochondral defects of the distal femur were mainly located at the lateral condyle and patello-femoral surface. Therefore, it is difficult to obtain good clinical outcomes using the above-named conventional arthroplasty procedures. Although 3D-printed prostheses have been commonly adopted for tumour-induced bone defect reconstruction, tumour-induced osteochondral defect reconstruction has rarely been reported. Ji et al. (2021) performed a retrospective study on 26 patients with unicondylar fractures of the distal femur GCT. Half of the patients treated with a 3D-printed custom unicondylar prosthesis had a shorter operation time, less intraoperative blood loss, higher MSTs scores, and better ROM than other patients treated with total knee arthroplasty. The satisfactory outcome of their study demonstrated the feasibility of a 3D-printed custom prosthesis for repairing unicondylar lesions.

Therefore, using 3D printing technique, we constructed a custom modular prosthesis for articular cartilage and bone defects. We obtained osseointegration between the prosthesis and surrounding bone and preserved more knee ligaments and residual bone, which were beneficial for the rehabilitation of the knee joint function. Furthermore, in our case, the patello-femoral cartilage was reconstructed with a favourable congruence of the 3D-printed prosthesis with the adjacent articular surface. The patient achieved good clinical outcomes without pain, local recurrence, or degeneration at the last follow-up. We propose that this could be an alternative option for patello-femoral large osteochondral defects caused by GCT or other reasons.

This patient achieved good clinical outcomes, possibly benefitting from the following 3D-printed prosthesis design

concepts. First, the front modular component of the prosthesis, which was made of a smooth titanium alloy for contact with the adjacent articular surface, could reduce joint friction and secondary cartilage degeneration. Further, the porous structure of the back components facilitates osseointegration and mechanical support. Moreover, the press-fit structure between the front and back components is firm, and four screws in the back components provide initial stabilisation by fixing it to the residual bone of the distal femur without an internal locking plate or intramedullary fixation. Finally, the size of the prosthesis was customised based on the specific osteochondral defects. Thus, we preserved more bone mass and tendon ligaments around the knee, which helped preserve knee function and stabilisation and would be easy to revise, if the tumour recurred, should a tumour-type total knee arthroplasty be easily performed.

Although no degeneration has been found thus far, the difference in elastic modulus between the titanium alloy material and the patella may lead to joint degeneration in the future. We originally planned to design the front part of the prosthesis with polyethylene to reconstruct the patello-femoral cartilage but failed because of insufficient manufacturing technology, which requires further study. Furthermore, our report had only one case with 27 months of follow-up, and long-term follow-up is needed to further investigate the clinical outcomes of this novel prosthesis.

In conclusion, a 3D-printed modular prosthesis may be a useful treatment option for the surgical reconstruction of GCT-induced patello-femoral large osteochondral defects. The firm fixation, osseointegration, and favourable congruency of the 3D-printed prosthesis with the adjacent articular surface can achieve long-term knee function and stability.

Data availability statement

The original contributions presented in the study are included in the article/Supplementary Material, further inquiries can be directed to the corresponding authors.

Ethics statement

The studies involving human participants were reviewed and approved by The Ethical Committee of West China Hospital, Sichuan University. The patients/participants provided their written informed consent to participate in this study.

Author contributions

DY and XF wrote the manuscript and produced the figures. WZ and HD supervised the process of writing the manuscript. XF, SL, WZ, and HD designed the prosthesis. XF, WZ, and HD performed the surgery. SL, NB, FK, and YG were responsible for English editing and reviewing the manuscript. All authors read and approved the final manuscript.

References

- Andrade, R., Nunes, J., Hinckel, B. B., Gruskay, J., Vasta, S., Bastos, R., et al. (2019). Cartilage restoration of patellofemoral lesions: A systematic review. *Cartilage* 13 57S–73S. doi:10.1177/1947603519893076
- Ayerza, M. A., Aponte-Tinao, L. A., Farfalli, G. L., Restrepo, C. A., and Muscolo, D. L. (2009). Joint preservation after extensive curettage of knee giant cell tumors. *Clin. Orthop. Relat. Res.* 467 (11), 2845–2851. doi:10.1007/s11999-009-0913-8
- Beard, D. J., Davies, L. J., Cook, J. A., MacLennan, G., Price, A., Kent, S., et al. (2020). Total versus partial knee replacement in patients with medial compartment knee osteoarthritis: The TOPKAT RCT. *Health Technol. Assess.* 24 (20), 1–98. doi:10.3310/hta24200
- Cotic, M., Forkel, P., and Imhoff, A. B. (2017). Patellofemoral arthroplasty. *Oper. Orthop. Traumatol.* 29 (1), 40–50. doi:10.1007/s00064-016-0477-1
- Degen, R. M., Coleman, N. W., Tetreault, D., Chang, B., Mahony, G. T., Camp, C. L., et al. (2017). Outcomes of patellofemoral osteochondral lesions treated with structural grafts in patients older than 40 years. *Cartilage* 8 (3), 255–262. doi:10.1177/1947603516665441
- Fang, X., Liu, H., Xiong, Y., Zhang, W., Luo, Y., Wu, F., et al. (2018). Total talar replacement with a novel 3D printed modular prosthesis for tumors. *Ther. Clin. Risk Manag.* 14, 1897–1905. doi:10.2147/tcrm.S172442
- Garner, A., van Arkel, R. J., and Cobb, J. (2019). Classification of combined partial knee arthroplasty. *Bone Jt. J.* 101-b (8), 922–928. doi:10.1302/0301-620x.101b8.Bjj-2019-0125.R1
- Ippolito, J. A., Campbell, M. L., Siracuse, B. L., and Benevenia, J. (2020). Reconstruction with custom unicondylar hemiarthroplasty following tumor resection: A case series and review of the literature. *J. Knee Surg.* 33 (8), 818–824. doi:10.1055/s-0039-1688556
- Jeong, S. H., Schneider, B., Pyne, A. S., Tishelman, J. C., and Strickland, S. M. (2020). Patellofemoral arthroplasty surgical technique: Lateral or medial parapatellar approach. *J. Arthroplasty* 35 (9), 2429–2434. doi:10.1016/j.arth.2020.04.026
- Ji, Y., Wu, Y., and Li, J. (2021). Use of three-dimensional-printed custom-made prosthesis to treat unicondylar femoral defect secondary to pathological fracture caused by giant cell tumor. *J. Int. Med. Res.* 49 (7), 030006052110253. doi:10.1177/03000605211025347
- Kamal, A. F., Simbolon, E. L., Prabowo, Y., and Hutagalung, E. U. (2016). Wide resection versus curettage with adjuvant therapy for giant cell tumour of bone. *J. Orthop. Surg. Hong. Kong.* 24 (2), 228–231. doi:10.1177/1602400221
- Kundu, Z. S., Gogna, P., Singla, R., Sangwan, S. S., Kamboj, P., and Goyal, S. (2015). Joint salvage using sandwich technique for giant cell tumors around knee. *J. Knee Surg.* 28 (2), 157–164. doi:10.1055/s-0034-1373738

Conflict of interest

The authors declare that the research was conducted in the absence of any commercial or financial relationships that could be construed as a potential conflict of interest.

Publisher's note

All claims expressed in this article are solely those of the authors and do not necessarily represent those of their affiliated organizations, or those of the publisher, the editors and the reviewers. Any product that may be evaluated in this article, or claim that may be made by its manufacturer, is not guaranteed or endorsed by the publisher.

Supplementary material

The Supplementary Material for this article can be found online at: <https://www.frontiersin.org/articles/10.3389/fbioe.2022.995879/full#supplementary-material>

- Lattermann, C., Kremser, V., and Altintas, B. (2018). Use of fresh osteochondral allografts in the patellofemoral joint. *J. Knee Surg.* 31 (3), 227–230. doi:10.1055/s-0037-1607324
- Lu, M., Wang, J., Tang, F., Min, L., Zhou, Y., Zhang, W., et al. (2019). A three-dimensional printed porous implant combined with bone grafting following curettage of a subchondral giant cell tumour of the proximal tibia: A case report. *BMC Surg.* 19 (1), 29. doi:10.1186/s12893-019-0491-y
- Palmerini, E., Picci, P., Reichardt, P., and Downey, G. (2019). Malignancy in giant cell tumor of bone: A review of the literature. *Technol. Cancer Res. Treat.* 18, 153303381984000. doi:10.1177/1533033819840000
- Rezzadeh, K., Behery, O. A., Kester, B. S., Dogra, T., Vigdorichik, J., and Schwarzkopf, R. (2020). Patellofemoral arthroplasty: Short-term complications and risk factors. *J. Knee Surg.* 33 (9), 912–918. doi:10.1055/s-0039-1688960
- Teng, W., Lin, P., Li, Y., Yan, X., Li, H., Li, B., et al. (2019). Bone combined cement grafting in giant cell tumor around the knee reduces mechanical failure. *Int. Orthop.* 43 (2), 475–482. doi:10.1007/s00264-018-3939-2
- Wang, C., Zhang, G., Li, Z., Zeng, X., Xu, Y., Zhao, S., et al. (2019). Tribological behavior of Ti-6Al-4V against cortical bone in different biolubricants. *J. Mech. Behav. Biomed. Mat.* 90, 460–471. doi:10.1016/j.jmbbm.2018.10.031
- Wu, M., Yao, S., Xie, Y., Yan, F., Deng, Z., Lei, J., et al. (2018). A novel subchondral bone-grafting procedure for the treatment of giant-cell tumor around the knee: A retrospective study of 27 cases. *Med. Baltim.* 97 (45), e13154. doi:10.1097/md.00000000000013154
- Xu, S., Yu, X., Xu, M., and Fu, Z. (2013). Inactivated autograft–prosthesis composite have a role for grade III giant cell tumor of bone around the knee. *BMC Musculoskelet. Disord.* 14, 319. doi:10.1186/1471-2474-14-319
- Yu, M., Wan, Y., Ren, B., Wang, H., Zhang, X., Qiu, C., et al. (2020). 3D printed Ti-6Al-4V implant with a micro/nanostructured surface and its cellular responses. *ACS Omega* 5 (49), 31738–31743. doi:10.1021/acsomega.0c04373
- Yu, X. C., Xu, M., Song, R. X., Fu, Z. H., and Liu, X. P. (2010). Long-term outcome of giant cell tumors of bone around the knee treated by *en bloc* resection of tumor and reconstruction with prosthesis. *Orthop. Surg.* 2 (3), 211–217. doi:10.1111/j.1757-7861.2010.00089.x
- Yu, Z., Zhang, W., Fang, X., Tu, C., and Duan, H. (2021). Pelvic reconstruction with a novel three-dimensional-printed, multimodality imaging based endoprosthesis following enneking type I + IV resection. *Front. Oncol.* 11, 629582. doi:10.3389/fonc.2021.629582



OPEN ACCESS

EDITED BY

Changhui Song,
South China University of Technology,
China

REVIEWED BY

Wei Chu,
ZhangJiang LAB, China
Nuno M. Alves,
Polytechnic Institute of Leiria, Portugal
Luca Pezzato,
University of Padua, Italy

*CORRESPONDENCE

Miao Zhang,
779482594@qq.com
Zhong Li,
545890312@qq.com
Xiaohong Li,
lixiaohong@swust.edu.cn

SPECIALTY SECTION

This article was submitted to
Biomaterials,
a section of the journal
Frontiers in Bioengineering and
Biotechnology

RECEIVED 06 June 2022

ACCEPTED 26 August 2022

PUBLISHED 23 September 2022

CITATION

Wang S, Zhang M, Liu L, Xu R, Huang Z,
Shi Z, Liu J, Li Z, Li X, Hao P and Hao Y
(2022), Femtosecond laser treatment
promotes the surface bioactivity and
bone ingrowth of Ti₆Al₄V
bone scaffolds.
Front. Bioeng. Biotechnol. 10:962483.
doi: 10.3389/fbioe.2022.962483

COPYRIGHT

© 2022 Wang, Zhang, Liu, Xu, Huang,
Shi, Liu, Li, Li, Hao and Hao. This is an
open-access article distributed under
the terms of the [Creative Commons
Attribution License \(CC BY\)](#). The use,
distribution or reproduction in other
forums is permitted, provided the
original author(s) and the copyright
owner(s) are credited and that the
original publication in this journal is
cited, in accordance with accepted
academic practice. No use, distribution
or reproduction is permitted which does
not comply with these terms.

Femtosecond laser treatment promotes the surface bioactivity and bone ingrowth of Ti₆Al₄V bone scaffolds

Su Wang¹, Miao Zhang^{1*}, Linlin Liu¹, Rongwei Xu¹, Zhili Huang¹,
Zhang'ao Shi¹, Juncai Liu², Zhong Li^{2*}, Xiaohong Li^{3*},
Peng Hao⁴ and Yongqiang Hao⁵

¹School of Mechanical Engineering, Sichuan University, Chengdu, China, ²Department of Orthopaedics, The Affiliated Hospital of Southwest Medical University, Sichuan Provincial Laboratory of Orthopedics Engineering, Luzhou, China, ³School of Science, Southwest University of Science and Technology, Mianyang, China, ⁴Sichuan Provincial People's Hospital, Chengdu, China, ⁵Department of Orthopedics Surgery, Ninth People's Hospital, Shanghai Jiaotong University School of Medicine, Shanghai, China

In this study, a femtosecond laser with a wavelength of 800 nm was used to modify the surface of a titanium alloy bone scaffold created *via* selective laser melting (SLM). The outcomes demonstrated that the surface morphology of the bone scaffold after femtosecond laser treatment was micro-nano morphology. The hydrophobic structure of the scaffold was changed into a super-hydrophilic structure, improving the surface roughness, which was highly helpful for osteoblast adhesion and differentiation. The femtosecond laser surface treatment *in vitro* samples produced a thick layer of hydroxyapatite (HAP) with improved surface bioactivity. The effectiveness of osseointegration and interstitial growth of the specimens treated with the femtosecond laser surface were found to be better when bone scaffolds were implanted into the epiphysis of the tibia of rabbits. As a result, femtosecond laser therapy dramatically enhanced the surface activity of bone scaffolds and their capacity to integrate with the surrounding bone tissues, serving as a trustworthy benchmark for future biological scaffold research.

KEYWORDS

femtosecond laser, micro-nano surface morphology, super hydrophilic structure, surface bioactivity, bone tissue growth

Introduction

Due to its superior mechanical qualities, corrosion resistance, and biocompatibility, titanium (Ti) and its alloys have been the most popular choice of implant materials. In the additive manufacturing process known as selective laser melting (SLM), powder is melted and stacked one layer at a time into complicated three-dimensional parts. In the biomedical arena, it is unquestionably appealing for the tailored preparation of orthopedic implants. At this time, clinical tests using porous titanium alloy scaffolds

made by SLM have been successful (Van Hooreweder et al., 2017; Wang et al., 2019; Zhao X. et al., 2020).

Bone scaffolds with strong biocompatibility are implanted into the defected area in bone tissue engineering to give growing space for cells and growth factors and encourage bone tissue regeneration. This approach is seen to be a promising one for repairing bone defects (Turnbull et al., 2018; Wubneh et al., 2018). The failure rate of stent implantation has increased significantly as a result of the inadequate connection between the scaffold and the bone in the initial stage of implantation as it is not favorable for the growth of bone tissue into the scaffold (Gnilitskiy et al., 2019). The micro–nano morphology, roughness, hydrophilicity, and bioactivity of the scaffold surface, which are significant elements determining the effectiveness of osseointegration, have been demonstrated in pertinent research to be able to encourage the formation of bone tissue (Luo et al., 2014; Raimbault et al., 2016). To increase the effectiveness of osseointegration between bone tissue and Ti implants, surface modification is crucial.

With the development of surface modification technology, the osseointegration of different surface modification methods has attracted extensive attention of researchers. Many surface modification methods for bone scaffolds have been reported in previous studies, including chemical methods such as alkali heat, acid etching, and oxidation (Amin Yavari et al., 2015; Pylypchuk et al., 2015; Tan et al., 2016), and physical methods such as grinding, sandblasting, and roughening (Le Guéhennec et al., 2007; Coelho et al., 2009; Abdel-Haq et al., 2011). Fanny (Hilario et al., 2017) synthesized TiO₂ nanotubes on the surface of a titanium plate by anodic oxidation to obtain better corrosion resistance and biological activity. Wang and Xiong (2018) prepared novel composite coatings using two different surface modification technologies (micro-arc oxidation and grafting hydrophilic polymers), demonstrating better hydrophilicity and abrasive resistance.

Dingyun Zhao et al. (2020) quickly prepared the sodium titanate rutile TiO₂ bioactive structure on the titanium surface by induction heating, acid etching, and alkali heat. This structure had good adhesion, corrosion resistance, and a strong ability to induce the formation of hydroxyapatite (HAP) in a simulated body fluid, and the formed HAP had excellent long-term stability. Calcium and phosphate, which are necessary for bone formation, are found in HAP, a biocompatible and osteoconduction bioactive ceramic Ca₁₀(PO₄)₆(OH)₂. It deposits on the surface of Ti, which is conducive to combining with living bone and promoting the growth of osseous tissue. Kostelac et al. (2022) prepared a 2-grade titanium alloy bioactive coating with HAP as the main component by the plasma electrolytic oxidation process. The cell adhesion biological test showed that the coating had excellent cytocompatibility with human cells, and the cell adhesion performance was improved compared with that of untreated samples. The aforementioned surface modification methods can improve the bioactivity of bone scaffolds. However, problems such as the coating adhesion being so poor that it is easy to peel, chemical

pollution, and difficult control of the surface structure are difficult to ignore.

Because laser processing is non-contact, highly repeatable, and produces very little pollution, it is a dependable technique for surface modification (Cunha et al., 2015). Compared to nanosecond and picosecond pulse lasers, femtosecond lasers can prevent thermal diffusion and cause less thermal damage to nearby materials (Lu et al., 2018). Furthermore, by concentrating a femtosecond laser at micro-level spots, the etching trajectory and surface morphology can be accurately controlled. Based on the aforementioned benefits, femtosecond laser technology can stand out from other surface modification techniques and take the top spot among them.

In recent years, we have seen an increase in studies on the surface bioactivity of titanium and its alloys by femtosecond laser therapy, with the aim of directing the femtosecond laser ablation on the surface of titanium alloys to generate micro–nano morphology. The multiscale shape of micro/nano combinations accelerated the development of osteoblasts, according to Tsukanaka et al. (2016). In order to give the titanium surface good hydrophilicity, which is more beneficial for the deposition of HAP and accelerates the adhesion and differentiation of osteoblasts, Lin et al. (2020) conducted a series of regular lattice microstructures on the titanium surface using the femtosecond laser micro–nano-processing technology. Bouet et al. (2019) used a femtosecond laser to change the surface morphology of the Ti alloy which is formed by SLM technology. The results showed that the stent surface modified by the femtosecond laser had more spikes; the surface with more spikes had better hydrophilic performance, stronger bone integration ability, and better antibacterial effect. Although some researchers have studied how to increase the biological activity by applying a femtosecond laser to the surface of Ti/Ti alloy slices, there are few reports on how to increase the biological activity of a Ti alloy bone scaffold and then watch bone tissue grow after implantation.

In this study, the SLM-produced Ti₆Al₄V bone scaffolds were directly ablated using the femtosecond laser micro–nano-processing technology. Surface morphology, roughness, and hydrophilicity define the surface properties of the scaffolds. To determine the promoting impact of femtosecond laser surface treatment on the surface activity and osteogenic growth ability of the bone scaffold and to obtain a bone scaffold with better osseointegration ability in the early stage of implantation, the *in vitro* activity and rabbit tibial implantation experiment were carried out.

Experiment

Preparation of samples

In this study, the particle size of Ti₆Al₄V powder (Avimetal Powder Metallurgy Technology (Beijing) Co., Ltd.) ranges from 15 to 53 μm. The degree of sphericity is quite well (Figure 1A).

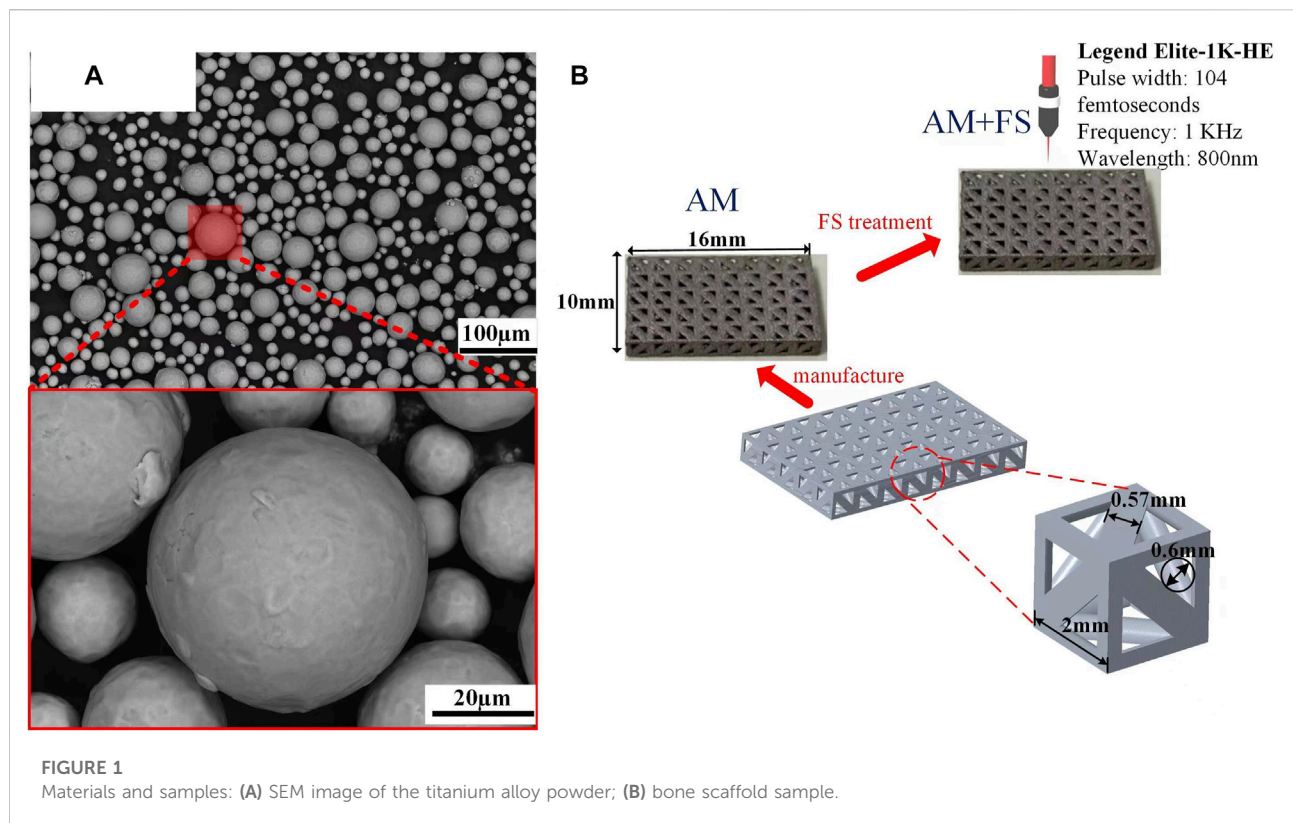


TABLE 1 Chemical composition of the titanium alloy powder.

Ti	V	Al	C	Fe	O
Bal	3.82	5.83	0.023	0.068	0.12

The main components of the titanium alloy powder are presented in Table 1. The bone scaffold is generated by a periodic array of pillar tetrahedral basic cells (TBCs) and designed by Unigraphics NX (Siemens PLM Software, Germany). The design method and structural parameter relationship can be found in our previous articles (Wang et al., 2019). The unit porosity is 65 %, and the typical dimension is 16 mm by 10 mm (Figure 1B).

Commercial SLM tools were used to create the bone scaffolds (FS271M, Sichuan Huashu Turing additive manufacturing technology Co., Ltd., Chengdu, Sichuan). The parameters of this equipment are as follows: the laser power is 500 W (W), the radius of the laser facula is 35 µm, the layer thickness is 30 µm, and the laser scanning speed is 240 mm/s. The scanning technique was designed as 67°- and 125°-angled laser channels for the neighboring layers to melt powder molding in order to eliminate internal residual stress. To ensure that printing was carried out in a pure argon gas environment, oxygen in the

forming cavity was removed before printing with argon gas that had a purity of 99.999 %. The bone scaffolds were created in the end (Figure 1B). After printing, wire electrical discharge machining (WEDM) technology was used to separate bone scaffold samples, which was created by additive manufacturing (AM), from the substrate. To eliminate contaminants and pollutants, the samples were then ultrasonically cleaned in industrial alcohol for 5 minutes.

The laser beam from the regeneratively amplified titanium gem femtosecond laser system abraded the surfaces of the AM samples with pulse times of 104 femtoseconds, repetition rates of 1 kHz, and center wavelengths of 800 nm (Legend Elite-1K-HE, Coherent, United States). The femtosecond laser surface treatment experiment was carried out at room temperature with air as the medium. During the ablation process, the laser beam guided the AM sample surfaces through the galvanometer scanning system (intelliSCAN III 14, SCANLAB), focusing the laser beam and scanning along with the linear scanning method. The scanning laser power was 50 mW, the speed was 0.5 mm/s, the focus spot was circular, the radius of the laser facula was 25 µm, the chirp of the pulse was 0.5 µm, and the line spacing was 0.04 mm. The new additive manufacturing (AM + FS) samples were taken after the femtosecond laser treatment and immersed in acetone for 5 min of ultrasonication to remove any remaining debris from the surface.

Surface characteristics of bone scaffolds

The surface morphology of the AM samples and the AM + FS samples was quantitatively analyzed using an atomic force microscope (AFM, NT-MDT, Russia). Five samples from each group were measured for their roughness average (Ra), roughness kurtosis (Rku), and roughness skewness (Rsk), and their averages were computed. Samples were scanned using an AFM at a width of 20 F0B4 20 mm. A field emission scanning electron microscope (SEM, JSE-5900 L V, Japan) was used to examine the surface morphology of the AM and AM + FS samples.

The hydrophilicity of the bone scaffold surface was evaluated by measuring the contact angle of droplets on the sample surfaces, which were detected by an optical contact angle-measuring instrument system (SDC-350, Shengding Precision Instrument Co., Ltd., Dongguan, China). Deionized water was used as the test solution, and a microliter syringe was used to control the droplet size to 2 μ L. Contact angle (CA) represents the average value obtained from different plane measurements.

In vitro bioactivity test of bone scaffolds

For 14 days at 37°C, five samples from the AM and AM + FS groups were immersed in a simulated bodily fluid (SBF) to examine the scaffold surface's capacity to promote HAP formation. The SBF used in the experiment was purchased from Fuzhou Beijing Biotechnology Co., Ltd. The ratio of the SBF solution volume to scaffold mass was 200 ml/g. It was noted that the volume of the SBF solution remained constant during the soaking process to ensure sufficient reaction ions for HAP formation. After soaking, the sample was taken out and repeatedly washed with ethanol three times to prevent further reaction. Then, the HAP deposition on the surface of the bone scaffold was evaluated and confirmed by SEM and energy-dispersive spectroscopy (EDS).

Rabbit tibial stent implantation experiment

In vivo implantation of bone scaffolds

This experiment was carried out in the experimental animal center of Southwest Medical University (Ethics No.: 2020878). A tibial metaphysis implantation experiment was conducted on 36 rabbits (weighing about 2.5 and 3 kg) at the age of 3 months.

Three groups of 12 rabbits each, made up of 36 rabbits, were randomly selected to represent three time-points (2, 4, and 8 weeks). At each time-point, the right tibial epiphysis of 12 rabbits was randomized to receive AM and AM + FS sample implants. A rectangular defect was drilled with a dental drill at the epiphysis of the tibial shaft after the rabbits were anesthetized with 3 % pentobarbital sodium (30 mg/kg),

then a bone scaffold was randomly implanted in the defect area, and the incision was sutured (Figures 2A,B). The rabbits were treated with penicillin for 3 days after the operation and fed separately. The rabbits were killed by intravenous injection of excessive sodium pentobarbital at 2, 4, and 8 weeks after implantation. For further analysis, the bone scaffold around the tibial metaphysis was immersed in 10 % formalin solution.

Micro-CT experimental evaluation

Micro-CT (SCANCO Medical, Switzerland) scanning was performed on the tibia metaphysis-containing stent at weeks 2, 4, and 8, respectively, and the scanned files were imported into Mimics 21.0 (Materialise, Belgium) software for reconstruction. Micro-CT was used to quantitatively analyze the growth of bone tissue into bone scaffolds. The bone tissue's interstitial growth capacity was quantified by the ratio of the new bone volume (BV) of the scaffold to the total volume (TV) of the analysis area.

Histological experimental evaluation

After Micro CT scanning, the specimens were dehydrated with 70 %, 80 %, 90 %, and 100 % ethanol, respectively, and then soaked in a formalin solution at 37°C for 1 week. A hard tissue section machine (SP1600, Leica, Germany) was used to slice the tissue along the radial and axial directions of the tibia. The slice thickness was 50 μ m, and the schematic diagram showed the tissue slice line (Figure 2C). The radial and axial directions of the femur were labeled as Line1 and Line2, respectively. After cutting it into sections, van Gieson stain, which contains 1.2 % trinitrophenol and 1 % acid fuchsin, was applied, and the development of bone tissue was seen under an optical microscope (DMCA, Leica, DM2500, Germany).

Results and Discussion

Surface characteristics of bone scaffolds

Figures 3A, B present the surface morphology of SEM images and optical microscopic images of AM samples and AM + FS samples. It might be seen that the surface morphology of the AM sample was relatively smooth, while that of the AM + FS sample after femtosecond laser surface treatment changes, forming a micro/nano-structure surface with a similar osteoporosis structure. Previous research has demonstrated that a critical feature influencing the bioactivity of metal implants is their surface morphology. Cells respond by detecting the surface morphology properties of implants, leading to adhesion, proliferation, and differentiation (Feller et al., 2014; Li et al., 2016; Liu et al., 2020). In particular, the surface morphology of

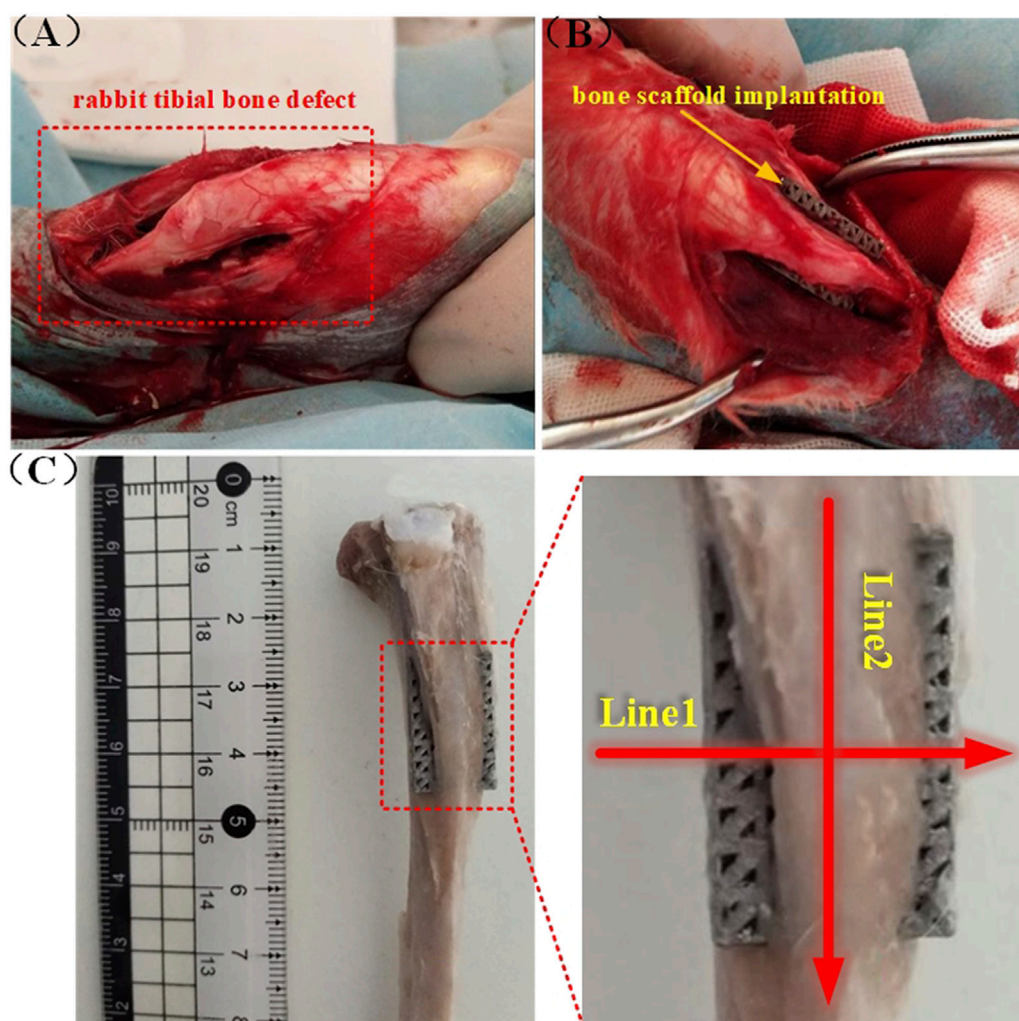


FIGURE 2

Rabbit tibial implantation experiment: (A) Rabbit tibial defect; (B) bone scaffold implantation; (C) schematic diagram of the cutting line of the hard tissue section after removal of the implanted bone scaffold.

the micro/nano-level combination improved the surface roughness and hydrophilicity, which was beneficial to the adhesion and differentiation of osteoblasts (Gittens et al., 2014a; Chen et al., 2017; Shaikh et al., 2018).

AFM was utilized to capture the three-dimensional surface morphology of AM and AM + FS samples, and roughness parameters were employed to quantitatively explain the surface morphology difference brought about by the femtosecond laser treatment of bone scaffolds (Figures 3C,D). The roughness of the two sets of samples was assessed in this study using the roughness metrics Ra, Rku, and Rsk. Ra represents the unevenness of the surface, and the larger the value, the rougher is the surface; Rku indicates the sharpness of the surface, and the higher its value, the sharper is the peak surface ($Rku > 3$ indicates that the surface is the peak surface); Rsk

represents the asymmetry of the surface, where a positive value represents the dominant number of surface peaks, and a negative value represents the dominant number of surface valleys. The results show that the surface roughness parameters of Ra, Rku, and Rsk of the bone scaffold AM + FS samples were higher than those of AM samples, indicating that the surface of the bone scaffold treated by femtosecond laser had higher roughness (Figures 3F, H).

The surface of the bone scaffolds underwent femtosecond laser treatment, which caused the unevenness to worsen and a sharper surface peak to develop. The analysis results of the skewness value demonstrated that although the surfaces of the bone scaffold AM samples and AM + FS samples were peak surfaces ($Rku > 3$), the surface Rsk of the AM samples were negative, and the number of surface valleys was more than

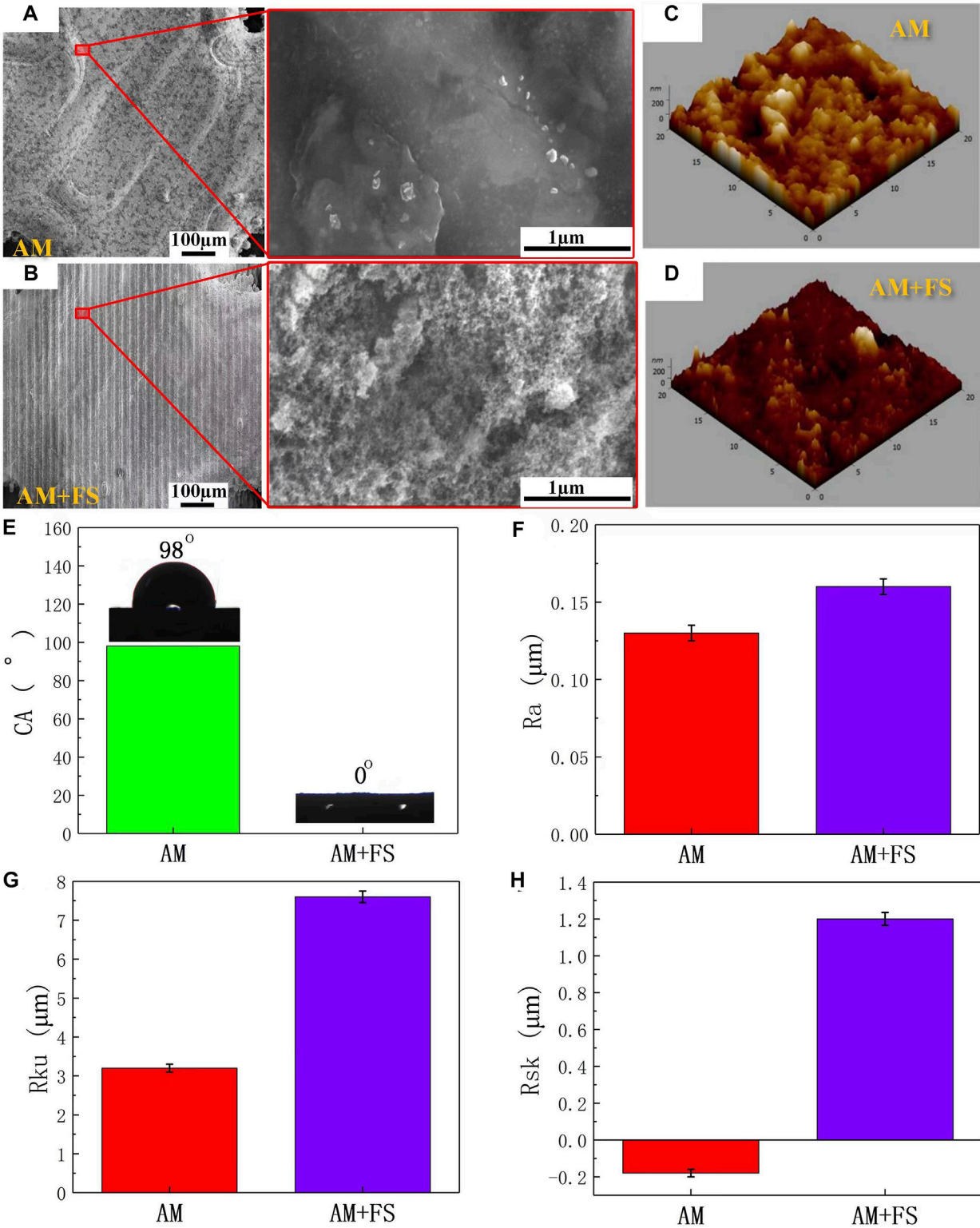


FIGURE 3 Surface characteristics: (A–B) SEM images and optical microscopic images of the surface of AM and AM + FS samples; (C–D) AFM three-dimensional morphologies of the AM and AM + FS samples; (E) the water contact angles of the sample surface; (F–H) surface parameters of Ra, Rku, and Rsk of samples.

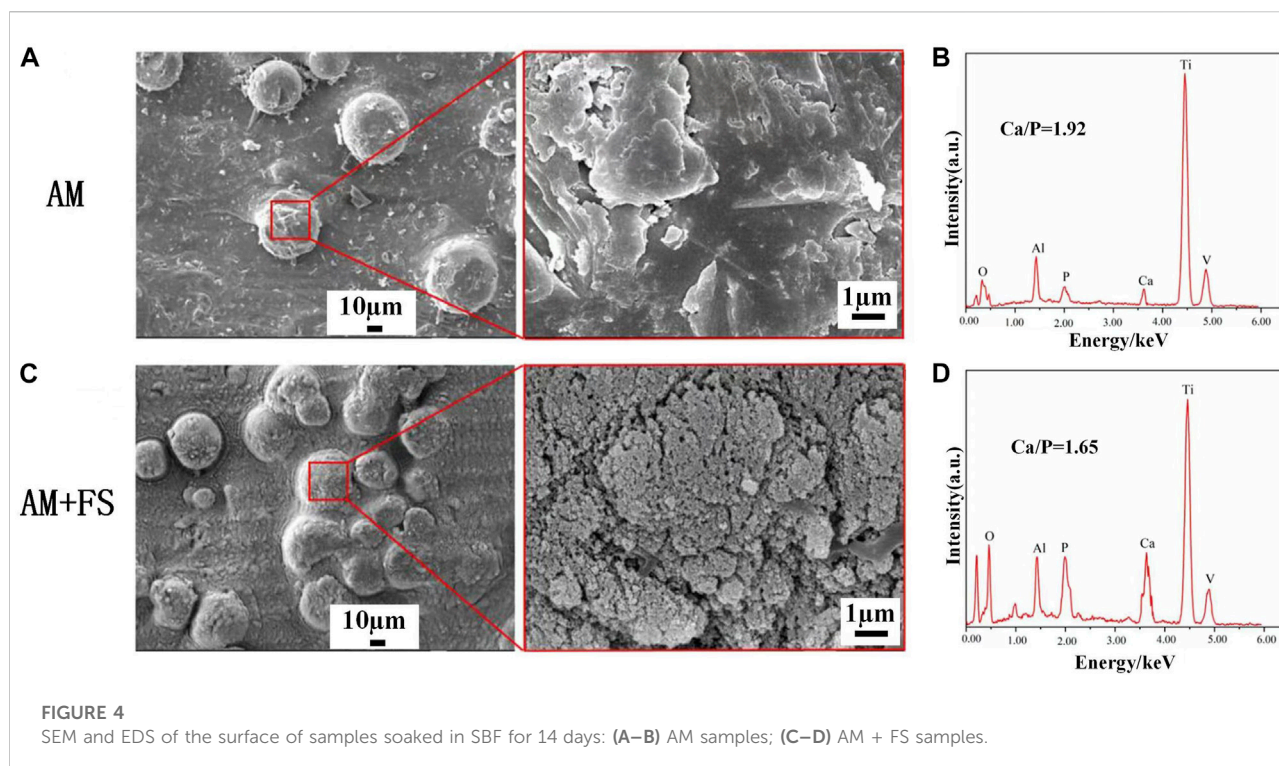


FIGURE 4
SEM and EDS of the surface of samples soaked in SBF for 14 days: (A–B) AM samples; (C–D) AM + FS samples.

that of the surface peaks. After femtosecond laser surface treatment, the surface tended to form surface peaks rather than surface valleys, and the number of surface peaks on the surface of the AM + FS sample was much greater than that of the surface valleys. It is more conducive to cell adhesion and speeds up the proliferation and differentiation of bone tissue cells when the surface area of a bone scaffold in contact with bone tissue cells rises (Chan et al., 2017; Spriano et al., 2018).

Surface hydrophilicity is another crucial factor determining the interaction between the surface of the bone scaffold and surrounding osseous tissue in addition to the surface morphology and roughness (Gittens et al., 2014b; Rupp et al., 2014). The water contact angles were measured to evaluate the hydrophilicity of the sample surfaces (Figure 3E). The average water contact angle on the surface of the AM samples was 98°, which was the hydrophobic structure. The average water contact angle on the surface of the AM + FS samples was almost 0°, which was the super-hydrophilic structure. The effectiveness of HAP deposition, cell adhesion, and bioactivity is significantly influenced by the hydrophilicity of the bone scaffold surface (Chen et al., 2014; Zhang et al., 2019; Menazea and Ahmed, 2020). The adhesion of cells at the initial stage of implantation has a significant impact on the proliferation and differentiation of subsequent cells, and relevant studies have shown that fibronectin and other important extracellular matrices (ECM) related to cell adhesion tend to be adsorbed on the hydrophilic surface (Wilson et al., 2005). As a result, the hydrophilic scaffold

surface can bind to osseous tissue *in vivo* more than the hydrophobic scaffold surface.

In vitro bioactivity evaluation of bone scaffolds

The formation of HAP is an important sign of the bioactivity of materials. It is also one of the criteria for evaluating the bioactivity of bone repair materials *in vitro*. The AM samples and AM + FS samples were soaked in SBF for 14 days. The surface morphology of the bone scaffolds soaked for 14 days was observed by SEM (Figures 4A–C).

HAP is clustered and composed of many nanocrystals. This is the typical form of HAP deposited in SBF. HAP was observed on the surface of AM samples and AM + FS samples, indicating that the titanium alloy bone scaffold had the ability to induce HAP deposition before and after femtosecond laser surface treatment. It is worth mentioning that only few HAP particles were generated on the surface of the AM samples, and the HAP coverage was low. However, a dense HAP layer was formed on the surface of the AM + FS samples, and the coverage was significantly increased. As a result, the bone scaffolds treated with the femtosecond laser had a stronger ability to induce HAP deposition and better bioactivity.

The elemental composition of the sample surface was analyzed by EDS (Figures 4B–D). The AM + FS sample's Ca/P ratio was about 1.65 after 14 days of soaking in the SBF

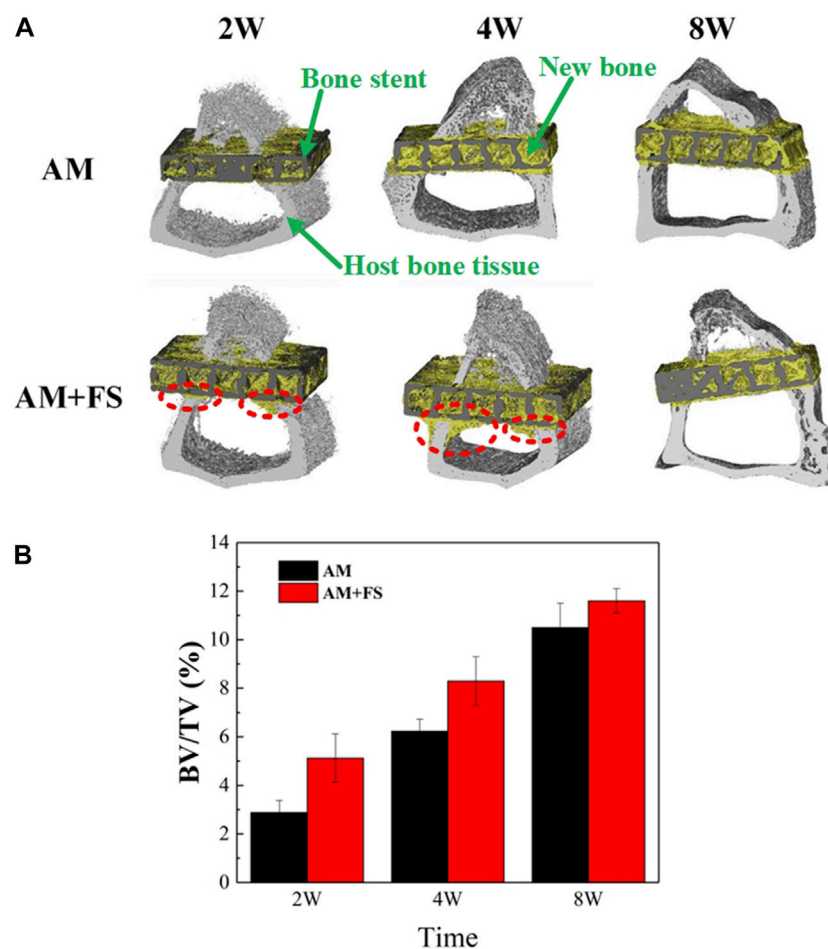


FIGURE 5

Micro-CT evaluation: (A) micro-CT reconstruction model of bone stent implantation in rabbits at different time-points; (B) BV/TV values at different time-points of bone scaffold implantation in rabbits (* $p < 0.05$).

solution, comparable to the Ca/P ratio of HAP typically seen in human bones. Compared to the typical Ca/p value of HAP in human bones, the AM samples had a higher Ca/p ratio of around 1.92. In an *in vitro* SBF immersion experiment, calcium ions were first deposited on the surface, and then, HAP grew there (Zhao and Xiong, 2012). Even while HAP is generated on the surface, it happens significantly more slowly in AM samples than in AM + FS samples, according to the AM sample's greater Ca/P ratio. The results of the EDS analysis and the SEM observation findings are in agreement.

Evaluation of the bone ingrowth ability of bone scaffolds *in vivo*

Micro-CT evaluation

In vitro experimental results have shown that femtosecond laser treatment can improve the surface bioactivity of bone

scaffolds. To further test the efficiency of osseointegration *in vivo*, the AM and AM + FS samples were implanted into the epiphysis of the rabbit tibial shaft for 2, 4, and 8 weeks, respectively. The ratio of the BV to the TV was used as an index to evaluate the bone ingrowth ability of the bone scaffold. The higher the value of BV/TV, the more the scaffold grows into bone tissue and the better is the osteogenic growth performance of the scaffold. The micro-CT three-dimensional model was reconstructed at different time-points after the bone scaffold was implanted into the rabbit tibia, in which the black part was the titanium alloy scaffold, the yellow part was the new bone tissue, and the gray part was the host's original bone tissue (Figure 5A). It was noted that due to the length of the bone scaffold implant, only a 5-mm long section was intercepted for analysis during 3D reconstruction. Since there were a certain number of bone tissue cells in the bone marrow cavity, a small amount of bone tissue cells had adhered and proliferated on the surface of the bone scaffold in the early stage of implantation.

This indicated that the titanium alloy bone scaffold manufactured by SLM had excellent biocompatibility.

As can be seen from the three-dimensional reconstruction model (Figure 5A), with the increase in implantation time, there was an increasing number of new bone tissues in the scaffold. In the first 2 weeks of implantation, it might be seen that the cortical bone tissue of the AM + FS samples extended to the marrow cavity along the contour of the scaffold, which was not the case in the AM samples. At the fourth week after implantation, the new bone tissue of cortical bone cells in the AM + FS samples increased gradually along the contour of the scaffold. In contrast, the bone tissue in the AM samples did not grow to the bone marrow cavity along the contour of the scaffold, which showed that the surface of the bone scaffold had better biocompatibility and osteoconduction after the femtosecond laser surface treatment. At the eighth week of implantation, it might be seen that many new bone tissues were growing in the AM samples and AM + FS samples. Nevertheless, compared with the AM samples, there were more new bone tissues in the pores of AM + FS samples. Bone tissue and scaffolds have become a whole, forming good osteointegration.

The quantitative analysis results of the bone growth ability after bone scaffold implantation by micro-CT were described by the BV/TV ratio (Figure 5B). It can be seen from the second week of implantation, the new bone volume of the AM + FS sample was almost twice that of the AM sample, indicating that the surface bioactivity and bone ingrowth ability of the bone scaffold were significantly improved after the femtosecond laser surface treatment. In the early stage of bone scaffold implantation, osteoblasts first adhered to the scaffold surface and then gradually grew into the scaffold pores. The surface of the bone scaffold treated by the femtosecond laser provided a good place for cell adhesion in the early stage of growth. At the fourth and eighth weeks after implantation, the volume difference of the new bone between the two groups' scaffolds decreased gradually, which was mainly attributed to the limited space provided by the 2 mm thickness of the scaffold for bone tissue growth. Therefore, the growth of bone tissue in the AM + FS samples slowed down gradually in the later stage.

Histological evaluation

The hard-tissue section machine was used to slice the tissue along with the schematic diagram of the slicing line (Figure 2C), stain after slicing, and observe the growth of bone tissue under an optical microscope.

After the implantation of bone scaffolds, at weeks 2, 4, and 8, bone tissue development was seen (Figure 6). In the figure, the scaffold is shown in black, the new bone is shown in red, and the fibrous tissue is shown in blue. The radial and axial directions of the femur are shown by lines 1 and 2, respectively.

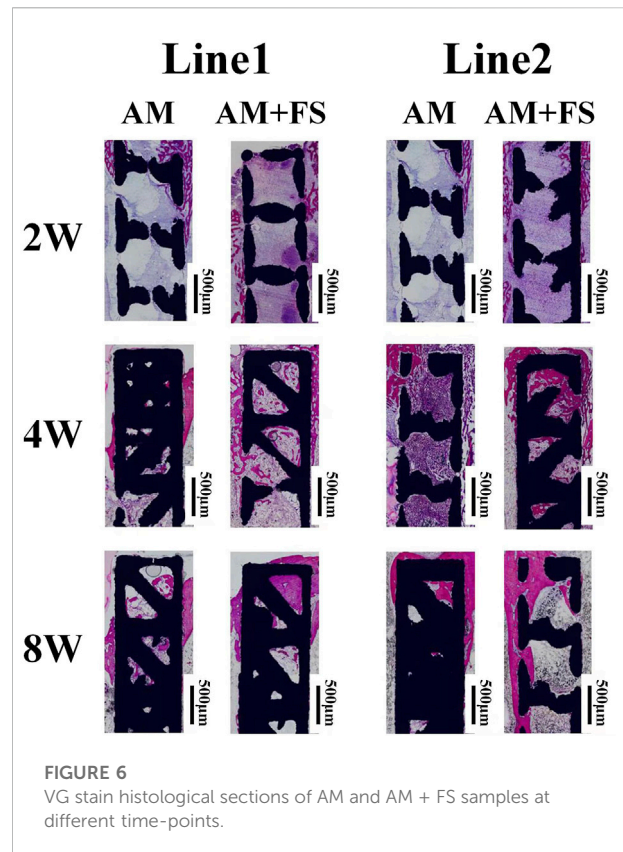


FIGURE 6
VG stain histological sections of AM and AM + FS samples at different time-points.

For the Line1 direction, the bone tissue first grew from the place where the cortical bone contacted the scaffold to both sides (Figure 6). In the second week, the bone tissue cells of the AM + FS samples proliferated bilaterally. However, only a few cells proliferated bilaterally in the AM samples. In the fourth week, the bone tissue cells of the AM + FS samples proliferated bilaterally and expanded into the inner pores of the scaffold. In the AM samples, bone tissue cell growth remained mostly unaltered. There were considerably less bone tissue cells in the inner pores of the AM samples than the AM + FS samples. In the eighth week, bone tissue could be found to be present in the inner pores of the AM samples and the AM + FS samples in contact with the cortical bone. The AM + FS samples had a wider contact area with bone tissue than the AM samples did, and the bone tissue interlocked well with the scaffold.

For the Line2 direction, because the scaffold was not in direct contact with the cortical bone, the bone tissue cells on the scaffold proliferated from the contact part between the cortical bone and scaffold. The capacity of bone tissue cells on the scaffold to proliferate and differentiate is directly reflected in the direction in which the bone tissue is growing. In the second week of the AM + FS samples, it can be seen from the Line2 direction that a few bone tissue cells proliferated to the center of the scaffold (Figure 6). At the same time, for the AM samples, only a few bone tissue units proliferated at the edge of the cortical bone. At

the fourth week, there was only a small amount of bone tissue cells in the middle of the AM samples, while more bone tissue cells had adhered to the middle of the AM + FS samples and proliferated and differentiated in the pores of the scaffold. At the eighth week, bone tissue cells had proliferated and differentiated well along the lateral side of the AM + FS samples, and the degree of cell proliferation on the AM samples was significantly lower than that of the AM + FS samples.

In conclusion, the *in vivo* implantation experiment showed that AM + FS samples in the Line1 direction might see the adhesion and growth of bone tissue cells on the scaffold surface after 2 weeks of implantation, showing good osseointegration ability. Compared with the AM samples at the same time point, the AM + FS samples showed more new bone tissue growth, indicating that the surface after femtosecond laser treatment can promote the adhesion of bone tissue cells. More bone tissue in the Line2 direction showed proliferation along the surface of the AM + FS samples, and bone tissue and bone scaffolds showed good mechanical interlocking characteristics at the eighth week of implantation.

Conclusion

In this study, the surface of Ti alloy bone scaffolds made by SLM was treated with a femtosecond laser, and the changes in the surface morphology, roughness, and hydrophilicity of the bone scaffolds following treatment were noted. The bioactivity of the AM and AM + FS samples was measured using the simulated bodily fluid immersion technique. To assess the bone development performance *in vivo*, the bone scaffolds were transplanted into the metaphysis of the rabbit tibia. The most innovative aspect of this study is how thoroughly and methodically the aforementioned tests have been conducted and studied. The key findings are as follows:

- 1) Bone scaffolds that had been surface-treated with a femtosecond laser developed micro–nano surface topography, which increased surface roughness and hydrophilicity.
- 2) *In vitro* activity tests revealed that treating the surface of the bone scaffold with a femtosecond laser resulted in dense HAP, which had improved bioactivity and promoted the adhesion and proliferation of bone tissue cells.
- 3) The implantation of a bone scaffold in the rabbit tibia metaphysis resulted in more new bone tissues growing in the AM + FS samples than in AM samples alone. It was further established that treating the bone scaffold with a femtosecond laser improves bone tissue cell adhesion and proliferation. Additionally, the growth of bone tissue on the surface of the AM + FS samples demonstrated strong mechanical interlocking properties with bone scaffolds.

Data availability statement

The original contributions presented in the study are included in the article/Supplementary Materials; further inquiries can be directed to the corresponding authors.

Ethics statement

The animal study was reviewed and approved by the experimental animal center of Southwest Medical University (Ethics No.: 2020878).

Author contributions

SW: conceptualization, validation, formal analysis, and supervision. MZ: writing—original draft and writing—review and editing. LL: investigation and visualization. RX: writing—review and editing. ZH: validation, methodology, and project administration. ZS: conceptualization, investigation, methodology, and formal analysis. ZL: resources and data curation. JL: supervision. XL: investigation. PH: funding acquisition. YH: resources.

Funding

This work was supported by the National Key R&D Program of China (No. 2016YFC1100600), the Applied Basic Research Project of Science & Technology Department of Sichuan Province (No. 2020YJ0265), the Sichuan University-Luzhou Municipal People's Government Strategic Cooperation Project (No. 2019CDLZ-17), and the Grant for Key Research Items from Sichuan Province of Science and Technology (No. 2020YFS0394).

Conflict of interest

The authors declare that the research was conducted in the absence of any commercial or financial relationships that could be construed as a potential conflict of interest.

Publisher's note

All claims expressed in this article are solely those of the authors and do not necessarily represent those of their affiliated organizations, or those of the publisher, the editors, and the reviewers. Any product that may be evaluated in this article, or claim that may be made by its manufacturer, is not guaranteed or endorsed by the publisher.

References

- Abdel-Haq, J., Karabuda, C. Z., Arisan, V., Mutlu, Z., and Kırkcı, M. (2011). Osseointegration and stability of a modified sand-blasted acid-etched implant: An experimental pilot study in sheep. *Clin. Oral Implants Res* 22, 265–274. doi:10.1111/j.1600-0501.2010.01990.x
- Amin Yavari, S., Chai, Y. C., Böttger, A. J., Wauthle, R., Schrooten, J., Weinans, H., et al. (2015). Effects of anodizing parameters and heat treatment on nanotopographical features, bioactivity, and cell culture response of additively manufactured porous titanium. *Mater. Sci. Eng. C* 51, 132–138. doi:10.1016/j.msec.2015.02.050
- Bouet, G., Cabanettes, F., Bidron, G., Guignandon, A., Peyroche, S., Bertrand, P., et al. (2019). Laser-based Hybrid manufacturing of Endosseous implants: Optimized titanium surfaces for enhancing osteogenic differentiation of human mesenchymal stem cells. *ACS Biomater. Sci. Eng.* 5, 4376–4385. doi:10.1021/acsbomaterials.9b00769
- Chan, C., Carson, L., Smith, G. C., Morelli, A., and Lee, S. (2017). Enhancing the antibacterial performance of orthopaedic implant materials by fibre laser surface engineering. *Appl. Surf. Sci.* 404, 67–81. doi:10.1016/j.apsusc.2017.01.233
- Chen, P., Aso, T., Sasaki, R., Tsutsumi, Y., Ashida, M., Doi, H., et al. (2017). Micron/submicron Hybrid topography of titanium surfaces Influences adhesion and differentiation Behaviors of the mesenchymal stem cells. *J. Biomed. Nanotechnol.* 13, 324–336. doi:10.1166/jbnn.2017.2335
- Chen, W., Chen, Y., Ko, C., Lin, Y., Kuo, T., and Kuo, H. (2014). Interaction of progenitor bone cells with different surface modifications of titanium implant. *Mater. Sci. Eng. C* 37, 305–313. doi:10.1016/j.msec.2014.01.022
- Coelho, P. G., Granjeiro, J. M., Romanos, G. E., Suzuki, M., Silva, N. R., Cardaropoli, G., et al. (2009). Basic research methods and current trends of dental implant surfaces. *J. Biomed. Mater. Res.* 88B, 579–596. doi:10.1002/jbm.b.31264
- Cunha, A., Zouani, O. F., Plawinski, L., Botelho do Rego, A. M., Almeida, A., Vilar, R., et al. (2015). Human mesenchymal stem cell behavior on femtosecond laser-textured Ti-6Al-4V surfaces. *Nanomedicine* 10, 725–739. doi:10.2217/nnm.15.19
- Feller, L., Chandran, R., Khammissa, R. A., Meyerov, R., Jadwat, Y., Bouckaert, M., et al. (2014). Osseointegration: Biological events in relation to characteristics of the implant surface. *SADJ* 69 (112), 112–117. doi:10.1163/157180807781870336
- Gittens, R. A., Olivares-Navarrete, R., Schwartz, Z., and Boyan, B. D. (2014a). Implant osseointegration and the role of microroughness and nanostructures: Lessons for spine implants. *Acta Biomater.* 10, 3363–3371. doi:10.1016/j.actbio.2014.03.037
- Gittens, R. A., Scheideler, L., Rupp, F., Hyzy, S. L., Geis-Gerstorf, J., Schwartz, Z., et al. (2014b). A review on the wettability of dental implant surfaces II: Biological and clinical aspects. *Acta Biomater.* 10, 2907–2918. doi:10.1016/j.actbio.2014.03.032
- Gnilitskiy, I., Pogorielov, M., Viter, R., Ferrara, A. M., Carapeto, A. P., Oleshko, O., et al. (2019). Cell and tissue response to nanotextured Ti6Al4V and Zr implants using high-speed femtosecond laser-induced periodic surface structures. *Nanomedicine Nanotechnol. Biol. Med.* 21, 102036. doi:10.1016/j.nano.2019.102036
- Hilario, F., Roche, V., Nogueira, R. P., and Junior, A. M. J. (2017). Influence of morphology and crystalline structure of TiO₂ nanotubes on their electrochemical properties and apatite-forming ability. *Electrochimica Acta* 245, 337–349. doi:10.1016/j.electacta.2017.05.160
- Kostelac, L., Pezzato, L., Settimi, A. G., Franceschi, M., Gennari, C., Brunelli, K., et al. (2022). Investigation of hydroxyapatite (HAP) containing coating on grade 2 titanium alloy prepared by plasma electrolytic oxidation (PEO) at low voltage. *Surfaces Interfaces* 30, 101888. doi:10.1016/j.surfin.2022.101888
- Le Guéhennec, L., Soueidan, A., Layrolle, P., and Amouriq, Y. (2007). Surface treatments of titanium dental implants for rapid osseointegration. *Dent. Mater.* 23, 844–854. doi:10.1016/j.dental.2006.06.025
- Li, X., Chen, T., Hu, J., Li, S., Zou, Q., Li, Y., et al. (2016). Modified surface morphology of a novel Ti-24Nb-4Zr-7.9Sn titanium alloy via anodic oxidation for enhanced interfacial biocompatibility and osseointegration. *Colloids Surfaces B Biointerfaces* 144, 265–275. doi:10.1016/j.colsurfb.2016.04.020
- Lin, X., Li, X., Li, G., Zhang, Y., and Cui, Z. (2020). Micro-dot-matrix induced by femtosecond laser on titanium surface for Ca-P phase deposition. *Appl. Surf. Sci.* 499, 143925. doi:10.1016/j.apsusc.2019.143925
- Liu, L., Wang, S., Liu, J., Deng, F., Li, Z., and Hao, Y. (2020). Architectural design of Ti6Al4V scaffold controls the osteogenic volume and application area of the scaffold. *J. Mater. Res. Technol.* 9, 15849–15861. doi:10.1016/j.jmrt.2020.11.061
- Lu, J., Huang, T., Liu, Z., Zhang, X., and Xiao, R. (2018). Long-term wettability of titanium surfaces by combined femtosecond laser micro/nano structuring and chemical treatments. *Appl. Surf. Sci.* 459, 257–262. doi:10.1016/j.apsusc.2018.08.004
- Luo, L., Jiang, Z. Y., Wei, D. B., and He, X. F. (2014). Surface modification of titanium and its alloys for biomedical application. *Amr* 887–888, 1115–1120. doi:10.4028/www.scientific.net/amr.887-888.1115
- Menazea, A. A., and Ahmed, M. K. (2020). Nanosecond laser ablation assisted the enhancement of antibacterial activity of copper oxide nano particles embedded though Polyethylene Oxide/Polyvinyl pyrrolidone blend matrix. *Radiat. Phys. Chem.* 174, 108911. doi:10.1016/j.radphyschem.2020.108911
- Pylypchuk, I. V., Petranovskaya, A. L., Gorbyk, P. P., Korduban, A. M., Markovsky, P. E., and Ivashishin, O. M. (2015). Biomimetic hydroxyapatite growth on Functionalized surfaces of Ti-6Al-4V and Ti-Zr-Nb alloys. *Nanoscale Res. Lett.* 10, 338. doi:10.1186/s11671-015-1017-x
- Raimbault, O., Benayoun, S., Anselme, K., Maclair, C., Bourgade, T., Kietzig, A., et al. (2016). The effects of femtosecond laser-textured Ti-6Al-4V on wettability and cell response. *Mater. Sci. Eng. C* 69, 311–320. doi:10.1016/j.msec.2016.06.072
- Rupp, F., Gittens, R. A., Scheideler, L., Marmur, A., Boyan, B. D., Schwartz, Z., et al. (2014). A review on the wettability of dental implant surfaces I: Theoretical and experimental aspects. *Acta Biomater.* 10, 2894–2906. doi:10.1016/j.actbio.2014.02.040
- Shaikh, S., Kedia, S., Majumdar, A. G., Subramanian, M., and Sinha, S. (2018). *In vitro* bioactivity and biocompatibility of femtosecond laser-modified Ti6Al4V alloy. *Appl. Phys. A* 124, 821. doi:10.1007/s00339-018-2238-5
- Spriano, S., Yamaguchi, S., Baino, F., and Ferraris, S. (2018). A critical review of multifunctional titanium surfaces: New frontiers for improving osseointegration and host response, avoiding bacteria contamination. *Acta Biomater.* 79, 1–22. doi:10.1016/j.actbio.2018.08.013
- Tan, G., Ouyang, K., Wang, H., Zhou, L., Wang, X., Liu, Y., et al. (2016). Effect of Amino-, Methyl- and Epoxy-Silane Coupling as a Molecular Bridge for Formatting a Biomimetic hydroxyapatite coating on titanium by electrochemical deposition. *J. Mater. Sci. Technol.* 32, 956–965. doi:10.1016/j.jmst.2016.07.012
- Tsukanaka, M., Fujibayashi, S., Takemoto, M., Matsushita, T., Kokubo, T., Nakamura, T., et al. (2016). Bioactive treatment promotes osteoblast differentiation on titanium materials fabricated by selective laser melting technology. *Dent. Mater. J.* 35, 118–125. doi:10.4012/dmj.2015-127
- Turnbull, G., Clarke, J., Picard, F., Riches, P., Jia, L., Han, F., et al. (2018). 3D bioactive composite scaffolds for bone tissue engineering. *Bioact. Mater.* 3, 278–314. doi:10.1016/j.bioactmat.2017.10.001
- Van Hooreweder, B., Apers, Y., Lietaert, K., and Kruth, J. P. (2017). Improving the fatigue performance of porous metallic biomaterials produced by Selective Laser Melting. *Acta Biomater.* 47, 193–202. doi:10.1016/j.actbio.2016.10.005
- Wang, K., and Xiong, D. (2018). Construction of lubricant composite coating on Ti6Al4V alloy using micro-arc oxidation and grafting hydrophilic polymer. *Mater. Sci. Eng. C* 90, 219–226. doi:10.1016/j.msec.2018.04.057
- Wang, S., Liu, L., Li, K., Zhu, L., Chen, J., and Hao, Y. (2019). Pore functionally graded Ti6Al4V scaffolds for bone tissue engineering application. *Mater. Des.* 168, 107643. doi:10.1016/j.matdes.2019.107643
- Wilson, C. J., Clegg, R. E., Leavesley, D. I., and Percy, M. J. (2005). Mediation of biomaterial-cell interactions by adsorbed proteins: A review. *Tissue Eng.* 11, 1–18. doi:10.1089/ten.2005.11.1
- Wubneh, A., Tsekoura, E. K., Ayranci, C., and Uludağ, H. (2018). Current state of fabrication technologies and materials for bone tissue engineering. *Acta Biomater.* 80, 1–30. doi:10.1016/j.actbio.2018.09.031
- Zhang, J., Zhou, W., Wang, H., Lin, K., and Chen, F. (2019). 3D-printed surface promoting osteogenic differentiation and angiogenic factor expression of BMSCs on Ti6Al4V implants and early osseointegration *in vivo*. *J. Mater. Sci. Technol.* 35, 336–343. doi:10.1016/j.jmst.2018.09.063
- Zhao, D., Tang, F., Min, L., Lu, M., Wang, J., Zhang, Y., et al. (2020). Intercalary reconstruction of the "Ultra-Critical sized bone defect" by 3D-printed porous Prosthesis after Resection of tibial Malignant Tumor. *Cmar* Vol. 12, 2503–2512. doi:10.2147/cmar.s245949
- Zhao, X., Ren, X., Wang, C., Huang, B., Ma, J., Ge, B., et al. (2020). Enhancement of hydroxyapatite formation on titanium surface by alkali heat treatment combined with induction heating and acid etching. *Surf. Coatings Technol.* 399, 126173. doi:10.1016/j.surfcoat.2020.126173
- Zhao, Y., and Xiong, T. Y. (2012). Formation of bioactive titania films under specific anodisation conditions. *Surf. Eng.* 28 (5), 371–376. doi:10.1179/174329409x409512



OPEN ACCESS

EDITED BY

Yanjin Lu,
Fujian Institute of Research on the
Structure of Matter (CAS), China

REVIEWED BY

Longgang Wang,
Yanshan University, China
Xu Chen,
China Medical University, China
Wei Zheng,
Fujian Institute of Research on the
Structure of Matter (CAS), China

*CORRESPONDENCE

Shenghui Su,
sushenghui27@163.com
Jiuzao Lin,
gykndsy@163.com
Xiaoyong Wang,
wxyong1999@163.com

SPECIALTY SECTION

This article was submitted to
Biomaterials and Bio-Inspired Materials,
a section of the journal
Frontiers in Materials

RECEIVED 11 July 2022

ACCEPTED 15 August 2022

PUBLISHED 27 September 2022

CITATION

Zhou C, Su S, Fan J, Lin J and Wang X
(2022), Engineered electrospun
poly(lactic-co-glycolic acid)/Si₃N₄
nanofiber scaffold promotes
osteogenesis of mesenchymal
stem cell.
Front. Mater. 9:991018.
doi: 10.3389/fmats.2022.991018

COPYRIGHT

© 2022 Zhou, Su, Fan, Lin and Wang.
This is an open-access article
distributed under the terms of the
Creative Commons Attribution License
(CC BY). The use, distribution or
reproduction in other forums is
permitted, provided the original
author(s) and the copyright owner(s) are
credited and that the original
publication in this journal is cited, in
accordance with accepted academic
practice. No use, distribution or
reproduction is permitted which does
not comply with these terms.

Engineered electrospun poly(lactic-co-glycolic acid)/Si₃N₄ nanofiber scaffold promotes osteogenesis of mesenchymal stem cell

Changsong Zhou¹, Shenghui Su^{1*}, Jiwen Fan², Jiuzao Lin^{1*} and Xiaoyong Wang^{1*}

¹Department of Orthopaedics, Ningde Municipal Hospital of Ningde Normal University, Ningde, Fujian, China, ²Department of Orthopaedics, Nanfang Hospital, Southern Medical University, Guangzhou, China

Nanofibers show promise as bone tissue engineering scaffolds (BTESs). In this study, electrospun poly (lactic-co-glycolic acid) (PLGA)/silicon nitride (Si₃N₄) composite nanofiber membranes were formed and the osteogenesis capability of mesenchymal stem cells (MSC) from the scaffold marrow was investigated. By modifying the different properties of Si₃N₄ in the PLGA, two hybrid scaffolds were successfully prepared, including the PLGA/Si₃N₄ (1 wt.%) nanofiber scaffold and PLGA/Si₃N₄ (2 wt.%) nanofiber scaffold. The diameter of the fiber nanofiber scaffold PLGA/Si₃N₄ was decreased and the mechanical strength was increased compared to PLGA. *In vitro* studies showed better cell adhesion and proliferation on the PLGA/Si₃N₄ nanofiber scaffold compared to the PLGA nanofiber scaffold. The integration of Si₃N₄ promoted osteogenesis capacity by increasing the gene expression of bone-related proteins (BMP2, ALP, OPN, COL1a1, Runx2, and OCN), calcium deposits, and support of ALP activity compared to those for the PLGA nanofiber scaffold. Similarly, the PLGA/Si₃N₄ (2 wt.%) nanofiber scaffold showed better mechanics and biological activity compared to the PLGA/Si₃N₄ (1 wt.%) nanofiber scaffold. Overall, the PLGA/Si₃N₄ nanofiber scaffold showed potential as a promising hybrid scaffold for bone regeneration.

KEYWORDS

electrospinning, PLGA, Si₃N₄, bone tissue engineering scaffold, MSCs

Introduction

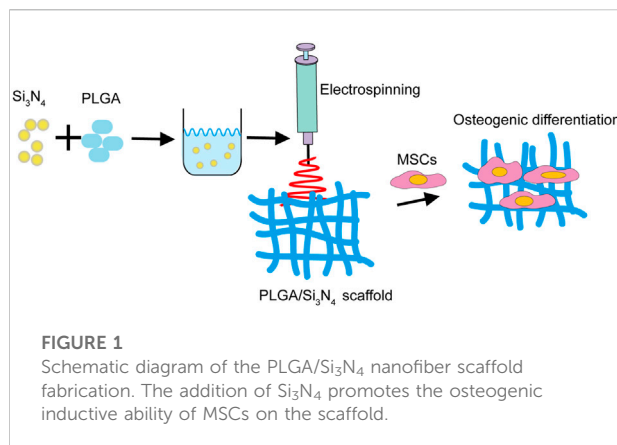
The demand is large for a graft or bone substitute to heal bone defects resulting from trauma, bone infections, osteomyelitis, necrosis, and tumors. BTES have been used as bone graft substitutes and overcome the limitations of all-/autografts.

From perspectives of developmental biology and tissue regeneration, an ideal BTES is designed by considering the following aspects: appropriate mechanical strength,

biological signaling factors, biomimetic structure, and selection of proper cell lineage (Lopes et al., 2018).

Natural and synthetic polymers with good biocompatibility are commonly used in the construction of BTES (Bharadwaz and Jayasuriya, 2020). While flexibility in processing and stability in artificial and mechanical strength are some advantages of synthetic polymers, they may lead to weak immune responses (Tamayol et al., 2013). Synthetic polymers such as polycaprolactone (PCL) (Heydari et al., 2017), poly (glycolic acid) (PGA) (Telemeco et al., 2005), poly (lactic-co-glycolic acid) (PLGA) (Loureiro et al., 2020), polyhydroxybutyrate (PHB) (Zhou et al., 2017), poly (propylene fumarate) (PPF) (Diez-Pascual and Diez-Vicente, 2017), and polycaprolactone (PLGA) show high-level mechanical properties (Bose et al., 2012). PLGA additionally shows high compatibility, as well as good biodegradability, chemical stability, thermal stability, nontoxicity, and histocompatibility and is widely used in the production and processing of drug carriers and tissue engineering scaffolds, and for wound healing [10]. The hydrophobic surface of PLGA results from ester bonds and high molecular weight, which lead to decreased surface wettability, which is a challenge in scaffold construction (Miguel et al., 2018). In addition, the low mechanical strength of pure PLGA scaffolds limits its application in osteogenic repair (Ji et al., 2011). Different forms of PLGA, such as porous scaffolds, films, fibers, nanoparticles, and microspheres, have been designed to overcome these shortcomings (Bose et al., 2018); Compounding with other materials is also another method used for the optimization of this polymer (Turnbull et al., 2018).

The most common fillers in BTES are bioactive glass (Turnbull et al., 2018), ceramic, and nanosheet materials such as Laponite, black phosphorus, graphene, and oxide. Compared to other organic 2D sheet materials, the covalent Si-N bonds of Si_3N_4 show cleavage. A silicon-rich layer is formed on the substrate surface, promoting hydroxyapatite formation and hydroxyapatite cell adhesion like bioactive glass. This method produces bioactive materials with the strongest known osseointegration ability (Zanocco et al., 2019). Moreover, the nitrogen released from Si_3N_4 plays a fundamental role in stimulating bone²¹ and also provides an antibacterial effect (Boschetto et al., 2020). The angiogenic and osteogenic activities of silicon ions have also been widely reported. Multiscale porous structures could provide enhanced protein adsorption (Zhu et al., 2017), regulation of cell behavior related to osteogenic differentiation (Kim et al., 2017), and vascular ingrowth, which is the precursor and basis for bone formation (Stegen et al., 2015). Electrospinning is a more effective and advantageous method to manage the final unique structures and properties of scaffolds compared



to 3D printing and other traditional methods (Jun et al., 2018).

Based on the excellent osteogenic regeneration potential of Si_3N_4 , this study fabricated a novel composite scaffold doped with PLGA and Si_3N_4 by electrospinning (Figure 1). This work aimed to integrate the desired properties of PLGA and Si_3N_4 in a nanofiber scaffold. The surface topography, mechanical characteristics, and bioactivity of the scaffolds were examined by SEM, tension test, and MTT assay. This nanofiber scaffold may contribute to improved bone regeneration.

Materials and methods

Fabrication of PLGA/ Si_3N_4 scaffolds

The desired amount of PLGA (240 mg) was dissolved in 2 ml of hexafluoroisopropanol (HFIP, Macklin, China) solvent and stirred for 24 h. Separately, Si_3N_4 (20–50 nm, XFnano, China) particle powders were well dispersed in HFIP solvent. The two solutions were mixed by stirring for 24 h. The concentration of PLGA in HFIP was 12% w/v, while the Si_3N_4 amounts varied according to PLGA. The scaffolds were constructed on an electrospinning machine (YFSP-T, Yunfan (Tianjin) Instrument Co., Ltd., China). Finally, PLGA, PLGA/ Si_3N_4 (1 wt.%), and PLGA/ Si_3N_4 (2 wt.%) nanofiber scaffolds were fabricated.

Characterization of the nanofiber scaffolds

A scanning electron microscope (SEM, Zeiss, Axiovert 200, Germany) was used to assess the morphology of the electrospun PLGA, PLGA/ Si_3N_4 (1 wt.%), and PLGA/ Si_3N_4

TABLE 1 Primers used for the qRT-PCR analysis.

Gene	Forward primer	Reverse primer
<i>GAPDH</i>	TCCAGTATGACTCTACCCACG	CACGACATACTCAGCACCAG
<i>BMP2</i>	TGCTCAGCTTCCATCACGAA	AATTTTGAGCTGGCTGTGGC
<i>OPN</i>	CCAGCCAAGGACCAACTACA	CCAAGTGGCTACAGCATCTGA
<i>COL1a1</i>	GATCCTGCCGATGTCGCTAT	GGGACTTCTTGAGGTTGCCA
<i>OCN</i>	GGCGCTACCTCAACAATGGA	GGCAACACATGCCCTAAACG
<i>ALP</i>	GTTACAAGGTGGTGGACGGT	ACAGTGGTCAAGGTTGGCTC
<i>Runx2</i>	GTGGCCAGGTTCAACGATCT	TGAGGAATGCGCCCTAAATCA

(2 wt.%) nanofiber scaffolds. All scaffolds were analyzed by SEM sputtered with a gold layer. Additionally, 30 pieces from each group were cached to calculate fiber diameters by using Image J pro.

The mechanical properties of the PLGA, PLGA/Si₃N₄ (1 wt.%), and PLGA/Si₃N₄ (2 wt.%) nanofiber scaffold were characterized using the same sample size (30 × 10 mm²). The mechanical properties were assessed using a universal mechanical testing machine (Instron 68SC-05, United States) at a crosshead speed of 1.5 mm/min.

Cytocompatibility assessment of MSCs

Marrow mesenchymal stem cells (MSCs) were cultured on the different scaffolds marked as control, PLGA nanofiber scaffold, PLGA/Si₃N₄ (1 wt.%) nanofiber scaffold, and PLGA/Si₃N₄ (2 wt.%) nanofiber scaffold for 3 days. The MTT assay (Sigma-Aldrich, United States) was used to evaluate MSC proliferation after cell seeding on the scaffolds and without a scaffold (control).

After the MSCs were cultured on the PLGA, PLGA/Si₃N₄ (1 wt.%), and PLGA/Si₃N₄ (2 wt.%) nanofiber scaffolds for 3 days, the MSCs-nanofiber scaffolds were incubated with 1 μM calcein-AM and 1 μM PI for 30 min while protected from light. After washing three times with phosphate-buffered saline (PBS), images of cell morphology and cell interaction with the nanofiber scaffold in each group were captured using a fluorescence imaging microscope (Zeiss, Axiovert 200, Germany).

Gene expression

After the MSCs were cultured on the Control and PLGA, PLGA/Si₃N₄ (1 wt.%), and PLGA/Si₃N₄ (2 wt.%) nanofiber scaffolds for 3, 7, and 14 days, real-time qPCR (qRT-qPCR) was performed. The primers for these are shown in Table 1.

Alkaline phosphatase activity assay

After the MSCs were cultured on the Control and PLGA, PLGA/Si₃N₄ (1 wt.%), and PLGA/Si₃N₄ (2 wt.%) nanofiber scaffolds for 7 days, alkaline phosphatase activity (ALP) was measured as previously described (Solarbio, China) (Yin et al., 2011).

Alizarin red S staining

After the MSCs were cultured on the Control and PLGA, PLGA/Si₃N₄ (1 wt.%), and PLGA/Si₃N₄ (2 wt.%) nanofiber scaffolds for 7 days, ARS (Sigma-Aldrich, United States) staining was performed.

Statistical analysis

One-way analysis of variances (ANOVA) was used to compare more than two groups. Quantitative data were expressed as mean ± SD, with **p* < 0.05, ***p* < 0.01, and ****p* < 0.001 considered statistically significant.

Results and discussion

Characterization of the nanofiber scaffolds

The microstructures of the PLGA, PLGA/Si₃N₄ (1 wt.%), and PLGA/Si₃N₄ (2 wt.%) nanofiber scaffolds were observed by SEM, as shown in Figure 2. The addition of Si₃N₄ made the nanofiber scaffolds more uniform in size (Figure 2A). The diameter of pure PLGA nanofiber scaffold fibers ranged from 200 to 900 nm, with an average diameter of 429.3 ± 136.7 nm (Figures 2B,C). The composite PLGA/Si₃N₄ (1 wt.%) nanofiber scaffold showed a fiber diameter of around 100–500 nm, with an average diameter of 268.2 ± 66.7 nm. The further increase of Si₃N₄ up to 2 wt.% in the

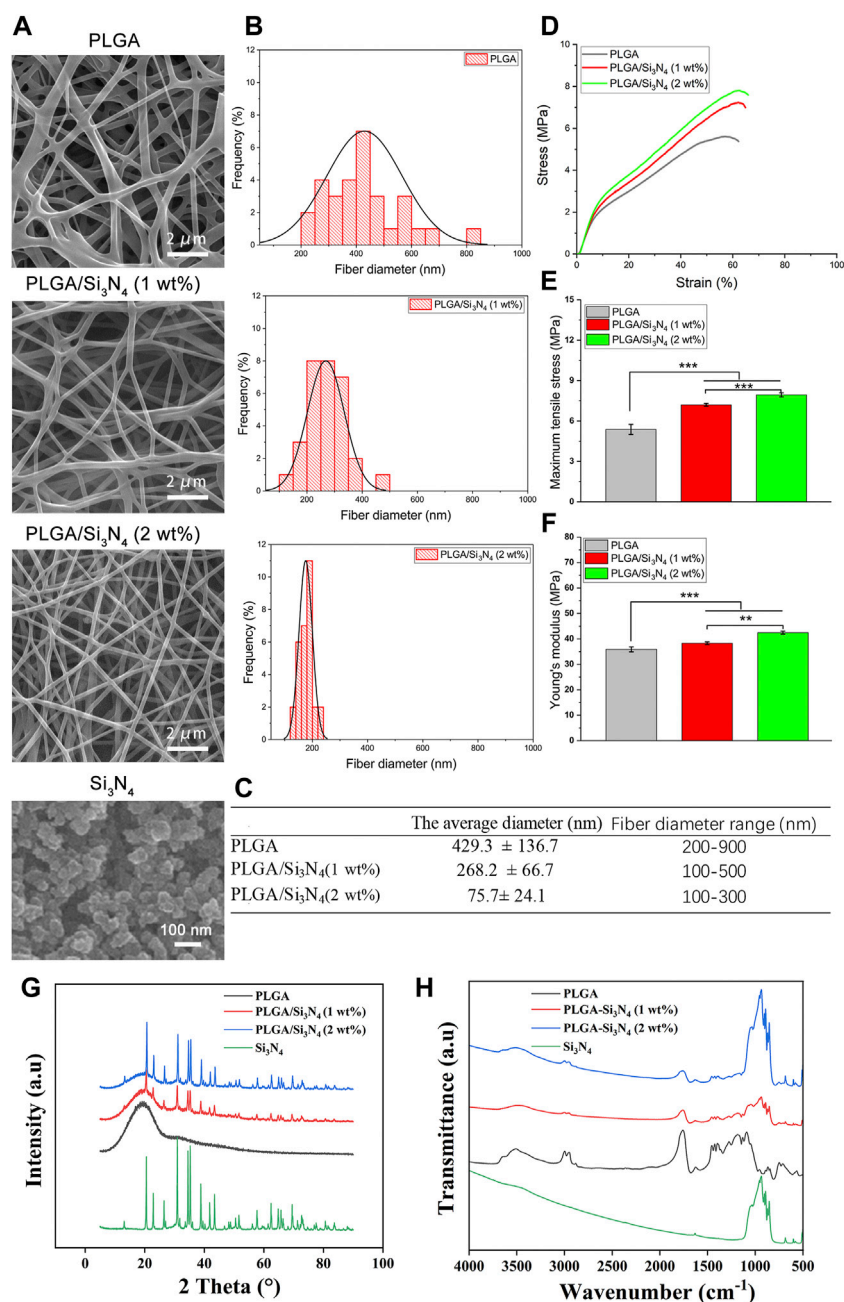


FIGURE 2

Characterization of the PLGA nanofiber scaffold, PLGA/Si₃N₄ (1 wt%), and PLGA/Si₃N₄ (2 wt%) nanofiber scaffold. (A) SEM images of the electrospinning fibrous scaffolds and Si₃N₄. Scale bar: 2000 nm. (B) distribution of fiber diameters in the nanofiber scaffolds. (C) average fiber diameter of the nanofiber scaffolds. (D) typical tensile stress-strain curves of the nanofiber scaffolds. (E) maximum tensile stress of the nanofiber scaffolds. (F) Young's modulus of the nanofiber scaffolds. (G) XRD and (H) FTIR results for different groups of Si₃N₄, PLGA, PLGA/Si₃N₄ (1 wt%), and PLGA/Si₃N₄ (2 wt%).

PLGA/Si₃N₄ (1 wt%) nanofiber scaffold decreased the range of fibers to 100–300 nm, with an average diameter of 175.7 ± 24.1 nm. Compared to the PLGA nanofiber scaffold and PLGA/Si₃N₄ (1 wt%) nanofiber scaffold, the PLGA/Si₃N₄ (2 wt%) nanofiber scaffold showed a smaller average diameter.

The stress-strain curves for the PLGA, PLGA/Si₃N₄ (1 wt%), and PLGA/Si₃N₄ (2 wt%) nanofiber scaffolds are shown in Figure 2D. The mechanical properties of the scaffolds are shown in Figures 2E,F. In the case of PLGA nanofiber scaffolds, the average maximum tensile strength and tensile modulus were 5.38 ± 0.37

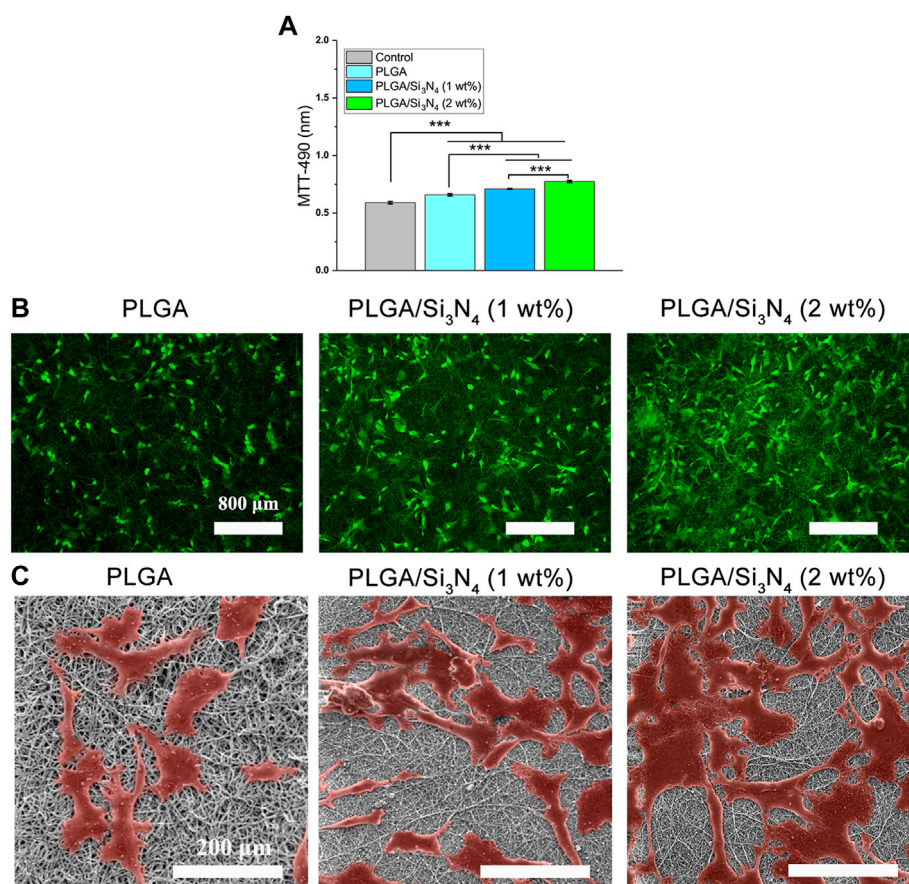


FIGURE 3

Control, PLGA nanofiber scaffold, PLGA/Si₃N₄ (1 wt.%) nanofiber scaffold, and PLGA/Si₃N₄ (2 wt.%) nanofiber scaffold cultured with MSCs for 3 days. **(A)** MTT assay results. **(B)** calcein-AM/PI stained for cell viability. scale bar: 800 μ m. **(C)** SEM results. Scale bar: 200 μ m.

(MPa) and 35.86 ± 0.95 (MPa), respectively. At 1 wt.% and 2 wt.% of Si₃N₄, the average final tensile strength significantly increased to 7.19 ± 0.11 (MPa) and 7.94 ± 0.15 (MPa), respectively. The Young's modulus also significantly increased to 38.28 ± 0.52 (MPa) and 42.46 ± 0.57 (MPa), respectively.

The mechanism by which inorganic nanoparticles enhance the polymer phase was summarized in a previous study (Li et al., 2018). Similarly, PLGA nanofiber scaffold chains combine on the surface of Si₃N₄, producing more loops, tails, and strands. As a result, the fiber diameter of the PLGA/Si₃N₄ nanofiber scaffolds decreased with increasing Si₃N₄ content. A higher mechanical strength of the periosteum is more favorable for the osteogenic differentiation of BMSCs (Yang et al., 2021). Compared to smooth surfaces, the rougher surfaces of the PLGA/Si₃N₄ nanofiber scaffolds were favorable for osteogenic differentiation of bone marrow mesenchymal stem cells. Finally, interconnected porosity with an adequate pore size benefits the diffusion of growth factors, cells, oxygen, and

nutrients and the exchange of waste products throughout the scaffold.

The results of XRD and FTIR showed that Si₃N₄ was compounded into the PLGA matrix. The mainly XRD diffraction peaks of Si₃N₄ appeared clearly in the Si₃N₄, PLGA/Si₃N₄ (1 wt.%), and PLGA/Si₃N₄ (2 wt.%) groups, while PLGA showed amorphous peaks from 20° to 30°. Regarding the FTIR of Si₃N₄, the absorption peak of the Si-N bond is in the range of 800–1100 cm⁻¹ while 1631 cm⁻¹ is the shear vibration of -NH. Regarding the FTIR of PLGA, the absorption peaks at 2954 cm⁻¹ and 2923 cm⁻¹ are caused by the stretching vibrations of methyl and methylene, while the strong absorption peaks at 1759, 1182, and 1132 cm⁻¹ represent the stretching vibrations of C=O, C-O-C, and C-O bonds, respectively. Most of the characteristic peaks from different materials were displayed on PLGA/Si₃N₄ (1 wt.%) and PLGA/Si₃N₄ (2 wt.%), as in XRD, which proved the addition of Si₃N₄ to the PLGA matrix.

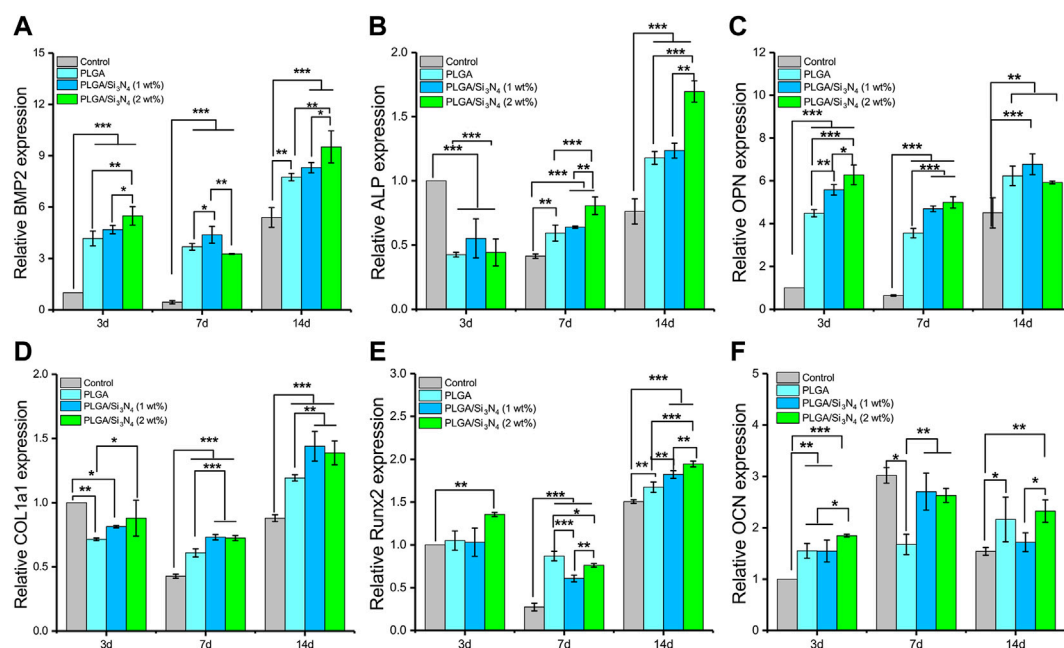


FIGURE 4

Gene expression of MSCs cultured on the PLGA nanofiber scaffold, PLGA/Si₃N₄ (1 wt.%) nanofiber scaffold, and PLGA/Si₃N₄ (2 wt.%) nanofiber scaffold for 3, 7, and 14 days. (A) BMP2 expression. (B) ALP expression. (C) OPN expression. (D) COL1a1 expression. (E) Runx2 expression. (F) OCN expression.

Biocompatibility of the nanofiber scaffolds

To verify cell proliferation and cytotoxicity of the nanofiber, the cell viability on the scaffolds was assessed by MTT assay. As shown in Figure 3A, a higher number of live cells was observed on the PLGA/Si₃N₄ (2 wt.%) scaffold compared to those on the pure PLGA and PLGA/Si₃N₄ (1 wt.%) scaffolds.

The results of staining to assess the viability of MSCs using live and dead cells are shown in Figure 3B. More surviving cells were observed on the PLGA/Si₃N₄ nanofiber scaffolds. A slightly higher number of cells was present on the PLGA/Si₃N₄ (2 wt.%) nanofiber scaffold compared to the PLGA/Si₃N₄ (1 wt.%) nanofiber scaffold. Moreover, the MSCs on the PLGA/Si₃N₄ (2 wt.%) nanofiber scaffold showed abundant acicular tentacles, which indicated better cell adhesion. The results showed that the PLGA/Si₃N₄ (2 wt.%) nanofiber scaffold effectively supported MSC proliferation.

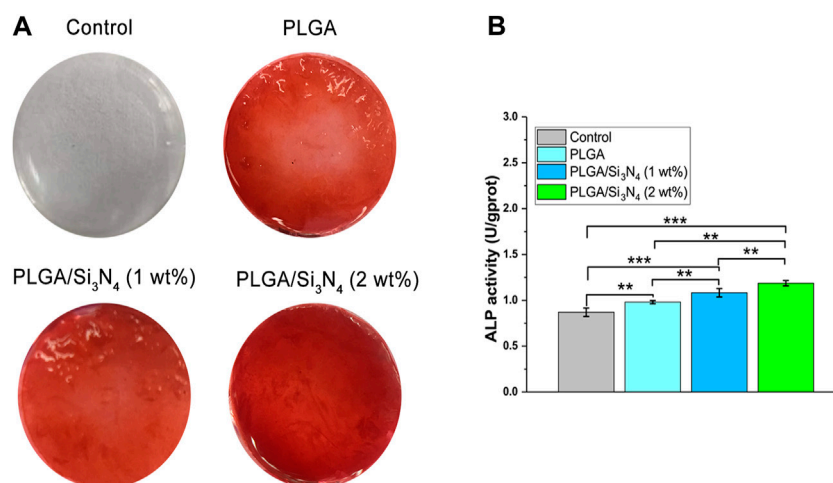
In vitro cellular responses including cell morphology and spreading are shown in Figure 3C. The PLGA matrix surfaces showed fewer cells compared to the PLGA/Si₃N₄ nanofiber scaffolds, likely due to the hydrophobic surface of the PLGA nanofiber scaffold. The overall cell morphology could be profoundly influenced by the micro-scale patterns (Rahmati et al., 2020). Several cells that were more spread out were observed on the PLGA/

Si₃N₄ (1 wt.%) nanofiber scaffold. Higher numbers of adherent and spreading cells were observed on the PLGA/Si₃N₄ (2 wt.%) nanofiber scaffold due to the additional Si₃N₄.

PLGA/Si₃N₄ nanofiber scaffolds showed good biocompatibility and supported MSC adhesion, as shown by the results of the MTT assays, calcein-AM/PI staining, and SEM (Figure 3). Increased Si₃N₄ in the scaffold showed better effects on supporting cell growth, as demonstrated by the higher OD value of PLGA/Si₃N₄ (2 wt.%) nanofiber scaffold compared to that for the PLGA/Si₃N₄ (1 wt.%) nanofiber scaffold. The biocompatibility of silicon nitride has been established since the late 1980s. Three months after the implantation of silicon nitride ceramics into the bone marrow cavity of the rabbit femur, no inflammatory reaction in the tissue around the implant was observed (Howlett et al., 1989). Based on these results, scaffolds consisting of Si₃N₄ could enable efficient cell adhesion and proliferation.

Enhanced osteogenic differentiation by PLGA/Si₃N₄ *in vitro*

To evaluate the effect of Si₃N₄ nanoparticles on promoting osteogenic differentiation, qRT-PCR was performed to

**FIGURE 5**

Nanofiber scaffolds supported osteogenic differentiation. **(A)** ARS staining of the nanofiber scaffolds at 7 days. The ARS solution stains calcium deposits red, with darker red indicating more calcium deposits. **(B)** ALP activity assay at 7 days for the nanofiber scaffold, PLGA/Si₃N₄ (1 wt.%) nanofiber scaffold, and PLGA/Si₃N₄ (2 wt.%) nanofiber scaffold.

determine the gene expression levels of *BMP2*, *ALP*, *OPN*, *COL1a1*, *Runx2*, and *OCN*. PLGA/Si₃N₄ (1 wt.%) and PLGA/Si₃N₄ (2 wt.%) showed increased gene expression levels compared to those in PLGA (Figure 4). With the addition of a higher Si₃N₄ dose (2 wt.%), the nanofiber scaffold showed higher expression levels of osteogenic markers compared to a lower Si₃N₄ dose (1 wt.%). More specifically, as shown in Figure 4, PLGA/Si₃N₄ with 1 wt.% and 2 wt.% showed higher gene expression levels of *BMP2* (on days 3 and 14), *ALP* (on days 7 and 14), *OPN* (on days 3 and 7), *COL1a1* (on days 3 and 14), *Runx2* (on day 14), and *OCN* (on day 3). PLGA/Si₃N₄ (1 wt.%) showed higher gene expression levels than those in PLGA for *BMP2* (days 3 and 14), *ALP* (days 7 and 14), *OPN* (days 3 and 7), *COL1a1* (day 3), *Runx2* (day 14), and *OCN* (day 14). PLGA/Si₃N₄ (2 wt.%) had higher gene expression levels than those in PLGA for *BMP2* (days 3 and 14), *ALP* (days 7 and 14), *OPN* (days 3 and 7), *COL1a1* (days 3, 7, and 14), *Runx2* (days 3 and 14), and *OCN* (days 3, 7, and 14). Overall, PLGA/Si₃N₄ (2 wt.%) showed a nearly 2-fold increase in *BMP2* expression, 3.1-fold in *ALP*, 1.4-fold in *OPN*, 1.5-fold in *COL1a1*, 0.6-fold in *Runx2*, and 1.9-fold in *OCN* to 14 days. Overall, PLGA containing Si₃N₄ (1 wt.%) and Si₃N₄ (2 wt.%) significantly supported the gene expression of bone-related proteins.

In addition, the PLGA/Si₃N₄ scaffold osteogenic performance was assessed according to mineralization measured by ARS (Figure 5A) and ALP activity (Figure 5B). On the seventh day, the PLGA/Si₃N₄ (1 wt.%) nanofiber membrane gradually showed deeper ARS staining compared to that in the PLGA nanofiber membrane. With an increase in Si₃N₄ from 1 wt.% to 2 wt.%, the PLGA/Si₃N₄ (2 wt.%) nanofiber membrane showed the darkest red

and most calcium nodes in MSC. ARS staining increased with increased Si₃N₄ concentration, suggesting that Si₃N₄ may support the formation of calcium nodes. Additionally, the ALP activity was consistent with the results of alizarine red staining. Compared to the PLGA nanofiber membrane, ALP activity increased from 1 wt.% to 2 wt.% Si₃N₄, with the PLGA/Si₃N₄ (2 wt.%) nanofiber membrane showing the highest ALP activity. PLGA/Si₃N₄ (2 wt.%) also stimulated higher levels of *in vitro* mineralization compared to PLGA/Si₃N₄ (1 wt.%).

As a regulated molecule in osteogenic differentiation, BMP2 plays important roles in the whole process of endochondral ossification (Peng et al., 2005). The addition of Si₃N₄ can significantly promote the autocrine and paracrine signals of BMP2 to promote osteogenesis. Furthermore, bone formation and regeneration is a complex multi-factor process, in which transcription factors are important influencing factors. High expression of active ALP and RUNX2 indicates osteoblast differentiation into mature osteocytes (Chen et al., 2016). As the Si₃N₄ content increased, the expression of osteogenic promoter genes significantly increased, thus demonstrating the ability of Si₃N₄ to promote osteogenesis. Similarly, the expression and maintenance of the extracellular matrix are also important signals for BMSCs in osteogenic differentiation. During long-term culture (14 days), *COL1a1* and *OCN* expression levels were significantly higher in PLGA/Si₃N₄ (2 wt.%) nanofiber scaffolds compared to the levels in the other scaffolds.

The control showed hardly any ARS coloring, while each composite membrane showed bright red coloring. Among them, PLGA/Si₃N₄ nanofiber scaffold (2 wt.%) showed the deepest red due to an appropriate osteogenic mechanical microenvironment. These results validate the osteogenic effects of PLGA/Si₃N₄ electrospun films.

Conclusion

This study successfully manufactured a Si_3N_4 -integrated PLGA nanofiber scaffold using the electrospinning technique. This scaffold showed good biological and mechanical properties. The Si_3N_4 nanoparticle composition significantly facilitated osteogenic differentiation and mineralization of MSCs *in vitro* based on different Si_3N_4 content, revealing the role of Si_3N_4 in electrospun nanofiber scaffolds. These results verify the potential of PLGA/ Si_3N_4 scaffolds for BTES.

Data availability statement

The original contributions presented in the study are included in the article/supplementary material; further inquiries can be directed to the corresponding authors.

Author contributions

Conceptualization, CZ; methodology, CZ and SS; formal analysis, SS and JL; data curation, CZ and JF; writing-

original draft preparation, CZ; writing-review and editing, JL and XW.

Funding

This study was supported by the Scientific Research Project of Medical Technology Improvement of Ningde Health Committee, Fujian Province, China (Grant number: 2020003).

Conflict of interest

The authors declare that the research was conducted in the absence of any commercial or financial relationships that could be construed as a potential conflict of interest.

Publisher's note

All claims expressed in this article are solely those of the authors and do not necessarily represent those of their affiliated organizations, or those of the publisher, the editors, and the reviewers. Any product that may be evaluated in this article, or claim that may be made by its manufacturer, is not guaranteed or endorsed by the publisher.

References

- Bharadwaz, A., and Jayasuriya, A. C. (2020). Recent trends in the application of widely used natural and synthetic polymer nanocomposites in bone tissue regeneration. *Mater. Sci. Eng. C* 110, 110698. doi:10.1016/j.msec.2020.110698
- Boschetto, F., Marin, E., Ohgiani, E., Adachi, T., Zanocco, M., Horiguchi, S., et al. (2020). Surface functionalization of PEEK with silicon nitride. *Biomed. Mat.* 16, 015015. doi:10.1088/1748-605x/abb6b1
- Bose, S., Ke, D., Sahasrabudhe, H., and Bandyopadhyay, A. (2018). Additive manufacturing of biomaterials. *Prog. Mat. Sci.* 93, 45–111. doi:10.1016/j.pmatsci.2017.08.003
- Bose, S., Roy, M., and Bandyopadhyay, A. (2012). Recent advances in bone tissue engineering scaffolds. *Trends Biotechnol.* 30, 546–554. doi:10.1016/j.tibtech.2012.07.005
- Chen, Q., Shou, P., Zheng, C., Jiang, M., Cao, G., Yang, Q., et al. (2016). Fate decision of mesenchymal stem cells: Adipocytes or osteoblasts? *Cell Death Differ.* 23, 1128–1139. doi:10.1038/cdd.2015.168
- Diez-Pascual, A. M., and Diez-Vicente, A. L. (2017). Multifunctional poly(glycolic acid-co-pyrene fumarate) electrospun fibers reinforced with graphene oxide and hydroxyapatite nanorods. *J. Mat. Chem. B* 5, 4084–4096. doi:10.1039/c7tb00497d
- Heydari, Z., Mohebbi-Kalhor, D., and Afarani, M. S. (2017). Engineered electrospun polycaprolactone (PCL)/octacalcium phosphate (OCP) scaffold for bone tissue engineering. *Mater. Sci. Eng. C* 81, 127–132. doi:10.1016/j.msec.2017.07.041
- Howlett, C. R., McCartney, E., and Ching, W. (1989). The effect of silicon nitride ceramic on rabbit skeletal cells and tissue. An *in vitro* and *in vivo* investigation. *Clin. Orthop. Relat. Res.* 244, 293–304. doi:10.1097/00003086-198907000-00032
- Ji, W., Sun, Y., Yang, F., van den Beucken, J. J., Fan, M., Chen, Z., et al. (2011). Bioactive electrospun scaffolds delivering growth factors and genes for tissue engineering applications. *Pharm. Res.* 28, 1259–1272. doi:10.1007/s11095-010-0320-6
- Jun, I., Han, H. S., Edwards, J. R., and Jeon, H. (2018). Electrospun fibrous scaffolds for tissue engineering: Viewpoints on architecture and fabrication. *Int. J. Mol. Sci.* 19, 745. doi:10.3390/ijms19030745
- Kim, J. J., El-Fiqi, A., and Kim, H. W. (2017). Synergetic cues of bioactive nanoparticles and nanofibrous structure in bone scaffolds to stimulate osteogenesis and angiogenesis. *ACS Appl. Mat. Interfaces* 9, 2059–2073. doi:10.1021/acsami.6b12089
- Li, A., Jia, Y., Sun, S., Xu, Y., Minsky, B. B., Stuart, M. A. C., et al. (2018). Mineral-enhanced polyacrylic acid hydrogel as an oyster-inspired organic-inorganic hybrid adhesive. *ACS Appl. Mat. Interfaces* 10, 10471–10479. doi:10.1021/acsami.8b01082
- Lopes, D. L., Martins-Cruz, C., Oliveira, M. B., and Mano, J. F. (2018). Bone physiology as inspiration for tissue regenerative therapies. *Biomaterials* 9, 240–275. doi:10.1016/j.biomaterials.2018.09.028
- Loureiro, J., Torres, A. L., Neto, T., Aguiar, P., Barrias, C. C., Pinto, M. T., et al. (2020). Corrigendum to "Conjugation of the T1 sequence from CCN1 to fibrin hydrogels for therapeutic vascularization" [Mater. Sci. & Eng. C. 104 (2019) 109847]. *Mater. Sci. Eng. C* 108, 110514. doi:10.1016/j.msec.2019.110514
- Miguel, S. P., Figueira, D. R., Simoes, D., Ribeiro, M. P., Coutinho, P., Ferreira, P., et al. (2018). Electrospun polymeric nanofibers as wound dressings: A review. *Colloids Surfaces B Biointerfaces* 169, 60–71. doi:10.1016/j.colsurfb.2018.05.011
- Peng, H., Usas, A., Olshanski, A., Ho, A. M., Gearhart, B., Cooper, G. M., et al. (2005). VEGF improves, whereas sFlt1 inhibits, BMP2-induced bone formation and bone healing through modulation of angiogenesis. *J. Bone Min. Res.* 20, 2017–2027. doi:10.1359/jbmr.050708
- Rahmati, M., Silva, E. A., Reseland, J. E., and Haugen, H. J. (2020). Biological responses to physicochemical properties of biomaterial surface. *Chem. Soc. Rev.* 49, 5178–5224. doi:10.1039/d0cs00103a
- Stegen, S., van Gestel, N., and Carmeliet, G. (2015). Bringing new life to damaged bone: The importance of angiogenesis in bone repair and regeneration. *Bone* 70, 19–27. doi:10.1016/j.bone.2014.09.017

- Tamayol, A., Akbari, M., Annabi, N., Paul, A., Khademhosseini, A., and Juncker, D. (2013). Fiber-based tissue engineering: Progress, challenges, and opportunities. *Biotechnol. Adv.* 31, 669–687. doi:10.1016/j.biotechadv.2012.11.007
- Telemeco, T. A., Ayres, C., Bowlin, G. L., Wnek, G. E., Boland, E. D., Cohen, N., et al. (2005). Regulation of cellular infiltration into tissue engineering scaffolds composed of submicron diameter fibrils produced by electrospinning. *Acta Biomater.* 1, 377–385. doi:10.1016/j.actbio.2005.04.006
- Turnbull, G., Clarke, J., Picard, F., Riches, P., Jia, L., Han, F., et al. (2018). 3D bioactive composite scaffolds for bone tissue engineering. *Bioact. Mat.* 3, 278–314. doi:10.1016/j.bioactmat.2017.10.001
- Yang, G., Liu, H., Cui, Y., Li, J., Zhou, X., Wang, N., et al. (2021). Bioinspired membrane provides periosteum-mimetic microenvironment for accelerating vascularized bone regeneration. *Biomaterials* 268, 120561. doi:10.1016/j.biomaterials.2020.120561
- Yin, G., Huang, Z., Deng, M., Zeng, J., and Gu, J. (2011). Preparation and cell response of bio-mineralized Fe₃O₄ nanoparticles. *J. Colloid Interface Sci.* 363, 393–402. doi:10.1016/j.jcis.2011.07.009
- Zanocco, M., Marin, E., Rondinella, A., Boschetto, F., Horiguchi, S., Zhu, W., et al. (2019). The role of nitrogen off-stoichiometry in the osteogenic behavior of silicon nitride bioceramics. *Mater. Sci. Eng. C* 105, 110053. doi:10.1016/j.msec.2019.110053
- Zhou, T., Li, G., Lin, S., Tian, T., Ma, Q., Zhang, Q., et al. (2017). Electrospun poly(3-hydroxybutyrate-co-4-hydroxybutyrate)/graphene oxide scaffold: Enhanced properties and promoted *in vivo* bone repair in rats. *ACS Appl. Mat. Interfaces* 9, 42589–42600. doi:10.1021/acsami.7b14267
- Zhu, K., Shin, S. R., van Kempen, T., Li, Y. C., Ponraj, V., Nasajpour, A., et al. (2017). Gold nanocomposite bioink for printing 3D cardiac constructs. *Adv. Funct. Mat.* 27, 1605352. doi:10.1002/adfm.201605352



OPEN ACCESS

EDITED BY

Chunguang Yang,
Institute of Metal Research (CAS), China

REVIEWED BY

Wei-Jen Chang,
Taipei Medical University, Taiwan
Nils-Claudius Gellrich,
Hannover Medical School, Germany
Yonggang Yan,
Sichuan University, China

*CORRESPONDENCE

Andrea Meyer-Lindenberg,
Andrea.Meyer-Lindenberg@
chir.vetmed.uni-muenchen.de

SPECIALTY SECTION

This article was submitted to
Biomaterials,
a section of the journal
Frontiers in Bioengineering and
Biotechnology

RECEIVED 19 July 2022

ACCEPTED 05 September 2022

PUBLISHED 28 September 2022

CITATION

Kowalewicz K, Waselau A-C,
Feichtner F, Schmitt A-M, Brückner M,
Vorndran E and Meyer-Lindenberg A
(2022), Comparison of degradation
behavior and osseointegration of 3D
powder-printed calcium magnesium
phosphate cement scaffolds with
alkaline or acid post-treatment.
Front. Bioeng. Biotechnol. 10:998254.
doi: 10.3389/fbioe.2022.998254

COPYRIGHT

© 2022 Kowalewicz, Waselau,
Feichtner, Schmitt, Brückner, Vorndran
and Meyer-Lindenberg. This is an open-
access article distributed under the
terms of the [Creative Commons
Attribution License \(CC BY\)](#). The use,
distribution or reproduction in other
forums is permitted, provided the
original author(s) and the copyright
owner(s) are credited and that the
original publication in this journal is
cited, in accordance with accepted
academic practice. No use, distribution
or reproduction is permitted which does
not comply with these terms.

Comparison of degradation behavior and osseointegration of 3D powder-printed calcium magnesium phosphate cement scaffolds with alkaline or acid post-treatment

Katharina Kowalewicz¹, Anja-Christina Waselau¹,
Franziska Feichtner¹, Anna-Maria Schmitt², Manuel Brückner²,
Elke Vorndran² and Andrea Meyer-Lindenberg^{1*}

¹Clinic for Small Animal Surgery and Reproduction, Ludwig-Maximilians-University of Munich, Munich, Germany, ²Department for Functional Materials in Medicine and Dentistry, University of Würzburg, Würzburg, Germany

Due to the positive effects of magnesium substitution on the mechanical properties and the degradation rate of the clinically well-established calcium phosphate cements (CPCs), calcium magnesium phosphate cements (CMPCs) are increasingly being researched as bone substitutes. A post-treatment alters the materials' physical properties and chemical composition, reinforcing the structure and modifying the degradation rate. By alkaline post-treatment with diammonium hydrogen phosphate (DAHP, $(\text{NH}_4)_2\text{HPO}_4$), the precipitation product struvite is formed, while post-treatment with an acidic phosphate solution [e.g., phosphoric acid (PA, H_3PO_4)] results in precipitation of newberyite and brushite. However, little research has yet been conducted on newberyite as a bone substitute and PA post-treatment of CMPCs has not been described in the accessible literature so far. Therefore, in the present study, the influence of an alkaline (DAHP) or acid (PA) post-treatment on the biocompatibility, degradation behavior, and osseointegration of cylindrical scaffolds ($h = 5.1\text{ mm}$, $\varnothing = 4.2\text{ mm}$) produced from the ceramic cement powder $\text{Ca}_{0.75}\text{Mg}_{2.25}(\text{PO}_4)_2$ by the advantageous manufacturing technique of three-dimensional (3D) powder printing was investigated *in vivo*. Scaffolds of the material groups Mg225d (DAHP post-treatment) and Mg225p (PA post-treatment) were implanted into the cancellous part of the lateral femoral condyles in rabbits. They were evaluated up to 24 weeks by regular clinical, X-ray, micro-computed tomographic (μCT), and histological examinations as well as scanning electron microscopy (SEM) and energy dispersive X-ray spectroscopy (EDX) analysis and compared with tricalcium phosphate (TCP). All materials showed excellent biocompatibility and rapid osseointegration. While TCP degraded only slightly, the CMPCs showed almost complete degradation. Mg225d demonstrated significantly faster loss of form and demarcability from surrounding bone, scaffold volume reduction, and significantly greater degradation on the side towards the bone marrow than

to the cortex than Mg225p. Simultaneously, numerous bone trabeculae have grown into the implantation site. While these were mostly located on the side towards the cortex in Mg225d, they were more evenly distributed in Mg225p and showed almost the same structural characteristics as physiological bone after 24 weeks in Mg225p. Based on these results, the acid post-treated 3D powder-printed Mg225p is a promising degradable bone substitute that should be further investigated.

KEYWORDS

stanfieldite, farringtonite, newberyite, 3D powder printing, scaffold, biocompatibility, osseointegration, degradable bone substitute

1 Introduction

Bone substitutes are needed for the reconstruction of large bone defects that occur for example due to trauma, tumors, infections or congenital defects (Kheirallah and Almeshaly, 2016). Due to a longer life expectancy, there is a sharp increase in musculoskeletal diseases such as osteoporosis, bone infections or metastases and fractures, leading to an increase in bone-related medical treatments (Agarwal and García, 2015). Autografts are still the gold standard in the surgical management of critical size bone defects (Kolk et al., 2012). However, natural bone substitutes do not apply to all types of bone defects and carry various risks such as donor site infections or additional trauma in autografts and allografts (Laurie et al., 1984; Arrington et al., 1996) as well as rejection of the implanted material or transmission of diseases through allografts and xenografts (Keating and McQueen, 2001; Campana et al., 2014). Due to these disadvantages, there has been constant research into the development of synthetic bone substitutes in recent years, which have the advantages of defined porosity and chemical composition, precision-fit for any bone defect, sterility and unlimited availability (Zimmermann and Moghaddam, 2011; Kolk et al., 2012; Kheirallah and Almeshaly, 2016). Synthetic bone substitutes exist in various application forms such as granules, scaffolds, blocks or injectable pastes (Fillingham and Jacobs, 2016; Kheirallah and Almeshaly, 2016).

For the production of three-dimensional (3D), dimensionally stable bone substitutes, various additive manufacturing techniques are currently being investigated (Castilho et al., 2014a; Roseti et al., 2017). Using medical imaging data [e.g., computed tomography (CT)] or computer-aided design (CAD) models, the precision-fit production of patient specific implants is possible, which is particularly advantageous in case of large and anatomically complex bone defects (Peters et al., 2006; Castilho et al., 2014a; Castilho et al., 2014b; Brunello et al., 2016; Roseti et al., 2017; Zhang et al., 2019). 3D powder printing has emerged as a promising additive manufacturing technique with great potential for the layer-by-layer production of individual synthetic bone substitutes (Vorndran et al., 2008; Castilho et al., 2014a; Roseti et al., 2017). Raw materials are for example calcium phosphate (CaP), magnesium phosphate

(MgP) or calcium magnesium phosphate (CaMgP) cement powders (Klammert et al., 2010b; Castilho et al., 2014b; Kowalewicz et al., 2021). Due to the high printing accuracy of 3D powder printing, dimensionally stable objects with specifically adjustable macro- and microstructure can be optimally produced, allowing the best possible adjustment of the scaffold properties to the tissue type to be replaced and therefore causing an optimal cell reaction *in vivo* (Castilho et al., 2014b; Brunello et al., 2016; Zhang et al., 2019). 3D powder-printed scaffolds also have a high microporosity (up to more than 30 vol%) (Castilho et al., 2014b), which promotes nutrient diffusion, vascularization of the scaffold and cell ingrowth (Boyan et al., 1996; Karageorgiou and Kaplan, 2005).

The ideal synthetic bone graft substitute is biocompatible, has similar mechanical properties as bone and undergoes physicochemical as well as cellular degradation while being replaced by newly formed bone (Moore et al., 2001; Kolk et al., 2012). Due to the similarity of their chemical composition to the mineral phase of bone, an excellent biocompatibility as well as osteoconductive and in some cases even osteoinductive properties, CaPs represent the currently favored synthetic bone substitutes (Dorozhkin and Epple, 2002; Gross and Berndt, 2002; LeGeros, 2002; Habibovic et al., 2008; LeGeros, 2008; Böhner et al., 2020). The majority of CaP bioceramics are chemically based on hydroxyapatite (HA), both types of tricalcium phosphate (α -TCP, β -TCP) and/or their multiphase formulations (Dorozhkin, 2013). Calcium phosphate cements (CPCs) have been commercially available for years and are clinically applied as solids and cement pastes (Dorozhkin, 2008; Rentsch et al., 2012; Lodoso-Torrecilla et al., 2021). However, many CPCs, like most CaPs, have the disadvantage of incomplete degradation over months to years due to a low solubility under physiological conditions (Kurashina et al., 1997; Frakenburg et al., 1998; Böhner et al., 2003; Ambard and Mueninghoff, 2006; Kanter et al., 2014). The wider clinical application of these cements is also limited by their mechanical properties, as CPCs are brittle, have low impact resistance, and variable compressive strengths (Ambard and Mueninghoff, 2006; Dorozhkin, 2008). Magnesium phosphate cements (MPCs) have a higher compressive strength and, due to their higher solubility, exhibit a greater chemical degradation potential than CPCs, which is associated with faster *in-vivo* resorption and higher bone ingrowth,

qualifying them as a suitable alternative bone substitute (Mestres and Ginebra, 2011; Ostrowski et al., 2016; Nabiyouni et al., 2018; Haque and Chen, 2020; Gefel et al., 2022). However, unlike CPCs, the biomedical application of MPCs has hardly been investigated so far. It is therefore reasonable to combine the MPCs with their superior biological properties with the well-established CPCs (Ostrowski et al., 2016; Nabiyouni et al., 2018). Several studies have shown that calcium magnesium phosphate cements (CMPCs) exhibit improved biological properties as bone substitutes than the single components and an excellent biocompatibility, good and increasing osseointegration, fast degradation, and rapid replacement by newly formed trabecular bone have been described (Wu et al., 2008a; Wu et al., 2008b; Klammert et al., 2010a; Jia et al., 2010; Wei et al., 2010; Vorndran et al., 2011; Zeng et al., 2012; Ewald et al., 2019; Fuchs et al., 2021).

In a previous short-term *in-vivo* study by Kowalewicz et al. (2021), CMPC scaffolds fabricated with the advantageous production method of 3D powder printing have yet been investigated and especially the alkaline (diammonium hydrogen phosphate, DAHP) post-treated material Mg225d showed promising initial results regarding degradation and osseointegration. Besides post-treatment with DAHP, which results in precipitation of struvite and has yet also been investigated *in vivo* for CMPC pastes or granules by other authors (Ewald et al., 2019; Fuchs et al., 2021), the post-treatment can also be carried out with an acidic phosphate solution (Klammert et al., 2010a; Klammert et al., 2011; Gefel et al., 2022), resulting in precipitation of newberyite and brushite. However, newberyite has been little researched as bone substitute so far and there is no accessible literature available on the post-treatment of CMPCs with phosphoric acid (PA). Therefore, the aim of the present study was the development, characterization, and first *in-vivo* long-term investigation of 3D powder-printed CMPC scaffolds with different physical and chemical properties due to alkaline (DAHP) or acid (PA) post-treatment. The two CMPC material groups Mg225d (DAHP post-treatment) and Mg225p (PA post-treatment) were compared with each other. TCP scaffolds served as reference. For 6, 12, and 24 weeks, respectively, the influence of the different post-treatments on biocompatibility, degradation, and osseointegration behavior of the cylindrical scaffolds was evaluated in a non-weight-bearing borehole defect in the cancellous part of the lateral femoral condyles in rabbits.

2 Materials and methods

2.1 Production and characterization of the scaffolds

2.1.1 Production of the scaffolds

Raw material for the production of the cylindrical CMPC scaffolds ($h = 5.1$ mm, $\varnothing = 4.2$ mm) was the ceramic cement powder $\text{Ca}_{0.75}\text{Mg}_{2.25}(\text{PO}_4)_2$. Reference implants with the same

dimensions were made of tricalcium phosphate (TCP, $\text{Ca}_3(\text{PO}_4)_2$) cement (Figure 1A). Therefore, mixtures of calcium hydrogen phosphate (CaHPO_4 , J.T. Baker, Philippsburg, United States), calcium carbonate (CaCO_3 , Merck KGaA, Darmstadt, Germany), magnesium hydrogen phosphate ($\text{MgHPO}_4 \cdot 3\text{H}_2\text{O}$, Alfa Aesar, Kandel, Germany), and magnesium hydroxide ($\text{Mg}(\text{OH})_2$, VWR International GmbH, Darmstadt, Germany) were prepared in specific molar ratios (Table 1). These powder mixtures were sintered, ground to powders with a particle size <355 μm using a ball mill, and mixed with 4 wt% hydroxypropyl methylcellulose (HPMC) before processing in powder printing (Kowalewicz et al., 2021). The scaffolds were fabricated using a 3D powder printer (ZP310, ZCorp., Burlington, United States) (Kowalewicz et al., 2021). After depowdering of the scaffolds with compressed air, the scaffolds underwent a heat treatment to compact the ceramic and burn out the HPMC, which included a debinding step at 500°C for 2 h and a phase-dependent final sintering temperature. $\text{Ca}_{0.75}\text{Mg}_{2.25}(\text{PO}_4)_2$ scaffolds were sintered at a final temperature of $1,100^\circ\text{C}$ for 4 h, while TCP scaffolds were sintered at $1,350^\circ\text{C}$ for 4 h. After this sintering process, a second sintering of TCP was performed at $1,000^\circ\text{C}$ for 4 h in order to increase the conversion rate of α -TCP into β -TCP.

The CMPC scaffolds were then divided into two material groups, which were subjected to different post-treatments. Both post-treatment variants were carried out at room temperature. One half of the scaffolds (Mg225d) received post-treatment by immersion (24 h) in an aqueous diammonium hydrogen phosphate solution (3.5 M DAHP, $(\text{NH}_4)_2\text{HPO}_4$, Merck KGaA, Darmstadt, Germany), the other half (Mg225p) was completely infiltrated four times with a phosphoric acid solution (2.0 M PA, H_3PO_4 , Merck KGaA, Darmstadt, Germany). The infiltrations with PA were done with a sufficient amount of liquid (100–160 μl PA per scaffold) to completely fill the pores and the scaffolds were dried at room temperature for 24 h after each infiltration. The post-treated scaffolds were washed in distilled water for 1 h and in phosphate-buffered saline (PBS) (Sigma-Aldrich, Taufkirchen, Germany) for 10 min. For this purpose, the scaffolds were placed in a Petri dish, completely covered with the washing medium and placed on a rocking table for uniform mixing of the medium.

Before implantation, all scaffolds were γ -sterilized by BBF Sterilisationsservice GmbH (Kernen, Germany) with a radiation of >25 kGy.

2.1.2 Physical and chemical properties of the scaffolds

The compressive strength was measured using a static universal testing machine (Z010, Zwick GmbH, Ulm, Germany). For this purpose, the post-treated scaffolds ($n = 14$ per material), which had been stored in PBS for 1 h, were measured in a wet condition with a 10 kN load cell, at a pre-load of 1 N and a test speed of 1 mm/min.

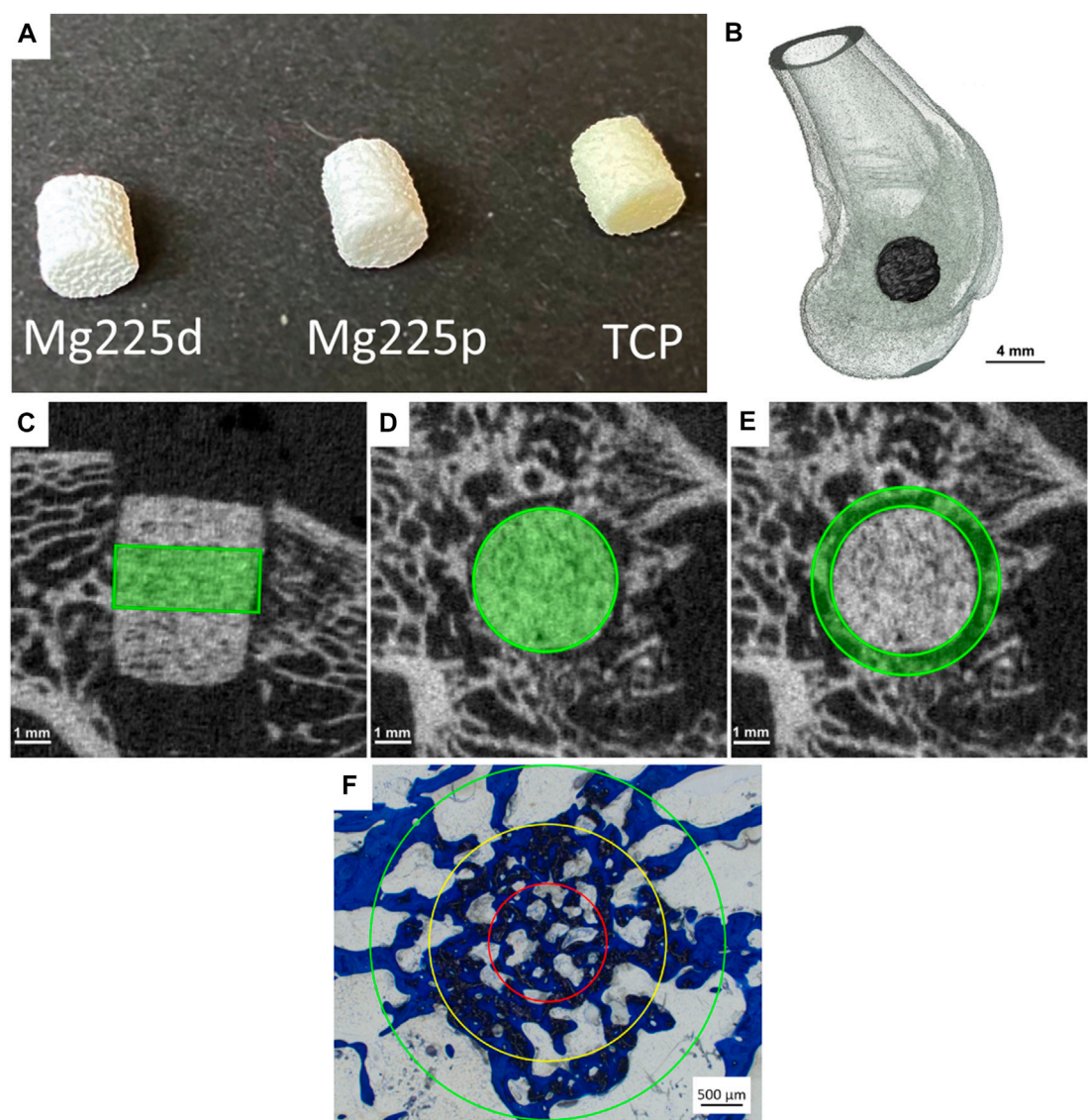


FIGURE 1
(A) Mg225d, Mg225p and TCP scaffolds prior to implantation ($h = 5.1$ mm, $\varnothing = 4.2$ mm). (B) Three-dimensional (3D) reconstruction of the distal rabbit femur with implanted scaffold in the lateral condyle in lateral view. (C) Cylindrical region of interest (ROI) in the scaffold center for measurement of scaffold volume (SV) and scaffold surface/scaffold volume (SS/SV) in the original *in-vivo* μ CT scan ($h = 60$ slices ≈ 1.82 mm) and (D) in the reoriented *in-vivo* μ CT scan ($\varnothing = 140$ voxels (≈ 4.24 mm)). (E) Second hollow cylindrical ROI for measurement of bone volume (BV), trabecular number (Tb.N), trabecular thickness (Tb.Th) and trabecular separation (Tb.Sp) in the scaffold environment in the reoriented *in-vivo* μ CT scan (inner ring: $\varnothing = 144$ voxels (≈ 4.36 mm), outer ring: $\varnothing = 180$ voxels (≈ 5.45 mm), $h = 60$ slices ≈ 1.82 mm). (F) ROIs for the semi-quantitative histological examination: red = inner ring (IR), yellow = medial ring (MR), green = outer ring (OR). \varnothing (OR) = 4.24 mm.

TABLE 1 Powder synthesis: Composition of the cement powders and sintering temperature of the raw powders.

Cement powder	Raw material (mol)				Sintering temperature (°C)
	CaHPO ₄	CaCO ₃	MgHPO ₄ · 3H ₂ O	Mg(OH) ₂	
Ca _{0.75} Mg _{2.25} (PO ₄) ₂	0.50	0.25	1.50	0.75	1,100
Ca ₃ (PO ₄) ₂	2.00	1.00	—	—	1,350

Open porosity and pore size distribution were determined on three scaffolds per material type using a mercury porosimeter (Pascal 140/440, Thermo Fisher Scientific Inc., Waltham, MA, United States). For each measurement, an entire cylindrical scaffold was used. Porosity was measured in a pressure range from 0.01 kPa to 400 MPa and data was analyzed using the software SOLID (SOLver of Intrusion Data Ver. 1.6.5, Thermo Fisher Scientific Inc. Waltham, MA, United States).

The chemical composition of the post-treated and sterile scaffolds was determined by X-ray powder diffraction and Rietveld analysis. For qualitative phase composition, three scaffolds per material type were ground into powder and each powder was analyzed individually using the Bruker Corporations D8 Advance X-ray diffractometer (Bruker Corporations, Karlsruhe, Germany) with monochromatic radiation ($\lambda = 1.541 \text{ \AA}$). The measurement was performed in the scan type locked coupled, within a 2θ -angular range of $10\text{--}40^\circ$ with an increment of 0.02° , a measurement speed of 0.5 s/step , and under rotation of the measurement cuvette of 15 rpm . The following reference files from the JCPDS database were used for analysis: $\beta\text{-Ca}_3(\text{PO}_4)_2$ (β -tricalcium phosphate, PDF Ref. 09-0169), $\alpha\text{-Ca}_3(\text{PO}_4)_2$ (α -tricalcium phosphate, PDF Ref. 09-0348), $\text{Mg}_3(\text{PO}_4)_2$ (farringtonite; PDF Ref. 33-0876), $\text{MgHPO}_4 \cdot 3\text{H}_2\text{O}$ (newberyite, PDF Ref. 35-0780), $\text{Ca}_4\text{Mg}_5(\text{PO}_4)_6$ (stanfieldite; PDF Ref. 11-0231), and $\text{NH}_4\text{MgPO}_4 \cdot 6\text{H}_2\text{O}$ (struvite, PDF Ref. 15-0762). Using the Rietveld method (Rietveld, 1969; Reid and Hendry, 2006), a quantitative phase analysis was carried out. Bruker Corporations' TOPAS V6 software (Bruker Corporations, Billerica, MA, United States) was used to perform this analysis.

2.1.3 Scanning electron microscopy and energy dispersive X-ray spectroscopy analysis of the scaffolds before implantation

For SEM (scanning electron microscopy) and EDX (energy dispersive X-ray spectroscopy) analysis, the scaffolds were fixed in 4% buffered formalin solution (Roth, Karlsruhe, Germany), dehydrated in an ascending series of alcohol (Roth, Karlsruhe, Germany) and defatted with xylene (Roth, Karlsruhe, Germany). Embedding was performed with a resin embedding system based on methyl methacrylate (Technovit[®] 9100, Heraeus Kulzer, Wehrheim, Germany) according to the manufacturer's instructions. After polymerization, thin sections (thickness = $4 \mu\text{m}$, $n = 1$ per material) were prepared using an automatic rotary microtome (RM2255 Leica, Wetzlar, Germany). After transfer to a water bath, the thin sections were mounted on glass slides (Glaswarenfabrik Karl Hecht, Sondheim, Germany) coated with ponal-poly-L-lysine. They were then stretched with 96% ethanol, covered with a polyethylene film (Heraeus Kulzer, Hanau, Germany) and dried in a slide press at 37°C for 2 days. Prior to SEM with a field emission electron microscope (Crossbeam CB 340, Zeiss, Oberkochen, Germany), the thin sections were coated with platinum (thickness = 4 nm) using a sputter coater (Leica EM ACE600, Leica Mikrosysteme GmbH,

Wetzlar, Germany). For EDX imaging, a system with silicon drift detector (INCA Energy 350 AzTec Advanced system with silicon drift detector) from Oxford Instruments, Abingdon, United Kingdom was used. Using an accelerating voltage of $5\text{--}10 \text{ keV}$, the scaffolds were examined at a magnification of $\times 24$ and $\times 100$. SEM was used to assess the surface texture and pore structure of the scaffolds, while EDX was used to analyze the distribution of chemical phases based on the occurrence of magnesium (Mg), calcium (Ca) and phosphorus (P).

2.2 Animal model

The animal experiment was approved by the competent authority (Government of Upper Bavaria) according to paragraph 8 of the German Animal Welfare Act (approval number ROB 55.2-2532.Vet_02-19-64). For this study, 36 female adult Zika rabbits (Asamhof, Kissing, Germany) weighing $4.26 \pm 0.27 \text{ kg}$ were divided into three groups with an observation period of 6, 12 and 24 weeks post-surgery, respectively. According to a fixed implantation scheme, eight scaffolds per material (Mg225d, Mg225p, TCP) and time group were implanted and examined.

The implantation of the scaffolds into the lateral femoral condyles of both hind limbs was performed following a previous study by Kowalewicz et al. (2021). The animals received enrofloxacin (10 mg/kg , Orniflox[®], CP-Pharma GmbH, Burgdorf, Germany) as antibiotic and meloxicam (0.3 mg/kg , Melosus[®], Albrecht GmbH, Aulendorf, Germany) as analgesic per os prior to surgery. Induction of anesthesia was performed by intramuscular application of ketamine (15 mg/kg , Aneskin[®], Albrecht GmbH, Aulendorf, Germany) and medetomidine (0.25 mg/kg , Dorbene vet[®], Zoetis Deutschland GmbH, Berlin, Germany). The airways were secured by endotracheal intubation and the animals were placed in supine position after shaving and aseptic preparation of the surgical area. Anesthesia was maintained by inhalation of isoflurane ($1.5\text{--}2 \text{ vol\%}$, simultaneously supply of oxygen 1 L/min). During surgery, the rabbits received $10 \mu\text{g/kg/h}$ fentanyl intravenously (Fentadon[®], CP-Pharma GmbH, Burgdorf, Germany) as pain medication.

Surgical access was performed through a skin incision in the area of the right lateral femoral condyle. After dissection of the muscles and visualization of the condyle using a raspatory, an approximately 5 mm deep hole was drilled in the cancellous part of the condyle directly above the attachment of the lateral collateral ligament. The cylindrical scaffold was inserted accurately into the borehole (Figure 1B). Wound closure of the soft tissue (Monosyn 4/0, B. Braun SE, Melsungen, Germany) and the skin (Optilene 4/0, B. Braun SE, Melsungen, Germany) was performed. After completion of the surgical procedure on the first side, the animals received

intravenous buprenorphine (20 µg/kg, Bupresol®, CP-Pharma GmbH, Burgdorf, Germany) for pain management. The contralateral femur was operated using the same surgical procedure. Immediately after surgery, an *in-vivo* micro-computed tomographic (µCT) examination (see Section 2.4) was performed of both hindlimbs, and radiographs (see Section 2.3) were obtained in two views. Finally, medetomidine was antagonized by intramuscular application of atipamezole (25 mg/kg, Atipam®, Albrecht GmbH, Aulendorf, Germany).

During the first 14 days after surgery, the animals were clinically and orthopedically examined daily, especially with regard to lameness and pain, and a daily wound assessment was performed. For 5 days, the animals received enrofloxacin (10 mg/kg, Orniflox®, CP-Pharma GmbH, Burgdorf, Germany) as antibiotic and meloxicam (0.3 mg/kg, Melosus®, Albrecht GmbH, Aulendorf, Germany) for pain management per os once daily. At fixed time points (6, 12, and 24 weeks after surgery, respectively), euthanasia of the animals was carried out in accordance with animal welfare regulations by intravenous application of propofol (5 mg/kg, Narcofol®, CP-Pharma GmbH, Burgdorf, Germany) and pentobarbital (200–230 mg/kg, Narkodorm®, CP-Pharma GmbH, Burgdorf, Germany). The femora were collected and adherent soft tissue was removed. The scaffold-bone-complexes were extracted using a diamond band saw (cut-grinder, Walter Messner GmbH, Oststeinbek, Germany).

2.3 X-ray examination

Immediately after surgery and at predefined time points (every 2 weeks until week 12, hereinafter every 4 weeks until week 24), a radiological examination of the rabbits' hind limbs was performed in two views [ventrodorsal (VD), mediolateral (ML)]. The examinations were conducted with the settings 54.9 kV and 4.5 mA (Multix Select DR, Siemens GmbH, Erlangen, Germany). Using the software dicomPACS® vet (Ver.8.9.5, Oehm und Rehbein GmbH, Rostock, Germany), the visibility of the scaffolds in the different X-ray views was assessed by two observers.

2.4 *In-vivo* µCT examination

Immediately after surgery and at the same predefined time points as the radiological examinations, the lateral femoral condyles of the rabbits were examined in an *in-vivo* µCT (Xtreme CT II, Scanco Medical, Zurich, Switzerland). The scans were performed with the settings 30.3 µm isotropic voxel size, 68 kV voltage, 1,000/180° projections, and 200 ms integration time. For this purpose, the rabbits were placed in supine position with stretched hindlimbs. For the scan immediately after surgery, anesthesia was maintained with

isoflurane (0.8–1.0 vol%, simultaneously oxygen supply 1.5–2 L/min). For the subsequent scans, anesthesia was induced as for surgery. Due to the shorter duration of anesthesia, the animals were not intubated for these scans but received oxygen (1.5–2 L/min) via a laryngeal mask (v-gel® rabbit, Docsinnovent Ltd., London, United Kingdom).

2.4.1 Semi-quantitative evaluation of *in-vivo* µCT scans

With a special modified scoring system (Kowalewicz et al., 2021), the following parameters were assessed by two observers: Scaffold demarcability based on gray value and structure, degradation properties, loss of cylindrical form, occurrence and distinctivity of a resorption zone (area within the scaffold volume characterized by a markedly lower gray value than the scaffold material), and scaffold-bone-contact. Score values from 0–2 were assigned for each parameter examined (Table 2). To obtain the cross-sectional view of the scaffolds with surrounding cancellous bone, it was necessary to rotate the original scan using the software µCT Evaluation Program V6.6 (Scanco Medical, Zurich, Switzerland).

2.4.2 Quantitative evaluation of *in-vivo* µCT scans

To calculate various degradation and osseointegration parameters, it was necessary to define material-specific thresholds. The following thresholds (Th) were established by assessing the grey values of the different scaffolds in the scans directly after surgery ($n = 6$ per material): Mg225d: 140, Mg225p: 149, TCP: 219. For cancellous bone at the same location, the Th 142 was determined using µCT scans of both lateral femoral condyles of adult Zika rabbit cadavers ($n = 4$) with intact femurs. Scaffold volume (SV) and scaffold surface area to volume ratio (SS/SV) were calculated following the studies of Kowalewicz et al. (2021), Augustin et al. (2020), and Kleer et al. (2019) in a region of interest (ROI) in the scaffold center. This ROI included a cylinder with a diameter of 140 voxels ($\hat{=}$ 4.24 mm) and a height of 60 slices ($\hat{=}$ 1.82 mm) (Figures 1C,D). Bone volume (BV), trabecular number (Tb.N), trabecular thickness (Tb.Th), and trabecular separation (Tb.Sp) in the scaffold environment were calculated also based on the studies of Kowalewicz et al. (2021), Augustin et al. (2020) and Kleer et al. (2019) in a second hollow cylindrical ROI (inner ring: $\varnothing = 144$ voxel ($\hat{=}$ 4.36 mm), outer ring: $\varnothing = 180$ voxel ($\hat{=}$ 5.45 mm), height = 60 slices) (Figure 1E). To establish reference values for cancellous bone, the cancellous part of both femoral condyles of cadavers of adult Zika rabbits ($n = 4$) with intact femora was examined. All calculations were performed using the software µCT Evaluation Program V6.6 (Scanco Medical, Zurich, Switzerland).

2.5 µCT 80 examination

After euthanasia of the animals and extraction of the scaffold-bone-complexes, these were processed as described

TABLE 2 Scoring system for the semi-quantitative evaluation of the *in-vivo* μ CT scans.

Parameter	Score 0	Score 1	Score 2
Scaffold demarcability (based on grey value and density/structure)	Scaffold not demarcable from surrounding bone tissue	Scaffold partially demarcable from surrounding bone tissue	Scaffold completely demarcable from surrounding bone tissue
Degradation properties	Scaffold uniformly degraded	Scaffold half close to the bone marrow more degraded	Scaffold half close to the bone marrow no longer visible
Loss of form	Cylindrical form no longer recognizable	Cylindrical form partially recognizable	Cylindrical form clearly recognizable
Distinctivity of a resorption zone (area within the scaffold volume with a markedly darker gray value than the scaffold material)	No resorption zone distinctive	Resorption zone indistinctly delineated	Resorption zone distinctly delineated
Scaffold-bone-contact	Broad contact area between scaffold and bone, numerous bone trabeculae on scaffold, no gap visible	Multiple bone trabeculae between scaffold and surrounding bone, barely visible gap	No contact between scaffold and surrounding bone, clear gap between bone and scaffold

TABLE 3 Scoring system for the semi-quantitative evaluation of the μ CT 80 scans.

Parameter	Score 0	Score 1	Score 2
Trabecular structures in the scaffold volume: Cross-sectional view	Numerous trabecular structures visible up to the center of the scaffold radius	Trabecular structures visible in >50% of the scaffold radius, not extending to the center	Trabecular structures visible in the outer <50% of the scaffold radius
Trabecular structures in the scaffold volume: Longitudinal view	Trabecular structures throughout the scaffold volume	Amount of trabecular structures close to the cortex markedly larger than close to the bone marrow	Trabeculae mainly located close to the cortex, few trabeculae close to the bone marrow

previously in [Section 2.1.3](#). After polymerization, the sample blocks were scanned using a μ CT 80 (Scanco Medical, Zurich, Switzerland). The scans were performed with settings of 10 μ m isotropic voxel size, 70 kV voltage and 600 ms integration time.

2.5.1 Semi-quantitative evaluation of μ CT 80 scans

Using a scoring system developed for this study, the occurrence and location of trabecular structures in cross and longitudinal section of the scaffold volume were assessed in the complete scan by two observers. Score values from 0–2 were assigned for both parameters examined ([Table 3](#)).

2.5.2 Quantitative evaluation of μ CT 80 scans

Trabecular number (Tb.N), trabecular thickness (Tb.Th), and trabecular separation (Tb.Sp) were measured within a defined cylindrical ROI in the scaffold center [$h = 182$ voxels ($\hat{=}$ 1.82 mm), $\varnothing = 424$ voxels ($\hat{=}$ 4.24 mm)]. Eight scans per material were used to determine the Ths for cancellous bone (144–235). Reference values for cancellous bone at the same location were determined using scans of eight lateral femoral condyles from adult Zika rabbit cadavers with intact femora. All calculations were performed using the software μ CT Evaluation Program V6.6 (Scanco Medical, Zurich, Switzerland).

2.6 Histological examination

Thick sections (thickness = 40 μ m) of the embedded scaffold-bone-complexes were produced according to the cutting-grinding technique of [Donath and Breuner \(1982\)](#) using a diamond band saw (cut-grinder, Walter Messner GmbH, Oststeinbek, Germany) and a grinding machine (lap-grinder, Walter Messner GmbH, Oststeinbek, Germany). A central section of each implanted scaffold was routinely stained with toluidine blue (0.1% toluidine blue O solution, Waldeck, Münster, Germany) ([Willbold and Witte, 2010](#); [Huehnerschulte et al., 2012](#)). The longitudinal axis of the cylinder was perpendicular to the cutting surface. The μ CT 80 scans were used to determine the scaffold position within the condyle.

2.6.1 Semi-quantitative evaluation of histological sections

The stained histological sections were assessed by two observers using a microscope (Zeiss Axio Imager Z.2, Carl Zeiss Microscopy GmbH, Jena, Germany). Following [von Doernberg et al. \(2006\)](#), the implantation area was divided into three ROIs at $\times 25$ magnification using three rings (IR = inner ring, MR = medial ring, OR = outer ring), with the diameter of the OR ($\varnothing = 4.24$ mm) corresponding to the scaffold diameter ([Figure 1F](#)). In each ROI, a scoring system modified according to [von Doernberg et al. \(2006\)](#), [Kleer-Reiter et al. \(2021\)](#) and

TABLE 4 Scoring system for the semi-quantitative histological evaluation of tissue and cells.

Parameter	Score 0	Score 1	Score 2	Score 3
Tissue level				
Scaffold material	0%	1%–25%	26%–50%	>50%
Scaffold material enclosed by bone	0%	1%–25%	26%–50%	>50%
New bone (thin trabeculae, dark blue colored)	0%	1%–25%	26%–50%	>50%
Remodeled bone (trabecular thickness as in environment, light blue colored)	0%	1%–25%	26%–50%	>50%
Granulation tissue/bone marrow	0%	1%–25%	26%–50%	>50%
Cell-rich resorption zone (fibrous tissue)	0%	1%–25%	26%–50%	>50%
Cell level				
Tissue ingrowth				
Fibrous cells/tissue	None/physiological for bone marrow	Slightly increased	Medium increased	Highly increased
Adipocytes	None	Few	Moderate	Many
Precursor cells (bone marrow activity)	None	Few	Moderate	Many
Vascularization ^a (blood vessels)	None	Few	Moderate	Many
Foreign body reaction				
Macrophages ^b	None	Few	Moderate	Many
Foreign body cells ^b	None	Few	Moderate	Many
Bone tissue and cells				
Osteoblasts ^b	None	Few	Moderate	Many
Osteoclasts ^b	None	Few	Moderate	Many
Osteoid	None	Sporadic	Thin layer	Thick layer

^aNone = 0, Few = 1–3, Moderate = 4–6, Many = 7+ blood vessels.

^bNone = 0, Few = 1–5, Moderate = 6–10, Many = 10+ cells.

Augustin et al. (2022) was used to assess in the initial scaffold cross section the percentage area of scaffold material, bone, granulation tissue/bone marrow and resorption zone (cell- and connective tissue-rich annular zone within the scaffold cross section) as well as the percentage of scaffold material enclosed by bone (Table 4). In each ROI, a second scoring system (Table 4) was used to evaluate the ingrowing tissue at cellular level (fibrous cells/tissue, adipocytes, precursor cells, vascularization/blood vessels, macrophages, foreign body cells (FBC), osteoblasts, osteoclasts, osteoid) in a field of view with fixed position at $\times 100$ magnification. Score values from 0–3 were assigned for each parameter examined (Table 4).

2.6.2 Quantitative evaluation (histomorphometry)

In addition to the semi-quantitative analysis, the thick sections from the scaffold center were quantitatively analyzed by histomorphometry. For this purpose, images of the cross sections (Zeiss Axio Imager 2, Carl Zeiss Microscopy GmbH, Jena, Germany) were taken at $\times 20$ magnification using the Zeiss Axio Cam Mrc digital camera and the software Zeiss ZEN 3.0 (Carl Zeiss Microscopy GmbH, Jena, Germany). The images were evaluated using the software Zeiss ZEN 3.0 (Carl Zeiss Microscopy GmbH, Jena, Germany). The percentage area of scaffold material, ingrown

bone tissue, and soft tissue (granulation tissue, bone marrow) was measured within a predefined circle ($\varnothing = 1,060$ pixels $\hat{=}$ diameter of the OR of the semiquantitative examination ($\varnothing = 4.24$ mm) $\hat{=}$ scaffold diameter), which was placed centrally around the initial implantation area.

2.7 SEM and EDX analysis of the unstained histological sections

Histological thin sections ($n = 2$ per material and time group) were prepared and examined by SEM and EDX analysis as previously described in Section 2.1.3. The scaffold center was examined with a magnification of $\times 28$ and $\times 500$. In SEM, the osseointegration of the scaffolds was assessed morphologically based on the surface texture of the thin sections, while in EDX, the presence of material particles was determined based on the occurrence of magnesium ions (CMPCs).

2.8 Statistics

Statistical analysis of the compressive strength and porosity of the scaffolds was performed by analysis of variance (ANOVA) followed by Tukey's post hoc test using Origin

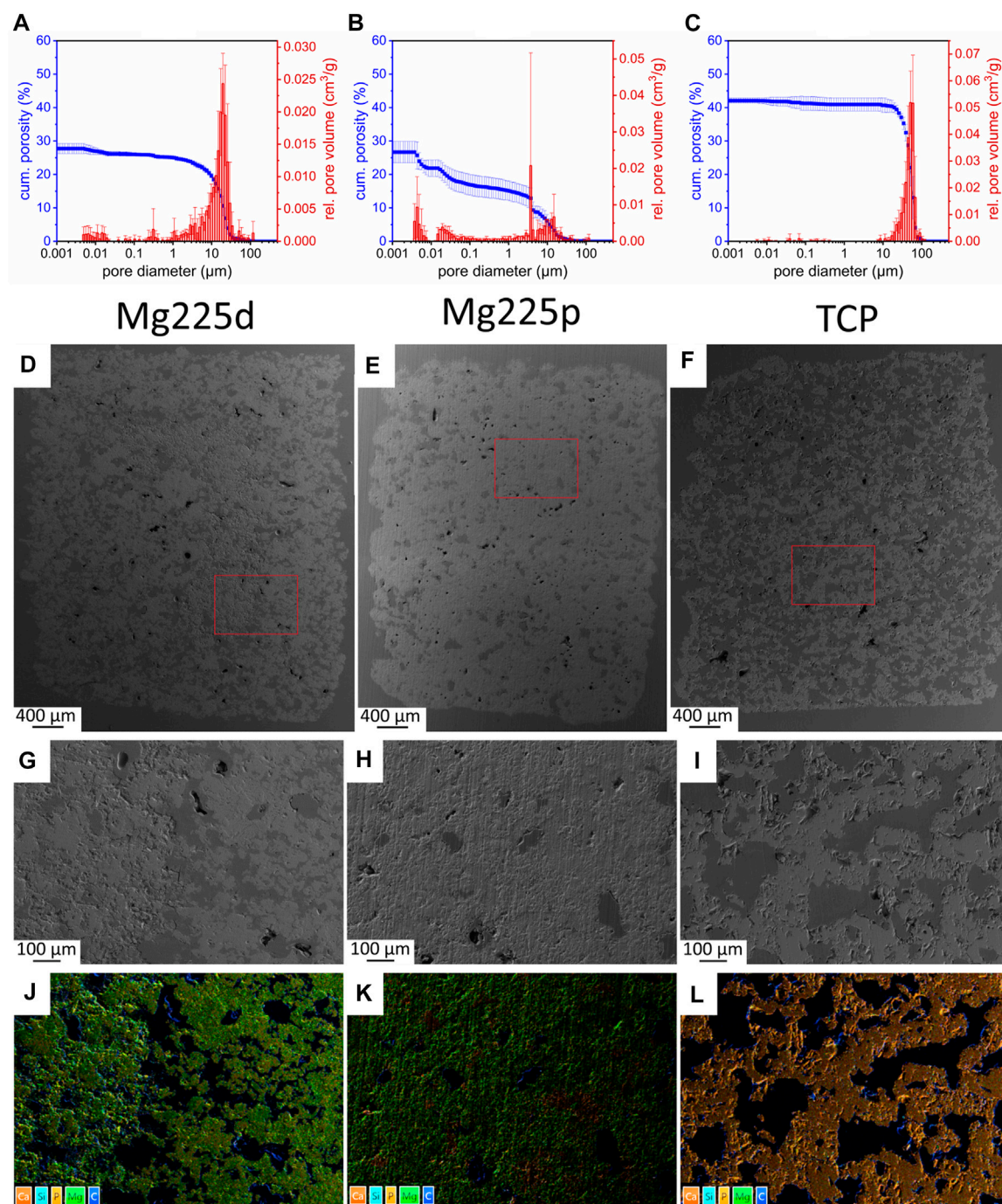


FIGURE 2

(A–C) Porosity, pore diameter and relative pore volume of (A) Mg225d, (B) Mg225p and (C) TCP. (D–F) SEM analysis (×24 magnification) of (D) Mg225d, (E) Mg225p and (F) TCP scaffold prior to implantation with (G–I) ×100 magnification from the scaffold center of (G) Mg225d, (H) Mg225p and (I) TCP. (D–I) Dark gray areas: pores, light gray areas: scaffold material. (J–L) EDX analysis from the scaffold center of (J) Mg225d, (K) Mg225p and (L) TCP prior to implantation with the same position and magnification as (G–I).

(OriginPro 2022, OriginLab, Northampton, MA, United States). The collected *in-vivo* data were analyzed with SPSS Statistics 26 (IBM Company, Armonk, United States). Using the Shapiro–Wilk test, data were tested for normal

distribution. Normally distributed data were analyzed using analysis of variance (ANOVA followed by Tukey post hoc test/ Welch-ANOVA followed by Games–Howell post-hoc test). For non-normally distributed data, testing for significant

differences was done using Kruskal–Wallis test with one-way analysis of variance (ANOVA) followed by Bonferroni's post hoc test. A significance level of $p < 0.05$ was set for all tests.

3 Results

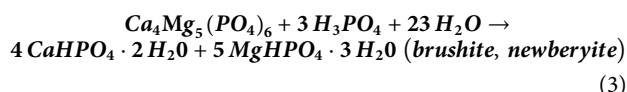
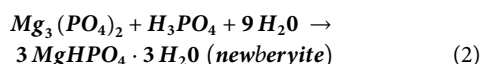
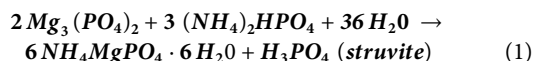
3.1 Characterization of the scaffolds

3.1.1 Physical and chemical properties of the scaffolds

The compressive strengths of the scaffolds prior to implantation differed significantly from each other ($p < 0.001$) [Mg225d: (6.00 ± 1.04) MPa, Mg225p: (14.12 ± 3.16) MPa, TCP: (1.95 ± 0.40) MPa].

Mercury porosimeter analysis revealed an open porosity of $(27.85 \pm 1.67)\%$ for Mg225d (Figure 2A). For Mg225p, an open porosity of $(26.85 \pm 3.02)\%$ was determined (Figure 2B), while TCP had an open porosity of $(42.11 \pm 0.78)\%$ (Figure 2C). The porosity of both CMPCs was significantly different compared to TCP ($p < 0.001$).

Due to the post-treatment of the scaffolds with DAHP (Mg225d) and PA (Mg225p), the following chemical reactions resulted in the partial transformation of stanfieldite and farringtonite into struvite (Mg225d (Eq. 1)), newberyite (Mg225p (Eqs. 2, 3)), and brushite (Mg225p (Eq. 3)), respectively.



The quantitative chemical composition of the scaffolds in wt % is listed in Table 5.

3.1.2 SEM and EDX analysis of the scaffolds before implantation

Analysis of the scaffolds by SEM and EDX showed an increasing porosity of the materials as listed: Mg225p < Mg225d < TCP. Mg225d showed large, interconnected pores as well as rough-appearing areas inside the scaffold, which probably contained unreacted raw powder (stanfieldite, farringtonite) (Figures 2D,G,J; Supplementary Figure S1A). EDX analysis also revealed a lower amount of Ca in the peripheral region of Mg225d than in the rough-appearing center, whereas Mg was homogeneously distributed. The matrix of Mg225p appeared more homogeneous and denser in EDX than in Mg225d (Figures 2E,H,K; Supplementary Figure S1B). The reddish

areas visible in the EDX analysis (high Ca concentration) were probably comprised of brushite, which is a precipitation product of the reaction with the phosphoric acid (Figure 2K). The TCP scaffolds were composed of morphologically and chemically homogeneous CaP (Figures 2F,I,L; Supplementary Figure S1C).

3.2 Clinical examination

All rabbits were in good general condition following surgery for the duration of the respective observation periods. No animal showed signs of pain or lameness. Physiological wound healing occurred.

3.3 X-ray examination

Since Mg225d and Mg225p showed a radiopacity comparable to that of bone, some scaffolds could not be distinguished from the surrounding bone tissue already directly after surgery. Over the study period, the percentage of visible CMPC scaffolds rapidly decreased in both views and was significantly lower than with TCP from week 4 in ML view ($p \leq 0.042$) and from week 6 in VD view ($p < 0.001$), respectively (Figure 3). The CMPC scaffolds were more difficult to delineate in the VD view due to overlap by the sesamoid bones, and therefore visible less frequent and for shorter periods (Mg225d up to week 12, Mg225p up to week 16) than in the ML view (Mg225d up to week 16, Mg225p up to week 20). All TCP scaffolds were clearly visible in both radiographic views at each examination time point.

3.4 In-vivo μ CT examination

3.4.1 Semi-quantitative evaluation of in-vivo μ CT scans

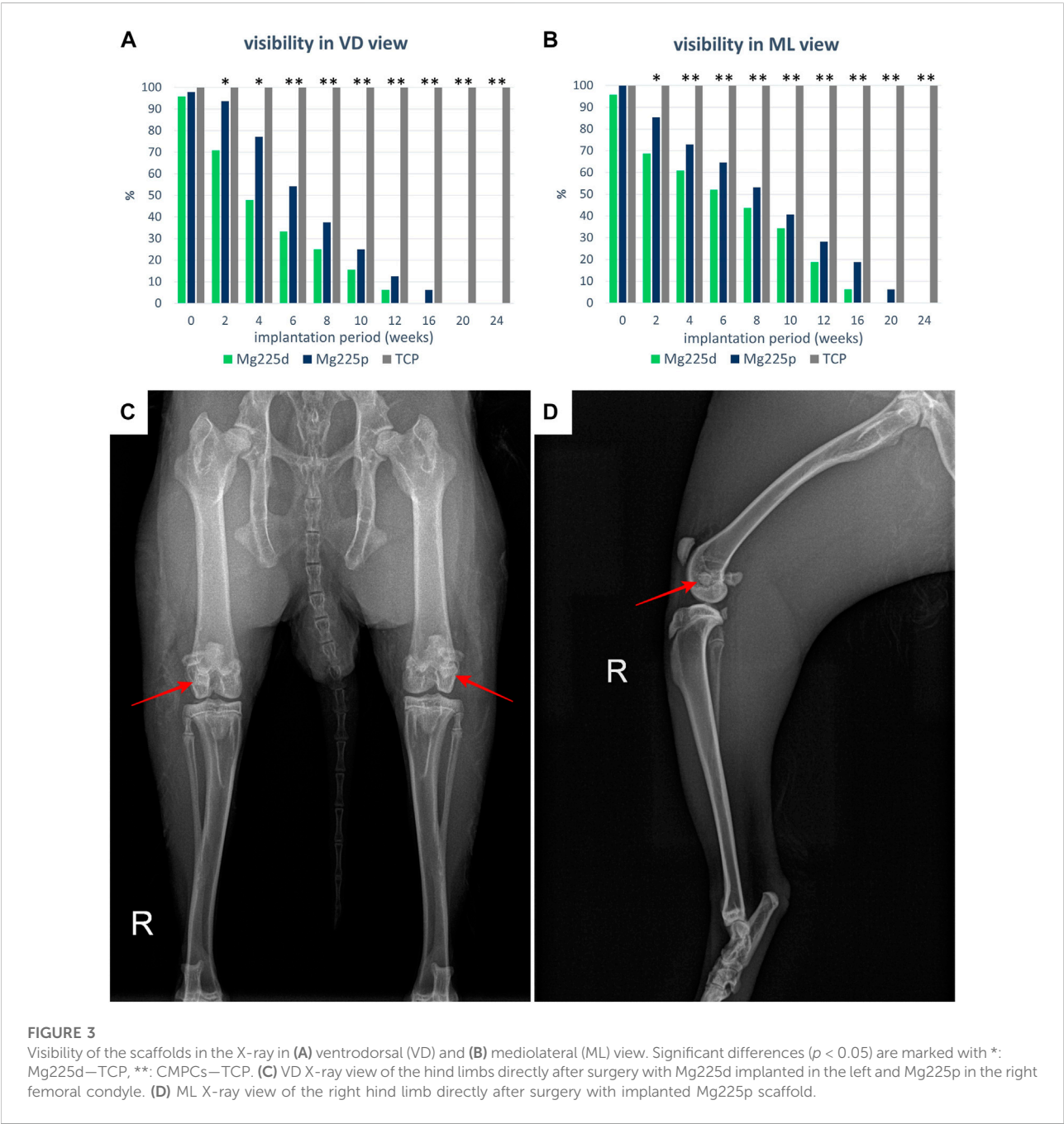
The demarcability of the CMPC scaffolds from surrounding bone decreased steadily over the 24-weeks study period (Figures 4, 5A; Supplementary Table S1). Between weeks 2 and 6 as well as at weeks 10 and 12, Mg225d was significantly less clearly demarcable from surrounding bone than Mg225p ($p \leq 0.023$). From week 16 onwards, the demarcation of all Mg225d scaffolds was no longer possible. All TCP scaffolds were completely demarcable from the surrounding bone by week 24 and thus differed significantly from the CMPC scaffolds from week 6 onwards ($p < 0.001$).

The phenomenon of faster scaffold degradation on the side towards the bone marrow compared to the side towards the cortex was observed in all materials (Figure 5B; Supplementary Table S2). 6 and 12 weeks after surgery, at least half of the

TABLE 5 Chemical composition of Mg225d, Mg225p and TCP in wt%.

	Stan	Far	New	Bru	Stru	Periclas	α-TCP	β-TCP
Mg225d	59.84 ± 1.05	31.92 ± 1.05			5.91 ± 1.38	2.33 ± 0.53		
Mg225p	25.04 ± 1.29	13.19 ± 0.52	53.33 ± 0.69	8.42 ± 1.10				
TCP							1.49 ± 0.83	98.51 ± 0.83

Stan, Stanfieldit $\text{Ca}_4\text{Mg}_5(\text{PO}_4)_6$; Far, Farringtonit $\text{Mg}_3(\text{PO}_4)_2$; New, Newberyit $\text{MgHPO}_4 \cdot 3\text{H}_2\text{O}$; Bru, Brushit $\text{CaHPO}_4 \cdot 2\text{H}_2\text{O}$; Stru, Struvit $\text{NH}_4\text{MgPO}_4 \cdot 6\text{H}_2\text{O}$; Periclas, MgO ; α-TCP, alpha-Tricalciumphosphat $\text{Ca}_3(\text{PO}_4)_2$; β-TCP, beta-Tricalciumphosphat $\text{Ca}_3(\text{PO}_4)_2$.



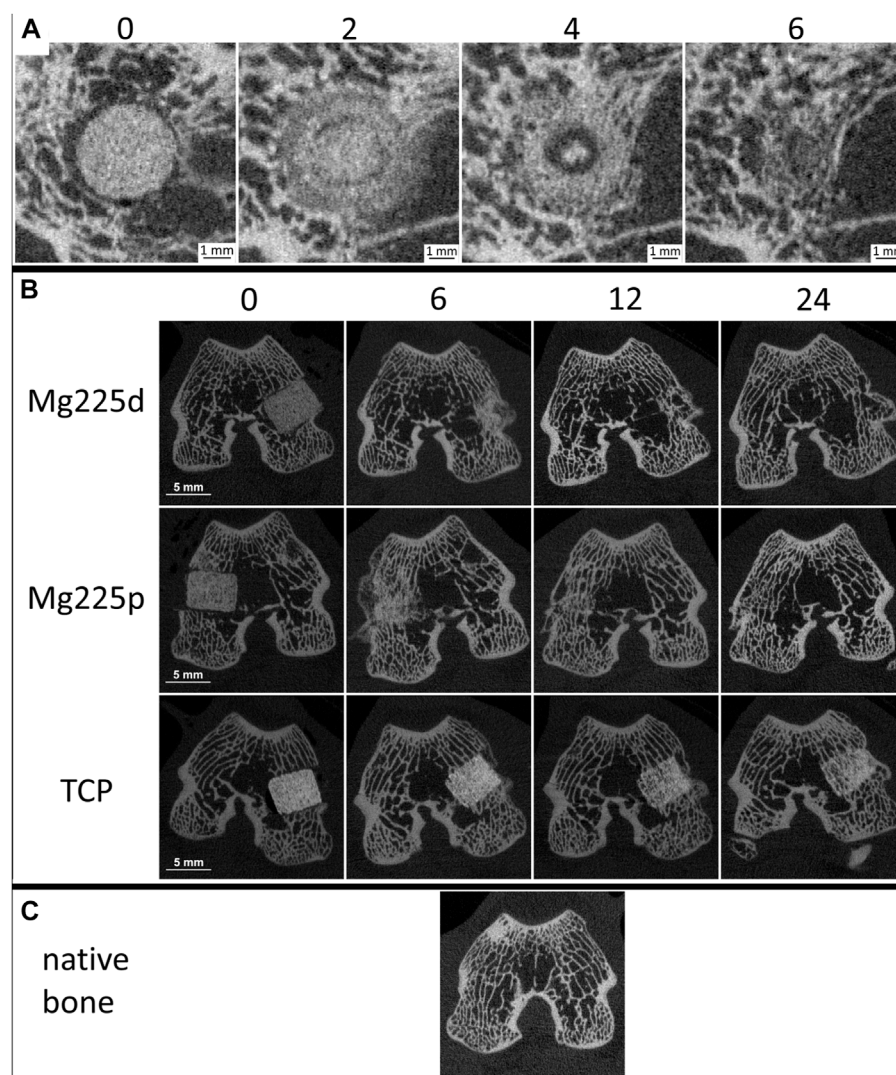


FIGURE 4

(A) *In-vivo* μ CT images of Mg225d and surrounding cancellous bone in cross section over time (directly after surgery up to 6 weeks) with increasing scaffold-bone-contact and resorption zone. (B) *In-vivo* μ CT images of the scaffolds (Mg225d, Mg225p and TCP) implanted in the distal femoral condyles over time (directly after surgery up to 24 weeks) (C) compared to native cancellous bone of the distal femoral condyle.

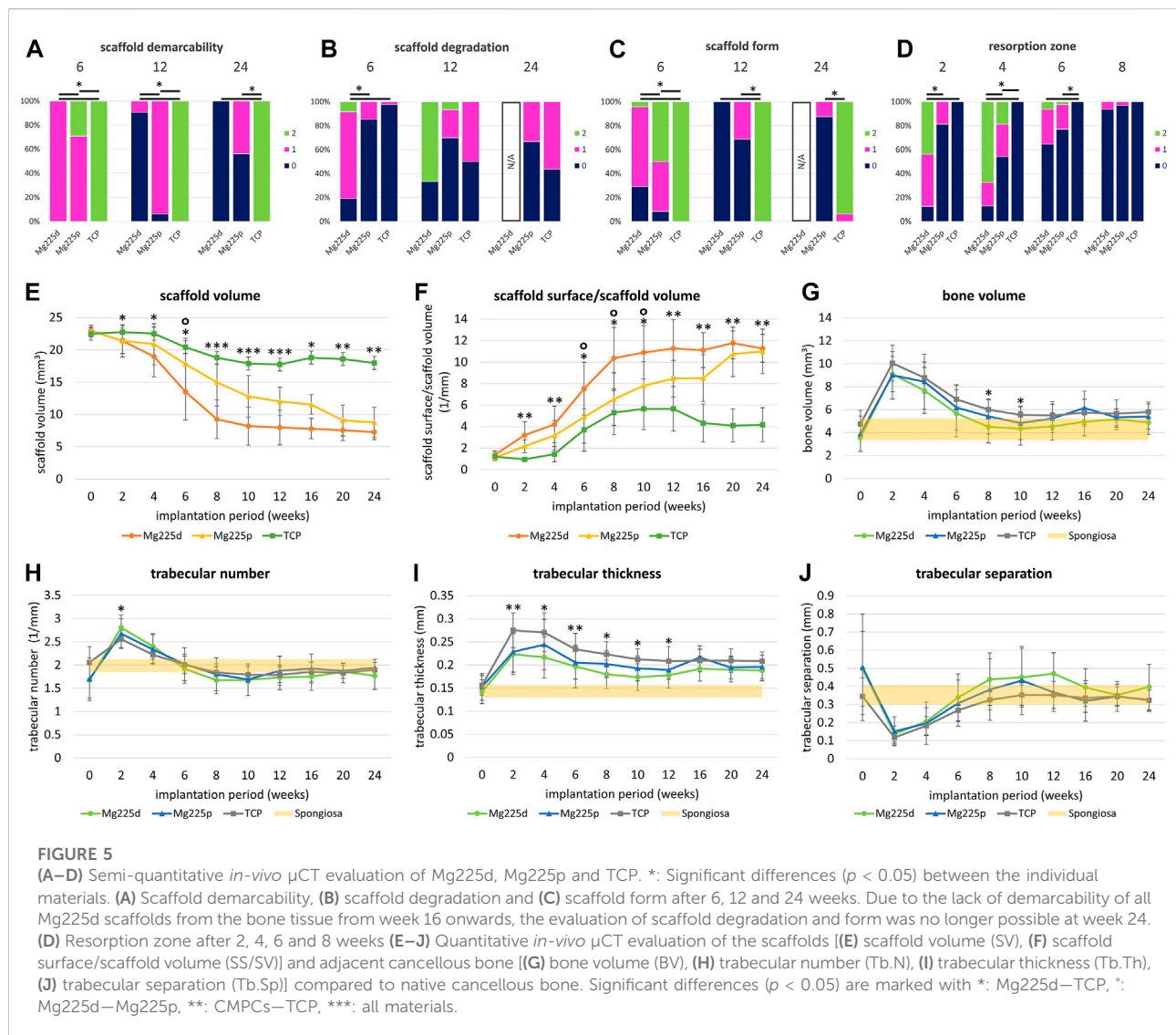
Mg225p and TCP scaffolds were equally degraded on the side towards the bone marrow and the cortex. At 24 weeks, more severe degradation was observed in the majority of TCP scaffolds on the side towards the bone marrow compared to the side towards the cortex. Mg225d exhibited significantly greater degradation close to the bone marrow than Mg225p and TCP between weeks 2 and 6 ($p < 0.001$). After 12 weeks, the majority of Mg225d scaffolds (67%) were no longer visible at the side towards the bone marrow.

Over the study period, the loss of cylindrical form of both CMPCs increased steadily and was significantly more pronounced than in TCP from week 4 onwards ($p \leq 0.003$), which almost always exhibited a distinct cylindrical form until

week 24 (Figures 4B, 5C; Supplementary Table S3). After 6 weeks, Mg225p (50% of scaffolds) still showed a distinct cylindrical form significantly more often than Mg225d (4% of scaffolds) ($p < 0.001$).

The CMPCs showed a resorption zone within the scaffolds between weeks 2 and 8, which was observed significantly more frequent and distinct in Mg225d than in Mg225p at weeks 2 and 4 ($p < 0.001$) (Figures 4A, 5D; Supplementary Table S4). In TCP, such a zone was indistinctly delineated in only a single scaffold at weeks 20 and 24.

Two weeks after surgery, several trabeculae were visible between the scaffold and the surrounding bone in the majority of scaffolds of all materials (Figure 4A,



Supplementary Table S5). After 8 weeks at the latest, there was always a broad contact area existing between the scaffold and the surrounding bone.

3.4.2 Quantitative evaluation of *in-vivo* μ CT scans

Within the study period (immediately after surgery up to week 24), a significant decrease in SV was observed in the CMPCs ($p < 0.001$) (Figure 5E). The volume decrease was greatest for Mg225d (Mg225d: 68.47%, Mg225p: 61.75%, TCP: 20.14%). From week 2 onwards, the SV of Mg225d was significantly lower than that of TCP ($p \leq 0.042$). Between weeks 6 and 12, Mg225d also had a significantly lower SV than Mg225p ($p \leq 0.049$). From week 12 onwards, the CMPCs showed only a slight decrease in volume. In TCP, a significant decrease in SV was observed when comparing between week 12 and immediately

after surgery ($p = 0.002$), which was followed briefly by a small increase in SV.

SS/SV increased significantly in the CMPCs over the study period of 24 weeks ($p \leq 0.001$) (Figure 5F). In TCP, a significant increase was observed between immediately after surgery and week 12 ($p = 0.009$). For Mg225d, SS/SV was significantly higher than for TCP from week 2 onwards ($p \leq 0.001$), for Mg225p this was the case at weeks 2 and 4 and from week 12 ($p \leq 0.049$). Between weeks 6 and 10, the SS/SV of Mg225d was significantly greater than that of Mg225p ($p \leq 0.023$).

BV in the scaffold environment increased slightly for all materials when comparing immediately after surgery with week 24 (Figure 5G). The significant increase in week 2 ($p \leq 0.005$) was striking for all materials, followed by a continuous decrease until week 10 (Mg225d, Mg225p) and week 12 (TCP), respectively. At subsequent time points, the BV was within or slightly above the

physiological range for cancellous bone at this site for all materials.

All materials showed an increase in the Tb.N at week 2, which was significant ($p = 0.005$) for the CMPCs (Figure 5H). This peak was followed by a continuous decrease until week 8 (Mg225d), week 10 (Mg225p) and week 12 (TCP), respectively. From week 6 onwards, the Tb.N was always within the physiological range for cancellous bone at this site or slightly lower.

After a significant increase until week 2 (Mg225d, TCP) or week 4 (Mg225p) ($p \leq 0.007$), the Tb.Th decreased slightly in all materials (Figure 5I). From week 2 onwards, the Tb.Th was higher in every material than in cancellous bone at this site.

Tb.Sp was significantly lower in the CMPCs after 2 weeks than immediately after surgery ($p \leq 0.013$) (Figure 5J). From week 2, the Tb.Sp increased again until week 10 (Mg225p) or week 12 (Mg225d, TCP) and was within or slightly above the physiological range for cancellous bone at this site from week 8 onwards.

3.5 μ CT 80 examination

3.5.1 Semi-quantitative evaluation of μ CT 80 scans

After 6 weeks, all TCP and the majority of CMPC scaffolds showed trabeculae reaching into the center of the scaffold radius in cross section (Figures 6, 7A; Supplementary Figure S2). 12 and 24 weeks after surgery, new bone trabeculae had grown into the center of the scaffold radius in all Mg225p and all TCP scaffolds, whereas this was significantly less frequent in Mg225d ($p \leq 0.005$).

In longitudinal section, at 6 weeks trabeculae were present and evenly distributed (same amount of trabeculae on the side towards the bone marrow as towards the cortex) throughout the scaffold volume in the majority of the CMPC scaffolds (Figure 7B). At 12 weeks, the proportion of Mg225p scaffolds with trabeculae evenly distributed throughout the scaffold volume increased, whereas Mg225d was significantly more likely to have a larger amount of trabeculae towards the cortex than towards the side of the bone marrow ($p = 0.001$). With TCP, the trabeculae were always evenly distributed throughout the scaffold volume, significantly differing this material from Mg225d at all observation time points ($p \leq 0.02$).

3.5.2 Quantitative evaluation of μ CT 80 scans

Various changes of bone structure parameters were observed at the implantation sites over the study period. The Tb.N decreased significantly with the CMPCs between weeks 6 and 24 ($p \leq 0.013$), while it decreased only slightly with TCP, resulting in significant differences of the Tb.N between all materials at weeks 12 and 24 ($p \leq 0.036$) (Figure 7C).

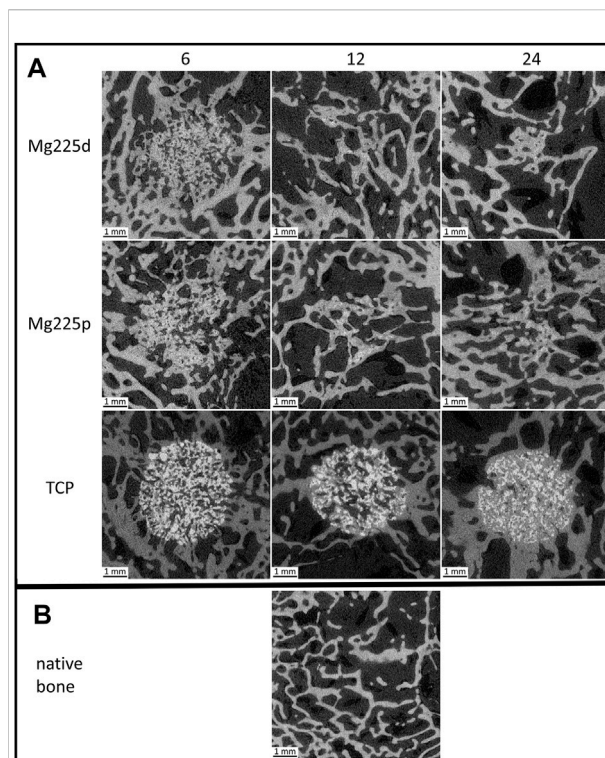


FIGURE 6

Cross-sectional μ CT 80 images (A) of the scaffolds (Mg225d, Mg225p and TCP) implanted in the distal femoral condyles at 6, 12 and 24 weeks after surgery (B) compared to native cancellous bone of the lateral femoral condyle.

The Tb.Th increased significantly in Mg225d and Mg225p between weeks 6 and 24 ($p \leq 0.001$) and was always significantly higher with the CMPCs than with TCP ($p \leq 0.040$) (Figure 7D).

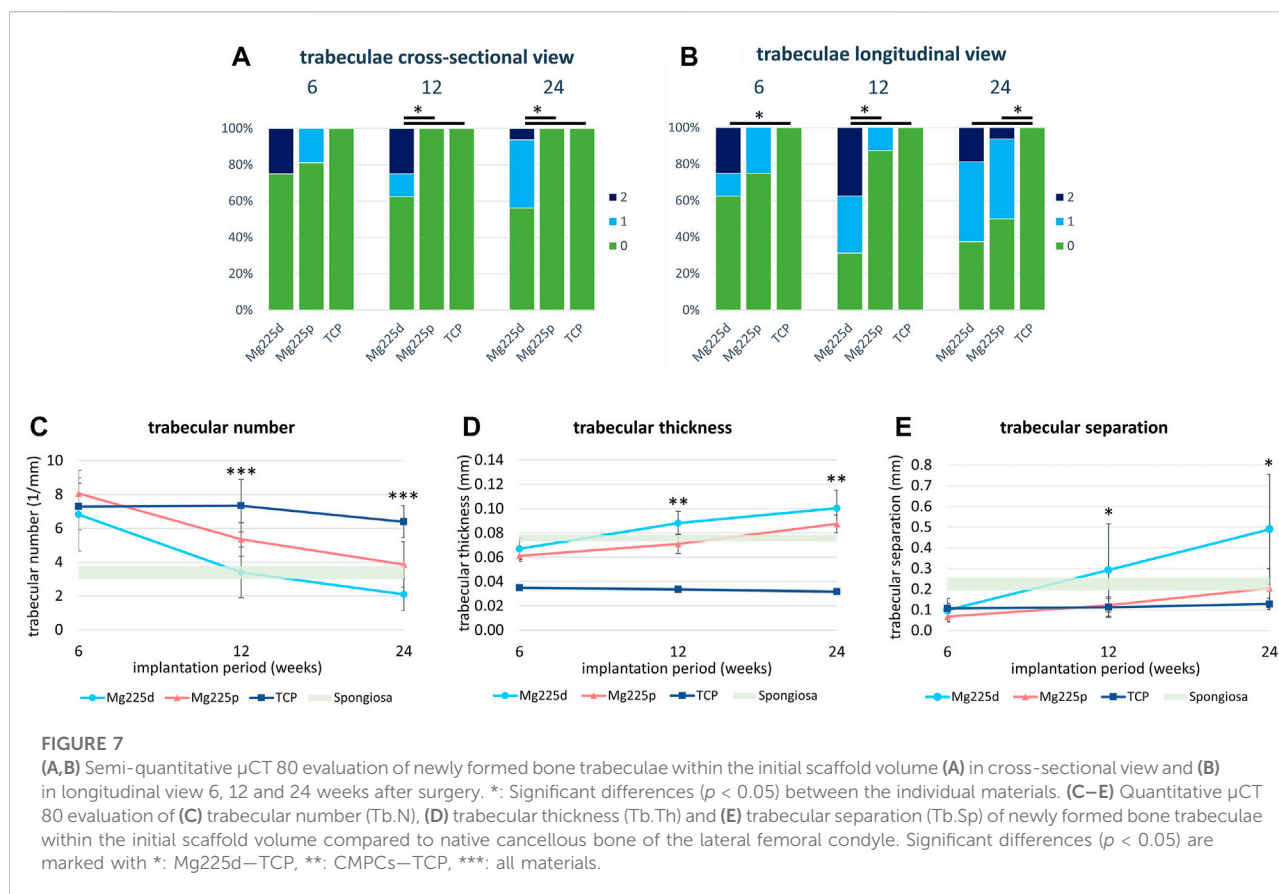
A significant increase in Tb.Sp was observed in the CMPCs in contrast to TCP, when comparing week 6 with week 24 ($p \leq 0.002$) (Figure 7E). At weeks 12 and 24, the Tb.Sp was significantly higher with Mg225d than with TCP ($p \leq 0.036$).

3.6 Histological examination

3.6.1 Semi-quantitative evaluation of histological sections

Histologically, a centripetal directed degradation was visible in all materials, steadily increasing over the study period (Figures 8, 9A). At each observation time point, the percentage area of scaffold material in the scaffold cross section of the CMPCs differed significantly from TCP ($p \leq 0.041$). The least material was always present from Mg225d, the most from TCP.

The material of all scaffolds was $>50\%$ surrounded by bone in the MR and OR after 6 weeks, in the IR this was observed in the majority ($\geq 71.4\%$) of the scaffolds (Supplementary Figure S3A). At 6 weeks, significantly more bone had grown into the CMPC



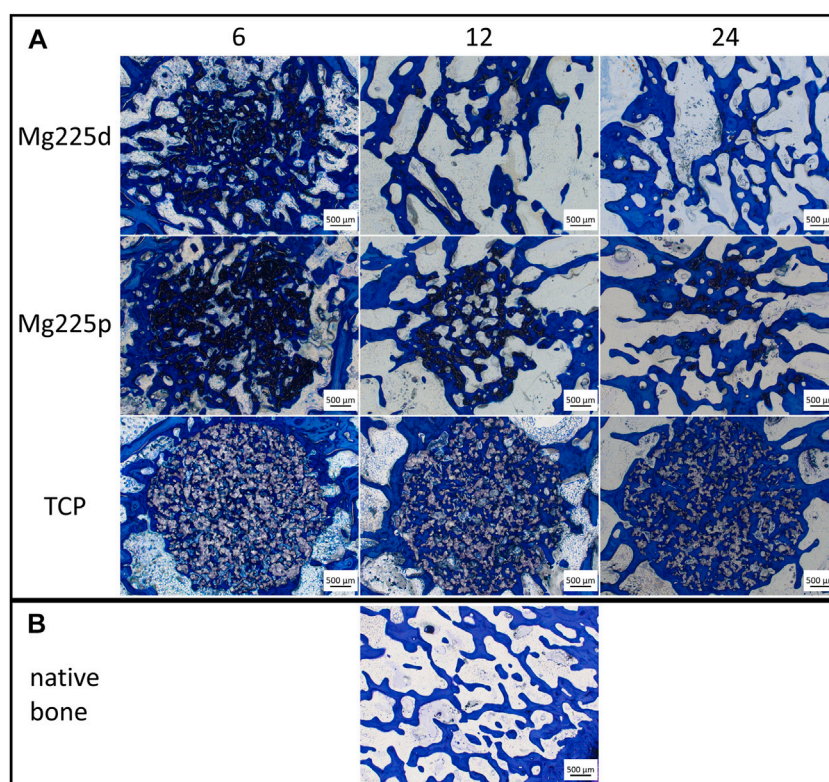
scaffolds than into TCP ($p \leq 0.004$) (Figure 9B). At 12 and at 24 weeks, the proportion of new, immature bone steadily decreased, while the proportion of remodeled bone increased (Figures 9B,C). This remodeling of newly formed bone occurred more slowly in TCP than in the CMPCs, as evidenced by a still significantly greater amount of newly formed bone at week 12 in TCP compared to the CMPCs ($p < 0.001$). Nevertheless, after 24 weeks, TCP showed significantly more remodeled bone than the CMPCs ($p < 0.001$). With increasing bone maturity, the number of osteoblasts and the amount of osteoid at the newly formed bone trabeculae decreased over the course of the study in all materials (Supplementary Figures S3B,C). However, at week 24, TCP still exhibited significantly more osteoid than the CMPCs ($p \leq 0.017$).

After 6 weeks, a low to moderate amount of granulation tissue/bone marrow (<50% of scaffold cross-sectional area) with a low to moderate number of adipocytes occurred in most scaffolds (Figures 9D,E). The percentage area of granulation tissue/bone marrow and the number of adipocytes increased markedly in the CMPCs over the study period. At each observation time point, the CMPCs showed significantly more adipocytes ($p < 0.001$) and at weeks 12 and 24 significantly more granulation tissue/bone marrow than TCP ($p < 0.001$). Mg225d always exhibited more granulation tissue/bone marrow than

Mg225p. After 24 weeks, all CMPC scaffolds showed numerous adipocytes throughout the implantation area and in the majority of the CMPC scaffolds (Mg225d: 95.8%, Mg225p: 62.5% of ROIs), >50% of the scaffold cross-sectional area consisted of granulation tissue/bone marrow. In contrast, granulation tissue/bone marrow in TCP almost always accounted for a maximum of 25% of the scaffold cross-sectional area and in less than half of the ROIs many adipocytes were present after 24 weeks.

Except for the IR of one TCP scaffold, precursor cells were observed in all scaffolds of all materials in each ROI as early as after 6 weeks (Supplementary Figure S3D). An increase in their amount at 12 weeks was followed by a decrease in the amount of precursor cells at week 24 in all materials. Numerous blood vessels were present in all materials at each observation time point, with Mg225p always showing significantly greater vascularization than TCP ($p \leq 0.001$) (Supplementary Figure S3E).

Connective tissue with fibrocytes was present in low to moderate amounts in the majority of scaffolds of all materials after 6 weeks (Figure 9F). In the CMPCs, the amount of connective tissue had decreased markedly at 12 weeks and after 24 weeks, it was no longer observed in Mg225d and only sporadically present in Mg225p. In TCP, however, significantly

**FIGURE 8**

Histological thick sections (toluidine blue staining, magnification $\times 2.5/0.085$) (A) from the center of the Mg225d, Mg225p and TCP scaffolds in cross section after 6, 12 and 24 weeks and (B) comparison to native cancellous bone of the lateral femoral condyle.

more connective tissue with fibrocytes than in the CMPCs was observed at each observation time point ($p < 0.001$). In all materials, connective tissue was almost always more abundant in the IR than in the MR and OR. A resorption zone (annular zone within the scaffold cross section, containing many cells and connective tissue) was observed after 6 weeks in 25% of the Mg225d scaffolds and in 12.5% of the TCP scaffolds in the IR (score 1) and after 24 weeks in 12.5% of the TCP scaffolds in the MR (score 1) and the IR (score 2) (scoring system in Table 4), respectively (Supplementary Figure S3F).

In the CMPCs, many macrophages were observed in $>54\%$ of ROIs at weeks 6 and 12 (Figure 9G). After 24 weeks, only a small or moderate number of macrophages was present in $\geq 75\%$ of ROIs in the CMPCs. As many macrophages were observed in TCP throughout the study period, TCP differed significantly from the CMPCs at week 24 ($p \leq 0.001$).

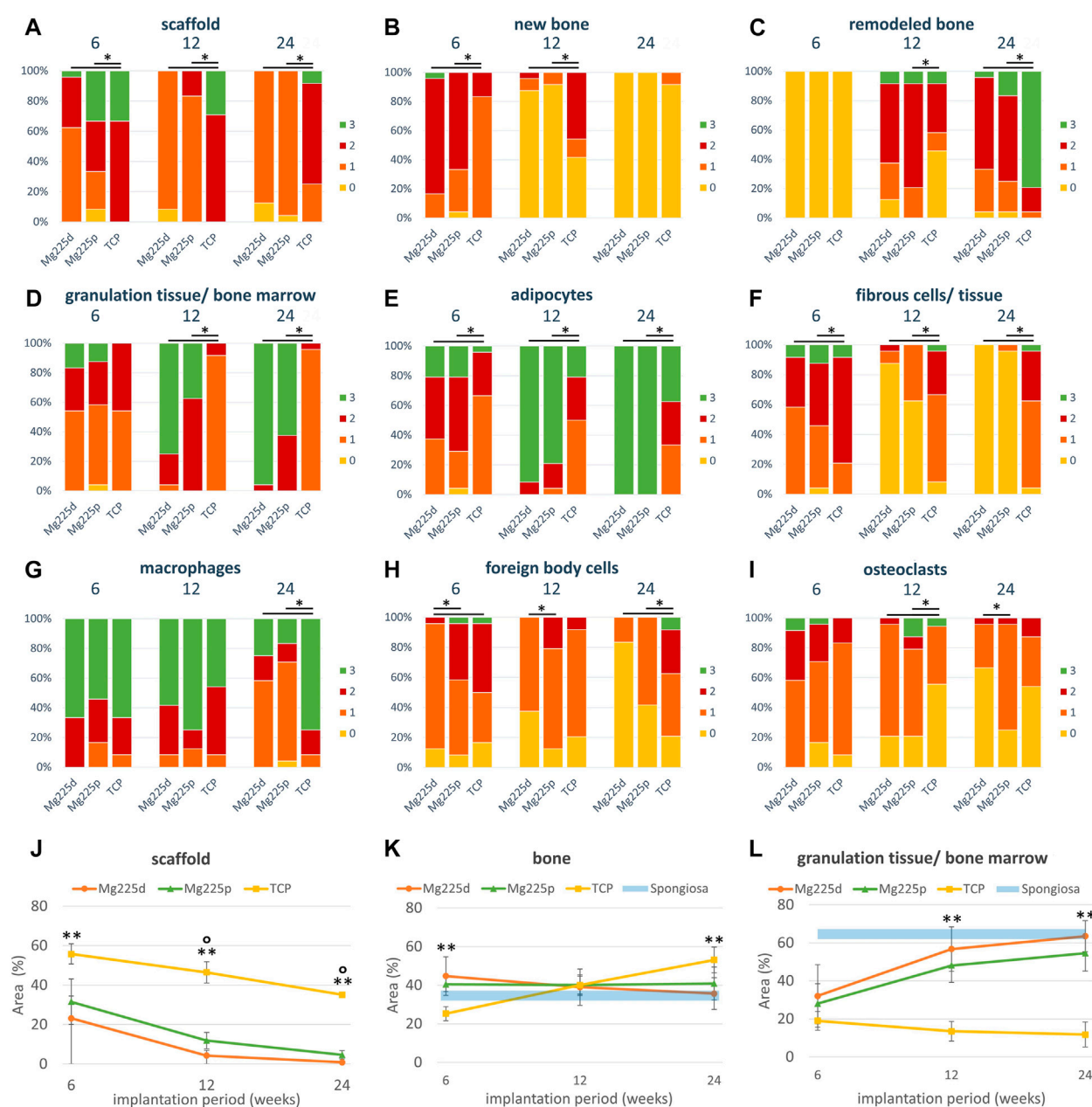
At weeks 6 and 12, few FBCs were present in $\geq 50\%$ of the ROIs of the CMPC scaffolds (Figure 9H). In Mg225p, they were significantly more frequent than in Mg225d ($p \leq 0.017$). In TCP, moderate to many FBCs were present at each observation time point (week 6: 50%, week 12: 8.3%, week 24: 37.5% of ROIs), differing it significantly from the CMPCs at week 24 ($p \leq 0.042$).

Overall, however, the number of FBCs decreased over the study period for all materials.

After 6 weeks, moderate to many osteoclasts were present in 41.7% of ROIs in Mg225d and 29.2% of ROIs in Mg225p, and their amount decreased with increasing implantation time (Figure 9I). TCP showed fewer osteoclasts than the CMPCs at 6 weeks and significantly fewer at 12 weeks ($p \leq 0.018$). After 24 weeks, no or few osteoclasts were observed in $\geq 87.5\%$ of ROIs in all materials.

3.6.2 Quantitative evaluation (histomorphometry)

All scaffolds showed a significant material loss over the study period ($p \leq 0.003$) (Figure 9J). After 24 weeks, the CMPC scaffolds were almost completely degraded (percentage of area of scaffold material in the scaffold cross section: Mg225d: 0.85%, Mg225p: 4.63%), while the remaining TCP material comprised 35.14% of the scaffold cross-sectional area. There was always significantly less material present from Mg225d and Mg225p than from TCP ($p < 0.001$). Additionally, in weeks 12 and 24, there was significantly less material present from Mg225d than from Mg225p ($p \leq 0.007$).



After 6 weeks, significantly more bone had grown into the CMPC scaffolds than into the TCP scaffolds ($p \leq 0.001$) (Figure 9K). After 12 weeks, the percentage of bone was approximately the same for all materials. After 24 weeks, it was significantly higher in TCP than in the CMPCs ($p \leq 0.022$).

Over the study period, the amount of soft tissue (granulation tissue, bone marrow) increased significantly in Mg225d and Mg225p, resulting in significantly more soft tissue with the CMPCs than with TCP at weeks 12 and 24 ($p < 0.001$) (Figure 9L).

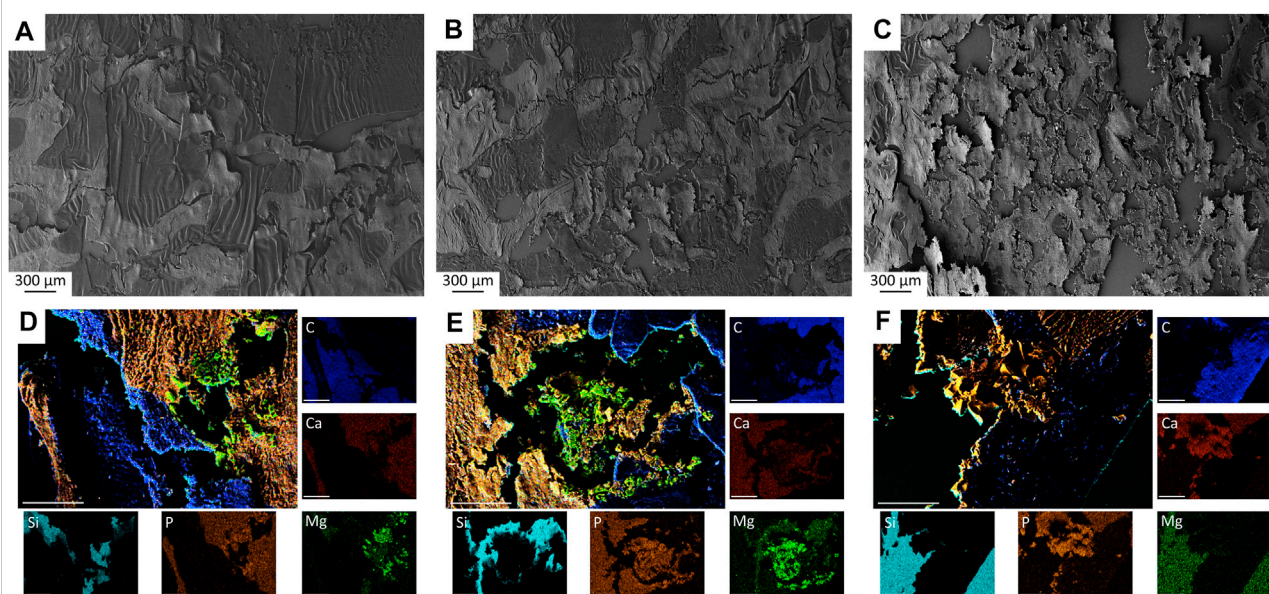


FIGURE 10

(A–C) SEM analysis of histological thin sections (×28 magnification) with (A) Mg225d, (B) Mg225p and (C) TCP scaffold incorporated by newly formed cancellous bone after 12 weeks. (D–F) EDX analysis of histological thin sections (×500 magnification) with (D) Mg225d, (E) Mg225p and (F) TCP particles incorporated by newly formed cancellous bone after 12 weeks. Scale bar = 50 µm.

3.7 SEM and EDX analysis of the unstained histological sections

Small scaffold particles could be detected in SEM and EDX analysis in all materials at all observation time points (Figure 10; Supplementary Figures S4, S5). A continuously increasing material degradation was observed. The material residues appeared as small, sharp-edged particles that were excellently integrated into the surrounding bone. After only 6 weeks, the entire implantation area of Mg225d was infiltrated by bone (Supplementary Figure S4A). The scaffold structure was no longer recognizable, the material was largely replaced by newly formed bone and the remaining particles were enclosed by it (Supplementary Figure S4D). After 12 weeks, the scaffolds were already degraded to a large extent, and after 24 weeks, only smallest particles of Mg225d were still present, incorporated into bone trabeculae (Figure 10A,D; Supplementary Figures S5A,D). The degradation of Mg225p showed a similar course, with always slightly more material present than with Mg225d. From week 12 onwards, the scaffold structure was no longer evident in Mg225p either. As with Mg225d, the scaffold was completely traversed by new bone trabeculae after 6 weeks. Mg225p also showed an excellent osseointegration and almost complete degradation after 24 weeks (Figure 10B,E; Supplementary Figures S4B,E, S5B,E). A greater amount of cement matrix was present with TCP than with the CMPCs at each time point examined, and less extensive material degradation was

observed over time. As of 6 weeks, the entire implant site was also infiltrated by new bone. As with the CMPCs, good osseointegration of the scaffold material was observed throughout the study period (Figure 10C,F; Supplementary Figures S4C,F, S5C,F).

4 Discussion

Due to their better mechanical properties as well as their faster degradation compared to CPCs, CMPCs have been increasingly researched in recent years in the form of cement pastes and granules (Wu et al., 2008a; Wu et al., 2008b; Klammert et al., 2010a; Jia et al., 2010; Wei et al., 2010; Vorndran et al., 2011; Zeng et al., 2012; Ewald et al., 2019; Fuchs et al., 2021; Götz et al., 2021). However, for the treatment of many bone defects, three-dimensional, dimensionally stable scaffolds are required, that can be produced patient-specifically. Therefore, 3D powder printing has emerged as a promising manufacturing technique for bone substitutes (Castilho et al., 2014a; Roseti et al., 2017; Zhang et al., 2019). This study varied the post-treatment of 3D powder printed CMPC scaffolds produced from the ceramic cement powder $\text{Ca}_{0.75}\text{Mg}_{2.25}(\text{PO}_4)_2$ by either immersion in DAHP (alkaline post-treatment) or by infiltration with PA (acid post-treatment), affecting the physical and chemical properties of the scaffolds. The influence of DAHP (Mg225d) or PA (Mg225p) post-treatment on biocompatibility, osseointegration and

degradation behavior of the scaffolds was investigated *in vivo* and compared between the two materials. Scaffolds of the established material TCP served as reference. The scaffolds were implanted into the lateral femoral condyles of rabbits and assessed by regular clinical and radiological (X-Ray and μ CT) examinations up to 24 weeks. After euthanasia of the animals, higher-resolution μ CT 80 and histological examinations were performed on the explanted scaffold-bone-complexes, as well as an analysis by SEM and EDX.

When the compressive strength of the scaffolds was investigated prior to implantation, all materials differed significantly from each other, with TCP having the lowest compressive strength and Mg225p the highest. The examination of the porosity with the mercury porosimeter as well as SEM analysis of the scaffolds before implantation showed that TCP had the highest porosity and Mg225p the lowest. As an increase in pore size and porosity affects the structural integrity of the scaffolds and reduces their mechanical properties (Karageorgiou and Kaplan, 2005), an inverse relationship between porosity and compressive strength has been described in the literature (Vorndran et al., 2011; Zhang et al., 2014; Wang et al., 2019), which was also observed with the materials investigated in this study.

As previously described in studies on CMPCs with the application form of granules, pastes or cylindrical scaffolds (Wu et al., 2008b; Wei et al., 2010; Ewald et al., 2019; Fuchs et al., 2021; Götz et al., 2021; Kowalewicz et al., 2021), the CMPCs investigated in this study as well as TCP showed excellent clinical tolerability with physiological wound healing. No animal showed lameness or pain.

Radiographically, the visibility of the CMPC scaffolds decreased rapidly and was significantly lower than that of TCP in both views from week 6 at the latest, whereas the latter was always still clearly delineable from surrounding bone until week 24. The longer visibility of the TCP scaffolds can be explained by the higher content of radiopaque Ca. However, it could also be an indication of a slower degradation compared to the CMPC scaffolds, which Fuchs et al. (2021) also observed when investigating granules of CMPCs and CPC (HA) in a rabbit model.

The CMPCs showed a significant volume loss as well as a significant increase of the surface area to volume ratio upon *in-vivo* μ CT examination over the study period. The volume loss was significantly more pronounced with the CMPCs than with TCP. The significantly faster volume degradation of Mg225d compared to Mg225p can be explained by the different chemical and physical properties of the scaffolds. The chemical solubility of the individual phases of the CMPCs increases as listed: farringtonite < struvite < brushite < newberyite (Ostrowski et al., 2016). No data on the solubility of stanfieldite are available in the accessible literature. The cement raw materials farringtonite and stanfieldite are mainly cohered by the binder phases struvite (Mg225d), newberyite and brushite (Mg225p)

formed during post-treatment with DAHP and PA, respectively (cf. Eqs. 1–3 in Section 3.1.1). The importance of the wt% fraction of the binder phase on the chemical degradation rate has previously been shown in the *in-vitro* study on scaffolds of farringtonite (76 wt%) and struvite (24 wt%) (TMP-D) and farringtonite (57 wt%) and newberyite (43 wt%) (TMP-P), respectively (Gefel et al., 2022). Despite the higher proportion of the chemically less soluble phase farringtonite, a faster and greater chemical solubility of TMP-D was observed compared to TMP-P. This phenomenon was based on the faster degradation of the low proportion of the binder phase struvite (24 wt%) compared to newberyite (43 wt%), as a result of which the degradation of the cement raw materials proceeded more rapidly (Gefel et al., 2022). In the present study, the same process can be assumed. In Mg225d, the binder phase struvite was probably degraded relatively quickly due to its low wt% content (<6 wt%). Based on the SEM and EDX analysis of Mg225d, it can also be assumed that due to the lower Ca-occurrence, more struvite and less stanfieldite was present in the peripheral region of the scaffolds, while areas of unreacted raw powder with low mechanical strength were probably present in the scaffold center. As soon as the outer areas with more struvite had dissolved, the scaffolds lost stability, the remaining cement matrix was no longer sufficiently cohered and rapidly disintegrated into individual particles, which was particularly accelerated by the ingrowth of bone and cells. Despite the higher chemical solubility of newberyite and brushite, the degradation of these binder phases took more time in Mg225p due to the higher wt% content (63.75 wt%) as well as the uniform distribution. Consequently, the scaffold matrix was cohered for a longer time and the degradation was slower than for Mg225d. Since dissolution is a physico-chemical process, it is controlled not only by solubility but also by porosity, pore size and surface area to volume ratio (Dorozhkin, 2013). SEM and EDX analysis of the scaffolds prior to implantation showed that Mg225d had large ($\varnothing > 100 \mu\text{m}$), interconnected pores, which were not detected in the mercury porosimeter measurement because they were either occluded or beyond the accessible measurement range. Therefore, the porosity and pore size of Mg225d can be assumed to be much larger than in Mg225p. Wei et al. (2010) observed significantly greater weight degradation for CPC and MPC scaffolds with higher microporosity and larger surface area in simulated body fluid (SBF) solution. Also, Kim et al. (2016) observed a faster material degradation with larger pore size during *in-vivo* investigation of MPC scaffolds. Therefore, it can be assumed that the higher porosity and larger pore size of Mg225d compared to Mg225p investigated in this study had an additional accelerating effect on the degradation rate. The solubility of the scaffolds was also likely enhanced by an increase in the scaffold surface area to volume ratio (SS/SV), which was accompanied by the loss of the cohesive scaffold structure. The significantly larger SS/SV between weeks 6 and 10 for Mg225d compared to Mg225p confirms that the Mg225d scaffolds

disintegrated into individual material particles much faster than Mg225p, which further accelerated the degradation of Mg225d. Since TCP has a relatively low solubility (Wang and Nancollas, 2008; Dorozhkin, 2013), dissolution of the TCP scaffolds investigated in this study occurred only to a very small extent.

Due to the very comparable radiopacity of the scaffolds and bone, distinct differentiation between scaffold material and bone that had grown into the implantation area was not always possible in *in-vivo* μ CT. In this regard, difficulties have also occurred in various other *in-vivo* studies on CaPs, CPCs or MPCs (Chopra et al., 2009; Huber et al., 2009; Kasuya et al., 2012; Kanter, 2014). Therefore, it is likely that newly formed bone was erroneously attributed to the scaffold volume, especially at the later observation time points, which also explains the increase in SV at TCP once again between weeks 12 and 16. However, the histomorphometric examinations in the present study clearly demonstrated the almost complete degradation of the CMPC scaffolds after 24 weeks.

The faster scaffold degradation on the side towards the bone marrow observed in the CMPCs in the present study has also been described by other authors for magnesium-based implants. It is assumed that degradation progresses more rapidly on the side towards the medullary cavity due to the higher blood vessel supply and the weaker trabecular network in the scaffold environment (Xu et al., 2007; Höh et al., 2009; Zhang et al., 2009). In the present study, it can be assumed that due to the overall faster degradation of Mg225d compared to Mg225p, increased material degradation on the side towards the medullary cavity was significantly more pronounced in Mg225d than in Mg225p.

Both CMPCs as well as TCP investigated in this study showed rapid and comprehensive osseointegration in the *in-vivo* μ CT examination by the presence of a broad direct scaffold-bone-contact after 8 weeks at the latest. This indicates optimal surface properties as well as excellent biocompatibility and osteogenesis of the scaffolds. The formation of an extensive direct bone-implant contact has also been demonstrated in other studies on CMPCs (Wu et al., 2008b; Wei et al., 2010; Ewald et al., 2019; Fuchs et al., 2021). The high microporosity of the 3D powder-printed scaffolds compared to cement pastes results in a large surface area, which has a positive effect on the integration into the surrounding bone. Various *in-vivo* studies have shown that improved osteogenesis and osseointegration occur with porous compared to solid implants, as pores allow cell migration and proliferation as well as vascularization (Karageorgiou and Kaplan, 2005). *In-vitro* investigations of CPC and MPC scaffolds have shown that the presence of micropores in particular has a positive effect on cell growth (Wei et al., 2010). A porous surface also improves mechanical interlocking and stability at the critical interface between scaffold and surrounding bone (Karageorgiou and Kaplan, 2005).

In the present study, the significant increase in BV observed in the adjacent scaffold environment at week 2 for all materials

was striking, suggesting an osteoconductive and even possible osteoinductive effect of the materials. Kanter (2014) also observed an increased BV in the implant environment compared to peripheral bone when studying CPCs and MPCs in a sheep model. However, she also observed increased bone formation in direct proximity around empty borehole defects. Albrektsson and Johansson (2001) assumed that even a trauma to the bone results in osteoinduction. Therefore, it is also possible that in the present study, increased BV and osteoinduction in the scaffold vicinity was only induced by the trauma of drilling. However, as no comparative empty borehole defect was assessed in the present study, this phenomenon could not be clarified conclusively. The maximum increase in BV at week 2 was followed by a continuous decrease in BV until week 10 (CMPCs) or week 12 (TCP) and an approach to the physiological volume of cancellous bone. An osteoconductive and even slightly osteoinductive effect of the materials investigated in this study is nevertheless suspected, as the BV in the immediate vicinity of the CMPCs as well as of TCP was always slightly higher or in the upper reference range of physiological bone at this location. It is known, that the release of ions from degrading implants can greatly influence the formation of new bone around an implant (Ostrowski et al., 2016). A high Mg-concentration promotes osteoblast proliferation and differentiation and increases their activity (Wu et al., 2015; He et al., 2016) and a local increase of Ca- and PO_4 -ions to a supra-physiological level has a positive effect on new bone formation (Chai et al., 2012). The higher BV in the vicinity of TCP at 24 weeks is probably caused by the higher Ca-content of the material compared with the CMPCs and the higher amount of remaining scaffold material releasing ions until the end of the study. The osteoconductive character as well as the promotion of osteogenesis and bone regeneration by CMPCs has yet been described by other authors (Wu et al., 2008b; Wei et al., 2010; Ewald et al., 2019; Fuchs et al., 2021). Studies on MPCs (Kim et al., 2016; Ostrowski et al., 2016; Kanter et al., 2018; Nabiyouni et al., 2018; Sarkar et al., 2019) and TCP (Walsh et al., 2008; Samavedi et al., 2013; Böhner et al., 2020) also demonstrated an osteoconductive behavior of these materials as well as the stimulation of bone formation.

In the present study, a decrease in Tb.N as well as an increase in Tb.Th and Tb.Sp over the study period was observed for all materials in the *in-vivo* μ CT in the scaffold vicinity, as well as for the CMPCs in the higher-resolution μ CT 80 within the initial scaffold volume. This progression was also observed by Kanter et al. (2018) when investigating MPCs. It suggests that the newly formed bone remodeled, adapted to the physiological situation and matured over the study period, resulting in the renewed presence of nearly physiological cancellous bone within the initial scaffold volume of Mg225p after 24 weeks. By week 24, a high Tb.N with small Tb.Th and Tb.Sp occurred within the scaffold volume of TCP, revealing a slower speed of bone remodeling, possibly because the large amount of remaining material spatially

inhibited trabecular growth and bone maturation. Additionally, μ CT 80 examinations of the scaffold longitudinal sections showed that the newly formed bone trabeculae within the initial scaffold volume were mostly located in the implantation area close to the cortex in Mg225d, whereas they were more evenly distributed in Mg225p with regard to their localization. This can be explained by the fact that Mg225d degraded significantly faster on the side towards the bone marrow than Mg225p and that new bone formation close to the bone marrow could not follow the degradation rate of the scaffold. Ewald et al. (2019) observed a decrease in bone-implant-contact in the faster degrading material when comparing 6 to 12 weeks during the *in-vivo* investigation of CMPC pastes and also assumed too rapid material degradation as a reason. In Mg225p, the material particles probably served as a guide for the new bone for a longer period of time, allowing a more uniform trabecular network to be formed.

In histology, all scaffolds examined in the present study quickly showed good osseointegration and replacement by newly formed trabecular bone increasing over time. Within the observation period, the amount of immature bone and osteoid and the number of osteoblasts in the initial implantation area of all materials decreased, while simultaneously the amount of remodeled, mature bone increased, which is typical for bone maturation (Hadjidakis and Androulakis, 2006; Katsimbri, 2017). The large amount of precursor cells in the bone marrow observed mainly after 12 weeks was also studied by Kanter et al. (2018). It can be considered as an active state of cell organization, resulting in centripetally directed formation of trabecular bone (Kanter et al., 2018). In TCP, significantly more immature bone after 12 weeks and significantly more osteoid after 24 weeks than in the CMPCs was still observed. This suggests that bone maturation occurred more slowly with TCP and was not yet completed at the end of the study period. The significantly higher proportion of bone in TCP compared to the CMPCs after 24 weeks is in contradiction with results from other *in-vivo* studies on CPCs and CMPCs in rabbits (Wu et al., 2008b; Wei et al., 2010). As bone ingrowth is facilitated by increased porosity and pore size (Karageorgiou and Kaplan, 2005), the greater amount of bone observed with TCP in the present study could be attributed to the significantly higher porosity of TCP compared to the CMPCs.

Within the implantation area of the CMPCs, the amount of granulation tissue rich of blood vessels and cells as well as the number of adipocytes increased continuously over the study period. At the same time, the amount of connective tissue with fibrocytes decreased markedly, resulting in no (Mg225d) or only sporadic (Mg225p) appearance after 24 weeks. This indicates that the ingrowing tissue has transformed into mature, physiological bone marrow, as this is also described in the literature (Travlos, 2006; Horowitz et al., 2017; Nombela-Arrieta and Manz, 2017; Lucas, 2021). TCP demonstrated significantly less granulation tissue/bone marrow at weeks

12 and 24 and at each observation time point significantly more connective tissue with fibrocytes than the CMPCs. It is likely that in TCP, due to the slower bone maturation, only little bone marrow was yet formed within the numerous small fibrovascular islets over the study period of 24 weeks. Possibly, the high amount of bone observed with TCP slowed down this remodeling process due to the spatial restriction of the granulation tissue. However, since complete bone replacement with *restitutio ad integrum* of the bone tissue is described in the literature for TCP (Wiltfang et al., 2002; Horch et al., 2006; Kolk et al., 2012), the formation of physiological bone marrow is also likely with a longer observation time.

FBCs express important growth factors for new blood vessel formation and a correlation between the amount of FBCs and the vascularization rate was observed in a study on TCP granules (Ghanaati et al., 2010; Al-Maawi et al., 2021), which could not be confirmed in the present study. Even though moderate to many FBCs were frequently present with TCP, at each observation time point significantly fewer blood vessels occurred within the implantation area of TCP than with Mg225p. Possibly, this could also be due to the spatial limitation of bone and scaffold material with TCP.

For all materials in the present study, centripetal directed degradation was observed in the histological examination, continuously increasing over the course of the investigation. The CMPCs differed significantly from TCP at each observation time point and were almost completely degraded after 24 weeks, whereas numerous particles of TCP were still present at the end of the study. As supposed for the *in-vivo* degradation of CMPCs by Wu et al. (2008b) and Wei et al. (2010), a two-step degradation mechanism is also assumed for the CMPC scaffolds investigated in this study. The previously described first step of chemical dissolution of the cements during the early implantation time resulted in surface enlargement and thus alteration of the microstructure of the scaffolds, which likely facilitated the cell-mediated resorption that occurred later in the second step. *In-vivo* degradation of CaP-based biomaterials is also thought to occur by a combination of chemical dissolution and cell-mediated resorption (Theiss et al., 2005; Dorozhkin, 2013). For rapidly resorbable CPCs such as brushite, mainly macrophages and FBCs are involved in the resorption process, whereas slowly resorbable CPCs such as apatite are degraded by osteoclasts (Apelt et al., 2004; Theiss et al., 2005; Dorozhkin, 2008, 2013). For MPCs, passive resorption by chemical dissolution in magnesium and phosphate ions has been described (Klammert et al., 2011; Kim et al., 2016). Gefel et al. (2022) could not detect an involvement of osteoclasts in the degradation of MPCs in *in-vitro* studies. In various *in-vivo* studies, however, osteoclasts were observed at the implantation site of MPCs, indicating a possible active cellular resorption as well (Zeng et al., 2012; Kim et al., 2016; Kanter et al., 2018). In the present study, both numerous macrophages and multinucleated cells located directly at the scaffold material were

observed. The number of macrophages decreased strongly in the CMPCs with advanced implantation time and degradation of the scaffolds, suggesting that they were involved to a large extent in material degradation. The FBCs observed with the CMPCs especially at the early observation time points were probably also involved in the cellular degradation. The significantly more frequent occurrence of FBCs at weeks 6 and 12 in Mg225p than in Mg225d correlates with the still greater amount of remaining scaffold material in Mg225p at these time points and supports this hypothesis. Furthermore, since with the CMPCs, slightly (week 6) or even significant (week 12) more osteoclasts were observed than with TCP, it is reasonable to assume that they were also participating in the degradation of the MPC phases. However, the increased occurrence of osteoclasts with the CMPCs could also be due to the fact that these cells were substantially involved in physiological bone remodeling, as also described in the literature (Hadjidakis and Androulakis, 2006). With TCP, many macrophages and some FBCs were present at each observation time point, and their amount was significantly higher than with the CMPCs at week 24. Therefore, it can be assumed that these two cell types were mainly responsible for the material degradation of TCP. Since the complete degradation of TCP happens rather slowly (Moore et al., 2001; Kolk et al., 2012; Bohner et al., 2020) and at the end of the study period larger amounts of potentially material-resorbing cells were still present, it can be assumed that the degradation of TCP was not yet completed after 24 weeks. However, as also described in the literature (Wiltfang et al., 2002), in the present study cellular degradation may have been impaired by the fact that a very high proportion of the numerous TCP fragments still present after 24 weeks were completely surrounded by the newly formed bone trabeculae and were therefore not accessible for further degradation for the time being. The final degradation of these particles occurs only when the material is exposed during remodeling processes of the newly formed bone (Wiltfang et al., 2002).

The resorption zone, found with an annular area of darker gray value within the scaffold volume of the CMPCs between weeks 2 and 8 in the *in-vivo* μ CT scans, could be identified in the histological examination as fibrovascular, macrophage-rich stroma between the material core and the ingrowing bone trabeculae. Investigating brushite or K-struvite cements, other authors have also observed such a fibrovascular resorption zone around the cement during the early implantation period (up to 2 months) (Constantz et al., 1998; Frayssinet et al., 2000; Apelt et al., 2004; Kaiser et al., 2022). As this zone was significantly more frequent in Mg225d than in Mg225p and TCP, it is reasonable to assume a connection with the scaffold degradation rate. It is likely that the volume degradation in Mg225d and in some cases also in Mg225p proceeded too rapidly, rendering the attachment of the newly formed bone trabeculae to the scaffold material impossible, as also assumed for K-struvite by Kaiser et al. (2022). However, the fibrovascular

zone formed to bridge the defect was in the present study at the latest after 10 weeks replaced by ingrowing trabecular bone.

Using SEM and EDX analysis, the surface texture of the thin sections of the scaffold-bone-complexes and the occurrence, respectively amount, of Mg in the implantation area have clearly demonstrated the presence of small scaffold particles in all materials by week 24. The results are consistent with the histological findings and confirm excellent osseointegration, almost complete degradation of the CMPCs, and replacement of the scaffolds by trabecular bone. In a study by Fuchs et al. (2021), EDX analysis of CMPCs granules also showed increasing degradation over time and their replacement by bone tissue based on the detection of Mg, Ca, and P. For TCP, very good osseointegration and osteoneogenesis were also observed in the present study, but only a slight progression of degradation occurred.

5 Conclusion

This study varied the post-treatment of 3D powder printed CMPC scaffolds by either immersion in DAHP or by infiltration with PA, and the influence of the post-treatment on the *in-vivo* performance of the scaffolds was examined. In a non-weight-bearing borehole defect in rabbits, both investigated CMPCs, Mg225d (alkaline post-treatment with DAHP) and Mg225p (acid post-treatment with PA), showed excellent biocompatibility and osseointegration, over time continuously increasing and almost complete degradation, and replacement of the scaffolds by newly formed bone trabeculae, which underwent continuous remodeling and adaption to the physiological situation. Post-treatment with DAHP resulted in significantly faster degradation with loss of cylindrical form, demarcability from surrounding bone, and scaffold volume in Mg225d than in Mg225p and TCP. Mg225d also showed significantly greater degradation on the side towards the medullary cavity than Mg225p and TCP. In TCP, degradation was significantly less than in the CMPCs after 24 weeks. All materials rapidly showed an ingrowth of numerous bone trabeculae into the scaffold. While in Mg225d, the trabeculae were predominantly located in the implantation area towards the cortex, in Mg225p they were more evenly distributed and showed almost the same structural properties as physiological bone at this localization after 24 weeks. The rapid degradation of Mg225d as well as the rapid breakdown of the scaffold framework into individual material particles probably had a negative effect on the uniform trabecular ingrowth. Therefore, and due to the low compressive strength of Mg225d, which presumably further decreased with increasing implantation time, this material is not suitable for application in weight-bearing bone. Since Mg225d nevertheless had a positive influence on osteoneogenesis, its use as a bone substitute in non-weight-bearing bone, such as for a sinus lift, would be feasible. In the present study, Mg225p showed, due to its higher compressive strength, optimal degradation rate for concurrent new bone formation, and excellent osteoneogenesis throughout the scaffold

volume, promising properties for use as degradable bone substitute to be further investigated in weight-bearing bone.

Data availability statement

The original contributions presented in the study are included in the article/Supplementary Material, further inquiries can be directed to the corresponding author.

Ethics statement

The animal study was reviewed and approved by the Regional Government of Upper Bavaria, Munich, Germany (approval number: ROB 55.2-2532.Vet_02-19-64).

Author contributions

Conceptualization and methodology, EV and AM-L; Investigation KK, A-CW, FF, A-MS, MB, EV, and AM-L; Resources, A-CW, EV, and AM-L; Writing-original draft preparation, KK; Writing-review and editing, A-CW, FF, EV, and AM-L; Visualization, KK and EV; Supervision, A-CW, FF, EV, and AM-L; Project administration, A-CW, EV, and AM-L; Funding acquisition, EV and AM-L. All authors have read and agreed to the published version of the manuscript.

Funding

This research was funded by the German Research Foundation (DFG), grant number 417069397, as part of the

collaboration project “Additive manufacturing of personalized bone implants for application in human and veterinary medicine based on calcium magnesium phosphates” between the Ludwig-Maximilians-University of Munich and the University of Würzburg. The authors would like to thank for the financial support. We also thank the DFG for funding the Zeiss CB 340 crossbeam scanning electron microscope (INST 105022/58-1 FUGG) within the DFG’s FUGG State Major Instrumentation Programme.

Conflict of interest

The authors declare that the research was conducted in the absence of any commercial or financial relationships that could be construed as a potential conflict of interest.

Publisher’s note

All claims expressed in this article are solely those of the authors and do not necessarily represent those of their affiliated organizations, or those of the publisher, the editors and the reviewers. Any product that may be evaluated in this article, or claim that may be made by its manufacturer, is not guaranteed or endorsed by the publisher.

Supplementary material

The Supplementary Material for this article can be found online at: <https://www.frontiersin.org/articles/10.3389/fbioe.2022.998254/full#supplementary-material>

References

- Agarwal, R., and García, A. J. (2015). Biomaterial strategies for engineering implants for enhanced osseointegration and bone repair. *Adv. Drug Deliv. Rev.* 94, 53–62. doi:10.1016/j.addr.2015.03.013
- Al-Maawi, S., Barbeck, M., Vizcaino, C. H., Egli, R., Sader, R., Kirkpatrick, C. J., et al. (2021). Thermal treatment at 500°C significantly reduces the reaction to irregular tricalcium phosphate granules as foreign bodies: An *in vivo* study. *Acta Biomater.* 121, 621–636. doi:10.1016/j.actbio.2020.11.034
- Albrektsson, T., and Johansson, C. (2001). Osteoinduction, osteoconduction and osseointegration. *Eur. Spine J.* 10 (2), 96–101. doi:10.1007/s005860100282
- Ambard, A. J., and Mueninghoff, L. (2006). Calcium phosphate cement: Review of mechanical and biological properties. *J. Prosthodont.* 15 (5), 321–328. doi:10.1111/j.1532-849X.2006.00129.x
- Apelt, D., Theiss, F., El-Warrak, A., Zlinszky, K., Bettschart-Wolfisberger, R., Bohner, M., et al. (2004). *In vivo* behavior of three different injectable hydraulic calcium phosphate cements. *Biomaterials* 25 (7–8), 1439–1451. doi:10.1016/j.biomaterials.2003.08.073
- Arrington, E. D., Smith, W. J., Chambers, H. G., Bucknell, A. L., and Davino, N. A. (1996). Complications of iliac crest bone graft harvesting. *Clin. Orthop. Relat. Res.* 329, 300–309. doi:10.1097/00003086-199608000-00037
- Augustin, J., Feichtner, F., Waselau, A. C., Julmi, S., Klose, C., Wriggers, P., et al. (2020). Comparison of two pore sizes of LAE442 scaffolds and their effect on degradation and osseointegration behavior in the rabbit model. *J. Biomed. Mat. Res.* 108 (7), 2776–2788. doi:10.1002/jbm.b.34607
- Augustin, J., Feichtner, F., Waselau, A. C., Julmi, S., Klose, C., Wriggers, P., et al. (2022). Effect of pore size on tissue ingrowth and osteoconductivity in biodegradable Mg alloy scaffolds. *J. Appl. Biomater. Funct. Mat.* 20, 228080002210781. doi:10.1177/22808000221078168
- Bohner, M., Santoni, B. L. G., and Döbelin, N. (2020). β -tricalcium phosphate for bone substitution: Synthesis and properties. *Acta Biomater.* 113, 23–41. doi:10.1016/j.actbio.2020.06.022
- Bohner, M., Theiss, F., Apelt, D., Hirsiger, W., Houriet, R., Rizzoli, G., et al. (2003). Compositional changes of a dicalcium phosphate dihydrate cement after implantation in sheep. *Biomaterials* 24 (20), 3463–3474. doi:10.1016/s0142-9612(03)00234-5
- Boyan, B. D., Hummert, T. W., Dean, D. D., and Schwartz, Z. (1996). Role of material surfaces in regulating bone and cartilage cell response. *Biomaterials* 17 (2), 137–146. doi:10.1016/0142-9612(96)85758-9
- Brunello, G., Sivolella, S., Meneghello, R., Ferroni, L., Gardin, C., Piattelli, A., et al. (2016). Powder-based 3D printing for bone tissue engineering. *Biotechnol. Adv.* 34 (5), 740–753. doi:10.1016/j.biotechadv.2016.03.009
- Campana, V., Milano, G., Pagano, E., Barba, M., Cicione, C., Salonna, G., et al. (2014). Bone substitutes in orthopaedic surgery: From basic science to clinical practice. *J. Mat. Sci. Mat. Med.* 25 (10), 2445–2461. doi:10.1007/s10856-014-5240-2

- Castilho, M., Dias, M., Vorndran, E., Gbureck, U., Fernandes, P., Pires, I., et al. (2014a). Application of a 3D printed customized implant for canine cruciate ligament treatment by tibial tuberosity advancement. *Biofabrication* 6 (2), 025005. doi:10.1088/1758-5082/6/2/025005
- Castilho, M., Moseke, C., Ewald, A., Gbureck, U., Groll, J., Pires, I., et al. (2014b). Direct 3D powder printing of biphasic calcium phosphate scaffolds for substitution of complex bone defects. *Biofabrication* 6 (1), 015006. doi:10.1088/1758-5082/6/1/015006
- Chai, Y. C., Carlier, A., Bolander, J., Roberts, S. J., Geris, L., Schrooten, J., et al. (2012). Current views on calcium phosphate osteogenicity and the translation into effective bone regeneration strategies. *Acta Biomater.* 8 (11), 3876–3887. doi:10.1016/j.actbio.2012.07.002
- Chopra, P. M., Johnson, M., Nagy, T. R., and Lemons, J. E. (2009). Micro-computed tomographic analysis of bone healing subsequent to graft placement. *J. Biomed. Mat. Res.* 88 (2), 611–618. doi:10.1002/jbm.b.31232
- Constantz, B. R., Barr, B. M., Ison, I. C., Fulmer, M. T., Baker, J., McKinney, L., et al. (1998). Histological, chemical, and crystallographic analysis of four calcium phosphate cements in different rabbit osseous sites. *J. Biomed. Mat. Res.* 43 (4), 451–461. doi:10.1002/(sici)1097-4636(199824)43:4<451::aid-jbm13>3.0.co;2-q
- Donath, K., and Breuner, G. (1982). A method for the study of undecalcified bones and teeth with attached soft tissues. The Säge-Schliff (sawing and grinding) Technique. *J. Oral Pathol. Med.* 11 (4), 318–326. doi:10.1111/j.1600-0714.1982.tb00172.x
- Dorozhkin, S. V. (2008). Calcium orthophosphate cements for biomedical application. *J. Mat. Sci.* 43 (9), 3028–3057. doi:10.1007/s10853-008-2527-z
- Dorozhkin, S. V. (2013). Calcium orthophosphate-based bioceramics. *Mater. (Basel)* 6 (9), 3840–3942. doi:10.3390/ma6093840
- Dorozhkin, S. V., and Epple, M. (2002). Biological and medical significance of calcium phosphates. *Angew. Chem. Int. Ed. Engl.* 41 (17), 3130–3146. doi:10.1002/1521-3773(20020902)41:17<3130::AID-ANIE3130>3.0.CO;2-1
- Ewald, A., Kreczy, D., Brückner, T., Gbureck, U., Bengel, M., Hoess, A., et al. (2019). Development and bone regeneration capacity of premixed magnesium phosphate cement pastes. *Mater. (Basel)* 12 (13), 2119. doi:10.3390/ma12132119
- Fillingham, Y., and Jacobs, J. (2016). Bone grafts and their substitutes. *Bone Jt. J.* 98-b (1), 6–9. doi:10.1302/0301-620x.98b.36350
- Frakenburg, E. P., Goldstein, S. A., Bauer, T. W., Harris, S. A., and Poser, R. D. (1998). Biomechanical and histological evaluation of a calcium phosphate cement. *J. Bone Jt. Surg.* 80 (8), 1112–1124. doi:10.2106/00004623-199808000-00004
- Frayssinet, P., Roudier, M., Lerch, A., Ceolin, J. L., Deprès, E., and Rouquet, N. (2000). Tissue reaction against a self-setting calcium phosphate cement set in bone or outside the organism. *J. Mat. Sci. Mat. Med.* 11 (12), 811–815. doi:10.1023/a:1008909714090
- Fuchs, A., Kreczy, D., Brückner, T., Gbureck, U., Stahlhut, P., Bengel, M., et al. (2021). Bone regeneration capacity of newly developed spherical magnesium phosphate cement granules. *Clin. Oral Investig.* 26, 2619–2633. doi:10.1007/s00784-021-04231-w
- Gefel, E., Moseke, C., Schmitt, A.-M., Dümmler, N., Stahlhut, P., Ewald, A., et al. (2022). Degradation of 3D-printed magnesium phosphate ceramics *in vitro* and a prognosis on their bone regeneration potential. *Bioact. Mat.* 19, 376–391. doi:10.1016/j.bioactmat.2022.04.015
- Ghanaati, S., Barbeck, M., Orth, C., Willershausen, I., Thimm, B. W., Hoffmann, C., et al. (2010). Influence of β -tricalcium phosphate granule size and morphology on tissue reaction *in vivo*. *Acta Biomater.* 6 (12), 4476–4487. doi:10.1016/j.actbio.2010.07.006
- Götz, L. M., Holeczek, K., Groll, J., Jüngst, T., and Gbureck, U. (2021). Extrusion-based 3D printing of calcium magnesium phosphate cement pastes for degradable bone implants. *Mater. (Basel)* 14 (18), 5197. doi:10.3390/ma14185197
- Gross, K. A., and Berndt, C. C. (2002). Biomedical application of apatites. *Rev. Mineral. Geochem.* 48 (1), 631–672. doi:10.2138/rmg.2002.48.17
- Habibovic, P., Gbureck, U., Doillon, C. J., Bassett, D. C., van Blitterswijk, C. A., and Barralet, J. E. (2008). Osteoconduction and osteoinduction of low-temperature 3D printed bioceramic implants. *Biomaterials* 29 (7), 944–953. doi:10.1016/j.biomaterials.2007.10.023
- Hadjidakis, D. J., and Androulakis, I. I. (2006). Bone remodeling. *Ann. N. Y. Acad. Sci.* 1092, 385–396. doi:10.1196/annals.1365.035
- Haque, M. A., and Chen, B. (2020). *In vitro* and *in vivo* research advancements on the magnesium phosphate cement biomaterials: A review. *Materialia* 13, 100852. doi:10.1016/j.mtla.2020.100852
- He, L., Zhang, X., Liu, B., Tian, Y., and Ma, W. (2016). Effect of magnesium ion on human osteoblast activity. *Braz. J. Med. Biol. Res.* 49 (7), S0100879X2016000700604. doi:10.1590/1414-431X20165257
- Höh, N. v. d., Bormann, D., Lucas, A., Denkena, B., Hackenbroich, C., and Meyer-Lindenber, A. (2009). Influence of different surface machining treatments of magnesium-based resorbable implants on the degradation behavior in rabbits. *Adv. Eng. Mat.* 11 (5), B47–B54. doi:10.1002/adem.200800273
- Horch, H. H., Sader, R., Pautke, C., Neff, A., Deppe, H., and Kolk, A. (2006). Synthetic, pure-phase beta-tricalcium phosphate ceramic granules (Cerasorb) for bone regeneration in the reconstructive surgery of the jaws. *Int. J. Oral Maxillofac. Surg.* 35 (8), 708–713. doi:10.1016/j.ijom.2006.03.017
- Horowitz, M. C., Berry, R., Holtrup, B., Sebo, Z., Nelson, T., Fretz, J. A., et al. (2017). Bone marrow adipocytes. *Adipocyte* 6 (3), 193–204. doi:10.1080/21623945.2017.1367881
- Huber, F. X., McArthur, N., Heimann, L., Dingeldein, E., Cavey, H., Palazzi, X., et al. (2009). Evaluation of a novel nanocrystalline hydroxyapatite paste Ostim in comparison to Alpha-BSM - more bone ingrowth inside the implanted material with Ostim compared to Alpha BSM. *BMC Musculoskelet. Disord.* 10, 164. doi:10.1186/1471-2474-10-164
- Huehnerschulte, T. A., Reifensrath, J., von Rechenberg, B., Dziuba, D., Seitz, J. M., Bormann, D., et al. (2012). *In vivo* assessment of the host reactions to the biodegradation of the two novel magnesium alloys ZEK100 and AX30 in an animal model. *Biomed. Eng. Online* 11 (1), 14. doi:10.1186/1475-925X-11-14
- Jia, J., Zhou, H., Wei, J., Jiang, X., Hua, H., Chen, F., et al. (2010). Development of magnesium calcium phosphate biocement for bone regeneration. *J. R. Soc. Interface* 7 (49), 1171–1180. doi:10.1098/rsif.2009.0559
- Kaiser, F., Schröter, L., Stein, S., Krüger, B., Weichhold, J., Stahlhut, P., et al. (2022). Accelerated bone regeneration through rational design of magnesium phosphate cements. *Acta Biomater.* 145, 358–371. doi:10.1016/j.actbio.2022.04.019
- Kanter, B., Geffers, M., Ignatius, A., and Gbureck, U. (2014). Control of *in vivo* mineral bone cement degradation. *Acta Biomater.* 10 (7), 3279–3287. doi:10.1016/j.actbio.2014.04.020
- Kanter, B. (2014). *Osseointegration kalthärtender Knochenzemente im Schafmodell*. Ludwig-Maximilians-University Munich. dissertation. Munich.
- Kanter, B., Vikman, A., Brückner, T., Schamel, M., Gbureck, U., and Ignatius, A. (2018). Bone regeneration capacity of magnesium phosphate cements in a large animal model. *Acta Biomater.* 69, 352–361. doi:10.1016/j.actbio.2018.01.035
- Karageorgiou, V., and Kaplan, D. (2005). Porosity of 3D biomaterial scaffolds and osteogenesis. *Biomaterials* 26 (27), 5474–5491. doi:10.1016/j.biomaterials.2005.02.002
- Kasuya, A., Sobajima, S., and Kinoshita, M. (2012). *In vivo* degradation and new bone formation of calcium phosphate cement-gelatin powder composite related to macroporosity after *in situ* gelatin degradation. *J. Orthop. Res.* 30 (7), 1103–1111. doi:10.1002/jor.22044
- Katsimbri, P. (2017). The biology of normal bone remodelling. *Eur. J. Cancer Care* 26 (6), e12740. doi:10.1111/ecc.12740
- Keating, J. F., and McQueen, M. M. (2001). Substitutes for autologous bone graft in orthopaedic trauma. *J. Bone Jt. Surg. Br. volume* 83 (1), 3–8. doi:10.1302/0301-620x.83b1.0830003
- Kheirallah, M., and Almeshaly, H. (2016). Bone graft substitutes for bone defect regeneration. A collective review. *Int. J. Dent. Oral Sci.* 3 (5), 247–255. doi:10.19070/2377-8075-1600051
- Kim, J.-A., Lim, J., Naren, R., Yun, H.-S., and Park, E. K. (2016). Effect of the biodegradation rate controlled by pore structures in magnesium phosphate ceramic scaffolds on bone tissue regeneration *in vivo*. *Acta Biomater.* 44, 155–167. doi:10.1016/j.actbio.2016.08.039
- Klammert, U., Ignatius, A., Wolfram, U., Reuther, T., and Gbureck, U. (2011). *In vivo* degradation of low temperature calcium and magnesium phosphate ceramics in a heterotopic model. *Acta Biomater.* 7 (9), 3469–3475. doi:10.1016/j.actbio.2011.05.022
- Klammert, U., Reuther, T., Blank, M., Reske, I., Barralet, J. E., Grover, L. M., et al. (2010a). Phase composition, mechanical performance and *in vitro* biocompatibility of hydraulic setting calcium magnesium phosphate cement. *Acta Biomater.* 6 (4), 1529–1535. doi:10.1016/j.actbio.2009.10.021
- Klammert, U., Vorndran, E., Reuther, T., Müller, F. A., Zorn, K., and Gbureck, U. (2010b). Low temperature fabrication of magnesium phosphate cement scaffolds by 3D powder printing. *J. Mat. Sci. Mat. Med.* 21 (11), 2947–2953. doi:10.1007/s10856-010-4148-8
- Kleer, N., Julmi, S., Gartzke, A.-K., Augustin, J., Feichtner, F., Waselau, A.-C., et al. (2019). Comparison of degradation behaviour and osseointegration of the two magnesium scaffolds, LAE442 and La2, *in vivo*. *Materialia* 8, 100436. doi:10.1016/j.mtla.2019.100436
- Kleer-Reiter, N., Julmi, S., Feichtner, F., Waselau, A. C., Klose, C., Wriggers, P., et al. (2021). Biocompatibility and degradation of the open-pored magnesium

- scaffolds LAE442 and La2. *Biomed. Mat.* 16 (3), 035037. doi:10.1088/1748-605X/abf5c5
- Kolk, A., Handschel, J., Drescher, W., Rothamel, D., Kloss, F., Blessmann, M., et al. (2012). Current trends and future perspectives of bone substitute materials—from space holders to innovative biomaterials. *J. Cranio-Maxillofacial Surg.* 40 (8), 706–718. doi:10.1016/j.jcms.2012.01.002
- Kowalewicz, K., Vorndran, E., Feichtner, F., Waselau, A.-C., Brueckner, M., and Meyer-Lindenberg, A. (2021). *In-vivo* degradation behavior and osseointegration of 3D powder-printed calcium magnesium phosphate cement scaffolds. *Mater. (Basel)* 14 (4), 946. doi:10.3390/ma14040946
- Kurashina, K., Kurita, H., Kotani, A., Takeuchi, H., and Hirano, M. (1997). *In vivo* study of a calcium phosphate cement consisting of α -tricalcium phosphate/dicalcium phosphate dibasic/tetracalcium phosphate monoxide. *Biomaterials* 18 (2), 147–151. doi:10.1016/s0142-9612(96)00173-1
- Laurie, S. W., Kaban, L. B., Mulliken, J. B., and Murray, J. E. (1984). Donor-site morbidity after harvesting rib and iliac bone. *Plastic Reconstr. Surg.* 73 (6), 933–938. doi:10.1097/00006534-198406000-00014
- LeGeros, R. Z. (2008). Calcium phosphate-based osteoinductive materials. *Chem. Rev.* 108 (11), 4742–4753. doi:10.1021/cr800427g
- LeGeros, R. Z. (2002). Properties of osteoconductive biomaterials: Calcium phosphates. *Clin. Orthop. Relat. Res.* 395, 81–98. doi:10.1097/00003086-200202000-00009
- Lodoso-Torrecilla, I., van den Beucken, J., and Jansen, J. A. (2021). Calcium phosphate cements: Optimization toward biodegradability. *Acta Biomater.* 119, 1–12. doi:10.1016/j.actbio.2020.10.013
- Lucas, D. (2021). Structural organization of the bone marrow and its role in hematopoiesis. *Curr. Opin. Hematol.* 28 (1), 36–42. doi:10.1097/moh.0000000000000621
- Mestres, G., and Ginebra, M.-P. (2011). Novel magnesium phosphate cements with high early strength and antibacterial properties. *Acta Biomater.* 7 (4), 1853–1861. doi:10.1016/j.actbio.2010.12.008
- Moore, W. R., Graves, S. E., and Bain, G. I. (2001). Synthetic bone graft substitutes. *ANZ J. Surg.* 71 (6), 354–361. doi:10.1046/j.1440-1622.2001.02128.x
- Nabiyouni, M., Brückner, T., Zhou, H., Gbureck, U., and Bhaduri, S. B. (2018). Magnesium-based bioceramics in orthopedic applications. *Acta Biomater.* 66, 23–43. doi:10.1016/j.actbio.2017.11.033
- Nombela-Arrieta, C., and Manz, M. G. (2017). Quantification and three-dimensional microanatomical organization of the bone marrow. *Blood Adv.* 1 (6), 407–416. doi:10.1182/bloodadvances.2016003194
- Ostrowski, N., Roy, A., and Kumta, P. N. (2016). Magnesium phosphate cement systems for hard tissue applications: A review. *ACS Biomater. Sci. Eng.* 2 (7), 1067–1083. doi:10.1021/acsbomaterials.6b00056
- Peters, F., Groisman, D., Davids, R., Hänel, T., Dürr, H., and Klein, M. (2006). Comparative study of patient individual implants from β -tricalcium phosphate made by different techniques based on CT data. *Materwiss. Werkstofftech.* 37 (6), 457–461. doi:10.1002/mawe.200600019
- Reid, J. W., and Hendry, J. A. (2006). Rapid, accurate phase quantification of multiphase calcium phosphate materials using Rietveld refinement. *J. Appl. Cryst.* 39 (4), 536–543. doi:10.1107/S0021889806020395
- Rentsch, C., Rentsch, B., Scharnweber, D., Zwipp, H., and Rammelt, S. (2012). [Bone substitute. Transplants and replacement materials—an update]. *Knochenersatz. Unfallchirurg* 115 (10), 938–949. doi:10.1007/s00113-012-2238-4
- Rietveld, H. M. (1969). A profile refinement method for nuclear and magnetic structures. *J. Appl. Cryst.* 2 (2), 65–71. doi:10.1107/S0021889869006558
- Roseti, L., Parisi, V., Petretta, M., Cavallo, C., Desando, G., Bartolotti, I., et al. (2017). Scaffolds for bone tissue engineering: State of the art and new perspectives. *Mater. Sci. Eng. C* 78, 1246–1262. doi:10.1016/j.msec.2017.05.017
- Samavedi, S., Whittington, A. R., and Goldstein, A. S. (2013). Calcium phosphate ceramics in bone tissue engineering: A review of properties and their influence on cell behavior. *Acta Biomater.* 9 (9), 8037–8045. doi:10.1016/j.actbio.2013.06.014
- Sarkar, K., Kumar, V., Devi, K. B., Ghosh, D., Nandi, S. K., and Roy, M. (2019). Effects of Sr doping on biodegradation and bone regeneration of magnesium phosphate bioceramics. *Materialia* 5, 100211. doi:10.1016/j.mtla.2019.100211
- Theiss, F., Apelt, D., Brand, B., Kutter, A., Zlinszky, K., Bohner, M., et al. (2005). Biocompatibility and resorption of a brushite calcium phosphate cement. *Biomaterials* 26 (21), 4383–4394. doi:10.1016/j.biomaterials.2004.11.056
- Travlos, G. S. (2006). Normal structure, function, and histology of the bone marrow. *Toxicol. Pathol.* 34 (5), 548–565. doi:10.1080/01926230600939856
- von Doernberg, M.-C., von Rechenberg, B., Bohner, M., Grünenfelder, S., van Lenthe, G. H., Müller, R., et al. (2006). *In vivo* behavior of calcium phosphate scaffolds with four different pore sizes. *Biomaterials* 27 (30), 5186–5198. doi:10.1016/j.biomaterials.2006.05.051
- Vorndran, E., Ewald, A., Müller, F. A., Zorn, K., Kufner, A., and Gbureck, U. (2011). Formation and properties of magnesium-ammonium-phosphate hexahydrate bioceramics in the Ca-Mg-PO₄ system. *J. Mat. Sci. Mat. Med.* 22 (3), 429–436. doi:10.1007/s10856-010-4220-4
- Vorndran, E., Klarner, M., Klammert, U., Grover, L. M., Patel, S., Barralet, J. E., et al. (2008). 3D powder printing of β -tricalcium phosphate ceramics using different strategies. *Adv. Eng. Mat.* 10 (12), B67–B71. doi:10.1002/adem.200800179
- Walsh, W. R., Vizesi, F., Michael, D., Auld, J., Langdown, A., Oliver, R., et al. (2008). β -TCP bone graft substitutes in a bilateral rabbit tibial defect model. *Biomaterials* 29 (3), 266–271. doi:10.1016/j.biomaterials.2007.09.035
- Wang, L., and Nancollas, G. H. (2008). Calcium orthophosphates: Crystallization and dissolution. *Chem. Rev.* 108 (11), 4628–4669. doi:10.1021/cr782574
- Wang, S., Xu, C., Yu, S., Wu, X., Jie, Z., and Dai, H. (2019). Citric acid enhances the physical properties, cytocompatibility and osteogenesis of magnesium calcium phosphate cement. *J. Mech. Behav. Biomed. Mat.* 94, 42–50. doi:10.1016/j.jmbbm.2019.02.026
- Wei, J., Jia, J., Wu, F., Wei, S., Zhou, H., Zhang, H., et al. (2010). Hierarchically microporous/macroporous scaffold of magnesium–calcium phosphate for bone tissue regeneration. *Biomaterials* 31 (6), 1260–1269. doi:10.1016/j.biomaterials.2009.11.005
- Willbold, E., and Witte, F. (2010). Histology and research at the hard tissue–implant interface using Technovit 9100 New embedding technique. *Acta Biomater.* 6 (11), 4447–4455. doi:10.1016/j.actbio.2010.06.022
- Wiltfang, J., Merten, H. A., Schlegel, K. A., Schultze-Mosgau, S., Kloss, F. R., Rupprecht, S., et al. (2002). Degradation characteristics of alpha and beta tricalcium-phosphate (TCP) in minipigs. *J. Biomed. Mat. Res.* 63 (2), 115–121. doi:10.1002/jbm.10084
- Wu, F., Su, J., Wei, J., Guo, H., and Liu, C. (2008a). Injectable bioactive calcium–magnesium phosphate cement for bone regeneration. *Biomed. Mat.* 3 (4), 044105. doi:10.1088/1748-6041/3/4/044105
- Wu, F., Wei, J., Guo, H., Chen, F., Hong, H., and Liu, C. (2008b). Self-setting bioactive calcium–magnesium phosphate cement with high strength and degradability for bone regeneration. *Acta Biomater.* 4 (6), 1873–1884. doi:10.1016/j.actbio.2008.06.020
- Wu, L., Feyerabend, F., Schilling, A. F., Willumeit-Römer, R., and Luthringer, B. J. (2015). Effects of extracellular magnesium extract on the proliferation and differentiation of human osteoblasts and osteoclasts in coculture. *Acta Biomater.* 27, 294–304. doi:10.1016/j.actbio.2015.08.042
- Xu, L., Yu, G., Zhang, E., Pan, F., and Yang, K. (2007). *In vivo* corrosion behavior of Mg–Mn–Zn alloy for bone implant application. *J. Biomed. Mat. Res. A* 83 (3), 703–711. doi:10.1002/jbm.a.31273
- Zeng, D., Xia, L., Zhang, W., Huang, H., Wei, B., Huang, Q., et al. (2012). Maxillary sinus floor elevation using a tissue-engineered bone with calcium-magnesium phosphate cement and bone marrow stromal cells in rabbits. *Tissue Eng. Part A* 18 (7–8), 870–881. doi:10.1089/ten.TEA.2011.0379
- Zhang, E., Xu, L., Yu, G., Pan, F., and Yang, K. (2009). *In vivo* evaluation of biodegradable magnesium alloy bone implant in the first 6 months implantation. *J. Biomed. Mat. Res. A* 90 (3), 882–893. doi:10.1002/jbm.a.32132
- Zhang, J., Liu, W., Schnitzler, V., Tancret, F., and Boulter, J. M. (2014). Calcium phosphate cements for bone substitution: Chemistry, handling and mechanical properties. *Acta Biomater.* 10 (3), 1035–1049. doi:10.1016/j.actbio.2013.11.001
- Zhang, L., Yang, G., Johnson, B. N., and Jia, X. (2019). Three-dimensional (3D) printed scaffold and material selection for bone repair. *Acta Biomater.* 84, 16–33. doi:10.1016/j.actbio.2018.11.039
- Zimmermann, G., and Moghaddam, A. (2011). Allograft bone matrix versus synthetic bone graft substitutes. *Injury* 42, 16–21. doi:10.1016/j.injury.2011.06.199



OPEN ACCESS

EDITED BY

Yanjin Lu,
Fujian Institute of Research on the
Structure of Matter (CAS), China

REVIEWED BY

Kannan Sanjeevi,
Pondicherry University, India
Narayana Kalkura,
Anna University, India

*CORRESPONDENCE

Zhifan Bao,
zfbao@cmu.edu.cn
Zhe Yi,
zheyi@cmu.edu.cn

SPECIALTY SECTION

This article was submitted to
Biomaterials and Bio-Inspired Materials,
a section of the journal
Frontiers in Materials

RECEIVED 21 July 2022

ACCEPTED 20 September 2022

PUBLISHED 06 October 2022

CITATION

Ma Y, Yan J, Yan T, Wang Q, Bao Z and
Yi Z (2022), Biological properties of Cu-
bearing and Ag-bearing titanium-based
alloys and their surface modifications: A
review of antibacterial aspect.
Front. Mater. 9:999794.
doi: 10.3389/fmats.2022.999794

COPYRIGHT

© 2022 Ma, Yan, Yan, Wang, Bao and Yi.
This is an open-access article
distributed under the terms of the
[Creative Commons Attribution License](https://creativecommons.org/licenses/by/4.0/)
(CC BY). The use, distribution or
reproduction in other forums is
permitted, provided the original
author(s) and the copyright owner(s) are
credited and that the original
publication in this journal is cited, in
accordance with accepted academic
practice. No use, distribution or
reproduction is permitted which does
not comply with these terms.

Biological properties of Cu-bearing and Ag-bearing titanium-based alloys and their surface modifications: A review of antibacterial aspect

Yidan Ma¹, Jiao Yan¹, Tingting Yan², Qiang Wang¹, Zhifan Bao^{1*}
and Zhe Yi^{1*}

¹Liaoning Provincial Key Laboratory of Oral Diseases, School and Hospital of Stomatology, China
Medical University, Shenyang, China, ²Faculty of Materials Science and Engineering, Kunming
University of Science and Technology, Kunming, China

The use of titanium dental implants to replace missing teeth represents an important field of daily dental practice worldwide, which is highly reliable for long-term survival and success rates. However, titanium dental implants still have intrinsic problems that cannot meet the clinical requirements. Improving the performance of implants is an increasingly important area of dental research to reduce infection rates. Improved properties can be achieved by two main methods: 1) the overall change in the materials by changing the elemental composition and 2) surface modifications. This review provides an overview of various titanium-based alloys that have been employed to achieve a higher survival rate of implantation by adding elements or modifying the surface, with a special focus on their antibacterial applications. Recent developments in titanium-based alloys containing various antibacterial agents have been described in detail, including Cu-bearing, Ag-bearing, and Zr-bearing Ti alloys. Moreover, the applications of bioactive coatings and 3D printing materials with antibacterial properties are reviewed. This review aims to highlight the antibacterial challenges associated with titanium-based alloys to promote the further development and clinical application of antibacterial alloys.

KEYWORDS

titanium, implants, infection, antibacterial properties, surface treatments, 3D-printed

1 Introduction

Population ageing is a global phenomenon, and the number of people requiring fixation or total replacement of hard tissue is increasing (Lu et al., 2021b). Over the past few decades, the use of dental implants has become an indispensable part of clinical dentistry and a standard treatment procedure for dental reconstructive therapy (Alghamdi and Jansen, 2020). It is a highly successful treatment option for replacing

missing teeth, with a documented long-term (>10 years) survival rate of over 90% for dental implants (Howe et al., 2019; Frisch et al., 2020).

In recent years, titanium-based alloys have been widely applied as dental implants because of their competitive properties, including excellent corrosion resistance, biocompatibility, non-magnetic properties, and non-toxicity (Liu et al., 2018; El-Bagoury et al., 2019). As a desirable material for implants, titanium-based alloys should have certain properties, such as a proper elastic modulus, antibacterial properties, and a higher osseointegration rate. A thin passive oxide layer is formed on the titanium-based implant, which makes it stable in bodily fluids and resistant to corrosion. It also facilitates osseointegration into the surrounding bone tissue (Prestat and Thierry, 2021).

However, pure titanium has no antibacterial property; therefore, bacteria tend to adhere to the neck of implants, resulting in peri-implant disease (Buser et al., 2002; Zadpoor, 2019). Infections, especially during or after implantation surgery, are serious complications for patients and cause huge pain and economic burden on them (Shimabukuro, 2020). Generally, patients need systemic antibiotic treatment to prevent infections after surgery, but the rising bacterial resistance can make existing antibiotics ineffective (Park et al., 2019). Invasive therapies used to fight infections, such as implantoplasty, might lead to other adverse outcomes (Toledano-Serrabona et al., 2021). In general, interactions between bacteria and materials can be divided into four stages. The primary step in this process is bacterial adhesion to the metal surface. The secondary step is the colonisation of bacteria on the metal surface. The third step involves biofilm formation and maturation. The final step is the proliferation of the bacteria (Zhang et al., 2021a). Many studies have reported that peri-implant infections are usually related to the formation of biofilms, which can protect bacteria from fluid shear stress and pharmacological therapies to a great extent (Norowski and Bumgardner, 2009; Quinn et al., 2020). The concentration of antibiotics at the focal site is insufficient, leading to rapid proliferation and secretion of extracellular polymers to form a biofilm after some pathogens assemble and adhere to the surface of the implant (Gristina and Costerton, 1985). Moreover, once a biofilm has formed, it will be extremely difficult to remove completely. Bacterial adhesion is also the critical stage of biofilm formation on teeth and subsequent tooth demineralization, especially the tissues around the oral treatment instruments are attached to more easily by bacteria (Fan et al., 2021). Worse still, it is difficult to clean by mechanical methods or mouthwashes. Taken together, it is of great significance to enable titanium-based implants, restorations or orthodontic archwires to be resistant to biofilm formation and to possess long-term antibacterial properties.

The agar diffusion plate test, plate-count method, live/dead stain, and dilution method can be used to assess antibacterial properties in the laboratory (Zhang et al., 2021a). According to SN/T 2399-2010, a material is considered antibacterial if the antibacterial rate is > 90%. When the antibacterial rate is less than 90%, the material has certain antibacterial properties; however, it is not an antibacterial material. When the antibacterial rate is > 99%, the material exhibits strong antibacterial properties (Lei et al., 2020). In addition, the methods commonly used to quantify the microbial biofilm or to observe the morphological changes include colony forming unit (CFU), scanning electron microscopy (SEM), confocal laser scanning microscopy (CLSM), real-time quantitative polymerase chain reaction, fluorescence *in situ* hybridization (FISH), etc. (Scheeren Brum et al., 2021). The methods like crystal violet assay, percentage transmission (%T) or percent transmittance (%T) and XTT reduction assay are characterized by high reliability, low-cost effectiveness and high sensitivity (Dhale et al., 2014). More recently developed methods of biofilm detection are ultrasonic Coda Wave Interferometry (Chen et al., 2021a), MgZnO dual-gate TFT biosensor (Li et al., 2020a), real-time quantitative polymerase chain reaction (Ríos-Castillo et al., 2020), Electrochemical detection (Abdelraheem et al., 2020), etc. These detection methods are more sensitive, lower consumption, more suitable for rapid detection, and the test results are more reliable and accurate.

This review focuses on various promising methods to improve the antibacterial properties of titanium dental implants as well as their relative mechanisms.

2 Titanium alloys with antibacterial elements copper and silver

Currently, inorganic elements added to alloys as antibacterial agents mainly include antibacterial metallic elements, such as silver (Ag) and copper (Cu). Copper is an essential trace element in organisms and plays important role in human health, as well as in the maturation of the nervous, haematopoietic, bone, and other systems (Wang et al., 2021). Owing to its excellent properties in protecting the cardiovascular system, exerting antibacterial effects, and promoting bone fracture healing (Ren et al., 2015), Cu has become an important alloying element in many alloys such as Ti-Cu alloys (Borkow, 2012; Zhuang et al., 2021). Ag, due to its well-performing antibacterial and anti-biofilm formation capability, has been used as an antibacterial agent for thousands of years. Various Ag-related techniques have been introduced to modify biomedical devices for improved anti-infective properties, including doped solid coatings, nanoparticle-loaded thin films, hydrogel materials, and alloy applications (Zhang et al., 2021a). The titanium alloys containing antibacterial elements are listed in Table 1.

TABLE 1 Summary of various alloys containing antibacterial elements.

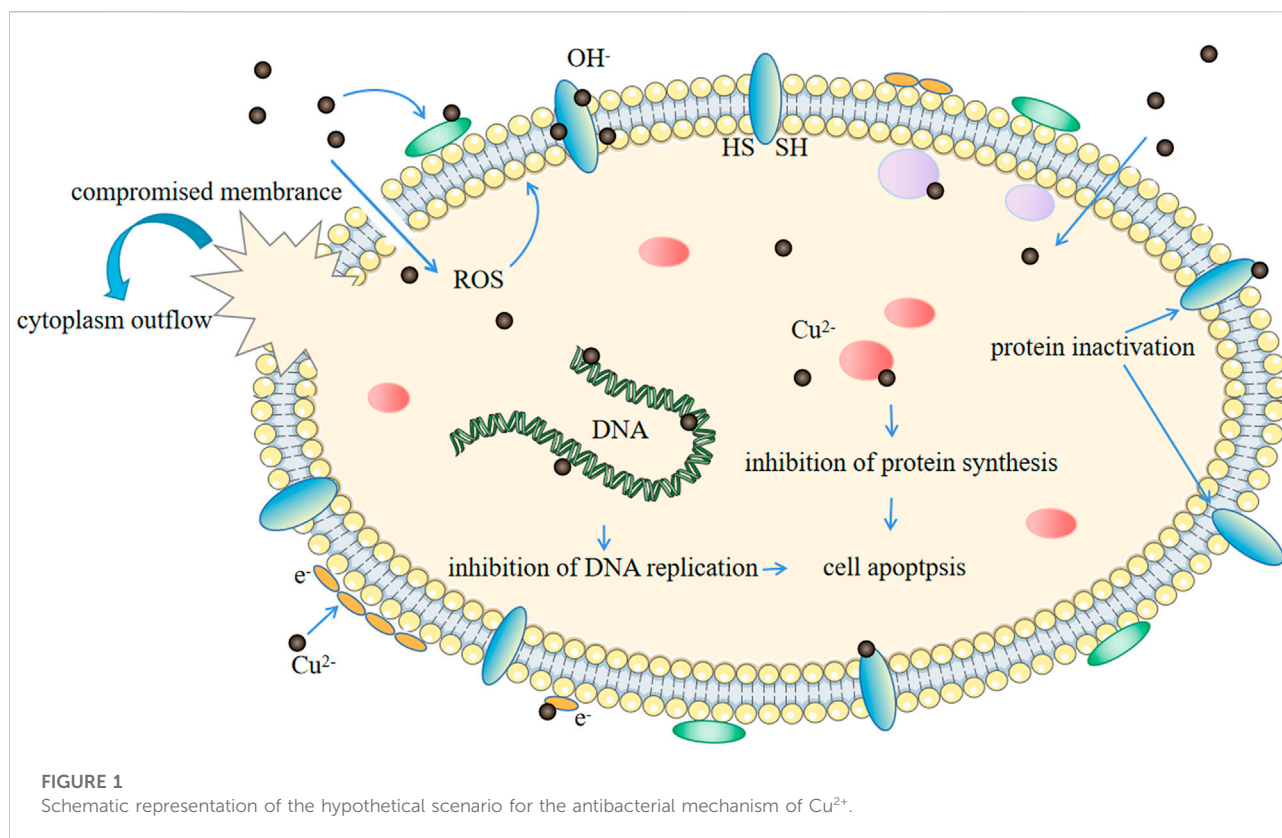
Material	Composition	Manufacture method	Tested bacteria	Antibacterial effects	The antibacterial mechanism	References
Ti6Al4V-5Cu/Ti6Al4V	Ti6Al4V powder and Ti6Al4V-5Cu powder	Selective laser melting (SLM) with computer-aided design data (CAD) modeling	<i>S. mutans</i>	This alloy significant against sessile bacteria and reduce biofilm formation, has little antibacterial effect on planktonic bacteria.	Down regulate the expression of genes related to bacterial adhesion and acid production	Fan et al. (2021)
Ti6Al4V-xCu	Commercial Ti6Al4V powder and commercial pure Cu powder Cu content: 2, 4, 6wt%	Selective laser melting (SLM)	<i>E. coli</i> <i>S. aureus</i>	The antibacterial rates against <i>E. coli</i> and <i>S. aureus</i> : Ti6Al4V-2wt.%Cu: 51.54% and 60.94% Ti6Al4V-4wt.%Cu: 97.40% and 93.56% Ti6Al4V-6wt.%Cu: >99%	The release behavior of Cu ion	Guo et al. (2017)
Ti-xCu	Purity titanium powder (99.99%) and purity copper powder (99.99%) Cu content: 2, 5, 10, 25wt%	Powder metallurgy	<i>E. coli</i> <i>S. aureus</i>	The antibacterial rates against <i>E. coli</i> and <i>S. aureus</i> : Ti-2wt% Cu: 57% and 79% Ti-5wt% Cu: 99.2% and 99.0% Ti-10wt% Cu: >99.99% Ti-25wt% Cu: >99.99%	The release behavior of Cu ion	Liu et al. (2014a)
Ti-xCu	Cu content: 3, 5, 7wt%	—	<i>S. aureus</i>	The antibacterial rates against <i>S. aureus</i> : Ti-3wt% Cu: 92.5% Ti-5wt% Cu: 99.4% Ti-7wt% Cu: 99.99%	The release behavior of Cu ion	Zhang et al. (2021b)
Ti-xCu	Commercial pure titanium and copper Cu content: 3, 5wt%	Vacuum arc melting and Selective acid etching (SAE)	<i>S. aureus</i>	The antibacterial rates against <i>S. aureus</i> : Ti-3 wt% Cu: 79%, Ti-5 wt% Cu: 87% Ti-3Cu-SAE: >99.9% Ti-5Cu-SAE: >99.9%	The release behavior of Cu ion; “Contact killing” of Ti ₂ Cu phase	Lu et al. (2021a)
Ti-xAg	Purity titanium powder (99.99%) and purity Ag powder (99.99%) with 75 μm and 10 μm in size Ag content: 1, 3, 5wt%	Powder metallurgy	<i>S. aureus</i>	The antibacterial rates against <i>S. aureus</i> : Ti-1Ag(S75): about 15% Ti-3Ag(S75): about 15% Ti-5Ag (S75): 85.2% Ti-1Ag(S10): 32% Ti-3Ag(S10): about 98.2% Ti-5Ag (S10): 99.99%	“Contact killing” of Ti ₂ Cu phase	Chen et al. (2016)

2.1 The antibacterial mechanism of copper and silver element

The antibacterial and antifungal mechanisms of Cu have been studied for a long time, involving the release of ionic copper from the surface and bacteria-metal contact. A large number of bacterial species, fungi, and viruses are vulnerable to copper, although some bacteria may be tolerant rather than resistant to copper (Grass et al., 2011; Borkow, 2012).

According to the classic view, the antimicrobial activity of Cu is based on its ability to form deleterious hydroxyl radicals *via* a Fenton-like mechanism. The direct production of reactive

oxygen species (ROS) not only causes damages to lipids, proteins, membrane and DNA but also depletes bacterial antioxidants (Fu et al., 2014). The binding of the Cu²⁺ to the copper-binding site of the DNA will leads to disorders in helical structures and the denaturation of deoxyribonucleic acid (DNA) (Borkow and Gabbay, 2005). Cu impairs the function of cell membranes by peroxidizing lipids in the bilayer (Hong et al., 2012). It has also been suggested that the membrane damage caused by Cu is associated with the fact that Cu ions can interact with sh-groups and lead to their inactivation (Fu et al., 2014). The influence of Cu on proteins can come from two aspects. First, Cu is capable of inhibiting the expression of related genes of bacteria



(Li et al., 2016c). And second, Cu ions may change the structure of proteins, or disrupt the enzyme structure and function by binding to the sulfur-containing or carboxylate-containing group (Sterritt and Lester, 1980). Specifically, the bacterial killing process runs as follows. First, Cu dissolves from the Cu-containing surface or material and causes cell damage. The cell membrane ruptures leading to a loss of membrane potential and cytoplasmic content. Next, the generation of ROS causes further cell damage by acting on proteins and lipids and finally genomic and plasmid DNA is degraded, leading to cell death (Grass et al., 2011). More explicit information regarding the mechanism is presented in Figure 1. Additionally, membrane depolarization is also considered to be one of the main mechanisms of Cu ions' antimicrobial activity (Santo and Lam, 2011; Warnes et al., 2012; Fan et al., 2021). Copper ions can bind to negatively charged regions of the bacterial cell membrane (both outer and inner), reducing the potential difference and causing membrane depolarization. Membrane leakiness or even rupture can occur when the potential difference decreases to zero.

Ag is also regarded as one of the most promising antibacterial agents (Ferraris and Spriano, 2016). Despite extensive research on Ag, the precise mechanism of antimicrobial effect remains to be defined. Similar to Cu, the most probable antimicrobial mechanism of silver compounds may include extensive

disruption of cellular functions due to the interference with 1) cell membrane or 2) intracellular biomolecules including enzyme, protein and DNA (Yan et al., 2018), 3) the induction of oxidative stress by metal-mediated reactive oxygen species generation, culminating in associated oxidative damages (Morones-Ramirez et al., 2013). Sukumaran and Eldho described the mechanism by which silver ions prevent cell function and induce cell death by interacting with the bacterial membranes (Sukumaran and Eldho, 2012). Similarly, (Iqbal et al., 2015) proposed that silver ions interact with the proteins and enzymes of the germ membrane to cause cell damage. Upon contacting Ag ions, the zeta potential of the cell surface changes, causing cell membrane hyperpermeability, membrane depolarization and a decreased respiratory potential. At last, the disturbance of membrane integrity leads to an irreversible cell damage and consequently to cell death (Gomaa, 2017). Mocanu et al. (2014) thought that silver ions penetrate the cell membrane, bind to bacterial DNA, and inhibit the bacterial replication. Although Ag ions cannot donate or receive electrons, the electron transfer between Ag nanoparticles and the titanium substrate may cause a reactive oxidation stress (Wang et al., 2017). However, there have been some reports of bacterial resistance to the ionic silver (Losasso et al., 2014). Such resistance may involve the reduction of Ag ions to the less toxic neutral oxidation state or the active efflux of Ag

ions from the cell by P-type adenosine triphosphatases or chemiosmotic Ag^+/H^+ antiporters (Silver et al., 2006). However, there is an inevitable problem. Ag, which is different from Cu, tends to accumulate in the human body and increase the level of serum Ag, which is harmful to human health (Masse' et al., 2000).

2.2 Copper-containing titanium alloys

2.2.1 Ti-Cu alloys

One of the basic requirements of novel materials used in biomedical sciences is their cytocompatibility. Cu is a highly bioactive element that exhibits strong bactericidal and cytotoxic effects (Park et al., 2013). The World Health Organization recommends that an adult should take copper 0.03 mg/kg per day and the tolerated amount is 10 mg (Filippini et al., 2018). Liu et al. (2014a) found that the antibacterial rate can be greater than 99% when the Cu immersion concentration is greater than 0.036 mg/L which is far less than the recommended daily intake. To a certain extent, Cu-bearing Ti alloys are safe.

Recently, due to the antibacterial activity, Ti-Cu alloys have attracted more attention, followed by meaningful advances. A case in point is that the hydrogen fluoride (HF) etching + anodised Ti-Cu alloy possessed strong antibacterial properties, good biological compatibility, and osteogenic ability. Among these, increasing the Cu content contributed significantly to antibacterial and osteogenic properties, and a higher and more stable antibacterial rate was obtained when the Cu content was $\geq 5\%$ (Zhang et al., 2021b). Liu et al. (2014a) also agreed that at least 5 wt% Cu is necessary for stable antibacterial properties. However, the antibacterial properties of Ti-Cu alloys are not always positively correlated with copper content. Zhang et al. (2016a) reported that after different treatment methods, Ti-5Cu alloy exhibited a much higher antibacterial rate than Ti-10Cu alloy, which may be due to the different existing forms of Cu in the alloy. They also noted that the contact sterilisation caused by the Ti_2Cu phase was the main controlling mechanism for the antibacterial capabilities of Ti-Cu alloys, and fine Ti_2Cu phases with a higher surface area could result in better antibacterial ability. Many studies have obtained similar results, showing that a high-volume fraction of the Ti_2Cu phase (or Cu-rich phase) improves the antibacterial ability of the Ti-xCu alloys (Fowler et al., 2019b; Lu et al., 2021a). By incrementally adding the Ti_2Cu phase to alloys, some treatments may improve their antibacterial ability. The heat treatment process can change the existing form of Cu, which in turn affects the final antibacterial activity of the titanium alloy (Zhang et al., 2016a). Likewise, the ageing treatment improved the antibacterial property owing to the large amount of nano-scale Ti_2Cu precipitated from the matrix. Lu et al. (2021a) prepared special Ti-Cu samples by selective acid (SAE) etching to further improve their antibacterial properties. The results showed that more Ti_2Cu particles were

exposed on the surface of the samples after SAE, and the antibacterial activity against *Staphylococcus aureus* (*S. aureus*) was significantly enhanced. Moreover, the morphology of the Ti_2Cu phase also affected the antibacterial properties of the Ti-Cu alloy. In research conducted by Xin et al. (2022), it was found that the lamellar Ti_2Cu phase (L- Ti_2Cu) has a higher Cu ions release rate than the granular Ti_2Cu phase (G- Ti_2Cu), which is due to the formation of elongated “micro-galvanic cell” between L- Ti_2Cu phase and α -Ti matrix. An increased Cu ion release rate can improve the antibacterial activity of Ti-Cu. Such a galvanic cell, in addition, will deplete the electrons in the system and even inhibit the power of protons, which is not conducive to the formation of ATP (adenosine triphosphate) in bacterial cells (Li et al., 2016a; Wang et al., 2019).

2.2.2 Ti-6Al-4V-xCu alloys

Ti-6Al-4V, which has excellent biocompatibility coupled with superior mechanical properties, accounts for over 50% of all commercially used titanium alloys (Quinn et al., 2020). Adding Cu element to Ti-6Al-4V offers a means not only to improve the mechanical properties, but also, crucially, to improve the antibacterial activity. Some research indicated that Ti-6Al-4V-5Cu behaved better wear resistance and higher hardness than Ti-6Al-4V (Wang et al., 2015). Xu et al. suggested that cell viability and corrosion resistance of Ti-6Al-4V-5Cu was better than Ti-6Al-4V. Meanwhile, this alloy showed prominent antibacterial ability. They speculated that the improvement of antibacterial property of Ti-6Al-4V-5Cu might be related to the contact sterilization *via* the extensive precipitation of Ti_2Cu (Xu et al., 2021). In the study of Ren et al. (2014), they examined the antibacterial ability of Ti-6Al-4V- xCu ($x = 1, 3, 5$ wt%) and found that these alloys showed strong abilities to kill the sessile bacteria. Furthermore, with the increase of the Cu content, the antibacterial activity of the Ti-6Al-4V- xCu alloys was advanced. By using co-culture, they found Ti-6Al-4V-5Cu is capable of killing nearly all bacterial colonies (Ren et al., 2014). In addition, extra treatment and heat treatment, for example, can improve the Ti-6Al-4V-Cu antibacterial property (Macpherson et al., 2017; Peng et al., 2018). This may occur because the content, amount and size of Ti_2Cu in Ti-6Al-4V- xCu increased after the heat treatment, and the greater effective contact surface area exposure brings better antibacterial ability (Xu et al., 2021).

2.2.3 Ti-Zr-Cu alloys

Recently, Ti-Zr alloys have been developed for dental applications which are comparable to those of the commercially pure titanium (cp-Ti) (Niinomi, 2003). Zirconium (Zr), which is a neutral element, is a transition metal with an atomic number of 40 and an atomic weight of 91.22 amu. Zirconium belongs to Group 4 (according to the new IUPAC name) in the periodic table and is identical to titanium and hafnium. Thus, no wonder it has a similar chemical structure and properties to titanium. Additionally, Zr, similar to Ti, is

biologically inert and is well accepted by the human tissue (Steinemann, 1998). Ti-Zr alloys are non-toxic and exhibit superior biomechanics compared to cp-Ti. Moreover, the use of Ti-Zr alloys can further improve the mechanical properties of implants. The hardness of the Ti-Zr alloys increased with increasing Zr content and ranged from 266 HV (Ti-10Zr) to 350 HV (Ti-40Zr) (Ho et al., 2008). Ti-45Zr has the optimum strength/elastic modulus ratio and osteogenic activity, which would be advantageous for reducing the fracture risk of implant materials (Ou et al., 2021). Due to these properties, Ti-Zr alloys are suitable for making narrow dental implants (NDIs), which are an alternative treatment when there is insufficient bone for regular implants (Gonzalez-Valls et al., 2021).

The corrosion behaviour of implant materials strongly influences foreign body reactions in the vicinity of the implantation site and thus plays a significant role in the biocompatibility of implants. Ti is well known for its high corrosion resistance (Medvedev et al., 2016). When exposed to oxygen, Ti-Zr alloy forms a stable oxide layer on its surface within nanoseconds, like titanium, which makes it a highly biocompatible and corrosion-resistant metal (Fujita, 1993). Akimoto et al. (2018) found that 90% fewer Ti ions were released from Ti-30Zr than from pure Ti after 1 week of immersion in a physiological fluid. This indicates that the ZrO₂ film is more stable and resilient to dissolution as compared to the Ti oxide, and the addition of Zr can significantly reduce Ti ion dissolution, further reducing the implant-induced foreign body reaction.

Despite the excellent biocompatibility of Ti-Zr alloys, the deficiency of antibacterial activity is a disadvantage associated with Ti-Zr implants. To prevent infection and ensure high success rates in clinical applications of medical devices and implants made from Ti-Zr alloys, antimicrobial performance should be improved. Chen et al. (2020) confirmed that Ti-Zr has a lower occurrence of *Candida Albicans* (*C. Albicans*) which might be clinically advantageous for medical devices, but the antibacterial mechanism still needs to be explored. To further improve the antibacterial properties of Ti-Zr alloys, adding antibacterial elements like Cu to improve their antibacterial properties is a good choice. Kolawole et al. (2020) confirmed that adding Cu to Ti-Zr alloys did not result in a decrease in the mechanical properties. They investigated the bactericidal effect of Ti-15Zr-xCu ($3 \leq x \leq 7$, wt%) on the survival of *Escherichia coli* (*E. coli*) and *S. aureus*. The results show that the antibacterial ability of such alloys is as high as 98.2%; thus, their antibacterial performance has been confirmed. Lee et al. claimed that the Ti-Nb-Ta-Zr (TNTZ) system showed promising properties for biocompatibility and strength comparable to those of Ti-6Al-4V. The alloys in the range of 3–10 wt% Cu all had Ti₂Cu, which may cause the potential antibacterial ability of the material (Fowler et al., 2019a). Shi et al. developed a

new titanium alloy, Ti-13Nb-13Zr-5Cu (TNZ-5Cu), with a low elastic modulus and good antibacterial properties. It exhibited strong antibacterial ability (>90%) against *S. aureus*, which increased with the extension of the ageing duration owing to the precipitation of the Ti₂Cu phase (Shi et al., 2021). It has been reported that Ti-13Nb-13Zr-10Cu has antibacterial activity against *S. aureus* and a low elastic modulus of 66 GPa, which might reduce bacterial infection and “stress shielding” in bone implants (Ke et al., 2019).

2.3 Silver-containing titanium alloys

2.3.1 Ti-Ag alloys promising antimicrobial materials

In the past few years, Ti-Ag alloys have become promising antibacterial candidates. Many studies have shown that Ag content is related to antibacterial properties, and a high Ag content usually results in a high antibacterial activity (Chen et al., 2017; Lei et al., 2020; Shi et al., 2020). However, too much Ag works contrary to expectations. In a study by Nakajo et al. (2014), with up to 30 wt% Ag, Ti-Ag alloys had no effect on bacteria. Ti₂Ag, like Ti₂Cu, plays an important role in the antibacterial ability of the Ti-Ag alloys (Chen et al., 2017). Ag ion release contributed to the antibacterial effect, while Ti₂Ag particles were the key factors in contact with the germs. Surface treatments such as acid etching can further enhance the antibacterial properties of Ti-Ag alloys by exposing more Ti₂Ag particles (Lei et al., 2020; Shi et al., 2020).

2.3.2 Other silver containing titanium alloys

According to Macpherson et al., selective laser melting Ti-6Al-4V containing 0.5 wt% Ag appeared to possess little antibacterial effect, possibly due to the low alloying content (Macpherson et al., 2017). In order to achieve effective antibacterial rates (>99%), the addition of Ag should be at least 3 wt% (Chen et al., 2016).

Young's modulus mismatch between the metallic prosthesis and human bone results in a stress shielding effect, which has been identified as a major reason for loosening or failure of the implants (Alqattan et al., 2021). Ti-Ni alloys are commonly used in orthodontics for shape memory and other applications. They display a lower Young's modulus than human bone. In addition, the results obtained by Zheng et al. (2011) showed that the number of bacteria on Ti-Ni-Ag alloy samples was less than that in other groups. Ti-Ni-Ag alloys may provide a new solution to this modulus problem. However, some reports claim nickel is harmful (Zhao et al., 2018; Pan et al., 2020).

Ag can also be added to the Ti-Nb alloy to obtain an alloy with low modulus and better antibacterial activity. Karbownik et al. (2017) confirmed that Ti-Nb-1Ag showed antibacterial

TABLE 2 Summary of studies about surface modification.

Substrate material	Coating material	Treatment processing	Tested bacteria	Antibacterial effects	The antibacterial mechanism	References
Ti	Zn	Micro-arc oxidation (MAO)	<i>E. coli</i>	The specimens incubated exhibited antibacterial activity against <i>E. coli</i> , while the specimens before incubation did not.	Zn was converted to ZnO, and ZnO could produce ROS	Shimabukuro et al. (2019)
Ti	Zinc substituted hydroxyapatite/bismuth substituted hydroxyapatite (Zn-HA/Bi-HA) biphasic coatings	Sol-gel and dip-coating processes	<i>E. coli</i> <i>S. aureus</i>	The specimens showed antibacterial activity against <i>E. coli</i> and <i>S. aureus</i>	The toxicity of zinc and bismuth ions to bacteria	Bi et al. (2020)
Ti	A layered double hydroxide (LDH) composed of Ga and Sr	Hydrothermal method and calcined in 250°C	<i>E. coli</i> <i>S. aureus</i>	The antibacterial rates against <i>E. coli</i> and <i>S. aureus</i> : LDH: 54.2% and 58.2% LDH250: 86.9% and 87.1% The anti-biofilm effects against <i>E. coli</i> and <i>S. aureus</i> : LDH: 68.5% and 74.7% LDH250: 82.9% and 82.0%	The Ga ³⁺ could destroy the bacterial iron metabolism; local alkaline environment; the production of ROS	Li et al. (2022)
Ti	LL37-loaded NP samples (NP/LL37)	Anodic oxidation treatment and simplified lyophilization method	<i>S. aureus</i> MRSA	Bacterial concentrations of <i>S. aureus</i> (on surface and in medium): NP: 3.7×10^4 and 6.2×10^4 cfu/ml NP/LL37: 0.3×10^4 and 1.8×10^4 cfu/ml Bacterial concentrations of MRSA (on surface and in medium) NP: 2.4×10^4 and 1.9×10^4 cfu/ml NP/LL37: 0.5×10^4 and 1.2×10^4 cfu/ml	The carpet model, barrel stave model and toroidal pore model of LL37	Shen et al. (2019)
Ti	MnO ₂ , IR780 photosensitizer and polydopamine (PDA).	—	<i>E. coli</i> <i>S. aureus</i>	The antibacterial rates: <i>E. coli</i> : 99.89% <i>S. aureus</i> : 99.94%	The synergistic action of both ROS and hyperthermia	Teng et al. (2020)
Ti	Calcium phosphate and chlorhexidine	Pulsed electrodeposition	<i>E. coli</i> <i>S. aureus</i>	0.75mM and 1.5 mM chlorhexidine inhibited <i>S. aureus</i> and <i>E. coli</i>	The toxicity of Chlorhexidine	Vidal et al. (2021)
Ti6Al4V	Hydroxyapatite and Ag nanoparticles	PEO treatment	<i>E. coli</i> <i>S. aureus</i>	Could eradicate <i>S. aureus</i> and <i>E. coli</i>	The toxicity of Ag nanoparticles	Sobolev et al. (2019)
Ti6Al4V	Fluorine-doped TiO ₂ layers with controlled nanostructure	Anodizing treatments	<i>S. epidermidis</i> <i>S. aureus</i> <i>E. coli</i> <i>P. aeruginosa</i> <i>C. albicans</i>	There is a slight decrease in the overall biofilm accumulation, both for <i>S. epidermidis</i> as for <i>E. coli</i> .	Nanostructure decreased bacterial adhesion and fluorine showed antibacterial properties	Perez-Jorge et al. (2017)
Ti6Al4V	F-P doped Bottle-shaped TiO ₂ nanotubes (bNT)	Anodizing treatments	<i>S. aureus</i> <i>S. epidermidis</i> <i>E. coli</i> <i>P. aeruginosa</i> <i>Stenotrophomonas maltophilia</i>	Bacterial adhesion decreased on bNT Ti-6Al-4V compared to CP Ti-6Al-4V: <i>S. aureus</i> : 20% <i>S. epidermidis</i> : 45% <i>E. coli</i> : 9% <i>P. aeruginosa</i> : 2% <i>S. maltophilia</i> : 80%	Effects of Al on cell membranes and enzymes	Aguilera-Correa et al. (2019)

(Continued on following page)

TABLE 2 (Continued) Summary of studies about surface modification.

Substrate material	Coating material	Treatment processing	Tested bacteria	Antibacterial effects	The antibacterial mechanism	References
Ti6Al4V scaffolds (3D printed)	PDA/heparin/vancomycin (TS-M and TS-M/P/V)	MAO and PDA/heparin/vancomycin treatments	MRSA	Average bacterial counts in the TS-M/P/V group were significantly lower than those from the TS and TS-M groups	The pH-responsive release of vancomycin	Zhang et al. (2020)

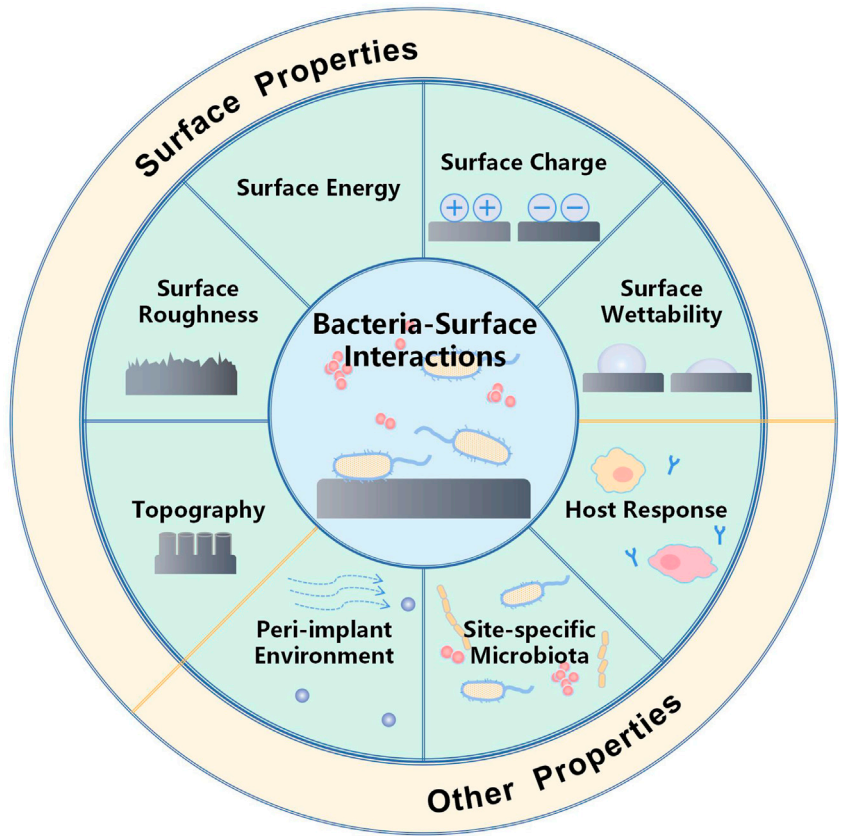
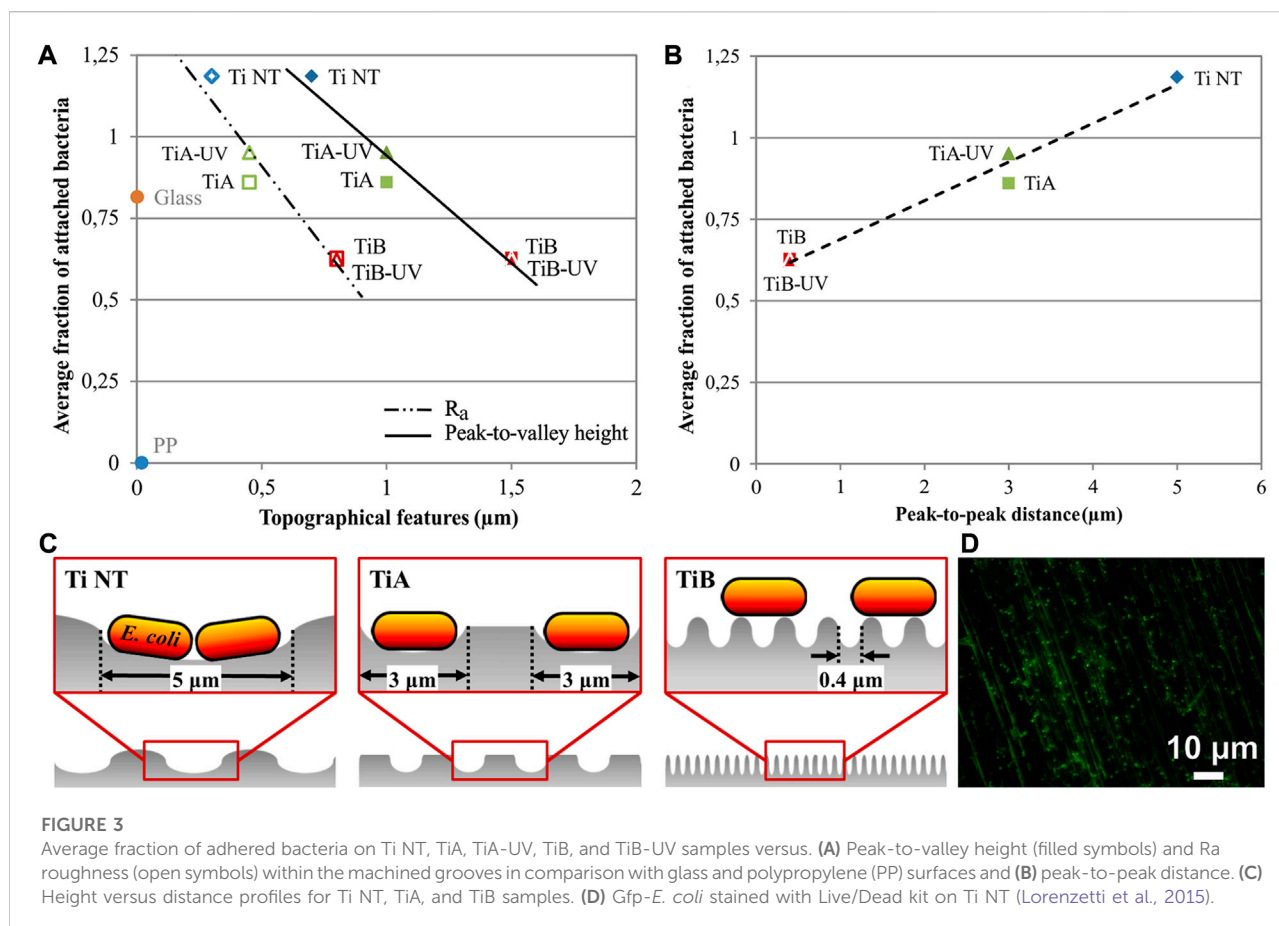


FIGURE 2
Schematic illustration of various factors that influence bacterial adhesion. Bacterial adhesion is governed by diverse surface properties including surface roughness, charge, wettability, and topography. Other factors, such as the peri-implant environment, site-specific microbiota, and host response, can also affect bacteria-surface interactions.

activity of 71.4% against *E. coli*. Ou et al. obtained similar results. Ti-27.5Nb alloy with 0.2–1.2 wt% Ag showed an extremely strong antibacterial effect (>90% against both *S. aureus* and *E. coli*) (Ou et al., 2017). Cai et al. (2021) designed a novel Ti-13Nb-13Zr-12.5Ag alloy in an ageing state with a low elastic modulus of 79 GPa and strong antibacterial activity. They

suggested that the precipitation of Ag-rich phase is a leading cause of antibacterial properties, and high amount of the Ag-rich particle resulted in a high antibacterial ability. However, the presence of Ti₂Ag phase will increases the Young’s modulus. Therefore, how to balance them is still a challenge for the develop of low modulus antibacterial titanium alloy.



3 Surface modification

Surface modification is a promising approach for improving the antibacterial properties of Ti-based alloys. This section summarises representative strategies for surface modification for antibacterial purposes (Table 2).

3.1 Antibacterial effect of surface properties

For dental implants, the overwhelming majority of commercial surface modifications focus on changes in the roughness of the titanium surface, primarily on improving the bone-healing process and osseointegration capability. Bacterial-surface interactions, especially the process of bacterial adhesion, may be affected by several surface properties of materials, such as roughness, surface energy, surface charge, surface wettability, and topography. In addition, other factors such as the peri-implant environment, site-specific microbiota, and host response can also be affected by bacteria-surface interactions, as illustrated in Figure 2 (Belibasakis and Manoil, 2021). Therefore, various strategies

have been developed to prevent biofilm formation at an early stage by engineering the anti-adhesive surface properties.

The desired as-modified surface should promote osteoblast adhesion and improve osseointegration but reduce the colonisation of bacteria, which is, in part, a conflicting demand. It is generally assumed that rougher surfaces promote bacterial biofilm formation because the surface area for adhesion is larger than that of flat surfaces, thereby protecting bacteria from shear forces. However, Lorenzetti et al. (2015) have shown in their study how the microscopic roughness dramatically affects bacterial adhesion, i.e., peak-to-peak distances equal to or larger than the bacterial size that could facilitate bacterial attachment (Figure 3). This is because bacteria can adhere to the grooves and are protected from direct exposure to external forces. As a result, structures with gaps smaller than the bacterial size provided only contact points for bacterial adhesion on the surface, reducing the contact area and the number of bacteria that successfully attached to the surface.

In addition, surface energy is believed to play a key role in the adhesion process. According to general results, the surface energy increases with increasing roughness of the Ti or TiO₂ panel (Rupp et al., 2006). The surface energy of approximately 42.5 mJ/m² (1 mJ/m² = 1 mN/m) was most effective at restricting the

proliferation of bacteria. The study by Bassouset al. (2019) also supported that the optimal surface energy (42.5 mJ/m^2) could reduce fibrosis, improve osteogenesis, and restrict the adhesion of bacteria in a drug-free manner to prevent infection in Ti-6Al-4V implants.

The wettability of a surface depends primarily on its surface characteristics such as surface roughness and surface energy (Song et al., 2019). Superhydrophobic or superhydrophilic surfaces have been confirmed to possess antibacterial effects by reducing protein adsorption and bacterial adhesion (Montgomerie and Popat, 2021; Tian et al., 2022). The superhydrophobic surface is defined as a surface exhibiting a static water contact angle (WCA) greater than 150° , contact angle hysteresis (CAH) below 10° , and sliding angle less than 10° (Hoshian et al., 2017). As its resistance to the adhesion of organic substances, such as blood cells and microorganisms, superhydrophobic surface has been investigated for their use in blood-contacting medical devices (Wu et al., 2021). In contrast, superhydrophilic surface is generally defined by very low WCA (less than 10°) (Si et al., 2018). Artificial superhydrophobic or superhydrophilic surfaces can be formed *via* different routes and techniques, such as surface treatment, changing the surface composition, or altering the surface texture. Many surface modification methods are available for the changing of surface wettability, such as MAO, ion irradiation (Karthikeyan et al., 2020; Kolanthai et al., 2022), UV light irradiation, thermal annealing or chemical treatment (Liu et al., 2014b).

Surface charge is also an important surface property that can affect bacterial adhesion and biofilm formation on surfaces. More bacterial adhesion was observed on positively charged surfaces, probably because bacteria generally possess a net negative charge owing to amino, carboxyl, and phosphate groups on their cell wall surface (Rijnaarts et al., 1999). In addition, some studies have shown that the surface charge also affects the subsequent accumulation of biofilms on the material surface (Kao et al., 2017; Shen et al., 2020).

Surface topography can significantly affect bacterial adhesion and subsequent biofilm formation. It was found that specific ranges of dimensions (i.e., height, diameter, and interspacing) of nanopillars lead to a strong bactericidal effect (He et al., 2021), and the mechanism was suggested to occur by mechanical rupture of the cell. However, Jenkins et al. (2020) reported that nanopillars did not result in mechanical rupture or cell lysis. The deformation and subsequent penetration of bacteria may be caused by the induction of oxidative stress within bacterial cells upon contact with nanopillars.

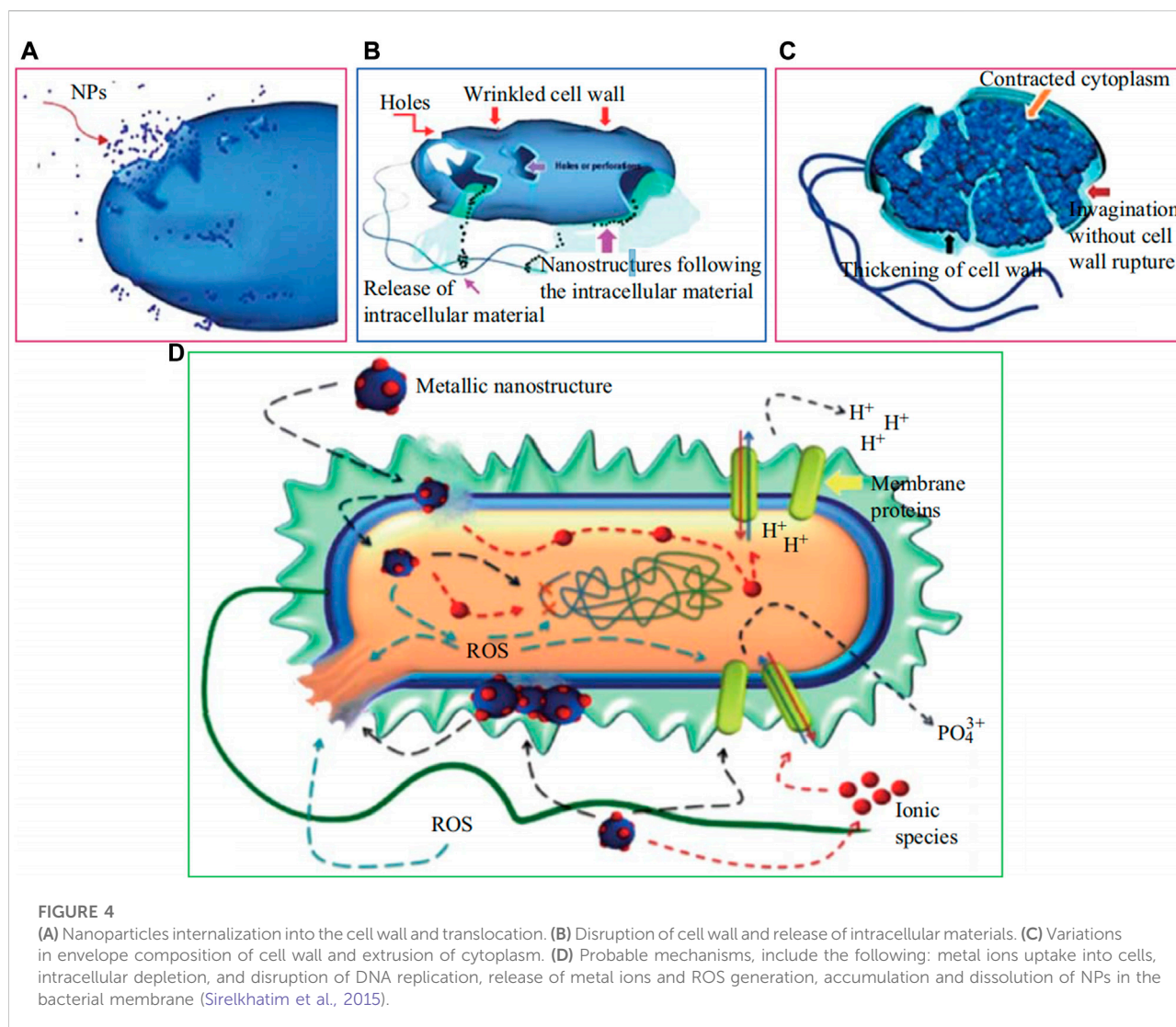
3.2 Metal nanoparticles coatings on titanium implants

As the antibiotic resistance of microbes to drugs increases, nanotechnology provides an opportunity to resolve this problem (Li et al., 2020c). Metal nanoparticles (NPs), which are referred to

as nanobiotics, have been proposed as novel antimicrobial agents. They can potentially reduce or eliminate the continuous emergence of bacterial resistance (Lee et al., 2019). Implant surfaces functionalized by coating them with NPs were found to have antibacterial properties as well as resistance to bacterial adhesion (Li et al., 2020b).

Although the exact antibacterial mechanisms of NPs remain unknown, several hypotheses have been proposed. It is generally believed that the main antibacterial mechanism is the interaction between bacteria and ions released from the NPs (Panáček et al., 2006; Mcquillan et al., 2012; Dorobantu et al., 2015). Under humid conditions, the ions released from NPs can induce excess ROS generation (Applerot et al., 2009; Wang et al., 2017; Korzekwa et al., 2021), which can kill bacteria by destroying intracellular biomolecules (Choi and Zhiqiang, 2008). The possible antibacterial mechanisms of NPs are shown in Figure 4. Although NPs do not release ions and electrons under dry conditions, some studies have demonstrated that they still possess antimicrobial properties under such conditions. This indicates that direct contact is a potential antimicrobial mechanism (Sami et al., 2018; Loran et al., 2019). This hypothesis was confirmed by Loran et al. (2019)'s experiment which showed that ion production does not increase the antibacterial effect of NPs. Moreover, the sharp edges of nanostructures can destroy microbial membranes, thus preventing biofilm formation, but are toxic to human cells as well (Pashkuleva et al., 2010).

The nano-scale size can be similar to the dimensions of water-filled channels in biofilm structures and possesses good affinity with a negatively charged extracellular matrix. Furthermore, their high surface-to-volume ratio also has excellent advantages (Ding et al., 2021). The metals used for these nanoparticles are almost exclusively heavy metals, such as Ag, Cu, zinc (Zn), and ZnO nanoparticles, with Ag particles being more common (Sanchez-Lopez et al., 2020). Rodríguez-Contreras et al. (2021) fabricated a coating incorporating Ag NPs and Ca on the surface of Ti using a new thermochemical treatment method. This coating not only generated non-cytotoxic surfaces and maintained the bioactivity provided by Ca, but also endowed the surfaces of Ti with antimicrobial activity against both gram-positive and gram-negative bacterial strains. Similarly, Surmeneva et al. (2019) confirmed that the calcium phosphate (CaP) layers formed on the Ti surface by plasma electrolytic oxidation (PEO) treatment comprised of approximate 0.02 mg/cm^2 Ag nanoparticles, hindered *E. coli* and *S. aureus* growth. Li et al. (2016b) also proved that Ag nanoparticles with gelatin microspheres incorporated into porous titanium showed a high antibacterial effect on both *E. coli* and *S. aureus*. Usually, Ag nanoparticles are reported to kill bacteria without resistance (Sobolev et al., 2019). Unfortunately, a study (Gunawan et al., 2013) revealed resistance, resulting from the adaptation of nanosilver. In a study by Panáček et al. (2018), some gram-



negative bacteria were also reported to be resistant to AgNPs under repeated contact. Panáček et al. (2015) suggested that this may be related to flagellin production, causing nanoparticle aggregation. Despite resistance without genetic changes, it cannot be handled easily. However, the pomegranate rind extract did. There is a strategy that combines NPs and antibiotics to overcome microbial resistance. The combination of Ag NPs and conventional antibiotics has been found to provide a much better antibacterial effect than Ag NPs or antibiotics alone (Naqvi et al., 2013; Hemeg, 2017). The enhanced microbial susceptibility to this combination which can facilitate the entry of antibiotics into cells may be due to the increased permeability of the microbial walls modulated by NPs. Another reason may be that the enzymes that play key roles in antibiotic resistance are inactivated by NPs (Panáček et al., 2015). Another study (Sobolev et al., 2019) found that combining up to 75% Ag NPs and 25% Zn NPs on

the implant surface had antibacterial effects on both adherent and planktonic bacteria *in vitro* and *in vivo*. The addition of Zn nanoparticles can reduce Ag release and enhance the mechanical properties of the alloy.

3.3 Zinc-containing surface modification

3.3.1 The antibacterial mechanism of zinc

Similar to Cu and Ag, zinc (Zn) possesses antibacterial properties. It is widely used as an antibacterial agent in dental products. The antibacterial activity of Zn was relatively weak compared to those of Ag and Cu. However, Zn ions show non-cytotoxicity in the range from 10^{-6} to 10^{-5} M. What's more, Zn is a significant element in metabolism activity, which can promote osteogenic responses and bone formation by upregulating the pre-expression of ossification-related genes and the synthesis of

extracellular matrix (Zhang et al., 2016b; Almoudi et al., 2018; Shimabukuro et al., 2019; Shimabukuro et al., 2020).

Zn ions have multiple antibacterial effects on bacteria by interacting with intact cell membranes and inhibiting relative enzyme activities (Almoudi et al., 2018). It plays a crucial role in preventing the initial adhesion of bacteria (Singh et al., 2021). ZnO is the chemical state of Zn, which functions by means of ROS generation and Zn ion release. Some researchers have suggested that ROS generation plays a leading role in the antibacterial properties of Zn (Dutta et al., 2012; Prasanna and Vijayaraghavan, 2015; Almoudi et al., 2018; Shimabukuro et al., 2019).

3.3.2 Antibacterial performance of zinc-coatings

To prevent implant-related infections, various techniques have been introduced to confer bacteriostasis to biomaterials, such as Zn incorporation into the implant surface. The results obtained by Petrini et al. (2006) showed that Ti oxide surfaces modified with Zn could significantly reduce the viability of five streptococcal oral strains. With increasing Zn content, the bacteriostasis of the coating was enhanced, while the cytoactivity of osteoblast cells was inhibited. Therefore, Zhao et al. (2013) proposed a range of Zn contents in the micro-arc oxidation (MAO) coating (from 0.199 at % to 0.574 at%) which may be beneficial to balance cytotoxicity and antibacterial capacity. Bi et al. (2020) fabricated biphasic Zn-HA/Bi-HA coatings which incorporated Zn and bismuth (Bi) ions onto titanium plates. They found that such coatings exhibited improved antimicrobial activity against *E. coli* and *S. aureus* and that Zn^{2+} ions may play an important role in this antimicrobial action owing to the lower release rate of Bi^{3+} ions from the coatings. For the purpose of improving biological properties, several other methods exist for adding elements to the surface of implants, like plasma-based low-energy ion implanted, ion beam or coatings prepared by wet chemical precipitation method followed by microwave irradiation (Karthikeyan et al., 2019; Arul et al., 2021).

3.4 Applications of other antibacterial elements in coatings

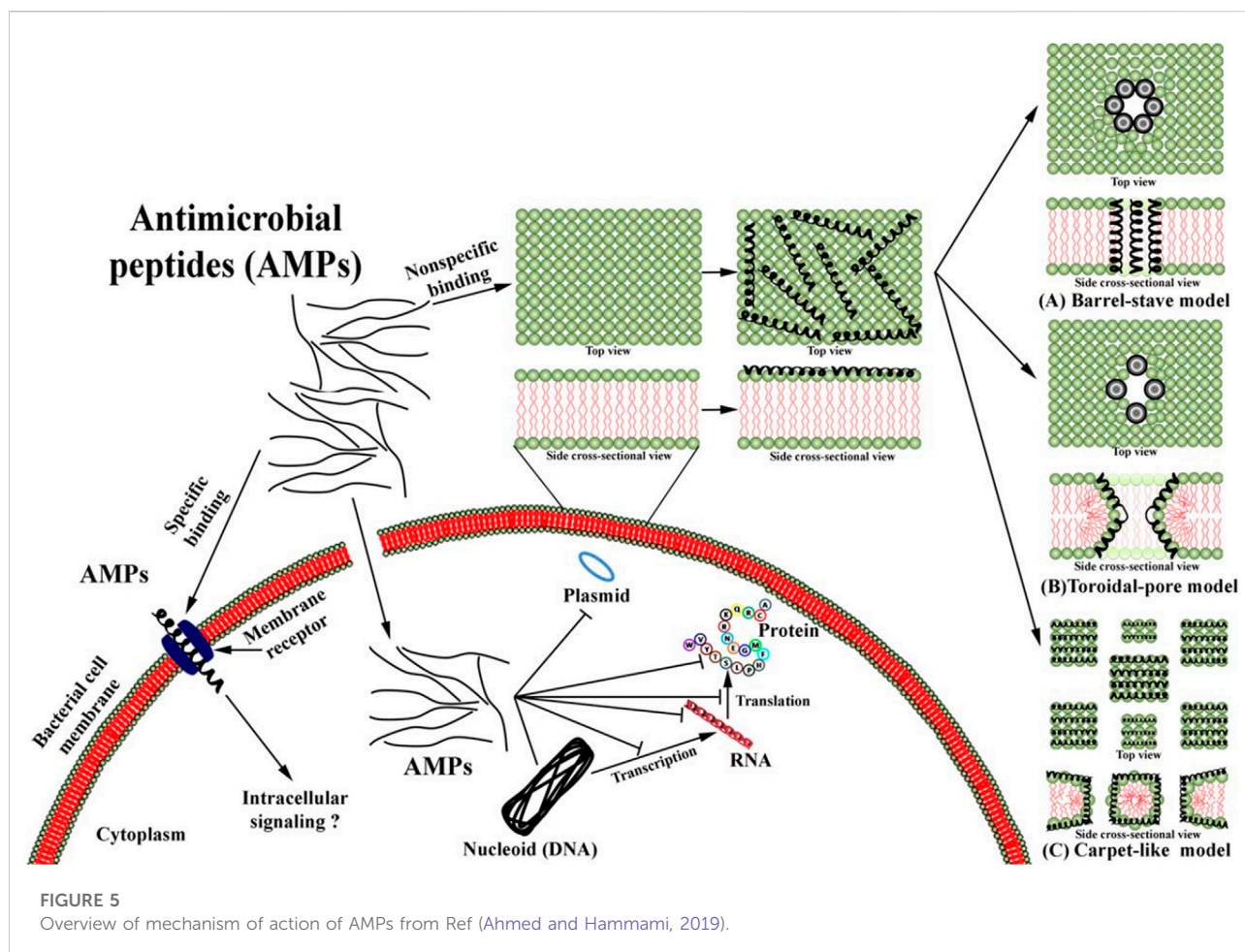
3.4.1 Fluorine

Fluorine is a necessary trace element in the human body, 93%–97% is stored in the skeletal system (Ciosek et al., 2021). Fluoride is essential for the proper development of bones and teeth. It increases the proliferation of osteoblastic cells and promotes bone formation, at the same time, inhibiting the activity of osteoclasts; thus, leading to an increase in bone mass (Liu et al., 2019). Therefore, fluorine compounds have been used in the treatment of osteoporosis. In addition, fluoride has been used in preventive dentistry for decades. They are added to mouthwash, toothpaste, and topical gels to reduce dental caries

by inhibiting the demineralisation of the natural tooth tissue (Goudouri et al., 2014). Fluorine also appears in surface modifications as an antimicrobial agent (Chen et al., 2021b). Up to now, two mechanisms of have been identified for the antibacterial effect of fluorine-treated materials. So far, two mechanisms have been suggested to explain the antibacterial action of Fluorine. One such mechanism is ascribed to the fluoride ions which can act directly as an enzyme inhibitor to the glycolytic enzyme and enolase. And the formation of metal-fluoride compounds is another potential mechanism. Metal-fluoride complexes is known to inhibit proton translocating F-ATPases and disrupt the bacterial metabolism and aciduric capability (Zhou et al., 2018). Prepared by the MAO method or plasma-based deposition methods, fluorine-containing coatings have shown antibacterial abilities in many studies (Perez-Jorge et al., 2017; Zhou et al., 2018; Zhao et al., 2019). However, some studies have confirmed that titanium dioxide/calcium phosphide coatings with a high fluorine content have obvious antibacterial effects, whereas coatings with a low fluorine content lack antibacterial activity (Zhou et al., 2018).

3.4.2 Gallium

Gallium (Ga) is a semi-metallic element in Group 13 of the periodic table. Over the past decades, Ga has shown a potential therapeutic effect on numerous disorders, such as bone loss, haemostasis, hypercalcaemia, autoimmune diseases, allograft rejection, and certain types of cancers (Kurtuldu et al., 2022). In 2003, the citrate-buffered nitrate form was approved by the United States Food and Drug Administration (FDA) for the treatment of malignant tumour-related hypercalcaemia and autoimmune diseases (Leyland-Jones, 2003). Notably, its antibacterial effects have attracted considerable attention in recent years. Ga ions (Ga^{3+}) can be mistakenly absorbed as Fe^{3+} owing to their similarities, which is known as “the Trojan horse strategy” (Li et al., 2022). Iron (Fe) is an essential element in the growth process of almost all bacteria, especially those that are predisposed to infections *in vivo*. When Ga^{3+} is actively transported into bacteria, it cannot be used in any metabolic pathways and iron metabolism is disturbed, ultimately resulting in the death of the bacteria (Minandri et al., 2014). Such an antimicrobial mechanism makes it difficult for bacteria to evolve resistance by reducing the uptake of Ga, as it would reduce iron uptake as well. Furthermore, Li et al. (2022) revealed that the alkaline microenvironment and ROS produced by the samples could contribute to the antibacterial effect. Recent studies have reported that Ga exerts significant inhibitory activity against numerous bacteria, including *S. aureus*, *E. coli*, *Pseudomonas aeruginosa*, and *Acinetobacter baumannii* (Xu et al., 2017; Cochis et al., 2019). Owing to Ga^{3+} and Sr^{2+} ions, the implant with a gallium-loaded SrTiO_3 nanotube coating exhibited better osteoinductivity and antibacterial properties (Qiao et al., 2019). However, a high Ga content may decrease the cytocompatibility of bone-related materials. Co-doping with



cerium (Ce), which exhibits good cytocompatibility and antibacterial properties, can mitigate the cytotoxicity of Ga (Łapa et al., 2020).

3.5 Antibiotic-containing surface modification

Although several disadvantages have been demonstrated, antibiotics still play a crucial role in the treatment of infections. The application of antibiotics to implant surfaces is another strategy to improve their antibacterial performance. Gentamycin is commonly used for infection therapy in the orthopaedics (Sarin et al., 2019). Using the direct oxidation method in Khodaei et al. (2017)'s study, gentamicin combined with strontium-containing gelatin microspheres was synthesized and deposited on the surface of a porous titanium scaffold, which was found to postpone strontium release and enhance antibacterial ability. Zhang et al. (2020) found that 3D printed porous Ti-6Al-4V implants with vancomycin displayed a remarkable inhibition of bone infection. Furthermore, the pH-

responsive release of vancomycin was proposed. However, from my perspective, *in vivo*, the pH did not change significantly for a long time because of homeostasis. Chlorhexidine, an antiseptic, is a common antibacterial drug that is usually used as a mouthwash. By interacting with the negatively charged bacterial membrane, chlorhexidine can become bacteriostatic or bactericidal as its concentration increases. Vidal et al. (2021) reported that samples coated with CaP and chlorhexidine which were processed by direct ink writing (DIW), showed antibacterial ability.

3.6 Antibacterial peptides

The emergence of Antibacterial peptides (AMPs) offers new approaches to overcoming antimicrobial resistance which is a significant challenge in the current healthcare industry (Zhang et al., 2021a). Lozeau et al. (2018) concluded from a series of studies that AMPs are short (10–50), cationic (+2 to +9), amphiphilic, and broad-spectrum antimicrobial proteins that are part of the innate immune systems of many species, including humans. It is difficult for bacteria to develop

resistance owing to their antimicrobial mechanisms. Ahmed and Hammami (2019) provided a clear picture to elucidate this, as shown in Figure 5, in which the barrel-stave model, toroidal-pore model, carpet-like mode and non-membrane binding activity, receptors, and internal activity are illustrated in detail.

3.7 Photo-sensitive antibacterial surface modification

Photosensitizers triggered by light can act as antibacterial agents owing to their photodynamic and photothermal properties. Under light irradiation, photosensitizers such as MoSe₂, MnO₂, TiO₂, ZnO, IR780 phosphorus, and graphene oxide can generate reactive oxygen species and/or increase local temperature, thereby killing the bacteria (Kubiak et al., 2021). For light, visible (>410 nm or 660 nm), infrared (808 nm) simulated sunlight (SSL), and LED have been found to be useful (Dutta et al., 2012; Jing et al., 2020; Teng et al., 2020; Zhu et al., 2020; Chai et al., 2021). Combined with photosensitizers, chitosan and polydopamine (PDA) are components of the coat that enhance biocompatibility and help absorb light (Teng et al., 2020; Zhu et al., 2020). Zhu et al. (2020) designed a chitosan-modified MoS₂ coating with antibacterial Ag nanoparticles was incorporated. According to their results, the antibacterial rate of the coating on *S. aureus* and *E. coli* was 98.66% and 99.77%, respectively, while chitosan within the system could reduce the cytotoxicity of Ag NPs. The advantage of photodynamic antibacterial and photothermal antibacterial strategies is that they can eliminate bacterial infection on implants safely and effectively within a short time and do not cause antibiotic resistance in bacteria. However, whether they can be applied on the surface of implants requires further research because light cannot pass through hard or soft tissue, and long-time infrared irradiation is harmful.

4 Antibacterial effects of 3D printing materials

Selective laser melting (SLM) is an additive manufacturing AM technology that can be used to manufacture metal components. So far, bone prostheses manufactured via these technologies have primarily been used clinically in relatively low load-bearing areas. The currently available 3D printing technology and new research in dentistry involve different specialities, such as oral surgery, prosthodontics, orthodontics, endodontics, periodontal disease, and temporomandibular joint rehabilitation (Christina et al., 2022). In terms of prosthodontics, 3D printing technology can be applied to interim prostheses, fixed and removable prosthodontics, etc., with the main purpose of improving accuracy and saving time and costs (Jin et al., 2018; Tahayeri et al., 2018). Surgical implant guides, dental implants, and regenerative periodontology are the primary applications of

3D printing in the periodontics (Hämmerle et al., 2009; Park et al., 2012). In addition, 3D printing has also been used to treat TMJ diseases, including making occlusal stabilisation splints (SS) for patients with temporomandibular disorders (TMDs) (Salmi et al., 2013), TMJ replacement (Zheng et al., 2019), and TMJ tissue engineering (Legemate et al., 2016). Whether used for restorations, prostheses, or implants, the material needs to have an antibacterial activity to reduce the occurrence of caries and infections of soft or hard tissues (Fan et al., 2021).

Implants made by 3D printing technology possess a larger surface area than an equally sized solid material, which increases the difficulty of sterilising the implant because of the difficult-to-reach internal surface (Zadpoor, 2019). However, to date, no clear evidence has shown an increased risk of infection in 3D printed implants (Zadpoor, 2019). Moreover, research completed by Bassous et al. (2019) corroborated that 3D printed Ti-6Al-4V scaffolds can exhibit antibacterial activity while improving osseointegration. They suggested that the probable antibacterial nature of the scaffolds might be because the concentration of adsorbed hydrophilic proteins increased with an increasing polar component of the surface energy. Some researchers have improved the antibacterial effects of 3D printed materials by adding coatings to their surfaces. Sedelnikova et al. (2022) created Zn- and Ag-containing coatings on the surface of 3D printing materials using the MAO method. It confirmed that the material has good biocompatibility and high antibacterial activity against MRSA and *E. coli*. In comparison to conventional methods, this method has greater design flexibility, therefore it enables the development of novel implants. Cox et al. (2016) incorporated the antibiotic (gentamicin sulphate) cement within the 3d-printed titanium-based (Ti-6Al-4V) implants containing a reservoir. After immersing implant models containing injected cement in phosphate buffered saline (PBS), they observed that gentamicin sulphate achieved a controlled release and exceed the minimum inhibitory concentrations of *S. aureus* (16 µg/ml) and *S. epidermidis* after 6 h (1 µg/ml).

5 Conclusion and perspectives

Ti-based orthopaedic and dental implants have been widely used and have been successful in the past few decades. However, the major limitations of their success in clinical applications are poor osseointegration and bacterial infection, which are the two main reasons for implant failure and revision surgery. Recently, novel alloys or surface modifications designed to fight microbial infections and enhance implant survival rates have been the focus of intense biomedical research. In this review, we summarise recent progress in techniques that have been explored to modify materials with the aim of addressing issues of conventional Ti implants, especially antibacterial applications, including the addition of antibacterial elements in materials, NPs,

Antibacterial peptide photosensitive coatings, and some other surface modifications. Although these techniques have proven to be effective in improving the antibacterial properties of implants, they have drawbacks. For example, for novel alloys, the entire alteration of the materials is expensive and time-consuming, which may cause changes in the mechanical properties. Numerous surface modification techniques have been investigated to optimise the interfacial properties of implants without disrupting the bulk properties of Ti biomaterials. However, in terms of coatings of Ti biomaterial, there are three main barriers to the design of these surfaces: 1) thin coatings may not adhere to the substrate in some cases, 2) long-term and stable antibacterial effects, and 3) maintenance of an effective local antibacterial effect at the implant surface without influencing the host response, and not causing cytotoxicity to the tissue surrounding the implant or allowing increased drug-resistant strains at the site. Another major setback to implant longevity is that the implant processing and surface modification methods could result in cracking and deteriorated ageing resistance of the implant surface. These drawbacks have motivated us to explore other approaches. Therefore, more suitable methods are needed to improve implant performance.

Recently, more scholars have explored solutions from a novel perspective. The future development direction of antibacterial materials should be “smart” and “synergistic”. An ideal antibacterial material should remain “bio-inert” in the absence of bacteria, activate when bacteria are present, and kill bacteria when they adhere to the surface. They should combine multiple bactericidal mechanisms to synergistically improve antibacterial efficacy and avoid resistance and should also be able to remove dead bacteria that may cause the development of a multi-structured biofilm and restore clean surfaces, thus guaranteeing long-term antibacterial properties. It is common sense that the microenvironment of biofilms is different from that of normal tissue around infection sites. Therefore, some substances can act as triggers for the response of antibacterial materials. As for stimulations, in the study of Ding et al. (2021) many products of bacteria such as enzymes, lipases, and some external stimuli such as pH, light, and microwaves have been reported. However, most of the process of experiments based on that were conducted *in vitro* which does not represent a real infection environment. However, the future of stimuli-responsive antibacterial materials remains bright because of their outstanding properties, functions, and irreplaceable advantages over conventional therapies.

Undoubtedly, the performance of titanium-based alloys must be further improved to adapt to inter-patient and inter-disease variations. They will be designed and tested to fight against more types of bacteria, especially gram-negative bacteria. The elastic modulus of titanium-based alloys can be reduced to resemble natural bone without damaging their properties. New-generation

titanium-based alloys should be able to fight against a wide range of pathogens, have a long-lasting antibacterial effect, possess high biocompatibility and stability, and shorten the treatment time. With the advancement of technology, the cost, time, and risk will reduce dramatically. Recent developments in materials engineering, nanotechnology, and additive manufacturing approaches are expected to have a considerable impact on the medical implants industry and drive further development for the design of a new generation of intelligent and multifunctional orthopedic implants. The highly reproducibility, cost-effectiveness, stability, and durability of these novel implants will be critical factors to consider for their widespread commercialisation. Upon fabrication of these novel implants, the next critical step would be their implementation in clinical practice which requires extensive *in vivo* experiments and long-term performances.

Author contributions

ZB and ZY contributed to the study's conception and design. YM and JY wrote the manuscript and TY and QW polished the language of the manuscript. All authors contributed to manuscript revision and read and approved the submitted version.

Funding

This work was supported by the Science and Technology Project of Liaoning Province (2018020205-101), Key Research and Development Projects of Liaoning Province (2020020184-JH2/103), and Yanglei Academician Expert Workstation of Yunnan Province (202205 AF150025).

Conflict of interest

The authors declare that the research was conducted in the absence of any commercial or financial relationships that could be construed as a potential conflict of interest.

Publisher's note

All claims expressed in this article are solely those of the authors and do not necessarily represent those of their affiliated organizations, or those of the publisher, the editors and the reviewers. Any product that may be evaluated in this article, or claim that may be made by its manufacturer, is not guaranteed or endorsed by the publisher.

References

- Abdelraheem, W. M., Abdelkader, A. E., Mohamed, E. S., and Mohammed, M. S. (2020). Detection of biofilm formation and assessment of biofilm genes expression in different *Pseudomonas aeruginosa* clinical isolates. *Meta Gene* 23, 100646. doi:10.1016/j.mgene.2020.100646
- Aguilera-Correa, J. J., Mediero, A., Conesa-Buendia, F. M., Conde, A., Arenas, M. A., de-Damborenea, J. J., et al. (2019). Microbiological and cellular evaluation of a fluorine-phosphorus-doped titanium alloy, a novel antibacterial and osteostimulatory biomaterial with potential applications in orthopedic surgery. *Appl. Environ. Microbiol.* 85 (2), e02271-18. doi:10.1128/AEM.02271-18
- Ahmed, T. A. E., and Hammami, R. (2019). Recent insights into structure-function relationships of antimicrobial peptides. *J. Food Biochem.* 43 (1), e12546. doi:10.1111/jfbc.12546
- Akimoto, T., Ueno, T., Tsutsumi, Y., Doi, H., Hanawa, T., and Wakabayashi, N. (2018). Evaluation of corrosion resistance of implant-use Ti-Zr binary alloys with a range of compositions. *J. Biomed. Mat. Res.* 106 (1), 73–79. doi:10.1002/jbm.b.33811
- Alghamdi, H. S., and Jansen, J. A. (2020). The development and future of dental implants. *Dent. Mat. J.* 39 (2), 167–172. doi:10.4012/dmj.2019-140
- Almoudi, M. M., Hussein, A. S., Abu Hassan, M. I., and Mohamad Zain, N. (2018). A systematic review on antibacterial activity of zinc against *Streptococcus mutans*. *Saudi Dent. J.* 30 (4), 283–291. doi:10.1016/j.sdentj.2018.06.003
- Alqattan, M., Peters, L., Alshammari, Y., Yang, F., and Bolzoni, L. (2021). Antibacterial Ti-Mn-Cu alloys for biomedical applications. *Regen. Biomater.* 8 (1), rbaa050. doi:10.1093/rb/rbaa050
- Applerot, G., Lipovsky, A., Dror, R., Perkas, N., Nitzan, Y., Lubart, R., et al. (2009). Enhanced antibacterial activity of nanocrystalline ZnO due to increased ROS-mediated cell injury. *Adv. Funct. Mat.* 19 (6), 842–852. doi:10.1002/adfm.200801081
- Arul, K. T., Manikandan, E., Ramya, J. R., Indira, K., Mudali, U. K., Henini, M., et al. (2021). Enhanced anticorrosion properties of nitrogen ions modified polyvinyl alcohol/Mg-Ag ions co-incorporated calcium phosphate coatings. *Mater. Chem. Phys.* 261, 124182. doi:10.1016/j.matchemphys.2020.124182
- Bassous, N. J., Jones, C. L., and Webster, T. J. (2019). 3-D printed Ti-6Al-4V scaffolds for supporting osteoblast and restricting bacterial functions without using drugs: Predictive equations and experiments. *Acta Biomater.* 96, 662–673. doi:10.1016/j.actbio.2019.06.055
- Belibasakis, G. N., and Manoil, D. (2021). Microbial community-driven etiopathogenesis of peri-implantitis. *J. Dent. Res.* 100 (1), 21–28. doi:10.1177/0022034520949851
- Bi, Q., Song, X., Chen, Y., Zheng, Y., Yin, P., and Lei, T. (2020). Zn-HA/Bi-HA biphasic coatings on Titanium: Fabrication, characterization, antibacterial and biological activity. *Colloids Surfaces B Biointerfaces* 189, 110813. doi:10.1016/j.colsurfb.2020.110813
- Borkow, G., and Gabbay, J. (2005). Copper as a biocidal tool. *Curr. Med. Chem.* 12 (18), 2163–2175. doi:10.2174/0929867054637617
- Borkow, G. (2012). Using copper to fight microorganisms. *Curr. Chem. Biol.* 6 (2), 93–103. doi:10.2174/187231312801254723
- Buser, D., Ingimarsson, S., Dula, K., Lussi, A., Hirt, H. P., and Belser, U. C. (2002). Long-term stability of osseointegrated implants in augmented bone: A 5-year prospective study in partially edentulous patients. *Int. J. Periodontics Restor. Dent.* 22 (2), 109–117.
- Cai, D., Zhao, X., Yang, L., Wa Ng, R., Zhang, E., Chen, D. F., et al. (2021). A novel biomedical titanium alloy with high antibacterial property and low elastic modulus. *J. Mat. Sci. Technol.* 81, 13–25. doi:10.1016/j.jmst.2021.01.015
- Chai, M., An, M., and Zhang, X. (2021). Construction of a TiO₂/MoSe₂/CHI coating on dental implants for combating *Streptococcus mutans* infection. *Mater. Sci. Eng. C* 129, 112416. doi:10.1016/j.msec.2021.112416
- Chen, B., Abdallah, M., Campistron, P., Moulin, E., Callens, D., Khelissa, S. O., et al. (2021a). Detection of biofilm formation by ultrasonic Coda Wave Interferometry. *J. Food Eng.* 290, 110219. doi:10.1016/j.jfoodeng.2020.110219
- Chen, M., Wang, X.-Q., Zhang, E.-L., Wan, Y.-Z., and Hu, J. (2021b). Antibacterial ability and biocompatibility of fluorinated titanium by plasma-based surface modification. *Rare Met.* 41, 689–699. doi:10.1007/s12598-021-01808-y
- Chen, M., Yang, L., Zhang, L., Han, Y., Lu, Z., Qin, G., et al. (2017). Effect of nano/micro-Ag compound particles on the bio-corrosion, antibacterial properties and cell biocompatibility of Ti-Ag alloys. *Mater. Sci. Eng. C* 75, 906–917. doi:10.1016/j.msec.2017.02.142
- Chen, M., Zhang, E., and Zhang, L. (2016). Microstructure, mechanical properties, bio-corrosion properties and antibacterial properties of Ti-Ag sintered alloys. *Mater. Sci. Eng. C* 62, 350–360. doi:10.1016/j.msec.2016.01.081
- Chen, S., Tsoi, J. K. H., Tsang, P. C. S., Park, Y. J., Song, H. J., and Matinlinna, J. P. (2020). Candida albicans aspects of binary titanium alloys for biomedical applications. *Regen. Biomater.* 7 (2), 213–220. doi:10.1093/rb/rbz052
- Choi, O., and Zhiqiang, H. U. (2008). Size dependent and reactive oxygen species related nanosilver toxicity to nitrifying bacteria. *Environ. Sci. Technol.* 42 (12), 4583–4588. doi:10.1021/es703238h
- Christina, H., Maria, B., Athina, B., and Petros, K. (2022). “Chapter 9 - 3D printing in dentistry with emphasis on prosthetic rehabilitation and regenerative approaches,” in *3D printing: Applications in medicine and surgery volume 2*. Editors V. N. Papadopoulos, V. Tsioukas, and J. S. Suri (Elsevier), 195–219.
- Ciosek, Z., Kot, K., Kosik-Bogacka, D., Lanocha-Arendarczyk, N., and Rotter, I. (2021). The effects of calcium, magnesium, phosphorus, fluoride, and lead on bone tissue. *Biomolecules* 11 (4), 506. doi:10.3390/biom11040506
- Cochis, A., Azzimonti, B., Chiesa, R., Rimondini, L., and Gasik, M. (2019). Metallurgical gallium additions to titanium alloys demonstrate a strong time-increasing antibacterial activity without any cellular toxicity. *ACS Biomater. Sci. Eng.* 5 (6), 2815–2820. doi:10.1021/acsbomaterials.9b00147
- Cox, S. C., Jamshidi, P., Eisenstein, N. M., Webber, M. A., Hassani, H., Attallah, M. M., et al. (2016). Adding functionality with additive manufacturing: Fabrication of titanium-based antibiotic eluting implants. *Mater. Sci. Eng. C* 64, 407–415. doi:10.1016/j.msec.2016.04.006
- Dhale, R. P., Ghorpade, M. V., and Dharmadhikari, C. A. (2014). Comparison of various methods used to detect biofilm production of *Candida* species. *J. Clin. Diagn. Res.* 8 (11), DC18–c20. doi:10.7860/jcdr/2014/10445.5147
- Ding, M., Zhao, W., Song, L.-J., and Luan, S.-F. (2021). Stimuli-responsive nanocarriers for bacterial biofilm treatment. *Rare Met.* 4, 482–498. doi:10.1007/s12598-021-01802-4
- Dorobantu, L. S., Fallone, C., Noble, A. J., Veinot, J., Burrell, R. E., Goss, G. G., et al. (2015). Toxicity of silver nanoparticles against bacteria, yeast, and algae. *J. Nanopart. Res.* 17 (4), 172. doi:10.1007/s11051-015-2984-7
- Dutta, R. K., Nenavathu, B. P., Gangishetty, M. K., and Reddy, A. V. (2012). Studies on antibacterial activity of ZnO nanoparticles by ROS induced lipid peroxidation. *Colloids Surfaces B Biointerfaces* 94, 143–150. doi:10.1016/j.colsurfb.2012.01.046
- El-Bagoury, N., Ahmed, S. I., Ahmed Abu Ali, O., El-Hadad, S., Fallatah, A. M., Mersal, G. A. M., et al. (2019). The influence of microstructure on the passive layer chemistry and corrosion resistance for some titanium-based alloys. *Mater. (Basel)* 12 (8), 1233. doi:10.3390/ma12081233
- Fan, D.-Y., Yi, Z., Feng, X., Tian, W.-Z., Xu, D.-K., Cristino Valentino, A. M., et al. (2021). Antibacterial property of a gradient Cu-bearing titanium alloy by laser additive manufacturing. *Rare Met.* 41, 580–593. doi:10.1007/s12598-021-01826-w
- Ferraris, S., and Spriano, S. (2016). Antibacterial titanium surfaces for medical implants. *Mater. Sci. Eng. C* 61, 965–978. doi:10.1016/j.msec.2015.12.062
- Filippini, T., Cilloni, S., Malavolti, M., Violi, F., Malagoli, C., Tesaro, M., et al. (2018). Dietary intake of cadmium, chromium, copper, manganese, selenium and zinc in a Northern Italy community. *J. Trace Elem. Med. Biol.* 50, 508–517. doi:10.1016/j.jtemb.2018.03.001
- Fowler, L., Janse Van Vuuren, A., Goosen, W., Engqvist, H., Ohman-Magi, C., and Norgren, S. (2019a). Investigation of copper alloying in a TNTZ-cux alloy. *Mater. (Basel)* 12 (22), 3691. doi:10.3390/ma12223691
- Fowler, L., Janson, O., Engqvist, H., Norgren, S., and Ohman-Magi, C. (2019b). Antibacterial investigation of titanium-copper alloys using luminescent *Staphylococcus epidermidis* in a direct contact test. *Mater. Sci. Eng. C* 97, 707–714. doi:10.1016/j.msec.2018.12.050
- Frisch, E., Wild, V., Ratka-Krüger, P., Vach, K., and Sennhenn-Kirchner, S. (2020). Long-term results of implants and implant-supported prostheses under systematic supportive implant therapy: A retrospective 25-year study. *Clin. Implant Dent. Relat. Res.* 22 (6), 689–696. doi:10.1111/cid.12944
- Fu, Y., Chang, F. M., and Giedroc, D. P. (2014). Copper transport and trafficking at the host-bacterial pathogen interface. *Acc. Chem. Res.* 47 (12), 3605–3613. doi:10.1021/ar500300n
- Fujita, M. (1993). *In vitro* study on biocompatibility of zirconium and titanium. *Kokubyo Gakkai Zasshi.* 60 (1), 54–65. doi:10.5357/koubyou.60.54
- Gomaa, E. Z. (2017). Silver nanoparticles as an antimicrobial agent: A case study on *Staphylococcus aureus* and *Escherichia coli* as models for gram-positive and

- gram-negative bacteria. *J. Gen. Appl. Microbiol.* 63 (1), 36–43. doi:10.2323/jgam.2016.07.004
- Gonzalez-Valls, G., Roca-Millan, E., Cespedes-Sanchez, J. M., Gonzalez-Navarro, B., Torrejon-Moya, A., and Lopez-Lopez, J. (2021). Narrow diameter dental implants as an alternative treatment for atrophic alveolar ridges. Systematic review and meta-analysis. *Mater. (Basel)* 14 (12), 3234. doi:10.3390/ma14123234
- Goudouri, O. M., Kontonasi, E., Lohbauer, U., and Boccacini, A. R. (2014). Antibacterial properties of metal and metalloid ions in chronic periodontitis and peri-implantitis therapy. *Acta Biomater.* 10 (8), 3795–3810. doi:10.1016/j.actbio.2014.03.028
- Grass, G., Rensing, C., and Solioz, M. (2011). Metallic copper as an antimicrobial surface. *Appl. Environ. Microbiol.* 77 (5), 1541–1547. doi:10.1128/AEM.02766-10
- Gristina, A. G., and Costerton, J. W. (1985). Bacterial adherence to biomaterials and tissue. The significance of its role in clinical sepsis. *J. Bone Jt. Surg.* 67 (2), 264–273. doi:10.2106/00004623-198567020-00014
- Gunawan, C., Teoh, W. Y., Marquis, C. P., and Amal, R. (2013). Induced adaptation of *Bacillus* sp. to antimicrobial nanosilver. *Small* 9 (21), 3554–3560. doi:10.1002/sml.201300761
- Guo, S., Lu, Y., Wu, S., Liu, L., He, M., Zhao, C., et al. (2017). Preliminary study on the corrosion resistance, antibacterial activity and cytotoxicity of selective-laser-melted Ti6Al4V-xCu alloys. *Mater. Sci. Eng. C* 72, 631–640. doi:10.1016/j.msec.2016.11.126
- Hämmerle, C. H., Stone, P., Jung, R. E., Kapos, T., and Brodala, N. (2009). Consensus statements and recommended clinical procedures regarding computer-assisted implant dentistry. *Int. J. Oral Maxillofac. Implants* 24, 126–131.
- He, Z., Yang, X., Wang, N., Mu, L., Pan, J., Lan, X., et al. (2021). Anti-biofouling polymers with special surface wettability for biomedical applications. *Front. Bioeng. Biotechnol.* 9, 807357. doi:10.3389/fbioe.2021.807357
- Hemeg, H. A. (2017). Nanomaterials for alternative antibacterial therapy. *Int. J. Nanomedicine* 12, 8211–8225. doi:10.2147/ijn.s132163
- Ho, W. F., Chen, W. K., Wu, S. C., and Hsu, H. C. (2008). Structure, mechanical properties, and grindability of dental Ti-Zr alloys. *J. Mat. Sci. Mat. Med.* 19 (10), 3179–3186. doi:10.1007/s10856-008-3454-x
- Hong, R., Kang, T. Y., Michels, C. A., and Gadura, N. (2012). Membrane lipid peroxidation in copper alloy-mediated contact killing of *Escherichia coli*. *Appl. Environ. Microbiol.* 78 (6), 1776–1784. doi:10.1128/aem.07068-11
- Hoshian, S., Kankuri, E., Ras, R. H. A., Franssila, S., and Jokinen, V. (2017). Water and blood repellent flexible tubes. *Sci. Rep.* 7 (1), 16019. doi:10.1038/s41598-017-16369-3
- Howe, M.-S., Keys, W., and Richards, D. (2019). Long-term (10-year) dental implant survival: A systematic review and sensitivity meta-analysis. *J. Dent.* 84, 9–21. doi:10.1016/j.jdent.2019.03.008
- Iqbal, N., Abdul Kadir, M. R., Bin Mahmood, N. H., Iqbal, S., Almasi, D., Naghizadeh, F., et al. (2015). Characterization and biological evaluation of silver containing fluorapatite nanoparticles prepared through microwave synthesis. *Ceram. Int.* 41 (5), 6470–6477. doi:10.1016/j.ceramint.2015.01.086
- Jenkins, J., Mantell, J., Neal, C., Gholinia, A., Verkade, P., Nobbs, A. H., et al. (2020). Antibacterial effects of nanopillar surfaces are mediated by cell impedance, penetration and induction of oxidative stress. *Nat. Commun.* 11 (1), 1626. doi:10.1038/s41467-020-15471-x
- Jin, S. J., Jeong, I. D., Kim, J. H., and Kim, W. C. (2018). Accuracy (trueness and precision) of dental models fabricated using additive manufacturing methods. *Int. J. Comput. Dent.* 21 (2), 107–113.
- Jing, Z., Zhang, T., Xiu, P., Cai, H., Wei, Q., Fan, D., et al. (2020). Functionalization of 3D-printed titanium alloy orthopedic implants: A literature review. *Biomed. Mat.* 15 (5), 052003. doi:10.1088/1748-605X/ab9078
- Kao, W. K., Gagnon, P. M., Vogel, J. P., and Chole, R. A. (2017). Surface charge modification decreases *Pseudomonas aeruginosa* adherence *in vitro* and bacterial persistence in an *in vivo* implant model. *Laryngoscope* 127 (7), 1655–1661. doi:10.1002/lary.26499
- Karbowiczek, J., Cordero-Arias, L., Virtanen, S., Misra, S. K., Valsami-Jones, E., Tuschscherr, L., et al. (2017). Electrophoretic deposition of organic/inorganic composite coatings containing ZnO nanoparticles exhibiting antibacterial properties. *Mater. Sci. Eng. C* 77, 780–789. doi:10.1016/j.msec.2017.03.180
- Karthikeyan, K. R., Arul, K. T., Ramya, J. R., Nabhiraj, P. Y., Menon, R., Krishna, J. B. M., et al. (2019). Core/shell structures on argon ions implanted polymer based zinc ions incorporated HAp nanocomposite coatings. *Mater. Sci. Semicond. Process.* 104, 104687. doi:10.1016/j.mssp.2019.104687
- Karthikeyan, K. R., Arul, K. T., Ramya, J. R., Nabhiraj, P. Y., Menon, R., Krishna, J. B. M., et al. (2020). Novel microporous surface and blue emission of argon ion implanted polyvinylalcohol/bionanohydroxyapatite coatings. *Radiat. Phys. Chem.* 171, 108678. doi:10.1016/j.radphyschem.2020.108678
- Ke, Z., Yi, C., Zhang, L., He, Z. Y., Tan, J., and Jiang, Y. H. (2019). Characterization of a new Ti-13Nb-13Zr-10Cu alloy with enhanced antibacterial activity for biomedical applications. *Mat. Lett.* 253, 335–338. doi:10.1016/j.matlet.2019.07.008
- Khodaei, M., Valanezhad, A., and Watanabe, I. (2017). Controlled gentamicin-strontium release as a dual action bone agent: Combination of the porous titanium scaffold and biodegradable polymers. *J. Alloys Compd.* 720, 22–28. doi:10.1016/j.jallcom.2017.05.236
- Kolanthai, E., Ahymah Joshy, M. I., Thanigai Arul, K., Manojkumar, P., Rameshbabu, N., Ashok, M., et al. (2022). Effect of swift heavy silicon ion irradiation on TiO₂ thin film prepared by micro arc oxidized technique. *Mater. Today Proc.* 58, 932–941. doi:10.1016/j.matpr.2021.12.312
- Kolawole, S. K., Hai, W., Zhang, S., Sun, Z., Siddiqui, M. A., Ullah, I., et al. (2020). Preliminary study of microstructure, mechanical properties and corrosion resistance of antibacterial Ti-15Zr-xCu alloy for dental application. *J. Mater. Sci. Technol.* 50, 31–43. doi:10.1016/j.jmst.2020.03.003
- Korzekwa, K., Kedziora, A., Stanczykiewicz, B., Bugla-Ploskonska, G., and Wojnicz, D. (2021). Benefits of usage of immobilized silver nanoparticles as *Pseudomonas aeruginosa* antibiofilm factors. *Int. J. Mol. Sci.* 23 (1), 284. doi:10.3390/ijms23010284
- Kubiak, B., Radtke, A., Topolski, A., Wrzeszcz, G., Golinska, P., Kaszkowiak, E., et al. (2021). The composites of PCL and tetranuclear titanium(IV)-oxo complexes as materials exhibiting the photocatalytic and the antimicrobial activity. *Int. J. Mol. Sci.* 22 (13), 7021. doi:10.3390/ijms22137021
- Kurtuldu, F., Mutlu, N., Boccacini, A. R., and Galusek, D. (2022). Gallium containing bioactive materials: A review of anticancer, antibacterial, and osteogenic properties. *Bioact. Mat.* 17, 125–146. doi:10.1016/j.bioactmat.2021.12.034
- Lapa, A., Cresswell, M., Campbell, I., Jackson, P., Goldmann, W. H., Detsch, R., et al. (2020). Gallium- and cerium-doped phosphate glasses with antibacterial properties for medical applications. *Adv. Eng. Mat.* 22 (9), 1901577. doi:10.1002/adem.201901577
- Lee, N. Y., Ko, W. C., and Hsueh, P. R. (2019). Nanoparticles in the treatment of infections caused by multidrug-resistant organisms. *Front. Pharmacol.* 10, 1153. doi:10.3389/fphar.2019.01153
- Legemate, K., Tarafder, S., Jun, Y., and Lee, C. H. (2016). Engineering human TMJ discs with protein-releasing 3D-printed scaffolds. *J. Dent. Res.* 95 (7), 800–807. doi:10.1177/0022034516642404
- Lei, Z., Zhang, H., Zhang, E., You, J., Ma, X., and Bai, X. (2020). Antibacterial activities and cell responses of Ti-Ag alloys with a hybrid micro- to nanostructured surface. *J. Biomater. Appl.* 34 (10), 1368–1380. doi:10.1177/0885328220905103
- Leyland-Jones, B. (2003). Treatment of cancer-related hypercalcemia: The role of gallium nitrate. *Semin. Oncol.* 30 (5), as0093775403001714–19. doi:10.1016/s0093-7754(03)00171-4
- Li, G., Wu, Y., Li, Y., Hong, Y., Zhao, X., Reyes, P. I., et al. (2020a). Early stage detection of *Staphylococcus epidermidis* biofilm formation using MgZnO dual-gate TFT biosensor. *Biosens. Bioelectron.* 151, 111993. doi:10.1016/j.bios.2019.111993
- Li, K., Tian, H., Guo, A., Jin, L., Chen, W., and Tao, B. (2022). Gallium (Ga)-strontium (Sr) layered double hydroxide composite coating on titanium substrates for enhanced osteogenic and antibacterial abilities. *J. Biomed. Mat. Res. A* 110 (2), 273–286. doi:10.1002/jbm.a.37284
- Li, M., Ma, Z., Zhu, Y., Xia, H., Yao, M., Chu, X., et al. (2016a). Toward a molecular understanding of the antibacterial mechanism of copper-bearing titanium alloys against *Staphylococcus aureus*. *Adv. Healthc. Mat.* 5 (5), 557–566. doi:10.1002/adhm.201500712
- Li, M., Wang, Y., Gao, L., Sun, Y., Wang, J., Qu, S., et al. (2016b). Porous titanium scaffold surfaces modified with silver loaded gelatin microspheres and their antibacterial behavior. *Surf. Coat. Technol.* 286, 140–147. doi:10.1016/j.surfcoat.2015.12.006
- Li, S., Liu, Y., Tian, Z., Liu, X., Han, Z., and Ren, L. (2020b). Biomimetic superhydrophobic and antibacterial stainless-steel mesh via double-potentiostatic electrodeposition and modification. *Surf. Coatings Technol.* 403, 126355. doi:10.1016/j.surfcoat.2020.126355
- Li, Y., Liu, L., Wan, P., Zhai, Z., Mao, Z., Ouyang, Z., et al. (2016c). Biodegradable Mg-Cu alloy implants with antibacterial activity for the treatment of osteomyelitis: *In vitro* and *in vivo* evaluations. *Biomaterials* 106, 250–263. doi:10.1016/j.biomaterials.2016.08.031
- Li, Y., Xiao, P., Wang, Y., and Hao, Y. (2020c). Mechanisms and control measures of mature biofilm resistance to antimicrobial agents in the clinical context. *ACS Omega* 5 (36), 22684–22690. doi:10.1021/acsomega.0c02294
- Liu, J., Li, F., Liu, C., Wang, H., Ren, B., Yang, K., et al. (2014a). Effect of Cu content on the antibacterial activity of titanium-copper sintered alloys. *Mater. Sci. Eng. C* 35, 392–400. doi:10.1016/j.msec.2013.11.028

- Liu, K., Cao, M., Fujishima, A., and Jiang, L. (2014b). Bio-inspired titanium dioxide materials with special wettability and their applications. *Chem. Rev.* 114 (19), 10044–10094. doi:10.1021/cr4006796
- Liu, R., Tang, Y., Zeng, L., Zhao, Y., Ma, Z., Sun, Z., et al. (2018). *In vitro* and *in vivo* studies of anti-bacterial copper-bearing titanium alloy for dental application. *Dent. Mat.* 34 (8), 1112–1126. doi:10.1016/j.dental.2018.04.007
- Liu, S., Zhou, H., Liu, H., Ji, H., Fei, W., and Luo, E. (2019). Fluorine-contained hydroxyapatite suppresses bone resorption through inhibiting osteoclasts differentiation and function *in vitro* and *in vivo*. *Cell Prolif.* 52 (3), e12613. doi:10.1111/cpr.12613
- Loran, S., Cheng, S., Botton, G. A., Yahia, L., Yelon, A., and Sacher, E. (2019). The physicochemical characterization of the Cu nanoparticle surface, and of its evolution on atmospheric exposure: Application to antimicrobial bandages for wound dressings. *Appl. Surf. Sci.* 473 (APR.15), 25–30. doi:10.1016/j.apsusc.2018.12.149
- Lorenzetti, M., Dogsa, I., Stosicki, T., Stopar, D., Kalin, M., Kobe, S., et al. (2015). The influence of surface modification on bacterial adhesion to titanium-based substrates. *ACS Appl. Mat. Interfaces* 7 (3), 1644–1651. doi:10.1021/am507148n
- Losasso, C., Belluco, S., Cibir, V., Zavagnin, P., Micetic, I., Gallochio, F., et al. (2014). Antibacterial activity of silver nanoparticles: Sensitivity of different *Salmonella* serovars. *Front. Microbiol.* 5, 227. doi:10.3389/fmicb.2014.00227
- Lozeau, L. D., Rolle, M. W., and Camesano, T. A. (2018). A QCM-D study of the concentration- and time-dependent interactions of human LL37 with model mammalian lipid bilayers. *Colloids Surfaces B Biointerfaces* 167, 229–238. doi:10.1016/j.colsurfb.2018.04.016
- Lu, M., Zhang, Z., Zhang, J., Wang, X., Qin, G., and Zhang, E. (2021a). Enhanced antibacterial activity of Ti-Cu alloy by selective acid etching. *Surf. Coatings Technol.* 421, 127478. doi:10.1016/j.surfcoat.2021.127478
- Lu, X., Wu, Z., Xu, K., Wang, X., Wang, S., Qiu, H., et al. (2021b). Multifunctional coatings of titanium implants toward promoting osseointegration and preventing infection: Recent developments. *Front. Bioeng. Biotechnol.* 9, 783816. doi:10.3389/fbioe.2021.783816
- Macpherson, A., Li, X., McCormick, P., Ren, L., Yang, K., and Sercombe, T. B. (2017). Antibacterial titanium produced using selective laser melting. *Jom* 69 (12), 2719–2724. doi:10.1007/s11837-017-2589-y
- Masse, V., Bruno, A., Bosetti, M., Biasibetti, A., Cannas, M., and Gallinaro, P. (2000). Prevention of pin track infection in external fixation with silver coated pins: Clinical and microbiological results. *J. Biomed. Mat. Res.* 53 (5), 600–604. doi:10.1002/1097-4636(200009)53:5<600::aid-jbm21>3.0.co;2-d
- Mcquillan, J. S., Infante, H. G., Stokes, E., and Shaw, A. M. (2012). Silver nanoparticle enhanced silver ion stress response in *Escherichia coli* K12. *Nanotoxicology* 6 (8), 857–866. doi:10.3109/17435390.2011.626532
- Medvedev, A. E., Molotnikov, A., Lapovok, R., Zeller, R., Berner, S., Habersetzer, P., et al. (2016). Microstructure and mechanical properties of Ti-15Zr alloy used as dental implant material. *J. Mech. Behav. Biomed. Mat.* 62, 384–398. doi:10.1016/j.jmbbm.2016.05.008
- Minandri, F., Bonchi, C., Frangipani, E., Imperi, F., and Visca, P. (2014). Promises and failures of gallium as an antibacterial agent. *Future Microbiol.* 9 (3), 379–397. doi:10.2217/fmb.14.3
- Mocanu, A., Furtos, G., Rapuntean, S., Horovitz, O., Flore, C., Garbo, C., et al. (2014). Synthesis, characterization and antimicrobial effects of composites based on multi-substituted hydroxyapatite and silver nanoparticles. *Appl. Surf. Sci.* 298, 225–235. doi:10.1016/j.apsusc.2014.01.166
- Montgomerie, Z., and Popat, K. C. (2021). Improved hemocompatibility and reduced bacterial adhesion on superhydrophobic titania nanoflower surfaces. *Material. Sci. Eng. C* 119, 111503. doi:10.1016/j.msec.2020.111503
- Morones-Ramirez, J. R., Winkler, J. A., Spina, C. S., and Collins, J. J. (2013). Silver enhances antibiotic activity against gram-negative bacteria. *Sci. Transl. Med.* 5 (190), 190ra81. doi:10.1126/scitranslmed.3006276
- Nakajo, K., Takahashi, M., Kikuchi, M., Takada, Y., Okuno, O., Sasaki, K., et al. (2014). Inhibitory effect of Ti-Ag alloy on artificial biofilm formation. *Dent. Mat. J.* 33 (3), 389–393. doi:10.4012/dmj.2013-334
- Naqvi, S. Z., Kiran, U., Ali, M. I., Jamal, A., Hameed, A., Ahmed, S., et al. (2013). Combined efficacy of biologically synthesized silver nanoparticles and different antibiotics against multidrug-resistant bacteria. *Int. J. Nanomedicine* 8, 3187–3195. doi:10.2147/ijn.s49284
- Niinomi, M. (2003). Fatigue performance and cyto-toxicity of low rigidity titanium alloy, Ti-29Nb-13Ta-4.6Zr. *Biomaterials* 24 (16), 2673–2683. doi:10.1016/s0142-9612(03)00069-3
- Norowski, P. A., Jr., and Bumgardner, J. D. (2009). Biomaterial and antibiotic strategies for peri-implantitis: A review. *J. Biomed. Mat. Res.* 88 (2), 530–543. doi:10.1002/jbm.b.31152
- Ou, K.-L., Weng, C.-C., Lin, Y.-H., and Huang, M.-S. (2017). A promising of alloying modified beta-type Titanium-Niobium implant for biomedical applications: Microstructural characteristics, *in vitro* biocompatibility and antibacterial performance. *J. Alloys Compd.* 697, 231–238. doi:10.1016/j.jallcom.2016.12.120
- Ou, P., Hao, C., Liu, J., He, R., Wang, B., and Ruan, J. (2021). Cytocompatibility of Ti-xZr alloys as dental implant materials. *J. Mat. Sci. Mat. Med.* 32 (5), 50. doi:10.1007/s10856-021-06522-w
- Pan, Y., Lin, Y., Jiang, L., Lin, H., Xu, C., Lin, D., et al. (2020). Removal of dental alloys and titanium attenuates trace metals and biological effects on liver and kidney. *Chemosphere* 243, 125205. doi:10.1016/j.chemosphere.2019.125205
- Panáček, A., Kvítek, L., Prucek, R., Pizurova, N., and Pizurová, N. d. (2006). Kolář, M., Vecěřová Silver colloid nanoparticles: Synthesis, characterization, and their antibacterial activity. *J. Phys. Chem. B* 110 (33), 16248–16253. doi:10.1021/jp063826h
- Panáček, A., Kvítek, L., Smekalova, M., Vecerova, R., Kolar, M., Roderova, M., et al. (2018). Bacterial resistance to silver nanoparticles and how to overcome it. *Nat. Nanotechnol.* 13 (1), 65–71. doi:10.1038/s41565-017-0013-y
- Panáček, A., Směkalová, M., Kilianová, M., Prucek, R., Bogdanová, K., Večeřová, R., et al. (2015). Strong and nonspecific synergistic antibacterial efficiency of antibiotics combined with silver nanoparticles at very low concentrations showing No cytotoxic effect. *Molecules* 21 (1), E26. doi:10.3390/molecules21010026
- Park, C. H., Rios, H. F., Jin, Q., Sugai, J. V., Padial-Molina, M., Taut, A. D., et al. (2012). Tissue engineering bone-ligament complexes using fiber-guiding scaffolds. *Biomaterials* 33 (1), 137–145. doi:10.1016/j.biomaterials.2011.09.057
- Park, C., Seong, Y. J., Kang, I. G., Song, E. H., Lee, H., Kim, J., et al. (2019). Enhanced osseointegration ability of poly(lactic acid) via tantalum sputtering-based plasma immersion ion implantation. *ACS Appl. Mat. Interfaces* 11 (11), 10492–10504. doi:10.1021/acsami.8b21363
- Park, Y. J., Song, Y. H., An, J. H., Song, H. J., and Anusavice, K. J. (2013). Cytocompatibility of pure metals and experimental binary titanium alloys for implant materials. *J. Dent. (Shiraz)* 41 (12), 1251–1258. doi:10.1016/j.jdent.2013.09.003
- Pashkuleva, I., Marques, A. P., Vaz, F., and Rui, L. R. (2010). Surface modification of starch based biomaterials by oxygen plasma or UV-irradiation. *J. Mat. Sci. Mat. Med.* 21 (1), 21–32. doi:10.1007/s10856-009-3831-0
- Peng, C., Zhang, S., Sun, Z., Ren, L., and Yang, K. (2018). Effect of annealing temperature on mechanical and antibacterial properties of Cu-bearing titanium alloy and its preliminary study of antibacterial mechanism. *Mater. Sci. Eng. C* 93, 495–504. doi:10.1016/j.msec.2018.08.018
- Perez-Jorge, C., Arenas, M. A., Conde, A., Hernandez-Lopez, J. M., de Damborenea, J. J., Fisher, S., et al. (2017). Bacterial and fungal biofilm formation on anodized titanium alloys with fluorine. *J. Mat. Sci. Mat. Med.* 28 (1), 8. doi:10.1007/s10856-016-5811-5
- Petrini, P., Arciola, C. R., Pezzali, I., Bozzini, S., Montanaro, L., Tanzi, M. C., et al. (2006). Antibacterial activity of zinc modified titanium oxide surface. *Int. J. Artif. Organs* 29 (4), 434–442. doi:10.1177/039139880602900414
- Prasanna, V. L., and Vijayaraghavan, R. (2015). Insight into the mechanism of antibacterial activity of ZnO – surface defects mediated reactive oxygen species even in Dark+. *Langmuir* 31 (33), 9155–9162.
- Prestat, M., and Thierry, D. (2021). Corrosion of titanium under simulated inflammation conditions: Clinical context and *in vitro* investigations. *Acta Biomater.* 136, 72–87. doi:10.1016/j.actbio.2021.10.002
- Qiao, H., Zhang, C., Dang, X., Yang, H., Huang, Y., Chen, Y., et al. (2019). Gallium loading into a polydopamine-functionalised SrTiO₃ nanotube with combined osteoinductive and antimicrobial activities. *Ceram. Int.* 45 (17), 22183–22195. doi:10.1016/j.ceramint.2019.07.240
- Quinn, J., McFadden, R., Chan, C. W., and Carson, L. (2020). Titanium for orthopedic applications: An overview of surface modification to improve biocompatibility and prevent bacterial biofilm formation. *iScience* 23 (11), 101745. doi:10.1016/j.isci.2020.101745
- Ren, L., Ma, Z., Li, M., Zhang, Y., Liu, W., Liao, Z., et al. (2014). Antibacterial properties of Ti-6Al-4V-xCu alloys. *J. Mat. Sci. Technol.* 30 (7), 699–705. doi:10.1016/j.jmst.2013.12.014
- Ren, L., Wong, H., Yan, C., Yeung, K., and Yang, K. (2015). Osteogenic ability of Cu-bearing stainless steel. *J. Biomed. Mat. Res.* 103 (7), 1433–1444. doi:10.1002/jbm.b.33318
- Rijnaarts, H. H. M., Norde, W., Lyklema, J., and Zehnder, A. J. B. (1999). DLVO and steric contributions to bacterial deposition in media of different ionic strengths. *Colloids Surfaces B Biointerfaces* 14 (1), 179–195. doi:10.1016/S0927-7765(99)00035-1

- Ríos-Castillo, A. G., Ripolles-Avila, C., and Rodríguez-Jerez, J. J. (2020). Detection of *Salmonella* Typhimurium and *Listeria monocytogenes* biofilm cells exposed to different drying and pre-enrichment times using conventional and rapid methods. *Int. J. Food Microbiol.* 324, 108611. doi:10.1016/j.jfoodmicro.2020.108611
- Rodríguez-Contreras, A., Torres, D., Rafik, B., Ortiz-Hernandez, M., Ginebra, M. P., Calero, J. A., et al. (2021). Bioactivity and antibacterial properties of calcium- and silver-doped coatings on 3D printed titanium scaffolds. *Surf. Coatings Technol.* 421, 127476. doi:10.1016/j.surfcoat.2021.127476
- Rupp, F., Scheideler, L., Olshanska, N., de Wild, M., Wieland, M., and Geis-Gerstorf, J. (2006). Enhancing surface free energy and hydrophilicity through chemical modification of microstructured titanium implant surfaces. *J. Biomed. Mat. Res. A* 76 (2), 323–334. doi:10.1002/jbm.a.30518
- Salmi, M., Paloheimo, K. S., Tuomi, J., Ingman, T., and Mäkitie, A. (2013). A digital process for additive manufacturing of occlusal splints: A clinical pilot study. *J. R. Soc. Interface* 10 (84), 20130203. doi:10.1098/rsif.2013.0203
- Sami, R., Dionysiou, D. D., Pillai, S. C., and John, K. (2018). Advances in catalytic/ photocatalytic bacterial inactivation by nano Ag and Cu coated surfaces and medical devices. *Appl. Catal. B Environ.* 240, 291–318. doi:10.1016/j.apcatb.2018.07.025
- Sanchez-Lopez, E., Gomes, D., Esteruelas, G., Bonilla, L., Lopez-Machado, A. L., Galindo, R., et al. (2020). Metal-based nanoparticles as antimicrobial agents: An overview. *Nanomater. (Basel)* 10 (2), 292. doi:10.3390/nano10020292
- Santo, C. E., Lam, E. W., Elowsky, C. G., Quaranta, D., Domaille, D. W., Chang, C. J., et al. (2011). Bacterial killing by dry metallic copper surfaces. *Appl. Environ. Microbiol.* 77, 794–802. doi:10.1128/AEM.01599-10
- Sarin, N., Singh, K. J., Kaur, H., Kaur, R., and Singh, J. (2019). Preliminary studies of the effect of doping of chromium oxide in SiO₂-CaO-P₂O₅ bioceramics for bone regeneration applications. *Spectrochimica Acta Part A Mol. Biomol. Spectrosc.* 229, 118000. doi:10.1016/j.saa.2019.118000
- Scheeren Brum, R., Apaza-Bedoya, K., Labes, L. G., Volpato, C. A. M., Pimenta, A. L., and Benfatti, C. A. M. (2021). Early biofilm formation on rough and smooth titanium specimens: A systematic review of clinical studies. *J. Oral Maxillofac. Res.* 12 (4), e1. doi:10.5037/jomr.2021.12401
- Sedelnikova, M. B., Sharkeev, Y. P., Tolkacheva, T. V., Uvarkin, P. V., Chebodaeva, V. V., Proslolov, K. A., et al. (2022). Additively manufactured porous titanium 3D-scaffolds with antibacterial Zn-Ag- calcium phosphate biocoatings. *Mater. Charact.* 186, 111782. doi:10.1016/j.matchar.2022.111782
- Shen, J., Gao, P., Han, S., Kao, R. Y. T., Wu, S., Liu, X., et al. (2020). A tailored positively-charged hydrophobic surface reduces the risk of implant associated infections. *Acta Biomater.* 114, 421–430. doi:10.1016/j.actbio.2020.07.040
- Shen, X., Al-Baadani, M. A., He, H., Cai, L., Wu, Z., Yao, L., et al. (2019). Antibacterial and osteogenesis performances of LL37-loaded titania nanopores *in vitro* and *in vivo*. *Int. J. Nanomedicine* 14, 3043–3054. doi:10.2147/IJN.S198583
- Shi, A., Cai, D., Hu, J., Zhao, X., Qin, G., Han, Y., et al. (2021). Development of a low elastic modulus and antibacterial Ti-13Nb-13Zr-5Cu titanium alloy by microstructure controlling. *Mater. Sci. Eng. C* 126, 112116. doi:10.1016/j.msec.2021.112116
- Shi, A., Zhu, C., Fu, S., Wang, R., Qin, G., Chen, D., et al. (2020). What controls the antibacterial activity of Ti-Ag alloy, Ag ion or Ti₂Ag particles? *Mater. Sci. Eng. C* 109, 110548. doi:10.1016/j.msec.2019.110548
- Shimabukuro, M. (2020). Antibacterial property and biocompatibility of silver, copper, and zinc in titanium dioxide layers incorporated by one-step micro-arc oxidation: A review. *Antibiot. (Basel)* 9 (10), 716. doi:10.3390/antibiotics9100716
- Shimabukuro, M., Hiji, A., Manaka, T., Nozaki, K., Chen, P., Ashida, M., et al. (2020). Time-transient effects of silver and copper in the porous titanium dioxide layer on antibacterial properties. *J. Funct. Biomater.* 11 (2), 44. doi:10.3390/jfb11020044
- Shimabukuro, M., Tsutsumi, Y., Nozaki, K., Chen, P., Yamada, R., Ashida, M., et al. (2019). Chemical and biological roles of zinc in a porous titanium dioxide layer formed by micro-arc oxidation. *Coatings* 9 (11), 705. doi:10.3390/coatings9110705
- Si, Y., Dong, Z., and Jiang, L. (2018). Bioinspired designs of superhydrophobic and superhydrophilic materials. *ACS Cent. Sci.* 4 (9), 1102–1112. doi:10.1021/acscentsci.8b00504
- Silver, S., Phung le, T., and Silver, G. (2006). Silver as biocides in burn and wound dressings and bacterial resistance to silver compounds. *J. Ind. Microbiol. Biotechnol.* 33 (7), 627–634. doi:10.1007/s10295-006-0139-7
- Singh, T. A., Sharma, A., Tejwan, N., Ghosh, N., Das, J., and Sil, P. C. (2021). A state of the art review on the synthesis, antibacterial, antioxidant, antidiabetic and tissue regeneration activities of zinc oxide nanoparticles. *Adv. Colloid Interface Sci.* 295, 102495. doi:10.1016/j.cis.2021.102495
- Sirelkhatim, A., Mahmud, S., Seeni, A., Kaus, N. H. M., Ann, L. C., Bakhori, S. K. M., et al. (2015). Review on zinc oxide nanoparticles: Antibacterial activity and toxicity mechanism. *Nanomicro. Lett.* 7 (3), 219–242. doi:10.1007/s40820-015-0040-x
- Sobolev, A., Valkov, A., Kossenko, A., Wolicki, I., Zinigrad, M., and Borodianskiy, K. (2019). Bioactive coating on Ti alloy with high osseointegration and antibacterial Ag nanoparticles. *ACS Appl. Mat. Interfaces* 11 (43), 39534–39544. doi:10.1021/acsami.9b13849
- Song, K., Lee, J., Choi, S. O., and Kim, J. (2019). Interaction of surface energy components between solid and liquid on wettability, and its application to textile anti-wetting finish. *Polym. (Basel)* 11 (3), 498. doi:10.3390/polym11030498
- Steinmann, S. G. (1998). Titanium-the material of choice? *Periodontol.* 2000 17, 7–21. doi:10.1111/j.1600-0757.1998.tb00119.x
- Sterritt, R. M., and Lester, J. N. (1980). Interactions of heavy metals with bacteria. *Sci. Total Environ.* 14 (1), 5–17. doi:10.1016/0048-9697(80)90122-9
- Sukumaran, P., and Eldho, K. P. (2012). Silver nanoparticles: Mechanism of antimicrobial action, synthesis, medical applications, and toxicity effects. *Int. Nano Lett.* 2 (1), 32. doi:10.1186/2228-5326-2-32
- Surmeneva, M., Lapanje, A., Chudinova, E., Ivanova, A., Koptuyug, A., Loza, K., et al. (2019). Decreased bacterial colonization of additively manufactured Ti6Al4V metallic scaffolds with immobilized silver and calcium phosphate nanoparticles. *Appl. Surf. Sci.* 480, 822–829. doi:10.1016/j.apsusc.2019.03.003
- Tahayeri, A., Morgan, M., Fugolin, A. P., Bompalaki, D., Athirasala, A., Pfeifer, C. S., et al. (2018). 3D printed versus conventionally cured provisional crown and bridge dental materials. *Dent. Mat.* 34 (2), 192–200. doi:10.1016/j.dental.2017.10.003
- Teng, X., Liu, X., Cui, Z., Zheng, Y., Chen, D.-f., Li, Z., et al. (2020). Rapid and highly effective bacteria-killing by polydopamine/IR780@MnO₂-Ti using near-infrared light. *Prog. Nat. Sci. Mater. Int.* 30 (5), 677–685. doi:10.1016/j.pnsc.2020.06.003
- Tian, M., Cai, S., Ling, L., Zuo, Y., Wang, Z., Liu, P., et al. (2022). Superhydrophilic hydroxyapatite/hydroxypropyltrimethyl ammonium chloride chitosan composite coating for enhancing the antibacterial and corrosion resistance of magnesium alloy. *Prog. Org. Coatings* 165, 106745. doi:10.1016/j.porgcoat.2022.106745
- Toledano-Serrabona, J., Gil, F. J., Camps-Font, O., Valmaseda-Castellón, E., Gay-Escoda, C., and Sánchez-Garcés, M. A. (2021). Physicochemical and biological characterization of Ti6Al4V particles obtained by implantoplasty: An *in vitro* study. Part I. *Materials* 14 (21), 6507. doi:10.3390/ma14216507
- Vidal, E., Guillem-Marti, J., Ginebra, M.-P., Combes, C., Rupérez, E., and Rodríguez, D. (2021). Multifunctional homogeneous calcium phosphate coatings: Toward antibacterial and cell adhesive titanium scaffolds. *Surf. Coatings Technol.* 405, 126557. doi:10.1016/j.surfcoat.2020.126557
- Wang, G., Jin, W., Qasim, A. M., Gao, A., Peng, X., Li, W., et al. (2017). Antibacterial effects of titanium embedded with silver nanoparticles based on electron-transfer-induced reactive oxygen species. *Biomaterials* 124, 25–34. doi:10.1016/j.biomaterials.2017.01.028
- Wang, J., Zhang, S., Sun, Z., Wang, H., Ren, L., and Yang, K. (2019). Optimization of mechanical property, antibacterial property and corrosion resistance of Ti-Cu alloy for dental implant. *J. Mater. Sci. Technol.* 35 (10), 2336–2344. doi:10.1016/j.jmst.2019.03.044
- Wang, P., Yuan, Y., Xu, K., Zhong, H., Yang, Y., Jin, S., et al. (2021). Biological applications of copper-containing materials. *Bioact. Mat.* 6 (4), 916–927. doi:10.1016/j.bioactmat.2020.09.017
- Wang, S., Ma, Z., Liao, Z., Song, J., Yang, K., and Liu, W. (2015). Study on improved tribological properties by alloying copper to CP-Ti and Ti-6Al-4V alloy. *Mater. Sci. Eng. C* 57, 123–132. doi:10.1016/j.msec.2015.07.046
- Warnes, S. L., Caves, V., and Keevil, C. W. (2012). Mechanism of copper surface toxicity in *Escherichia coli* O157:H7 and *Salmonella* involves immediate membrane depolarization followed by slower rate of DNA destruction which differs from that observed for Gram-positive bacteria. *Environ. Microbiol.* 14 (7), 1730–1743. doi:10.1111/j.1462-2920.2011.02677.x
- Wu, X. H., Liew, Y. K., Mai, C. W., and Then, Y. Y. (2021). Potential of superhydrophobic surface for blood-contacting medical devices. *Int. J. Mol. Sci.* 22 (7), 3341. doi:10.3390/ijms22073341
- Xin, C., Wang, N., Chen, Y., He, B., Zhao, Q., Chen, L., et al. (2022). Biological corrosion behaviour and antibacterial properties of Ti-Cu alloy with different Ti₂Cu morphologies for dental applications. *Mater. Des.* 215, 110540. doi:10.1016/j.matdes.2022.110540
- Xu, D., Wang, T., Lu, Z., Wang, Y., Sun, B., Wang, S., et al. (2021). Ti-6Al-4V-5Cu synthesized for antibacterial effect *in vitro* and *in vivo* via contact sterilization. *J. Mater. Sci. Technol.* 90, 133–142. doi:10.1016/j.jmst.2021.03.007

- Xu, Z., Zhao, X., Chen, X., Chen, Z., and Xia, Z. (2017). Antimicrobial effect of gallium nitrate against bacteria encountered in burn wound infections. *RSC Adv.* 7 (82), 52266–52273. doi:10.1039/c7ra10265h
- Yan, X., He, B., Liu, L., Qu, G., Shi, J., Hu, L., et al. (2018). Antibacterial mechanism of silver nanoparticles in *Pseudomonas aeruginosa*: Proteomics approach. *Metallomics* 10 (4), 557–564. doi:10.1039/c7mt00328e
- Zadpoor, A. A. (2019). Additively manufactured porous metallic biomaterials. *J. Mat. Chem. B* 7 (26), 4088–4117. doi:10.1039/c9tb00420c
- Zhang, E., Wang, X., Chen, M., and Hou, B. (2016a). Effect of the existing form of Cu element on the mechanical properties, bio-corrosion and antibacterial properties of Ti-Cu alloys for biomedical application. *Mater. Sci. Eng. C* 69, 1210–1221. doi:10.1016/j.msec.2016.08.033
- Zhang, E., Zhao, X., Hu, J., Wang, R., Fu, S., and Qin, G. (2021a). Antibacterial metals and alloys for potential biomedical implants. *Bioact. Mat.* 6 (8), 2569–2612. doi:10.1016/j.bioactmat.2021.01.030
- Zhang, L., Gao, Q., and Han, Y. (2016b). Zn and Ag Co-doped anti-microbial TiO₂ coatings on Ti by micro-arc oxidation. *J. Mat. Sci. Technol.* 32 (9), 919–924. doi:10.1016/j.jmst.2016.01.008
- Zhang, T., Wei, Q., Zhou, H., Zhou, W., Fan, D., Lin, X., et al. (2020). Sustainable release of vancomycin from micro-arc oxidised 3D-printed porous Ti6Al4V for treating methicillin-resistant *Staphylococcus aureus* bone infection and enhancing osteogenesis in a rabbit tibia osteomyelitis model. *Biomater. Sci.* 8 (11), 3106–3115. doi:10.1039/c9bm01968e
- Zhang, W., Zhang, S., Liu, H., Ren, L., Wang, Q., and Zhang, Y. (2021b). Effects of surface roughening on antibacterial and osteogenic properties of Ti-Cu alloys with different Cu contents. *J. Mat. Sci. Technol.* 88, 158–167. doi:10.1016/j.jmst.2021.01.067
- Zhao, B. H., Zhang, W., Wang, D. N., Feng, W., Liu, Y., Lin, Z., et al. (2013). Effect of Zn content on cytoactivity and bacteriostasis of micro-arc oxidation coatings on pure titanium. *Surf. Coatings Technol.* 228, S428–S432. doi:10.1016/j.surfcoat.2012.05.037
- Zhao, L., Si, J., Wei, Y., Li, S., Jiang, Y., Zhou, R., et al. (2018). Toxicity of porcelain-fused-to-metal substrate to zebrafish (*Danio rerio*) embryos and larvae. *Life Sci.* 203, 66–71. doi:10.1016/j.lfs.2018.04.019
- Zhao, Q., Yi, L., Hu, A., Jiang, L., Hong, L., and Dong, J. (2019). Antibacterial and osteogenic activity of a multifunctional microporous coating codoped with Mg, Cu and F on titanium. *J. Mat. Chem. B* 7 (14), 2284–2299. doi:10.1039/c8tb03377c
- Zheng, J., Chen, X., Jiang, W., Zhang, S., Chen, M., and Yang, C. (2019). An innovative total temporomandibular joint prosthesis with customized design and 3D printing additive fabrication: A prospective clinical study. *J. Transl. Med.* 17 (1), 4. doi:10.1186/s12967-018-1759-1
- Zheng, Y. F., Zhang, B. B., Wang, B. L., Wang, Y. B., Li, L., Yang, Q. B., et al. (2011). Introduction of antibacterial function into biomedical TiNi shape memory alloy by the addition of element Ag. *Acta Biomater.* 7 (6), 2758–2767. doi:10.1016/j.actbio.2011.02.010
- Zhou, J., Li, B., and Han, Y. (2018). F-doped TiO₂ microporous coating on titanium with enhanced antibacterial and osteogenic activities. *Sci. Rep.* 8 (1), 17858. doi:10.1038/s41598-018-35875-6
- Zhu, M., Liu, X., Tan, L., Cui, Z., Liang, Y., Li, Z., et al. (2020). Photo-responsive chitosan/Ag/MoS₂ for rapid bacteria-killing. *J. Hazard. Mat.* 383, 121122. doi:10.1016/j.jhazmat.2019.121122
- Zhuang, Y., Ren, L., Zhang, S., Wei, X., Yang, K., and Dai, K. (2021). Antibacterial effect of a copper-containing titanium alloy against implant-associated infection induced by methicillin-resistant *Staphylococcus aureus*. *Acta Biomater.* 119, 472–484. doi:10.1016/j.actbio.2020.10.026



OPEN ACCESS

EDITED BY

Yanjin Lu,
Fujian Institute of Research on the
Structure of Matter, Chinese Academy
of Sciences (CAS), China

REVIEWED BY

Esther Potier,
Centre National de la Recherche
Scientifique (CNRS), France
Mehdi Dadashpour,
Semnan University of Medical
Sciences, Iran
Nicola Green,
The University of Sheffield,
United Kingdom

*CORRESPONDENCE

Elaheh Ferdosi-Shahandashti,
elaheh.ferdosi@yahoo.com,
e.ferdosi@mubabol.ac.ir
Ehsan Seyedjafari,
seyedjafari@ut.ac.ir

SPECIALTY SECTION

This article was submitted to
Biomaterials,
a section of the journal
Frontiers in Bioengineering and
Biotechnology

RECEIVED 27 July 2022

ACCEPTED 26 September 2022

PUBLISHED 17 October 2022

CITATION

Shariati S, Seyedjafari E, Mahdavi FS,
Maali A and Ferdosi-Shahandashti E
(2022), NiFe₂O₄/ZnO-coated Poly(L-
Lactide) nanofibrous scaffold enhances
osteogenic differentiation of human
mesenchymal stem cells.
Front. Bioeng. Biotechnol. 10:1005028.
doi: 10.3389/fbioe.2022.1005028

COPYRIGHT

© 2022 Shariati, Seyedjafari, Mahdavi,
Maali and Ferdosi-Shahandashti. This is
an open-access article distributed
under the terms of the [Creative
Commons Attribution License \(CC BY\)](#).
The use, distribution or reproduction in
other forums is permitted, provided the
original author(s) and the copyright
owner(s) are credited and that the
original publication in this journal is
cited, in accordance with accepted
academic practice. No use, distribution
or reproduction is permitted which does
not comply with these terms.

NiFe₂O₄/ZnO-coated Poly(L-Lactide) nanofibrous scaffold enhances osteogenic differentiation of human mesenchymal stem cells

Shiva Shariati^{1,2,3}, Ehsan Seyedjafari^{4*}, Fatemeh Sadat Mahdavi⁴,
Amirhosein Maali^{5,6} and Elaheh Ferdosi-Shahandashti^{1,7*}

¹Department of Medical Biotechnology, School of Medicine, Babol University of Medical Sciences, Babol, Iran, ²Department of Medical Biotechnology, School of Advanced Medical Sciences, Golestan University of Medical Sciences, Golestan, Iran, ³Student Research Committee, Babol University of Medical Sciences, Babol, Iran, ⁴Department of Biotechnology, College of Sciences, University of Tehran, Tehran, Iran, ⁵Department of Immunology, Pasteur Institute of Iran, Tehran, Iran, ⁶Department of Medical Biotechnology, Faculty of Allied Medicine, Qazvin University of Medical Sciences, Qazvin, Iran, ⁷Cellular and Molecular Biology Research Center, Health Research Institute, Babol University of Medical Sciences, Babol, Iran

Background: A combination of bioceramics and polymeric materials has attracted the research community's interest in bone tissue engineering. These composites are essential to support cell attachment, proliferation, and osteogenesis differentiation, which are vital as a classic strategy in bone tissue engineering. In this study, NiFe₂O₄/ZnO-coated poly L-Lactide (PLLA) was employed as a scaffold to evaluate the osteogenic differentiation capability of human adipose tissue derived mesenchymal stem cells (hAMSCs).

Material and methods: The electrospun PLLA nanofibers were fabricated, coated with nanocomposite (NiFe₂O₄/ZnO), and evaluated by the water contact angle (WCA), tensile test, attenuated total reflectance fourier-transform infrared (ATR-FTIR) and scanning electron microscopy (SEM). Then, the osteogenic differentiation potential of hAMSCs was assessed using NiFe₂O₄/ZnO-coated PLLA compared to tissue culture plastic (TCP) and a simple scaffold (PLLA) *in vitro* conditions.

Results: The adhesion, proliferation, and differentiation of hAMSCs were supported by the mechanical and biological properties of the NiFe₂O₄/

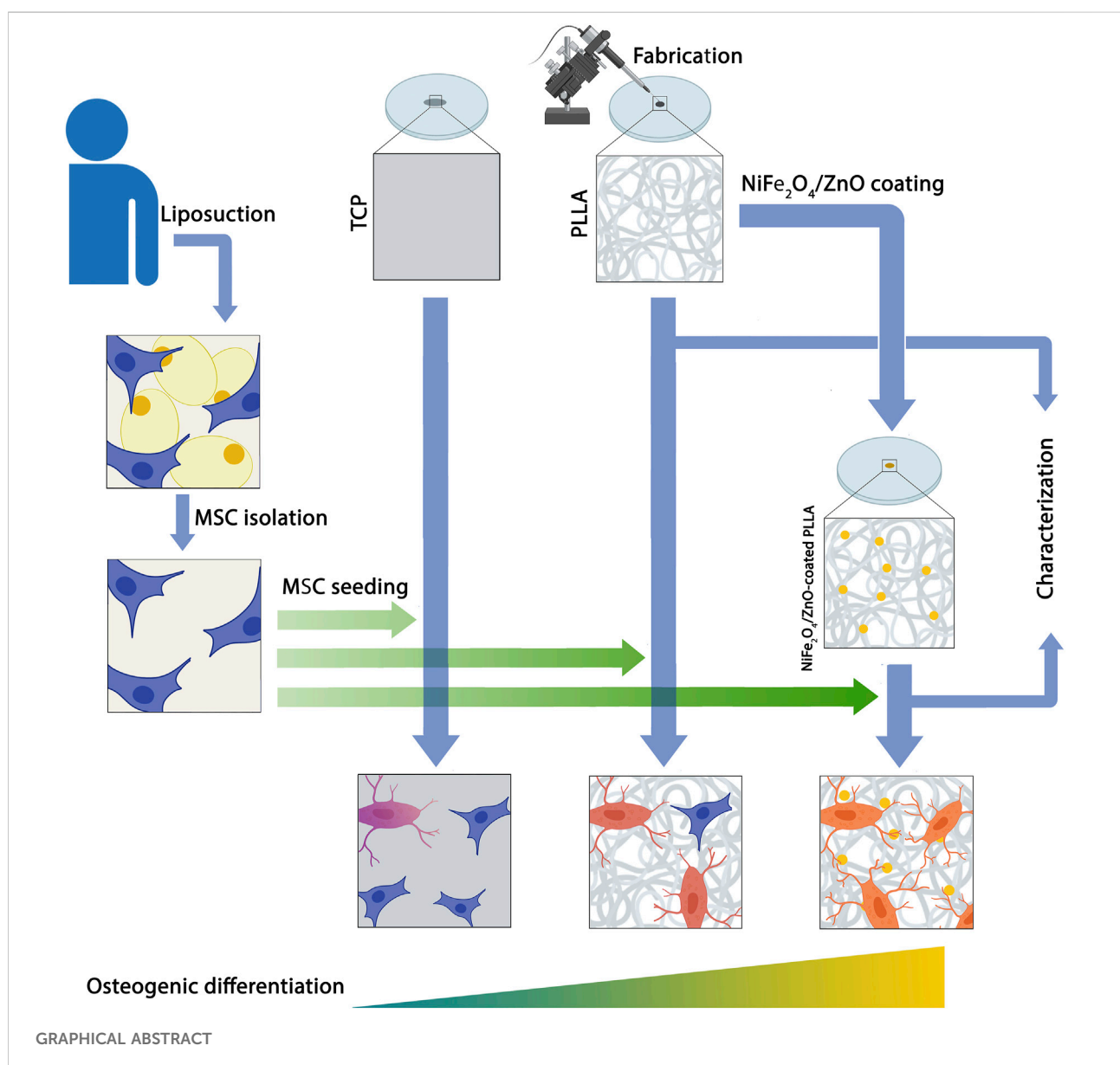
Abbreviations: ATR-FTIR, Attenuated Total Reflectance Fourier-Transform Infrared; ALP, Alkaline phosphatase; ARS, Alizarin-red staining; BGP, Bone growth protein; BMP9, Bone morphogenic protein-9; BTE, Bone tissue engineering; DAPI, 4',6-Diamidino-2-phenylindole dihydrochloride; diH₂O, deionized water; DMF, Dimethylformamide; DMEM, Dulbecco's Modified Eagle's Medium; DMSO, Dimethyl sulfoxide; ECM, Extracellular matrix; FBS, Fetal bovine serum; H, Hour; hAMSCs, human Adipose tissue-derived Mesenchymal Stem Cells; HG-DMEM, High glucose- Dulbecco's Modified Eagle's Medium; HP, H₂O₂ Plasma; EtO, Ethylene Oxide; MTT(3-(4,5-Dimethylthiazol-2-yl)-2,5-diphenyl Tetrazolium Bromide); PLLA, Poly L-Lactide; PBS, Phosphate-buffered saline; Pen-strep, penicillin and streptomycin; RIPA, Radioimmunoprecipitation assay; ROS, Reactive oxygen species; Runx2, Runt-related transcription factor 2; SEM, Scanning Electron Microscopy; OD, Optical density; TCP, Tissue culture plastic; UV, Ultraviolet light; WCA, Water contact angle; ZnO, Zinc oxide.

ZnO-coated PLLA scaffold, according to SEM and 4',6-Diamidino-2-phenylindole dihydrochloride (DAPI) staining patterns. During bone differentiation, Alkaline phosphatase (ALP) enzyme activity, biomineralization, calcium content, and osteogenic gene expression (ALP, Osteonectin, Osteocalcin, Collagen type I, and Runx2) were higher on NiFe₂O₄/ZnO-coated PLLA scaffold than on PLLA scaffold and TCP.

Conclusion: Based on our results, the osteogenic differentiation of hAMSCs on the improved biological scaffold (PLLA coated with NiFe₂O₄/ZnO) could accelerate due to the stimulating effect of this nanocomposite.

KEYWORDS

nanocomposites, adipose tissue-derived mesenchymal stem cell, poly-L-lactide, osteogenesis, cell differentiation



1 Highlights

- Bone tissue engineering is a dynamic, regenerative medicine procedure that aims to provide structural support for cell development, proliferation, and adhesion, as well as growth factors or other active substances.
- One scaffold frequently employed for this purpose is Poly (L-lactide) or (PLLA), an aliphatic thermoplastic polyester.
- It is assumed that magnetic nanostructures could bind to cell surfaces, regulating cell function and increasing bone cells activity, resulting in bone tissue regeneration.
- In this study, a NiFe₂O₄/ZnO-coated PLLA scaffold was used to assess the osteogenic differentiation capability of human adipose tissue-derived Mesenchymal Stem Cells (hAMSCs) with the aim of bone tissue regeneration *in vivo* condition.
- The differentiation of hAMSC into the osteogenic lineage demonstrates that NiFe₂O₄/ZnO coated PLLA could provide a proper support role by mimicking the ECM architecture and culminating in osteoblast adhesion, proliferation, differentiation, and maturation.
- It is thought that NiFe₂O₄/ZnO-coated PLLA could have favorable magnetic and mechanical properties and serves as a proper platform for directing connections and cellular activity toward the osteogenic lineage

2 Introduction

Natural bone is a dynamic and multifaceted organ with the hierarchical and architectural arrangement of nanoscale to microscopic dimensions that performs fundamental biological functions such as body mobility, organ protection, and regulation of homeostasis of the hematopoietic cell, etc., (Ye et al., 2020; Zhang et al., 2020). Repairing and regenerating bone tissue depends on the injury's extent, which can adequately repair slight injuries, such as microcracks and some minor fractures. Nevertheless, bone fractures that exceed the threshold (more than 2 cm) are beyond the capacity of this tissue, which can be induced by trauma, congenital disabilities, tumor resection, and other causes (Koons et al., 2020). Depending on the anatomical location, it cannot be entirely and permanently repaired without clinical intervention (Yousefi et al., 2016; Koons et al., 2020).

Bone tissue engineering (BTE) is a dynamic and regenerative medicine process that establishes structural support for cell growth, proliferation, and adhesion through growth factors or active substances. BTE is critical for accelerating differentiation and extracellular matrix (ECM) development. It can potentially integrate and

regenerate a specific functional tissue compared to conventional approaches (Baino et al., 2015; Kumar et al., 2018; Porgham Daryasari et al., 2019). Scaffolds provide surfaces that promote stem cell cohesion, survival, migration, proliferation, and differentiation. Also, their porous structure facilitates the formation of arteries, angiogenesis, and a bone-like environment, which results in bone tissue regeneration by mimicking the configuration of ECM (Yousefi et al., 2016; Kumar et al., 2018).

PLLA, an aliphatic thermoplastic polyester, is a frequently employed scaffold for mimicking the bone ECM structure (Kumar et al., 2018). This hydrophilic polymer with electrospinning fabrication is a cost-effective method that is widely used in tissue engineering (Tavangar et al., 2018; Porgham Daryasari et al., 2019). PLLA nanofibers with a high surface-to-volume ratio and a high porosity mimic the role of the bone ECM, promoting hydroxyapatite production, mineral deposition, and optimum vascular integration. Additionally, its strength and stiffness provide a proper framework for developing osteogenic progenitor cells and bone conduction (Liu et al., 2016; Tavangar et al., 2018). Despite their benefits in tissue engineering, Pure PLLA stereoisomers have low biologic activity and surface characteristics. Mixing nanoparticles with a polymer matrix to replicate the architecture of bone nanocomposites makes it possible to increase their mechanical and biological properties (Kumar et al., 2018; Tavangar et al., 2018).

Recent research indicates that the magnetic field generated by nanostructures that have magnetic properties promotes mineralization, cohesion, proliferation, and cell differentiation (Fan et al., 2020). Along with influencing biomineralization behavior during the early stages of gene expression and protein synthesis, the magnetic field affects the structure and crystallization of biomineral products. Also, it alters the spatial structure of proteins in the cytoskeleton. Thus, magnetic nanostructures can adhere to cell surfaces, regulating cell function and increasing bone cell activity, resulting in tissue regeneration. Magnetic nanoparticles primarily comprise cobalt, iron, or nickel that can produce a magnetic field directly and indirectly (Peng et al., 2019). Zinc is a critical nutrient that plays a role in growth, calcium metabolism, ALP activity, and bone metabolism. The absence or inadequacy of these chemical agents retards bone development (Ramezanifard et al., 2016; Laurenti and Cauda, 2017; Peng et al., 2019). Zinc oxide (ZnO) nanostructures have been studied for their potential to enhance cell adhesion, proliferation, and differentiation. Additionally, ZnO characteristics uniquely function in cellular drift, the opening of Ca²⁺ channels in the plasma membrane of osteoblast cells, intracellular calcium transfer, proliferation, and the effect of reactive oxygen species (ROS) on blood vessel development (Laurenti and Cauda, 2017).

In this study, to improve the structure and performance of the scaffold, NiFe₂O₄/ZnO-coated PLLA was used as a scaffold to evaluate the potential osteogenic differentiation of hAMSCs, aimed at the regeneration of bone tissue in *in-vivo* conditions.

3 Materials and methods

3.1 Scaffold synthesis

3.1.1 Fabrication of poly l-lactide scaffold

The electrospinning (Nanoazma, ESI-I, Iran) process was used to fabricate PLLA nanofibers. Briefly, 12% (wt/vol) solution of PLLA (Sigma-Aldrich, MO, United States) in chloroform (Merck, Germany) and dimethylformamide (DMF; Merck, Germany) was drawn into a 5 ml syringe with a 21-gauge needle. Two nozzles were set at an injection rate of 1 ml/h at a distance of 15 cm from the collector. Then, nanofibers were collected on a cylindrical collector with a rotational speed of 600rpm and voltage of 20 kV. Finally, the sheet with a relative thickness of about 200 μ m was vacuumed to evaporate the remaining chloroform solution completely.

3.1.2 Scaffolds surface modification

A Plasma quartz reactor (Diener Electronics, Ebhausen, Germany) was applied to induce hydrophilicity in a hydrophobic PLLA scaffold using a low-frequency plasma generator at 90 GHz. The scaffold was put in the reactor chamber, and a vacuum was generated using a dual trap vacuum pump before performing a glow discharge. The PLLA scaffold was subjected to pure oxygen at 0.4 mBar pressure and a flow rate of 10 ml/min for 3 min.

3.1.3 Water contact angle

WCA was determined before and after plasma treatment using a goniometer (GO EDMUND Optic, United States) to evaluate scaffold surface hydrophilicity. PLLA scaffold before and after plasma treatment received one drop of deionized water at room temperature. The images were taken after 10 s, and the contact angle was measured by ImageJ software (NIH United States).

3.1.4. Coating nanofibers with nanocomposite

The NiFe₂O₄/ZnO nanocomposite was synthesized using the solid-state method. Briefly, the thiourea was extensively mixed with ZnO and nickel ferrite nanoparticles and then calcined at an 800°C (Yeganeh et al., 2020). After preparation, the nanoparticle powder was dissolved in deionized water at a concentration of (0.1% wt/vol). Then, the solution was placed in an ultrasonic bath for 30 min at 37°C to disperse. The plasma-treated scaffold was immersed overnight in a nanocomposite solution, rinsed twice with deionized water, and dried in a vacuum.

3.2 Scaffold characterization

3.2.1 Attenuated total reflectance fourier-transform infrared spectroscopy

The vibrational spectrum of NiFe₂O₄/ZnO-coated PLLA and PLLA scaffolds were determined using ATR-FTIR spectroscopy (PerkinElmer-Frontier, United States) with a reading range of 400–4000 cm⁻¹ that used a DTGS detector and diamond ATR crystal. PerkinElmer Spectrum version 10.03.06 (PerkinElmer-Frontier, United States) was used to analyze the data.

3.2.2 Tensile test

The SANTAM (STM-20, Iran) device was used to evaluate the mechanical properties of electrospun scaffolds before and after plasma treatment with nanocomposite loading. The scaffolds were carved into a rectangular shape with dimensions of 1 cm \times 4 cm, a gauge length of 2 cm, and an 80 μ m thickness. Then, it was inserted into the device at room temperature at 5 mm/min crosshead speed. The calculation of tensile was determined by SANTAM machine controller software (STM- 20, Iran).

3.2.3 Scanning electron microscopy

The microstructure of NiFe₂O₄/ZnO coated PLLA and the morphology of a PLLA scaffold surface was analyzed. The cell-free scaffolds do not require preparation. Both scaffolds were mounted to an aluminum sample holder with conductive adhesive tape and coated with gold using a KYKY SBC12 sputtering machine at 1 kV and 10 mA for 120 s. Samples were visualized by SEM (AIS2700, SERON technology, South Korea) at 20 kV. The scale of selected SEM images was set to analyze the diameters, then 60 fibers and 10 particles were chosen randomly, and the diameters were measured with ImageJ software (NIH, United States).

3.3 Isolation of human adipose tissue-derived mesenchymal stem cell

Adipose tissue was taken from a patient undergoing liposuction surgery in Omid Hospital, Amol, Iran, according to the guidelines of the Medical Ethics Committee, Babol University of Medical Sciences and Health Services (approval code: IR. MUBABOL.HRI. REC 1398.137). Written informed consent was obtained from the next of kin of a 36-year-old man participant for the publication of any potentially identifiable data included in this article. The tissue was transported to the lab under sterile conditions using a solution containing Dulbecco's Modified Eagle's Medium (DMEM, Gibco) and penicillin/streptomycin (Pen-strep) (Gibco, United States). Then the tissue was rinsed multiple times with sterile phosphate-buffered saline (PBS, Zistmavad, Iran) containing Pen-strep to eliminate any remaining blood. After discarding the PBS, the

adipose tissue was incubated with 0.1% collagenase type I (Gibco, United States) at 37°C for 1 h (hour) in a shaker incubator and then centrifuged at 1200 g for 10 min. The supernatant was discarded, and the pellet was suspended in 10 ml of high glucose DMEM (HG-DMEM, Gibco) supplemented with 1% Pen-strep and 10% fetal bovine serum (FBS, Gibco, United States). Then transferred to a T75 cell culture flask; incubated at 37°C and CO₂ concentration of 5%. The leftover blood cells were eliminated after 24 h by changing the medium. The culture medium was replaced with fresh medium every 3 days. In this article, basal media refers to HG-DMEM without supplementary material, culture media refers to HG-DMEM with 10% FBS, and osteogenic media (HG-DMEM, which contains 10% FBS, Pen-strep, 10 mM β -glycerophosphate (Sigma-Aldrich, United States), 0.2 mM ascorbic acid (Sigma-Aldrich, United States), and 0.1 μ M dexamethasone (Sigma-Aldrich, United States).

3.4 Human adipose tissue-derived mesenchymal stem cell characterization

In the second passage, the hAMSCs surface markers, i.e., CD90, CD105, CD45, and CD34, were characterized by flow cytometry. The cells were detached from the T25 culture flask with trypsin-EDTA (Gibco, United States) and centrifuged at 1500 rpm for 5 min. Then the final volume of cell sediment reached 1 ml with PBS. 5 μ l of anti-CD90-APC (BioLegend, United States), anti-CD45-FITC (BD Bioscience, United Kingdom), anti-CD105-PE (BioLegend, United States), anti-CD34-PE (IQ Product, United States) were added to 100 μ l of cell suspension of each flow cytometry tube and incubated for 30 min at 4°C. Afterward, 500 μ l of PBS was added to each tube and centrifuged at 1500 rpm for 5 min. Finally, 250 μ l PBS was added to each tube, and cell suspensions were read by BD FACS Calibur (BD Biosciences, United States) and analyzed with Flowjo software version 10.5.3.

3.5 Cell culture, adhesion, and differentiation

The effect of PLLA and NiFe₂O₄/ZnO coated PLLA scaffolds on cell adhesion, and osteogenic differentiation was examined. On the fourth day after plasma treatment, both Scaffolds were punched to a diameter of 16 mm and subjected to ultraviolet light (UV) for 20 min, then immersed in 70% alcohol for 2 h and rinsed 3 times with sterile PBS to remove any traces of alcohol, then incubated overnight with FBS to enhance cell adhesion. To determine the adherence and proliferation capacity, 2×10^4 hAMSCs were suspended in 100 μ l of culture media and seeded on PLLA and NiFe₂O₄/ZnO-coated PLLA; 1 h after seeding the cells, the culture media was added to fill each well

to the specified volume. After 7 days of culture, the medium was removed and rinsed with PBS. Then, 2.5% Glutaraldehyde (Merck, Germany) in distilled water was added to each well to cover the surface and left over for 1 h. Then scaffolds were dehydrated with 50%–90% methanol solution series left overnight under laminar flow at room temperature to dry and kept in a desiccator.

Additionally, to assess hAMSC differentiation, 2×10^4 cells were seeded in PLLA and NiFe₂O₄/ZnO-coated on PLLA. After 24 h, the culture medium was replaced with an osteogenic medium (described above), and every 3 days were changed. On day 21 of differentiation, cells were fixed according to the above procedure; then scaffolds were mounted to an aluminum sample holder with conductive adhesive tape and coated with gold using a KYKY SBC12 sputtering machine at 1 kV and 10 mA for 120 s. Samples were visualized using an SEM (AIS2700, SERON technology, South Korea) at 20 kV.

3.6 Bioassays

3.6.1 MTT assay

On days 1, 4, and 7, the metabolic activity of hAMSCs on PLLA, NiFe₂O₄/ZnO-coated PLLA, and TCP scaffolds were used to examine. 2×10^4 cells were seeded with a culture medium for this purpose. After discarding the culture media, basal media (described above) containing 50 μ l of MTT solution (3-(4,5-Dimethylthiazol-2-yl)-2,5-diphenyl Tetrazolium Bromide) (Sigma-Aldrich, United States) (5 mg/ml MTT in HG-DMEM) was added to each well and incubated at 37°C for 3.5 h. Then, dark-blue intracellular formazan crystals were dissolved in 200 μ l dimethyl sulfoxide (DMSO; Sigma-Aldrich, United States) and vortexed for 8 min. The optical density (OD) was determined using a microplate reader (Bio-Tek Instruments, Winooski, VT, United States) at a wavelength of 570 nm.

3.6.2 DAPI staining

DAPI staining was used to determine cell adhesion. For this aim, 2×10^4 hAMSCs were seeded on NiFe₂O₄/ZnO-coated PLLA, PLLA, and TCP and cultured in a culture medium, then incubated at 37 °C and 5% CO₂. After 7 days of incubation, each group was washed twice with PBS and incubated with 2.5% Glutaraldehyde for 1 h. Then glutaraldehyde was removed and washed with PBS. 50 μ l DAPI solution (5 μ g/ml in diH₂O; Sigma-Aldrich, Germany) was added to each well of groups and incubated for 5 min. To remove excess and unbounded DAPI stains, they were washed with PBS. The plate was covered and left in the dark, and images were captured using an Immunofluorescence Microscope (Labomed, United States). The scale and threshold of the photos were set and processed. Then, the number of stained cells was determined by analyzing the particle option *via* ImageJ software (NIH, United States).

TABLE 1 Primers used in Real-time PCR.

Gene name	Primer sequences	Product size (bp)	
<i>β-2-Micro globulin (β2M)</i>	Forward	5'-TGGAAAGAAGATACCAAATATCGA-3'	201
	Reverse	5'-GATGATTCAGAGCTCCATAGAGCT-3'	
<i>Osteonectin</i>	Forward	5'-AGGTATCTGTGGGAGCTAATC-3'	224
	Reverse	5'-ATTGCTGCACACCTTCTC-3'	
<i>Osteocalcin</i>	Forward	5'-GCAAAGGTGCAGCCTTTGTG-3'	86
	Reverse	5'-GGCTCCCAGCCATTGATACAG-3'	
<i>Alkaline phosphatase (ALP)</i>	Forward	5'-GCACCTGCCTTACTAACTC-3'	162
	Reverse	5'-AGACACCCATCCCATCTC-3'	
<i>Collagen I</i>	Forward	5'-TGGAGCAAGAGGCGAGAG-3'	121
	Reverse	5'-CACCAGCATCACCCTTAGC-3'	
<i>Runx2</i>	Forward Reverse	5'-GCCTTCAAGGTGGTAGCCC-3' 5'-CGTTACCCGCCATGACAGTA-3'	86

3.6.3 Alkaline phosphatase activity assay

On days 7, 14, and 21, 2×10^4 hAMSCs were seeded on PLLA, NiFe₂O₄/ZnO-coated PLLA, and TCP in the presence of osteogenic media (described above) to determine ALP enzyme activity. The culture media was removed on the appointed days, then rinsed with PBS. After adding 200 μl of radioimmunoprecipitation assay (RIPA) lysis buffer to each well, gently agitated, and cell lysate was centrifuged at 1500 g for 15 min at 4°C. After centrifugation, the supernatant containing total proteins was collected. ALP activity was determined using a procedure provided with an ALP assay kit (Pars Azmoon, Iran). A microplate reader (Bio-Tek Instruments, Winooski, VT, United States) was used to determine the fluorescence intensity at 405 nm. Finally, the enzyme activity (IU/L) was adjusted to the total protein concentration (mg/dl).

3.6.4 Calcium content assay

On days 7, 14, and 21, in the presence of the osteogenic media (described above), the calcium content of hAMSC was determined using the O-cresolphthalein method on PLLA, NiFe₂O₄/ZnO-coated PLLA, and TCP. The medium was removed, and each well was rinsed with PBS for calcium extraction. Then, 0.6 N HCL (Merck, Germany) was added to each well and incubated for 1 h by mild shaking at 4°C. Then, the reagent buffer of the calcium content assay kit (Pars Azmoon, Iran) was added and allowed for incubation. A microplate reader (Bio-Tek Instruments, Winooski, VT, United States) read the OD of samples at 570 nm. The standard curve was generated using repeated dilutions of 0.1 M calcium chloride solution.

3.6.5 Alizarin-red staining

To assess mineral sediments formed as a result of differentiation, on days 7, 14, and 21, 2×10^4 cells were seeded on PLLA, NiFe₂O₄/ZnO-coated PLLA, and TCP scaffolds in the presence of osteogenic media (explained

above). After removing the culture media and washing with PBS, the cells were fixed with the same procedure described above. Each well received 200 μl Alizarin red (Sigma-Aldrich) solution (2 mM in deionized water (diH₂O) and incubated at room temperature for 15 min by mild agitation, then rinsed with PBS several times until the color was removed entirely and only a purple halo remained. Ultimately, the photos were captured using a stereomicroscope (Olympus, Japan).

3.7 Quantitative-Real-time PCR

The real-time PCR was used to determine the mRNA expression levels of *Osteonectin*, *Osteocalcin*, *ALP*, *Collagen type I*, and Runt-related transcription factor 2 (*Runx2*) genes on days 7, 14, and 21 of the culture on scaffolds. The primer sequences used for qRT-PCR are shown in [table 1](#). First, RNA was isolated from hAMSCs cultured on TCP, PLLA, and NiFe₂O₄/ZnO-coated PLLA scaffolds in osteogenic media using the RNA extraction kit (MaxSpin, Maxcell, Iran). To synthesize cDNA, 5 μg of RNA was mixed with 2 μl of BON-RTmix primer (1 mM) (Bonbiotech, IRAN), 11 μl of DEPS water, 1 μl of BON-RT enzyme (5U/ml; Bonbiotech, IRAN), 3 μl of dNTP mix (Bonbiotech, Iran), and 6 μl RT buffer (Bonbiotech, Iran). The samples were incubated in a thermocycler (Bio-Rad) for 10 min at 25°C, 15 min at 37°C, 45 min at 42°C, and 10 min at 72°C, respectively. Then, 6.5 μl of master mix SYBR green 2x (BON-QPCR, Bonbiotech, Iran), 1 μl of specific F and R primers, 1 μl of cDNA, and 0.25 μl ROX Reference Dye were combined and incubated for 2 min at 95°C, followed by 5 s at 95°C and 30 s at 60°C for 40 cycles on an ABI Applied Biosystems™ thermal cycler (Thermo Fisher, United States). The relative expression of genes was determined by the $2^{-\Delta\Delta CT}$ method. The *B2-microglobulin* gene was used as the internal control. Also, Rest software 2009 was used for analyzing the data.

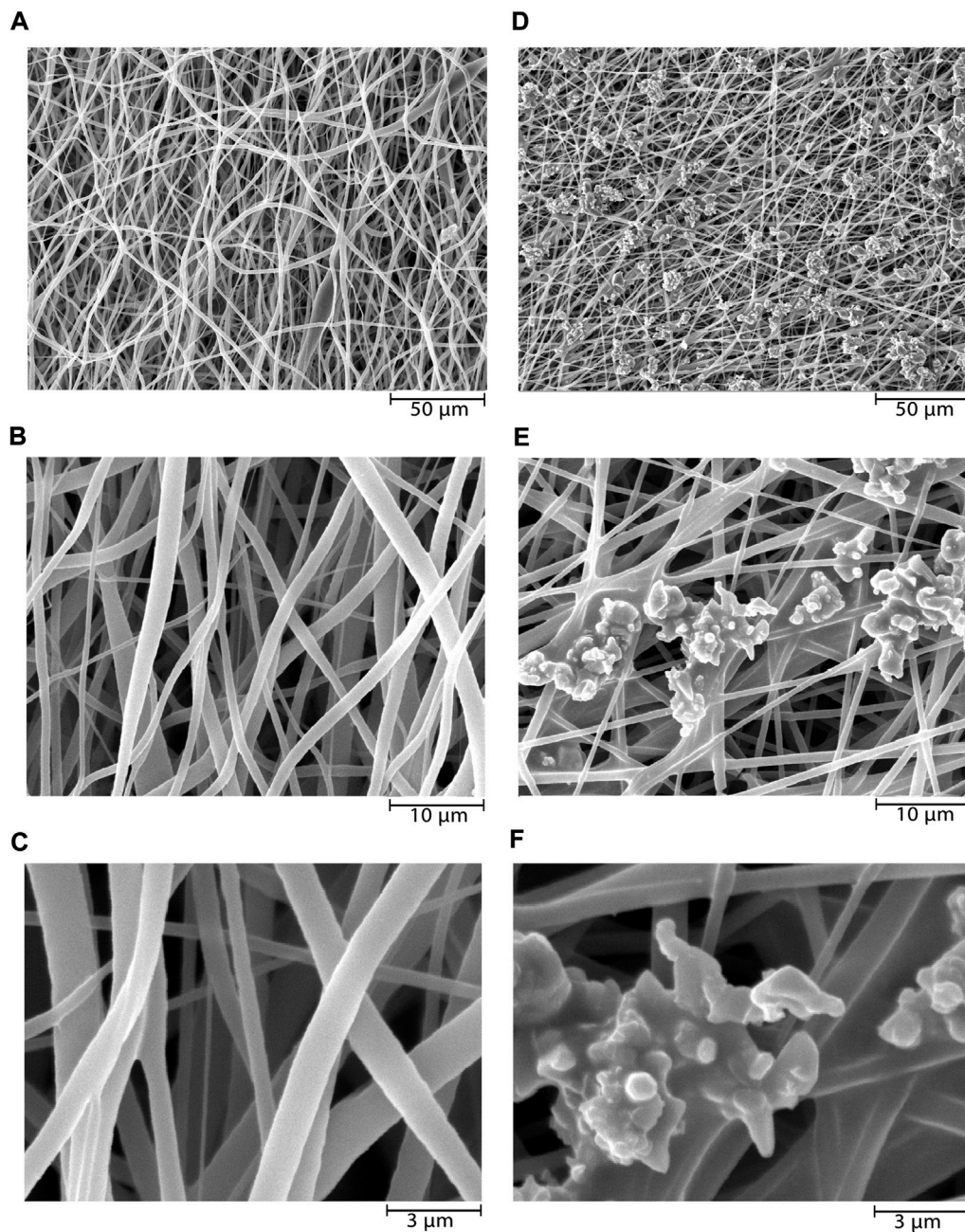


FIGURE 1

SEM microstructure of electrospun PLLA nanofibers before and after nanocomposites deposition. PLLA nanofibers at x1000 (A), x5000 (B), and x15,000 (C) magnifications, and NiFe₂O₄/ZnO-coated PLLA nanofibers at x1000 (D), x5000 (E), and x15,000 (F) magnifications.

3.8 Statistical analysis

All experiments were performed in triplicate, and mechanical experiments were performed with $n = 6$. Obtained data were shown as mean \pm SD. The MTT assay, ALP enzyme, calcium content, and gene expression were analyzed *via* two-way analysis of variance (ANOVA), and

DAPI staining was analyzed *via* one-way ANOVA. Also, Tukey's multiple comparisons tests were used for means that are significantly different from each other in all analyses by GraphPad Prism software version 8.3.1 and Microsoft Excel software version 16.11.1. Also, the p -value was used to show statistical significance ($p < 0.05$ was considered significant).

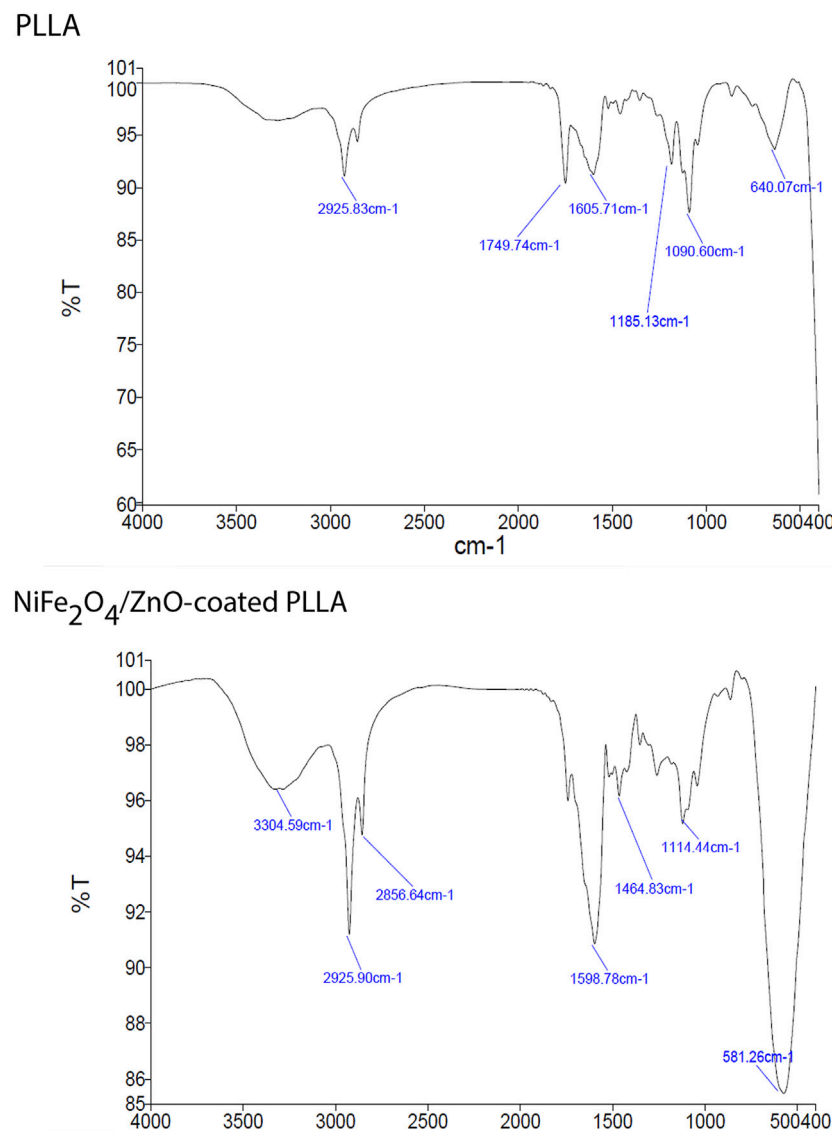


FIGURE 2
ATR-FTIR spectra of PLLA and NiFe₂O₄/ZnO-coated PLLA scaffolds.

4 Result

4.1 Morphology and microstructure of electrospun nanofibers

In this study, SEM micrographs of nanofibers morphology depict entirely random and nearly homogenous fibers which have lacked a bead and porous cavities (Figure 1A–C). After coating the NiFe₂O₄/ZnO on the PLLA scaffold with a mean size of $83 \text{ nm} \pm 9.01$, a nearly homogeneous distribution of nanocomposite was found on the surfaces. However, it may have an aggregation number. The nanocomposite had a uniform aggregated spherical morphology with some voids

(Figure 1D–F). The mean diameters of nanofibers were about $678 \text{ nm} \pm 7.43$ when measured using ImageJ software (NIH United States). The diameter of nanofibers did not change after coating the nanocomposite (Figure 1D–E).

Hydrophilicity was determined by measuring the water contact angle of PLLA nanofibers before and after plasma treatment. This angle was 117° before plasma treatment and decreased to 0° following plasma treatment. Before plasma treatment, the tensile strength of the PLLA nanofiber scaffold was $0.36 \pm 0.18 \text{ MPa}$, and elongation at peak break was 67.26%. Still, after plasma treatment and nanocomposite presence, the tensile strength increased to $1.21 \pm 0.41 \text{ MPa}$, and elongation at break peak was 53.54%. As a result, the PLLA scaffold's

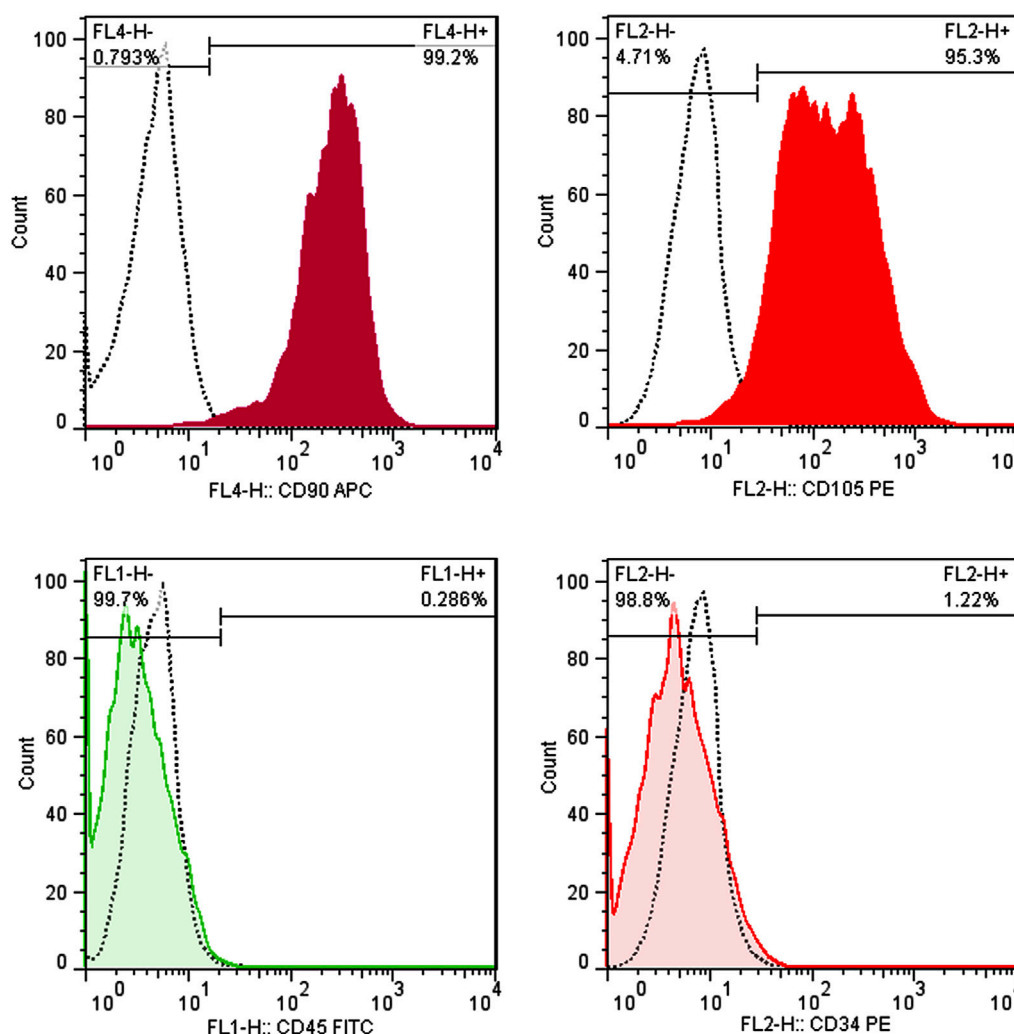


FIGURE 3
Immunophenotyping of hAMSCs using flow cytometry. hAMSCs were positive for CD105 and CD90 and negative for CD34 and CD45. (dotted curve: unstained samples, color curve: stained samples).

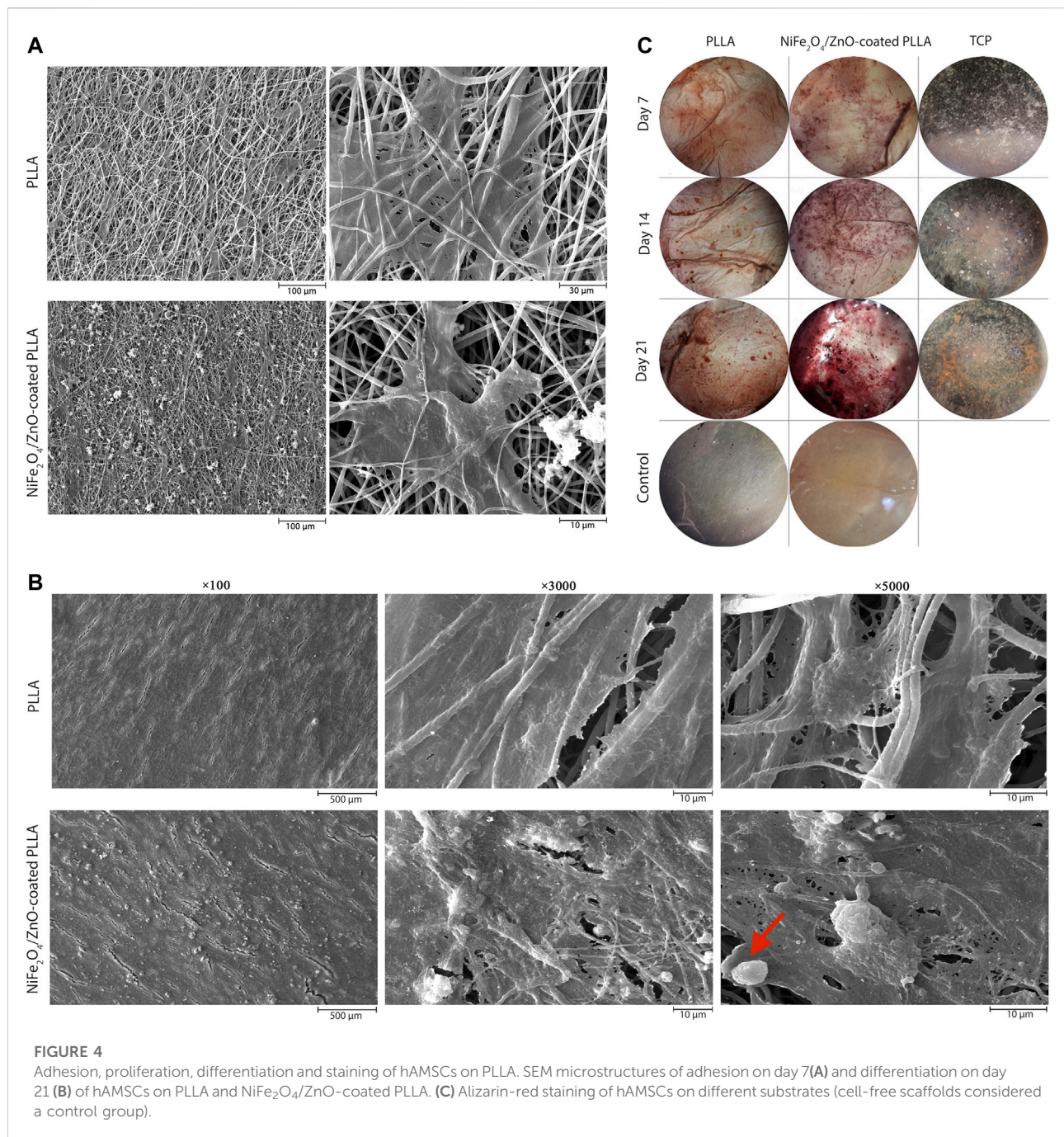
mechanical characteristics were enhanced after plasma treatment and coating of the nanocomposite.

Due to the vibrations of PLLA nanofibers described previously (Ramezanifard et al., 2016), FTIR measurements revealed peaks at 1749.74 cm^{-1} corresponding to C=O tensile of the carbonyl group, 1090.60 cm^{-1} corresponding to C—O antisymmetric stretching, and 1185.13 cm^{-1} corresponding to (C—O—C stretching). The O—H vibration has a broad peak at 3304.59 cm^{-1} . The vibration at 581.26 cm^{-1} is a stretching vibration of oxygen metal ($\text{Fe}^{3+}\text{—O}^{2-}$) or a combination of ZnO and ferrite stretching. Nanocomposite' OH bending vibrations cause the peak at 1114 cm^{-1} . The increase in the strength of vibrations in this group confirms the presence of nanocomposite on PLLA (Figure 2).

4.2 Characterization, adhesion, and differentiation of human adipose tissue-derived mesenchymal stem cell on scaffolds

As shown in Figure 3, positive markers (CD105, CD90) have an expression level of more than 95% of cells when surface antigens were analyzed by flow cytometry. Additionally, the hematopoietic markers CD34 and CD45 were expressed at 1.22% and 0.29%, respectively, confirming that the separated cells' have a mesenchymal origin.

On day 7, adhesion and proliferation of hAMSCs on PLLA and $\text{NiFe}_2\text{O}_4/\text{ZnO}$ -coated PLLA scaffolds demonstrates the distribution of cells on the scaffold



surface, indicating proper contact and integration of cells with PLLA and NiFe₂O₄/ZnO-coated PLLA scaffolds have occurred (Figure 4A). On both types of scaffold surface, cell adhesion and proliferation are seen, suggesting the low toxicity of PLLA and NiFe₂O₄/ZnO-coated PLLA scaffolds (Figure 4A).

After 21 days of differentiation, the mineral deposits on NiFe₂O₄/ZnO-coated PLLA were much more significant than

PLLA. The deposition of calcium and hydroxyapatite granules on the surface of nanofibers was discovered to have a significant association with mineral mass. Mineral deposits shown in the red arrow (Figure 4B) seem to have a porous and rough shape at high magnification; this appearance may be due to the accumulation of sediments on top of each other, which shows spherical aggregates of minerals. Sedimentation occurred at a meager rate in PLLA (Figure 4B).

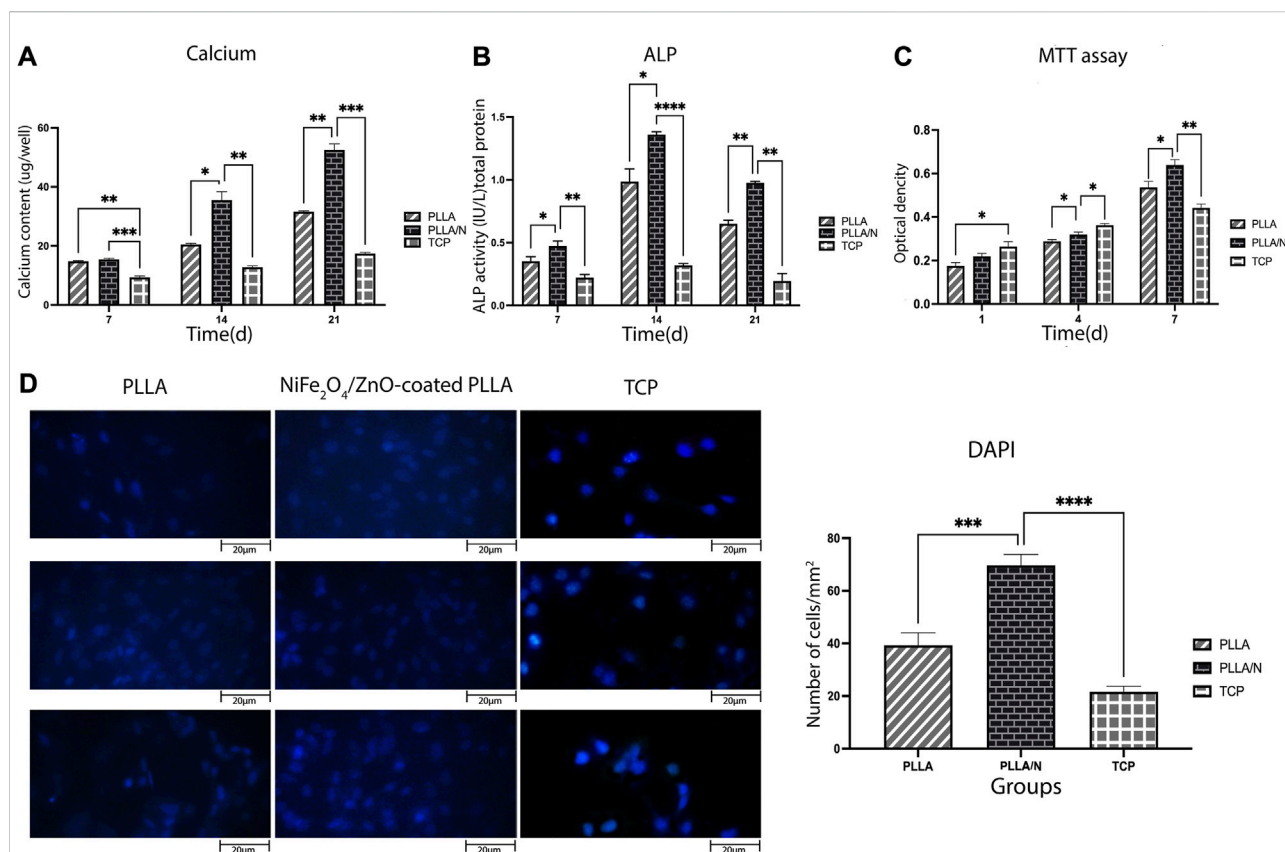


FIGURE 5

Bioassays in the osteogenic differentiation process. Mineralized calcium deposition (A) and Alkaline phosphatase (ALP) activity of osteogenic differentiation of hAMSCs on different scaffolds (B) Cell viability of hAMSCs on different scaffolds (C) and DAPI staining of hAMSCs cultured on different substrates(D) (mean \pm SD; p -value < 0.05). (* p < 0.01, ** p < 0.001, *** p < 0.0001, **** p < 0.0001).

4.3 Bioassays

4.3.1 Alizarin-red staining (biomineralization)

ARS was utilized to assess the osteogenic differentiation of hAMSC on different surfaces qualitatively. The amount of alizarin-red dots associated with mineral deposits and calcium increased on days 14 and 21. On the 21st day of differentiation, the largest values of these sediments were observed on the NiFe₂O₄/ZnO-coated PLLA scaffold. Additionally, there was no color on cell-free scaffolds (control), indicating that PLLA and NiFe₂O₄/ZnO are achromatic in the absence of cells (Figure 4C).

4.3.2 Calcium content

On days 7, 14, and 21, the calcification rate was determined in an osteogenic environment. On days 14 (PLLA = 20.50 \pm 0.36, PLLA/n = 35.53 \pm 2.80, TCP = 12.80 \pm 0.45) and 21, the calcium concentration of the NiFe₂O₄/ZnO-coated PLLA scaffold was

higher than that of the PLLA and TCP scaffolds (p < 0.05). However, on day 7, no statistically significant variation in calcium concentration was observed between the NiFe₂O₄/ZnO-coated PLLA and the PLLA scaffold (PLLA = 14.83 \pm 0.20, PLLA/n = 15.46 \pm 0.32, TCP = 9.33 \pm 0.50) (p > 0.05). On day 21 of differentiation, a higher calcium level was reported in the NiFe₂O₄/ZnO-coated PLLA scaffold than PLLA scaffold and TCP (PLLA = 31.60 \pm 0.26, PLLA/n = 52.53 \pm 2.04, TCP = 17.43 \pm 0.35) (Figure 5A).

4.3.3 Alkaline phosphatase

ALP activity indicates early osteoblastic differentiation and commitment of stem cells to the osteoblastic phenotype. Results showed that ALP activity has increased from day 7 (PLLA = 0.3 \pm 0.035, PLLA/n = 0.4 \pm 0.3, TCP = 0.22 \pm 0.02) to day 14 (PLLA = 0.98 \pm 0.1, PLLA/n = 1.36 \pm 0.02, TCP = 0.31 \pm 0.01) in cells cultured on both scaffolds. Each day, the mean absorption ALP activity in NiFe₂O₄/ZnO-coated PLLA

scaffold was higher than PLLA and TCP ($p < 0.05$). On day 21, the ALP enzyme activity decreased in all groups (PLLA = 0.64 ± 0.03 , PLLA/n = 0.97 ± 0.01 , TCP = 0.19 ± 0.06) (Figure 5B).

4.3.4 Human adipose tissue-derived mesenchymal stem cell viability on different substrates

The viability and adherence of hAMSCs on different scaffolds were assessed with MTT assay (on days 1, 4, and 7 after seeding) and DAPI staining (on day 7). On days 1 (PLLA = 0.17 ± 0.016 , PLLA/n = 0.21 ± 0.014 , TCP = 0.26 ± 0.022) and 4 (PLLA = 0.28 ± 0.009 , PLLA/n = 0.32 ± 0.01 , TCP = 0.36 ± 0.008) the cell viability (proliferation) was higher on TCP compared to PLLA and NiFe₂O₄/ZnO-coated PLLA scaffolds. Still, on day 7 (PLLA = 0.53 ± 0.028 , PLLA/n = 0.63 ± 0.02 , TCP = 0.44 ± 0.018), most of the cell's metabolic activity occurred on the NiFe₂O₄/ZnO-coated PLLA scaffold ($p < 0.05$) (Figure 5C).

On day 7, hAMSCs cultivated on NiFe₂O₄/ZnO-coated PLLA scaffold had a higher population density per mm² surface area than TCP and PLLA scaffold ($p < 0.05$). It provides a bioactive and biocompatible environment where cells can adhere and proliferate (PLLA = 39.33 ± 4.7 , PLLA/n = 69.66 ± 4.16 , TCP = 21.66 ± 2.08) (Figure 5D).

5 Osteogenic gene expression

To evaluate the osteogenic differentiation in cells cultured on scaffolds and TCP, the expression of critical osteogenic genes (*Osteonectin*, *Osteocalcin*, *ALP*, *Runx2*, and *Collagen type I*) were measured. On all days (Ghobeira et al., 2017; Porgham Daryasari et al., 2019; Yeganeh et al., 2020; Yeganeh et al., 2020), a higher expression of the *ALP* gene was observed in the differentiation on NiFe₂O₄/ZnO-coated PLLA scaffold compared to TCP and PLLA ($p < 0.05$) (day7; PLLA = 0.94 ± 0.0 , PLLA/n = 1.11 ± 0.03 , and TCP = 0.72 ± 0.14).

The transcription of the *ALP* gene during differentiation was more on day 14 (PLLA = 1.24 ± 0.16 , PLLA/n = 2.87 ± 0.09 , and TCP = 1 ± 0.03) than on day 21 (PLLA = 0.93 ± 0.03 , PLLA/n = 1.32 ± 0.17 , and TCP = 0.70 ± 0.19). On day 7 (PLLA = 0.95 ± 0.04 , PLLA/n = 1.21 ± 0.09 , and TCP = 0.73 ± 0.07) Day 14 (PLLA = 1.57 ± 0.08 , PLLA/n = 1.91 ± 0.07 , TCP = 1.11 ± 0.05) to 21, the expressions of *Osteonectin* on NiFe₂O₄/ZnO-coated PLLA scaffold was increased compared to the PLLA and TCP ($p < 0.05$). On day 21 of differentiation, osteonectin gene expression decreased in PLLA and TCP but increased on NiFe₂O₄/ZnO-coated PLLA scaffold (PLLA = 1.50 ± 0.19 , PLLA/n = 2.67 ± 0.09 , and TCP = 1.02 ± 0.23). Regarding the expression of the *Osteocalcin* in this study, no significant statistical difference was observed in all three groups on day 7 (PLLA = 1.1 ± 0.18 , PLLA/n = 1.31 ± 0.10 , and TCP = 1 ± 0.01) ($p > 0.05$). In contrast, on days 14 (PLLA = 1.20 ± 0.04 , PLLA/n = 1.9 ± 1.06 , and TCP = 1.0 ± 0.15) and

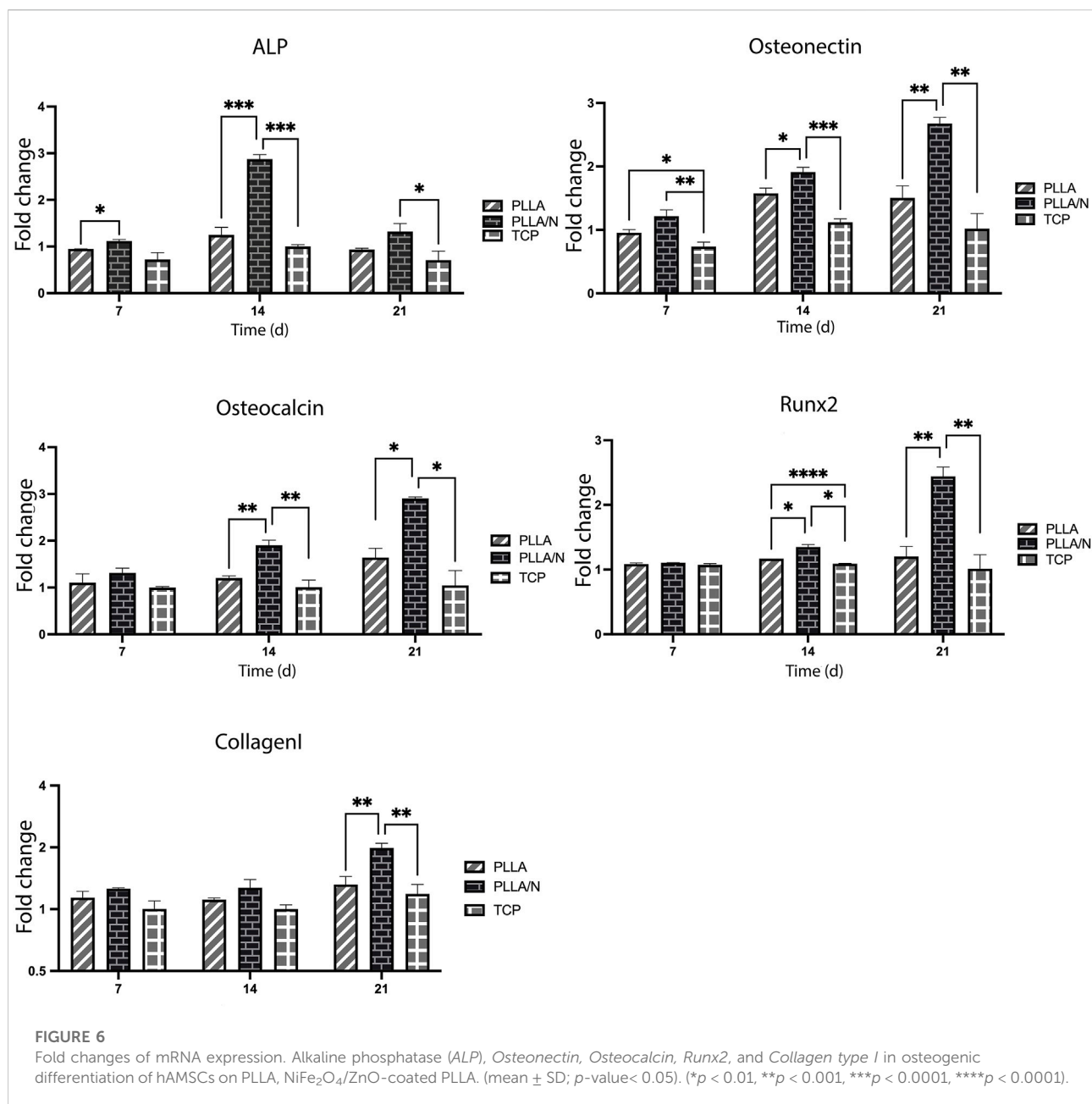
21 (PLLA = 1.61 ± 0.2 , PLLA/N = 2.9 ± 0.03 , and TCP = 1.04 ± 0.31), the expression of *Osteocalcin* was much increased in cultured cells on NiFe₂O₄/ZnO-coated PLLA scaffold compared to PLLA and TCP ($p < 0.05$). On days 14 (PLLA = 1.17 ± 0.02 , PLLA/N = 1.34 ± 0.04 , and TCP = 1.09 ± 0.0) and 21, the expression of the *Runx2* gene in cultured cells on the NiFe₂O₄/ZnO-coated PLLA scaffold was more than PLLA and TCP ($p < 0.05$). However, on day 7 (PLLA = 1.0 ± 0.01 , PLLA/n = 1.08 ± 0.0 , TCP = 1.07 ± 0.01), there was no significant statistical difference in *Runx2* gene expression between the three groups. On day 21 (PLLA = 1.2 ± 0.15 , PLLA/N = 2.44 ± 0.14 , and TCP = 1.01 ± 0.21) of differentiation, the expression of this gene increased in cultured cells on the NiFe₂O₄/ZnO-coated PLLA scaffold. The level of *Runx2* gene expression has remained almost constant for PLLA and TCP; a slight downward trend was observed.

On days 7 (PLLA = 1.13 ± 0.0 , PLLA/N = 1.25 ± 0.01 , and TCP = 1 ± 0.09) and 14 (PLLA = 1.11 ± 0.02 , PLLA/n = 1.27 ± 0.12 , and TCP = 1 ± 0.04) of differentiation, there was no significant difference in the *Collagen type I* gene expression level between all three groups ($p > 0.05$). Still, on day 21, the expression of the *Collagen type I* in cultured cells on NiFe₂O₄/ZnO-coated PLLA scaffold was increased compared to the PLLA and TCP (PLLA = 1.31 ± 0.1 , PLLA/n = 1.98 ± 0.11 , and TCP = 1.18 ± 0.13) ($p < 0.05$).

6 Discussion

Bone tissue engineering aims to create materials that enter irreparable bone tissue lesions and regenerate through resident cells. Biomaterials can mimic the ECM's function, resulting in cellular and vascular infiltration and structure of the bone matrix in injured tissue (Laurenti and Cauda, 2017; Koons et al., 2020; Troy et al., 2021). Numerous studies have been conducted to determine the best ability of nanofiber scaffolds incorporating nanoparticles, such as bioceramic, metal, etc., to repair bone defects. Even without bone growth agents, nanostructured materials operate as an effective signal in the mechanism of osteoblastic differentiation (Dang et al., 2018; Petersen et al., 2018; Tavangar et al., 2018). On the other hand, ideas such as bone protein uptake, topography, and surface calcification are proposed for assessing the ossification function of chemicals that can cause it (Tavangar et al., 2018; Montoya et al., 2021).

The ability of hAMSCs to differentiate into osteogenic cells was evaluated in this experiment using NiFe₂O₄/ZnO-coated PLLA as a scaffold to target bone tissue engineering. According to this, the mechanical properties of the PLLA scaffold improved following plasma treatment and nanocomposite coating. This method revealed evidence of additional tensile strength. Plasma therapy leads to carboxyl and hydroxyl groups forming electrostatic bonds with soluble ions such as calcium and growth hormones (Karimi et al.,



2019). We hypothesize that this effect is due to the stiffness of NiFe₂O₄/ZnO-coated PLLA scaffolds. The stiffness of the scaffold promoted osteogenic proteins (Osteonectin and Osteopontin) and vascularization, resulting in a significant correlation between vascular growth, bone formation, and bone matrix deposition (Karimi et al., 2019; Montoya et al., 2021).

Wettability is essential for cell adhesion, and expansion and sterilization methods may affect it. About 60%–80% ethanol solution is a common disinfection technique that does not affect the chemical and morphological properties of the scaffold, but its high

concentrations may cause fiber shrinkage (Ghobeira et al., 2017; Łopianiak and Butruk-Raszeja, 2020). Effective sterilization is ensured by combining ethanol and UV radiation, which is an effective method because the physical and chemical changes caused by H₂O₂ Plasma (HP) or Ethylene Oxide (ETO) occur far less and maintain the biocompatibility of sterilized nanofibers. In the studies done after UV sterilization, WCA remains constant, which indicates that 3 h of UV exposure does not cause surface chemical changes. Still, long-term UV radiation for 5–24 h can cause drastic differences in topography and chemical composition (Park et al., 2011; Ghobeira et al., 2017).

The nanocomposites applied to the scaffold surface, as shown in (Figure 1D–F), did not obstruct the porosity space of the scaffold. Also, nanocomposites coated on the scaffold surface have no inhibitory effect on adhesion cell proliferation and survival but rather enhance cell proliferation (Figure 4A). Connected pore networks can facilitate the movement of nutrients, oxygen, waste products, and angiogenesis. Roughness on the surface and other topological properties can enhance cell adhesion and fate (Gaharwar et al., 2020).

On day 7, DAPI staining revealed that the number of cells in the NiFe₂O₄/ZnO-coated PLLA scaffold was much higher (Figure 5D). We hypothesize that this effect can be attributed to the presence of magnetic nanoparticles to modulate and proliferate hAMSCs. Nanocomposites with magnetic properties, i.e., nickel and ferrite, affect cell proliferation and survival, achieved with surface modifiers. The broad porous nanofibers contain anchors that promote cell attachment and proliferation while boosting cell cohesion and diffusion (Seyedjafari et al., 2010; Vieira et al., 2017; Fan et al., 2020).

Cell growth and proliferation were increased on both scaffolds throughout the 21-day monitoring of hAMSCs differentiation into the osteogenic lineage (Figure 4B) but were higher on the nanocomposites-coated scaffold, which also had more cell layers on the surface. We hypothesized that hydroxyapatite granules on the surface of the NiFe₂O₄/ZnO-coated PLLA promote differentiation into the osteogenic lineage. Carbonate hydroxyapatite is a bone mineral necessary for forming phosphate and calcium. It is found between collagen fibers. These compounds are responsible for bone hierarchical and mechanical structural properties (Koons et al., 2020). We observed a slight cellular infiltration (Figure 4B), which is unclear in the image due to surface coating with cells. The major limitation of electrospun scaffolds is that they have solid layers with only a single surface porous network, which is limited to the sheet-like formation (Wu and Hong, 2016). Although electrospun scaffolds have high porosity, the pore diameter of these scaffolds is much smaller than the diameter of cells in the micrometer range. This unavoidable feature limits cell penetration through the scaffolds. But the depth of cell penetration into the Electrospun scaffolds varies from approach to approach (Blakeney et al., 2011; Khorshidi et al., 2016). Microporous scaffolds have been shown to promote hAMSC adhesion and osteogenic differentiation. Through intracellular and intercellular signaling, the material's topographic and biochemical properties can alter the microenvironment of the desired location. These microenvironmental modifications affect cell differentiation by regulating enzymes, cells, and ions containing radical species (Gaharwar et al., 2020).

ALP activity was assessed based on our findings from the process of osteoblastic differentiation of hAMSC on PLLA,

NiFe₂O₄/ZnO-coated PLLA, and TCP. The most activity of the ALP enzyme (Figure 5) was seen in nanofibers of NiFe₂O₄/ZnO-coated PLLA throughout this procedure. We assume this is due to Zinc in this nanocomposite. Zinc acts as a cofactor in ALP activity and promotes the development of osteoblastic activity (Laurenti and Cauda, 2017). ALP activity in osteoblasts is the primary marker of osteogenesis and hard tissue (Jaiswal et al., 2013).

As a significant factor, calcium functions in creating osteogenesis (Khader and Arinze, 2020). On the NiFe₂O₄/ZnO-coated PLLA scaffold (Figure 5), calcium levels rise during the differentiation phase from day 7 to day 21 due to the support of ALP activity, which initiates the mineralization process. By releasing signaling ions, biodegradable biomaterials can alter the environment. Calcium can excite calcium sensory receptors, essential for cell proliferation, differentiation, and chemotaxis. In addition, releasing ions from the phosphate, calcium, and biomaterial bases can stimulate endogenous cells, causing them to develop into the osteogenic lineage (Gaharwar et al., 2020).

On day 21, the highest amount of calcium mineralization occurred in the NiFe₂O₄/ZnO-coated PLLA, as shown in Figure 4C of Alizarin red staining, which serves as a seal of approval for the process of osteoblast cell mineralization and maturation during the differentiation process into the osteogenic lineage. Studies show that the magnetic mechanism of action is mediated through the calcium ion transport channel in the cell membrane. Additionally, it could affect the structure and crystallization of biomineral products, alter the spatial organization of proteins in the cytoskeleton, and affects the biomineralization behavior during the early stages of gene expression and protein synthesis (Fan et al., 2020). Cell receptors, proteins, and peptides interact to enable the cell to store minerals and ECM proteins (Koons et al., 2020).

During the 21-day observation of osteogenic lineage development, bone-related mRNAs (*Osteonectin*, *Osteocalcin*, *ALP*, *Runx2*, and *Collagen type I*) were detected during the molecular behavior of hAMSC. The nanocomposites on the scaffold surface boosted and maintained Runx2 expression until day 21 (Figure 6). The *Runx2* gene regulates the expression of phenotypic markers such as osteocalcin and ALP during the differentiation of hAMSCs into pre-osteoblasts (Abe et al., 2019). The highest level of ALP mRNA expression on day 14 indicated the nanocomposites' osteoblastic activity; we hypothesize this can be attributed to the action of Zinc, an essential element. ZnO significantly affected the amount of ALP and the magnetic field produced by nickel ferrite, which is effective at interacting with cells and their ossifying role (Ramezanifard et al., 2016; Abe et al., 2019).

The *Runx2* gene expression on the 21st day of differentiation was increased on the NiFe₂O₄/ZnO-coated

PLLA scaffold. The high expression of the *Runx2* gene was shown to increase the Bone Morphogenetic Protein-9 (Bmp9) gene expression (Karimi et al., 2019). Osteonectin is a calcium-binding glycoprotein that plays a function in the crystallization of osteoblasts during their early stages of development (Nafary et al., 2017). The highest level of Osteonectin gene expression was seen on day 21 on the NiFe₂O₄/ZnO-coated PLLA scaffold, which corresponds to the mineralization stage (2 weeks of differentiation) in the previous studies (Seyedjafari et al., 2010; Nafary et al., 2017). The *Osteocalcin* gene is known as a bone-growth protein (BGP) that osteoblasts generate and release during their maturation (3 weeks of differentiation) (Nafary et al., 2017; Nguyen et al., 2019). The highest level of *Osteocalcin* mRNA expression on day 21 indicates the osteoblastic activity of the NiFe₂O₄/ZnO-coated PLLA scaffold. We hypothesize that it can be attributed to the magnetic properties of the nanocomposite. *Collagen type I* is the most abundant protein in the bone matrix, as it aids in mineralization during bone formation (Peng et al., 2019). The expression of *Collagen type I* was increased on day 21 in this study, while there was no statistically significant difference between the groups on days 7 and 14 of osteoconductive culture. As a result, they provide surfaces capable of transmitting biological signals by mimicking the structure of the ECM (Chen et al., 2017; Dang et al., 2018; Komori, 2019). Numerous Studies indicated that moving electrons provide magnetic properties to stem cells, aiding their cohesion, survival, migration, proliferation, and differentiation. Their porosity space can result in the formation of arteries, angiogenesis, and a bone-like environment, enabling bone tissue regeneration (Chen et al., 2017; Komori, 2019; Dixon and Gomillion, 2022). Our results indicate that NiFe₂O₄/ZnO-coated PLLA and PLLA nanofibers prolong the osteoblastic obligation process in hAMSC. Combining PLLA nanofibers with nanocomposite (NiFe₂O₄/ZnO) promotes cell interaction and ossification in an osteogenic environment. The NiFe₂O₄/ZnO-coated PLLA scaffold may be used in animal models of bone injury to confirm this work's findings, consistent with the link between osteogenic function *in vitro* and *in vivo*.

7 Conclusion

The differentiation of hAMSC into the osteogenic lineage demonstrated that interaction of cells with NiFe₂O₄/ZnO coated PLLA scaffold could provide a support role, like bone ECM architecture, culminating in osteoblast adhesion, proliferation, differentiation, and maturation. We assume that NiFe₂O₄/ZnO-coated PLLA could be the proper platform for directing connections and cellular activity toward the osteogenic lineage by hypothesizing having piezoelectric, magnetic, and proper

mechanical properties. However, Future studies should be conducted to deepen the study of these properties and the potential of NiFe₂O₄/ZnO-coated PLLA scaffold designed as an *in vivo* osteoinduction material.

Data availability statement

The raw data supporting the conclusions of this article will be made available by the authors, without undue reservation.

Author contributions

ES and EF conceived, designed and supervised the project. SS conducted all experiments, processed and analyzed data. FS helped processed and analyzed data. AM drew graphical abstract and helped to draft the manuscript. All authors discussed the data, read, commented and approved the manuscript.

Funding

This master's thesis study was conducted with the financial support of Babol University of Medical Sciences and the supply of some tools and materials from the University of Tehran.

Acknowledgments

Thank all colleagues in the tissue engineering lab in the Biotechnology Department of the University of Tehran for their contributions to this work.

Conflict of interest

The authors declare that the research was conducted in the absence of any commercial or financial relationships that could be construed as a potential conflict of interest.

Publisher's note

All claims expressed in this article are solely those of the authors and do not necessarily represent those of their affiliated organizations, or those of the publisher, the editors and the reviewers. Any product that may be evaluated in this article, or claim that may be made by its manufacturer, is not guaranteed or endorsed by the publisher.

References

- Abe, Y., Chiba, M., Yaklai, S., Pechayco, R. S., Suzuki, H., and Takahashi, T. (2019). Increase in bone metabolic markers and circulating osteoblast-lineage cells after orthognathic surgery. *Sci. Rep.* 9 (1), 20106–20110. doi:10.1038/s41598-019-56484-x
- Baino, F., Novajra, G., and Vitale-Brovarone, C. (2015). Bioceramics and scaffolds: A winning combination for tissue engineering. *Front. Bioeng. Biotechnol.* 3, 202. doi:10.3389/fbioe.2015.00202
- Blakeney, B. A., Tambralli, A., Anderson, J. M., Andukuri, A., Lim, D. J., Dean, D. R., et al. (2011). Cell infiltration and growth in a low density, uncompressed three-dimensional electrospun nanofibrous scaffold. *Biomaterials* 32 (6), 1583–1590. doi:10.1016/j.biomaterials.2010.10.056
- Chen, Y., Xu, J., Huang, Z., Yu, M., Zhang, Y., Chen, H., et al. (2017). An innovative approach for enhancing bone defect healing using PLGA scaffolds seeded with extracorporeal-shock-wave-treated bone marrow mesenchymal stem cells (BMSCs). *Sci. Rep.* 7 (1), 44130–44213. doi:10.1038/srep44130
- Dang, M., Saunders, L., Niu, X., Fan, Y., and Ma, P. X. (2018). Biomimetic delivery of signals for bone tissue engineering. *Bone Res.* 6 (1), 25–12. doi:10.1038/s41413-018-0025-8
- Dixon, D. T., and Gomillion, C. T. (2022). Conductive scaffolds for bone tissue engineering: Current state and future outlook. *J. Funct. Biomater.* 13 (1), 1. doi:10.3390/jfb13010001
- Fan, D., Wang, Q., Zhu, T., Wang, H., Liu, B., Wang, Y., et al. (2020). Recent advances of magnetic nanomaterials in bone tissue repair. *Front. Chem.* 8, 745. doi:10.3389/fchem.2020.00745
- Gaharwar, A. K., Singh, I., and Khademhosseini, A. (2020). Engineered biomaterials for *in situ* tissue regeneration. *Nat. Rev. Mat.* 5 (9), 686–705. doi:10.1038/s41578-020-0209-x
- Ghobeira, R., Philips, C., Declercq, H., Cools, P., De Geyter, N., Cornelissen, R., et al. (2017). Effects of different sterilization methods on the physico-chemical and bioresponsive properties of plasma-treated polycaprolactone films. *Biomed. Mat.* 12 (1), 015017. doi:10.1088/1748-605x/aa51d5
- Jaiswal, A. K., Chhabra, H., Kadam, S. S., Londhe, K., Soni, V. P., and Bellare, J. R. (2013). Hardystonite improves biocompatibility and strength of electrospun polycaprolactone nanofibers over hydroxyapatite: A comparative study. *Mater. Sci. Eng. C* 33 (5), 2926–2936. doi:10.1016/j.msec.2013.03.020
- Karimi, Z., Seyedjafari, E., Mahdavi, F. S., Hashemi, S. M., Khojasteh, A., Kazemi, B., et al. (2019). Baghdadite nanoparticle-coated poly l-lactic acid (PLLA) ceramics scaffold improved osteogenic differentiation of adipose tissue-derived mesenchymal stem cells. *J. Biomed. Mat. Res. A* 107 (6), 1284–1293. doi:10.1002/jbm.a.36638
- Khader, A., and Arinze, T. L. (2020). Biodegradable zinc oxide composite scaffolds promote osteochondral differentiation of mesenchymal stem cells. *Biotechnol. Bioeng.* 117 (1), 194–209. doi:10.1002/bit.27173
- Khorshidi, S., Solouk, A., Mirzadeh, H., Mazinani, S., Lagaron, J. M., Sharifi, S., et al. (2016). A review of key challenges of electrospun scaffolds for tissue-engineering applications. *J. Tissue Eng. Regen. Med.* 10 (9), 715–738. doi:10.1002/term.1978
- Komori, T. (2019). Regulation of proliferation, differentiation and functions of osteoblasts by Runx2. *Int. J. Mol. Sci.* 20 (7), 1694. doi:10.3390/ijms20071694
- Koons, G. L., Diba, M., and Mikos, A. G. (2020). Materials design for bone-tissue engineering. *Nat. Rev. Mat.* 5 (8), 584–603. doi:10.1038/s41578-020-0204-2
- Kumar, P., Dehiya, B. S., and Sindhu, A. (2018). Bioceramics for hard tissue engineering applications: A review. *Int. J. Appl. Eng. Res.* 13 (5), 2744–2752.
- Laurenti, M., and Cauda, V. (2017). ZnO nanostructures for tissue engineering applications. *Nanomaterials* 7 (11), 374. doi:10.3390/nano7110374
- Liu, W., Li, Z., Zheng, L., Zhang, X., Liu, P., Yang, T., et al. (2016). Electrospun fibrous silk fibroin/poly (L-lactic acid) scaffold for cartilage tissue engineering. *Tissue Eng. Regen. Med.* 13 (5), 516–526. doi:10.1007/s13770-016-9099-9
- Lopianiak, I., and Butruk-Raszeja, B. A. (2020). Evaluation of sterilization/disinfection methods of fibrous polyurethane scaffolds designed for tissue engineering applications. *Int. J. Mol. Sci.* 21 (21), 8092. doi:10.3390/ijms21218092
- Montoya, C., Du, Y., Gianforaro, A. L., Orrego, S., Yang, M., and Lelkes, P. I. (2021). On the road to smart biomaterials for bone research: Definitions, concepts, advances, and outlook. *Bone Res.* 9 (1), 12–16. doi:10.1038/s41413-020-00131-z
- Nafary, A., Seyedjafari, E., and Salimi, A. (2017). Electrospun poly-L-lactic acid coated with silicate bioceramic nanoparticles enhance osteogenic differentiation of adipose tissue derived mesenchymal stem cells. *J. Biomater. tissue Eng.* 7 (2), 91–100. doi:10.1166/jbt.2017.1544
- Nguyen, T. D. T., Jang, Y. S., Kim, Y. K., Kim, S. Y., Lee, M. H., and Bae, T. S. (2019). Osteogenesis-related gene expression and guided bone regeneration of a strontium-doped calcium-phosphate-coated titanium mesh. *ACS Biomater. Sci. Eng.* 5 (12), 6715–6724. doi:10.1021/acsbomaterials.9b01042
- Park, K. H., Koak, J. Y., Kim, S. K., and Heo, S. J. (2011). Wettability and cellular response of UV light irradiated anodized titanium surface. *J. Adv. Prosthodont.* 3 (2), 63–68. doi:10.4047/jap.2011.3.2.63
- Peng, J., Zhao, J., Long, Y., Xie, Y., Nie, J., and Chen, L. (2019). Magnetic materials in promoting bone regeneration. *Front. Mat.* 6, 268. doi:10.3389/fmats.2019.00268
- Petersen, A., Princ, A., Korus, G., Ellinghaus, A., Leemhuis, H., Herrera, A., et al. (2018). A biomaterial with a channel-like pore architecture induces endochondral healing of bone defects. *Nat. Commun.* 9 (1), 4430–4516. doi:10.1038/s41467-018-06504-7
- Porgham Daryasari, M., Dusti Telgerd, M., Hossein Karami, M., Zandi-Karimi, A., Akbarijavar, H., Khoobi, M., et al. (2019). Poly-L-lactic acid scaffold incorporated chitosan-coated mesoporous silica nanoparticles as pH-sensitive composite for enhanced osteogenic differentiation of human adipose tissue stem cells by dexamethasone delivery. *Artif. Cells Nanomed. Biotechnol.* 47 (1), 4020–4029. doi:10.1080/21691401.2019.1658594
- Ramezanifard, R., Seyedjafari, E., Ardeshtyrlajimi, A., and Soleimani, M. (2016). Biomimetic scaffolds containing nanofibers coated with willemite nanoparticles for improvement of stem cell osteogenesis. *Mater. Sci. Eng. C* 62, 398–406. doi:10.1016/j.msec.2016.01.089
- Seyedjafari, E., Soleimani, M., Ghaemi, N., and Shabani, I. (2010). Nanohydroxyapatite-coated electrospun poly (L-lactide) nanofibers enhance osteogenic differentiation of stem cells and induce ectopic bone formation. *Biomacromolecules* 11 (11), 3118–3125. doi:10.1021/bm1009238
- Tavangar, B., Arasteh, S., Edalatkhah, H., Salimi, A., Doostmohammadi, A., and Seyedjafari, E. (2018). Hardystonite-coated poly (L-lactide) nanofibrous scaffold and efficient osteogenic differentiation of adipose-derived mesenchymal stem cells. *Artif. Organs* 42 (11), E335–E348. doi:10.1111/aor.12891
- Troy, E., Tilbury, M. A., Power, A. M., and Wall, J. G. (2021). Nature-based biomaterials and their application in biomedicine. *Polymers* 13 (19), 3321. doi:10.3390/polym13193321
- Vieira, S., Vial, S., Reis, R. L., and Oliveira, J. M. (2017). Nanoparticles for bone tissue engineering. *Biotechnol. Prog.* 33 (3), 590–611. doi:10.1002/btpr.2469
- Wu, J., and Hong, Y. (2016). Enhancing cell infiltration of electrospun fibrous scaffolds in tissue regeneration. *Bioact. Mat.* 1 (1), 56–64. doi:10.1016/j.bioactmat.2016.07.001
- Ye, Z., Xu, W., Shen, R., and Yan, Y. (2020). Emulsion electrospun PLA/calcium alginate nanofibers for periodontal tissue engineering. *J. Biomater. Appl.* 34 (6), 763–777. doi:10.1177/0885328219873561
- Yeganeh, F. E., Yousefi, M., Hekmati, M., and Bikhof, M. (2020). Photocatalytic degradation of coomassie blue G-250 by magnetic NiFe₂O₄/ZnO nanocomposite. *Comptes Rendus Chim.* 23 (6–7), 385–393. doi:10.5802/crchim.36
- Yousefi, A. M., James, P. F., Akbarzadeh, R., Subramanian, A., Flavin, C., and Oudadesse, H. (2016). Prospect of stem cells in bone tissue engineering: A review. *Stem Cells Int.* 2016, 1–13. doi:10.1155/2016/6180487
- Zhang, Y., Di Wu, X. Z., Pakvasa, M., Tucker, A. B., Luo, H., Qin, K. H., et al. (2020). Stem cell-friendly scaffold biomaterials: Applications for bone tissue engineering and regenerative medicine. *Front. Bioeng. Biotechnol.* 8, 598607. doi:10.3389/fbioe.2020.598607



OPEN ACCESS

EDITED BY

Changhui Song,
South China University of Technology,
China

REVIEWED BY

Yuting Lv,
Shandong University of Science and
Technology, China
Youwen Yang,
Jiangxi University of Science and
Technology, China

*CORRESPONDENCE

Cheng Wang,
✉ 2598166583@qq.com

SPECIALTY SECTION

This article was submitted
to Biomaterials,
a section of the journal
Frontiers in Bioengineering
and Biotechnology

RECEIVED 27 October 2022

ACCEPTED 16 December 2022

PUBLISHED 04 January 2023

CITATION

Peng W, Liu Y and Wang C (2023),
Definition, measurement, and function
of pore structure dimensions of
bioengineered porous bone tissue
materials based on additive
manufacturing: A review.
Front. Bioeng. Biotechnol. 10:1081548.
doi: 10.3389/fbioe.2022.1081548

COPYRIGHT

© 2023 Peng, Liu and Wang. This is an
open-access article distributed under
the terms of the [Creative Commons
Attribution License \(CC BY\)](https://creativecommons.org/licenses/by/4.0/). The use,
distribution or reproduction in other
forums is permitted, provided the
original author(s) and the copyright
owner(s) are credited and that the
original publication in this journal is
cited, in accordance with accepted
academic practice. No use, distribution
or reproduction is permitted which does
not comply with these terms.

Definition, measurement, and function of pore structure dimensions of bioengineered porous bone tissue materials based on additive manufacturing: A review

Wen Peng^{1,2}, Yami Liu^{1,2} and Cheng Wang^{1*}

¹Department of Orthopaedic Surgery, The First Affiliated Hospital, Hengyang Medical School, University of South China, Hengyang, China, ²Foshan Orthopedic Implant (Stable) Engineering Technology Research Center, Foshan, China

Bioengineered porous bone tissue materials based on additive manufacturing technology have gradually become a research hotspot in bone tissue-related bioengineering. Research on structural design, preparation and processing processes, and performance optimization has been carried out for this material, and further industrial translation and clinical applications have been implemented. However, based on previous studies, there is controversy in the academic community about characterizing the pore structure dimensions of porous materials, with problems in the definition logic and measurement method for specific parameters. In addition, there are significant differences in the specific morphological and functional concepts for the pore structure due to differences in defining the dimensional characterization parameters of the pore structure, leading to some conflicts in perceptions and discussions among researchers. To further clarify the definitions, measurements, and dimensional parameters of porous structures in bioengineered bone materials, this literature review analyzes different dimensional characterization parameters of pore structures of porous materials to provide a theoretical basis for unified definitions and the standardized use of parameters.

KEYWORDS

additive manufacturing, bioengineered materials, bone tissue, pore structure, dimension characterization

Introduction

Technical background

Repair of bone tissue defects caused by tumors, infections, trauma, and medically induced injuries are the main applications of bioengineered porous bone tissue materials. The ability of these materials to promote bone tissue repair and reconstruction has been widely recognized (Xia et al., 2023; Dall'Ava et al., 2020; Chen et al., 2018). The bioengineered porous bone tissue materials promote bone tissue reconstruction and repair by providing an effective support effect and maintaining a good mechanical environment at the defect site after implantation (Ponader et al., 2010; Wang et al., 2020; Lehder et al., 2021). They also act as a scaffold for tissue growth, enabling the growth and formation of fibers, blood vessels, and bone tissue (Harrison et al., 2014; Taniguchi et al., 2016; Wu et al., 2022). Moreover, due to their unique porous structure, the overall elastic modulus of the implants can be effectively reduced to avoid stress shielding and provide the necessary stress stimulation for bone tissue growth (Shah et al., 2016; Cheong et al., 2018; Jette et al., 2018; Chao et al., 2021). In addition, such materials can promote the integration of the tissue–scaffold interface by constructing special morphologies on the material surface (Stevenson et al., 2016; Shuai et al., 2018; Kopp et al., 2019). They can also accelerate the bone defect repair and reconstruction process by relying on active substances, such as bone growth factors, that contribute to the formation of bone tissue (Li et al., 2015; Li et al., 2019a; Huang et al., 2020). They can also be prepared as slowly degradable porous materials using degradable metals, polymers, or other biomaterials, *etc.*, eventually leading to complete bone tissue replacement (Carluccio et al., 2020; Cockerill et al., 2020; Wu et al., 2021; Qin et al., 2022a; Qin et al., 2022b). At present, such bioengineered porous bone materials constructed by additive manufacturing technology have replaced traditional techniques such as the direct foaming method, pore-forming agent method, and powder sintering method due to their controlled pore structure, reliable mechanical properties, and flexible formulation mechanism (Zaharin et al., 2018; Cao et al., 2020; Sharma et al., 2020).

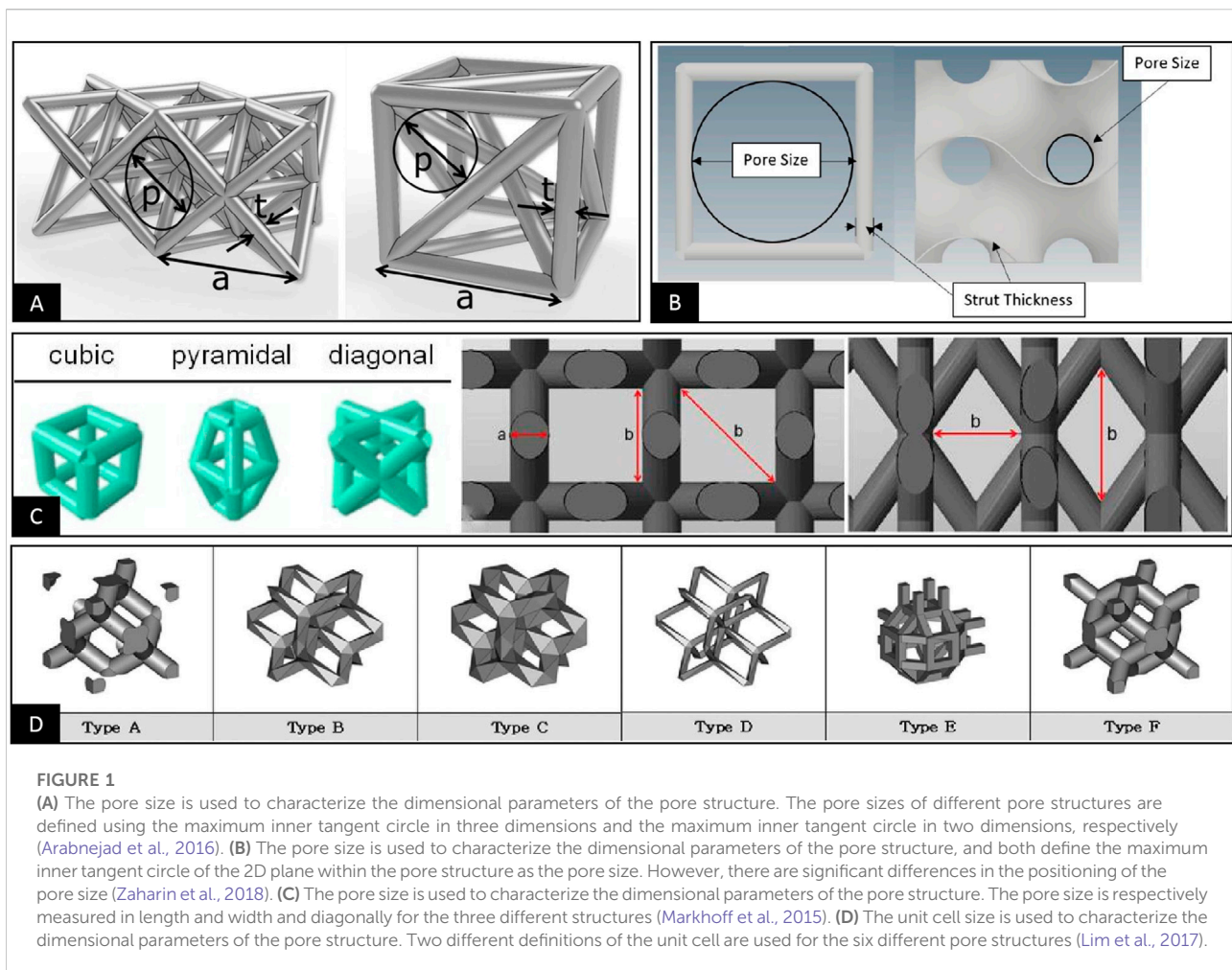
Structure design

Currently, the pore structure design used for bioengineered porous bone tissue materials mainly includes two approaches: regular and irregular pore structures. In this line, there are two main technical solutions to constructing a regular pore structure: through the regular arrangement of rod structures in 2D planes and through the superposition of 2D planes in the

Z axis (Cubo-Mateo and Rodriguez-Lorenzo, 2020; Sakthiabirami et al., 2021; Kilian et al., 2022). On the other hand, rod structures form the unit cells in 3D spaces through angular connections, and then the whole structure is formed by stacking the unit cells in the X/Y/Z axes (Li et al., 2018a; Li et al., 2018b). In recent years, the pore structure based on triply periodic minimal surface (TPMS) has emerged. It mainly involves the periodic extension of parametric surface sheets in three directions, culminating in the formation of walls in a 3D space state and a complete pore structure (Kelly et al., 2019; Corona-Castuera et al., 2021; Lu et al., 2022a; Lv et al., 2022). However, the design of irregular pore structures is more complex. It requires CT scanning of bone tissue to obtain the 3D structure of bone trabeculae, which are then rotated, stitched, and superimposed to achieve the overall design of the pore structure (Cheng et al., 2014). Alternatively, by employing Voronoi structures, it generates randomly distributed points within the spatial structure under certain conditions in a functional manner, subsequently forming pore structures with unspecified arrangements by connecting points to points (Deering et al., 2021; Zhao et al., 2021; Zhu et al., 2021). In addition to the above structures, the gradient pore structure has gradually become a research hotspot in recent years as the knowledge of the pore structure of bioengineered porous bone tissue materials has gradually deepened. These structures are usually implemented by parameterized adjustments of the pore structure sizes (Li et al., 2020a; Kamboj et al., 2020), rod diameters (Li et al., 2019b; Zhang et al., 2019; Li et al., 2020b; Liu et al., 2020; Xiong et al., 2020), or wall thicknesses (Afshar et al., 2016), changing the random distribution conditions of the point arrangement (Zhao et al., 2021; Zhu et al., 2021), or directly splicing different pore structures (Wieding et al., 2014; Wysocki et al., 2016; Kayacan et al., 2018) based on conventional pore structures.

Current problems

To characterize the pore structure dimension of porous materials, the pore size is often used as an important parameter and as the main control index to study the mechanical and biological properties of porous materials. However, after summarizing the relevant literature, we found that the definition of pore size is not clear in some literature sources. Furthermore, no unified positioning and measurement methods are available (Yavari et al., 2013; Amin Yavari et al., 2014; Soro et al., 2019; Liu et al., 2022). This problem has prompted some studies to cite findings from other literature with significant differences in the definition, localization, and measurement of pore size, leading to questioning the conclusions in their papers (Zadpoor, 2015; Dziaduszevska and Zielinski, 2021). More importantly, some studies have even used different definitions and positioning methods of pore sizes to describe



different pore structures, possibly leading to some bias in comparative analyses of different structures, as shown in Figures 1A–C–C (Markhoff et al., 2015; Arabnejad et al., 2016; Zaharin et al., 2018; Hossein Ehsani et al., 2022). Probably due to this uncertainty regarding the definition of pore size, some studies have abandoned using pore size for evaluating pore structure and have instead used the unit cell size as a measure to characterize pore structure dimension in porous materials (Yan et al., 2015; Hedayati et al., 2017; Lim et al., 2017; Ahmadi et al., 2019; Lu et al., 2020; Yang et al., 2020). However, differences in the definition of the unit cell size ultimately lead to the inconsistent characterization of the pore structure size, as shown in Figure 1D (Lim et al., 2017). Considering the current confusing situation, we analyze and summarize the definition and measurements of the pore structure dimensions. In addition, the specific mechanisms affecting osteogenesis and bioengineered porous bone tissue materials are evaluated to clarify definitions and facilitate further material research and industrial applications based on previous research.

Definition of pore structure dimension

Conventional porous materials

Early in the field of bone tissue bioengineering, porous materials were mostly made by processes such as vapor-phase porogenesis (Oppenheimer and Dunand, 2010; Ji et al., 2012), blowing agent porogenesis (Kato et al., 2013; Kapat et al., 2017; Liu et al., 2017), and solid-phase porogenesis (Maya et al., 2012; Hsu et al., 2013; Yamanoglu et al., 2016), in which the porosity of porous materials can usually be precisely controlled by the volume of added porogenic agents or binders. However, the morphology of the internal pore structure and the pore size of porous materials cannot be effectively controlled. Considering the irregular pore shape, uneven distribution, and easy formation of closed pores in porous materials, technicians use spherical porogenic agents filled with regular particles and controlled particle size to form a uniformly distributed and regular morphological pore structure in porous materials (Jia et al.,

2015). The preparation of porous materials by controlled particle porogenic agents enables the precise control of the morphology of the pore structure within porous materials, further making the pore size in the pore structure an important parameter to influence the mechanical and biological properties of these materials (Imwinkelried, 2007; Zhao et al., 2016). This molding technique involves mixing the granular material with the target material, casting, molding, and then removing the granular material by solution elution or high-temperature sintering after the material is formed to finally form a porous structure within the material with the outline of a granular material (Ye and Dunand, 2010). From the summary analysis, we concluded that the pore diameter in this type of porous material should represent the size of the 3D space inside the pore structure of the material, which is used to evaluate the maximum size to which the cells within the pore structure can grow (Cao et al., 2020). The pore throat size represents the size of the 2D planar channel used to achieve communication between adjacent pore structures on the surface of porous materials. It is used to evaluate the maximum planar size of the pore structure that can accommodate cells growing into the pore structure (Otsuki et al., 2006). Although the shape of porous materials produced by the conventional process can only achieve a simple geometry, this defect restricts the industrial application of these materials in bone tissue engineering. However, this method to characterize the pore structure dimension using both pore size and pore throat size is straightforward and should be used as an important reference and guide for defining pore structure dimensions.

Additive manufacturing of porous materials

The application of material-extrusion-based 3D printing (ME-3DP), such as fused deposition modeling (FDM) (Diez-Escudero et al., 2020) and direct ink writing (DIW) (Lewis, 2006) in the preparation of bioengineered porous bone tissue materials has, to some extent, solved the problems of inability to achieve a specific shape and inaccurate connectivity of the pore structure of porous materials prepared by conventional processes (Li et al., 2021). This technique is mainly used to extrude solid or slurry materials in 2D planes according to a specific scanning path and form a planar structure with pore morphology. It is followed by superimposing multiple planar structures with a certain thickness in the Z axis sequentially to finally build pore structures of porous materials (Cubo-Mateo and Rodriguez-Lorenzo, 2020; Sakthibirami et al., 2021; Yang et al., 2021; Kilian et al., 2022). Considering this molding technology's characteristics, the prepared material's structure in the 2D plane can be controlled. Thus, its structure definition in the 2D plane is also accurate, but the 3D space structure cannot be accurately defined and positioned because the layer thickness cannot be precisely controlled. Therefore, the literature continues

to use pore size as a specific parameter to define the pore structure dimension, defining it as the spacing of two parallel rods in a 2D plane (Shanjani et al., 2017; Gupta et al., 2021). However, some literature ignores the rod diameter size and uses the scan spacing directly as the pore size (Kilian et al., 2022). Nevertheless, according to the original definition of pore size and pore throat size, such parameters should be defined as the pore throat size in the 2D plane, not pore size in 3D space. The fundamental reason for this discrepancy is the objective drawback of the preparation technique of insufficient strength in molding and accuracy after molding.

With further developments in additive manufacturing technology, preparation techniques such as DLP (Schmidleithner et al., 2019), SLM (Yang et al., 2018; Pei et al., 2020), or EBM (Nune et al., 2017a; Zhang et al., 2020) have been gradually applied to bioengineered porous bone tissue materials, benefiting from the high-precision material formation of light-cured materials or powder materials by high-precision light sources or energy beams. In this context, the most typical and widely used technology is SLM, which mainly uses a micron laser beam to melt the micron powder material with high precision. Then the 2D plane structure is prepared by the movement of the laser beam, and the overall target structure is finally prepared by layer-by-layer processing (Wei et al., 2017). The advantages of these techniques over ME-3DP are the improved precision processing accuracy and the ability to build porous structures with controlled diameter, length, and tilt angle support structures in the Z axis through the individual superposition of 2D point structures in the Z axis. This results in a complete 3D space morphology in the porous structures; thus, most printed porous structures have controlled, regular, and connected 3D space shapes (Li et al., 2018a; Li et al., 2018b; Li et al., 2020c). Furthermore, as porous materials are prepared by relying on this molding technology, the control of various parameters of the structure during the molding process is more accurate, contributing to the appearance of different pore structure dimension definitions in the same type of structure. We found two definitions of pore diameter that follow the conventional molding process and ME-3DP, respectively, where the maximum internal tangent spherical diameter in the 3D space of the pore structure is taken as the pore diameter (Ambu and Morabito, 2019). In addition, the maximum internal tangent circular diameter in the 2D plane of the pore structure is defined as the pore diameter (Wauthle et al., 2015; Liang et al., 2022) in the relevant literature sources. According to the original definition of pore size and pore throat size, these two structures should be defined as pore size and pore throat size. Therefore, we believe this difference is the source of the current confusion in the academic community about the definition of the pore structure dimension of porous materials.

Recommended definition method

Two different ways of defining the pore structure dimensions and specific schemes were finally summarized by analyzing the

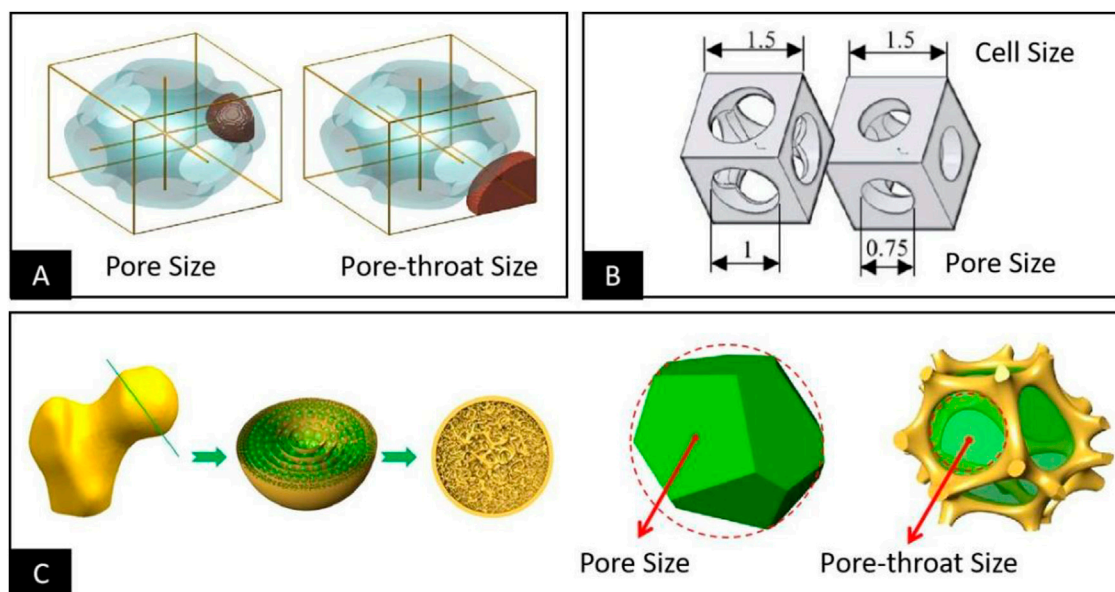


FIGURE 2

(A) Defining the maximum 3D space dimension that can be accommodated within the pore structure as the pore size and the maximum 2D plane dimension to interconnect the pore structure with other adjacent pore structures in the vicinity of the pore throat size (Afshar et al., 2016). (B) Defining the maximum 3D space dimension that can be accommodated within the pore structure as the unit cell size and the maximum 2D plane dimension to interconnect the pore structure with other adjacent structures in the vicinity as the pore size (Liverani et al., 2021). (C) Considering the structural morphology of human bone tissue, the bone trabecular structure consists of a large number of pore structures of different sizes; the pore size should be defined as the size of the 3D space structure in which the cells grow, and the pore throat diameter should be defined as the size of the 2D plane structure that allows the cells to be accommodated within the pore structure (Wang et al., 2018a).

relevant studies involving bioengineered porous bone tissue materials in recent years. The first one defines the maximum 3D space dimension that can be accommodated within the smallest pore structure within the porous material as the pore size. Then it defines the maximum 2D plane dimension that interconnects the pore structure inside the porous material with other adjacent pore structures as the pore throat size, as shown in Figure 2A (Afshar et al., 2016; Jette et al., 2018; Ambu and Morabito, 2019; Wang et al., 2020; Lehder et al., 2021; Timercan et al., 2021). The second one defines the maximum 2D plane dimension of the pore within the porous material that interconnects with other adjacent pore structures as the pore diameter. It also introduces the unit cell size that contains a minimum pore structure and can be accumulated by repetition to form a complete porous material for measuring the maximum 3D spatial dimension within the pore structure, as shown in Figure 2B (Nune et al., 2017b; Melancon et al., 2017; Dallago et al., 2018; Barba et al., 2019; Liverani et al., 2021). These two methods of definition do not contradict each other in a practical sense; both describe the pore structure in 3D space and 2D plane simultaneously in different ways, and both meet the basic requirements for the pore structure dimensional characterization. However, the basic morphology of the cell is still different from that of the pore structure. Therefore, it usually contains some structures attributed to other adjacent pore

structures, leading to the problem that the unit cell size is larger than the actual value when used to describe the maximum space for cell growth within the porous structure. Based on the above reasons and combined with the basic characteristics of human bone trabeculae (Wang et al., 2018a), as shown in Figure 2C, the bone trabecular structure is composed of many pore structures. However, their pore size and distribution follow stress stimulation. The pore size in the trabecular structure should be defined as the size of the 3D spatial structure in which cells, tissues, and tissue fluids grow, while the pore throat diameter should be defined as the size of the 2D planar structure that allows cells, tissues, and tissue fluids to enter the porous structure. We believe that adopting the first definition scheme is more consistent with the practical needs of bioengineered porous bone tissue materials to define and describe pore structure.

Measurement of pore structure dimensions

Positioning method

As analyzed previously, characterizing the 3D space shape of simple, rod, interleaved structures prepared by ME-3DP is

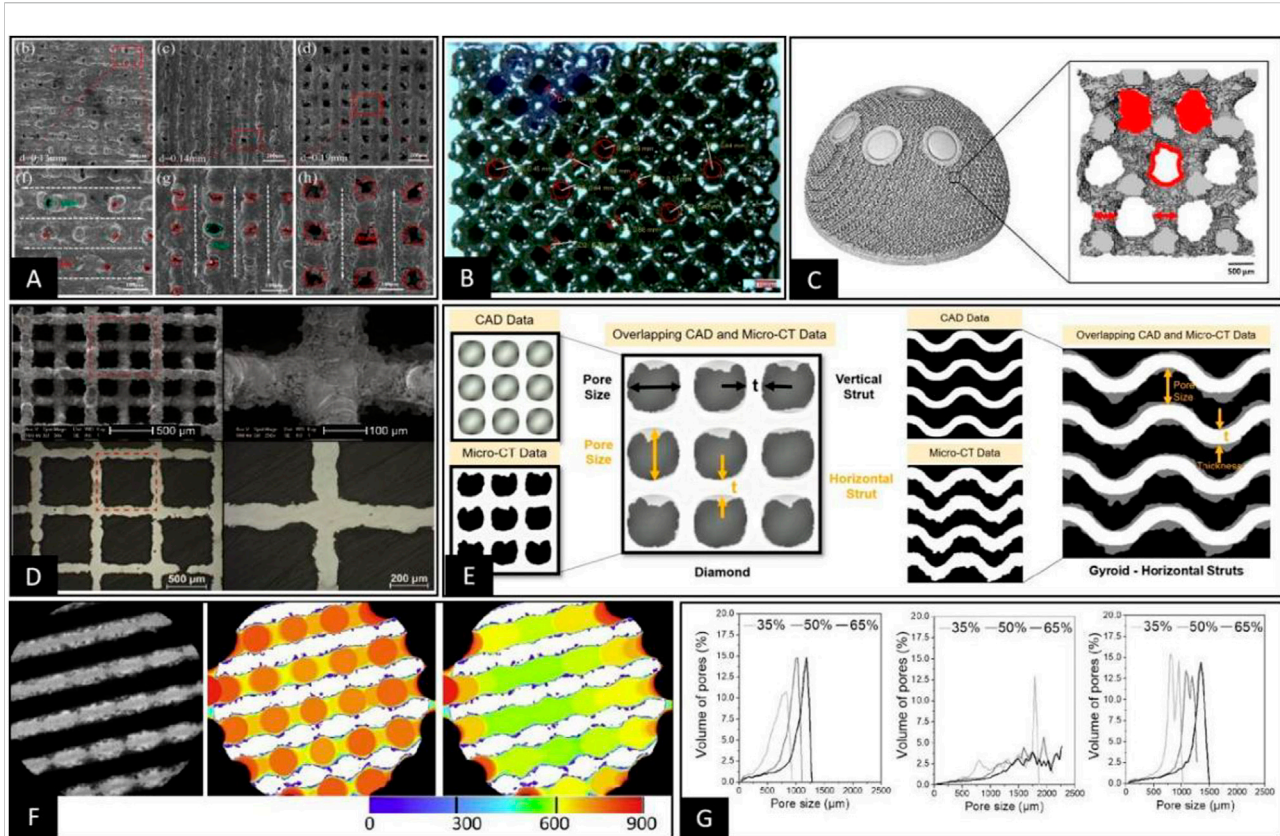


FIGURE 3

(A) Direct measurement of the inner tangent circle diameter of circular pore throats on the pore structure of porous materials prepared using SLM was performed under SEM (Lei et al., 2021). (B) Pore throat size was characterized by the 2D plane transformation of 3D space pore throats on the pore structure of porous materials prepared using EBM under a stereomicroscope, followed by measurement of the inner tangent circle diameter on the 2D plane (Moiduddin, 2018). (C) The 3D model of the pore structure of the porous material was obtained by Micro-CT, and a specific plane representing the pore throat size was selected. Then the pore throat size was measured by calculating the equivalent circle diameter of the pore throat (Dall'Ava et al., 2020). (D) The 3D pore structure was transformed into 2D planes using sample cutting, and the pore size data were measured indirectly by metallographic microscopy in 2D planes (Wauthle et al., 2015). (E) Representative cross-sections were obtained by Micro-CT, which adequately represent the pore morphology and measurements of the distance between two points or lines that are representative of the pore size within the 2D cross-section (Naghavi et al., 2022). (F,G) Using Micro-CT to obtain 2D cross-sectional images or 3D stereoscopic models of porous materials, the filling of different sizes of circular or spherical bodies was performed, as in Figure F (Taniguchi et al., 2016). Then the pore size distribution curves were plotted according to the size and number of different sizes of circular or spherical bodies, as in Figure G (Diez-Escudero et al., 2020).

difficult due to the inability to control the Z axis effectively. Therefore, to further position the pore size, most of the measurements in such porous materials are performed only for the pore throat size in the 2D plane (Lee et al., 2018). The rod lengths and thicknesses usually exhibit relatively disparate differences during the pore throat diameter measurement of this porous structure. Therefore, usually, two different sizes of pore throats are characterized separately in the horizontal and vertical planes, with the horizontal pore throat consisting of the lengths of interwoven rods in the X and Y axes and the vertical pore throat consisting of the thickness and length of the rod (Shanjani et al., 2017; Cubo-Mateo and Rodriguez-Lorenzo, 2020; Diaz-Gomez et al., 2020). Therefore, it is accurate to describe the pore throat size simply by using

one of the parameter dimensions of length and width when the pore throat shape is described as a square (Hossein Ehsani et al., 2022). However, when its pore throat shape is described as a rectangle, its length and width should be reported separately, and the pore throat size should be expressed as length*width (Lee et al., 2018). However, considering the possibility of collapse and deformation of the material during the preparation process, which leads to an irregular shape of the hole throat (Baptista and Guedes, 2021), it is recommended to evaluate the pore throat size using the inner tangent circle diameter or equivalent circle diameter for such structures.

In contrast, pore structures made by high-precision additive manufacturing technologies, such as SLM and

EBM, have controllable dimensions in the X, Y, and Z axes and form a clear 3D space within the porous structure. This allows the pore size and the pore throat size of such structures to be clearly distinguished and located. For example, when the pore throat has a 2D plane geometry, such as octahedron type, in the measurement process, it is only necessary to select the 2D plane where the pore throat is located to measure the inner tangent circle of the pore throat, as shown in Figure 3A (Lei et al., 2021). However, when the pore structure is diamond-shaped, the quadrilateral structure forming the pore throat is distributed in 3D space. Therefore, the vertical direction of the maximum projected area of the quadrilateral structure should be selected to observe the pore throat size as a method to convert the 3D space to a 2D plane and then measure the inner tangent circle of the pore throat, as shown in Figures 3B,C (Dall'Ava et al., 2020; Moiduddin, 2018). However, when the pore throat is not a simple 2D structure or a 3D structure that can be planarly transformed, such as the TPMS-G type where the pore throat behaves as a spiral 3D channel, the results obtained by measuring the pore throat size only from a 2D plane do not necessarily match the actual situation (Zaharin et al., 2018; Wang et al., 2021; Su et al., 2022). Considering the gradual deepening of pore structure research, the complex shape of the pore structure will continue to be clarified. However, the complex 3D shape of the pore throat for accurately positioning the size poses a significant challenge, pending further research.

However, pore size, as a 3D space parameter, can be defined, located, and measured only when the 3D space form of the pore structure is complete and specific. Based on the localization methods for pore throat size summarized in the previous section, it is currently relatively difficult to perform pore size localization under 3D space conditions using a direct microscopic view. However, since the pore in the 3D state is the same as the pore throat in the 3D state, the transformation of the 2D plane can be performed by changing the observation angle and cutting the material when the pore structure is regular, as shown in Figure 3D (Wauthle et al., 2015; Zhang et al., 2020). However, in the 3D state, the pore has a more complex morphological structure compared to the pore throat, and sometimes it is only used to measure the pore size by considering the distance between two rods or walls that can roughly represent the pore size (Gorgin Karaji et al., 2017; Ma et al., 2019; Naghavi et al., 2022). Nevertheless, there are some special structures, such as TPMS-Split *p*, lidinoid types, and bionic trabecular structures, where it is impossible to specify the morphology of the aperture, making it impossible to determine the specific dimensions from 2D or 3D morphology based on the relative relationship between points, lines, and surfaces (Wang et al., 2018a; Zhao et al., 2021; Zhu et al., 2021). Therefore, in this situation, it is necessary to introduce the technical means in the 3D space

state to measure the pore size directly based on the definition of pore size for the dimensions of the tangential spheres within the pore structure. This approach reduces the human bias in selecting 2D cross-sections and viewing the orientation; however, the accuracy of measurements in this technique depends heavily on the accuracy of Micro-CT scans and data processing.

Measurement technology

The oldest pore size detection methods mostly started in the chemical and physical fields, including Mercury intrusion porosimetry (Zhang et al., 2013; Jiao et al., 2020). Although they can obtain pore size data more accurately, they are not suitable for detecting bioengineered bone materials because they are invasive methods and may be associated with other biological risks. In addition, since the core purpose of bioengineered bone materials is to realize the industrialization and clinical application of these materials, their detection method should be non-destructive, rapid, and accurate. Current methods for detecting pore size or pore throat size in bioengineered bone tissue materials include direct measurements performed by optical instruments such as SEM (Shuai et al., 2018; Lei et al., 2021) and indirect measurements relying on scanning devices such as Micro-CT (Cheng et al., 2014; Li et al., 2018a; Li et al., 2020c). Optical measuring instruments are, in essence, only a direct way of measuring in 2D plane conditions because their images cannot perceive the depth of the 3D space. Therefore, these techniques are only suitable for measuring 2D plane dimensions or 3D space dimensions that can be transformed through 2D planes (Wauthle et al., 2015; Shuai et al., 2018; Lei et al., 2021; Wu et al., 2021). This measurement method also has unique advantages. For example, the accuracy of direct measurement by optical instruments is significantly higher than that of Micro-CT-based 2D and 3D imaging measurements when the measurement target and evaluation method are specified. However, with the gradual advancement of pore structure-related research, the pore structure design is becoming increasingly complex. With the application of bionic non-regular pore structure and more different kinds of TPMS, the method used to measure pore structure dimension parameters, such as pore size or pore throat size on a 2D plane relying solely on optical instruments, is gradually replaced by other techniques.

Optical instruments are limited to 2D plane measurements in direct view and require destructive methods such as cutting or polishing. However, if planar switching of internal spatial structures is required, a highly accurate layer-by-layer scanning method of materials, such as Micro-CT or industrial CT, allows the acquisition of tomographic images for characterizing the layered morphology of materials and

measuring local planes on tomographic 2D images (Yavari et al., 2013; Li et al., 2018a; Li et al., 2018b; Schmidleithner et al., 2019; Li et al., 2020c). The approach is, in essence, similar to that of direct measurement by optical instruments in the 2D plane, where the actual data measurement process is still highly dependent on the selection of 2D cross-section and view orientation, but its selection for 2D images are more accessible and accurate, as shown in Figure 3E (Otsuki et al., 2006; Dong et al., 2020; Naghavi et al., 2022). Because of the limitations of this technical solution in terms of subjective judgment, the aperture diameter is measured using the maximal covering spheres (MCS) method after the 3D reconstruction of images based on techniques such as Micro-CT. This automatic measurement technique works with spheres of different diameters by moving and filling the space structure until the boundary conditions are reached after the spheres form a tangent to the structure. Then the diameters of the spheres are included in the statistics and counted, eventually resulting in aperture diameter distribution curves related to the diameter and number of spheres, as shown in Figure 3F (Jones et al., 2007; Taniguchi et al., 2016; Timercan et al., 2021). In this measurement, the definition of pore size and pore throat diameter is ignored. Therefore, in the pore size distribution curves, we can observe a single pore structure, usually with a double or multiple peak pattern, respectively representing pore size and pore throat size, as shown in Figure 3G (Diez-Escudero et al., 2020). Another comparable technique is automatically measuring the trabecular separation (Tb.Sp) from Micro-CT 3D-reconstructed post data by software and using it to measure the pore size (Li et al., 2019b). Both of the above approaches are purely based on a comprehensive test of the 3D space size or distance, reflecting the approximate size of the pore and pore throat path in the form of average values and distribution curves. This type of measurement can accomplish pore size measurements for complex pore structures such as bone tissue trabecular structures, irregular structures, TPMS, gradient structures, and other porous scaffolds (Cheng et al., 2014; Wang et al., 2018a; Corona-Castuera et al., 2021; Zhu et al., 2021). However, this is more consistent with our specific needs for evaluating porous structures since the underlying logic of MCS in its measurement approach simulates the maximum size of cells that can pass and grow within the pore structure. In addition, clear distribution curves of pore and pore throat size can be obtained. Based on the above study, we believe that in the early development stage of porous structures and actual product quality sampling, techniques such as Micro-CT should be used to describe the pore size and pore throat size distribution curves. However, in the subsequent product treatment control process, optical instruments should be used for rapid and low-cost measurement of some of these structures that are easy to observe directly.

Significance of pore structure dimension

Function of pore throat size

Since the relationship between pore throat size and pore size is determined by the shape of the pore structure, controlling changes in pore throat size usually results in changes in parameters such as pore size, porosity, and elastic modulus. Therefore, there are reports that independent control of the pore throat size parameters depends on using a single 2D plane structure with a deficiency of 3D space for *in vitro* cell tests. On this basis, studies have shown that when the pore throat size range is 50–100 μm , cells can form a membrane across the whole pore surface through morphological changes to block the pore, affecting the nutrient interaction and cell entry inside the pore structure, as shown in Figure 4A (Egles et al., 2013; Lei et al., 2021). However, when the pore throat size is $> 200 \mu\text{m}$, the cells no longer grow across the pores but show growth along the rod direction, and there is cell growth into the porous structure below its surface pores, as shown in Figure 4B (Liu et al., 2020; Sakthiabirami et al., 2021). This conclusion reflects the original implication of the pore throat size, which is a passage for cell entry. This size determines whether the cells can successfully enter the interior portion of the porous scaffold to perform their actual function (Deb et al., 2018). When the pore structure and pore throat size meet the above requirements, studies have shown that the smaller the pore throat size, the better the cell adhesion, proliferation, and differentiation for bone formation, as shown in Figure 4C (Yang et al., 2021). The main reason is that since the pore throat size reflects the angle, distance, and curvature between rods or walls in the pore structure, the specific mechanism by which the pore throat size causes differences in the cellular state may be related to differences in intracellular stress stimulation due to the morphology of cell adhesion and growth (Bershadsky et al., 2003; Rumpler et al., 2008; Bidan et al., 2013). On this basis, Fukuda et al. (2011) prepared cubic columnar canals of different sizes within the same scaffold to investigate the effect of pore throat size on the osteogenic effect of the scaffold pore structure *in vivo*. The results showed that the best internal bone tissue formation was achieved at a scaffold pore throat size of 500 μm and 5 mm from the end face, as shown in Figure 4D. It was also suggested that this might be related to the circulation of body fluids within the scaffold at different pore throat diameters. This conclusion further suggests that the pore throat size also interferes with the bone tissue formation within the porous material to some extent through the circulation of body fluids (Takahashi and Tabata, 2004; Van Bael et al., 2012). Considering the above studies, we believe that the main influence of pore throat size on bioengineered porous bone materials is mediated by

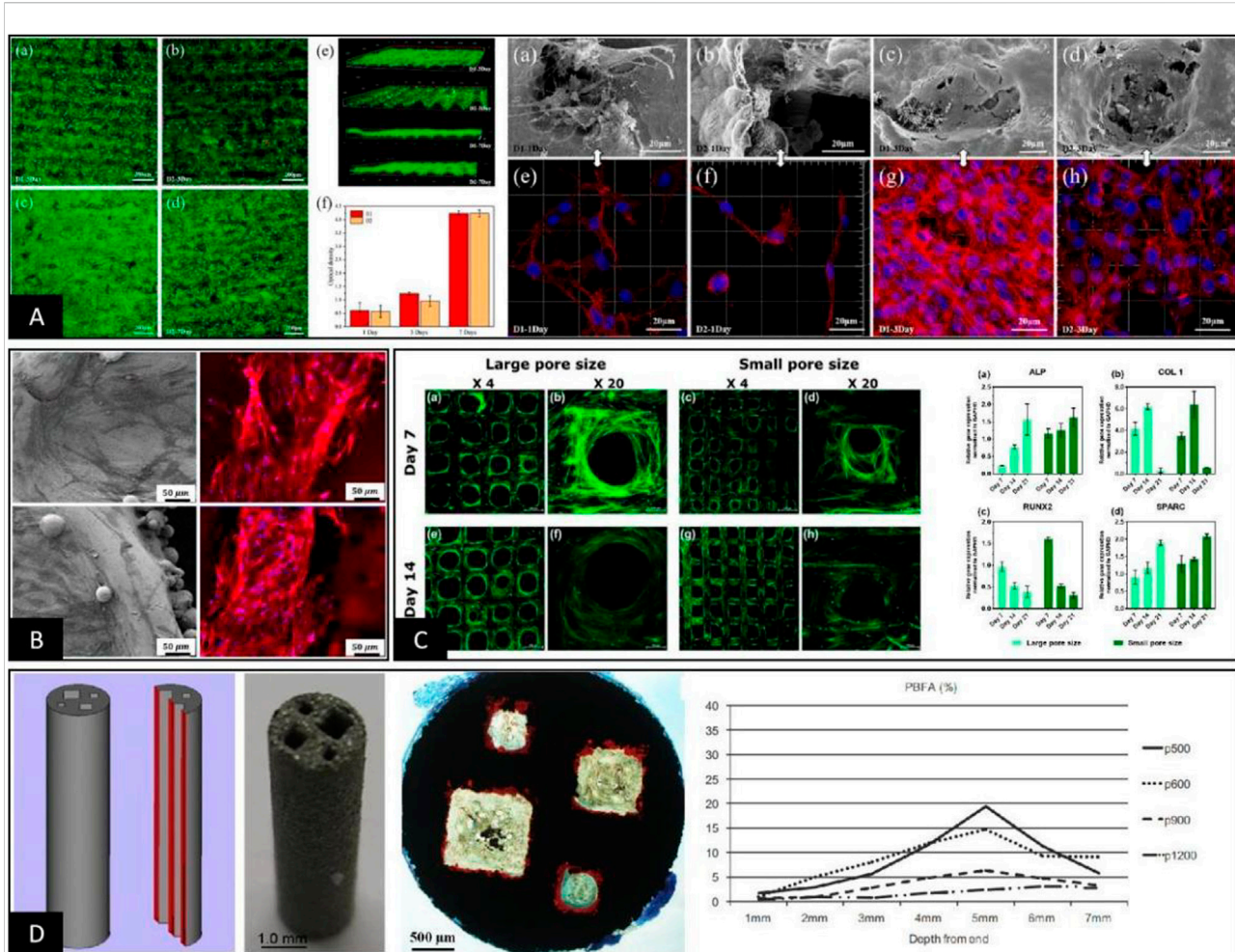


FIGURE 4

(A) When the pore throat sizes were 33 μm and 81 μm , the cells inoculated on the surface of the scaffold grew across the top of the pore structure and blocked the surface pore structure so that other cells could not enter the pore structure (Lei et al., 2021). (B) When the pore throat diameter was $>100 \mu\text{m}$, the cells grew on the internal rod or wall surface of the pore structure, and the pore throat of pore structure was not blocked by cell coverage, maintaining a good environment for nutrient exchange (Liu et al., 2020). (C) When the pore throat size met the basic requirements for cell growth into the pore, the smaller the pore throat size was, the better the state of cell adhesion, proliferation, and differentiation into bone, the mechanism of which may be related to the morphological differences in cell growth on the rod (Yang et al., 2021). (D) Cubic columnar pores with different pore throat sizes were significantly different in the osteogenic area within each pore during *in vivo* animal experiments, and the area of bone tissue varied depending on the distance from the end surfaces (Fukuda et al., 2011).

controlling whether cells can enter the pore structure properly and circulating body fluids to influence cell adhesion and morphology.

Function of pore size

Comparatively, *in vitro* cellular and *in vivo* animal studies on the effect of pore size on bone ingrowth and osteogenesis of porous scaffolds by pore structure shape or pore size are more complex than those related to pore throat size. In vitro cell studies, mostly after inoculating cells on the surface of different porous materials, the pore structure is adjusted to change the cell

adhesion state and the intracellular stress, affecting the physiological activity of the cells (Diez-Escudero et al., 2020; Wu et al., 2022). This is the same mechanism by which the pore throat size interferes with cell adhesion and growth on the surface of porous scaffolds. However, Papaefstathiou et al. (2022) showed differences in early cell proliferation and final total cell number due to differences in surface morphology and surface area between the two groups of solid and porous disc samples. However, their normalized treatment did not show significant differences in ALP expression. In addition, Liang et al. (2022) reported no significant difference in the proliferation activity of cells inoculated on the surface of the materials, while there were differences in the pore size and pore

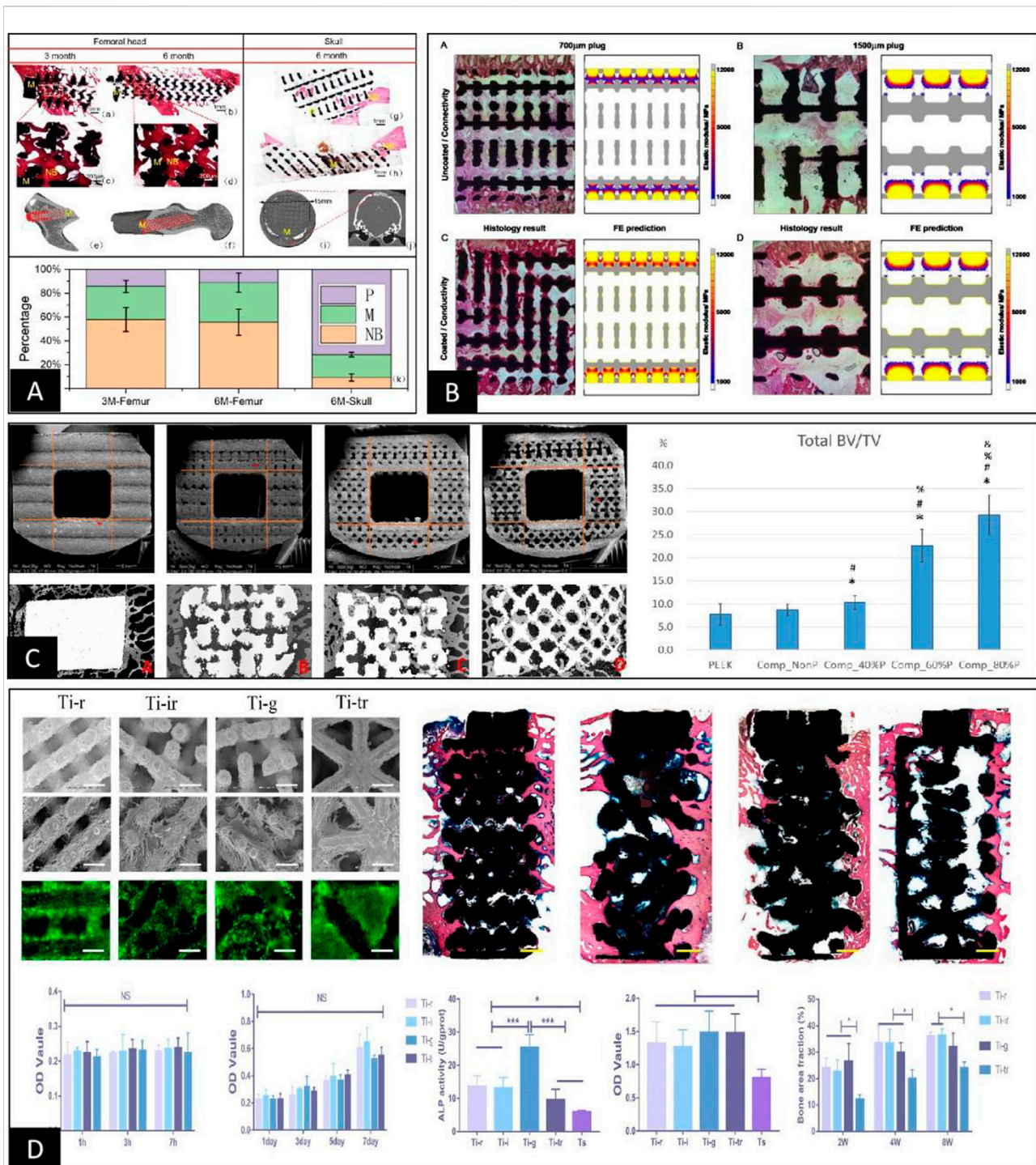


FIGURE 5

(A) Porous scaffolds with the same pore structure implanted in the femur and skull of the same animal were very different in the final osteogenic effect due to the difference in their local skeletal stresses (Pei et al., 2020). (B) Comparative analysis between finite element stress analysis and animal implantation experiments of porous scaffolds showed that the osteogenic region within the porous scaffold clearly correlated with stress distribution (Cheong et al., 2018). (C) The final post-implantation osteogenic effect of porous scaffolds with different elastic moduli constructed solely by rod diameter control was inversely correlated with the elastic modulus (Tsai et al., 2021). (D) After constructing porous scaffolds with different elastic moduli simply by different pore structures, their cellular assays showed no differences in cell adhesion, proliferation, and quantitative analysis of calcium nodules between the groups except for ALP activity. In contrast, animal tests showed differences in the final osteogenic effect between the groups, with no apparent correlation with the differences in elastic modulus and ALP activity of the porous scaffolds (Wang et al., 2018b).

morphology of porous materials. Wang et al. (2018b) carried out comprehensive cellular and animal experiments on porous scaffolds with four different pore structures. The results showed that the osteogenic effect within the porous scaffolds did not significantly correlate with cell adhesion, proliferation, and differentiation statuses. Therefore, we believe that because *in vitro* cellular experiments cannot simulate the complex growth environment and stress state of cells within the pore structure of porous materials, they are limited to studying the surface and 3D morphology of the pore structure of porous scaffolds. In addition, the results at the cellular level alone do not accurately represent the actual effects of porous materials after implantation *in vivo*. This is in general agreement with the conclusion reached by Karageorgiou and Kaplan, (2005) that the osteogenic effect of the pore structure of porous materials has two opposite tendencies *in vivo* and *in vitro*. However, with technological developments, some studies have been conducted on hydrogels to achieve a 3D co-culture system between porous scaffolds and cells. The results of these *in vitro* cell experiments will be closer to the actual *in vivo* state (Ji et al., 2020; Ma et al., 2021). Meanwhile, hydrodynamics is gradually becoming a new hotspot in the study of porous materials, where changes in pore shape, pore throat size, and pore size interfere with the permeability or fluid environment within the porous structure (Ma et al., 2019; Chao et al., 2021; Timercan et al., 2021), ultimately affecting changes in cell adhesion and proliferation (Markhoff et al., 2015; Liu et al., 2020). With the innovation of such experimental approaches, it will become a trend to further elucidate the mechanisms related to the cell growth condition within porous materials by constructing a bionic growth environment and applying specific mechanical stimuli to the cells within porous scaffolds *in vitro*.

At this stage, to make up for the shortcomings of *in vitro* cell experiments, researchers usually supplement *in vitro* animal experiments for further validation. However, the experimental results obtained through animal experiments are still highly controversial, mainly because parameters such as pore throat diameter, porosity, and elastic modulus change while adjusting the pore structure and pore size in 3D spaces (Zadpoor, 2015). First, even when porous scaffolds with the same material, preparation process, and pore structure are implanted in the skull and femur of the same animal, the effect of osteogenesis within the porous material is not uniform, mainly due to the different stress stimuli on the scaffold at different implantation sites, as shown in Figure 5A (Walsh et al., 2019; Pei et al., 2020). Furthermore, when a clear stress stimulus is missing at the implantation site, the osteogenic outcome is relatively poor, suggesting that osteogenesis within porous materials may be positively correlated with stress stimuli (Li et al., 2015; Taniguchi et al., 2016; Li et al., 2021; Lu et al., 2022b). The idea was also confirmed by Tsai et al. (2021) in an *in vivo* study by designing porous materials with the same pore size and different rod sizes. The results showed that the smaller the modulus of elasticity and

the higher the porosity, the better the percentage of bone tissue volume within the porous material, as shown in Figure 5C. In addition, according to Cheong et al. (2018), the distribution range of osteogenesis within the porous scaffold observed by histomorphology in animal experiments was highly consistent with the stress distribution region within the pore structure under finite element analysis. This finding further suggests that the specific mechanism by which the pore structure affects osteogenesis may be related to the difference in the elastic modulus under the intervention of pore size, as shown in Figure 5B. However, Shah et al. (2016) showed that porous scaffolds using the same pore structure and different materials had essentially the same volume fraction of bone tissue at each site within both scaffolds after implantation and only differed in the integration of the bone–metal interface. In addition, Wang et al. (2018b) undertook comprehensive animal experiments using porous scaffolds with four pore structures. The results showed no clear linear relationship between the osteogenic effect within the porous scaffold and parameters such as pore size, porosity, and elastic modulus, as shown in Figure 5D. Therefore, based on the results of different animal experimental osteogenesis analyses, we believe there is a clear correlation between the osteogenic effect within porous materials and the pore size. However, the specific mechanism of action is often related to the pore throat size, elastic modulus, and other related parameters that are not yet completely clear and still need further in-depth studies.

Conclusion

We analyzed the origin and internal logic of different definition methods for the evolution of pore structure dimension characterization in bioengineered porous bone materials and proposed that it is more practical to characterize pore structure dimension by pore throat size and pore size together.

- 1) The pore throat size is the maximum cross-sectional diameter of the penetration channel of the cells into the interior portion of the pore structure. It is the maximum internal tangent circle diameter in the 2D plane at the surface of the pore structure. It can be calculated using SEM or Micro-CT or other methods by directly measuring the internal tangent circle diameter or cross-sectional equivalent circle diameter under 2D conditions by selecting a specific plane or cross-section.
- 2) The pore diameter is the maximum space diameter that can allow the cells to grow after entering the interior portion of the pore structure. It is the maximum internal tangential sphere diameter in the 3D spatial environment within the pore structure and can be measured by the rod or wall spacing equivalent to the pore diameter within the pore structure

using SEM or Micro-CT or based on the reconstructed 3D model after Micro-CT scanning. The software simulation can be used to obtain its internal pore diameter distribution data. However, it is worth noting that the pore size distribution curve obtained in this way includes the pore throat size.

At the same time, based on the joint definition of pore throat size and pore size, the specific functions and mechanisms of their respective roles in bioengineered porous bone materials were analyzed. The results showed that both pore throat size and pore size could affect the cell growth state and the final osteogenesis in porous scaffolds in different ways.

1) The pore throat size, which is the size of the channel that characterizes the internal access of cells to the pore structure, directly determines whether the cells can enter the pore structure smoothly. It also determines the specific state of the circulation of body fluids between the internal and external shelf tissues of the pore structure, which influences the specific process of osteogenesis within the pore structure in the form of nutrient supply. At the same time, the morphology and size of the pore throat, as a direct morphological structure perceived by cells adhering to the surface of the pore structure, can also affect the specific functions of cell proliferation and differentiation by changing the cell adhesion status. However, this conclusion is limited to the cellular level and has not been confirmed in animal experiments.

2) As a characterization of the size of the space in which cells can grow within the pore structure, the pore size also represents the pore structure dimensions. The function of pore size at the cellular level is similar to that of pore throat size in that it changes the cellular adhesion state through morphology and size, affecting the specific functions of cell proliferation and differentiation. However, the conclusions of such cellular-level studies are not fully consistent with the results of actual porous scaffold implantation *in vivo*, mainly because the cellular experiments lack the complex physiological environment and the mechanical stimuli *in vivo*. The function of the pore size *in vivo* is to co-intervene with parameters such as pore shape and rod diameter in the elastic modulus of the material to change the distribution of stress stimuli within the porous scaffold and influence the osteogenic state within the pore structure.

Currently, bioengineered porous bone tissue materials and their related products are initially applied in the first line of clinical practice. However, there are still various problems, such

as intraoperative sinking, non-fusion of bone graft, pseudo-joint formation, postoperative implant infection, *etc.* The root cause of these problems is the lack of in-depth research on the pore structure and the inability to clarify the specific mechanisms of osteogenesis, vascularization, and fibrogenesis within the pore structure of porous materials, which cannot be precisely controlled and regulated. This paper proposed the characterization of pore structure dimension by pore size and pore throat size by reviewing, summarizing, and unifying the specific definition and measurement methods of pore size and pore throat size. On this basis, the possible roles and mechanisms of specific parameters of pore structure dimension that influence osteogenesis within porous materials were proposed to provide further theoretical references for the subsequent in-depth studies of pore structure.

Author contributions

WP contributed to conception and writing, YL contributed to proofreading, and CW contributed to conception and funding. All the authors contributed to the article and approved the submitted version.

Acknowledgments

Authors gratefully acknowledge the partial financial support from The Project of Health Commission in Hunan Province (20201961), The Natural Science Foundation in Hunan Province (2022JJ30537).

Conflict of interest

The authors declare that the research was conducted in the absence of any commercial or financial relationships that could be construed as a potential conflict of interest.

Publisher's note

All claims expressed in this article are solely those of the authors and do not necessarily represent those of their affiliated organizations, or those of the publisher, the editors and the reviewers. Any product that may be evaluated in this article, or claim that may be made by its manufacturer, is not guaranteed or endorsed by the publisher.

References

- Afshar, M., Anaraki, A. P., Montazerian, H., and Kadkhodapour, J. (2016). Additive manufacturing and mechanical characterization of graded porosity scaffolds designed based on triply periodic minimal surface architectures. *J. Mech. Behav. Biomed. Mater* 62, 481–494. doi:10.1016/j.jmbbm.2016.05.027
- Ahmadi, S. M., Kumar, R., Borisov, E. V., Petrov, R., Leeflang, S., Li, Y., et al. (2019). From microstructural design to surface engineering: A tailored approach for improving fatigue life of additively manufactured meta-biomaterials. *Acta Biomater.* 83, 153–166. doi:10.1016/j.actbio.2018.10.043
- Ambu, R., and Morabito, A. E. (2019). Modeling, assessment, and design of porous cells based on schwartz primitive surface for bone scaffolds. *ScientificWorldJournal* 2019, 7060847. doi:10.1155/2019/7060847
- Amin Yavari, S., Ahmadi, S. M., van der Stok, J., Wauthle, R., Riemsag, A. C., Janssen, M., et al. (2014). Effects of bio-functionalizing surface treatments on the mechanical behavior of open porous titanium biomaterials. *J. Mech. Behav. Biomed. Mater* 36, 109–119. doi:10.1016/j.jmbbm.2014.04.010
- Arabnejad, S., Burnett Johnston, R., Pura, J. A., Singh, B., Tanzer, M., and Pasini, D. (2016). High-strength porous biomaterials for bone replacement: A strategy to assess the interplay between cell morphology, mechanical properties, bone ingrowth and manufacturing constraints. *Acta Biomater.* 30, 345–356. doi:10.1016/j.actbio.2015.10.048
- Baptista, R., and Guedes, M. (2021). Morphological and mechanical characterization of 3D printed PLA scaffolds with controlled porosity for trabecular bone tissue replacement. *Mater. Sci. Eng. C Mater. Biol. Appl.* 118, 111528. doi:10.1016/j.msec.2020.111528
- Barba, D., Alabort, E., and Reed, R. C. (2019). Synthetic bone: Design by additive manufacturing. *Acta Biomater.* 97, 637–656. doi:10.1016/j.actbio.2019.07.049
- Bershadsky, A. D., Balaban, N. Q., and Geiger, B. (2003). Adhesion-dependent cell mechanosensitivity. *Annu. Rev. Cell Dev. Biol.* 19, 677–695. doi:10.1146/annurev.cellbio.19.111301.153011
- Bidan, C. M., Kommareddy, K. P., Rumpel, M., Kollmannsberger, P., Fratzl, P., and Dunlop, J. W. (2013). Geometry as a factor for tissue growth: Towards shape optimization of tissue engineering scaffolds. *Adv. Healthc. Mater* 2, 186–194. doi:10.1002/adhm.201200159
- Cao, S., Han, J., Sharma, N., Msallem, B., Jeong, W., Son, J., et al. (2020). *In vitro* mechanical and biological properties of 3D printed polymer composite and β -tricalcium phosphate scaffold on human dental pulp stem cells. *Mater. (Basel)* 13, 3057. doi:10.3390/ma13143057
- Carluccio, D., Xu, C., Venezuela, J., Cao, Y., Kent, D., Bermingham, M., et al. (2020). Additively manufactured iron-manganese for biodegradable porous load-bearing bone scaffold applications. *Acta Biomater.* 103, 346–360. doi:10.1016/j.actbio.2019.12.018
- Chao, L., Jiao, C., Liang, H., Xie, D., Shen, L., and Liu, Z. (2021). Analysis of mechanical properties and permeability of trabecular-like porous scaffold by additive manufacturing. *Front. Bioeng. Biotechnol.* 9, 779854. doi:10.3389/fbioe.2021.779854
- Chen, Y. W., Shen, Y. F., Ho, C. C., Yu, J., Wu, Y. A., Wang, K., et al. (2018). Osteogenic and angiogenic potentials of the cell-laden hydrogel/mussel-inspired calcium silicate complex hierarchical porous scaffold fabricated by 3D bioprinting. *Mater. Sci. Eng. C Mater. Biol. Appl.* 91, 679–687. doi:10.1016/j.msec.2018.06.005
- Cheng, A., Humayun, A., Cohen, D. J., Boyan, B. D., and Schwartz, Z. (2014). Additively manufactured 3D porous Ti-6Al-4V constructs mimic trabecular bone structure and regulate osteoblast proliferation, differentiation and local factor production in a porosity and surface roughness dependent manner. *Biofabrication* 6, 045007. doi:10.1088/1758-5082/6/4/045007
- Cheong, V. S., Fromme, P., Mumith, A., Coathup, M. J., and Blunn, G. W. (2018). Novel adaptive finite element algorithms to predict bone ingrowth in additive manufactured porous implants. *J. Mech. Behav. Biomed. Mater* 87, 230–239. doi:10.1016/j.jmbbm.2018.07.019
- Cockerill, I., Su, Y., Sinha, S., Qin, Y. X., Zheng, Y., Young, M. L., et al. (2020). Porous zinc scaffolds for bone tissue engineering applications: A novel additive manufacturing and casting approach. *Mater. Sci. Eng. C Mater. Biol. Appl.* 110, 110738. doi:10.1016/j.msec.2020.110738
- Corona-Castuera, J., Rodriguez-Delgado, D., Henao, J., Castro-Sandoval, J. C., and Poblano-Salas, C. A. (2021). Design and fabrication of a customized partial hip prosthesis employing CT-scan data and lattice porous structures. *ACS Omega* 6, 6902–6913. doi:10.1021/acsomega.0c06144
- Cubo-Mateo, N., and Rodriguez-Lorenzo, L. M. (2020). Design of thermoplastic 3D-printed scaffolds for bone tissue engineering: Influence of parameters of "hidden" importance in the physical properties of scaffolds. *Polym. (Basel)* 12, 1546. doi:10.3390/polym12071546
- Dall'Ava, L., Hothi, H., Henckel, J., Di Laura, A., Shearing, P., and Hart, A. (2020). Characterization of dimensional, morphological and morphometric features of retrieved 3D-printed acetabular cups for hip arthroplasty. *J. Orthop. Surg. Res.* 15, 157. doi:10.1186/s13018-020-01665-y
- Dallago, M., Fontanari, V., Torresani, E., Leoni, M., Pederzoli, C., Potrich, C., et al. (2018). Fatigue and biological properties of Ti-6Al-4V ELI cellular structures with variously arranged cubic cells made by selective laser melting. *J. Mech. Behav. Biomed. Mater* 78, 381–394. doi:10.1016/j.jmbbm.2017.11.044
- Deb, P., Deoghare, A. B., Borah, A., Barua, E., and Das Lala, S. (2018). Scaffold development using biomaterials: A review. *Mater. Today Proc.* 5, 12909–12919. doi:10.1016/j.matpr.2018.02.276
- Deering, J., Dowling, K. I., DiCecco, L. A., McLean, G. D., Yu, B., and Grandfield, K. (2021). Selective Voronoi tessellation as a method to design anisotropic and biomimetic implants. *J. Mech. Behav. Biomed. Mater* 116, 104361. doi:10.1016/j.jmbbm.2021.104361
- Diaz-Gomez, L., Elizondo, M. E., Kontoyiannis, P. D., Koons, G. L., Dacunha-Marinho, B., Zhang, X., et al. (2020). Three-dimensional extrusion printing of porous scaffolds using storable ceramic inks. *Tissue Eng. Part C Methods* 26, 292–305. doi:10.1089/ten.tec.2020.0050
- Diez-Escudero, A., Harlin, H., Isaksson, P., and Persson, C. (2020). Porous polylactic acid scaffolds for bone regeneration: A study of additively manufactured triply periodic minimal surfaces and their osteogenic potential. *J. Tissue Eng.* 11, 204173142095654. doi:10.1177/2041731420956541
- Dong, J., Li, Y., Lin, P., Leeflang, M. A., van Asperen, S., Yu, K., et al. (2020). Solvent-cast 3D printing of magnesium scaffolds. *Acta Biomater.* 114, 497–514. doi:10.1016/j.actbio.2020.08.002
- Dziazduszevska, M., and Zielinski, A. (2021). Structural and material determinants influencing the behavior of porous Ti and its alloys made by additive manufacturing techniques for biomedical applications. *Mater. (Basel)* 14, 712. doi:10.3390/ma14040712
- Egles, C., Joly, P., Duda, G. N., Schöne, M., Welzel, P. B., Freudenberg, U., et al. (2013). Geometry-driven cell organization determines tissue growths in scaffold pores: Consequences for fibronectin organization. *PLoS ONE* 8, e73545. doi:10.1371/journal.pone.0073545
- Fukuda, A., Takemoto, M., Saito, T., Fujibayashi, S., Neo, M., Pattanayak, D. K., et al. (2011). Osteoinduction of porous Ti implants with a channel structure fabricated by selective laser melting. *Acta Biomater.* 7, 2327–2336. doi:10.1016/j.actbio.2011.01.037
- Gorgin Karaji, Z., Speirs, M., Dadbakhsh, S., Kruth, J. P., Weinans, H., Zadpoor, A. A., et al. (2017). Additively manufactured and surface biofunctionalized porous nitinol. *ACS Appl. Mater. Interfaces* 9, 1293–1304. doi:10.1021/acsami.6b14026
- Gupta, D., Vashisth, P., and Bellare, J. (2021). Multiscale porosity in a 3D printed gellan-gelatin composite for bone tissue engineering. *Biomed. Mater* 16, 034103. doi:10.1088/1748-605x/abf1a7
- Harrison, N., Field, J. R., Quondamatteo, F., Curtin, W., McHugh, P. E., and Mc Donnell, P. (2014). Preclinical trial of a novel surface architecture for improved primary fixation of cementless orthopaedic implants. *Clin. Biomech. (Bristol, Avon)* 29, 861–868. doi:10.1016/j.clinbiomech.2014.07.007
- Hedayati, R., Janbaz, S., Sadighi, M., Mohammadi-Aghdam, M., and Zadpoor, A. A. (2017). How does tissue regeneration influence the mechanical behavior of additively manufactured porous biomaterials? *J. Mech. Behav. Biomed. Mater* 65, 831–841. doi:10.1016/j.jmbbm.2016.10.003
- Hossein Ehsani, A., Rahmati, S., Nikkhoo, M., Etemadi Haghighi, S., and Haghpasahi, M. (2022). Using different unit-cell geometries to generate bone tissue scaffolds by additive manufacturing technology. *Proc. Inst. Mech. Eng. H* 236, 896–908. doi:10.1177/09544119221099786
- Hsu, H.-C., Wu, S.-C., Hsu, S.-K., Tsai, M.-S., Chang, T.-Y., and Ho, W.-F. (2013). Processing and mechanical properties of porous Ti-7.5Mo alloy. *Mater. Des.* 47, 21–26. doi:10.1016/j.matdes.2012.12.043
- Huang, B., Vyas, C., Byun, J. J., El-Newehy, M., Huang, Z., and Bartolo, P. (2020). Aligned multi-walled carbon nanotubes with nanohydroxyapatite in a 3D printed polycaprolactone scaffold stimulates osteogenic differentiation. *Mater. Sci. Eng. C Mater. Biol. Appl.* 108, 110374. doi:10.1016/j.msec.2019.110374
- Imwinkelried, T. (2007). Mechanical properties of open-pore titanium foam. *J. Biomed. Mater. Res.* A 81, 964–970. doi:10.1002/jbm.a.31118
- Jette, B., Brailovski, V., Dumas, M., Simoneau, C., and Terriault, P. (2018). Femoral stem incorporating a diamond cubic lattice structure: Design, manufacture and testing. *J. Mech. Behav. Biomed. Mater* 77, 58–72. doi:10.1016/j.jmbbm.2017.08.034

- Ji, C., Annabi, N., Hosseinkhani, M., Sivaloganathan, S., and Dehghani, F. (2012). Fabrication of poly-DL-lactide/polyethylene glycol scaffolds using the gas foaming technique. *Acta Biomater.* 8, 570–578. doi:10.1016/j.actbio.2011.09.028
- Ji, X., Yuan, X., Ma, L., Bi, B., Zhu, H., Lei, Z., et al. (2020). Mesenchymal stem cell-loaded thermosensitive hydroxypropyl chitin hydrogel combined with a three-dimensional-printed poly(ϵ -caprolactone)/nano-hydroxyapatite scaffold to repair bone defects via osteogenesis, angiogenesis and immunomodulation. *Theranostics* 10, 725–740. doi:10.7150/thno.39167
- Jia, J., Siddiq, A. R., and Kennedy, A. R. (2015). Porous titanium manufactured by a novel powder tapping method using spherical salt bead space holders: Characterisation and mechanical properties. *J. Mech. Behav. Biomed. Mater* 48, 229–240. doi:10.1016/j.jmbbm.2015.04.018
- Jiao, C., Gu, J., Cao, Y., Xie, D., Liang, H., Chen, R., et al. (2020). Preparation of Al₂O₃-ZrO₂ scaffolds with controllable multi-level pores via digital light processing. *J. Eur. Ceram. Soc.* 40, 6087–6094. doi:10.1016/j.jeurceramsoc.2020.06.024
- Jones, A. C., Arns, C. H., Sheppard, A. P., Huttmacher, D. W., Milthorpe, B. K., and Knackstedt, M. A. (2007). Assessment of bone ingrowth into porous biomaterials using MICRO-CT. *Biomaterials* 28, 2491–2504. doi:10.1016/j.biomaterials.2007.01.046
- Kamboj, N., Kazantseva, J., Rahmani, R., Rodriguez, M. A., and Hussainova, I. (2020). Selective laser sintered bio-inspired silicon-wollastonite scaffolds for bone tissue engineering. *Mater. Sci. Eng. C Mater. Biol. Appl.* 116, 111223. doi:10.1016/j.msec.2020.111223
- Kapat, K., Srivas, P. K., and Dhara, S. (2017). Coagulant assisted foaming – a method for cellular Ti6Al4V: Influence of microstructure on mechanical properties. *Mater. Sci. Eng. A* 689, 63–71. doi:10.1016/j.msea.2017.02.040
- Karageorgiou, V., and Kaplan, D. (2005). Porosity of 3D biomaterial scaffolds and osteogenesis. *Biomaterials* 26, 5474–5491. doi:10.1016/j.biomaterials.2005.02.002
- Kato, K., Ochiai, S., Yamamoto, A., Daigo, Y., Honma, K., Matano, S., et al. (2013). Novel multilayer Ti foam with cortical bone strength and cytocompatibility. *Acta Biomater.* 9, 5802–5809. doi:10.1016/j.actbio.2012.11.018
- Kayacan, M. C., Baykal, Y. B., Karaaslan, T., Ozsoy, K., Alaca, I., Duman, B., et al. (2018). Monitoring the osseointegration process in porous Ti6Al4V implants produced by additive manufacturing: An experimental study in sheep. *J. Appl. Biomater. Funct. Mater* 16, 68–75. doi:10.5301/jabfm.5000385
- Kelly, C. N., Francovich, J., Julmi, S., Safranski, D., Guldborg, R. E., Maier, H. J., et al. (2019). Fatigue behavior of As-built selective laser melted titanium scaffolds with sheet-based gyroid microarchitecture for bone tissue engineering. *Acta Biomater.* 94, 610–626. doi:10.1016/j.actbio.2019.05.046
- Kilian, D., von Witzleben, M., Lanaro, M., Wong, C. S., Vater, C., Lode, A., et al. (2022). 3D plotting of calcium phosphate cement and melt electrowriting of polycaprolactone microfibers in one scaffold: A hybrid additive manufacturing process. *J. Funct. Biomater.* 13, 75. doi:10.3390/jfb13020075
- Kopp, A., Derra, T., Muther, M., Jauer, L., Schleifenbaum, J. H., Voshage, M., et al. (2019). Influence of design and postprocessing parameters on the degradation behavior and mechanical properties of additively manufactured magnesium scaffolds. *Acta Biomater.* 98, 23–35. doi:10.1016/j.actbio.2019.04.012
- Lee, J. B., Maeng, W. Y., Koh, Y. H., and Kim, H. E. (2018). Porous calcium phosphate ceramic scaffolds with tailored pore orientations and mechanical properties using lithography-based ceramic 3D printing technique. *Mater. (Basel)* 11, 1711. doi:10.3390/ma11091711
- Lehder, E. F., Ashcroft, I. A., Wildman, R. D., Ruiz-Cantu, L. A., and Maskery, I. (2021). A multiscale optimisation method for bone growth scaffolds based on triply periodic minimal surfaces. *Biomech. Model. Mechanobiol.* 20, 2085–2096. doi:10.1007/s10237-021-01496-8
- Lei, H., Yi, T., Fan, H., Pei, X., Wu, L., Xing, F., et al. (2021). Customized additive manufacturing of porous Ti6Al4V scaffold with micro-topological structures to regulate cell behavior in bone tissue engineering. *Mater. Sci. Eng. C Mater. Biol. Appl.* 120, 111789. doi:10.1016/j.msec.2020.111789
- Lewis, J. A. (2006). Direct ink writing of 3D functional materials. *Adv. Funct. Mater.* 16, 2193–2204. doi:10.1002/adfm.200600434
- Li, J., Yuan, H., Chandrakar, A., Moroni, L., and Habibovic, P. (2021). 3D porous Ti6Al4V-beta-tricalcium phosphate scaffolds directly fabricated by additive manufacturing. *Acta Biomater.* 126, 496–510. doi:10.1016/j.actbio.2021.03.021
- Li, J., Zhao, Z., Yan, R., and Yang, Y. (2020). Mechanical properties of graded scaffolds developed by curve interference coupled with selective laser sintering. *Mater. Sci. Eng. C Mater. Biol. Appl.* 116, 111181. doi:10.1016/j.msec.2020.111181
- Li, L., Li, Y., Yang, L., Yu, F., Zhang, K., Jin, J., et al. (2019). Polydopamine coating promotes early osteogenesis in 3D printing porous Ti6Al4V scaffolds. *Ann. Transl. Med.* 7, 240. doi:10.21037/atm.2019.04.79
- Li, Y., Jahr, H., Lietaert, K., Pavanram, P., Yilmaz, A., Fockaert, L. I., et al. (2018). Additively manufactured biodegradable porous iron. *Acta Biomater.* 77, 380–393. doi:10.1016/j.actbio.2018.07.011
- Li, Y., Jahr, H., Pavanram, P., Bobbert, F. S. L., Paggi, U., Zhang, X. Y., et al. (2019). Additively manufactured functionally graded biodegradable porous iron. *Acta Biomater.* 96, 646–661. doi:10.1016/j.actbio.2019.07.013
- Li, Y., Li, W., Bobbert, F. S. L., Lietaert, K., Dong, J. H., Leeftang, M. A., et al. (2020). Corrosion fatigue behavior of additively manufactured biodegradable porous zinc. *Acta Biomater.* 106, 439–449. doi:10.1016/j.actbio.2020.02.001
- Li, Y., Pavanram, P., Zhou, J., Lietaert, K., Taheri, P., Li, W., et al. (2020). Additively manufactured biodegradable porous zinc. *Acta Biomater.* 101, 609–623. doi:10.1016/j.actbio.2019.10.034
- Li, Y., Yang, W., Li, X., Zhang, X., Wang, C., Meng, X., et al. (2015). Improving osteointegration and osteogenesis of three-dimensional porous Ti6Al4V scaffolds by polydopamine-assisted biomimetic hydroxyapatite coating. *ACS Appl. Mater. Interfaces* 7, 5715–5724. doi:10.1021/acsami.5b00331
- Li, Y., Zhou, J., Pavanram, P., Leeftang, M. A., Fockaert, L. I., Pouran, B., et al. (2018). Additively manufactured biodegradable porous magnesium. *Acta Biomater.* 67, 378–392. doi:10.1016/j.actbio.2017.12.008
- Liang, H., Wang, Y., Chen, S., Liu, Y., Liu, Z., and Bai, J. (2022). Nano-Hydroxyapatite bone scaffolds with different porous structures processed by digital light processing 3D printing. *Int. J. Bioprint* 8, 502. doi:10.18063/ijb.v8i1.502
- Lim, J. Y., Kim, N., Park, J. C., Yoo, S. K., Shin, D. A., and Shim, K. W. (2017). Exploring the optimal structural design for the 3D-printing technology for cranial reconstruction: A biomechanical and histological study comparison of solid vs. porous structure. *Childs Nerv. Syst.* 33, 1553–1562. doi:10.1007/s00381-017-3486-y
- Liu, F., Ran, Q., Zhao, M., Zhang, T., Zhang, D. Z., and Su, Z. (2020). Additively manufactured continuous cell-size gradient porous scaffolds: Pore characteristics, mechanical properties and biological responses *in vitro*. *Mater. (Basel)* 13, 2589. doi:10.3390/ma13112589
- Liu, J., Liu, B., Min, S., Yin, B., Peng, B., Yu, Z., et al. (2022). Biodegradable magnesium alloy WE43 porous scaffolds fabricated by laser powder bed fusion for orthopedic applications: Process optimization, *in vitro* and *in vivo* investigation. *Bioact. Mater* 16, 301–319. doi:10.1016/j.bioactmat.2022.02.020
- Liu, J., Ruan, J., Chang, L., Yang, H., and Ruan, W. (2017). Porous Nb-Ti-Ta alloy scaffolds for bone tissue engineering: Fabrication, mechanical properties and *in vitro/vivo* biocompatibility. *Mater. Sci. Eng. C Mater. Biol. Appl.* 78, 503–512. doi:10.1016/j.msec.2017.04.088
- Liverani, E., Rogati, G., Pagani, S., Brogini, S., Fortunato, A., and Caravaggi, P. (2021). Mechanical interaction between additive-manufactured metal lattice structures and bone in compression: Implications for stress shielding of orthopaedic implants. *J. Mech. Behav. Biomed. Mater* 121, 104608. doi:10.1016/j.jmbbm.2021.104608
- Lu, S., Jiang, D., Liu, S., Liang, H., Lu, J., Xu, H., et al. (2022). Effect of different structures fabricated by additive manufacturing on bone ingrowth. *J. Biomater. Appl.* 36, 1863–1872. doi:10.1177/08853282211064398
- Lu, Y., Cui, Z., Cheng, L., Li, J., Yang, Z., Zhu, H., et al. (2020). Quantifying the discrepancies in the geometric and mechanical properties of the theoretically designed and additively manufactured scaffolds. *J. Mech. Behav. Biomed. Mater* 112, 104080. doi:10.1016/j.jmbbm.2020.104080
- Lu, Y., Huo, Y., Zou, J., Li, Y., Yang, Z., Zhu, H., et al. (2022). Comparison of the design maps of TPMS based bone scaffolds using a computational modeling framework simultaneously considering various conditions. *Proc. Inst. Mech. Eng. H* 236, 1157–1168. doi:10.1177/09544119221102704
- Lv, J., Jin, W., Liu, W., Qin, X., Feng, Y., Bai, J., et al. (2022). Selective laser melting fabrication of porous Ti6Al4V scaffolds with triply periodic minimal surface architectures: Structural features, cytocompatibility, and osteogenesis. *Front. Bioeng. Biotechnol.* 10, 899531. doi:10.3389/fbioe.2022.899531
- Ma, L., Wang, X., Zhou, Y., Ji, X., Cheng, S., Bian, D., et al. (2021). Biomimetic Ti-6Al-4V alloy/gelatin methacrylate hybrid scaffold with enhanced osteogenic and angiogenic capabilities for large bone defect restoration. *Bioact. Mater* 6, 3437–3448. doi:10.1016/j.bioactmat.2021.03.010
- Ma, S., Tang, Q., Feng, Q., Song, J., Han, X., and Guo, F. (2019). Mechanical behaviours and mass transport properties of bone-mimicking scaffolds consisted of gyroid structures manufactured using selective laser melting. *J. Mech. Behav. Biomed. Mater* 93, 158–169. doi:10.1016/j.jmbbm.2019.01.023
- Markhoff, J., Wieding, J., Weissmann, V., Pasold, J., Jonitz-Heincke, A., and Bader, R. (2015). Influence of different three-dimensional open porous titanium scaffold designs on human osteoblasts behavior in static and dynamic cell investigations. *Mater. (Basel)* 8, 5490–5507. doi:10.3390/ma8085259

- Maya, A. E. A., Grana, D. R., Hazarabedian, A., Kokubu, G. A., Luppo, M. I., and Vigna, G. (2012). Zr–Ti–Nb porous alloys for biomedical application. *Mater. Sci. Eng. C* 32, 321–329. doi:10.1016/j.msec.2011.10.035
- Melancon, D., Bagheri, Z. S., Johnston, R. B., Liu, L., Tanzer, M., and Pasini, D. (2017). Mechanical characterization of structurally porous biomaterials built via additive manufacturing: Experiments, predictive models, and design maps for load-bearing bone replacement implants. *Acta Biomater.* 63, 350–368. doi:10.1016/j.actbio.2017.09.013
- Moiduddin, K. (2018). Retracted: Microstructure and mechanical properties of porous titanium structures fabricated by electron beam melting for cranial implants. *Proc. Inst. Mech. Eng. H* 232, 185–199. doi:10.1177/0954411917751558
- Naghavi, S. A., Wang, H., Varma, S. N., Tamaddon, M., Marghoub, A., Galbraith, R., et al. (2022). On the morphological deviation in additive manufacturing of porous Ti6Al4V scaffold: A design consideration. *Mater. (Basel)* 15, 4729. doi:10.3390/ma15144729
- Nune, K. C., Kumar, A., Misra, R. D. K., Li, S. J., Hao, Y. L., and Yang, R. (2017). Functional response of osteoblasts in functionally gradient titanium alloy mesh arrays processed by 3D additive manufacturing. *Colloids Surf. B Biointerfaces* 150, 78–88. doi:10.1016/j.colsurf.2016.09.050
- Nune, K. C., Misra, R. D., Li, S. J., Hao, Y. L., and Yang, R. (2017). Cellular response of osteoblasts to low modulus Ti–24Nb–4Zr–8Sn alloy mesh structure. *J. Biomed. Mater. Res. A* 105, 859–870. doi:10.1002/jbma.a.35963
- Oppenheimer, S., and Dunand, D. C. (2010). Solid-state foaming of Ti–6Al–4V by creep or superplastic expansion of argon-filled pores. *Acta Mater.* 58, 4387–4397. doi:10.1016/j.actamat.2010.04.034
- Otsuki, B., Takemoto, M., Fujibayashi, S., Neo, M., Kokubo, T., and Nakamura, T. (2006). Pore throat size and connectivity determine bone and tissue ingrowth into porous implants: Three-dimensional micro-CT based structural analyses of porous bioactive titanium implants. *Biomaterials* 27, 5892–5900. doi:10.1016/j.biomaterials.2006.08.013
- Papaefstathiou, S., Larochette, N., Liste, R. M. V., Potier, E., Petite, H., Vivace, B. J., et al. (2022). Three-dimensional printing of biomimetic titanium mimicking trabecular bone induces human mesenchymal stem cell proliferation: An *in-vitro* analysis. *Spine (Phila Pa 1976)* 47, 1027–1035. doi:10.1097/brs.00000000000004317
- Pei, X., Wu, L., Zhou, C., Fan, H., Gou, M., Li, Z., et al. (2020). 3D printed titanium scaffolds with homogeneous diamond-like structures mimicking that of the osteocyte microenvironment and its bone regeneration study. *Biofabrication* 13, 015008. doi:10.1088/1758-5090/abc060
- Ponader, S., von Wilmowsky, C., Widenmayer, M., Lutz, R., Heintz, P., Korner, C., et al. (2010). *In vivo* performance of selective electron beam-melted Ti–6Al–4V structures. *J. Biomed. Mater. Res. A* 92, 56–62. doi:10.1002/jbma.a.32337
- Qin, Y., Liu, A., Guo, H., Shen, Y., Wen, P., Lin, H., et al. (2022). Additive manufacturing of Zn–Mg alloy porous scaffolds with enhanced osseointegration: *In vitro* and *in vivo* studies. *Acta Biomater.* 145, 403–415. doi:10.1016/j.actbio.2022.03.055
- Qin, Y., Yang, H., Liu, A., Dai, J., Wen, P., Zheng, Y., et al. (2022). Processing optimization, mechanical properties, corrosion behavior and cytocompatibility of additively manufactured Zn–0.7Li biodegradable metals. *Acta Biomater.* 142, 388–401. doi:10.1016/j.actbio.2022.01.049
- Rumpler, M., Woesz, A., Dunlop, J. W., van Dongen, J. T., and Fratzl, P. (2008). The effect of geometry on three-dimensional tissue growth. *J. R. Soc. Interface* 5, 1173–1180. doi:10.1098/rsif.2008.0064
- Sakthiabirami, K., Kang, J. H., Jang, J. G., Soundharajan, V., Lim, H. P., Yun, K. D., et al. (2021). Hybrid porous zirconia scaffolds fabricated using additive manufacturing for bone tissue engineering applications. *Mater. Sci. Eng. C Mater. Biol. Appl.* 123, 111950. doi:10.1016/j.msec.2021.111950
- Schmidleithner, C., Malferarri, S., Palgrave, R., Bomze, D., Schwentenwein, M., and Kalaskar, D. M. (2019). Application of high resolution DLP stereolithography for fabrication of tricalcium phosphate scaffolds for bone regeneration. *Biomed. Mater.* 14, 045018. doi:10.1088/1748-605x/ab279d
- Shah, F. A., Omar, O., Suska, F., Snis, A., Matic, A., Emanuelsson, L., et al. (2016). Long-term osseointegration of 3D printed CoCr constructs with an interconnected open-pore architecture prepared by electron beam melting. *Acta Biomater.* 36, 296–309. doi:10.1016/j.actbio.2016.03.033
- Shanjani, Y., Kang, Y., Zarnescu, L., Ellerbee Bowden, A. K., Koh, J. T., Ker, D. F. E., et al. (2017). Endothelial pattern formation in hybrid constructs of additive manufactured porous rigid scaffolds and cell-laden hydrogels for orthopedic applications. *J. Mech. Behav. Biomed. Mater.* 65, 356–372. doi:10.1016/j.jmbbm.2016.08.037
- Sharma, P., Jain, K. G., Pandey, P. M., and Mohanty, S. (2020). *In vitro* degradation behaviour, cytocompatibility and hemocompatibility of topologically ordered porous iron scaffold prepared using 3D printing and pressureless microwave sintering. *Mater. Sci. Eng. C Mater. Biol. Appl.* 106, 110247. doi:10.1016/j.msec.2019.110247
- Shuai, C., Yang, Y., Feng, P., Peng, S., Guo, W., Min, A., et al. (2018). A multi-scale porous scaffold fabricated by a combined additive manufacturing and chemical etching process for bone tissue engineering. *Int. J. Bioprint* 4, 133. doi:10.18063/IJB.v4i2.133
- Soro, N., Attar, H., Brodie, E., Veidt, M., Molotnikov, A., and Dargusch, M. S. (2019). Evaluation of the mechanical compatibility of additively manufactured porous Ti–25Ta alloy for load-bearing implant applications. *J. Mech. Behav. Biomed. Mater.* 97, 149–158. doi:10.1016/j.jmbbm.2019.05.019
- Stevenson, G., Rehman, S., Draper, E., Hernandez-Nava, E., Hunt, J., and Haycock, J. W. (2016). Combining 3D human *in vitro* methods for a 3Rs evaluation of novel titanium surfaces in orthopaedic applications. *Biotechnol. Bioeng.* 113, 1586–1599. doi:10.1002/bit.25919
- Su, J., Hua, S., Chen, A., Chen, P., Yang, L., Yuan, X., et al. (2022). Three-dimensional printing of gyroid-structured composite bioceramic scaffolds with tuneable degradability. *Biomater. Adv.* 133, 112595. doi:10.1016/j.msec.2021.112595
- Takahashi, Y., and Tabata, Y. (2004). Effect of the fiber diameter and porosity of non-woven PET fabrics on the osteogenic differentiation of mesenchymal stem cells. *J. Biomater. Sci. Polym. Ed.* 15, 41–57. doi:10.1163/156856204322752228
- Taniguchi, N., Fujibayashi, S., Takemoto, M., Sasaki, K., Otsuki, B., Nakamura, T., et al. (2016). Effect of pore size on bone ingrowth into porous titanium implants fabricated by additive manufacturing: An *in vivo* experiment. *Mater. Sci. Eng. C Mater. Biol. Appl.* 59, 690–701. doi:10.1016/j.msec.2015.10.069
- Timercan, A., Sheremetyev, V., and Brailovski, V. (2021). Mechanical properties and fluid permeability of gyroid and diamond lattice structures for intervertebral devices: Functional requirements and comparative analysis. *Sci. Technol. Adv. Mater.* 22, 285–300. doi:10.1080/14686996.2021.1907222
- Tsai, P. I., Wu, M. H., Li, Y. Y., Lin, T. H., Tsai, J. S. C., Huang, H. I., et al. (2021). Additive-manufactured Ti–6Al–4 V/polyetheretherketone composite porous cage for interbody fusion: Bone growth and biocompatibility evaluation in a porcine model. *BMC Musculoskelet. Disord.* 22, 171. doi:10.1186/s12891-021-04022-0
- Van Bael, S., Chai, Y. C., Truscetto, S., Moesen, M., Kerckhofs, G., Van Oosterwyck, H., et al. (2012). The effect of pore geometry on the *in vitro* biological behavior of human periosteum-derived cells seeded on selective laser-melted Ti6Al4V bone scaffolds. *Acta Biomater.* 8, 2824–2834. doi:10.1016/j.actbio.2012.04.001
- Walsh, W. R., Pelletier, M. H., Wang, T., Lovric, V., Morberg, P., and Mobbs, R. J. (2019). Does implantation site influence bone ingrowth into 3D-printed porous implants? *Spine J.* 19, 1885–1898. doi:10.1016/j.spinee.2019.06.020
- Wang, G., Shen, L., Zhao, J., Liang, H., Xie, D., Tian, Z., et al. (2018). Design and compressive behavior of controllable irregular porous scaffolds: Based on voronoi-tessellation and for additive manufacturing. *ACS Biomater. Sci. Eng.* 4, 719–727. doi:10.1021/acsbomaterials.7b00916
- Wang, H., Su, K., Su, L., Liang, P., Ji, P., and Wang, C. (2018). The effect of 3D-printed Ti6Al4V scaffolds with various macropore structures on osteointegration and osteogenesis: A biomechanical evaluation. *J. Mech. Behav. Biomed. Mater.* 88, 488–496. doi:10.1016/j.jmbbm.2018.08.049
- Wang, S., Zhou, X., Liu, L., Shi, Z., and Hao, Y. (2020). On the design and properties of porous femoral stems with adjustable stiffness gradient. *Med. Eng. Phys.* 81, 30–38. doi:10.1016/j.medengphy.2020.05.003
- Wang, Y., Huang, H., Jia, G., Zeng, H., and Yuan, G. (2021). Fatigue and dynamic biodegradation behavior of additively manufactured Mg scaffolds. *Acta Biomater.* 135, 705–722. doi:10.1016/j.actbio.2021.08.040
- Wauthle, R., van der Stok, J., Amin Yavari, S., Van Humbeeck, J., Kruth, J. P., Zadpoor, A. A., et al. (2015). Additively manufactured porous tantalum implants. *Acta Biomater.* 14, 217–225. doi:10.1016/j.actbio.2014.12.003
- Wei, P., Wei, Z., Chen, Z., Du, J., He, Y., Li, J., et al. (2017). The AlSi10Mg samples produced by selective laser melting: Single track, densification, microstructure and mechanical behavior. *Appl. Surf. Sci.* 408, 38–50. doi:10.1016/j.apsusc.2017.02.215
- Wieding, J., Wolf, A., and Bader, R. (2014). Numerical optimization of open-porous bone scaffold structures to match the elastic properties of human cortical bone. *J. Mech. Behav. Biomed. Mater.* 37, 56–68. doi:10.1016/j.jmbbm.2014.05.002
- Wu, M. H., Lee, M. H., Wu, C., Tsai, P. I., Hsu, W. B., Huang, S. I., et al. (2022). *In vitro* and *in vivo* comparison of bone growth characteristics in additive-manufactured porous titanium, nonporous titanium, and porous tantalum interbody cages. *Mater. (Basel)* 15, 3670. doi:10.3390/ma15103670
- Wu, R., Li, Y., Shen, M., Yang, X., Zhang, L., Ke, X., et al. (2021). Bone tissue regeneration: The role of finely tuned pore architecture of bioactive scaffolds before clinical translation. *Bioact. Mater.* 6, 1242–1254. doi:10.1016/j.bioactmat.2020.11.003

- Wysocki, B., Idaszek, J., Szlajak, K., Strzelczyk, K., Brynk, T., Kurzydowski, K. J., et al. (2016). Post processing and biological evaluation of the titanium scaffolds for bone tissue engineering. *Mater. (Basel)* 9, 197. doi:10.3390/ma9030197
- Xia, D., Qin, Y., Guo, H., Wen, P., Lin, H., Voshage, M., et al. (2023). Additively manufactured pure zinc porous scaffolds for critical-sized bone defects of rabbit femur. *Bioact. Mater.* 19, 12–23. doi:10.1016/j.bioactmat.2022.03.010
- Xiong, Y. Z., Gao, R. N., Zhang, H., Dong, L. L., Li, J. T., and Li, X. (2020). Rationally designed functionally graded porous Ti6Al4V scaffolds with high strength and toughness built via selective laser melting for load-bearing orthopedic applications. *J. Mech. Behav. Biomed. Mater.* 104, 103673. doi:10.1016/j.jmbbm.2020.103673
- Yamanoglu, R., Gulsoy, N., Olevsky, E. A., and Gulsoy, H. O. (2016). Production of porous Ti5Al2.5Fe alloy via pressureless spark plasma sintering. *J. Alloys Compd.* 680, 654–658. doi:10.1016/j.jallcom.2016.04.176
- Yan, C., Hao, L., Hussein, A., and Young, P. (2015). Ti-6Al-4V triply periodic minimal surface structures for bone implants fabricated via selective laser melting. *J. Mech. Behav. Biomed. Mater.* 51, 61–73. doi:10.1016/j.jmbbm.2015.06.024
- Yang, H., Zhu, Q., Qi, H., Liu, X., Ma, M., and Chen, Q. (2018). A facile flow-casting production of bioactive glass coatings on porous titanium for bone tissue engineering. *Mater. (Basel)* 11, 1540. doi:10.3390/ma11091540
- Yang, L., Han, C., Wu, H., Hao, L., Wei, Q., Yan, C., et al. (2020). Insights into unit cell size effect on mechanical responses and energy absorption capability of titanium graded porous structures manufactured by laser powder bed fusion. *J. Mech. Behav. Biomed. Mater.* 109, 103843. doi:10.1016/j.jmbbm.2020.103843
- Yang, Y., Kulkarni, A., Soraru, G. D., Pearce, J. M., and Motta, A. (2021). 3D printed SiOC(N) ceramic scaffolds for bone tissue regeneration: Improved osteogenic differentiation of human bone marrow-derived mesenchymal stem cells. *Int. J. Mol. Sci.* 22, 13676. doi:10.3390/ijms222413676
- Yavari, S. A., Wauthle, R., van der Stok, J., Riemsagel, A. C., Janssen, M., Mulier, M., et al. (2013). Fatigue behavior of porous biomaterials manufactured using selective laser melting. *Mater. Sci. Eng. C Mater. Biol. Appl.* 33, 4849–4858. doi:10.1016/j.msec.2013.08.006
- Ye, B., and Dunand, D. C. (2010). Titanium foams produced by solid-state replication of NaCl powders. *Mater. Sci. Eng. A* 528, 691–697. doi:10.1016/j.msea.2010.09.054
- Zadpoor, A. A. (2015). Bone tissue regeneration: The role of scaffold geometry. *Biomater. Sci.* 3, 231–245. doi:10.1039/c4bm00291a
- Zaharin, H. A., Abdul Rani, A. M., Azam, F. I., Ginta, T. L., Sallih, N., Ahmad, A., et al. (2018). Effect of unit cell type and pore size on porosity and mechanical behavior of additively manufactured Ti6Al4V scaffolds. *Mater. (Basel)* 11, 2402. doi:10.3390/ma11122402
- Zhang, C., Zhang, L., Liu, L., Lv, L., Gao, L., Liu, N., et al. (2020). Mechanical behavior of a titanium alloy scaffold mimicking trabecular structure. *J. Orthop. Surg. Res.* 15, 40. doi:10.1186/s13018-019-1489-y
- Zhang, X. Y., Fang, G., Leeflang, S., Zadpoor, A. A., and Zhou, J. (2019). Topological design, permeability and mechanical behavior of additively manufactured functionally graded porous metallic biomaterials. *Acta Biomater.* 84, 437–452. doi:10.1016/j.actbio.2018.12.013
- Zhang, Z., Jones, D., Yue, S., Lee, P. D., Jones, J. R., Sutcliffe, C. J., et al. (2013). Hierarchical tailoring of strut architecture to control permeability of additive manufactured titanium implants. *Mater. Sci. Eng. C Mater. Biol. Appl.* 33, 4055–4062. doi:10.1016/j.msec.2013.05.050
- Zhao, H., Han, Y., Pan, C., Yang, D., Wang, H., Wang, T., et al. (2021). Design and mechanical properties verification of gradient Voronoi scaffold for bone tissue engineering. *Micromachines (Basel)* 12, 664. doi:10.3390/mi12060664
- Zhao, Y., Tan, K., Zhou, Y., Ye, Z., and Tan, W. S. (2016). A combinatorial variation in surface chemistry and pore size of three-dimensional porous poly(ϵ -caprolactone) scaffolds modulates the behaviors of mesenchymal stem cells. *Mater. Sci. Eng. C Mater. Biol. Appl.* 59, 193–202. doi:10.1016/j.msec.2015.10.017
- Zhu, L., Liang, H., Lv, F., Xie, D., Wang, C., Mao, Y., et al. (2021). Design and compressive fatigue properties of irregular porous scaffolds for orthopedics fabricated using selective laser melting. *ACS Biomater. Sci. Eng.* 7, 1663–1672. doi:10.1021/acsbomaterials.0c01392



OPEN ACCESS

EDITED BY
Chunguang Yang,
Institute of Metal Research (CAS), China

REVIEWED BY
Xinhua Qu,
Shanghai Jiao Tong University, China
Liqun Yang,
China Medical University, China

*CORRESPONDENCE
Li Min,
✉ minli1204@scu.edu.cn
Chongqi Tu,
✉ tucq@scu.edu.cn

[†]These authors have contributed equally to this work

SPECIALTY SECTION
This article was submitted to Biomaterials, a section of the journal Frontiers in Bioengineering and Biotechnology

RECEIVED 15 November 2022
ACCEPTED 30 December 2022
PUBLISHED 12 January 2023

CITATION
Zhang Y, Lu M, Hu X, Li Z, Wang J, Gong T, Zhou Y, Luo L, Min L and Tu C (2023), Three-dimensional-printed porous prosthesis for the joint-sparing reconstruction of the proximal humeral tumorous defect.
Front. Bioeng. Biotechnol. 10:1098973. doi: 10.3389/fbioe.2022.1098973

COPYRIGHT
© 2023 Zhang, Lu, Hu, Li, Wang, Gong, Zhou, Luo, Min and Tu. This is an open-access article distributed under the terms of the [Creative Commons Attribution License \(CC BY\)](https://creativecommons.org/licenses/by/4.0/). The use, distribution or reproduction in other forums is permitted, provided the original author(s) and the copyright owner(s) are credited and that the original publication in this journal is cited, in accordance with accepted academic practice. No use, distribution or reproduction is permitted which does not comply with these terms.

Three-dimensional-printed porous prosthesis for the joint-sparing reconstruction of the proximal humeral tumorous defect

Yuqi Zhang^{1,2†}, Minxun Lu^{1,2†}, Xin Hu^{1,2}, Zhuangzhuang Li^{1,2}, Jie Wang^{1,2}, Taojun Gong^{1,2}, Yong Zhou^{1,2}, Li Luo^{1,2}, Li Min^{1,2*} and Chongqi Tu^{1,2*}

¹Department of Orthopedics, Orthopedic Research Institute, West China Hospital, Sichuan University, Chengdu, Sichuan, China, ²Model Worker and Craftsman Talent Innovation Workshop of Sichuan province, Chengdu, Sichuan, China

Background: Tumorous bone defect reconstructions of the proximal humerus with joint sparing is a challenge. Numerous reconstruction methods have been proposed but the proximal residual humerus is commonly sacrificed because of its extremely short length. To preserve the proximal humerus and improve clinical outcomes, we designed a three-dimensional (3D) printed uncemented prosthesis with a porous structure to treat tumorous bone defects of the proximal humerus.

Methods: Our analysis included seven patients treated between March 2018 and July 2019. A 3D model was established, and related data were obtained, including the diameter of the humeral head, the resection length, and the residual length. A prosthesis was designed and fabricated based on these data. Functional and oncologic outcomes were recorded, and complications and osseointegration were evaluated.

Results: The mean age of the patients was 20.3 years, and the median follow-up period was 26 months. The lengths of the residual proximal humerus were 17.9 mm on average. All the patients had preserved humeral heads and most of the rotator cuff was intact. The average postoperative range of motion (ROM) of the affected shoulder was 83.8°; flexion was 82.5°, extension was 43.8°, and adduction was 16.3°. The average Musculoskeletal Tumor Society score (MSTS) was 94.3%. Good osseointegration was observed on the interface between the bone and prosthesis.

Conclusion: A 3D printed porous prosthesis with cone-like structures successfully achieved joint-sparing reconstruction of proximal humeral tumorous defects with satisfying functional outcomes. The preservation of the rotator cuff and humeral head plays an essential role in the function of the shoulder joint.

KEYWORDS

3D printed, arthroplasty, prosthesis, intercalary prosthesis, proximal humerus

Abbreviations: 3D, Three dimensional; 3D-CT, Three-dimensional computed tomography; MRI, Magnetic resonance imaging; SPECT, Single-photon emission computed tomography; PET/CT, Positron emission tomography/computerized tomography; STL, Stereolithography; T-SMART, Tomosynthesis-Shimadzu Metal Artefact Reduction Technology; MSTS, Musculoskeletal Tumor Society.

1 Introduction

The metaphysis of the proximal humerus is the most commonly affected site for primary malignant bone tumors (Bielack et al., 2002; Arndt et al., 2012). Although segmental resection with a safe margin has been widely accepted as the standard treatment for malignant bone tumors (Potter et al., 2009), joint preservation is still demanding due to the extremely short axial length of the residual proximal humerus (Liu et al., 2014).

There are currently some approaches available for the repair of tumorous defects involving the metaphysis, such as autograft, allograft, and prostheses (Ruggieri et al., 2011; Wieser et al., 2013; King et al., 2016; Maclean et al., 2017; Rafalla and Abdullah, 2017; Nota et al., 2018; Chauhan et al., 2019). Autologous fibula graft has been widely applied in clinical settings because of its excellent biocompatibility and osteoinductivity (Li et al., 2012; Pilge et al., 2018). However, the interface may not integrate well due to the severe mismatch between the fibula head and the remaining proximal humerus, and subsequent bone absorption and fracture frequently occur (Ceruso et al., 2001). Therefore, an allograft with various options for appropriate size and shape could provide an ideal interface contact, but unexpected immunological rejection and disease transmission are still major concerns (Gupta et al., 2017). As a result, prostheses seem to be one of the most acceptable choices for the reconstruction of segmental bone defects in the proximal humerus (Damron et al., 2008).

Hemiarthroplasty, total arthroplasty, and intercalary prosthesis replacements are all reasonable options for the reconstruction of proximal humeral tumorous defects. As for defects involving the metaphysis, hemiarthroplasty or total arthroplasty would inevitably sacrifice the humeral head, which could have been preserved. Compared with hemiarthroplasty or total arthroplasty, an intercalary prosthesis could not only preserve the humeral head anatomically to retain shoulder function but also provide early stability and rapid function recovery (Yoshida et al., 2010; Panagopoulos et al., 2017). However, current intercalary prostheses are cemented and fixed by an intramedullary stem, which requires at least 3 cm of bone to maintain acceptable stability (McGrath et al., 2011). Moreover, plates and screws are still required for extra fixation due to the lack of osteoinductive activity and bone ingrowth ability (Zekry et al., 2019; Zheng et al., 2019). Additionally, for a shorter proximal humerus (length < 3 cm), reconstruction with joint sparing cannot be achieved by intercalary prosthesis.

Recently, it has been accepted that the porous structure could significantly improve the integration ability of a prosthesis (Batta et al., 2014). In our previous clinical evaluation of three-dimensionally (3D)-printed porous intercalary prostheses, excellent interfacial integration was observed, even with a residual bone length shorter than .7 cm (Lu et al., 2018; Zhao et al., 2020). In this study, we aimed to design and apply a new 3D printed uncemented prosthesis with special features and evaluate its feasibility for the treatment of proximal humeral defects. The detailed design and features of the prosthesis, surgical techniques, and early-term clinical outcomes are presented and analyzed.

2 Materials and methods

2.1 Patients

Between March 2018 and July 2019, seven patients (two females and five males) with humeral malignant tumors received 3D printed

uncemented prosthesis reconstructions in our institution. The average age was 19.25 years (range, 16–24 years). All the patients received preoperative radiographic assessments, including x-rays, 3D computed tomography (CT) scans (Philips Brilliance 64 Slice, thickness: .4 mm), magnetic resonance imaging (MRI) scans, and bone scans (SPECT) or positron emission tomography/computerized tomography (PET/CT) scans (Figure 1). A preoperative biopsy was performed for all patients. An Enneking surgical staging system was used to evaluate the surgical stage (Enneking, 1986). Tumor locations were classified with reference to the epiphyseal plate proposed by Kumta et al. (Kumta et al., 1999). Neoadjuvant chemotherapy was performed for patients with high-grade sarcoma according to the NCCN guidelines for bone cancer. The detailed characteristics of the patients are summarized in Table 1.

This study was performed in accordance with the Declaration of Helsinki as revised in 2008 and was approved by the Ethics Committee of the West China Hospital. All patients signed an informed consent form before surgery and provided consent to publish and report individual clinical data.

2.2 Anatomical data measurement

The 3D CT data of patients were imported to Mimics V20.0 software (Materialise Corp., Leuven, Belgium) to build virtual 3D models of the tumor and bone. The tumor edge was determined using the combination of x-ray, MRI, and SPECT. Anatomical data, including the diameter of the humeral head, the proximal and distal osteotomy location, the resection length, the length of the residual humerus, and the diameters of the intramedullary cavity, were obtained. The curative margin was subsequently obtained to determine the tumor resection and residual bone parts, and an operation simulation was performed using Geomagic Wrap software (Geomagic inc., Morrisville, NC) (Figure 2A).

2.3 Prosthesis design and fabrication

All prostheses were designed by our clinical team according to the anatomical data, and were fabricated by Chunli Co., Ltd., Tongzhou, Beijing, China. The prostheses consisted of a head, shaft, and stem. A hemisphere-like structure was selected for the design of the head shape, and the size of the head was customized in all patients as per the host humeral head. In addition, specific features, including suture holes and cone-like structures, were added to enhance the initial stability of the bone-implant interface. In detail, a solid core porous shell complicated structure concept was applied to design the prosthesis head. The thickness of the porous shell layer was 3–4 mm. Furthermore, 600-μm pores with 70% porosity were suggested for the setting of the porous shell (Karageorgiou and Kaplan, 2005; Palmquist et al., 2013; Hara et al., 2016; Shah et al., 2016; Wang et al., 2019). The shaft length depended on the bone defect length of the patient (Figures 2B, C).

The prosthesis was made of titanium alloy (Ti6Al4V powder, Chunlizhengda Corp., Beijing, China) and was fabricated using the electron beam melting technique (ARCAM Q10 plus, Molndal, Sweden) with the powder bed fusion technique. The metal powder was placed in a vacuum and fused by heat from an electron beam. The

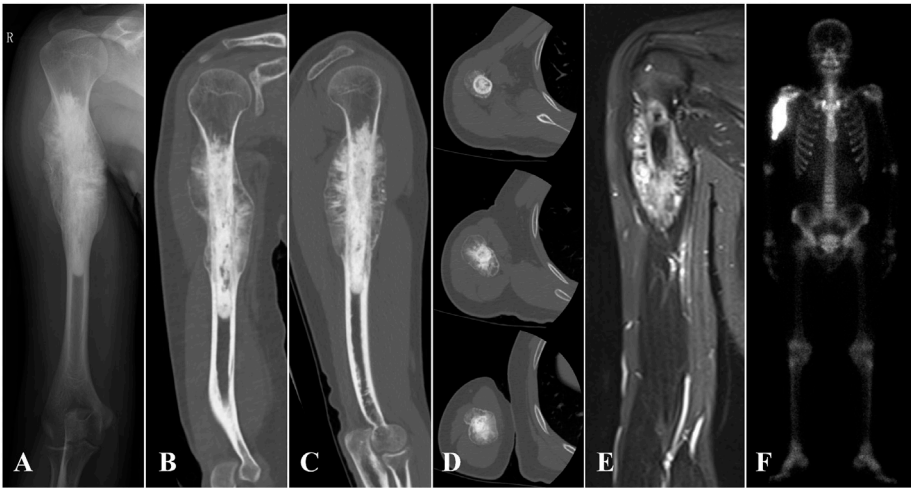


FIGURE 1
(A) X-ray, (B–D) 3D CT, (E) MRI, and (F) SPE/CT of case 1 with proximal humerus osteosarcoma are shown.

TABLE 1 Patient characteristics.

Case	Age	Gender	Follow up (months)	Stage	Classification	Pathological type
1	17	Male	33	IIB	II	Osteosarcoma
2	20	Male	25	IB	III	Chondrosarcoma
3	24	Female	29	IIB	III	Osteosarcoma
4	16	Male	18	IIB	II	Osteosarcoma
5	16	Male	21	IIB	II	Osteosarcoma
6	19	Female	30	IB	II	Chondrosarcoma
7	30	Male	25	IIB	III	Chondrosarcoma

components were then fabricated as per the previously designed model by the continuous addition of pre-alloyed powder layers. The plastic patient-specific instruments and trial models were fabricated *via* stereo lithography apparatus techniques (UnionTech Lite 450HD, Shanghai, China) (Figure 3).

2.4 Surgical techniques

All patients were placed in a supine position. Through an anterior longitudinal humeral incision, the radial nerve was exposed and well protected. The preservation of the rotator cuff insertions was performed before the segmental resection. The osteotomy was performed with patient-specific instruments, in reference to the greater tubercle of the humerus. The remaining proximal humerus was trimmed, while reaming was performed to press-fit the prosthesis. The bone marrow from the reamed canal and trabecular bone trimmings were collected for subsequent autograft (Figure 4A).

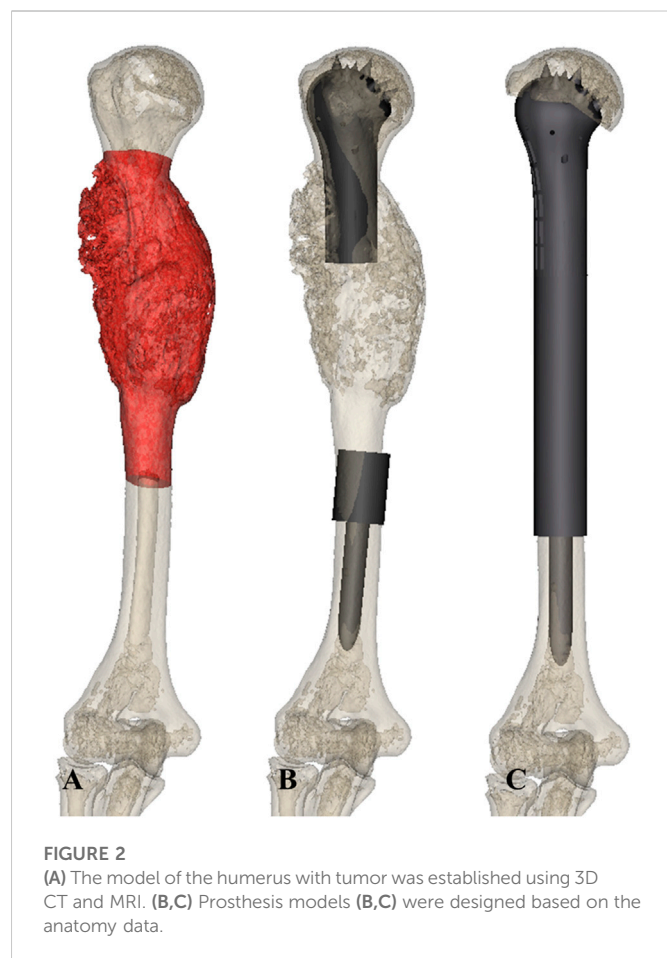
The prosthesis was implanted after autografting. Extra fixation depended on the intraoperative initial stability of the prosthesis.

When the prosthesis was appropriately in place, axial compression was carried out to press the cone-like structure into the proximal cancellous bone. The remaining proximal humeral cortex was sutured to the prosthesis head with the rivet lines, and the sutured cortex needed to be sufficiently stable to prevent avulsion (Figure 4B).

The residual muscles were anatomically relocated to the prosthesis surface with rivet lines but without knotting. The muscles posterior and medial to the humerus were sutured first, followed by the muscles anterior and lateral to the humerus. The knots to suture the rotator cuff were finished together to balance perisoulder muscle tension. The deltoid, pectoralis major, and pectoralis minor, which are important for shoulder ROM, were finally reconstructed, and soft tissue coverage was achieved. Intraoperative time and blood loss were recorded (Figure 4C).

2.5 Postoperative treatment and follow up

The affected limbs of patients were immobilized at 80° of abduction and 60° of flexion for 4 weeks. Passive movements were

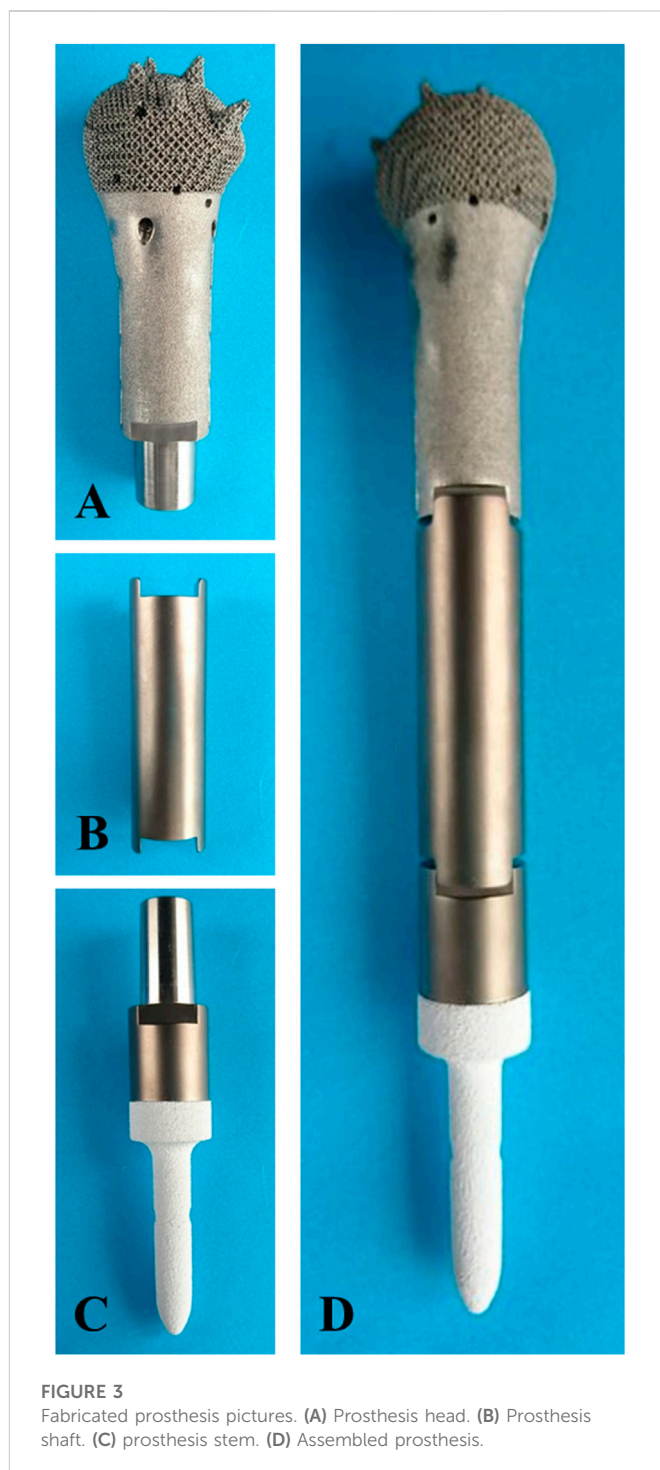


allowed after week 4, and patients were gradually transited to active movement at week 6. The exact time of lifting and exercise depended on the degree of osseointegration. Postoperative chemotherapy was started 2 weeks after surgery.

All patients underwent evaluations, including monthly physical examinations and radiography, during the first 3 months postoperatively and every 3 months thereafter. The absence of periprosthetic radiolucency or the observation of bone bridging, spot welding, and neocortex formation between the trabecular structures and the implant surface on x-rays or Tomosynthesis-Shimadzu Metal Artefact Reduction Technology (T-SMART) was considered good osseointegration. Chest CT scans were used to evaluate lung metastasis every 3 months. Functional outcomes were assessed using the Musculoskeletal Tumor Society score (MSTS), ROM of the glenohumeral joint was recorded, and complication rates were assessed.

2.6 Statistical analysis

Statistical analyses were performed using IBM SPSS Statistics software, version 22 (IBM SPSS, Armonk, NY, United States). Continuous data are represented as mean \pm standard deviation. Student's *t*-test was used to compare continuous variables. $p < .05$ was considered statistically significant.



3 Results

Detailed measurement data are summarized in Table 2. The mean diameter of the humeral head was 42.4 ± 2.0 mm. The mean resection length was 130.5 ± 47.5 mm, and the mean lengths of the residual proximal humerus and residual distal humerus were 17.9 ± 1.3 and 155.5 ± 50.2 mm, respectively.

Detailed prostheses data are summarized in Table 3. The mean diameter of the prosthesis head was 34.7 ± 1.3 mm. According to

**FIGURE 4**

Intraoperative pictures. (A) The remaining proximal humerus was trimmed after segmental resection. (B) The prosthesis stem was press-fit after assembly. (C) The prosthesis was implanted, and muscles were reconstructed using Marlex mesh.

TABLE 2 Anatomy data.

Case	Diameter of the head	Proximal OP distance ^a	Distal OP distance	Resection length	Length of the RPH	Length of the RDH	Diameter of the RDH intramedullary cavity
1	42.24	19.82	201.67	181.85	19.82	103.66	10.29
2	45.93	16.59	92.21	75.62	16.59	237.31	11.94
3	43.33	17.85	169.35	151.5	17.85	142.42	11.01
4	40.23	16.22	101.38	85.16	16.22	193.64	10.03
5	40.11	19.01	180.5	161.49	19.01	118.56	11.21
6	42.56	18.55	100.5	81.95	18.55	182.34	11.66
7	42.65	17.21	193.23	176.02	17.21	110.19	9.86
Mean	42.44	17.89	148.41	130.51	17.89	155.45	10.86

^aOsteotomy plane distance indicates the distance from the osteotomy plane to the proximal end of the humerus.

OP, osteotomy plane; RPH, residual proximal humerus; RDH, residual distal humerus.

TABLE 3 Prosthesis data (mm).

Case	Prosthesis length	Length of the stem	Diameter of the stem	Diameter of the head	Diameter of the body
1	240	55	10	35	20
2	120	45	12	36	22
3	200	50	11	36	20
4	130	45	10	33	18
5	210	50	11	33	20
6	130	50	11	35	22
7	220	45	10	35	20
Mean	178.57	48.57	10.71	34.71	20.29

different resection lengths, the mean length of the prosthesis was 178.6 ± 50.1 mm. Based on the residual length and the diameter of the intramedullary cavity, the mean length and diameter of the prosthesis stem were 48.6 ± 3.8 mm and $10.7 \pm .8$ mm, respectively.

Surgeries took $3.3 \pm .7$ h and the mean volume of intraoperative hemorrhage was 225.7 ± 59.1 ml. The entire supraspinatus and most of the infraspinatus were preserved in every case. The teres minor was rarely preserved, and part of the subscapularis was preserved.

The mean follow-up period was 26 months (range, 18–33 months). The average MSTS score was 94.3%, which increased with statistical

difference ($p < .05$). Average abduction was 83.8° , flexion was 82.5° , extension was 43.8° , and adduction was 16.3° in this series (Figure 5). No aseptic loosening, breakage, dislocation, and infection of prostheses were found until the last follow up. No local recurrence and distant metastasis were observed in all cases. One patient had radial nerve palsy, which recovered completely 5 weeks after surgery. The absence of radiolucency between the prosthesis and the bone was observed with T-SMART 6 months postoperatively (Figure 6). Intraoperative data and oncologic and functional outcomes are summarized in Table 4.



FIGURE 5
The shoulder abduction of case 1 was normal 6 months after surgery.

4 Discussion

Tumorous defect reconstructions with shoulder joint preservation involving the metaphysis are challenging due to the limited surgical techniques and prosthesis designs. Our 3D printed porous prosthesis with cone-like structures successfully achieved joint-sparing reconstruction of proximal humeral tumorous defects with satisfying functional outcomes.

Prosthetic reconstruction is probably the most widely used method because of its availability, low complication rates, and acceptable functional results compared with other approaches (Ceruso et al., 2001; Gupta et al., 2017). The resection length and residual bone are important parameters for the application of an intercalary prosthesis. Benevenia et al. suggested that an intercalary prosthesis is a good reconstruction method for humeral defects when residual bone length is ≥ 4 cm (Benevenia et al., 2016). However, the length of intramedullary fixation severely restricted the application of the prosthesis. Abudu et al. (1996) showed that an intercalary prosthesis has a high risk of early loosening when the intramedullary fixation length is < 5 cm. When the fixation length is < 4 cm, a previous study advocated for extracortical plates to enhance fixation (Sewell et al., 2011). When the residual bone length is < 3 cm, or even 2 cm, the remaining humeral head has to be sacrificed for arthroplasty, which leads to potentially increased instability and a permanent reduction in limb function (Hardes et al., 2013).

In our study, the newly porous prosthesis successfully reconstructed the humeral defect and preserved the shoulder joint. Average ROM was 83.75° for abduction, 82.5° for flexion, 43.75° for extension, and 16.25° for adduction. The functional results showed an average MSTS score of 94.29%, which is better than those of other series (Wittig et al., 2002; Li et al., 2012; Zheng et al., 2019). In all cases, periprosthetic radiolucency disappeared 6 months postoperatively, and bone ingrowth could be observed with T-SMART.

Good osseointegration induced by uncemented fixation is essential for the long-term survival of the prosthesis with joint preservation. By

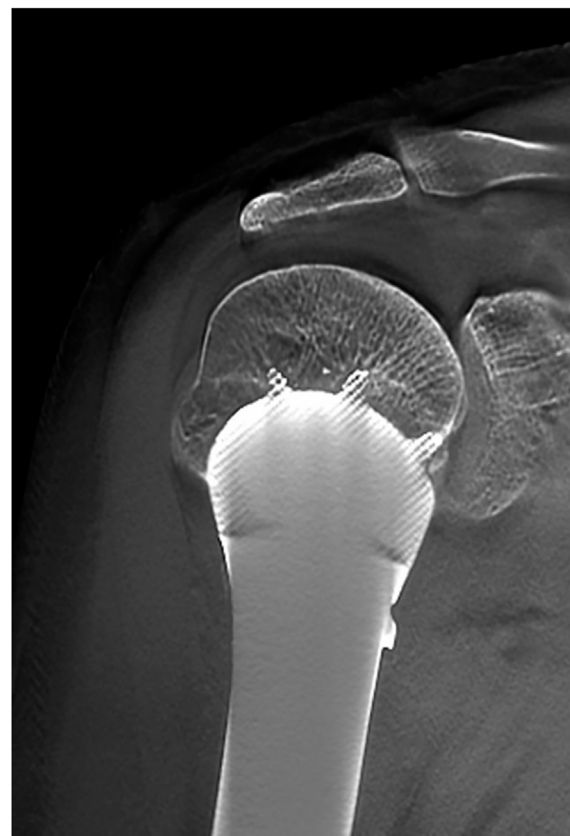


FIGURE 6
T-SMART showed preliminary osseointegration 6 months after surgery.

contrast, cemented fixation failed to achieve joint-preserving reconstruction in cases of residual bone length of < 2 cm, and certainly cannot achieve interfacial integration, which inevitably results in prosthesis loosening or dislocation. McGrath et al. reported on 13 patients who underwent cemented intercalary prosthetic reconstruction (the shortest intramedullary stem = 3 cm) for malignant bone disease of the humerus (McGrath et al., 2011). Aseptic loosening occurred in four cases, and two patients presented with periprosthetic fractures. The overall complication rate related to the prosthesis was 31%. To promote osseointegration, the structure of the prosthesis was optimized. Previous studies showed that the porous structures (pore size of $300\text{--}800\text{ }\mu\text{m}$ and porosity of 70%) at the interface could enhance bone ingrowth (Karageorgiou and Kaplan, 2005; Palmquist et al., 2013; Hara et al., 2016; Shah et al., 2016; Wang et al., 2019). So, porous structures with a porosity of 70% and pore size of $600\text{ }\mu\text{m}$ were applied in the shell layer of the prosthesis head in our study.

However, osseointegration could be affected by micromotion through the formation of fibrous tissues and the induction of bone resorption (Pilliar et al., 1986). To reduce micromotion, we designed cone-like structures with uniform distribution on the prosthesis head. The advantages of the cone design are as follows. First, the design increases the contact surface and friction to reduce micromotion. Second, axial pressure makes the cones anchor into the spongy bone, which improves the initial rotational stability. Third, the contact of the

TABLE 4 Intraoperative data and oncologic and functional outcomes.

Case	Surgery time (h)	Intraoperative hemorrhage (ml)	Tissue preservation				Closest margin (mm)	Local recurrence	Limb shortening (mm)	Complication	MSTS score (%)
			Musculus infraspinatus	Musculus supraspinatus	Musculus teres minor	Musculus subscapularis					
1	2.1	150	Most	All	None	Partial	10.0	No	3.25	—	93
2	3.5	230	Most	All	Little	Partial	10.0	No	5.53	Radial nerve palsy	90
3	2.7	200	Most	All	Little	Partial	9.0	No	-2.67	—	97
4	4.2	340	Most	All	Little	Partial	9.0	No	3.60	—	93
5	3.0	200	Most	All	Little	Partial	9.5	No	-1.49	—	97
6	3.1	250	Most	All	Little	Partial	9.0	No	-1.95	—	97
7	4.0	210	Most	All	Little	Partial	10.0	No	-1.02	—	93
Mean	3.23	225.71	—	—	—	—	9.5	—	.75	—	94.29

cancellous bone and cones increases the shear force of the interface to avoid possible relative displacement. Furthermore, the tight sutures of the humeral head to the prosthesis provide axial stability to prevent the separation of the bone and the prosthesis. Moreover, all patients were restricted to passive movements of the involved shoulder by limb immobilization within the first 4 weeks, during which time bone ingrowth occurred. The optimization of the porous shell and the control of micromotion laid the foundation for subsequent functional rehabilitation. Comparatively, cemented intramedullary fixation relies on the adhesive properties of cement to provide initial stability. [Zhao et al. \(2020\)](#) suggested that high rotational stress and traction play a role in the early loosening of cemented fixation and recommended adding a preventive additional extracortical plate to share the partial stress of the intramedullary fixation. However, extracortical plate implantation increases the risk of prosthesis related complications, such as infection and rupture.

There were no cases of subluxation or dislocation in our study. Patients could even complete circumduction movements in the sagittal plane ([Supplementary Video S1](#)). Dynamic x-rays showed smooth movement of the shoulder joint ([Supplementary Video S2](#)). By comparison, patients have been reported to present with decreased shoulder abduction after resection of the proximal humerus, even after undergoing arthroplasty or bone graft ([Wittig et al., 2002](#)). In Dubina's review, 84 patients from eight studies of shoulder arthroplasty were analyzed. The mean MSTS score was 70%, and 26% patients presented with mechanical failure. The favorable result of our study depends not only on the prosthesis design rationale but also on important anatomic structure preservation and precise surgical techniques. First, the preservation of the shoulder joint and rotator cuff directly resulted in good function of the shoulder joint. Although direct attachment of the residual rotator cuff to the allograft or prosthesis was performed, some proximal subluxation inevitably occurs because of the improper reconstruction of the rotator cuff ([Ayoub et al., 1999](#); [Black et al., 2007](#)). Joint preservation reduced the difficulty of muscle reconstruction and the damage to the muscle insertions, which enhanced postoperative recovery. Second, the preservation of the articular capsule and rotator cuff maintained the passive tension of the joint. When the shoulder joint is in motion, passive tension in the rotator cuff provides compressive stress between the articular surfaces, which forms concavity compression to stabilize the joint ([Halder et al., 2001](#)). Additionally, the coordination of rotator cuff muscle contraction keeps the stress in balance in all directions, which is conducive to the stability of the shoulder joint ([Lee et al., 2000](#); [Abboud and Soslowsky, 2002](#)). In our study, all patients had their entire humeral head and most of the rotator cuff preserved. Each insertion of the rotator cuff around the anatomical neck was marked with suture traction before the osteotomy and was sutured *in situ* after prosthesis implantation. The supraspinatus was intact and most of the infraspinatus was preserved because the insertion position was superior to the osteotomy plane. However, part of the subscapularis and most of the teres minor were removed to ensure a curative margin. Thus, we used Marlex mesh to repair the insufficient muscles. Therefore, the stability of the glenohumeral joint was well preserved and joint tension was maintained. On the basis of the stability of the glenohumeral joint, other muscles that also influence shoulder abduction, such as the deltoid muscle and pectoralis major, were carefully sutured through the designed holes on the prosthesis surface.

Our study has some limitations. First, because of the differences in the extent of the resections and disease processes, it was difficult to formulate a comparative control group. Second, there was no biomechanical analysis included in our study. Future studies should include a finite element analysis. Third, it is possible that more complications might arise after a longer follow up, but a safe surgical margin was obtained and no local recurrence was recorded at our last follow up. Therefore, further research should be performed and a longer follow up is needed.

5 Conclusion

A 3D printed prosthesis with cone-like structures can successfully achieve joint-sparing reconstruction of proximal humeral tumorous defects. The prosthesis was designed to improve initial stability and promote osteointegration, which ensured good survival. A surgical technique that considers shoulder joint integrity and passive tension balance results in favorable function.

Data availability statement

The original contributions presented in the study are included in the article/[Supplementary Material](#), further inquiries can be directed to the corresponding authors.

Ethics statement

Written informed consent was obtained from the individual(s) for the publication of any potentially identifiable images or data included in this article.

Author contributions

YuZ, ML, LM, and CT were involved with the concept and design of this manuscript. JW, XH, and YuZ were involved with the acquisition of subjects and data. YuZ, ML, and CT were involved in the design of the prosthesis. LM, YL, ZL, TG, and CT were involved in the postsurgical evaluation of the patients. All authors contributed to the data analysis, drafted and critically revised the manuscript, and approved the submitted manuscript and agreed to be accountable for all aspects of the work.

References

- Abboud, J. A., and Soslowsky, L. J. (2002). Interplay of the static and dynamic restraints in glenohumeral instability. *Clin. Orthop. Relat. Res.* 400, 48–57. doi:10.1097/00003086-200207000-00007
- Abudu, A., Carter, S. R., and Grimer, R. J. (1996). The outcome and functional results of diaphyseal endoprostheses after tumour excision. *J. Bone Jt. Surg. Br.* 78 (4), 652–657. doi:10.1302/0301-620x.78b4.0780652
- Arndt, C. A., Rose, P. S., Folpe, A. L., and Laack, N. N. (2012). Common musculoskeletal tumors of childhood and adolescence. *Mayo Clin. Proc.* 87 (5), 475–487. doi:10.1016/j.mayocp.2012.01.015
- Ayoub, K. S., Fiorenza, F., Grimer, R. J., Tillman, R. M., and Carter, S. R. (1999). Extensible endoprostheses of the humerus after resection of bone tumours. *J. Bone Jt. Surg. Br.* 81 (3), 495–500. doi:10.1302/0301-620x.81b3.0810495
- Batta, V., Coathup, M. J., Parratt, M. T., Pollock, R. C., Aston, W. J., Cannon, S. R., et al. (2014). Uncemented, custom-made, hydroxyapatite-coated collared distal femoral endoprostheses: Up to 18 years' follow-up. *Bone Jt. J.* 96-B (2), 263–269. doi:10.1302/0301-620x.96b2.32091
- Benevenia, J., Kirchner, R., Patterson, F., Beebe, K., Wirtz, D. C., Rivero, S., et al. (2016). Outcomes of a modular intercalary endoprosthesis as treatment for segmental defects of the femur, tibia, and humerus. *Clin. Orthop. Relat. Res.* 474 (2), 539–548. doi:10.1007/s11999-015-4588-z
- Bielack, S. S., Kempf-Bielack, B., Delling, G., Exner, G. U., Flege, S., Helmke, K., et al. (2002). Prognostic factors in high-grade osteosarcoma of the extremities or trunk: An analysis of 1,702 patients treated on neoadjuvant cooperative osteosarcoma study group protocols. *J. Clin. Oncol.* 20 (3), 776–790. doi:10.1200/jco.2002.20.3.776

Funding

This work was supported, in part, by the Sichuan Provincial Science and Technology Department Project (2020YFS0036), the 1-3-5 Project for Disciplines of Excellence of the West China Hospital of Sichuan University (ZYJC18036 and ZYJC18017), a project funded by China Postdoctoral Science Foundation (2021M702342), and the Clinical Research Incubation Project of West China Hospital of Sichuan University (2020HXFH004) for the design of the prosthesis, the collection, analysis, and interpretation of the data.

Acknowledgments

We thank Xianliang Zhang (Department of Pathology, West China Hospital, Sichuan, China) for pathology evaluation.

Conflict of interest

The authors declare that the research was conducted in the absence of any commercial or financial relationships that could be construed as a potential conflict of interest.

Publisher's note

All claims expressed in this article are solely those of the authors and do not necessarily represent those of their affiliated organizations, or those of the publisher, the editors and the reviewers. Any product that may be evaluated in this article, or claim that may be made by its manufacturer, is not guaranteed or endorsed by the publisher.

Supplementary material

The Supplementary Material for this article can be found online at: <https://www.frontiersin.org/articles/10.3389/fbioe.2022.1098973/full#supplementary-material>

SUPPLEMENTARY VIDEO S1

Circumduction movement in the sagittal plane of a patient.

SUPPLEMENTARY VIDEO S2

Dynamic x-ray of the shoulder joint movement of a patient.

- Black, A. W., Szabo, R. M., and Titelman, R. M. (2007). Treatment of malignant tumors of the proximal humerus with allograft-prosthesis composite reconstruction. *J. Shoulder Elb. Surg.* 16 (5), 525–533. doi:10.1016/j.jse.2006.12.006
- Ceruso, M., Falcone, C., Innocenti, M., Delcroix, L., Capanna, R., and Manfrini, M. (2001). Skeletal reconstruction with a free vascularized fibula graft associated to bone allograft after resection of malignant bone tumor of limbs. *Handchir Mikročir Plast. Chir.* 33 (4), 277–282. doi:10.1055/s-2001-16597
- Chauhan, V. S., Vaish, A., and Vaishya, R. (2019). Reverse shoulder arthroplasty after failed megaprosthesis for osteosarcoma of the proximal humerus: A case report and review of literature. *J. Clin. Orthop. Trauma* 10 (3), 526–530. doi:10.1016/j.jcot.2019.03.015
- Damron, T. A., Leerapun, T., Hugate, R. R., Shives, T. C., and Sim, F. H. (2008). Does the second-generation intercalary humeral spacer improve on the first? *Clin. Orthop. Relat. Res.* 466 (6), 1309–1317. doi:10.1007/s11999-008-0246-z
- Enneking, W. F. (1986). A system of staging musculoskeletal neoplasms. *Clin. Orthop. Relat. Res.* 204 (204), 9–24. doi:10.1097/00003086-198603000-00003
- Gupta, S., Kafchinski, L. A., Gundle, K. R., Saidi, K., Griffin, A. M., Wunder, J. S., et al. (2017). Intercalary allograft augmented with intramedullary cement and plate fixation is a reliable solution after resection of a diaphyseal tumour. *Bone Jt. J.* 99-B (7), 973–978. doi:10.1302/0301-620x.99b7.bjj-2016-0996
- Halder, A. M., Kuhl, S. G., Zobitz, M. E., Larson, D., and An, K. N. (2001). Effects of the glenoid labrum and glenohumeral abduction on stability of the shoulder joint through concavity-compression: An *in vitro* study. *J. Bone Jt. Surg. Am.* 83 (7), 1062–1069. doi:10.2106/00004623-200107000-00013
- Hara, D., Nakashima, Y., Sato, T., Hirata, M., Kanazawa, M., Kohno, Y., et al. (2016). Bone bonding strength of diamond-structured porous titanium-alloy implants manufactured using the electron beam-melting technique. *Mater. Sci. Eng. C Mater. Biol. Appl.* 59, 1047–1052. doi:10.1016/j.msec.2015.11.025
- Hardes, J., Henrichs, M. P., Gosheger, G., Gebert, C., Holl, S., Dieckmann, R., et al. (2013). Endoprosthetic replacement after extra-articular resection of bone and soft-tissue tumours around the knee. *Bone Jt. J.* 95-B (10), 1425–1431. doi:10.1302/0301-620x.95b10.31740
- Karageorgiou, V., and Kaplan, D. (2005). Porosity of 3D biomaterial scaffolds and osteogenesis. *Biomaterials* 26 (27), 5474–5491. doi:10.1016/j.biomaterials.2005.02.002
- King, J. J., Nystrom, L. M., Reimer, N. B., Gibbs, C. P., Jr., Scarborough, M. T., and Wright, T. W. (2016). Allograft-prosthetic composite reverse total shoulder arthroplasty for reconstruction of proximal humerus tumor resections. *J. Shoulder Elb. Surg.* 25 (1), 45–54. doi:10.1016/j.jse.2015.06.021
- Kumta, S. M., Chow, T. C., Griffith, J., Li, C. K., Kew, J., and Leung, P. C. (1999). Classifying the location of osteosarcoma with reference to the epiphyseal plate helps determine the optimal skeletal resection in limb salvage procedures. *Arch. Orthop. Trauma Surg.* 119 (5–6), 327–331. doi:10.1007/s004020050420
- Lee, S. B., Kim, K. J., O'Driscoll, S. W., Morrey, B. F., and An, K. N. (2000). Dynamic glenohumeral stability provided by the rotator cuff muscles in the mid-range and end-range of motion. A study in cadavera. *J. Bone Jt. Surg. Am.* 82 (6), 849–857. doi:10.2106/00004623-200006000-00012
- Li, J., Wang, Z., Guo, Z., Wu, Y., Chen, G., and Pei, G. (2012). Precise resection and biological reconstruction for patients with bone sarcomas in the proximal humerus. *J. Reconstr. Microsurg* 28 (6), 419–425. doi:10.1055/s-0032-1315766
- Liu, T., Zhang, Q., Guo, X., Zhang, X., Li, Z., and Li, X. (2014). Treatment and outcome of malignant bone tumors of the proximal humerus: Biological versus endoprosthetic reconstruction. *BMC Musculoskelet. Disord.* 15, 69. doi:10.1186/1471-2474-15-69
- Lu, M., Li, Y., Luo, Y., Zhang, W., Zhou, Y., and Tu, C. (2018). Uncemented three-dimensional-printed prosthetic reconstruction for massive bone defects of the proximal tibia. *World J. Surg. Oncol.* 16 (1), 47. doi:10.1186/s12957-018-1333-6
- Maclean, S., Malik, S. S., Evans, S., Gregory, J., and Jeys, L. (2017). Reverse shoulder endoprosthesis for pathologic lesions of the proximal humerus: A minimum 3-year follow-up. *J. Shoulder Elb. Surg.* 26 (11), 1990–1994. doi:10.1016/j.jse.2017.04.005
- McGrath, A., Sewell, M. D., Hanna, S. A., Pollock, R. C., Skinner, J. A., Cannon, S. R., et al. (2011). Custom endoprosthetic reconstruction for malignant bone disease in the humeral diaphysis. *Acta Orthop. Belg* 77 (2), 171–179.
- Nota, S., Teunis, T., Kortlever, J., Ferrone, M., Ready, J., Gebhardt, M., et al. (2018). Functional outcomes and complications after oncologic reconstruction of the proximal humerus. *J. Am. Acad. Orthop. Surg.* 26 (11), 403–409. doi:10.5435/jaaos-d-16-00551
- Palmquist, A., Snis, A., Emanuelsson, L., Browne, M., and Thomsen, P. (2013). Long-term biocompatibility and osseointegration of electron beam melted, free-form-fabricated solid and porous titanium alloy: Experimental studies in sheep. *J. Biomater. Appl.* 27 (8), 1003–1016. doi:10.1177/0885328211431857
- Panagopoulos, G. N., Mavrogenis, A. F., Mauffrey, C., Lesensky, J., Angelini, A., Megaloikonomos, P. D., et al. (2017). Intercalary reconstructions after bone tumor resections: A review of treatments. *Eur. J. Orthop. Surg. Traumatol.* 27 (6), 737–746. doi:10.1007/s00590-017-1985-x
- Pilge, H., Ruppert, M., Bittersohl, B., Westhoff, B., and Krauspe, R. (2018). Lengthening of newly formed humerus after autologous fibula graft transplantation following intercalary tumor resection. *J. Pediatr. Orthop. B* 27 (4), 322–325. doi:10.1097/bpb.0000000000000464
- Pilliar, R. M., Lee, J. M., and Maniopoulos, C. (1986). Observations on the effect of movement on bone ingrowth into porous-surfaced implants. *Clin. Orthop. Relat. Res.* 208 (208), 108–113. doi:10.1097/00003086-198607000-00023
- Potter, B. K., Adams, S. C., and Pitcher, J. D., Jr. (2009). Proximal humerus reconstructions for tumors. *Clin. Orthop. Relat. Res.* 467 (4), 1035–1041. doi:10.1007/s11999-008-0531-x
- Rafalla, A. A., and Abdullah, E. S. A. (2017). Endoprosthetic replacement versus cement spacer in reconstruction of proximal humerus after tumor resection: Cost and benefits. *J. Orthop. Surg. Hong. Kong* 25 (2), 230949901771393. doi:10.1177/2309499017713937
- Ruggieri, P., Mavrogenis, A. F., Guerra, G., and Mercuri, M. (2011). Preliminary results after reconstruction of bony defects of the proximal humerus with an allograft-resurfacing composite. *J. Bone Jt. Surg. Br.* 93 (8), 1098–1103. doi:10.1302/0301-620x.93b8.26011
- Sewell, M. D., Hanna, S. A., McGrath, A., Aston, W. J., Blunn, G. W., Pollock, R. C., et al. (2011). Intercalary diaphyseal endoprosthetic reconstruction for malignant tibial bone tumours. *J. Bone Jt. Surg. Br.* 93 (8), 1111–1117. doi:10.1302/0301-620x.93b8.25750
- Shah, F. A., Omar, O., Suska, F., Snis, A., Matic, A., Emanuelsson, L., et al. (2016). Long-term osseointegration of 3D printed CoCr constructs with an interconnected open-pore architecture prepared by electron beam melting. *Acta Biomater.* 36, 296–309. doi:10.1016/j.actbio.2016.03.033
- Wang, C., Liu, D., Xie, Q., Liu, J., Deng, S., Gong, K., et al. (2019). A 3D printed porous titanium alloy rod with diamond crystal lattice for treatment of the early-stage femoral head osteonecrosis in sheep. *Int. J. Med. Sci.* 16 (3), 486–493. doi:10.7150/ijms.30832
- Wieser, K., Modaresi, K., Seeli, F., and Fuchs, B. (2013). Autologous double-barrel vascularized fibula bone graft for arthrodesis of the shoulder after tumor resection. *Arch. Orthop. Trauma Surg.* 133 (9), 1219–1224. doi:10.1007/s00402-013-1795-5
- Wittig, J. C., Bickels, J., Kellar-Graney, K. L., Kim, F. H., and Malawer, M. M. (2002). Osteosarcoma of the proximal humerus: Long-term results with limb-sparing surgery. *Clin. Orthop. Relat. Res.* 397, 156–176. doi:10.1097/00003086-200204000-00021
- Yoshida, Y., Osaka, S., and Tokuhashi, Y. (2010). Analysis of limb function after various reconstruction methods according to tumor location following resection of pediatric malignant bone tumors. *World J. Surg. Oncol.* 8, 39. doi:10.1186/1477-7819-8-39
- Zekry, K. M., Yamamoto, N., Hayashi, K., Takeuchi, A., Alkhooly, A. Z. A., Abd-Elfattah, A. S., et al. (2019). Reconstruction of intercalary bone defect after resection of malignant bone tumor. *J. Orthop. Surg. Hong. Kong* 27 (1), 230949901983297. doi:10.1177/2309499019832970
- Zhao, D., Tang, F., Min, L., Lu, M., Wang, J., Zhang, Y., et al. (2020). Intercalary reconstruction of the “ultra-critical sized bone defect” by 3D-printed porous prosthesis after resection of tibial malignant tumor. *Cancer Manag. Res.* 12, 2503–2512. doi:10.2147/cmar.s245949
- Zheng, K., Yu, X. C., Hu, Y. C., Shao, Z. W., Xu, M., Wang, B. C., et al. (2019). Outcome of segmental prosthesis reconstruction for diaphyseal bone tumors: A multi-center retrospective study. *BMC Cancer* 19 (1), 638. doi:10.1186/s12885-019-5865-0



OPEN ACCESS

EDITED BY

Chunguang Yang,
Institute of Metal Research (CAS), China

REVIEWED BY

Vamsi Krishna Balla,
Central Glass and Ceramic Research
Institute (CSIR), India
Changlu Xu,
University of California, Los Angeles,
United States

*CORRESPONDENCE

Jingzhou Yang,
✉ yangjz@qut.edu.cn
Xinhua Qu,
✉ xinhua_qu@126.com
Bing Yue,
✉ advbmp2@163.com

[†]These authors have contributed equally to
this work

SPECIALTY SECTION

This article was submitted to Biomaterials,
a section of the journal
Frontiers in Bioengineering and
Biotechnology

RECEIVED 07 December 2022

ACCEPTED 18 January 2023

PUBLISHED 27 January 2023

CITATION

Jiao J, Hong Q, Zhang D, Wang M, Tang H,
Yang J, Qu X and Yue B (2023), Influence of
porosity on osteogenesis, bone growth
and osteointegration in trabecular
tantalum scaffolds fabricated by
additive manufacturing.
Front. Bioeng. Biotechnol. 11:1117954.
doi: 10.3389/fbioe.2023.1117954

COPYRIGHT

© 2023 Jiao, Hong, Zhang, Wang, Tang,
Yang, Qu and Yue. This is an open-access
article distributed under the terms of the
[Creative Commons Attribution License
\(CC BY\)](https://creativecommons.org/licenses/by/4.0/). The use, distribution or
reproduction in other forums is permitted,
provided the original author(s) and the
copyright owner(s) are credited and that
the original publication in this journal is
cited, in accordance with accepted
academic practice. No use, distribution or
reproduction is permitted which does not
comply with these terms.

Influence of porosity on osteogenesis, bone growth and osteointegration in trabecular tantalum scaffolds fabricated by additive manufacturing

Juyang Jiao^{1†}, Qimin Hong^{1†}, Dachen Zhang^{2,3}, Minqi Wang¹,
Haozheng Tang¹, Jingzhou Yang^{4,2,3*}, Xinhua Qu^{1*} and Bing Yue^{1*}

¹Department of Bone and Joint Surgery, Department of Orthopedics, Renji Hospital, Shanghai Jiao Tong University School of Medicine, Shanghai, China, ²Shenzhen Dazhou Medical Technology Co., Ltd., Shenzhen, Guangdong, China, ³Center of Biomedical Materials 3D Printing, National Engineering Laboratory for Polymer Complex Structure Additive Manufacturing, Baoding, Hebei, China, ⁴School of Mechanical and Automobile Engineering, Qingdao University of Technology, Qingdao, Shandong, China

Porous tantalum implants are a class of materials commonly used in clinical practice to repair bone defects. However, the cumbersome and problematic preparation procedure have limited their widespread application. Additive manufacturing has revolutionized the design and process of orthopedic implants, but the pore architecture feature of porous tantalum scaffolds prepared from additive materials for optimal osseointegration are unclear, particularly the influence of porosity. We prepared trabecular bone-mimicking tantalum scaffolds with three different porosities (60%, 70% and 80%) using the laser powder bed fusing technique to examine and compare the effects of adhesion, proliferation and osteogenic differentiation capacity of rat mesenchymal stem cells on the scaffolds *in vitro*. The *in vivo* bone ingrowth and osseointegration effects of each scaffold were analyzed in a rat femoral bone defect model. Three porous tantalum scaffolds were successfully prepared and characterized. *In vitro* studies showed that scaffolds with 70% and 80% porosity had a better ability to osteogenic proliferation and differentiation than scaffolds with 60% porosity. *In vivo* studies further confirmed that tantalum scaffolds with the 70% and 80% porosity had a better ability for bone ingrowth than the scaffold with 60% porosity. As for osseointegration, more bone was bound to the material in the scaffold with 70% porosity, suggesting that the 3D printed trabecular tantalum scaffold with 70% porosity could be the optimal choice for subsequent implant design, which we will further confirm in a large animal preclinical model for better clinical use.

KEYWORDS

additive manufacturing, bone repair, osseointegration, porosity, tantalum scaffold, trabecular

1 Introduction

Bone tissue has a natural regenerative and self-healing capacity to repair minor injuries such as cracks. However, large bone defects caused by severe trauma, degenerative disease, congenital malformations or surgical removal of malignant tumors often require surgical intervention to reconstruct bone morphology and function so as to achieve complete healing (McDermott et al., 2019; Koons et al., 2020). Moreover, changes in the bone microenvironment caused by

degenerative diseases, infections, osteoporosis, and bone metastases have a large influence on bone repair (Claes et al., 2012). Current bone repair materials successfully used in clinical settings are bioactive bone (homogeneous autologous bone/homogeneous allogeneous bone/xenogeneic bone), bioceramics (hydroxyapatite, calcium phosphate, tricalcium phosphate), inorganic/organic polymers (collagen, alginate, polylactic acid, polyethylene glycol) and biomedical metals (titanium, stainless steel and tantalum) (Webber et al., 2016; Gillman and Jayasuriya, 2021). Bioactive bone is the gold standard for bone repair materials due to its excellent osteogenic, osteoinductive and osteoconductive properties, but insufficient donor sources, collateral donor site damage, potential risk of infectious disease transmission and immunogenicity restrict its large-scale use (Amini et al., 2012). Bioceramics provide relatively high compression modulus and release bioactive ions, but are brittle (Jakus et al., 2016). Polymers are widely available and easy to modify, but also have weak mechanical properties and immunogenicity risks (Guo et al., 2021). Therefore, the above materials are mostly used to repair small, non-weight-bearing bone defects, while metal is the best solution for critical and weight-bearing bone defects due to its excellent mechanical properties and good biocompatibility (Pobloth et al., 2018). Pure titanium and titanium alloys (Ti6Al4V) are the most commonly used metal implants in clinical practice which have high mechanical strength, fatigue resistance and corrosion resistance, but they also suffer from aseptic loosening around the implant due to the stress-shielding effect caused by high elastic modulus, side effects related to corrosion-induced ion release, and poor osseointegration performance (Alipal et al., 2021).

Tantalum metal has excellent biological affinity, superior corrosion resistance, good mechanical ductility, bone formation and bone conduction properties, and is increasingly favored by clinicians and researchers (Levine et al., 2006). As an inert metal, tantalum can combine with oxygen to form a stable tantalum pentoxide (Ta_2O_5) passivation film, which is not easy to corrode; At the same time, the presence of oxide film is conducive to the formation of osteoid apatite coating and reduces the adhesion and colonization of bacteria (Han et al., 2019). Similar to the elastic modulus (110 GPa) of titanium alloys, the elastic modulus of dense bulk tantalum (186 GPa) is significantly higher than that of human cortical bone (3–30 GPa) and cancellous bone (0.02–2 GPa) (Wang et al., 2016; 2021). In addition, the high density (16.68 g/cm³) and high melting point (2,996°C) of tantalum constrain the industrial manufacturing and medical applications of tantalum materials (Black, 1994). It was not until the 1990s that a highly porous trabecular tantalum metal (Trabecular Metal™(TM), Zimmer, Warsaw, IN, United States) prepared by chemical vapor deposition (CVD) was introduced and successfully used in clinical applications, including but not limited to femoral or tibial cone and augmentation in knee/hip arthroplasty revision, monoblock/modular tibial component, acetabular cup prosthesis, femoral necrosis reconstruction rods, interbody fusion cage, artificial shoulder prosthesis and dental implants (Bobyn et al., 1999; Christie, 2002; Cohen, 2002; Huang et al., 2021). However, there are still some intractable key problems with the CVD method. First, this traditional preparation technology is costly, time-consuming, and inefficient; second, it is difficult to prepare bone implants that are individually tailored by the patient to fit the shape of the anatomical site; and third, it is impossible to guarantee the

accuracy of the design and control of the porous structural features of the scaffold.

Additive manufacturing, as an advanced, powerful and mature processing technology, overcomes the deficiencies of traditional techniques and can be used to manufacture porous metal scaffolds with complex layered structures and high precision, which has very attractive application prospects (Bose et al., 2018). Additive manufacturing technologies are still progressing rapidly, including but not limited to selective laser melting (SLM), electron beam melting (EBM), selective laser sintering (SLS), laser engineered net shaping (LENS), fused deposition modeling, binder jetting, and direct metal printing (Chen Y. et al., 2020). SLM (Wauthle et al., 2015; Guo et al., 2019; Wang et al., 2019; Yang et al., 2020) and LENS (Balla et al., 2010; Bandyopadhyay et al., 2019) has been successfully used in the preparation of porous tantalum scaffolds. Among them, SLM, in particular Laser-based powder bed fusion (LPBF), stands out for its good stability, high efficiency, smooth surface finish and the ability to precisely tune the internal pore architecture of the porous structure.

The porous structure is critical for the mechanical and biological properties of the implant. Porosity, pore geometry, pore size, strut diameter and interconnectivity of pores are important parameters for the topology design of porous architectures (Gao et al., 2021). Among these, porosity is regarded as the dominant effect affecting the mechanical (stiffness and hardness) and biological properties of the implant, with other parameters such as pore geometry being a non-negligible secondary effect (Al-Ketan et al., 2018; Kelly et al., 2018). On the one hand, high porosity reduces the mechanical strength of metal scaffolds and subsequently achieves an elastic modulus comparable to that of bone, which helps to reduce stress shielding; on the other hand, high porosity provides a large specific surface area to promote cell migration as well as nutrient delivery and improves osseointegration. Several studies have reported the effect of porosity on the performance of porous metal scaffolds (Cheng et al., 2014; Chen Z. et al., 2020; Pei et al., 2021). Cheng et al. prepared a titanium alloy scaffold mimicking the structure of human cancellous bone using SLS and compared the effects of three porosities (16%, 38% and 70%, respectively) on *in vitro* osteogenesis, and found that the scaffold with 70% porosity was more favorable for osteoblast proliferation and differentiation (Cheng et al., 2014). Chen et al. compared Ti6Al4V ELI scaffolds with 60% and 70% porosity and showed that the scaffold with 60% porosity had the best bone growth outcome (Chen Z. et al., 2020). Among the porous tantalums prepared by additive materials, Wauthle et al. prepared highly porous tantalum implants (80% porosity) using SLM and demonstrated their excellent osteoconductivity and mechanical properties *in vitro* and *in vivo* (Wauthle et al., 2015). The above contradictory results may be related to the pore structure, material properties, preparation process, etc. Therefore, further studies are needed to comprehensively adjust the porous structure characteristics to achieve the optimization of mechanical and biological properties. Human cancellous bone is a complex morphologically irregular porous structure with porosity ranging from 50% to 90% and pore size of 300–500 µm, with non-homogeneous anisotropic properties (Li et al., 2017). The only porous tantalum implant successfully used in clinical practice to date, Trabecular Metal, uses a bone trabecular structure with 70%–

TABLE 1 Primer sequences of rBMSCs used for qRT-PCR in this study.

Target gene	Direction	Primer sequence (5' to 3')
ALP	Forward	TCG CCT ATC AGC TAA TGC AC
	Reverse	GCC TTC TCA TCC AGT TCA TAT TCC
BMP-2	Forward	AGC ATG TTT GGC CTG AAG CAG AGA
	Reverse	TGA AAG TTC CTC GAT GGC TTC
CXCL-12	Forward	CCG ATT CTT TGA GAG CCA TGT
	Reverse	CAG ACT TGT CTG TTG TTG CTT
OCN	Forward	TAT GGC ACC ACC GTT TAG GG
	Reverse	CTG TGC CGT CCA TAC TTT CG
RUNX-2	Forward	CAA ACA ACC ACA GAA CCA CAA G
	Reverse	CTC AGA GCA CTC ACT GAC TC

85% porosity and an average pore size of 400–600 μm , a unique biomimetic structure that seems to have even more outstanding advantages (Wang et al., 2020). Yang et al. have successfully prepared porous tantalum scaffolds with a more refined trabecular bone mimetic structure using LPBF previously. Compared with the CVD-prepared TM, the trabecular bone tantalum scaffold prepared by SLM has the same porosity, interconnectivity of pores as well as larger pores and coarser filament diameter, and comparable mechanical properties to human cancellous bone (Yang et al., 2020). However, the biological properties of SLM-prepared trabecular tantalum scaffolds have not been fully investigated, especially the effect of porosity. In order to improve the reliability of implants in medical applications and for better clinical translation, there is an urgent need to systematically investigate the effects of porosity on bone formation, bone ingrowth and osseointegration of SLM-prepared trabecular tantalum scaffolds.

Therefore, the aim of this study was to explore the optimal porosity of SLM-prepared trabecular tantalum scaffolds for bone ongrowth and bone ingrowth. To this end, a series of trabecular bone tantalum scaffolds with different porosity were prepared by LPBF and characterized, followed by an *in vitro* study of their cytocompatibility and osteogenic ability, and finally a comparison of bone growth ability and biosafety in a rat femoral bone defect model.

2 Methods

2.1 Material preparation and characterization

We designed three types of porous tantalum scaffolds (60%, 70% and 80%) with different porosity of bionic trabeculae (denoted as Ta T60, Ta T70 and Ta T80, respectively) and prepared porous tantalum discs (10 mm in diameter \times 3 mm in height) for *in vitro* studies and porous tantalum cylinders (3 mm in diameter \times 5 mm in height) for *in vivo* studies with the above structures by 3D printing technology. Specifically, the bionic bone trabeculae structure and 3D conformation of the porous tantalum scaffold were designed by Rhino3D NURBS V7.0 (Robert McNeel & Assoc., Seattle, WA,

United States) and Materialise Magics V22.0 (Materialise N.V., Leuven, Belgium). Based on the aforementioned computer-aided design (CAD) model, The sample was prepared by Dazhou Medical Co., Ltd. (Shenzhen, Guangdong, China)] ulitizing PBLF additive manufacturing system Farsoon FM271M (Farsoon Technologies Co., Ltd., Changsha, Hunan, China). TEKMAT™ Ta-45 powder (TEKNA Advanced Materials Inc., Sherbrooke, QC, Canada) was used, and the powder was melted by the laser under reasonable laser parameter regulation, stacked layer by layer, and solidified into shape. The final sample is obtained after sandblasting and annealing treatment. Finally, sufficient ultrasonic shaking and cleaning were applied to remove the unfused particles from the support.

The pore characteristics, surface morphology and elemental composition of the samples were determined using field emission scanning electron microscopy (FE-SEM, Hitachi S4800, Japan), energy disperse spectroscopy (EDS) and ImageJ were used for the analysis. The actual porosity of the samples was calculated using the weight method at standard atmospheric pressure according to the following formula.

$$\text{Porosity (\%)} = \frac{\text{sample volume} \times \text{material density} - \text{actual sample weight}}{\text{sample volume} \times \text{material density}} \times 100\% \quad (1)$$

Static mechanical testing of porous tantalum scaffolds with different porosity including compression, bending and torsion experiments have been reported in previous studies (Yang et al., 2020).

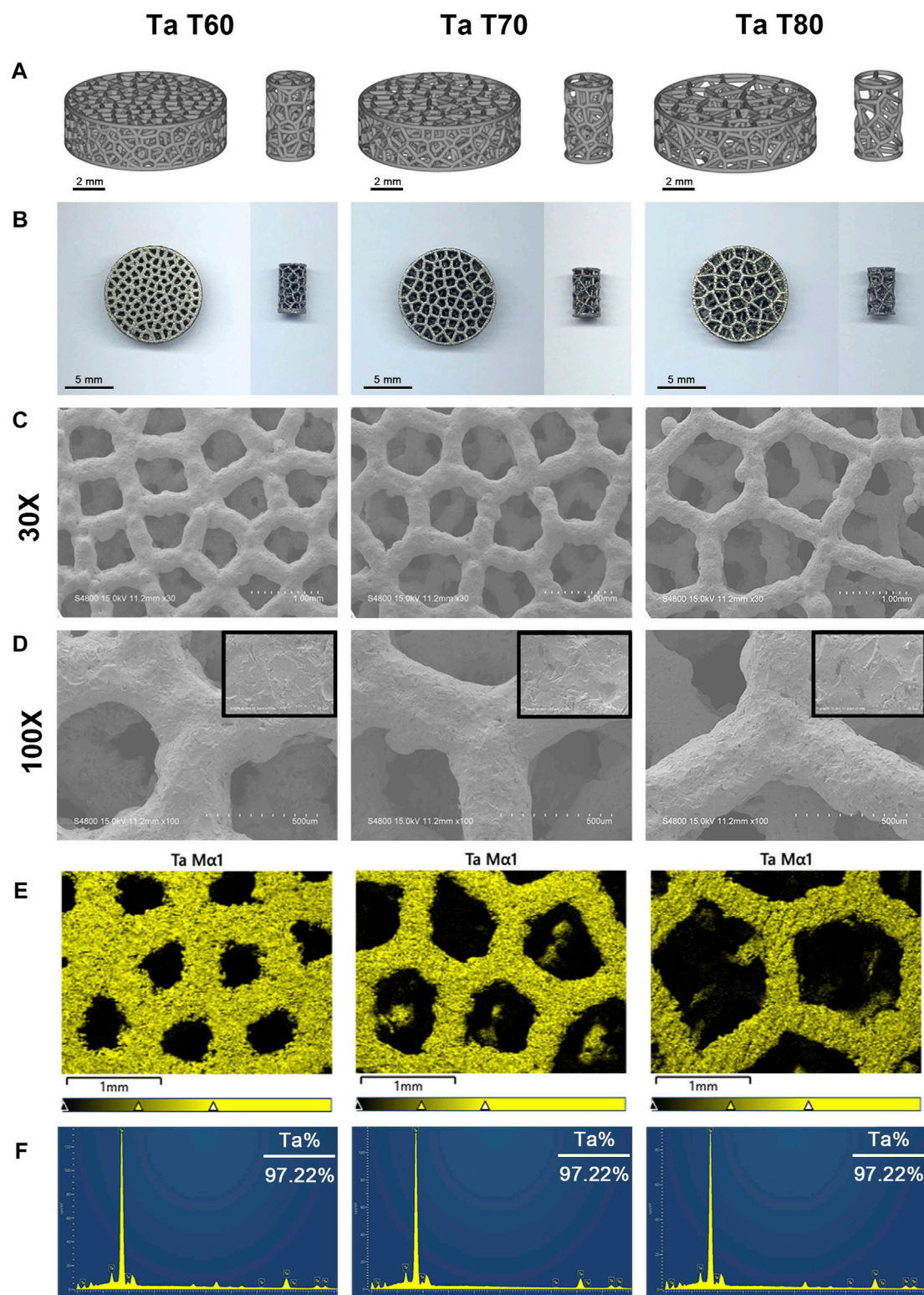
2.2 *In vitro* cytocompatibility assessment

2.2.1 Culture of cells on materials

All materials were sonicated and vortexed for 2 h and washed with ultraclean water to remove unmelted powder prior to use. After autoclaving and drying, porous tantalum scaffolds were placed in 48-well plates with a small amount of Minimum Essential Medium- α (α -MEM, Hyclone) for infiltration. Rat bone marrow mesenchymal stem cells (rBMSCs) were extracted and cultured as previously described (Huo et al., 2021). The cell harvesting was approved by the Animal Ethics Committee of Renji Hospital, Shanghai Jiao Tong University School of Medicine. Briefly, cells were cultured in α -MEM containing 1% penicillin-streptomycin and 10% fetal bovine serum (FBS, Hyclone, Logan, UT, United States) in an incubator (37°C, 5% CO₂ and 95% air) and maintained in an incubator with fluid exchange every 3 days. Cells passed to the second or third generation were used for subsequent experiments. If not otherwise specified, rBMSCs were inoculated on the surface of the scaffolds at a density of 2×10^4 cells/well in 48-well plates with α -MEM submerged scaffolds and fluid exchanges every other day.

2.2.2 Cytotoxicity and hemolytic reactions

Cytotoxicity and proliferation on the scaffold were assessed by Cell Counting Kit-8 (CCK-8) assay and hemolysis assay. The group inoculated with cells alone without scaffold served as control. Cells on scaffolds were assayed on days 1, 3, and 5 using CCK-8 reagent (Dojindo, Kumamoto, Japan). The original medium was replaced with fresh complete medium containing 10% CCK-8 and incubated in the incubator for 2 h. After incubation, 100 μL of supernatant per well was added to a new 96-well plate, and the optical density

**FIGURE 1**

Material characterization of three porous tantalum scaffolds with different porosities. 3D modeling (A) and general appearance (B) of porous tantalum scaffolds (left: disks, right: cylinders). (C) and (D) Surface morphology of porous tantalum scaffolds under electron microscopy at x30 (C) and x100 (D) magnification, respectively (The upper right corner of Figure D is 1,000x magnification). EDS mapping (E) and spectra (F) show the elemental distribution and composition of each scaffold.

(OD) values at 450 nm were measured using a microplate reader (BioTek microplate reader). Each experiment was repeated three times. In addition, fresh blood samples were taken from the tail

vein of rats for the hemolysis test, and the blood cells were collected by centrifugation at 3,000 rpm for 5 min. Phosphate buffer solution (PBS) was washed three times and resuspended to reach a final

TABLE 2 Structural parameters and mechanical properties of 3D-printed porous tantalum scaffolds with different porosities.

			Groups		
			Ta T60	Ta T70	Ta T80
Structural parameters	Porosity (%)	D	60	70	80
		A	56.4	66.7	79.3
	Average pore diameter (μm)	D	450	600	800
	Strut diameter (μm)	D	300	300	300
		A	316.8 ± 17.8	320.3 ± 15.4	330.1 ± 15.4
	Pore interconnectivity (%)	D	100	100	100
		A	99.99	99.99	99.99
Mechanical properties Yang et al. (2020)	Compressive strength (MPa)		59.5 ± 0.2	33.2 ± 0.4	14.2 ± 1
	Compressive modulus (GPa)		3.3 ± 0.3	3 ± 0.2	1.5 ± 0.4
	Bending strength (GPa)		97 ± 4.2	52.8 ± 2.6	23 ± 0.8
	Shear modulus (GPa)		6.8 ± 0.3	2.8 ± 0.6	1.2 ± 0.2
	Torsion strength (MPa)		41.2 ± 0.8	28 ± 0.3	11.2 ± 0.6

Values are represented as the mean ± SD (n = 5). A, actual; D, designed.

erythrocyte concentration of 4% (v/v). The sample was placed in a centrifuge tube, and a sufficient amount of fresh erythrocyte suspension was added. After 2 h incubation at 37°C, samples were centrifuged at 3,000 rpm for 3 min. 100 μL of supernatant was transferred from each tube to a 96-well plate, and the OD value was detected at 560 nm. The 0.1% Triton X-100 solution and PBS were used as positive control and negative control, respectively, and three parallel groups of each sample were used. The hemolysis rate (%) was calculated according to the following formula:

$$\text{Hemolysis rate (\%)} = \frac{\text{OD560 (Sample)} - \text{OD560 (PBS)}}{\text{OD560 (Triton)} - \text{OD560 (PBS)}} \times 100\% \quad (2)$$

(OD560 (Sample), OD560 (PBS) and OD560 (Triton) are the OD value of samples, PBS and Triton X-100 solution at 560 nm, respectively).

2.2.3 Live/dead cell staining

rBMSCs (4×10⁴ cells/well) on the different scaffold were cultured for 7 days, and cell viability was assessed using Calcein/PI Live/Dead Assay Kit (#C2015M, Beyotime Biotechnology, Shanghai) according to the instructions. Briefly, cells on the samples were added to the Calcein/PI working solution, incubated for 30 min at 37°C in the dark and the staining effect was observed under the confocal laser scanning microscope (CLSM).

2.2.4 SEM observation of cell morphology

Cells were cultured as above for 1 day (density of rBMSCs was 2×10⁴ cells/well), and the cells on the surface of the scaffolds were washed 3 times with PBS and fixed overnight at 4°C in 2.5% glutaraldehyde solution. Then, the cells were washed 3 times with deionized water, dehydrated in alcohol solution with stepwise concentrations (30%, 50%, 70%, 80%, 90%, and 100%) for 10 min, dried and sprayed with gold, and observed under a scanning electron microscope (Carl Zeiss, Germany).

2.3 In vitro osteogenic response assessment

2.3.1 Cell culture

rBMSCs were seeded at a density of 2 × 10⁴ cells/well on the surface of the material as described previously, and after 24 h the complete medium was replaced with an osteogenic induction solution (containing 10% FBS, 1% penicillin-streptomycin, 100 nmol/L dexamethasone, 10 mmol/L β-glycerolphosphate and 50 mmol/L ascorbic acid) and continue to incubate at 37°C in a humidified incubator with 5% CO₂, followed by fluid exchanges at 2-day intervals.

2.3.2 Alkaline phosphatase (ALP) staining and activity quantification

ALP staining and activity quantification of cells on the material surface were performed on days 7 and 14. Cells on the surface of the material were fixed with 4% paraformaldehyde for 1 min and stained by BCIP/NBT Alkaline Phosphatase Color Development Kit (#C3206, Beyotime Biotechnology, Shanghai) according to the instructions. Incubated for 30 min at room temperature in the dark, washed and dried, and took pictures. Meanwhile, ALP activity was assayed using the Alkaline Phosphatase Assay Kit (#P0321M, Beyotime Biotechnology, Shanghai). In brief, cells on the scaffold were washed with PBS, lysed on ice for 10 min with 0.1% Triton X-100, and the supernatant was removed. The absorbance was measured at 405 nm according to the operating instructions. In addition, total cellular protein of cells on the surface of each material was quantified using the BCA Protein Assay Kit (#23227, Thermo Scientific Pierce, Rockford, United States), and absorbance was measured at 562 nm. The ALP/total protein ratio was calculated to quantify ALP activity.

2.3.3 Alizarin red S staining and semi-quantification

Cells on scaffolds were examined after 14 and 21 days of culture using the Alizarin Red S Staining Kit for Osteogenesis (#C0138, Beyotime Biotechnology, Shanghai). Briefly, cells on scaffolds were

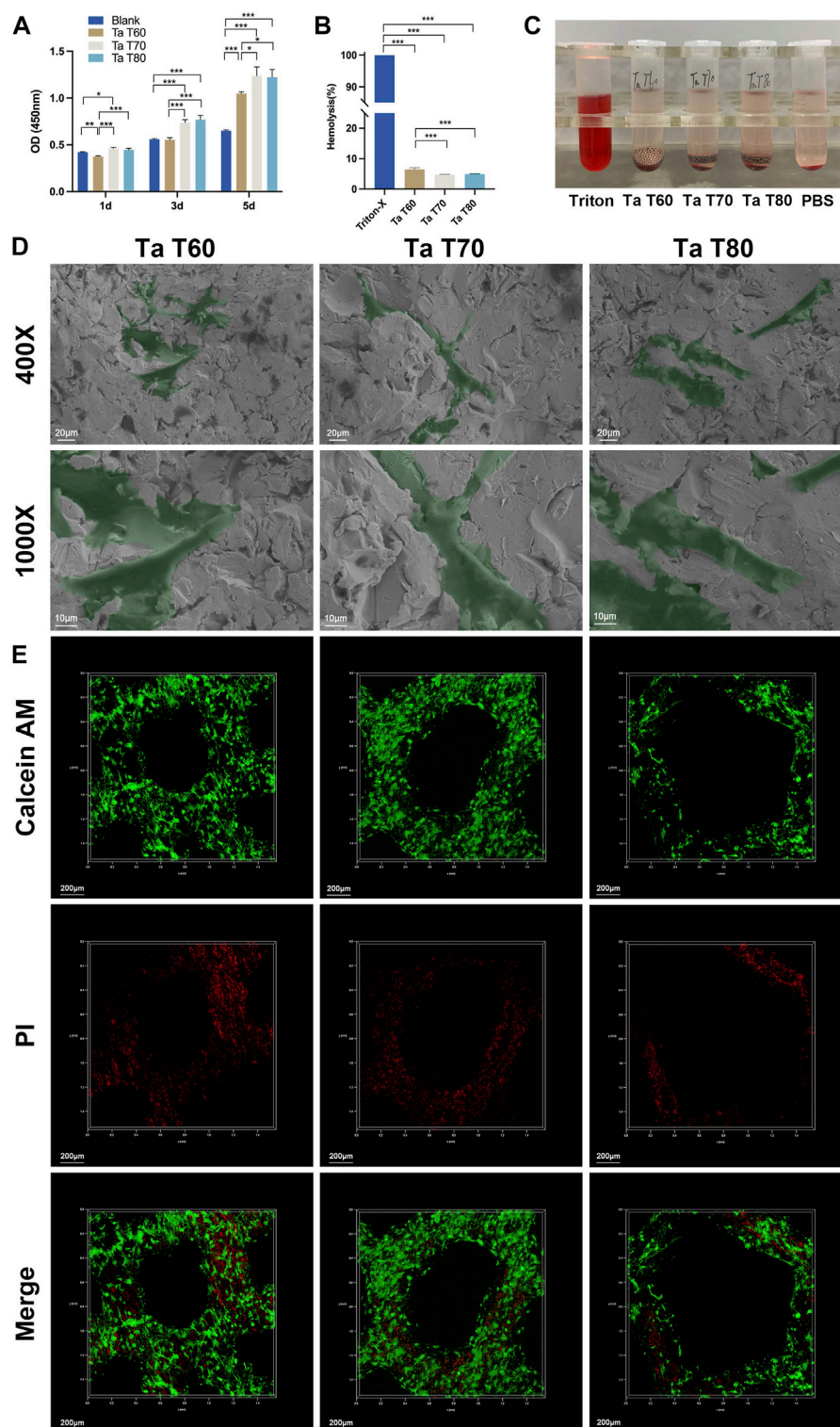


FIGURE 2

In vitro cytocompatibility of porous tantalum scaffolds and their effects on the growth of rBMSCs. (A) Activity of rBMSCs cultured on each tantalum scaffold for 1, 3 and 5 days. Quantitative analysis (B) and qualitative analysis (C) of hemolysis of blood cells cultured with tantalum scaffolds. (D) Representative SEM images of rBMSCs grown in the surface of tantalum scaffolds for 1 day. (E) Live/dead cell staining for rBMSCs cultured on tantalum scaffolds for 7 d. Data are represented as mean \pm standard deviation (SD). (n = 3, * p < 0.05; ** p < 0.01; *** p < 0.001).

fixed with 4% paraformaldehyde for 20 min, washed 3 times with PBS, stained with Alizarin Red S staining solution at room temperature for 30 min, washed with deionized water and photographed for

mineralized nodules. After that, 10% cetylpyridinium chloride was added to lyse the mineralized nodules and the absorbance was measured at 620 nm for semi-quantitative analysis.

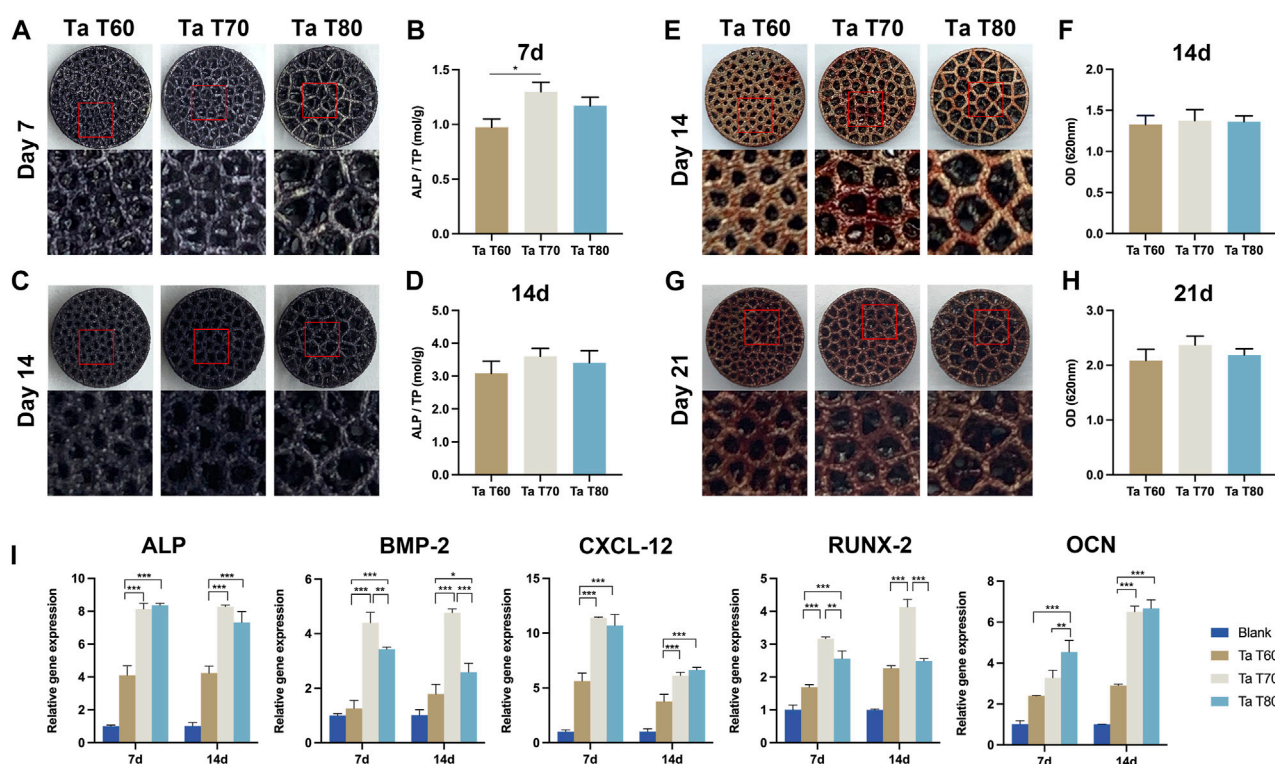


FIGURE 3

In vitro osteogenic effect of rBMSCs in each porous tantalum scaffold. (A) and (C) Appearance of ALP staining at 7d and 14d. (B) and (D) Quantitative assessment of ALP activity at 7d and 14d of culture. (E) and (G) Appearance of alizarin red staining at 14d and 21d. (F) and (H) Semi-quantitative analysis of alizarin red staining. (I) Osteogenesis-related gene expression at 7d and 14d of culture. Data represent mean \pm SD. (n = 3, * p < 0.05; ** p < 0.01; *** p < 0.001).

2.3.4 Quantitative real-time fluorescent PCR (qRT-PCR)

rBMSCs were inoculated at a density of 5×10^4 cells/well on the material surface in 24-well plates for 7 and 14 days. Total RNA was extracted from rBMSCs using Simply P Total RNA Extraction Kit (#BSC52M1, Bioer Technology, Hangzhou, China). Next, reverse transcription reactions of total RNA were performed with the Primerscript RT Master kit (as indicated) to obtain cDNA. Osteogenic-related genes including ALP, bone morphogenetic protein 2 (BMP2), C-X-C motif chemokine ligand 12 (CXCL12), Runt-related transcription factor 2 (RUNX2), and osteocalcin (OCN) were analyzed by qRT-PCR using a TB Green Premix Ex TaqII (Takara, Japan) on a fluorescent quantitative PCR instrument (QuantStudio 7, Thermo Scientific, United States) was performed. The relative expression of the above genes was calculated using the internal reference gene GAPDH as a control. The primers were synthesized by Sangon Biotech (Shanghai, China), and the sequences are shown in Table 1.

2.4 *In vivo* bone ingrowth and biosafety assessment

2.4.1 Surgical procedures

All animal experiments and operations were approved by the Animal Ethics Committee of Renji Hospital, Shanghai Jiao Tong University School of Medicine. We established a rat model of bone defect repair in the lateral femoral condyle. A total of 36 male SD rats

(12 weeks old, mean weight $350 \text{ g} \pm 25.2 \text{ g}$) were obtained from the Shanghai Lab. Animal Research Center and randomly divided into three groups: 1) porous tantalum scaffold with 60% porosity (denoted as Ta T60); 2) porous tantalum scaffold with 70% porosity (denoted as Ta T70), and 3) porous tantalum scaffold group with 80% porosity (denoted as Ta T80). Each rat was anesthetized with 2% pentobarbital sodium (0.2 mL/100 g, intraperitoneal injection). After shaving and disinfection of the right lower extremity of the rats, a 3-mm diameter, 5-mm deep bone defect perpendicular to the bone surface was made. After saline rinsing to remove the bone debris, porous tantalum scaffolds with different porosity were implanted. Finally, the wound was flushed with saline and sutured layer by layer. Six and 12 weeks after implantation, the rats (6 per group) were euthanized to collect femoral samples. At 4 and 2 weeks before rats were sacrificed, alizarin red (30 mg/kg) and calcein (20 mg/kg) were injected intraperitoneally to mark the new bone formation process.

2.4.2 Imaging assessment of the osteogenic properties of porous tantalum scaffolds *in vivo*

At 6 and 12 weeks postoperatively, intact right femurs of rats were obtained and fixed in 4% paraformaldehyde. The imaging characteristics of the porous tantalum scaffold were routinely evaluated using X-ray and micro-CT. X-ray frontal and lateral radiographs of the intact femur were taken using an X-ray imaging system (M-20, Faxitron, United States). Meanwhile, the femoral condyles and femur were scanned using micro-CT (SkyScan1076, Bruker, Belgium) to detect bone growth.

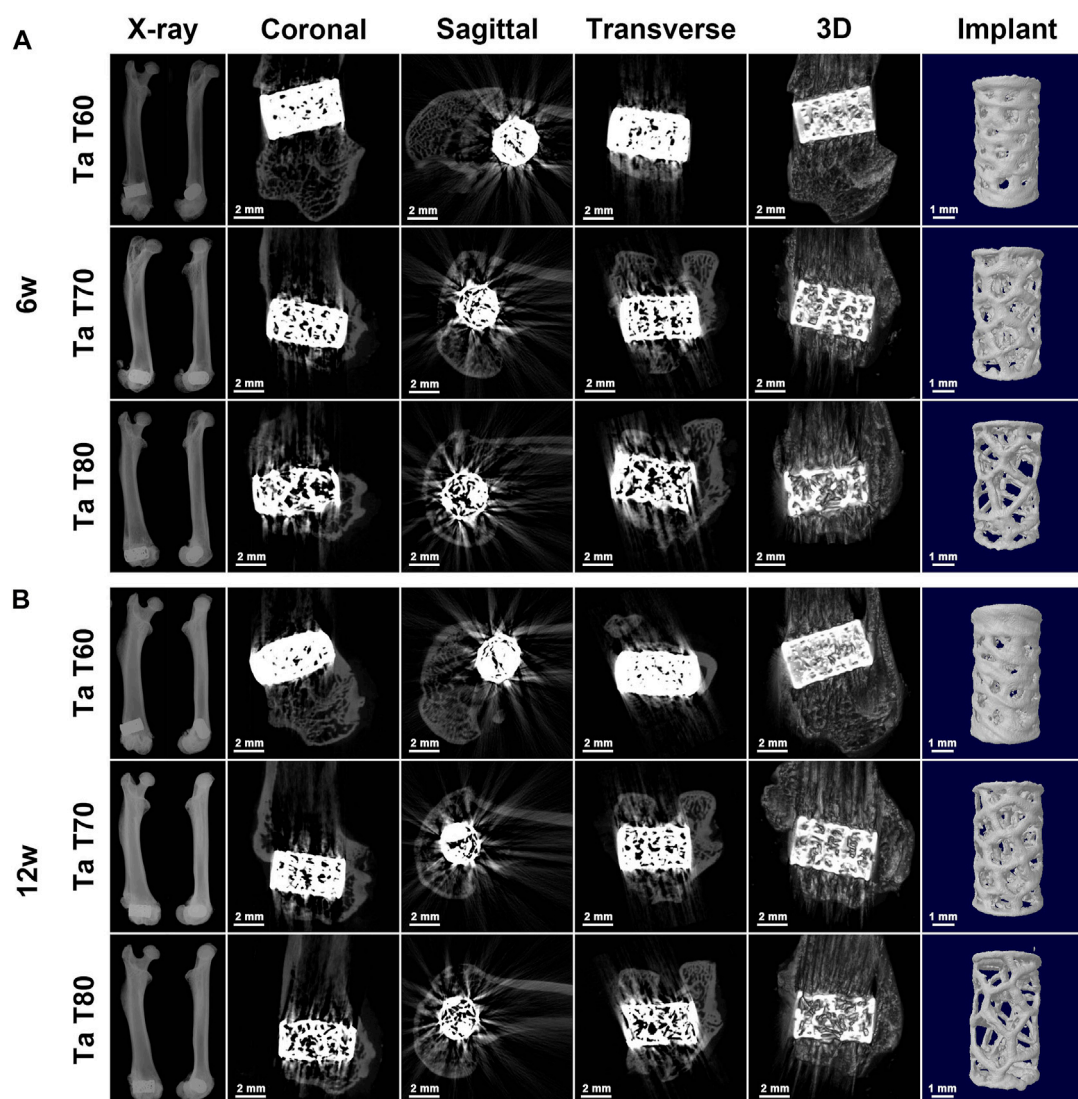


FIGURE 4

Radiological evaluation of tantalum scaffolds with different porosities implanted in rats. Representative X-ray images and corresponding 2D and 3D construction micro-CT images of the rat femoral condyle as well as the implant at 6w (A) and 12w (B) after surgery.

2.4.3 Histological and histometric analysis of bone ingrowth in porous tantalum scaffolds

After completion of imaging, rat femoral specimens were subjected to hard tissue sectioning stained with Van Gieson (VG) and methylene blue (MB). The stained sections were imaged by a high-resolution microscope and an automated digital section scanner. Images of bone ingrowth within the scaffold with different magnifications were obtained. Semi-quantitative analysis of bone ingrowth was performed by Image Pro Plus 6.0 software (Media Cybernetic, Rockville, MD, United States). Two methods were used to analyze bone ingrowth and osseointegration: one was to calculate the relative bone area (RBA), which is the area of new bone divided by the available void area (available void area = total area—metal area), and the other was to calculate the bone implant contact (BIC) index, which is the length of direct contact with bone at the interface/total length of the interface. Fluorescent labeling of

transverse sections was observed with a fluorescence microscope (Leica, Germany). The excitation/emission wavelengths of alizarin red and calcein were 543/580–670 and 488/500–550 nm, respectively. Other unstained hard tissue sections were gold sprayed and the morphological and compositional changes of bone and scaffold were characterized by SEM and EDS.

2.4.4 *In vivo* biosafety assessment of porous tantalum scaffolds

The general condition of the rats including body temperature, weight change, and wound healing were observed daily after surgery. At 12 weeks postoperatively, arterial blood was randomly drawn from rats in each experimental group by cardiac blood collection ($n = 3$). Routine blood and blood biochemical parameters, including alanine aminotransferase (ALT), blood urea nitrogen (BUN) and creatine kinase (CK), were measured and compared. Meanwhile, heart, liver, spleen,

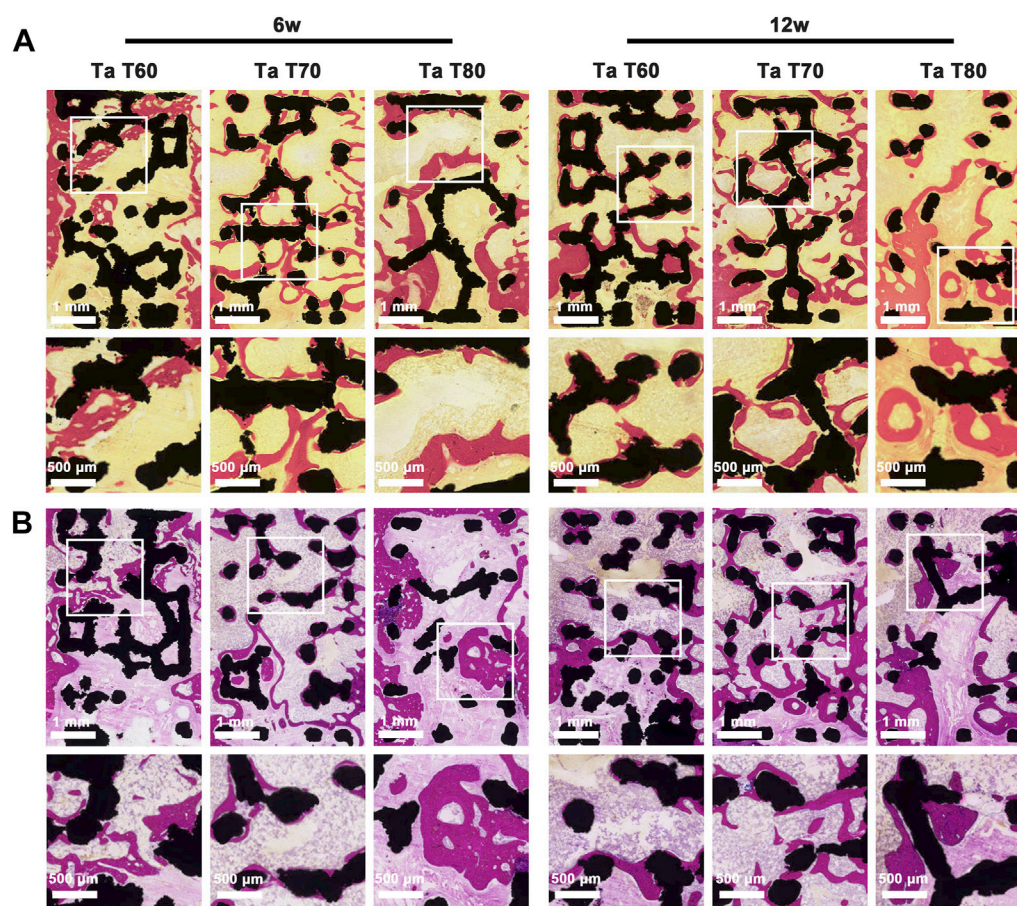


FIGURE 5

Bone growth *in vivo* evaluated by longitudinal-sectioning of porous tantalum scaffolds at 6w and 12w postoperatively. (A) Van Gieson staining and (B) methylene blue staining of undecalcified sections.

lung and kidney organ specimens were obtained from each experimental group and HE staining was performed to assess the possible organ pathological damage.

2.5 Data analysis

Data analysis was performed using SPSS 26.0 statistical software (SPSS Inc., Chicago, United States). Numerical data are reported as mean \pm standard deviation (SD). Statistical differences were analyzed by unpaired two-tailed Student's *t*-test or one-way ANOVA with Tukey *post hoc* comparisons. $p < 0.05$ were considered to be statistically significant.

3 Results

3.1 Characterization of porous tantalum scaffolds

Figure 1A show the modeling and general appearance of porous tantalum scaffolds (discs and cylinders) with different porosities. Macroscopically, the surface of the scaffolds is smooth and flat, the pore structure is trabecular bone mimetic, and the pore size of each

scaffold varies, which is consistent with the model. Then, we used SEM to further observe the microstructure of each scaffold (Figure 1C). The results showed that the strut diameter of each scaffold was uniform and complete, with the similar micro/nano rough surface, almost no unfused particles were present, and the pore size was consistent with the macroscopic one. In addition, the EDS results proved that all three porous tantalum scaffolds have only the presence of tantalum and oxygen elements, and the percentage of tantalum elements is basically the same (Figure 1D). The above results confirmed that pure tantalum porous scaffolds were successfully prepared by SLM with different pore sizes. Further, we compared the structural parameters such as porosity of each scaffold, and the structural parameters as well as mechanical properties of the three porous tantalum scaffolds are summarized in Table 2.

3.2 *In vitro* cytocompatibility

First, we assayed CCK-8 after culture of rBMSCs on tantalum scaffolds for 1, 3 and 5 days to assess cytotoxicity. As shown in Figure 2A, there was no significant difference between the cells on the three scaffolds and the blank control at day 1. On days 3 and 5, cells on the materials were statistically higher in each group than in the blank group (except for the Ta T60 group in day 3). The

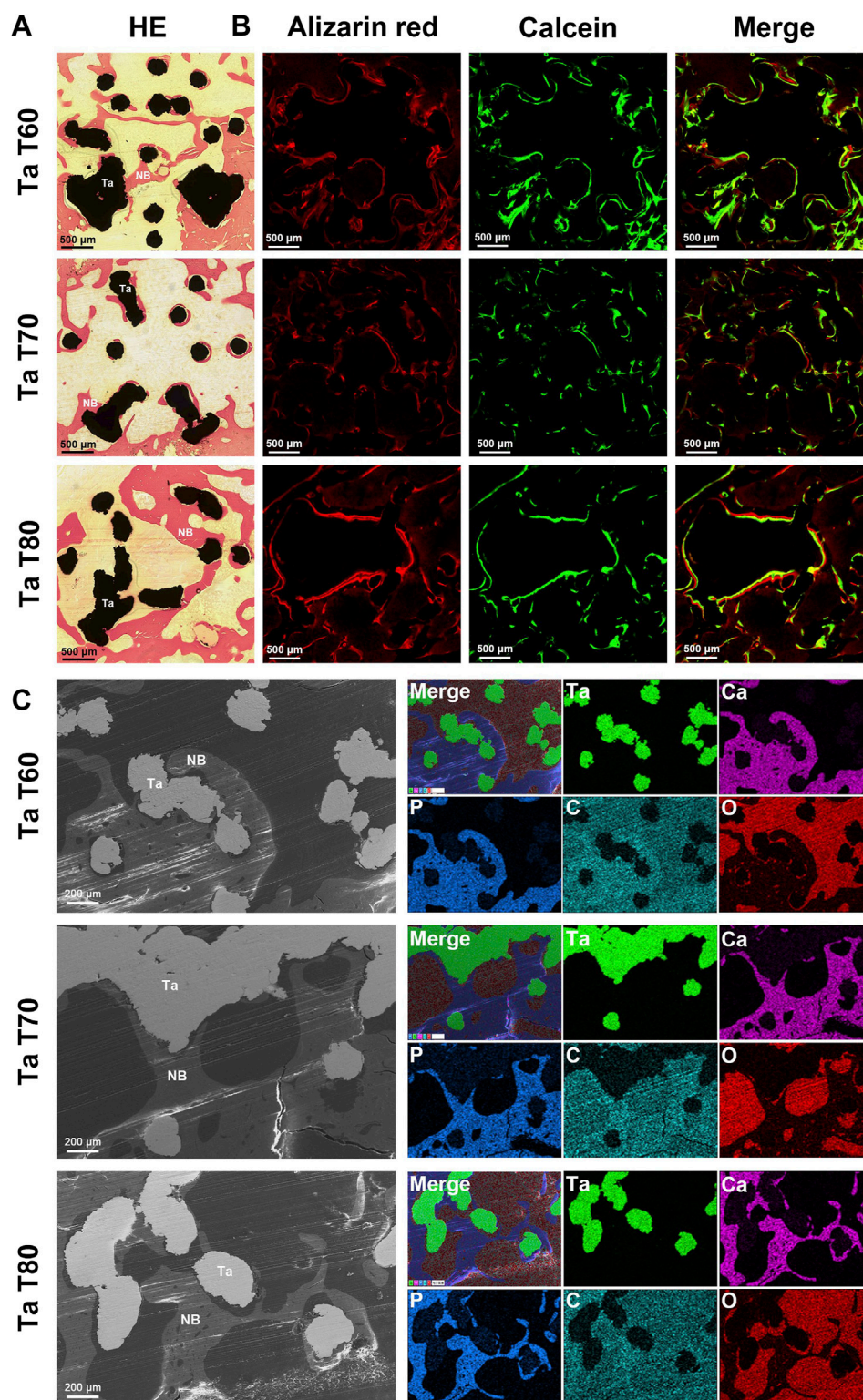
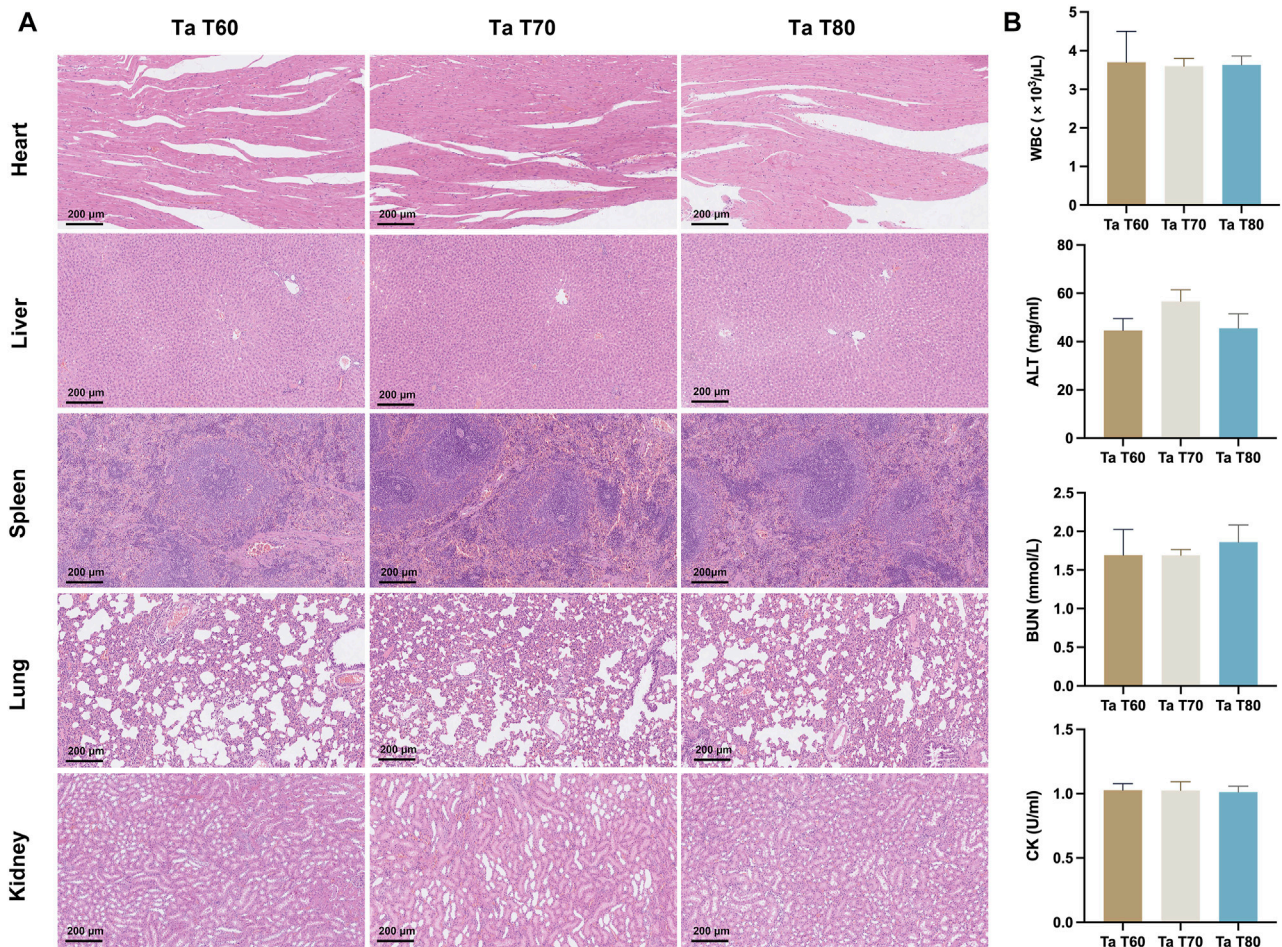


FIGURE 6

Bone growth *in vivo* evaluated by cross-sectioning of porous tantalum scaffolds at 12w after surgery. (A) Representative HE staining results of porous tantalum scaffolds. (B) Undecalcified sections of sequential fluorescence staining for bone: red (Alizarin red), green (Calcein) and blue (DAPI). (C) SEM micrographs and EDS mapping of bone growth in different porous tantalum scaffolds. Maps of element tantalum, calcium, phosphorus, carbon, and oxygen are in green, pink, blue, cyan, and red, respectively. NB, New bone; Ta, Tantalum.

materials showed an increasing trend at all three time points, and comparison between groups showed that cells in the Ta T70 and Ta T80 group were higher than that of Ta T60 group. The results

showed that all three porous tantalum scaffolds with different porosity were non-cytotoxic and promoted the proliferation of rBMSCs. Next, we used hemolysis assay to assess the compatibility

**FIGURE 7**

In vivo biosafety of porous tantalum scaffolds. (A) The HE staining results of rat heart, liver, spleen, lung, and kidney. (B) Blood routine and blood biochemical indexes in rats. (n = 3, * $p < 0.05$; ** $p < 0.01$; *** $p < 0.001$).

of the material and blood cells. Qualitative results (Figure 2B) showed that all tubes with the scaffold were clear and bright compared to the positive control. The quantitative results (Figure 2C) suggested that the hemolysis rates of Ta T60, Ta T70 and Ta T80 were 6.46%, 4.74% and 4.95%, respectively, which were within the normal range, indicating that there was no hemolytic side effect of the materials. We also performed live/dead cell staining on cells cultured on the materials for 7 days to assess the cell state. The CLSM results (Figure 2D) showed that most cells on all scaffolds were green fluorescent, and the green fluorescence intensity was in the order of Ta T60, Ta T70 and Ta T80 from highest to lowest (Supplementary Figure S1). Interestingly, the green fluorescence signal near the nodes on the surface of all materials was stronger than that on the struts. However, the green/red fluorescence signal of Ta T60 group was slightly lower than that of Ta T70 and Ta T80, but not statistically different. In addition, we observed the morphology of rBMSCs cultured on the material surface for 1 day by SEM, and as shown in Figure 2E, the cells on all materials were well spread, with flat morphology and extended multiple pseudopods. The above illustrates the superior cytocompatibility of the 3D-printed porous tantalum scaffold.

3.3 *In vitro* osteogenic properties

We performed qualitative and quantitative assays of ALP and calcium deposition by ALP staining and ARS staining, respectively, to assess the early and late osteogenic differentiation potential of porous tantalum scaffolds with different porosity. Figure 3A reflects the ALP assay on each group of material at 7 and 14 days, and the results showed that the amount of ALP was slightly higher in the Ta T60 group than in the Ta T70 and Ta T80 groups at 7 days, and the amount of ALP was significantly higher in all three groups at 14 days compared to 7 days, with no significant difference between the groups. ALP quantification (Figure 3B) suggested a higher ratio of ALP/total protein in the Ta T70 and Ta T80 groups than in Ta T60 at 7 and 14 days. Qualitative (Figure 3C) and semi-quantitative analysis of ARS staining (Figure 3D) showed a large number of red calcium nodules formed on the surface of all materials at 14 and 21 days, with no statistically significant difference between each other. In addition, we also used RT-PCR to detect the expression of some osteogenic-related genes (ALP, BMP-2, RUNX-2, CXCL-12 and OCN) to compare the osteogenic differentiation of cells on each group of materials at 7 and 14 days, and the results showed that at 7 and 14 days, the expression of ALP, RUNX-2, BMP-2 and CXCL-12 in Ta

T70 and Ta T80 groups were higher than those of Ta T60. At 7 days, the difference in OCN between the three groups was not significant, while by 14 days, the expression of Ta T70 and Ta T80 groups was slightly higher than that of Ta T60.

3.4 *In vivo* osteogenesis and safety evaluation

To further compare the osseointegration and bone ingrowth ability of three porous tantalum scaffolds with different porosity, we established a rat femoral condylar bone defect repair model. All animals recovered well after the operation, and no adverse reactions such as rejection and infection occurred.

3.4.1 Radiographic results

The postoperative X-ray results at 6 and 12 weeks (Figure 4) showed that all implants were well positioned and stably integrated with the host bone, with no loosening or dislocation. The porous structure of the implants could be faintly seen in all groups. We also performed micro-CT scans to better present the position of the implants in the femur and the structure of the implants. Figure 4 presents the coronal, sagittal, and transverse 2D images of the three tantalum implants in the femur at 6 and 12 weeks, as well as the reconstructed spatial distribution of the implants in the femur and the 3D morphology of the implants. Because of the high density of tantalum, which can easily absorb X-rays and make them impenetrable, it is not possible to compare the bone ingrowth of the implant well, as many attempts have been made to see more radiographic artifacts around the implant. However, with micro-CT, we can visualize the position of the implant in the femur and identify the shape of the implant.

3.4.2 Results of histological and histometrical analysis

Next, we performed hard tissue sections of the specimens at 6 and 12 weeks and further evaluated the effect of different porosity on osseointegration and bone ingrowth of porous tantalum scaffolds by VG staining, MB staining, CLSM observation by sequential fluorescence, and SEM. The results of MB staining of the postoperative samples at 6 and 12 weeks are shown in Figure 5A. The global images of the scaffold and the new bone confirmed that the amount of new bone in the three groups of porous tantalum scaffolds with different porosity increased over time, and that the new bone staining purple grew not only at the periphery of the black tantalum scaffold, but also to the interior. The vast majority of them grew against the surface of the tantalum scaffold, in addition to a large amount of granular bone marrow tissue and lamellar collagen fibrous tissue within the material. The large porosity of the scaffold was more favorable for new bone to grow in, and the amount of new bone at 6 weeks was in the order of Ta T80, Ta T70 and Ta T60, but it should be noted that in the Ta T80 group, the bone tissue and the material did not fit closely together and there was more lamellar collagen fiber formation. In contrast, the new bone in Ta T70 was mostly tightly adhered to the material and had more bone marrow tissue. At 12 weeks, the amount of new bone was, in descending order, Ta T70, Ta T80, and Ta T60. Histometric analysis of the ROI area showed that Ta T60, Ta T70, and Ta T80 had 14.3%, 28.6%, and 23.3% of new bone area at 12 weeks, respectively, with BIC indices of 35%, 60%, and 45%, respectively. This result supports that Ta T70 and Ta T80 have

better bone ingrowth than Ta T60, and Ta T70 has the best osseointegration ability. In Figure 5B we can see the panoramic and local magnified images of the VG staining of the samples. The red area represents the new bone tissue and the light yellow represents the bone marrow tissue. Similar to MB staining, the RBA at 6 and 12 weeks was in descending order for Ta T80, Ta T70, and Ta T60, but the new bone and material binding of the internal scaffold was not as good in Ta T80 as in Ta T70.

The results of the cross-section of porous tantalum scaffolds in each group are shown in Figure 6. The VG staining of the transverse section and the staining of the longitudinal section were similar (Figure 6A). New bone grew inward from the perimeter of the scaffold, and the bone growth into Ta T70 and Ta T80 was better than that of Ta T60. The sequential fluorescence staining showed stronger red and green fluorescence in Ta T70 and Ta T80 than in Ta T60 (Figure 6B). SEM and EDS confirmed the presence of new bone and close contact with the scaffold surface (Figure 6C).

3.4.3 *In vivo* biosafety results

Three groups of rats were euthanized at 12 weeks postoperatively, and heart, liver, spleen, lung and kidney tissues were taken and sections were stained for HE. The results showed that in Figure 7A, no significant abnormal pathological changes were observed in the organ tissue sections of each group. The blood samples from each group were also examined for blood biochemical parameters, and there were no significant statistical differences between the three groups of rats in terms of blood routine, ALT, BUN and CK, all of which were within the normal reference range (Figure 7B). The above results indicate that the porous tantalum scaffold has excellent *in vivo* biosafety.

4 Discussion

Bone defects, especially large-sized bone defects of weight-bearing bone, remain one of the most pressing clinical challenges, and porous tantalum stands out for its high porosity, excellent biocompatibility, and suitable elastic modulus. Trabecular Metal prepared by the conventional CVD method is currently widely used in the clinic. However, the disadvantages of the traditional process, such as time-consuming and inefficient, the inability to personalize the material and the lack of precision in its internal structure, have stimulated interest in developing 3D printing technology for the preparation of porous tantalum. The high precision, efficiency and personalization of 3D printing allow us to prepare trabecular porous tantalum scaffolds with different porosity and to study the effects of their mechanical and biological properties. In this study, we successfully prepared three trabecular bone porous tantalum scaffolds with different porosity (60%, 70%, and 80%, respectively) by SLM technology, and *in vitro* studies revealed that although the cell adhesion on the surface of the Ta T60 group was higher than that of the Ta T70 and Ta T80 groups, the proliferation and osteogenic differentiation were inferior to the latter two. The *in vivo* results further confirmed that the Ta T70 and Ta T80 groups showed better bone ingrowth than Ta T60, with Ta T70 having the best osseointegration effect.

In 2015, pure tantalum implants with a high degree of porosity and high interporous interconnectivity were first prepared by Ruben et al. using SLM technology, and a variety of porous tantalum implants with different pore structures have since been prepared (Wauthle et al.,

2015; Guo et al., 2019; Wang et al., 2019; Yang et al., 2020). Yang et al. first reported trabecular bone tantalum scaffolds fabricated by AM and compared them with bone trabecular tantalum metal prepared by conventional CVD (Yang et al., 2020). On this basis, porous trabecular tantalum scaffolds with different porosities were prepared. The actual porosity of the three scaffolds was essentially the same as the ideal porosity with an error within 5%, mainly due to the small size of the samples and the different evaluation methods, which was lower than the 99% previously reported (Yang et al., 2020). In addition, except for the differences in porosity and pore size, the strut diameter, inter-pore interconnectivity and micro/nano surface structure were basically the same among the scaffolds, ensuring comparability between groups. Residual powder is a problem that cannot be ignored in metal additive manufacturing processes (Maleki et al., 2021). It has been shown that the angle between the unfused particles and the substrate is less than 90°, which is considered to be beneficial particles that can improve the micro-nano roughness of the material surface and promote the integration with the bone, while if the angle is greater than 90°, it is considered to be harmful particles that can easily fall off from the substrate and cause undesirable performance such as surrounding osteolysis and prosthesis loosening (Pei et al., 2021). The porous tantalum scaffolds in this study were all post-treated by sandblasting, and the surface of the scaffolds was flat, showing a micro/nano-rough structure and essentially free of easily dislodged unfused particles (Figure 1). This post-treatment can better remove residual unfused particles and reduce the impact on 3D printing accuracy and material properties. The porous structure affects the mechanical properties of the material, and the elastic modulus of the trabecular tantalum scaffold fabricated by AM decreases with increasing porosity, but the elastic modulus of the porous tantalum scaffold with all three porosities is within the range of the elastic modulus of human cortical bone and cancellous bone (1.5–3 GPa, 3–30 GPa, and 0.02–2 GPa for porous tantalum scaffolds, human cortical bone, and human cancellous bone, respectively) (Wang et al., 2016; Yang et al., 2020; Wang et al., 2021). Therefore, trabecular tantalum scaffolds are ideal biomaterials for bone filling and bone repair due to their highly porous structure, human bone-matched mechanical properties and rough micro/nano surface structure.

Further, *in vitro* culture of MSCs on scaffolds confirmed the excellent cytocompatibility of trabecular tantalum scaffolds. Both the hemolysis and CCK-8 test confirmed the non-toxicity of the material. Cell adhesion is the first step in the reaction between cell and material, and the physicochemical properties and surface characteristics of the material can have an important impact. Tantalum's inherent high wettability and surface energy as well as its rough micro/nanosurface structure facilitate protein adsorption and cell adhesion (Huang et al., 2022). SEM showed that MSCs on the surface of each material were fully spread and protruding pseudopodia by 1 day of culture. Live/dead cell staining showed cell growth on the surface of each scaffold after 7 days of culture (Figure 2) and revealed a negative correlation between cell adhesion and the porosity of the material, and, moreover, cells were concentrated on the nodes rather than on the struts. These results are consistent with previous studies (Chen Z. et al., 2020; Pei et al., 2021). Previous studies have shown that the surface area of the material as well as the local curvature have an effect on cell growth. A high surface area facilitates cell adhesion and proliferation, especially under 2D cell culture. In addition, cells prefer to grow on concave ($k < 0$) and flat surfaces compared to convex surfaces ($k > 0$) (Zadpoor, 2015). Cells can sense local curvature at the

millimeter scale and tend to minimize surface tension at finite volumes, which is thought to be a mechanism that facilitates tissue growth (Rumpler et al., 2008). The struts of three scaffolds in this study had the similar diameter (similar local curvature). The smaller porosity had more scaffold junctions along with a larger surface area, implying relatively more cell adhesion on the surface of Ta T60 scaffold. However, the dead/live cell ratio was slightly higher in the Ta T60 group than in the Ta T70 and Ta T80 groups, and we speculate that the possible reasons for this are excessive cell aggregation or insufficient nutrients delivered due to low porosity. In addition, the relatively high number of residual unfused particles on the surface of Ta T60 may have an effect on the activity of cells.

ALP and calcium deposition were markers of early and late bone formation, respectively. ALP and ARS staining qualitatively and quantitatively showed that porous tantalum scaffolds of all porosities promoted osteogenic differentiation of MSCs, with the Ta T70 and Ta T80 groups outperforming the Ta T60 group. Further PCR assays also supported this result. The porous tantalum scaffolds with high porosity promoted the osteogenic differentiation of MSCs. This phenomenon is consistent with the results of some previous studies. Cheng et al. found that compared with lower porosity scaffolds, scaffolds with high porosities can promote the expression of OCN, OPN, BMP-2, BMP-4 and VEGF (Cheng et al., 2014). Wang et al. found that cellular genes such as ALP, RUNX-2, Col-1 and BMP-2 were more highly expressed in scaffolds with large pore size and porosity (Wang et al., 2022). Besides, in the study of Luo et al., they found that the calcium content of tantalum scaffolds with high pore size and porosity (400–600um/70%, 600–800um/80%) at 21 days of incubation was higher than that of scaffolds with low pore size (100–200um/23%, 200–400um/53%), although there was no significant difference in ALP content (Luo et al., 2021). We speculate that the possible reasons for this phenomenon are as follows. First, there would be relatively dense cell distribution, tighter cell contacts, and more extracellular matrix secretion on struts of the scaffold with large porosity after growing the same number of MSCs. This direct cell-to-cell communication induced by cell signaling molecular transmission through gap junctions may significantly enhance osteogenic differentiation of MSCs (Van Bael et al., 2012). Second, large porosity scaffolds have relatively more large pores and more space for cell growth, and the larger distance between struts during attachment and migration may cause cells to produce more stretch to cross the gaps, and more cell stretch facilitates cell differentiation (Kumar et al., 2011). Third, the high permeability due to large porosity could transport more nutrients and oxygen, which may facilitate cell growth. However, some studies have obtained the opposite result. Chen et al. found higher expression of ALP, BMP-2, OPN, OCN and RUNX-2 in Ti6Al4V ELI scaffolds with 60% porosity than in the group with 70% porosity, and attributed this to the low permeability, high inoculation efficiency and high attachment surface area due to the small porosity and small pore size (Chen Z. et al., 2020). In summary, small porosity is more conducive to initial cell adhesion, but the low permeability and easy clogging associated with too small porosity can limit inward cell growth; large porosity is more conducive to cell proliferation and growth, especially inside the scaffold, but too large porosity can affect the mechanical and biological properties of the scaffold (inability to anchor or migrate). Therefore, pore characteristics need to be carefully adjusted to achieve a balance between mechanical, biological and hydrodynamic properties of the scaffold.

We implanted three bionic trabecular tantalum scaffolds into femoral condylar bone defects in rats to further evaluate the osteoconductivity and osseointegration of the material. Radiographic performance at 6 and 12 weeks indicated stable *in vivo* osseointegration of the scaffolds without significant osteolysis or inflammation. Due to the high energy spectrum of tantalum resulting in no X-ray transmission and the large number of metallic artifacts produced in microCT, it was not possible to further assess bone growth within the scaffold by imaging means. Therefore, we chose to use hard tissue sectioning and staining to assess the bonding of the metallic material to the bone. The 3D printed porous tantalum scaffold has superior osteoconduction and osteoincorporation as seen in the hard tissue section results. Once the implant enters the bone defect site, it is in close contact with the surrounding bone, which provides initial stability for successful intraosseous healing of the implant (Davies, 2007). Then, the blood first comes into contact with the implant and a series of biological reactions occur: protein deposition, coagulation, inflammatory response and tissue formation (Kuzyk and Schemitsch, 2011). The surface properties and topology of the implant can have a significant impact on these processes (Gittens et al., 2014; Rupp et al., 2018). The deposition of proteins in turn activates platelets and promotes clotting, i.e., the formation of clots that attach to the implant, and the inflammatory response occurs simultaneously and interacts with platelet activation and clotting (Shiu et al., 2014). The recruitment and migration of osteogenic cells is regulated by fibrin through the clots and possibly by leukocytes and platelets. When osteogenic cells reach the implant surface, they initiate the secretion of bone matrix, preferentially forming a highly mineralized, collagen-free interfacial zone (similar to the cement line of lamellar osteon) (Shah et al., 2019). Differentiated mature osteoblasts continue to secrete collagen outside this zone as well as undergo mineralization to form immature woven bone, which provides secondary stability for implant healing within the host bone while bridging the gap between the implant and the surrounding bone (Davies, 2003). Bone remodeling then occurs in the host bone around the implant and in the immature bone in the interstitial space, resulting in mature lamellar bone and eventual functional healing (Davies, 2003). In this study, the high friction force due to the high friction coefficient of tantalum provided good initial stability, and porous tantalum was more conducive to leukocyte activation and promoted early inflammatory response (Schildhauer et al., 2009). The rough surface topography of the 3D printed tantalum implant provides a larger surface area for protein and platelet adhesion and good osteoconductivity. The porous structure is also more conducive to bone growth and ingrowth. Furthermore, the bone-matched elastic modulus resulting from the porous structure will have a significant impact on later bone remodeling, as there is no significant stress-shielding effect.

3D printing technology has revolutionized the design and preparation process of implants, and the characteristics of precisely tuned porous structures make it possible for us to study the optimal porosity of bone growth. According to RBA and BIC, Ta T70 and Ta T80 have better bone ingrowth effect than Ta T60, among which, Ta T70 has the best osseointegration effect. The large porosity and large pore size of the scaffold can provide more space and attachment area, which facilitates the long entry of bone tissue. In addition, large porosity means more blood and oxygen delivery, and these provide fertile nutrients for bone formation. Several studies have reported the effect of implants with different pore characteristics on bone ingrowth.

Taniguchi et al. designed three titanium implants with diamond structures of different pore sizes (300/600/900um) using the SLM technique. The rabbit diaphysis model suggested that the 300um scaffold was less effective in bone ingrowth than the other two groups, and separation experiments suggested that the 600um scaffold had the best bone ingrowth (Taniguchi et al., 2016). Similar results were reported in the study of Ran et al. (Ran et al., 2018). Luo et al. prepared four types of porous tantalum scaffolds with different pore sizes and porosities by SLM, and the *in vivo* results of the rabbit femoral condylar model confirmed that the osseointegration of tantalum scaffolds with large pore sizes (400–600um and 600–800um) was higher than that of scaffolds with low pore sizes (100–200um and 200–400um), with the best osseointegration ability of tantalum scaffolds with 400–600um. They concluded that the effective permeability increases with increasing porosity and pore size, but the effective contact area decreases with increasing porosity and pore size. Moreover, energy dissipation and cell seeding caused by high flow velocity and vortex formation in large pore size scaffolds also have an effect (Luo et al., 2021). Kelly et al. used LPBF to prepare titanium implants with gyroid-sheet architecture of various porosities (0%–90%) and implanted them into the sheep femoral shaft bicortical defect model to systematically investigate the relationship between porosity and implant stiffness, bone ingrowth, and implant-bone mechanical interlocking strength. They found a linear correlation between bone length entry and porosity, but a parabolic relationship between mechanical interlocking strength obtained by osseointegration and porosity, with peaks between 60% and 70%. The interfacial stiffness was inversely linearly related to porosity. The payoff effect of bone ingrowth on osseointegration strength diminished when porosity exceeded 80% (Kelly et al., 2021). The results of these studies are consistent with our results. Of course, there are some studies that do not support this conclusion. Chen et al. reported that the Ti6Al4V ELI porous scaffold prepared by SLM showed the best performance in bone formation (osteogenesis) and bone ingrowth for the scaffold with 500um pore size and 60% porosity compared to the scaffold with 600/700um pore size and 70% porosity (Chen Z. et al., 2020). In the study by Pei et al. (2021) they concluded that 3D printed titanium scaffolds with different pore characteristics (pore size and porosity) had no effect on bone ingrowth outcomes in a rabbit femoral stem cortical defect model and a beagle (beagles) femoral head necrosis model. Instead, implant site had a greater effect on bone ingrowth outcomes. The above results suggest that the design and preparation of materials, the selection of host species and sites, the implementation of experimental methods and the choice of evaluation methods all have an impact on the results, and that uniform and standardized protocols and systems for implant evaluation are needed.

There are still some disadvantages in this experiment. First, we used a rat femoral condylar defect model for the assessment of bone ingrowth effects. Although this is a very common assessment model, the faster bone growth ability of rats may have an impact on the results. Second, we used BIC, a common osseointegration evaluation method in dentistry and orthopedics, to indirectly assess the osseointegration effect, lacking indicators that can directly reflect the bone mechanical interlocking force, such as push-out force and torsion force. These will be further optimized in subsequent studies, such as the use of large animals (sheep, etc.) for modeling and the use of more intuitive mechanical tests for evaluation, for better clinical translation.

5 Conclusion

We prepared three porous tantalum implants with different porosity using LPBF. *In vitro* results showed that Ta T60 had more cell adhesion but less cell proliferation and osteogenic differentiation than Ta T70 and Ta T80. *In vivo* bone ingrowth results confirmed that Ta T70 and Ta T80 had better bone ongrowth and bone ingrowth than Ta T60, among which, Ta T70 had the best osseointegration effect. Combined with the *in vivo* and *ex vivo* results, the porous tantalum scaffold with 70% porosity has good osteogenesis, osteoconductivity, osseointegration, biosafety and mechanical properties, and is a very promising 3D printed implant for orthopedics and dentistry, and provides a strong support and reference for the design and optimization of porous tantalum implants afterwards.

Data availability statement

The raw data supporting the conclusions of this article will be made available by the authors, without undue reservation.

Author contributions

BY, JY, and XQ conceived the general idea and provided critical revision and final approval of the manuscript; JJ and QH conducted the experiment and participated in manuscript drafting; DZ and JY participated in the material design and preparation; HT and MW participated in the animal experiment. All authors contributed to the article and approved the submitted version.

Funding

This work was supported by the National Key Research and Development Project of China (Grant No. 2020YFC1107500 and

2020YFC1107503); National Natural Science Foundation of China (Grant No. 82225031, 32222042, 82172464, 82172453 and 81972086); Program of Shanghai Academic/Technology Research Leader (Grant No. 22XD1401900); The Shanghai Rising-Star Program (21QA1405500); Shanghai Municipal Health Commission & Shanghai “Rising Stars of Medical Talent” Youth Development Program-Outstanding Youth Medical Talents (Grant No. 20224Z0011); Clinical Scientific Innovation and Cultivation Fund of Renji Hospital, Shanghai JJ Tong University School of Medicine, (Grant no. RJPY-LX-009).

Conflict of interest

JY and DZ were employed by Shenzhen Dazhou Medical Technology Co, Ltd.

The remaining authors declare that the research was conducted in the absence of any commercial or financial relationships that could be construed as a potential conflict of interest.

Publisher's note

All claims expressed in this article are solely those of the authors and do not necessarily represent those of their affiliated organizations, or those of the publisher, the editors and the reviewers. Any product that may be evaluated in this article, or claim that may be made by its manufacturer, is not guaranteed or endorsed by the publisher.

Supplementary material

The Supplementary Material for this article can be found online at: <https://www.frontiersin.org/articles/10.3389/fbioe.2023.1117954/full#supplementary-material>

References

- Alipal, J., Mohd Pu'ad, N. A. S., Nayan, N. H. M., Sahari, N., Abdullah, H. Z., Idris, M. I., et al. (2021). An updated review on surface functionalisation of titanium and its alloys for implants applications. *Mater. Today Proc.* 42, 270–282. doi:10.1016/j.matpr.2021.01.499
- Al-Ketan, O., Rowshan, R., and Abu Al-Rub, R. K. (2018). Topology-mechanical property relationship of 3D printed strut, skeletal, and sheet based periodic metallic cellular materials. *Addit. Manuf.* 19, 167–183. doi:10.1016/j.addma.2017.12.006
- Amini, A. R., Laurencin, C. T., and Nukavarapu, S. P. (2012). Bone tissue engineering: Recent advances and challenges. *Bone Tissue Eng.* 40, 363–408. doi:10.1615/critrevbiomedeng.v40.i5.10
- Balla, V. K., Bodhak, S., Bose, S., and Bandyopadhyay, A. (2010). Porous tantalum structures for bone implants: Fabrication, mechanical and *in vitro* biological properties. *Acta Biomater.* 6, 3349–3359. doi:10.1016/j.actbio.2010.01.046
- Bandyopadhyay, A., Mitra, I., Shivaram, A., Dasgupta, N., and Bose, S. (2019). Direct comparison of additively manufactured porous titanium and tantalum implants towards *in vivo* osseointegration. *Addit. Manuf.* 28, 259–266. doi:10.1016/j.addma.2019.04.025
- Black, J. (1994). Biologic performance of tantalum. *Clin. Mater.* 16, 167–173. doi:10.1016/0267-6605(94)90113-9
- Bobyn, J. D., Stackpool, G. J., Hacking, S. A., Tanzer, M., and Krygier, J. J. (1999). Characteristics of bone ingrowth and interface mechanics of a new porous tantalum biomaterial. *J. Bone Jt. Surg.* 81, 907–914. doi:10.1302/0301-620x.81b5.9283
- Bose, S., Ke, D., Sahasrabudhe, H., and Bandyopadhyay, A. (2018). Additive manufacturing of biomaterials. *Prog. Mater. Sci.* 93, 45–111. doi:10.1016/j.pmatsci.2017.08.003
- Chen, Y., Li, W., Zhang, C., Wu, Z., and Liu, J. (2020). Recent developments of biomaterials for additive manufacturing of bone scaffolds. *Adv. Healthc. Mater.* 9, 2000724. doi:10.1002/adhm.202000724
- Chen, Z., Yan, X., Yin, S., Liu, L., Liu, X., Zhao, G., et al. (2020). Influence of the pore size and porosity of selective laser melted Ti6Al4V ELI porous scaffold on cell proliferation, osteogenesis and bone ingrowth. *Mater. Sci. Eng. C* 106, 110289. doi:10.1016/j.msec.2019.110289
- Cheng, A., Humayun, A., Cohen, D. J., Boyan, B. D., and Schwartz, Z. (2014). Additively manufactured 3D porous Ti-6Al-4V constructs mimic trabecular bone structure and regulate osteoblast proliferation, differentiation and local factor production in a porosity and surface roughness dependent manner. *Biofabrication* 6, 045007. doi:10.1088/1758-5082/6/4/045007
- Christie, M. J. (2002). Clinical applications of trabecular metal. *Am. J. Orthop. (Belle Mead, N.J.)* 31, 219–220.
- Claes, L., Recknagel, S., and Ignatius, A. (2012). Fracture healing under healthy and inflammatory conditions. *Nat. Rev. Rheumatol.* 8, 133–143. doi:10.1038/nrrheum.2012.1
- Cohen, R. (2002). A porous tantalum trabecular metal: Basic science. *Am. J. Orthop. (Belle Mead, N.J.)* 31, 216–217.
- Davies, J. E. (2003). Understanding peri-implant endosseous healing. *J. Dent. Educ.* 67, 932–949. doi:10.1002/j.0022-0337.2003.67.8.tb03681.x
- Davies, J. E. (2007). Bone bonding at natural and biomaterial surfaces. *Biomaterials* 28, 5058–5067. doi:10.1016/j.biomaterials.2007.07.049

- Gao, H., Yang, J., Jin, X., Qu, X., Zhang, F., Zhang, D., et al. (2021). Porous tantalum scaffolds: Fabrication, structure, properties, and orthopedic applications. *Mater. Des.* 210, 110095. doi:10.1016/j.matdes.2021.110095
- Gillman, C. E., and Jayasuriya, A. C. (2021). FDA-approved bone grafts and bone graft substitute devices in bone regeneration. *Mater. Sci. Eng. C* 130, 112466. doi:10.1016/j.msec.2021.112466
- Gittens, R. A., Olivares-Navarrete, R., Schwartz, Z., and Boyan, B. D. (2014). Implant osseointegration and the role of microroughness and nanostructures: Lessons for spine implants. *Acta Biomater.* 10, 3363–3371. doi:10.1016/j.actbio.2014.03.037
- Guo, Y., Xie, K., Jiang, W., Wang, L., Li, G., Zhao, S., et al. (2019). *In vitro* and *in vivo* study of 3D-printed porous tantalum scaffolds for repairing bone defects. *ACS Biomater. Sci. Eng.* 5, 1123–1133. doi:10.1021/acsbomaterials.8b01094
- Guo, L., Liang, Z., Yang, L., Du, W., Yu, T., Tang, H., et al. (2021). The role of natural polymers in bone tissue engineering. *J. Control. Release* 338, 571–582. doi:10.1016/j.jconrel.2021.08.055
- Han, Q., Wang, C., Chen, H., Zhao, X., and Wang, J. (2019). Porous tantalum and titanium in orthopedics: A review. *ACS Biomater. Sci. Eng.* 5, 5798–5824. doi:10.1021/acsbomaterials.9b00493
- Huang, G., Pan, S.-T., and Qiu, J.-X. (2021). The clinical application of porous tantalum and its new development for bone tissue engineering. *Materials* 14, 2647. doi:10.3390/ma14102647
- Huang, G., Pan, S.-T., and Qiu, J.-X. (2022). The osteogenic effects of porous Tantalum and Titanium alloy scaffolds with different unit cell structure. *Colloids Surfaces B Biointerfaces* 210, 112229. doi:10.1016/j.colsurfb.2021.112229
- Huo, S., Wang, F., Lyu, Z., Hong, Q., Nie, B. e., Wei, J., et al. (2021). Dual-functional polyetheretherketone surface modification for regulating immunity and bone metabolism. *Chem. Eng. J.* 426, 130806. doi:10.1016/j.cej.2021.130806
- Jakus, A. E., Rutz, A. L., Jordan, S. W., Kannan, A., Mitchell, S. M., Yun, C., et al. (2016). Hyperelastic “bone”: A highly versatile, growth factor-free, osteoregenerative, scalable, and surgically friendly biomaterial. *Sci. Transl. Med.* 8, 358ra127. doi:10.1126/scitranslmed.aaf7704
- Kelly, C. N., Miller, A. T., Hollister, S. J., Guldberg, R. E., and Gall, K. (2018). Design and structure-function characterization of 3D printed synthetic porous biomaterials for tissue engineering. *Adv. Healthc. Mater.* 7, 1701095. doi:10.1002/adhm.201701095
- Kelly, C. N., Wang, T., Crowley, J., Wills, D., Pelletier, M. H., Westrick, E. R., et al. (2021). High-strength, porous additively manufactured implants with optimized mechanical osseointegration. *Biomaterials* 279, 121206. doi:10.1016/j.biomaterials.2021.121206
- Koons, G. L., Diba, M., and Mikos, A. G. (2020). Materials design for bone-tissue engineering. *Nat. Rev. Mater.* 5, 584–603. doi:10.1038/s41578-020-0204-2
- Kumar, G., Tison, C. K., Chatterjee, K., Pine, P. S., McDaniel, J. H., Salit, M. L., et al. (2011). The determination of stem cell fate by 3D scaffold structures through the control of cell shape. *Biomaterials* 32, 9188–9196. doi:10.1016/j.biomaterials.2011.08.054
- Kuzyk, P. R. T., and Schemitsch, E. H. (2011). The basic science of peri-implant bone healing. *Indian J. Orthop.* 45, 108–115. doi:10.4103/0019-5413.77129
- Levine, B. R., Sporer, S., Poggie, R. A., Della Valle, C. J., and Jacobs, J. J. (2006). Experimental and clinical performance of porous tantalum in orthopedic surgery. *Biomaterials* 27, 4671–4681. doi:10.1016/j.biomaterials.2006.04.041
- Li, Y., Xiao, Y., and Liu, C. (2017). The horizon of materiobiology: A perspective on material-guided cell behaviors and tissue engineering. *Chem. Rev.* 117, 4376–4421. doi:10.1021/acs.chemrev.6b00654
- Luo, C., Wang, C., Wu, X., Xie, X., Wang, C., Zhao, C., et al. (2021). Influence of porous tantalum scaffold pore size on osteogenesis and osteointegration: A comprehensive study based on 3D-printing technology. *Mater. Sci. Eng. C* 129, 112382. doi:10.1016/j.msec.2021.112382
- Maleki, E., Bagherifard, S., Bandini, M., and Guagliano, M. (2021). Surface post-treatments for metal additive manufacturing: Progress, challenges, and opportunities. *Addit. Manuf.* 37, 101619. doi:10.1016/j.addma.2020.101619
- McDermott, A. M., Herberg, S., Mason, D. E., Collins, J. M., Pearson, H. B., Dawahare, J. H., et al. (2019). Recapitulating bone development through engineered mesenchymal condensations and mechanical cues for tissue regeneration. *Sci. Transl. Med.* 11, eaav7756. doi:10.1126/scitranslmed.aav7756
- Pei, X., Wu, L., Zhou, C., Fan, H., Gou, M., Li, Z., et al. (2021). 3D printed titanium scaffolds with homogeneous diamond-like structures mimicking that of the osteocyte microenvironment and its bone regeneration study. *Biofabrication* 13, 015008. doi:10.1088/1758-5090/abc060
- Pobloth, A.-M., Checa, S., Razi, H., Petersen, A., Weaver, J. C., Schmidt-Bleek, K., et al. (2018). Mechanobiologically optimized 3D titanium-mesh scaffolds enhance bone regeneration in critical segmental defects in sheep. *Sci. Transl. Med.* 10, eaam8828. doi:10.1126/scitranslmed.aam8828
- Ran, Q., Yang, W., Hu, Y., Shen, X., Yu, Y., Xiang, Y., et al. (2018). Osteogenesis of 3D printed porous Ti6Al4V implants with different pore sizes. *J. Mech. Behav. Biomed. Mater.* 84, 1–11. doi:10.1016/j.jmbbm.2018.04.010
- Rumpler, M., Woesz, A., Dunlop, J. W. C., van Dongen, J. T., and Fratzl, P. (2008). The effect of geometry on three-dimensional tissue growth. *J. R. Soc. Interface.* 5, 1173–1180. doi:10.1098/rsif.2008.0064
- Rupp, F., Liang, L., Geis-Gerstorfer, J., Scheidele, L., and Hüttig, F. (2018). Surface characteristics of dental implants: A review. *Dent. Mater.* 34, 40–57. doi:10.1016/j.dental.2017.09.007
- Schildhauer, T. A., Peter, E., Muhr, G., and Köller, M. (2009). Activation of human leukocytes on tantalum trabecular metal in comparison to commonly used orthopedic metal implant materials. *J. Biomed. Mater. Res.* 88A, 332–341. doi:10.1002/jbm.a.31850
- Shah, F. A., Thomsen, P., and Palmquist, A. (2019). Osseointegration and current interpretations of the bone-implant interface. *Acta Biomater.* 15, 1–15. doi:10.1016/j.actbio.2018.11.018
- Shiu, H. T., Goss, B., Lutton, C., Crawford, R., and Xiao, Y. (2014). formation of blood clot on biomaterial implants influences bone healing. *Tissue Eng. Part B Rev.* 20, 697–712. doi:10.1089/ten.teb.2013.0709
- Taniguchi, N., Fujibayashi, S., Takemoto, M., Sasaki, K., Otsuki, B., Nakamura, T., et al. (2016). Effect of pore size on bone ingrowth into porous titanium implants fabricated by additive manufacturing: An *in vivo* experiment. *Mater. Sci. Eng. C* 59, 690–701. doi:10.1016/j.msec.2015.10.069
- Van Bael, S., Chai, Y. C., Truscetto, S., Moesen, M., Kerckhofs, G., Van Oosterwyck, H., et al. (2012). The effect of pore geometry on the *in vitro* biological behavior of human periosteum-derived cells seeded on selective laser-melted Ti6Al4V bone scaffolds. *Acta Biomater.* 8, 2824–2834. doi:10.1016/j.actbio.2012.04.001
- Wang, X., Xu, S., Zhou, S., Xu, W., Leary, M., Choong, P., et al. (2016). Topological design and additive manufacturing of porous metals for bone scaffolds and orthopaedic implants: A review. *Biomaterials* 83, 127–141. doi:10.1016/j.biomaterials.2016.01.012
- Wang, H., Su, K., Su, L., Liang, P., Ji, P., and Wang, C. (2019). Comparison of 3D-printed porous tantalum and titanium scaffolds on osteointegration and osteogenesis. *Mater. Sci. Eng. C* 104, 109908. doi:10.1016/j.msec.2019.109908
- Wang, X., Zhu, Z., Xiao, H., Luo, C., Luo, X., Lv, F., et al. (2020). Three-Dimensional, MultiScale, and interconnected trabecular bone mimic porous tantalum scaffold for bone tissue engineering. *ACS Omega* 5, 22520–22528. doi:10.1021/acsomega.0c03127
- Wang, X., Ning, B., and Pei, X. (2021). Tantalum and its derivatives in orthopedic and dental implants: Osteogenesis and antibacterial properties. *Colloids Surfaces B Biointerfaces* 208, 112055. doi:10.1016/j.colsurfb.2021.112055
- Wang, Z., Zhang, M., Liu, Z., Wang, Y., Dong, W., Zhao, S., et al. (2022). Biomimetic design strategy of complex porous structure based on 3D printing Ti-6Al-4V scaffolds for enhanced osseointegration. *Mater. Des.* 218, 110721. doi:10.1016/j.matdes.2022.110721
- Wauthle, R., van der Stok, J., Amin Yavari, S., Van Humbeeck, J., Kruth, J.-P., Zadpoor, A. A., et al. (2015). Additively manufactured porous tantalum implants. *Acta Biomater.* 14, 217–225. doi:10.1016/j.actbio.2014.12.003
- Webber, M. J., Appel, E. A., Meijer, E. W., and Langer, R. (2016). Supramolecular biomaterials. *Nat. Mater.* 15, 13–26. doi:10.1038/nmat4474
- Yang, J., Jin, X., Gao, H., Zhang, D., Chen, H., Zhang, S., et al. (2020). Additive manufacturing of trabecular tantalum scaffolds by laser powder bed fusion: Mechanical property evaluation and porous structure characterization. *Mater. Charact.* 170, 110694. doi:10.1016/j.matchar.2020.110694
- Zadpoor, A. A. (2015). Bone tissue regeneration: The role of scaffold geometry. *Biomater. Sci.* 3, 231–245. doi:10.1039/C4BM00291A



OPEN ACCESS

EDITED BY

Yanjin Lu,
Fujian Institute of Research on the
Structure of Matter (CAS), China

REVIEWED BY

Changlu Xu,
University of California, Los Angeles,
United States
Lan-Yue Cui,
Shandong University of Science and
Technology, China

*CORRESPONDENCE

Lianhui Fan,
✉ 1841508661@qq.com
Jing Zhao,
✉ zhaojing@imr.ac.cn
Jianzhong Li,
✉ 174030098@qq.com

SPECIALTY SECTION

This article was submitted to Biomaterials
and Bio-Inspired Materials,
a section of the journal
Frontiers in Materials

RECEIVED 29 November 2022

ACCEPTED 18 January 2023

PUBLISHED 02 February 2023

CITATION

Li H, Zhao J, Wang Z, Hu J, Zhao J,
Awonusi BO, Li J and Fan L (2023), Cu-
loaded polyurethane to reduce ureteral
stent microbes adherence and regulation
of the inflammation response
to RAW264.7.
Front. Mater. 10:1110919.
doi: 10.3389/fmats.2023.1110919

COPYRIGHT

© 2023 Li, Zhao, Wang, Hu, Zhao, Awonusi,
Li and Fan. This is an open-access article
distributed under the terms of the [Creative
Commons Attribution License \(CC BY\)](#).
The use, distribution or reproduction in
other forums is permitted, provided the
original author(s) and the copyright
owner(s) are credited and that the original
publication in this journal is cited, in
accordance with accepted academic
practice. No use, distribution or
reproduction is permitted which does not
comply with these terms.

Cu-loaded polyurethane to reduce ureteral stent microbes adherence and regulation of the inflammation response to RAW264.7

Hongwei Li^{1,2}, Jing Zhao^{3*}, Zhenyu Wang², Jiyuan Hu³,
Jinlong Zhao³, Bukola O. Awonusi³, Jianzhong Li^{2*} and
Lianhui Fan^{1,2*}

¹Department of Urology, Jinzhou Medical University Graduate Training Base, General Hospital of Northern Theater Command, Shenyang, China, ²Department of Urology, General Hospital of Northern Theater Command, Shenyang, China, ³Institute of Metal Research, Chinese Academy of Sciences, Shenyang, China

Introduction: Ureteral stents blocked with encrustation are a common clinical complication and affect bacteria colonization and inflammatory response. In this study, different concentrations of copper (0.25, 0.5, 1, 1.5, and 2 g/L) were immobilized on polyurethane (PU) that showed functionalization of microbe resistance and regulation of the inflammation response to RAW264.7.

Methods: X-ray photoelectron spectroscopy (XPS), atomic force microscope (AFM) and static water contact angles were used to analyze the surface characterization. *Proteus mirabilis* resistance test and adhesion of cells by SEM were carried out to evaluate the antibacterial property of Cu-bearing samples. Cell cytotoxicity assay and apoptosis were used to obtain acceptable concentrations of PU-Cu. The morphology of cells was used to observe the occurrence of pseudopodia after contact with PU-Cu. Wound healing assay and Transwell invasion assay were carried out to observe the migration and recovery of macrophages. IL-6 and IL-10 were used to evaluate the secretion of pro-/anti-inflammatory cytokines.

Results: X-ray photoelectron spectroscopy (XPS), atomic force microscope (AFM), and static water contact angle measurement were used to confirm successful immobilization of Cu on PU. Plate counting assay and observation of adhered cells by SEM demonstrated that the antibacterial performance of PU-Cu against *Proteus mirabilis* increased with the amount of Cu loading in a dependent manner. Furthermore, the CCK-8 assay and apoptosis test suggested an acceptable cytotoxicity of PU-Cu at concentrations of 0.25, 0.5, and 1 g/L. The morphology of cells observed by SEM showed reduced occurrence of pseudopodia after contact with PU-Cu. Wound healing and transwell invasion assays manifested that migration and recovery of macrophages were improved by PU-Cu. ELISA of IL-6 and IL-10 demonstrated that PU-Cu could regulate inflammatory cytokines toward anti-inflammatory functionalization.

KEYWORDS

ureteral stent, copper, microbe resistance, inflammatory response, RAW264.7

1 Introduction

Ureteral stents are considered ideal devices for urolithiasis that have been widely used to maintain the patency of urine from renal to bladder and to relieve obstruction of the urinary tract (Li et al., 2021). However, implantation of a foreign object would cause many complications, such as inflammation, encrustation, and urinary symptoms (Sali and Joshi, 2020). More than 80% of the patients suffer from varying degrees of pains in daily life, attributing to the retention of ureteral stents (Soria et al., 2021). Therefore, it is necessary to solve these side effects by inspecting new comfortable materials.

Encrustation generally occurs on both lumen and outer surfaces of the ureteral stent, aggravated by the accumulation of biofilm formation and indwelling time duration (Barghouthy et al., 2021). It has been shown that organic molecules, glycoproteins, and microbes could adhere to the stent in a short-term period to facilitate crystal deposition (Torrecilla et al., 2020). Ureteral stents tender the surface of substrates and are conducive to formatting microbial immobilization and biofilm formation (Bhardwaj and Ingole, 2022). Urease-positive microbiome (*Proteus*, *Klebsiella*, etc.) predisposes urea to ammonia and contributes to the elevation of urine pH that can accelerate precipitation of minerals from urine and gather on the stent. These complicated conditional films and micro-environment around stents construct a mutual promotion to generate new stones (Wasfi et al., 2020; Tomer et al., 2021). The main components of encrustation are calcium phosphate (CaP) and calcium oxalate monohydrate (COM), a potent type of calcium oxalate (CaOx) (Kram et al., 2022). These nuclei gradually induce the formation of stones that result in several kidney stone diseases and deposition of CaOx crystals in infiltrating macrophages (Singhto and Thongboonkerd, 2018; Zhu et al., 2019).

In addition to lumen blocking, stones can also activate the inflammatory response of the human body and ultimately lead to tissue injury under the control of related inflammatory mediators (Li et al., 2020; Liu et al., 2022a). Macrophages play an important role in the early inflammatory response, and diverse cytokines such as interleukin-6 (IL-6), interleukin-1 β (IL-1 β), and tumor necrosis factor- α (TNF- α) are secreted (Liu et al., 2022b). Once bacterial colonization and crystal deposition occur on the catheter, chronic infection is caused by macrophages and induces overproduction of reactive oxygen species (ROS), chemokines, and pro-inflammatory cytokines (Xue et al., 2020). Consequently, more immune cells including monocytes, macrophages, and neutrophils can be recruited toward the inflammatory sites. In addition, macrophage-engulfed COM contributes to the activation of pyrin domain-containing protein (NLRP3) that influences the recruitment of leukocytes and regulates the corresponding pro-inflammatory cytokines (Anders et al., 2018; Singhto et al., 2018; Lin et al., 2019). Furthermore, during monocytes phagocytosing crystals, macrophages would be polarized into M₁ and M₂ and affect the inflammatory response (Liang et al., 2021). M₁ macrophages modulate promotion of the deposited crystals *via* regulating inflammation response and ROS by releasing pro-inflammatory cytokines like IL-6, leading to the deposition of crystals. Conversely, M₂ polarization positively alleviates inflammatory response with secretion of anti-inflammatory cytokines like IL-10 that are conducive to tissue-healing and phagocytizing crystals (Liu et al., 2020; Jiang et al., 2021).

In this study, copper immobilized on PU was prepared based on the previous successful performance of Cu-bearing stainless steel that reduces biofilm formation, and it was fabricated by using the

TABLE 1 Chemical components of the artificial urine.

Component	Quantity (g)
NaCl	6.17
NaH ₂ PO ₄	4.59
Na ₃ C ₆ H ₅ O ₇	0.944
MgSO ₄	0.463
Na ₂ SO ₄	2.408
KCl	4.75
Na ₂ C ₂ O ₄	0.043
CaCl ₂	0.638

encrustation deposition method (Zhao et al., 2019). X-ray photoelectron spectroscopy (XPS), atomic force microscope (AFM), and contact angle measurement were used to characterize the surface properties. In order to investigate the inflammation response induced by copper after incubation with RAW264.7, cell proliferation, morphology, invasion, and secretion of pro-/anti-inflammatory cytokines were tested by cell counting kit-8 (CCK-8) assay, flow cytometry, scanning electron microscopy (SEM), transwell invasion assay, and enzyme-linked immunosorbent assay (ELISA).

2 Materials and methods

2.1 Preparation of copper-loaded samples

Polyurethanes (PUs) purchased from Lubrizol Corporation (United States) were divided into 10 × 10 mm segments for the experiments. Samples were treated with 2 g/L dopamine hydrochloride (PDA) (Biotopped, China) solution in Tris-HCL buffer at 37 C for 24 h. Then, dopamine-immobilized PU (PU-PDA) was washed ultrasonically with deionized water and absolute ethanol. After drying, the substrates were immersed in different concentrations of CuCl₂ (0.25, 0.5, 1, 1.5, and 2 g) solution supplemented with 0.01 mol/L Tris-HCL and 0.1 mol/L dimethylaminoborane (DMAB) (Maya Reagent, China). The copper-bearing specimens were named PU-0.25Cu, PU-0.5Cu, PU-1Cu, PU-1.5Cu, and PU-2Cu according to the concentration of CuCl₂.

2.2 Surface characterization

X-ray photoelectron spectroscopy (XPS, Thermo VG, United States) was used to measure the surface chemical compositions of diverse groups of samples with an Al K α X-ray source. The peaks of copper and N element were analyzed using XPSPEAK41 software. An atomic force microscope (AFM, Agilent 5500) was utilized to detect roughness and surface morphology of coatings. Static water contact angles were measured using a contact angle goniometer (DSA-100, Kruss, Germany) with 5 μ L water droplet placed on three random areas of each sample.

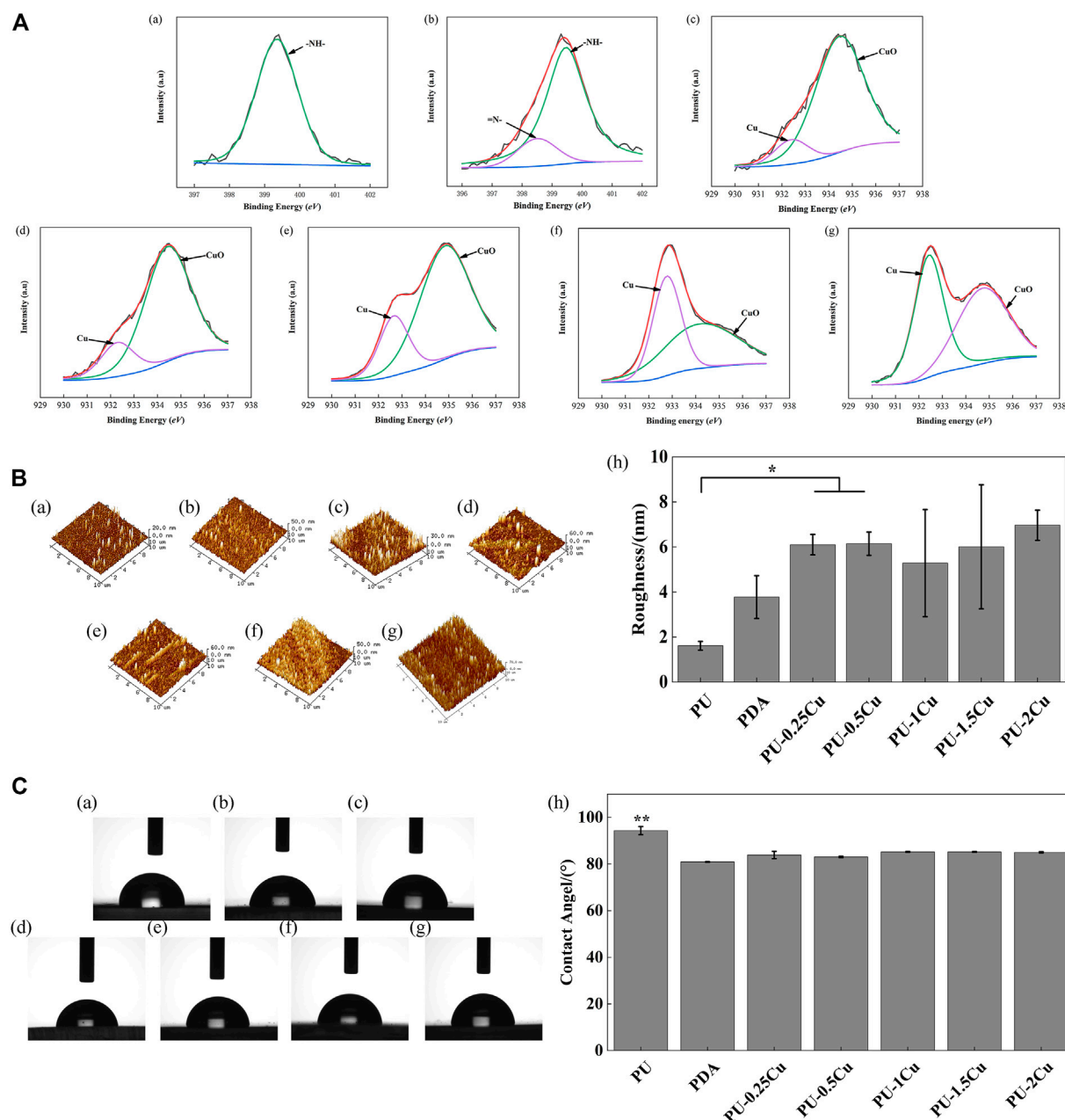


FIGURE 1

(A) (a)–(b) XPS results for PU and PDA, representing high-resolution spectra of N1s. (c)–(g) XPS results for PU-0.25Cu, PU-0.5Cu, PU-1Cu, PU-1.5Cu, and PU-2Cu, representing high-resolution spectra of Cu 2p_{3/2}. (B) (a)–(g) 3D topography images of PU, PDA, PU-0.25Cu, PU-0.5Cu, PU-1Cu, PU-1.5Cu, and PU-2Cu. (h) surface roughness values of samples. Data were presented as mean ± standard deviation (n=3), with *p<0.05 indicating a significant difference. (C) (a)–(g) Representative droplet images of PU, PDA, PU-0.25Cu, PU-0.5Cu, PU-1Cu, PU-1.5Cu, and PU-2Cu. (h) Statistical results of water contact angles, with **p<0.01 indicating a very significant difference.

2.3 *Proteus mirabilis* cultivation and *in vitro* bacteria resistance test

The *Proteus mirabilis* lyophilized powder (BeNa Culture Collection, China) was dissolved in a liquid medium and incubated overnight in a shaker at 150 rpm. Afterward, 100 μL bacterial droplets were cultured on a solid medium for 24 h and prepared for the subsequent test. The plate counting method was used to evaluate the antibacterial property of Cu-bearing samples. A measure of 100 μL

bacterial suspension at a concentration of 5.0×10^5 CFU/mL was dropped on the surface of sterilized samples. After incubating at 37°C for 24 h, samples were transferred into PBS solution and eluted by vortex-mixing for 1 min. The serially diluted suspensions were pipetted out for counting by coating on a solid agar. The antibacterial rate was calculated as follows:

$$\text{Antibacterial rate\%} = \frac{A - B}{A} \times 100\%, \quad (1)$$

TABLE 2 Proportion of Cu element determined by XPS.

Sample	Cu%
PU-0.25Cu	11.98
PU-0.5Cu	19.09
PU-1Cu	24.61
PU-1.5Cu	46.43
PU-2Cu	51.36

where A and B are the colonies of PU and PU-PDA or copper-loaded samples, respectively.

In addition, scanning electron microscopy (TESCAN MIRA, Czech Republic) was used to observe the distribution and

morphology of *P. mirabilis* adhered on the substrates incubated with 5.0×10^7 CFU/mL suspensions. After co-culturing for 24 h, samples were washed with PBS three times and then fixed with 2.5% glutaraldehyde (Macklin, China) at 4°C for 2 h. Then, serial dehydration was performed, and samples were dried.

2.4 Deposited encrustation assay

Each sample was immersed in 1 mL artificial urine containing 5.0×10^8 CFU of *P. mirabilis* and then incubated at 37°C for 7 days. The proportion of artificial urine is shown in Table 1. At the indicated time, samples were taken out and washed with deionized water. After immersing in 5% HCl solution and ultrasonically cleaning for 5 min, the contents of Ca^{2+} and Mg^{2+} ions were measured by ICP-MS7900 (Agilent, United States).

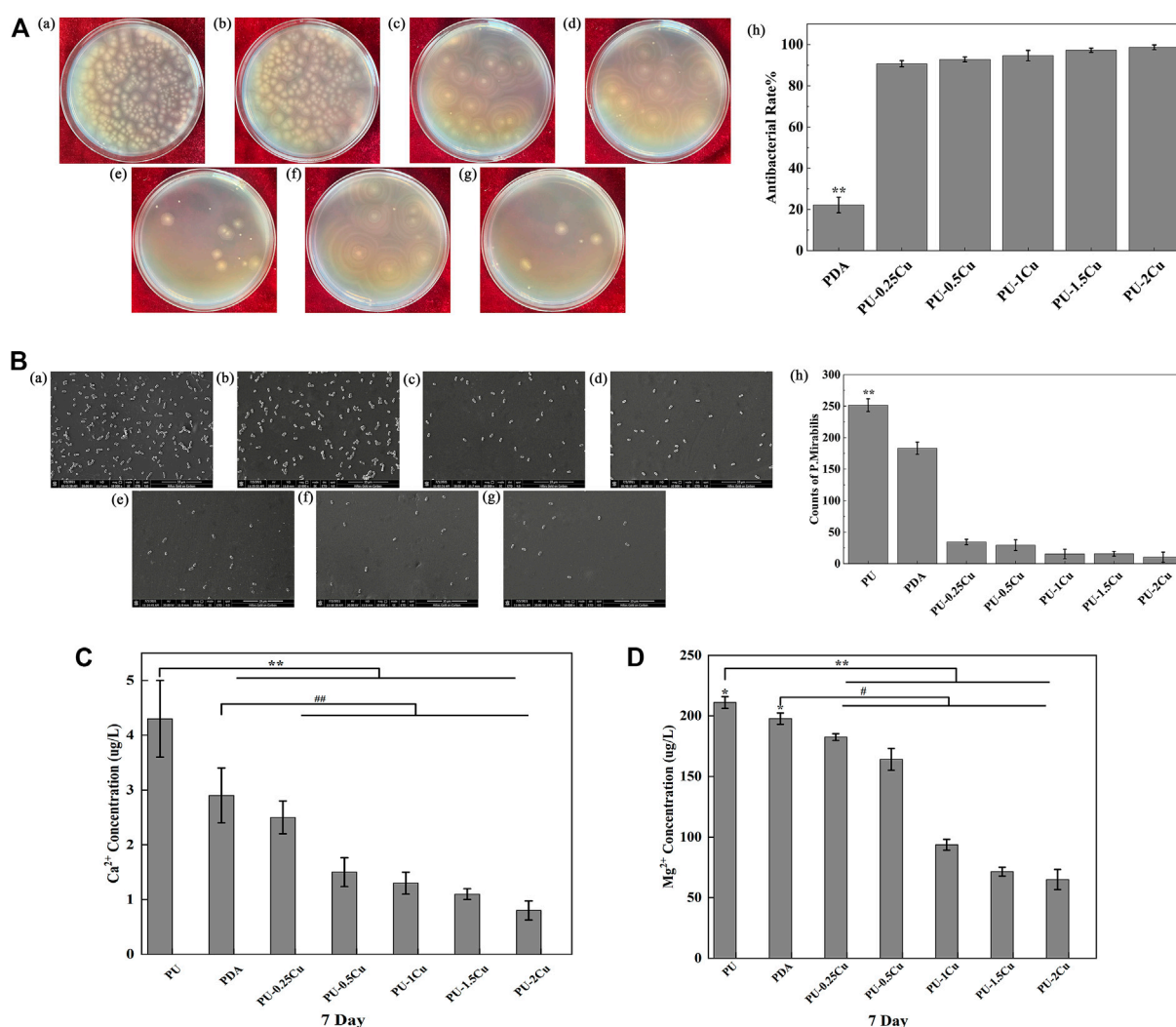


FIGURE 2

(A) (a)–(g) *P. mirabilis* colonies on plates for PU, PDA, PU-0.25Cu, PU-0.5Cu, PU-1Cu, PU-1.5Cu, and PU-2Cu. (h) Antibacterial rate of samples compared to PU. Data were presented as mean \pm SD (N=3), and a significant difference at $p < 0.01$ is shown as $**p < 0.01$. (B) (a)–(g) Morphology and distribution of *Proteus mirabilis* on the surface of PU, PDA, PU-0.25Cu, PU-0.5Cu, PU-1Cu, PU-1.5Cu, and PU-2Cu. (h) Amount of *Proteus mirabilis* on the samples. A significant difference at $p < 0.01$ is shown by $**p < 0.01$. (C,D) Contents of Ca^{2+} and Mg^{2+} in the encrustation on various samples by *P. mirabilis*. A significant difference at $p < 0.05$ is shown as $*p < 0.05$, $\#p < 0.05$ and $p < 0.01$ is shown as $**p < 0.01$ and $##p < 0.01$.

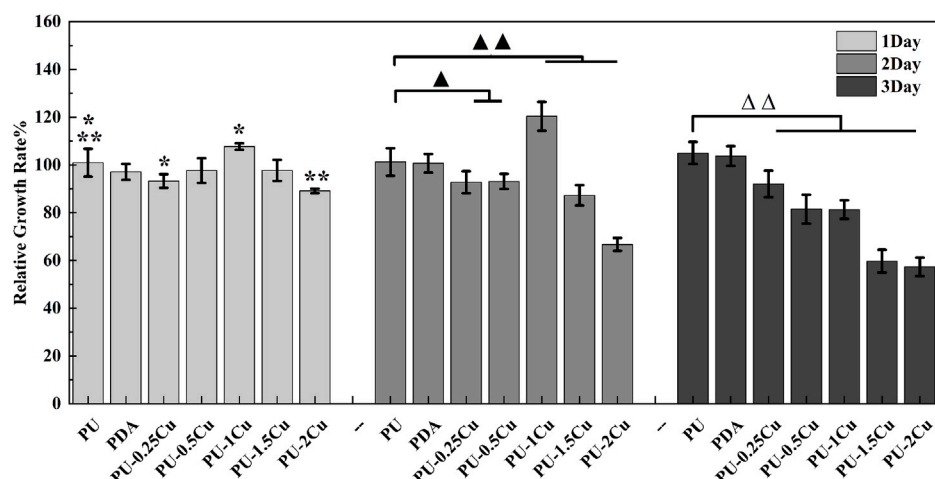


FIGURE 3

RGR of RAW264.7 cultured with the extracts for 24, 48, and 72 h. Significant differences are marked as * $p < 0.05$, $\blacktriangle p < 0.05$, ** $p < 0.01$, $\blacktriangle\blacktriangle p < 0.01$, and $\Delta\Delta p < 0.01$, respectively.

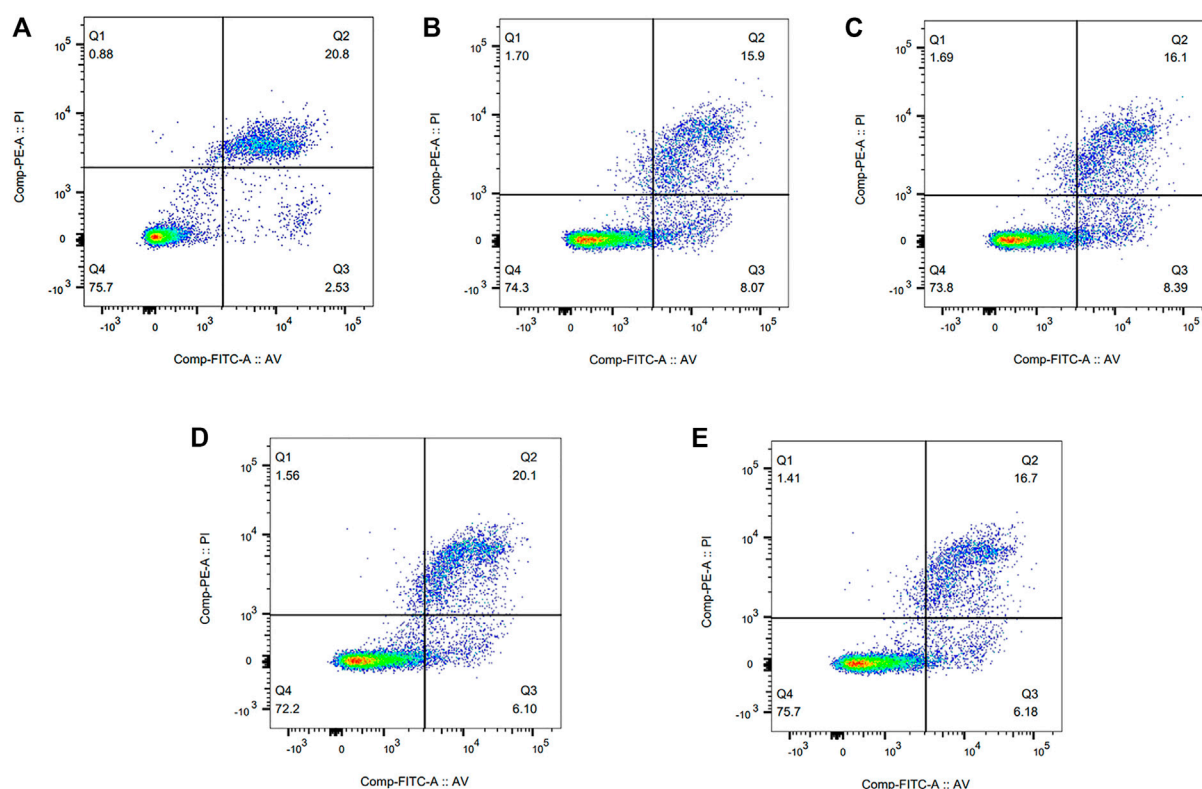


FIGURE 4

Flow cytometry results of RAW264.7 cultured with the extracts for 24 h. (A) PU, (B) PDA, (C) PU-0.25Cu, (D) PU-0.5Cu, and (E) PU-1Cu.

2.5 RAW264.7 cell line culture

Mouse leukemia cells of monocyte macrophage cell lines (RAW264.7), obtained from the National Collection of Authenticated Cell Cultures, were cultured in Dulbecco's modified Eagle medium (DMEM, HyClone,

United States) supplemented with 10% fetal bovine serum (Gibco), 100 U/mL penicillin, and 100 μ g/mL streptomycin (Genview, China) in a 5% CO₂ incubator (Shel Lab, United States) at 37°C. Cells were treated with 0.25% trypsin-EDTA (Gibco, Canada) and re-suspended in fresh DMEM, while 80% confluence was reached.

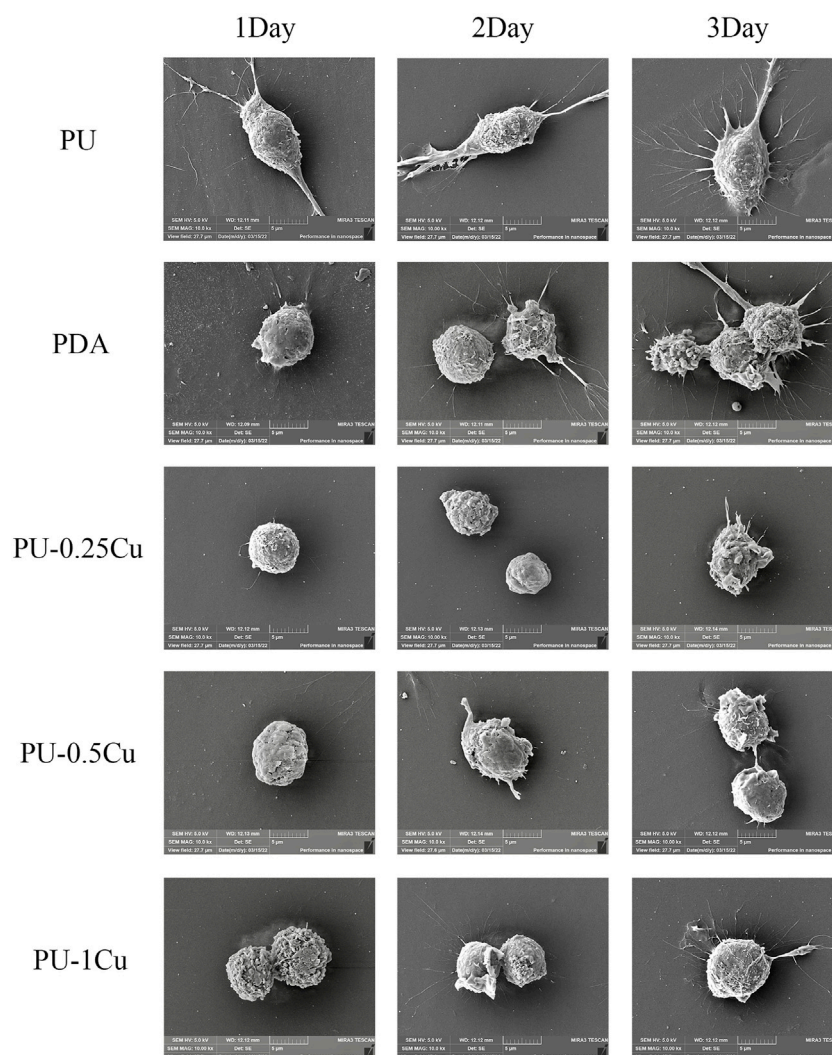


FIGURE 5
SEM images of RAW264.7 on the surface of samples.

2.6 Cytotoxicity assay

Cytotoxicity was used to evaluate the cell viability after treating with 24-h extracts of samples using CCK-8 (Biosharp, China). The ratio of samples' surface-area to culture medium volume ($3 \text{ cm}^2/\text{mL}$) was used to prepare the extracts according to ISO 10993-5. A measure of $100 \mu\text{L}$ of cell suspensions at a concentration of $3 \times 10^4/\text{mL}$ was seeded in a 96-well plate and incubated overnight. Afterward, the medium was replaced with $100 \mu\text{L}$ extracts or DMEM (negative control). After 24, 48, and 72 h of incubation, cell counting kit-8 was added and co-cultured for 2 h to measure the optical density (O.D.) at 450 nm (Bio-Rad, United States). The relative growth rate (RGR) was calculated by the following equation:

$$\text{Relative Growth Rate (\%)} = \frac{A - B}{B} \times 100\%, \quad (2)$$

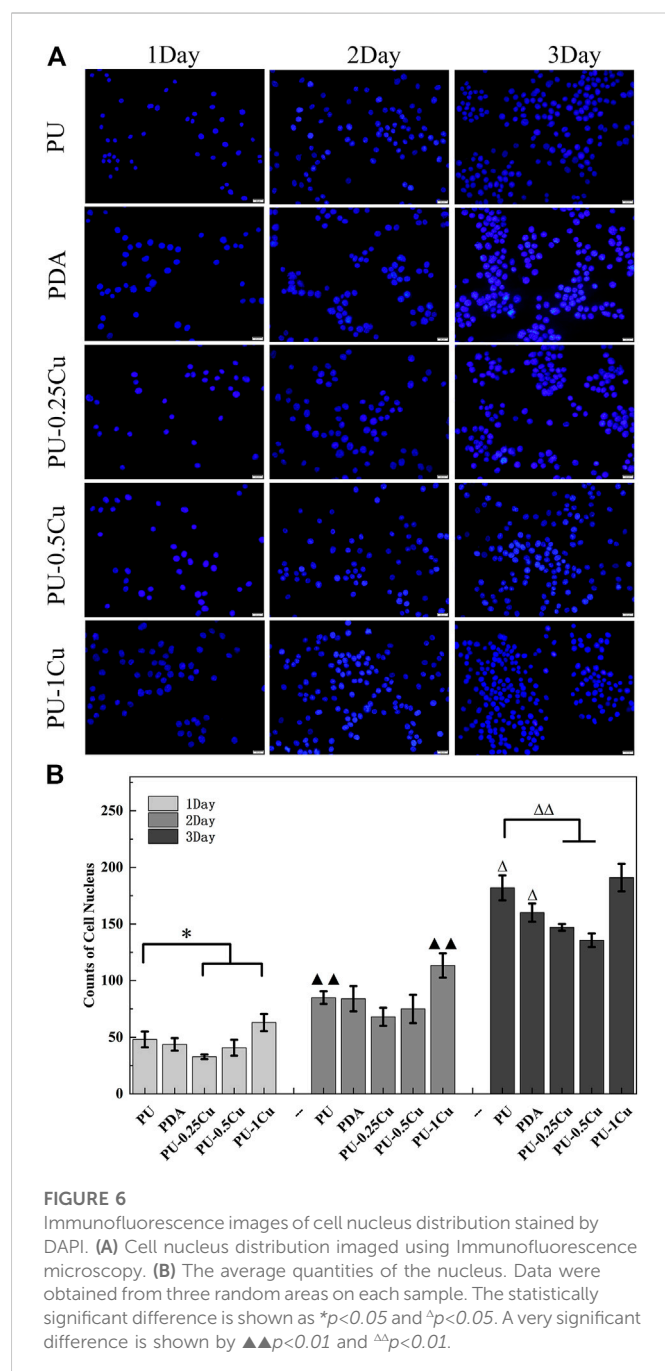
where A is O.D. for each experimental group and B is the control.

2.7 Annexin V-FITC/PI apoptosis assay

RAW264.7 cells at a density of 1×10^6 cells per well were incubated in a six-well plate with the sample extracts for 24 h, respectively. Trypsin solution with phenol red (EDTA-free) (Biosharp, China) was used to harvest the cells, then washed with ice-cold PBS, and re-suspended with Annexin V-FITC/PI apoptosis kit (Multisciences, China) according to the standard instructions. Afterward, flow cytometry was used to detect apoptosis of cells, and the corresponding data were analyzed using ModFit LT software.

2.8 Morphology of cells

RAW264.7 cells at a density of 1×10^4 cells were seeded on samples and incubated for 24, 48, and 72 h. Subsequently, substrates were fixed with 2.5% glutaraldehyde (Macklin, China) and dehydrated with serial concentrations of ethanol. After drying and gold spraying, SEM



(TESCAN MIRA, Czech Republic) was used to observe morphology of macrophages.

2.9 Cell distribution

The cell nucleus stained by DAPI (Beyotime, China) was used to observe distribution and counts of RAW264.7 cells seeded on the samples and incubated for 24, 48, and 72 h. At the indicated time, samples were taken out and fixed with 4% paraformaldehyde (Biosharp, China) for 30 min and then supplemented with 0.1% Triton-X-100 (Dingguo, China) for 5 min. After washing with PBS, DAPI was used to stain the cells out of light. Three random areas on each sample were

observed using an immunofluorescence microscope (Olympus, Japan), and the average amount of cells was stated.

2.10 Wound healing assay

Wound healing assay was carried out to investigate the cell migration capacity of RAW264.7 cells. A density of 1×10^6 cells were cultured in a six-well plate and incubated until confluent. A 10- μ L pipette tip was used to make a straight scratch. After washing three times, 2 mL of 24-h extracts was added, and photographs were taken using an optical microscope (Olympus, CKX53) at 0 h and after incubation for 24 h at a stable location. The wound areas were analyzed using Image J, and the relative migration area was calculated by the following equation:

$$\text{Relative Migration Area (\%)} = \frac{A - B}{A} \times 100\%, \quad (3)$$

where A and B are the scratch marks with no cells at 0 and 24 h, respectively.

2.11 Transwell invasion assay

A measure of 100 μ L of cell suspensions at a concentration of 5×10^5 /mL was added into the upper chambers and transferred to the wells of 24-well plates containing 600 μ L DMEM or 24-h extracts supplemented with 10% FBS. After incubation for 36 h, the membrane was fixed with 4% paraformaldehyde for 30 min at 4 C and then was stained with 0.1% crystal violet (Lengene, China). Three random locations of the membrane were imaged using an optical microscope (Olympus, CKX53), and the migration numbers were quantified.

2.12 ELISA of IL-10 and IL-6

The secretion of pro- or anti-inflammatory cytokines (IL-6 and IL-10) of RAW264.7 was detected using the ELISA kit (Multisciences, China). RAW264.7 cells at a density of 1×10^5 cells per well were cultured in a six-well plate with the extracts for 24, 48, and 72 h. The collected specimen from each well was centrifuged at 1,000 rpm for 20 min, and the supernatant was measured using IL-6 and IL-10 ELISA kits, respectively, according to the manufacturer's protocol. The mean values of cytokine secretion of samples were calculated in triplicate.

2.13 Statistical analysis

Data were presented as mean \pm standard deviation (SD). The statistical analysis was expressed by the t -test or one-way ANOVA with a *post hoc* test.

3 Results

3.1 XPS analysis

XPS was used to analyze the composition of substrates, and the corresponding spectra of N1s and Cu2p regions are shown in Figure 1A. A secondary amine ($-\text{NH}-$) with a binding energy of 399.5 eV appeared in

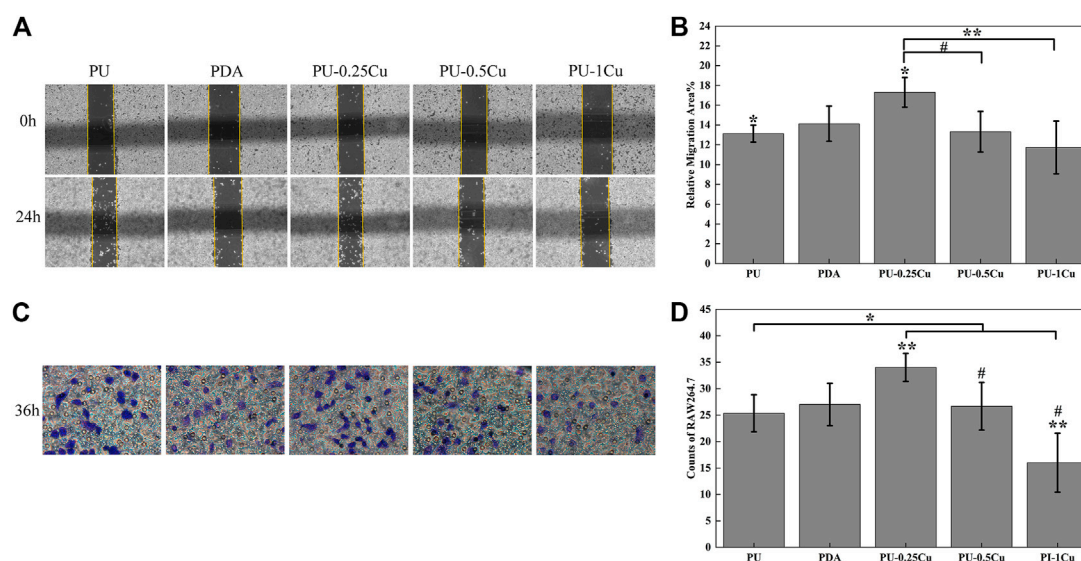


FIGURE 7

(A) Wound healing assay imaged using an optical microscope, magnified 100 times at 0 and 24 h. (B) Relative migration area of samples. (C) Transwell assay recorded using an optical microscope at 36 h. (D) Number of cells migrated through the membrane for 36 h. The statistically significant difference at $p < 0.05$ is shown as * $p < 0.05$ and # $p < 0.05$. $p < 0.01$ is shown by different letters ** $p < 0.01$.

PU, whereas an additional amino-rich tertiary group (=N-) with a binding energy of 398.5 eV, which was the characteristic peak of PDA, appeared in PU/PDA, indicating a successful coating of PDA on PU. The peaks of Cu2p, including Cu (932.50 eV) and CuO (934.60 eV), were considered important evidence to prove immobilization of Cu on the substrates as shown in Figure 1A (c)–(g). Table 2 depicts the proportion of Cu, which increases with concentrations of CuCl₂. The proportion of Cu loading on PU for concentrations of 0.25, 0.5, 1, 1.5, and 2 g/L were 11.98, 19.09, 24.61, 46.43, and 51.36%, respectively.

3.2 Topography and roughness

AFM was carried out to study surface topography and roughness of samples. The 3D images in Figure 1B depict that PU has a smooth surface; however, topography of Cu-loaded samples displays a certain fluctuation. It showed that Ra of PU was 1.61 ± 0.19 nm, which was enhanced after immobilizing copper, ranging from 5 to 7 nm with no significant difference.

3.3 Contact angles

As illustrated in Figure 1C, the contact angle of PU and PDA was 94.4° and 80.9°, respectively, indicating that PDA was successfully immobilized on PU with the help of a hydrophilic reagent. There was no significant difference in copper-loaded PU except for a slightly increasing tendency.

3.4 Antibacterial property

Figure 2A shows the antibacterial rate of samples cultured with *P. mirabilis* for 24 h. Compared to PU, an enormous improvement was seen in PU-Cu against microbes, increasing with the copper loading

content response. SEM was used to confirm adhesion of *P. mirabilis* on samples, as shown in Figure 2B. The morphology of *P. mirabilis* was rhabditiform and was distributed evenly on the majority of PU. However, fewer bacteria were adhered on PU-Cu samples.

3.5 Deposited encrustation assay

The primary elements of encrustation were Ca and Mg. It was shown that the concentrations of Ca²⁺ and Mg²⁺, which dissolved from the samples, gradually decreased with the increasing contents of copper, as depicted in Figures 2C, D.

3.6 Cytotoxicity

CCK-8 was used to measure cytotoxicity of RAW264.7 after culturing with the extracts for 24, 48, and 72 h. As shown in Figure 3, the RGRs were all above 80% in PU, PDA, and PU-(0.25–1)Cu, indicating an acceptable cytotoxicity, according to the standard of ISO 10993–5. However, the RGR of cells co-cultured with PU-2Cu for 48 h was decreased to 66.71%, showing negative effects on RAW264.7 due to additional release of copper ions. When cultivating for 72 h, RGR was reduced to 59.68% and 57.30% for PU-1.5Cu and PU-2Cu, respectively, demonstrating that there was an acceptable cytotoxicity against cells only within a certain concentration range of Cu loaded on substrates. Thus, samples with an acceptable cytotoxicity were subjected to the following tests besides PU-1.5Cu and PU-2Cu.

3.7 Annexin V-FITC/PI apoptosis assay

Flow cytometry was performed to evaluate cell viability of PU, PDA, and PU-Cu groups. After incubating for 24 h, the results are

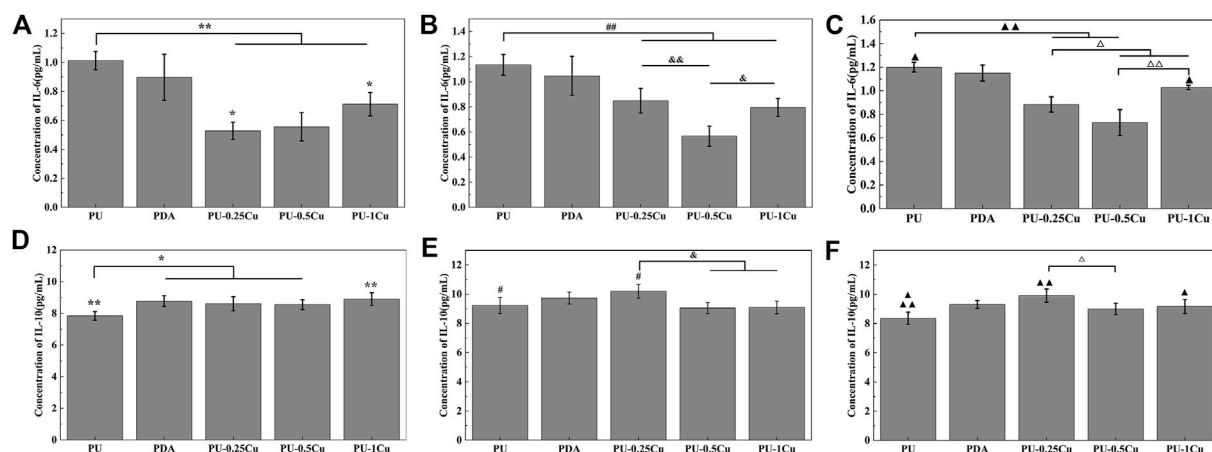


FIGURE 8

(A–C) Concentration of IL-6 secreted into the culture medium for 24, 48, and 72 h. Statistically significant differences are shown as * $p < 0.05$, [†] $p < 0.05$, [‡] $p < 0.05$, [§] $p < 0.01$, ^{||} $p < 0.01$, ^{¶¶} $p < 0.01$, ^{△△} $p < 0.01$, and ^{▲▲} $p < 0.01$. **(D–F)** Concentration of IL-10 secreted into the culture medium for 24, 48, and 72 h. Significant differences are represented as * $p < 0.05$, [†] $p < 0.05$, [‡] $p < 0.05$, [§] $p < 0.05$, [△] $p < 0.05$, ^{△△} $p < 0.05$, ^{△△} $p < 0.05$, and ^{▲▲} $p < 0.01$.

displayed in Figure 4. It could be concluded that the percentage of live cells (Q4) of PU was 75.7%, whereas that of PDA, PU-0.25Cu, PU-0.5Cu, and PU-1Cu was 74.3, 73.8, 72.2, and 75.7%, respectively.

3.8 Cell morphology

Cell morphology on the surface of samples was visualized by SEM. As shown in [Figure 5](#), RAW264.7 cells on PU and PDA were activated to become spindle-shaped with more pseudopod spreading. However, the cells adhered on PU-Cu showed a spherical shape with almost no pseudopods, which means less effect on macrophage irritation. There was no significant discrepancy of cell morphology among Cu-loaded PU substrates.

3.9 Staining assay for the cell nucleus

Immunofluorescence microscopy was used to observe the cell nucleus distribution, and the corresponding results are shown in Figure 6. The average quantities of the nucleus were increased with the prolonged incubation period for each material. Statistically significant differences of PU-0.25Cu and PU-1Cu compared to PU indicated a favorable probability of cell attachment after coating with Cu for 24 h.

3.10 Cell migration assay

The effect of PU-Cu on cell migration capacities was investigated by wound healing and transwell assays, respectively. As presented in [Figures 7A, B](#), the relative migration area of RAW264.7 incubated with PU-0.25Cu was 17.3%, which was significantly higher than that of PU (13.1%). However, the other PU-Cu samples showed a negative influence. In addition, [Figures 7C, D](#) illustrate cell longitudinal migration capacity evaluated by transwell assay. Similar to the results of wound healing and compared with PU or other PU-Cu samples, more stained cells were observed after incubating with PU-0.25Cu.

3.11 Detection of IL-6 and IL-10 secretion by ELISA

ELISA kits were used to detect concentrations of IL-6 and IL-10 secretion into the medium. As described in [Figures 8A–C](#), the contents of IL-6 were obviously decreased after culturing with 24-h PU-Cu extracts, compared to PU for 24, 48, and 72 h. The concentration of the pro-inflammatory cytokine, IL-6, in PU was 1.013 ± 0.0064 pg/mL, whereas that in PU-0.25Cu, PU-0.5Cu, and PU-1Cu was 0.528 ± 0.060 , 0.556 ± 0.098 , and 0.712 ± 0.081 pg/mL, respectively, with the statistical difference between PU and PU-Cu for 24 h. It was obvious that the secretion of IL-6 in the PU group was increased to 1.200 ± 0.041 pg/mL after incubation for 72 h, while that of PU-Cu samples was significantly lower. These observations demonstrated that copper loaded on samples has a preferable effect on inflammatory inhibition. [Figures 8D–F](#) depict the concentration of IL-10 secreted into the medium. It can be seen that cells incubated with PU secreted the lowest concentration of IL-10 with a significant difference between PU-Cu for 24, 48, and 72 h, indicating that the anti-inflammatory cytokine, IL-10, would be increased with the existence of moderate Cu ions released from PU-Cu samples.

4 Discussion

Ureteral stents are indispensable in urological procedures and used to relieve obstruction after performing shock wave lithotripsy (Arkusz et al., 2021; Yoshida et al., 2021). Multiple serious effects attributing to the encrustation on stents coupled with subsequent chronic inflammatory response show an adverse influence on the recovery of patients (Rebl et al., 2020; Van de Perre et al., 2020). Thus, inhibitory inflammation is favorable to ureteral stents by modulating surface property. In this study, copper loaded on PU bound via PDA was conducted to kill microbes, contributing to the inhibition of encrustation formation, and suppressed the related cytokine expression for alleviating inflammatory response.

In order to confirm the coating of PDA on PU samples, high-resolution spectra of N1s were measured. The presence of a secondary

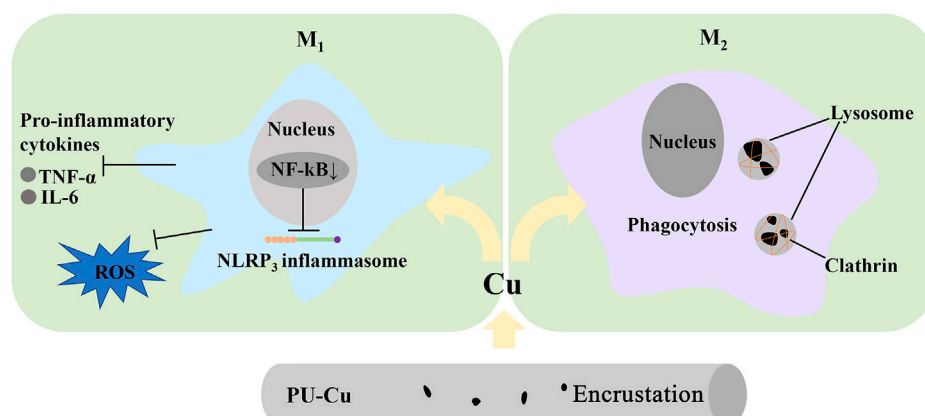
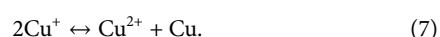
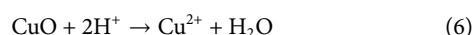
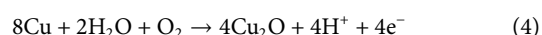


FIGURE 9
Schematic diagram of Cu-bearing stents, inhibiting encrustation via phagocytosis.

and tertiary amine group of PDA with binding energies of 399.5 eV and 398.5 eV, respectively, as shown in Figure 1A (b), indicated successful PDA deposition. Meanwhile, Cu and CuO peaks confirmed the successful immobilization of Cu on the substrates, as demonstrated by the roughness and hydrophilicity changes. Cu⁺ is toxic to biological surroundings and kills bacteria via destroying Fe-S protein; however, it is not stable in solution as Cu²⁺. The Cu-loaded samples reacted well with water and formed Cu₂O, which converted into CuO quickly (Eqs 4, 5) under an oxidation reaction. Cu²⁺ was then reproduced through the reaction with H⁺ in urine, and the dynamic equilibrium would be broken by the action of Cu. Therefore, disproportionation reactions (Eqs 6, 7) could be restricted to form more Cu⁺. Thus, in order to improve the antibacterial property, it is crucial to enhance the proportion of Cu on samples for more Cu⁺. The SEM results showed the inhibitory performance of PU-Cu samples against *P. mirabilis* in Figure 2B. The majority of PU was distributed with microbes, while a decreased number of cells were adhered on PU-Cu samples with the enhanced Cu proportion. Furthermore, Ma et al. (2019) confirmed that the release of Cu ions on the urinary implant materials could kill microbes, thus blocking the occurrence of the deposited encrustation. The depositions on samples were dissolved with HCl, and the corresponding concentrations of Ca²⁺ and Mg²⁺ were analyzed by ICP-MS. A significant decrease of crystal deposition on PU-Cu samples compared to PU or PDA was shown, which was due to continuous contact with PU-Cu.



However, it was indicated that PU-1.5Cu and PU-2Cu manifested certain cytotoxicity to macrophage compared to PU-(0.25–1)Cu, with the same toxic tendency with the proportion of Cu. Figure 3 shows that only an appropriate range of Cu is preferably vital for RAW264.7, affecting the regulating crystal deposition. Macrophages play a pivotal role in the inflammatory response, with the capability of phagocytosis and secretion of related inflammatory cytokines that are functional in immune defense

(Lee et al., 2021). The RAW264.7 cells were stimulated by samples to be activated and polarized to form pro-inflammatory M₁ macrophage or anti-inflammatory M₂ macrophage (Taguchi et al., 2016; Tu et al., 2021; Xiao et al., 2021). Pro-inflammatory M₁ macrophage enhances deposition of CaOx crystals and promotes tissue injury, whereas anti-inflammatory M₂ macrophage shows the opposite effect (Yang et al., 2020). Figure 5 confirms that the RAW264.7 cells adhered to PU were partly activated with the pseudopod spreading, whereas RAW264.7 cells on Cu-bearing samples were almost sphere plotting that showed anti-inflammatory tendency. In addition, macrophage recruitment and swallowing directly affect the eliminating crystals (Yan et al., 2022). Cell nucleus distribution as shown in Figure 6 was stained by DAPI, and the result identified that Cu ion plays an active role in RAW264.7 immobilization. Wound healing assay and transwell assay of cells indicated that RAW264.7 migrated faster and more with a certain concentration of Cu, which was conducive to enhancing chemotaxis. As mentioned previously, different secreted cytokines could promote inflammatory response or anti-inflammatory performance. ELISA for IL-6 secretion demonstrated that Cu can decrease secretion of the pro-inflammatory cytokine. However, it induced secretion of the anti-inflammatory cytokine, IL-10, suggesting that Cu modulated RAW264.7 for further immune response.

The mechanism of regulating encrustation response to macrophage is shown in Figure 9. M₁ and its corresponding pro-inflammatory cytokines, TNF-α and IL-6, and oxidative stress molecules, property to promote the development of CaOx stones, were downregulated via diminishing the nuclear factor κB (NF-κB) signal pathway after contacting with PU-Cu stents (Song et al., 2016; Liu et al., 2022a). Lysosome rupture, ROS generation, and NLRP3 inflammasome activation were blocked in the process of macrophage engulfing (Jin et al., 2011). Nevertheless, deposition of CaOx crystals was suppressed by PU-Cu through polarizing to M₂, which facilitates phagocytosis and contributes to eliminating crystals via lysosomes, clathrin mediation, and some related anti-inflammatory chemokines (Dominguez-Gutierrez et al., 2018; Taguchi et al., 2021). Further investigation should be focused on the related signal pathway targeting the regulation of macrophages converting into M₁ and M₂, and encrustation formation induced by the Cu-bearing ureteral stent in an infectious and crystal precipitation model.

5 Conclusion

In this study, Cu immobilized on PU was modified with the functionality of killing microbes and restraining encrustation. The antibacterial ability was increased with the concentration of Cu loading, whereas only PU-(0.25–1)Cu had an acceptable cytotoxicity to cells. In addition, RAW264.7 cells were recruited in the sustaining action of Cu and secreted the anti-inflammatory cytokine in response to phagocytized crystals, contributing to decreasing stone formation on the ureteral stent.

Data availability statement

The original contributions presented in the study are included in the article/Supplementary Material; further inquiries can be directed to the corresponding authors.

Author contributions

HL performed the experiments and investigation, analyzed the results, and drafted the manuscript. JZ revised the manuscript, approved the submitted version, and contributed to the design and conception of the study. ZW, JH, and BA searched for relevant literature works. JZ analyzed the results of the experiments. JL contributed to supervision, project administration, and acquisition of resources and management. LF performed acquisition of resources and management, supervision, and management of the project.

References

- Anders, H. J., Suarez-Alvarez, B., Grigorescu, M., Foresto-Neto, O., Steiger, S., Desai, J., et al. (2018). The macrophage phenotype and inflammasome component NLRP3 contributes to nephrocalcinosis-related chronic kidney disease independent from IL-1-mediated tissue injury. *Kidney Int.* 93 (3), 656–669. doi:10.1016/j.kint.2017.09.022
- Arkus, K., Pasik, K., Halinski, A., and Halinski, A. (2021). Surface analysis of ureteral stent before and after implantation in the bodies of child patients. *Urolithiasis* 49 (1), 83–92. doi:10.1007/s00240-020-01211-9
- Barghouthy, Y., Wiseman, O., Ventimiglia, E., Letendre, J., Cloutier, J., Daudon, M., et al. (2021). Silicone-hydrocoated ureteral stents encrustation and biofilm formation after 3-week dwell time: Results of a prospective randomized multicenter clinical study. *World J. Urol.* 39 (9), 3623–3629. doi:10.1007/s00345-021-03646-0
- Bhardwaj, M., and Ingole, N. (2022). Application, advancement, and complication of ureteral stent and encrustation: A major complication. *Cureus* 14 (8), e28639. doi:10.7759/cureus.28639
- Dominguez-Gutierrez, P. R., Kusmartsev, S., Canales, B. K., and Khan, S. R. (2018). Calcium oxalate differentiates human monocytes into inflammatory M1 macrophages. *Front. Immunol.* 9, 1863. doi:10.3389/fimmu.2018.01863
- Jiang, S., Wang, R., Han, L., Kuerban, K., Ye, L., Pan, S., et al. (2021). Activation of autophagy reverses gemcitabine-induced immune inhibition of RAW264.7 macrophages by promoting TNF- α , IL-6 and MHC-II expression. *Immunol. Res.* 69 (4), 352–362. doi:10.1007/s12026-021-09210-7
- Jin, C., Frayssinet, P., Pelker, R., Cwirka, D., Hu, B., Vignery, A., et al. (2011). NLRP3 inflammasome plays a critical role in the pathogenesis of hydroxyapatite-associated arthropathy. *Proc. Natl. Acad. Sci. U. S. A.* 108 (36), 14867–14872. doi:10.1073/pnas.1111101108
- Kram, W., Rebl, H., de la Cruz, J. E., Haag, A., Renner, J., Epting, T., et al. (2022). Interactive effects of copper-doped urological implants with tissue in the urinary tract for the inhibition of cell adhesion and encrustation in the animal model rat. *Polym. (Basel)* 14 (16), 3324. doi:10.3390/polym14163324
- Lee, G. H., Kim, J. Y., Jin, S. W., Pham, T. H., Park, J. S., Kim, C. Y., et al. (2021). Impressive acid attenuates the lipopolysaccharide-induced inflammatory response by activating the AMPK/GSK3 β /Nrf2 Axis in RAW264.7 macrophages. *Int. J. Mol. Sci.* 22 (2), 762. doi:10.3390/ijms22020762
- Li, L. C., Pan, Z. H., Ning, D. S., and Fu, Y. X. (2020). Anti-inflammatory effect of simonsinol on lipopolysaccharide stimulated RAW264.7 cells through inactivation of NF- κ B signaling pathway. *Molecules* 25 (16), 3573. doi:10.3390/molecules25163573
- Li, X., Gao, H., Sun, X., Huang, Z., Wang, B., Li, Y., et al. (2021). A preliminary study on the role of Bacteroides fragilis in stent encrustation. *World J. Urol.* 39 (2), 579–588. doi:10.1007/s00345-020-03185-0
- Liang, B., Wang, H., Wu, D., and Wang, Z. (2021). Macrophage M1/M2 polarization dynamically adapts to changes in microenvironment and modulates alveolar bone remodeling after dental implantation. *J. Leukoc. Biol.* 110 (3), 433–447. doi:10.1002/jlb.1ma0121-001r
- Lin, Q., Li, S., Jiang, N., Shao, X., Zhang, M., Jin, H., et al. (2019). PINK1-parkin pathway of mitophagy protects against contrast-induced acute kidney injury via decreasing mitochondrial ROS and NLRP3 inflammasome activation. *Redox Biol.* 26, 101254. doi:10.1016/j.redox.2019.101254
- Liu, H., Yang, X., Tang, K., Ye, T., Duan, C., Lv, P., et al. (2020). Sulfuraphane elicits dual therapeutic effects on renal inflammatory injury and crystal deposition in calcium oxalate nephrocalcinosis. *Theranostics* 10 (16), 7319–7334. doi:10.7150/thno.44054
- Liu, Y., Sun, Y., Kang, J., He, Z., Liu, Q., Wu, J., et al. (2022a). Role of ROS-induced NLRP3 inflammasome activation in the formation of calcium oxalate nephrolithiasis. *Front. Immunol.* 13, 818625. doi:10.3389/fimmu.2022.818625
- Liu, Y., Wu, X., Fang, Q., Li, Z. X., Xia, G. Q., Cai, J. N., et al. (2022b). CD73 attenuates alcohol-induced liver injury and inflammation via blocking TLR4/MyD88/NF- κ B signaling pathway. *J. Inflamm. Res.* 15, 53–70. doi:10.2147/jir.S341680
- Ma, Z., Gao, M., Na, D., Li, Y., Tan, L., and Yang, K. (2019). Study on a biodegradable antibacterial Fe-Mn-C-Cu alloy as urinary implant material. *Mater. Sci. Eng. C Mater. Biol. Appl.* 103, 109718. doi:10.1016/j.msec.2019.05.003
- Rebl, H., Renner, J., Kram, W., Springer, A., Fritsch, N., Hansmann, H., et al. (2020). Prevention of encrustation on ureteral stents: Which surface parameters provide guidance for the development of novel stent materials? *Polym. (Basel)* 12 (3), 558. doi:10.3390/polym12030558
- Sali, G. M., and Joshi, H. B. (2020). Ureteric stents: Overview of current clinical applications and economic implications. *Int. J. Urol.* 27 (1), 7–15. doi:10.1111/iju.14119

Funding

This work was supported by the Shenyang Public Health Science and Technology Project (No. 21-172-9-10) and Liaoning Science and Technology Program (No. 2020JH2/10300159).

Acknowledgments

The authors would like to express their gratitude to EditSprings (<https://www.editsprings.cn>) for the expert linguistic services provided.

Conflict of interest

The authors declare that the research was conducted in the absence of any commercial or financial relationships that could be construed as a potential conflict of interest.

Publisher's note

All claims expressed in this article are solely those of the authors and do not necessarily represent those of their affiliated organizations, or those of the publisher, the editors, and the reviewers. Any product that may be evaluated in this article, or claim that may be made by its manufacturer, is not guaranteed or endorsed by the publisher.

- Singhto, N., Kanlaya, R., Nilnumkhum, A., and Thongboonkerd, V. (2018). Roles of macrophage exosomes in immune response to calcium oxalate monohydrate crystals. *Front. Immunol.* 9, 316. doi:10.3389/fimmu.2018.00316
- Singhto, N., and Thongboonkerd, V. (2018). Exosomes derived from calcium oxalate-exposed macrophages enhance IL-8 production from renal cells, neutrophil migration and crystal invasion through extracellular matrix. *J. Proteomics* 185, 64–76. doi:10.1016/j.jprot.2018.06.015
- Song, H., Liu, B., Huai, W., Yu, Z., Wang, W., Zhao, J., et al. (2016). The E3 ubiquitin ligase TRIM31 attenuates NLRP3 inflammasome activation by promoting proteasomal degradation of NLRP3. *Nat. Commun.* 7, 13727. doi:10.1038/ncomms13727
- Soria, F., de La Cruz, J. E., Fernandez, T., Budia, A., Serrano, Á., and Sanchez-Margallo, F. M. (2021). Heparin coating in biodegradable ureteral stents does not decrease bacterial colonization-assessment in ureteral stricture endourological treatment in animal model. *Transl. Androl. Urol.* 10 (4), 1700–1710. doi:10.21037/tau-21-19
- Taguchi, K., Okada, A., Hamamoto, S., Unno, R., Moritoki, Y., Ando, R., et al. (2016). M1/M2-macrophage phenotypes regulate renal calcium oxalate crystal development. *Sci. Rep.* 6, 35167. doi:10.1038/srep35167
- Taguchi, K., Okada, A., Unno, R., Hamamoto, S., and Yasui, T. (2021). Macrophage function in calcium oxalate kidney stone formation: A systematic review of literature. *Front. Immunol.* 12, 673690. doi:10.3389/fimmu.2021.673690
- Tomer, N., Garden, E., Small, A., and Palese, M. (2021). Ureteral stent encrustation: Epidemiology, pathophysiology, management and current Technology. *J. Urol.* 205 (1), 68–77. doi:10.1097/ju.0000000000001343
- Torreclilla, C., Fernández-Concha, J., Cansino, J. R., Mainez, J. A., Amón, J. H., Costas, S., et al. (2020). Reduction of ureteral stent encrustation by modulating the urine pH and inhibiting the crystal film with a new oral composition: A multicenter, placebo controlled, double blind, randomized clinical trial. *BMC Urol.* 20 (1), 65. doi:10.1186/s12894-020-00633-2
- Tu, Y. J., Tan, B., Jiang, L., Wu, Z. H., Yu, H. J., Li, X. Q., et al. (2021). Emodin inhibits lipopolysaccharide-induced inflammation by activating autophagy in RAW 264.7 cells. *Chin. J. Integr. Med.* 27 (5), 345–352. doi:10.1007/s11655-020-3477-9
- Van de Perre, E., Reichman, G., De Geyter, D., Geers, C., Wissing, K. M., and Letavernier, E. (2020). Encrusted uropathy: A comprehensive overview-to the bottom of the crust. *Front. Med. (Lausanne)* 7, 609024. doi:10.3389/fmed.2020.609024
- Wafsi, R., Hamed, S. M., Amer, M. A., and Fahmy, L. I. (2020). *Proteus mirabilis* biofilm: Development and therapeutic strategies. *Front. Cell Infect. Microbiol.* 10, 414. doi:10.3389/fcimb.2020.00414
- Xiao, L., Shiwaku, Y., Hamai, R., Tsuchiya, K., Sasaki, K., and Suzuki, O. (2021). Macrophage polarization related to crystal phases of calcium phosphate biomaterials. *Int. J. Mol. Sci.* 22 (20), 11252. doi:10.3390/ijms222011252
- Xue, Y., Li, Q., Park, C. G., Klena, J. D., Anisimov, A. P., Sun, Z., et al. (2020). *Proteus mirabilis* targets atherosclerosis plaques in human coronary arteries via DC-SIGN (CD209). *Front. Immunol.* 11, 579010. doi:10.3389/fimmu.2020.579010
- Yan, L., Chen, J., and Fang, W. (2022). Exosomes derived from calcium oxalate-treated macrophages promote apoptosis of HK-2 cells by promoting autophagy. *Bioengineered* 13 (2), 2442–2450. doi:10.1080/21655979.2021.2012622
- Yang, X., Liu, H., Ye, T., Duan, C., Lv, P., Wu, X., et al. (2020). AhR activation attenuates calcium oxalate nephrocalcinosis by diminishing M1 macrophage polarization and promoting M2 macrophage polarization. *Theranostics* 10 (26), 12011–12025. doi:10.7150/thno.51144
- Yoshida, T., Takemoto, K., Sakata, Y., Matsuzaki, T., Koito, Y., Yamashita, S., et al. (2021). A randomized clinical trial evaluating the short-term results of ureteral stent encrustation in urolithiasis patients undergoing ureteroscopy: Micro-computed tomography evaluation. *Sci. Rep.* 11 (1), 10337. doi:10.1038/s41598-021-89808-x
- Zhao, J., Cao, Z., Lin, H., Yang, H., Li, J., Li, X., et al. (2019). *In vivo* research on Cu-bearing ureteral stent. *J. Mater. Sci. Mater. Med.* 30 (7), 83. doi:10.1007/s10856-019-6285-z
- Zhu, W., Zhao, Z., Chou, F., Zuo, L., Liu, T., Yeh, S., et al. (2019). Loss of the androgen receptor suppresses intrarenal calcium oxalate crystals deposition via altering macrophage recruitment/M2 polarization with change of the miR-185-5p/CSF-1 signals. *Cell Death Dis.* 10 (4), 275. doi:10.1038/s41419-019-1358-y



OPEN ACCESS

EDITED BY

Yanjin Lu,
Fujian Institute of Research on the
Structure of Matter (CAS), China

REVIEWED BY

Qiang Wang,
China Medical University, China
Junlei Li,
Affiliated Zhongshan Hospital of Dalian
University, China

*CORRESPONDENCE

Jiantao Liu,
✉ liujiantao2010xjtu@163.com
Jun Cheng,
✉ chengjun_851118@126.com

SPECIALTY SECTION

This article was submitted to
Biomaterials,
a section of the journal
Frontiers in Bioengineering and
Biotechnology

RECEIVED 20 December 2022

ACCEPTED 03 February 2023

PUBLISHED 10 February 2023

CITATION

Liu J, Wang K, Li X, Zhang X, Gong X,
Zhu Y, Ren Z, Zhang B and Cheng J
(2023), Biocompatibility and
osseointegration properties of a novel
high strength and low modulus β -
Ti10Mo6Zr4Sn3Nb alloy.
Front. Bioeng. Biotechnol. 11:1127929.
doi: 10.3389/fbioe.2023.1127929

COPYRIGHT

© 2023 Liu, Wang, Li, Zhang, Gong, Zhu,
Ren, Zhang and Cheng. This is an open-
access article distributed under the terms
of the [Creative Commons Attribution
License \(CC BY\)](https://creativecommons.org/licenses/by/4.0/). The use, distribution or
reproduction in other forums is
permitted, provided the original author(s)
and the copyright owner(s) are credited
and that the original publication in this
journal is cited, in accordance with
accepted academic practice. No use,
distribution or reproduction is permitted
which does not comply with these terms.

Biocompatibility and osseointegration properties of a novel high strength and low modulus β - Ti10Mo6Zr4Sn3Nb alloy

Jiantao Liu^{1,2*}, Kao Wang³, Xingyuan Li², Xiwei Zhang², Xi Gong²,
Yihan Zhu², Zhiwei Ren¹, Bin Zhang⁴ and Jun Cheng^{5*}

¹Department of Orthopedics, The First Affiliated Hospital of Xi'an Jiaotong University, Xi'an, Shaanxi, China, ²Xi'an Jiaotong University, Xi'an, Shaanxi, China, ³Medical School of Yan'an University, Yan'an, Shaanxi, China, ⁴Institute of Translational Medicine, Shenzhen Second People's Hospital, Shenzhen, China, ⁵Northwest Institute for Nonferrous Metal Research, Shaanxi Key Laboratory of Biomedical Metal Materials, Xi'an, China

Introduction: Ti6Al4V titanium alloy is widely used in producing orthopedic and maxillofacial implants, but drawbacks include high elastic modulus, poor osseointegration performance, and toxic elements. A new medical titanium alloy material with better comprehensive performance is urgently needed in the clinic.

Methods: Ti10Mo6Zr4Sn3Nb titanium alloy (referred to as Ti-B12) is a unique medical β titanium alloy material developed by us. The mechanical properties of Ti-B12 depict that it has advantages, such as high strength, low elastic modulus, and fatigue resistance. In our study, the biocompatibility and osseointegration properties of Ti-B12 titanium alloy are further studied to provide theoretical guidance for its clinical transformation.

Results and Discussion: The titanium alloy Ti-B12 displays no significant effect on MC3T3-E1 cell morphology, proliferation, or apoptosis *in vitro*. Neither Ti-B12 titanium alloy nor Ti6Al4V titanium alloy depicts a significant difference ($p > 0.05$); Ti-B12 material extract injected into the abdominal cavity of mice does not cause acute systemic toxicity. The skin irritation test and intradermal irritation test reveal that Ti-B12 does not cause skin allergic reactions in rabbits. Compared to Ti6Al4V, Ti-B12 titanium alloy material has more advantages in promoting osteoblast adhesion and ALP secretion ($p < 0.05$). Although there is no significant difference in OCN and Runx2 gene expression between the three groups on the 7th and 14th days of differentiation induction ($p > 0.05$), the expression of Ti-B12 group is higher than that of Ti6Al4V group and blank control group. Furthermore, the rabbit *in vivo* test present that 3 months after the material is implanted in the lateral epicondyle of the rabbit femur, the Ti-B12 material fuses with the surrounding bone without connective tissue wrapping. This study confirms that the new β -titanium alloy Ti-B12 not only has low toxicity and does not cause rejection reaction but also has better osseointegration performance than the traditional titanium alloy Ti6Al4V. Therefore, Ti-B12 material is expected to be further promoted in clinical practice.

KEYWORDS

titanium alloys, biocompatibilities, osseointegrations, osteoblasts, biomaterials

1 Introduction

For decades, Ti6Al4V has been one of the most widely used materials for orthopedics and oral implants due to its lightweight, corrosion resistance, fatigue resistance, and non-toxic and non-magnetic properties (Trevisan et al., 2018; Xi and Wong, 2021). However, clinical studies have found complications, such as loosening and displacement of the Ti6Al4V implants (Liu et al., 2019; Gkias et al., 2021). The reason is closely related to the defect of Ti6Al4V (Jing et al., 2020; Zhan et al., 2020; Zheng et al., 2020). Firstly, as compared to cortical bone (17–20 GPa) and cancellous bone (about 4 GPa), Ti6Al4V has an elastic modulus of about 110 GPa (Murr, 2017). A higher elastic modulus will cause a “stress shielding” effect (Pehlivan et al., 2020), causing excessive stress on the local cortical bone and low stress on the underlying bone, leading to osteolysis. Second, Ti6Al4V is a bioinert material without biological activity and osteoinducibility, and it is challenging to osteointegrate with surrounding bone tissues after implantation in the human body (Backes et al., 2021; Su et al., 2021). Additionally, these alloys use two toxic elements, V and Al. Studies have confirmed that V even shows higher toxicity than Cr and Ni and will accumulate in various organs after long-term implantation, which can induce cancer (Mello et al., 2019). However, the element Al enters the human body in the form of Al salt, which causes organ damage and side effects such as bone softening, nervous system disorder, and anemia (Willis et al., 2021). Al element may be related to Alzheimer’s disease (Vojdani, 2021).

Because of the defects of Ti6Al4V materials, domestic and foreign researchers have been committed to researching and developing new medical titanium alloys with better comprehensive properties (Sarraf et al., 2022; Szczesny et al., 2022). In the mid-1990s, Switzerland and Germany successively developed the second generation of medical titanium alloys Ti6Al7Nb and Ti5Al2.5Fe, which replaced V with Nb and Fe. However, these two alloys still contain an Al element that has adverse reactions to the human body, and the elastic modulus is still as high as 4–10 times that of bone tissue. The mismatch between the mechanical properties of implant and bone tissue was unsolved. Recently, researchers have begun to focus on new β titanium alloys (Nadammal et al., 2022; Sing, 2022; Vonavkova et al., 2022). This material can retain the unstable phase, such as the sub-stable β phase or martensite structure, at room temperature, giving the material good processing plasticity and toughness. Adjusting the microstructure of material through post-processing, heat treatment, strength, toughness, elastic modulus, corrosion resistance, wear resistance, and fatigue properties can be significantly enhanced (Sidhu et al., 2021).

Additionally, Zr, Mo, Sn, Ti, Ta, Nb, Pd, Hf, and other non-toxic elements to human tissue are used in the new β -type titanium alloy to improve biocompatibility (Sidhu et al., 2021). The United States, Japan, Russia, and other countries have made some achievements in the research and development of biomedical β -type titanium alloys, such as Ti12Mo6Zr2Fe, TiNbTaZr, and Ti51Zr18Nb. These β -type titanium alloys have been successively applied in the medical field.

Using non-toxic elements, we developed a novel β type of biomedical titanium alloy -- Ti10Mo6Zr4Sn3Nb, referred to as Ti-B12, and obtained the national invention patent (ZL.201110184053.X) (Cheng et al., 2020). Mechanical tests demonstrate that when the elastic modulus of Ti-B12 titanium alloy is as low as 50 GPa, the tensile strength is about 970 MPa, and the elongation can reach more than 40%, which has obvious advantages over pure Ti. The elastic modulus is about 60.7 GPa when the tensile strength reaches 1,010 MPa, while the elongation of material can still reach 15%, which is much less than Ti6Al4V. Additionally, Ti-B12 titanium alloy can obtain high strength, low modulus, and excellent comprehensive mechanical properties that match degree through the ‘martensite transition’ and the intermediate transition phase “ ω phase” in the process of processing and heat treatment. Hence, it shows good biomechanical compatibility under static conditions. The Ti-B12 titanium alloy still has a high fatigue strength limit ($\sigma_N \geq 500$ MPa, the number of cycles is 10^7) and recoverable strain ($\epsilon_{\max-R} \leq 2.25\%$) after cyclic loading and fatigue test, which is conducive to the implant material maintaining its original excellent biomechanical compatibility under long-term dynamic loading conditions. The results of this study illustrate that the biocompatibility of Ti-B12 titanium alloy is superior to that of Ti6Al4V material. However, it has better bone integration properties and is an excellent medical titanium alloy material, which is expected to achieve clinical transformation in the future.

2 Methods

2.1 Statement of animal rights

Procedures for the care and use of animals were approved by the Ethics Committee of the First Hospital of Xi’an Jiaotong University (2022-196). All applicable institutional and governmental regulations concerning the ethical use of animals were followed.

2.2 Alloy design and composition

The biomedical metastable β -type titanium alloy with independent intellectual property rights of the Northwest Institute of Non-ferrous Metals was selected as the experimental material. Zero-grade small-particle sponge titanium, industrial grade sponge zirconium (Zr-1), Ti-32Mo, Ti-60Sn, and Nb-47Ti intermediate alloys were selected for three times melting by consumable vacuum arc melting furnace to ensure the uniform chemical composition of alloy ingot and avoid the occurrence of composition segregation and high and low-density inclusion. The measured results of chemical composition of Ti-B12 alloy ingot are as follows: Mo: 10.1%, Zr: 6.05%, Sn: 4.11%, Nb: 2.98%, O: 0.19%. The transus temperature is about 765 °C by conventional quenching metallography. Under the condition of 1,000 °C, using a 1-ton air-free forging hammer, the alloy ingot was upset and pulled many times to break the coarse cast structure, and finally, the square bar of 50 × 50 × L mm was obtained. Under 850 °C, the transverse pass mill was used to roll the bar. After peeling and

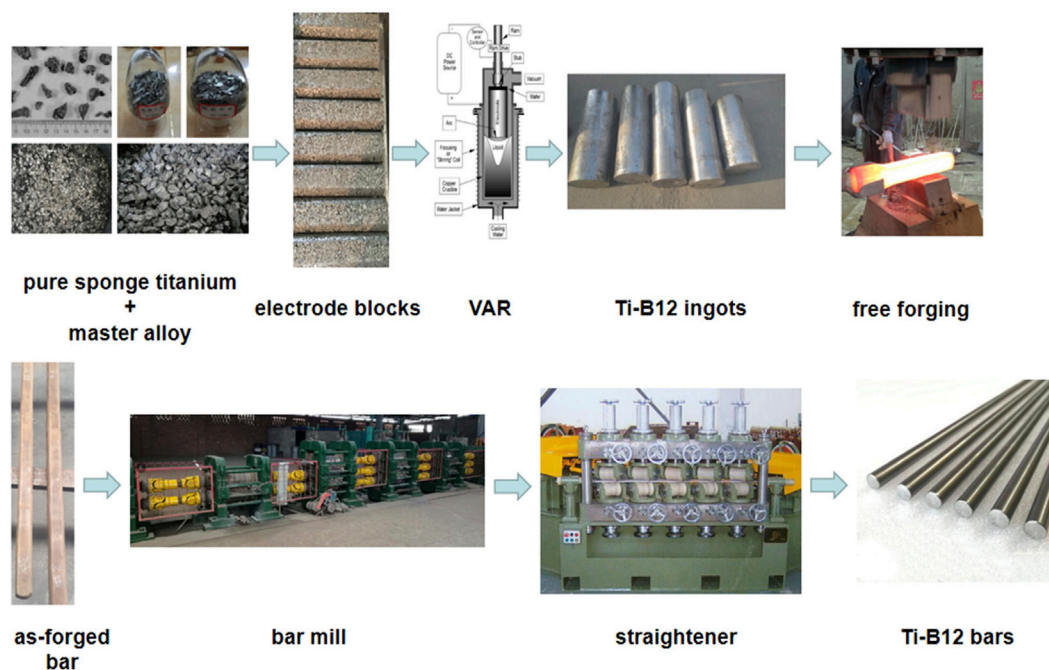


FIGURE 1
Synthesis process of Ti-B12 titanium alloy.

straightening, the alloy bar with a diameter of 8 mm was finally obtained. The synthesis process is shown in Figure 1.

2.3 Materials preparation

Using a numerical control lathe and Edm wire cutting equipment, a disc with a diameter of 8 mm and thickness of 1 mm and a cylinder with a diameter of 5 mm and height of 10 mm were manufactured, which were used for the comprehensive evaluation experiment of biocompatibility and bone integration performance. Ti6Al4V was used as the control material. All samples were cleaned by ultrasonic wave with distilled water, acetone, 95% ethanol, and distilled water in turn, each step for 30 min. The above operation was repeated three times. The cleaned samples were autoclaved at 121 °C for 40 min, dried in a vacuum, and put into sterile tubes for subsequent cell and animal experiments.

2.4 Biocompatibility of Ti-B12

2.4.1 Cell morphology observation and proliferation experiment

The sterilized Ti-B12 and Ti6Al4V materials were placed in sterile Petri dishes, and the growth medium containing α -MEM medium (Cellmax), 10% FBS (MRC), and 1% penicillin-streptomycin mixture (Solarbio) was added and placed in the cell incubator for 72 h to prepare the extract. MC3T3-E1 cells in the logarithmic growth phase were collected and seeded in 96-well cell culture plates at $1 \times 10^5 \text{ mL}^{-1}$ (100 μL per well). They

were divided into three groups: A, B, and C, with five wells set at each time point in each group. The culture medium was changed after 24 h in the cell incubator. Groups A and B were added with 200 μL of Ti-B12 and Ti6Al4V material extract, respectively. Group C was added with an ordinary growth medium, which was changed every 3 days. At 1, 3, and 7 days, cell growth status was observed by microscope and photographed, and then cell proliferation rate was detected by the Cell Counting Kit 8 (CCK8) kit (Biyuntian, Shanghai, China).

2.4.2 Cell apoptosis assay

MC3T3-E1 cells in good growth state were inoculated into sterile 6-well plates containing Ti-B12 and Ti6Al4V, respectively, at the concentration of $1 \times 10^5 \text{ mL}^{-1}$, and each well was inoculated with 3 mL. In the blank control group, only osteoblasts were inoculated with three multiple wells in each group, and cells were cultured in the cell incubator for 24 h. Annexin V-PE/7-AAD Apoptosis Detection Kit (Yeast) was used to detect cell apoptosis by flow cytometry.

2.4.3 Acute systemic toxicity test

A total of twelve healthy adult male mice were randomly assigned to three groups, Ti-B12 group, Ti6Al4V group, and control group, each consisting of four mice. The ethics committee of Xi, a Jiaotong University, approved the experiment. According to the systemic toxicity detection method of national standard GBT 16886.11-1997, mice in Ti-B12 group and Ti6Al4V group were intraperitoneally injected with metal material normal saline extract (50 mL kg^{-1}), while mice in the control group were intraperitoneally injected with normal saline (50 mL kg^{-1}). Status, body weight, toxic reactions, and the number of dead mice were

TABLE 1 Evaluation criteria for systemic toxicity.

Toxicity level	Performance of toxicity
Non-toxic	No symptoms of toxicity were observed
Mild poisoning	The symptoms were mild, without reduced movement or dyspnea
Moderate poisoning	Symptoms of abdominal irritation were obvious, with less exercise, dyspnea, drooping eyelids, diarrhea, and significant weight loss to 15–17 g or 20% \pm 3% of body weight loss
Severe poisoning	Respiratory failure, cyanosis, tremors, severe abdominal irritation. Eyelids droop, and weight drops to less than 15 g
Death	Death after injection

TABLE 2 Skin and intradermal stimulation response scoring system.

Type	0	1	2	3	4
Erythema and eschar	No erythema	Very subtle erythema	Clear erythema	Moderate erythema	Severe erythema (purple-red) to eschar formation
edema	No edema	Very subtle edema	Clear edema (swelling, not beyond the edge of area)	Moderate edema (swelling about 1 mm)	Severe edema (swelling of more than 1 mm, beyond the range of application)

observed daily for 5 days after injection. According to its manifestations, acute systemic toxicity can be classified into non-toxic, mildly toxic, moderately toxic, severely toxic, and death. Table 1 illustrates the specific evaluation indicators.

2.4.4 Skin irritation test

Six adult male New Zealand white rabbits, weighing 2.5–3 kg, were provided and raised by the Laboratory Animal Center of Xi'an Jiaotong University. Before the experiment, hair on both sides of the rabbit spine was removed (about 10 \times 15 cm), and the two materials were placed in the hair removal area on both sides of the spine, respectively. The material surface was covered with 2.5 \times 2.5 cm gauze, soaked with 0.9% normal saline, and fixed with bandages for 4 h. After removing the materials, the skin conditions at the contact sites on both sides of the skin were continuously observed for 1, 48, and 72 h, and the type of skin irritation response was evaluated according to the scoring system (Tables 2, 3).

2.4.5 Intradermal stimulation test

After sterilization, Ti-B12 and Ti6Al4V materials were placed into sterile six-well plates, 0.9% normal saline (polar extract) and olive oil (non-polar extract) were added, and placed in an incubator for 72 h to obtain the material extract. Six adult male New Zealand white rabbits, weighing 2.5–3 kg, were provided by the Laboratory Animal Center of Xi'an Jiaotong University. Before the experiment, the hair on both sides of the rabbit spine (about 10 \times 15 cm) was removed, and six injection points were set on both sides. The test material saline extract and normal saline were injected at six intradermal injection points before and after one side of each rabbit spine. Olive oil extract of the same material and olive oil was injected at six intradermal injection points before and after the other side. Skin conditions at each injection site were recorded at 1, 48, and 72 h after injection and the types of intradermal stimulation responses were evaluated according to the scoring system (Tables 2, 3).

TABLE 3 Type of stimulus-response.

Reaction type	Very mild	Mild	Moderate	Severe
The average score	0–0.4	0.5–1.9	2.0–4.9	5.0–8.0

2.5 Osteointegrative properties of Ti-B12

2.5.1 Osteoblast adhesion ability

Cell adhesion was detected by acridine orange staining and cell counting. MC3T3-E1 cells at a concentration of 1×10^5 mL⁻¹ were seeded in sterile 24-well plates containing Ti-B12 and Ti6Al4V, respectively, with 1 mL per well. Acridine orange staining was performed at 1, 3, and 5 h of co-culture, respectively. Three re-wells were set for each material and each time point.

2.5.2 Osteoblast adhesion status

MC3T3-E1 cells in the logarithmic growth phase were seeded in sterile 12-well plates with Ti-B12 and Ti6Al4V materials at a concentration of 1×10^5 mL⁻¹ and incubated at 37 °C, 95% relative humidity, and 5% CO₂ for 72 h. Before scanning electron microscopy, the culture was terminated for fixation, dislocation, critical point drying, and gold spraying.

2.5.3 Detection of IL-6 secretion

MC3T3-E1 cells were seeded at a concentration of 1×10^5 mL⁻¹ were seeded in 24-well plates containing Ti-B12, the Ti6Al4V group, and the control group. Each time point of each group was set with three re-holes. Cells were cultured in the cell incubator for 2, 4, and 6 days, respectively. At the end of culture, 10 μ L of cell culture medium was taken to detect the concentration of IL-6 according to the interleukin 6 (IL-6) ELISA kit (Biyuntian, Shanghai, China).

2.5.4 Alkaline phosphatase activity

MC3T3-E1 cells in the logarithmic growth phase were digested in a cell suspension and seeded in a 24-well plate containing two

TABLE 4 The upper and lower primer sequences.

Gene	The upper primer sequences	The lower primer sequences
ALP	5'-gaggtcacatccatcctgcgtgg-3'	5'-gagtaccagtcgccgatcgccgag-3'
OCN	5'-ctgctcactctgctgacctggct-3'	5'-gctttgtcagactcaggccgctg-3'
Runx2	5'-gcaacaagaccctgccctgg-3'	5'-gaaactctgctcgtccgctcg-3'
GAPDH	5'-atcactgccaccagaagac-3'	5'-gtgagttccggtcagctc-3'

types of materials at a concentration of $1 \times 10^5 \text{ mL}^{-1}$. The blank control group contained no materials. Three re-wells were set for each time point in each group. The cells were incubated at 37°C and 5% CO_2 for 1, 3, and 5 days, respectively. At the time of termination of culture, 10 μL of cell culture medium sample was taken to detect ALP concentration according to the instruction of ALP ELISA kit (Biyuntian, Shanghai, China).

2.5.5 Expression of osteogenic related genes

The growth medium was replaced with an osteogenic differentiation medium after 24 h in the Ti-B12, Ti6Al4V, and blank control groups, and the growth medium was replaced every 3 days. After 7 and 14 days of induction, the culture medium was carefully sucked and discarded, the branch samples were washed twice with PBS, RNA was extracted, and osteogenic-related genes (ALP, OCN, and Runx2) were detected by RT-PCR. Table 4 illustrates the primer sequences.

2.5.6 Osteoblast mineralization

MC3T3-E1 cells were seeded in 12-well plates containing Ti-B12, Ti6Al4V, or not at a cell concentration of $1 \times 10^5 \text{ mL}^{-1}$. After 24 h, the medium was changed to osteoblast mineralization medium (α -mem medium containing 10% FBS, 10 mmol/L β -sodium glycerophosphate, 10 nmol/L dexamethasone, and 50 mg/L vitamin C). The mineralized medium was changed every 3 days. After 30 days of culture, the medium was discarded, and the bottom of well and the material were washed three times with PBS, fixed with 4% paraformaldehyde for 30 min, and stained with 40 mmol.L⁻¹ alizarin red for 20 min. Calcified nodules after staining were observed under an inverted microscope. Finally, 10% cetylpyridine chloride was added to dissolve mineralized nodules, and absorbance was detected at a wavelength of 590 nm.

2.5.7 In vivo experiments on animals

Ten adult male New Zealand white rabbits weighing 2.5–3 kg were divided into two groups, group A was implanted with Ti-B12 material, and group B was implanted with Ti6Al4V material. After administration of pentobarbital through the ear vein, the epicondyle of both rabbit femurs of rabbits was exposed, and a hole was made perpendicular to the femur with a 2.0 g Schnur wire. The sterilized material was implanted and sutured layer by layer (Figure 2). Penicillin (10,000 U.kg⁻¹) was used to prevent infection 3 days after the operation, and an X-ray examination was performed 3 months after the procedure. Three months after the operation, the animals were sacrificed by overdose of anesthesia to obtain specimens for hard tissue sections to observe bone growth around the material. The production process of hard tissue section is rough as follows: the femur specimen containing



FIGURE 2
The prostheses were implanted in the lateral epicondyle of the rabbit femur.

titanium alloy is made into a resin block after formalin fixation, gradient alcohol dehydration, and resin immersion. A diamond band saw was used to cut the resin blocks into sheets with a thickness of 200–300 μm , and the sheets were cleaned and adhered to the resin slides. The sample was ground to a thickness of approximately 50 μm using an EXAKT tissue mill (E400CS), and the sample surface was polished and stained with toluidine blue. The prepared sections were observed under a microscope.

2.6 Statistical analysis

Data were expressed as mean \pm standard deviation (SD) and analyzed statistically using one-way analysis of variance (ANOVA). Differences between the two groups and each time point were analyzed by independent sample *t*-test. The significance level of data is set at $p < 0.05$.

3 Results

3.1 Biocompatibility of Ti-B12

3.1.1 Cell morphology observation and proliferation experiment

MC3T3-E1 cells grew well in Ti-B12 material extract, Ti6Al4V extract, and blank control group, but no significant differences in cell

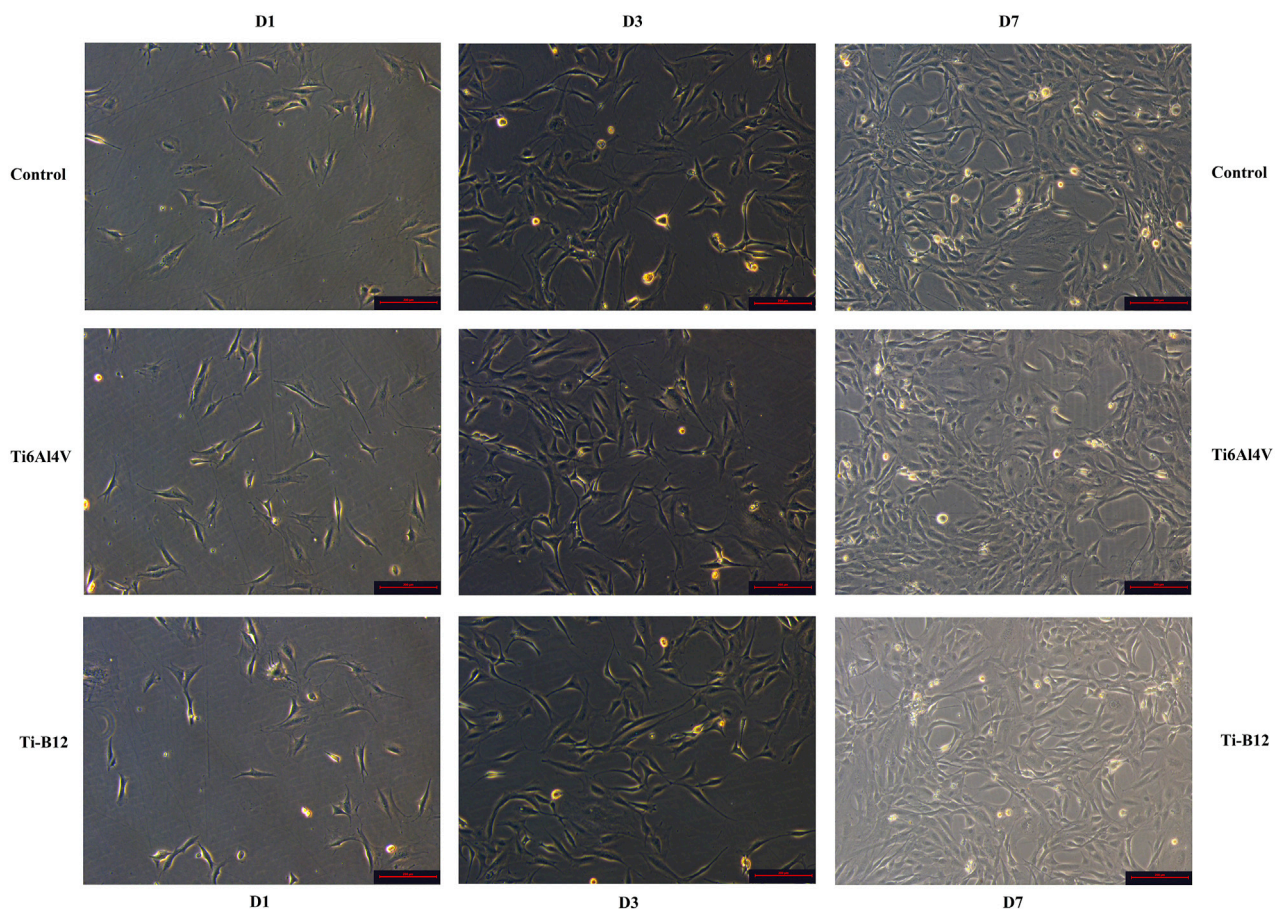


FIGURE 3
MC3T3-E1 Cell morphology observation of three groups on the 1st, 3rd, and 7th days.

morphology were observed at each time point. On the first day, the cells adhered to the wall and grew in spindle shape or dendritic shape. On the third day, the cells increased significantly, grew rapidly, and the refractive index was strong. On the seventh day, the cells were in good condition, with entire cytoplasm and an increased number, almost covering the bottom of pore (Figure 3).

Figure 4A presents that cells in the three groups proliferated with the increase in culture time. Although the Ti-B12 group demonstrated a higher proliferation rate than the Ti6Al4V and blank control groups, there was no significant difference ($p > 0.05$). Therefore, MC3T3-E1 cells can proliferate normally in Ti-B12 material extract, which meets the cytotoxicity requirements of biomedical materials and products.

3.1.2 Cell apoptosis assay

Figure 4B displays the flow cytometry detection results, where quadrants B1, B2, B3, and B4 depict the proportion of necrotic cells, middle and late apoptotic cells, viable cells, and early apoptotic cells in all cells, respectively. Statistical analysis of the early apoptosis rate of three groups found that the early apoptosis rate of the Ti-B12 group, the Ti6Al4V group, and the blank control group was similar (Figure 4C), and there was no statistical difference ($p > 0.05$). The

results revealed that Ti-B12 alloy did not induce early apoptosis of osteoblasts and had good biological activity.

3.1.3 Acute systemic toxicity test

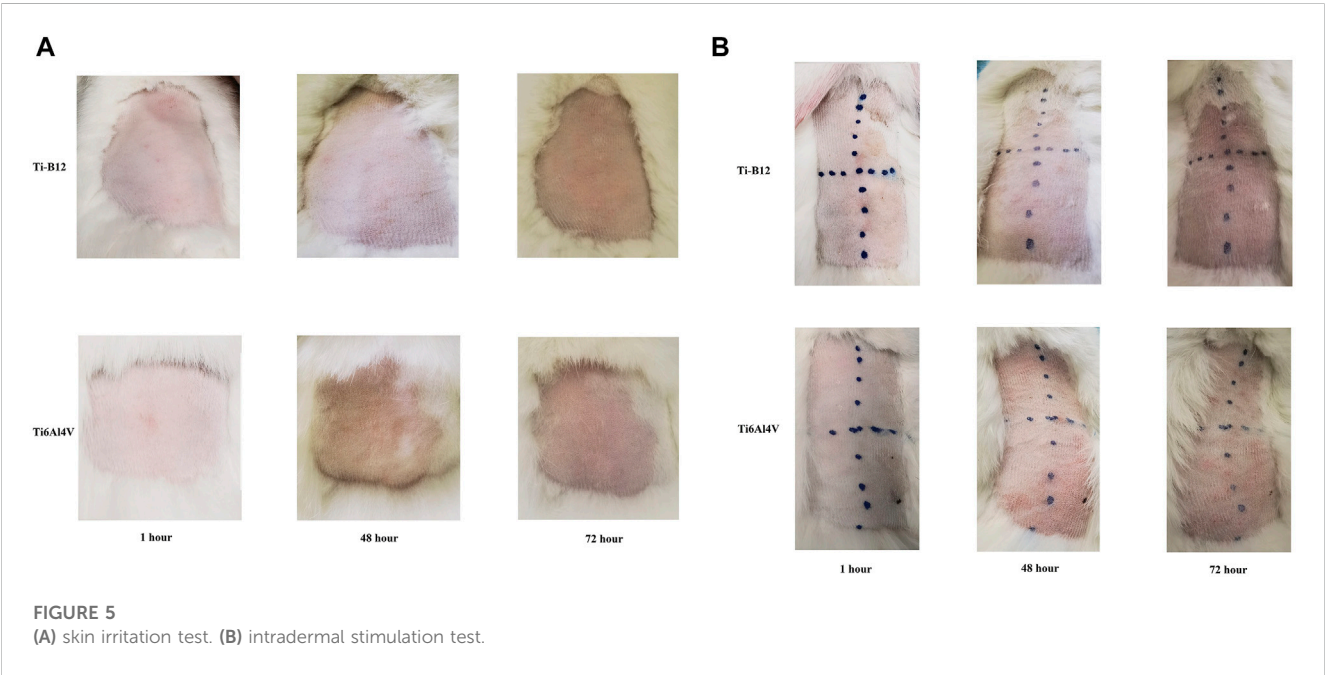
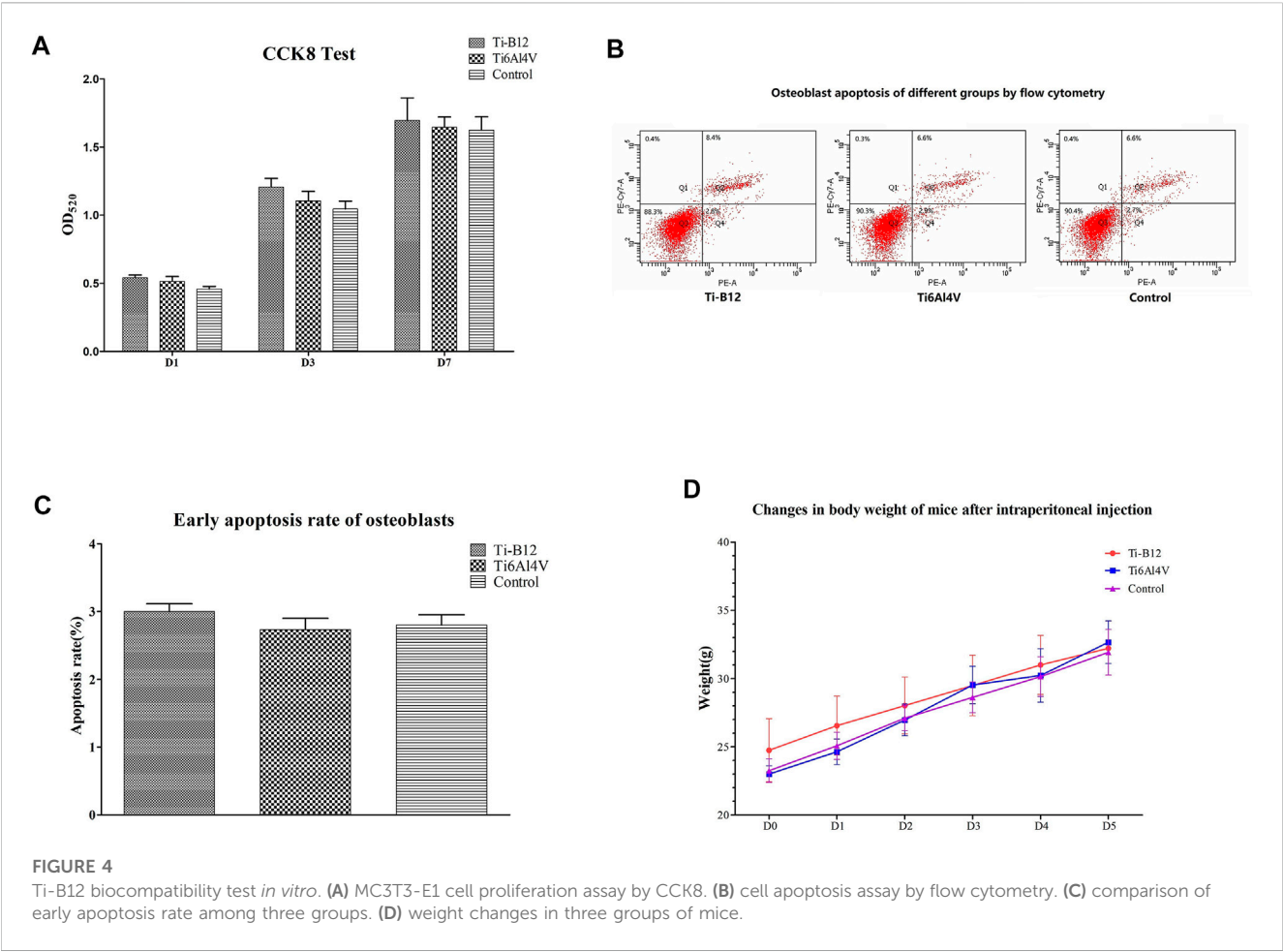
All mice were observed after injection. Within 5 days, the weight of mice in the three groups increased continuously (Figure 4D), and no symptoms of peritoneal irritation, respiratory depression, decreased movement, cyanosis, diarrhea, tremor, or death occurred. It can be concluded that Ti-B12 meets the requirements of biological materials and products.

3.1.4 Skin irritation test

Figure 5A presents that erythema, eschar, and edema did not appear in the application site of Ti-B12 and Ti6Al4V materials in 1, 48, and 72 h, and their scores were all 0. The type of stimulation reaction was very mild, which met the requirements of the skin irritation experiment with biological materials and products.

3.1.5 Intradermal stimulation test

Figure 5B presents that the skin at the injection site demonstrated no erythema, eschar and edema at 1, 48, and 72 h after intradermal injection of polar and non-polar extracts of Ti-B12



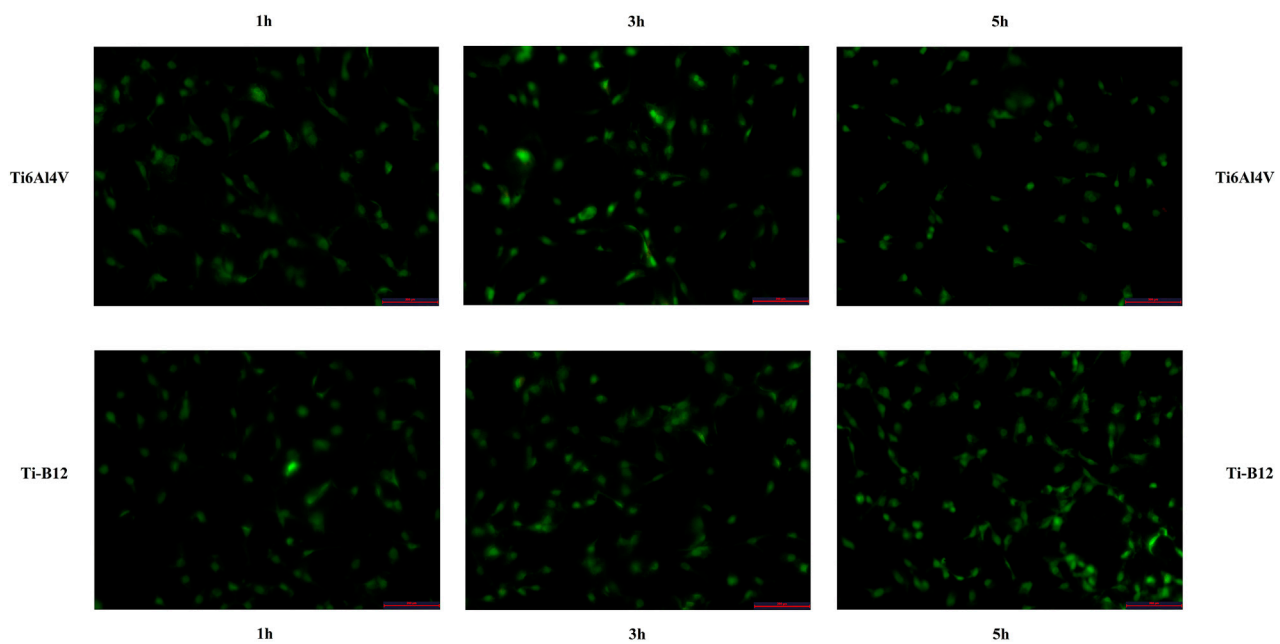


FIGURE 6

The adhesion ability of MC3T3-E1 on the surface of osteoblasts of two materials was observed under a fluorescence microscope.

and Ti6Al4V materials; this was the same as the performance after the intradermal injection of polar and non-polar control solvents, with an average score of 0; this indicates that Ti-B12 meets the requirements of subcutaneous stimulation of biological materials and products.

3.2 Osteointegrative properties of Ti-B12

3.2.1 Osteoblast adhesion ability

The number of adherent cells on the surface of two materials was counted under a fluorescence microscope (Figure 6), and the number of adherent cells of Ti-B12 and Ti6Al4V increased with the extension of culture time. At different times, the number of adherent cells on the surface of Ti-B12 material was higher than that of Ti6Al4V material. It can be seen that Ti-B12 has a better adhesion capacity for osteoblasts.

3.2.2 Osteoblast adhesion status

Scanning electron microscope observation of cells on the surface of Ti-B12 and Ti6Al4V demonstrated that a large number of MC3T3-E1 cells were attached to the surface of the material, which was elongated and spindle-shaped, with many pseudopodia, and the growth status of the cells was good (Figure 7). The number and morphology of Ti-B12 adhesion cells were significantly better than that of Ti6Al4V, indicating that Ti-B12 material was more conducive to osteoblast adhesion.

3.2.3 Detection of IL-6 secretion

The IL-6 content in the supernatant of the three groups was compared and analyzed at each time point. As we can see from the results (Figure 8A), there was no significant difference in IL-6

secretion between the two alloys and the blank control group at 2, 4, and 6 days of culture ($p > 0.05$); this indicates that the Ti-B12 titanium alloy does not stimulate osteoblast secretion of IL-6 and does not increase the immunogenic response.

3.2.4 Alkaline phosphatase activity

Compared to the Ti6Al4V group (Figure 8B), the expression of osteoblast alkaline phosphatase in the Ti-B12 group was significantly increased on the third and fifth day of culture ($p < 0.05$) but also significantly higher than the blank control group on the third day ($p < 0.05$), indicating that the Ti-B12 alloy had a better promotion effect on early differentiation of osteoblasts.

3.2.5 Expression of osteogenic related genes

Figure 8C presents that on the seventh day of differentiation induction, ALP gene expression in Ti-B12 group was highest in the three groups ($p < 0.05$). ALP gene expression in Ti-B12 group was higher than that in the blank control group on day 14 of induced differentiation ($p < 0.05$). Although there were no significant differences in the expression of the OCN and Runx2 gene between the three groups at 7 and 14 days after differentiation induction ($p > 0.05$), the expression of the OCN and Runx2 gene in the Ti-B12 group was higher than that in the Ti6Al4V group and the blank control group.

3.2.6 Osteoblast mineralization

The results revealed that the deposition of calcium salt was significantly more in the Ti-B12 group than in the Ti6Al4V group and the blank control group ($p < 0.05$), and there was no significant difference between the latter two groups ($p > 0.05$), indicating that Ti-B12 material has a better promotion effect on osteoblast mineralization *in vitro* (Figures 9A, B).

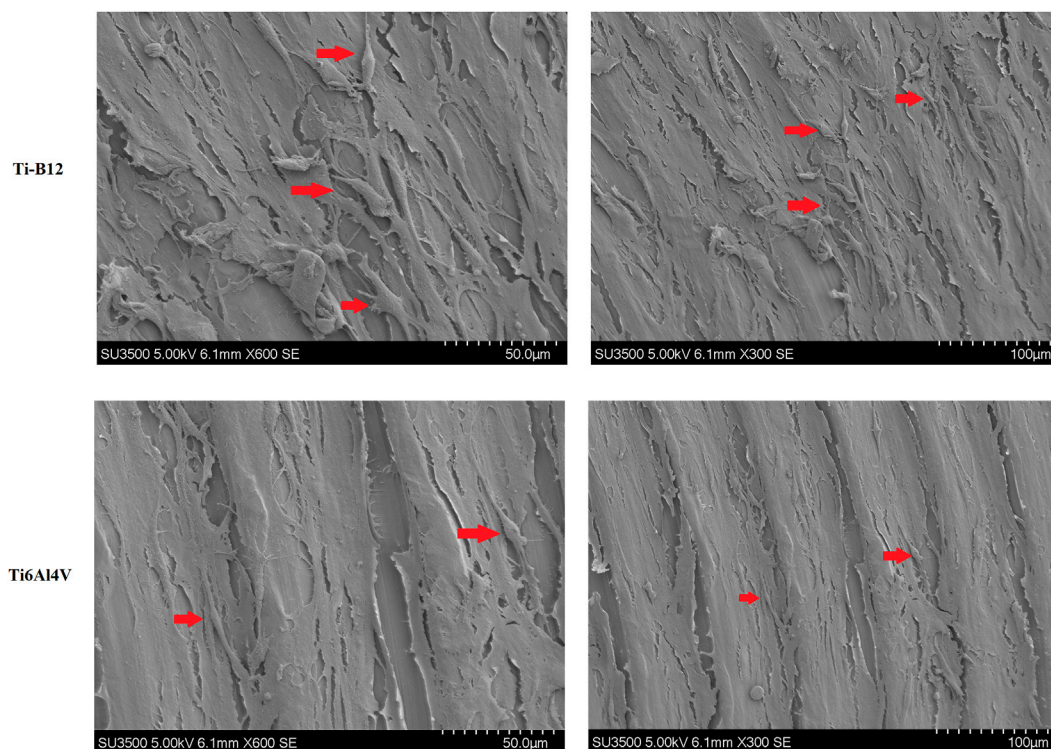


FIGURE 7
Observation by scanning electron microscope of MC3T3-E1 cells on the surface of Ti-B12 and Ti6Al4V.

3.2.7 *In vivo* experiments on animals

Figure 10A displays the X-ray examination results 3 months after the operation, showing that both alloys were perfectly embedded in the lateral epicondyle of femur, and no peeling or displacement was found. The samples were well integrated with the surrounding bone, and no osteoporosis or inflammation was observed. Figure 10B presents the toluidine blue staining results of hard tissue sections of experimental rabbits 3 months after implantation of different alloys into the lateral epicondyle of femur. It was observed that the two alloys were closely bound to bone and that no connective tissue was found at the junction between the material and bone. However, the contact rate of bone tissue around Ti-B12 titanium alloy is better than that of Ti6Al4V.

4 Discussion

Titanium alloys are widely used in orthopedic implants due to their good biocompatibility and mechanical properties (Kaur and Singh, 2019). However, some studies illustrated that Ti6Al4V ($\alpha+\beta$ titanium alloy), commonly used in clinical practice, has the drawbacks of excessive elastic modulus and toxic elements (Ottaria et al., 2018). Therefore, many scholars have researched to exploit titanium-based materials with non-toxic and mechanical properties matching natural bone (Bedouin et al., 2019; Shi et al., 2021). To achieve this goal, the effects of different β -stabilizers such as Ta, Zr, Mo, and Nb on the properties of tailored titanium alloys

have attracted the great attention of researchers (Mendes et al., 2016; Zhao et al., 2018; Zhang et al., 2021). These β -stabilizers have good shape memory effects, superelasticity, and a low Young modulus in titanium alloys. It can be seen from the recently published literature that the development of β -titanium alloy materials without Al and V elements has been a research hot spot (Kaur and Singh, 2019). Our group developed a new β -titanium alloy Ti-B12 with high strength and low elastic modulus using Mo, Zr, Sn, and Nb β stabilizers. Preliminary mechanical tests have also confirmed that the new material has excellent mechanical properties. However, the ultimate goal of customized β -Ti alloys is to obtain alloy properties similar to the physiological properties of tissues, which requires the new materials to have excellent mechanical properties, as well as excellent biocompatibility and osseointegration properties. Therefore, this study aims to identify the biological properties of Ti-B12 titanium alloy and provide theoretical guidance for its application in orthopedic implants.

Using biological materials replaces or repairs living tissues to enhance organ and tissue functions and treat diseases. The premise of its function is implantation in the human body. Therefore, in addition to providing specific functions, good biocompatibility is the basic condition that biomaterials must meet (Rahmati and Mozafari, 2019; Shahi et al., 2019). Biocompatibility refers to the reaction of medical materials and human tissues when interacting (Apostu et al., 2018). After the biological material is implanted into the human body, the implant is subjected to the fatigue of body fluids and various external forces. The material components will enter the human body due to corrosion or wear. Biocompatibility in cells

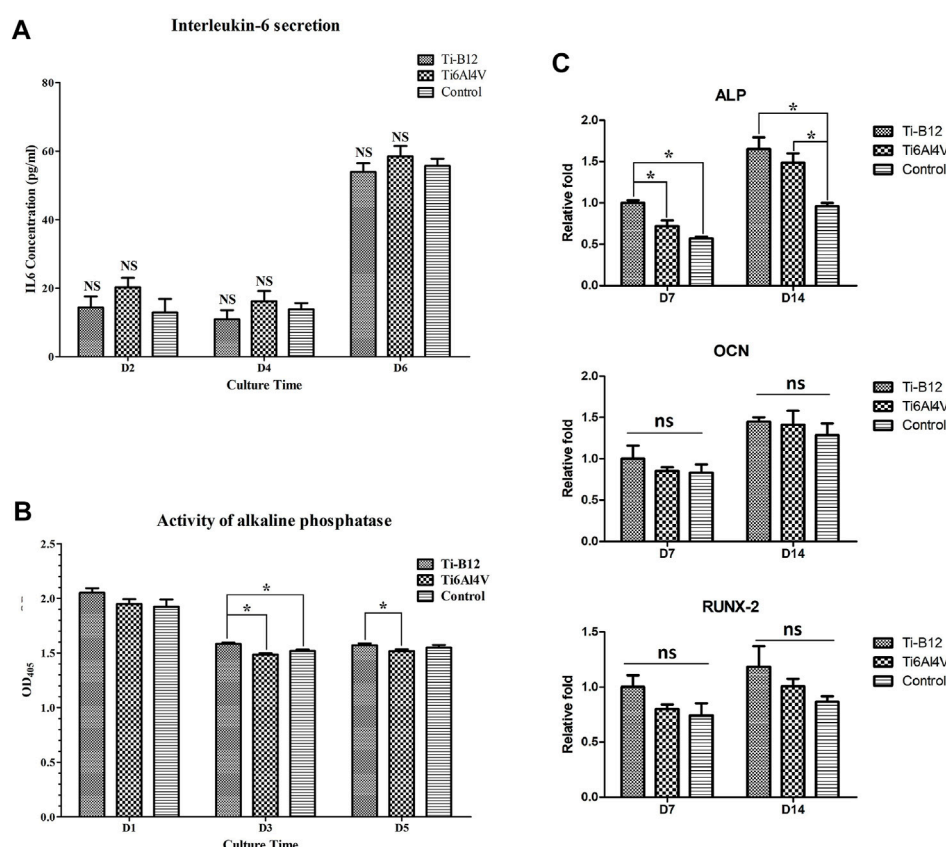


FIGURE 8

Detection of osteogenic properties *in vitro*. (A) detection of IL-6 secretion. (B) comparison of alkaline phosphatase activity. (C) expression of osteogenic-related genes.

means that the material has little or no cytotoxicity and does not cause cell necrosis or apoptosis. In the body, the local rejection of the contact site is small and does not cause local congestion, edema, erythema, and other inflammatory and allergic reactions. The overall response of tested animals is good, and no systemic symptoms such as agitation, anorexia, or even death occur. *In vivo* and *in vitro* experiments are essential components of the biocompatibility evaluation of medical materials. Using *in vivo* experiments, the biocompatibility of material is evaluated by inflammation, allergy, and other reactions of body tissue. The advantage of *in vivo* experiments is that the whole organism is used as the test object, and the result is similar to that of the implanted human body. However, it is difficult to distinguish the influence of complex factors on the experimental results. The *in vitro* experiment refers to the direct study (material itself) or indirect study (material extract) study of the effect of material effect on the growth, differentiation, or activity of tissue cells (Declercq et al., 2004). *In vivo* experiments need to consider the complexity of biological systems, and it is difficult to analyze a single factor objectively. Therefore, *in vitro* experiments are more sensitive to distinguishing biotoxicity and its effects on tissues and cells. Some studies revealed that some medical materials depict mild toxicity *in vitro* experiments but show good biocompatibility *in vivo* experiments (Suggs et al., 1999; Xie et al., 2016). This difference

may be because cytotoxic substances released by material degradation are attenuated or eliminated by the complex biological regulatory system of the subject, thus masking their toxic effects. Therefore, only *in vivo* experiments cannot fully reflect the biocompatibility of tested materials. *In vivo* and *in vitro* experiments can counteract the influence of complex factors in the body to some extent and more fully reflect the impact of materials on cells.

To detect the toxicity of Ti-B12 material, MC3T3-E1 cells were cultured with Ti-B12 material extract, and cell morphology and proliferation were detected. At the same time, MC3T3-E1 cells and Ti-B12 were co-cultured, and cell apoptosis was detected by flow cytometry. Compared to the Ti6Al4V group and the blank control group, Ti-B12 material did not cause abnormal growth and apoptosis of MC3T3-E1 cells and had no adverse effect on cell proliferation rate. These results indicate that Ti-B12 material has low toxicity and meets the toxicity requirements of biological materials.

The implantation of biomaterials is like a foreign object invasion or trauma to the body, so it is necessary to evaluate the local and systemic reactions of materials in contact with the body. We injected the saline extract of Ti-B12 material into the abdominal cavity of mice and observed them for five consecutive days. No adverse reactions such as diarrhea, cyanosis, decreased exercise, and weight loss was found in mice. Additionally, the skin irritation

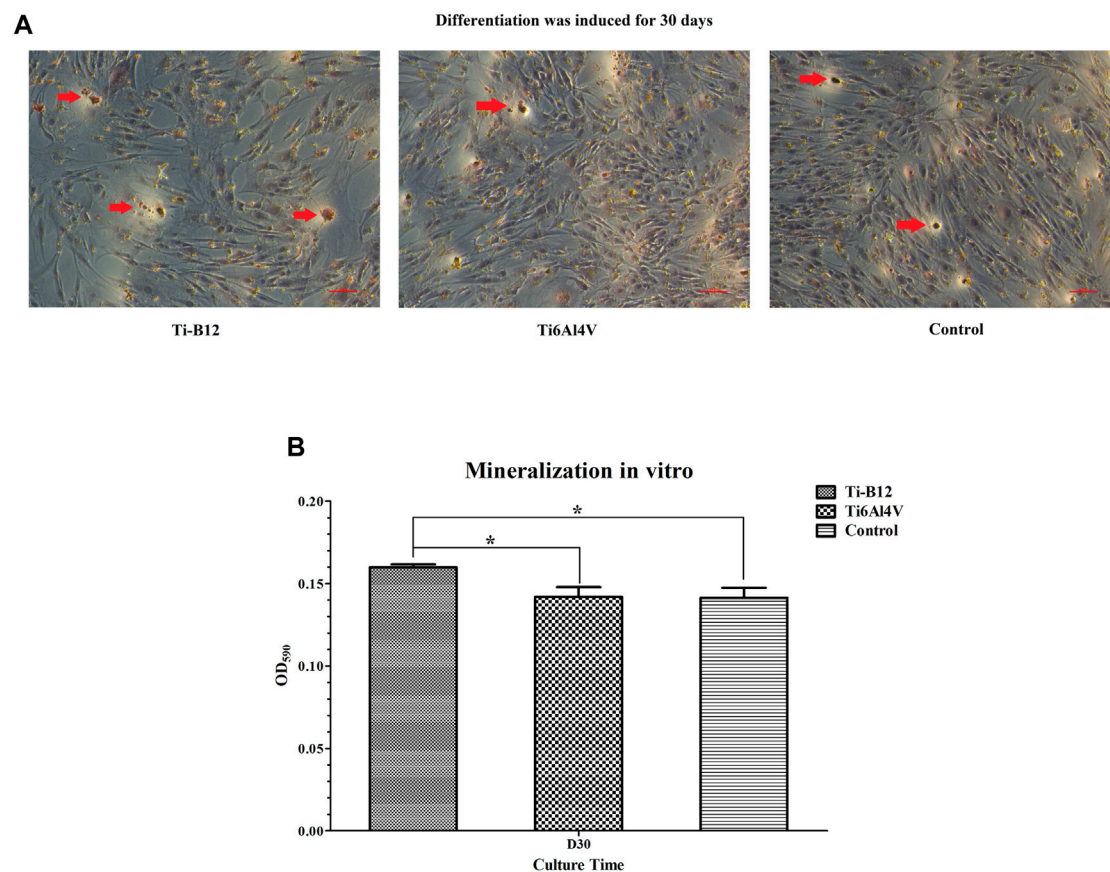


FIGURE 9

Osteoblast mineralization. (A) calcium salts in mineralized nodules were stained dark red by alizarin red staining, shown by the red arrow. (B) quantitative determination of calcium salt deposition.

experiment was carried out by directly contacting Ti-B12 with rabbit skin. The intradermal irritation experiment was conducted by injecting the Ti-B12 saline and olive oil extract into rabbit skin. The above studies demonstrated no erythema, lump, or swelling of the skin at the contact and injection sites, as in the Ti6Al4V group and the blank control group, with a score of 0, indicating that Ti-B12 implantation would not cause rejection.

Currently, some metal ions in commonly used medical alloy materials have a certain toxic effect on the human body. For example, Cr and Co have greater cytotoxicity and are metal metamorphosis sources. Ni can limit the growth of fibroblasts but also may cause allergic reactions or cancer; Al is neurotoxic, and V may be teratogenic or carcinogenic. However, Ti, Nb, Zr, Mo, Sn, and Nb are non-toxic or low-toxic elements. Yamamoto et al. reported that the toxicity of Nb to osteoblasts and fibroblasts was very low (Yamamoto et al., 1999). Zr might significantly improve osteoblast adhesion (Sista et al., 2013), which is currently marketed as Roxolid (Straumann, Basel, Switzerland). Sn has been found non-toxic and non-allergic (Niinomi, 2003). Thus, Tin (Sn) seems to be an alloying element that is safe to use with Ti. In several previous studies, Mo elements have shown good biocompatibility. The components of Ti10Mo6Zr4Sn3Nb alloy are all elements with good biocompatibility. The research results also present that the

material has good biocompatibility and meets the safety standards of biological materials.

The osseointegration performance of orthopedic implant material refers to the bony fusion of material with surrounding bone without connective tissue growth, which can improve the binding force of the material-bone interface and ensure the long-term stability of the prosthesis. Osteoblasts are one of the most important cells in bone tissue repair. An osteoblast adheres to the surface of a material which is essential for osseointegration. Acridine orange cell staining can count the number of cells, distinguish normal growth, apoptotic, and necrotic cells, and depict the growth state of cells. The results of acridine orange cell adhesion assay revealed that when MC3T3-E1 cells were co-cultured with Ti-B12 alloy, osteoblasts could adhere to the surface of alloy, and the number of adherent cells was higher than that of Ti6Al4V alloy ($p < 0.05$), thus it can be proved that Ti-B12 alloy has better adhesion ability to osteoblasts.

Further verification of the adhesion of the Ti-B12 alloy to osteoblasts was performed using scanning electron microscopy to evaluate the osteoblast morphology adhering to the material surface. Most osteoblasts adhered to the material in the form of elongated spindles, with more pseudopodia, and the cell growth status was good, which was more than that of the Ti6Al4V group. These results indicated that Ti-B12 was more conducive to osteoblast adhesion.

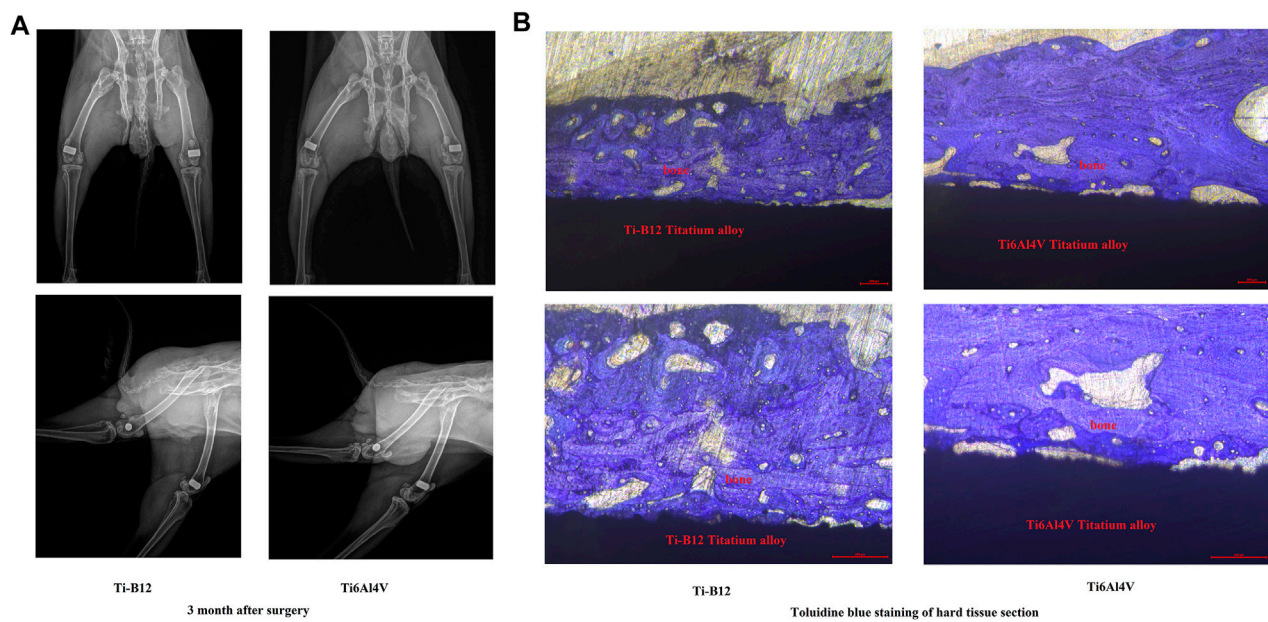


FIGURE 10

In vivo experiments on animals. (A) results of the X-ray examination 3 months after the operation; (B) results of the toluidine blue staining of hard tissue sections.

ALP is an essential indicator for detecting the degree of osteoblast differentiation of osteogenic cells, which has a high content in bone tissue and plays a key role in the calcification process (Vimalraj, 2020). Osteoblast function can be evaluated by measuring ALP secretion and is also a specific index for evaluating tissue calcification ability and osteoblast activity (Nakamura et al., 2020). The ALP content test of osteoblasts demonstrated that osteoblasts in the Ti-B12 group secrete more ALP than the Ti6Al4V and blank control groups ($p < 0.05$); this indicated that the alloy could enhance the secretion of ALP in osteoblasts. ALP was expressed in the process of formation and maturity of extracellular bone matrix expression, OCN expression in the bone matrix mineralization process is the main index of osteogenetic differentiation, and Runx2 is one of the important transcription factors for osteogenesis cell differentiation throughout the various stages of the directional differentiation process, the main control cell division cycle, and other transcription factors also play a role. This study illustrated that gene expression levels for ALP, OCN, and Runx2 demonstrated no significant difference between Ti-B12 group, Ti6Al4V group, and blank control group at 7 and 14 days after induction of differentiation. However, the Ti-B12 group was slightly higher than the latter two, indicating that Ti-B12 alloy has more advantages in promoting osteogenic differentiation.

Mineralized nodules are the final expression of the osteogenic phenotype of osteoblasts *in vitro* (Park et al., 2021) and are also characteristic indicators of mineralized matrix formation. Therefore, the study of terminal differentiation and functional status of osteoblasts can be achieved indirectly by detecting mineralized nodules. Calcium salts in mineralized nodules were stained dark red by alizarin red staining, and 10% hexapylpyridine chloride dissolved the red-stained mineralized nodules. Calcium ion

content was proportional to absorbance value. Alizarin red staining of mineralized nodules demonstrated that there were larger and more dark red mineralized nodules in Ti-B12 group, which were higher in number and size than those in Ti6Al4V and blank control group. After solubilization, the OD values of mineralized nodules depicted that Ti-B12 group was significantly higher than Ti6Al4V and blank control group ($p < 0.05$). Ti-B12 can enhance the mineralization of extracellular matrix of osteoblasts and promote bone formation.

To further evaluate the integration of new titanium alloy Ti-B12 with the surrounding bone, we implanted it in rabbits and studied it by X-ray and histological analysis. In this study, X-rays displayed that the implant was in a good position and the surrounding tissues demonstrated no signs of bone density loss, demonstrating good osseointegration between the implant and the bone tissue. Additionally, hard tissue sections can be used to slice bone tissues containing metal materials. The tested materials do not need to be predecalfified, and the position relationship between implanted metal materials and bone tissues remains unchanged, which can reflect the growth status of implanted bone tissues without damaging the original tissue structure of implant-bone interface. After toluidine blue staining of hard tissue sections, it is possible to observe the growth of surrounding bone tissue, and the ability of the material to directly combine with bone tissue can be directly evaluated. In this study, both materials were wrapped in bone tissue, and there was no fibrous tissue space between the materials and the new bone. However, the binding rate between Ti-B12 and surrounding bone tissue was better than that of Ti6Al4V, which proved that Ti-B12 alloy with low elastic modulus was similar to the elastic modulus of human bone and could provide good stress conduction, thus promoting the formation and reconstruction of surrounding bone tissue.

There are some defects and deficiencies in this study: 1) Only MC3T3-E1 cells were used in the experiment, and several more cells were needed to evaluate the biocompatibility of the material in the follow-up; 2) This study only evaluated the biocompatibility and bone integration properties of the new titanium alloy materials prepared by forging process, which lacked the research on the properties of the new titanium alloy materials under different processing methods, and needed to be further supplemented by subsequent research.

5 Conclusion

β -titanium alloy material has broad application potential in orthopedics and maxillofacial surgery due to its excellent mechanical properties. The premise of its clinical transformation is excellent biocompatibility and osseointegration performance. According to this study, the new β -titanium alloy Ti-B12 has low toxicity, does not cause rejection reactions, and has better osseointegration performance than the traditional titanium alloy Ti6Al4V. Therefore, Ti-B12 material is expected to be further promoted in clinical practice.

Data availability statement

The raw data supporting the conclusion of this article will be made available by the authors, without undue reservation.

Ethics statement

The animal study was reviewed and approved by the Ethics Committee of the First Hospital of Xi'an Jiaotong University.

Author contributions

JL and JC contributed to the conception and design of the study. JL, KW, XL, XZ, XG, and YZ conduct a research process, specifically

performing the experiments and data collection. ZR and BZ design of methodology. JL performed the statistical analysis. JL and JC wrote the first draft of the manuscript. All authors contributed to the manuscript revision, read, and approved the submitted version.

Funding

This work was financially supported by Key Research and Development Plan of Shaanxi Province—General Project (2022GY-390), Institutional Foundation of The First Affiliated Hospital of Xi'an Jiaotong University (2020QN-36) and National Natural Science Foundation of China (52271249, 51901193). Key Research and Development Program of Shaanxi (2023-YBGY-488).

Acknowledgments

We want to express our special thanks to the Northwest Research Institute for Non-ferrous Metals and State Key Laboratory of Powder Metallurgy of Central South University, which provided the titanium alloy material for this experiment, and to the Animal Center of Xi'an Jiaotong University, which provided us with the required experimental animals.

Conflict of interest

The authors declare that the research was conducted in the absence of any commercial or financial relationships that could be construed as a potential conflict of interest.

Publisher's note

All claims expressed in this article are solely those of the authors and do not necessarily represent those of their affiliated organizations, or those of the publisher, the editors and the reviewers. Any product that may be evaluated in this article, or claim that may be made by its manufacturer, is not guaranteed or endorsed by the publisher.

References

- Apostu, D., Lucaciu, O., Berce, C., Lucaciu, D., and Cosma, D. (2018). Current methods of preventing aseptic loosening and improving osseointegration of titanium implants in cementless total hip arthroplasty: a review. *J. Int. Med. Res.* 46 (6), 2104–2119. doi:10.1177/0300060517732697
- Backes, E. H., Fernandes, E. M., Diogo, G. S., Marques, C. F., Silva, T. H., Costa, L. C., et al. (2021). Engineering 3D printed bioactive composite scaffolds based on the combination of aliphatic polyester and calcium phosphates for bone tissue regeneration. *Mater. Sci. Eng. C Mater. Biol. Appl.* 122, 111928. doi:10.1016/j.msec.2021.111928
- Bedouin, Y., Gordin, D., Pellen-Mussi, P., Perez, F., Tricot-Doleux, S., Vasilescu, C., et al. (2019). Enhancement of the biocompatibility by surface nitriding of a low-modulus titanium alloy for dental implant applications. *J. Biomed. Mater. Res. B Appl. Biomater.* 107 (5), 1483–1490. doi:10.1002/jbm.b.34240
- Cheng, J., Wang, H., Li, J., Gai, J., Ru, J., Du, Z., et al. (2020). The effect of cold swaging deformation on the microstructures and mechanical properties of a novel metastable β type Ti-10Mo-6Zr-4Sn-3Nb alloy for biomedical devices. *Front. Mater.* 7, 228. doi:10.3389/fmats.2020.00228
- Declercq, H., Van den Vreken, N., De Maeyer, E., Verbeeck, R., Schacht, E., De Ridder, L., et al. (2004). Isolation, proliferation and differentiation of osteoblastic cells to study cell/biomaterial interactions: comparison of different isolation techniques and source. *Biomaterials* 25 (5), 757–768. doi:10.1016/s0142-9612(03)00580-5
- Gkias, I., Sharma, A. K., Driscoll, D. A., McLawhorn, A. S., Chalmers, B. P., and Sculco, P. K. (2021). Nonconcentric and irregular dislocations of total hip arthroplasties: Radiographic analysis and review of the literature. *J. Emerg. Med.* 60 (4), 451–459. doi:10.1016/j.jemermed.2020.11.023
- Jing, Z., Zhang, T., Xiu, P., Cai, H., Wei, Q., Fan, D., et al. (2020). Functionalization of 3D-printed titanium alloy orthopedic implants: a literature review. *Biomed. Mater.* 15 (5), 052003. doi:10.1088/1748-605x/ab9078
- Kaur, M., and Singh, K. (2019). Review on titanium and titanium based alloys as biomaterials for orthopaedic applications. *Mater. Sci. Eng. C Mater. Biol. Appl.* 102, 844–862. doi:10.1016/j.msec.2019.04.064
- Liu, T., Hua, X., Yu, W., Lin, J., Zhao, M., Liu, J., et al. (2019). Long-term follow-up outcomes for patients undergoing primary total hip arthroplasty with uncemented versus cemented femoral components: a retrospective observational study with a 5-year minimum follow-up. *J. Orthop. Surg. Res.* 14 (1), 371. doi:10.1186/s13018-019-1415-3
- Mello, D. C. R., de Oliveira, J. R., Cairo, C. A. A., Ramos, L. S. d. B., Vegian, M. R. d. C., de Vasconcellos, L. G. O., et al. (2019). Titanium alloys: *in vitro* biological analyzes on

biofilm formation, biocompatibility, cell differentiation to induce bone formation, and immunological response. *J. Mater. Sci. Mater. Med.* 30 (9), 108. doi:10.1007/s10856-019-6310-2

Mendes, M. W., Agreda, C. G., Bressiani, A. H., and Bressiani, J. C. (2016). A new titanium based alloy Ti-27Nb-13Zr produced by powder metallurgy with biomimetic coating for use as a biomaterial. *Mater. Sci. Eng. C Mater. Biol. Appl.* 63, 671–677. doi:10.1016/j.msec.2016.03.052

Murr, L. E. (2017). Open-cellular metal implant design and fabrication for biomechanical compatibility with bone using electron beam melting. *J. Mech. Behav. Biomed. Mater.* 76, 164–177. doi:10.1016/j.jmbbm.2017.02.019

Nadammal, N., Rajput, M., Gupta, S. K., Ivanov, E., Reddy, A. S., Suwas, S., et al. (2022). Laser powder bed fusion additive manufacturing of a low-modulus Ti-35Nb-7Zr-5Ta alloy for orthopedic applications. *ACS Omega* 7 (10), 8506–8517. doi:10.1021/acsomega.1c06261

Nakamura, T., Nakamura-Takahashi, A., Kasahara, M., Yamaguchi, A., and Azuma, T. (2020). Tissue-nonspecific alkaline phosphatase promotes the osteogenic differentiation of osteoprogenitor cells. *Biochem. Biophys. Res. Commun.* 524 (3), 702–709. doi:10.1016/j.bbrc.2020.01.136

Niinomi, M. (2003). Recent research and development in titanium alloys for biomedical applications and healthcare goods. *Sci. Technol. Adv. Mater.* 4, 445–454. doi:10.1016/j.stam.2003.09.002

Ottaria, L., Lauritano, D., Andreasi Bassi, M., Palmieri, A., Candotto, V., Tagliabue, A., et al. (2018). Mechanical, chemical and biological aspects of titanium and titanium alloys in implant dentistry. *J. Biol. Regul. Homeost. Agents* 32, 81–90.

Park, K. R., Lee, J. Y., Cho, M., Hong, J. T., and Yun, H. M. (2021). Biological mechanisms of paeonin in the differentiation of pre-osteoblasts and the formation of mineralized nodules. *Int. J. Mol. Sci.* 22 (13), 6899. doi:10.3390/ijms22136899

Pehlivan, E., Dzugan, J., Fojt, J., Sedlacek, R., Rzepa, S., and Daniel, M. (2020). Post-processing treatment impact on mechanical properties of SLM deposited Ti-6Al-4 V porous structure for biomedical application. *Mater. (Basel)* 13 (22), 5167. doi:10.3390/ma13225167

Rahmati, M., and Mozafari, M. (2019). Biocompatibility of alumina-based biomaterials-A review. *J. Cell Physiol.* 234 (4), 3321–3335. doi:10.1002/jcp.27292

Sarraf, M., Rezvani Ghomi, E., Alipour, S., Ramakrishna, S., and Liana Sukiman, N. (2022). A state-of-the-art review of the fabrication and characteristics of titanium and its alloys for biomedical applications. *Biores. Manuf.* 5 (2), 371–395. doi:10.1007/s42242-021-00170-3

Shahi, S., Ozcan, M., Maleki Dizaj, S., Sharifi, S., Al-Haj Husain, N., Eftekhari, A., et al. (2019). A review on potential toxicity of dental material and screening their biocompatibility. *Toxicol. Mech. Methods* 29 (5), 368–377. doi:10.1080/15376516.2019.1566424

Shi, A., Cai, D., Hu, J., Zhao, X., Qin, G., Han, Y., et al. (2021). Development of a low elastic modulus and antibacterial Ti-13Nb-13Zr-5Cu titanium alloy by microstructure controlling. *Mater. Sci. Eng. C Mater. Biol. Appl.* 126, 112116. doi:10.1016/j.msec.2021.112116

Sidhu, S. S., Singh, H., and Gepreel, M. A. (2021). A review on alloy design, biological response, and strengthening of beta-titanium alloys as biomaterials. *Mater. Sci. Eng. C Mater. Biol. Appl.* 121, 111661. doi:10.1016/j.msec.2020.111661

Sing, S. L. (2022). Perspectives on additive manufacturing enabled beta-titanium alloys for biomedical applications. *Int. J. Bioprint* 8 (1), 478. doi:10.18063/ijb.v8i1.478

Sista, S., Nouri, A., Li, Y., Wen, C., Hodgson, P. D., and Pande, G. (2013). Cell biological responses of osteoblasts on anodized nanotubular surface of a titanium-zirconium alloy. *J. Biomed. Mater. Res. A* 101, 3416–3430. doi:10.1002/jbm.a.34638

Su, X., Wang, T., and Guo, S. (2021). Applications of 3D printed bone tissue engineering scaffolds in the stem cell field. *Regen. Ther.* 16, 63–72. doi:10.1016/j.reth.2021.01.007

Suggs, L. J., Shive, M. S., Garcia, C. A., Anderson, J. M., and Mikos, A. G. (1999). *In vitro* cytotoxicity and *in vivo* biocompatibility of poly(propylene fumarate-co-ethylene glycol) hydrogels. *J. Biomed. Mater. Res. B Appl. Biomater.* 46, 22–32. doi:10.1002/(sici)1097-4636(199907)46:1<22::aid-jbm3>3.0.co;2-r

Szczesny, G., Kopec, M., Politis, D. J., Kowalewski, Z. L., Lazarski, A., and Szolc, T. (2022). A review on biomaterials for orthopaedic surgery and traumatology: From past to present. *Mater. (Basel)* 15 (10), 3622. doi:10.3390/ma15103622

Trevisan, F., Calignano, F., Aversa, A., Marchese, G., Lombardi, M., Biamino, S., et al. (2018). Additive manufacturing of titanium alloys in the biomedical field: processes, properties and applications. *J. Appl. Biomater. Funct. Mater* 16 (2), 57–67. doi:10.5301/jabfm.5000371

Vimalraj, S. (2020). Alkaline phosphatase: Structure, expression and its function in bone mineralization. *Gene* 754, 144855. doi:10.1016/j.gene.2020.144855

Vojdani, A. (2021). Elevated IgG antibody to aluminum bound to human serum albumin in patients with crohn's, celiac and Alzheimer's disease. *Toxics* 9 (9), 212. doi:10.3390/toxics9090212

Vonavkova, I., Prusa, F., Kubasek, J., Michalcova, A., and Vojtech, D. (2022). Microstructure and mechanical properties of Ti-25Nb-4Ta-8Sn alloy prepared by spark plasma sintering. *Mater. (Basel)* 15 (6), 2158. doi:10.3390/ma15062158

Willis, J., Crean, S. J., and Barrak, F. N. (2021). Is titanium alloy Ti-6Al-4 V cytotoxic to gingival fibroblasts-A systematic review. *Clin. Exp. Dent. Res.* 7 (6), 1037–1044. doi:10.1002/cre2.444

Xi, D., and Wong, L. (2021). Titanium and implantology: a review in dentistry. *J. Biol. Regul. Homeost. Agents* 35, 63–72.

Xie, L., Yu, H., Yang, W., Zhu, Z., and Yue, L. (2016). Preparation, *in vitro* degradability, cytotoxicity, and *in vivo* biocompatibility of porous hydroxyapatite whisker-reinforced poly(L-lactide) biocomposite scaffolds. *J. Biomater. Sci. Polym. Ed.* 27 (6), 505–528. doi:10.1080/09205063.2016.1140613

Yamamoto, A., Honma, H., Tanaka, A., and Sumita, M. (1999). Generic tendency of metal salt cytotoxicity for six cell lines. *J. Biomed. Mater. Res. B Appl. Biomater.* 47, 396–403. doi:10.1002/(sici)1097-4636(19991205)47:3<396::aid-jbm15>3.0.co;2-r

Zhan, X., Li, S., Cui, Y., Tao, A., Wang, C., Li, H., et al. (2020). Comparison of the osteoblastic activity of low elastic modulus Ti-24Nb-4Zr-8Sn alloy and pure titanium modified by physical and chemical methods. *Mater. Sci. Eng. C Mater. Biol. Appl.* 113, 111018. doi:10.1016/j.msec.2020.111018

Zhang, T., Ou, P., Ruan, J., and Yang, H. (2021). Nb-Ti-Zr alloys for orthopedic implants. *J. Biomater. Appl.* 35 (10), 1284–1293. doi:10.1177/0885328220970756

Zhao, X., Zhang, P., Wang, X., Chen, Y., Liu, H., Chen, L., et al. (2018). *In-situ* formation of textured TiN coatings on biomedical titanium alloy by laser irradiation. *J. Mech. Behav. Biomed. Mater.* 78, 143–153. doi:10.1016/j.jmbbm.2017.11.019

Zheng, Y., Han, Q., Wang, J., Li, D., Song, Z., and Yu, J. (2020). Promotion of osseointegration between implant and bone interface by titanium alloy porous scaffolds prepared by 3D printing. *ACS Biomater. Sci. Eng.* 6 (9), 5181–5190. doi:10.1021/acsbmaterials.0c00662



OPEN ACCESS

EDITED BY

Yanjin Lu,
Fujian Institute of Research on the
Structure of Matter (CAS), China

REVIEWED BY

Jiabing Ran,
China Three Gorges University, China
Zhen Geng,
Shanghai University, China

*CORRESPONDENCE

Jianfeng Gao,
✉ jfgao@shzu.edu.cn
Lei Wang,
✉ leiwang@yic.ac.cn

SPECIALTY SECTION

This article was submitted to Biomaterials,
a section of the journal
Frontiers in Bioengineering and
Biotechnology

RECEIVED 31 December 2022

ACCEPTED 30 January 2023

PUBLISHED 13 February 2023

CITATION

Liu Z, Jiang X, Wang K, Zhou Y, Li T, Gao J
and Wang L (2023), Preparation of fish
decalcified bone matrix and its bone repair
effect in rats.
Front. Bioeng. Biotechnol. 11:1134992.
doi: 10.3389/fbioe.2023.1134992

COPYRIGHT

© 2023 Liu, Jiang, Wang, Zhou, Li, Gao and
Wang. This is an open-access article
distributed under the terms of the [Creative
Commons Attribution License \(CC BY\)](#).
The use, distribution or reproduction in
other forums is permitted, provided the
original author(s) and the copyright
owner(s) are credited and that the original
publication in this journal is cited, in
accordance with accepted academic
practice. No use, distribution or
reproduction is permitted which does not
comply with these terms.

Preparation of fish decalcified bone matrix and its bone repair effect in rats

Zichao Liu¹, Xiaorui Jiang², Kai Wang², Yongshun Zhou¹,
Tingting Li¹, Jianfeng Gao^{1*} and Lei Wang^{3*}

¹College of Life Sciences, Shihezi University, Shihezi, Xinjiang, China, ²Department of Hand and foot Surgery, The Affiliated Yantai Yuhuangding Hospital of Qingdao University, Yantai, China, ³The Affiliated Hospital of Weifang Medical University, Yantai, China

Decalcified bone matrix has great potential and application prospects in the repair of bone defects due to its good biocompatibility and osteogenic activity. In order to verify whether fish decalcified bone matrix (FDBM) has similar structure and efficacy, this study used the principle of HCl decalcification to prepare the FDBM by using fresh halibut bone as the raw material, and then degreasing, decalcifying, dehydrating and freeze-drying it. Its physicochemical properties were analyzed by scanning electron microscopy and other methods, and then its biocompatibility was tested by *in vitro* and *in vivo* experiments. At the same time, an animal model of femoral defect in rats was established, and commercially available bovine decalcified bone matrix (BDBM) was used as the control group, and the area of femoral defect in rats was filled with the two materials respectively. The changes in the implant material and the repair of the defect area were observed by various aspects such as imaging and histology, and its osteoinductive repair capacity and degradation properties were studied. The experiments showed that the FDBM is a form of biomaterial with high bone repair capacity and lower economic cost than other related materials such as bovine decalcified bone matrix. FDBM is simpler to extract and the raw materials are more abundant, which can greatly improve the utilization of marine resources. Our results show that FDBM not only has a good repair effect on bone defects, but also has good physicochemical properties, biosafety and cell adhesion, and is a promising medical biomaterial for the treatment of bone defects, which can basically meet the clinical requirements for bone tissue repair engineering materials.

KEYWORDS

decalcified bone matrix, artificial bone material, bone defect, tissue regeneration, Hydrophilic

1 Introduction

Bone tissue repair has always been a hot topic in biomedical research. In recent years, the number of patients with bone defects due to an ageing population, trauma, infections, bone tumors and congenital malformations has remained high and the demand for bone repair materials is increasing day by day (Henkel et al., 2013). Bone defects can disrupt bone continuity and lead to loss of bone function, making wound healing difficult, affecting the patient's life and career and causing many problems for themselves and their families (Dimitriou et al., 2011). How to repair bone defects and restore normal function in a short period of time is the greatest demand of patients and the direction that the majority of medical workers are striving for.

Bone grafting or implantation of bone materials such as autologous bone, allogeneic bone and artificial bone materials are often required in the treatment of patients with bone defects. Autologous bone grafting is often seen as the best means of repairing bone defects in medicine

(Pereira et al., 2017), but bone grafting operation can cause secondary injury to the body, damage the normal bone structure of the donor area and making it vulnerable to risks such as bleeding, infection and pain (De Ponte et al., 2017; Pan et al., 2018). Allogeneic bone is prone to fracture due to resorption after transplantation. On the other hand, it is also immunogenic and immune rejection and has a potential risk of epidemic transmission (Ippolito et al., 2019). In order to overcome these limitations in treatment, researchers have turned their attention to artificial bone materials with excellent properties, such as inorganic bone materials, polymer bone materials, composite bone materials and tissue engineering materials (Bian et al., 2019). Among them, biomaterials have been widely used in clinical practice for their excellent performance.

DBM is an artificial bone material obtained by decalcifying biological bone. It is a bone tissue engineering scaffold material with collagen as the main component and also contains non-collagenous proteins and lower concentrations of growth factors, with good biocompatibility and biodegradability (Hu et al., 2018; Cho et al., 2020; Hao et al., 2022). Among these, bone morphogenetic protein is the key factor in the induction of osteogenic activity, which can induce the differentiation of mesenchymal cells into chondrogenic cells and thus the formation of new bone (Chen et al., 2007; Salonijs et al., 2020). The decalcification treatment removes the constraint imposed by calcium salts on bone morphogenetic protein, allowing it to be released and to fulfil its osteogenic potential (Zhang et al., 1997). Collagen is conducive to the synthesis of osteocalcin and can increase the activity level of osteoblast alkaline phosphatase. It is also conducive to the attachment of cells and the deposition of hard tissue. Loose porous structure can also promote the inward growth of osteoprogenitor cells and capillaries, so as to better play the role of bone conduction (Caballe-Serrano et al., 2020).

Currently, the DBM used in clinical practice is mainly derived from the skull, femur and tibia of terrestrial animals such as pigs, cattle, dogs and rabbits. Although they are easy to obtain, they carry a risk of transmitting diseases such as avian influenza, swine influenza and odontogenic diseases. Especially, the DBM of bovine origin carries a high risk of transmissible spongiform encephalopathy (TSE), bovine spongiform encephalopathy (BSE) and other potential viruses that may be transmitted to humans (Jonglareonrak et al., 2005; Widdowson et al., 2018). In addition to this, the DBM which derived from pigs is also banned in some countries for religious or ethical reasons. Compared with terrestrial animals, marine animals are rich in sources, easy to extract, and have higher safety. There are no animal disease risks and religious issues mentioned above (Lim et al., 2019). Marine animal collagen is similar in amino acid structure to terrestrial mammals and has a sequence structure similar to RGD amino acid sequence, which can effectively promote cell adhesion to biological materials and guide tissue regeneration, making it an ideal raw material for medical use (Silva et al., 2014; Chen et al., 2019). In addition, the presence of a large number of diaminodicarboxyl groups in the peptide chain makes the collagen of marine animals extremely hydrophilic, which can effectively solve the problem of difficult cell adhesion and proliferation on the DBM. (Wang et al., 2022).

This study was conducted to determine whether a decalcified bone matrix prepared from fish bones meets the requirements for a bone repair material and whether it has the ability to promote bone repair. In this study, fish bone from flounder was used as raw material, and the FDBM was obtained after a series of treatments, and its physicochemical properties and biocompatibility were tested. At the

same time, an animal model of femoral defect in rats was established, and commercially available BDBM was used as the control group, and the area of femoral defect in rats was filled with the two materials respectively. The changes in the implant material and the repair of the defect area were observed by various aspects such as imaging and histology, and its osteoinductive repair capacity and degradation properties were studied.

2 Materials and methods

2.1 Materials

FDBM was prepared by the laboratory itself using halibut bone. BDBM was purchased from a conventional medical equipment manufacturer. Female Sprague Dawley (SD) rats (200–220 g) were purchased from Jinan Pengyue Experimental Animal Breeding Co Ltd (Jinan, China). New Zealand White rabbits (2–2.5 kg) were purchased from Qingdao Kangda Biotechnology Co Ltd (Qingdao, China). All other chemicals were of analytical grade and no further purification was required for use. All animal experiments were approved by the Animal Theory Committee of Yantai Lundy Biotechnology Co Ltd (approval number: LDSW2022037).

2.2 Preparation of fish decalcified bone matrix

This preparation process uses fresh halibut fish bones as raw material (Figure 1). We take 50 g of fish bones, cut it into 0.5 cm*0.5 cm cylinders, and rinse with pure water for 3 times. Soak the treated fish bones in 9% NaCl solution for 8 h with a material-to-liquid ratio of 1:20 (w/v) (remove impurities such as oil). The fish bones were soaked in 1% SDS solution for 8 h and the ratio of material-to-liquid was 1:20 (w/v) (remove impurities such as oil). After washing them with pure water for 3 times, the fish bones were soaked in propanetriol, and the ratio of material-to-liquid was 1:10 (w/v) (remove fat). It was stirred at 120 rpm for 8 h and filter out the solution. Then the fish bones were soaked in 3% hydrogen peroxide (H₂O₂) solution for 6 h, the ratio of material-to-liquid was 1:10 (w/v), and the fish bones was bleached. Wash with pure water for 3 times. The fish bones were soaked in anhydrous ether for 8 h, the ratio of material-to-liquid was 1:10 (w/v). Afterwards, the fish bones were soaked in 0.1 mol/L hydrochloric acid (HCl) and stirred with the same speed for 12 h, the ratio of material-to-liquid was 1:50 (w/v) (remove calcium). Then the fish bones were soaked in 0.5% pepsin for 30 min, the ratio of material-to-liquid was 1:30 (w/v). Finally, clean the FDBM with pure water, freeze-dry it in a freeze dryer, and sterilize it with 60Co.

2.3 Physical and chemical properties

2.3.1 Characterisation and structural observations

The shape and morphology of the prepared FDBM was observed. Then, the structures of FDBM were observed by scanning electron microscope (SEM). The FDBM was cut into small pieces of 0.1 cm*0.1 cm and fixed on the sample table by conductive adhesive. After the surface was sprayed with gold, the surface, porosity, pore size and internal structure of the FDBM was observed by SEM (S-4800, HITACHI, Japan).

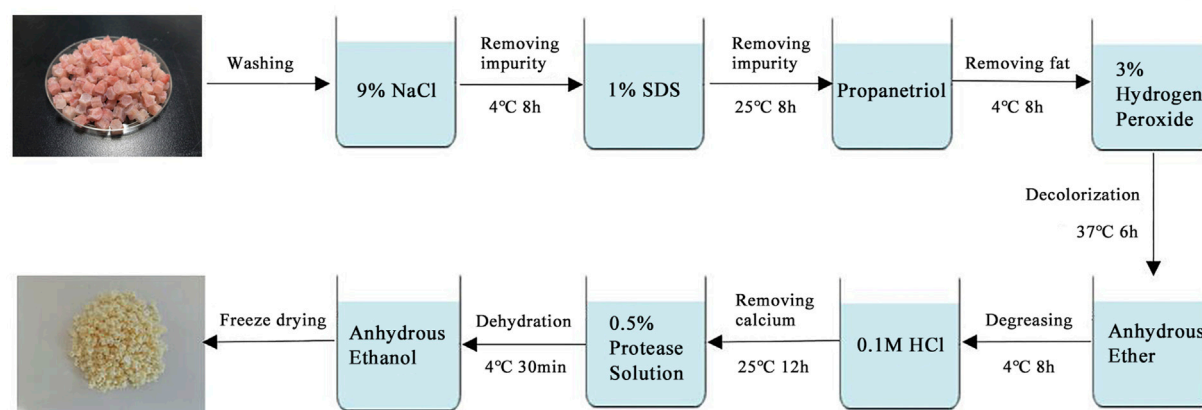


FIGURE 1

Preparation of fish decalcified bone matrix (FDBM).

2.3.2 Mechanical strength

The FDBM (cylinders of 0.5 cm diameter and 0.5 cm height) were fixed on a universal testing machine at room temperature and the specimens were crushed at a rate of 2 mm/min until the FDBM pellets were crushed into flakes (CMT8502, MTS systems, China). The compressive strength was calculated from the measured pressure values. The mean value was taken from three parallel measurements under the same conditions. The standard deviation was calculated and presented as mean \pm standard deviation ($\bar{x} \pm s$).

2.3.3 Porosity testing

Anhydrous ethanol was added to the measuring cylinder and the volume was recorded as V_1 . The cylinder was then placed in a vacuum desiccator and evacuated to allow the ethanol to enter the pores of the material until no air bubbles escaped, at which point the volume was recorded as V_2 . Finally, the FDBM was removed and the remaining volume of ethanol was recorded as V_3 . The porosity of the FDBM was calculated according to the equation and the data are presented as mean \pm standard deviation ($\bar{x} \pm s$).

$$\text{Porosity (\%)} = \frac{V_1 - V_3}{V_2 - V_3} \times 100\%$$

In the formula: V_1 is the initial ethanol volume; V_2 is the total volume of FDBM after submersion in ethanol; V_3 is the remaining ethanol volume.

2.3.4 Calcium content

1) Establishment of calcium standard curve: Weigh 10 g analytically pure CaCO_3 powder at 110°C in a beaker and gradually add 1 M HCl dropwise to the beaker until it is completely dissolved. The volume is then fixed to 100 ml in a volumetric flask. This calcium standard solution has a Ca^{2+} concentration of 1 mol/L. Dilute them into 5 parts of calcium standard solution of 1 mol/L, 0.8 mol/L, 0.6 mol/L, 0.4 mol/L and 0.2 mol/L respectively. The absorbance of the Ca^{2+} concentration of each group was observed under visible spectrophotometer 422.7 nm and the value was recorded as A. The relationship between n and A was analyzed and fitted to give the calcium standard curve equation:

$$\rho = 0.9078n + 0.0585 \quad (R^2 = 0.9995)$$

In the formula: ρ is the absorbance value corresponding to the concentration of Ca^{2+} ; n is the amount-of-substance concentration of calcium ions, mol/L.

- (2) Determination of total calcium in fish bones: 1 g undecalcified fish bone was placed in a beaker, 5 ml concentrated H_2SO_4 was added and the beaker was placed on the electrothermal furnace. Continue to raise the temperature when the fish bones are black and sticky. Gradually add HClO_4 solution dropwise to the beaker and continue heating to make it clear and transparent. After cooling, the final volume was adjusted to 50 ml by adding deionized water. A suitable volume of liquid was taken and the absorbance was measured under visible spectrophotometer 422.7 nm. The value was recorded as A. The total calcium content of the fish bones was calculated from the regression equation in 1).
- (3) Determination of calcium content in fish bone decalcification solution: A suitable volume of decalcifying solution was taken and the absorbance was measured under visible spectrophotometer 422.7 nm. The value was recorded as A. The calcium content of the fish bone decalcification solution was calculated according to the regression equation in 1).
- (4) Calculation of decalcification rate:

$$\text{Decalcification rate (\%)} = \frac{S}{T} \times 100\%$$

In the formula: S is the calcium content in decalcification solution; T is the total calcium in fish bones.

2.3.5 Water absorption

Six pieces of prepared FDBM were divided into six groups at room temperature, immersed in deionized water for 10 min and then suspended on a table. When no water drops fell from the samples, each group was weighed and the mass recorded as m. The samples were then freeze-dried, weighed again and the mass recorded as m1. Each group was repeated 3 times and the average was taken.

$$\text{Water absorption (\%)} = \frac{m - m_1}{m} \times 100\%$$

In the formula, m is the mass of FDBM after immersion in water, and m_1 is the mass of FDBM after freeze-drying.

2.3.6 In Vitro degradation

Six pieces of FDBM were taken, weighed and placed in a 6-well culture plate, one piece per well. 6 ml of artificial degradation solution (0.1 mol/L PBS) was added to each well, and then placed the plate in a 37°C incubator for degradation. The FDBM was removed at weeks 2, 4, 6, 8 and 10, freeze-dried and weighed, and the rate of mass loss was calculated by averaging. After each recording was completed, the physiological degradation solution was replaced with an equal amount to continue the degradation. The degradation rate of the FDBM was calculated for each time period (2 weeks for each time period) and a degradation rate curve was plotted.

$$\text{Degradation rate (\%)} = \frac{A_0 - A_1}{A_0} \times 100\%$$

In the formula, A_0 is the mass of FDBM at one time point before degradation, and A_1 is the mass of FDBM at one time point after degradation.

2.4 Biocompatibility

2.4.1 Cytocompatibility

In order to evaluate the cytotoxicity, proliferation rate and adhesion of FDBM, we chose mouse fibroblasts (L929) as co-cultured cells with FDBM.

2.4.1.1 Cytotoxicity

Under aseptic condition, 5 g FDBM were placed in 30 ml DMEM high glucose (DMEM-H) complete medium and extracted at 37°C with 80 rpm for 24 h to obtain cell culture medium. The cytotoxicity was detected by CCK-8 method. L929 cells are cultured with the DMEM-H system containing 10% FBS. According to the standard of 8×10^3 /well, L929 cells at logarithmic growth stage were inoculated in a 96-well plate with a volume of 100 μ L per well. The upper layer of the cell culture medium was discarded after the cells adhered to the wall and formed monolayers. Then the mixture of 200 μ L cell culture medium and extraction solution were sequentially added to the 96-well plate according to the proportion of 25, 50%, and 100%. After co-culture with cells for 24 h, each well was equipped with 100 μ L CCK-8 solution (10 μ L CCK-8 in 90 μ L medium) according to the instructions of CCK-8 kit (Biosharp, China). Then the culture plate was incubated at 37°C and 5% CO₂ for 2 h, and the optical density (OD) value was detected at 450 nm by microplate reader (Infinite F50, Tecan, Switzerland).

$$\text{Cell proliferation rate (\%)} = \frac{A_s - A_b}{A_c - A_b} \times 100\%$$

In the formula, A_s is the absorbance of wells with cells, CCK8 solution and leachate, A_c is the absorbance of wells with cells, CCK8 solution and no extraction solution, and A_b is the absorbance of wells with medium and CCK8 solution and no cells.

2.4.1.2 Live/Dead Cell staining

According to the standard of 1×10^5 cells per well, 500 μ L cell suspension was put into 48-well plate. After the cells adhered to the wall, the original cell culture medium was replaced with the extraction solution. After culturing for 3 days, replace the normal cell culture medium with 1.5 μ L propidium iodide and 1 μ L calcein-AM (Solarbio, China) in PBS solution, and incubate for another 30 min. After the sample was gently washed with PBS, fluorescence was excited by 490 nm wavelength under inverted fluorescence microscope (ECHO RVL-100-G, United States), and the distribution of living dead cells was observed.

2.4.1.3 Observation of Cell adhesion

L929 cells were cultured in a cell incubator at 37°C and 5% CO₂. The cells were digested and counted when the cells grew to the logarithmic phase. After 1 ml cell suspension was inserted into a 24-well plate. FDBM was put into the cell suspension, co-cultured with the cells for 24 h, fixed with 2.5% glutaraldehyde solution for 24 h and lyophilized. The cells were observed for adhesion, infiltration and growth on the surface and inside the bone material by scanning electron microscope.

2.4.2 In Vivo safety and degradation

2.4.2.1 In vivo implantation

Twelve SD rats were randomly divided into four groups and each group consists of seven rats. After the rats were anesthetized with 10% chloral hydrate at a dose of 0.4 ml/100g, their backs were depilated within the 1 cm² area. After alcohol disinfection, the full-thickness skin openings of 0.5 cm were opened at 1.5 cm on both sides of the dorsal spine. Then FDBM and BDBM were placed on the left and right sides, respectively, and sutured. After all rats were awakened, the rats were observed for their living condition, mental status and feeding.

2.4.2.2 Histopathological Examination

On the 3rd, 7th, 14th, and 28th day after the operation, one group of rats were sacrificed respectively, and the embedded FDBM and BDBM were took out, which were fixed with 4% paraformaldehyde. After 24 h of fixation, the tissues were embedded in paraffin and sectioned in routine paraffin for HE and Masson staining. Finally, the morphology and cell infiltration of FDBM and BDBM were observed under light microscope.

2.4.3 Haemolysis rate

Under aseptic condition, 5 g FDBM were placed in 30 ml normal saline and extracted at 37°C with 80 rpm for 24 h to obtain the extraction solution of FDBM. 2 ml fresh anticoagulant blood was taken from healthy SD rats and 8 ml normal saline was added to dilute it. 10 ml FDBM extraction solution were prepared as experimental group. At the same time, the same amount of deionized water was used as the positive control group and the same amount of normal saline as the negative control group. Then 200 μ L SD rats' blood was added to test tubes from three groups, which are mixed thoroughly and incubated at 37°C for 60 min. After incubation, the tubes were centrifuged at 2500 rpm speed for 5 min in a high-speed centrifuge. After centrifugation, the hemolysis was observed, and the absorbance was measured with an ultraviolet spectrophotometer at 545 nm wavelength.

$$\text{Haemolysis rate (\%)} = \frac{A_1 - A_2}{A_3 - A_2} \times 100\%$$

In the formula, A_1 is the average absorbance of FDBM group, A_2 is the average absorbance of normal saline group, and A_3 is the average absorbance of deionized water group.

2.4.4 Pyrogen testing

The FDBM was tested for pyrogen by reference to the Chinese Pharmacopoeia (2020 edition). The extraction solution of FDBM was obtained by the method in 2.4.3, placed in a water bath and preheated to 38°C. Then three normal New Zealand White rabbits were taken and their body temperature was measured. 25 ml extraction solution of FDBM was slowly injected from each rabbit's ear marginal vein, and then the temperature change was measured in real time over a 3 h period using the same online real-time thermometer. After the measurement was complete, the highest temperature during the entire test was used to subtract the normal body temperature of the rabbit as the number of degrees of increase in body temperature for this test. If all temperatures measured throughout are lower than normal body temperature, record as 0°C.

2.5 Ability to repair bone defects

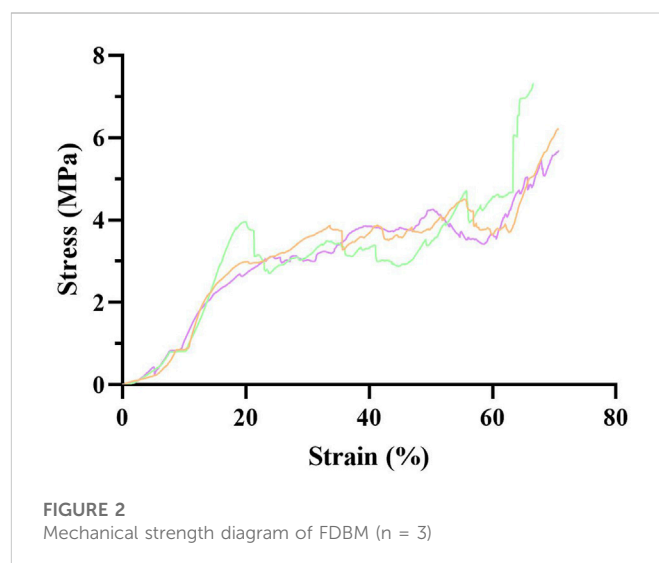
2.5.1 Establishment of bone defects model

Forty-five SPF-grade 10-week-old female rats (200–220 g) were randomly divided into three groups of fifteen rats each. 10% chloral hydrate was injected intraperitoneally according to 0.4 ml/100 g body weight ratio. Aseptic operation was maintained during the operation. After rats were placed in a supine position, the hair on the inner side of the leg was removed and the skin was exposed and disinfected with 75% alcohol. Then a 1 cm skin incision was made along the left femur, the skin and muscle layers were spread along the femur in turn to expose the femoral stem. The periosteum was then separated to expose the middle and upper part of the femoral stem. The rat's femur was drilled with a 2 mm diameter drill, the drill was moved up and down to create a bone defect area of approximately $2 \times 3 \text{ mm}^2$. The holes were flushed with sterile saline to quickly remove the bone fragments.

After the bone defects model was prepared, FDBM and BDBM were implanted into the bone defect area of different group, and the defect area was adequately filled. The self-healing group did not do any treatment. After implantation, the wound was closed with sutures and 400,000 units of penicillin were injected into the other thigh muscle to prevent infection. Normal feeding after operation.

2.5.2 Postoperative status observation

After the operation, the rats' spirit, feeding, activity and wound healing were recorded daily. The effect of the surgery and the implant material on the rats was judged according to their behavior and reaction status. At the same time, the occurrence of redness, swelling, oozing and pus at the operative site was recorded. Five rats in each group were euthanized at the fourth, 8th and 12th weeks after operation, and the whole femur was removed. The muscles, fascia and other tissues on the femur were cleared and then the bone defect area was observed for the state of the material, the state of healing and the presence of infection.



2.5.3 CT radiographic observation

The femur in 2.4.2 was fixed in 4% paraformaldehyde for 24 h. The specimen was removed and washed three times with PBS buffer (pH 7.0) before CT radiography was performed to observe the bone repair of the defect site and the degradation of the implant material.

2.5.4 Histopathological examination

The rat femurs were put into the EDTA decalcification solution and placed in a constant temperature shaker at 37°C, 50 rpm for 1 month, during which time the EDTA decalcification solution was changed once a week. After decalcification was completed, the rat femurs were washed with distilled water, routinely dehydrated, embedded in paraffin, sectioned and then subjected to HE and Masson staining. The ability of the bone material to repair bone defects was evaluated by observing the degradation of the bone materials, the cell type and status of the bone defect area, and the bone repair at the defect site. New bone formation was evaluated semi-quantitatively at the 4-week time point with reference to the histological outcome assessment criteria in "YY/T 1680–2020 *In vivo* evaluation of osteoinductive potential for materials containing demineralized bone". The results were evaluated independently by two investigators blinded and counted.

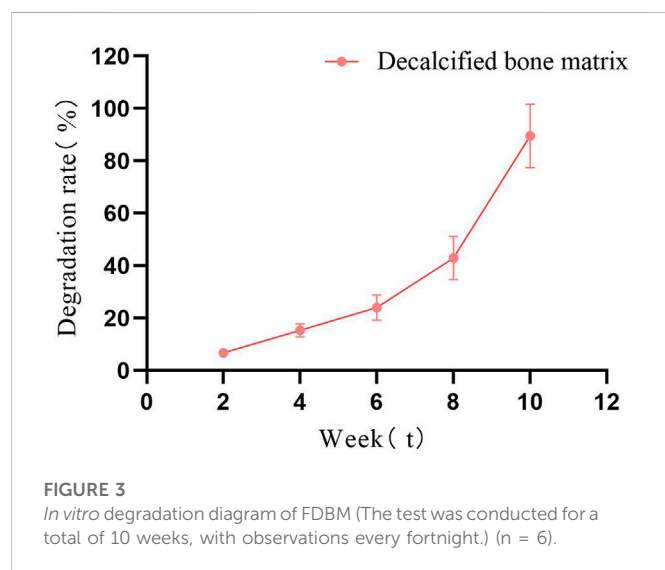
3 Result

3.1 Physical and chemical properties of FDBM

The FDBM was prepared from flounder fish bones through a process of defatting, decalcifying and freeze-drying. The freeze-dried FDBM is faintly yellow, hard and dense. As a whole, its shape resembles that of a cylinder with a diameter and height of 0.5 cm. From the side, its shape is irregular, with two large ends and a thin middle part. In the determination of calcium content in FDBM, the relationship between n and A was analyzed and fitted to give the calcium standard curve equation: $\rho = 0.9078n + 0.0585$ ($R^2 = 0.9995$). In the formula: ρ is the absorbance value corresponding to the concentration of Ca^{2+} ; n is the amount-of-substance concentration

TABLE 1 Water absorption in each group (n = 3, per group).

Groups	Before absorbing water ($\bar{x} \pm SD$)	After absorbing water ($\bar{x} \pm SD$)	Water absorption (%)
1	0.0351 \pm 0.0026	0.0674 \pm 0.0046	92.11
2	0.0324 \pm 0.0027	0.0604 \pm 0.0045	86.47
3	0.0273 \pm 0.0033	0.0515 \pm 0.0051	88.83
4	0.0311 \pm 0.0025	0.0572 \pm 0.0047	83.72
5	0.0333 \pm 0.0024	0.0590 \pm 0.0049	77.31
6	0.0316 \pm 0.0032	0.0602 \pm 0.0065	90.30



of calcium ions, mol/L. After calculation, the average decalcification rate of FDBM is $78.41 \pm 5.73\%$. Normally DBM has the disadvantage of poor mechanical properties, so we did not completely decalcify it during the preparation of FDBM. This approach allows the FDBM to maintain good mechanical strength without compromising the repair effect. This facilitates the better use of FDBM in bone tissue engineering. In the process of tissue repair, materials with higher porosity can provide a wider space for cell adhesion, proliferation and differentiation. The results show that the porosity of FDBM is $72.56 \pm 4.67\%$, which basically meets the requirements of an ideal bone tissue engineering material.

The mechanical strength of the FDBM was measured using the compression test method and the first turning point of the compression curve was defined as the mechanical strength. Figure 2 shows that the stress increases as the FDBM is continuously compressed, with a turning point when the strain reaches about 30%. The compressive stress when FDBM was destroyed was 4.03 ± 0.17 MPa which is close to the strength of human cancellous bone (2–20 MPa) (Bose et al., 2012). The results indicating that FDBM has excellent mechanical strength and is very suitable for biomedical materials.

The hydrophilicity of biomaterials is an important parameter in tissue engineering applications, and good hydrophilicity facilitates cell adhesion, growth and differentiation (Mishra et al., 2019). HCl treatment can fully expose the hydrophilic groups of fish bone, so that the FDBM has good hydrophilicity.

Experiments showed that the water absorption rate of the FDBM can reach 86.41% (Table 1). The ideal bone tissue engineering scaffold should also have good biodegradability. The degradation rate of the scaffold after implantation should be commensurate with the growth rate of the tissue and should maintain its shape over a period of time, which can provide a shaping effect on the new tissue. Too fast or too slow a degradation rate of the scaffold can affect the structure of the new tissue. Figure 3 shows that the FDBM degrades *in vitro* in a physiological degradation solution at a slow rate for the first 6 weeks, with a significantly faster rate after 6 weeks and rapid cleavage as it approaches 10 weeks. The results show that the *in vitro* degradation time of FDBM is approximately 8–10 weeks.

The ideal bone repair scaffold should have a highly interconnected porous structure that provides a biological environment conducive to cell adhesion and proliferation as well as tissue growth and nutrient flow (Zhang et al., 2019). Figure 4 shows that the freeze-dried FDBM showed a porous honeycomb shape with a dense and regular arrangement in the electron microscopic field of view. At high magnification, the FDBM shows a loose and porous structure with good connectivity between the porous structures. The pores of the FDBM range from 10 μm to 50 μm , and its loose and porous structure provides good access and storage for small molecules, which provides a structural basis for cell crawling and growth inside the scaffold (Lv et al., 2021).

3.2 Biocompatibility assessment of FDBM

3.2.1 Cytocompatibility

Cell metabolism can be affected by cytotoxic materials. After the Calcein AM-PI staining, the living cells were green and the dead cells were red (Zhang et al., 2021). From the staining results of live/dead cells cultured to 3 days (Figure 5), the cells cultured by FDBM extraction solution grow well compared with the control group, and there is no significant difference in the proportion of dead cells, indicating that the FDBM scaffold has no cytotoxicity. Similarly, the results of CCK-8 test (Figure 6) also proved that the prepared FDBM is non-cytotoxic. The cells cultured in all three concentrations of FDBM extraction solution had a cell proliferation rate of around 95%. The cellular value-added rates at the three concentration tests were approximately equal and the differences were not statistically significant. According to the grading standard of cytotoxicity evaluation, the cytotoxicity is level 1. According to the standard, it is deemed to be non-cytotoxic when the cytotoxicity is at the first level. The cytocompatibility of TADM was satisfactory.

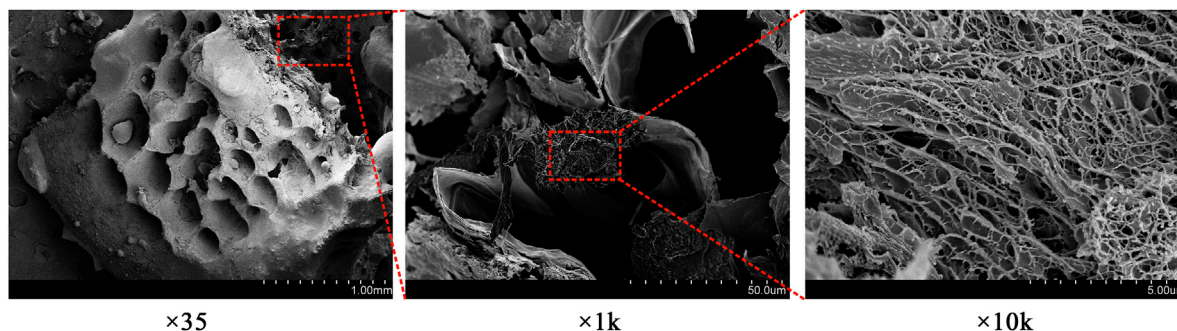


FIGURE 4
Electron microscope scan of FDBM.

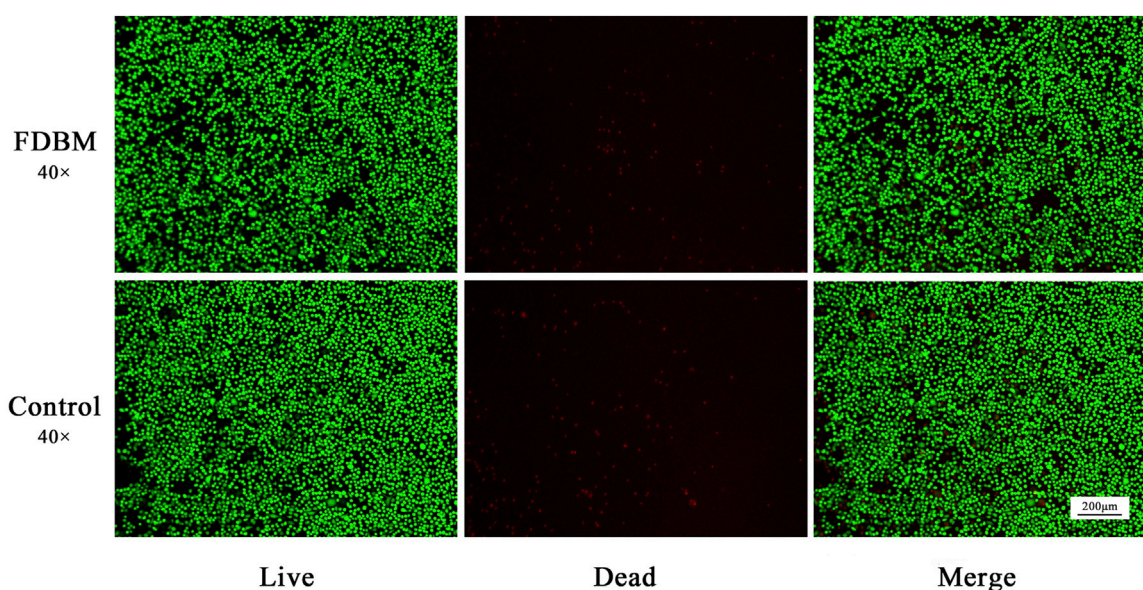


FIGURE 5
Live-Dead staining of L929 cells cultured by FDBM extraction solution after culturing for 3 days (green for living cells and red for dead cells; magnification, $\times 40$).

Figure 7 shows that L929 cells can normally infiltrate the FDBM and adhere to it. A large number of cells adhere to the interior of the material, but the cells mainly adhere to the collagen surface and extend pseudopods on its surface, showing some crawling behavior. In addition, some of the cells replicate and proliferate inside the material. This again demonstrates the good cytocompatibility of the FDBM. The results show that the FDBM not only has high porosity, but also has good fibroblast adhesion and potential to induce fibroblast migration and growth, which fully indicates that the FDBM has good cell compatibility.

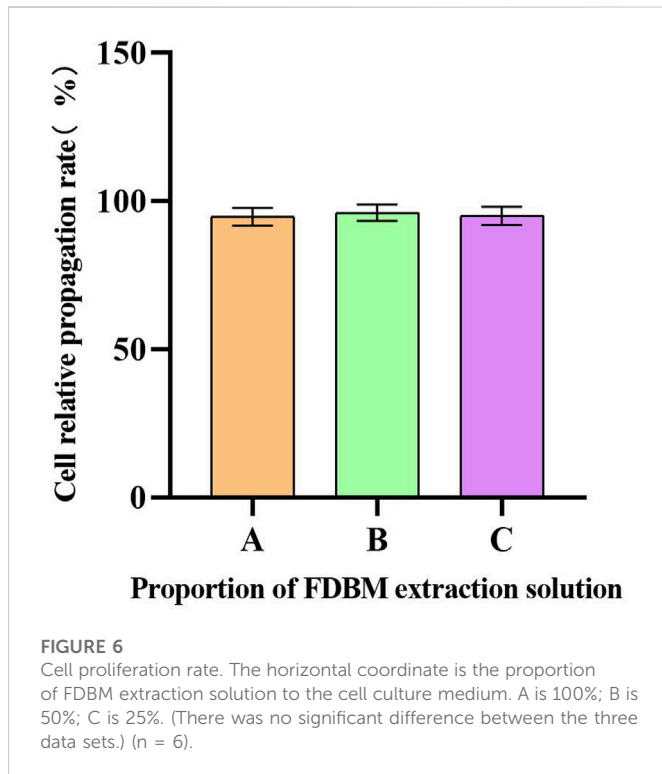
3.2.2 Destructive effect on blood cells

The results of the hemolysis test (Figure 8) showed that the supernatant of the normal saline group was clear and transparent, and no hemolysis occurred. The supernatant of the FDBM group was slightly red, and most of the red blood cells were precipitated to the bottom of the tube, only a very small number of red blood cells were

lysed. The distilled water group had no red blood cell precipitation, and the liquid in the tube appeared uniformly red. The absorbance was measured by adjusting the wavelength of the UV spectrophotometer to 545 nm. General standards stipulate that if hemolysis rate is less than 5%, the material could meet the clinical blood safety requirements. The average hemolysis rate of the FDBM group was only 1.55% (Table 2), which was much less than 5%. It can be determined that it will not cause a hemolytic reaction.

3.2.3 Pyrogen testing

The entry of substances with immunogenicity into the body induces an immune rejection reaction, which is manifested externally by increased body temperature and poor mental status (Gil-Castell et al., 2020). All New Zealand White rabbits were in good spirits and could eat normally without any abnormal reaction after the injection of the FDBM extraction solution. Body temperature testing (Figure 9) showed that the rabbits' temperature had no significant



change at a total of 6 time points over a period of 3 h after injection. All rabbits did not have an increase in body temperature of more than 0.6°C and the sum did not exceed 1.3°C. The results showed that the FDBM was free of pyrogenic reactions and complied with the provisions of the standard results composite related to pyrogenic reactions of biomedical materials.

3.2.4 Degradation in the body

After the DBM was buried subcutaneously in the rats, the rats lived in good condition and ate normally during the observation period. There was no immune rejection and allergic reactions such as swelling, redness, or seeping pus in the area of the implantation. The histological staining of subcutaneously implanted DBM is shown in Figure 10. The results showed that both groups of material were encapsulated by the fibrous capsule wall on day 3, along with a large infiltration of tissue fluid. There were some inflammatory cells entering the scaffold along the larger pores. On day 7, a small number of inflammatory cells have infiltrated the pores

of the scaffold, and the collagen fibers in the scaffold have begun to degrade and adhere to the connective tissue of the skin. On day 14, the fibrous capsule that encases the material was significantly smaller. The collagen fibrous structure became incomplete and gradually fused with the skin and cells as with normal soft tissue. On day 28, the volume of the remaining bone material was approximately 1/2 of the initial volume and degradation was evident. The inflammatory cells largely disappeared. The results show that the fish decalcified bone matrix has good biocompatibility and does not cause inflammatory reactions or immune rejection in rats. Its good *in vivo* degradability is also demonstrated.

3.3 Femoral defect repair in rats

3.3.1 Postoperative status observation

All the rats in the bone defect model woke up within 1 h after surgery, and their mental and dietary conditions were slightly poor for the first 3 days, and returned to normal after 3 days. During the whole experimental cycle, the surgical area of the rats healed well and no obvious symptoms of infection such as swelling, redness, or seeping pus were observed. Figure 11 showed that all three groups of rats had formed a larger volume of bone crust structure at the site of the bone defect at week 4 postoperatively. Among them, the self-healing group had the largest bone crust structure, and the FDBM group had a smaller bone crust structure compared with the BDBM group. The area of the femoral defect was significantly reduced in all three groups, with the FDBM group showing the greatest reduction and the self-healing group the smallest. At 8 weeks postoperatively, the bone defect area in the FDBM group was almost completely healed and the bone surface had been repaired, but the bone crust structure was still present and significantly smaller than at 4 weeks. The repair status of the BDBM group was similar to that of the FDBM group, but the bone crust structure was relatively larger. The bone defect area in the self-healing group was not completely healed in all rats, and the remaining defect area was significantly larger than the other two groups, and the bone crust structure was still significantly. At 12 weeks postoperatively, the FDBM group had the best healing status, with no capsule or encapsulation around the material. The defect surface was largely intact, with the bone crust structure largely gone. The bone defect area in the BDBM group also healed better, but there was still a relatively small bone crust structure in all rats. The defect area in the self-healing group was not repaired, and the bone crust structure was significantly larger in all rats than in the other two groups.

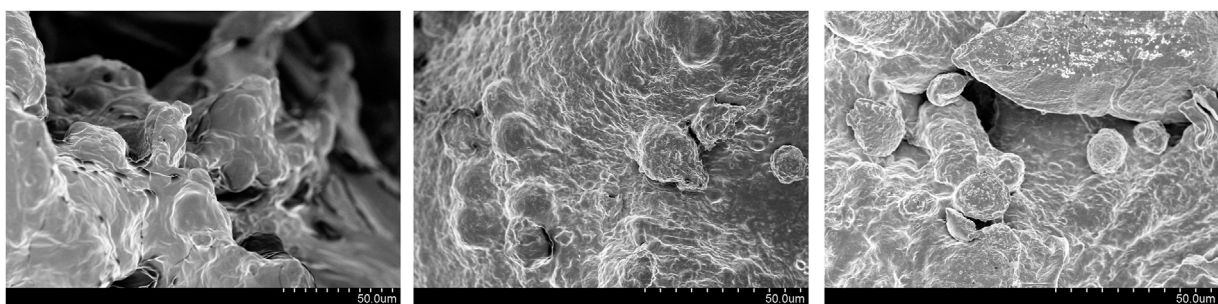


FIGURE 7
Electron microscope picture of the adhesion and growth of L929 cells on FDBM.

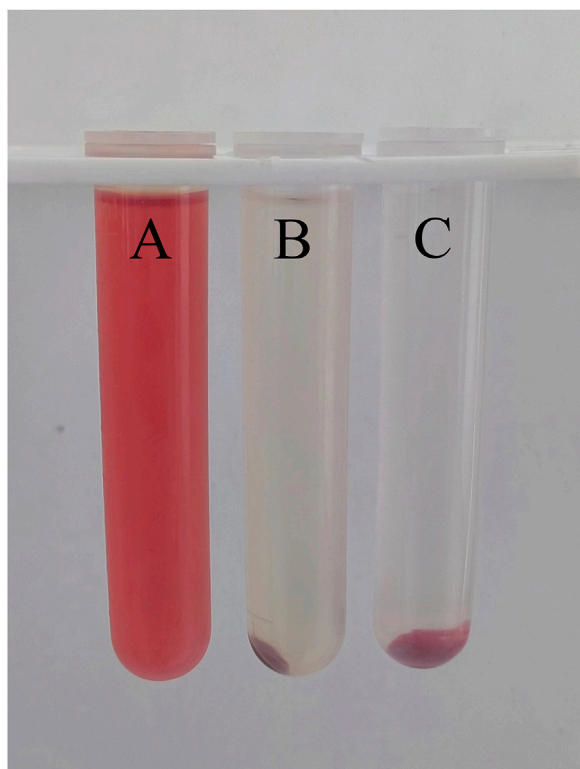


FIGURE 8

The result diagram of FDBM hemolysis (A is distilled water, B is FDBM extraction solution, C is normal saline) (n = 10 per group).

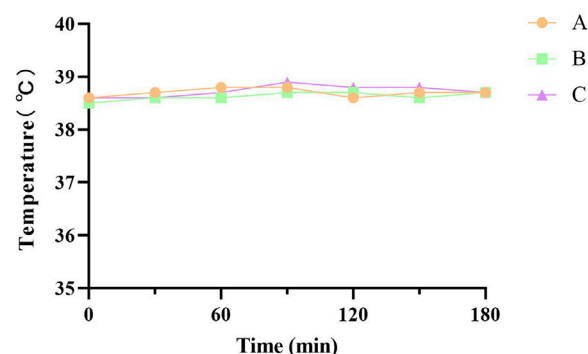


FIGURE 9

Temperature test curve of New Zealand white rabbits. A, B and C are tests on three New Zealand White rabbits (Test every 30 min Six tests in total).

At week 8 postoperatively, CT images showed varying degrees of shrinkage of the bone crust in the area of the bone defect in all three groups. In the self-healing group, the bone scab structure was the largest, and the FDBM group had a smaller bone scab structure compared to the BDBM group. In addition, the area of hypodense shadow was significantly reduced in the FDBM group, and the density of the defect area was close to that of normal femoral tissue, indicating that new bone tissue was being produced along the edges of the defect area towards the center, but complete healing of the entire defect area had not yet been achieved. In contrast, the femoral defect area in the BDBM group recovered slightly less well.

At week 12 postoperatively, only about 1/4 of the defect area in the FDBM group was slightly less dense than the high-density area, while the rest of the area was not significantly different from normal femoral tissue. This indicates that the FDBM has been resorbed, degraded and mature new bone tissue has formed at the edges and within the defect area. There is no longer any bone crust structure present on the image. The difference between the BDBM group and the FDBM group was not significant, with only a small portion of the defective area being slightly less dense than the high-density area, while the rest of the repaired defective area did not differ significantly in bone structure and density from the normal area. The self-healing group still had a large amount of bone scab structure present and the defect area showed a large hypodense shadow, mostly not replaced by new bone tissue, with poor recovery.

The CT results showed that the FDBM was superior to the BDBM in terms of speed of bone healing and denseness of the bone tissue formed, indicating that the FDBM has good osteogenic ability and is a good material for bone repair.

TABLE 2 OD and hemolysis rate in each group (n = 10, per group).

Groups	OD ($\bar{x} \pm SD$)	Average hemolysis rate (%)
Fish decalcified bone matrix (FDBM)	0.031 ± 0.004	1.55
Physiological saline (NS)	0.012 ± 0.002	-
Distilled water (DI)	1.235 ± 0.005	-

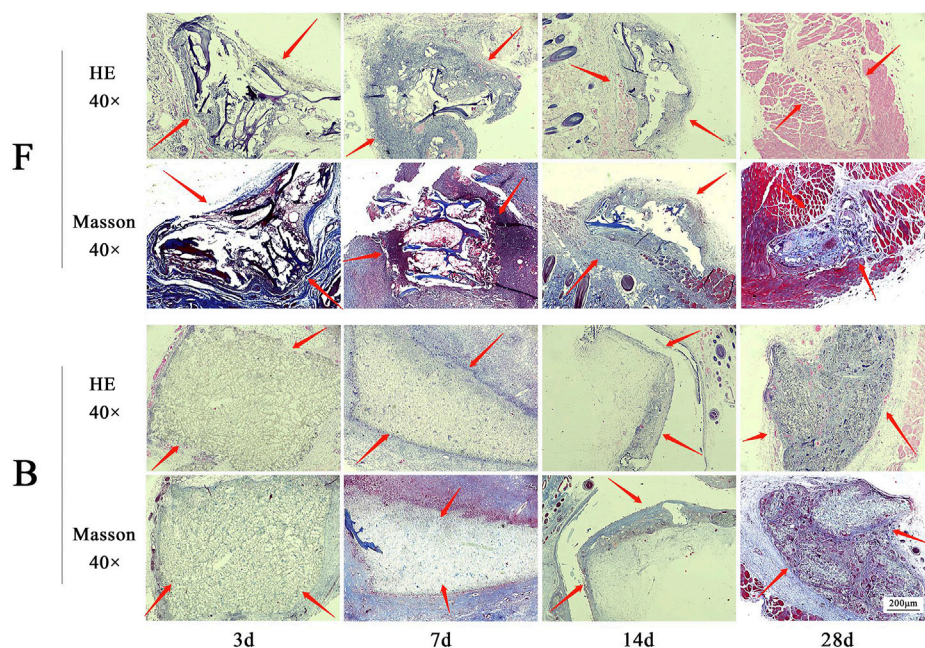
From this, it can be tentatively judged that the prepared FDBM has good ability to induce bone repair and that it repairs bone defects faster than commercially available BDBM. It can be used as a potential clinical bone repair material.

3.3.2 CT radiographic observation

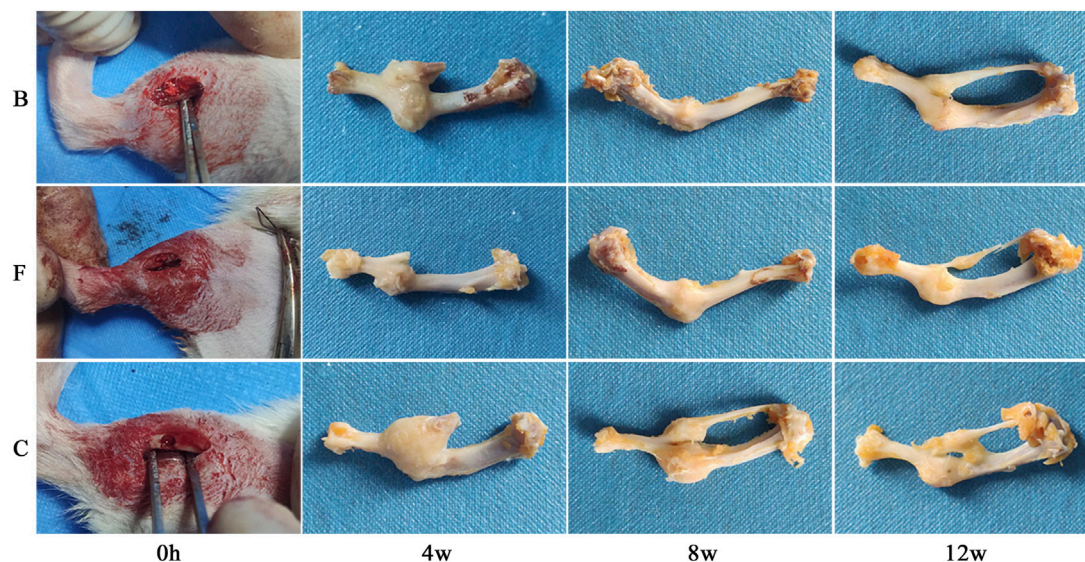
The femurs of the rats removed in 3.3.1 were subjected to CT radiographs and the image data were analyzed to observe bone repair at the defect site and degradation of the implant material (Figure 12). At week 4 postoperatively, both the self-healing group and the group filled with bone material showed varying degrees of fracture at the site of the bone defect. The edges of the defect area were clear and the size of the defect was not significantly reduced. The bone material in both groups showed a hypodense shadow that could be completely visualized and differed significantly from normal femoral tissue. There was no new bone production on the marginal bone surface of the material and the femoral defect area.

3.3.3 Histopathological analysis

The results of HE staining (Figure 13) showed that the FDBM group had been partially degraded at week 4 and the remaining material was wrapped in fibrous tissue. Newly generated bone tissue and bone trabeculae were interspersed between and at the edges of the fibrous tissue. There were also a number of inflammatory cells and osteoblasts distributed in the fibrous tissue. At week 8 postoperatively, the interior of the bone defect was covered with new bone tissue. The osteocytes are distributed among the newly created bone tissue and there are no inflammatory cells. There was still a small amount of artificial bone material located in the middle of the new bone tissue. At week

**FIGURE 10**

The results of HE and Masson staining are obtained by subcutaneously embedded FDBM and BDBM. The tissues were taken for H&E and Masson staining on the third, seventh, 14th and 28th day after implantation (magnification, $\times 40$). F is the FDBM group, B is the BDBM group (The red arrows show the implanted bone matrix).

**FIGURE 11**

Effect of repairing femoral defect (B: BDBM group; F: FDBM group; C: Self-healing group).

12 postoperatively, the entire defect area had been filled with new bone tissue and there was a significant number of osteoblasts present in the bone tissue. The area was fully integrated with the original femoral tissue, except for a small intermediate area which was slightly less integrated with the surrounding bone tissue. The BDBM group showed the same trend of bone repair as the FDBM group at the first two time points. However, at week 12, a small portion of the defective area was still filled with collagen

fibers and was not fully osteogenic. The repair effect was slightly lower than in the FDBM group. The self-healing group had the worst bone repair effect, with significantly worse bone trabeculae numbers and new bone tissue density at each time point than the FDBM group and the BDBM group. At week 12, the interior of the defect area was still relatively sparse with new bone tissue and fibrous tissue, and large areas were not completely filled.

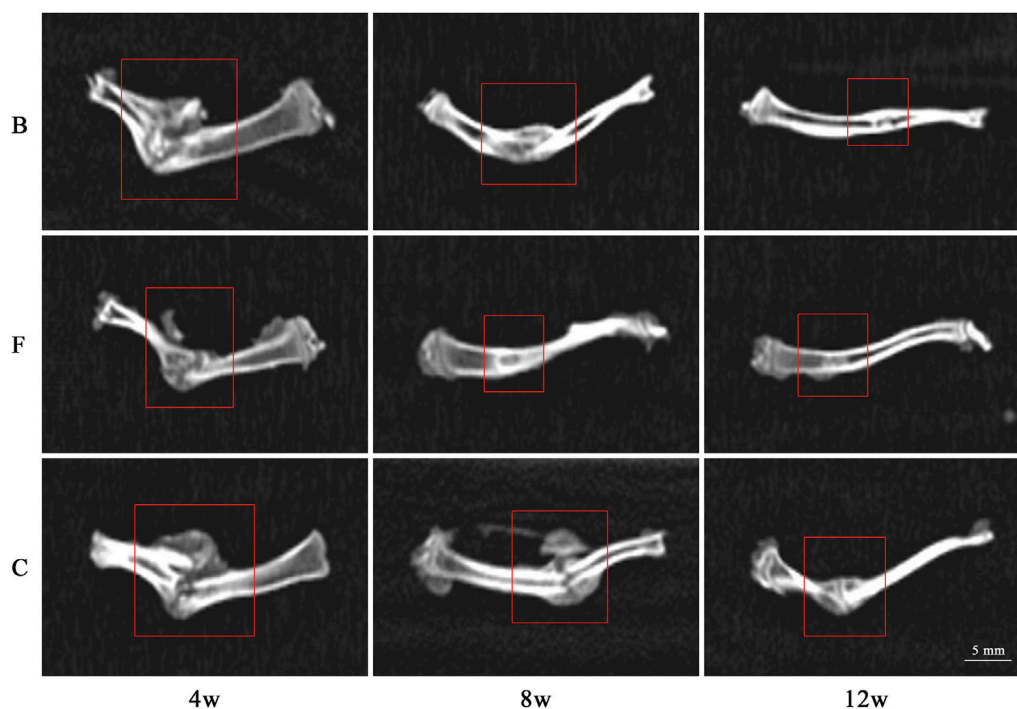


FIGURE 12
CT radiographic observation (B: BDBM group; F: FDBM group; C: Self-healing group).

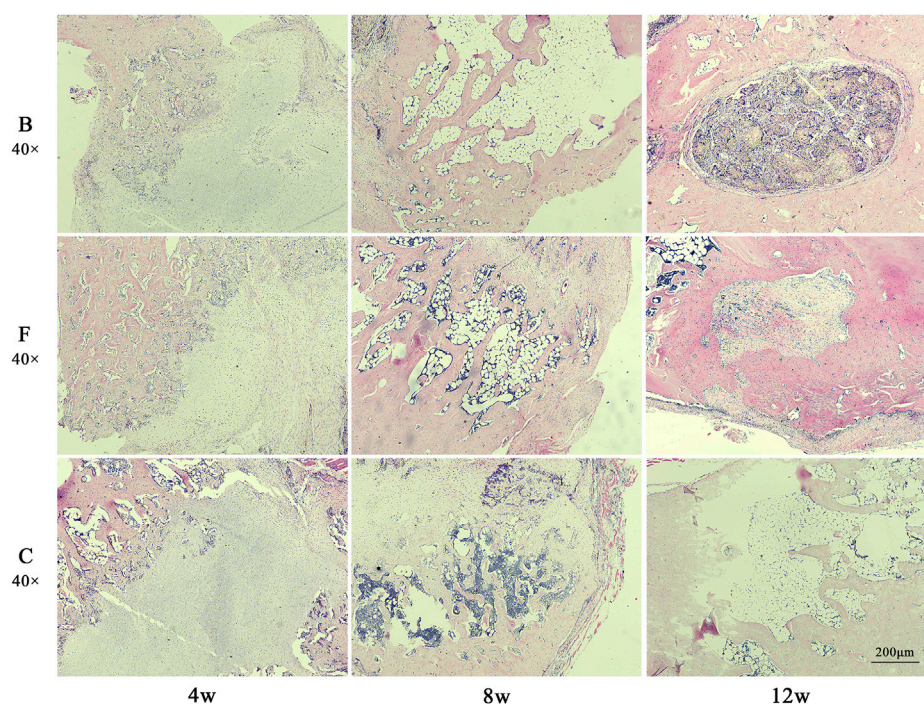
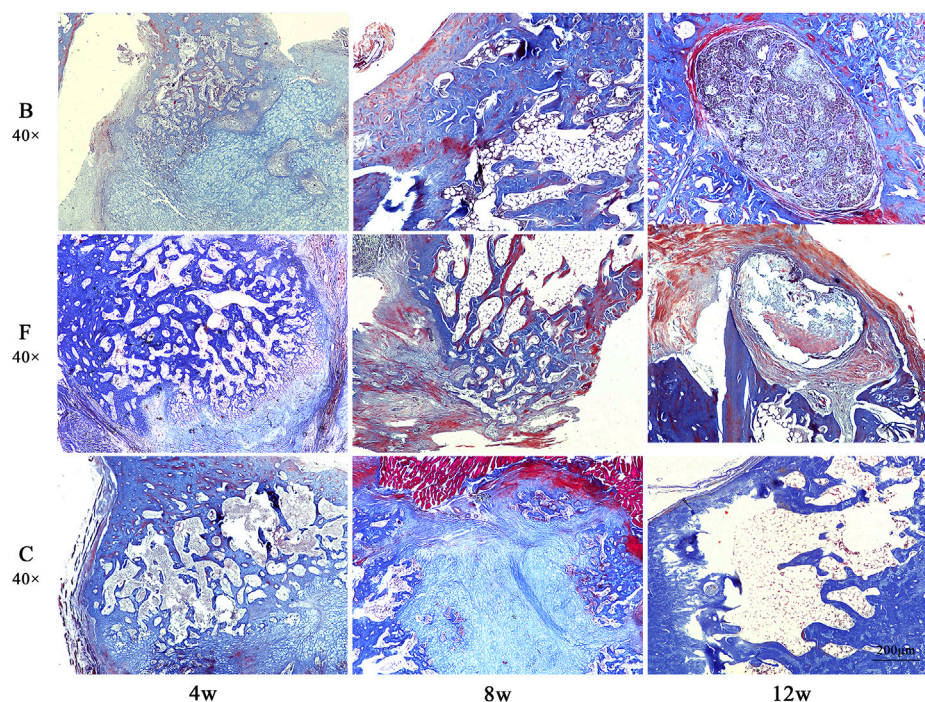


FIGURE 13
The H&E staining map of bone defects in rats. The tissues were taken for H&E staining at weeks 4, 8 and 12 after implantation (magnification, $\times 40$).

Masson staining showed (Figure 14) that at week 4 postoperatively, all three groups of defect areas were heavily filled with collagen fibers internally. A portion of the FDBM and the BDBM

were encapsulated by collagen fibers. In both bone material groups, there was some newly generated collagen and mature collagen from the edges of the defect area towards the interior, and the defect area

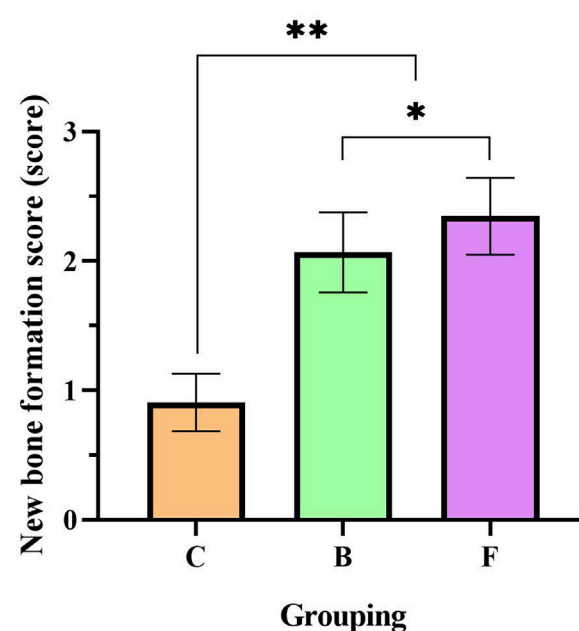
**FIGURE 14**

The Masson staining map of bone defects in rats. The tissues were taken for Masson staining at weeks 4, 8 and 12 after implantation (magnification, $\times 40$).

was not clearly demarcated. In the self-healing group, there was no new collagen around or inside the defect area and the boundary with the original bone tissue was clearly visible. At week 8 postoperatively, there was a large amount of mature and new bone tissue filling the defect area in all three groups, but the filling density was significantly higher in the two bone material groups than in the self-healing group. At week 12 postoperatively, most of the bone defect area in the FDBM group had been replaced by new bone tissue, with only a small portion of the area remaining filled with relatively sparse bone tissue, which had not yet formed a mature and dense bone structure. In the bovine decalcified bone matrix group, a small area remained filled with collagen fibers, with a small amount of new bone tissue scattered within. In the self-healing group, most of the defect area was still filled with new bone tissue and collagen fibers, and no dense bone tissue was formed.

Combining the two staining results, it was found that the FDBM did not cause any immune response in the rats and had good biocompatibility. It also has good osteogenic induction, which can guide osteoblasts to grow in and form mature bone, new bone and osteoid at the edges of the defect area and within the material to fuse with the autologous femur. The FDBM group produced more new bone tissue and trabeculae in the early stages of repair than the BDBM group, and had better overall repair capacity. While new bone was formed, the material gradually degraded and had good degradation properties in the animals. The results show that the FDBM has the ability to be used as a bone repair material.

Semi-quantitative analysis showed (Figure 15) that the new bone formation score in the self-healing group was 0.9. Compared with the self-healing group, the new bone formation score was significantly higher in the DBM group ($p < 0.01$). And the FDBM group scoring

**FIGURE 15**

New bone formation score for femoral repair at 4 weeks. (C: Self-healing group; B: BDBM group; F: FDBM group) (**: Significant difference compared to the self-healing group, $p < 0.01$; *: Significant difference compared to BDBM, $p < 0.05$).

slightly higher than the BDBM group ($p < 0.05$). With reference to the criteria of YY/T 1680–2020, it can be concluded that the FDBM has good osteoinductive potential.

4 Discussion

In reality, it is very common for people to suffer from bone defects as a result of work-related injuries, accidental injuries or injuries of medical origin. Currently, the implantation of bone tissue engineering repair materials remains the most effective method of treating patients with bone defects. Various types of bone tissue engineering materials have been widely used in clinical practice due to their excellent bone repair properties (Geng et al., 2022). However, there is still a problem of low osteogenic activity in clinical practice, which makes it difficult to meet the needs of a large number of clinical patients. In general, an ideal bone tissue engineering material should have sufficient osteoconductivity, osteoinductivity, good biocompatibility and degradability. DBM is a bone material that has been acid-treated to remove the mineral matrix, while retaining organic matter and growth factors. DBM was first reported to have an important osteogenic effect in 1965, with collagen as its main component and bone morphogenetic proteins (BMPs) with osteogenic activity but no species specificity as the rest. It is now generally accepted that the repair mechanism of implanted bone materials is to heal bone defects by promoting osteoblast growth and angiogenesis. DBM induces osteogenesis by removing the calcium salt barrier through decalcification, removing the encapsulation of calcium salts around BMPs and other osteogenic active factors and stimulating the conversion of MSCs into cartilage and osteoblasts. At the same time the decalcification process gives the DBM a natural pore structure. This not only allows the DBM to develop good plasticity, but also facilitates the slow release of BMPs and the growth of new bone and other tissues into it, thus improving the mechanical strength and enhancing the efficiency of the repair. And the antigenic surface structure of the DBM is disrupted during the acid treatment, resulting in no immune rejection and reduced morbidity at the surgical site. In our study, we use halibut fish bone that is left from the former procedure and obtained FDBM after a series of treatments, which effectively improved the utilization efficiency of fish bone and reduced solid waste.

4.1 Physicochemical properties and biocompatibility evaluation of FDBM

As a tissue engineering scaffold for bone defect repair medicine, it must have the characteristics of good porosity, mechanical strength, biocompatibility and biodegradability. The porosity of collagen materials increases with their internal surface area. During tissue repair, higher porosity of collagen materials can provide a wider space for cell adhesion, proliferation and differentiation. The results of scanning electron microscopy show that FDBM has a high porosity and basically meets the requirements of an ideal bone tissue engineering material. The mechanical strength is an important indicator to evaluate the mechanical properties of the scaffold, which indicates the effective load-bearing capacity of the material and determines the tolerance to mechanical loading during the process from new tissue growth to the degradation of the scaffold matrix (Tao et al., 2017). The mechanical strength of the prepared FDBM is similar to that of human cancellous bone. It can withstand a large degree of deformation without rupture and basically meets the requirements of bone repair materials in terms of mechanical

properties. The results showed that the treatment of incompletely decalcified can enable the scaffold to maintain a certain mechanical strength based on its good performance, which is beneficial for its application in bone tissue engineering. Additionally, because of its biodegradability, the FDBM can be de-graded by itself at the bone defects, so there is no need to take it out again, which reduces the occurrence of secondary trauma.

The rate of degradation of bone tissue engineered scaffolds is mainly determined by the nature of the material itself and the local physiological environment after implantation. *In vivo* degradation is mainly related to the action of osteoclasts and multinucleated macrophages. The rate of bone resorption by osteoclasts is higher than the rate of bone formation by osteoclasts, which can result in poor bone repair (Geng et al., 2021). During the formation of new bone, the scaffold material is broken down by components such as lysosomal enzymes released by osteoclasts. The residual fragments are engulfed by macrophages, thus allowing the scaffold material to be gradually degraded and resorbed. The results showed that the FDBM could be gradually degraded in the body, indicating it has good biosafety and biodegradability. Cell adhesion and spreading are two key factors in the regulation of cell functions (Geng et al., 2020). The results of the co-culture of cells and materials showed that the FDBM not only has high porosity, but also has good fibroblast adhesion and potential to induce fibroblast migration and growth, which fully indicates that the FDBM has good cell compatibility. Important means including hemolysis test, pyrogen test, subcutaneous implantation test, cytotoxicity test whether implanted bone tissue engineering materials are qualified. It was found that no adverse reactions occurred. The FDBM has an excellent biosafety profile and meets the requirements of a medical device.

4.2 Bone defect repair capacity of FDBM

The critical size defect (CSD) is the most commonly used model for evaluating materials for bone defect repair. Schmitz et al. define CSD as the smallest bone defect in a particular bone of a particular animal that does not heal over its lifetime (Gordon et al., 2008). Hollinger et al. define CSD as a bone defect that heals less than 10% over the life of the animal, and if this level is not reached within 1 year, the model is considered to meet the criteria for CSD (Gordon et al., 2008). However, most preclinical studies have a time limit for assessment and Gosia et al. state that “the critical size defect in animal studies is the size of the defect that does not heal during the study period” (Song et al., 2016). Female rats at 10 weeks of age were used for this experiment to ensure that the femur was of sufficient width. A 2 × 3 mm bone defect was created on the medial side of the upper middle femur of the rat. Throughout the experiment, the imaging and histological findings of the blank control group showed that the bone defect was not completely repaired and met the CSD criteria. The results show that the rat femoral bone defect model meets the requirements for discussing FDBM-based repair of femoral bone defects.

The repair of bone defects is a long and complex process. The safety and efficacy of the obtained FDBM were evaluated by bone defect repair testing in rats for 12 weeks, and compared with BDBM that have been used in clinical practice for many years. The results show that FDBM is slightly more effective than BDBM in repairing bone defects, and that it has a good *in vivo* biosafety profile, making it a promising medical biomaterial for the treatment of bone

defects. It has been suggested that DBM alone has limited osteoinductive potential and does not have the ability to promote complete repair of bone defects (Giannoudis et al., 2005; Gerhardt et al., 2011; Yannas, 2013), and some experiments have demonstrated a lack of bone regeneration despite the use of DBM in critical size defects (Larranaga et al., 2014; Tainio et al., 2017). Up to 12 weeks postoperatively, the imaging results of the DBM group still showed incomplete healing of the bone defect, possibly due to partial loss and insufficient concentration of bone forming proteins during preparation, making it difficult to develop a dose effect. However, for the time being, the prepared FDBM is better than commercially available BDBM in the treatment of bone defects and has good biocompatibility. It also effectively improves the utilization of marine resources and reduces solid waste. In conclusion, FDBM is a promising medical biomaterial for the treatment of bone defects and is expected to replace BDBM in clinical practice.

5 Conclusion

In this study, we prepared FDBM from halibut fish bone and characterized its properties. The results showed that the FDBM has good porosity, mechanical strength, biodegradability and biocompatibility, which is conducive to cell infiltration, adhesion and growth. Its good bone repair ability was confirmed in a rat bone defect model, and it can effectively induce the growth of new bone tissue, and its repair speed and quality are better than those of the commercially available BDBM. The FDBM is an artificial bone material with good application prospects, which can basically meet the clinical requirements for bone tissue repair materials.

Data availability statement

The original contributions presented in the study are included in the article/supplementary material, further inquiries can be directed to the corresponding authors.

References

- Bian, T., Zhao, K., Meng, Q., Tang, Y., Jiao, H., and Luo, J. (2019). The construction and performance of multi-level hierarchical hydroxyapatite (HA)/collagen composite implant based on biomimetic bone Haversian motif. *Mater. Des.* 162, 60–69. doi:10.1016/j.matdes.2018.11.040
- Bose, S., Roy, M., and Bandyopadhyay, A. (2012). Recent advances in bone tissue engineering scaffolds. *Trends Biotechnol.* 30, 546–554. doi:10.1016/j.tibtech.2012.07.005
- Caballe-Serrano, J., Zhang, S., Sculean, A., Staehli, A., and Bosshardt, D. D. (2020). Tissue integration and degradation of a porous collagen-based scaffold used for soft tissue augmentation. *Materials (Basel)*, 13. doi:10.3390/ma13102420
- Chen, B., Lin, H., Wang, J. H., Zhao, Y. N., Wang, B., Zhao, W. X., et al. (2007). Homogeneous osteogenesis and bone regeneration by demineralized bone matrix loading with collagen-targeting bone morphogenetic protein-2. *Biomaterials* 28, 1027–1035. doi:10.1016/j.biomaterials.2006.10.013
- Chen, J. J., Gao, K. L., Liu, S., Wang, S. J., Elango, J., Bao, B., et al. (2019). Fish collagen surgical compress repairing characteristics on wound healing process *in vivo*. *Mar. Drugs* 17, 33. doi:10.3390/md17010033
- Cho, H., Bucciarelli, A., Kim, W., Jeong, Y., Kim, N., Jung, J., et al. (2020). "Natural sources and applications of demineralized bone matrix in the field of bone and cartilage tissue engineering," in *Bioinspired biomaterials: Advances in tissue engineering and regenerative medicine* Editors H. J. Chun, R. L. Reis, A. Motta, and G. Khang.
- De Ponte, F. S., Falzea, R., Runci, M., Siniscalchi, E. N., Lauritano, F., Bramanti, E., et al. (2017). Histomorphological and clinical evaluation of maxillary alveolar ridge

Ethics statement

The animal study was reviewed and approved by the Animal Theory Committee of Yantai Lundy Biotechnology Co Ltd (approval number: LDSW2022037).

Author contributions

Conceptualization, ZL and LW; methodology, ZL, LW, XJ, and KW; validation, ZL, YZ and TL; formal analysis, ZL, YZ, and TL; resources, ZL and LW; data curation, ZL; writing—original draft preparation, ZL; writing—review and editing, ZL, LW, and JG; funding acquisition, LW and JG. All authors have read and agreed to the published version of the manuscript.

Funding

This work was supported by Department of Science and Technology of Shandong Province (No. 2019JZZY011103).

Conflict of interest

The authors declare that the research was conducted in the absence of any commercial or financial relationships that could be construed as a potential conflict of interest.

Publisher's note

All claims expressed in this article are solely those of the authors and do not necessarily represent those of their affiliated organizations, or those of the publisher, the editors and the reviewers. Any product that may be evaluated in this article, or claim that may be made by its manufacturer, is not guaranteed or endorsed by the publisher.

reconstruction after craniofacial trauma by applying combination of allogeneic and autogenous bone graft. *Chin. J. Traumatol.* 20, 14–17. doi:10.1016/j.cjtee.2016.10.005

Dimitriou, R., Jones, E., McGonagle, D., and Giannoudis, P. V. (2011). Bone regeneration: Current concepts and future directions. *Bmc Med.* 9, 66. doi:10.1186/1741-7015-9-66

Geng, Z., Ji, L., Li, Z., Wang, J., He, H., Cui, Z., et al. (2021). Nano-needle strontium-substituted apatite coating enhances osteoporotic osseointegration through promoting osteogenesis and inhibiting osteoclastogenesis. *Bioact. Mater.* 6, 905–915. doi:10.1016/j.bioactmat.2020.09.024

Geng, Z., Li, Z., Cui, Z., Wang, J., Yang, X., and Liu, C. (2020). Novel bionic topography with MiR-21 coating for improving bone-implant integration through regulating cell adhesion and angiogenesis. *Nano Lett.* 20, 7716–7721. doi:10.1021/acs.nanolett.0c03240

Geng, Z., Sang, S., Wang, S., Meng, F., Li, Z., Zhu, S., et al. (2022). Optimizing the strontium content to achieve an ideal osseointegration through balancing apatite-forming ability and osteogenic activity. *Biomater. Adv.* 133, 112647. doi:10.1016/j.msec.2022.112647

Gerhardt, L. C., Widdows, K. L., Erol, M. M., Burch, C. W., Sanz-Herrera, J. A., Ochoa, I., et al. (2011). The pro-angiogenic properties of multi-functional bioactive glass composite scaffolds. *Biomaterials* 32, 4096–4108. doi:10.1016/j.biomaterials.2011.02.032

Giannoudis, P. V., Dinopoulos, H., and Tsiridis, E. (2005). Bone substitutes: An update. *Injury-International J. Care Inj.* 36, 20–27. doi:10.1016/j.injury.2005.07.029

Gil-Castell, O., Badia, J. D., Ontoria-Oviedo, I., Castellano, D., Sepulveda, P., and Ribes-Greus, A. (2020). Polycaprolactone/gelatin-based scaffolds with tailored performance: *In vitro* and *in vivo* validation. *Mater Sci. Eng. C Mater Biol. Appl.* 107, 110296. doi:10.1016/j.msec.2019.110296

- Gordon, T., Brushart, T. M., and Chan, K. M. (2008). Augmenting nerve regeneration with electrical stimulation. *Neurological Res.* 30, 1012–1022. doi:10.1179/174313208x362488
- Hao, J. X., Bai, B. S., Ci, Z., Tang, J. C., Hu, G. H., Dai, C. X., et al. (2022). Large-sized bone defect repair by combining a decalcified bone matrix framework and bone regeneration units based on photo-crosslinkable osteogenic microgels. *Bioact. Mater.* 14, 97–109. doi:10.1016/j.bioactmat.2021.12.013
- Henkel, J., Woodruff, M. A., Epari, D. R., Steck, R., Glatt, V., Dickinson, I. C., et al. (2013). Bone regeneration based on tissue engineering conceptions - a 21st century perspective. *Bone Res.* 1, 216–248. doi:10.4248/br201303002
- Hu, Q. X., Liu, M. Y., Chen, G. B., Xu, Z. L., and Lv, Y. G. (2018). Demineralized bone scaffolds with tunable matrix stiffness for efficient bone integration. *ACS Appl. Mater. Interfaces* 10, 27669–27680. doi:10.1021/acsami.8b08668
- Ippolito, J. A., Martinez, M., Thomson, J. E., Willis, A. R., Beebe, K. S., Patterson, F. R., et al. (2019). Complications following allograft reconstruction for primary bone tumors: Considerations for management. *J. Orthop.* 16, 49–54. doi:10.1016/j.jor.2018.12.013
- Jonglareonrak, A., Benjakul, S., Visessanguan, W., Nagai, T., and Tanaka, M. (2005). Isolation and characterisation of acid and pepsin-solubilised collagens from the skin of Brownstripe red snapper (*Lutjanus vitta*). *Food Chem.* 93, 475–484. doi:10.1016/j.foodchem.2004.10.026
- Larranaga, A., Aldazabal, P., Martin, F. J., and Sarasua, J. R. (2014). Hydrolytic degradation and bioactivity of lactide and caprolactone based sponge-like scaffolds loaded with bioactive glass particles. *Polym. Degrad. Stab.* 110, 121–128. doi:10.1016/j.polymdegradstab.2014.08.021
- Lim, Y. S., Ok, Y. J., Hwang, S. Y., Kwak, J. Y., and Yoon, S. (2019). Marine collagen as A promising biomaterial for biomedical applications. *Mar. Drugs* 17, 467. doi:10.3390/md17080467
- Lv, K., Wang, L., He, X., Li, W., Han, L., and Qin, S. (2021). Application of Tilapia skin cellular dermal matrix to induce acute skin wound repair in rats. *Front. Bioeng. Biotechnol.* 9, 792344. doi:10.3389/fbioe.2021.792344
- Mishra, R., Varshney, R., Das, N., Sircar, D., and Roy, P. (2019). Synthesis and characterization of gelatin-PVP polymer composite scaffold for potential application in bone tissue engineering. *Eur. Polym. J.* 119, 155–168. doi:10.1016/j.eurpolymj.2019.07.007
- Pan, Y. X., Yang, G. G., Li, Z. W., Shi, Z. M., and Sun, Z. D. (2018). Clinical observation of biomimetic mineralized collagen artificial bone putty for bone reconstruction of calcaneus fracture. *Regen. Biomater.* 5, 61–67. doi:10.1093/rb/rbx033
- Pereira, R. S., Gorla, L. F., Boos, F., Okamoto, R., Garcia Junior, I. R., and Hochuli-Vieira, E. (2017). Use of autogenous bone and beta-tricalcium phosphate in maxillary sinus lifting: Histomorphometric study and immunohistochemical assessment of RUNX2 and VEGF. *Int. J. Oral Maxillofac. Surg.* 46, 503–510. doi:10.1016/j.ijom.2017.01.002
- Salonius, E., Kontturi, L., Laitinen, A., Haaparanta, A. M., Korhonen, M., Nystedt, J., et al. (2020). Chondrogenic differentiation of human bone marrow-derived mesenchymal stromal cells in a three-dimensional environment. *J. Cell Physiol.* 235, 3497–3507. doi:10.1002/jcp.29238
- Silva, T. H., Moreira-Silva, J., Marques, A. L. P., Domingues, A., Bayon, Y., and Reis, R. L. (2014). Marine origin collagens and its potential applications. *Mar. Drugs* 12, 5881–5901. doi:10.3390/md12125881
- Song, J. L., Sun, B. B., Liu, S., Chen, W., Zhang, Y. Z., Wang, C. Y., et al. (2016). Polymerizing pyrrole coated poly (l-lactic acid-co-ε-caprolactone) (PLCL) conductive nanofibrous conduit combined with electric stimulation for long-range peripheral nerve regeneration. *Front. Mol. Neurosci.* 9, 117. doi:10.3389/fnmol.2016.00117
- Tainio, J., Paakinaho, K., Ahola, N., Hannula, M., Hyttinen, J., Kellomaki, M., et al. (2017). *In vitro* degradation of borosilicate bioactive glass and poly(l-lactide-co-ε-caprolactone) composite scaffolds. *Materials* 10, 1274. doi:10.3390/ma10111274
- Tao, L., Zhonglong, L., Ming, X., Zezheng, Y., Zhiyuan, L., Xiaojun, Z., et al. (2017). *In vitro* and *in vivo* studies of a gelatin/carboxymethyl chitosan/LAPONITE® composite scaffold for bone tissue engineering. *RSC Adv.* 7, 54100–54110. doi:10.1039/c7ra06913h
- Wang, L., Li, W., Qu, Y., Wang, K., Lv, K., He, X., et al. (2022). Preparation of super absorbent and highly active fish collagen sponge and its hemostatic effect *in vivo* and *in vitro*. *Front. Bioeng. Biotechnol.* 10, 862532. doi:10.3389/fbioe.2022.862532
- Widdowson, J. P., Picton, A. J., Vince, V., Wright, C. J., and Mearns-Spragg, A. (2018). *In vivo* comparison of jellyfish and bovine collagen sponges as prototype medical devices. *J. Biomed. Mater. Res. B Appl. Biomater.* 106, 1524–1533. doi:10.1002/jbm.b.33959
- Yannas, I. V. (2013). Emerging rules for inducing organ regeneration. *Biomaterials* 34, 321–330. doi:10.1016/j.biomaterials.2012.10.006
- Zhang, D., Hou, J., Gu, Y., Shao, J., Zhou, S., Zhuang, J., et al. (2021). Cryopreserved skin epithelial cell sheet combined with acellular amniotic membrane as an off-the-shelf scaffold for urethral regeneration. *Mater. Sci. Eng. C Mater. Biol. Appl.* 122, 111926. doi:10.1016/j.msec.2021.111926
- Zhang, M., Powers, R. M., and Wolfinbarger, L. (1997). Effect(s) of the demineralization process on the osteoinductivity of demineralized bone matrix. *J. Periodontology* 68, 1085–1092. doi:10.1902/jop.1997.68.11.1085
- Zhang, X. Y., Chen, Y. P., Han, J., Mo, J., Dong, P. F., Zhuo, Y. H., et al. (2019). Biocompatible silk fibroin/carboxymethyl chitosan/strontium substituted hydroxyapatite/cellulose nanocrystal composite scaffolds for bone tissue engineering. *Int. J. Biol. Macromol.* 136, 1247–1257. doi:10.1016/j.ijbiomac.2019.06.172



OPEN ACCESS

EDITED BY

Chunguang Yang,
Institute of Metal Research (CAS), China

REVIEWED BY

Zhen Geng,
Shanghai University, China
Changchun Zhou,
Sichuan University, China

*CORRESPONDENCE

Long Xiong,
✉ ncxionglong2@126.com

[†]These authors have contributed equally to this work and share first authorship

SPECIALTY SECTION

This article was submitted to Biomaterials, a section of the journal Frontiers in Bioengineering and Biotechnology

RECEIVED 19 December 2022

ACCEPTED 17 March 2023

PUBLISHED 27 March 2023

CITATION

Zhou J, Xiong S, Liu M, Yang H, Wei P, Yi F, Ouyang M, Xi H, Long Z, Liu Y, Li J, Ding L and Xiong L (2023), Study on the influence of scaffold morphology and structure on osteogenic performance. *Front. Bioeng. Biotechnol.* 11:1127162. doi: 10.3389/fbioe.2023.1127162

COPYRIGHT

© 2023 Zhou, Xiong, Liu, Yang, Wei, Yi, Ouyang, Xi, Long, Liu, Li, Ding and Xiong. This is an open-access article distributed under the terms of the [Creative Commons Attribution License \(CC BY\)](https://creativecommons.org/licenses/by/4.0/). The use, distribution or reproduction in other forums is permitted, provided the original author(s) and the copyright owner(s) are credited and that the original publication in this journal is cited, in accordance with accepted academic practice. No use, distribution or reproduction is permitted which does not comply with these terms.

Study on the influence of scaffold morphology and structure on osteogenic performance

Jingyu Zhou^{1,2,3†}, Shilang Xiong^{2,4†}, Min Liu^{1,3}, Hao Yang³, Peng Wei^{1,2,3}, Feng Yi^{1,3}, Min Ouyang^{1,3}, Hanrui Xi^{1,3}, Zhisheng Long⁵, Yayun Liu⁶, Jingtang Li⁶, Linghua Ding⁷ and Long Xiong^{1*}

¹Department of Orthopedics, The Second Affiliated Hospital of Nanchang University, Nanchang, Jiangxi, China, ²Institute of Clinical Medicine, Jiangxi Provincial People's Hospital, The First Affiliated Hospital of Nanchang Medical College, Nanchang, Jiangxi, China, ³The Second Clinical Medical College of Nanchang University, Nanchang, Jiangxi, China, ⁴Department of Orthopedics, The First Affiliated Hospital of Nanchang University, Nanchang, Jiangxi, China, ⁵Department of Orthopedics, Jiangxi Provincial People's Hospital, The First Affiliated Hospital of Nanchang Medical College, Nanchang, Jiangxi, China, ⁶Department of Traumatology, Jiangxi Provincial People's Hospital, The First Affiliated Hospital of Nanchang Medical College, Nanchang, Jiangxi, China, ⁷Department of Orthopedics, Jinhua People's Hospital, Jinhua, Zhejiang, China

The number of patients with bone defects caused by various bone diseases is increasing yearly in the aging population, and people are paying increasing attention to bone tissue engineering research. Currently, the application of bone tissue engineering mainly focuses on promoting fracture healing by carrying cytokines. However, cytokines implanted into the body easily cause an immune response, and the cost is high; therefore, the clinical treatment effect is not outstanding. In recent years, some scholars have proposed the concept of tissue-induced biomaterials that can induce bone regeneration through a scaffold structure without adding cytokines. By optimizing the scaffold structure, the performance of tissue-engineered bone scaffolds is improved and the osteogenesis effect is promoted, which provides ideas for the design and improvement of tissue-engineered bones in the future. In this study, the current understanding of the bone tissue structure is summarized through the discussion of current bone tissue engineering, and the current research on micro-nano bionic structure scaffolds and their osteogenesis mechanism is analyzed and discussed.

KEYWORDS

scaffold, nanotechnology, hierarchically structured scaffold, porosity, bone tissue regeneration

1 Introduction

With the aging population, the number of patients with bone defects caused by various bone diseases is increasing annually (El-Rashidy et al., 2017). Among them, large-scale bone defects are the biggest problem faced by orthopedic surgeons, which often require multiple operations, and the clinical treatment effect is poor, leading to delayed union or non-union, and even amputation. Presently, the gold standard for the clinical treatment of bone defects is pedicled autologous bone flap transplantation; however, the source of the autologous bone is limited, which increases the risk of wound infection, causes secondary injury to patients, and aggravates their pain. Biological factors, such as adding the vascular endothelial growth

factor and bone morphogenetic protein into scaffolds, can regulate the directional differentiation of mesenchymal stem cells into vascular endothelial cells and promote bone regeneration (Won et al., 2020); however, the clinical effect is not good, the action is limited, the osteogenic effect is not ideal, and there is the possibility of inducing tumors (Silva et al., 2020; Hanusek et al., 2022). Cell or gene treatment methods have limitations such as being time-consuming, expensive, difficult to master in clinical applications, and potentially carcinogenic. The repair of massive bone defects is a clinical challenge in modern medicine, hence there is an urgent need to find a safe, convenient, and efficient means to promote bone regeneration.

In recent years, biomaterial scientists, represented by Academician Xingdong Zhang of Sichuan University, proposed the concepts of “tissue-induced biomaterials” and “*in vivo* tissue engineering” (Xing et al., 2019; Zhou et al., 2021). In other words, the microstructure design of the material is carried out to endow the material with the ability to induce tissue regeneration (Xing et al., 2019). This promotes fracture healing without the addition of growth factors. This theory suggests a new method to guide the research and development of bone regeneration materials in the future. Additionally, by improving the internal structure of the bone scaffold, the performance of the scaffold can be further optimized. by adjusting its surface morphology, which can adjust the fate of the cells and promote the progression of osteogenesis. Therefore, through a reasonable design of the scaffold, the maximum therapeutic effect of the scaffold, promotion of healing of bone defects, and alleviation of pain in patients can be achieved.

In this study, structure influencing factors influence its characteristics, the current micro-nano structure scaffold design, and the structure influence mechanism of osteogenesis. The purpose of this study was to determine the influence of the scaffold structure on the scaffold performance and cell fate.

2 Bone structure

Bone tissue is a natural nanocomposite material that is mainly composed of bone cells and a matrix around the bone cells. Bone cells are deeply embedded in a mineralized matrix, which senses mechanical stimulation and converts it into biological signals, regulates mineral homeostasis, promotes hematopoiesis and regulates secretion (Divieti Pajevic, 2013). The matrix components around the bone cells are mainly composed of organic and inorganic compounds. The main component of inorganic matter is calcium phosphate, which exists in the form of nano-hydroxyapatite crystals (Weiner et al., 1999); 90% of organic components are mainly type I collagen, and the rest are composed of lipids, growth factors, osteopontin, proteoglycan, adhesion proteins, and other molecules (Carvalho et al., 2018). Macroscopically, the bone tissue is composed of cortical and cancellous bones. Cancellous bones are mainly composed of trabeculae of different sizes, forming a high-porosity structure (up to 30%–90%) and a low elastic modulus. Cortical bones are mainly composed of a Haval bone plate, an inner interosseous plate, and an outer ring bone plate, with low porosity (5%–30%). The special structure of the bone tissue determines its special function; the high porosity of cancellous bone ensures the exchange of intramedullary nutrients and participates in

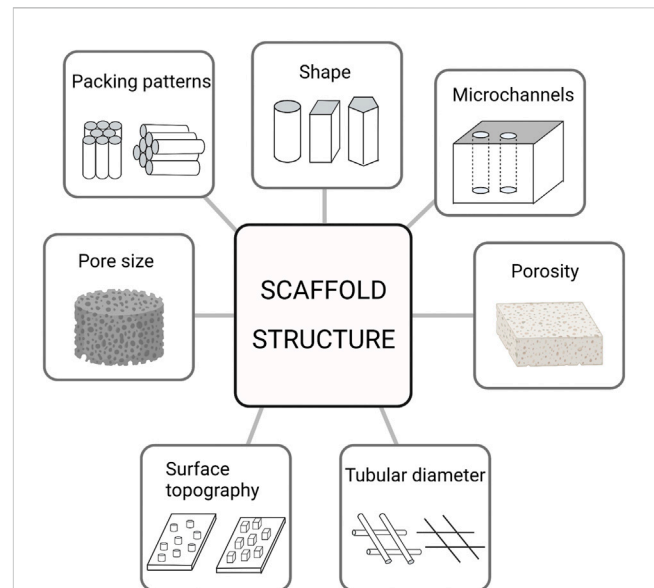


FIGURE 1
The primary structure of the scaffold at present.

the main metabolic process of bone tissue (Lin et al., 2016). The cortical bone plate is mainly composed of mineralized accumulation and precipitation of inorganic components, and the cortical bone has a high elastic modulus, high hardness, and low toughness, which play a major supporting role (Han et al., 2018). When the scaffold is implanted into a bone defect site, it mainly replaces the bone, temporarily supports the structure, and participates in the metabolism of the bone tissue. Therefore, scaffolds must have hierarchical structures and characteristics similar to those of the bone tissue. The hierarchical structure of scaffolds mainly includes macroscopic features such as the tubular diameter, shape, pore, and microchannels, and nano-microscopic features such as surface morphology and nano-pores (Figure 1). Its characteristics include inductivity, electrical conductivity, mechanical properties, hydrophilicity, hydrophobicity, cell compatibility, biodegradability, and biocompatibility. It is the key to the scaffold design for bone tissue engineering to adjust the scaffold structure and improve the scaffold characteristics (Giannitelli et al., 2014). Table 1 provides an overview about the influence of scaffold structure on scaffold characteristics.

3 Influence of structure on scaffold characteristics

3.1 Conductivity and inductivity of scaffolds

The scaffold, which has a certain conductivity, must provide a growth surface for osteoblasts from the periphery of the implant bed and directional osteoblasts in the bone marrow. The pore diameter between 0.1 mm and 0.5 mm is regarded as the best distance for bone conduction, which may be related to the proliferation of pre-osteoblasts and better initial adhesion of osteoblasts (Hollister, 2005; Murphy et al., 2010). The

TABLE 1 Influence of scaffold structure on scaffold characteristics.

Characteristic	Structure	Ref
Conductivity and inductivity	Surface characteristics	Graziano et al. (2007), Graziano et al. (2008)
	Pore size	Wang et al. (2013a), Zhang et al. (2022b)
Mechanical properties	Pore architectures	Lee et al. (2012)
	Stacking direction	Lee et al. (2012), Feng et al. (2017)
	Geometric shape	Zhao et al. (2019)
	Porosity	Boccaccio et al. (2016), Xiao et al. (2016)
Hydrophilicity and hydrophobicity	Atomic topology of Surface	Yu et al. (2018)
	Surface topography	Gagner et al. (2012), Wu et al. (2022)
	Tubular diameter	Gongadze et al. (2013)
Pore size and porosity	Pore size and porosity	Ma et al. (2000), Rnjak-Kovacina et al. (2011), Zhang et al. (2022a), Song et al. (2022)
Biodegradability	Cylindrical structure	Chew et al. (2016)
	Porosity	Zhang et al. (2019)
	Pore size	Kim et al. (2016)
Biocompatibility	Porosity	Dezfuli et al. (2012)
	Porosity distribution	Hamilton et al. (2009)

induction of scaffolds means that biomaterials directly induce peripheral mesenchymal stem cells to differentiate into bone precursor cells and osteoblasts and further form bone tissue. Presently, most artificial bone products used in clinics only have bone conductivity, poor osteo-inductivity, and weak osteogenesis, and it is still difficult to solve large bone defects clinically (Ho-Shui-Ling et al., 2018). Numerous studies have reported that the conductivity and inductivity of scaffolds are affected by their structures (Humbert et al., 2019). The surface characteristics of the scaffold are related to osteogenesis, and a concave surface of the scaffold is more conducive to osteogenesis than a convex one (Graziano et al., 2008). The cells on the microcavity-rich scaffold released a significant amount of *BMP-2* and *VEGF* into the culture medium and expressed higher alkaline phosphatase activity, which induced bone tissue formation (Graziano et al., 2007; Wang H. et al., 2013) deduced that the macro-porous structure of the HA stent is beneficial for angiogenesis and osteo-induction. Macro-porous structures ensure nutrient and metabolic waste transport, vascular ingrowth, and direct osteogenesis (Murphy et al., 2010; Wang et al., 2021). This type of pore has an optimum size. In the research by Zhang et al. (2022b), it was deduced that *in vivo* experiments, the porous structure with a size of 400 μm is more conducive to ectopic bone growth, whereas *in situ* bone defects, the porous structure with a size of 600 μm has the largest area of new bone tissue. Yamasaki and Sakai (1992) emphasized that the existence of interconnected microporous structures (2–10 μm) can endow scaffolds with osteo-inductive characteristics; inward bone growth was not observed in similar materials with a dense morphology. On one hand, micropores can provide niches for cells that preferentially undergo osteogenic differentiation, and adsorb cells to settle

in micropores by capillary forces (Polak et al., 2013). On the other hand, the microporous structure can increase the surface area of scaffolds and provides more adsorption sites for proteins or cells.

3.2 Mechanical properties of scaffolds

When the scaffold is implanted into the bone defect site, it should meet certain mechanical properties, provide support for the fracture end, and simultaneously, should be similar to the mechanical properties of human bone tissue. Otherwise, it would cause stress concentration and fracture recurrence. The mechanical properties of the scaffold are closely related to the structure, whereas those of the same material can be changed by changing the internal structure. Wang et al. (Feng et al., 2017) used a three-dimensional (3D) printing system to prepare three types of biomimetic scaffolds with different packing patterns (i.e., cross-packing, quartet close-packing, and hexagonal close-packing patterns). Among them, the compressive strength of the hexagonal dense stacked bionic scaffold was the highest (the range was 30–46 MPa). Furthermore, the mechanical properties of the scaffolds can be enhanced by controlling the pore architecture and stacking direction. Among the scaffolds made of PCL/PLGA blends, the highest compressive strength of the triangular scaffolds is 9.81 Mpa, which can be used to enhance their mechanical properties, whereas the compressive strength of lattice and staggered scaffolds is 6.05 Mpa and 7.43 Mpa, respectively (Lee et al., 2012). Presently, the influence of the differences in the construction direction, material structure, and geometric shape of the support on stress, can be determined using the finite element model to further design the support and improve its performance (Boccaccio et al., 2016; Zhao et al., 2019;

Xiao et al., 2016) used finite element modelling (FEM) to redesign the scaffold microstructure and improve its bending strength without significantly lowering its compressive strength and ability of bone regeneration *in vivo*. The data verified the prediction of the finite-element simulation. This scaffold, with a different pore gradient structure, composed of a less porous outer region and a more porous inner region, exhibited a flexural strength (34 ± 5 Mpa) that was more than twice the value of the uniform grid-like microstructure (15 ± 5 Mpa) and a higher compressive strength (88 ± 20 Mpa) than the grid-like microstructure (72 ± 10 Mpa). It can better imitate the microstructure of human long bones and provide a more reliable guarantee of bone repair.

3.3 Hydrophilicity and hydrophobicity

The hydrophilicity and hydrophobicity of the material surface affect the cell morphology and surface adhesion level. Cells can spread, proliferate, and differentiate on hydrophilic surfaces, whereas hydrophobic surfaces adsorb more proteins. The hydrophilicity and hydrophobicity of the scaffold surface are related to its topological structure, and Yu et al. (2018) showed that silica exhibits a hydrophilic-to-hydrophobic transition driven by its silanol surface density. The topological constraint theory was applied to show that the surface reactivity and hydrophilic/hydrophobic character of silica are regulated by the atomic topology of its surface. The surface structure of the scaffold can affect the hydrophilicity and hydrophobicity of the scaffold, and further, affect protein adsorption. Gagner et al. (2012) used wet chemical methods to synthesize gold nano-cubes (AuNC) with 100 facets and gold nano-ctahedra (AuNO) with 111 facets. Their chemical compositions are similar, but their protein adsorption level is different. When the protein concentration was saturated, the protein was adsorbed on AuNO with a higher surface density. The different surface structures may affect the packing density of the negatively charged ligands and further affect their affinity for protein adsorption. Wu et al. (2022) formed a nano-rod coating on a surface of the scaffold using a hydrothermal method, which improved the hydrophilicity of the scaffold. In contrast, nano-rod coating significantly increases biological activity. Moreover, by changing the internal tubular diameter of the scaffold, hydrophilicity and hydrophobicity can also be affected, thus affecting the protein adsorption level. Gongadze et al. (2013) quantitatively detected fibronectin content by ELISA and found that the adsorption of fibronectin on the surface of TiO₂ nanotubes with different diameters was quite different.

3.4 Pore size and porosity

Porosity refers to the ratio of the pore volume to the total volume of materials, which is a morphological property independent of materials (Karageorgiou and Kaplan, 2005). Natural bone, as a gradient porous structure, has a complex structure and can meet expected physiological functions. The cancellous bone is mainly composed of trabeculae with a high porosity of 50%–90%, whereas the cortical bone has only 5%–10% porosity. The pore structure is essential for cell nutrition, proliferation, migration, tissue vascularization, and new tissue formation (Salerno et al., 2012). Generally, larger pores are conducive to blood vessel growth and

abundant material exchange, which are more suitable for cell survival (Artel et al., 2011). For scaffolds with pore sizes between 250 and 500 μm , chondrocytes show preferential proliferation and ECM production (Lien et al., 2009). The pore structure facilitates cell adsorption and provides anoxic conditions that induce osteochondral formation before osteogenesis (Karageorgiou and Kaplan, 2005). However, the ability of larger pores to promote cell infiltration has been proven to override the beneficial effect of a larger initial cell attachment surface area provided by smaller pores (Loh and Choong, 2013). Presently, it is generally accepted that scaffolds with 300–800 μm through macropores and secondary capillary micropores ($\leq 10 \mu\text{m}$) inside the macropores show good osteo-inductivity (Li T.-T. et al., 2021). The porosity and pore size of a scaffold directly affect its function in biomedical applications. Porosity is proportional to the surface area, and the surface area of the scaffold material gradually increases with an increase in the porosity, which may help to transport nutrients and oxygen or make more cells grow inward; cells are more likely to adhere to the surface of the scaffold material (Cychosz et al., 2017). However, owing to the large void volume, compressive strength are reduced, and the degradation process of the scaffold is promoted (Karageorgiou and Kaplan, 2005). Additionally, the porosity and pore size affect cell proliferation and differentiation. Ma et al. (2000) constructed high porosity (HP, 89.6%, average pore size 39 μm) and low porosity (LP, 84.9%, average pore size 30 μm) using polyethylene terephthalate by hot compression technology. The proliferation rate of ED27 cells in the LP co-culture system was higher than that in the HP co-culture system, but the differentiation activity of the ED27 cells in the HP co-culture system was higher than that in the LP matrix, which may be related to the small pores in LP, limiting the cell cluster and affected cell differentiation. Additionally, the porosity and pore size can affect the ECM composition of the extracellular matrix. Fibronectin and type I collagen were deposited in fibroblasts cultured in a synthetic human elastin scaffold with high porosity and a large average pore size during cell culture, and the expression of the collagen-related marker genes was also up-regulated (Rnjak-Kovacina et al., 2011).

3.5 Biodegradability

Biomaterials should have the ability to degrade with time *in vivo* so that new tissues can grow and replace old ones, to increase the growth space for new tissues, and finally to make new bone tissues completely replace scaffolds and restore the normal physiological functions of bone defects (Yang et al., 2019). The tissue growth rate is different in different parts. For example, the lower limb requires negative weight, the fracture stabilization takes time, and material degradation time can be delayed; head and face or upper limb fracture stabilization time is relatively short, the material degradation rate can be accelerated, and the ideal biomaterial has controlled rate degradation according to the tissue growth rate. The scaffold structure is closely related to its degradability. Chew et al. (2016) prepared PLGA scaffolds with different structures to evaluate the influence of structures on scaffold degradation and found that the degradation ability of the thin strand scaffolds, which had the highest SVR, was stronger than that of the coarse and fine chain structures because the increase in the surface area allows more contact between water molecules and degradable ester groups in the

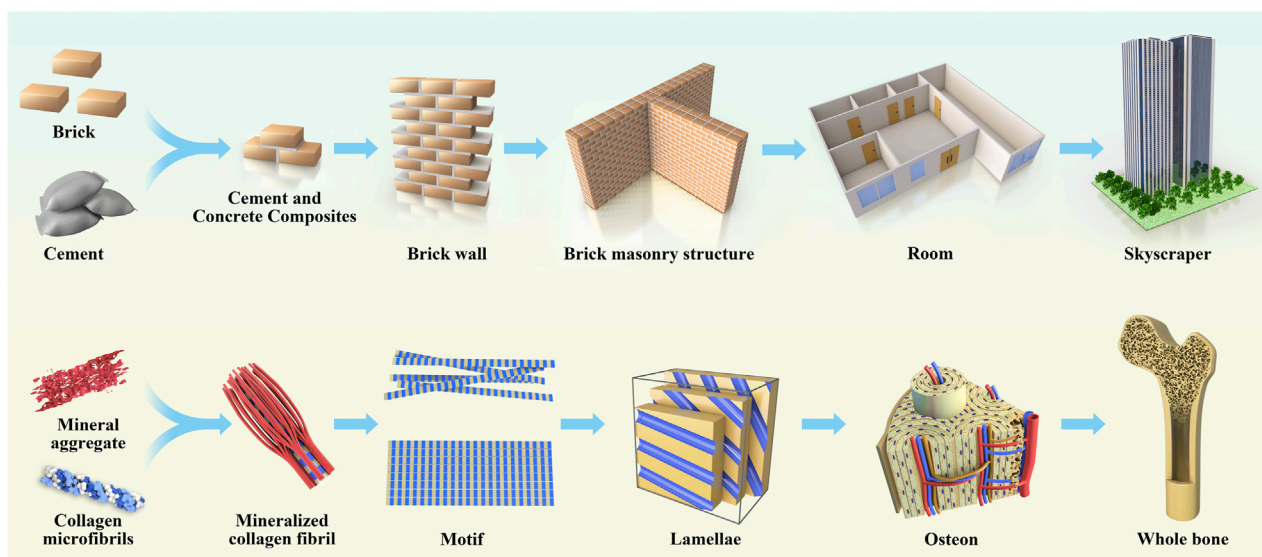


FIGURE 2

The anatomical structure of bone is analogical to architecture, which is divided according to hierarchy, and each hierarchy plays its own function and forms a whole together.

polymer. Zhang et al. (2019) prepared Ga-P scaffolds with different pores using 3D printing technology. The porosity increased non-linearly with an increase in the pore size, and the degradation rate of the scaffolds also increased. Kim et al. (2016) prepared magnesium phosphate ceramic scaffolds containing macropores (100 μm) but micropores of different sizes by combining 3D printing with salt immersion. Compared to scaffolds without micropores, scaffolds containing micropores exhibited faster biodegradation. Therefore, by improving the scaffold structure, individual schemes can be formulated to satisfy different degradation requirements.

3.6 Biocompatibility

Biocompatibility refers to the properties of living tissues that react with inactive materials (Crawford et al., 2021). Any implant in the body causes rejection. Currently, the purpose of the scaffold design is to regenerate tissues and support cell activity without causing toxic side effects or host reactions (Hussein et al., 2016). Therefore, in the design and application of stents, *in vivo* rejection must be minimized. Presently, the most common strategy is to increase the biocompatibility of scaffolds by combining them with natural materials. It is generally believed that scaffolds constructed from natural materials such as hydroxyapatite, chitosan, and collagen (Akilbekova et al., 2018) have good biocompatibility (Cheburu et al., 2011; Park et al., 2019; Cursaru et al., 2022), but natural materials are difficult to process, unstable in material properties, and poor mechanical properties, and some materials such as collagen can have immunogenicity (Shahab et al., 2012). Additionally, the scaffold structure can affect biocompatibility. Dezfali et al. (2012) deduced that the porosity distribution influences cell viability and proliferation. High porosity indicates a large surface area, and scaffold cells with a large surface area have

high viability. In addition to the shape of the scaffold, the shape of the internal particles also affects cell viability (Hamilton et al., 2009; Zhao et al., 2013) co-cultured cells with nano-sized hydroxyapatite (nHA) of different shapes. They found that needle- and plate-shaped nHA resulted in the most significant cell death in BEAS-2B cultures compared to sphere- and rod-shaped nHA.

4 Structure of scaffold

4.1 Hierarchical structure of bone

Natural bone is a non-homogeneous anisotropic nano-composite material whose main components are organized in layers into several structural levels ranging from macroscopic to nanoscale levels (Figure 2). The cognition of the hierarchical structure of bone tissue is a gradual process. Weiner et al. (1999) first proposed that the lamellar bone is composed of lamellar unit structures by measuring the angle deviation of the collagen fibers using an SEM microscope and proposed that the lamellar bone has seven hierarchical structures. In 2014, Reznikov et al. (2014) proposed a three-dimensional bone by the focused ion beam electron microscopy and serial surface observation method for further observation of the architecture and proposed further improvements to this theory by dividing the lamellar bone into nine structures. In 2018, the structure of mineralized collagen fibers was subdivided using STEM tomography, followed by the proposal in Science that the natural bone has a complex multilayered structure at different scales ranging from the millimeter level to the micro-nanometer level for a total of 12 levels (Reznikov et al., 2018). Natural bone contains a rich hierarchical structure that provides directions for scaffold construction and structural optimization. The construction of multi-level structural scaffolds from the macroscale to the microcosmic bone by simulating the natural bone structure is a major challenge in current bone tissue engineering.

4.2 Hierarchical structure of the scaffold

The rich hierarchical structure is a typical feature of the natural bone structure, which not only provides excellent biological properties to materials but also provides an ideal microenvironment *in vivo*, which contains rich and diverse signal clues affecting the cell fate (Iacoviello et al., 2020). Current bone repair biomaterial scaffolds aim to reproduce such a microenvironment, promote inward cell growth and differentiation, and be applied in the vascularization of osteogenesis. Therefore, biomaterial scaffolds with porous nanostructures and 3D layered structures are the most promising bone substitutes for simulating natural bones (Vordemvenne et al., 2020; Luo et al., 2020) simulated the dimensions of fibers in human extracellular matrix (ECM) using the membrane-liquid interface culture method, to produce a novel bacterial cellulose/cellulose acetate scaffold, which exhibited an interpenetrated nano (42 nm) and submicron (820 nm) fibrous structure and contained nanopores and macropores. The novel scaffold exhibited enhanced cell proliferation, alkaline phosphatase activity, and gene and protein expression compared to single bacterial cellulose and cellulose acetate scaffolds. Thomas et al. (Vordemvenne et al., 2020) studied collagen sponges. They observed that the collagen sponge had $60.66 \pm 24.48 \mu\text{m}$ pores and $32.97 \pm 1.41 \text{ nm}$ nano-pores, and coated it with SiO_2 nanoparticles with a size of approximately 146 nm to cover up the original morphology and structure. Subsequently, the levels of bone growth and healing decreased in the skull defect model. Zhang et al. (Wu et al., 2020) fabricated biomimetic natural wood-like hierarchically structured scaffolds with first-level macropores ($\sim 100\text{--}600 \mu\text{m}$) and second-level micro/nanoscale pores ($\sim 100\text{--}10,000 \text{ nm}$) by 3D printing technology. A micro/nano-whisker coating was prepared on the surface of the scaffold by hydrothermal treatment. This hierarchically structured scaffold exhibited excellent osteo-inductive activity. Li et al. (2019) inspired by the composition, structure, and function of hot dogs, printed hollow bioceramic tubes through improved 3D nozzles through 3D printing technology and bidirectional freezing technology and well-dispersed bioceramic slurry was placed in hollow ceramic tubes and fixed by bidirectional freezing technology. Finally, ice crystals were sublimated by the freeze-drying method. Finally, a hierarchical hot dog scaffold composed of a hollow tube structure embedded with a bioceramic rod and a uniformly arranged layered microstructure was successfully prepared. Compared to a non-hot dog-like system with the same chemical composition, this layered hot dog-like structure had a double-layer macro-porous and microporous structure, and its drug loading capacity and drug release time were significantly improved. The drug release time was 90 days. The scaffold has a large surface area, which is beneficial for cell adhesion and can promote the expression of osteogenic genes, such as *Runx2*, *OCN*, and *OPN*.

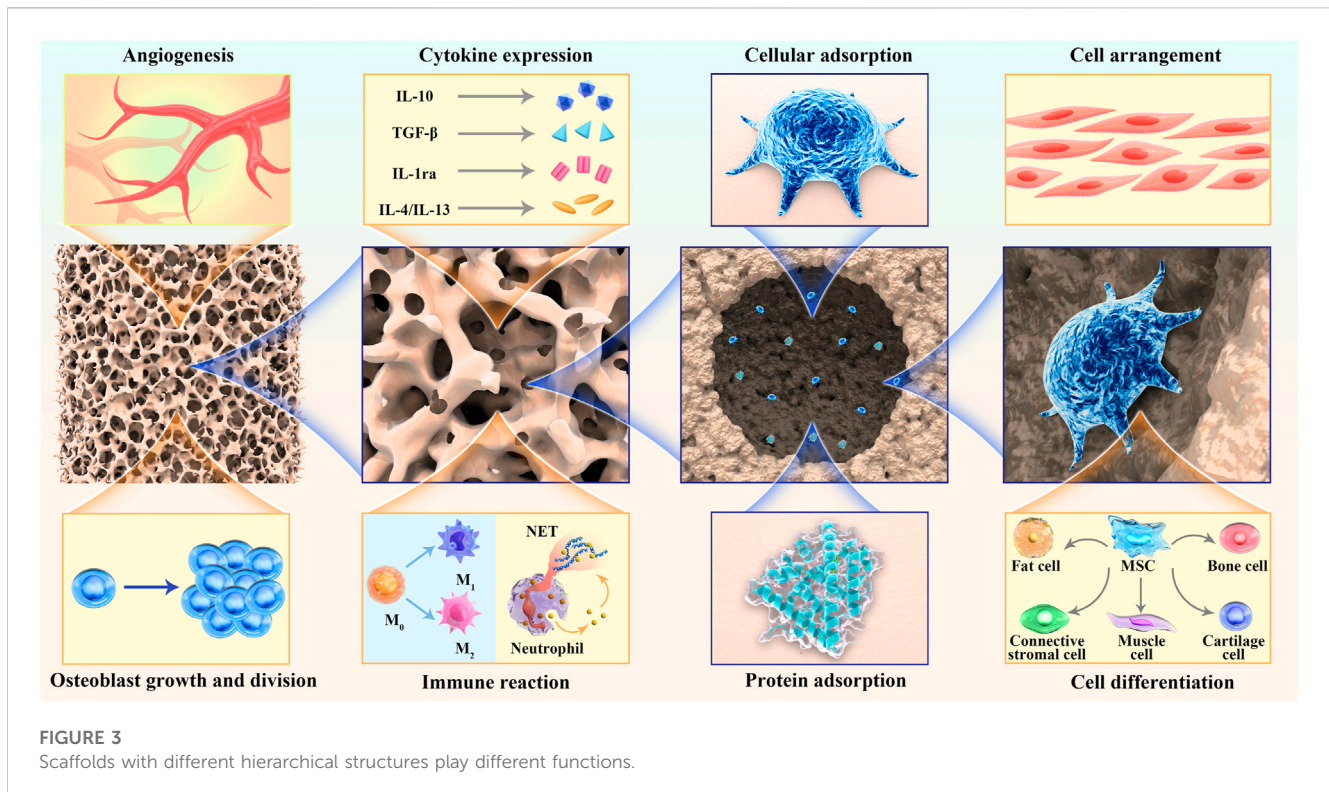
4.3 Macrostructure of scaffold

Current studies have confirmed that different scales of hierarchical structures have different functions (Figure 3): small structures ($<10 \mu\text{m}$) are more easily impregnated by tissue fluid, creating more sites for cell adsorption (Perez and Mestres, 2016); medium structures ($20\text{--}40 \mu\text{m}$) help promote the conversion of primary macrophages to the M2 type and upregulate anti-inflammatory gene expression to suppress the host immune response to grafts (Sadtler et al., 2016), which facilitates the inward growth of host cells, especially MSCs; the large scale structures

($>100 \mu\text{m}$) facilitate angiogenesis, cell homing, and colonization, and provide a site for cell colony formation (Karageorgiou and Kaplan, 2005; Murphy et al., 2010; Zhang et al., 2018). Additionally, the size of the pore structure affects cell proliferation and differentiation. Adipose stem cells were inoculated onto PCL stents prepared with different pore sizes ($100 \mu\text{m}$, $200 \mu\text{m}$, and $400 \mu\text{m}$) and placed under chondrogenic differentiation conditions for 21 days. The results showed that for the $100 \mu\text{m}$ and $200 \mu\text{m}$ pore sizes, the ASC cells were evenly distributed and proliferated in higher numbers, whereas in the $400 \mu\text{m}$ pore size scaffolds, the cells tended to aggregate, and proteoglycan production and chondrogenic markers were significantly higher in the $400 \mu\text{m}$ pore size scaffolds than in the $100 \mu\text{m}$ and $200 \mu\text{m}$ pore sizes (Im et al., 2012). Although many 3D-printed biological scaffolds with high porosity have been prepared for tissue regeneration, the micropores in the scaffolds cannot form channel structures, which hinders the formation of the basic vascular system and internal new bone tissue (Yan et al., 2019; Liu et al., 2023). Adding microchannels to the scaffold can induce endothelial cells to form a basic vascular system, promote oxygen/nutrition perfusion, and induce tissues to grow inward along these channels (Rnjak-Kovacina et al., 2019; Wen et al., 2021). Feng et al. (2017) fabricated lotus-root-like biomimetic materials with parallel multichannel structures *via* a modified 3D printing strategy. Owing to the existence of microchannels, the porosity and specific surface area of this bionic structure material were obviously improved. Compared with traditional 3D printing materials, lotus root-like bionic materials have significantly improved the attachment and proliferation of BMSCs *in vitro* and osteogenesis, as well as angiogenesis *in vivo*.

4.4 Nano-microstructure of scaffold

The nanostructured composition of the bone tissue consists mainly of nano-hydroxyapatite and collagen fibers. The main component of hydroxyapatite is calcium phosphate crystals, which are mainly located inside collagen fibers. In contrast, collagen, as an endogenous structural protein, makes up the organic component of the bone tissue, formed mainly by the self-assembly of three amino acid peptide chains with $31.93 \pm 14 \text{ nm}$ pores on the surface (Greiner et al., 2019), providing an attachment surface for the hydroxyapatite crystals (Xu et al., 2020) and promoting their better mineralization (Nudelman et al., 2010). During bone formation, nHA crystals are mainly arranged along the c-axis parallel to the collagen fibers and organize the biomineralization along the fibers in a periodic, staggered fashion, and thus constitute the main nanostructure of the bone tissue (He et al., 1999). This kind of nano-microstructure structure mainly involves nano-scale, including surface morphology and nano-pores. Nanostructures are essential for tissue engineering, not only to modulate hydroxyapatite crystal mineralization but to increase the mechanical strength of the bone and further influence physical and chemical properties, such as the crystal polymorphism and melting point after crystal nucleation (Hamilton et al., 2012; Jiang and Ward, 2014) but also to guide cells to assemble and attach in a specific way or a specific area on the scaffold, ultimately affecting the fate of the cells (Singh et al., 2014). Some studies have shown that the preparation of nanotube structures with diameters ranging from 30 to 50 nm by mimicking the surface pores of collagen fibers can promote mineralization (Yang et al., 2014; Minagar et al., 2015; Zhang et al., 2017). In a study by Cantaert et al. (2013), it was observed that the pore



size was closely related to the degree of crystal orientation, and the degree of crystal orientation at 50 nm was better than that at 200 nm. Moreover, numerous studies have shown that the nanosphere structure affects the biological properties (Manoukian et al., 2018). Zhen et al. deduced that nano-topology exhibits better cell adhesion and proliferation than micro-topology, thus increasing the biomechanical strength of implants (Geng et al., 2020b). Meanwhile, Xia and his research team (Xia et al., 2020) deduced that increasing the nanopore diameter inhibits the initial adhesion of BMSC cells, but can promote a larger diffusion area of cells and an increased expression level of ALP, osteopontin, osteocalcin, and type I collagen, which are more favorable for osteogenesis. Greiner et al. successfully constructed self-assembled silica nanoparticles by a thermally induced cross-linking reaction with oleic acid-silica nanocomposites with a pore size of approximately 34 ± 14 nm and demonstrated that the surface pore size of endogenous type I collagen fibers could promote stem cell osteogenic differentiation (Greiner et al., 2019). Moreover, surface nano-topography is sufficient to regulate cellular behavior. Park et al. prepared vertical titanium dioxide nanotubes with diameters of 15 nm and 100 nm, and MSCs grown on 15 nm diameter nanotubes exhibited increased expression of the bone morphogenetic protein-2, which promoted osteogenic differentiation, whereas the 100 nm diameter nanotubes exhibited reduced cell adhesion levels, increased apoptosis, and promoted chondrogenic differentiation (Oh et al., 2009). Dalby et al. prepared nanogroove structures of different depths using polymer layering and colloid lithography. Cytoskeleton staining of the HMSCs cell co-culture revealed that the cell spreading area increased and the expression of the stress fibers increased. Additionally, HMSCs react strongly to surface features down to 10 nm in height with a low aspect ratio and enriched osteoblast differentiation (Dalby et al., 2006a).

In conclusion, the microstructure of the scaffold plays a different role depending on the surrounding bone tissue hierarchy, constructing bone regeneration scaffolds, further studying the biological properties of different layers of bone tissue, and providing a basis for subsequent studies on multilevel structural scaffolds. However, the effect of these scaffold structures on osteogenesis can be summarized as follows.

5 Mechanism of scaffold structure promoting osteogenesis

5.1 Biomechanics of material morphology

The internal structure of a material can induce cell deformation and regulate gene expression (Liu and Ding, 2020). When the material is implanted into the body, the cells adhere to the surface of the material, and the material morphology induces cell deformation, causing changes in the cell surface pressure and internal tension, which are transmitted to the nucleus through a series of signals, which finally causes the cells to respond (Campbell and Humphries, 2011; Könnig et al., 2018). Therefore, extracellular matrix mechanical signals play a crucial role in the regulation of physiological processes, such as the maintenance of the cell behavior and function (Hannezo and Heisenberg, 2019). It is important for the development, growth, and maintenance of the bone. Numerous receptors (Nguyen and Jacobs, 2013; Bertrand et al., 2020), are distributed on the surface of bone cells and participate in cell mechanical transduction. Integrin-containing focal adhesions, *Wnt* receptors, including Lrp5, primary cilia, voltage-gated calcium channels, and connexin-based gap junctions are the major

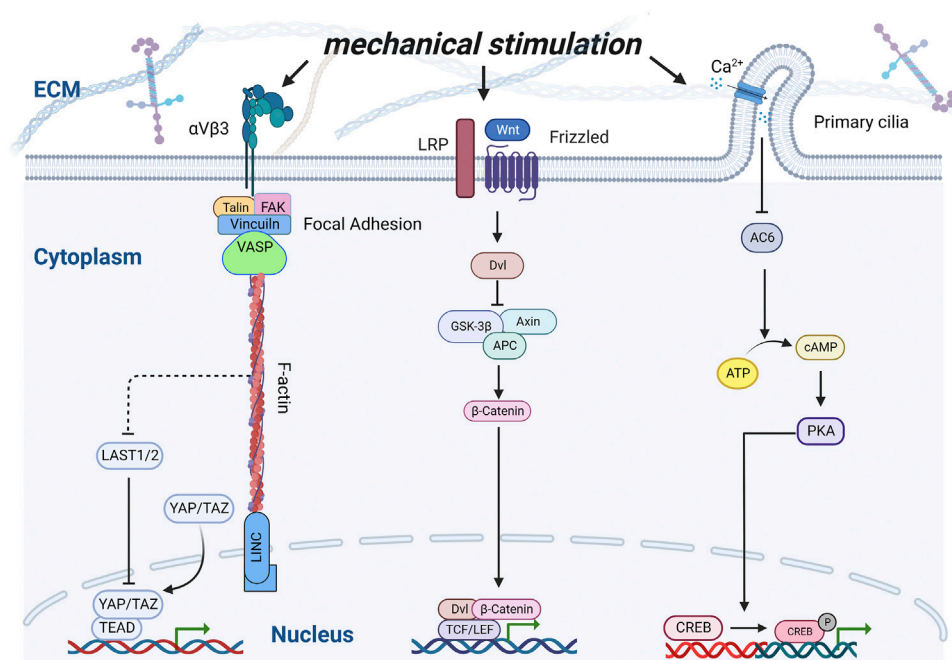


FIGURE 4

Schematic of interactions of various signaling pathways under mechanical stimulation. Integrins, Wnt receptors, and Ca^{2+} channels were stimulated by mechanical stimulation, thereby inducing a series of transcription factors to regulate osteoblast proliferation and differentiation.

mechanisms implicated in bone cells (Li X. et al., 2021) (Figure 4). When a mechanical force acts on the cell membrane, it stimulates the autophosphorylation of the focal adhesion kinase (Michael et al., 2009), and further promotes the sliding of F-actin on myosin II, which causes the contraction of the cytoskeleton and finally transmits it to the linker of the nucleoskeleton and cytoskeleton complex, thus regulating the transport of the transcription factors (Wang et al., 2005; Speight et al., 2016). Zhen et al. affected the mineralization of the surface coating by adjusting the pH. Compared with the flake morphology prepared at low pH, the expression levels of ITG $\alpha 5$ and ITG $\beta 1$ related to the cell adhesion level increased on the surface nano-needle strontium-substituted apatite coating prepared at high pH, and the expression of related osteogenesis related genes such as Runx2, ALP, Col-I, and OCN also increased significantly (Geng et al., 2021). Moreover, F-actin opposes the Yes-associated protein (YAP) and transcriptional coactivator with PDZ-binding motif (TAZ) phosphorylation through inhibition of the kinases *LATS1* and *LATS2* (Halder et al., 2012). As a transcriptional co-activator, YAP/TAZ can up-regulate the expression of the vascular endothelial growth factor, transforming growth factor- β (TGF- β), bone morphogenetic protein-2 (BMP-2), and other growth factors (Pefani et al., 2016; Azad et al., 2018; Sivaraj et al., 2020), and plays an important role in the fracture healing process (Zarka et al., 2021). In scaffolds, high curvature surfaces or small pores (<125 μm diameter) can up-regulate the phosphorylation of YAP-related proteins, whereas relatively low curvature or large pores (>250 μm diameter) can down-regulate the phosphorylation of YAP and increase its nuclear translocation, and transcriptional activation reverses osteogenic differentiation (Swanson et al., 2022). The mechanical stimulation of the *Wnt* pathway involves binding of the *Wnt* ligand to the transmembrane receptor *Fzd*, which forms a

complex with *LRP5*. *Wnt-Fzd* binding causes *Dvl* to inhibit *Axin/APC/GSK-3 β* , releasing β -catenin to the nucleus and binding to the *TCF/LEF* family as a coactivator of transcription (Bertrand et al., 2020), which can up-regulate the expression of osteoblast-related genes, such as *Col-1*, *ALP* and *OCN*, thus controlling the osteoblast differentiation and bone development (Li et al., 2018). Primary cilia are mechanically sensitive to flow and serve as part of the calcium signaling system (Saternos et al., 2020). Flow-induced calcium influx inhibits adenylyl cyclase 6, which in turn leads to a decrease in the cyclic AMP and activated protein kinase levels, thus promoting the transformation of MSC into osteoblasts (Siddappa et al., 2009; Nguyen and Jacobs, 2013).

5.2 Bone immune mechanism

Although tissue-engineered bone scaffolds have biocompatibility, the host immune response is an inevitable stage after tissue-engineered bone implantation (Vishwakarma et al., 2016). The initial inflammatory response following biomaterial implantation aids in tissue repair and regeneration; however, persistent inflammation impairs the wound-healing response (Julier et al., 2017).

The material structure and morphology can regulate the bone immune response and promote bone repair (Zheng et al., 2019). When the scaffold was implanted, neutrophils migrated around the scaffold within 24 h and prepared to recruit immune cells by secreting cytokines and releasing neutrophil extracellular traps (NETs). When neutrophils adhere to the surface of the scaffold (extracellular matrix), they are activated to excrete DNA and form neutrophil extracellular traps (NETs) (Schoen et al., 2022; Won

et al., 2020) fabricated hierarchically structured “microchannel” 3D printed scaffolds by the 3D printing of a polycaprolactone polymer. Compared to non-microchannel scaffolds made of the same material, the neutrophil-capturing net can be reduced, which is beneficial for tissue repair. Additionally, different levels of extracellular neutrophil capture can be induced by adjusting the template components and diameters during electrospinning, and the capture net can be significantly reduced by increasing the fiber diameter (Fetz et al., 2017).

Macrophages are among the most important immune cells. As early responders after biomaterial implantation, they play a significant role in guiding angiogenesis and tissue remodeling and are closely related to bone remodeling (Guo et al., 2020). Macrophages are usually divided into M1 and M2 phenotypes: M1 macrophages act as pro-inflammatory factors and can release a large number of cytokines such as IL1 β , IL8, and TNF α through exosomes, which can cause a series of immune responses (Recalcati et al., 2010; Gao et al., 2016); in contrast to M1, the M2 macrophages mainly release cytokines such as IL10, which inhibit inflammatory responses, promote anabolism such as osteogenesis and angiogenesis, and play a key role in wound healing, tissue repair and other processes (Italiani and Boraschi, 2014; Lee et al., 2019). The surface morphology and microstructure of scaffolds can influence the immune response of the body. The special scaffold structure can reduce macrophages to M1, polarize them to M2, and further regulate angiogenesis and osteogenesis. The most important factors are the particle size (Lebre et al., 2017), porosity (Jordan et al., 2018), and pore size (Chan et al., 2022) of the scaffold structure. Tylek et al. (2020) constructed square porous polycaprolactone fiber scaffolds with different structural shapes using 3D printing technology, with pore sizes ranging from 100 μ m to 40 μ m. These scaffolds promoted the extension of macrophages and are differentiated into the M2 type, which was most obvious on scaffolds with a pore size of 40 μ m. Zheng et al. (2019) regulated the surface structure of the scaffold using near-infrared radiation from a flat surface to a groove-like surface structure, which causes macrophage phenotype changes. Garg et al. (2013) deduced that an increase in the fiber diameter in the electro spun scaffold can promote the transformation of macrophages to M2 macrophages *in vitro*. The 100 nm nanostructure produced on Ti by anodic oxidation is beneficial to M1 macrophages, whereas 30 nm is beneficial to M2 polarization. Cell elongation induces the release of cytokines (IL-4 and IL-13) and polarizes macrophages to the M2-like phenotype, indicating that the cell shape plays a role in the regulation of phenotypic polarization (McWhorter et al., 2013).

5.3 Adsorption mechanism of peripheral protein

The influence of the material structure on cells or host reactions is mainly realized by affecting the adsorption behavior of proteins on the surface of materials. When a biomaterial is implanted as a foreign body, its surface is in contact with the extracellular environment, and proteins are usually adsorbed on the surface of the biomaterial earlier than the cells (Puleo and Nanci, 1999). Cells can recognize specific peptide domains in this protein, further regulate their fate, and ultimately affect the biological properties

of the scaffolds (Lutolf and Hubbell, 2005). Therefore, increasing protein surface coverage can improve cell adhesion and diffusion (Atif et al., 2022). The structure of the scaffold affects the protein adsorption level. Increasing the number of micropore structures can also increase the interaction between the scaffold and serum proteins, which may be an attractive strategy to promote the osteo-inductivity and osteo-conductivity of scaffolds (Perez and Mestres, 2016). These proteins can then stimulate osteogenic-related cell functions, such as attachment, proliferation, osteogenic differentiation, and biomineralization (Wang et al., 2014). The microporosity and micropore size of the scaffolds have a significant influence on the protein adsorption characteristics. HA and BCP particles with higher and/or more micropores can adsorb more fibrinogen and insulin (Zhu et al., 2010). The rich microporous structure and relatively high body surface area of the scaffold can promote the adsorption of osteogenesis-related proteins, which leads to new bone formation (Campion et al., 2011; Wang J. et al., 2013) studied the effects of calcium phosphate ceramic particles with different structures on protein adsorption using a dynamic protein adsorption device. Under simulated dynamic conditions, the phase composition and microstructure of the CaP ceramics affect their protein adsorption capacity. Among them, spherical hydroxyapatite and biphasic calcium phosphate ceramic particles prepared by spray drying sintering with abundant micropores and high specific surface area have a higher adsorption capacity for serum proteins such as fibronectin and vitronectin, which is beneficial for cell adhesion. Simultaneously, the protein adsorbed on the implanted scaffold can regulate immune activity and play a significant role in macrophage adhesion, activation, and foreign body giant cell formation (Dadsetan et al., 2004).

5.4 Cell adhesion mechanism

Cell adhesion is one of the basic life activities of cells, and plays a key role in regulating proliferation, maintaining activity, differentiation and migration. Cell adhesion is related to transmembrane proteins on the cell surface, such as integrin and cadherin (Niessen et al., 2011). These transmembrane proteins can interact with the ECM, directly or indirectly regulate the proliferation of stem cells, and promote cell adhesion and multidirectional differentiation (Abdal Dayem et al., 2018). Some related studies have shown that the micro-nanomorphology of the scaffold surface can affect the adsorption level of cells (Acevedo-Morantes et al., 2012; Li H. et al., 2021). Geng et al. (2020a) simulated a continuous deep pit-like surface structure inside the gill cover of a snail on the surface of a titanium implant to increase the adsorption level of cells. Filova et al. (2015) prepared nanotubes with different diameters by adjusting the voltage of the Ti-6Al-4V alloy. After the co-culture of Saos-2 cells, the adsorption level of the former cells increased significantly compared with that of the cells cultured on glass plates. The surface of this type of metal stent is negatively charged and the surface charge density at the sharp edge is high. Therefore, the surface charge density of small-diameter nanotubes is high, which promotes the adsorption of the fibronectin and vitronectin molecules and proteins with a quadrupolar internal charge distribution, resulting in more

effective adhesion and diffusion of osteoblasts to scaffolds and the promotion of osteogenic effects (Kabaso et al., 2011; Gongadze et al., 2013). Different fiber diameters also affect cell adhesion and morphology. When cells contact coarse fibers, they tend to adhere to the surface of the coarse fibers as a whole and fill pores in a circular manner; When coming into contact with fine fibers, the cells tend to wrap fine fibers at one end, thus forming a “bypass”. Consequently, the cells exhibited an obvious directional growth trend on a specific arrangement of thick and thin fibers (Xie et al., 2019). Moreover, the richer the hierarchical structure of the materials, the richer the adsorption effect. Wang et al. prepared a TiO₂ nanotube structure based on a micron trabecular bone structure by anodic oxidation and formed a micro-nano gradient coexistence bionic structure. Compared to pure titanium and micron-trabecular bone groups with lower structural levels, it was deduced that a rich hierarchical structure can effectively promote the adhesion, proliferation, and osteogenic differentiation of BMSCs (Jang et al., 2017). For example, adding nanoscale structures on the surface of the scaffold using a laser can promote the adhesion function of BMSCs and promote osteogenesis (Šugár et al., 2021). Bone progenitor cell differentiation can point to the osteoblast phenotype by reducing the size of the nano-morphology to 10 nm (Dalby et al., 2006b).

6 Influence of manufacturing process on scaffold structure

The fabrication process affects the structure of the scaffold. Generally, to prepare a specific scaffold structure, it is necessary to use a specific preparation method. Presently, the most common methods for preparing pore scaffolds are freeze-drying (Brougham et al., 2017), electrospinning (Yan et al., 2020), and gas foaming (Chen et al., 2021); however, these methods cannot effectively control the pore structure. With the update of 3D printing technology, new technologies such as digital light projection printing can quickly manufacture composites with complex pore structures, adjust the pore structure parameters (Zhang et al., 2022a; Song et al., 2022), and accurately control the shape of scaffolding. Therefore, geometric structures with different shapes can be accurately manufactured by computer aided design (CAD) (Zopf et al., 2015), such as complex geometric objects or artificial organ frames. For the topological structure of the scaffold surface, nano-coating is often used to cover the scaffold surface by hydrothermal deposition, or the scaffold surface is patterned directly by laser micromachining (Aguilar et al., 2005; Geng et al., 2020) prepared the texture topology of the operculum of a river snail on a Ti surface using electrochemical corrosion and anodic oxidation. Strontium-doped apatite was then deposited on the surface by hydrothermal deposition. Moreover, 3D printing technology can be easily processed for microchannel structures with a simple structure. Microchannels with complex structures can be constructed using the sacrificial template method (Jeon et al., 2023; Saggiomo and Velders, 2015) proposed a simple two-step acrylonitrile butadiene styrene (ABS) scaffold removal method that can be used to realize 3D multilayer complex micron channels in a single block of polydimethylsiloxane.

7 Outlook, perspective, and conclusion

The process of the osteogenic differentiation of mesenchymal stem cells is influenced by the external matrix. In natural bone, cells grow in an external matrix with a hierarchical structure, after which, the scaffold is implanted into the body and the extracellular environment is exposed in the scaffold. Therefore, by imitating the natural bone structure, optimizing the scaffold structure can regulate cell growth and differentiation and provide a suitable external environment for cells. Scaffolds with different structures have different functions, such as macropores and microchannels, which are beneficial for blood vessel growth; a concave surface is beneficial for bone formation and micropores are beneficial for cell adsorption. These functions can affect the characteristics of the scaffold, and the scaffold can be used to the maximum extent using a reasonable design. Technological innovations in preparation methods such as photo-curing 3D printing and the sacrificial template method, or through scaffold hierarchical structure innovations such as bionic technology to improve the scaffold structure, create new possibilities for new micro-nano bionic scaffolds and the development of bone tissue engineering. Moreover, the osteogenic mechanism of the scaffold structures remains unclear. It mainly is in the classical pathway but lacks the interaction between scaffolds and signal molecules. In the future, through transcriptome analysis, single-cell sequencing and other technologies can be used to deeply explore the principle of the structural influence on osteogenesis.

Author contributions

LX and JZ initiated the project and made suggestions and revised the article. JZ and SX wrote the manuscript. JZ, ML, HY, PW, FY, HX, and MO searched the database, wrote, and made the figures. LX, JZ, ZL, YL, JL, and LD offered the support of the fund. All authors reviewed and commented on the entire manuscript and approved it for publication.

Funding

This work was supported by the National Natural Science Foundation of China (32060222, 82160354, 82160528), the Natural Science Foundation of Jiangxi Province (2021BAB206059, 20224ACB206012), the Jiangxi Graduate Innovation Special Fund (No. YC2022-s208), the Jinhua Science and Technology Plan Project (No. 2022-4-148).

Acknowledgments

Figure 1 and Figure 4 created with BioRender.com.

Conflict of interest

The authors declare that the research was conducted in the absence of any commercial or financial relationships that could be construed as a potential conflict of interest.

Publisher's note

All claims expressed in this article are solely those of the authors and do not necessarily represent those of their affiliated

References

- Abdal Dayem, A., Lee, S., Y Choi, H., and Cho, S.-G. (2018). The impact of adhesion molecules on the *in vitro* culture and differentiation of stem cells. *Biotechnol. J.* 13 (2), 1700575. doi:10.1002/biot.201700575
- Acedo-Morantes, C. Y., Irizarry-Ortiz, R. A., Caceres-Valencia, P. G., Singh, S. P., and Ramirez-Vick, J. E. (2012). Combinatorial growth of oxide nanoscaffolds and its influence in osteoblast cell adhesion. *J. Appl. Phys.* 111 (10), 102810. doi:10.1063/1.4714727
- Aguilar, C. A., Lu, Y., Mao, S., and Chen, S. (2005). Direct micro-patterning of biodegradable polymers using ultraviolet and femtosecond lasers. *Biomaterials* 26 (36), 7642–7649. doi:10.1016/j.biomaterials.2005.04.053
- Akilbekova, D., Shaimerdenova, M., Adilov, S., and Berillo, D. (2018). Biocompatible scaffolds based on natural polymers for regenerative medicine. *Int. J. Biol. Macromol.* 114, 324–333. doi:10.1016/j.jbiomac.2018.03.116
- Artel, A., Mehdiadeh, H., Chiu, Y.-C., Brey, E. M., and Cinar, A. (2011). An agent-based model for the investigation of neovascularization within porous scaffolds. *Tissue Eng. Part A* 17 (17–18), 2133–2141. doi:10.1089/ten.tea.2010.0571
- Atif, A.-R., La Cis, U., Engqvist, H., Tenje, M., Bagheri, S., and Mestres, G. (2022). Experimental characterization and mathematical modeling of the adsorption of proteins and cells on biomimetic hydroxyapatite. *ACS Omega* 7 (1), 908–920. doi:10.1021/acsomega.1c05540
- Azad, T., Janse van Rensburg, H. J., Lightbody, E. D., Neveu, B., Champagne, A., Ghaffari, A., et al. (2018). A LATS biosensor screen identifies VEGFR as a regulator of the Hippo pathway in angiogenesis. *Nat. Commun.* 9 (1), 1061. doi:10.1038/s41467-018-03278-w
- Bertrand, A. A., Malapati, S. H., Yamaguchi, D. T., and Lee, J. C. (2020). The intersection of mechanotransduction and regenerative osteogenic materials. *Adv. Healthc. Mater.* 9 (20), e2000709. doi:10.1002/adhm.202000709
- Boccaccio, A., Uva, A. E., Fiorentino, M., Mori, G., and Monno, G. (2016). Geometry design optimization of functionally graded scaffolds for bone tissue engineering: A mechanobiological approach. *PloS One* 11 (1), e0146935. doi:10.1371/journal.pone.0146935
- Brougham, C. M., Levingstone, T. J., Shen, N., Cooney, G. M., Jockenhoevel, S., Flanagan, T. C., et al. (2017). Freeze-drying as a novel biofabrication method for achieving a controlled microarchitecture within large, complex natural biomaterial scaffolds. *Adv. Healthc. Mater.* 6 (21), 1700598. doi:10.1002/adhm.201700598
- Campbell, I. D., and Humphries, M. J. (2011). Integrin structure, activation, and interactions. *Cold Spring Harb. Perspect. Biol.* 3 (3), a004994. doi:10.1101/cshperspect.a004994
- Campion, C. R., Chander, C., Buckland, T., and Hing, K. (2011). Increasing strut porosity in silicate-substituted calcium-phosphate bone graft substitutes enhances osteogenesis. *J. Biomed. Mater. Res. Part B, Appl. Biomaterials* 97 (2), 245–254. doi:10.1002/jbm.b.31807
- Cantaert, B., Benias, E., and Meldrum, F. C. (2013). Nanoscale confinement controls the crystallization of calcium phosphate: Relevance to bone formation. *Chem. (Weinheim Der Bergstrasse, Ger.)* 19 (44), 14918–14924. doi:10.1002/chem.201302835
- Carvalho, M. S., Poundarik, A. A., Cabral, J. M. S., da Silva, C. L., and Vashishth, D. (2018). Biomimetic matrices for rapidly forming mineralized bone tissue based on stem cell-mediated osteogenesis. *Sci. Rep.* 8 (1), 14388. doi:10.1038/s41598-018-32794-4
- Chan, N. R., Hwang, B., Ratner, B. D., and Bryers, J. D. (2022). Monocytes contribute to a pro-healing response in 40 μ m diameter uniform-pore, precision-templated scaffolds. *J. Tissue Eng. Regen. Med.* 16 (3), 297–310. doi:10.1002/term.3280
- Cheburu, C.-N., Stoica, B., Neamtu, A., and Vasile, C. (2011). Biocompatibility testing of chitosan hydrogels. *Rev. Medico-chirurgica Soc. Medici Si Nat. Din Iasi* 115 (3), 864–870.
- Chen, Y., Jia, Z., Shafiq, M., Xie, X., Xiao, X., Castro, R., et al. (2021). Gas foaming of electrospun poly(L-lactide-co-caprolactone)/silk fibroin nanofiber scaffolds to promote cellular infiltration and tissue regeneration. *Colloids Surfaces. B, Biointerfaces* 201, 111637. doi:10.1016/j.colsurfb.2021.111637
- Chew, S. A., Arriaga, M. A., and Hinojosa, V. A. (2016). Effects of surface area to volume ratio of PLGA scaffolds with different architectures on scaffold degradation characteristics and drug release kinetics. *J. Biomed. Mater. Res. Part A* 104 (5), 1202–1211. doi:10.1002/jbm.a.35657
- Crawford, L., Wyatt, M., Bryers, J., and Ratner, B. (2021). Biocompatibility evolves: Phenomenology to toxicology to regeneration. *Adv. Healthc. Mater.* 10 (11), e2002153. doi:10.1002/adhm.202002153
- Cursaru, L. M., Iota, M., Piticescu, R. M., Tarnita, D., Savu, S. V., Savu, I. D., et al. (2022). Hydroxyapatite from natural sources for medical applications. *Mater. (Basel, Switz.)* 15 (15), 5091. doi:10.3390/ma15155091
- Cychosz, K. A., Guillet-Nicolas, R., Garcia-Martinez, J., and Thommes, M. (2017). Recent advances in the textural characterization of hierarchically structured nanoporous materials. *Chem. Soc. Rev.* 46 (2), 389–414. doi:10.1039/c6cs00391e
- Dadsetan, M., Jones, J. A., Hiltner, A., and Anderson, J. M. (2004). Surface chemistry mediates adhesive structure, cytoskeletal organization, and fusion of macrophages. *J. Biomed. Mater. Res. Part A* 71 (3), 439–448. doi:10.1002/jbm.a.30165
- Dalby, M. J., McCloy, D., Robertson, M., Agheli, H., Sutherland, D., Affrossman, S., et al. (2006a). Osteoprogenitor response to semi-ordered and random nanotopographies. *Biomaterials* 27 (15), 2980–2987. doi:10.1016/j.biomaterials.2006.01.010
- Dalby, M. J., McCloy, D., Robertson, M., Wilkinson, C. D. W., and Oreffo, R. O. C. (2006b). Osteoprogenitor response to defined topographies with nanoscale depths. *Biomaterials* 27 (8), 1306–1315. doi:10.1016/j.biomaterials.2005.08.028
- Dezfuli, S. N., Sadrnezhad, S. K., Shokrgozar, M. A., and Bonakdar, S. (2012). Fabrication of biocompatible titanium scaffolds using space holder technique. *J. Mater. Sci. Mater. Med.* 23 (10), 2483–2488. doi:10.1007/s10856-012-4706-3
- Divieti Pajevic, P. (2013). Recent progress in osteocyte research. *Endocrinol. Metabolism (Seoul, Korea)* 28 (4), 255–261. doi:10.3803/EnM.2013.28.4.255
- El-Rashidy, A. A., Roether, J. A., Harhaus, L., Kneser, U., and Boccaccini, A. R. (2017). Regenerating bone with bioactive glass scaffolds: A review of *in vivo* studies in bone defect models. *Acta Biomater.* 62, 1–28. doi:10.1016/j.actbio.2017.08.030
- Feng, C., Zhang, W., Deng, C., Li, G., Chang, J., Zhang, Z., et al. (2017). 3D printing of Lotus root-like biomimetic materials for cell delivery and tissue regeneration. *Adv. Sci. (Weinheim, Baden-Wuerttemberg, Ger.)* 4 (12), 1700401. doi:10.1002/advs.201700401
- Fetz, A. E., Neeli, I., Rodriguez, I. A., Radic, M. Z., and Bowlin, G. L. (2017). Electrospun template architecture and composition regulate neutrophil NETosis *in vitro* and *in vivo*. *Tissue Eng. Part A* 23 (19–20), 1054–1063. doi:10.1089/ten.TEA.2016.0452
- Filova, E., Fojt, J., Kryslava, M., Moravec, H., Joska, L., and Bacakova, L. (2015). The diameter of nanotubes formed on Ti-6Al-4V alloy controls the adhesion and differentiation of Saos-2 cells. *Int. J. Nanomedicine* 10, 7145–7163. doi:10.2147/IJN.S87474
- Gagner, J. E., Qian, X., Lopez, M. M., Dordick, J. S., and Siegel, R. W. (2012). Effect of gold nanoparticle structure on the conformation and function of adsorbed proteins. *Biomaterials* 33 (33), 8503–8516. doi:10.1016/j.biomaterials.2012.07.009
- Gao, X., Wang, Y.-S., Li, X.-Q., Hou, H.-Y., Su, J.-B., Yao, L.-B., et al. (2016). Macrophages promote vasculogenesis of retinal neovascularization in an oxygen-induced retinopathy model in mice. *Cell Tissue Res.* 364 (3), 599–610. doi:10.1007/s00441-015-2353-y
- Garg, K., Pullen, N. A., Oskertizian, C. A., Ryan, J. J., and Bowlin, G. L. (2013). Macrophage functional polarization (M1/M2) in response to varying fiber and pore dimensions of electrospun scaffolds. *Biomaterials* 34 (18), 4439–4451. doi:10.1016/j.biomaterials.2013.02.065
- Geng, Z., Ji, L., Li, Z., Wang, J., He, H., Cui, Z., et al. (2021). Nano-needle strontium-substituted apatite coating enhances osteoporotic osseointegration through promoting osteogenesis and inhibiting osteoclastogenesis. *Bioact. Mater.* 6 (4), 905–915. doi:10.1016/j.bioactmat.2020.09.024
- Geng, Z., Li, X., Ji, L., Li, Z., Zhu, S., Cui, Z., et al. (2020b). A novel snail-inspired bionic design of titanium with strontium-substituted hydroxyapatite coating for promoting osseointegration. *J. Mater. Sci. Technol.* 79 (0), 35–45. doi:10.1016/j.jmst.2020.11.041
- Geng, Z., Li, Z., Cui, Z., Wang, J., Yang, X., and Liu, C. (2020a). Novel bionic topography with MiR-21 coating for improving bone-implant integration through regulating cell adhesion and angiogenesis. *Nano Lett.* 20 (10), 7716–7721. doi:10.1021/acs.nanolett.0c03240
- Giannitelli, S. M., Accoto, D., Trombetta, M., and Rainer, A. (2014). Current trends in the design of scaffolds for computer-aided tissue engineering. *Acta Biomater.* 10 (2), 580–594. doi:10.1016/j.actbio.2013.10.024

- Gongadze, E., Kabaso, D., Bauer, S., Park, J., Schmuki, P., and Igljč, A. (2013). Adhesion of osteoblasts to a vertically aligned TiO₂ nanotube surface. *Mini Rev. Med. Chem.* 13 (2), 194–200. doi:10.2174/1389557511313020002
- Graziano, A., d'Aquino, R., Cusella-De Angelis, M. G., De Francesco, F., Giordano, A., Laino, G., et al. (2008). Scaffold's surface geometry significantly affects human stem cell bone tissue engineering. *J. Cell. Physiology* 214 (1), 166–172. doi:10.1002/jcp.21175
- Graziano, A., d'Aquino, R., Cusella-De Angelis, M. G., Laino, G., Piattelli, A., Pacifici, M., et al. (2007). Concave pit-containing scaffold surfaces improve stem cell-derived osteoblast performance and lead to significant bone tissue formation. *PLoS One* 2 (6), e496. doi:10.1371/journal.pone.0000496
- Greiner, J. F., Gottschalk, M., Fokin, N., Bükler, B., Kaltschmidt, B. P., Dreyer, A., et al. (2019). Natural and synthetic nanopores directing osteogenic differentiation of human stem cells. *Nanomedicine Nanotechnol. Biol. Med.* 17, 319–328. doi:10.1016/j.nano.2019.01.018
- Guo, S., Yu, D., Xiao, X., Liu, W., Wu, Z., Shi, L., et al. (2020). A vessel subtype beneficial for osteogenesis enhanced by strontium-doped sodium titanate nanorods by modulating macrophage polarization. *J. Mater. Chem. B* 8 (28), 6048–6058. doi:10.1039/d0tb00282h
- Halder, G., Dupont, S., and Piccolo, S. (2012). Transduction of mechanical and cytoskeletal cues by YAP and TAZ. *Nat. Rev. Mol. Cell Biol.* 13 (9), 591–600. doi:10.1038/nrm3416
- Hamilton, B. D., Ha, J.-M., Hillmyer, M. A., and Ward, M. D. (2012). Manipulating crystal growth and polymorphism by confinement in nanoscale crystallization chambers. *Accounts Chem. Res.* 45 (3), 414–423. doi:10.1021/ar200147v
- Hamilton, R. F., Wu, N., Porter, D., Buford, M., Wolfarth, M., and Holian, A. (2009). Particle length-dependent titanium dioxide nanomaterials toxicity and bioactivity. *Part. Fibre Toxicol.* 6, 35. doi:10.1186/1743-8977-6-35
- Han, C., Li, Y., Wang, Q., Wen, S., Wei, Q., Yan, C., et al. (2018). Continuous functionally graded porous titanium scaffolds manufactured by selective laser melting for bone implants. *J. Mech. Behav. Biomed. Mater.* 80, 119–127. doi:10.1016/j.jmbm.2018.01.013
- Hannezo, E., and Heisenberg, C.-P. (2019). Mechanochemical feedback loops in development and disease. *Cell* 178 (1), 12–25. doi:10.1016/j.cell.2019.05.052
- Hanusek, K., Rybicka, B., Poplawski, P., Adamiak-Ostrowska, A., Gluchowska, K., Pieklik-Witkowska, A., et al. (2022). TGF- β 1 affects the renal cancer miRNome and regulates tumor cells proliferation. *Int. J. Mol. Med.* 49 (4), 52. doi:10.3892/ijmm.2022.5108
- He, C., Chen, H., Li, L., Chen, M., Chen, Y., and Wu, W. (1999). Changes of biomechanical properties in goats at different times after ovariectomy. *Sheng Wu Yi Xue Gong Cheng Xue Za Zhi* 16 (3), 295–299.
- Ho-Shui-Ling, A., Bolander, J., Rustom, L. E., Johnson, A. W., Luyten, F. P., and Picart, C. (2018). Bone regeneration strategies: Engineered scaffolds, bioactive molecules and stem cells current stage and future perspectives. *Biomaterials* 180, 143–162. doi:10.1016/j.biomaterials.2018.07.017
- Hollister, S. J. (2005). Porous scaffold design for tissue engineering. *Nat. Mater.* 4 (7), 518–524. doi:10.1038/nmat1421
- Humbert, P., Brennan, M. A., Davison, N., Rosset, P., Trichet, V., Blanchard, F., et al. (2019). Immune modulation by transplanted calcium phosphate biomaterials and human mesenchymal stromal cells in bone regeneration. *Front. Immunol.* 10, 663. doi:10.3389/fimmu.2019.00663
- Hussein, K. H., Park, K.-M., Kang, K.-S., and Woo, H.-M. (2016). Biocompatibility evaluation of tissue-engineered decellularized scaffolds for biomedical application. *Mater. Sci. Eng. C, Mater. For Biol. Appl.* 67, 766–778. doi:10.1016/j.msec.2016.05.068
- Iacoviello, F., Kirby, A. C., Javanmardi, Y., Moendarbary, E., Shabanli, M., Tsolaki, E., et al. (2020). The multiscale hierarchical structure of *Heloderma suspectum* osteoderms and their mechanical properties. *Acta Biomater.* 107, 194–203. doi:10.1016/j.actbio.2020.02.029
- Im, G.-I., Ko, J.-Y., and Lee, J. H. (2012). Chondrogenesis of adipose stem cells in a porous polymer scaffold: Influence of the pore size. *Cell Transplant.* 21 (11), 2397–2405. doi:10.3727/096368912X638865
- Italiani, P., and Boraschi, D. (2014). From monocytes to M1/M2 macrophages: Phenotypical vs. Functional differentiation. *Front. Immunol.* 5, 514. doi:10.3389/fimmu.2014.00514
- Jang, I., Choi, D.-S., Lee, J.-K., Kim, W.-T., Cha, B.-K., and Choi, W.-Y. (2017). Effect of drug-loaded TiO₂ nanotube arrays on osseointegration in an orthodontic miniscrew: An *in-vivo* pilot study. *Biomed. Microdevices* 19 (4), 94. doi:10.1007/s10544-017-0237-5
- Jeon, D.-G., Lee, M., Heo, J., Lee, S., Boo, Y., and Nam, S.-W. (2023). 3D sacrificial microchannels by scaffold removal process for electrical characterization of electrolytes. *Electron. Mater. Lett.* 2023. doi:10.1007/s13391-022-00402-3
- Jiang, Q., and Ward, M. D. (2014). Crystallization under nanoscale confinement. *Chem. Soc. Rev.* 43 (7), 2066–2079. doi:10.1039/c3cs60234f
- Jordan, S. W., Fligor, J. E., Janes, L. E., and Dumanian, G. A. (2018). Implant porosity and the foreign body response. *Plastic Reconstr. Surg.* 141 (1), 103e–112e. doi:10.1097/PRS.00000000000003930
- Julier, Z., Park, A. J., Briquez, P. S., and Martino, M. M. (2017). Promoting tissue regeneration by modulating the immune system. *Acta Biomater.* 53, 13–28. doi:10.1016/j.actbio.2017.01.056
- Kabaso, D., Gongadze, E., Perutková, S., Matschegewski, C., Kraljic-Igljč, V., Beck, U., et al. (2011). Mechanics and electrostatics of the interactions between osteoblasts and titanium surface. *Comput. Methods Biomechanics Biomed. Eng.* 14 (5), 469–482. doi:10.1080/10255842.2010.534986
- Karageorgiou, V., and Kaplan, D. (2005). Porosity of 3D biomaterial scaffolds and osteogenesis. *Biomaterials* 26 (27), 5474–5491. doi:10.1016/j.biomaterials.2005.02.002
- Kim, J.-A., Lim, J., Naren, R., Yun, H.-S., and Park, E. K. (2016). Effect of the biodegradation rate controlled by pore structures in magnesium phosphate ceramic scaffolds on bone tissue regeneration *in vivo*. *Acta Biomater.* 44, 155–167. doi:10.1016/j.actbio.2016.08.039
- Könnig, D., Herrera, A., Duda, G. N., and Petersen, A. (2018). Mechanosensation across borders: Fibroblasts inside a macroporous scaffold sense and respond to the mechanical environment beyond the scaffold walls. *J. Tissue Eng. Regen. Med.* 12 (1), 265–275. doi:10.1002/term.2410
- Lebre, F., Sridharan, R., Sawkins, M. J., Kelly, D. J., O'Brien, F. J., and Lavelle, E. C. (2017). The shape and size of hydroxyapatite particles dictate inflammatory responses following implantation. *Sci. Rep.* 7 (1), 2922. doi:10.1038/s41598-017-03086-0
- Lee, J.-S., Cha, H. D., Shim, J.-H., Jung, J. W., Kim, J. Y., and Cho, D.-W. (2012). Effect of pore architecture and stacking direction on mechanical properties of solid freeform fabrication-based scaffold for bone tissue engineering. *J. Biomed. Mater. Res. Part A* 100 (7), 1846–1853. doi:10.1002/jbm.a.34149
- Lee, J., Byun, H., Madhurakkt Perikamana, S. K., Lee, S., and Shin, H. (2019). Current advances in immunomodulatory biomaterials for bone regeneration. *Adv. Healthc. Mater.* 8 (4), e1801106. doi:10.1002/adhm.201801106
- Li, H., Zheng, L., and Wang, M. (2021a). Biofunctionalized nanofibrous bilayer scaffolds for enhancing cell adhesion, proliferation and osteogenesis. *ACS Appl. Bio Mater.* 4 (6), 5276–5294. doi:10.1021/acsabm.1c00414
- Li, T.-T., Zhang, Y., Ren, H.-T., Peng, H.-K., Lou, C.-W., and Lin, J.-H. (2021b). Two-step strategy for constructing hierarchical pore structured chitosan-hydroxyapatite composite scaffolds for bone tissue engineering. *Carbohydr. Polym.* 260, 117765. doi:10.1016/j.carbpol.2021.117765
- Li, T., Zhai, D., Ma, B., Xue, J., Zhao, P., Chang, J., et al. (2019). 3D printing of hot dog-like biomaterials with hierarchical architecture and distinct bioactivity. *Adv. Sci. (Weinheim, Baden-Württemberg, Ger.)* 6 (19), 1901146. doi:10.1002/advs.201901146
- Li, X., Kordsmeier, J., and Xiong, J. (2021c). New advances in osteocyte mechanotransduction. *Curr. Osteoporos. Rep.* 19 (1), 101–106. doi:10.1007/s1914-020-00650-y
- Li, Z., Xu, Z., Duan, C., Liu, W., Sun, J., and Han, B. (2018). Role of TCF/LEF transcription factors in bone development and osteogenesis. *Int. J. Med. Sci.* 15 (12), 1415–1422. doi:10.1016/j.ijms.2018.07.041
- Lien, S.-M., Ko, L.-Y., and Huang, T.-J. (2009). Effect of pore size on ECM secretion and cell growth in gelatin scaffold for articular cartilage tissue engineering. *Acta Biomater.* 5 (2), 670–679. doi:10.1016/j.actbio.2008.09.020
- Lin, K.-F., He, S., Song, Y., Wang, C.-M., Gao, Y., Li, J.-Q., et al. (2016). Low-temperature additive manufacturing of biomimetic three-dimensional hydroxyapatite/collagen scaffolds for bone regeneration. *ACS Appl. Mater. Interfaces* 8 (11), 6905–6916. doi:10.1021/acsami.6b00815
- Liu, R., and Ding, J. (2020). Chromosomal repositioning and gene regulation of cells on a micropillar array. *ACS Appl. Mater. Interfaces* 12 (32), 35799–35812. doi:10.1021/acsami.0c05883
- Liu, S., Yao, L., Wang, Y., Li, Y., Jia, Y., Yang, Y., et al. (2023). Immunomodulatory hybrid micro-nanofiber scaffolds enhance vascular regeneration. *Bioact. Mater.* 21, 464–482. doi:10.1016/j.bioactmat.2022.08.018
- Loh, Q. L., and Choong, C. (2013). Three-dimensional scaffolds for tissue engineering applications: Role of porosity and pore size. *Tissue Eng. Part B, Rev.* 19 (6), 485–502. doi:10.1089/ten.TEB.2012.0437
- Luo, H., Gan, D., Gama, M., Tu, J., Yao, F., Zhang, Q., et al. (2020). Interpenetrated nano- and submicro-fibrous biomimetic scaffolds towards enhanced mechanical and biological performances. *Mater. Sci. Eng. C, Mater. For Biol. Appl.* 108, 110416. doi:10.1016/j.msec.2019.110416
- Lutolf, M. P., and Hubbell, J. A. (2005). Synthetic biomaterials as instructive extracellular microenvironments for morphogenesis in tissue engineering. *Nat. Biotechnol.* 23 (1), 47–55. doi:10.1038/nbt1055
- Ma, T., Li, Y., Yang, S. T., and Kniss, D. A. (2000). Effects of pore size in 3-D fibrous matrix on human trophoblast tissue development. *Biotechnol. Bioeng.* 70 (6), 606–618. doi:10.1002/1097-0290(20001220)70:6<606::aid-bit2>3.0.co;2-h
- Manoukian, O. S., Aravamudan, A., Lee, P., Arul, M. R., Yu, X., Rudraiah, S., et al. (2018). Spiral layer-by-layer micro-nanostructured scaffolds for bone tissue engineering. *ACS Biomaterials Sci. Eng.* 4 (6), 2181–2192. doi:10.1021/acsbiomaterials.8b00393
- McWhorter, F. Y., Wang, T., Nguyen, P., Chung, T., and Liu, W. F. (2013). Modulation of macrophage phenotype by cell shape. *Proc. Natl. Acad. Sci. U. S. A.* 110 (43), 17253–17258. doi:10.1073/pnas.1308887110

- Michael, K. E., Dumbauld, D. W., Burns, K. L., Hanks, S. K., and García, A. J. (2009). Focal adhesion kinase modulates cell adhesion strengthening via integrin activation. *Mol. Biol. Cell* 20 (9), 2508–2519. doi:10.1091/mbc.e08-01-0076
- Minagar, S., Li, Y., Berndt, C. C., and Wen, C. (2015). The influence of titania-zirconia-zirconium titanate nanotube characteristics on osteoblast cell adhesion. *Acta Biomater.* 12, 281–289. doi:10.1016/j.actbio.2014.10.037
- Murphy, C. M., Haugh, M. G., and O'Brien, F. J. (2010). The effect of mean pore size on cell attachment, proliferation and migration in collagen-glycosaminoglycan scaffolds for bone tissue engineering. *Biomaterials* 31 (3), 461–466. doi:10.1016/j.biomaterials.2009.09.063
- Nguyen, A. M., and Jacobs, C. R. (2013). Emerging role of primary cilia as mechanosensors in osteocytes. *Bone* 54 (2), 196–204. doi:10.1016/j.bone.2012.11.016
- Niessen, C. M., Leckband, D., and Yap, A. S. (2011). Tissue organization by cadherin adhesion molecules: Dynamic molecular and cellular mechanisms of morphogenetic regulation. *Physiol. Rev.* 91 (2), 691–731. doi:10.1152/physrev.00004.2010
- Nudelman, F., Pieterse, K., George, A., Bomans, P. H. H., Friedrich, H., Brylka, L. J., et al. (2010). The role of collagen in bone apatite formation in the presence of hydroxyapatite nucleation inhibitors. *Nat. Mater.* 9 (12), 1004–1009. doi:10.1038/nmat2875
- Oh, S., Brammer, K. S., Li, Y. S. J., Teng, D., Engler, A. J., Chien, S., et al. (2009). Stem cell fate dictated solely by altered nanotube dimension. *Proc. Natl. Acad. Sci. U. S. A.* 106 (7), 2130–2135. doi:10.1073/pnas.0813200106
- Park, J.-E., Jang, Y.-S., Bae, T.-S., and Lee, M.-H. (2019). Biocompatibility characteristics of titanium coated with multi walled carbon nanotubes-hydroxyapatite nanocomposites. *Mater. (Basel, Switz.)* 12 (2), 224. doi:10.3390/ma12020224
- Pefani, D.-E., Pankova, D., Abraham, A. G., Grawenda, A. M., Vlahov, N., Scrase, S., et al. (2016). TGF- β targets the hippo pathway scaffold RASSF1A to facilitate YAP/SMAD2 nuclear translocation. *Mol. Cell* 63 (1), 156–166. doi:10.1016/j.molcel.2016.05.012
- Perez, R. A., and Mestres, G. (2016). Role of pore size and morphology in musculo-skeletal tissue regeneration. *Mater. Sci. Eng. C, Mater. For Biol. Appl.* 61, 922–939. doi:10.1016/j.msec.2015.12.087
- Polak, S. J., Rustom, L. E., Genin, G. M., Talcott, M., and Wagoner Johnson, A. J. (2013). A mechanism for effective cell-seeding in rigid, microporous substrates. *Acta Biomater.* 9 (8), 7977–7986. doi:10.1016/j.actbio.2013.04.040
- Puleo, D. A., and Nanci, A. (1999). Understanding and controlling the bone-implant interface. *Biomaterials* 20 (23–24), 2311–2321. doi:10.1016/s0142-9612(99)00160-x
- Recalcati, S., Locati, M., Marini, A., Santambrogio, P., Zaninotto, F., De Pizzol, M., et al. (2010). Differential regulation of iron homeostasis during human macrophage polarized activation. *Eur. J. Immunol.* 40 (3), 824–835. doi:10.1002/eji.200939889
- Reznikov, N., Bilton, M., Lari, L., Stevens, M. M., and Kröger, R. (2018). Fractal-like hierarchical organization of bone begins at the nanoscale. *Science* 360 (6388), eaao2189. doi:10.1126/science.aao2189
- Reznikov, N., Shahar, R., and Weiner, S. (2014). Bone hierarchical structure in three dimensions. *Acta Biomater.* 10 (9), 3815–3826. doi:10.1016/j.actbio.2014.05.024
- Rnjak-Kovacina, J., Gerrand, Y.-W., Wray, L. S., Tan, B., Joukhdar, H., Kaplan, D. L., et al. (2019). Vascular pedicle and microchannels: Simple methods toward effective *in vivo* vascularization of 3D scaffolds. *Adv. Healthc. Mater.* 8 (24), e1901106. doi:10.1002/adhm.201901106
- Rnjak-Kovacina, J., Wise, S. G., Li, Z., Maitz, P. K. M., Young, C. J., Wang, Y., et al. (2011). Tailoring the porosity and pore size of electrospun synthetic human elastin scaffolds for dermal tissue engineering. *Biomaterials* 32 (28), 6729–6736. doi:10.1016/j.biomaterials.2011.05.065
- Sadtler, K., Estrellas, K., Allen, B. W., Wolf, M. T., Fan, H., Tam, A. J., et al. (2016). Developing a pro-regenerative biomaterial scaffold microenvironment requires T helper 2 cells. *Sci. (New York, N.Y.)* 352 (6283), 366–370. doi:10.1126/science.aad9272
- Saggiomo, V., and Velders, A. H. (2015). Simple 3D printed scaffold-removal method for the fabrication of intricate microfluidic devices. *Adv. Sci. (Weinheim, Baden-Württemberg, Ger.)* 2 (9), 1500125. doi:10.1002/advs.201500125
- Salerno, A., Di Maio, E., Iannace, S., and Netti, P. A. (2012). Tailoring the pore structure of PCL scaffolds for tissue engineering prepared via gas foaming of multi-phase blends. *J. Porous Mater.* 19 (2), 181–188. doi:10.1007/s10934-011-9458-9
- Saternos, H., Ley, S., and AbouAlaiwi, W. (2020). Primary cilia and calcium signaling interactions. *Int. J. Mol. Sci.* 21 (19), 7109. doi:10.3390/ijms21197109
- Schoen, J., Euler, M., Schauer, C., Schett, G., Herrmann, M., Knopf, J., et al. (2022). Neutrophils' extracellular trap mechanisms: From physiology to pathology. *Int. J. Mol. Sci.* 23 (21), 12855. doi:10.3390/ijms232112855
- Shahab, U., Ahmad, S., MoinuddinDixit, K., Habib, S., Alam, K., Ali, A., et al. (2012). Hydroxyl radical modification of collagen type II increases its arthritogenicity and immunogenicity. *PLoS One* 7 (2), e31199. doi:10.1371/journal.pone.0031199
- Siddappa, R., Mulder, W., Steeghs, I., van de Klundert, C., Fernandes, H., Liu, J., et al. (2009). cAMP/PKA signaling inhibits osteogenic differentiation and bone formation in rodent models. *Tissue Eng. Part A* 15 (8), 2135–2143. doi:10.1089/ten.tea.2008.0512
- Silva, A. S., Santos, L. F., Mendes, M. C., and Mano, J. F. (2020). Multi-layer pre-vascularized magnetic cell sheets for bone regeneration. *Biomaterials* 231, 119664. doi:10.1016/j.biomaterials.2019.119664
- Singh, D., Singh, D., Zo, S., and Han, S. S. (2014). Nano-biomimetics for nano/micro tissue regeneration. *J. Biomed. Nanotechnol.* 10 (10), 3141–3161. doi:10.1166/jbn.2014.1941
- Sivaraj, K. K., Dharmalingam, B., Mohanakrishnan, V., Jeong, H.-W., Kato, K., Schröder, S., et al. (2020). YAP1 and TAZ negatively control bone angiogenesis by limiting hypoxia-inducible factor signaling in endothelial cells. *ELife* 9, e50770. doi:10.7554/eLife.50770
- Song, P., Li, M., Zhang, B., Gui, X., Han, Y., Wang, L., et al. (2022). DLP fabricating of precision GelMA/HAP porous composite scaffold for bone tissue engineering application. *Compos. Part B Eng.* 244, 110163. doi:10.1016/j.compositesb.2022.110163
- Speight, P., Kofler, M., Szász, K., and Kapus, A. (2016). Context-dependent switch in chemo/mechanotransduction via multilevel crosstalk among cytoskeleton-regulated MRTF and TAZ and TGF β -regulated Smad3. *Nat. Commun.* 7, 11642. doi:10.1038/ncomms11642
- Šugar, P., Pudrovcová, B., Kalbáčová, M. H., Šugarová, J., Sahul, M., and Kováčik, J. (2021). Laser surface modification of powder metallurgy-processed Ti-graphite composite which can enhance cells' osteo-differentiation. *Mater. (Basel, Switz.)* 14 (20), 6067. doi:10.3390/ma14206067
- Swanson, W. B., Omi, M., Woodbury, S. M., Douglas, L. M., Eberle, M., Ma, P. X., et al. (2022). Scaffold pore curvature influences μ sc fate through differential cellular organization and YAP/TAZ activity. *Int. J. Mol. Sci.* 23 (9), 4499. doi:10.3390/ijms23094499
- Tylek, T., Blum, C., Hrynevich, A., Schlegelmilch, K., Schilling, T., Dalton, P. D., et al. (2020). Precisely defined fiber scaffolds with 40 μ m porosity induce elongation driven M2-like polarization of human macrophages. *Biofabrication* 12 (2), 025007. doi:10.1088/1758-5090/ab5f4e
- Vishwakarma, A., Bhise, N. S., Evangelista, M. B., Rouwkema, J., Dokmeci, M. R., Ghaemmaghami, A. M., et al. (2016). Engineering immunomodulatory biomaterials to tune the inflammatory response. *Trends Biotechnol.* 34 (6), 470–482. doi:10.1016/j.tibtech.2016.03.009
- Vordemvenne, T., Wähnert, D., Koettnitz, J., Merten, M., Fokin, N., Becker, A., et al. (2020). Bone regeneration: A novel osteoinductive function of spongostan by the interplay between its nano- and microtopography. *Cells* 9 (3), 654. doi:10.3390/cells9030654
- Wang, C., Xu, D., Lin, L., Li, S., Hou, W., He, Y., et al. (2021). Large-pore-size Ti6Al4V scaffolds with different pore structures for vascularized bone regeneration. *Mater. Sci. Eng. C, Mater. For Biol. Appl.* 131, 112499. doi:10.1016/j.msec.2021.112499
- Wang, H., Zhi, W., Lu, X., Li, X., Duan, K., Duan, R., et al. (2013a). Comparative studies on ectopic bone formation in porous hydroxyapatite scaffolds with complementary pore structures. *Acta Biomater.* 9 (9), 8413–8421. doi:10.1016/j.actbio.2013.05.026
- Wang, J., Chen, Y., Zhu, X., Yuan, T., Tan, Y., Fan, Y., et al. (2014). Effect of phase composition on protein adsorption and osteoinduction of porous calcium phosphate ceramics in mice. *J. Biomed. Mater. Res. Part A* 102 (12), 4234–4243. doi:10.1002/jbm.a.35102
- Wang, J., Zhang, H., Zhu, X., Fan, H., Fan, Y., and Zhang, X. (2013b). Dynamic competitive adsorption of bone-related proteins on calcium phosphate ceramic particles with different phase composition and microstructure. *J. Biomed. Mater. Res. Part B, Appl. Biomaterials* 101 (6), 1069–1077. doi:10.1002/jbm.b.32917
- Wang, Y., Botvinick, E. L., Zhao, Y., Berns, M. W., Usami, S., Tsien, R. Y., et al. (2005). Visualizing the mechanical activation of Src. *Nature* 434 (7036), 1040–1045. doi:10.1038/nature03469
- Weiner, S., Traub, W., and Wagner, H. D. (1999). Lamellar bone: Structure-function relations. *J. Struct. Biol.* 126 (3), 241–255. doi:10.1006/jsbi.1999.4107
- Wen, N., Qian, E., and Kang, Y. (2021). Effects of macro-/micro-channels on vascularization and immune response of tissue engineering scaffolds. *Cells* 10 (6), 1514. doi:10.3390/cells10061514
- Won, J.-E., Lee, Y. S., Park, J.-H., Lee, J.-H., Shin, Y. S., Kim, C.-H., et al. (2020). Hierarchical microchanneled scaffolds modulate multiple tissue-regenerative processes of immune-responses, angiogenesis, and stem cell homing. *Biomaterials* 227, 119548. doi:10.1016/j.biomaterials.2019.119548
- Wu, L., Pei, X., Zhang, B., Su, Z., Gui, X., Gao, C., et al. (2022). 3D-printed HAp bone regeneration scaffolds enable nano-scale manipulation of cellular mechanotransduction signals. *Chem. Eng. J.* 455, 140699. doi:10.1016/j.cej.2022.140699
- Wu, L., Zhou, C., Zhang, B., Lei, H., Wang, W., Pu, X., et al. (2020). Construction of biomimetic natural wood hierarchical porous-structure bioceramic with micro/nanowhisker coating to modulate cellular behavior and osteoinductive activity. *ACS Appl. Mater. Interfaces* 12 (43), 48395–48407. doi:10.1021/acsami.0c15205
- Xia, J., Yuan, Y., Wu, H., Huang, Y., and Weitz, D. A. (2020). Decoupling the effects of nanopore size and surface roughness on the attachment, spreading and differentiation of bone marrow-derived stem cells. *Biomaterials* 248, 120014. doi:10.1016/j.biomaterials.2020.120014

- Xiao, W., Zaeem, M. A., Bal, B. S., and Rahaman, M. N. (2016). Creation of bioactive glass (13-93) scaffolds for structural bone repair using a combined finite element modeling and rapid prototyping approach. *Mater. Sci. Eng. C, Mater. For Biol. Appl.* 68, 651–662. doi:10.1016/j.msec.2016.06.011
- Xie, C., Gao, Q., Wang, P., Shao, L., Yuan, H., Fu, J., et al. (2019). Structure-induced cell growth by 3D printing of heterogeneous scaffolds with ultrafine fibers. *Mater. Des.* 181, 108092. doi:10.1016/j.matdes.2019.108092
- Xing, F., Li, L., Zhou, C., Long, C., Wu, L., Lei, H., et al. (2019). Regulation and directing stem cell fate by tissue engineering functional microenvironments: Scaffold physical and chemical cues. *Stem Cells Int.* 2019, 1–16. doi:10.1155/2019/2180925
- Xu, Y., Nudelman, F., Eren, E. D., Wirix, M. J. M., Cantaert, B., Nijhuis, W. H., et al. (2020). Intermolecular channels direct crystal orientation in mineralized collagen. *Nat. Commun.* 11 (1), 5068. doi:10.1038/s41467-020-18846-2
- Yamasaki, H., and Sakai, H. (1992). Osteogenic response to porous hydroxyapatite ceramics under the skin of dogs. *Biomaterials* 13 (5), 308–312. doi:10.1016/0142-9612(92)90054-r
- Yan, L., Yang, X., Long, J., Cheng, X., Pan, D., Huang, Y., et al. (2020). Universal unilateral electro-spinning/spraying strategy to construct water-unidirectional Janus membranes with well-tuned hierarchical micro/nanostructures. *Chem. Commun. Camb. Engl.* 56 (3), 478–481. doi:10.1039/c9cc08088k
- Yan, Y., Chen, H., Zhang, H., Guo, C., Yang, K., Chen, K., et al. (2019). Vascularized 3D printed scaffolds for promoting bone regeneration. *Biomaterials* 190–191, 97. doi:10.1016/j.biomaterials.2018.10.033
- Yang, D., Xiao, J., Wang, B., Li, L., Kong, X., and Liao, J. (2019). The immune reaction and degradation fate of scaffold in cartilage/bone tissue engineering. *Mater. Sci. Eng. C, Mater. For Biol. Appl.* 104, 109927. doi:10.1016/j.msec.2019.109927
- Yang, W., Xi, X., Shen, X., Liu, P., Hu, Y., and Cai, K. (2014). Titania nanotubes dimensions-dependent protein adsorption and its effect on the growth of osteoblasts. *J. Biomed. Mater. Res. Part A* 102 (10), 3598–3608. doi:10.1002/jbm.a.35021
- Yu, Y., Krishnan, N. M. A., Smedskjaer, M. M., Sant, G., and Bauchy, M. (2018). The hydrophilic-to-hydrophobic transition in glassy silica is driven by the atomic topology of its surface. *J. Chem. Phys.* 148 (7), 074503. doi:10.1063/1.5010934
- Zarka, M., Haÿ, E., and Cohen-Solal, M. (2021). YAP/TAZ in bone and cartilage biology. *Front. Cell Dev. Biol.* 9, 788773. doi:10.3389/fcell.2021.788773
- Zhang, B., Gui, X., Song, P., Xu, X., Guo, L., Han, Y., et al. (2022a). Three-dimensional printing of large-scale, high-resolution bioceramics with micronano inner porosity and customized surface characterization design for bone regeneration. *ACS Appl. Mater. Interfaces* 14 (7), 8804–8815. doi:10.1021/acsami.1c22868
- Zhang, B., Sun, H., Wu, L., Ma, L., Xing, F., Kong, Q., et al. (2019). 3D printing of calcium phosphate bioceramic with tailored biodegradation rate for skull bone tissue reconstruction. *Bio-Design Manuf.* 2 (3), 161–171. doi:10.1007/s42242-019-00046-7
- Zhang, B., Wang, W., Gui, X., Song, P., Lei, H., Li, Z., et al. (2022b). 3D printing of customized key biomaterials genomics for bone regeneration. *Appl. Mater. Today* 26, 101346. doi:10.1016/j.apmt.2021.101346
- Zhang, R., Elkhooly, T. A., Huang, Q., Liu, X., Yang, X., Yan, H., et al. (2018). Effects of the hierarchical macro/mesoporous structure on the osteoblast-like cell response. *J. Biomed. Mater. Res. Part A* 106 (7), 1896–1902. doi:10.1002/jbm.a.36387
- Zhang, Y., Luo, R., Tan, J., Wang, J., Lu, X., Qu, S., et al. (2017). Osteoblast behaviors on titania nanotube and mesopore layers. *Regen. Biomater.* 4 (2), 81–87. doi:10.1093/rb/rbw042
- Zhao, L., Pei, X., Jiang, L., Hu, C., Sun, J., Xing, F., et al. (2019). Bionic design and 3D printing of porous titanium alloy scaffolds for bone tissue repair. *Compos. Part B Eng.* 162, 154–161. doi:10.1016/j.compositesb.2018.10.094
- Zhao, X., Ng, S., Heng, B. C., Guo, J., Ma, L., Tan, T. T. Y., et al. (2013). Cytotoxicity of hydroxyapatite nanoparticles is shape and cell dependent. *Archives Toxicol.* 87 (6), 1037–1052. doi:10.1007/s00204-012-0827-1
- Zheng, X., Xin, L., Luo, Y., Yang, H., Ye, X., Mao, Z., et al. (2019). Near-infrared-triggered dynamic surface topography for sequential modulation of macrophage phenotypes. *ACS Appl. Mater. Interfaces* 11 (46), 43689–43697. doi:10.1021/acsami.9b14808
- Zhou, C., Wang, K., Sun, Y., Wang, Q., Jiang, Q., Liang, J., et al. (2021). Biofabrication (3D bioprinting) laboratory at sichuan university. *Bio-Design Manuf.* 4 (2), 432–439. doi:10.1007/s42242-020-00115-2
- Zhu, X. D., Zhang, H. J., Fan, H. S., Li, W., and Zhang, X. D. (2010). Effect of phase composition and microstructure of calcium phosphate ceramic particles on protein adsorption. *Acta Biomater.* 6 (4), 1536–1541. doi:10.1016/j.actbio.2009.10.032
- Zopf, D. A., Mitsak, A. G., Flanagan, C. L., Wheeler, M., Green, G. E., and Hollister, S. J. (2015). Computer aided-designed, 3-dimensionally printed porous tissue bioscaffolds for craniofacial soft tissue reconstruction. *Otolaryngology-head Neck Surg.* 152 (1), 57–62. doi:10.1177/0194599814552065



OPEN ACCESS

EDITED BY

Yanjin Lu,
Chinese Academy of Sciences (CAS),
China

REVIEWED BY

Xiaodong Tang,
Peking University People's Hospital,
China
Tao Ji,
Peking University People's Hospital,
China

*CORRESPONDENCE

Zhenfeng Li,
✉ 199862000206@email.sdu.edu.cn

RECEIVED 30 January 2023

ACCEPTED 27 April 2023

PUBLISHED 05 May 2023

CITATION

Lv Z, Li J, Yang Z, Li X, Yang Q and Li Z (2023), A novel three dimensional-printed biomechanically evaluated patient-specific sacral implant in spinopelvic reconstruction after total *en bloc* sacrectomy. *Front. Bioeng. Biotechnol.* 11:1153801. doi: 10.3389/fbioe.2023.1153801

COPYRIGHT

© 2023 Lv, Li, Yang, Li, Yang and Li. This is an open-access article distributed under the terms of the [Creative Commons Attribution License \(CC BY\)](https://creativecommons.org/licenses/by/4.0/). The use, distribution or reproduction in other forums is permitted, provided the original author(s) and the copyright owner(s) are credited and that the original publication in this journal is cited, in accordance with accepted academic practice. No use, distribution or reproduction is permitted which does not comply with these terms.

A novel three dimensional-printed biomechanically evaluated patient-specific sacral implant in spinopelvic reconstruction after total *en bloc* sacrectomy

Zhaorui Lv^{1,2}, Jianmin Li¹, Zhiping Yang¹, Xin Li¹, Qiang Yang¹ and Zhenfeng Li^{1*}

¹Qilu Hospital, Shandong University, Jinan, China, ²Cheeloo College of Medicine, Shandong University, Jinan, Shandong, China

Background: Reconstruction after a total sacrectomy is a challenge due to the special anatomical and biomechanical factors. Conventional techniques of spinal-pelvic reconstruction do not reconstruct satisfactorily. We describe a novel three-dimensional-printed patient-specific sacral implant in spinopelvic reconstruction after total *en bloc* sacrectomy.

Methods: We performed a retrospective cohort study including 12 patients with primary malignant sacral tumors, including 5 men and 7 women with a mean age of 58.25 years (range 20–66 years), undergoing total *en bloc* sacrectomy with 3D printed implant reconstruction from 2016 to 2021. There were 7 cases of chordoma, 3 cases of osteosarcoma, 1 case of chondrosarcoma and 1 case of undifferentiated pleomorphic sarcoma. We use CAD technology to determine surgical resection boundaries, design cutting guides, and individualized prostheses, and perform surgical simulations before surgery. The implant design was biomechanically evaluated by finite element analysis. Operative data, oncological and functional outcomes, complications, and implant osseointegration status of 12 consecutive patients were reviewed.

Results: The implants were implanted successfully in 12 cases without death or severe complications during the perioperative period. Resection margins were wide in 11 patients and marginal in one patient. The average blood loss was 3875 mL (range, 2000–5,000 mL). The average surgical time was 520 min (range, 380–735 min). The mean follow-up was 38.5 months. Nine patients were alive with no evidence of disease, two patients died due to pulmonary metastases, and one patient survived with disease due to local recurrence. Overall survival was 83.33% at 24 months. The Mean VAS was 1.5 (range, 0–2). The mean MSTS score was 21 (range, 17–24). Wound complications occurred in 2 cases. A deep infection occurred in one patient and the implant was removed. No implant mechanical failure was identified. Satisfactory osseointegration was found in all patients, with a mean fusion time of 5 months (range 3–6 months).

Conclusion: The 3D-printed custom sacral prosthesis has been effective in reconstructing spinal-pelvic stability after total *en bloc* sacrectomy with satisfactory clinical outcomes, excellent osseointegration, and excellent durability.

KEYWORDS

implant, sacral tumor, spinopelvic reconstruction, total *en bloc* sacrectomy, 3D-printed

1 Introduction

Primary malignant sacral tumors are rare and include chordoma, chondrosarcoma, osteosarcoma, and Ewing sarcoma (Senne et al., 2021). En-bloc wide resection is the recommended surgical treatment for the management of sacral malignancies, which can prolong survival time (Chatain and Finn, 2020). Large bone defect after total sacrectomy resulting in spinopelvic discontinuity leads to significant instability. Unless reconstruction restores continuity and stability, the patient's postoperative function and quality of life will be severely limited (Kim et al., 2021).

Reconstruction after a total sacrectomy is a complex procedure due to the special anatomical and biomechanical factors of the lumbosacral region. The reconstruction technique should provide sound stability, which facilitates early pain-free mobility and bone healing. Many types of spinopelvic reconstruction have been described but long-term success is limited and remains controversial (Bederman et al., 2014). Traditional methods of spinal-pelvic reconstruction do not reconstruct satisfactorily.

The use of customized 3D-printed implants for the reconstruction of severe oncologic bone defects in selected cases is increasing when the use of conventional techniques is difficult or impossible (Wang and Yang, 2021; Meng et al., 2022). Customized implants are used for spinopelvic reconstruction in complex clinical cases (Wei et al., 2017; Chatain and Finn, 2020; Peng et al., 2020). However, there are still 30% of patients with implant failure (breakage of screws and/or rods) and other defects (Wei et al., 2019), lack long-term follow-up results, and can not provide reliable clinical prognosis information for doctors, and the prosthesis needs further optimization. We previously reported that the use of a prosthesis to restore continuity after sacral GCT resection is safe and effective and facilitates better functional outcomes (Lv et al., 2020). The design concept was of an implant with porous bone-implant interfaces to connect the posterior lumbar spine, anterior spinal column, and both sides of the ilium in one step. Given the rarity of these cases, robust data on the use of prosthetic reconstruction are lacking.

Currently, to our knowledge, a 3D-printed custom-made prosthesis with a two-wing design is rare for spinopelvic reconstruction. The purpose of this study was to describe the design concept and surgical skills of the 3D-printed prosthesis in primary malignancies of the sacrum, and explore the function, complications, and osseointegration.

2 Materials and methods

2.1 Patients

We performed a retrospective cohort study including 12 patients with primary malignant sacral tumors, including 5 men and 7 women with a mean age of 58.25 years (range 20–66 years), undergoing total sacral osteotomy with 3D printed prosthesis reconstruction from 2016 to 2021.

Twelve patients presented with complaints of lumbosacral pain and eight patients had bladder and bowel symptoms. Preoperative puncture biopsies were performed to determine the pathological classification of the tumors. 7 cases were diagnosed as chordoma, 3 as osteosarcoma, 1 as chondrosarcoma, and 1 as undifferentiated pleomorphic sarcoma. This study was approved by the Medical Ethics Committee of Qilu Hospital of Shandong University. Informed consent was obtained from all participants. Details are shown in Table 1.

2.2 Prosthesis design and fabrication

Pelvic CT in DICOM format was exported to the software MIMICS (Materialise, Leuven, and Belgium) to reconstruct a 3D rendering to identify anatomical details (Figure 1A). We determined the osteotomy plane and the morphology of the bone defect (Figure 1B). The osteotomy guides were highly conformed to the surface morphology of bone and had positioning holes for Kirschner wire drilling (Figure 1C). The two-wing-like sacral implant fully adapting to the bone defect was designed as a patient-specific structure (Figure 2). The central portion is attached to the lower endplate of the L5 vertebrae and the two wings are attached to the osteotomy plane of the bilateral iliac bones. The small holes facilitate the suture of the surrounding soft tissue. The lumbar pedicle screws are attached to the implant with titanium rods. The bone-implant connection is a porous structure and is firmly fixed by screws. The implant design was biomechanically evaluated by individualized finite element analysis using Abaqus (Dassault Systèmes, Velizy Villacoublay, and France) before the actual fabrication of the implant. After evaluation of the finite element analysis, we found that the bone loading neither causes fractures nor stress shielding and that the implant design is sufficiently strong (Figure 3). It takes about 2 weeks from implant design to surgery.

2.3 Surgical techniques

Selective arterial embolization and abdominal aortic balloon occlusion were used to reduce intraoperative bleeding. An adequate preoperative enema was performed to minimize any intraoperative disturbance. An artificial vessel was prepared and if the vessel was damaged, an anastomosis was performed. After anesthesia, all patients were placed in the prone position using a posterior-only approach. The incision is an inverted Y-shaped incision. The deep fascia is incised to reach the sacrospinous muscle, exposing the dorsal sacrococcygeal, bilateral sacroiliac joints, part of the iliac crest, and the L5 spinous process. Bilateral pedicle screws are placed at L4 and L5. The sacrospinous muscle and sacral and coccygeal ligaments were removed. The space between the rectum and the sacrum is then filled with gauze and the rectum is pushed forward to ensure that the bowel wall is not damaged during the separation. The iliac vessels, ureter, sciatic nerve, and other vital structures are protected. The sacral spine was excised to expose the sacral canal and dural sac and ligated. The bilateral L5 nerve roots are carefully

TABLE 1 Diagnoses, operative data, oncologic, functional outcomes and complications of patients.

Patient number	Age (years)	Sex	Diagnosis (stage)	Tumor level	Tumor size (cm)	Blood loss (mL)	Operative time (min)	Surgical margin	Follow-up (months)	VAS	MSTS score (%)	Metastasis	Local recurrence	Patient status	Complications	Time of osseointegration (months)
1	64	F	Chondrosarcoma	S1–S4	10	5,000	735	Marginal	62	2	18	Yes	Yes	Died of disease	wound dehiscence, recurrence	3
2	66	F	Undifferentiated pleomorphic sarcoma	S1–S3	10	3,000	720	Wide	53	1	18	No	No	No evidence of disease	None	6
3	65	M	Osteosarcoma	S1–S4	8	4,500	520	Wide	48	2	17	Yes	No	Died of disease	wound dehiscence	6
4	20	F	Osteosarcoma	S1–S3	6	2000	395	Wide	46	1	25	No	No	No evidence of disease	None	3
5	53	M	chordoma	S1–S4	7	4,000	420	Wide	45	0	23	No	No	No evidence of disease	None	6
6	56	F	chordoma	S1–S4	8	3,500	600	Wide	42	2	23	Yes	No	Alive with disease	Deep infection	6
7	60	M	chordoma	S1–S4	10	5,000	540	Wide	36	2	18	No	No	No evidence of disease	None	6
8	55	M	chordoma	S1–S4	8	3,500	480	Wide	34	1	24	No	No	No evidence of disease	None	6
9	69	F	chordoma	S1–S3	8	4,000	380	Wide	27	2	20	No	No	No evidence of disease	None	6
10	62	F	chordoma	S1–S3	10	3,500	520	Wide	21	2	23	No	No	No evidence of disease	None	6
11	64	F	Osteosarcoma	S1–S3	12	5,000	480	Wide	28	2	20	No	No	No evidence of disease	None	3
12	65	M	chordoma	S1–S3	8	3,500	450	Wide	20	1	23	No	No	No evidence of disease	None	3

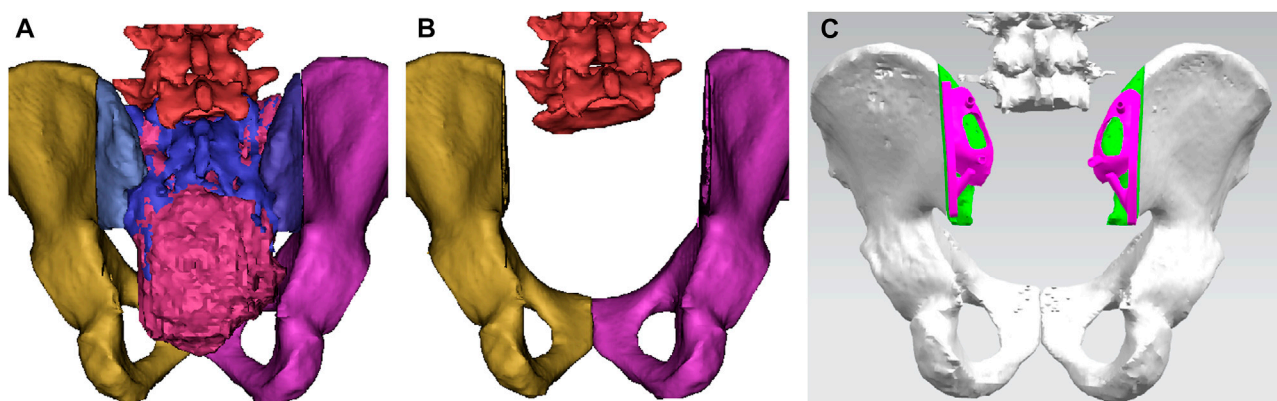


FIGURE 1

A 3D bone tumor model from CT data was created for surgical planning (A). Bone defect model after tumor resection (B). Design of the cutting guide (C).

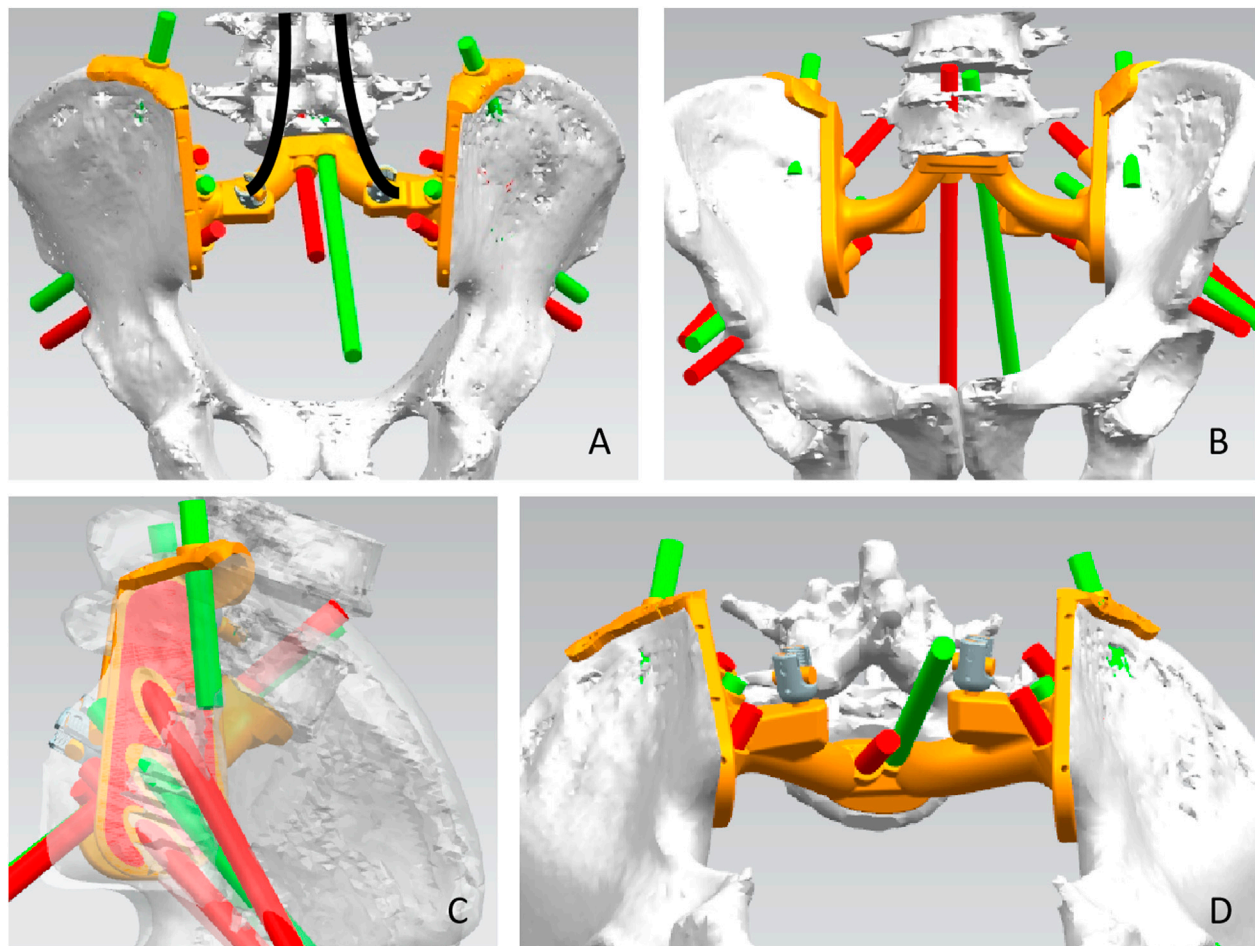


FIGURE 2

Design of the sacral implant. Dorsal view (A), front view (B), side view (C), and upward view (D) of the sacral implant 3D model.

separated. The L5-S1 intervertebral disc is excised. A cutting guide was placed according to the preoperative simulation and fixed with a Kirsch pin, the iliac bones were osteotomized bilaterally, and the

entire sacrum was then removed in one piece along with the tumor (Figure 4). A plastic implant test is used to confirm the match, followed by pulsed irrigation with isotonic sodium chloride solution,

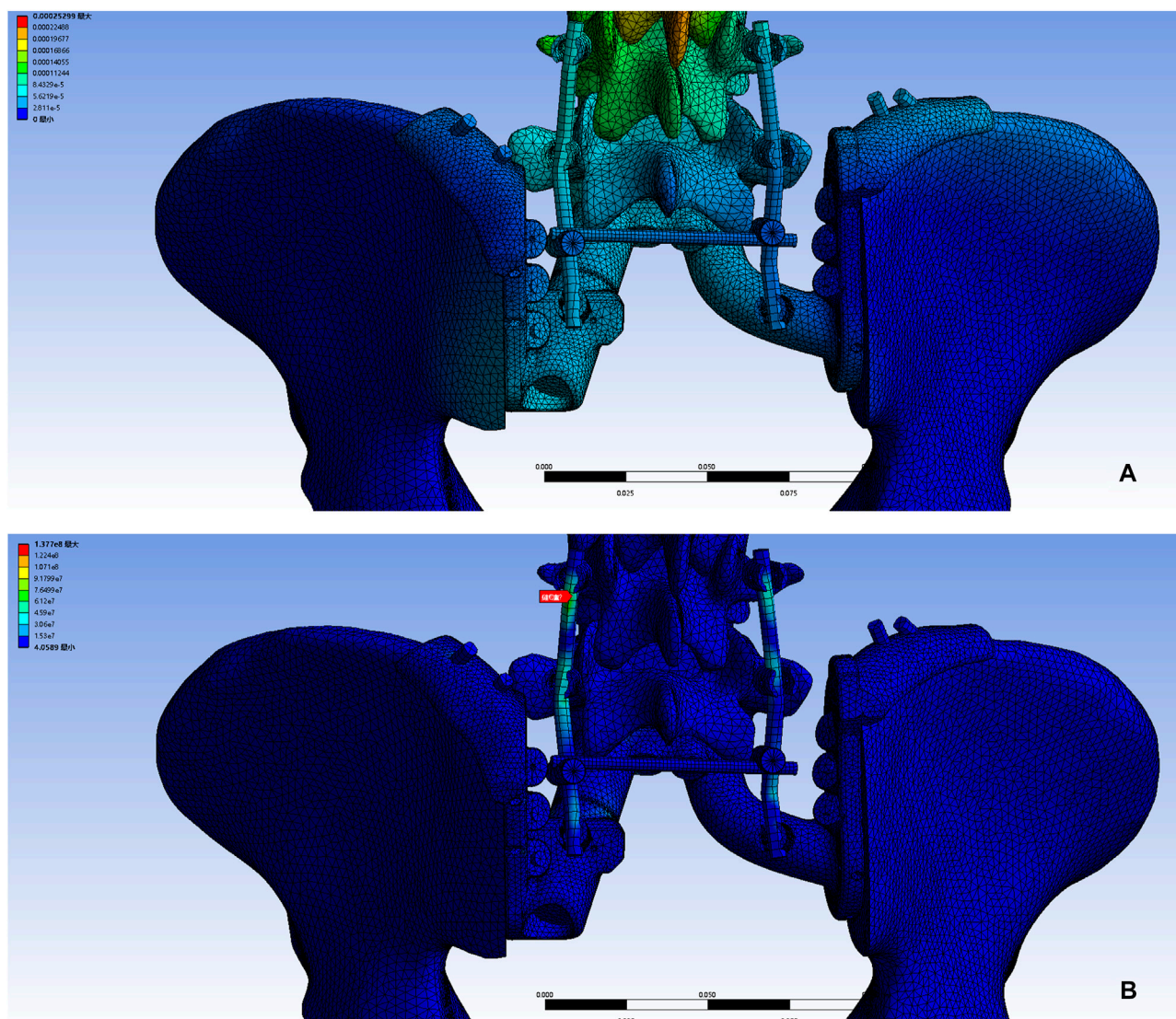


FIGURE 3
A 3D bone tumor model from CT data was created for surgical planning (A). Bone defect model after tumor resection (B). Design of the cutting guide (C).

followed by a 3-min wound soak with iodophor, and then pulsed irrigation. Prosthesis installation usually begins with sublumbar endplate fixation, resetting the entire pelvis and fixing the prosthesis to the remaining iliac bone with a metal rod attached posteriorly to the lumbar spine (Figure 4). Re-irrigation is performed, followed by autograft filling with bone chips at the bone-implant interface. The soft tissue is tightly sutured to the prosthesis to reduce dead space. There was enough tissue to tightly close the wound, and we did not use a rotational or free flap in these patients.

2.4 Postoperative treatment and follow up

Postoperative antibiotic therapy was administered and an inflatable leg pump was used to prevent lower extremity venous

thrombosis. The drainage tube was removed when the daily drainage was less than 50 mL. The length of time the catheter is left in place is determined by whether the patient can urinate. If the patient was unable to urinate, the indwelling catheter was kept in place and functional bladder exercises were continued. At 6 weeks postoperatively, patients were instructed to stand up using crutches and to perform progressive lower extremity walking exercises. One patient received adjuvant radiotherapy. Patients with osteosarcoma received adjuvant chemotherapy.

Patients have regular outpatient follow-ups for pelvic radiographic review in the third, sixth and twelfth months after surgery. After 1 year, reviews were performed every 6 months; after 3 years, reviews were performed annually. The Visual Analog Scale (VAS) was used to assess pain levels. Functional outcome was determined using the MSTs 93 system at the latest follow-up. The complications, including surgery-related complications and

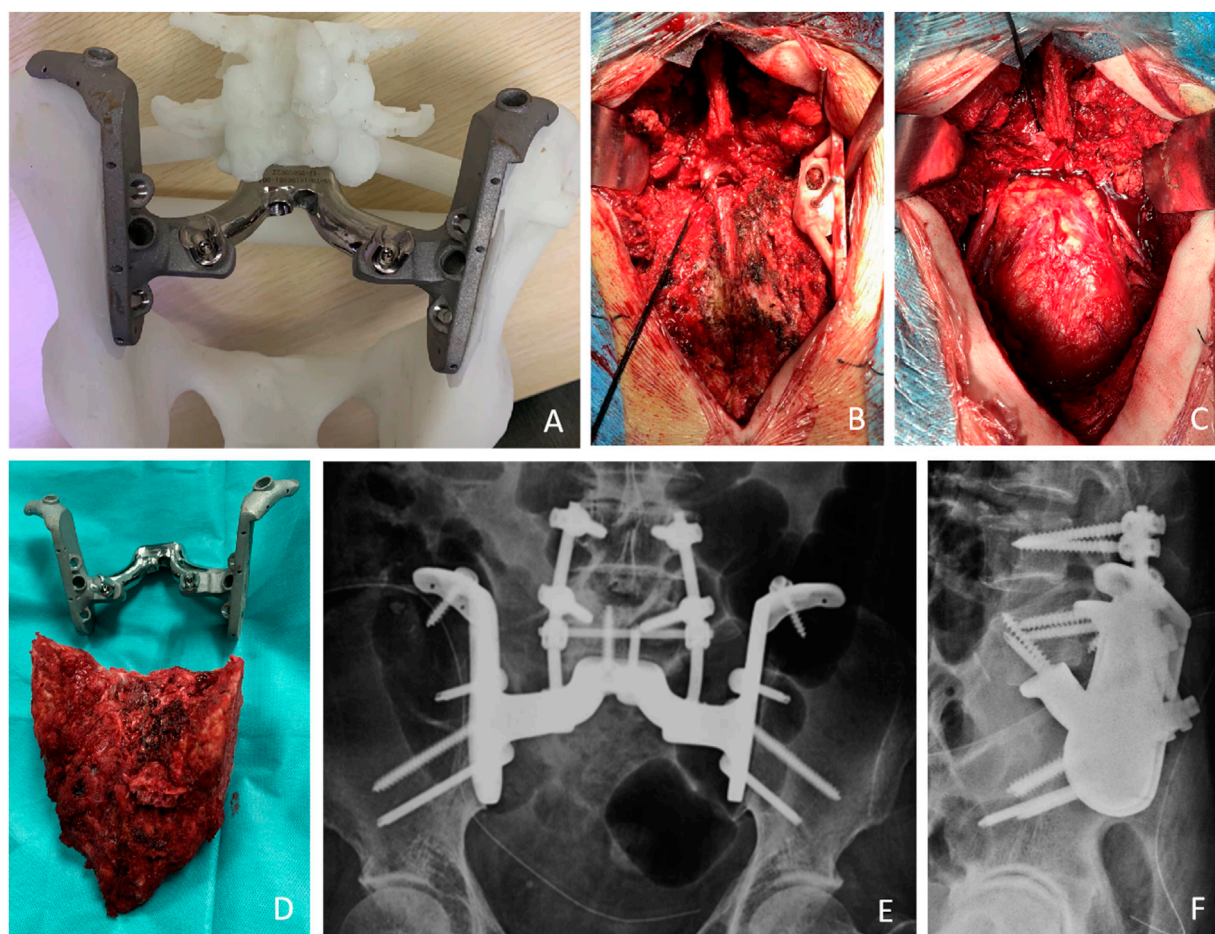


FIGURE 4

Preoperative simulation and intraoperative images. **(A)** The outer view of the implant. These models included the implant trial and the remaining bone after tumor resection allowed the surgeon to practice the procedures before the real surgery. **(B)** The cutting guide was placed according to the preoperative simulation and fixed with a Kirsch pin, the iliac bones were osteotomized bilaterally. **(C)** Bone defect after excision. **(D)** The entire sacrum was then removed in one piece along with the tumor. **(E,F)** The X-ray shows that the prosthesis has been properly placed.

mechanical failures, were determined at the final follow-up. Osseointegration was assessed every 3 months using radiographs or computed tomography scans. The criterion for osseointegration is the continuous trabecular structure of the bone on the surface of the implant viewed on CT.

2.5 Statistical analysis

Statistical analyses were performed using IBM SPSS Statistics software, version 22 (IBM SPSS, Armonk, NY, United States). Continuous data are represented as mean.

3 Results

3.1 Operational outcomes

Resection margins were wide in 12 patients and marginal in one patient (Table 1). The average blood loss was 3,875 mL (range,

2000–5,000 mL). The average surgical time was 520 min (range, 380–735 min). No patient died of intra/perioperative complications.

3.2 Oncologic outcomes

At a mean follow-up of 38.5 months (range, 20–62 months), 9 patients were alive with no evidence of disease, and one patient survived with disease due to local recurrence. Two patients with osteosarcoma were found to have distant metastasis at a mean of 14.5 months postoperatively and died due to rapid tumor progression at a mean of 20.2 months. One patient had a local recurrence at 11.2 months postoperatively. Overall survival was 83.33% at 24 months.

3.3 Functional outcome

After surgery, all patients experienced an improvement in quality of life resulting from the reduction or resolution of pain.

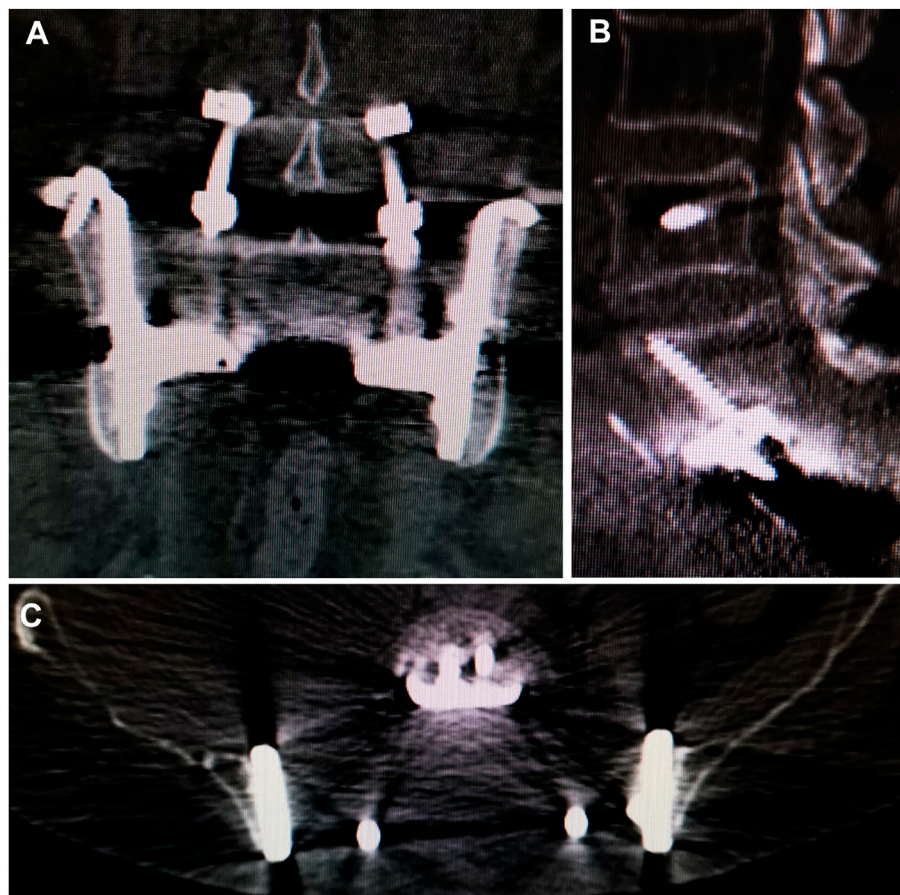


FIGURE 5

CT showed excellent osseointegration at the bone–implant junctions in coronal (A), sagittal (B), and axial (C) views.

The Mean VAS was 1.5 (range, 0–2). All patients experienced an improvement in limb function at the final follow-up. At the last follow-up, 12 patients were able to walk independently, while 2 patients could only walk at home with walking aids. The mean MSTS score was 21 (range, 17–24). Patients all experienced postoperative bowel, bladder, and sexual function loss. After 2–6 months of bladder function exercises (mean 4 months), these patients were able to compress the bladder or pass urine on their own. Patients were instructed to perform defecation exercises, follow a controlled diet, and participate in medication-assisted therapy to defecate by regularly squeezing the lower abdomen.

3.4 Complications

Wound complications occurred in 2 cases as post-operative. Wound dehiscence was successfully treated with surgical wound debridement, antibiotic therapy, and VSD therapy. A deep infection occurred in one patient and the implants were removed 1 year after the operation. Local recurrence occurred in one patient.

3.5 Implant status

No aseptic loosening and fracture were identified. Osseointegration at the all bone-implant interface was radiographically confirmed in all patients using CT (Figure 5).

4 Discussion

The treatment of extensive sacral bone loss and spinopelvic discontinuity is challenging. Spinal pelvic reconstruction after total sacrectomy is very difficult. In recent years, several studies have begun using custom-made 3D-printed prostheses in spinopelvic reconstruction, with encouraging results. Paul Wuisman et al. applied a custom-made prosthesis consisting of five components in a patient with sacral osteosarcoma involving both iliac bones, and at a 3-year postoperative follow-up, the patient was able to walk short distances outdoors with crutches (Wuisman et al., 2001). Guo Wei et al. reported a kind of total sacral reconstruction using a 3D-printed one-piece prosthesis and found that the prosthesis significantly outperformed the conventional approach in terms of reconstructive stability and motor pain function scores and that the

integration between the prosthesis and bone remained strong even with the presence of broken nails (Wei et al., 2019). Doyoung Kim et al. used a 3D-printed prosthesis for reconstruction in a Hemisacrectomy, and CT at 1-year follow-up showed that bone ingrowth had occurred at the prosthesis-bone interface (Kim et al., 2017). Previously, our team used a modular prosthesis for reconstruction in the resection of sacral giant cell tumor with preservation of the sacral nerve and found that the modular design was easy to install, had excellent osseointegration properties, and helped maintain long-term stability (Lv et al., 2020). Currently, the design and application of the prosthesis are in the exploratory stage, and the surgeon's surgical philosophy has a strong influence on the design of the prosthesis, integrated or grouped, preferring anatomical or functional reconstruction, but also showing certain commonalities, such as better matching of the bone defect structure, design of holes that can be fixed with screws, and the use of holes that facilitate lightweight and bone ingrowth. In our series, all patients regained walking function after surgery, and good bone ingrowth was found during follow-up, showing some superiority over traditional reconstruction methods. These prostheses show satisfactory results in terms of surgical technique, operating time, safety, and functional outcomes. The complication rate is comparable to other complex reconstructions.

The use of 3D printing technology in bone tumor treatment is safe and effective, reducing operative time and complication rates, obtaining satisfactory functional and oncological outcomes and has become cost-effective and reliable, making it suitable for orthopedic oncology (Yen et al., 2021). The 3D-printed prosthesis conforms to the current concept of lumbar-pelvic reconstruction (Kim et al., 2021). The prosthesis is implanted to reconstruct the anterior lumbar column and the posterior pelvic ring and is connected to the posterior lumbar spine in combination with a nail rod system to achieve all-around fixation. The 3D-printed prosthesis can be customized to fit any shape of the sacral defect. The preoperative planning and the use of osteotomy guides allow for a very good fit of the prosthesis to the bone defect. The porous structure and rough surface inside the prosthesis provide a scaffold for cellular adhesion and proliferation, and the new bone can be cross-locked inside the pores to form a strong osseointegration (Guyer et al., 2016). At our follow-up, bone osseointegration at the prosthesis-bone interface was also observed, even as the new bone shell wrapped around the edges of the prosthesis, and the L5 position and posterior pelvic ring opening remained unchanged significantly during the follow-up period, indicating very high reconstructive stability of the prosthesis. The elastic modulus of the porous structure is close to that of human cortical bone, and the elastic modulus can be adjusted by changing the structure, and porosity, or achieving a gradient porosity distribution to avoid stress fractures. In conclusion, the advantages of conforming to current reconstruction concepts, having the advantage of individualized matching, a porous structure that facilitates osseointegration, and an elastic modulus similar to that of cortical bone make 3D printed prosthesis an optimistic prospect for lumbar-pelvic stability reconstruction.

It is very important to choose the appropriate surgical approach, protect the nerves and blood vessels, avoid damaging the bowel or ureter, control the risk of bleeding, and restore stability to the lumbosacral region (Houdek et al., 2020). *En bloc* sacrectomy is a procedure with a high rate of major complications, often

necessitating secondary interventions (Verlaan et al., 2015). Although most patients have permanent neurological deficits after tumor resection, extensive resection is the best way to treat sacral tumors to reduce the chance of local recurrence and prolong survival time (van Wulfften Palthe et al., 2017). Depending on the pathology of the tumor, adjuvant radiotherapy should be considered as a postoperative treatment. Unfortunately, despite total *En bloc* sacrectomy and adjuvant therapy, both older patients developed recurrence and passed away. Throughout the follow-up period, all patients steadily improved their ambulatory function and regained the ability to walk long distances to climb stairs. Patients' MSTS scores continued to improve, reflecting the fact that the use of prosthetic reconstruction was very beneficial to the recovery of functional activity of the patient's lower extremities. Patients in this study had a total *En bloc* sacrectomy with immediate postoperative urinary and fecal incontinence, but there was no impact on the motor ability and no loss of plantar flexion of the foot, but there was residual numbness of the lower extremity to varying degrees. A total of 2 patients experienced wound complications. Poor healing, such as wound infection and dehiscence, was reported in 29.2% of sacral tumor surgeries (Li et al., 2013). The incidence of wound infection or poor healing after resection of high sacral tumors can be 25% and 53.5% (Ruggieri et al., 2012). High suture tension at the skin margin, inadequate blood flow, and local fecal contamination are common causes. Some studies have shown that high sacral tumors, tumor volume over 200 cm³, and abundant tumor blood supply are independent risk factors for intraoperative hemorrhage (Tang et al., 2009). In this study, the overall bleeding was lower than that reported in the literature due to the use of preoperative embolization and balloon block to control bleeding.

Our study has some limitations. This study had a limited sample size and lacked an appropriate control group; therefore, we believe that a larger sample size, appropriate control group, and longer follow-up period are necessary. For 3D-printed prostheses, the relatively short follow-up period in this study may underestimate the potential for late complications in these patients. We consider the absence of gaps at the bone-prosthesis interface with the presence of continuous trabeculae as good osseointegration. Patients with good osseointegration did not experience displacement or screw loosening. Therefore, the impact of assessment bias was not significant. In addition, studies analyzing changes in spinal biomechanical status due to internal fixation devices could provide additional clinical evidence for optimizing treatment options. The widespread use and familiarity with the latest generation of 3D printed custom prostheses over the past 5 years or so has made this new reconstruction technique possible and therefore allows for long-term follow-up of patients. We believe the real value is the opportunity to share this experience and technical description in the hope that it will stimulate the potential for multi-institutional research and collaboration to further refine the options for this challenging clinical problem.

5 Conclusion

The 3D-printed custom sacral prosthesis has been effective in reconstructing spinal-pelvic stability after total *en bloc* sacrectomy

with satisfactory clinical outcomes, excellent osseointegration, and excellent durability, which is worth further promotion in clinical practice.

Data availability statement

The raw data supporting the conclusion of this article will be made available by the authors, without undue reservation.

Ethics statement

The studies involving human participants were reviewed and approved by the Medical Ethics Committee of Qilu Hospital of Shandong University. The patients/participants provided their written informed consent to participate in this study.

Author contributions

ZfL, ZrL, and JL were involved with the concept and design of this manuscript. ZY, XL, and QY were involved with the acquisition of subjects and data. ZfL and JL were involved in the design of the prosthesis. ZrL and ZfL were involved in the postsurgical evaluation of the patients. All authors contributed to the data analysis, drafted and critically revised the manuscript, and approved the submitted

manuscript, and agreed to be accountable for all aspects of the work. All authors contributed to the article and approved the submitted version.

Funding

This research was funded by Shandong Provincial Natural Science Foundation, grant number “ZR2021MH114”.

Conflict of interest

The authors declare that the research was conducted in the absence of any commercial or financial relationships that could be construed as a potential conflict of interest.

Publisher's note

All claims expressed in this article are solely those of the authors and do not necessarily represent those of their affiliated organizations, or those of the publisher, the editors and the reviewers. Any product that may be evaluated in this article, or claim that may be made by its manufacturer, is not guaranteed or endorsed by the publisher.

References

- Bederman, S. S., Shah, K. N., Hassan, J. M., Hoang, B. H., Kiester, P. D., and Bhatia, N. N. (2014). Surgical techniques for spinopelvic reconstruction following total sacrectomy: A systematic review. *Eur. Spine J.* 23, 305–319. doi:10.1007/s00586-013-3075-z
- Chatain, G. P., and Finn, M. (2020). Compassionate use of a custom 3D-printed sacral implant for revision of failing sacrectomy: Case report. *J. Neurosurg. Spine* 1, 513–518. doi:10.3171/2020.3.SPINE191497
- Guyot, R. D., Abitbol, J. J., Ohnmeiss, D. D., and Yao, C. (2016). Evaluating osseointegration into a deeply porous titanium scaffold: A biomechanical comparison with peck and allograft. *Spine* 41, E1146–E1150. doi:10.1097/BRS.0000000000001672
- Houdek, M. T., Wellings, E. P., Moran, S. L., Bakri, K., Dozois, E. J., Mathis, K. L., et al. (2020). Outcome of sacropelvic resection and reconstruction based on a novel classification system. *J. Bone Jt. Surg. Am.* 102, 1956–1965. doi:10.2106/JBJS.20.00135
- Kim, D., Lim, J. Y., Shim, K. W., Han, J. W., Yi, S., Yoon, D. H., et al. (2017). Sacral reconstruction with a 3D-printed implant after hemisacrectomy in a patient with sacral osteosarcoma: 1-Year follow-up result. *Yonsei Med. J.* 58, 453–457. doi:10.3349/ymj.2017.58.2.453
- Kim, K. R., Kim, K. H., Park, J. Y., Shin, D. A., Ha, Y., Kim, K. N., et al. (2021). Surgical strategy for sacral tumor resection. *Yonsei Med. J.* 62, 59–67. doi:10.3349/ymj.2021.62.1.59
- Li, D., Guo, W., Qu, H., Yang, R., Tang, X., Yan, T., et al. (2013). Experience with wound complications after surgery for sacral tumors. *Eur. Spine J.* 22, 2069–2076. doi:10.1007/s00586-013-2765-x
- Lv, Z. R., Li, Z. F., Yang, Z. P., Li, X., Yang, Q., Li, K., et al. (2020). One-Step reconstruction with a novel suspended, modular, and 3D-printed total sacral implant resection of sacral giant cell tumor with preservation of bilateral S(1-3) nerve roots via a posterior-only approach. *Orthop. Surg.* 12, 58–66. doi:10.1111/os.12582
- Meng, M., Wang, J., Sun, T., Zhang, W., Zhang, J., Shu, L., et al. (2022). Clinical applications and prospects of 3D printing guide templates in orthopaedics. *J. Orthop. Transl.* 34, 22–41. doi:10.1016/j.jot.2022.03.001
- Peng, L., Wang, P., Jiang, W., Cheng, C., Zuo, W., Qu, Y., et al. (2020). Reconstruction with a 3D-printed prosthesis and internal fixation with novel four-rod technique after *en bloc* resection of meningiomas in the lumbosacral region (L5-S3) without rectum/bladder function sacrifice: Technical case report. *Turk Neurosurg.* 30, 632–635. doi:10.5137/1019-5149.JTN.28031-19.2
- Ruggieri, P., Angelini, A., Pala, E., and Mercuri, M. (2012). Infections in surgery of primary tumors of the sacrum. *Spine* 37, 420–428. doi:10.1097/BRS.0b013e3182213a44
- Senne, J., Nguyen, V., Staner, D., Stensby, J. D., and Bhat, A. P. (2021). Demystifying sacral masses: A pictorial review. *Indian J. Radiol. Imaging* 31, 185–192. doi:10.1055/s-0041-1729766
- Tang, X., Guo, W., Yang, R., Tang, S., and Ji, T. (2009). Risk factors for blood loss during sacral tumor resection. *Clin. Orthop. Relat. Res.* 467, 1599–1604. doi:10.1007/s11999-008-0483-1
- van Wulfften Palthe, O. D., Houdek, M. T., Rose, P. S., Yaszemski, M. J., Sim, F. H., Boland, P. J., et al. (2017). How does the level of nerve root resection in *en bloc* sacrectomy influence patient-reported outcomes. *Clin. Orthop. Relat. Res.* 475, 607–616. doi:10.1007/s11999-016-4794-3
- Verlaan, J. J., Kuperus, J. S., Slooff, W. B., Hennipman, A., and Oner, F. C. (2015). Complications, secondary interventions and long term morbidity after *en bloc* sacrectomy. *Eur. Spine J.* 24, 2209–2219. doi:10.1007/s00586-014-3729-5
- Wang, Z., and Yang, Y. (2021). Application of 3D printing in implantable medical devices. *Biomed. Res. Int.* 2021, 1–13. doi:10.1155/2021/6653967
- Wei, R., Guo, W., Ji, T., Zhang, Y., and Liang, H. (2017). One-step reconstruction with a 3D-printed, custom-made prosthesis after total *en bloc* sacrectomy: A technical note. *Eur. Spine J.* 26, 1902–1909. doi:10.1007/s00586-016-4871-z
- Wei, R., Guo, W., Yang, R., Tang, X., Yang, Y., Ji, T., et al. (2019). Reconstruction of the pelvic ring after total *en bloc* sacrectomy using a 3D-printed sacral endoprosthesis with re-establishment of spinopelvic stability: A retrospective comparative study. *Bone Jt. J.* 101-B, 880–888. doi:10.1302/0301-620X.101B7.BJJ-2018-1010.R2
- Wuisman, P., Lieshout, O., van Dijk, M., and van Diest, P. (2001). Reconstruction after total *en bloc* sacrectomy for osteosarcoma using a custom-made prosthesis: A technical note. *Spine* 26, 431–439. doi:10.1097/00007632-200102150-00021
- Yen, W. W., Baksh, N., Gallo, V., Jamil, Z., Tischler, E. H., and Maheshwari, A. V. (2021). Current concepts and advances of three-dimensional printing in reconstructive musculoskeletal oncology: A systematic review. *J. Long. Term. Eff. Med. Implants* 31, 59–71. doi:10.1615/JLongTermEffMedImplants.2021038735



OPEN ACCESS

EDITED BY

Chunguang Yang,
Chinese Academy of Sciences (CAS),
China

REVIEWED BY

Sarath Chandra Veerla,
Associate Professor, India
Xinhua Qu,
Shanghai Jiao Tong University, China
Hui Deng,
Wenzhou Medical University, China

*CORRESPONDENCE

Jinxin Lin,
✉ jicheng@fjirsm.ac.cn

RECEIVED 25 March 2023

ACCEPTED 25 April 2023

PUBLISHED 09 May 2023

CITATION

Ji C, Zhang C, Xu Z, Chen Y, Gan Y,
Zhou M, Li L, Duan Q, Huang T and Lin J
(2023), Mussel-inspired HA@TA-CS/SA
biomimetic 3D printed scaffolds with
antibacterial activity for bone repair.
Front. Bioeng. Biotechnol. 11:1193605.
doi: 10.3389/fbioe.2023.1193605

COPYRIGHT

© 2023 Ji, Zhang, Xu, Chen, Gan, Zhou, Li,
Duan, Huang and Lin. This is an open-
access article distributed under the terms
of the [Creative Commons Attribution
License \(CC BY\)](https://creativecommons.org/licenses/by/4.0/). The use, distribution or
reproduction in other forums is
permitted, provided the original author(s)
and the copyright owner(s) are credited
and that the original publication in this
journal is cited, in accordance with
accepted academic practice. No use,
distribution or reproduction is permitted
which does not comply with these terms.

Mussel-inspired HA@TA-CS/SA biomimetic 3D printed scaffolds with antibacterial activity for bone repair

Cheng Ji^{1,2,3,4}, Chengcheng Zhang⁵, Zeya Xu^{1,2}, Yan Chen^{1,2},
Yanming Gan^{1,2,4}, Minghui Zhou^{1,2,4}, Lan Li^{1,2}, Qinying Duan^{1,2,4},
Tingting Huang^{1,2} and Jinxin Lin^{1,2,3*}

¹Quanzhou Institute of Equipment Manufacturing, Fujian Institute of Research on the Structure of Matter, Chinese Academy of Sciences, Quanzhou, Fujian, China, ²Fujian Science and Technology Innovation Laboratory for Optoelectronic Information of China, Fuzhou, Fujian, China, ³College of Chemistry and Materials Science, Fujian Normal University, Fuzhou, China, ⁴Fujian College, University of Chinese Academy of Sciences, Fuzhou, China, ⁵Fujian Medical University, Fuzhou, China

Bacterial infection is a major challenge that could threaten the patient's life in repairing bone defects with implant materials. Developing functional scaffolds with an intelligent antibacterial function that can be used for bone repair is very important. We constructed a drug delivery (HA@TA-CS/SA) scaffold with curcumin-loaded dendritic mesoporous organic silica nanoparticles (DMON@Cur) via 3D printing for antibacterial bone repair. Inspired by the adhesion mechanism of mussels, the HA@TA-CS/SA scaffold of hydroxyapatite (HA) and chitosan (CS) is bridged by tannic acid (TA), which in turn binds sodium alginate (SA) using electrostatic interactions. The results showed that the HA@TA-CS/SA composite scaffold had better mechanical properties compared with recent literature data, reaching 68.09 MPa. It displayed excellent degradation and mineralization capabilities with strong biocompatibility *in vitro*. Furthermore, the antibacterial test results indicated that the curcumin-loaded scaffold inhibited *S.aureus* and *E.coli* with 99.99% and 96.56% effectiveness, respectively. These findings show that 3D printed curcumin-loaded HA@TA-CS/SA scaffold has considerable promise for bone tissue engineering.

KEYWORDS

3D printing, curcumin, scaffolds, DMON, antibacterial

1 Introduction

Bone defects that exceed critical size deficiencies require surgical intervention to use bone grafts to repair the damaged tissue (Boos et al., 2010). Traditional treatment methods include autologous bone grafting and allogeneic bone grafting by obtaining bone tissue from the patient or donor and then implanting it into the bone defect site. Among them, autologous bone graft has complete histocompatibility without immune reaction and is also known as the gold standard of clinical treatment. However, conventional treatment is limited by the lack of bone donors, inflammation, infection, chronic pain at the donor site, and long-term medical care (Koushik et al., 2023; Mirkhalaf et al., 2023). In addition to the traditional treatment methods, Bioactive scaffolds have emerged as an alternative strategy for treating bone defects since interconnected pore structures allow space for inward tissue growth and oxygen and nutrient delivery (Zhang et al., 2019; Jodati et al., 2020). Moreover,

bioactive scaffolds avoid the drawbacks of traditional bone repair procedures, such as lack of bone cells and immune rejection, which can considerably reduce the patient's suffering from bone diseases (O'Brien, 2011; Delloye et al., 2007). The ideal scaffold is also required to have superior osteoinductivity, matching the new bone production rate's degradation rate, mechanical strength compatible with the original bone, etc., (Lee et al., 2022; Shi et al., 2022). Generally, bone tissue engineering scaffolds are available in four categories: natural polymers, synthetic polymers, bioceramic materials, and composite biomaterials (Boos et al., 2010; Lee et al., 2022; O'Brien, 2011; Zhang et al., 2019). Organic/inorganic composites as bone scaffolds have been the subject of extensive research to imitate the structure of natural bone, which comprises 60–65 wt% inorganic hydroxyapatite (HA) embedded in an organic collagen matrix (Olszta et al., 2007; Shi et al., 2022). There are various ways to make these bone scaffolds, but 3D printing has shown excellent capabilities in fabricating scaffold materials with complex shapes and individual customization (Zhang et al., 2019). 3D printing has structural design advantages and can couple functional designs to achieve structural and functional integration (Brunello et al., 2016; Zafar et al., 2019; Zhang et al., 2019; Wang et al., 2020; Yadav et al., 2021; MacDonald et al., 2022). Our previous research reported that 3D-printed La³⁺ ions-doped OCP/PLA scaffolds could promote osteogenic differentiation of BMSCs and accelerate bone defect healing *in vivo* (Xu et al., 2022). Nevertheless, synthetic polymers' hydrophobicity frequently causes cell adhesion problems, which limits their use. Natural polymers (like chitosan, sodium alginate, collagen, etc.) are similar to the extracellular matrix (ECM) structure. They have outstanding biocompatibility, cell adhesion, and cell growth-promoting qualities (Donnaloja et al., 2020; Guo et al., 2021; Ressler, 2022; Ye et al., 2022). Because of this, researchers are paying more and more attention to them. Mussels, marine organisms, can adhere firmly to a range of non-specific surfaces by secreting protein fibres containing the catechol fraction (Barros et al., 2021; Radulescu et al., 2022). In recent years, there had been remarkable success in the functionalization of mussel-inspired material surfaces (Lee et al., 2007; Mehdizadeh et al., 2012; Guo et al., 2016; Guo et al., 2017; Guo et al., 2018; Lu et al., 2020). Tannins with catechol moieties had been shown to adhere strongly to inorganic surfaces, enhancing the interfacial forces of the complexes (Guo et al., 2020; Yan et al., 2020; Yu et al., 2023).

In clinical, however, implant-related infection is the major concern for implant failure. *Staphylococcus aureus* is the most common pathogen of infections (Lew and Waldvogel, 2004). It can lead to the failure of bone repair and even the death of the patient. Antibiotics was the most effective treatment strategy for bone implant infections, but systemic delivery may cause significant adverse effects and bacterial medication resistance (Ribeiro et al., 2012; Fernandes et al., 2017; Filipovic et al., 2020). Developing and manufacturing bone scaffolds with antibacterial activity is necessary. For instance, Lei et al. reported a ZIF-8-loaded vancomycin bone scaffold with an inhibition efficiency of about 93.5% against *S.aureus*, which exhibited a faster VAN release rate in a weakly acidic solution (Han et al., 2022). In addition, many other types of drugs are used for the antimicrobial functionalization of bone scaffolds, such as doxycycline (Bakhsheshi-Rad et al., 2018; Wang et al., 2021a), tannic acid (TA) (Zhang et al., 2022a; Liao et al., 2022; Zhou et al., 2022), etc. Turmeric is used in Traditional Chinese

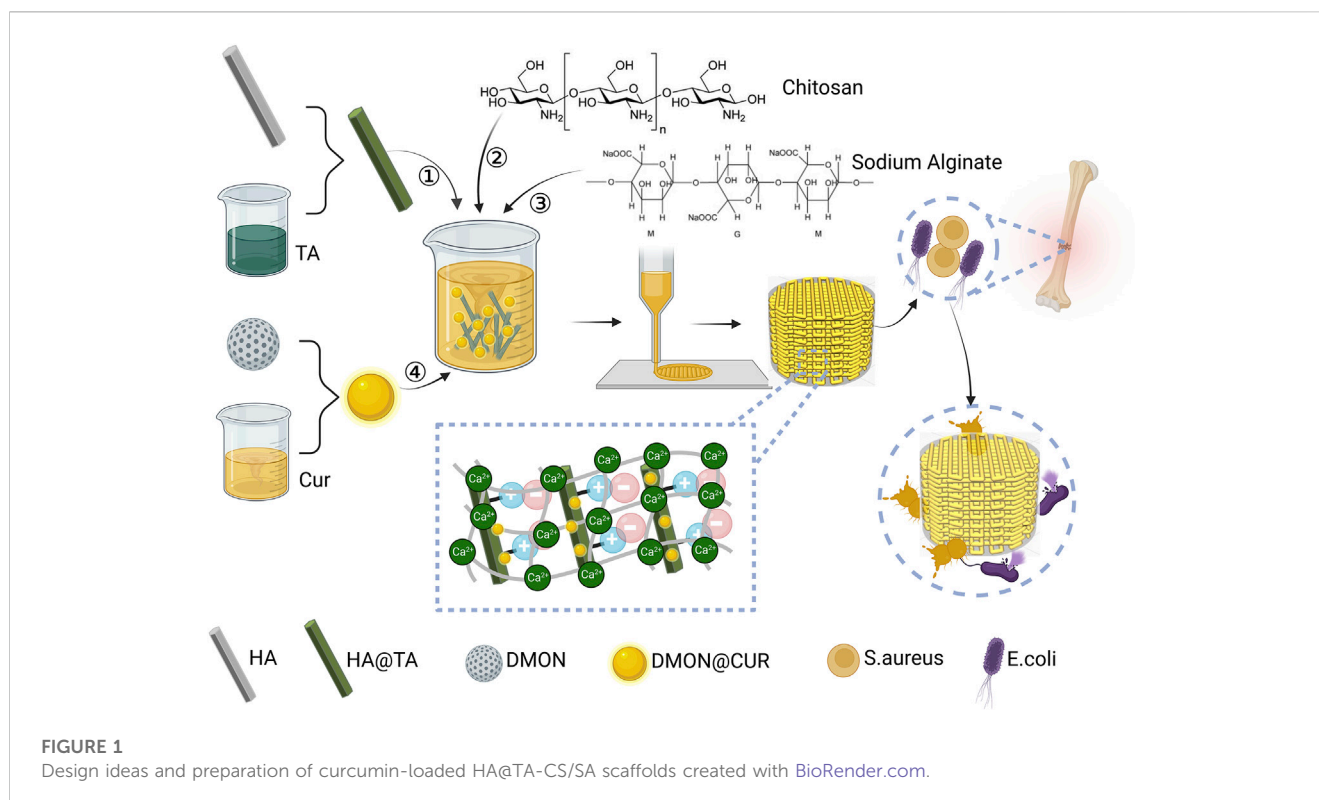
Medicine (TCM) to treat and prevent various diseases such as osteoarthritis, cancer, stomach ulcers, etc., (Chen et al., 2022). Turmeric has more than 300 bioactive components, including curcumin (Cur), a class of natural orange-yellow polyphenolic compounds found in turmeric (Iweala et al., 2023). Extensive studies had shown it has good antioxidant, anti-inflammatory, antibacterial, and antiviral activities (Benameur et al., 2022; Benameur et al., 2023; Nasiry and Khalatbary, 2023). But curcumin has very low solubility in an aqueous solution and is easily degraded, which limits its clinical application (Hamilton and Gilbert, 2023; Jiang et al., 2023). Therefore, a suitable curcumin carrier is important to improve its bioavailability. There had been several drug release studies for curcumin, such as cellulose nanocrystals containing curcumin for an antimicrobial delivery system for diabetic wound excipients, and the drug can be released stable for 36 h (Ou et al., 2018; Tong et al., 2018). Studies have shown that porous materials combined with low-solubility drugs can significantly improve drug solubility (Kong et al., 2016; Pezzini et al., 2016; Riachy et al., 2016). Dendritic mesoporous organic silica nanoparticles (DMON) can significantly enhance low-solubility drug delivery and release due to their large surface area, high porosity, excellent biocompatibility, and biodegradability (Wang et al., 2021b). Tannin acid is a class of natural water-soluble polyphenol dendrimers with antioxidant and antibacterial properties. Studies have shown that redox-active antioxidants can improve curcumin's chemical stability and biological activity (Nimiya et al., 2016). In addition, Tannin acid is an efficient precursor for surface treatment, capable of layer-by-layer assembly and deposition with polymer molecules through non-covalent bonds (Zhang et al., 2022a; Liao et al., 2022; Zhou et al., 2022). As a strong adhesive, tannic acid can also easily adhere to the surface of hydroxyapatite (Guo et al., 2020). Therefore, tannins are increasingly used in antibacterial bone scaffolds.

Inspired by the adhesion mechanism of mussels, this study prepared HA@TA powder by adhering TA to HA surface. TA was then used as a "bridge" to connect HA and CS, compounded with SA using electrostatic interactions, and doped with DMON@Cur nanoparticles of different mass fractions to produce curcumin-loaded HA@TA-CS/SA scaffolds by 3D printing. As shown in Figure 1, this bionic scaffold had a fully interconnected porous structure that provides a site for tissue ingrowth and nutrient transport, and a rough surface microstructure that promotes cellular and bacterial adhesion. All components of the scaffold are biologically active and degradable compared to other biomaterials, with curcumin providing significant antibacterial properties to the scaffold. This bionic antimicrobial scaffold has great potential in reducing bacterial infections during bone defect repair.

2 Experimental section

2.1 Materials

Analytical reagent diammonium hydrogen phosphate ((NH₄)₂HPO₄), sodium alginate (SA.), chitosan (CS, high viscosity, >400 mPa.s), and glycolic acid (GA, 70% aqueous) were purchased from Shanghai Aladdin Bio-Chem Technology Co., Ltd



(China). Acetamide (AA), hexadecyl trimethyl ammonium bromide (CTAB), bis(3-(triethoxysilyl)propyl) tetrasulfide (BTES), tetraethoxy-silane (TEOS), curcumin(Cur) and tannic acid (TA) were procured from Macklin Biochemical Technology Co., Ltd (China). Calcium chloride dehydrate ($\text{CaCl}_2 \cdot 2\text{H}_2\text{O}$, 99%), Tris(hydroxymethyl)amino-methane ($\text{C}_4\text{H}_{11}\text{NO}_3$, 99.8%), and calciumnitrate tetrahydrate ($\text{Ca}(\text{NO}_3)_2 \cdot 4\text{H}_2\text{O}$ analytically pure) were purchased from Sinopharm Chemical Reagent Co., Ltd (China). All chemicals were used as received without further purification.

2.2 Preparation and characterization of powder

2.2.1 Preparation of DMON and DMON@Cur

The DMON synthesis was based on the previously published technique with certain modifications (Dong et al., 2022). The following procedures were carried out in the dark to produce DMON@Cur powder. Ultrasonically dispersing 0.1 g of curcumin and 0.1 g of DMON powder in 50 mL of PBS-Tween 80 (0.09 wt%) took 10 min. This was followed by magnetic stirring at 37°C and 500 rpm for 12 h. The bottom precipitated pellet was then dried under a vacuum at 37°C after high-speed centrifugation. The process's supernatant was collected, and its UV absorbance at 425 nm was measured using a UV-6100 UV spectrophotometer (Mwere dissolved in 200 mL of Acetamide (AA) solution (1 mol/L) aAPADA) to determine the encapsulation efficiency and loading. A standard calibration curve of Cur in PBS-Tween 80 (0.09 wt%) was used to determine how much Cur was in the supernatant. Eq. 1, 2

were used to determine encapsulation efficiency and loading capacity.

$$\text{Encapsulation efficiency (\%)} = \frac{\text{Loaded amount of CUR}}{\text{Total amount of CUR}} \quad (1)$$

$$\text{Loading capacity (\%)} = \frac{\text{Loaded amount of CUR}}{\text{Total amount of DMON}} \quad (2)$$

2.2.2 Synthesis of long rod-shaped hydroxyapatite modified with tannic acid

Hydroxyapatite (HAp, $\text{Ca}_{10}(\text{PO}_4)_6(\text{OH})_2$) powder samples were prepared via the pH-adjusting agents-assisted hydrothermal synthesis. In a typical experiment (Zhang and Darvell, 2010), 0.025 mol of $\text{Ca}(\text{NO}_3)_2 \cdot 4\text{H}_2\text{O}$ and $(\text{NH}_4)_2\text{HPO}_4$ were dissolved in 200 mL of Acetamide (AA) solution (1 mol/L) and then mixed slowly at a Ca/P ratio of 1.67. Then the pH was adjusted to 3.0 with 0.1 mol/L of HNO_3 . The resulting reaction system was reacted hydrothermally at 180°C for 6 h and then filtered and washed to obtain pure HA powder.

To synthesize HA@TA powder (Guo et al., 2020), first dissolved an appropriate amount of Tris(hydroxymethyl)aminomethane in deionized water and adjusted the pH to 9.0 with 1 mol/L hydrochloric acid to form 50 mM Tris-HCl solution. Then, 5 g of tannic acid was added to 100 mL of Tris-HCl solution and stirred until clear, and an equal mass of HA powder was dispersed in 150 mL of Tris-HCl solution. The above solutions were mixed and sealed at room temperature under mechanical stirring for 24 h. Finally, the above yellow-green suspension was centrifuged at 4500 rpm for 10 min, washed 3 times with deionized water, and dried in an oven at 60°C for 6 h.

TABLE 1 The names and codes of the prepared scaffolds.

Scaffold name	Code	DMON@Cur (wt%)
Hydroxyapatite-Sodium alginate	HA-SA	0
Hydroxyapatite@ Tannin-Sodium alginate	HA@TA-SA	0
Hydroxyapatite@ Tannin-Chitosan/Sodium alginate	HA@TA-CS/SA	0
Hydroxyapatite@ Tannin-Chitosan/Sodium alginate-3 wt% DMON curcumin	HA@TA-CS/SA-3 wt% DMON	3
Hydroxyapatite@ Tannin-Chitosan/Sodium alginate-6 wt% DMON curcumin	HA@TA-CS/SA-6 wt% DMON	6
Hydroxyapatite@ Tannin-Chitosan/Sodium alginate-9 wt% DMON curcumin	HA@TA-CS/SA-9 wt% DMON	9

2.2.3 Characterization of powder

Field emission scanning electron microscopy (FESEM; SU8010, Hitachi) and transmission electron microscopy (TEM; TecnaiG2F20S-TWIN, FEI) analyses were used to examine the microstructure and distribution of the synthesized HA and DMON. The products' corresponding elemental mapping and energy-dispersive X-ray spectra (EDS) were obtained from the TEM. The surface area and pore size of DMON were measured on a Micromeritics TristarII 3020 system using an N₂ adsorption-desorption isotherm. The samples were degassed under vacuum at 120 °C for 24 h before testing. The crystalline nature of HA, HA@TA powders were identified by X-ray diffraction (XRD, Miniflex600, Rigaku) using Cu K α radiation at 40 kV and 15 mA current. The 2 θ angles were scanned from 10° to 65° at a scan rate of 2°/min. The chemical and functional characteristics of HA, HA@TA, DMON, and DMON@Cur powders were examined by FTIR spectroscopy (Lambda 950, Perkin Elmer). Raman spectrophotometer (LabRAM HR, HORIBA) was also used to characterize the KBr integrated samples, using an Nd: YAG laser with a wavelength of 633 nm, a displacement range of 400–4000 cm⁻¹, and a resolution of 2 cm⁻¹. The surface potential of HA, HA@TA powders identified with the BI-200SM dynamic light scattering particle size analyzer.

2.3 Preparation of scaffolds

Table 1 lists the names of all the scaffolds prepared in this work.

2.3.1 Preparation of HA@TA-CS/SA scaffolds and 3D printing

The slurry of the HA@TA-CS/SA scaffold for printing requires an inorganic-organic mass ratio mimicking natural human bone of 6:4, which is prepared by the *in situ* compounding method. Specifically, 1 g of CS was dissolved in 200 mL of ethanolic acid (2 wt%) to prepare a 5 g/L solution of CS. 2 g of the prepared HA@TA powder was dispersed in 150 mL of deionized water and stirred continuously with a magnetic stirrer for 20 min to achieve uniform dispersion. 53.33 mL of CS solution was added to the above solution by high-speed magnetic stirring for 30 min, and the pH of the solution was adjusted to 7.6 by adding 1% sodium hydroxide solution dropwise. Some of the above-stirred slurries were dried in the oven at 60 °C to obtain HA@TA-CS powder, which was then used for subsequent characterization tests. Then, 1.07 g of SA powder was weighed and slowly added to the above solution

under high-speed mechanical stirring so that the mass ratio of CS to SA was 2:8. Stirring was continued until the SA was dissolved entirely so that the slurry was well mixed. Some of the above-stirred slurries were dried in an oven at 60 °C to obtain HA@TA-CS/SA powder, which was used for subsequent characterization tests. The resulting solution was frozen in a refrigerator at -20 °C for 12 h and then freeze-dried for 48 h until complete. The freeze-dried "foamy" solid was mixed with deionized water in a ratio of 1:3 by mass and stirred with a glass rod until it was in the form of a slurry. The prepared slurry is then loaded into a 50cc cylinder and waited for printing.

The cylindrical models of $\Phi 15 \times 5$ mm and $\Phi 15 \times 30$ mm were constructed using SolidWorks2020 modeling software, saved as stl format files, imported into the model slices using CurA slicing software, set specific process parameters: layer thickness 0.6 mm, filling density 50%, filling path serrated, filling direction 90°, printing speed 25 mm/min. After that, the Gcode file is generated, and the porous scaffold is printed layer by layer by an extrusion 3D printer whose needle diameter is 0.6 mm under the control of a computer program. After printing, the scaffolds were crosslinked in 10 wt% CaCl₂ solution for 5 h, then washed three times with deionized water to remove the CaCl₂ solution from the surface and dried in an oven at 37°C for 24 h.

2.3.2 Characterization of HA@TA-CS/SA scaffolds

The crystalline nature of HA@TA-CS and HA@TA-CS/SA powders were identified by X-ray diffraction (XRD, Miniflex600, Rigaku). The chemical and functional characteristics of HA@TA-CS and HA@TA-CS/SA powders were examined by FTIR spectroscopy (Lambda 950, Perkin Elmer) and Raman spectrophotometer (LabRAM HR, HORIBA) to explore their interactions in the scaffold composites. Elemental and bond composition of HA@TA-CS/SA powders used by x-ray photoelectron spectroscopy (XPS). The surface potential of HA@TA-CS and HA@TA-CS/SA powders were identified with the BI-200SM dynamic light scattering particle size analyzer.

The rheology and viscoelasticity of the printed slurry were tested at 25°C using a rheometer (TA Instruments, DHR-2). The rheology of the slurry was tested in flow scan mode using a 25 mm diameter 5.805° conical-plate-shaped rotor with a measurement gap of 150 μ m. The viscoelasticity of the slurry was tested using the same rotor in amplitude scan mode at 1 Hz and with a measurement gap of 150 μ m. FESEM carried out the microscopic morphology of the prepared HA@TA-CS/SA scaffold at 5 kV after gold sputter coating.

2.3.3 Preparation of curcumin-loaded HA@TA-CS/SA scaffolds

DMON@Cur nanoparticles with varying mass ratios (3.0, 6.0, and 9.0 wt%) were added to the above HA@TA-CS/SA slurry to make the scaffolds antibacterial. It is worth noting that the remainder of the preparation procedure was identical. Portions of the above-stirred slurries were baked in a 60 °C oven to produce curcumin-loaded HA@TA-CS/SA powder for future characterization testing.

2.3.4 Characterization of curcumin-loaded HA@TA-CS/SA scaffolds

The chemical and functional characteristics of curcumin-loaded HA@TA-CS/SA powder were examined by Fourier transform infrared spectroscopy (Lambda 950, Perkin Elmer).

The rheology and viscoelasticity of the printed slurry were tested at 25°C using a rheometer (TA Instruments, DHR-2). The rheology of the slurry was tested in flow scan mode using a 25 mm diameter 5.805° conical-plate-shaped rotor with a measurement gap of 150 µm. The viscoelasticity of the slurry was tested using the same rotor in amplitude scan mode at 1 Hz and with a measurement gap of 150 µm. FESEM carried out the microscopic morphology of the prepared curcumin-loaded HA@TA-CS/SA scaffolds at 5 kV after gold sputter coating. The thermal stability of the scaffold's powder was measured using a comprehensive thermal analyzer (STA449-F3, Netzsch), with a heating rate of 10 k/min and a measurement interval of 30°C–900°C.

2.4 Compression testing

For the compressive strength tests, two more control scaffolds (HA-SA and HA@TA-SA) were prepared using the controlled variable method to see how the different parts of the HA@TA-CS/SA scaffolds worked together. The HA-SA and HA@TA-SA scaffolds were fabricated using the same fabrication process, and both had an organic/inorganic component ratio of 4:6. The 3D-printed HA-SA, HA@TA-SA, HA@TA-CS/SA, and curcumin-loaded HA@TA-CS/SA scaffolds were all $\Phi 15 \times 30$ mm in size. The compressive stress and Young's modulus of the porous scaffolds were measured using a universal testing machine (CMT4304, SANS).

2.5 Immersion tests

The *in vitro* degradation test of the curcumin-loaded HA@TA-CS/SA scaffolds was conducted in PBS solution (pH = 7.4) at 37°C to evaluate the weight loss. The exact weight of the scaffold (W_i) was measured, and then the scaffold was put into a beaker with PBS. Under the aforementioned conditions, the beakers were sealed entirely and kept at 37°C for 14 days. At set times, samples were taken out, washed, freeze-dried, and weighed (W_f), and the shape of the degraded scaffold was examined using a FESEM microscope. Eq. 3 was used to determine the percentage degradation rate (DR):

$$DR (\%) = \frac{W_i - W_f}{W_i} \quad (3)$$

2.6 Curcumin release studies

To evaluate the drug release pattern of curcumin-loaded scaffolds in normal and inflammatory environments, scaffolds containing different concentrations (3.0, 6.0, 9.0 wt%) of DMON@Cur particles were placed into dialysis bags (30 kDa, Solarbio, China). Meanwhile, A set of HA@TA-CS/SA-loaded curcumin scaffolds without DMON nanoparticles, in which the curcumin loading concentration was 9 wt%, was also prepared and put into the dialysis bag as a comparative test. The dialysis bags were placed in 50 mL of PBS-Tween80 (0.9 wt%, 100 rpm/min) solution at pH 5.3 and pH 7.4, respectively, as a release medium without ambient light. At defined time intervals, 3 mL of the solution was removed and replaced with a new PBS-Tween80 solution. Samples obtained from the release medium were characterized using a UV spectrophotometer at 425 nm to determine the concentration of released Cur.

2.7 Cytocompatibility assay

Bone marrow mesenchymal stem cells (BMSCs) of 3–5 generations were used for the study of *in vitro* cellular experiments. Primary rat bone marrow MSCs were isolated and cultured following previously reported procedures. BMSCs were cultured in culture flasks and maintained at 37°C as well as 5% CO₂ in a cell culture chamber (SCO5W-2, Shellab, United States). Cells were cultured with DMEM/F12 medium containing 10% fetal bovine serum, 1% streptomycin-penicillin double antibody and 1% glutamine, renewed every 2 days. All curcumin-loaded HA@TA-CS/SA scaffold extracts were prepared according to ISO 10993–12 2017. The curcumin-loaded HA@TA-CS/SA scaffolds were immersed in ethanol (75 v/v%) for 2 h, then rinsed with sterile PBS and immersed in the medium at 10 ± 0 mg/mL (same as cell culture medium) and incubated on a shaker at 37°C. The medium was collected, renewed every other day with a sterile syringe, and filtered through 0.22 µm. The filtrate was collected in a 15 mL centrifuge tube and stored in a refrigerator at 4°C for later use.

The cell viability of the curcumin-loaded HA@TA-CS/SA scaffolds was measured by the Cell Counting Kit-8 (CCK-8) assay. In a typical experiment, BMSCs were incubated with extracts at a density of 8×10^4 cells/cm² in 96-well plates. 10 µL CCK-8 solution was added to each well at different time points (1, 3, and 5 days). After 1 h of incubation, each well's optical density (OD) was measured at 450 nm using an enzyme marker to quantify cell proliferation.

After 1, 3, and 5 days of incubation, bone marrow BMSCs were stained with a calcein-AM/PI double staining kit (Dalian Meilun Biotechnology Co., Ltd.) The fluorescence images of bone marrow MSCs obtained by inverted fluorescence microscopy.

The results of osteogenic differentiation were observed under the microscope after incubation of the three generations of BMSCs cells with the infiltrates of four curcumin-loaded scaffolds for 7 days using alkaline phosphatase staining. ALP activity was then quantified using an alkaline phosphatase assay kit (p0321, Beyotime).

2.8 Antibacterial test

With the inhibition circle method, the inhibition ability of the curcumin-loaded HA@TA-CS/SA scaffold against *E.coli* and *S.aureus* was measured. The slant strains of *E.coli* and *S.aureus* used in the experiment were bought from the Shanghai Conservation Biotechnology Centre. Inoculation loops put *E.coli* and *S.aureus* on nutrient agar plates. The plates were then incubated at 90% humidity and 37°C for 20 h until the bacteria entered the exponential growth phase. A small number of bacteria entering the exponential growth phase was picked up with an inoculation loop, dissolved in PBS solution, and diluted to 1×10^8 cfu/mL using the medium diffusion method.

Bacterial inhibition loop experiment using *E.coli* and *S.aureus*: Dilute the above 1×10^8 cfu/mL *E.coli* and *S.aureus* bacterial solution 100 times with PBS solution, use a pipette to take 100 μ L of the diluted bacterial solution on an agar plate, spread it evenly with a spreader, allow the bacterial solution to dry and then take a $\Phi 15 \times 5$ mm size curcumin-loaded HA@TA-CS/SA (0,3,6, and 9 wt%) porous scaffolds were evenly placed in the Petri dishes and incubated upside down in a constant temperature incubator at 37°C for 24 h before comparing the size of the inhibition rings.

The bactericidal rate test is an important measure of whether the scaffold could kill the bacteria in contact with it in the surrounding environment. The above 1×10^8 cfu/mL *Staphylococcus aureus* and *Escherichia coli* solutions were diluted 10 times to 105 cfu/mL in PBS solution. Curcumin-loaded HA@TA-CS/SA (0,3,0,6,0 and 9.0 wt%) scaffolds were placed in a bacterial suspension at a 105 cfu/mL concentration rate of 1 g/100 mL and placed in a 37°C incubator. Plates were counted at 24 h of incubation at 10-fold dilution, each group was repeated three times, and the bactericidal rate was calculated. Bactericidal rates were assessed using Eq. 4:

$$\text{Bactericidal rate} = \frac{\text{colony count}_{\text{blank}} - \text{colony count}_{\text{sample}}}{\text{colony count}_{\text{blank}}} \quad (4)$$

The bacteria were diluted with PBS buffer until the absorbance OD value was 0.1 and then co-cultured with the scaffolds for 12 h. Using the BCA kit, protein concentration was measured.

3 Results and discussion

3.1 Characterization of DMON@Cur

FESEM analysis showed that the organic dendritic mesoporous silica microspheres (DMON) appeared as uniformly sized spherical particles with fullness (Figure 2A). Meanwhile, TEM analysis (Figures 2B, C) revealed the fine surface structure of DMON, highlighting the presence of distinct dendritic mesopores. Mappings (Figure 2D) showed that element C was uniformly distributed on the microspheres' surface and internal pores, proving that curcumin had been loaded onto the DMON microspheres. The specific surface area and pore size distribution of the prepared DMON and DMON@Cur nanoparticles were measured using N_2 adsorption-desorption isotherms (Figures 2E, F). The N_2 adsorption-desorption isotherms of both nanoparticles

could be classified as type IV, indicating a mesoporous structure (Yao et al., 2020). The specific surface area rapidly reduced after total absorption (from 632.6 m^2/g to 170.8 m^2/g). Furthermore, the pore size of DMON was 17.5 nm, which dropped to 15.6 nm in DMON@Cur, suggesting the successful production of Cur-loaded DMON nanosystems. The average size of DMON@Cur particles was approximately 228 ± 5 nm (Figure 2G). The encapsulation efficiency and drug loading capacity of DMON were 73.81% and 70.25%, respectively, calculated by Eqs 1, 2. X-ray diffraction (Figure 2H) and FTIR (Figure 2I) showed the DMON and DMON@Cur structural characteristics spectroscopy. As shown in the XRD patterns (Figure 2H), characteristic diffraction peaks of amorphous SiO_2 within 15° – 30° for mesoporous silica and the main diffraction peaks of curcumin appeared at $2\theta = 17$ – 28° (Ou et al., 2018; Oboudatian and Safaei-Ghomi, 2022). The FTIR (Figure 2I) showed the typical peaks of the DMON could be observed in the region of 1092–1150 cm^{-1} , reflecting the Si–O–Si asymmetric stretching vibration, Si–O–Si peak was observed at 812 cm^{-1} , which represented the symmetric stretching vibration. Moreover, the peaks at 463 cm^{-1} , 1621 cm^{-1} , and 3446 cm^{-1} correspond to the Si–O bending vibration, the O–H bending vibration, and the stretching vibration, respectively (Oboudatian and Safaei-Ghomi, 2022). The main characteristic peaks of curcumin were the unsaturated carbonyl vibrations at 1630 cm^{-1} , the hydroxyl vibrations at 3510 cm^{-1} , and the benzene ring peaks at 1600 cm^{-1} and 1510 cm^{-1} (Benassi et al., 2008). It was found that Cur and DMON interacted by hydrogen bonding. All the above results showed that the synthesized DMON nanoparticles could bind well with curcumin through hydrogen bonding.

3.2 Characterization of scaffolds

The SEM (Figure 3) showed the scaffolds doped with DMON@Cur particles of various mass fractions (0,3,0,6,0, and 9.0 wt%) microscopic morphology. All scaffolds had an interconnected porous structure with a rough uncracked surface and pore size of 300 ± 60 μ m. The scaffolds became deeper in color as the proportion of Cur-loaded particles increased. The rod-shaped HA was faintly visible and encapsulated inside the scaffolds.

The hydroxyapatite (HA) prepared by the hydrothermal method was demonstrated by FESEM (Figure 4A) as homogenous hexagonal long rods (60–170 μ m) with a diameter of 818 ± 207 nm and a high aspect ratio (59–278), which was similar to the results of previous studies (Zhang and Darvell, 2010). After TA modification, the surface morphological roughness of HA crystals changed, and some fine HA particles could be seen adsorbed on the surface. It also showed that TA had a high capacity to adsorb and bond to the HA surface (Figure 4B). The HA lattice spacing (Figure 4C) was 0.34 nm, corresponding to the (002) crystal plane of the standard card (JCPDS PDF 9–432), and showed that the HA crystals were developing in a C-axis orientation (Zhang and Zhu, 2005). The elemental distribution of the HA@TA powder was analyzed by EDS (Figure 4D), which showed that the main composition consisted of C (13.87wt%), Ca (29.72wt%), P (18.1wt%), and O (38.31wt%) elements. The presence of C indicated that TA was adsorbed on the surface of HA.

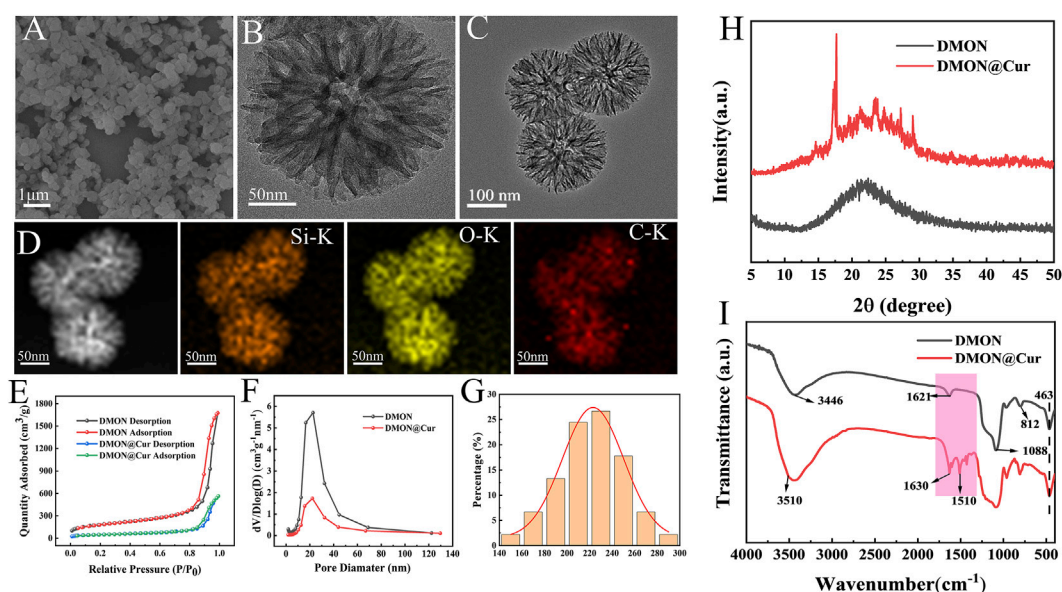


FIGURE 2

(A) SEM micrographs of DMON. (B) TEM micrographs of DMON. (C) TEM micrographs of DMON@Cur. (D) Elemental mappings. (E) Nitrogen adsorption-desorption isotherm. (F) the corresponding pore-size distribution of DMON and DMON@Cur. (G) Size distribution of DMON@Cur. (H) XRD of DMON and DMON@Cur. (I) FTIR of DMON and DMON@Cur.

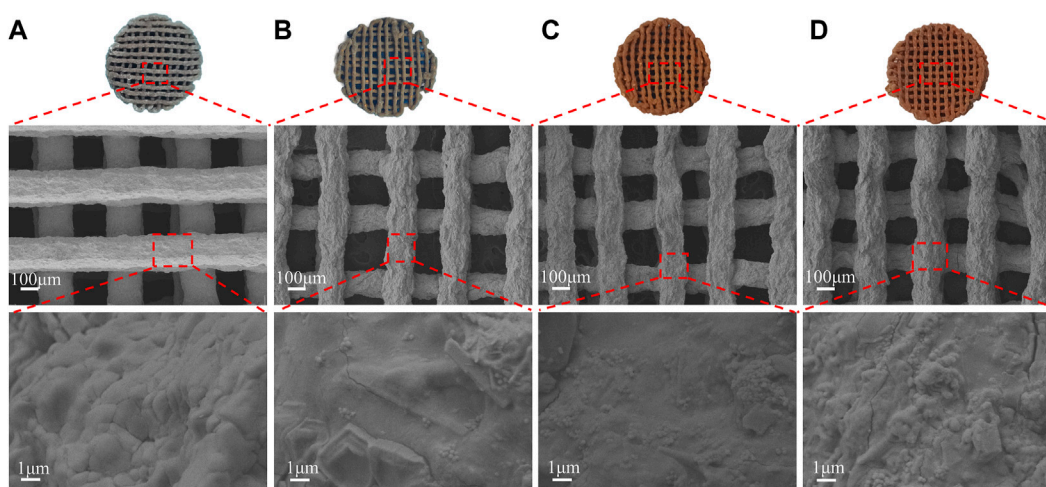


FIGURE 3

Surface morphology of scaffolds with different DMON@Cur loadings (A) 0 wt% (B) 3.0 wt% (C) 6.0 wt% (D) 9.0 wt%.

The X-ray diffraction (Figure 5A) showed patterns of HA, HA@TA, HA@TA-CS, and HA@TA-CS/SA powders to determine their crystalline properties. The sharp characteristic peaks of HA powders (Figure 5A) were consistent with those of the standard XRD card (JCPDS PDF 9–432) of hydroxyapatite. The characteristic peaks at 10.82° , 21.819° , 25.897° , 28.126° , 28.966° , 31.773° , 32.196° , 32.902° , 39.818° , 46.711° , 49.468° correspond to the planar diffraction peaks of HA (100), (202), (002), (102), (210), (211), (112), (300), (202), (310), (222), (213), where the diffraction peak at (211) crystal plane

is the strongest. It indicated that HA powders with high crystallinity were successfully synthesized using the hydrothermal method (Zhang and Zhu, 2005). As previously reported, the most vigorous peak intensity occurred in the (211) lattice plane (Yang et al., 2005). After the surface modification, however, the intensity diffraction peak of HA powders was decreased. Moreover, the functional groups of the material and their possible interactions within the scaffold were assessed using FTIR and Raman techniques. The FTIR spectra (Figure 5B) showed the HA powder and after

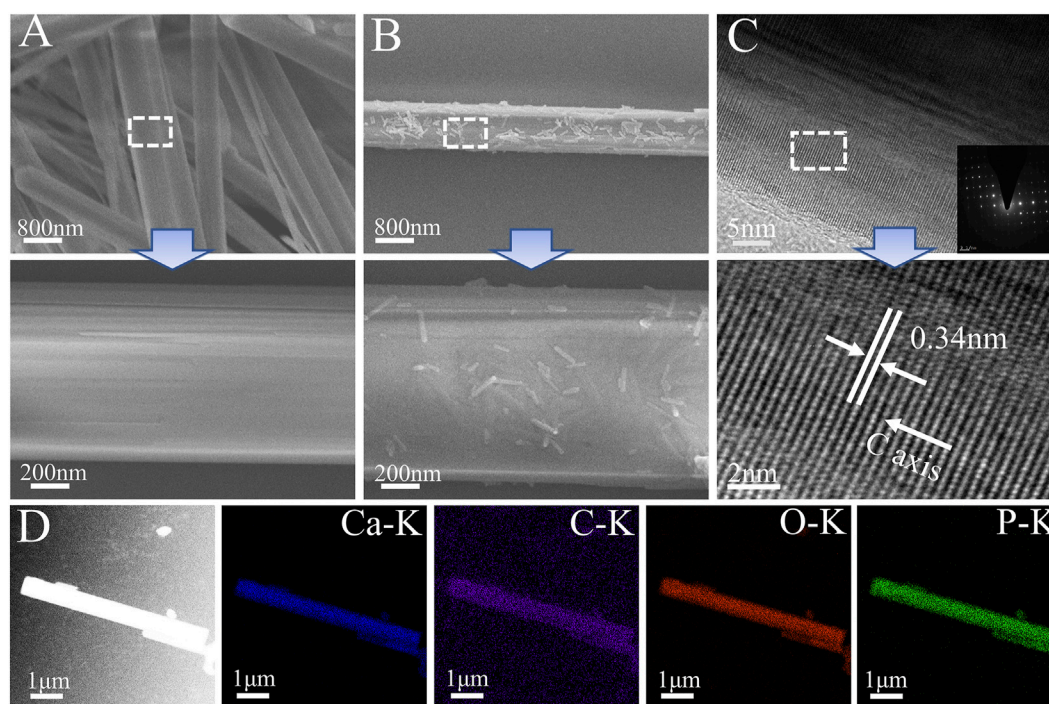


FIGURE 4

(A) SEM micromorphology of HA. (B) SEM micromorphology of HA@TA. (C) TEM microscopic morphology and electron diffraction of HA. (D) Elemental mappings.

organic modified HA powder. The characteristic peaks at 1093, 1034, 602, and 564 cm^{-1} were PO_4^{3-} and the absorption peaks at 3571 and 633 cm^{-1} were attributed to hydroxyl groups. These main vibrational peaks were typical of the characteristic peaks of HA (Koutsopoulos, 2002; Zhang and Darvell, 2010). Compared to the pure HA powder, the HA@TA powder had C-O stretching peak (1707 cm^{-1}), C-O stretching peak (1609 cm^{-1}), C-C-C aromatic ring stretching peak (1444 cm^{-1}), and C-C bond corresponding to the aromatic ring 754 cm^{-1} peak (Hussain et al., 2022). The absorption peak at 1552 cm^{-1} of the HA@TA-CS powder spectrum corresponded to the $-\text{NH}_2$ bending vibration. The absorption peak (1440 cm^{-1}) was related to the electrostatic interaction between the NH_3^+ group of CS and the phenoxy (Ph-O-) group of HA@TA (Lee et al., 2023). The absorption peaks of the HA@TA-CS/SA powder were C-O-C stretching at 1030 cm^{-1} and OH-stretching at 3450 cm^{-1} . The observed bands at 1625 and 1420 cm^{-1} for SA were attributed to carboxyl groups and asymmetric and symmetric COO^- stretching vibrations, respectively. The antisymmetric stretching of COO^- in SA shifts towards the lower band, and wave numbers overlap the antisymmetric stretching peaks of COO^- at 1546 cm^{-1} and 1595 cm^{-1} . It confirmed the presence of ionic interactions between cationic CS and anionic SA via electrostatic interactions (Ke et al., 2010). The Raman spectra (Figure 5C) also showed the typical characteristic peaks of HA, with the modified powder having CH- and C=C double bonded peaks at 1350 cm^{-1} and 1550 cm^{-1} , respectively. The most pronounced peaks on the surface of the scaffold demonstrated successful modification on the surface of HA. Based on the XPS spectra of HA@TA-CS/SA scaffold powders

results (Figure 5D), the deconvolution peaks of Ca2p and P2p were typical of the elements and families of HA crystals (Yang et al., 2005). The deconvolution peaks of C-C (284.8 eV), C-O-C (286.41 eV), O=C-O (288.61 eV), and $\pi-\pi^*$ (291.0 eV) in the C1s spectrum and C=O (533.02 eV) and C-O (531.55 eV) in the O1s spectrum reflected organic bonding on the HA ceramic surfaces (Hussain et al., 2022; Lee et al., 2023). The appearance of C-NH2 (400.15 eV) in the N1s spectrum also demonstrated the introduction of CS in the scaffold (Lee et al., 2023).

Rheological performance is an essential judgment in examining the printable properties of the slurry. After adding DMON@Cur particles with mass fractions of 0, 3.0, 6.0, 9.0 wt% to the HA@TA-CS/SA slurry, the pastes' rheological characteristics (Figure 6A) were examined. The apparent viscosity of all slurry decreased significantly with increasing shear rate showing an apparent "shear thinning" phenomenon typical of pseudoplastic fluids. In addition, the higher the mass fraction of DMON@Cur particles added, the apparent viscosity of the slurry was slightly reduced, but the effect was not significant. Frequency scans (Figure 6B) of the slurries showed that the G' values for all slurries remained essentially constant throughout the frequency range, indicating good crosslinking (Dong et al., 2022). The addition of DMON@Cur carrier particles had little effect on the internal crosslinking mechanism of the slurries, which were stable and continuous.

We performed zeta potential tests during each step of the scaffold preparation to determine the binding pattern within the material (Figure 6C). At the initial stage, the synthesized HA surface displayed a positive charge of 4.32 mv. After the TA modification, the material exhibited a negative charge of -3.43 mv (Hussain et al.,

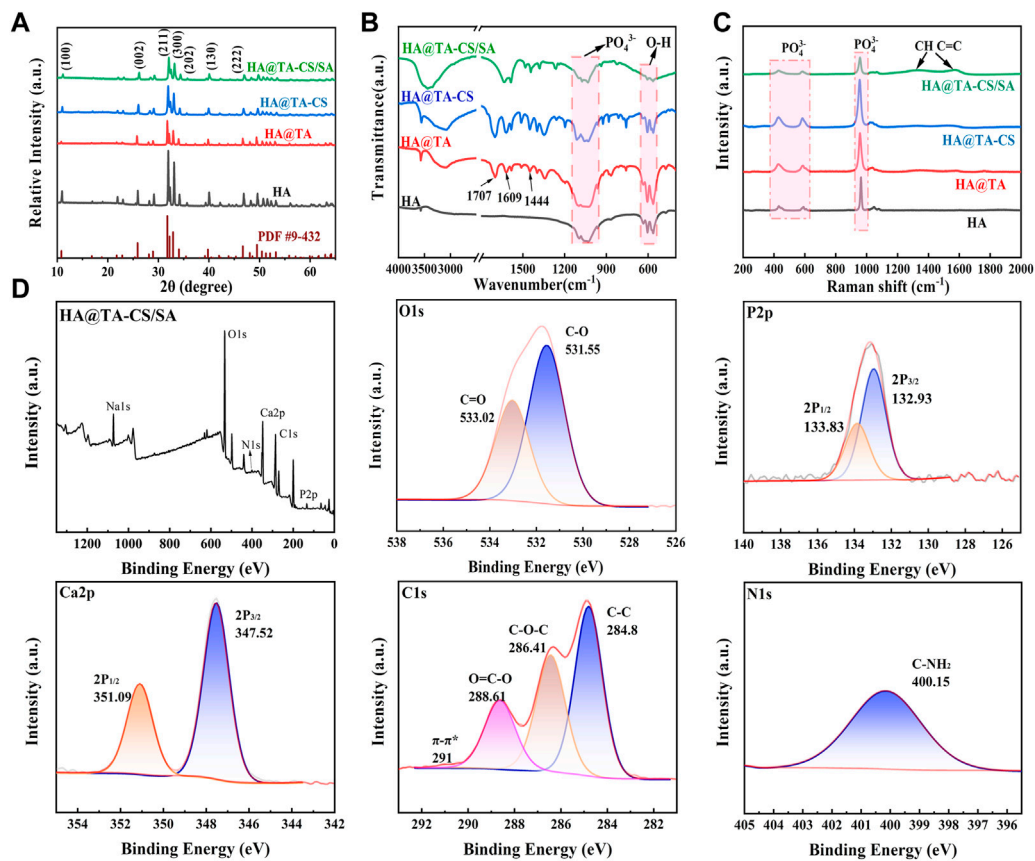


FIGURE 5

(A) XRD spectra of powders. (B) FTIR spectra of powders. (C) Raman spectra of powders. (D) XPS spectra of HA@TA-CS/SA scaffold powders.

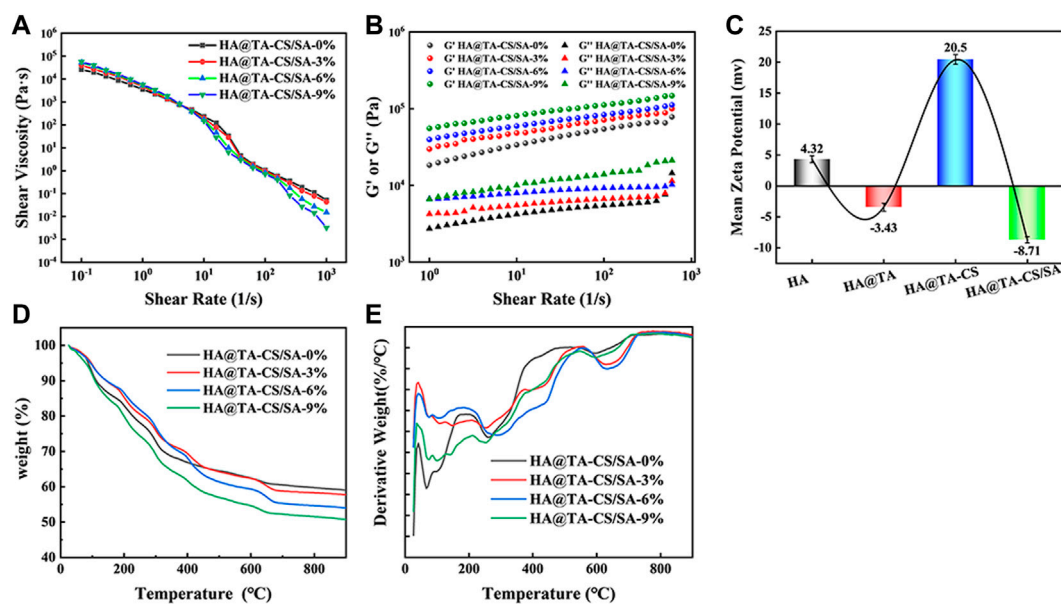


FIGURE 6

(A) Variation curve of viscosity with the shear rate for curcumin-loaded HA@TA-CS/SA scaffolds. (B) Variation curves of G' and G'' with the shear rate for curcumin-loaded HA@TA-CS/SA scaffolds. (C) zeta potential (D) TG curves of curcumin-loaded scaffolds (E) DTG curves of curcumin-loaded scaffolds.

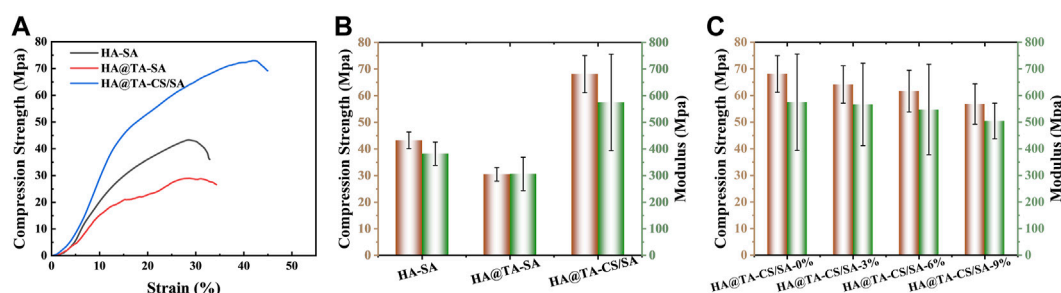


FIGURE 7

(A) The presentative compressive stress-strain curves of the HA-SA, HA@TA-SA, and HA@TA-CS/SA scaffolds. (B) compressive stress and Young's modulus of the HA-SA, HA@TA-SA, and HA@TA-CS/SA scaffolds. (C) compressive stress and Young's modulus of the DMON@Cur loaded scaffolds.

2022). Following the introduction of CS, the material displayed another positive charge of 20.5 mv. Finally, after the binding of SA, the material displayed a negative charge of -8.71 mv. It had been reported that TA could easily adhere to the HA surface mainly through hydrogen bonding. Based on the combined results of XRD, FT-IR, Raman, and XPS analysis, we speculated that the catechol group of TA formed a hydrogen bond with the hydroxyl group of HA and wrapped tightly on the surface of HA to form a TA film. At this time, the HA@TA particle had a negative charge. After cationic CS was introduced, the NH_3^{3+} group in CS adsorbed on the surface of HA@TA particles through electrostatic interaction (Shu et al., 2001). By stirring and electrostatic mutual repulsion, the charged particles could be uniformly dispersed in the slurry. After adding SA, all positively charged HA@TA-CS particles were attracted to each other by electrostatic interaction with the negative charge of SA, and finally, the slurry was formed. The alternating positive and negative changes in Zeta potential with each step of material modification proved that the material components were bonded through hydrogen bonding and electrostatic interactions.

Figures 6D, E showed the TG and DTG curves of the scaffolds loaded with different mass fractions (0, 3, 6, 9 wt%) of DMON@Cur nanoparticles. The weightlessness process of all scaffolds went through roughly three stages. The first stage was roughly 40°C – 150°C due to the evaporation of free water in the scaffold. The main thermal decomposition stage occurred at 200°C – 700°C . This stage saw the decomposition of polymer tannins, chitosan, sodium alginate, and curcumin. The weight loss of the scaffold gradually stabilized in the third stage 700°C – 900°C , and the hydroxyapatite in the scaffold underwent a slow phase transition. All scaffolds' final weight loss ratio was positively correlated with the mass of loaded curcumin.

3.3 Compressive strength of scaffolds

The compressive stress-strain curves of the HA-SA, HA@TA-SA, and HA@TA-CS/SA scaffolds are shown in Figure 7A. The strains were in the range of 0%–45% for all three groups of scaffolds. It could be seen that the compressive strength of the HA-SA scaffold without TA and CS modification was 43.23 Mpa. When TA and CS modified the HA-SA scaffold, the prepared HA@TA-CS/SA scaffold had the highest compressive strength increasing to 68.09 Mpa. The

prepared scaffolds were still competitive in terms of mechanical properties when compared with published studies (Chi et al., 2022; Rezanian et al., 2022; Zhao et al., 2022). To confirm the great increase of compressive strength for the HA@TA-CS/SA scaffold was due to the solid electrostatic interactions by CS, the HA@TA-SA scaffold was designed and produced without CS modification. It is notable that the HA@TA-SAC scaffold, however, was less intense than the HA-SA scaffold, being the least strong of the three groups at 30.47 Mpa. In addition, the HA@TA-CS/SA scaffold had the highest maximum strain of the three groups at 43%. At the yield stress point of the other two groups of scaffolds, the compressive strength of the prepared HA@TA-CS/SA scaffold for the same period was 65 Mpa.

The three groups of scaffolds compared Young's modulus (Figure 7B), with the HA@TA-CS/SA scaffold still having the best modulus (574.92 Mpa), which was higher than the HA-SA scaffold without CS and TA modifications (381.75 Mpa) by 50.6%. As a comparison, Young's modulus of the HA@TA-SA scaffold (305.99 Mpa) decreased by 46.77%. Compared the results with the Zeta potential data (Figure 6C), the HA@TA was negatively charged and repelled the negative charge of SA, which was the main reason for the deterioration in mechanical strength. After introducing positive charged CS as a bridge between the TA and SA, part of the TA's hydroxyl group made hydrogen bonds with the CS, as indicated in the IR spectrum. While the other portion protonates the $-\text{NH}_2$ group of the CS, forming an electrostatic connection with the TA's phenoxy group (Ph-O-). Particles with a positively charged outer layer were generated during the slurry preparation process and then added to the anionic SA solution.

The CS in the outer layer could create hydrogen and amide bonds with the SA, as revealed by the XPS spectra (Figure 5D). The anionic SA and cationic CS rely on electrostatic interactions for homogenous binding. At last, Ca^{2+} ions chelated the SA in the slurry to generate a double network structure maximized scaffold strength (Song et al., 2022). The compressive strength and Young's modulus of scaffolds (Figure 7C) with the addition of different mass fractions of particles showed that both the compressive strength and Young's modulus of the scaffolds were decreased slightly. Owing to their stiffness differences, microspheres produce stress concentrations in materials, making them more brittle. The microspheres may also propagate defects and cracks in the material, leading to the fragmentation of the cross-linkage network between the internal

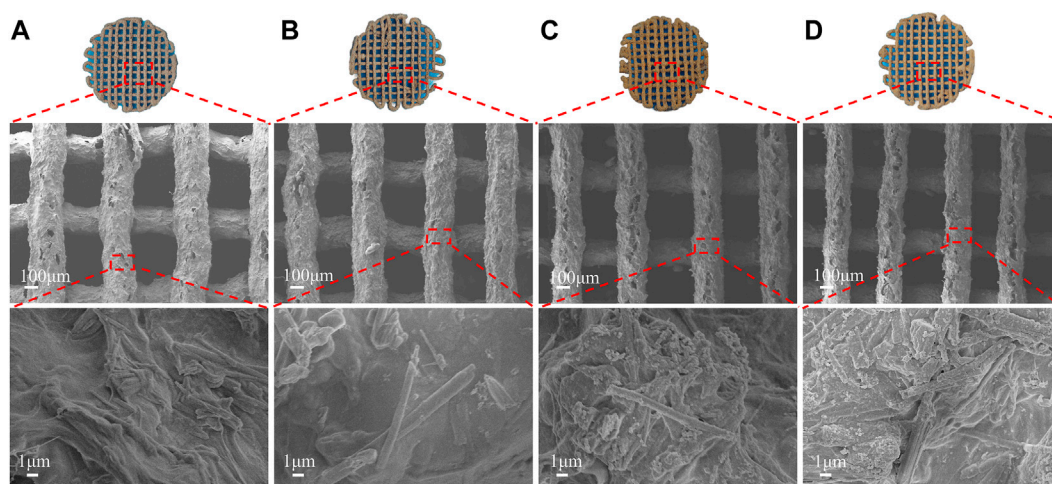


FIGURE 8
Surface morphology of the DMON@Cur loaded scaffolds after 14 days of *in vitro* degradation. (A) 0 wt%. (B) 3 wt%. (C) 6 wt%. (D) 9 wt%.

components of the scaffolds, which weakens their mechanical properties.

The mechanical properties of bone repair scaffolds have an important role in bone tissue regeneration. Especially in the initial stage of tissue regeneration, it can provide the necessary mechanical support and sufficient stability for the bone repair site, so that the conditions for tissue growth and nutrient delivery exchange during bone tissue regeneration can be created. Secondly, the high modulus bone repair scaffold can simulate the mechanical properties of normal bone, reduce the displacement and stress concentration during bone reconstruction, promote the growth and regeneration of bone cells, and facilitate bone repair (Zhang et al., 2021a; Zhang et al., 2022b).

3.4 *In vitro* degradation and mineralization

The rate of deterioration *in vitro* of bone tissue engineering scaffolds is an essential characteristic. The optimal pace of scaffold breakdown should be proportional to the rate of new bone formation. It is also vital to research the long-term behaviour of the scaffold in the same physiological context for medication application. Following 14 days in PBS media, (Figure 8), optical photos of the dried scaffolds revealed that all scaffolds retained their structure and that additional fractures were discovered on the surface of the scaffolds, but no substantial deformation occurred. More rod-shaped HA and DMON@Cur particles were observed on the surface of the scaffolds when the microstructure was examined using SEM (Figure 8). The number of particles exposed exhibited a similar pattern to the amount of medication loaded. Figure 10A depicted the DMON@Cur-loaded scaffolds' weight degradation curves, revealing that all scaffolds degraded similarly, with an overall sluggish, fast, and slow degradation rate. The greatest rate of deterioration occurred on day 7, followed by a slowing on day 12. The total mass on day

14 decreased to 23.47, 21.85, 21.56, and 19.38%, respectively, with small variances in degradation mass closely proportional to the drug-loaded mass.

It is used to measure the biological activity of osteogenesis *in vitro* that the capacity to generate apatite on the surface of biological materials in simulated body fluids (SBF) (Chen et al., 2020). Figure 9 depicted optical and SEM photos of the scaffold after 14 days of immersion in SBF. The optical pictures revealed that the structure suffered no significant damage due to the immersion. Ca/P or hydroxyapatite deposits appeared on the surface, and the morphology was intact. SEM revealed similarly dispersed white spherical particles of identical size on the surface of all scaffolds (Olad et al., 2019; Chen et al., 2020). There were no significant differences between the four scaffold groups. The presence of calcium and phosphorus on the surface of the scaffolds was confirmed by EDS elemental analysis of the white spherical particles detected. Calcium cations have been found to play a vital function in the mineralization of scaffolds as crosslinking agents in scaffold preparation (Song et al., 2022). Moreover, the amino group of CS may enhance the deposition of biominerals (Xu and Liang, 2022; Hakimi et al., 2023). Consistent with our findings, all DMON@Cur-loaded scaffolds exhibited excellent mineralization virtually uniformly, indicating the scaffolds' potential capacity to promote new bone formation.

3.5 *In vitro* release of curcumin

Curcumin is often used to prevent and treat various diseases and has various pharmacological properties, including anticancer, anti-osteoarthritis, antioxidant, and antibacterial. Nevertheless, its insolubility in water (only 0.4 μg/ml) and rapid degradability at physiological pH severely reduce its bioavailability (Hamilton and Gilbert, 2023; Jiang et al., 2023). As a result, this investigation employed curcumin as a typical drug template being loaded into the scaffold to explore the scaffolds' *in vitro* drug release at

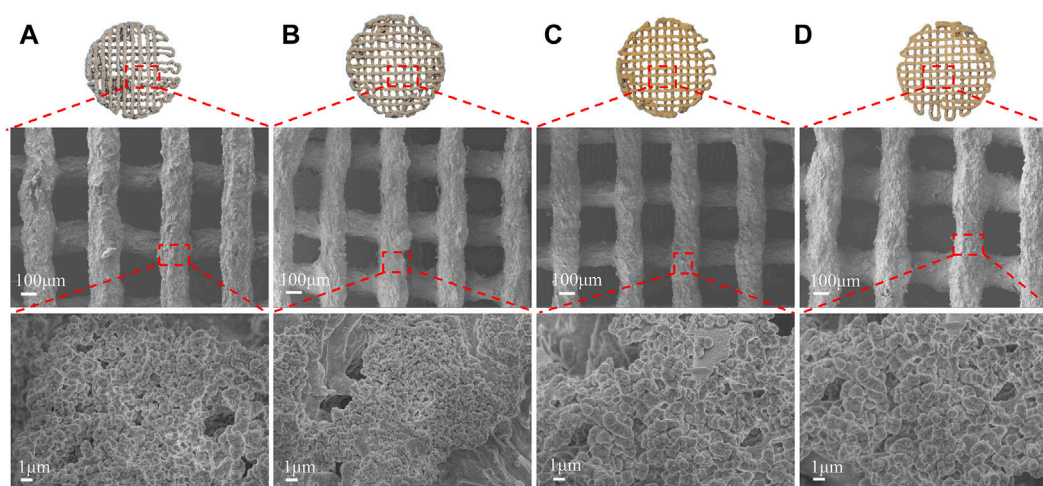


FIGURE 9
Surface morphology of scaffolds with different drug loadings after 14 days of immersion in SBF. (A) 0 wt% (B) 3 wt% (C) 6 wt% (D) 9 wt%.

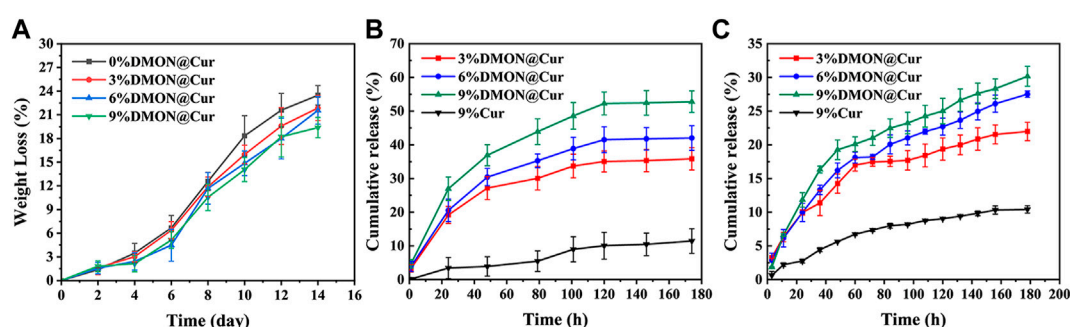


FIGURE 10
(A) The degradation rate of curcumin-loaded scaffolds. (B) Drug release from curcumin-loaded scaffolds at pH 7.4 (C) Drug release from curcumin-loaded scaffolds at pH 5.3.

pH 7.4 and pH 5.3. As shown in Figure 10B, the cumulative curcumin release rates of the DMON@Cur-loaded (3.0, 6.0, and 9.0 wt%) scaffolds at pH 7.4 over 180 h were $52.78\% \pm 3.2\%$, $42.02\% \pm 3.67\%$, and $35.84\% \pm 3.32\%$, respectively. Also at pH 5.3, the release rates of cumulative curcumin over 180 h were $21.98\% \pm 1.35\%$, $27.51\% \pm 0.46\%$, and $30.16\% \pm 1.46\%$ (Figure 10C). As a comparison, the cumulative release rate of the scaffolds directly doped with 9 wt% curcumin was only 11.45% and 10.41% during the same period. The release of curcumin-loaded scaffolds was slower and more sustained at the pH of the inflammatory environment. It showed that the scaffolds loaded with DMON@Cur particles exhibited better drug release performance for all gradient concentrations than the control group. There was an overall rapid release trend at pH 7.4, followed by a gradual smoothing out, reaching the maximum drug release concentration at 120 h. In contrast, at pH 5.3, the release pattern of curcumin was first rapid and then slow, with an inflection point at 60 h. The scaffolds loaded with a more mass fraction of DMON@Cur particles simultaneously had greater drug release concentrations.

It is presumably because more DMON@Cur particles were exposed on the surface as the scaffolds continued to degrade in PBS, leading to more drug release. Acidic inflammatory environments protonate chitosan in the scaffold and form more amide bonds with sodium alginate, leading to tighter binding, slower degradation and more sustained drug release during scaffold degradation. The composite of curcumin with mesoporous material might restrict curcumin in monomorphous form within the spaces of a porous material (Ananth et al., 2022). In this way, the solubility and bioavailability of curcumin could be significantly improved.

3.6 Biocompatibility assay

In vitro cell assay is an essential tool to detect growth inhibition, functional changes, cell lysis, death, or other toxic reactions of cells after exposure to biological materials in an isolated environment that simulates the growth environment of

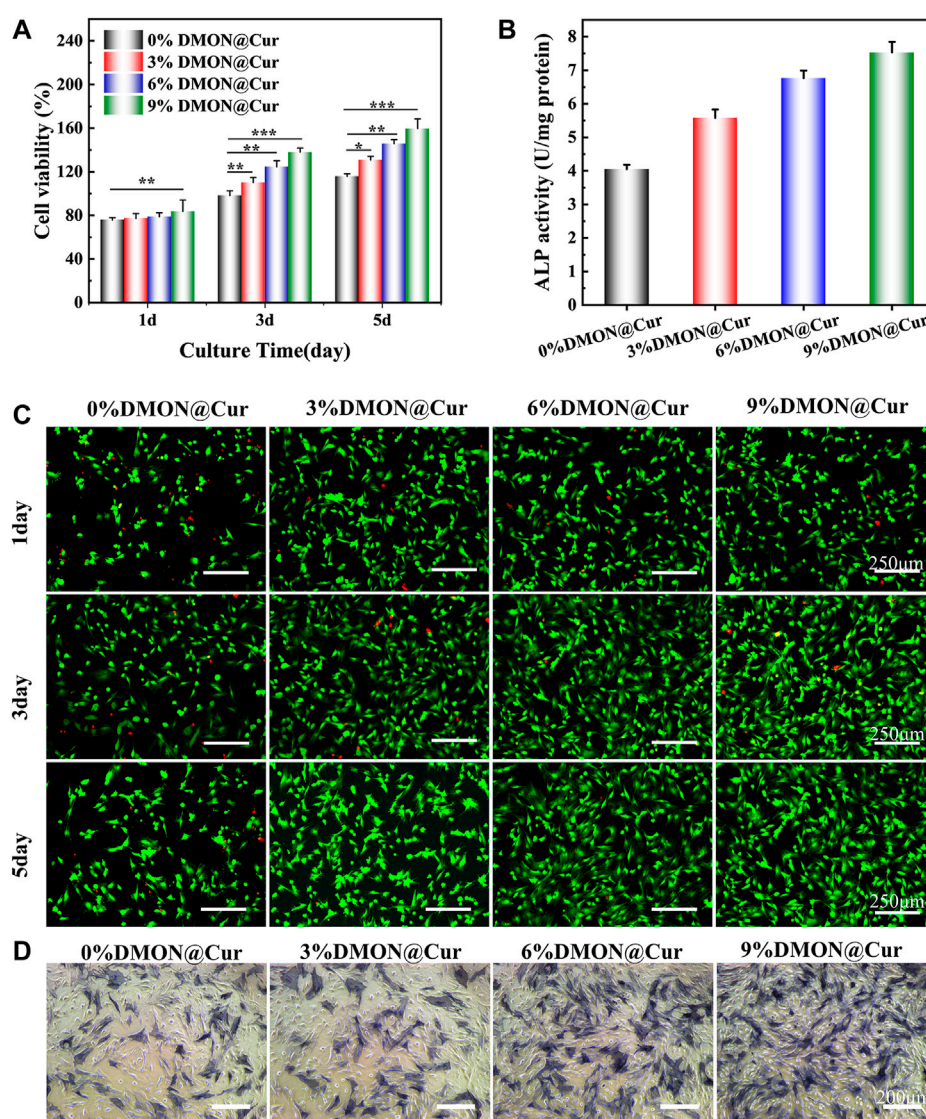


FIGURE 11

(A) CCK-8 assay for scaffold cytotoxicity. (B) ALP quantitative analysis (C) Live-dead staining of cells (D) ALP osteogenic differentiation staining.

an organism (Ananth et al., 2022; Claro et al., 2023). The cell viability of BMSCs cultured in DMON@Cur-loaded HA@TA-CS/SA scaffold extracts assayed by the CCK-8 method is demonstrated in Figure 11A. The results showed that all scaffolds were non-toxic. There was no significant difference between the groups on the first day. Still, with time, the cell proliferation of the DMON@Cur-loaded scaffolds was significantly better than that of the positive control group. The cell survival rate reflected an increasing trend, and the proliferation was positively correlated with the DMON@Cur loading, showing good biocompatibility. Figure 11C showed the results of BMSCs cells stained under a fluorescence microscope, and the overall situation is consistent with the detection of the CCK-8 assay. The cell morphology of the DMON@Cur-loaded scaffolds was more spreading and numerous, which strongly confirmed that the

scaffold had good biocompatibility and could promote the proliferation of BMSCs cells (Zhang et al., 2021b). The synthesized scaffold materials using natural polymers have shown very good biocompatibility. Figures 11B, D showed the quantitative analysis and staining results of alkaline phosphatase (ALP) after BMSCs cells were cultured for 7 days in the infiltrate of HA@TA-CS/SA-loaded curcumin scaffold. The results showed that the scaffold with more drug loading had a deeper and denser ALP staining status, indicating that the curcumin-loaded scaffold could significantly promote the differentiation of BMSCs cells (Li and Zhang, 2018; Chen et al., 2021; Inchingolo et al., 2022).

On the other hand, curcumin could promote the survival and proliferation of osteoblasts by eliminating the inhibitory effect of reactive oxygen species on the Nrf2 signaling pathway to reduce osteoblast apoptosis and maintain their differentiation function, as

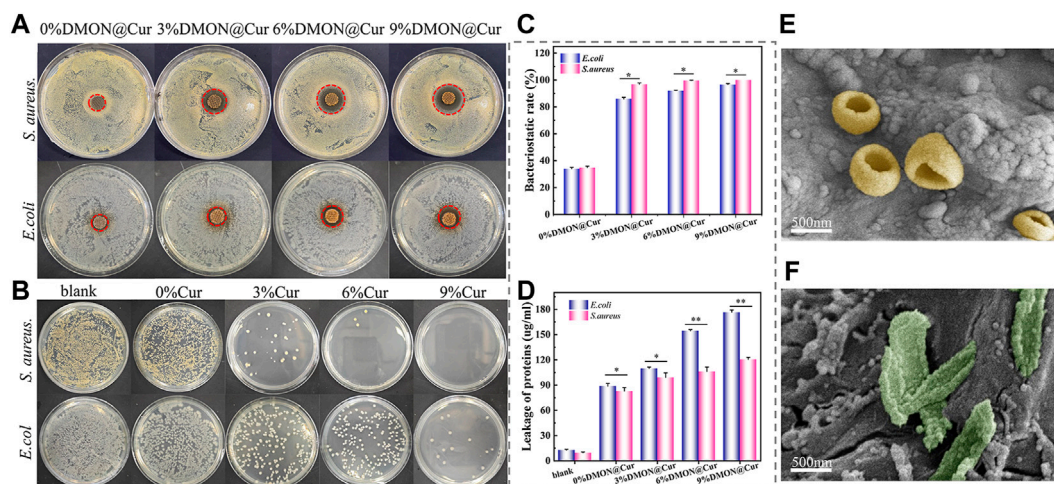


FIGURE 12

(A) and (B) Antibacterial capacity of curcumin-loaded scaffolds for testing *S. aureus* and *E. coli* by disk diffusion and plate coating methods. (C) BCA kit detects protein concentrations released by bacteria co-cultured with curcumin-loaded scaffolds. (D) bactericidal rate of *S. aureus* and *E. coli* after treatment with the curcumin-loaded scaffolds. (E, F) SEM after co-cultivation of *S. aureus* and *E. coli* with curcumin-loaded scaffolds for 24 h.

reported by Li et al. (Wu et al., 2019; Dang et al., 2021). In conclusion, all curcumin-loaded scaffolds have good proliferation-promoting and differentiation effects on BMSCs cells, showing their great potential in bone repair properties.

3.7 Antibacterial performance

Selected representative *S. aureus* and *E. coli* characterize the antibacterial activity of the scaffolds, qualitatively and quantitatively, by using the disk diffusion method and plate coating method, respectively. As shown in Figure 12A, the inhibition ring diameters of the scaffolds were 15.4 ± 0.6 mm, 19.3 ± 0.8 mm, 23.6 ± 0.5 mm, and 27.4 ± 0.8 mm after 24 h incubation with DMON@Cur-loaded scaffolds (0, 3, 6, and 9 wt %) in *S. aureus* medium. The inhibition ring diameters were 15.8 ± 0.3 , 16.4 ± 0.2 , 17.2 ± 0.3 and 18.0 ± 0.2 mm, respectively, after 24 h incubation with the same concentration gradient of DMON@Cur-loaded scaffolds in *E. coli* culture dishes. All concentration gradients of DMON@Cur-loaded scaffolds showed inhibition, and the inhibition effect was significantly stronger for *S. aureus* than for *E. coli*. Adding 0% DMON@Cur-loaded particles to the scaffolds also produced a small amount of inhibition, attributed to the antimicrobial properties of TA and CS in the scaffolds. It is noteworthy that the TA and CS added to the scaffold were only in small amounts, and the bacterial inhibitory effect of the scaffold increased significantly with the increase of the curcumin-loaded drug content, which was mainly influenced by curcumin. Figure 12B showed the results of the DMON@Cur-loaded scaffold co-cultured with *S. aureus* and *E. coli* bacteria for 24 h after plate coating. It coincided with the results of the inhibition test; Figure 12C showed the bactericidal rate of *S. aureus* and *E. coli* after treatment with the DMON@Cur-loaded HA@TA-CS/SA scaffolds. Adding 9 wt% of DMON@Cur-loaded microspheres to the scaffold produced 99.99% and 96.56% bactericidal effects against *S. aureus* and *E. coli*,

respectively. The above test proved that the DMON@Cur-loaded HA@TA-CS/SA scaffolds had a good antibacterial effect, especially on *S. aureus* bacteria, which was also in line with the results of previous studies (Doustdar et al., 2022).

The bacteria morphology was observed under SEM after co-cultivation of *S. aureus* and *E. coli* with DMON@Cur-loaded scaffolds for 24 h, respectively (Figures 12E, F). The rough surface of the scaffolds was favourable for bacterial adhesion. It was also observed that the cell membrane of *S. aureus* and *E. coli* were broken to expose the intracellular material, and DMON@Cur-loaded microspheres were distributed around them. In contrast, most *S. aureus* had more intact cell structures than *E. coli*, and more folds could be seen on their cell surfaces. It is theorized that curcumin disrupted bacteria's cell membrane structure, ultimately resulting in their demise. Despite the qualitative results observed for visualization in electron micrographs, it had been shown that the intracellular leaked-out proteins could be quantitatively characterized using the BCA protein kit. As shown in Figure 12D, according to the protein assay, both the *E. coli* groups and the *S. aureus* groups were able to cause a large amount of intracellular protein leakage after co-culture with the DMON@Cur-loaded scaffolds compared to the blank groups. Among them, the curcumin-loaded scaffolds containing 9 wt% of DMON@Cur particles were co-cultured with *Escherichia coli* and *Staphylococcus aureus* with protein concentrations up to 176.59 ± 2.6 and 120.54 ± 2.53 μg/mL, respectively. It is consistent with the results visualized in the electron micrographs, indicating that our hypothesized mechanism of bacterial inhibition of the DMON@Cur-loaded scaffold was bio-compatible. In addition, the *S. aureus* group shed less intracellular material. That could be because the thick layer of peptidoglycan on the outside of Gram-positive bacteria acts as a barrier to releasing intracellular chemicals. Gram-negative bacteria lack such a robust protective barrier, causing *E. coli* to break down and spill out vast amounts of intracellular protein (Yuan et al., 2022).

4 Conclusion

In summary, we prepared a series of HA@TA-CS/SA scaffolds with different curcumin-loaded silica microspheres (0.3, 0.6, 0.9, and 9.0 wt%) using 3D printing. XRD and TEM showed that the synthesized long rod-shaped hydroxyapatite grew directionally along the C-axis with a high aspect ratio. IR, Raman, XPS, and zeta potential showed that the components within the scaffold were bound to each other in layers by hydrogen bonding and solid electrostatic interactions. The rheological test revealed that the slurry was a pseudoplastic fluid with a stable bond. Their rheological properties were unaffected by the addition of silica-loaded particles. The scaffolds also had good mechanical qualities (compressive strength 68.09 Mpa). In addition, SEM and EDX demonstrated that the scaffolds had high biomineralization capability and a good degradation rate. The synthesized scaffold's have high cytocompatibility which can boost the proliferation of BMSCs significantly. Curcumin's solubility and bioavailability were enhanced by the scaffold, as demonstrated by *in vitro* drug release test. Moreover, the HA@TA-CS/SA-9% DMON@Cur scaffolds inhibited *S.aureus* and *E.coli* with 99.99% and 96.56% effectiveness, respectively. The scaffolds' antibacterial activity mechanism was confirmed using SEM, and the BCA protein assay, which was curcumin disrupts bacteria's cell membrane structure. Overall, the results indicated that HA@TA-CS/SA-9% DMON@Cur scaffolds had considerable potential for therapeutic bone tissue engineering.

Data availability statement

The original contributions presented in the study are included in the article/supplementary material, further inquiries can be directed to the corresponding author.

References

- Ananth, A. N., Nagarajan, V., Kumar, S. S., Sasikumar, P., Chirico, G., D'Alfonso, L., et al. (2022). Water dynamics in competitive solvation assisted loading of colloidal curcumin nanoparticles onto mesoporous silica nanostructures. *Part. Part. Syst. Charact.* 39, 2200062. doi:10.1002/ppsc.202200062
- Bakhsheshi-Rad, H. R., Hamzah, E., Staiger, M. P., Dias, G. J., Hadisi, Z., Saheban, M., et al. (2018). Drug release, cytocompatibility, bioactivity, and antibacterial activity of doxycycline loaded Mg-Ca-TiO₂ composite scaffold. *Mater. Des.* 139, 212–221. doi:10.1016/j.matdes.2017.10.072
- Barros, N. R., Chen, Y., Hosseini, V., Wang, W., Nasiri, R., Mahmoodi, M., et al. (2021). Recent developments in mussel-inspired materials for biomedical applications. *Biomaterials Sci.* 9, 6653–6672. doi:10.1039/d1bm01126j
- Benameur, T., Frota Gaban, S. V., Giacomucci, G., Filannino, F. M., Trotta, T., Polito, R., et al. (2023). The effects of curcumin on inflammasome: Latest update. *Molecules* 28, 742. doi:10.3390/molecules28020742
- Benameur, T., Giacomucci, G., Panaro, M. A., Ruggiero, M., Trotta, T., Monda, V., et al. (2022). New promising therapeutic avenues of curcumin in brain diseases. *Molecules* 27, 236. doi:10.3390/molecules27010236
- Benassi, R., Ferrari, E., Lazzari, S., Spagnolo, F., and Saladini, M. (2008). Theoretical study on curcumin: A comparison of calculated spectroscopic properties with nmr, UV-vis and IR experimental data. *J. Mol. Struct.* 892, 168–176. doi:10.1016/j.molstruc.2008.05.024
- Boos, A. M., Arkudas, A., Kneser, U., Horch, R. E., and Beier, J. P. (2010). Bone tissue engineering for bone defect therapy. *Handchir. Mikrochir. Plast. Chir.* 42, 360–368. doi:10.1055/s-0030-1261964
- Brunello, G., Sivoletta, S., Meneghello, R., Ferroni, L., Gardin, C., Piattelli, A., et al. (2016). Powder-based 3D printing for bone tissue engineering. *Biotechnol. Adv.* 34, 740–753. doi:10.1016/j.biotechadv.2016.03.009
- Chen, C., Yang, H., Yang, X., and Ma, Q. (2022). Tannic acid: A crosslinker leading to versatile functional polymeric networks: A review. *Rsc Adv.* 12, 7689–7711. doi:10.1039/d1ra07657d
- Chen, J., Zhang, T., Hua, W., Li, P., and Wang, X. (2020). 3D Porous poly(lactic acid)/regenerated cellulose composite scaffolds based on electrospun nanofibers for biomineralization. *Colloids Surfaces a-Physicochemical Eng. Aspects* 585, 124048. doi:10.1016/j.colsurfa.2019.124048
- Chen, S., Liang, H., Ji, Y., Kou, H., Zhang, C., Shang, G., et al. (2021). Curcumin modulates the crosstalk between macrophages and bone mesenchymal stem cells to ameliorate osteogenesis. *Front. Cell Dev. Biol.* 9, 634650. doi:10.3389/fcell.2021.634650
- Chi, M., Li, N., Cui, J., Karlin, S., Rohr, N., Sharma, N., et al. (2022). Biomimetic, mussel-inspired surface modification of 3D-printed biodegradable polylactic acid scaffolds with nano-hydroxyapatite for bone tissue engineering. *Front. Bioeng. Biotechnol.* 10, 989729. doi:10.3389/fbioe.2022.989729
- Claro, A. M., Alves, C. C., Dos Santos, K. S., Da Rocha, E. G., Fontes, M. D. L., Monteiro, G. C., et al. (2023). Regenerated cellulose sponge as sacrificial template for the synthesis of three-dimensional porous alumina-silica scaffold for tissue engineering. *J. Sol-Gel Sci. Technol.* doi:10.1007/s10971-022-05990-y
- Dang, Y.-Y., Luo, H., Li, Y.-M., Zhou, Y., Luo, X., Lin, S.-M., et al. (2021). Curcumin prevents As₃₊-induced carcinogenesis through regulation of GSK3 β /Nrf2. *Chin. Med.* 16, 116. doi:10.1186/s13020-021-00527-x

Author contributions

JL and CJ contributed to the conception and design of the study. CJ, CZ, YC, YG, MZ, LL, QD, and TH conduct a research process, specifically performing the experiments and data collection. CJ and ZX design of methodology. CJ performed the statistical analysis. CJ wrote the first draft of the manuscript. All authors contributed to the manuscript revision, read, and approved the submitted version.

Funding

This work was financially supported by the National Natural Science Foundation of China (No. 51801198 and No. 82072074), Funds of Scientific and Technological Plan of Fujian Province (Nos 2020Y0083 and 2020L3026) and Fujian Science and Technology Innovation Laboratory for Optoelectronic Information of China (No. 2021ZZ111).

Conflict of interest

The authors declare that the research was conducted in the absence of any commercial or financial relationships that could be construed as a potential conflict of interest.

Publisher's note

All claims expressed in this article are solely those of the authors and do not necessarily represent those of their affiliated organizations, or those of the publisher, the editors and the reviewers. Any product that may be evaluated in this article, or claim that may be made by its manufacturer, is not guaranteed or endorsed by the publisher.

- Delloe, C., Cornu, O., Druez, V., and Barbier, O. (2007). Bone allografts - what they can offer and what they cannot. *J. Bone Jt. Surgery-British* 89B, 574–580. doi:10.1302/0301-620x.89b5.19039
- Dong, X., Li, C., Zhang, M., Zhao, Y., Zhao, Z., Li, W., et al. (2022). Multifunctional injectable hydrogel for effective promotion of cartilage regeneration and protection against osteoarthritis: Combined chondroinductive, antioxidative and anti-inflammatory strategy. *Sci. Technol. Adv. Mater.* 23, 361–375. doi:10.1080/14686996.2022.2076568
- Donnalaja, F., Jacchetti, E., Soncini, M., and Raimondi, M. T. (2020). Natural and synthetic polymers for bone scaffolds optimization. *Polymers* 12, 905. doi:10.3390/polym12040905
- Doustdar, F., Olad, A., and Ghorbani, M. (2022). Development of a novel reinforced scaffold based on chitosan/cellulose nanocrystals/halloysite nanotubes for curcumin delivery. *Carbohydr. Polym.* 282, 119127. doi:10.1016/j.carbpol.2022.119127
- Fernandes, J. S., Gentile, P., Pires, R. A., Reis, R. L., and Hatton, P. V. (2017). Multifunctional bioactive glass and glass-ceramic biomaterials with antibacterial properties for repair and regeneration of bone tissue. *Acta Biomater.* 59, 2–11. doi:10.1016/j.actbio.2017.06.046
- Filipovic, U., Dahmane, R. G., Ghannouchi, S., Zore, A., and Bohinc, K. (2020). Bacterial adhesion on orthopedic implants. *Adv. Colloid Interface Sci.* 283, 102228. doi:10.1016/j.cis.2020.102228
- Guo, J. S., Kim, G. B., Shan, D. Y., Kim, J. P., Hu, J. Q., Wang, W., et al. (2017). Click chemistry improved wet adhesion strength of mussel-inspired citrate-based antimicrobial bioadhesives. *Biomaterials* 112, 275–286. doi:10.1016/j.biomaterials.2016.10.010
- Guo, J. S., Sun, W., Kim, J. P., Lu, X. L., Li, Q. Y., Lin, M., et al. (2018). Development of tannin-inspired antimicrobial bioadhesives. *Acta Biomater.* 72, 35–44. doi:10.1016/j.actbio.2018.03.008
- Guo, J. S., Tian, X. G., Xie, D. H., Rahn, K., Gerhard, E., Kuzma, M. L., et al. (2020). Citrate-based tannin-bridged bone composites for lumbar fusion. *Adv. Funct. Mater.* 30, 2002438. doi:10.1002/adfm.202002438
- Guo, J. S., Wang, W., Hu, J. Q., Xie, D. H., Gerhard, E., Nisic, M., et al. (2016). Synthesis and characterization of anti-bacterial and anti-fungal citrate-based mussel-inspired bioadhesives. *Biomaterials* 85, 204–217. doi:10.1016/j.biomaterials.2016.01.069
- Guo, L., Liang, Z., Yang, L., DU, W., Yu, T., Tang, H., et al. (2021). The role of natural polymers in bone tissue engineering. *J. Control. Release* 338, 571–582. doi:10.1016/j.jconrel.2021.08.055
- Hakimi, F., Jafari, H., Hashemikia, S., Shabani, S., and Ramazani, A. (2023). Chitosan-polyethylene oxide/clay-alginate nanofiber hydrogel scaffold for bone tissue engineering: Preparation, physical characterization, and biomimetic mineralization. *Int. J. Biol. Macromol.* 233, 123453. doi:10.1016/j.ijbiomac.2023.123453
- Hamilton, A. E., and Gilbert, R. J. (2023). Curcumin release from biomaterials for enhanced tissue regeneration following injury or disease. *Bioengineering* 10, 262. doi:10.3390/bioengineering10020262
- Han, L., Huang, Z., Zhu, M., Zhu, Y., and Li, H. (2022). Drug-loaded zeolite imidazole framework-8-functionalized bioglass scaffolds with antibacterial activity for bone repair. *Ceram. Int.* 48, 6890–6898. doi:10.1016/j.ceramint.2021.11.243
- Hussain, Z., Ullah, I., Liu, X., Shen, W., Ding, P., Zhang, Y., et al. (2022). Tannin-reinforced iron substituted hydroxyapatite nanorods functionalized collagen-based composite nanofibrous coating as a cell-instructive bone-implant interface scaffold. *Chem. Eng. J.* 438, 135611. doi:10.1016/j.cej.2022.135611
- Inchingolo, A. D., Inchingolo, A. M., Malcangi, G., Avantario, P., Azzollini, D., Buongiorno, S., et al. (2022). Effects of resveratrol, curcumin and quercetin supplementation on bone metabolism-A systematic review. *Nutrients* 14, 3519. doi:10.3390/nu14173519
- Iweala, E. J., Uche, M. E., Dike, E. D., Etumnu, L. R., Dokunmu, T. M., Oluwapelumi, A. E., et al. (2023). Curcuma longa (turmeric): Ethnomedicinal uses, phytochemistry, pharmacological activities and toxicity profiles—a review. *Pharmacol. Res. - Mod. Chin. Med.* 6, 100222. doi:10.1016/j.prmcm.2023.100222
- Jiang, Z., Gan, J., Wang, L., and Lv, C. (2023). Binding of curcumin to barley protein Z improves its solubility, stability and bioavailability. *Food Chem.* 399, 133952. doi:10.1016/j.foodchem.2022.133952
- Jodati, H., Yilmaz, B., and Evis, Z. (2020). A review of bioceramic porous scaffolds for hard tissue applications: Effects of structural features. *Ceram. Int.* 46, 15725–15739. doi:10.1016/j.ceramint.2020.03.192
- Ke, G., Xu, W., and Yu, W. (2010). Preparation and properties of drug-loaded chitosan-sodium alginate complex membrane. *Int. J. Polym. Mater.* 59, 184–191. doi:10.1080/00914030903231332
- Kong, F., Zhang, H., Qu, X., Zhang, X., Chen, D., Ding, R., et al. (2016). Gold nanorods, DNA origami, and porous silicon nanoparticle-functionalized biocompatible double emulsion for versatile targeted therapeutics and antibody combination therapy. *Adv. Mater.* 28, 10195–10203. doi:10.1002/adma.201602763
- Koushik, T. M., Miller, C. M., and Antunes, E. (2023). Bone tissue engineering scaffolds: Function of multi-material hierarchically structured scaffolds. *Adv. Healthc. Mater.* 12, e2202766. doi:10.1002/adhm.202202766
- Koutsopoulos, S. (2002). Synthesis and characterization of hydroxyapatite crystals: A review study on the analytical methods. *J. Biomed. Mater. Res.* 62, 600–612. doi:10.1002/jbm.10280
- Lee, H., Lee, B. P., and Messersmith, P. B. (2007). A reversible wet/dry adhesive inspired by mussels and geckos. *Nature* 448, 338–341. doi:10.1038/nature05968
- Lee, S. J., Gwak, M. A., Chathuranga, K., LE, J. S., Koo, J., and Park, W. H. (2023). Multifunctional chitosan/tannic acid composite films with improved anti-UV, antioxidant, and antimicrobial properties for active food packaging. *Food Hydrocoll.* 136, 108249. doi:10.1016/j.foodhyd.2022.108249
- Lee, S. S., DU, X. Y., Kim, I., and Ferguson, S. J. (2022). Scaffolds for bone-tissue engineering. *Matter* 5, 2722–2759. doi:10.1016/j.matt.2022.06.003
- Lew, D. P., and Waldvogel, F. A. (2004). Osteomyelitis. *Lancet* 364, 369–379. doi:10.1016/s0140-6736(04)16727-5
- Li, Y., and Zhang, Z.-Z. (2018). Sustained curcumin release from PLGA microspheres improves bone formation under diabetic conditions by inhibiting the reactive oxygen species production. *Drug Des. Dev. Ther.* 12, 1453–1466. doi:10.2147/dddt.s154334
- Liao, B., Xu, C., Wang, Z., Li, W., Liu, X., and Lu, D. (2022). Preparation of chitosan-tannic acid coating and its anti-osteoclast and antibacterial activities in titanium implants. *J. Bone Mineral Metabolism* 40, 402–414. doi:10.1007/s00774-022-01309-7
- Lu, X. L., Shi, S. J., Li, H. M., Gerhard, E., Lu, Z. H., Tan, X. Y., et al. (2020). Magnesium oxide-crosslinked low-swelling citrate-based mussel-inspired tissue adhesives. *Biomaterials* 232, 119719. doi:10.1016/j.biomaterials.2019.119719
- Macdonald, A. F., Harley-Troxell, M. E., Newby, S. D., and Dhar, M. S. (2022). 3D-Printing graphene scaffolds for bone tissue engineering. *Pharmaceutics* 14, 1834. doi:10.3390/pharmaceutics14091834
- Mehdizadeh, M., Weng, H., Gyawali, D., Tang, L. P., and Yang, J. (2012). Injectable citrate-based mussel-inspired tissue bioadhesives with high wet strength for sutureless wound closure. *Biomaterials* 33, 7972–7983. doi:10.1016/j.biomaterials.2012.07.055
- Mirkhalaf, M., Men, Y., Wang, R., No, Y., and Zreiqat, H. (2023). Personalized 3D printed bone scaffolds: A review. *Acta Biomater.* 156, 110–124. doi:10.1016/j.actbio.2022.04.014
- Nasiry, D., and Khalatbary, A. R. (2023). Natural polyphenols for the management of autism spectrum disorder: A review of efficacy and molecular mechanisms. *Nutr. Neurosci.* 1–11. doi:10.1080/1028415x.2023.2180866
- Nimiya, Y., Wang, W., DU, Z., Sukamtoh, E., Zhu, J., Decker, E., et al. (2016). Redox modulation of curcumin stability: Redox active antioxidants increase chemical stability of curcumin. *Mol. Nutr. Food Res.* 60, 487–494. doi:10.1002/mnfr.201500681
- O'Brien, F. J. (2011). Biomaterials & scaffolds for tissue engineering. *Mater. Today* 14, 88–95. doi:10.1016/s1369-7021(11)70058-x
- Oboudat, H. S., and Safaei-Ghomi, J. (2022). Silica nanospheres KCC-1 as a good catalyst for the preparation of 2-amino-4H-chromenes by ultrasonic irradiation. *Sci. Rep.* 12, 2381. doi:10.1038/s41598-022-05993-3
- Olad, A., Hagh, H. B. K., Mirmohseni, A., and Azhar, F. F. (2019). Graphene oxide and montmorillonite enriched natural polymeric scaffold for bone tissue engineering. *Ceram. Int.* 45, 15609–15619. doi:10.1016/j.ceramint.2019.05.071
- Olszta, M. J., Cheng, X. G., Jee, S. S., Kumar, R., Kim, Y. Y., Kaufman, M. J., et al. (2007). Bone structure and formation: A new perspective. *Mater. Sci. Eng. R-Reports* 58, 77–116. doi:10.1016/j.mser.2007.05.001
- Ou, X. F., Zheng, J. Q., Zhao, X. J., and Liu, M. X. (2018). Chemically cross-linked chitin nanocrystal scaffolds for drug delivery. *ACS Appl. Nano Mater.* 1, 6790–6799. doi:10.1021/acsnanm.8b01585
- Pezzini, B. R., Beringhs, A. O., Ferraz, H. G., Segatto Silva, M. A., Stulzer, H. K., and Sonaglio, D. (2016). Liquesolid technology applied to pellets: Evaluation of the feasibility and dissolution performance using felodipine as a model drug. *Chem. Eng. Res. Des.* 110, 62–69. doi:10.1016/j.cherd.2016.01.037
- Radulescu, D.-E., Neacsu, I. A., Grumezescu, A.-M., and Andronescu, E. (2022). Novel trends into the development of natural hydroxyapatite-based polymeric composites for bone tissue engineering. *Polymers* 14, 899. doi:10.3390/polym14050899
- Ressler, A. (2022). Chitosan-based biomaterials for bone tissue engineering applications: A short review. *Polymers* 14, 3430. doi:10.3390/polym14163430
- Rezania, N., Asadi-Eydivand, M., Abolfathi, N., Bonakdar, S., Mehrjoo, M., and Solati-Hashjin, M. (2022). Three-dimensional printing of polycaprolactone/hydroxyapatite bone tissue engineering scaffolds mechanical properties and biological behavior. *J. Mater. Science-Materials Med.* 33, 31. doi:10.1007/s10856-022-06653-8
- Riachy, P., Roig, F., Garcia-Celma, M.-J., Stebe, M.-J., Pasc, A., Esquena, J., et al. (2016). Hybrid hierarchical porous silica templated in nanoemulsions for drug release. *Eur. J. Inorg. Chem.* 2016, 1989–1997. doi:10.1002/ejic.201501127
- Ribeiro, M., Monteiro, F. J., and Ferraz, M. P. (2012). Infection of orthopedic implants with emphasis on bacterial adhesion process and techniques used in studying bacterial-microbial interactions. *Biomater* 2, 176–194. doi:10.4161/biom.22905
- Shi, J. C., Dai, W. F., Gupta, A., Zhang, B. Q., Wu, Z. Q., Zhang, Y. H., et al. (2022). Frontiers of hydroxyapatite composites in bionic bone tissue engineering. *Materials* 15, 8475. doi:10.3390/ma15238475

- Shu, X. Z., Zhu, K. J., and Song, W. H. (2001). Novel pH-sensitive citrate cross-linked chitosan film for drug controlled release. *Int. J. Pharm.* 212, 19–28. doi:10.1016/s0378-5173(00)00582-2
- Song, X., Guo, J., Liu, Y., Li, F., Yang, Q., Guan, F., et al. (2022). Preparation and characterization of multi-network hydrogels based on sodium alginate/krill protein/polyacrylamide-Strength, shape memory, conductivity and biocompatibility. *Int. J. Biol. Macromol.* 207, 140–151. doi:10.1016/j.ijbiomac.2022.03.015
- Tong, W. Y., Bin Abdullah, A. Y. K., Rozman, N. A. S. B., Bin Wahid, M. I. A., Hossain, M. S., Ring, L. C., et al. (2018). Antimicrobial wound dressing film utilizing cellulose nanocrystal as drug delivery system for curcumin. *Cellulose* 25, 631–638. doi:10.1007/s10570-017-1562-9
- Wang, C., Huang, W., Zhou, Y., He, L., He, Z., Chen, Z., et al. (2020). 3D printing of bone tissue engineering scaffolds. *Bioact. Mater.* 5, 82–91. doi:10.1016/j.bioactmat.2020.01.004
- Wang, M., Li, H., Yang, Y., Yuan, K., Zhou, F., Liu, H., et al. (2021a). A 3D-bioprinted scaffold with doxycycline-controlled BMP2-expressing cells for inducing bone regeneration and inhibiting bacterial infection. *Bioact. Mater.* 6, 1318–1329. doi:10.1016/j.bioactmat.2020.10.022
- Wang, Y., Zhang, B., Ding, X., and DU, X. (2021b). Dendritic mesoporous organosilica nanoparticles (DMONs): Chemical composition, structural architecture, and promising applications. *Nano Today* 39, 101231. doi:10.1016/j.nantod.2021.101231
- Wu, J., Ibtisham, F., Niu, Y. F., Wang, Z., Li, G. H., Zhao, Y., et al. (2019). Curcumin inhibits heat-induced oxidative stress by activating the MAPK-Nrf2/ARE signaling pathway in chicken fibroblasts cells. *J. Therm. Biol.* 79, 112–119. doi:10.1016/j.jtherbio.2018.12.004
- Xu, H., and Liang, H. (2022). Chitosan-regulated biomimetic hybrid nanoflower for efficiently immobilizing enzymes to enhance stability and by-product tolerance. *Int. J. Biol. Macromol.* 220, 124–134. doi:10.1016/j.ijbiomac.2022.08.048
- Xu, Z. Y., Lin, B., Zhao, C. Q., Lu, Y. J., Huang, T. T., Chen, Y., et al. (2022). Lanthanum doped octacalcium phosphate/poly(lactic acid) scaffold fabricated by 3D printing for bone tissue engineering. *J. Mater. Sci. Technol.* 118, 229–242. doi:10.1016/j.jmst.2021.09.069
- Yadav, L. R., Chandran, S. V., Lavanya, K., and Selvamurugan, N. (2021). Chitosan-based 3D-printed scaffolds for bone tissue engineering. *Int. J. Biol. Macromol.* 183, 1925–1938. doi:10.1016/j.ijbiomac.2021.05.215
- Yan, G., Qiao, W., Cao, H., Shi, J., and Dong, N. (2020). Application of surface modification of polydopamine in tissue engineering. *Chin. Biotechnol.* 40, 75–81.
- Yang, Z., Huang, Y., Chen, S. T., Zhao, Y. Q., Li, H. L., and Hu, Z. A. (2005). Template synthesis of highly ordered hydroxyapatite nanowire arrays. *J. Mater. Sci.* 40, 1121–1125. doi:10.1007/s10853-005-6927-z
- Yao, X., Ma, S., Peng, S., Zhou, G., Xie, R., Jiang, Q., et al. (2020). Zwitterionic polymer coating of sulfur dioxide-releasing nanosystem augments tumor accumulation and treatment efficacy. *Adv. Healthc. Mater.* 9, 1901582. doi:10.1002/adhm.201901582
- Ye, B., Wu, B., Su, Y., Sun, T., and Guo, X. (2022). Recent advances in the application of natural and synthetic polymer-based scaffolds in musculoskeletal regeneration. *Polym. (Basel)* 14, 4566. doi:10.3390/polym14214566
- Yu, Y., Lv, B., Wu, J., and Chen, W. (2023). Mussel-based biomimetic strategies in musculoskeletal disorder treatment: From synthesis principles to diverse applications. *Int. J. Nanomedicine* 18, 455–472. doi:10.2147/ijn.s386635
- Yuan, Y., Liu, Q., Huang, Y., Qi, M., Yan, H., Li, W., et al. (2022). Antibacterial efficacy and mechanisms of curcumin-based photodynamic treatment against *Staphylococcus aureus* and its application in juices. *Molecules* 27, 7136. doi:10.3390/molecules27207136
- Zafar, M. J., Zhu, D., and Zhang, Z. (2019). 3D printing of bioceramics for bone tissue engineering. *Materials* 12, 3361. doi:10.3390/ma12203361
- Zhang, B., Wang, L., Song, P., Pei, X., Sun, H., Wu, L., et al. (2021a). 3D printed bone tissue regenerative PLA/HA scaffolds with comprehensive performance optimizations. *Mater. Des.* 201, 109490. doi:10.1016/j.matdes.2021.109490
- Zhang, H., and Darvell, B. W. (2010). Synthesis and characterization of hydroxyapatite whiskers by hydrothermal homogeneous precipitation using acetamide. *Acta Biomater.* 6, 3216–3222. doi:10.1016/j.actbio.2010.02.011
- Zhang, H. G., and Zhu, Q. S. (2005). Glutamic acid-mediated synthesis of ultralong hydroxyapatite nanoribbons under hydrothermal conditions. *Chem. Lett.* 34, 788–789. doi:10.1246/cl.2005.788
- Zhang, H., Shen, X., Fei, Z., Fan, X., Ma, L., Wang, H., et al. (2022a). Ag-incorporated polydopamine/tannic acid coating on titanium with enhanced cytocompatible and antibacterial properties. *Front. Bioeng. Biotechnol.* 10, 877738. doi:10.3389/fbioe.2022.877738
- Zhang, L., Yang, G., Johnson, B. N., and Jia, X. (2019). Three-dimensional (3D) printed scaffold and material selection for bone repair. *Acta Biomater.* 84, 16–33. doi:10.1016/j.actbio.2018.11.039
- Zhang, Q., Ma, L., Ji, X., He, Y., Cui, Y., Liu, X., et al. (2022b). High-strength hydroxyapatite scaffolds with minimal surface macrostructures for load-bearing bone regeneration. *Adv. Funct. Mater.* 32, 2204182. doi:10.1002/adfm.202204182
- Zhang, R., Zhang, Q., Zou, Z., Li, Z., Jin, M., An, J., et al. (2021b). Curcumin supplementation enhances bone marrow mesenchymal stem cells to promote the anabolism of articular chondrocytes and cartilage repair. *Cell Transplant.* 30, 963689721993776. doi:10.1177/0963689721993776
- Zhao, X., Liu, A., Zhou, L., Yang, Z., Wei, S., Zhao, Z., et al. (2022). 3D printing of bioactive macro/microporous continuous carbon fibre reinforced hydroxyapatite composite scaffolds with synchronously enhanced strength and toughness. *J. Eur. Ceram. Soc.* 42, 4396–4409. doi:10.1016/j.jeurceramsoc.2022.04.012
- Zhou, A., Zhang, Y., Zhang, X., Deng, Y., Huang, D., Huang, C., et al. (2022). Quaternized chitin/tannic acid bilayers layer-by-layer deposited poly(lactic acid)/polyurethane nanofibrous mats decorated with photoresponsive complex and silver nanoparticles for antibacterial activity. *Int. J. Biol. Macromol.* 201, 448–457. doi:10.1016/j.ijbiomac.2022.01.065



OPEN ACCESS

EDITED BY

Yanjin Lu,
Chinese Academy of Sciences (CAS),
China

REVIEWED BY

Qiang Wang,
China Medical University, China
Jinxin Lin,
Fujian Normal University, China

*CORRESPONDENCE

Xiaofeng Huang,
✉ xiaofengh@ccmu.edu.cn

RECEIVED 27 April 2023

ACCEPTED 13 June 2023

PUBLISHED 13 July 2023

CITATION

Li Y, Tang L, Shen M, Wang Z and Huang X
(2023), A comparative study of Sr-loaded
nano-textured Ti and TiO₂ nanotube
implants on osseointegration
immediately after tooth extraction in
Beagle dogs.
Front. Mater. 10:1213163.
doi: 10.3389/fmats.2023.1213163

COPYRIGHT

© 2023 Li, Tang, Shen, Wang and Huang.
This is an open-access article distributed
under the terms of the [Creative
Commons Attribution License \(CC BY\)](#).
The use, distribution or reproduction in
other forums is permitted, provided the
original author(s) and the copyright
owner(s) are credited and that the original
publication in this journal is cited, in
accordance with accepted academic
practice. No use, distribution or
reproduction is permitted which does not
comply with these terms.

A comparative study of Sr-loaded nano-textured Ti and TiO₂ nanotube implants on osseointegration immediately after tooth extraction in Beagle dogs

Yongfeng Li¹, Li Tang², Mingming Shen¹, Zhen Wang¹ and Xiaofeng Huang^{1*}

¹Department of Stomatology, Beijing Friendship Hospital, Capital Medical University, Beijing, China,

²School of Stomatology, Qingdao University, Qingdao, China

Dental implantation, when performed immediately after tooth extraction, simplifies the treatment procedure, resulting in satisfaction for dentists and patients. Dental implants with nanotopography surface modification have been used to promote osseointegration immediately after implantation. We compared two different nanotopography surface implants on the effects of osseointegration immediately after tooth extraction: TiO₂ nanotubes (NT-TiO₂) fabricated by anodization and Sr-loaded nanotopography Ti (NT-Sr) formed via magnetron sputtering technology. Sr-loaded nanotextured Ti nanotubes (NT-Sr) were fabricated via magnetron sputtering using 99.99% SrTiO₃ as the sputtering target. TiO₂ nanotubes (NT-TiO₂) were fabricated by anodization in 0.5 wt% hydrofluoric acid (HF). After the surface topography, hydrophilicity, chemical components, and interface bonding strength were analyzed, two different nano-topographies were applied for *in vivo* cellular activity evaluation. Subsequently, the implants with NT-Sr and NT-TiO₂ surfaces were inserted into the fresh socket immediately after tooth extraction. Radiological scanning, histological analysis, and biomechanical tests were carried out to investigate implant osseointegration. The results showed that nanotubes with diameters of 15–80 nm were distributed on the NT-TiO₂ surface, while the NT-Sr group showed 20–40 nm nanoparticles deposited on the surface. Compared to NT-Sr, the NT-TiO₂ surface possessed better hydrophilicity and favorable cellular adhesion and proliferation. The NT-Sr surface possessed greater interfacial bonding strength than the NT-TiO₂ group, and greater bone formation, higher bone-to-implant contact (BIC%), and maximum pull-out force were observed in the NT-Sr group. The above results indicated that although the NT-TiO₂ surface showed favorable *in vitro* bioactivity, the NT-Sr surface, with higher interface bonding strength, showed better *in vitro* osteogenesis, and would be more favorable for immediate implantation.

KEYWORDS

strontium, nano, magnetron sputtering, osseointegration, surface modification, immediate implantation

1 Introduction

Immediate implant placement after tooth extraction has led to much satisfaction for dentists and patients over the past decades (Seyssens et al., 2022). Compared to traditional delayed implantation, immediate implants can simplify the treatment procedure. In addition, immediate implantation is favorable for preservation of the extraction site and decreases alveolar bone resorption (Araújo et al., 2019). In order to attain comparable long-term clinical efficacy to delayed implantation, immediate implantation demands higher yields of early osteogenic ability around the implant and higher initial stability. Various strategies have been developed to achieve early osteogenesis and initial stability during immediate implantation, including implant thread optimization and implant surface roughening. Previous studies have demonstrated that rough implant surface modifications can induce osteogenesis around the implant and subsequently stabilize osseointegration (Robo et al., 2022). To date, the conventional topography of commercial implant is almost at the micro-scale (1–10 μm). At present, nano scale surface (1–100 nm) modification has received significant attention, owing to its favorable biological reaction compared to micro-scale surface implants (Mendonça et al., 2008; Cavalu et al., 2020).

Previous studies have reported that a nanotopography surface promotes the osseointegration of implants. Nanotopography structures are classified, according to their topography, as nanoparticles, nanotubes, nanofibers (Mendonça et al., 2008; Yeo, 2019), and so on. An *in vitro* study conducted by Long et al. reported that titanium dioxide (TiO_2) nanotubes can create a favorable osteoimmunomodulatory environment for bone regeneration and osseointegration (Bai et al., 2021). Parnia found that dental implants with nanoparticle coatings possess enhanced osseointegration and antimicrobial properties (Feridoun et al., 2017). Our previous studies have demonstrated that strontium (Sr)-loaded nanoparticle surfaces can promote osteogenesis in cellular and animal experiments under normal and osteoporotic conditions. However, surface roughness modification is a double-edged sword; an active roughness surface may decrease the coating interface bonding strength of the implant. Therefore, it is meaningful to fabricate surfaces possessing the dual properties of high coating interface bonding strength and active osteogenic ability. Few studies have investigated the effects of different nanotopographic surfaces on osseointegration in immediate implantation, especially when applied to large animal models.

Therefore, this study was performed to compare effects of two different typical nanotopographic surfaces on osseointegration during immediate implantation: Sr-loaded nanotextured Ti nanotubes (NT-Sr) and TiO_2 nanotubes (NT- TiO_2).

2 Materials and methods

2.1 Sample coating fabrication and investigation

Titanium disks (Φ 15 mm \times 1 mm) and titanium screw implants (Φ 4 mm \times 8 mm) were randomly divided into two groups. The NT- TiO_2 implant group was prepared via anodization

in a 0.5% (w/v) hydrofluoric (HF) acid electrolyte solution for 30 min, using a 20 V direct current (DC) power supply, and a platinum electrode as the cathode. NT-Sr group implants were fabricated via magnetron sputtering using an industrial physical vapor deposition (PVD) system. The films were deposited under the following conditions: Ar_2 gas composition at 0.5 Pa. After fabrication, all samples were cleaned sequentially with acetone, ethanol, and deionized water ultrasonically, and finally sterilized with γ irradiation for subsequent testing. The samples were tested using field-emission scanning electron microscopy (FE-SEM, HITACHI S-4800) to observe the surface topography and X-ray photoelectron spectroscopy (XPS, ESCALB MK-II) for chemical component analysis.

The interfacial bonding strength of nanotopography layers was evaluated using an epoxy resin docking tensile test, and the Ti samples after epoxy resin docking tensile testing were investigated using SEM to evaluate the collapsed surface characteristics. The surface hydrophilicity of the Ti samples was measured using a surface contact angle measurement machine (DSA30; Kruss, Germany).

The Sr release experiment was carried out using the following procedures: NT-Sr samples were immersed in 5 mL phosphate buffer solution (PBS, Gibco) at 37°C. The PBS was collected and replaced with fresh PBS after 1, 4, 7, and 14 days. The PBS solution containing released Sr was analyzed using inductively coupled plasma atomic emission spectrometry (ICP-AES; IRIS Advantage ER/S). The NT-Sr samples were completely dissolved in a HNO_3 and HF mixture with ultrasonic treatment at room temperature. The total amount of Sr was determined using ICP-AES.

2.2 *In vitro* cellular assay

The murine MC3T3-E1 osteoblast cell line was used for co-culture with Ti samples. The cells were cultured in a minimum essential medium (α -MEM, Gibco) containing 10% fetal calf serum (FCS, Gibco) at 37°C, with the medium changed every 3 days. The Ti samples were placed in a 24-well plate and the cells were seeded at a density of 2×10^4 cells/mL for the assays.

Cell adhesion analysis was carried out after incubation for 30, 60, and 120 min; the attached cells were stained using 4',6'-diamidino-2-phenylindole (DAPI) (Sigma-Aldrich Co., St Louis, MO, United States). Positive cells were counted under an optical microscope (Olympus FluoView FV1000).

Cell proliferation was assessed after culturing for 1, 4, and 7 days using a 3-(4,5-dimethylthiazol-2-yl)-2, 5-diphenyltetrazolium bromide (MTT) (Sigma-Aldrich Co.) assay. At prescribed time points, the Ti samples were gently rinsed with PBS and transferred to a new plate. The Ti samples were then incubated with the MTT solution at 37°C for 4 h. The formazan was then dissolved in dimethyl sulfoxide, and the optical density was measured at 490 nm using a spectrophotometer (Bio-Tek).

Alkaline phosphatase activity (ALP) analysis was performed after 7 days in culture. A colorimetric assay was used to determine the quantity of ALP present. This assay was based on an ALP reagent containing p-nitrophenyl phosphate (p-NPP) as the substrate. Moreover, cell morphology observation after incubation for 3 days was carried out to compare the *in vitro* cellular activity of the two nano-texture surfaces. After incubation for 3 days, the samples with

attached cells were fixed in 3% glutaraldehyde, dehydrated in a graded ethanol series, freeze dried, sputter coated with gold, and observed using FE-SEM. The details of the above *in vitro* cellular assay complied with our previous study (Li et al., 2015).

2.3 In vivo experiment

2.3.1 Animals and surgical procedures

Eight 2-year-old beagles were included in our study. The study was approved and supervised by the Laboratory Animal Ethical Inspection, School of the Fourth Military Medical University [Xi'an, China; approval document no. 2014 (058)]. Adequate measures were taken to minimize pain and discomfort in animals. Animals were anesthetized with sodium pentobarbital (30 mg/kg; Merck Drugs and Biotechnology). The two different surface implants were inserted into fresh extraction sockets immediately after bilateral mandibular premolar extraction. The NT-TiO₂ implants were implanted on the left side, and the NT-Sr implants on the right. The gaps between the implants and extraction sockets were filled with autologous bone chips and X-ray scanning (IntraOs 70, Blue X, Assago, Italy) was performed before teeth extraction, post-extraction, and post-implantation. Antibiotics (ampicillin, 0.5 mg/kg, China) were administered for 5 days to prevent infection post-operation, mouth care with normal saline rinsing was performed for 1 week, and a semi-fluid diet was fed to avoid excessive occlusal force. Twelve weeks after implantation, all animals were euthanized according to the following procedures: overanesthesia with pentobarbital (3%, 100 mg/kg) intravenous injection was applied before harvesting, after vital signs including breathing and heart rate were not detected and tongue cyanosis observed. Mandibles with implants were harvested for subsequent testing. Calcein (8 mg kg⁻¹, Sigma Chemicals Co., United States) and tetracycline (50 mg kg⁻¹, Amresco Ltd., United States) were administered via intramuscular injection on days 4 and 14 to evaluate new bone deposition.

2.3.2 Micro-CT scanning

After euthanasia, the samples were immersed in 75% alcohol and prepared for micro-CT scanning (Inveon, Siemens, Erlangen, Germany). A three-dimensional image was reconstructed using an isotropic voxel size of 15 µm. A region of interest (ROI) was defined as a ring 1 mm in radius from the implant surface. Images acquired from the ROI were used for quantitative analysis, which included bone volume/total volume (BV/TV), trabecular number (Tb.N), trabecular thickness (Tb.Th), and trabecular separation (Tb.Sp).

2.3.3 Histological analysis

The samples were prepared for non-decalcified sections after micro-CT scanning. The samples were immersed in 75% alcohol for 7 days and then dehydrated using a graded series of dilutions of ethanol and 100% acetone. Samples were embedded in polyester resin and cut mid-axially into slices of 150 µm, which were subsequently ground into 100 µm-thick slices using a sawing microtome (Leica SP 1600, Leica Microsystems). Images were captured using a fluorescence microscope (Leica).

After fluorescence observation, the sections were stained with methylene blue acid fuchsin and analyzed using a digitized image analysis system (Leica) coupled to a light microscope (Olympus).

BIC% was calculated as the linear percentage of direct bone-to-implant contact relative to the total implant interface in the cancellous bone.

2.3.4 Biomechanical testing

After the specimens were harvested, eight samples from each group were immediately subjected to a biomechanical pull-out test using a universal material testing system (AGS-10KNG, Shimadzu, Japan). The speed was set at 2 mm/min. The displacement–force curve was recorded to calculate the maximum pull-out force.

2.4 Statistical analysis

Data analysis was performed using the Statistical Package for the Social Sciences (SPSS, version 18). A paired-samples *t*-test was applied for comparisons between two groups. All data are expressed as the mean ± standard deviation (SD). Significant difference was defined as $p < 0.05$, and highly significant differences as $p < 0.01$.

3 Results

3.1 Surface characterization of the samples

SEM images clearly show the surface textures of the two different samples. Nanotubes with diameters of 15–80 nm were distributed on the NT-TiO₂ surface, whereas nanoparticles with diameters of 20–40 nm were deposited on the NT-Sr surface (Figure 1). XPS results showed that Ti, O, and fluorine (F) elements were detected in the NT-TiO₂ samples. The XPS survey of the NT-Sr samples detected the presence of Ti, O, and Sr (Figure 1).

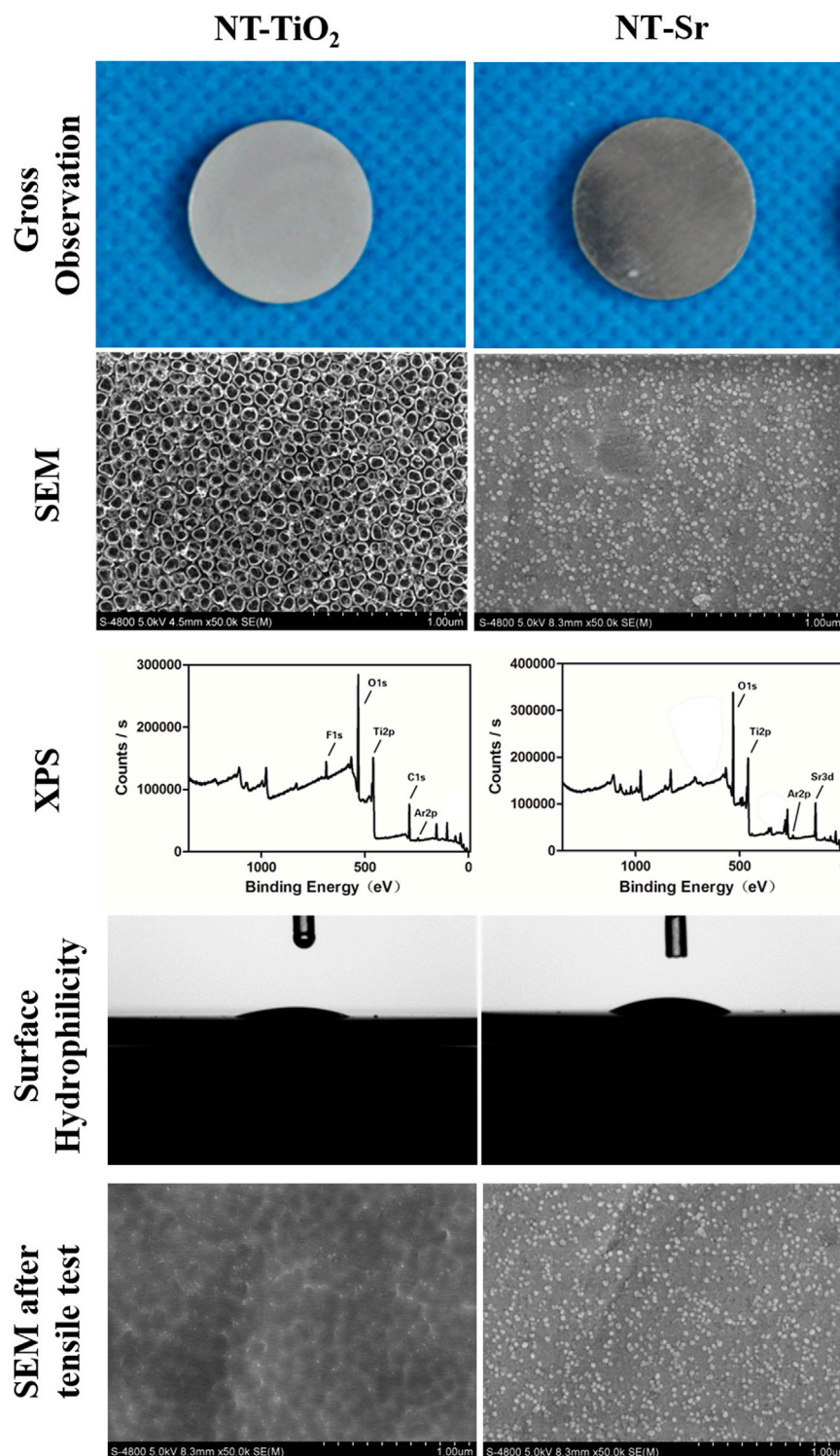
The interface bonding strength of NT-Sr and NT-TiO₂ samples were 52.40 ± 8.73 MPa and 18.20 ± 4.16 MPa, respectively, and a significant difference existed between the groups. SEM images show that the nanotube structure disappeared and that only a residual nanopitted texture remained, whereas the NT-Sr sample displayed a few nanoparticle splits (Figure 1). The contact angles of NT-TiO₂ and NT-Sr were $23.96^\circ \pm 3.64^\circ$ and $29.76^\circ \pm 5.18^\circ$, respectively, which indicated that the NT-TiO₂ surface possessed better hydrophilicity than the NT-Sr surface (Figure 1).

Furthermore, the initial Sr release occurred quickly and the release rate decreased with time. Seven days later, the Sr release rate was relatively constant (Figure 2); the approximate amount of Sr released from NT-Sr samples daily was 0.0156 ± 0.0092 µg/cm². The total Sr content loaded on the NT-Sr surfaces was 42.08 ± 2.52 µg. The results indicated that the total Sr content could be released continuously for over 1 year.

3.2 In vitro cellular assay

As shown in Figure 3, the number of adherent cells on all the Ti samples increased from 30 to 120 min, and the number of cells adhered on the NT-TiO₂ surface seemed to be higher than that on the NT-Sr group over the entire process.

Cell proliferation was evaluated using MTT assay (Figure 3). The cells of the two groups proliferated well, with culture times of

**FIGURE 1**

Surface characteristics evaluation of the two different samples. ($n = 8$). Scale bar is 200 nm. NT-TiO₂, TiO₂ nanotubes surface; NT-Sr, nano strontium-containing titanium surface; SEM, scanning electron microscopy; XPS, X-ray photoelectron spectroscopy.

1–7 days. On day 1, there was no discernible difference in cell proliferation among the different Ti samples. On days 4 and 7, the NT-TiO₂ samples showed better cell proliferation ability than the NT-Sr samples.

As shown in Figure 3, high-magnification SEM images reveal that osteoblasts had spread on the NT-Sr and NT-TiO₂ surfaces. Compared with the cells grown on NT-Sr, the lamellipodia of the cells grown on NT-TiO₂ spread more smoothly.

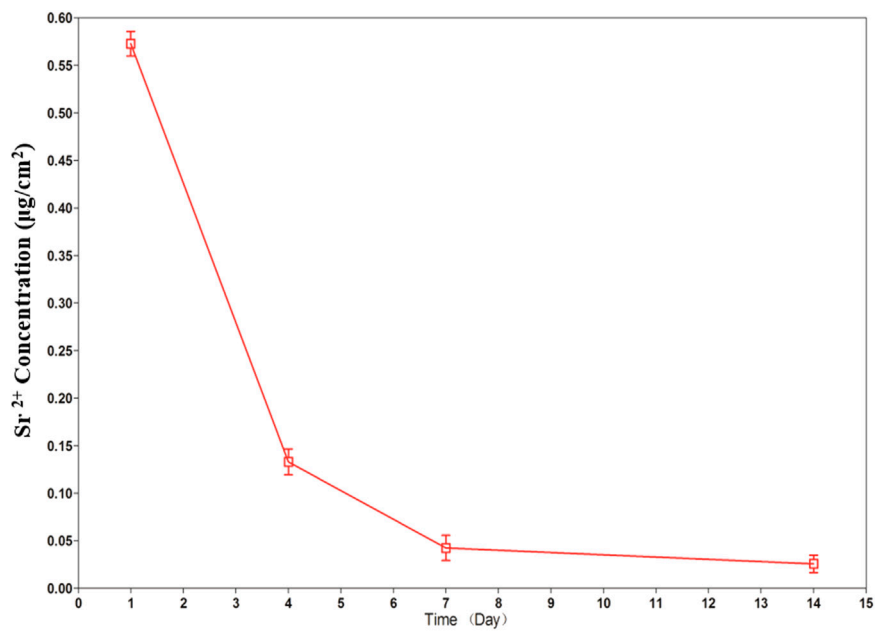


FIGURE 2
Non-cumulative Sr release time profile for NT-Sr into PBS ($n = 5$ at each time point).

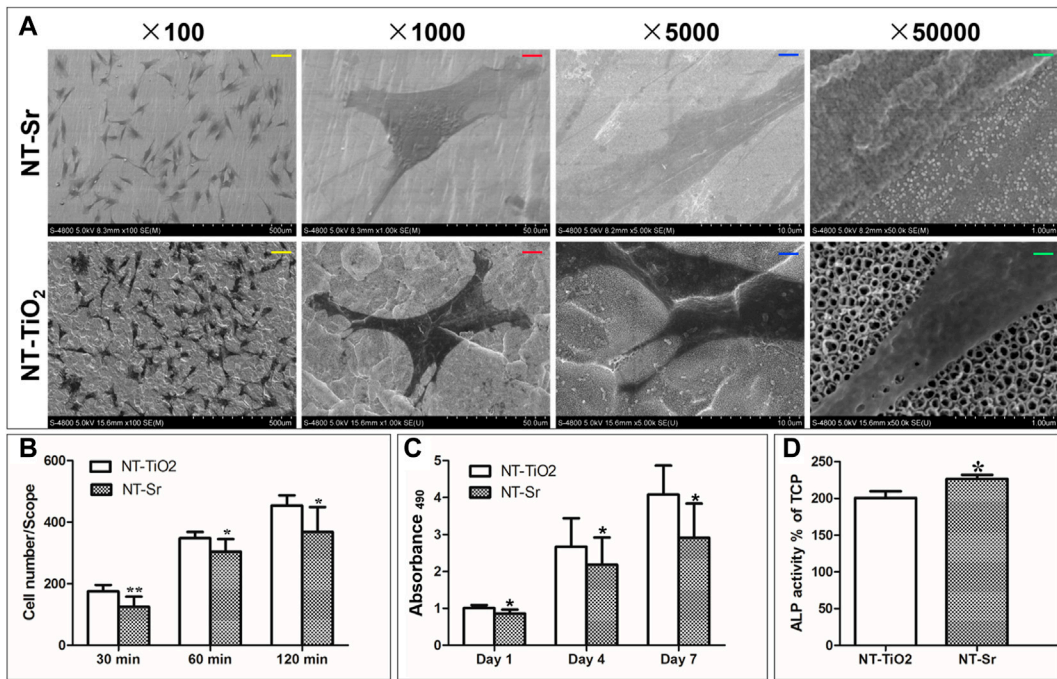


FIGURE 3
In vitro cellular activity evaluation of the two different samples. * $p < 0.05$ and ** $p < 0.01$ compared to NT-TiO₂ samples. ($n = 6$ at each time point). (A) SEM images of cellular adhesion on the two surfaces; (B) Cellular attachment on the two different samples; (C) Cellular proliferation after incubation for 1, 4, and 7 days. (D) ALP activity for two samples. Scale bars: yellow scale bar = 100 µm, red scale bar = 10 µm, blue scale bar = 2 µm, green scale bar = 200 nm.

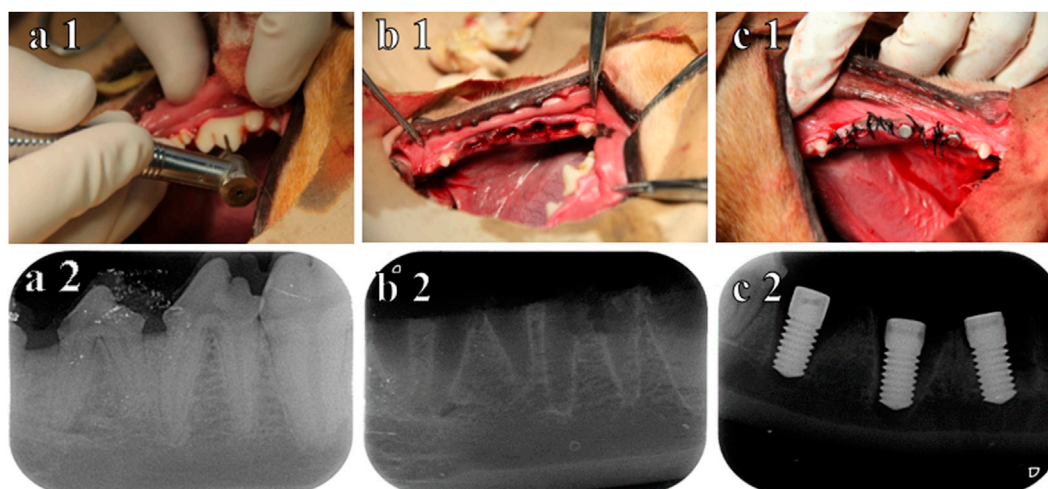


FIGURE 4

Procedure for immediate implantation and X-ray. (A1) before teeth extraction; (B1) after teeth extraction; (C1) immediately after implantation; (A2) X-ray before teeth extraction; (B2) X-ray after teeth extraction; (C2) X-ray immediately after implantation.

Furthermore, the results in Figure 3 indicate that the NT-Sr group showed significantly better ALP activity after 7 days in culture.

3.3 In vivo animal experiment

X-ray examination indicated that the teeth were extracted without additional trauma. Subsequently, the implants were inserted into the extraction socket, and the inferior alveolar neurovascular bundle was not injured (Figure 4). No implant loss occurred after 3 months of observation.

The 3D reconstructed images from micro-CT are shown in Figure 5, which depict bone remodeling around the implants. The bone volume of the NT-Sr group was higher than that of the NT-TiO₂ group. In the quantitative assessment, BV/TV, Tb.N, and Tb.Th were significantly higher for the NT-Sr group. Particularly, as the most important parameter reflecting bone remodeling, the BV/TV of the NT-Sr group increased 0.91-fold compared to the NT-TiO₂ group (Table 1).

As shown in the fluorescence microscopy images (Figure 5), the tissues labelled with calcein were observed with a green fluorescence marker, while those observed with a yellow fluorescence marker indicated tissues labelled with tetracycline; the markers were deposited along the implant surfaces. The mineral apposition ratio (MAR, $\mu\text{m}/\text{d}$) indicates the rate of new-bone mineralization, which is defined as the distance between two double-fluorescence markers. There were statistically significant differences in the MAR between the two groups, in the following order: NT-Sr > NT-TiO₂ ($p < 0.01$). Moreover, from images of the methylene blue/acid fuchsin staining, calcified bone was stained with its characteristic bright pink color and Ti implants were stained black on the slides (Figure 5). One section from each specimen was used for the analysis, and the results of histomorphometry were expressed

as BIC% (Table 1). Twelve weeks after implantation, the BIC% of the NT-TiO₂ and NT-Sr groups were $44.13\% \pm 6.2\%$ and $76.63\% \pm 8.16\%$, respectively, and a significant statistical difference in BIC% existed between the two groups.

Table 2 lists the results of the maximal pull-out force of the two groups 12 weeks after implantation. The pull-out force of the NT-Sr group was significantly higher than that of the NT-TiO₂ group ($p < 0.01$).

4 Discussion

Previous clinical and experimental studies have demonstrated that implants immediately inserted in fresh extraction sockets can prevent post-extraction bone loss. However, the immediate implantation strategy has two potential challenges: firstly, gaps between the regular implant and the irregular extraction socket prevent a part of the implant surface from making direct alveolar bone contact (Naji et al., 2021; Slagter et al., 2021). Secondly, unpredictable implant primary stability results from lower thread mechanical retention in the surrounding bone (Levin et al., 2021). Therefore, favorable osteogenic ability and primary stability are crucial for immediate implantation success.

Conventionally, the regions where the implant surface directly contacts the host bone facilitate favorable osseointegration, while the regions of mismatch gaps between the implant and extraction socket require better bone induction ability. Compared to micro-topography surfaces, nanotopography appears to positively affect cell behavior, including cell adhesion, spread, motility, and proliferation, and nanotopography can selectively adhere to osteoblasts (Price et al., 2003; McManus et al., 2005). For example, on nanosized materials, the affinity ratio between osteoblasts and fibroblasts was 3:1, but for conventional materials, the ratio was 1:1 (Webster et al., 2000).

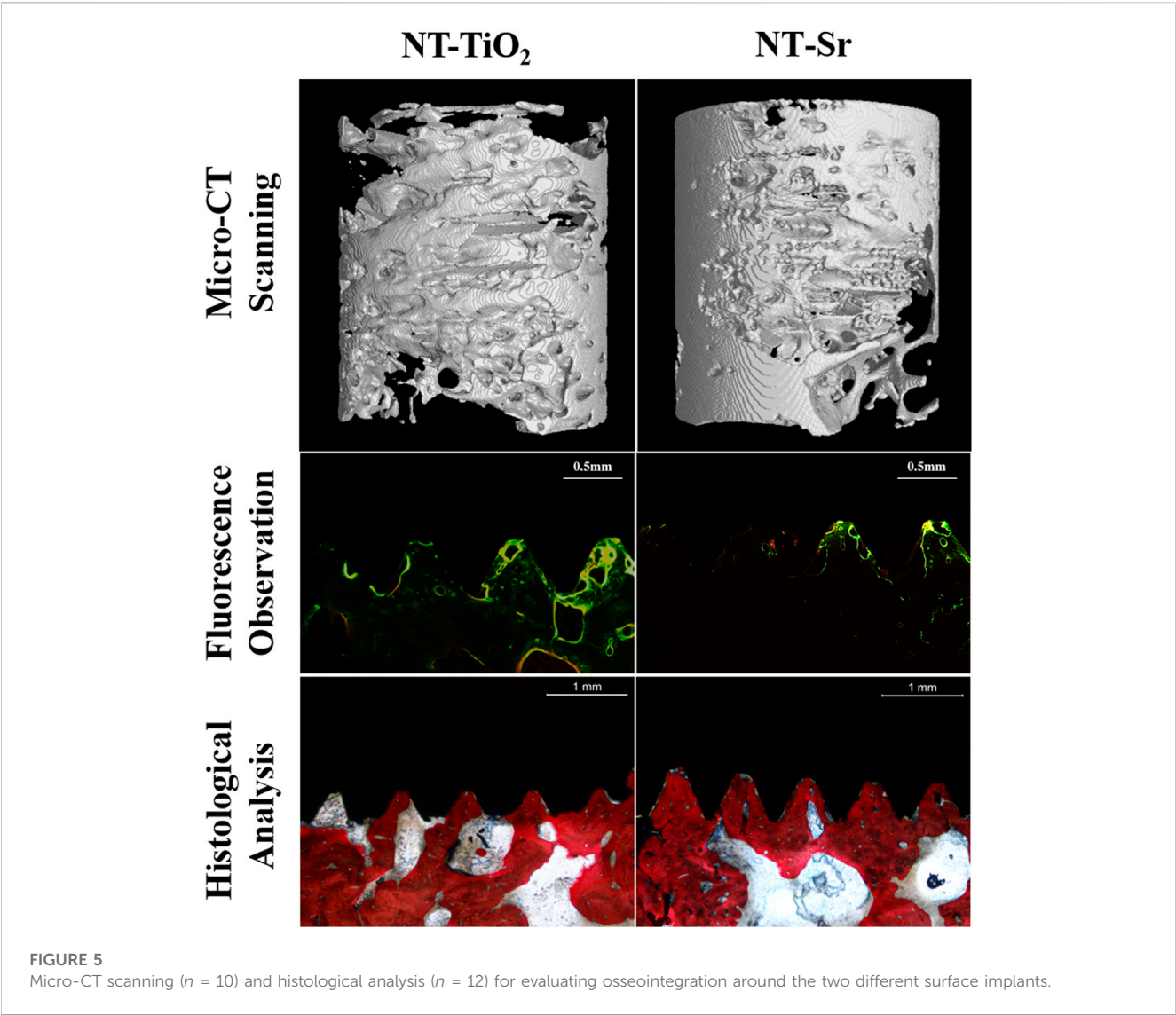


TABLE 1 Quantity analysis of trabecular bone from Micro-CT scanning for implantation immediately after teeth extraction * $p < 0.05$ and ** $p < 0.01$ compared with NT-TiO₂ ($n = 10$).

Parameters	Groups	
	NT-TiO ₂	NT-Sr
BV/TV (%)	28.79 ± 5.94	54.95 ± 9.97**
Tb.N (1/mm)	2.06 ± 0.76	2.38 ± 0.46
Tb.Th (μm)	131.6 ± 25.6	204.9 ± 29.7**
Tb.Sp (μm)	315.2 ± 112.7	196.7 ± 89.7*

Nanotopography is crucial for osteogenesis between gaps in the implant surface, which can ensure that osteoblasts, instead of fibroblasts, occupy the gaps between the implant and extraction socket. Therefore, in this study, two typical nanotopographic surfaces, NT-Sr and NT-TiO₂, were applied to promote osteogenesis around titanium implants. SEM imaging indicated

TABLE 2 Histological analysis and biomechanical test for evaluating osseointegration around two different surface implants: * $p < 0.05$ and ** $p < 0.01$ compared with NT-TiO₂ ($n = 12$).

Parameters	Groups	
	NT-TiO ₂	NT-Sr
BIC (%)	44.13 ± 6.2	76.63 ± 8.16**
MAR (μm/day)	1.78 ± 0.55	2.92 ± 0.58**
Maximal pullout force (N)	236.50 ± 40.86	342.75 ± 46.02**

that nanoparticles (20–40 nm) and nanotubes (15–80 nm), respectively, were fabricated on these titanium surfaces. Subsequent *in vitro* cellular assays showed a positive effect on cell adhesion, proliferation, and differentiation. Additionally, compared to the NT-Sr group, the NT-TiO₂ surface showed better cell adhesion and proliferation, which may be attributed to the superior hydrophilicity of the NT-TiO₂ surface. While higher ALP activity was observed on the NT-Sr surface, Sr loading may be

one of the most important factors that influenced bone remodeling. Previous studies have demonstrated that strontium has dual effects on promoting osteogenesis: stimulation of osteoblast differentiation and inhibition of osteoclast functions (Marx et al., 2020). The osseointegration effect of strontium-loaded surfaces under normal and osteoporotic conditions was verified by *in vitro* and *in vivo* experiments (Shi et al., 2017; Liu et al., 2019; López-Valverde, Muriel-Fernández, Gómez de Diego, Ramírez, and; López-Valverde et al., 2019). Moreover, the Sr release assay used in this study detected continuous Sr release at a slow rate, which can ensure active osteogenesis and mineralization. A similar phenomenon was observed in the double fluorescence labelled results, which indicated that the NT-Sr surface possessed a better mineralization ability than the NT-TiO₂ surface.

The animal experiment investigated osseointegration around the implants, and reversed trends from the *in vivo* assay were observed in the two nanotopography groups: the BIC%, MAR, and maximum pull-out strength of the NT-Sr group were higher than those of the NT-TiO₂ group. This can be explained by the results of the epoxy resin docking tensile test, which indicated that the nanocoating interfacial bonding strength of the NT-TiO₂ surface was only 34.73% of that of the NT-Sr surface. SEM imaging after the epoxy resin docking tensile test also showed completely desquamated nanotubes, whereas the NT-Sr surface showed no obvious changes. In clinical practice, a greater range difference is applied to obtain primary stability during immediate implantation; hence, the solid bonding strength between the coating and the titanium substrates is of great importance. Once the coating collapses from the substrates during implant insertion, the free collapsed particles result in potential adverse inflammatory responses, peri-implantitis, and implant loosening. Potential systemic toxicity resulting from desquamate nanoparticles and debris has been reported in previous studies (Hoet et al., 2004; Warheit et al., 2004; Zeman et al., 2018). Therefore, the interfacial bonding strength of the implant and surface coating was comparable to that of the coating and surrounding bones. Considering the above issues, we fabricated a bioactive nanotopography surface using magnetron sputtering technology, which can synthesize highly adherent thin films via physical vapor deposition (PVD) (Stan et al., 2011) (Qadir et al., 2019).

The positive results of the NT-Sr surface in *in vitro* osseointegration satisfied the two main demands of immediate implantation mentioned above. Firstly, nanotopography and Sr loading can promote osteogenesis, which is needed to simultaneously perform implant insertion and tooth extraction. Secondly, a high interfacial bonding strength can resist the strength of a greater insertion force, which is required for better primary stability. Therefore, compared to the NT-TiO₂ surface, the NT-Sr surface is more suitable for immediate implantation.

References

Araújo, M., Silva, C. O., Souza, A. B., and Sukekava, F. (2019). Socket healing with and without immediate implant placement. *Periodontol.* 79,168–177. doi:10.1111/prd.12252

5 Conclusion

Although we tried to take all aspects into consideration, limitations still inevitability existed, such as limited evaluation indicators and a short observation period. Nonetheless, we can conclude from our preliminary results that NT-TiO₂ and NT-Sr surfaces show favorable *in vivo* cellular activity. NT-TiO₂ possessed better cellular adhesion and proliferation due to its higher hydrophilicity. While NT-Sr surfaces with higher coating interfacial bonding strength would be more suitable for immediate implantation, Sr loading on the surface facilitating improved mineralization was another crucial factor.

Data availability statement

The original contributions presented in the study are included in the article/Supplementary material, further inquiries can be directed to the corresponding author.

Ethics statement

The animal study was reviewed and approved by the Laboratory Animal Ethical Inspection, School of the Fourth Military Medical University.

Author contributions

YL: conceptualization, investigation, writing-original draft. LT: investigation, data curation, visualization. MS: investigation, data curation, formal analysis. ZW: investigation, data curation, visualization. XH: conceptualization, revision, writing-review and editing, validation. All authors contributed to the article and approved the submitted version.

Conflict of interest

The authors declare that the research was conducted in the absence of any commercial or financial relationships that could be construed as a potential conflict of interest.

Publisher's note

All claims expressed in this article are solely those of the authors and do not necessarily represent those of their affiliated organizations, or those of the publisher, the editors and the reviewers. Any product that may be evaluated in this article, or claim that may be made by its manufacturer, is not guaranteed or endorsed by the publisher.

Bai, L., Zhao, Y., Chen, P., Zhang, X., Huang, X., Du, Z., et al. (2021). Targeting early healing phase with titania nanotube arrays on tunable diameters to accelerate bone regeneration and osseointegration. *Small* 17, e2006287. doi:10.1002/smll.202006287

- Cavalu, S., Antoniac, I. V., Mohan, A., Bodog, F., Doicin, C., Mates, I., et al. (2020). Nanoparticles and nanostructured surface fabrication for innovative cranial and maxillofacial surgery. *Mater. (Basel)* 13, 5391. doi:10.3390/ma13235391
- Feridoun, P., Javad, Y., Vahid, J., and Solmaz, M. D. (2017). Overview of nanoparticle coating of dental implants for enhanced osseointegration and antimicrobial purposes. *J. Pharm. Pharm. Sci.* 20, 148–160. doi:10.18433/J3GP6G
- Hoet, P. H., Brüske-Hohlfeld, I., and Salata, O. V. (2004). Nanoparticles - known and unknown health risks. *J. Nanobiotechnology*. 2, 12. doi:10.1186/1477-3155-2-12
- Levin, B. P., Chu, S. J., Saito, H., Nevins, M., and Levin, J. P. (2021). A novel implant design for immediate extraction sites: Determining primary stability. *Int. J. Periodontics. Restor. Dent.* 41, 357–364. doi:10.11607/prd.5527
- Li, Y., Qi, Y., Gao, Q., Niu, Q., Shen, M., Fu, Q., et al. (2015). Effects of a micro/nano rough strontium-loaded surface on osseointegration. *Int. J. Nanomedicine*. 10, 4549–4563. doi:10.2147/IJN.S84398
- Liu, F., Li, Y., Liang, J., Sui, W., Bellare, A., and Kong, L. (2019). Effects of micro/nano strontium-loaded surface implants on osseointegration in ovariectomized sheep. *Clin. Implant. Dent. Relat. Res.* 21, 377–385. doi:10.1111/cid.12719
- López-Valverde, N., Muriel-Fernández, J., Gómez de Diego, R., Ramírez, J. M., and López-Valverde, A. (2019). Effect of strontium-coated titanium implants on osseointegration in animal models: A literature systematic review. *Int. J. Oral. Maxillofac. Implants.* 34, 1389–1396. doi:10.11607/jomi.7827
- Marx, D., Rahimnejad Yazdi, A., Papini, M., and Towler, M. (2020). A review of the latest insights into the mechanism of action of strontium in bone. *Bone. Rep.* 12, 100273. doi:10.1016/j.bonr.2020.100273
- McManus, A. J., Doremus, R. H., Siegel, R. W., and Bizios, R. (2005). Evaluation of cytocompatibility and bending modulus of nanoceramic/polymer composites. *J. Biomed. Mat. Res. A* 72, 98–106. doi:10.1002/jbm.a.30204
- Mendonça, G., Mendonça, D. B., Aragão, F. J., and Cooper, L. F. (2008). Advancing dental implant surface technology-from micron-to nanotopography. *Biomaterials* 29, 3822–3835. doi:10.1016/j.biomaterials.2008.05.012
- Naji, B. M., Abdelsamea, S. S., Alqutaibi, A. Y., and Said Ahmed, W. M. (2021). Immediate dental implant placement with a horizontal gap more than two millimetres: A randomized clinical trial. *Int. J. Oral. Maxillofac. Surg.* 50, 683–690. doi:10.1016/j.ijom.2020.08.015
- Price, R. L., Gutwein, L. G., Kaledin, L., Tepper, F., and Webster, T. J. (2003). Osteoblast function on nanophase alumina materials: Influence of chemistry, phase, and topography. *J. Biomed. Mat. Res. A* 67, 1284–1293. doi:10.1002/jbm.a.20011
- Qadir, M., Li, Y., and Wen, C. (2019). Ion-substituted calcium phosphate coatings by physical vapor deposition magnetron sputtering for biomedical applications: A review. *Acta. Biomater.* 89, 14–32. doi:10.1016/j.actbio.2019.03.006
- Robo, I., Heta, S., Papakozma, D., and Ostreni, V. (2022). Modification of implant surfaces to stimulate mesenchymal cell activation. *Bull. Natl. Res. Cent.* 46, 52. doi:10.1186/s42269-022-00743-x
- Seyssens, L., Eeckhout, C., and Cosyn, J. (2022). Immediate implant placement with or without socket grafting: A systematic review and meta-analysis. *Clin. Implant. Dent. Relat. Res.* 24, 339–351. doi:10.1111/cid.13079
- Shi, J., Li, Y., Gu, Y., Qiao, S., Zhang, X., and Lai, H. (2017). Effect of titanium implants with strontium incorporation on bone apposition in animal models: A systematic review and meta-analysis. *Sci. Rep.* 7, 15563. doi:10.1038/s41598-017-15488-1
- Slagter, K. W., Meijer, H. J. A., Hentenaar, D. F. M., Vissink, A., and Raghoobar, G. M. (2021). Immediate single-tooth implant placement with simultaneous bone augmentation versus delayed implant placement after alveolar ridge preservation in bony defect sites in the esthetic region: A 5-year randomized controlled trial. *J. Periodontol.* 92, 1738–1748. doi:10.1002/jper.20-0845
- Stan, G. E., Pasuk, I., Husanu, M. A., Enculescu, I., Pina, S., Lemos, A. F., et al. (2011). Highly adherent bioactive glass thin films synthesized by magnetron sputtering at low temperature. *J. Mat. Sci. Mat. Med.* 22, 2693–2710. doi:10.1007/s10856-011-4441-1
- Warheit, D. B., Laurence, B. R., Reed, K. L., Roach, D. H., Reynolds, G. A., and Webb, T. R. (2004). Comparative pulmonary toxicity assessment of single-wall carbon nanotubes in rats. *Toxicol. Sci.* 77, 117–125. doi:10.1093/toxsci/kfg228
- Webster, T. J., Ergun, C., Doremus, R. H., Siegel, R. W., and Bizios, R. (2000). Specific proteins mediate enhanced osteoblast adhesion on nanophase ceramics. *J. Biomed. Mat. Res.* 51, 475–483. doi:10.1002/1097-4636(20000905)51:3<475::aid-jbm23>3.0.co;2-9
- Yeo, I. (2019). Modifications of dental implant surfaces at the micro- and nano-level for enhanced osseointegration. *Materials* 13, 89. doi:10.3390/ma13010089
- Zeman, T., Loh, E. W., Čierný, D., and Šerý, O. (2018). Penetration, distribution and brain toxicity of titanium nanoparticles in rodents' body: A review. *IET. Nanobiotechnol.* 12, 695–700. doi:10.1049/iet-nbt.2017.0109



OPEN ACCESS

EDITED BY

Chunguang Yang,
Chinese Academy of Sciences (CAS),
China

REVIEWED BY

Qiang Wang,
China Medical University, China
Gabriela Graziani,
Rizzoli Orthopedic Institute (IRCCS), Italy

*CORRESPONDENCE

Julian R. Jones,
✉ julian.r.jones@imperial.ac.uk

RECEIVED 17 May 2023

ACCEPTED 03 August 2023

PUBLISHED 17 August 2023

CITATION

Heyraud A, Tallia F, Sory D, Ting H-K,
Tchorzewska A, Liu J, Pilsworth HL,
Lee PD, Hanna JV, Rankin SM and
Jones JR (2023), 3D printed hybrid
scaffolds for bone regeneration using
calcium methoxyethoxide as a
calcium source.
Front. Bioeng. Biotechnol. 11:1224596.
doi: 10.3389/fbioe.2023.1224596

COPYRIGHT

© 2023 Heyraud, Tallia, Sory, Ting,
Tchorzewska, Liu, Pilsworth, Lee, Hanna,
Rankin and Jones. This is an open-access
article distributed under the terms of the
[Creative Commons Attribution License](https://creativecommons.org/licenses/by/4.0/)
(CC BY). The use, distribution or
reproduction in other forums is
permitted, provided the original author(s)
and the copyright owner(s) are credited
and that the original publication in this
journal is cited, in accordance with
accepted academic practice. No use,
distribution or reproduction is permitted
which does not comply with these terms.

3D printed hybrid scaffolds for bone regeneration using calcium methoxyethoxide as a calcium source

Agathe Heyraud¹, Francesca Tallia¹, David Sory², Hung-Kai Ting¹,
Anna Tchorzewska¹, Jingwen Liu³, Hannah L. Pilsworth⁴,
Peter D. Lee³, John V. Hanna⁴, Sara M. Rankin² and
Julian R. Jones^{1*}

¹Department of Materials, Imperial College London, London, United Kingdom, ²Faculty of Medicine, Imperial College London, National Heart and Lung Institute, London, United Kingdom, ³Department of Mechanical Engineering, Faculty of Engineering Science, University College London, London, United Kingdom, ⁴Department of Physics, University of Warwick, Coventry, United Kingdom

Introduction: Hybrids consist of inorganic and organic co-networks that are indistinguishable above the nanoscale, which can lead to unprecedented combinations of properties, such as high toughness and controlled degradation.

Methods: We present 3D printed bioactive hybrid scaffolds for bone regeneration, produced by incorporating calcium into our “Bouncy Bioglass”, using calcium methoxyethoxide (CME) as the calcium precursor. SiO₂-CaO_{CME}/PTHF/PCL-diCOOH hybrid “inks” for additive manufacturing (Direct Ink Writing) were optimised for synergy of mechanical properties and open interconnected pore channels.

Results and Discussion: Adding calcium improved printability. Changing calcium content (5, 10, 20, 30, and 40 mol.%) of the SiO₂-CaO_{CME}/PTHF/PCL-diCOOH hybrids affected printability and mechanical properties of the lattice-like scaffolds. Hybrids containing 30 mol.% calcium in the inorganic network (70S30C_{CME}-CL) printed with 500 μm channels and 100 μm strut size achieved the highest strength (0.90 ± 0.23 MPa) and modulus of toughness (0.22 ± 0.04 MPa). These values were higher than Ca-free SiO₂/PTHF/PCL-diCOOH hybrids (0.36 ± 0.14 MPa strength and 0.06 ± 0.01 MPa toughness modulus). Over a period of 90 days of immersion in simulated body fluid (SBF), the 70S30C_{CME}-CL hybrids also kept a stable strain to failure (30 %) and formed hydroxycarbonate apatite within three days. The extracts released by the 70S30C_{CME}-CL hybrids in growth medium did not cause cytotoxic effects on human bone marrow stromal cells over 24 h of culture.

KEYWORDS

sol-gel hybrid, bone regeneration, bioactive, Direct Ink Writing, calcium

Introduction

Non-union bone defects occur in up to 10% of all fracture cases (Calori et al., 2011), and may form critical size defects which do not correctly heal if unaided (2–2.5 times the diameter of the affected bone) (Lasanianos et al., 2010). These often require reconstructive grafts to fill the defect and repair the bone. The gold standard is autografts; however, the procedure has limitations such as donor site morbidity, pain, and the requirement of a second operation site to harvest the bone, increasing recovery time and risks of infection (Baino and Vitale-Brovarone, 2011). The amount of bone that can be harvested is limited and has mismatched mechanical properties compared to long bones (Lasanianos et al., 2010; Jones, 2013), due to being non-load bearing and may poorly fit the defect site. Bone grafts are also not recommended when the defect exceeds 4–5 cm in length as partial resorption of the graft and revascularisation result in weakness and susceptibility to fractures (Lasanianos et al., 2010). Therefore, non-union bone defects are an unmet clinical need. Novel techniques have been used for long-bone diaphyseal defects (>5 cm), such as vascularised bone grafts (Lasanianos et al., 2010), or induced membrane technique with external fixators (Roddy et al., 2018; Masquelet et al., 2019). This however highlights the need for more specialised interventions. Synthetic biomaterial medical devices could meet this unmet need for scaffolds (temporary templates) and: share load with the host bone; bond to the host bone; stimulate osteoprogenitor cells to produce new bone; support vascularised bone ingrowth in a 3D structure; biodegrade as the bone remodels (Jones, 2013).

Recent medical devices for bone regeneration focus on biodegradable materials, with the aim of bone replacing the graft as the material degrades, followed by continued bone remodelling. Bioglass and silicon substituted hydroxyapatite have been proven to stimulate osteogenesis *in vitro* (Xynos et al., 2001) and improved bone regeneration *in vivo* (Oonishi et al., 2000; Midha et al., 2013) compared to other synthetic bone grafts, but while they have good compressive strengths, they are brittle (Jones et al., 2006a; Poologasundarampillai et al., 2016). A hypothesis is that choosing a scaffold material that can share cyclic loading with the host tissue can avoid stress shielding and promote high quality bone regeneration (Wei et al., 2020). Biodegradable polymers (natural: collagen, or synthetic: aliphatic polyesters), provide elasticity but not suitable strength (Wei et al., 2020). Combining organic polymers and inorganic bioactive ceramics or glasses as composites would be a strategy for increasing the toughness of bioactive ceramics or glasses (Koons et al., 2020). However, this leads to bioactive phases being hidden from the *in vivo* environment and heterogeneous degradation rates between the phases, resulting in poor mechanical properties as the scaffold degrades during the bone regeneration process (Jones, 2013). A hybrid differs from composites as their inorganic and organic components are indistinguishable above the nanoscale (Jones, 2013), making them single phase materials. The hypothesis is that the fine scale integration of the co-networks will enable the hybrid biomaterial to degrade as one phase and allow cells to interact with the organic and inorganic networks simultaneously, with no masking of the bioactive phase (Valliant and Jones, 2011). Hybrid biomaterials are synthesised by incorporating a polymer into the sol-gel process, which is usually based on the hydrolysis of silicate based

alkoxides such as tetraethylorthosilicate (TEOS), prior to the gelation of the sol, which forms a silicate network. The synthesis and subsequent drying are carried out below 60°C to prevent polymer burnout or thermal degradation (Tallia et al., 2018). The specification of the organic polymer for the hybrid is important, as it must be: soluble in the sol; tough; able to form dynamic and covalent bonds with the inorganic network; degradable at a controllable rate. For hybrids designed for use as biomaterials, they must have covalent bonds between the organic and inorganic networks, otherwise water will penetrate and force the chains apart, causing dissolution (Poologasundarampillai et al., 2010). Covalent bonding can be achieved through covalent coupling molecules, such as (3-glycidyloxypropyl) trimethoxysilane (GPTMS), (3-isocyanatopropyl) triethoxysilane (ICPTS), or by co-polymerisation techniques (Tallia et al., 2018). Early examples used ICPTS as the coupling agent for PCL containing class II hybrids (Tian et al., 1996; Tian et al., 1997; Tian et al., 1998; Rhee et al., 2002; Rhee, 2004), but mechanical properties were low. Others used gelatin as the polymer, with its carboxylic groups opening the epoxide ring of the coupling agent, GPTMS. The gelatin therefore presented siloxane groups to the silica sol (Mahony et al., 2010). Hybrids with caprolactone co-polymers, GPTMS, and silica were also synthesised and showed adhesion of pre-osteoblast cells to the material (Sang et al., 2018).

For the inorganic network of the hybrids to have the bioactive properties of bioactive glass, calcium must be incorporated into the silicate network (Tallia et al., 2022). This will trigger hydroxycarbonate apatite (HCA) layer formation for bone bonding and release of calcium ions for osteogenic stimulation of cells (Jones, 2013). However, the addition of calcium to the inorganic component of the hybrid poses a challenge: the common calcium source used for sol-gel glass production is calcium nitrate, as it is soluble in the sol. However, it requires a heat treatment higher than 400°C to burn off toxic nitrate by-products and incorporate the calcium into the silicate network (Lin et al., 2009; Jones, 2013). While calcium can be introduced into hybrids at low temperatures as non-toxic calcium salts, such as calcium chloride, the calcium does not bond into the network, making its release uncontrolled on immersion in fluids. Low temperature (<60°C) calcium incorporation in hybrids is needed to prevent the polymer component from degrading (Valliant and Jones, 2011). As an alternative to calcium salts, calcium alkoxides have been used, such as calcium methoxyethoxide (CME) and calcium ethoxide (CE). CME has been shown to incorporate into the silica network at temperatures below 60 °C, where calcium salts did not (Yu et al., 2012). It was hypothesised that the CME hydrolyses when added to the hydrolysed TEOS solution, incorporating calcium into the wet gel. As the silica cross-links during ageing and drying, it maintains calcium in its network (Yu et al., 2012). Using calcium alkoxide instead of nitrate as the precursor for sol-gel glass synthesis was shown to produce thicker and more homogeneous HCA surface layers on glasses (Rámila et al., 2002). CME was successfully incorporated into a SiO₂-CaO/poly (γ-glutamic acid) bulk hybrids (Poologasundarampillai et al., 2014), SiO₂-CaO/polyethylene glycol bulk hybrids (Li et al., 2015), and SiO₂-CaO/PTHF/PCL-diCOOH bulk hybrids (Tallia et al., 2022) which all showed apatite formation after 3 days in simulated body fluid (SBF) and promising cell response. CE was also investigated as another calcium source in class II silica-gelatin hybrids with GPTMS as the coupling agent (Dieudonné et al., 2014; Lao et al., 2016). Calcium alkoxides being

highly sensitive to water meant the choice of water-soluble gelatin limited the synthesis process to avoid fast gelation, leading to uneven distribution of the calcium (Dieudonné et al., 2014; Lao et al., 2016).

None of these calcium-containing hybrid compositions were optimised for additive manufacturing. Tallia et al. recently reported hybrids of the SiO_2 /PTHF/PCL-diCOOH composition that could be printed through Direct Ink Writing and showed excellent resistance to cyclic loads (Tallia et al., 2018). The size of the pore channels was found to be critical for the specific tissue engineering application. When scaffolds were printed with $\sim 250\ \mu\text{m}$ wide pore channels, bone marrow stem cells cultured in the scaffolds progressed down the chondrogenic route, producing articular-like cartilage matrix rich in collagen Type II, Aggrecan, Sox9, and glycosaminoglycans, indicative of articular cartilage matrix. When the pore channels were increased to $500\ \mu\text{m}$, the cells produced matrix that was collagen Type I rich (Li et al., 2020). This underlined the importance of the geometry, as well as degradation by-products to trigger cell signalling and tissue regeneration. For bone regeneration applications, it was therefore important to consider the effect of calcium addition to the hybrid structure. Calcium was first successfully incorporated into the SiO_2 -CaO/PTHF/PCL-diCOOH hybrids using CME with a 60:40 TEOS:CME molar ratio (Tallia et al., 2022), but only in the form of cylindrical monoliths, reaching stress and strain to failure of 60 MPa and 55%, respectively (Tallia et al., 2022), compared to calcium free SiO_2 /PTHF/PCL-diCOOH hybrid monoliths with similar inorganic/organic ratio reaching only 3 MPa and 28%, respectively (Tallia et al., 2018). This increase in strength and toughness due to the addition of calcium showed a real potential for use in bone regeneration.

The aim of this work was to build on the previous research to develop a new hybrid with calcium fully incorporated into the silicate network and synthesise it into an “ink” for Direct Ink Writing to produce open channel interconnective scaffolds suitable for vascularised bone regeneration ($>400\ \mu\text{m}$) with mechanical properties similar to porous bone. The scaffold should also trigger apatite formation *in vitro* and maintain mechanical properties during the biodegradation.

Materials and methods

Materials

All materials were obtained from Sigma Aldrich (Dorset, UK) and VWR UK, unless specified otherwise.

Synthesis of calcium methoxyethoxide (CME)

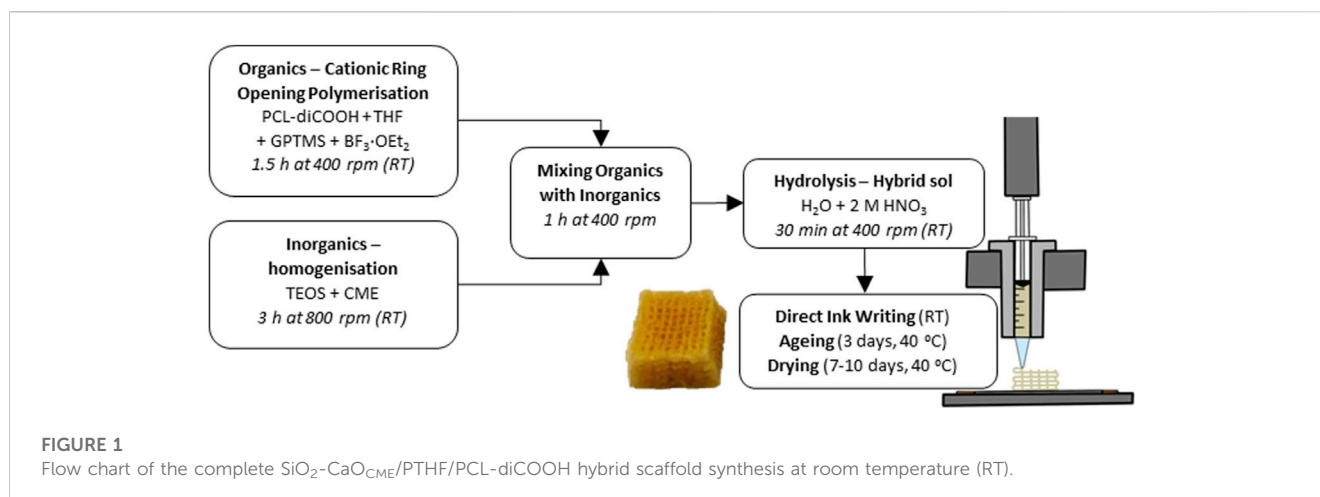
CME was prepared following the process established by Pickup et al. (2009): 2 g of calcium was reacted with 48 mL of anhydrous 2-methoxyethanol at 80°C under Argon for 24 h; the solution was then centrifuged for 20 min at 6,000 rpm to remove unreacted calcium metal and deposit. A transparent dark red solution was obtained. To measure its concentration, 1 mL of solution was transferred into a platinum crucible and heated to $1,050^\circ\text{C}$ for 10 h: the solvent evaporated, and the CME converted to CaO. The concentration was calculated as a ratio of the mass of CaO and the molecular weight of CaO. The CME concentration used in this work was 1 M.

Synthesis of SiO_2 -CaO_{CME}/PTHF/PCL-diCOOH hybrid inks for Direct Ink Writing

The synthesis of the hybrid ink was a two-step procedure developed previously (Tallia et al., 2018), starting with a TEMPO oxidation of the PCL diol to produce a dicarboxylic acid, PCL-diCOOH. The -COOH group was necessary to react with the coupling agent of the hybrid, GPTMS, to form covalent bonds between the silica network and the polymers (Tallia et al., 2018). PCL-diCOOH was used in the sol-gel hybrid synthesis in the organic precursor solution, Figure 1, consisting of PCL-diCOOH (1 mol), (3-glycidyloxypropyl) trimethoxysilane (GPTMS, 2 mol) and boron trifluoride diethyletherate ($\text{BF}_3\cdot\text{EOt}_2$, 0.5 mol) in tetrahydrofuran (THF, $100\ \text{mg mL}^{-1}$ with respect to PCL-diCOOH). This solution was stirred at room temperature for 1.5 h to allow the polymerisation of THF to occur, forming PTHF. GPTMS acted as the initiator for *in situ* cationic ring-opening polymerisation of the THF solvent. In parallel, the inorganic solution was prepared, with TEOS as a silica precursor, using a TEOS:PCL ratio of 70:30 wt.% to achieve a final inorganic:organic (I:O) ratio of 20:80 wt.%. The TEOS was mixed with the CME solution, a TEOS:CME ratio of 60:40 mol.% was initially used but altered throughout the work, down to 95:5 mol.%. The TEOS and CME were mixed at room temperature for 3 h. The organic solution was added dropwise to the inorganic sol and left to stir at room temperature (RT) for a further hour at $400\ \text{rpm}^{24}$. After which, the deionised water was added in stoichiometric volume to hydrolyse the TEOS and GPTMS, followed by 2 M nitric acid (1/3 volume of water). The sol was stirred for 30 min before removing the lid to increase the evaporation of excess solvent, this part was found to take from 10 up to 45 min, varying with temperature and humidity. When the appropriate viscosity was achieved it was then poured into 3 mL Luer-lock plastic syringes and stored in a freezer at -82°C .

Direct Ink Writing of SiO_2 -CaO_{CME}/PTHF/PCL-diCOOH hybrid

The SiO_2 -CaO_{CME}/PTHF/PCL-diCOOH sol-gel ink syringes were defrosted. Once the correct viscosity (degree of gelation) was reached for printing ($\sim 4\ \text{h}$), the syringe was placed in the Direct Ink Writing machine (Robocaster, 3d Inks LLC, USA), connected to a computer with the RoboCAD software (3d Inks LLC, USA). The strut size was determined by the nozzle used, and the strut separation and layer thickness by the scaffold design. The ideal viscosity, which was visually assessed, was reached when the ink was liquid enough to flow through the nozzle but viscous enough to hold its shape without collapsing. This ongoing gelation was utilised to form bonds between the printed layers. The printing window (length of time for which the ink could be printed) was between 1 and 2 h, increasing as calcium content increased. The printing speed and deposition rate also helped to determine the final strut size; with faster printing speed the ink filament could break. A speed of $10\ \text{mm s}^{-1}$ and deposition rate of $0.05\ \text{mL min}^{-1}$ were used. The latter was held constant during printing by an automatic force adjustment applied to the plunger on the z-axis, as the ink viscosity and resistance to extrusion increased with gelation. Strut spacing of 1 mm guaranteed a final pore size of $400\text{--}500\ \mu\text{m}$, post drying. The



layer thickness, or z-spacing, was set at 0.20 mm, matching the tip size. The printing substrate needed to allow for stability of the scaffold during extrusion but facilitate the removal after printing. Greaseproof paper was taped on a flat metal plate and used as the printing substrate. Once the scaffolds were printed, they were carefully removed from the substrate and placed in poly (methyl pentene), PMP, airtight pots for the ageing and drying process at 40°C. The ageing process lasted 3 days in an airtight container, followed by gradual loosening of the lid by a quarter of a revolution every day for 7 days, or until fully opened, to slowly dry the scaffolds.

Characterisation of the hybrid scaffolds

To evaluate the architecture of the hybrid scaffolds, Scanning Electron Microscopy (SEM, JEOL 6010 LA) was used in secondary electron mode with a voltage of 20 kV, a working distance between 13 and 20 mm and spot size between 40 and 60 μm. The samples were fixed on aluminium holders using carbon tape and coated in a 10–15 nm layer of gold using a EMITECH K575X Peltier cooled coater. The top surface and cross sections were imaged after manually cutting with a sharp blade to investigate the horizontal and vertical pore channels of the scaffolds. Post simulated body fluid (SBF) immersion, SEM was used to analyse signs of apatite formation or surface degradation.

To characterise the porosity percentage and interconnectivity of channels, 60S40C_{CME}-CL scaffolds (Table 1) were scanned using X-ray microtomography (μCT, Nikon XTH225 ST) at 70 kV and 140 μA, with a voxel size of 4.0 μm. The μCT images were reconstructed (Nikon's CT Pro 3D) and a sub volume of interest (VOI, 2,600 × 2,600 × 2,600 μm) was defined for quantification. First a 3 × 3 × 3 median filter was applied to reduce noise (Yue et al., 2011), then manual thresholding was performed, selecting the mid-point between attenuation peaks using Avizo (version 2021). "Label analysis" in Avizo was utilised for the measurement of porosity and interconnectivity (percentage of pores connected with each other and the exterior). Pore sizes and the strut equivalent diameter of 60S40C_{CME}-CL scaffolds were measured using the open-source image processing program ImageJ with the BoneJ plugin (Doubé et al., 2010). Two types of thickness maps were made: one illustrating

pore size and the other strut equivalent diameter (Atwood et al., 2004).

Fourier Transform Infra-red (FTIR) spectroscopy was used to verify the presence of the functional groups corresponding to the organic and inorganic components of the hybrid system and investigate the variation in the hybrid chemical structure and bonding due to the different addition of calcium. This technique also identified compositional changes after immersion in SBF. A Thermo Scientific Nicolet iS10 FTIR equipped with Smart Golden Gate for Single-Reflection Diamond ATR Analysis, with OMNIC software was used. 64 scans were collected at a resolution of 4 cm⁻¹ for a spectral range of 400–4,000 cm⁻¹. Solid samples were usually prepared by manually grinding them into a fine powder.

Simultaneous Differential Scanning Calorimetry and Thermogravimetric Analysis (DSC/TGA) were performed on Netzsch Jupiter STA 449C instrument with Proteus software to process the acquired data. The hybrid samples were manually ground to a fine powder, and between 10 and 15 mg was placed in a platinum crucible, the reference being an empty platinum crucible. A heating rate of 10°C min⁻¹ over a temperature range of 20–800°C under continuously flowing air was used. This technique was used to analyse the hybrids final I:O ratio and finding the characteristic burn-out temperature of both polymers present in the system: PCL-diCOOH and PTHF. The I:O ratios were also evaluated after various timepoints of immersion in SBF.

Compression testing was done to assess maximum stress and strain of the 3D printed hybrid scaffolds. A sharp blade was used to cut the scaffolds to 5 × 5 × 5 mm³ cubes, and the load was applied perpendicular to the plane of deposition during printing. A Bose Electroforce Series III mounted with a 450 N load cell was used for compression testing, with the Wintest software to collect the data. The displacement rate used was 0.5 mm min⁻¹. The engineering and true stress and strain at yield were calculated. Cyclic loading was also performed on scaffolds of the same dimensions to show their ability to recover deformation in a specific strain range. The test comprised of 10 cycles, all in the same conditions, in a strain-controlled manner to compress each sample to 20% of their original measured height. The loading and unloading steps were both performed at 0.5 mm min⁻¹, similar to the compression to failure tests. A dwell time of 30 s between each cycle was programmed to enable complete

recovery of the deformation after loading. DMA (Dynamic Mechanical Analysis) was performed on the same scaffold dimensions with the Bose Electroforce Series III used in parallel with the Wintest DMA software. The tests were done at strain ranges of 1%–5%, 5%–9% and 9%–13%, individually calculated for each scaffold from their measured height, collecting data at frequencies of 0.1, 1 and 10 Hz. DMA was performed to analyse the viscoelastic behaviour of the scaffolds and compare the stiffness of hybrids with varying calcium content and after immersion in SBF at various timepoints.

X-ray Diffraction (XRD) measurements were performed using a Bruker D2 PHASER desktop diffractometer, the data was analysed with a PANalytical X'Pert HighScore software. A Cu K α tube anode was used ($\lambda = 1.5418 \text{ \AA}$) and the generator settings fixed at a voltage of 30 kV and current intensity of 10 mA. A nickel filter was used to remove K β , though still visible from most intense peaks. Each pattern was recorded in the range of 5 to 120°, this is specified if changed to analyse a narrower range of angles. The step size and time per step were set at 0.035° and 0.35 s step⁻¹. Minimal sample preparation is required, hybrid samples were usually manually ground to a fine powder and flattened in a single crystal silicon sample holder, to prevent it showing background noise. This method provided information on the presence of crystallised apatite on otherwise amorphous hybrid scaffolds after immersion in SBF.

A Thermo Scientific ICAP 6300 Inductively coupled plasma-optical emission spectroscopy (ICP-OES) with autosampler was used in parallel with the iTEVA software to determine the concentration of Ca, Si and P in SBF solution after immersion of hybrid scaffolds. The aim was to analyse potential apatite formation on the hybrids for bone regeneration, as well as monitor the slow release of silica and calcium ions due to the controlled degradation of the hybrid (Tallia et al., 2022). Due to the high content of calcium in SBF itself, the samples were diluted by a factor of 10 with DI water (1 mL of the aqueous sample and 9 mL of DI water). The standard solutions for calibration were prepared containing Si, Ca, and P at 0, 0.1, 0.2, 0.4, 0.8, 1, 5, 10 and 20 $\mu\text{g mL}^{-1}$. For the dissolution studies, timepoints of 0–8 h, 1, 3, 7, 21, 30, 60 and 90 days were selected to analyse the effect of immersion of hybrid scaffolds with different calcium content in SBF. SBF was used, as opposed to phosphate buffered saline (PBS) or tris(hydroxymethyl)aminomethane (TRIS), as the deposition of apatite on the bone scaffold was investigated. Scaffolds were cut to the desired size ($5 \times 5 \times 5 \text{ mm}^3$) and weighed to measure mass loss post dissolution. They were then rinsed three times in DI water prior to the immersion in SBF to ensure no reaction by-product were left over (such as $\text{BF}_3 \cdot \text{EOt}_2$) and placed in SBF at a 1.5 mg mL^{-1} scaffold mass to SBF volume ratio. This concentration is commonly used for testing apatite formation on bioactive glasses in SBF (Jones et al., 2001; Tallia et al., 2022). The scaffolds were then kept in an incubator at 37 °C and 120 rpm (Maçon et al., 2015).

All ^{29}Si Magic-Angle-Spinning Nuclear Magnetic Resonance (MAS NMR) measurements were performed at 7.05 T using a Bruker Avance III HD-300 spectrometer operating at a ^{29}Si Larmor frequency of 59.5 MHz. These experiments were undertaken using a Bruker 7 mm HX probe which enabled a MAS frequency of 5 kHz for all ^{29}Si single pulse experiments

performed to assess the Si speciation quantitatively. The pulse time calibration was performed on solid kaolinite ($\text{Al}_2\text{O}_3 \cdot 2\text{SiO}_2 \cdot 2\text{H}_2\text{O}$) from which a $\pi/2$ pulse time of 6.0 μs was measured. All ^{29}Si MAS NMR data were acquired using a $\pi/2$ nutation angle, a recycle delay of 240 s, and a heteronuclear $^1\text{H}/^{29}\text{Si}$ decoupling field strength of 80 kHz during data acquisition. The reported ^{29}Si chemical shifts were referenced against the IUPAC recommended primary reference of Me_4Si (1% in CDCl_3 , $\delta_{\text{iso}} = 0.0 \text{ ppm}$), via a secondary solid kaolinite standard which has a known shift of $\delta_{\text{iso}} = -92.0 \text{ ppm}$ (Harris et al., 2002). The degree of condensation of the silica network, Dc, Equation 1, was calculated from quantitative measurement of the Qⁿ structures derived from TEOS ($\text{Si}(\text{OSi})_n(\text{OR})_{4-n}$ species, with R being Ca or H) and Tⁿ structures derived from the coupling agent GPTMS ($\text{C-Si}(\text{OSi})_n(\text{OR})_{3-n}$ species, with R being Ca or H), from the ^{29}Si MAS NMR data (Connell et al., 2014).

$$D_c = \left(\left[\frac{4Q^4 + 3Q^3 + 2Q^2}{4} \right] + \left[\frac{3T^3 + 2T^2 + T^1}{3} \right] \right) \quad (1)$$

Cell culture study: Conditioned medium, cell seeding, and plate preparation for *in vitro* cultures

Discs of 8 mm diameter were punched out of 1 mm thick 70S30C_{CME}-CL and 90S10C_{CME}-CL hybrid monoliths. The discs were sterilised by 3 washing cycles in DI water, 70% and 100% ethanol, then irradiated under UV light for 3 h and air dried under sterile conditions for 24 h.

The 70S30C_{CME}-CL and 90S10C_{CME}-CL hybrid conditioned media and vehicle medium (VC, fresh serum-free Dulbecco's Modified Eagle Medium, DMEM) were prepared as per ISO 10993-12 (ISO 10993-12: 2021 Biological evaluation of medical devices—Part 12: Sample preparation and reference materials, 2021) (3 discs mL^{-1} of fresh serum-free DMEM to give $300 \text{ mm}^2 \text{ mL}^{-1}$, 72 h incubation at 37 °C). The conditioned media were sterilised by filtration through a 0.2 μm non-pyrogenic sterile 28 mm syringe surfactant-free cellulose acetate filter (#431219, Corning). Dilution series of 0%, 25%, 50%, 75% and 100% were prepared with vehicle medium (VC or 0%). ICP-OES was used to analyse the release of soluble calcium, phosphate, and silica ions in the extracts. XRD was used to evaluate the deposition of hydroxyapatite on the samples after incubation. Prior to treating cells, all conditioned media were reconstituted with 10% (v/v) Fetal Bovine Serum (FBS), 1% (v/v) Penicillin/Streptomycin (P/S) and 1% (v/v) L-glutamine.

Fresh unprocessed human-bone marrow stromal cells (h-BMSCs, #PT2501, LONZA) were expanded and used up to passage 5 maximum. On the day prior to the cytotoxicity study, h-BMSCs were detached by enzymatic digestion (trypsin/EDTA) and seeded to 1×10^4 cells well^{-1} in the central wells of 96-well plate prefilled with 60 μL of freshly prepared non-selective growth medium. The cells were incubated for 24 h in standard sterile culture conditions (37°C, 5% CO_2) to allow the formation of a semi-confluent monolayer. Just prior to starting the *in vitro* cytotoxicity study, growth medium was replaced by freshly prepared conditioned media or VC.

Cell viability was assessed using an Alamar Blue HS kit, as per manufacturer's protocol. A decrease of Alamar Blue dye fluorescence reading in h-BMSCs exposed to hybrids extracts was used as marker of cytotoxicity. Cytotoxicity in h-BMSCs was recorded prior to and after 24 h of exposure to the dilution extracts from conditioned media.

Results and discussion

Ink formulation for Direct Ink Writing

The effect of calcium content on hybrid printability, chemical characteristics, and mechanical properties were analysed, using TEOS:CME molar ratios of 60:40, 70:30, 80:20, 90:10 and 95:5. To keep the hybrid I:O ratios consistent (approx. 25:75 wt.%), the TEOS:PCL-diCOOH ratios were altered as the TEOS:CME ratio changed. The ratios and composition of each ink are summarised in Table 1, with the I:O ratio determined by TGA. The hybrids are identified by their TEOS:CME ratios, with a hybrid with a molar ratio of x:y being named "xSyC_{CME}-CL".

The 80S20C_{CME}-CL hybrid composition was not printable due to phase separation. This composition was therefore used in understanding the chemical bonding of calcium in the hybrid but not to assess mechanical properties, as no scaffolds could be printed. All other composition "inks" appeared homogeneous and were printable, forming regular hybrid structures with open channel interconnectivity (Figure 2). After printing, the scaffolds were aged and dried, which caused shrinkage. The aim was to achieve x-y channels of approximately 500 μm and z channels of 100 μm post drying (Table 2) by setting a strut spacing of 1 mm and using a tip size of 0.20 mm. The channels of each scaffold were measured using ImageJ from SEM micrographs (Figure 2), showing drying and shrinkage variability between the compositions. x-y channel widths ranged from 399.2 ± 95.5 to $515.2 \pm 80.2 \mu\text{m}$, shrinkage of 50%–65% compared to the CAD file. Channel widths in the z direction were measured at 103.2 ± 32.8 to $150.5 \pm 52.5 \mu\text{m}$, 50%–75% of the CAD file, due to shrinkage and the weight of the struts in the z direction. The scaffold printed from these calcium containing inks shrank more than calcium-free (100S0C-CL) hybrid scaffolds previously printed by Li et al. to achieve the same 500 μm final channel size (Li et al., 2020) (x-y channel size was $503 \pm 82 \mu\text{m}$, with strut sizes ranging between

210–230 μm^{32}). This was expected due to the addition 2-methoxyethanol solvent introduced during the hybrid synthesis for the calcium addition. Increasing the amount of calcium with CME increased the gelation time to reach printability of the ink, as well as the printing window, meaning the ink was printable for longer (varying from 1 h to 2 h). It however increased the shrinkage of the hybrid scaffold during the drying stage, showing a difference of approximately 100 μm between compositions (Table 2). The aim to create scaffolds with an open interconnected channel network was achieved for hybrid compositions: 60S40C_{CME}-CL, 70S30C_{CME}-CL, 90S10C_{CME}-CL, and 95S5C_{CME}-CL. The variability observed did not impact the final structure, but the different hybrids need further testing to underline which composition shows the most potential for bone regeneration.

Approximately 50% porosity was achieved in the scaffolds, measure by analysis of the μCT rendering (Figure 3). This was below the porosity of trabecular bone (70%–95%) (Aspden, 2004); however, the importance of the porous structure was to have open pore channels, interconnectivity suitable for tissue ingrowth, i.e., to create a scaffold for bone to grow on rather than to recreate a bone structure directly. The 60S40C_{CME}-CL hybrid scaffold had a total porosity calculated at $51.2\% \pm 2.8\%$ with 99.9% of the pores were interconnected (i.e., connected to each other and the surface). The strut size is in Figure 3B by a 3D colour map; the mean strut equivalent diameter was $174 \pm 65 \mu\text{m}$, with a maximum of 473 μm . Due to the channel like structure of the porosity, it was difficult to classify the channels into pores and connecting apertures (as done in some prior studies (Atwood et al., 2004; Jones et al., 2006b; Jones et al., 2009; Yue et al., 2010)) but Figure 3C shows representation of the channels (with the scaffold removed); the mean pore equivalent diameter (most are channels, see Figure 3C) was $243 \pm 105 \mu\text{m}$, with a maximum of 476 μm . Figure 3D shows connections between channels, with the majority of the channels interconnected by passages over 200 μm in equivalent diameter. Interestingly the range of pore and interconnect sizes is similar, but the mean pore equivalent diameter is larger.

Mechanical properties

The effect of calcium on the mechanical properties of the hybrid scaffolds was assessed by compression to failure and DMA analysis. Representative stress-strain curves in Figure 4A show elastic deformation, and the values obtained from the curves are in Table 3, with the maximum stress corresponding to strut

TABLE 1 SiO₂-CaO_{CME}/PTHF/PCL-diCOOH hybrids synthesised with varying compositions and final I:O ratios.

Hybrid name (xSyC _{CME} -CL, where x:y is the TEOS:CME molar ratio)	TEOS:CME ratio (mol.%)	TEOS:PCL-diCOOH ratio (wt.%)	I:O ratio (wt.%)
60S40C _{CME} -CL	60:40	70:30	23.1:76.9
70S30C _{CME} -CL	70:30	72.5:27.5	25.5:74.5
80S20C _{CME} -CL	80:20	75:25	23.8:76.2
90S10C _{CME} -CL	90:10	77.5:22.5	26.3:73.7
95S5C _{CME} -CL	95:5	78.75:21.25	27.2:72.8
100S-CL	100:0	80:20	25.1:74.9

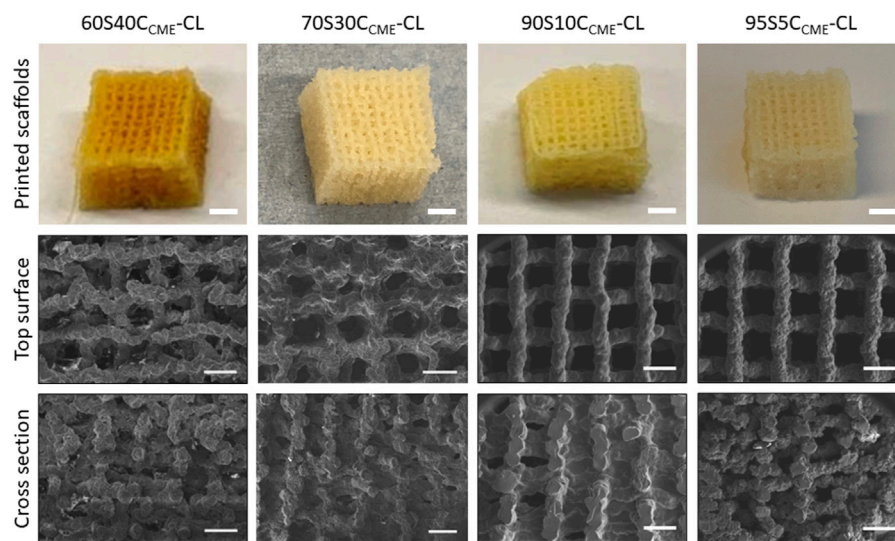


FIGURE 2

Photographs (scale bars 2 mm) and SEM micrographs (scale bars 500 μm) of 3D printed $\text{SiO}_2\text{-CaO}_{\text{CME}}/\text{PTHF}/\text{PCL}\text{-diCOOH}$ hybrid scaffolds of compositions $x\text{SyC}_{\text{CME}}\text{-CL}$, where $x:y$ is the TEOS:CME molar ratio, printed via Direct Ink Writing using a tip size of 0.20 mm and strut spacing of 1 mm.

fracture, which is equivalent to the yield stress. The corresponding strain at the yield point was taken as the maximum strain of the hybrid. An increase in strength as calcium content increased was expected, hypothesised to be due to calcium cations forming stabilising complexes with lone pairs on the ester linkages along the PCL backbone, and with any remaining unreacted carboxylate terminal groups. The carbonyl oxygen has two lone electron pairs and slight excess of negative charge to form a stabilising complex with calcium, oxygen acting as a ligand in the metal complex. It could act as a monodentate or bidentate ligand, binding through one or two donor sites (Tallia et al., 2022).

The $95\text{S}5\text{C}_{\text{CME}}\text{-CL}$ hybrids, which had the addition of 5 mol.% calcium compared to the $100\text{S}\text{-CL}$ (Ca-free) control, had a similar yield stress to the $100\text{S}\text{-CL}$ scaffolds, but the yield strain decreased by 6%. The slight reduction could be due to the less regular scaffold print due to the ink behaviour. As calcium content was increased, $90\text{S}10\text{C}_{\text{CME}}\text{-CL}$ and $70\text{S}30\text{C}_{\text{CME}}\text{-CL}$ hybrids showed an increase in yield stress by 0.3 and 0.5 MPa, respectively, to 0.71 ± 0.17 and 0.90 ± 0.23 MPa. This behaviour followed the expectation that calcium incorporation increases the hybrid strength (Tallia et al., 2022). Interestingly, the yield strain of $90\text{S}10\text{C}_{\text{CME}}\text{-CL}$ and $70\text{S}30\text{C}_{\text{CME}}\text{-CL}$ were similar to that of the Ca-free ($100\text{S}\text{-CL}$) scaffolds; however, properties of $90\text{S}10\text{C}_{\text{CME}}\text{-CL}$ had large variation between scaffolds tested. The $70\text{S}30\text{C}_{\text{CME}}\text{-CL}$ hybrid scaffolds exhibited the highest yield strength at 0.90 ± 0.23 MPa, at a strain of 30%, over all compositions tested, and the highest modulus of toughness (0.22 ± 0.04 MPa). As calcium content was increased further to $60\text{S}40\text{C}_{\text{CME}}\text{-CL}$, the yield stress dropped down to 0.38 MPa and the yield strain increased 13% compared to the control, illustrating the change in behaviour of the hybrid due to the addition of calcium. This increase in strain in the $60\text{S}40\text{C}_{\text{CME}}\text{-CL}$ hybrid scaffold showed the shear thinning property of the CME solution affected the final properties of the hybrid. The elastic region could not be accurately quantified from measuring the Young's

TABLE 2 Structure of $\text{SiO}_2\text{-CaO}_{\text{CME}}/\text{PTHF}/\text{PCL}\text{-diCOOH}$ hybrids of different compositions ($x\text{SyC}_{\text{CME}}\text{-CL}$, where $x:y$ is the TEOS:CME molar ratio) after Direct Ink Writing using a tip size of 0.20 mm and strut spacing of 1 mm. Mean values \pm standard deviation ($n \geq 3$).

Hybrid name	x-y channels (μm)	z channels (μm)
$60\text{S}40\text{C}_{\text{CME}}\text{-CL}$	399.2 ± 95.5	150.5 ± 52.5
$70\text{S}30\text{C}_{\text{CME}}\text{-CL}$	473.2 ± 73.6	103.2 ± 32.8
$90\text{S}10\text{C}_{\text{CME}}\text{-CL}$	439.8 ± 76.1	152.4 ± 71.5
$95\text{S}5\text{C}_{\text{CME}}\text{-CL}$	515.2 ± 80.2	117.3 ± 25.3

modulus as it exhibited a non-linear elastic deformation. Therefore, DMA was performed to quantify the elastic modulus at 1 Hz frequency, representative of the frequency range investigated, 0.1–10 Hz and physiological activities of humans (Khusainov et al., 2013). The strain ranges of 1%–5%, 5%–9% and 9%–13% were studied as deemed to be a safe range (i.e., damage-free elastic region) to analyse the elastic properties of the hybrids of each composition. The first observation for all compositions was that the damping values obtained by DMA (i.e., $\tan\delta$) were all close to zero with $E' \gg E''$. Due to the negligible damping values, it was concluded that all compositions showed an elastic behaviour in those strain ranges and the storage modulus could be directly related to the stiffness of the material. The $95\text{S}5\text{C}_{\text{CME}}\text{-CL}$ hybrids and the $90\text{S}10\text{C}_{\text{CME}}\text{-CL}$ showed similar values of stiffness, 3.54 ± 0.06 and 3.26 ± 0.45 MPa, respectively. However, the later composition had a larger variability, similarly to its stress strain values. As expected, from the stress-strain curves, the $60\text{S}40\text{C}_{\text{CME}}\text{-CL}$ hybrid showed the lowest stiffness of 2.14 ± 0.14 MPa. $70\text{S}30\text{C}_{\text{CME}}\text{-CL}$ reaching up to 4.48 ± 0.29 MPa.

Cyclic loading was performed on the $60\text{S}40\text{C}_{\text{CME}}\text{-CL}$ hybrid scaffolds to show that even with the maximal addition of CME, 60 mol.% with respect to TEOS, the hybrid was still able to recover

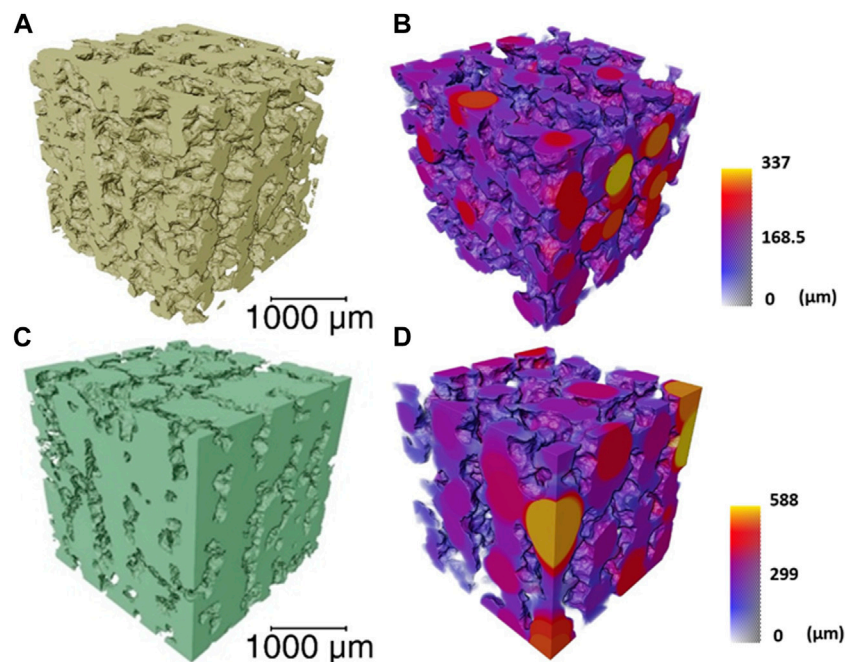


FIGURE 3

μCT imaging and analysis of a volume of interest ($2,600 \times 2,600 \times 2,600 \mu\text{m}$) of the 60S40C_{CME}-CL hybrid scaffold of overall porosity $51.2\% \pm 2.8\%$ and pore interconnectivity of 99.9%. (A) 3D rendering of the scaffold struts; (B) strut thickness map coloured by their diameter size; (C) 3D rendering of the interconnected pore network (negative of the strut rendering); and (D) a colour map to visualise the interconnecting channel thickness.

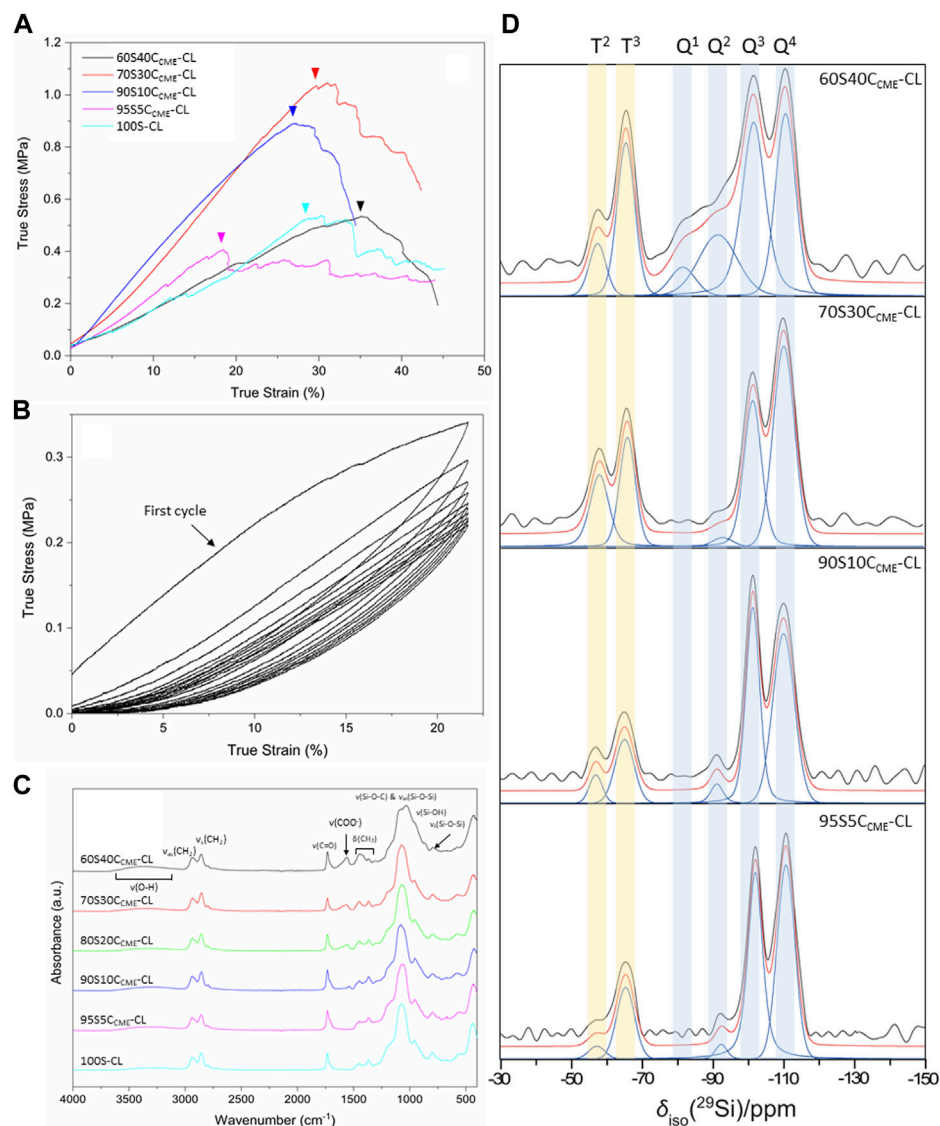
from deformation, similarly to the original 100S-CL hybrid (Tallia et al., 2018). A safe strain range was established with the compression data, 20% strain was inflicted on the scaffolds for 10 cycles (Figure 4B). Every cycle recovered the strain reached, after the first cycle. The maximum stress reduced with each cycle until it settled around 0.22 MPa. A hysteresis loop was observed, significative of a lag in deformation recovery, characteristic of viscoelastic behaviour (Tallia et al., 2018; Tallia et al., 2022). The first cycle showed initial higher stress reached, this behaviour seemed typical of hybrids tests in cubic form, with struts at the edge having a higher stress concentration and individually breaking (Tallia et al., 2018), whilst the bulk stayed intact. The Mullins effect could also have an impact; it is a characteristic of pure elastomer with mechanical softening occurring due to the transformation of hard domains to soft domains (Cantournet et al., 2009). This shows a decrease in stress on unloading compared to loading, characterised by the hysteresis visible in Figure 4B. Despite the first cycles showing a slightly different behaviour, the 60S40C_{CME}-CL did sustain cyclic loading, making it an option for trabecular bone repair, with preconditioning potentially required before use. This slow reduction until settling at 0.22 MPa was not seen in the calcium-free 100S-CL hybrids (Tallia et al., 2018), the increased elasticity of 60S40C_{CME}-CL scaffolds and higher strain reached could explain this initial compression.

Calcium incorporation into the silicate network

FTIR spectra show features of the organic and inorganic networks. Bands corresponding to bonds in the inorganic network are mostly found at wavenumbers below $1,200 \text{ cm}^{-1}$,

with the band between $1,100$ and $1,000 \text{ cm}^{-1}$ corresponding to the Si-O-Si asymmetric stretching and Si-O-C stretching (Figure 4C). For calcium contents less than 70S30C_{CME}-CL, one prominent band was observed, with a small shoulder towards higher wavelengths. For the 60S40C_{CME}-CL hybrid, two bands were observed, at $1,078$ and $1,031 \text{ cm}^{-1}$; the band at $1,078 \text{ cm}^{-1}$ being of lower relative intensity. The band at $1,000\text{--}900 \text{ cm}^{-1}$ corresponds to the Si-OH stretching vibration, characteristic of non-bridging oxygens (NBOs). This band was of higher relative intensity in hybrids with highest calcium content, merging in with the Si-O-Si and Si-O-C bands. Calcium's role as a network modifier of the silicate network explains this disruption, ionically bonding with the silica network. The band at 790 cm^{-1} , corresponding to the symmetric Si-O-Si stretching, was more intense in the control and lower calcium content hybrids.

The main difference between the FTIR spectra of the calcium-free control and 95S5C_{CME}-CL hybrids compared to all other hybrid compositions was the carboxylate anion band, COO^- , at $1,580 \text{ cm}^{-1}$. This band was not present for both the control and the 95S5C_{CME}-CL hybrid, and its intensity increased as the calcium content increased in SiO₂-CaO_{CME}/PTHF/PCL-diCOOH hybrids (90S10C_{CME}-CL, 80S20C_{CME}-CL, 70S30C_{CME}-CL, and 60S40C_{CME}-CL). It is possible that the calcium only remained bonded to the PCL-diCOOH if present in excess and sites for integration into the silica network were saturated. In the hybrid network, PCL-diCOOH will form covalent bonds with GPTMS or act as a chain terminator for THF polymerisation (Tallia et al., 2018); both these reactions will therefore reduce the amount of carboxyl bonds available in the hybrid network, mainly having carbonyl groups characteristic of the ester. It is

**FIGURE 4**

$\text{SiO}_2\text{-CaO}_{\text{CME}}/\text{PTHF}/\text{PCL-diCOOH}$ hybrid scaffolds, with compositions $x\text{SyC}_{\text{CME}}\text{-CL}$ ($x:y$ is the TEOS:CME molar ratio) and control 100S-CL were characterised: (A) true stress versus strain under compression; (B) stress versus strain under cyclic compression (curves shown for 60S40C_{CME}-CL scaffolds); (C) FTIR spectra; (D) Single pulse solid-state ²⁹Si MAS NMR spectra - shaded regions highlight peaks attributed to Tⁿ and Qⁿ species.

TABLE 3 $\text{SiO}_2\text{-CaO}_{\text{CME}}/\text{PTHF}/\text{PCL-diCOOH}$ hybrid scaffolds with composition $x\text{SyC}_{\text{CME}}\text{-CL}$, where $x:y$ is the TEOS:CME molar ratio and control 100S-CL true stress, true strain, toughness modulus and elastic modulus. Mean values \pm standard deviation ($n \geq 3$).

	True stress (MPa)	True strain (%)	Toughness modulus (MPa)	Elastic modulus - 1 Hz - strain 5%–9% (MPa)
60S40C _{CME} -CL	0.38 \pm 0.15	44.9 \pm 14.6	0.11 \pm 0.02	2.14 \pm 0.14
70S30C _{CME} -CL	0.90 \pm 0.23	29.9 \pm 1.9	0.22 \pm 0.04	4.48 \pm 0.29
90S10C _{CME} -CL	0.71 \pm 0.17	30.4 \pm 13.5	0.14 \pm 0.04	3.26 \pm 0.45
95S5C _{CME} -CL	0.33 \pm 0.10	24.8 \pm 16.9	0.10 \pm 0.06	3.54 \pm 0.06
100S-CL	0.36 \pm 0.14	31.3 \pm 9.5	0.06 \pm 0.01	-

hypothesised that the calcium cations could form stabilising complexes with lone pairs on the ester linkages along the PCL backbone as well as any remaining unreacted carboxylate

terminal groups. The carbonyl oxygen has two lone electron pairs and slight excess of negative charge to form a stabilising complex with calcium, oxygen acting as a ligand in the metal

TABLE 4 Chemical shifts from ^{29}Si CP-MAS NMR and percentage abundance from ^{29}Si single-pulse MAS NMR of silicon T and Q species (from GPTMS and TEOS, respectively), and the corresponding degree of condensation (D_c) of the silica network of the $\text{SiO}_2\text{-CaO}_{\text{CME}}/\text{PTHF}/\text{PCL-diCOOH}$ hybrids.

Sample ID	T ²		T ³		Q ¹		Q ²		Q ³		Q ⁴		D _c
	δ_{iso} [ppm]	/	δ_{iso} [ppm]	/	δ_{iso} [ppm]	/	δ_{iso} [ppm]	/	δ_{iso} [ppm]	/	δ_{iso} [ppm]	/	
100S-CL Tallia et al. (2022)	-58.8	3.8	-66.0	14.5	-	-	-	-	-102.5	27.9	-111.5	53.8	91.8
95S5C _{CME} -CL	-57.5	2.5	-65.4	15.2	-	-	-92.4	2.1	-102.0	39.2	-110.7	41.0	88.3
90S10C _{CME} -CL	-57.1	4.3	-65.2	14.2	-	-	-91.3	3.3	-101.4	35.2	-110.1	43.1	88.2
70S30C _{CME} -CL	-58.5	14.4	-66.4	17.1	-	-	-93.3	1.7	-101.8	26.3	-110.6	40.5	87.8
60S40C _{CME} -CL	-57.9	6.0	-65.9	18.3	-82	5.0	-91.9	15.9	-102.0	30.2	-111	24.7	78.9

complex. It could act as a monodentate or bidentate ligand, binding through one or two donor sites (Tallia et al., 2022). This should not affect the C=O band intensity.

The hypothesis is that calcium preferentially bonds to Si-O bonds in the silica network once hydrolysis of the TEOS occurs, and that the CME and TEOS homogenisation step does not result in any interactions between them. When the organic and inorganic solutions are mixed, no hydrolysis of the TEOS has occurred (no water present), so calcium bonds to the PCL-diCOOH via carboxyl or carbonyl interactions. Excess calcium remains unreacted until after the water and acid are added and hydrolysis of TEOS and GPTMS begins, the calcium is then scavenged from the carboxylate complex and as it is free in sol, can enter the silica network, bonding to the Si-O⁻ groups. If excess calcium is still present after, it will stay bonded to PCL-diCOOH, forming stabilising complexes with the lone pairs on the ester linkages and any unreacted carboxylate terminal groups. For the hybrid composition with no or a barely visible carboxylate band (95S5C_{CME}-CL and 90S10C_{CME}-CL hybrids), it can be assumed that all the calcium integrated into the inorganic network.

To confirm calcium entered the silica network, solid state ^{29}Si MAS NMR of the different $\text{SiO}_2\text{-CaO}_{\text{CME}}/\text{PTHF}/\text{PCL-diCOOH}$ hybrid compositions were obtained, comparing them to spectra from the calcium free control, 100S-CL (Tallia et al., 2022). The molecular conditions of silane groups were assessed by measuring the relative quantities of the Qⁿ (TEOS) and T^m (GPTMS) species (Figure 4D) and calculating the D_c (Table 4). Qⁿ values indicate the number (n) of bridging Si-O-Si bonds between silicon atoms, which form the silicate network, with n having a maximum of 4. The Qⁿ values (Table 4) indicate increased incorporation of calcium into the silicate network as CME precursor increased, with % Q⁴ reducing from 54% to 41% as CME was introduced at 5% (95S5C_{CME}-CL). Q³ and Q² also increased. As calcium content was increased to 90S10C_{CME}-CL and 70S30C_{CME}-CL, little change was seen in the Q speciation. However, for 60S40C_{CME}-CL, Q⁴ reduced to 25%, and Q² increased from 2% to 16% and Q¹ units were detected (5%), indicating more calcium incorporation.

The degree of condensation calculation, Equation 1 (Table 4), confirms calcium incorporation into the silicate network. The calcium-free control showed the highest degree of condensation (91.8%), this is due to the absence of calcium as a network modifier. 95S5C_{CME}-CL, 90S10C_{CME}-CL, and 70S30C_{CME}-CL all had a similar degree of condensation, all approximately 4% less than the control. 60S40C_{CME}-CL calcium showed a drop of approximately 10% compared to these compositions. In terms of D_c values, from the carboxylate band in the FTIR spectra (Figure 4C), it seems the additional calcium of the 70S30C_{CME}-CL composition formed stabilising complexes between the lone pairs on the ester linkages and any unreacted carboxylate terminal groups. The degree of condensation of the silica network of the 60S40C_{CME}-CL composition dropped a further 10%, leading to the hypothesis of the lone pairs on the ester linkages and carboxylate terminal groups being saturated, forcing the calcium to further modify the silica network. This also explained the drop in mechanical properties seen in Figure 4A for this composition (Tian et al., 1996). Previous work by Tallia et al. on the calcium-free control, showed a degree of condensation of 91.8% (Tallia et al., 2018). Their 60S40C_{CME}-CL hybrids had a degree of condensation of 84.8% (Tallia et al., 2022),

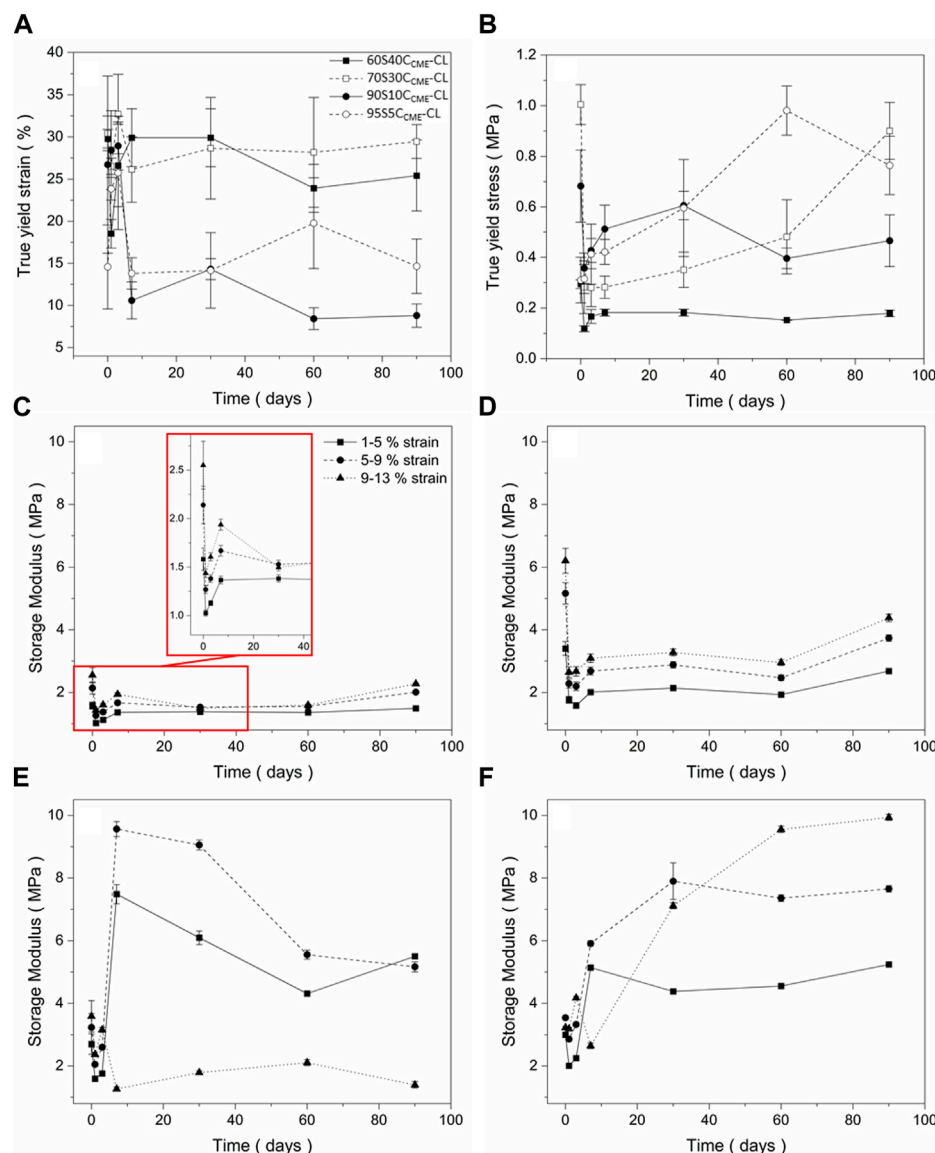


FIGURE 5

Mechanical assessment as a function of degradation, of the $\text{SiO}_2\text{-CaO}_{\text{CME}}/\text{PTHF}/\text{PCL-diCOOH}$ hybrid scaffolds with compositions $x\text{SyC}_{\text{CME-CL}}$, where x:y is the TEOS:CME molar ratio, from compression tests following immersion in simulated body fluid (SBF) for 0, 1, 3, 7, 30, 60, and 90 days: (A) true strain at yield; (B) true stress at yield (C–F) storage modulus values at strain ranges of 1%–5%, 5%–9%, 9%–13% for (C) 60S40CME-CL, (D) 70S30CME-CL, (E) 90S10CME-CL, and (F) 95S5CME-CL. Error bars are standard deviations from the mean values for $n = 4$.

indicating Ca incorporation. The degree of condensation of 60S40CME-CL hybrid in this work (78.9%) was lower due to the reduction in TEOS during synthesis to enable final I:O ratios of all the compositions, to match with the 100S-CL control. The degree of condensation of the silica network agreed with FTIR spectra as the Si-OH stretch at 950 cm^{-1} (Figure 4C) increased as the calcium content in the hybrid increased, significant of a lower degree of condensation, which was expected as calcium acts as a network modifier.

Scaffold mechanical properties during dissolution in SBF

The degradation properties of each composition needed to be investigated before choosing a final composition to assess

osteogenesis abilities. The mechanical properties must be maintained as the scaffold decomposes *in vivo* and the degradation by-product should stimulate HCA formation of the surface of the structure, showing bioactivity. Figures 5A, B show the yield stress and strain of each hybrid scaffold composition, recorded at different times of immersion in SBF.

All compositions underwent an initial drop in yield stress after 24 h. This could be due to the change in condition, from dry to wet testing the scaffolds after immersing in SBF. The 60S40CME-CL and 90S10CME-CL scaffolds did not revert to their original strength and plateau at 0.2 MPa and 0.4 MPa, respectively. The 70S30CME-CL and 95S5CME-CL both showed a gradual increase in strength, with 70S30CME-CL reaching its original value after 90 days immersion and 95S5CME-CL exceeding its dry value, reaching 0.98 MPa after

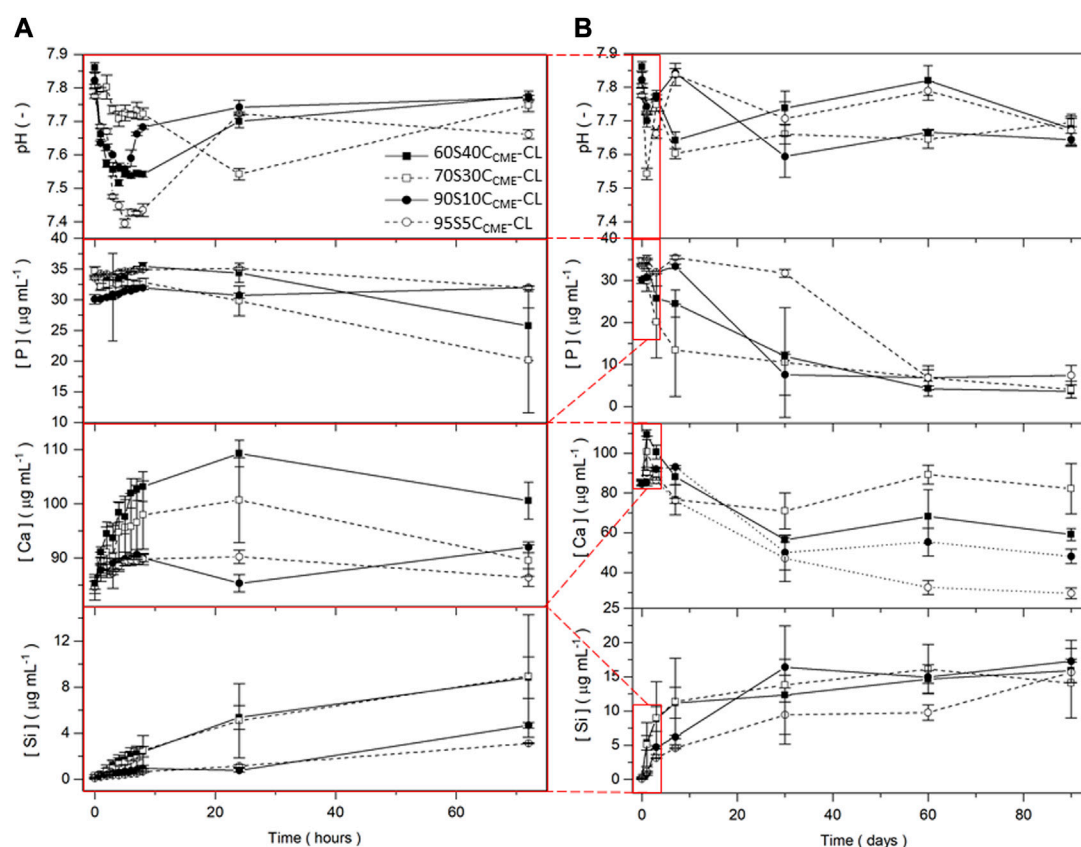


FIGURE 6

pH measurements and silicon, calcium, and phosphorous content in SBF (measured by ICP) for the $\text{SiO}_2\text{-CaO}_{\text{CME}}/\text{PTHF}/\text{PCL-dicOOH}$ hybrid scaffolds with composition $x\text{SyC}_{\text{CME}}\text{-CL}$, where $x:y$ is the TEOS:CME molar ratio, for immersion up to 90 days. Expanded view of the first 72 h including hourly time points for the first 8 h are presented (A) to show details of ion release from the 90 days timeframe (B). Error bars are standard deviations from the mean values for $n = 5$.

60 days of immersion. The yield strain is an important factor to consider, with both $90\text{S}10\text{C}_{\text{CME}}\text{-CL}$ and $95\text{S}5\text{C}_{\text{CME}}\text{-CL}$ dropping to approximately 10%, indicating increase in brittleness, although 10% strain is higher than that sustained by trabecular bone. The $60\text{S}40\text{C}_{\text{CME}}\text{-CL}$ and $70\text{S}30\text{C}_{\text{CME}}\text{-CL}$ scaffolds showed similar strain at yield to their dry values, at approximately 30%. This showed an increased stability from these compositions, when exposed to simulated body conditions. From this behaviour, the $70\text{S}30\text{C}_{\text{CME}}\text{-CL}$ composition was the most consistent when subjected to SBF immersion.

The storage modulus (Figures 5C–F) initially decreased over the first 3 days of immersion, for all compositions at all strain ranges. $60\text{S}40\text{C}_{\text{CME}}\text{-CL}$ and $70\text{S}30\text{C}_{\text{CME}}\text{-CL}$ showed little change in modulus as strain ranges increased. As immersion time increased, storage modulus reached up to 2.3 and 4.4 MPa, respectively. The $90\text{S}10\text{C}_{\text{CME}}\text{-CL}$ scaffolds showed a sharp increase in modulus after 7 days, followed by a reduction, due to the scaffolds breaking during the test. The $95\text{S}5\text{C}_{\text{CME}}\text{-CL}$ showed a less drastic change after 7 days, apart for the 9%–13% strain range as scaffold failure occurred during the test. This showed these two compositions were more unreliable, especially the $90\text{S}10\text{C}_{\text{CME}}\text{-CL}$, breaking at strains within the trabecular bone range, $\leq 7\%$. Values of elastic compressive modulus of trabecular bone ranges from 0.8 to 2.7 GPa (Carter and Spengler, 1978; Keaveny et al., 2004; Gibson and

Ashby, 2014; Mirzaali et al., 2016; Morgan et al., 2018). The $70\text{S}30\text{C}_{\text{CME}}\text{-CL}$ showed the highest initial modulus, whilst ensuring no failure, its value of 6.2 MPa was however not within the range required to mimic bone tissue.

Apatite formation in SBF

To evaluate the *in vitro* bioactivity of these hybrids, the pH variation in SBF was evaluated, as well as the release of silica, calcium, and phosphate ions (Figure 6). As expected, silica release was gradual from the inorganic glass network.

After 7 days immersion in SBF, the $90\text{S}10\text{C}_{\text{CME}}\text{-CL}$ and $95\text{S}5\text{C}_{\text{CME}}\text{-CL}$ compositions released $\sim 5 \mu\text{g mL}^{-1}$ of Si and the $60\text{S}40\text{C}_{\text{CME}}\text{-CL}$ and $70\text{S}30\text{C}_{\text{CME}}\text{-CL}$ compositions released more than $11 \mu\text{g mL}^{-1}$. The calcium disruption of the silica network, seen in the NMR data Table 4, clearly increased silica network dissolution; all compositions plateaued after 30 days. Over the first 8 h, calcium released increased with calcium content in the hybrid, at rates of $\sim 1 \mu\text{g mL}^{-1}$ and $4 \mu\text{g mL}^{-1}$ per hour for the $95\text{S}5\text{C}_{\text{CME}}\text{-CL}$ and $60\text{S}40\text{C}_{\text{CME}}\text{-CL}$ hybrids, respectively. After 24 h, a drop in calcium concentration in the SBF was visible for all scaffold compositions, especially between day 7 and 30, from on average of $90 \mu\text{g mL}^{-1}$ down to $55 \mu\text{g mL}^{-1}$. The $70\text{S}30\text{C}_{\text{CME}}\text{-CL}$ composition dropped to $70 \mu\text{g mL}^{-1}$, increasing back up to $90 \mu\text{g mL}^{-1}$ at day 60.

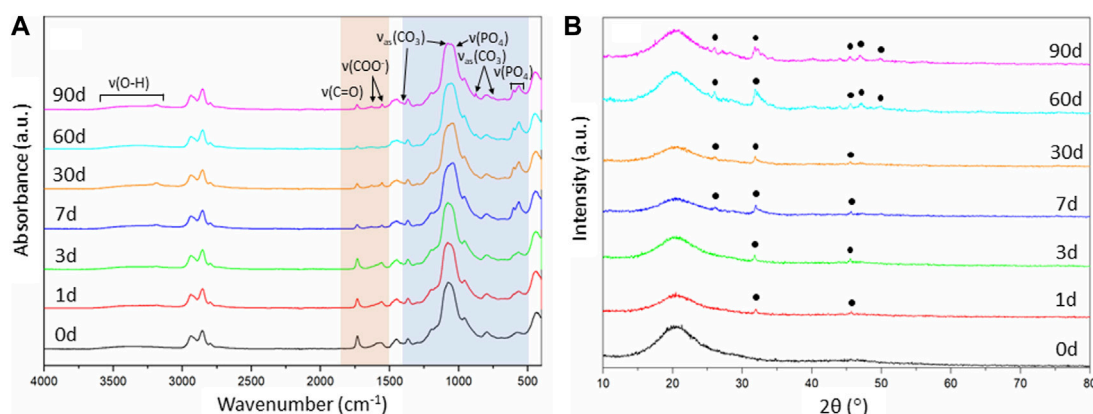


FIGURE 7

Evaluation of the $\text{SiO}_2\text{-CaO}_{\text{CME}}/\text{PTHF}/\text{PCL-diCOOH}$ hybrid scaffolds of composition 70S30C_{CME}-CL after immersion in SBF over 90 days: (A) FTIR spectra, section highlighted in blue is where all bands for calcium phosphate are found, the bands highlighted in orange are the carboxyl and carboxylate bands from the calcium reacting with the polymer; and (B) XRD patterns with annotated peaks characteristic of carbonate-hydroxyapatite (Legeros et al., 1967).

Between 30 and 60 days, the calcium concentration increased for all compositions, apart from 95S5C_{CME}-CL. This early behaviour was mirrored in the phosphate concentration; it was initially stable as no phosphate was released by the hybrid, and when the calcium concentration started to drop between day 1 and 3, so did the phosphate. It decreased fastest for the 70S30C_{CME}-CL hybrid, followed by the 60S40C_{CME}-CL, 90S10C_{CME}-CL and 95S5C_{CME}-CL. The drop in both calcium and phosphate after 3 days confirmed the formation of calcium phosphate, characteristic of hydroxyapatite, as seen in FTIR spectra and XRD patterns of the scaffolds after immersion (Figure 7). This correlated with the white deposit observed on the hybrids at day 3 (Figure 8). The slow increase in calcium after 30 days could be due to the rate of calcium release overtaking the rate of calcium deposition. There seems to be a limit to how much calcium phosphate can form, due to the limited phosphate content.

The pH of SBF fluctuated during the dissolution study (Figure 6), initially increasing as Ca^{2+} from the hybrid was rapidly exchanged by H^+ from the SBF (Tallia et al., 2022) and remained between 7.4 and 7.8 for the duration of the study, which is conducive to HCA formation as OH^- and $(\text{CO}_3)^{2-}$ need to be incorporated into the calcium phosphate layer (Clark et al., 1976; Hench, 1991; Tallia et al., 2022).

As the 70S30C_{CME}-CL hybrid composition was the most promising in terms of mechanical properties as a function of immersion time in SBF and showed a larger drop of calcium and phosphate in SBF, FTIR and XRD were performed to assess this formation (Figure 7).

FTIR spectra of 70S30C_{CME}-CL showed the appearance of a band at around 874 cm^{-1} after 60 days in SBF (Figure 7A). This band corresponded to the formation of carbonate (Rodriguez-Blanco et al., 2011), CO_3^{2-} . A visible shoulder at $1,409\text{ cm}^{-1}$ formed at the same time as the band at 874 cm^{-1} , in accordance with the characteristic bands of HCA (Notingher et al., 2003). P-O bending bands (Salma et al., 2008; Malakauskaite-Petruleviciene et al., 2016) were visible after 7 days, at $550\text{--}600\text{ cm}^{-1}$ which are characteristic of orthophosphate, the phosphate units in HCA. P-O stretch ($1,020\text{--}1,100\text{ cm}^{-1}$) were also

present, indicative of the formation of a crystalline calcium phosphate layer (Lei et al., 2009). This layer was visible on the scaffolds after immersion in SBF (Figure 8) as a white deposit intertwined within the pores. HCA formation was confirmed using XRD. After 60 days immersion in SBF, XRD peaks were found at 26° , $32^\circ\text{--}34^\circ$, 46° , 47° and 49° 2θ (Figure 7B), corresponding to the (002), (211), (112), (222) and (213) reflections of the hydroxyapatite phase (Balamurugan et al., 2006; Lei et al., 2009). Some of the peaks were visible as early as 1 day in SBF. The crystalline HCA peaks were slightly different to those found on bioactive glasses (Lei et al., 2009), indicating that the HCA crystals formed on the hybrid had different preferred growth orientation. These results confirm that the hybrids were able to induce HCA formation after only 1 day in SBF. Peaks increase in intensity the longer the immersion time.

Changes in the FTIR were also observed for the organic part. The carboxyl band reduced with soaking time; $1,730\text{ cm}^{-1}$ due to the degradation of PCL-diCOOH within the hybrid in SBF. The carboxylate band at $1,550\text{ cm}^{-1}$, characteristic of the excess calcium bonded to PCL-diCOOH in 70S30C_{CME}-CL hybrid compositions, also reduced and almost completely disappeared, the ionic bonds breaking faster in solution, releasing the calcium at a faster rate than the covalent bonds between the PCL-diCOOH and GPTMS from the silica network or to the PTHF as a chain terminator. The carboxylate band seemed to be replaced by two very small bands at $1,550$ and $1,625\text{ cm}^{-1}$. The calcium in the SBF could potentially initially ionically bond to PCL-diCOOH free radicals. Two bands could form from the COO^- interacting with different ions, such as calcium, and potentially themselves. A low intensity OH^- ions derived band at 630 cm^{-1} is visible for all compositions, mostly after 3 months in SBF, typical of stoichiometric hydroxyapatite (HA) (Destainville et al., 2003; Salma et al., 2008).

SEM images of the scaffolds showed little difference at low magnification after 3 days of immersion in SBF, but significant HCA formation could be seen after 7 days with the naked eye. At day 3, the scaffold showed a whiter aspect corresponding to HCA formation, which correlated with the HCA peaks being visible under XRD

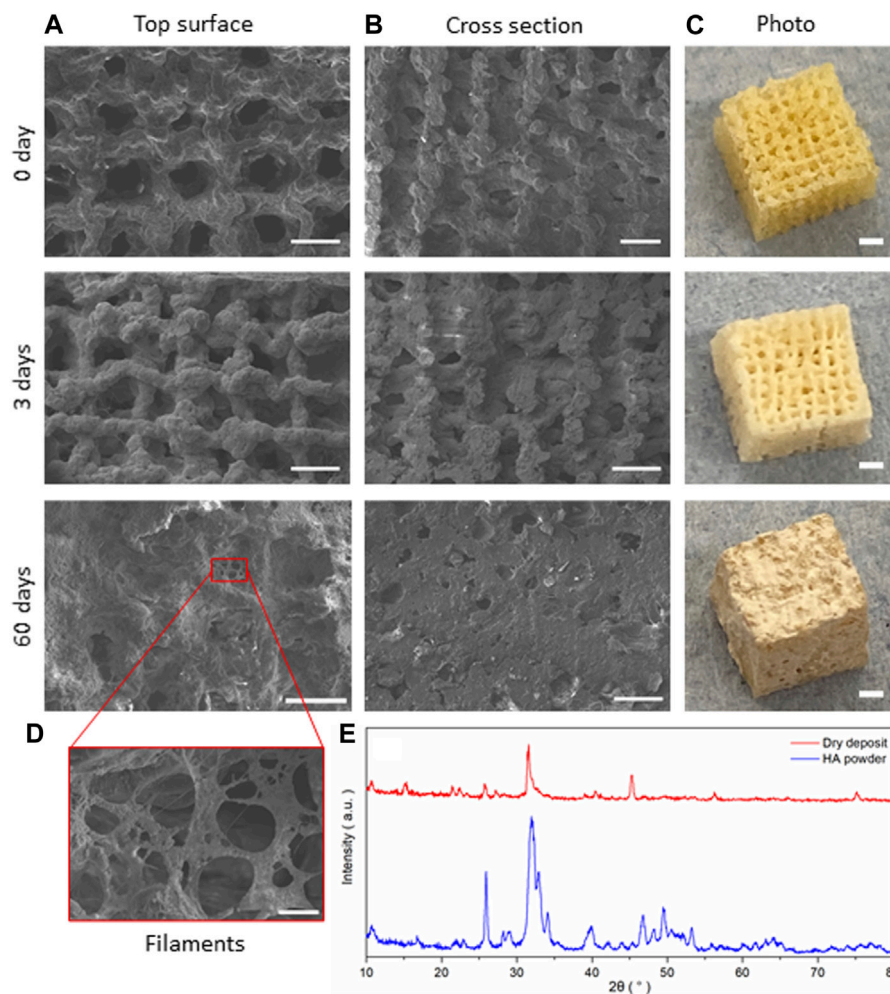


FIGURE 8

SiO₂-CaO_{CME}/PTHF/PCL-diCOOH hybrid scaffolds of composition 70S30C_{CME}-CL after immersion in SBF for 0, 3, and 60 days; SEM micrographs showing (A) the top surface, (B) cross section (scale bar 500 μm), and (C) photographs of the scaffolds (scale bars 2 mm); (D) SEM image of the details of the growth on the scaffolds (scale bar 50 μm); and (E) the XRD patterns comparing the dried deposit from the scaffold to commercial HA powder (Sigma-Aldrich, UK).

(Figure 7B). The deposit densified the longer the scaffold was immersed in SBF, forming filaments and plaques covering the entirety of the scaffold after 60 days (Figure 8), filling in the pores in the cross-section view. A deposit dried after 3 days immersion was investigated with XRD and compared to commercial HA powder (Sigma-Aldrich, UK), showing a close match of the peaks obtained (Figure 8E).

Biological response of human bone marrow stromal cells to hybrids

The performances of implantable biomaterials for bone and orthopaedic applications are determined by their interactions with cells mineralising bone tissues. *In vitro* cytotoxicity tests were performed with 70S30C_{CME}-CL and 90S10C_{CME}-CL conditioned media to assess the effects of ionic release on human bone marrow stromal cell (h-BMSC) health. These two hybrid compositions were chosen as they showed the highest mechanical properties and comparing two calcium contents would help understand its effect

on cell health. Multipotent h-BMSCs are the most suited cells for the initial cytocompatibility assessment as they are the cells responsible for bone regeneration in bone defects. Cell health, as indicator of cytotoxic effects, was assessed in samples prior to and after 24 h exposure to serial dilution of ionic release from hybrids to basal DMEM (CM 0%) or growth medium (GM), Figure 9.

70S30C_{CME}-CL hybrid ionic release did not cause cytotoxic effects in h-BMSCs, with results similar to the basal media. However, 90S10C_{CME}-CL extracts did cause toxicity, unless they were diluted to at least 50%. Live-cell monitoring assessment (15 min framing rate) also confirmed loss of cell adhesion and the presence of apoptosis-like features in monolayers for 90S10C_{CME}-CL extracts at 100% and 75% dilution (Figure 9C). Fluorescence readings in all 70S30C_{CME}-CL conditions remained similar to levels measured in the non-exposed h-BMSCs. A slight but non-significant drop of fluorescence (equivalent to 12%) was noted in the 100% 70S30C_{CME}-CL hybrid extracts. On the contrary, cell health dropped by more than 50% when cells were exposed to higher concentrations 90S10C_{CME}-CL hybrid extracts.

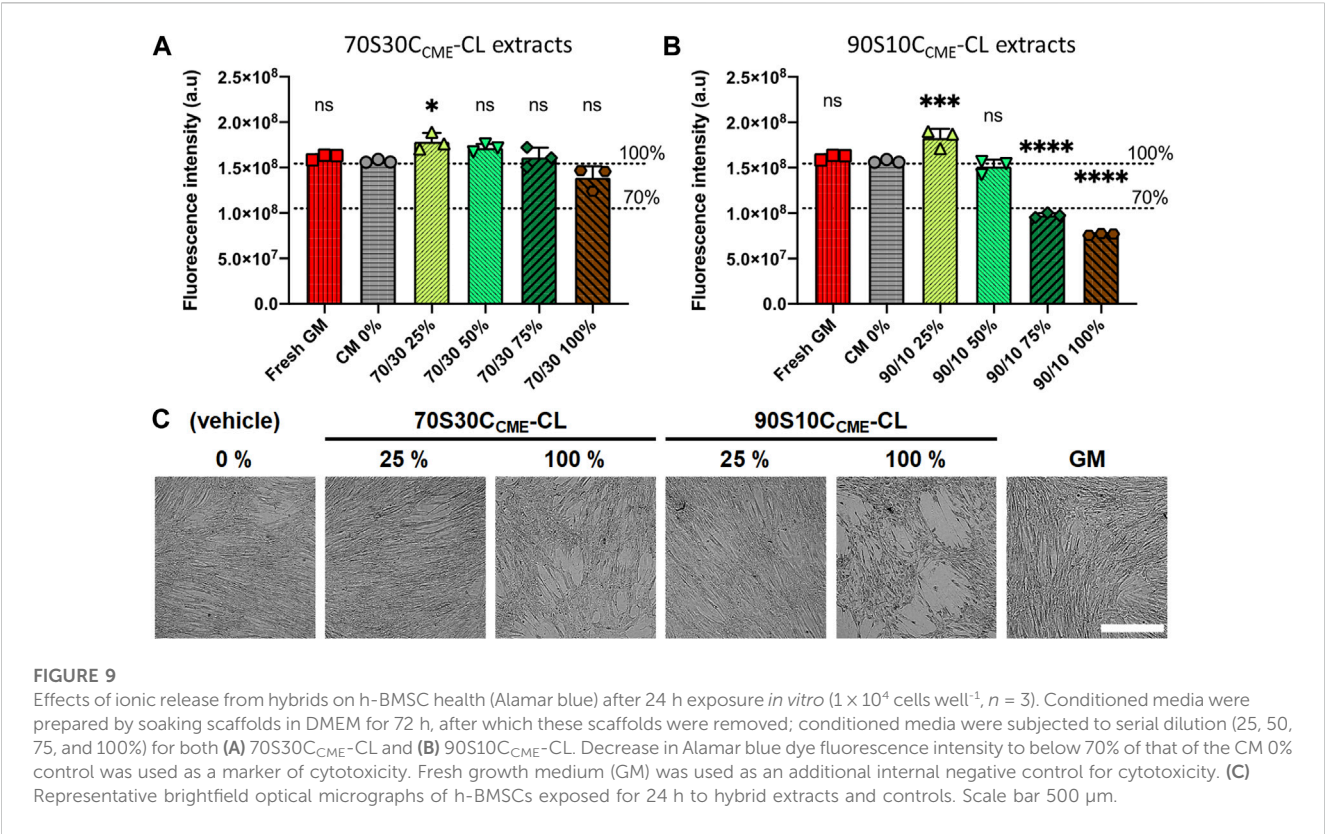


FIGURE 9 Effects of ionic release from hybrids on h-BMSC health (Alamar blue) after 24 h exposure *in vitro* (1×10^4 cells well⁻¹, $n = 3$). Conditioned media were prepared by soaking scaffolds in DMEM for 72 h, after which these scaffolds were removed; conditioned media were subjected to serial dilution (25, 50, 75, and 100%) for both (A) 70S30C_{CME}-CL and (B) 90S10C_{CME}-CL. Decrease in Alamar blue dye fluorescence intensity to below 70% of that of the CM 0% control was used as a marker of cytotoxicity. Fresh growth medium (GM) was used as an additional internal negative control for cytotoxicity. (C) Representative brightfield optical micrographs of h-BMSCs exposed for 24 h to hybrid extracts and controls. Scale bar 500 μ m.

TABLE 5 Elemental concentration of phosphorous, calcium, and silicon content in vehicle medium (VC) after 72 h incubation of 70S30C_{CME}-CL or 90S10C_{CME}-CL hybrid discs (37°C, 5% CO₂) ($n = 3$).

	[P] (μ g mL ⁻¹)	[Ca] (μ g mL ⁻¹)	[Si] (μ g mL ⁻¹)
VC (0%, vehicle)	32.9 \pm 0.3	72.9 \pm 1.3	1.6 \pm 0.4
90S10C _{CME} -CL	32.4 \pm 0.6	82.3 \pm 3.2	26.5 \pm 2.9
70S30C _{CME} -CL	1.2 \pm 0.4	187.3 \pm 12.5	70 \pm 3.1

Prior to using the extracts, ICP analysis of the media showed calcium ions in 70S30C_{CME}-CL extracts were over double the concentration of that of the media conditioned with 90S10C_{CME}-CL discs (Table 5). The media conditioned with the 90S10C_{CME}-CL hybrid had a calcium content < 10 μ g mL⁻¹, less than the control media. Media conditioned with 70S30C_{CME}-CL also showed a reduction in phosphate, from 32.9 \pm 0.3 μ g mL⁻¹ before incubation to 1.2 \pm 0.4 μ g mL⁻¹ after soaking for 72 h in vehicle. A drop of phosphate concentration associated to high levels of soluble calcium ions strongly suggests the early formation of calcium phosphate during incubation (Figure 6). Calcium is a pivotal signalling messenger to a myriad of cellular functions, from cell growth to differentiation to cell death (Viti et al., 2016). HA possesses osteoconductive properties (Khotib et al., 2021). In the 90S10C_{CME}-CL hybrid composition, however, the phosphate concentration stayed equal to the vehicle baseline levels. Silica concentration in solution was minimal for the control; the 90S10C_{CME}-CL composition showed a release of 26.5 \pm 2.9 μ g mL⁻¹ and the 70S30C_{CME}-CL, 70.0 \pm 3.1 μ g mL⁻¹. Calcium acts as a network modifier and disrupts the glass network, making it more

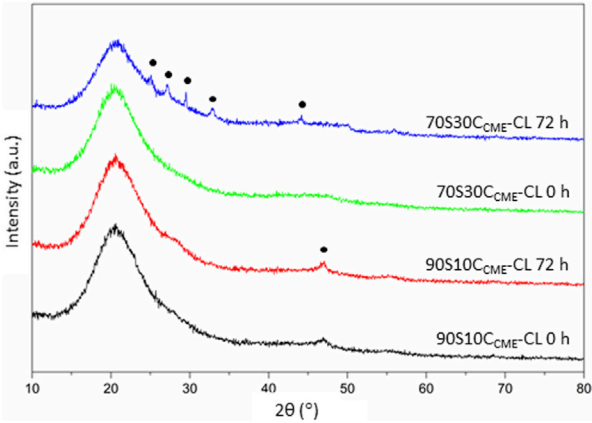


FIGURE 10 XRD patterns of the 90S10C_{CME}-CL and 70S30C_{CME}-CL hybrids before (0 h) and after 72 h incubation in serum-free DMEM. Annotated peaks characteristic of carbonate-hydroxyapatite (Legeros et al., 1967).

susceptible to dissolution for hybrids with higher calcium content. The release in both hybrids was higher than expected as, when incubated in SBF for 72 h, the 70S30C_{CME}-CL composition had a Si concentration of $\sim 9 \mu$ g mL⁻¹. The discrepancies between the *in vitro* cell and SBF ICP results are explained by different volume to weight ratios used during incubation. A typical ratio of 1.5 mg mL⁻¹ hybrid disc to buffer (Jones et al., 2001) was used in the hybrid scaffold SBF studies, whereas extraction ratios followed

the $3 \text{ cm}^2 \text{ mL}^{-1}$ ISO guideline for 1 mm thick discs (equiv. 150 mg mL^{-1}) in the *in vitro* cytotoxicity (ISO 10993-12: 2021 Biological evaluation of medical devices—Part 12: Sample preparation and reference materials, 2021). The increased concentration explains the higher ion concentration, minimised by the fact that scaffolds show a higher surface area than discs. The higher release of calcium ions from 70S30C_{CME}-CL hybrids facilitated the formation of calcium phosphate, a major component of HCA.

XRD analyses performed on discs after incubation confirmed the presence of phosphate and calcium in the form of HCA on the 70S30C_{CME}-CL hybrids (Figure 10). The XRD patterns showed similar peak pattern than that recorded in the SBF studies on the 70S30C_{CME}-CL hybrids (Figure 8). HA stimulates osteoblastic differentiation by increasing the expression of osteogenic transcription factors. However, the intracellular mechanisms involved are not fully understood yet (Khotib et al., 2021). Further studies should be focused on the 70S30C_{CME}-CL hybrid composition, as it showed the best mechanical properties, HCA formation after 72 h when incubated in DMEM, and had a relative cell viability of 88% when h-BMSCs were exposed to this 100% extract serial dilution.

Further research is required to investigate how 70S30C_{CME}-CL hybrid extract does not affect cell survival and growth in more complex *in vitro* models and to determine whether long-term contact to 70S30C_{CME}-CL substrate is sufficient in inducing osteogenesis exists. Similarly, future work is warranted to investigate whether other key osteogenic genes are upregulated at later time points and indeed whether h-BMSCs exhibit physical characteristics of osteoblasts at these later times.

Conclusion

SiO₂-CaO_{CME}/PTHF/PCL-diCOOH hybrids of composition 60S40C_{CME}-CL, 70S30C_{CME}-CL, 90S10C_{CME}-CL, and 95S5C_{CME}-CL were successfully synthesised, printed with pore channels of $> 400 \mu\text{m}$, and characterised. The 70S30C_{CME}-CL composition reached the highest yield strength ($0.90 \pm 0.23 \text{ MPa}$), toughness modulus ($0.22 \pm 0.04 \text{ MPa}$), and storage modulus ($4.48 \pm 0.29 \text{ MPa}$). The mechanical properties and bioactivity of these hybrids were assessed in SBF up to 90 days. This confirmed the formation of HCA within all hybrid scaffolds that contained calcium in their composition. Increasing the calcium content produced faster HCA formation and strength up to a threshold of 70S30C_{CME}-CL; at higher calcium content (60S40C_{CME}-CL), the printability and strength of the hybrid reduced. At lower calcium contents, the hybrid was more brittle and took longer to fully form HCA, e.g., the 90S10C_{CME}-CL and 95S5C_{CME}-CL hybrid. The serial dilution of the 70S30C_{CME}-CL extracts after dissolution in DMEM for 72 h showed a cell health not dropping below 100% for dilutions to 25, 50, and 75%. Cell health dropped by 10% relative to the non-exposed cells for the undiluted media. Apatite formation occurred on 70S30C_{CME}-CL after only 72 h of incubation in DMEM. The 70S30C_{CME}-CL hybrid composition also showed the best mechanical properties during degradation of 90 days, having a stable yield stress of 30% when submerged in SBF, not showing any sudden brittleness. Its yield stress was almost double that of the

60S40C_{CME}-CL and 95S5C_{CME}-CL compositions, which dropped when submerged, and steadily recovered over 90 days. The 70S30C_{CME}-CL printed with final strut size of $100 \mu\text{m}$ and pores of $400\text{--}500 \mu\text{m}$ did not reach mechanical values close to trabecular bone. Optimisation is necessary with work ongoing using different calcium sources and altering the final implant structure and chemical composition, utilising this optimised calcium content.

Data availability statement

The raw data supporting the conclusion of this article will be made available by the authors, without undue reservation.

Ethics statement

Ethical approval was not required for the studies on humans in accordance with the local legislation and institutional requirements because only commercially available established cell lines were used.

Author contributions

AH, FT, H-KT, and JJ developed experimental protocols and designed the experiments. AH produced all the samples used in the experiment, conducted experiments, analysed and interpreted the data. AT conducted experiments and analysed data. JL and PL conducted the micro CT experiments, analysed and interpreted the results. HP and JH conducted the solid-state NMR experiments, analysed and interpreted the results. DS and SR conducted the *in vitro* cell experiments analysed and interpreted the results. JJ, PL, JH, and SR obtained funding and supervised the project. AH and JJ wrote the manuscript. All authors contributed to the article and approved the submitted version.

Acknowledgments

The authors acknowledge the EPSRC (EP/M019950/1, EP/N025059/1, EP/S025782/1 and IAA EP/X52556X/1) and National Institute for Health Global Health Research (grant number 1613745: NIHR Group on POsT Conflict Trauma in Sri Lanka; ProTeCT). JH acknowledges financial support for the solid state NMR instrumentation at Warwick used in this research which was funded by EPSRC (grants EP/M028186/1 and EP/K024418/1), the University of Warwick, and the Birmingham Science City AM1 and AM2 projects, which, in turn, were supported by Advantage West Midlands (AWM) and the European Regional Development Fund (ERDF). Raw data can be obtained from rdm-enquiries@imperial.ac.uk.

Conflict of interest

The authors declare that the research was conducted in the absence of any commercial or financial relationships that could be construed as a potential conflict of interest.

Publisher's note

All claims expressed in this article are solely those of the authors and do not necessarily represent those of their affiliated

References

- Aspden, R. M. (2004). Mechanical testing of bone *ex vivo*. *Methods Mol. Med.* 80, 369–380.
- Atwood, R. C., Jones, J. R., Lee, P. D., and Hench, L. L. (2004). Analysis of pore interconnectivity in bioactive glass foams using X-ray microtomography. *Scr. Mater* 51, 1029–1033. doi:10.1016/j.scriptamat.2004.08.014
- Baino, F., and Vitale-Brovarone, C. (2011). Three-dimensional glass-derived scaffolds for bone tissue engineering: current trends and forecasts for the future. *J. Biomed. Mater. Res. A* 97 A, 514–535. doi:10.1002/jbm.a.33072
- Balamurugan, A., Sockalingum, G., Michel, J., Fauré, J., Banchet, V., Wortham, L., et al. (2006). Synthesis and characterisation of sol gel derived bioactive glass for biomedical applications. *Mater. Lett.* 60, 3752–3757. doi:10.1016/j.matlet.2006.03.102
- Calori, G. M., Mazza, E., Colombo, M., Ripamonti, C., and Tagliabue, L. (2011). Treatment of long bone non-unions with polytherapy: indications and clinical results. *Injury* 42, 587–590. doi:10.1016/j.injury.2011.03.046
- Cantournet, S., Desmorat, R., and Besson, J. (2009). Mullins effect and cyclic stress softening of filled elastomers by internal sliding and friction thermodynamics model. *Int. J. Solids Struct.* 46, 2255–2264. doi:10.1016/j.ijsolstr.2008.12.025
- Carter, D. R., and Spengler, D. M. (1978). Mechanical properties and composition of cortical bone. *Clin. Orthop. Relat. Res.* 135, 192–217. doi:10.1097/00003086-197809000-00041
- Clark, A. E., Pantano, C. G., and Hench, L. L. (1976). Auger spectroscopic analysis of Bioglass corrosion films. *J. Am. Ceram. Soc.* 59, 37–39. doi:10.1111/j.1151-2916.1976.tb09382.x
- Connell, L. S., Romer, F., Suárez, M., Valliant, E. M., Zhang, Z., Lee, P. D., et al. (2014). Chemical characterisation and fabrication of chitosan-silica hybrid scaffolds with 3-glycidoxypentyl trimethoxysilane. *J. Mater. Chem. B* 2, 668–680. doi:10.1039/c3tb21507e
- Destainville, A., Champion, E., Bernache-Assollant, D., and Laborde, E. (2003). Synthesis, characterization and thermal behavior of apatitic tricalcium phosphate. *Mater. Chem. Phys.* 80, 269–277. doi:10.1016/s0254-0584(02)00466-2
- Dieudonné, X., Montouillout, V., Jallot, E., Fayon, F., and Lao, J. (2014). Bioactive glass hybrids: a simple route towards the gelatin-SiO₂-CaO system. *Chem. Commun.* 50, 8701–8704. doi:10.1039/c3cc49113g
- Doube, M., Klosowski, M. M., Arganda-Carreras, I., Cordelières, F. P., Dougherty, R. P., Jackson, J. S., et al. (2010). Bone: free and extensible bone image analysis in ImageJ. *Bone* 47, 1076–1079. doi:10.1016/j.bone.2010.08.023
- Gibson, L. J., and Ashby, M. F. (2014). *Cellular solids: Structure and properties*. second edition. Cambridge University Press. Cellular solids: structure and properties.
- Harris, R. K., Becker, E. D., de Menezes, S. M. C., Goodfellow, R., and Granger, P. (2002). NMR nomenclature: nuclear spin properties and conventions for chemical shifts. *Solid State Nucl. Magn. Reson.* 22, 458–483. doi:10.1006/ssnmr.2002.0063
- Hench, L. L. (1991). Bioceramics: from concept to clinic. *J. Am. Ceram. Soc.* 74, 1487–1510. doi:10.1111/j.1151-2916.1991.tb07132.x
- ISO 10993-12:2021 Biological evaluation of medical devices — Part 12: Sample preparation and reference materials. (2021).
- Jones, J. R., Atwood, R. C., Poologasundarapillai, G., Yue, S., and Lee, P. D. (2009). Quantifying the 3D macrostructure of tissue scaffolds. *J. Mater. Sci. Mater. Med.* 20, 463–471. doi:10.1007/s10856-008-3597-9
- Jones, J. R., Ehrenfried, L. M., and Hench, L. L. (2006a). Optimising bioactive glass scaffolds for bone tissue engineering. *Biomaterials* 27, 964–973. doi:10.1016/j.biomaterials.2005.07.017
- Jones, J. R., Lee, P. D., and Hench, L. L. (2006b). Hierarchical porous materials for tissue engineering. *Philosophical Trans. R. Soc. A Math. Phys. Eng. Sci.* 364, 263–281. doi:10.1098/rsta.2005.1689
- Jones, J. R. (2013). Review of bioactive glass: from Hench to hybrids. *Acta Biomater.* 9, 4457–4486. doi:10.1016/j.actbio.2012.08.023
- Jones, J. R., Sepulveda, P., and Hench, L. L. (2001). Dose-dependent behavior of bioactive glass dissolution. *J. Biomed. Mater. Res.* 58, 720–726. doi:10.1002/jbm.10053
- Keaveny, T. M., Morgan, E. F., and Yeh, O. C. (2004). *Bone mechanics*.
- Khotib, J., Gani, M. A., Budiati, A. S., Lestari, M. L. A. D., Rahadiansyah, E., and Ardianto, C. (2021). Signaling pathway and transcriptional regulation in osteoblasts during bone healing: direct involvement of hydroxyapatite as a biomaterial. *Pharmaceuticals* 14, 615. doi:10.3390/ph14070615
- Khusainov, R., Azzi, D., Achumba, I. E., and Bersch, S. D. (2013). Real-time human ambulation, activity, and physiological monitoring: taxonomy of issues, techniques, applications, challenges and limitations. *Sensors* 13, 12852–12902. doi:10.3390/s131012852
- Koons, G. L., Diba, M., and Mikos, A. G. (2020). Materials design for bone-tissue engineering. *Nat. Rev. Mater.* 5, 584–603. doi:10.1038/s41578-020-0204-2
- Lao, J., Dieudonné, X., Fayon, F., Montouillout, V., and Jallot, E. (2016). Bioactive glass-gelatin hybrids: building scaffolds with enhanced calcium incorporation and controlled porosity for bone regeneration. *J. Mater. Chem. B* 4, 2486–2497. doi:10.1039/c5tb02345a
- Lasanianos, N. G., Kanakaris, N. K., and Giannoudis, P. V. (2010). Current management of long bone large segmental defects. *Orthop. Trauma* 24, 149–163. doi:10.1016/j.mprth.2009.10.003
- Legeros, R. Z., Trautz, O. R., Legeros, E. K., and Shirra, W. P. (1967). Apatite crystallites: effects of carbonate on morphology. *Science* 155, 1409–1411. doi:10.1126/science.155.3768.1409
- Lei, B., Chen, X., Wang, Y., Zhao, N., Du, C., and Fang, L. (2009). Synthesis and bioactive properties of macroporous nanoscale SiO₂-CaO-P₂O₅ bioactive glass. *J. Non Cryst. Solids* 355, 2678–2681. doi:10.1016/j.jnoncrysol.2009.09.029
- Li, A., Shen, H., Ren, H., Wang, C., Wu, D., Martin, R. A., et al. (2015). Bioactive organic/inorganic hybrids with improved mechanical performance. *J. Mater. Chem. B* 3, 1379–1390. doi:10.1039/c4tb01776e
- Li, S., Tallia, F., Mohammed, A. A., Stevens, M. M., and Jones, J. R. (2020). Scaffold channel size influences stem cell differentiation pathway in 3-D printed silica hybrid scaffolds for cartilage regeneration. *Biomater. Sci.* 8, 4458–4466. doi:10.1039/c9bm01829h
- Lin, S., Ionescu, C., Pike, K. J., Smith, M. E., and Jones, J. R. (2009). Nanostructure evolution and calcium distribution in sol-gel derived bioactive glass. *J. Mater. Chem.* 19, 1276–1282. doi:10.1039/b814292k
- Maçon, A. L. B., Kim, T. B., Valliant, E. M., Goetschius, K., Brow, R. K., Day, D. E., et al. (2015). A unified *in vitro* evaluation for apatite-forming ability of bioactive glasses and their variants. *J. Mater. Sci. Mater. Med.* 26, 115–210. doi:10.1007/s10856-015-5403-9
- Mahony, O., Tsigkou, O., Ionescu, C., Minelli, C., Ling, L., Hanly, R., et al. (2010). Silica-gelatin hybrids with tailorable degradation and mechanical properties for tissue regeneration. *Adv. Funct. Mater.* 20, 3835–3845. doi:10.1002/adfm.201000838
- Malakauskaite-Petrukeviciene, M., Stankeviciute, Z., Niaura, G., Garskaite, E., Beganskiene, A., and Kareiva, A. (2016). Characterization of sol-gel processing of calcium phosphate thin films on silicon substrate by FTIR spectroscopy. *Vib. Spectrosc.* 85, 16–21. doi:10.1016/j.vibspec.2016.03.023
- Masquelet, A., Kanakaris, N. K., Obert, L., Stafford, P., and Giannoudis, P. V. (2019). Bone repair using the masquelet technique. *J. Bone Jt. Surg. - Am.* 101, 1024–1036. doi:10.2106/jbjs.18.00842
- Midha, S., Kim, T. B., van den Bergh, W., Lee, P. D., Jones, J. R., and Mitchell, C. A. (2013). Preconditioned 70S30C bioactive glass foams promote osteogenesis *in vivo*. *Acta Biomater.* 9, 9169–9182. doi:10.1016/j.actbio.2013.07.014
- Mirzaali, M. J., Schwiedrzik, J. J., Thaiwichai, S., Best, J. P., Michler, J., Zysset, P. K., et al. (2016). Mechanical properties of cortical bone and their relationships with age, gender, composition and microindentation properties in the elderly. *Bone* 93, 196–211. doi:10.1016/j.bone.2015.11.018
- Morgan, E. F., Unnikrisnan, G. U., and Hussein, A. I. (2018). Bone mechanical properties in healthy and diseased states. *Annu. Rev. Biomed. Eng.* 20, 119–143. doi:10.1146/annurev-bioeng-062117-121139
- Nottingham, L., Jones, J. R., Verrier, S., Bisson, I., Embanga, P., Edwards, P., et al. (2003). Application of FTIR and Raman spectroscopy to characterisation of bioactive materials and living cells. *Spectroscopy* 17, 275–288. doi:10.1155/2003/893584
- Oonishi, H., Hench, L. L., Wilson, J., Sugihara, F., Tsuji, E., Matsuura, M., et al. (2000). Quantitative comparison of bone growth behavior in granules of Bioglass, A-W glass-ceramic, and hydroxyapatite. *J. Biomed. Mater. Res.* 51, 37–46. doi:10.1002/(sici)1097-4636(200007)51:1<37::aid-jbm6>3.0.co;2-t
- Pickup, D. M., Valappil, S. P., Moss, R. M., Twyman, H. L., Guerry, P., Smith, M. E., et al. (2009). Preparation, structural characterisation and antibacterial properties of Ga-doped sol-gel phosphate-based glass. *J. Mater. Sci.* 44, 1858–1867. doi:10.1007/s10853-008-3237-2

- Poologasundarampillai, G., Ionescu, C., Tsigkou, O., Murugesan, M., Hill, R. G., Stevens, M. M., et al. (2010). Synthesis of bioactive class II poly(γ -glutamic acid)/silica hybrids for bone regeneration. *J. Mater. Chem.* 20, 8952. doi:10.1039/c0jm00930j
- Poologasundarampillai, G., Lee, P. D., Lam, C., Kourkouta, A. M., and Jones, J. R. (2016). Compressive strength of bioactive sol-gel glass foam scaffolds. *Int. J. Appl. Glass Sci.* 7, 229–237. doi:10.1111/ijag.12211
- Poologasundarampillai, G., Tsigkou, O., Wang, D., Romer, F., Bhakhri, V., et al. (2014). Poly(γ -glutamic acid)/silica hybrids with calcium incorporated in the silica network by use of a calcium alkoxide precursor. *Chem. - A Eur. J.* 20, 8149–8160. doi:10.1002/chem.201304013
- Rámila, A., Balas, F., and Vallet-Regí, M. (2002). Synthesis routes for bioactive sol-gel glasses: alkoxides versus nitrates. *Chem. Mater.* 14, 542–548. doi:10.1021/cm0110876
- Rhee, S. H. (2004). Bone-like apatite-forming ability and mechanical properties of poly(ϵ -caprolactone)/silica hybrid as a function of poly(ϵ -caprolactone) content. *Biomaterials* 25, 1167–1175. doi:10.1016/j.biomaterials.2003.08.004
- Rhee, S. H., Choi, J. Y., and Kim, H. M. (2002). Preparation of a bioactive and degradable poly(ϵ -caprolactone)/silica hybrid through a sol-gel method. *Biomaterials* 23, 4915–4921. doi:10.1016/s0142-9612(02)00251-x
- Roddy, E., DeBaun, M. R., Daoud-Gray, A., Yang, Y. P., and Gardner, M. J. (2018). Treatment of critical-sized bone defects: clinical and tissue engineering perspectives. *Eur. J. Orthop. Surg. Traumatology* 28, 351–362. doi:10.1007/s00590-017-2063-0
- Rodriguez-Blanco, J. D., Shaw, S., and Benning, L. G. (2011). The kinetics and mechanisms of amorphous calcium carbonate (ACC) crystallization to calcite, via vaterite. *Nanoscale* 3, 265–271. doi:10.1039/c0nr00589d
- Salma, K., Borodajenko, N., Plata, A., Berzina-Cimdina, L., and Stunda, A. (2008). Fourier Transform infrared spectra of technologically modified calcium phosphates. *IFMBE Proc.* 20, 68–71.
- Sang, T., Ting, H. K., Stevens, M. M., Becer, C. R., and Jones, J. R. (2018). Hybrids of Silica/Poly(caprolactone coglycidoxypopyl trimethoxysilane) as Biomaterials. *Chem. Mater.* 30, 3743–3751. doi:10.1021/acs.chemmater.8b00751
- Tallia, F., Russo, L., Li, S., Orrin, A. L. H., Shi, X., Chen, S., et al. (2018). Bouncing and 3D printable hybrids with self-healing properties. *Mater. Horiz.* 5, 849–860. doi:10.1039/c8mh00027a
- Tallia, F., Ting, H. K., Page, S. J., Clark, J. P., Li, S., Sang, T., et al. (2022). Bioactive, degradable and tough hybrids through calcium and phosphate incorporation. *Front. Mater.* 9. doi:10.3389/fmats.2022.901196
- Tian, D., Blacher, S., Dubois, P., and Jérôme, R. (1998). Biodegradable and biocompatible inorganic-organic hybrid materials: 2. Dynamic mechanical properties, structure and morphology. *Polym. Guildf.* 39, 855–864. doi:10.1016/s0032-3861(97)00343-1
- Tian, D., Dubois, P., and Jerome, R. (1996). A new poly(ϵ -caprolactone) containing hybrid ceramer prepared by the sol-gel process. *Polym. Guildf.* 37, 3983–3987. doi:10.1016/0032-3861(96)00199-1
- Tian, D., Dubois, P., and Jérôme, R. (1997). Biodegradable and biocompatible inorganic-organic hybrid materials. I. Synthesis and characterization. *J. Polym. Sci. A Polym. Chem.* 35, 2295–2309. doi:10.1002/(sici)1099-0518(199708)35:11<2295::aid-pola21>3.0.co;2-8
- Valliant, E. M., and Jones, J. R. (2011). Softening bioactive glass for bone regeneration: sol-gel hybrid materials. *Soft Matter* 7, 5083–5095. doi:10.1039/c0sm01348j
- Viti, F., Landini, M., Mezzelani, A., Petecchia, L., Milanese, L., and Scaglione, S. (2016). Osteogenic differentiation of MSC through calcium signaling activation: transcriptomics and functional analysis. *PLoS One* 11, e0148173. doi:10.1371/journal.pone.0148173
- Wei, S., Ma, J. X., Xu, L., Gu, X. S., and Ma, X. L. (2020). Biodegradable materials for bone defect repair. *Mil. Med. Res.* 7, 54. doi:10.1186/s40779-020-00280-6
- Xynos, I. D., Edgar, A. J., Buttery, L. D., Hench, L. L., and Polak, J. M. (2001). Gene-expression profiling of human osteoblasts following treatment with the ionic products of Bioglass 45S5 dissolution. *J. Biomed. Mater. Res.* 55, 151–157. doi:10.1002/1097-4636(200105)55:2<151::aid-jbm1001>3.0.co;2-d
- Yu, B., Turdean-Ionescu, C. A., Martin, R. A., Newport, R. J., Hanna, J. V., Smith, M. E., et al. (2012). Effect of calcium source on structure and properties of sol-gel derived bioactive glasses. *Langmuir* 28, 17465–17476. doi:10.1021/la303768b
- Yue, S., Lee, P. D., Poologasundarampillai, G., and Jones, J. R. (2011). Evaluation of 3-D bioactive glass scaffolds dissolution in a perfusion flow system with X-ray microtomography. *Acta Biomater.* 7, 2637–2643. doi:10.1016/j.actbio.2011.02.009
- Yue, S., Lee, P. D., Poologasundarampillai, G., Yao, Z., Rockett, P., Devlin, A. H., et al. (2010). Synchrotron X-ray microtomography for assessment of bone tissue scaffolds. *J. Mater. Sci. Mater. Med.* 21, 21 847–853. doi:10.1007/s10856-009-3888-9

Frontiers in Bioengineering and Biotechnology

Accelerates the development of therapies,
devices, and technologies to improve our lives

A multidisciplinary journal that accelerates the
development of biological therapies, devices,
processes and technologies to improve our lives
by bridging the gap between discoveries and their
application.

Discover the latest Research Topics

[See more →](#)

Frontiers

Avenue du Tribunal-Fédéral 34
1005 Lausanne, Switzerland
frontiersin.org

Contact us

+41 (0)21 510 17 00
frontiersin.org/about/contact



Frontiers in
Bioengineering
and Biotechnology

